EIGHTH INTERNATIONAL SYMPOSIUM ON APPLICATIONS OF LASER TECHNIQUES TO FLUID MECHANICS

VOLUME I

DISTRIBUTION STATEMENT A
Approved for public release

19970516 051

July 8th to 11th 1996
Lisbon, Portugal

DTIC QUALITY INSPECTED 1

EIGHTH INTERNATIONAL SYMPOSIUM ON APPLICATIONS OF LASER TECHNIQUES TO FLUID MECHANICS

VOLUME I

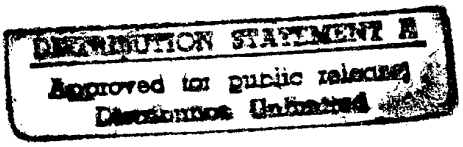

July 8 - 11, 1996

Lisbon, Portugal

PREFACE

The proceedings volumes I and II comprised the papers that were accepted for presentation at the ***Eighth International Symposium on Applications of Laser Techniques to Fluids Mechanics***, which was held at The Calouste Gulbenkian in Lisbon, during the period of July 8 to 11, 1996. The prime objective of this Eighth Symposium is to provide a forum for the presentation of the most advanced research on laser techniques for flow measurements, and reveal significant results to fluid mechanics. The applications of laser techniques to scientific and engineering fluid flow research is emphasised, but contributions to the theory and practice of laser methods are also considered where they facilitate new improved fluid mechanic research. Attention is focused on laser-Doppler anemometry, particle sizing and other methods for the measurement of velocity and scalars, such as particle image velocimetry and laser induced fluorescence.

The papers comprising the formal record of the meeting were selected following high standard reviews, by members of the Advisory Committee, from approximately 300 extended abstracts submitted for presentation at this meeting.

Volume I comprises the papers to be presented during the first and second Days of the Symposium, namely July 8 and 9, while Volume II includes the papers of the following days, Wednesday, July 10, and Thursday, July 11.

We would like to take this opportunity to thank those who assisted us. The assistance provided by the Advisory Committee is highly appreciated. We are highly indebted for the financial support provided by the Sponsoring Organisations that made this Symposium possible. Many thanks are also due to the Secretariat of the Symposium, Graça Pereira, Carlos Carvalho, Anabela Almeida, Luisa Martins and Ana Nunes.

THE ORGANIZING COMMITTEE

ORGANIZING COMMITTEE

- **Ronald J. Adrian**
  Department of Theoretical and Applied Mechanics
  University of Illinois at Urbana - Champaign
  Urbana, Illinois 61801
  USA

- **Diamantino F. G. Durão**
  Department of Mechanical Engineering
  Instituto Superior Técnico
  Av. Rovisco Pais
  1096 Lisboa Codex
  PORTUGAL

- **Franz Durst**
  Lehrstuhl für Strömungsmechanik
  Erlangen Universität - Nurenberg
  Egerlandstraße 13
  D-8520 Erlangen
  GERMANY

- **Manuel V. Heitor**
  Department of Mechanical Engineering
  Instituto Superior Técnico
  Av. Rovisco Pais
  1096 Lisboa Codex
  PORTUGAL

- **Masanobu Maeda**
  Department of Mechanical Engineering
  Keio University
  1-14-1 Hioshi, Kohuku
  Yokohama 223
  JAPAN

- **James H. Whitelaw**
  Imperial College of Science, Technology and Medicine
  Department of Mechanical Engineering
  Exhibition Road
  London SW7 2BX
  England, United Kingdom

ADVISORY COMMITTEE

R. A. Antonia
C. Arcoumanis
W. D. Bachalo
A. Boutier
C. H. CAspersen
A. Coghe
W. J. A. Dahm
D. Dopheide
H. Eickhoff
M. Escudier
A. F. Falcão
L. Fingerson
M. Gharib
G. Gouesbet
I. Grant
J. A. C. Humphrey
D. A. Jackson
R. Karlsson
K. Ishida
J. Kompenhans
L. Lading
B. Lehmann
A. Leipertz
A. Melling
W. Merzkirch
J. F. Meyers
R. H. Miles
E. A. Müller
T. Nakajima
N. Nakatani
A. Naqwi
K. Ohba
T. Obokata
J. C. Pereira
H. J. Pfeifer
F. Pinho
M. L. Riethmüller
D. Rockwell
X. Shen
R. L. Simpson
R. N. Syred
A. M. K. P. Taylor
E. P. Tomasini
C. Tropea
J. T. Turner
J. E. S. Venart
P. O. Witze
G. Wigley
M. Yanneskis

SPONSORING ORGANISATIONS

- Caixa Geral de Depósitos
- DHL
- Direcção Geral de Turismo
- European Commission
- European Research Office:
  United States Army,
  Navy and Air Force Departments
- Calouste Gulbenkian Foundation
- FLAD, Portuguese-American Foundation for the Development
- IST - Instituto Superior Técnico
- ITEC/CRAPS
  Centro de Robótica, Automação e Processamento de Sinal
- JNICT - Junta Nacional de Investigação Científica e Tecnológica
  (Portuguese Research Council)
- TAP, Air Portugal

LOCAL SECRETARIAT

Graça Pereira

Carlos Carvalho

Anabela Almeida

Luisa Martins

Ana Paula Nunes

Instituto Superior Técnico

Departamento de Engenharia Mecânica

Pavilhão de Mestrados

Av. Rovisco Pais, 1096 Lisboa Codex

Portugal

Telephone: (351 1) 841 73 79

Fax: (351 1) 849 61 56

EMail: mheitor@tercomb.ist.utl.pt

LIST OF CONTENTS

VOLUME I (SESSION 1-20)

SESSION 1. PLENARY SESSION

1.1. Effects of Centrebody Rotation on Laminar Flow Through an Eccentric Annulus
M.P. Escudier and I. W. Gouldson

1.2. Molecular Tagging Diagnostics for the Study of Kinematics and Mixing in Liquid Phase Flows
M. M. Koochesfahani, R.K. Cohn, C.P. Gendrich and D.G. Nocera

1.3. Two-dimensional Laser Diagnostics For Sooting Flames
S. Schrami, S. Will, D. Hofmann, K.-U. Münch and A. Leipertz

SESSION 2. 2 PHASE FLOWS INSTRUMENTATION I

2.1. A Device For Phase Shift Measurement in an Advanced Phase Doppler Velocimeter
J. Evenstad, A. Naqwi and R. Menon

2.2. Optimization of the Shape of Receiving Aperture in a Phase Doppler System
A. Naqwi

2.3. A Novel Architecture for Real-Time Phase Measurement
K.M. Ibrahim and W.D. Bachalo

2.4. The Influence of Flame on Phase Doppler Anemometry
S. Tsushima, F. Akamatsu, M. Katsuki, Y. Mizutani and Y.-D. Cho

2.5. Determination of Effective Measurment Area in a Conventional Phase-Doppler Anemometry
T. Maeda, H. Morikita, K. Hishida and M. Maeda

2.6. Measurement Uncertainties of Phase Doppler Technique Due To Effect of Slit Location, Control Volume Size and Flame Front Presence (in Application for Combusting Spray)
Y. Ikeda, T. Hirohata and T. Nakajima

SESSION 3. COMBUSTION I

3.1. Investigations of Turbulent Jet Diffusion Flames by Spontaneous Raman Scattering and Laser-Induced Fluorescence
W. Meier, A. Vyrodov, V. Bergmann, U. Meier and W. Stricker

3.2. Quantitative LIF and Rayleigh Measurements of Temperature and Absolute Concentration of OH Radical in Strained Diffusion Flames
T. Croonenbroek, Th. Daguse, N. Darabiha and J.C. Rolon

3.3. Application of PIV to Turbulent Reacting Flows
L. Muñiz, R.E. Martinez and M.G. Mungal

3.4. Velocity Measurements in Highly Turbulent Premixed Flames by a PIV Measurement System
N. Paone, G.M. Revel and E. Nino

3.5. Flame Surface Density Measurements in Turbulent Premixed Combustion
C. Martel, J. Piana, V. Liard, N. Darabiha and D. Veynante

3.6. Whole-Field Measurements on an Excited Premixed Flame Using On-Line PIV
H. Shen, L. Lourenco, A. Krothapalli and P. Strykowski

SESSION 4. 3D-IMAGING VELOCIMETRY

4.1. Dual-Plane Correlation for Three-Dimensional Particle Image Velocimetry on Planar Domains
M. Raffel, C. Willert, A. Derville, O. Ronneberger and J. Kompenhans

4.2. Spatial Correlation Analysis for 3-D Scanning PIV: Simulation and Application of Dual-Color Light-Sheet Scanning
Ch. Brücker

4.3. Three Dimensional Velocity Measurements using Hybrid HPIV
J. Zhang, B. Tao and J. Katz

4.4. Improvements of Holographic Particle Image Velocimetry (HPIV) by Light-in-Flight Holography
M. Böhmer, H. Hinrichs, K.D. Hinsch and J. Kickstein

4.5. Scalar Imaging Velocimetry Measurements of the Velocity Gradient Tensor Field in Turbulent Flows
L.S. Su and W.J. Dahm *CANCELLED*

4.6. Some Statistical Results from Concentration and Velocity Field Measurements using Laser Induced Fluorescence Tomography
G. J. Merkel, P. Rys, F.S. Rys and T.A. Dracos

SESSION 5. MANUFACTURER'S TECHNICAL PRESENTATION

SESSION 6. 2-PHASE FLOWS INSTRUMENTATION II

6.1. Characteristics of a Miniaturized Probe Employing the Pulse Displacement Technique
C. F. Hess

6.2. Determination of Submicronic Particles Size by Analysis of Light Scattered By a Gas Stream
L. Azizi, P. Herve and A. Kleitz

6.3. Advantages of UV Lasers in Laser and Phase Doppler Anemometers for Submicrometer Particles
F. Durst, A. Melling and P. Volkholz

6.4. On Particle Flux and Concentration Measurement by Shadow Doppler Velocimetry
M. Maeda, H. Morikita, I. Prassas, A.M.K.P. Taylor and J.H. Whitelaw

6.5. Scattering of a Gaussian Beam by an Infinite Cylinder: Numerical Results in GLMT-Framework
K.F. Ren, G. Gouesbet and G. Gréhan

6.6. Time Domain Single Tone Analysis using Quadrature Algorithm
V. Strunck, H. Müller and D. Dopheide

SESSION 7. COMBUSTION II

7.1. Turbulent Propagation Velocity and Mean Reaction Rates of Premixed Turbulent Flames in Stagnation Flows
E. Bourguignon, Y. Michou and I. Gökalp

7.2. Combustion-Turbulence Interaction in Stagnation Flows
F.I.E. Doolaar and T.H. van der Meer

7.3 On the Use of Laser Rayleigh Scattering to Study the Aerothermochemistry of Recirculating Premixed Flames
F. Caldas, D. Duarte, P.C. Ferrão, M. V. Heitor and C. Poppe

7.4. A PIV Investigation in an Axisymetric non Premixed Bluff Body Burner Flame
A. Susset, M. Perrin, D. Jaffre, C. Gray and J.B. Richon

7.5. Methane Concentration by MIE Scattering Imaging Technique in Axisymmetric Non-Premixed Bluff Body Flames
K. Mokaddem, J.C. Rolon, D. Jaffre and M. Perrin

7.6. Non-Intrusive Spectroscopic Measurements with a Tunable Excimer Laser in an Atmospheric Combustor with Premixing and Prevaporization
R. Lachner, D. Theisen, H. Kettl, D. Rist, G. Kappler and A. Schmid

SESSION 8. AERODYNAMIC FLOWS AND ROTATING MACHINES I

8.1. LDA-Investigations on Turbulent Shear Stress in full Scale Centrifugal Pump
M. Lutz, V. Denk and A. Delgado

8.2. Velocity Measurement in the Impeller and in the Volute of a Centrifugal Pump by Particle Image Displacement Velocimetry
M. Oldenburg and E. Pap

8.3. Mean and Turbulent Flow Characteristics of Single Hyperboloid Impeller Stirred Vessels
F.M. Piqueiro, M.F. Proença, F.T. Pinho and A.M. Santos

8.4. Detailed LDV-Measurements for Visualisation of the Flow Field Within a Rushton-Turbine
M. Höfken, M. Schäfer and F. Durst

8.5. The Decay of the Trailing Vortices from Impeller Blades
N.J. Fentiman, N. A. Borrett, K.C. Lee and M. Yianneskis

8.6. Particle Tracking Velocimetry Measurements in a Radial Pump with Particle Pair Detection using the HOUGH Transform
C. Rothlübbers, T. Scheffler, R. Orglmeister and H. Siekamann

SESSION 9. 2-PHASE FLOWS INSTRUMENTATION III

9.1. A Single-Beam Velocimeter based on Rainbow-Interferometry
J.P.A.J. van Beeck and M.L. Riethmuller

9.2. Size Insensitive Rainbow Refractometry: Theoretical Aspects
N. Roth, K. Anders and A. Frohn

9.3. An Advanced Rainbow Signal Processor for Improved Accuracy in Droplet Temperature Measurements
S.V. Sankar, D.M. Robart and W.D. Bachalo

9.4. Investigations on Accuracy and Resolution of Refractive Index Measurements with an Extended Phase-Doppler Anemometer
G. Brenn, C. Tropea, and T. -H. Xu

9.5. Phase Doppler Particle Sizing with Off-Axis Angles in Alexander's Darkband - A Promising Approach for Complex Technical Spray Systems
M. Willmann, A. Glahn and S. Wittig

SESSION 10. COMBUSTION III

10.1. The Development of Spark Ignited Turbulent Flames
R. A. Hicks, M. Lawes, C. G. W. Sheppard and R. Woolley

10.2. Aerodynamic Flow Characterisation of a Swirl Burner
B. Poireault, J.-M. Most and J. Imbach

10.3. Mixing Processes and Combustion of a Gas Jet Flame Surrounded by a Shroud of Combustion Air
P.X. Tran, M.P. Mathur and J.M. Ekmann

10.4. Visualisation of Coherent Structures in a Highly Turbulent Swirling Flame
W. Fick, A. J. Griffiths and T. O'Doherty

10.5 Size-Classified Droplet Dynamics of Combusting Spray in 0.1 MW Oil Furnace
N. Kawahara, Y. Ikeda, T. Hirohata and T. Nakajima

SESSION 11. DOPPLER GLOBAL VELOCIMETRY AND INTERFEROMETRY

11.1. Evolution of Doppler Global Velocimetry Data Processing
J. Meyers

11.2. Doppler Global Velocimetry in the Flow of a Swirler
I. Röehle and R. Schodl

11.3. Development of Doppler Global Velocimetry for Turbomachinery Applications
H. D. Ford and R.P. Tatam

11.4. An Improvement in Doppler Global Velocimetry: The Use of a CW Dye Laser
B. Leporcq, J. F. Le Roy, B. Pinchemel and C. Dufour

11.5 Combined Techniques of Holographic Interferometry and Particle Track Laser Sheet to Study Flame Spread Over Liquids
G. Tashtoush, A. Narumi, A. Ito, K. Saito and C. Cremers

SESSION 12. 2-PHASE FLOWS INSTRUMENTATION IV

12.1. Usage of the Spatial Filter Method for Measurements of Local Particle Velocities in Circulating Fluidized Beds
O. Fiedler, N. Labahn, J. Kumpart, K. Christofori

12.2. Frequency Response of Solid Particles in Oscillating Flows
G. Tedeschi and R.K. Menon

12.3. Size and Velocity Measurements in a Two-Phase Flow using Stereoscopic Particle Image Velocimetry
V. Palero and P. Arroyo

12.4. Comparison Between Velocity Measurements by LDV Techniques and Double Fiber Optic Sensors in Two Phase Jets
M. Gasparetti, G.L. Rossi, A. Campi and R. Onori

12.5. The Locus of Centres Method for LDA and PDA Measurements
Th. Panidis and M. Sommerfeld

12.6. A Fourier Optics Method for the Simulation of Measurement-Volume-Effect by the Slit Constraint
H. -H. Qiu and C.T. Hsu

SESSION 13. ENGINES I

13.1. Spray Characteristics in the Manifold , Port and Cylinder of a Four-Valve Spark-Ignition Engine
B. Cousyn, F. Neveu, M. Posylkin, D. S. Whitelaw and J.H. Whitelaw

13.2. Turbulent Flow Field Characteristics in a Reciprocating Engine: Appropriate Cut-off Frequencies for Cycle-resolved Turbulence, an Analysis of Co-incident 3D LDV Data Based on Combustion-related Dimensional-arguments
P. Dimopoulos, K. Boulouchos and G. Valentino

13.3. LIF Visualization of Liquid Fuel in the Cylinder of a Spark Ignition Engine
P. O. Witze and R. M. Green

13.4. Investigation of the Structure of Injection Sprays in Diesel Engines by Means of a Light-Scattering Technique
K. Prescher, A. Astachow, G. Krüger, J. Henße and D. Potz

13.5. Characterization of Spray Flows under High Fuel Temperature using Phase Doppler Anemometer
T. Obokata, T. Ishima, T. Koyama, K. Uehara, K. Kobayashi and M. Tukagoshi

13.6. Spray Formation and Dispersion of Size-Classified Fuel Droplet of Air-Assist Injector
Y. Ikeda, T. Nakajima and N. Kurihara

SESSION 14. AERODYNAMIC FLOWS AND ROTATING MACHINES II

14.1. Near Wake L.V. Investigation on Hovering Rotor Blades
J. Ramos, M. Mba, D. Favier and E. Berton

14.2. The Application of Laser Anemometry to Eddy Capture in a Propeller Inflow
J.M. Harden and M.V. Lowson

14.3. Measurement of Vortical Structures on a Helicopter Rotor Model in a Wind Tunnel by LDV and PIV
M. Raffel, U. Seelhorst and K.A. Bütefisch

14.4. Three Component LDA Study of the Flow Field Surrounding the Helicopter Landing Pad of a Frigate
C. Swales, J. Rickards, M. Crompton, N. Terry and G. Breeze

14.5. Vortex Investigation on a Retreating Helicopter Blade with 3D Laser Velocimetry in DNW
A. Boutier, J. Lefevre and F. Micheli

14.6. Secondary Flow in Axial Flow Fans of Non-Free Vortex Operation
J. Vad and F. Bencze

SESSION 15. PARTICLES & MARKERS

15.1. Seeding for Laser Velocimetry in Confined Supersonic Flows with Shocks
J. Lepicovsky and R.J. Bruckner

15.2. A Repeatable Laser-Generated Localized Perturbation for Application to Fluid Mechanics
J. D. Schmisseur, S. P. Schneider, T.R. Salyer and S.H. Collicot

15.3. Observations of Fluid Flow Produced in a Closed Cylinder by a Rotating Lid using the PHANTOMM (Photo-Activated Non Intrusive Tracking of Molecular Motion) Flow Tagging Technique
S. R. Harris, R.B. Miles and W.R. Lempert

15.4. Quantitative Velocity Measurements in Turbulent Taylor-Couette Flow by PHANTOMM Flow Tagging
M. Biage, S.R. Harris, W.R. Lempert and A.J. Smits

15.5. Measurements of Velocity and Temperature In Turbulent Flow using Laser Photothermal Effect with the New Interferometers
N. Nakatani, Oshio and T. Sakabe

SESSION 16. ENGINES II

16.1. Evaluation of Time and Spatial Turbulence Scales in a D.I. Diesel Engine
M. Auriemma, F.E. Corcione, R. Macchioni and G. Valentino

16.2. Characteristics of Steady Flows through the Inlet Ports of Multi-Valve Engines
Z. Mahmood and M. Yianneskis

16.3. Steady Flow Characteristics through the Intake Valves of a FORD Four-Valve Cylinder Head
C. Arcoumanis, B. French and J.M. Nouri

16.4. Laser Doppler Measurements of the Instantaneous Volume Flow Rate in Periodically Operating Systems
D. Trimis, M. Weclas and F. Durst

SESSION 17. WALL FLOWS I

17.1. A Study of Streaky Structures in a Turbulent Channel Flow With Particle Image Velocimetry
Z. -C. Liu, R. Adrian and T.J. Hanratty

17.2. Spanwise Vorticity Measurements in a Turbulent Boundary Layer using LDV
C.L. Gan, L. Djenidi and R.A. Antonia

17.3. An LDA Study of Longitudinal Vortices Embedded in a Turbulent Boundary Layer
H.-L-Zhang, X. Zhang and D.W. Hurst

17.4. The Differential Speckle Strophometry - A Light Scattering Technique for the Measurement of Velocity Gradients in Turbulent Fluid Flow
R. Schulz and W. Staude

SESSION 18. 2 D PIV AND PTV

18.1. High-Speed Digital Video Camera Systems and Related Software for Application of PIV in Wind Tunnel Flows
C. Willert, B. Stasicki, M. Raffel and J. Kompenhans

18.2. High Resolution Digital Two-Color PIV (D2CPIV) and its Application to High Free Stream Turbulent Flows
S. P. Gogineni, D.D. Trump, L. P. Goss, R.B. Rivir and D.J. Pestian

18.3. Measurement of Turbulent Boundary Layer using Stereoscopic Particle Image Velocimetry
W.T. Lai and Z.-C. Liu

18.4. Fibre Optic PIV Studies in an Industrial Combustor
D. J. Anderson, C.A. Greated, J.D.C. Jones, G. Nimmo and S. Wiseall

18.5. Measurement of Vortical Flows in a Low Speed Wind Tunnel using Particle Image Velocimetry
J.N. Stewart, Q. Wang, R.P. Moseley, P. W. Bearman and J.K. Harvey

18.6. PIV, LDA and CTA: Common Features and Differences
D.R. McCluskey, F.E. Jorgensen and P. Gjelstrup

SESSION 19. FLOWS WITH ROTATION

19.1. Combined Application of Particle Image Velocimetry (PIV) and Laser Doppler Anemometry (LDA) to Swirling Flows under Compression
J. Volkert, C. Tropea, R. Domann, W. Hübner and I. Lengyel

19.2. A Laser-Doppler of Cooling and Swirling in a Research Combustor
P.Anacleto, M.V. Heitor and A.L.N. Moreira

19.3. Interaction of Swirling Flows from Two Adjacent Coal Burners
A. Aroussi, S. Tarr and S.J. Pickering

19.4. The Turbulent 3D Flow Field in a Rotating Annular Flume
V. Spork, A. Cüppers and J. Köngeter

19.5. A Study of the Flows in a TORE® Slurry Transportation Unit
M.G. Faram, N. Syred, and T.O'Doherty

19.6. LDA Measurements of Axial and Tangential Velocity Components in a DMS Cylindrical Cyclone
B. Chiné, F. Concha and G. Ferrara

SESSION 20. SPRAYS

20.1. Comparative Mass Flux Measurements in Sprays using Patternator and Phase Doppler Anemometers
K. Dullenkopf, M. Willmann, S. Wittig, F. Schöne, M. Stieglmeier, C. Tropea and Chr. Mundo

20.2. Spray Visualization and Phase Doppler Anemometry Measurements of Charged Hydrocarbon Sprays
J.S. Shrimpton, A.J. Yule and A.P. Watkins

20.3. Characterization of a Pulsed Fuel Injector
E. Haile, F. Lacas, D. Veynante and D. Durox

20.4. Application of Extended Phase-Doppler Anemometry in Liquid-Gas Atomization
J. Domnick, J . Raimann and G. Wolf

20.5. Control of Droplet Atomisation in an 'Air-Assist' Atomizer
A.K. Gupta, R. Aftel, C. Cook and C. Presser

20.6. Dual-Mode PDA Measurements in Large Twin-Fluid Atomizers
J. Domnick, F. Durst, S. Gerstner and U. Weiss

VOLUME II (SESSION 21-40)

SESSION 21. PIV AND PTV SIGNAL PROCESSING I

21.1 Sparse Array Image Correlation
D. P. Hart

21.2. Young's Fringes Analysis by Neural Networks
F. Carosone and A. Cenedese

21.3. Double Image Two-Phase Flow PIV
J.I. Garcia-Palacin and M.G. Mungal

21.4. Quantitative Flow Visualization of Velocity Distributions by Parallel Image Processing using PPH (Photo-Conductor Plastic Hologram)
P.M.F. Kato, I. Shimizu, Y. Shibata, T. Isago and H. Taki

21.5. Simultaneous Multiple Pixel Processing Algorithms for PTV and PIV
T. Uemura, M. Yoshimoto and M. Tatumi

SESSION 22. ENGINES III

22.1. LDA-Measurements of the Coolant Flow of a Highly Complex Reciprocating Engine
J. Reuber and E. Blümcke

22.2. Measurement of Axial Flow Velocity in a Cylinder of an S.I. Engine by a Single-Incidence-Beam Reference-Mode LDA
C. Takeda, Y. Ohta, T. Ishima, K. Ishii and T. Obokata

22.3. PIV Measurements and Characterisation of In-Cylinder Flows in Combustion Engines
M.R. Heikal, M. Faure and N.S. Jackson

22.4. A Novel Diode PTV System for the Investigation of Intake Flows in I.C. Engines
C. Freek, A. Wüste and W. Hentschel

22.5. A Study on the Speed Dependence of the Intake Flow of a Motored Four - Stroke Engine, using Laser - Doppler Velocimetry
M. Socoliuc and M. Brun

SESSION 23. STRATIFIED FLOWS

23.1. Investigation of Turbulent Penetrative Convection
V. Troy and R. Adrian

23.2. PIV-Measurements in a Separated Flow Bounded by a Free Surface
G. Janke and L.P. Bernal *CANCELLED*

23.3. Application of DPIV to the Experimental Investigation of a Spilling Water Wave
D. Dabiri and M. Gharib *CANCELLED*

23.4. LDV-Measurements on Thermal Convective Instabilities in Spherical Gap Flow
C. Egbers, W. Beyer and H. Rath

23.5. Mixing in Gravity Current Heads Flowing over Rough Surfaces
W.D. Peters, J.E.S. Venart and S.R. Cogswell

SESSION 24. SCALAR MEASUREMENTS

24.1. Single-Shot Spectrally Resolved UV Rayleigh Scattering Measurements in High Speed Flow
R. G. Seasholtz

24.2. Measurement of the Transient Three-Dimensional Density Distribution using Photoconductor-Plastic
K. Ikeda, K. Okamoto, F. Kato and I. Shimizu

24.3. LIF Investigation of the Flow Pressure Chemical Vapor Deposition (LPCVD) Using CuI as Precursor
R. Kall, A. Möller, V. Till, G. Wortberg, G. Adomeit

24.4. Degenerate Four-Wave Mixing Investigations of Boundary Layer Chemistry in a Thermal Plasma CVD System
T. Owano, E. H. Wahl, and C. Kruger

24.5. UV Laser Diagnostics of Compressible Flows
M. Rodenburg, N. Dam, P.M. Huisman-Kleinherenbrink and J.J. ter Meulen

24.6. Temperature Measurement of 3-D Thermal Flow Fields using Color Image Processing
I. Kimura and M. Ozawa

SESSION 25. LIQUID FILMS

25.1. Droplet Concentration and Velocity Fields in Spark-Ignition Engines
C. Arcoumanis, D.S. Whitelaw and J.H. Whitelaw

25.2. Velocity Profiles in Shear-Driven Liquid Films: LDV-Measurements
S. Wittig, A. Elsässer, W. Samenfink, J. Ebner and K. Dullenkopf

25.3. Internal Transport Mechanisms of Shear-Driven Liquid Films
J. Ebner, W. Samenfink, A. Elsäßer, S. Wittig, and K. Dullenkopf

25.4. Microscopic Super Laminar Flow Measurements in a Journal Bearing using a 2D Solid-State LDA
E.B. Li, A.K. Tieu and M.R. MacKenzie

25.5. Applications of Low Coherence Interferometry to Dynamic Oil Film Thickness Measurement
S. R. Taplin, A. Gh. Podoleanu, D. J. Webb, D. A. Jackson and S. R. Nattrass

25.6. Experimental Analysis by Laser Extinction of the Evolution of the Liquid Crown Produced by the Splash of a Drop on Thin Liquid Film
A. Coghe and G.E. Cossali

SESSION 26. COMPLEX FLOWS I

26.1. Phase-Shifted Two-Camera DPIV For the Study of Flow Past Artificial Heart Valves
Ch. Brücker

26.2. LDV Measurement in a Full Scale Passenger-Car-Cabin
P. Castellini, M. Gasparetti and N. Paone

26.3. A Comparison Between LDA Measurements and Numerical Simulations for a Flow in a Tridimensional Cavity
E. Ovalle and A. Barrientos

26.4. LDV Measurements of the Flow Around a Fence in a Three-Dimensionally Stretched Channel
J.M.M. Sousa, N. Garcia and J.C.F. Pereira

26.5. Velocity Field Characteristics of Multiple Jets Impinging on a Flat Plate
A. Bernard and J.L. Bousgarbiès

26.6. Three-Component Laser-Doppler Measurements of the Confined Model Flow behind a Swirl Nozzle
B. Lehmann, C. Hassa and J. Helbig

SESSION 27. PIV & PTV SIGNAL PROCESSING II

27.1. Temporal Mapping of the Spring Model for Particle Image Velocimetry
K. Okamoto, M. Koiumi, H. Madarame and Y. A. Hassan

27.2. Subpixel Interpolation and Filters for PIV
A. Host-Madsen, A.H. Nielsen and M. R. Schmidt *CANCELLED*

27.3. Error Detection in the Analysis of PTV Images using Proper Orthogonal Decomposition
A. Cenedese, M. Miozzi and G.P. Romano

27.4. Tackling the Problem of Trajectory Occlusion in Multi-Frame PIV (PTV) Using a Neural Network Method
X. Pan and I. Grant

SESSION 28. AERODYNAMIC FLOWS AND ROTATING MACHINES III

28.1. Experimental Aspects of PIV Measurements of Transonic Flow Fields at a Trailing Edge Model of a Turbine Blade
M. Raffel, F. Kost, C. Willert and J. Kompenhans

28.2. 3D Fibre Optic Laser Doppler Velocimetry
S.W. James, R.A. Lockey, D.A. Egan, R.P. Tatam and R.L. Elder

28.3. LDV Investigation of the Rotor-Stator Aerodynamic Interaction in a Centrifugal Turbomachine
M. Ubaldi, P. Zunino, A. Ghiglione and G. Barigozzi

28.4. Aeroacoustic Measurements on an Aerofoil
C. Swales, E.C. Nash, and M.V. Lowson

SESSION 29. WALL FLOWS II

29.1. A Check of Taylor's Hypothesis using Two-Point LDV Measurements in a Turbulent Boundary Layer
R. Elavarasan, L. Djenidi and R.A. Antonia

29.2. LDA Measurements of Laminar-Turbulent Transition in a Flat-Plate Boundary Layer
M. Kruse and S. Wagner

29.3. Measurement of Temporal and Spatial Evolution of Transitional Pipe Flow with PIV
A.A. Draad and J. Westerweel

29.4. Turbulent Transport Mechanism in a Drag Reducing Flow with Surfactant Additive Investigated by Two Component LDV
Y. Kawaguchi, Y. Tawaraya, A. Yabe, K. Hishida and M. Maeda

SESSION 30. FREE FLOWS I

30.1. On the Relationship Between the Formation Number and Passive Scalar Pinch-Off in Starting Jets
H. Johari, D. Dabiri, A. Weigand and M. Gharib

30.2. Planar Doppler Velocimetry in Supersonic Jets
J.-H. Kim, P. Clancy and M. Samimy *CANCELLED*

30.3. Large Scale Vortical Structures in a Turbulent Coaxial Jet
A. Talamelli, G. Buresti, A, Mordacci and G. Tanzini

30.4. Simultaneous Velocity and Concentration Measurements in Confined Coaxial Jets
M.M.C.L. Lima, J.M.L.M. Palma and N.A. Silva

30.5. Coupled Multiple-Jets Excitation
U. Vandsburger and S. D. LePera

SESSION 31. LDV SIGNAL PROCESSING

31.1. Development of a PC-Based Miniature Signal Processor for LDA and PDA Measurements
M. Zhongming and X. Shen

31.2. Velocity Doppler Measurements in a High Speed Water Flow using a Fabry-Perot Interferometer
B. Leporcq, J. F. Le Roy, B. Pinchemel, C. Dufour and G. Houssaye

31.3. New Processing Methods for LDA Signals
A. Host-Madsen and P.Gjelstrup

31.4. Application of the Wavelet Transform to Laser-Doppler Signal Processors
H.R.E. van Maanen and F. J. Nijenboer

31.5. Development of a Velocity Profile Monitor in an Unsteady Flow by Using Semiconductor Laser Velocimeter with FFT-based Multi-Channel Signal Processing
T. Hachiga, N. Furuichi, J. Mimatsu, K. Hishida and M. Kumada

SESSION 32. 2-PHASE FLOWS I

32.1. Particle Dispersion in an Acoustically Excited Round Jet
M. V. Heitor, A.L. N. Moreira and R. Hoffmann

32.2. Influence of Cavitation on the Water Flow in a Pipe with a sudden Expansion
G. Wigley, R. Klasinc, R.H. Logar and T. Dum

32.3. Eddy Diffusivity of Liquid Droplets in a Vertical Flow of Vapor Produced at Boiling Liquid Surface
K . Ohtake, T. Miyata and F. Ogino

32.4. Experimental Study of Turbulent Flow with Bubble Injection at the Wall
T. Tjiptahasdja, C. Gabillet, C. Colin, J. Borée and J. Fabre

32.5. Experiments on Particulate Turbulent Jets
J.A. Garcia, L.M. Cerecedo, J.I. Garcia-Palacin and L. A. Aisa

SESSION 33. FLOWS WITH UNSTEADINESS

33.1. Measurements of Unsteady Velocity and Heat Transfer for Cylinders in Cross Flow
J. W. Scholten, D.B. Murray and J.A. Fitzpatrick

33.2. Measurements of Flow around Two-Dimensional Circular Cylinder Bundles with LDV
K. Tsunoda, S. Okamoto, N. Abe, M. Kijima and S. Higashi

33.3. Turbulence Scales and Spectra in Staggered Tube Bundle Flows
S. Balabhani and M. Yianneskis

33.4. Simultaneous Flow Velocity and Boundary Pressure Measurement for the Investigation of Flow-Induced Multiple-Mode Gate Vibrations
P. Billeter and M. Benesch *CANCELLED*

33.5. Pulsatile Flow Behaviour Near Cardiac Prostheses:
Application and Limitation of Laser and MRI Techniques
F. Hirt, K. Eisele, Z. Zhang, E. Jud, R. Botnar, P. Bösiger, J. Kepner And T. Baldwin

SESSION 34. OPTICS 1

34.1. Power and Sensitivity Improvement of LDA-Systems by Fiber Amplifiers
H. Többen, H. Müller, D. Dopheide

34.2. Two-Component Directional Laser Doppler Anemometer based on a Frequency Modulated Nd:YAG Ring Laser and Fiber Delay Lines
J.W. Czarske and H. Müller

34.3. Fibre Optical Multicomponent LDA-System using the Optical Frequency Difference of Powerful DBR-Laser Diodes
H. Müller, H. Wang and D. Dopheide

34.4. Integrated Laser Doppler Anemometer Made By Ion-Exchange in Glass Substrate
P.L. Auger, A. Cartellier, P. Benech and I. S. Dupont

34.5. Laser Resonance Anemometer Optics
N. Kurihara and M. Takamoto

SESSION 35. FREE FLOWS II

35.1. Two-Scale Grid Turbulence Mixing
M. Gottero, G. Iuso and M. Onorato

35.2. The Effect of a Single Bubble on Turbulence Structure in Grid Turbulence Flow by Combined Shadow-Image and PIV Technique
A. Tokuhiro, M. Maekawa, K. Lizuka, K. Hishida and M. Maeda

35.3. The Separation of Large-Scale and Small-Scale Turbulence in a Shallow Mixing Layer
J. Tukker and R. Booij

35.4. Damping of a Vortex Ring in a Stratified Fluid
T. S. Laursen, J.J. Rasmussen, B. Stenum and D.R. McCluskey

35.5. Flow of Shear-Thinning Fluids around a Cylinder: Vortex Shedding and Drag Characteristics
P.M. Coelho, F.T. Pinho and A.H. Rodrigues

35.6. Turbulent Natural Convection around a Heated Vertical Slender Cylinder
J. Persson and R.I. Karlsson

SESSION 36. LDV DATA PROCESSING

36.1. Uncertainty Estimates for any Turbulence Statistic
L.H. Benedict and R.D. Gould

36.2. Refined Reconstruction Techniques for LDA Data Analysis
H. Nobach, E. Müller and C. Tropea

36.3. Analysis of Randomly Sampled Data using Fuzzy and Non-Linear Techniques
A. Porporato and l. Ridolfi

36.4. Estimation of the Auto Correlation Function of Turbulent Velocity Fluctuations using the Slotting Technique with Local Normalisation
H.R.E. van Maanen and M. Tummers

36.5. Minimizing Errors for Cross Spectral Analysis using Laser Doppler Anemometry Measurements
J. Scholten, S. Dawson, J.A. Fitzpatrick and L. Simon

36.6. Understanding Biases in the Near-Field Region of Two-Point Correlation Measurements using LDA
L.H. Benedict and R.D. Gould

SESSION 37. COMPLEX FLOWS II

37.1. Use of the Complementary PIV and LDV Techniques to Study Industrial Complex Flows
C. Cahen, J. Bénard, M. Barcouda and F. Hofmann

37.2. LDA-Study For Modelling Flows through Screens
U. Ullum, J.P. Frederiksen, E. Akoh, N.F. Nielsen and P.S. Larsen

37.3. Filtration of Dirty Gases by Ceramic Candle Filters
A. Aroussi, K. Simmons and S.J. Pickering

37.4. The Holographic Determination of the Particle Dynamics in an Electro-Hydrodynamic Flow-Field
H.-J. Schmid and H. Umhauer

37.5. LDA Experiments on a Multiple Split Flow at 90°
G. Bäumer, V.A. Campos and J.C.F. Teixeira

37.6. Pulsatile Flow Through Tapered U-Bends as Simulated Aortic Arch (Velocity Field Measurements by Laser-Induced Fluorescence Method)
K. Ohba, A. Sakurai, S. Ikedo, T. Urabe and K. Sawa

SESSION 38. 2-PHASE FLOWS II

38.1. Application of Laser-Doppler Anemometry to Flows in Liquid/Liquid and Solid/Liquid-Extraction Columns
G. Wigley, C. Weiss and R. Marr

38.2. Insights into Grain Entrainment Using Particle Image Velocimetry
M.W. Gallagher and I.K. McEwan

38.3. Flow and Particle Aerodynamic Properties in Aerial Dispersion of Pathogen Spores
A. Rambert, P. Gougat and L. Huber

38.4. An Experimental Study of the Aerodynamic Break-Up of Liquid Drops using Laser Diffraction Technique
S. H. Zaidi and B. J. Azzopardi

38.5. Experimental Investigation and Visualisation of Particle Motion in a Model of a Beater Wheel Mill Model
M. Founti, Th. Achimastos and D.A. Dimopoulos

SESSION 39. OSCILLATING FLOWS AND FLAMES

39.1. Velocity, Temperature and Pressure Characteristics of Pulsed Premixed Flame
E.C. Fernandes and M V. Heitor

39.2. Measurement of the Periodic Flow Instability during a Self Excited Combustion Oscillation by LDV
P. Zangl, J. Hermann, A. Orthmann and D. Vortmeyer

39.3. Characteristics of Oscillating Control Spray for the Suppression of Low Frequency Combustion Instabilities
E. Lubarsky and Y. Levy

39.4. Acoustic Velocity Measurements by Means of Laser Doppler Velocimetry
Ph. Herzog, J.C. Valière, V. Valeau and G. Tournois

SESSION 40. OPTICS II

40.1. Evaluation of the Gaussian Beam Model for the Prediction of LDV Fringe Fields
P.C. Miles and P.O. Witze

40.2. Miniaturizing and Ruggedising Laser Anemometers
L. Lading, L.R. Lindvold, S.G. Hanson, H. Imam and B. Rose

40.3. Effects of Particle Size on Reference LDA Scanning Probe for Profile Measurements
V. Strunck and D. Dopheide

40.4. Development of Fiber Optic Laser Doppler Velocimeter Sensor for Measurement of Local Blood Velocity
K. Ohba and K. Korenaga

40.5. Velocity Distribution using a Transmission Grating
T. Nakajima and Y. Ikeda

AUTHORS' INDEX

SESSION 1

Plenary Session

EFFECTS OF CENTREBODY ROTATION ON LAMINAR FLOW THROUGH AN ECCENTRIC ANNULUS

M P Escudier and I W Gouldson

Department of Mechanical Engineering
University of Liverpool, P O Box 147
Liverpool, L69 3BX, UK

ABSTRACT

The work discussed here is part of a programme of research, motivated by drilling hydraulics, in which the flow of both Newtonian and non-Newtonian liquids is being investigated in pipes and annuli. The present results are limited to laminar flow of a Newtonian liquid in an eccentric annulus with a) an imposed bulk flow without centrebody rotation (axial velocity profiles), b) centrebody rotation with zero bulk flow (tangential velocity profiles) and c) combined bulk flow and centrebody rotation (axial and tangential velocity profiles). The measured velocity profiles are in excellent agreement with available theory. In the absence of an imposed bulk flow, the critical Taylor number at which Taylor vortices appeared in the eccentric annulus geometry was determined by monitoring the onset on an axial velocity in the widest sector of the annulus. Detailed measurements are restricted to sub-critical Taylor numbers.

1. INTRODUCTION

Operational constraints often limit the flow of a drilling fluid (mud) in the annulus (usually eccentric) between the drillpipe and wellbore wall during the drilling of oil and gas wells to the laminar regime (Ooms and Kampman-Reinhartz, 1995). Such flows thus represent a relatively rare example of laminar flows with major industrial relevance. The rheology of a drilling mud is generally non-Newtonian in character: almost invariably shear thinning, and often exhibiting viscoelastic and thixotropic properties as well as a yield stress. The combination of a fluid exhibiting all of these characteristics and an eccentric annulus with centrebody rotation represents a flow of extraordinary complexity, the more so if the rotation rate exceeds the critical condition at which Taylor vortices are generated. Various elements of the flow of liquids in annular geometries are being tackled in an extensive programme of research at the University of Liverpool, motivated by wellbore hydraulics. The present contribution is limited to fully developed laminar flow of a Newtonian liquid in an annulus of radius ratio 0.506 with an offset centrebody rotated at subcritical speeds. The experimental results compare well with the classical analytical expressions for flow in a concentric annulus without rotation, for circular Couette flow a concentric annulus in the absence of an imposed axial flow, and with the recent numerical calculations of Manglik and Fang (1995) for axial flow in an eccentric annulus without rotation. There is also good qualitative agreement with the work of Bakhtiyarov and Siginer (1995) on the flow of a linear fluidity fluid in an eccentric annulus with centrebody rotation but zero bulk flow.

2. EXPERIMENTAL CONDITIONS

Measurements were performed on a 5.8 m long pipe consisting of six modules of precision-bore glass tubing (100.4 mm ID) with a stainless steel centrebody (50.8 mm OD) providing an annulus with a radius ratio $\kappa = 0.506$. The glass tubing was supported on linear bearings which permitted the geometry to be eccentered between $\varepsilon = 0$ and $\varepsilon = 1$. A DC motor and gearbox allowed the centrebody to be rotated at speeds of up to 126 rpm, monitored by an optical encoder with a resolution of 0.1 rpm. Bulk flow through the annulus was provided by a progressive cavity Mono pump, with the flowrate monitored by a Fischer and Porter electromagnetic flowmeter. A Dantec fibreflow LDA system with a measuring volume length in water of 0.19 mm was used to measure the radial variation of axial and tangential velocities. Velocity profiles were measured in the four orthogonal planes shown in **Figure 1** (sectors A-D) for axial velocities with and without rotation and tangential velocities with and without axial flow. The test fluid used was a 2.5:1 w/w glucose- water mixture with density $\rho = 1290$ kg/m^3 and viscosity $\mu = 0.125$ N.s/m^2 at 20°C. The bulk axial velocity was nominally 0.22 m/s and the rotation speed 78 rpm which corresponds to $U/\omega R_i$ of

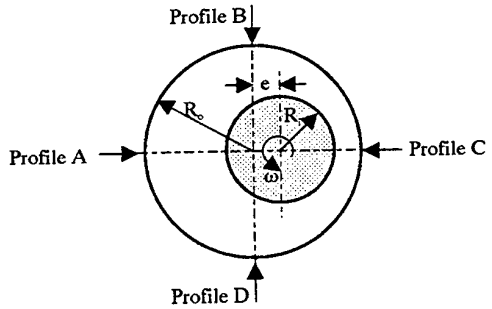

Figure 1 Definition of eccentric geometry and circumferential locations at which velocity profiles were measured

Figure No.	ε	Re	Ro	Ta	$U/\omega R_i$
2 (a)	0	105	-	-	-
2 (b)	0.2	105	-	-	-
2 (c)	0.5	105	-	-	-
2 (d)	0.8	110	-	-	-
6 (a)	0	-	50	2300	-
6 (b)	0.2	-	51	2430	-
6 (c)	0.5	-	53	2600	-
6 (d)	0.8	-	53	2600	-
7(a) & 8(a)	0	105	55	2800	0.99
7(b) & 8(b)	0.2	105	55	2700	1.00
7(c) & 8(c)	0.5	115	57	3000	1.03
7(d) & 8(d)	0.8	120	56	2900	1.08

Table 1 Reynolds and Taylor numbers for individual experiments

1.06. The corresponding bulk flow Reynolds number Re was 113, the Taylor number Ta = 2900, and the rotational Reynolds number Ro = 54. Table 1 gives the exact values for Re, Ro, Ta and $U/\omega R_i$ for individual experiments.

3. EXPERIMENTAL RESULTS

3.1 Bulk axial flow without rotation

The integrity of the measurements is evident from the agreement of the velocity profile for ε = 0 (**Figure 2a**) with the theoretical profile

$$\frac{u}{U} = \frac{2[1-(r/R_o)^2-(1-\kappa^2)ln(r/R_o)/ln\kappa]}{(1+\kappa^2)+(1-\kappa^2)/ln\kappa} \qquad (1)$$

That even slight eccentricity has a major influence on the azimuthal variation of the axial velocity is apparent from **Figure 2b** (ε = 0.2). The highest velocities occur in the widest part of the annulus (A) with a peak velocity twice the bulk average and 30% higher than for the concentric case. The velocities in the narrowest part of the annulus (C) are correspondingly reduced - essentially the source of problems in the cement:mud displacement process. These results for ε = 0.2 are in good agreement with the calculation of Manglik and Fang (1995) for κ = 0.5 who find $u_{max}/U = 2$ for sector A and $u_{max}/U = 0.92$ for sector C. Slight deviations from symmetry are evident in planes B and D, attributable to minor imperfections in the geometry, but the profiles are little changed from those for ε = 0. The trends of **Figure 2b** are further exaggerated for ε = 0.5 (**Figure 2c**), whilst for ε = 0.8 (**Figure 2d**) the fluid in the narrow part of the annulus is practically at rest.

Frictional pressure drop data represented as $f.Re$ versus ε (**Figure 3**) are in reasonable agreement with the

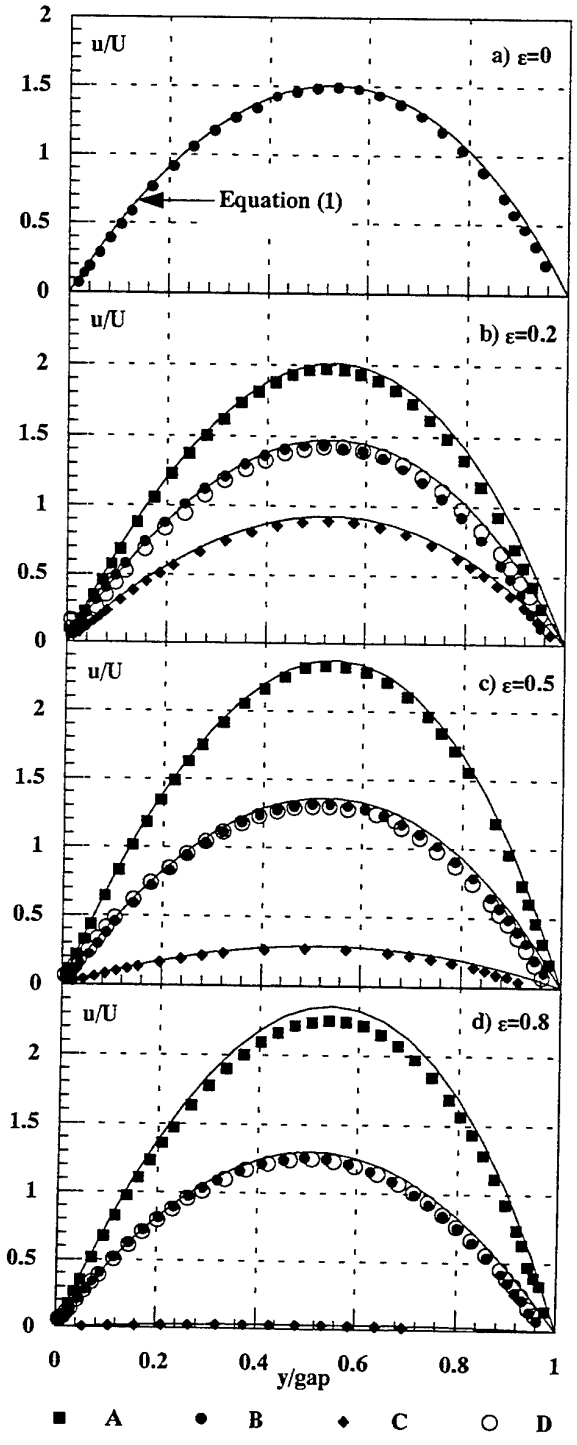

Figure 2 Influence of eccentricity on axial velocity profiles for Ta = 0, Re ≈ 106. Theoretical curves for ε > 0 from Manglik and Fang (1995)

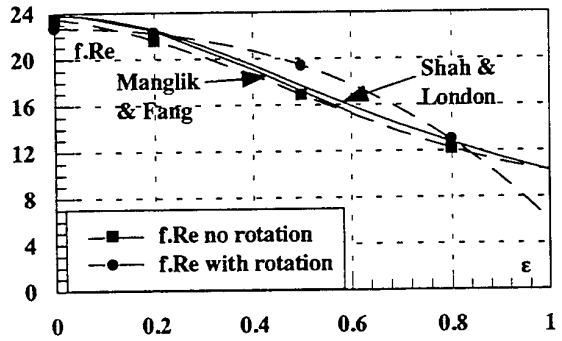

Figure 3 Variation of f.Re with eccentricity:
■ Ta = 0, ● Ta ≈ 2500

numerical calculations of Manglik and Fang for $0 < \varepsilon < 0.6$ and also with the earlier work of Shah and London (1978) which extends to higher values of ε.

3.2 Rotation without bulk axial flow

The variation of critical Taylor number Ta_c with eccentricity (**Figure 5**) was determined by monitoring the onset of an axial velocity in sector A at a point 2/3 g from the outer wall (**Figure 4**). The results are in fair agreement with the numerical calculations of Lockett

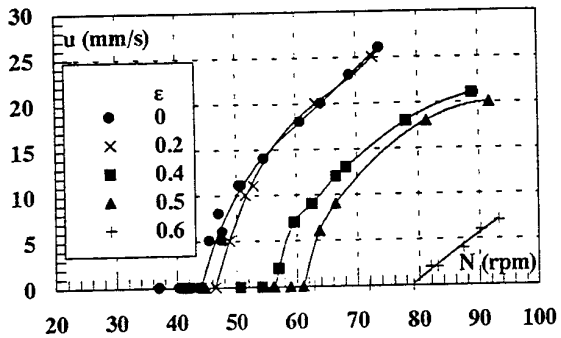

Figure 4 Influence of eccentricity on Taylor vortex onset

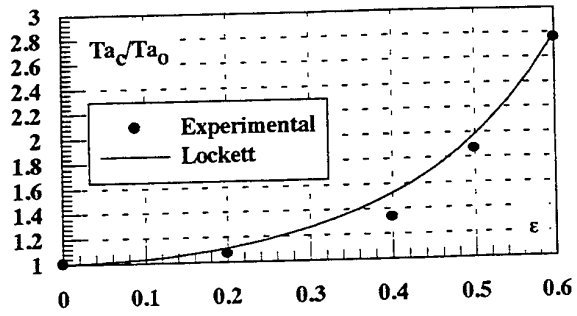

Figure 5 Dependence of critical Taylor number on eccentricity

(1992) which he showed are well represented by

$$\frac{Ta_c}{Ta_o} = 1 + 2.6185\,\varepsilon^2 + 2.13\,\varepsilon^4 + 12.1\,\varepsilon^6 \quad (2)$$

independent of κ. All other measurements were made for Taylor numbers in the range 2430-3000, well below the critical value for any eccentricity since $Ta_o \approx 4500$.

For ε = 0 (**Figure 6a**) the agreement with the theoretical profile for circular Couette flow

$$\text{i.e.} \quad \frac{w}{\omega R_i} = \frac{R_i/r - \kappa^2 r/R_i}{1-\kappa^2} \quad (3)$$

is excellent. The effect of slight eccentricity (ε = 0.2, **Figure 6b**) is again evident with increased tangential velocities in the narrow side (sector C) of the annulus and decreases in the other three sectors. This trend is considerably enhanced for ε = 0.5 (**Figure 6c**) with evidence of a counter-rotating vortex ($w<0$) centred 40% from the outer wall in the wide side (sector A) of the annulus. The reduced velocity on the surface of the inner cylinder in sectors B and D is a consequence of the eccentric geometry - the orientation of the LDA system is not sensitive to the radial (with respect of the outer wall) component of ωR_i. The trends of **Figure 6c** continue with increasing eccentricity: for ε = 0.8 (**Figure 6d**) a counter rotating kidney-shaped vortex has penetrated sectors B and D and a clear asymmetry has developed. Although detailed comparisons are difficult to make, the observed influence of eccentricity is in complete qualitative agreement with the theoretical calculations of San Andreas and Szeri (1984) and also with the observations and calculations of Bakhtiyarov and Siginer (1995).

3.3 Combined bulk axial flow and rotation

For all eccentricities, the distributions of tangential velocity (**Figure 7**) for the situation of combined bulk axial flow and centrebody rotation reveal only slight quantitative differences compared with the situation for zero bulk axial flow.

In contrast to the tangential velocities, with the exception of the concentric geometry, the axial velocity distributions (**Figure 8**) are markedly different from their zero rotation counterparts. This is particularly the case for the lowest eccentricity (ε = 0.2, **Figure 8b**) which has a very significant influence on the axial flow. The symmetry about AC is replaced by an apparent AB/DC symmetry, i.e. symmetries in the profile shape and magnitude of the velocities in sectors A and D, and B and C. The overall flow distribution is closer to axisymmetric, with a reduction of about 15% in the highest velocities and an increase of 30% in the lowest compared with the case for zero rotation. For ε = 0.5 (**Figure 8c**) and, to a lesser degree, for ε = 0.8 (**Figure 8d**) the influence of

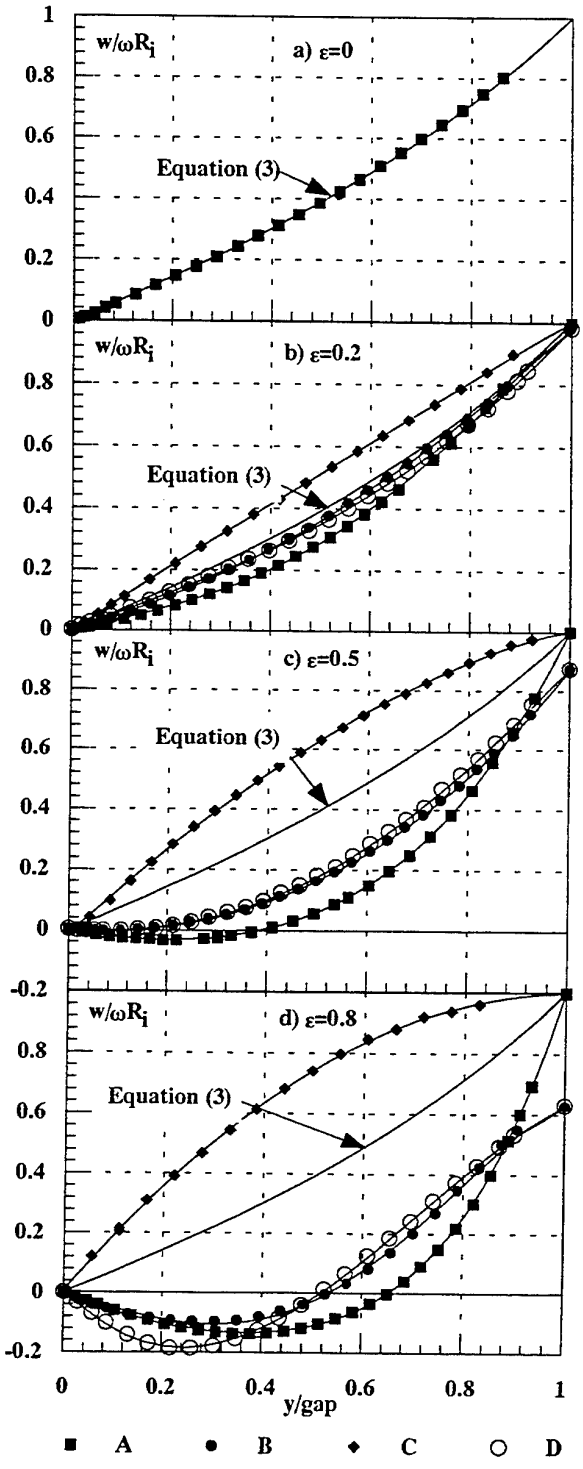

Figure 6 Influence of eccentricity on tangential velocity profiles for Ta ≈ 2500, Ro ≈ 52, Re = 0

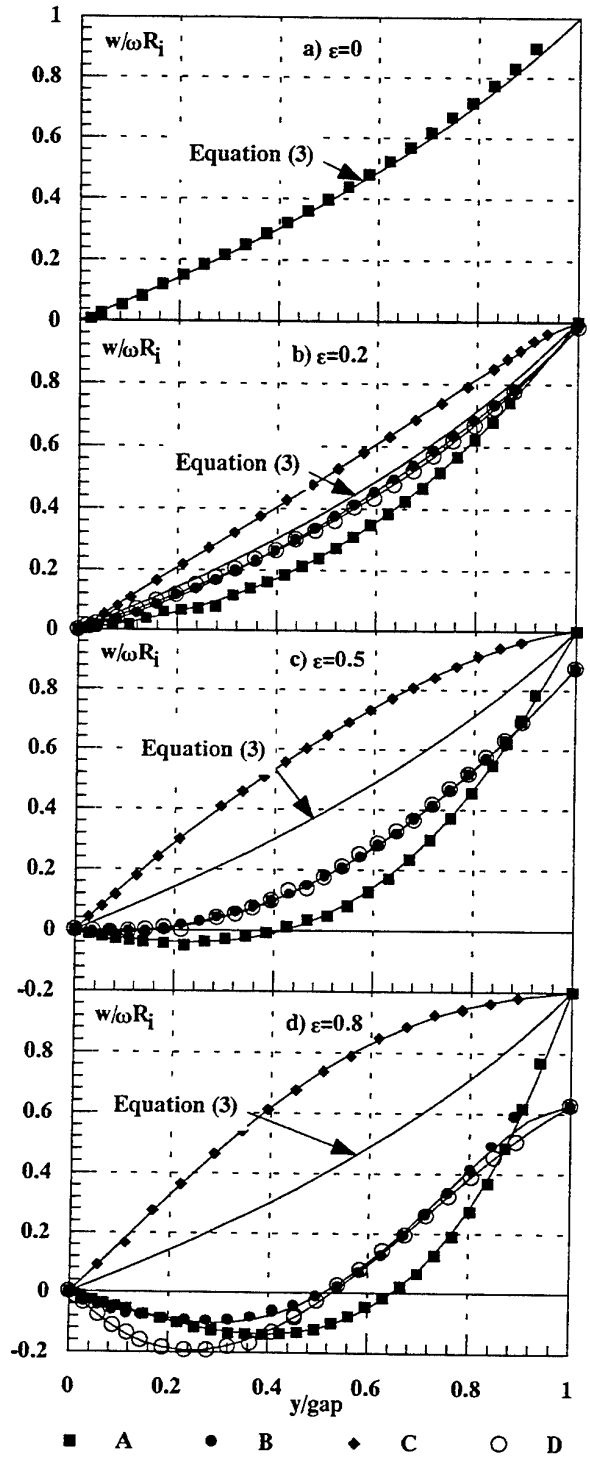

Figure 7 Influence of eccentricity on tangential velocity profiles for Ta ≈ 2850, Ro ≈ 56, Re ≈ 110, U/ωR$_i$ ≈ 1

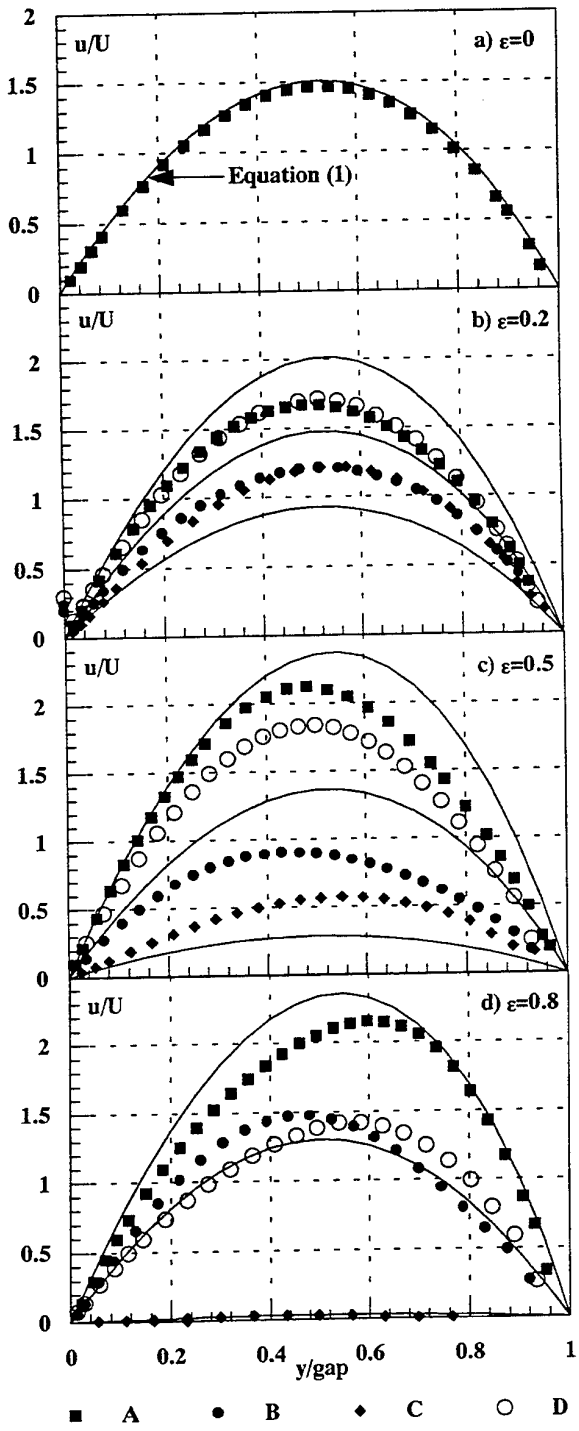

Figure 8 Influence of eccentricity on axial velocity profiles for Ta ≈ 2850, Ro ≈ 56, Re ≈ 110, $U/\omega R_i \approx 1$. Theoretical curves for $\varepsilon > 0$ from Manglik and Fang (1995)

rotation is significant but less dramatic - the highest velocities are again in the widest part of the annulus, the lowest in the narrowest, and the peak locations are shifted radially. It is apparent that the essential influence of rotation is to move fluid of high axial momentum into regions which, in its absence, were momentum deficient.

The influence of rotation on f.Re (**Figure 3**) is greatest for $\varepsilon = 0.5$ where there is a 15% increase compared with the zero rotation case. Significant changes in f.Re were to be anticipated given the strong effect of rotation on the axial velocity profiles. The laminar flow situation may be contrasted with turbulent flow where the effect of rotation on both the axial flow and f(Re) is negligibly small (Escudier and Gouldson, 1995).

4. CONCLUSIONS

In the absence of centrebody rotation, increasing eccentricity results in progressive departures from axisymmetry of the laminar axial flow in an annulus with $\kappa = 0.506$. For $\varepsilon = 0.8$ the peak velocity in the widest part of the annulus is 50% higher than for a concentric geometry whilst there is practically no flow through the narrowest section.

Centrebody rotation at sub-critical Taylor numbers, in the absence of a bulk throughflow, generates a radial/tangential velocity field with a counter-rotating kidney shaped vortex in the widest part of the annulus for eccentricities of about 0.5 or higher.

Bulk axial flow at the low Reynolds numbers investigated here ($\sim 10^2$) has no significant influence on the radial/tangential velocity field generated by centrebody rotation.

At all eccentricities, and particularly the lowest value investigated (0.2), centrebody rotation produces a significant reduction in the azimuthal variation in the axial velocity distributions.

5. ACKNOWLEDGEMENTS

The authors gratefully acknowledge the financial support of EPSRC/MTD (research grant GR/F87813), Shell Research BV and British Gas plc. We are also indebted to Professor R Manglik, University of Cincinnati for providing full details of the computations reported in Manglik and Fang (1995).

6. NOMENCLATURE AND DEFINITIONS

d	mean annular gap R_o-R_i (m)
e	displacement of centrebody axis from outer pipe axis (m)
g	gap width (A, B, C or D)
R_i	outer radius of centrebody (m)
R_o	inner radius of outer tube (m)
Re	bulk axial Reynolds number $2\rho Ud/\mu$
Ro	rotational Reynolds number $\rho\omega R_i^2/\mu$
Ta	Taylor number $(\rho\omega/\mu)^2 R_i d^3$

Ta_c	critical Taylor number
Ta_o	value of Ta_c for $\varepsilon = 0$
u	axial component of velocity (m/s)
u_{max}	peak value of u in any sector of the annulus
U	bulk axial velocity (m/s)
w	tangential component of velocity (m/s)
y	distance from inner wall of outer tube (m)
ε	eccentricity e/d
κ	radius ratio R_i/R_o
μ	fluid dynamic viscosity ($N.s/m^2$)
ξ	non-dimensional distance from outer wall y/g
ρ	fluid density (kg/m^3)
ω	angular velocity of centrebody (rad/s)

7. REFERENCES

Bakhtiyarov S and Siginer D A, 1995, Flow of linear fluidity fluids in eccentric annuli, Proc ASME Symposium Developments and Applications of non-Newtonian Flows, FED-Vol 231/MD-Vol 68.

Escudier M.P. and Gouldson I.W., 1995, Concentric annular flow with centrebody rotation of a Newtonian and a shear-thinning liquid, Int. J. Ht and Fluid Flow, **16**, no 3, pp 156-162.

Lockett T.J., 1992, Numerical simulation of inelastic non-Newtonian fluid flows in annuli, PhD Thesis Imperial College of Science, Technology and Medicine.

Manglik R.M. and Fang P.P., 1995, Effects of eccentricity and thermal boundary conditions on laminar and fully developed flow in annular ducts, Int. J. Ht. and Fluid Flow, **16**, no 4, pp 298-306.

Ooms G. and Kampman-Reinhartz B.E., 1995, Influence of drillpipe rotation and eccentricity on pressure drop over borehole during drilling, Submitted to European J. Mechanics.

San Andreas A. and Szeri A.Z., 1984, Flow between eccentric rotating cylinders, ASME J. Appl. Mech., **51**.

Shah R.K. and London A.L., 1978, Laminar flow forced convection in ducts, Advances in Heat Transfer, Academic, New York.

MOLECULAR TAGGING DIAGNOSTICS FOR THE STUDY OF KINEMATICS AND MIXING IN LIQUID PHASE FLOWS

M. M. Koochesfahani[a], R. K. Cohn[a], C. P. Gendrich[a], and D. G. Nocera[b]

Departments of Mechanical Engineering[a] and Chemistry[b]
Michigan State University, East Lansing, MI 48824

ABSTRACT

This paper reports our recent developments of novel techniques for velocimetry and studies of the Lagrangian evolution of mixing interfaces based on molecular tagging approaches. These developments take advantage of a class of newly engineered phosphorescent supramolecules that are water soluble. Previous implementations using photochromic molecules and caged fluorescein are briefly discussed and compared. The application of molecular tagging velocimetry is demonstrated in several flow fields including examples which illustrate its unique capability in flows with significant out-of-plane motion, and its potential for simultaneous passive scalar and velocity measurements.

1. INTRODUCTION

The capability to tag a portion of a flow non-intrusively and observe its subsequent evolution offers new possibilities for velocimetry and the study of entrainment and mixing in fluid flows. Chemical compounds with long luminescence lifetimes are needed for this approach. Current laser induced fluorescence (LIF) techniques are generally not suitable for this purpose because of the short lifetime of the fluorescence process (τ = a few nanoseconds).

The majority of past efforts in the use of molecular tagging have concentrated on flow velocimetry. Regardless of the details of the photophysics in each molecular design, all of these efforts can be characterized under a broader common heading of Molecular Tagging Velocimetry (MTV). In this method of velocimetry, the flowing medium is premixed with molecules that can be turned into long lifetime tracers upon excitation by photons. Typically a pulsed laser is used to "tag" small regions of interest. The tagged regions are imaged at two successive times within the lifetime of the tracer. The measured displacement vector provides the estimate of the velocity vector.

Past implementations of MTV in liquid phase flows primarily include the use of photochromic molecules (Popovich & Hummel 1967; Falco & Chu 1987; Ojha, et. al. 1989; and Chu & Liao 1992, among others), caged fluorescein (Lempert, et. al. 1995; Harris, et. al. 1996), and specially engineered phosphorescent supramolecules (Koochesfahani, et. al. 1993; Stier, 1994; Gendrich, et. al. 1994; Hill & Klewicki, 1995, Cohn, et. al. 1995, and Gendrich & Koochesfahani 1996). In gas phase flows, the fluorescence of excited-state oxygen (Miles, et. al. 1987; 1989; 1993) and the phosphorescence of biacetyl (Hilbert & Falco 1991, Stier, et. al. 1995) have typically been utilized. The review by Falco & Nocera (1993) discusses some of these and other efforts known at that time.

The purpose of this paper is to give a brief summary of various MTV implementations and their chemical mechanisms, followed by our recent contributions to improve and extend this technique. This includes a discussion of the ideas behind the design of the new phosphorescent complexes and our approach to imaging and tracking the tagged regions. Examples of the application of MTV to different flow fields will be provided, one of which highlights the ability to make measurements when strong out-of-plane motions are present. Other examples will illustrate the potential for simultaneous passive scalar and velocity measurements.

2. CHEMICAL MECHANISMS

A molecular complex is suitable for molecular tagging applications if its lifetime after excitation is

long enough relative to the flow convection time scale to allow sufficient displacement of the tagged regions. The discussion in this paper focuses primarily on liquid phase applications, however it is worthwhile to briefly note some highlights of work in gas phase. The use of excited-state oxygen fluorescence, pioneered by Miles, et. al. (1987, 1989, 1993) under the acronym RELIEF, is the only tagging method currently available in an oxygen environment (i.e. air). The lifetime of the tracer (vibrationally excited O_2) is of order 100 μs, making it suitable for high speed flows. The phosphorescence of biacetyl, which has a reported lifetime of order 1 ms, has also been used for velocimetry (Hilbert & Falco 1991, Stier, et. al. 1995). However, its use is limited to oxygen-free environments due to the phosphorescence quenching by oxygen.

2.1. Photochromics

In a photochromic process a molecule M is excited to produce a high energy form of M, designated M′, which has a different absorption spectrum giving rise to a color change (e.g. from clear to dark blue). The long lifetime tracer is the newly produced M′, which persists for several seconds to minutes. The nonradiative conversion from M to M′, i.e. the tagging process, occurs rapidly (within the duration of a few nanosecond long laser pulse). The photochromic process is reversible; M′ thermally converts back to M over time, therefore the chemical is reusable. Photochromic dyes are generally insoluble in water, so organic liquids such as kerosene are typically used as the flowing medium. The use of photochromic chemicals requires two photon sources; typically a UV laser (e.g. λ = 351 nm from an excimer laser) to induce the color change and a white light source to interrogate the tagged regions.

Hummel and his group (e.g. Popovich & Hummel 1967, Ojha, et. al. 1989) originated the use of photochromic chemicals as a velocity measurement tool by tagging the flow along single lines. Significant improvements were made in the pioneering work of Falco & Chu (1987), who used a laser grid to tag the flow and coined the acronym LIPA (**L**aser **I**nduced **P**hotochemical **A**nemometry). The distinction between these different tagging approaches is a very important one, which will be discussed in Section 3.

Some of the advantages of photochromics (long lifetime, reusable) are offset by the need to use special fluids such as kerosene. It is possible to ease this restriction by making chemical modifications to enable many photochromic dyes to dissolve in water. One such example has been reported by Yurechko & Ryazantsev (1991). The most significant drawback in using photochromic chemicals is that the image is produced by a change in absorbance, thereby requiring a measurement of the difference between incident and transmitted light. Emitted light (against a black background) is more easily and accurately detected than transmitted light; consequently, images based on luminescence are better suited to MTV applications. Despite some of these difficulties, photochromics are being used very effectively to advance the understanding of flow physics (Chu & Liao, 1992; Chu, et. al. 1993).

2.2. Caged Fluorescein

In this compound a chemical group is attached to fluorescein in order to render it non-fluorescent. The caging group is removed upon absorption of UV photons (λ = 350 nm), thereby creating regular fluorescein which fluoresces with very high quantum efficiency. In this case, the long lifetime tracer is the uncaged fluorescein, which persists for a very long time and can be interrogated at the time of interest through its luminescence upon re-irradiation. Two sources of photons are therefore needed, one to break the cage and the other to excite fluorescence. The use of caged fluorescein and similar compounds for molecular tagging velocimetry was first introduced by Lempert, et. al. (1995) under the acronym PHANTOMM (**PH**oto-Activated **N**on-intrusive **T**racking of **M**olecular **M**otion). In both this work and a recent novel application of it (Harris, et. al. 1996), laser line tagging is used (see Section 3 for further discussion).

There are two aspects of caged fluorescein that one must be aware of in designing an experiment. The cage-breaking process is irreversible; each caged molecule can be used only once. The cage-breaking process is not rapid and occurs with a time constant of the order of a few milliseconds. This delay between laser tagging and generation of enough fluorescein to obtain an image with sufficient signal/noise will dictate the fastest flow speeds that can be accommodated. Obviously, very slow speeds can be handled with ease considering the very long lifetime (practically infinite) of the uncaged fluorescein. It is anticipated that future research will lead to the design of new generations of caged fluorescent molecules without these drawbacks.

2.3. Phosphorescent Supramolecules

In using a phosphorescent compound for molecular tagging, excitation by photons is used to produce a long-lived excited state which is interrogated through its phosphorescence emission as it radiatively returns

to its ground state. The long lifetime tracer is the excited state molecule itself. In this case only one source of photons is needed, and the excitation/emission process is reversible. The difficulty is that long-lived excited states (i.e. phosphorescence) suffer from O_2 and H_2O quenching, and as a result, suitable molecular complexes have not been available until recently.

New findings by Nocera and his group (Ponce, et. al. 1993, Mortellaro & Nocera 1996, Hartmann, et. al. 1996) show that supramolecules may be designed that exhibit long-lived phosphorescence, which are not quenched. A successful design by Ponce, et. al. (1993) indicates that the quenching of a lumophore can be stopped, and the phosphorescence emission recovered, by mixing certain alcohols with an aqueous solution of a cyclodextrin (CD) cup that contains the lumophore. Cyclodextrins are molecules constructed from sugars connected in a head-to-tail arrangement. The molecule is cup-shaped with its size determined by the number of sugars in the structure. The CD used in our application is Gß-CD, which is constructed of 7 glucose subunits, resulting in an outer cup dimension of 15.3 Å and an inner cup cavity dimension of 7.8 Å. The size of the cavity is important for effective binding to the guest molecule, in our case 1-bromonaphthalene (1-BrNp), which is the lumophore.

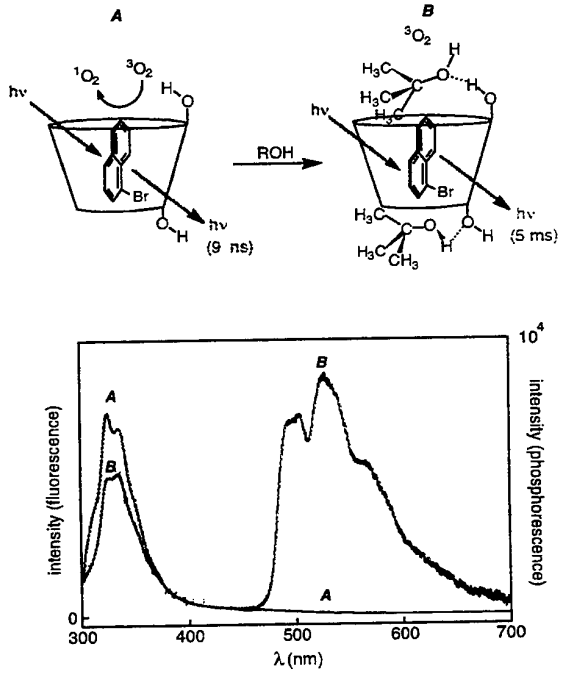

Figure 1. Emission from 1-BrNp in CD's (A) Only blue fluorescence is exhibited in the absence of an appropriate alcohol (ROH); (B) A bright green phosphorescence plus the initial fluorescence is seen upon the addition of ROH, which prevents the quenching of 1-BrNp phosphorescence by O_2.

The long-lived, green phosphorescence (lifetime $\tau \approx 5$ ms) of 1-BrNp is efficiently quenched by oxygen, even when the lumophore is inside a CD cup. The phosphorescence can be recovered upon adding an alcohol (ROH) to the solution as shown in Figure 1. Detailed studies of Ponce, et. al. (1993) and Hartmann, et. al. (1996) show that a ternary complex (1-BrNp · Gß-CD · ROH) is formed where the alcohol hydrogen bonds to the rim of the CD cup and acts as a lid for the cup, thereby shielding 1-BrNp from oxygen. The phosphorescence enhancement can be very large, approaching 10^4-10^5, depending on the fit of the alcohol lid to the CD cup. For the studies described in this paper, cyclohexanol was used as the alcohol

When using this phosphorescent complex, it is useful to recall that luminescence lifetime refers to the time when the emission has decayed to 37% (e^{-1}) of its initial intensity. The actual usable delay time between laser tagging and interrogation can be considerably longer and is dictated by the type of detection used. We have, for example, measured flows with delays of up to 30 ms using image-intensified cameras. Nevertheless, the lifetime of this molecular design is not suitable for very low speed flows. Such cases are best investigated using caged fluorescein or photochromics.

Depending on the placement of the three components of the phosphorescent complex in the flow, we have devised methods for (1) purely velocimetry, (2) molecularly tagging a passive scalar mixing region and monitoring its Lagrangian evolution, and (3) molecularly tagging a chemical reaction interface between two streams and observing its Lagrangian evolution. The first two of these implementations are described in this paper.

3. TAGGING, DETECTION, AND PROCESSING SCHEMES

3.1. Tagging

Tagging the flow along single lines was originally used by Hummel and his group (e.g. Popovich & Hummel 1967, Ojha, et. al. 1989). The velocity is determined from the displacement of the tagged lines in much the same manner as using hydrogen bubble lines generated by a wire (for example, see Lu & Smith 1985). Laser line tagging is still the only method used to date in the works utilizing caged fluorescein (Lempert, et. al. 1995; Harris, et. al. 1996) and excited-state oxygen fluorescence (Miles, et. al. 1987, 1989, 1993). It is very important to recognize that line tagging allows the measurement of only one component of velocity, that normal to the tagged line. In addition, the

estimate of this velocity component has an inherent error associated with it. Following the analysis of Hill & Klewicki (1995), and referring to Figure 2, this error can be cast in the form

$$\frac{\Delta u}{u} = \tan\theta \, \frac{\partial u}{\partial y} \, \Delta t$$

In this expression, u is the estimated velocity component normal to the tagged line, $\Delta u = u_{actual} - u$ is the error in the estimated velocity, θ is the local flow angle given by $\tan\theta = v/u$ with v being the flow velocity parallel to the tagged line, and Δt is the time delay between tagging and interrogation. Clearly an *a priori* knowledge of the flow field is necessary in order to provide an estimate of the error. It can be observed, however, that this inherent error is identically zero only in flows where the velocity component v along the tagged line is zero (i.e. unidirectional flows) or where velocity gradient $\partial u/\partial y = 0$. In a general flow field where these constraints are not met, the error can be reduced by decreasing the delay time Δt, but it cannot be made arbitrarily small, since Δt has to be large enough for the resulting displacement of the tagged line to be measured with adequate accuracy. While keeping these issues in mind, it is sometimes possible to take advantage of an *a priori* knowledge of the flow field under investigation to design the experimental parameters such that the inherent error discussed here becomes minimal compared to other measurement errors. In cases where this can be done (see Hill & Klewicki 1995, for example) the line tagging approach can provide reliable information on one component of the velocity vector.

In order to unambiguously measure two components of the velocity in a plane, the luminescence intensity field from a tagged region must have spatial gradients along two, preferably orthogonal, directions. For single-point velocimetry, this is easily achieved using a pair of crossing laser beams; a grid of intersecting laser lines allows multi-point velocity measurements. Use of this tagging scheme was pioneered by Falco & Chu (1987). An example of a region in a flow tagged in this manner using our new phosphorescent supramolecules, and the same region interrogated subsequently at two different delay times, is depicted in Figure 3. The flow field is that generated by a vortex ring impacting a solid wall at normal incidence, which will be discussed as one of the examples in Section 4. The superposition of the image at the longer time delay (Figure 3d) onto the initially tagged image (Figure 3a), shown in Figure 4, serves to highlight the velocity error inherent in the line tagging approach discussed earlier. The image at the shorter time delay in Figure 3c is more typical of that used in

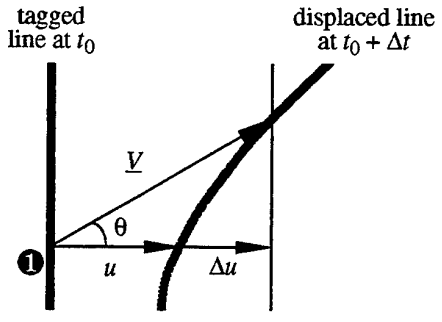

Figure 2. The velocity at point ❶ is V. Using the line center displacement gives a lateral velocity estimate u, with error Δu. The vertical velocity component cannot be estimated with the flow tagged in this manner.

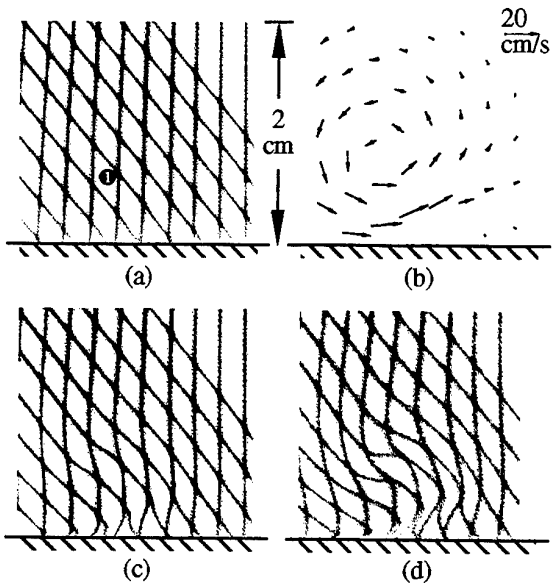

Figure 3. The undistorted grid in (a) is displaced by the velocity field shown in (b) for 5 ms and 19 ms to produce the distorted grids shown in (c) and (d), respectively.

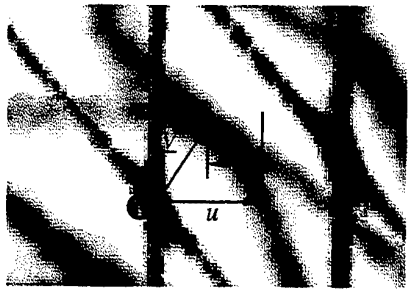

Figure 4. The superposition of Figure 3d (red) over Figure 3a (green) in the neighborhood of the point marked ❶ in Figure 3a. The notation is the same as that used in Figure 2.

our velocimetry applications.

As will be seen later, laser grid tagging is only a special case of a more generalized approach to induce a spatially non-uniform luminescence intensity in a tagged region. For example, the non-uniform passive scalar concentration field typical of most turbulent flows can sometimes be used as a natural source of luminescence non-uniformity without the need for grid illumination.

3.2. Detection

Depending on the specific requirements of a particular application, a variety of image acquisition methods have been used in the past including cameras recording on film, CCD cameras, and gated image-intensified cameras. The common element among all previous studies is that a single detector is used; the initial tagging pattern is recorded once, usually at the beginning of the experiment, and then the delayed images are acquired. The implicit assumption in this approach is that the initial tagging pattern remains spatially invariant throughout the experiment. Because current processing schemes (see Section 3.3) measure the displacement of the tagged regions with sub-pixel accuracy, small variations in the initial pattern will be misinterpreted as flow velocity fluctuations. We have improved the accuracy of the MTV technique by employing a two-detector imaging scheme.

The experimental arrangement, shown in Figure 5, involves a link between the pulsed excimer laser (λ = 308 nm) and two image detectors through a digital delay generator. Immediately after the laser fires, the first detector records an image of the tagged flow, and after a prescribed time delay Δt, the second detector records a delayed image. These images are digitally acquired in real time by two separate acquisition systems. The advantage of this arrangement is that any spatial "wandering" of the tagged regions (e.g. due to laser beam pointing instability, vibration of the optics, etc.) does not contribute to error in the measurement of the displacement of these regions. Furthermore, the two-detector setup is clearly indispensable when the intensity field in the initial tagging pattern cannot be assumed, for example in the case of a non-uniform scalar mixing field.

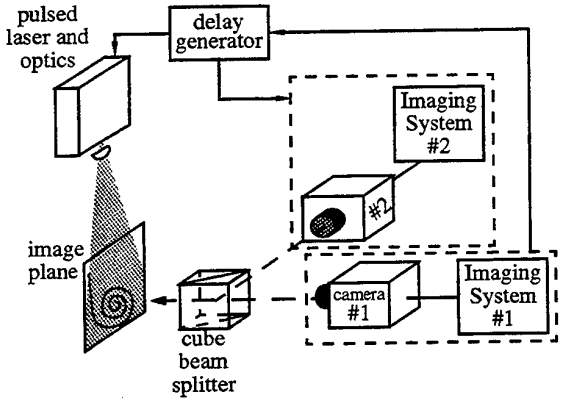

Figure 5. Optical and electronic arrangement for 2-camera MTV experiments. Both cameras view the same image plane through the cube beam splitter. Synchronization between the two cameras and laser is provided by a digital delay generator.

The data shown in this paper were acquired using the arrangement shown in Figure 5 in conjunction with a variety of CCD detectors (interlaced cameras, electronically-shuttered frame transfer cameras, and gated image-intensified cameras) depending on the optical/imaging requirements unique to the particular experiment. Each image was digitized to 8 bits into a 512 x 512 pixel array. Time series data were acquired at a rate of 30 image pairs per second directly onto hard disk.

3.3. Processing

The traditional method for finding the displacement of tagged lines or grids has been to locate the center of each line through various techniques. Most of the recent techniques use the best fit to an assumed laser line shape, for example, a gaussian intensity distribution. We are not aware of a systematic statistical study of the performance of this approach while considering the effects of experimental parameters such as image contrast, signal to noise ratio, etc. The recent study of Hill & Klewicki (1995) reports the accuracy in determining the displacement vector to be $\pm$0.35 pixel rms. Even though efforts are under way to improve the accuracy further using better algorithms, the basic premise behind this approach is the use of a known line shape for the tagged line, which may not be known *a priori* in some situations, due to a variety of reasons associated with laser beam transmission through a flowing medium, bleaching effects, etc.

We have taken a different approach in an attempt to implement a generalized scheme that is independent of the details within a tagged region, and can accommodate arbitrary tagging patterns including those due to non-uniform scalar mixing fields. The displacement of the tagged regions is determined using a direct digital spatial correlation technique. The example provided in Figure 6 illustrates a region in an actual experiment tagged by a laser grid, the tagged region at a later time, and the corresponding spatial correlation coefficient field for one of the grid crossings. A well-

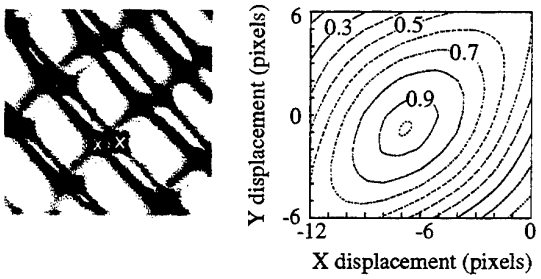

(a) (b)

Figure 6. Experimental MTV grid. (a) ■ lines are the grid at t = 0; ■ lines are the grid after a 6 ms delay. (b) Correlation coefficient contours for the indicated intersection in (a)

defined correlation peak occurs at the location corresponding to the displacement of the tagged region by the flow; the displacement peak is located to sub-pixel accuracy using a multi-dimensional polynomial fit. This procedure is similar to what could be used in DPIV processing of particle image pairs. One advantage of our processing technique over traditional line-center methods is robustness to the presence of noise due to the averaging process inherent in the correlation procedure. Based on both experiments and an extensive statistical study on the performance of this correlation approach, we have found that we can typically measure the displacement of the tagged regions with a 95% confidence limit of ±0.1 sub-pixel accuracy (i.e. 95% of the displacement measurements are accurate to better than 0.1 pixel). This corresponds to an rms accuracy of ±0.05 pixel, assuming a Gaussian distribution for error. The details can be found in Gendrich & Koochesfahani (1996).

It should be noted that the spatial correlation method just described, though of more general utility than the line-center methods, may lead to a somewhat degraded spatial resolution. The contrast is similar to that between PIV (using a group of seed particles) versus individual particle tracking.

4. EXAMPLES OF MTV MEASUREMENTS

When the three components of the phosphorescent complex (1-BrNp · Gß-CD · ROH) are premixed with water in the entire flow facility, we obtain a technique intended solely for velocity measurements. Since the flowing medium is homogeneously mixed, a pulsed laser grid pattern is used to molecularly tag the regions of interest.

An example of the type of time series data obtained from a single MTV grid intersection is shown in Figure 7. This figure illustrates the time evolution of

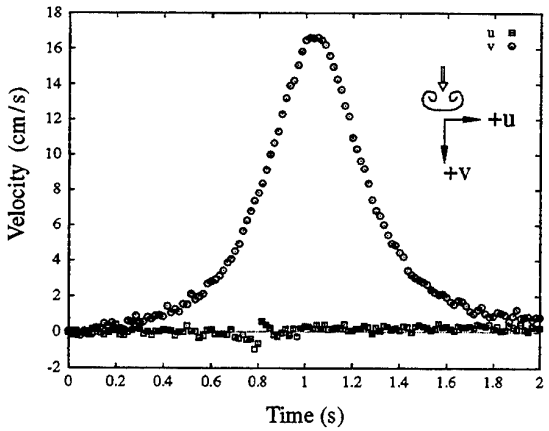

Figure 7. The time evolution of (u, v) velocity components measured by MTV near the center of a passing vortex ring.

two components of the velocity vector near the axis of symmetry of a passing vortex ring. We note that this represents raw data (i.e. no filtering or smoothing) from one of many grid points where simultaneous velocity data were obtained.

The next example provides a sample of the instantaneous whole-field measurements of two components of the velocity vector over a plane in a study of unsteady boundary layer separation in a vortex-wall interaction. A vortex ring approaching a wall at normal incidence generates an unsteady adverse pressure gradient on the wall which results in boundary layer separation and formation of a secondary vortex. An LIF flow visualization of this flow right after the formation of the secondary vortex is depicted on top in Figure 8(a) (only the left half of the flow is included). Figure 8(b) shows the corresponding instantaneous MTV velocity data (1 mm grid spacing with first grid 0.5 mm away from the wall) and the computed vorticity field. The data sequence in Figure 9 is selected from a much longer time series sequence showing an enlarged view of the details of the velocity and vorticity fields during the boundary layer separation process. Except for the inherent smoothing involved in mapping the velocity data from the irregular MTV grid onto a regular grid, the data shown in Figures 8 and 9 represent raw data, i.e. no attempt was made to remove a "bad" vector, replace it, or apply spatial filtering

At this stage, a comparison between the MTV and PIV methods is warranted. The MTV technique can be thought of as the *molecular* version of PIV with two major advantages. First, since particles are replaced by molecules dissolved in the flowing medium, the problems related to particles tracking the flow, density mismatch between particles and the fluid, particle seeding

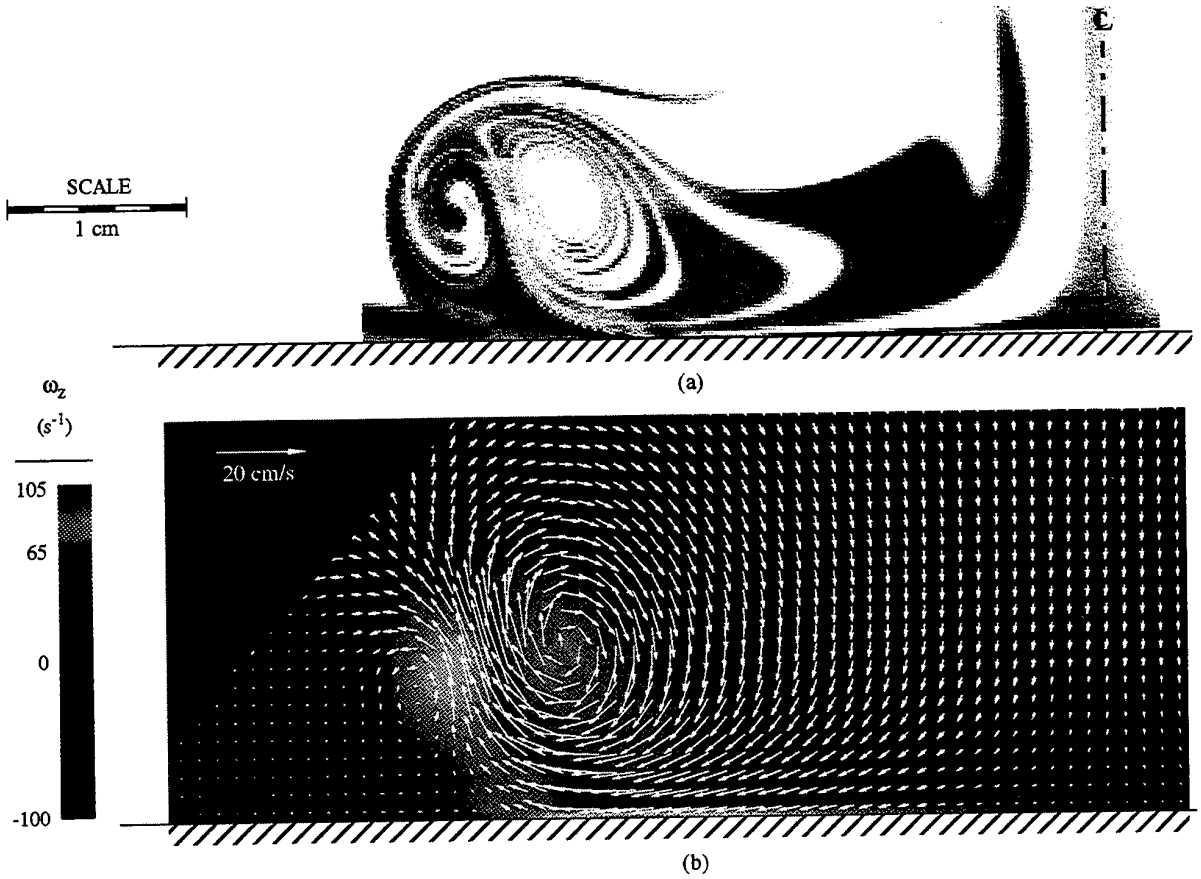

Figure 8. (a) LIF image of the left-half of a downward moving vortex ring. The ring and wall-layer fluids are marked by green- and red-emitting laser dyes, respectively. (b) Velocity and vorticity fields measured using MTV.

density, etc. are absent from MTV. Second, the performance and accuracy of PIV in measuring the in-plane velocity vector can degrade considerably in 3-D velocity fields due to particle motion in/out of the plane of the laser sheet. In MTV, the measurement of in-plane velocity vectors is quite insensitive to the out-of-plane velocity component. The reason is that only the tagged region is luminescent; the motion of any molecules located outside of this tagged region into or out of the image field of view does not contaminate the spatial correlation process since those molecules are not luminescent.

The latter advantage of MTV offers a unique capability for velocimetry in highly 3-D flows, which we demonstrate in an application to a forced wake. We have previously reported that forcing a low Reynolds number 2-D wake can lead to a highly three-dimensional flow and a large increase in mixing (MacKinnon & Koochesfahani 1993, Koochesfahani, et. al. 1994). Figure 10 illustrates preliminary instantaneous velocity vectors (v, w components) in the cross-stream (y-z) plane at three different instances during the perturbation period at a downstream station x = 13 cm. The estimated streamwise vorticity fields at two of those instances are included in Figure 11. The region shown in these figures covers an area 1.8 cm × 4 cm. As before, except for remapping onto a regular grid, these are raw data. It is important to recognize that the mean streamwise flow direction is actually out of the page in this flow field. The high degree of three-dimensionality and the spatial structure of the streamwise vorticity are apparent. The maximum cross-stream velocity in Figure 10 is about 40% of the wake freestream velocity.

5. PASSIVE SCALAR MIXING DYNAMICS

In the non-reacting (passive scalar) implementation, the alcohol, CD, and lumophore are premixed in

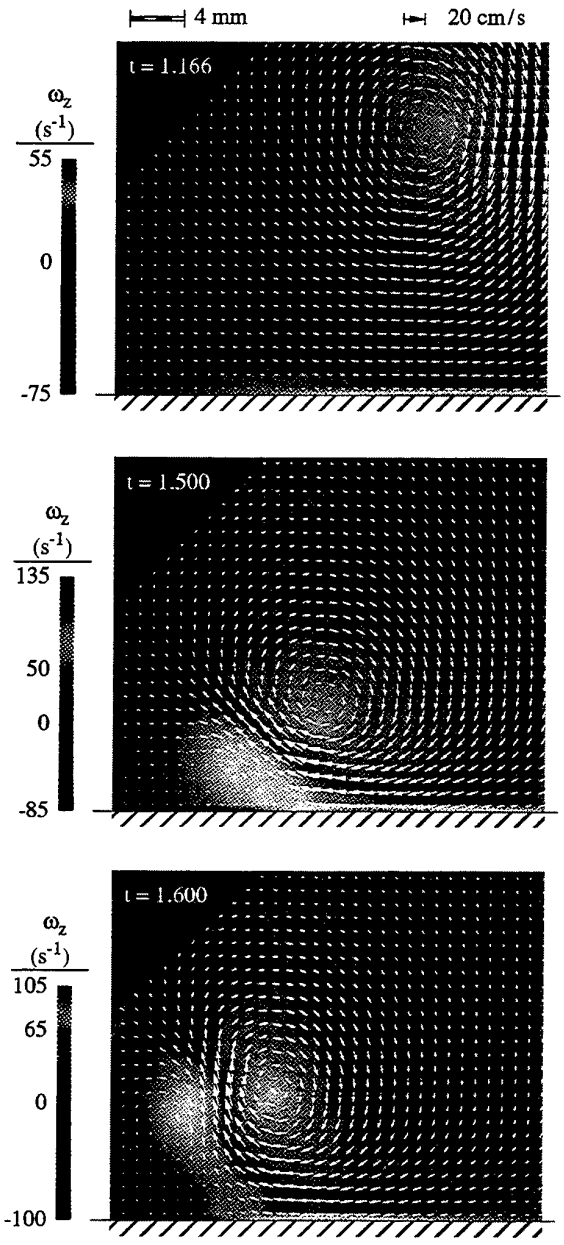

Figure 9. Velocity and vorticity details of the ring/wall interaction measured using MTV. Only the left-half of the flow field is shown.

one stream, and the other mixing stream is for example pure water or contains an alcohol solution. The Lagrangian evolution of the scalar mixing field is then monitored over the luminescence lifetime. An example of this implementation is shown in Figure 12. A vortex ring's fluid is premixed with the alcohol/CD/lumophore solution, and the ambient fluid contains only the alcohol solution. The UV laser is arranged to illuminate a series of parallel "bands" in the flow. Figure 12 shows the molecularly-tagged patches of the vortex ring fluid at the initial time (20 μs after laser firing), marked green, and the evolution of the same patches 9 ms later (marked red). The velocity vectors at the corners of the patches are determined by the same direct spatial correlation technique described earlier. Figures 13(a,b) show the velocity vectors in the laboratory frame and the vortex frame, respectively.

Even though the vortex ring example just shown has a rather simple concentration field (i.e. uniform within the tagged patches), it does highlight the potential of a molecular tagging approach for simultaneous concentration (from the first image) and velocity (using image pairs as in Figure 12) measurements in more complex and turbulent flows. In this case the spatially non-uniform scalar concentration field typical of most turbulent flows can be used as a natural source of the luminescence intensity variation described earlier. Where this can be accomplished, a much simpler optical arrangement with a laser sheet can replace the more involved technique of "writing" a prescribed laser pattern into the flow (e.g. the usual grid pattern). An example is given in Figure 14, illustrating the vortex ring of a starting jet illuminated by a pair of crossing laser sheets. The placement of the chemical components is the same as that in the example of Figure 12.

Figure 14(a) is the first image of the tagged flow acquired 20 μs after the laser firing; the second image, not shown here, is acquired 6 ms later. In a manner similar to that already described, the Lagrangian displacement of small regions (source windows) in the first image can be obtained using spatial correlation with "roam windows" from the second image. One example of a suitable source window is illustrated in Figure 14(b) along with the roam window from the second image in Figure 14(c); the dashed black square in the roam window indicates the initial location of the source window. The resulting correlation coefficient field indicates a well-defined peak whose pixel coordinates are determined to be $(\Delta x, \Delta y) = (-0.9, -5.3)$. Figure 14(e) shows the superposition of (b) over (c), after (b) has been moved to the location of the peak correlation (the solid black square).

It is implicitly understood that the correlation procedure applied to continuously distributed luminescence fields such as Figure 14(a) will yield accurate displacement information in two directions only if sufficient intensity gradients are present within the selected source windows. In the areas of the flow where this requirement is not satisfied, a non-uniform laser illumination can be used instead. The example of Figure 14 again highlights the potential for simulta-

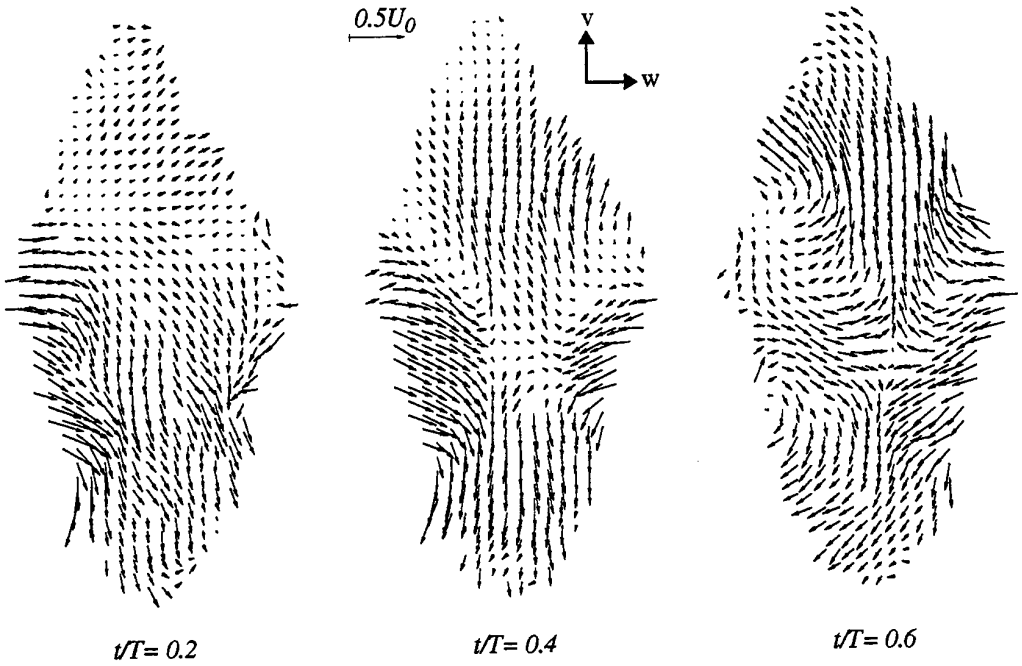

Figure 10. Raw instantaneous MTV velocity vectors of the cross-stream flow in a forced wake at three different instances in the forcing cycle. Note that the mean flow is out of the page.

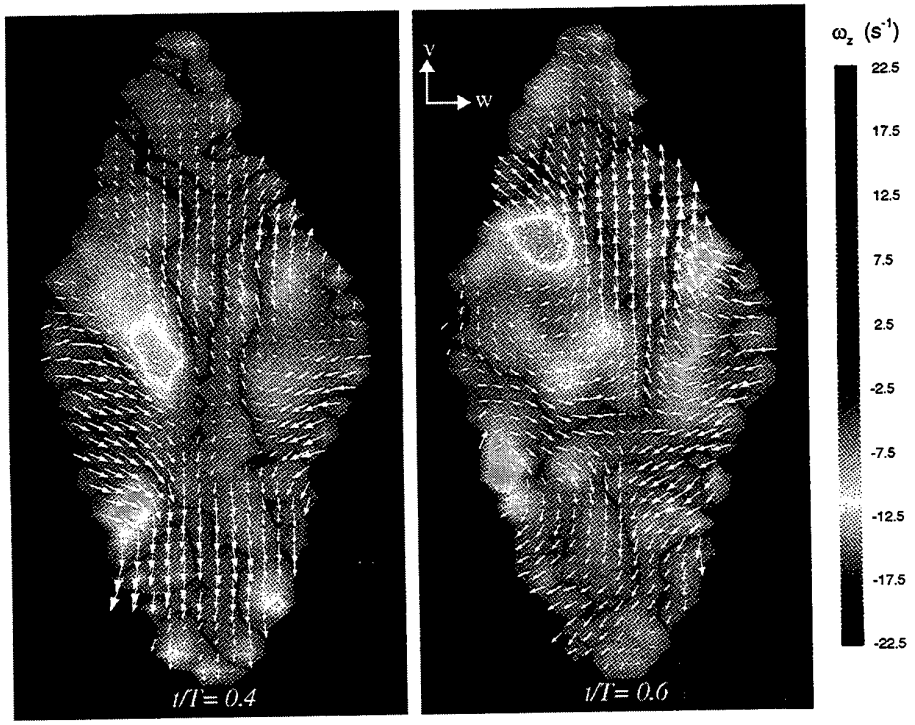

Figure 11. Instantaneous MTV velocity vectors and streamwise vorticity of the cross-stream flow in a forced wake.

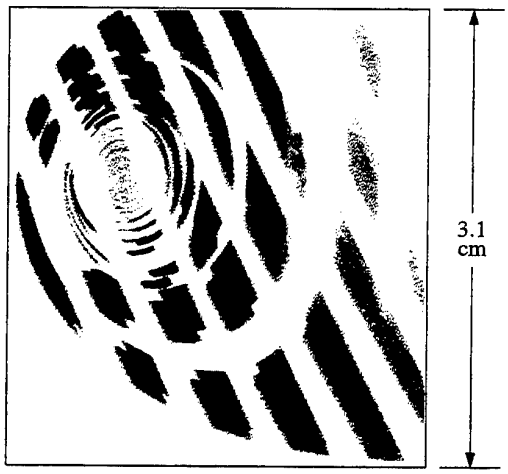

Figure 12. Lagrangian evolution of molecularly tagged fluid patches in a vortex ring. Only the left half of a downward-moving ring is shown. The ■ patches are regions imaged 20 μs after laser firing; the ■ patches are the same regions 9 ms later.

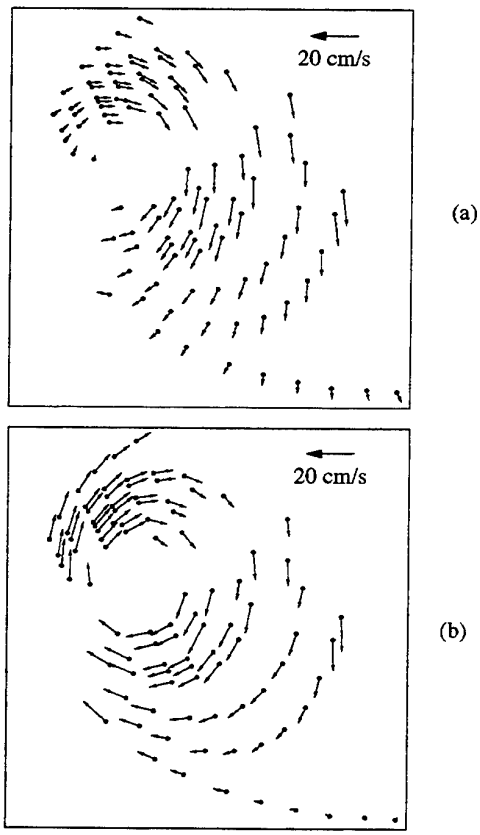

Figure 13. (a) Velocity vectors estimated using the corners of the patches in Figure 12. (b) The velocity field of (a) with the core convection velocity subtracted

neous concentration (from the first image) and velocity (using image pairs) measurements. Similar to the discussion earlier in Section 2.3, in cases where monitoring the evolution of the passive scalar field over very long time periods is desired, a much longer lifetime tracer such as caged fluorescein would have to be used.

6. CONCLUSIONS

New developments in molecular tagging diagnostics for velocimetry (MTV) and the study of the Lagrangian evolution of scalar mixing fields have been

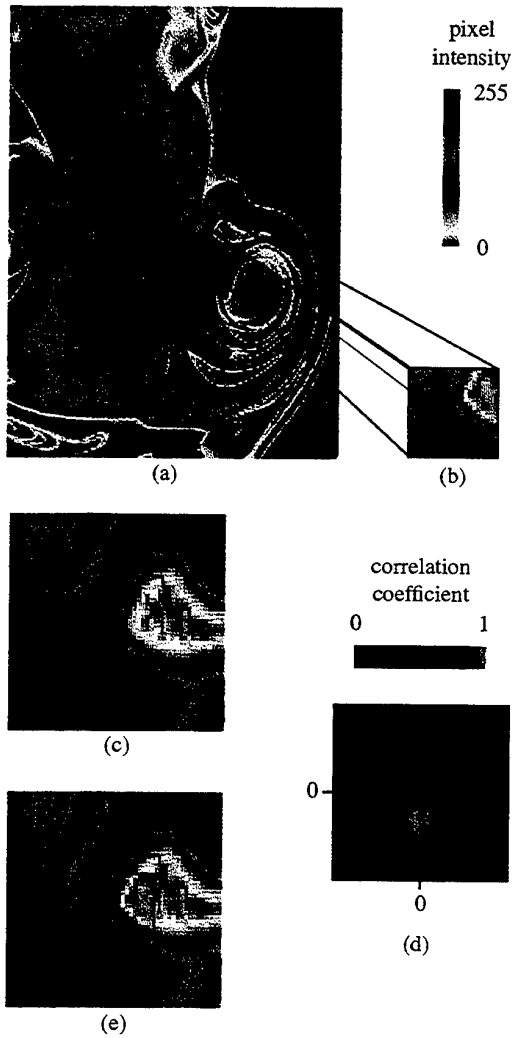

Figure 14. Correlation technique applied to experimental data from a mixing jet flow field. (a) Earlier image. (b) 21 x 21 pixel source window from (a). (c) 51 x 51 pixel roam window from the second image (not shown here). (d) correlation coefficient field. (e) superposition of source window over roam window.

described. The MTV approach is the molecular counterpart of PIV and offers certain advantages over PIV, primarily its lack of sensitivity to out-of-plane motion contaminating in-plane velocity data. This aspect has been demonstrated in an application of MTV to the highly 3-D velocity field of a forced wake. The potential of the molecular tagging approach for studying the dynamic evolution of mixing interfaces and combined scalar/velocity measurements has also been demonstrated.

ACKNOWLEDGMENTS

This work was supported in part by the Air Force Office of Scientific Research under grants F49620-92-J-0338 and F49620-95-1-0391, and the MRSEC Program of the National Science Foundation Award Number DMR-9400417.

7. REFERENCES

Chu, C. C. and Liao, Y. Y. 1992, A quantitative study of the flow around an impulsively started circular cylinder, *Exp. Fluids*, vol. 13, 137-146.

Chu, C. C., Wang, C. T. and Hsieh, C. H. 1993, An experimental investigation of vortex motions near surfaces, *Phys. Fluids A.*, vol. 5, no. 3, 662-676.

Cohn, R. K., Gendrich, C. P., Mackinnon, C. G., and Koochesfahani, M. M. 1995, Crossflow velocimetry measurements in a wake flow, *Bull. Am. Phys. Soc.*, vol. 40, no. 12, 1962.

Falco, R. E. and Chu, C. C. 1987, Measurement of two-dimensional fluid dynamic quantities using a photochromic grid tracing technique, *SPIE*, vol. 814, 706-710.

Falco, R. E. and Nocera, D. G. 1993, Quantitative multipoint measurements and visualization of dense solid-liquid flows using laser induced photochemical anemometry (LIPA), in *Particulate Two-Phase Flow*, Ed. M. C. Rocco; Butterworth-Heinemann, 59-126.

Gendrich, C. P., Koochesfahani, M. M. and Nocera, D. G. 1994, Analysis of molecular tagging velocimetry images for obtaining simultaneous multi-point velocity vectors, *Bull. Am. Phys. Soc.*, vol. 39, no. 9, 1980.

Gendrich, C. P. and Koochesfahani, M. M. 1996, A spatial correlation technique for estimating velocity fields using Molecular Tagging Velocimetry (MTV), *Exp. Fluids*, to appear.

Harris, S. R., Lempert, W. R., Hersh, L., Burcham, C. L., Saville, A., Miles, R. B., Gee, K. and Haughland, R. P. 1996, Quantitative measurements on internal circulation in droplets using flow tagging velocimetry, *AIAA J.*, vol. 34, no. 3, 449-454.

Hartmann, W. K., Gray, M. H. B., Ponce, A. and Nocera, D. G. 1996, Substrate induced phosphorescence from cyclodextrin · lumophore host-guest complexes, *Inorg. Chim. Acta*, vol. 243, 239.

Hilbert, H. S. and Falco, R. E. 1991, Measurements of flows during scavenging in a two-stroke engine, SAE Technical Paper 910671.

Hill, R. B. and Klewicki, J. C. 1995, Data reduction methods for flow tagging velocity measurements, *Exp. Fluids*, vol. 20, no. 3, 142-152.

Koochesfahani, M. M., Gendrich, C. P. and Nocera, D. G. 1993, A new technique for studying the Lagrangian evolution of mixing interfaces in water flows, *Bull. Am. Phys. Soc.*, vol. 38, no. 12, 2287.

Koochesfahani, M. M., Beresh, S. J. and MacKinnon, C. G. 1994, Volumetric visualization of 3-D flow structure in a low Reynolds number forced wake, *Bull. Am. Phys. Soc.*, vol. 39, no. 9, 1947.

Lempert, W. R., Magee, K., Ronney, P., Gee, K. R. and Haughland, R. P. 1995, Flow tagging velocimetry in incompressible flow using photo-activated nonintrusive tracking of molecular motion (PHANTOMM), *Exp. Fluids*, vol. 18, 249-257.

Lu, L. J. and Smith, C. R. 1985, Image processing of hydrogen bubble visualization for determination of turbulence statistics and bursting characteristics, *Exp. Fluids*, vol. 3, 349-356.

MacKinnon, C. G. and Koochesfahani, M. M. 1993, Three-dimensional structure and mixing of a forced wake inside a confined channel, AIAA Paper 93-0658.

Miles, R., Cohen, C., Conners, J., Howard, P., Huang, S., Markovitz, E. and Russell, G. 1987, Velocity measurements by vibrational tagging and fluorescent probing of oxygen, *Optics Letters*, vol. 12, no. 11, 861-863.

Miles, R. B., Connors, J. J., Markovitz, E. C., Howard, P. J. and Roth, G. J. 1989, Instantaneous profiles and turbulence statistics of supersonic free shear layers by Raman excitation plus laser-induced electronic fluorescence (Relief) velocity tagging of oxygen, *Exp. Fluids*, vol. 8, 17-24.

Miles, R. B., Zhou, D., Zhang, B., Lempert, W. R., and She, Z. S. 1993, Fundamental turbulence measurements by Relief flow tagging, *AIAA J.*, vol. 31, no. 3, 447-452.

Mortellaro, M. A. and Nocera, D. G. 1996, A turn-on for optical sensing, *Chemtech*, vol. 26, 17-23.

Ojha, M., Cobbold, R. S.C., Johnston, K. W., and Hummel, R. 1989, Pulsatile flow through constricted tubes: an experimental investigation using photochro-

mic tracer methods, *J. Fluid Mech.*, vol. 203, 173-197.

Ponce, A., Wong, P. A., Way, J. J. and Nocera, D. G. 1993, Intense phosphorescence triggered by alcohols upon formation of a cyclodextrin ternary complex, *J. Physical Chem.*, vol. 97, 11137-11142.

Popovich, A. T. and Hummel, R. L. 1967, A new method for non-disturbing turbulent flow measurement very close to a wall, *Chem. Engng. Soc.*, vol. 22, 21-25.

Stier, B. 1994, An investigation of fluid flow during the induction stroke of a water analog model of an IC engine using an innovative optical velocimetry concept -- LIPA, PhD thesis, Michigan State University, East Lansing, Michigan.

Stier, B., Koochesfahani, M. M., Nocera, D. G. and Schock, H. J. 1995, Molecular tagging velocimetry in gas phase flow, *Bull. Am. Phys. Soc.*, vol. 40, no. 12, 1962.

Yurechko, V. N. and Ryazantsev, Yu. S. 1991 Fluid motion investigation by the photochromic flow visualization technique, *Exp. Thermal and Fluid Sci.* Vol. 4, pp. 273-288.

TWO-DIMENSIONAL LASER DIAGNOSTICS FOR SOOTING FLAMES

S. Schraml, S. Will, D. Hofmann, K.-U. Münch, and A. Leipertz
Lehrstuhl für Technische Thermodynamik (LTT), Universität Erlangen-Nürnberg, Erlangen, Germany

ABSTRACT

The paper describes new laser-based diagnostic strategies towards a complete description of sooting flames. One technique presented is laser-induced incandescence (LII), which, in part in conjuction with extinction and scattering techniques, allows to obtain ample information on soot concentration and size, both of primary particles and clusters. The other technique introduced is filtered Rayleigh scattering (FRS), an extention of conventional Rayleigh scattering, which makes it possible to gather temperature information also in a sooting environment, yielding important information both for the evaluation of LII data and for a basic understanding of combustion.

Either method may be used in an imaging way enabling the acquisition of complete maps of soot parameters or temperature, respectively.

1. INTRODUCTION

The understanding of soot formation and oxidation both in model laboratory flames and in technical combustion processes heavily relies on suitable diagnostic techniques for both soot data and the underlying temperature field. For the measurement of the soot quantities required optical techniques are of major importance, as discussed by Charamlampopoulos (1992). Among these there are dynamic light scattering for the cluster size, as applied by Scrivner et al (1986), and various scattering and extinction methods, which have been used by Bockhorn et al (1981) and Puri et al (1993) to acquire information on both cluster size and structure and soot volume fraction. These methods are basically pointwise or show a line of sight character, in the latter case they are often combined with a tomographic reconstruction for axisymmetric problems in order to recover distributions at a given plane above a burner, as shown by Shaddix et al (1994). Besides a considerable effort necessary for a full information of the soot distribution these well-established optical techniques suffer from two substantial drawbacks. One disadvantage is that it is not possible to obtain data on the whole combustion field simultaneously, which limits the utility for non-stationary processes. Another limitation is that they most often require input data for the size of primary particles, which is not accessible directly by these techniques and is usually gained by a sample probe and subsequent electron microscopy, as used by Bockhorn et al (1981).

Alternatively, laser induced incandescence (LII) techniques have successfully been used for two-dimensional soot diagnostics, e.g. by Shaddix et al (1994). and Quay et al (1994), especially on soot volume-fraction. Will et al. (1995) have described a way to measure primary soot particle sizes by time-resolved LII (TIRE-LII).

A point of major importance to obtain accurate results is the provision of information on local gas temperature.

For instantaneous two-dimensional temperature measurement in gas combustion, Rayleigh scattering has proven to be a useful tool (see e.g. Kampmann (1994)). Its major disadvantage is the interference from elastic scattering from particles and surfaces that made investigation of sooting flames impossible. Here a novel filtering technique is presented that permits the detection of gas phase Rayleigh scattering in the presence of the orders of magnitudes stronger scattering of soot particles, enabling temperature determination in sooting flames.

2. LII - THEORY AND QANTITIES ACCESIBLE

2.1. Soot Volume Fraction

Basic principle of LII is to increase the temperature of the soot particles to slightly above vaporisation temperatures by means of an highly-energetic laser pulse and to detect the enhanced thermal radiation. The differential equation for the temperature of the primary particles assumed as spherical with diameter d_p follows from the conservation of energy and reads

$$Q_{abs}\cdot\frac{\pi d_p^{\,2}}{4}\cdot E_i-\Lambda\cdot(T-T_0)\cdot\pi d_p^{\,2}-\frac{\Delta H_V}{M}\cdot\frac{dm}{dt}-$$

$$-\bar{\varepsilon}(T)\cdot\sigma_{SB}T^4\cdot\pi d_p^{\,2}-\frac{\pi d_p^{\,3}}{6}\rho C\frac{dT}{dt}=0$$

The individual terms denote absorption of the laser irradiation (absorption efficiency Q_{abs}, irradiance E_i), heat transfer to the surrounding medium (heat transfer coefficient Λ, temperature T_0 of surrounding gas), vaporisation of soot particles (heat of vaporisation ΔH_v and molar mass M of carbon, loss of mass dm/dt), thermal radiation (mean

emission coefficient $\bar{\varepsilon}$, Stefan-Boltzmann-constant σ_{SB}) and raise of internal energy (density ρ and specific heat C of carbon).

According to Melton (1984) the radiative emission for a given wavelength λ_{em} and thus the detected signal S in the moment of maximum temperature (dT/dt = 0) can be calculated to give

$$S \propto N_p d_p^{\,x},$$

where the exponent is $x = 3 + 154\ nm / \lambda_{em}$ with emission wavelength λ_{em}. Thus, the LII technique may be used for the approximate determination of soot volume fraction f_v in spite of a slight overestimation and a bias towards larger particles, which may be tolerated for most practical applications.

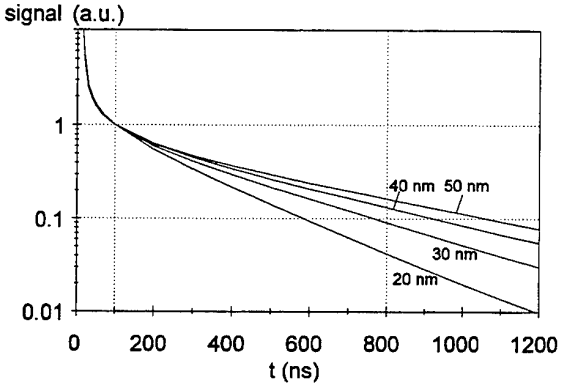

Fig. 1 Temporal behavior of the LII signal for various particle sizes

2.2. TIRE-LII and Primary Particle Size

The time-resolved LII technique is based on the fact that after an initial laser pulse smaller particles cool down faster than larger ones due to their larger specific surface. There are three paths for energy loss, namely vaporisation, heat conduction to the surrounding gas and radiation. High enough initial laser power provided, vaporisation is the dominant path for a period of order 100 ns, after which heat conduction is the most important heat transfer mechanism. It should be pointed out that radiative heat transfer contributes little (less than 5 % for all times) to the total temperature decrease, although there exists a detectable signal, and that all three paths are included in the heat transfer calculations.

From a numerical integration of the power balance a model for the particle temperature as a function of time can be set up. The relative LII signal S can then be calculated with the help of Planck's radiation function, where the emissivity, which equals the absorption efficiency, can be obtained from the usual Mie-formulae.

There are several aspects which have to be taken into consideration for a favorable application of TIRE-LII. One important point is how the moments of detection should be chosen. As to the first moment of observation it is favourable to avoid the first tens of nanoseconds of the decay, where the effects of vaporisation are predominant; a value of about 100 ns is a reasonable selection. As to the selection of the second point, signal statistics are of great importance, which obviously strongly depend on the detection system employed.

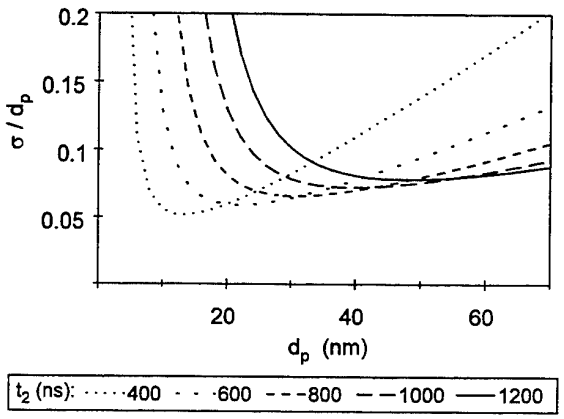

Fig. 2 Theoretical standard deviation of the particle diameter d_p measured, as it is obtained from photoelectron statistics.

With the use of a two-dimensional ICCD-camera a second moment of observation in the range of 600 - 1000 ns is favorable. The final choice also depends on the particle sizes to be expected. Short times appear advantageous for small particles, but only marginally suitable for larger ones.

The accurate determination of absolute values for monomer size relies heavily on the models used for the heat transfer mechanism and the LII signal and on correct physical data for the quantities involved therein. As the model calculations take into account particle shrinkage, the influence of parameters like refractive index or laser irradiance on the determination of original monomer size is present, yet not dominant. In general, as the energy transfer after some 100 ns is mainly determined by the internal energy of the soot particles and the heat transfer to the surrounding gas, the density and heat capacity of soot and the heat transfer coefficient Λ gain major importance. Following Melton's (1984) model, our calculations are also based on air as the surrounding medium due to a lack of knowledge on local gas composition, yet a differing thermal conductivity of the local gas mixture may affect the results considerably.

Furthermore, errors regarding local gas temperatures must be taken into account. Model calculations are based on a combustion temperature of 1800 K. Figure 3 illustrates the relative error in size obtained for a 30 nm particle for various values of t_2 and as a function of the gas temperature T_0, which is to represent the true local temperature. As it can be seen, the error increases with increasing t_2, because at later detection times an error in the temperature difference between the particles and the surrounding gas amounts to an increased error in the cooling rate. Yet the error is smaller as it may be expected, especially for large delay times, as the dependence of the thermal conductivity on temperature in part compensates for the effect of a wrong assumption of gas temperature. The local variation of monomer size may be determined more reliably in systems with moderate local temperature changes. Yet, generally, TIRE-LII performance may be significantly improved by providing information on local gas temperature.

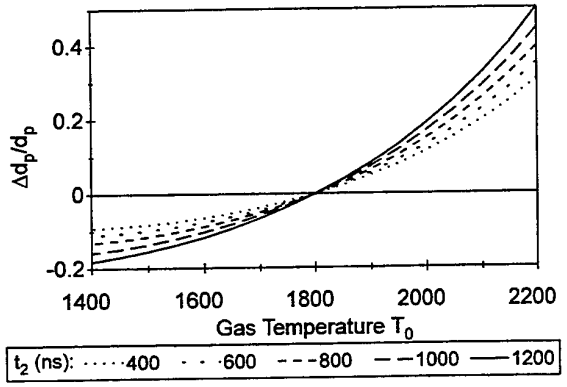

Fig. 3 Relative error in particle size for a 30 nm particle and various delays t_2, if the true gas temperature T_0 differs from the assumed value of 1800 K.

2.3. Combinative Techniques And Other Quantities Of Interest

Besides information about primary particle sizes also knowledge about cluster size is highly desirable. This may be achieved by a combination of LII and elastic scattering (ES). With the relationships for the signals of either technique, i.e.

$$S_{LII} \propto N_a n d_p^{\,3}$$

for the prompt LII signal and

$$S_{ES} \propto N_a n^2 d_p^{\,6}$$

for elastic scattering in the Rayleigh approximation, a relative value for the volume equivalent diameter D of a soot cluster may be obtained:

$$\left(\frac{S_{ES}}{S_{LII}}\right)^{1/3} \propto \left(\frac{N_a n^2 d_p^{\,6}}{N_a n d_p^{\,3}}\right)^{1/3} = n^{1/3} d_p = D.$$

Both for aggregate size and for soot volume fraction it is necessary to obtain at least one calibration point. In the case of f_V, this may be most easily accomplished by extinction measurements, where a laser beam with wavelength λ and incident energy flux I_0 is attenuated to a value I along the total length L of the combustion zone. For the determination of soot volume fraction a common approach is to approximate the extinction efficiency by the absorption efficiency, thus neglecting scattering, and to calculate absorption in the Rayleigh approximation, which according to Santoro et al (1984) results in the relationship

$$\ln\left(\frac{I_0}{I}\right) = \int_0^L 6\pi\, f_v\, E(\tilde{m})\lambda^{-1} dl,$$

where $E(\tilde{m})$ follows from the complex index of refraction. In an axisymmetric flame the volume fraction at each point may be achieved from scanning the laser beam through the whole flame and applying a subsequent tomographic reconstruction, as it has been demostrated by Puri et al (1984). In order to obtain a calibration constant for the LII measurements, it is sufficient, however, to compare the total absorption along a line of sight with the corresponding integral of the LII values.

A calibration value for the aggregate size may be obtained from a combination of extinction and scattering measurements, as shown by Pinson et al (1993).

With the volume fraction and the cluster size calibrated, it is a straightforward task to calculate other quantities required for the individual volume elements. The average number n of monomers in an aggregate follows directly from the relationship between aggregate and monomer size, the number concentrations of primary particles and aggregates, N_p and N_a, respectively, can be derived from the soot volume fraction and the corresponding sizes.

3. THEORY OF FILTERED RAYLEIGH SCATTERING

The frequency spectrum of scattered light from molecules stays constant in the centre frequency but can be broadened spectrally relative to the incident radiation. Due to the higher inertia, broadening of elastically scattered light of particles is neglegible while laser induced glare on surfaces is not broadened. A very narrowband absorption

filter at the centre frequency of the incident radiation can such be used to suppress the interfering unbroadend scattered light (Fig. 4). Unfortunately the major part of the Rayleigh signal is absorbed as well and only the shaded part in Fig. 4 can be detected.

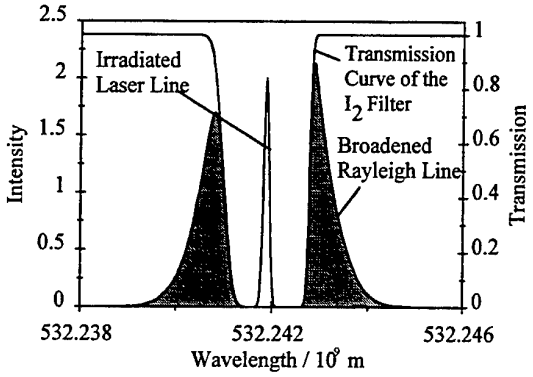

Fig. 4 Frequency distribution of the scattered light and the transmission of the filter

For the used frequency doubled Nd:YAG laser molecular iodine vapour exhibits the proper absorption characteristics concerning centre wavelength, halfwidth, cut off steepness and optical depth (Miles et al. (1994) and Gerstenkorn and Luc (1978)).

3.1. FRS Broadening Mechanisms

Boley et al. (1972) defined two regimes for the broadening of the Rayleigh line.

The kinetic regime discribes diluted gases where the mean free path of the molecules is large compared to the wavelenght of the irradiated light. The light is scattered by individual and undisturbed molecules, so the line shape of the broadened light is given by the Gaussian profile characteristic for Doppler broadening due to thermal motion (Fig 5):

$$S_{kin}(q,\varpi) = \left[(2\pi)^{0.5} / q v_0\right] \exp\left(-\varpi^2 / 2q^2 v_0^2\right)$$

Here v_0 is the speed of sound, ϖ is the frequency shift relative to the wavelength λ_0 of the incident laser and $|q| = 4\pi n \sin(\theta/2)/\lambda_0$ is the wave vector (n: the index of refraction, θ: the scattering angle between irradiation direction and detection path).

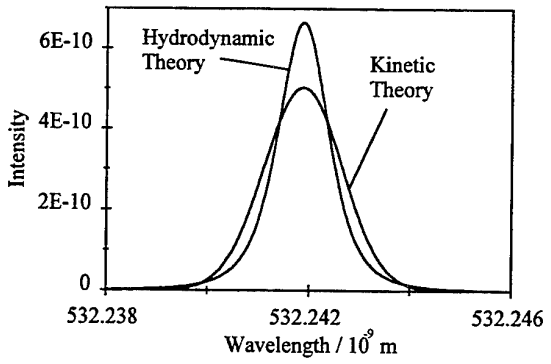

Fig. 5 Frequency distribution of the scattered light for nitrogen at 1 bar and 300 K

In the case of higher densities, the so called hydrodynamic regime, the Rayleigh scattering is due to density fluctuations, and thus to adiabatic pressure fluctuations and the fluctuation of entropy. The former fluctuations propagate and give rise to two distinct, shifted Brillouin lines. The latter fluctuations do not propagate and result in the unshifted component of the Rayleigh line. The composed line shape in the hydrodynamic regime is given by Kraft (1995) to:

$$S_{hd}(q,\varpi) = 2\frac{c_p - c_v}{c_p}\left(\frac{aq^2}{\varpi^2 + (aq^2)^2}\right) +$$

$$+2\frac{c_v}{c_p}\left(\frac{D_s q^2}{(\varpi - c_s q)^2 + (D_s q^2)} + \frac{D_s q^2}{(\varpi + c_s q)^2 + (D_s q^2)}\right)$$

with the thermal diffusivity a, the speed of sound c_s, the sound attenuation D_s and the isobaric and isochoric heat capacities c_p and c_v. The resulting curve in Fig. 5 does not show distinct Brillouin peaks as they merge with the unshifted component for the given conditions.

3.2. Temperature Determination by FRS

As in conventional Rayleigh scattering experiments, the gas phase temperature is derived from measured intensity distributions for isobaric conditions by comparing the scattered intensity I_M, measured e.g. in the flame, with the intensity I_N scattered by a known gas composition under known conditions (T_N, x_N, σ_N) corrected with the background intensity I_B for detector noise and flame luminosity (e.g. Fourguette et al. (1986) and Kampmann (1994)).

$$T_M = T_N \frac{I_N - I_B}{I_M - I_B}\frac{\sigma_M}{\sigma_N}$$

Contrary to conventional Rayleigh scattering, the effective scattering cross sections σ_i are defined by the ratio of the detectable intensity for the filtered case I_{FRS} to the detectable intensity for conventional Rayleigh scattering I_{Ray} times the conventional scattering cross section.

$$\sigma_{FRS} = \sigma_{Ray} \frac{I_{FRS}}{I_{Ray}}$$

The such derived FRS scattering cross sections depend on temperature, pressure, composition and filter characteristics. For temperature evaluation the first formular in this section is split into two ratios, a calculated and a measured one.

$$\frac{T_M}{T_N}\frac{\sigma_N}{\sigma_M} = R_C = \frac{I_N - I_B}{I_M - I_B} = R_M = f(T_M)$$

4. EXPERIMENTAL ARRANGEMENTS

The diagnostic techniques described above have been applied to laminar diffusion flames, where the fuel flow in a metal tube is stabilised by an air coflow in an outer tube; for the FRS experiments the flame was partly premixed. In the case of the LII experiments ethene, for FRS methane was used as fuel. Different burner gases have turned out to be necessary at the present state of the development of either technique and the technical equipment available, as on the one hand the weak LII signal in the lightly sooting methane flame prevents reasonable measurements with a larger time delay and on the other hand the suppression of the light scattered from soot particles is not sufficient in the strongly sooting ethene flames for the FRS technique.

Both kinds of measurements were performed with irradiation from a frequency-doubled Nd:YAG laser with a pulse duration of 8 ns (FWHM). For LII a light sheet is formed with an height of approximately 15 mm and a minimum thickness of about 300 µm by expanding the beam parallel to the burner axis and weakly focusing it in the perpendicular direction by cylindrical lenses. For a better definition of the light sheet rectangular stops were employed close to the burner. For FRS the same light sheet without the beam stops was used. Signal observation is performed by an intensified two-dimensional CCD-camera aligned perpendicularly to the light sheet and operated with a gate width of 20 ns.

For LII both a short-pass filter with a cut-off wavelength of 450 nm and an additional mirror for 532 nm are placed in front of the camera objective, resulting in a complete suppression of elastic scattering. The nominal resolution of the detection system was 0.15 × 0.15 mm^2. TIRE-LII experiments were carried out with delay times of 100 ns and 800 ns, respectively. For either LII technique 30 frames were averaged at a given time in order to reduce noise, and an averaged picture without laser irradiation was subtracted in order to account for the natural flame luminosity.

For elastic scattering images were taken with the help of an interference filter with a centre wavelength of 532 nm and a width of 8 nm (FWHM) instead of the filters used for LII. Extinction measurements were carried out with a HeNe laser at 633 nm where the beam waist was reduced to approximately 0.2 mm. In order to compensate for fluctuations in laser intensity, an additional reference photo diode was used. The accuracy of the transmission values obtained in this way is estimated to be about 0.2 - 0.3 %.

For FRS measurements an interference filter with a centre wavelength of 532 nm and a width of 8 nm (FWHM) was used in front of the camera to suppress flame luminosity and ambient light. The filter cell is a 230 mm long stainless steel tube with windows of 80 mm diameter at both sides. Cristalline iodine is placed into a side arm of the cell and the cell is evacuated to the partial pressure of iodine. The cell is placed into the detection path. Due to the higher distance to the flame, the effective resolution was 0.38 x 0.38 mm^2.

As for FRS a single absorption line of iodine is used, the laser has to have a strictly single mode behavior. Furthermore, the laser wavelength has to be tuneable to a strong absorption line of iodine. By using an external seed laser, the host laser could be tuned to four strong absorption lines by temperature control of the seed laser. The one with the least detuning of the gain centre frequency was chosen for most stable performance of the laser.

5. RESULTS AND DISCUSSION

5.1 Soot Parameters by LII

Figure 6a shows the soot volume fraction f_v for a height of 19 mm to 34 mm above the burner exit, as it was obtained from the prompt LII signal with a calibration by comparison to the integral extinction signal at 20 mm. In agreement with the expected behaviour for a laminar diffusion flame an annular region of maximum soot concentration and a decrease of f_v due to oxidation processes with increasing height can be observed. The comparison of volume fractions measured by LII and laser extinction with a subsequent tomographic reconstruction shows good agreement, also for different heights.

Primary particle sizes determined by TIRE-LII at acquisition times of 100 ns and 800 ns are depicted in Figure 6b, which in the annular region of high soot concentration exhibit a fairly constant plateau value and the expected decrease with an increasing residence time due to oxidation processes. There remains some uncertainty, however, regarding the absolute values, which are in a range

of approximately 20 nm to 80 nm and thus slightly larger as they have been reported by Dobbins et al (1990) for other ethene diffusion flames. This may be due to the lack of knowledge on local gas composition and temperature, which results in a considerable uncertainty, as discussed above. In order to reduce uncertainties due to local temperature variations, a measurement series for the temperature field has been started at our laboratory, based on the pure rotational CARS technique, as described by Seeger and Leipertz (1996). As first results indicate, the temperature in the upper region of the flame and in the annular zone of a high soot concentration are in part well above the 1800 K assumed throughout, and these corrections may result in reductions of particle size of more than 20 % in some instances.

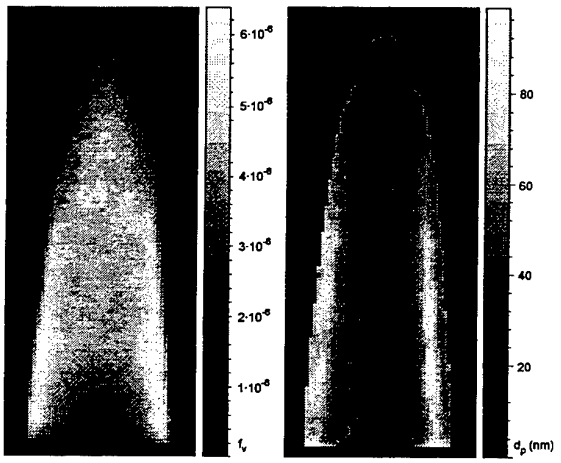

Fig. 6a Map of soot volume fractions f_v in the upper region of a laminar ethene diffusion flame.

Fig. 6b Primary particle sizes d_p from TIRE-LII measurements.

Combining prompt LII and elastic scattering information on aggregate size D may be deduced, which is shown in Fig. 7a. Due to the fact that an independent calibration has not been performed yet, cluster sizes can only be given on a relative basis, yet a decrease of cluster size can be observed with increasing residence time.

This observation is consistent with the concept of a decrease of primary particle size which is only partly balanced by an increase of the mean number n of monomers within a cluster. This quantity may be derived from the size information obtained by the combination LII/ES and TIRE-LII, respectively, but is again limited to give a relative information due to the lack of an absolute calibration standard for D. Although there might be considerable experimental error in this quantity, as two pictures both for TIRE-LII and the LII/ES combination and a third power are involved, the expected increase can be observed in Fig. 7b.

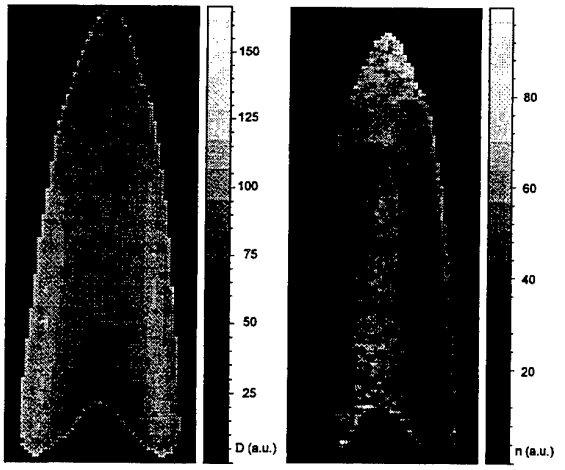

Fig. 7a Relative aggregate sizes D from the combination of prompt LII and elastic scattering.

Fig. 7b Relative distribution of the average number n of monomers within a cluster.

5.2. Calibration of FRS with Conventional Rayleigh Scattering

Temperature measurements in a non sooting methane-air flame with conventional Rayleigh scattering and FRS were made for verification. Unfortunately, for methane combustion at ambient pressure and detection of FRS in the visible neither of the introduced broading mechansims is strictly applicable. The broadening mechanism for that intermediate regime has to be between kinetic and hydrodynamic regime. The measurements yielded, as expected, to high temperatures with the kinetic line shape and too low temperatures with the hydrodynamic line shape. As up to now no combined theory can be presented, the measurements on the non-sooting flame were used for calibration of the FRS technique by fitting the kinetic model to the temperatures measured by conventional Rayleigh scattering (Hofmann et al. (1996)). This calibration factor was used for the measurements in the sooting flame as well, as the relevant factors for broadening mechanisms are of the same order for both cases. The deviations in the FRS scattering cross sections between fresh gas and exhaust gas are less than 4 % for the temperature range between 300 K and 2000 K.

5.3. FRS in a Sooting Flame

FRS measurementes were performed in a weakly sooting methane-air flame. From the volume fluxes of the feed gases the stochiometry was found to be $\lambda = 0.09$. This flame was adjusted such, that the scattered light of the soot

particles could completely be filtered out by the present iodine cell. Even though the flame was only weakly sooting, the scattered light of the soot particles obscures a significant part of the combustion field (Fig. 8) and limits the usable detector dynamic.

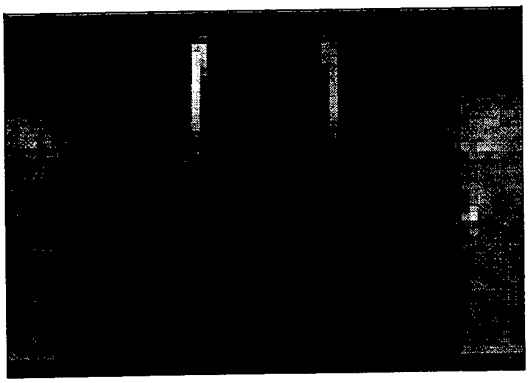

Fig. 8 Unfiltered scattering intensity in a sooting flame

With the absorption filter in the detection path, the scattering of the soot particles is supressed and the undisturbed temperature field can be derived (Fig. 9). The displayed cross sections show that no residuals of the soot scattered light can be seen in the temperature distribution. The crosses in Fig. 8 and 9 indicate the positions where the probability density functions in Fig. 10 were taken. They lie within the hottest detected region (PDF1) and the region of highest soot scattering intensity (PDF2). The PDFs have been calculated from 25 single-shot temperature distributions. The mean temperatures for the two points are found to be 1800 K and 1656 K, respectively.

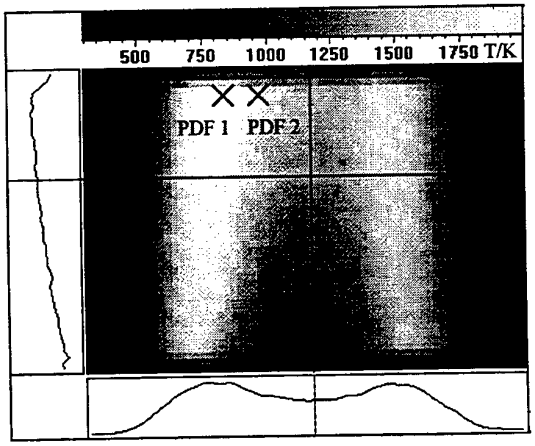

Fig. 9 Temperature distribution in a sooting flame

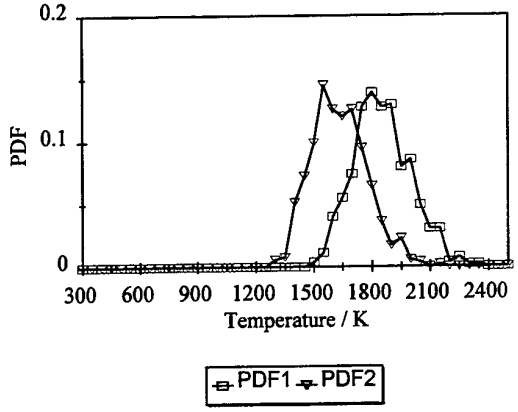

Fig. 10 Temperature probability density function at two selected points in the combustion field

6. CONCLUSIONS

It has been shown that laser induced incandescence data may form the basis for a comprehensive description of soot in combustion processes, where a two-dimensional information of soot volume fractions and particle sizes is required. Time-resolved LII offers the chance of obtaining a complete map of monomer sizes, which is not easily possible by any other technique known. Filtered Rayleigh scattering is an important tool for temperature measurements in sooting flames and can provide the information essential for understanding combustion processes, modelling the formation of soot and also for accurate measurements of other quantities, such as primary particle size by means of TIRE-LII.

Regrettably, mainly technical limitations did not allow to obtain information on soot parameters and temperature in a common object of investigation to date. Thus, the outstanding challenge for future work is to close the gap between the fields, in which either technique can be utilised now. Achievements are possible by the use of more advanced detection systems on the one hand and filter cells with a better suppression of light scattered from soot on the other hand. With these tasks solved it will be possible to obtain even more information required on sooting flames simultaneously.

ACKOWLEDGEMENT

The authors would like to thank A. Thumann for performing temperature measurements by the CARS technique. Burner plans have been made available by the Institute for Physical Electronics of the University of Stuttgart. Financial support for parts of the work by the German Ministry for Education and Research (BMBF) under conduct of the VDI-TZ

Physical Technologies in the frame of the project 13N6175 is gratefully acknowledged.

REFERENCES

Bockhorn, H., Fettig, F., Meyer, U., Reck, R. & Wannemacher, G. 1981, Measurement of the soot concentration and soot particle sizes in propane oxygen flames, Eighteenth Symposium (International) on Combustion, The Combustion Institute, Pittsburgh, pp. 1137- 1147.

Boley, C. D., Desai, R. C. & Tenti, G. 1972, Kinetic models and Brillouin scattering in a molecular gas, Can. J. Phys.,vol. 50, pp. 2158-2173

Charalampopoulos, T. T. 1992, Morphology and dynamics of agglomerated particulates in combustion systems using light scattering techniques, Prog. Energy Combust Sci., vol. 18, pp. 13-45.

Dobbins, R. A., Santoro, R. J. & Semerjian, H. G. 1990, Analysis of light scattering from soot using optical cross sections for aggregates, Twenty-Third Symposium (International) on Combustion, The Combustion Institute, Pittsburgh, pp. 1525- 1532.

Fourguette, D. C., Zurn, R. M. & Long, M. B. 1986, Two-dimensional Rayleigh thermometry in a turbulent nonpremixed methane-hydrogen flame, Comb. Sci. Technol., vol 44, pp. 307-317

Gerstenkorn, S. & Luc, P., 1978, Atlas du Specre d` absorption de la molecule d` Iode, Part 3, Centre National de la Recherche Scientifique, Paris

Hofmann, D., Münch, K.-U. & Leipertz, A. 1996, Two-dimensional temperature determination in sooting flames using Filtered Rayleigh Scattering (RS), accepted for publication, Opt. Lett.

Kampmann, S., 1994, Entwicklung einer zweidimensionalen Laser-Rayleigh-Temperatur-meßsonde zur Untersuchung hochturbulenter Verbrennungsvorgänge in einem industriellen Drallbrenner, Berichte zur Energie- und Verfahrenstechnik -BEV-, Heft 94.2, Esytec, Erlangen

Kraft, K. 1995, Bestimmung von Schallgeschwindigkeit und Schalldämpfung transparenter Fluide mittels der Dynamischen Lichtstreuung, Berichte zur Energie- und Verfahrenstechnik -BEV-, Heft 95.4, Esytec, Erlangen

Melton, L. A. 1984, Soot diagnostics based on laser heating, Appl. Opt., vol 23, pp. 2201-2208.

Miles, R. B., Forkey, J. N., Finkelstein, N. & Lempert, W. R. 1994, Precision whole-field velocity measurements with frequency-scanned filtered Rayleigh scattering, Proc. Seventh International Symposium on Application of Laser Technique to Fluid Mechanics, Lisbon, pp. 26.6.1-26.6.6

Pinson, J. A., Mitchell, D. L., Santoro, R. J. & Litzinger, T. A. 1993, Quantitative, Planar Soot Measurements in a D.I. Diesel Engine Using Laser-Induced Incandescence and Light Scattering, SAE Paper No. 932650.

Puri, R., Richardson, T. F., Santoro, R. J & Dobbins, R. A. 1993, Aerosol Dynamic Processes of Soot Aggregates in a Laminar Ethene Diffusion Flame, Combust. Flame, vol. 92, pp. 320-333.

Quay, B., Lee, T.-W., Ni, T. & Santoro, R. J. 1994, Spatially Resolved Measurements of Soot Volume Fraction Using Laser-Induced Incandescence, Combust. Flame, vol. 97, pp. 384-392.

Santoro, R. J., Semerjian, H. G. & Dobbins, R. A. 1983, Soot Particle Measurements in Diffusion Flames, Comb. Flame, vol. 51, pp. 203 - 218.

Scrivner, S. M., Taylor, T. W. Sorensen, C. M. & Merklin, J. F. 1986, Soot particle size distribution measurements in a premixed flame using photon correlation spectroscopy, Appl. Opt., vol. 25, pp. 291-297.

Seeger, T. & Leipertz, A. 1996, Experimental comparison of single-shot broadband vibrational and dual-broadband pure rotational coherent anti-Stokes Raman scattering in hot air, Appl. Opt. (accepted).

Shaddix, C. R., Harrington, J. E. & Smyth, K. C. 1994, Quantitative Measurements of Enhanced Soot Production in a Flickering Methane / Air Diffusion Flame, Combust. Flame, vol. 99, pp. 723-732.

Will, S., Schraml, S. & Leipertz, A. 1995, Two-dimensional soot particle sizing by time-resolved laser-induced incandescence, Opt. Lett., vol. 20, pp. 2342-2344.

SESSION 2

Two-Phase Flows
Instrumentation I

A device for phase shift measurement in an advanced phase Doppler velocimeter

James Evenstad, Amir Naqwi and Rajan Menon

TSI Incorporated, P. O. Box 64394, St. Paul, MN 55164, USA

Abstract

Construction and performance of a printed circuit board is described that is built for phase measurement in a state-of-the-art phase Doppler system. Special requirements in treating phase Doppler signals are highlighted and shown to be met satisfactorily by an innovative electronic design that involves signal burst detection, multi-bit sampling, frequency-band narrowing, and phase signal validation based on integrated amplitude and waveform recognition. Performance of the device is measured in terms of phase accuracy for various signal-to-noise ratios, signal frequencies and operating temperatures. The present device is also compared with some alternative techniques for phase measurement.

1. Introduction

A standard phase/Doppler system, for simultaneous measurement of particle size and velocity, is shown in Fig. 1. The output beam of an Argon-Ion laser is transmitted to the beam conditioning optics (ColorBurst™ of TSI), where the laser beam is split into two beams, such that one of the beams has a 40 MHz shift in frequency relative to the other one. The laser beams exiting the beam conditioning assembly are coupled into single-mode polarization preserving fibers, connected to the transmitting probe, which focuses a pair of monochromatic beams to intersect and produce interference fringes in a small volume. These fringes move with a frequency of 40 Mhz.

The particles under investigation scatter light as they cross the fringes. This light is collected by the phase/Doppler receivers and coupled to multi-mode fibers attached to them. These optical signals are transported to the transducer module (ColorLink™ of TSI), where they are converted into electrical signals using photomultipliers. The electrical signals, which have a carrier frequency of 40 MHz, are further conditioned using filters and downmixers, so that the signal pedestal is removed, noise is suppressed and signal frequency is brought into a desirable range. A transducer module designed for phase/Doppler applications employs common oscillators for downmixing various phase shifted signals, so that the phase difference between the signals is unaffected.

The downmixed signals are transferred to the signal processor, where phase and frequency measurements are conducted in parallel, in order to measure particle size and velocity respectively. The operating principle of the frequency processors under consideration (i.e. IFA 755 & 655 of TSI) is described in detail by Jenson (1990, 1992). This processor consists of a *burst detector* and a *double-clipped auto-correlator*. Single-bit digital auto-correlation is used to isolate the signal from the noise and to determine the signal frequency.

The auto-correlation process is made most effective by guiding it with the burst detector that continuously monitors the coherence in the electrical input to the processor, so that it determines the beginning and the end of a signal and provides this information as a *burst gate*. It also ascertains the optimal sampling rate for a fixed number (i.e. 256) of samples, so that there are always 10–20 samples per cycle (5–10 samples per cycle for the frequencies exceeding 50 MHz) of the signal.

Optimization of the sampling rate is important, as a lower than optimal sampling rate would result in too few samples per cycle, whereas an excessively large sampling rate would lead to too few cycles per burst. The optimal sampling rate is provided as a 4-bit output, referred to as the *burst code*.

The phase detector uses the burst gate and the burst code to optimize the measurement of phase lead of the first phase/Doppler signal relative to the second phase/Doppler signal, as illustrated in Fig. 2. Two such phase detectors can be housed in a standard IFA processor.

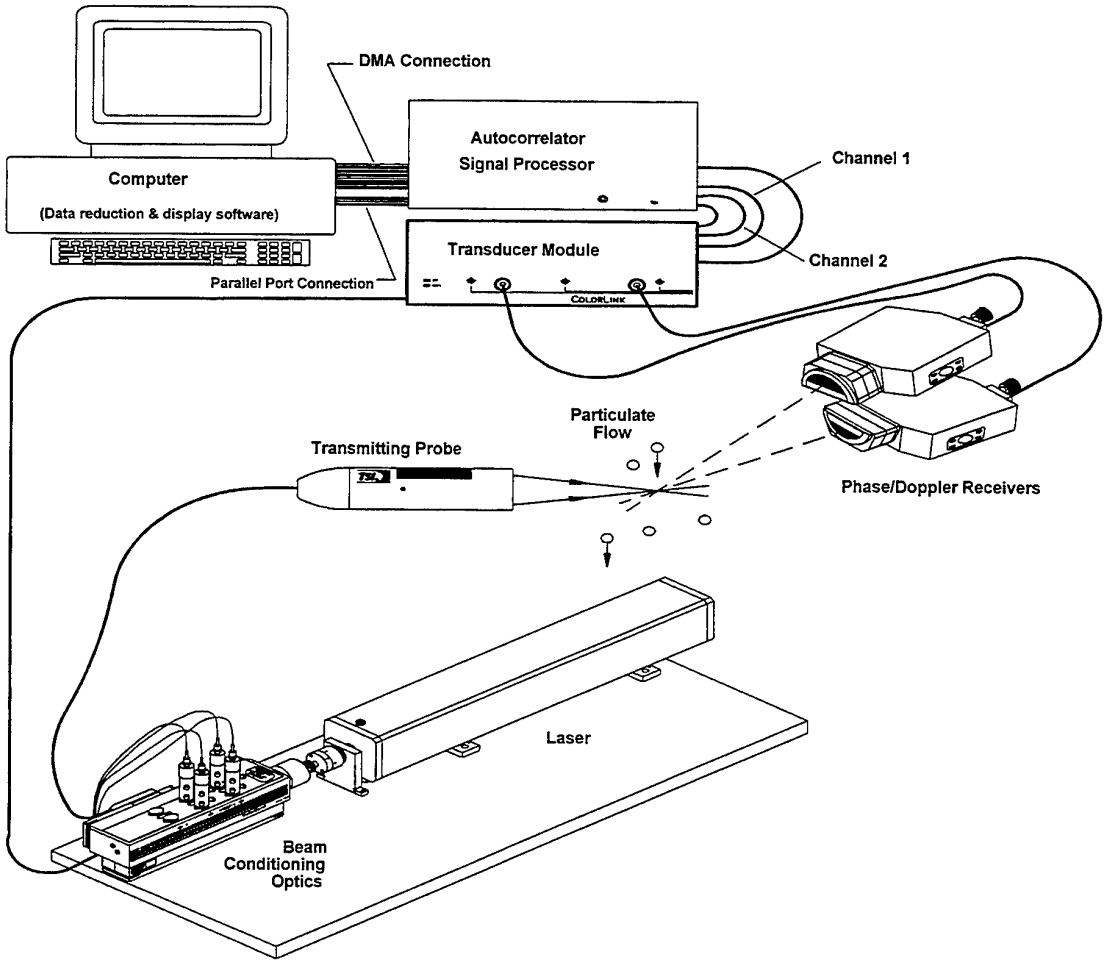

Figure 1: A standard phase Doppler setup

2. Phase Measuring Hardware

The phase detector is built as a printed circuit board and is included in IFA signal processors configured for phase/Doppler systems (APV). Hereafter, this phase measuring device will be referred to as *APV Board*. It combines several techniques to obtain accurate phase measurements on LDV type (i.e. burst-like) signals with low SNR.

The first APV signal is sent to a velocity channel as well as the APV Board. The velocity channel (see Fig. 2), delivers the burst gate and an estimate of signal frequency back to the APV Board.

The APV Board uses an 8-bit A/D converter for phase measurements. Using multi-bit A/D conversion, the sinusoidal waveform of the signals is preserved, which significantly enhances the resolution of the phase measurement in the present device.

The sampling process of these A/D converters is controlled by the burst gate and the frequency estimation code generated by the burst detector. Signals are digitized at a sampling rate of 5-10 samples per cycle and transferred to a first-in-first-out (FIFO) memory.

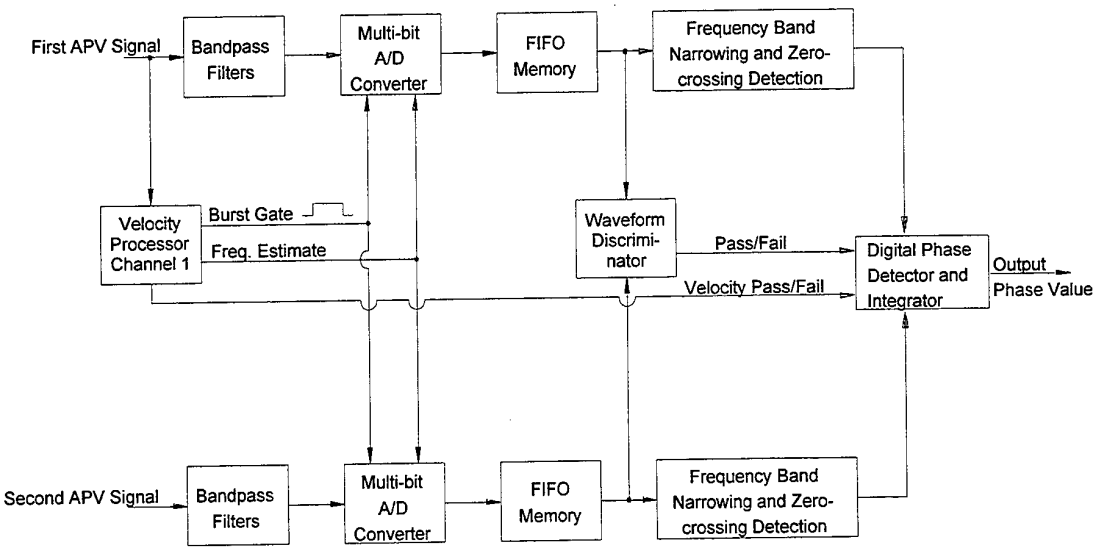

Figure 2: Schematic diagram of the APV Board

After the burst gate has ended, data from the FIFOs is read out and converted back to an analog signal to allow fast processing. The digitized data is read at a fixed rate of 40 MHz. Since the data was originally sampled at 5–10 samples per cycle, the reconstructed analog waveform has a frequency of 4 to 8 MHz, regardless of the input frequency.

Since the signals used to determine phase are now narrow band, there is less susceptibility to phase errors as the phase detectors can be optimized for a narrow (one octave) range. This technique has led to TSI's patent on frequency translation, see Evenstad (1995).

During frequency translation, waveform discrimination is performed and is very precise since it is done in the digital domain over a single octave bandwidth. The waveform discriminator monitors the digitized signals for minimum power level, sinusoidal shape and a minimum of 16 cycles. In order to validate the phase measurement, each input signal must have a qualifying burst.

Finally, the measured phase value is 10-bit digitized and placed in the output buffer. The phase shift measurement is completed prior to the frequency measurement and resides in the output buffer until the frequency measurement is available. Phase and frequency measurements are combined and delivered to the computer along with other auxiliary data.

3. Principle of Operation

The Basic Concept

As shown in Fig. 2, the reconstructed signals are provided to the zero-crossing detectors. Output of each zero-crossing detector is logic high for analog values above zero volts and logic low for analog values below zero volts.

The output of both the zero-crossing detectors is presented to a *pulse-width modulator* (PWM). The output of this device turns to logic high on the rising edge of the first signal and switches to logic low on the rising edge of the second signal, as shown in Fig. 3. The occurrence of high-level increases consistently with the increasing lead of the first signal relative to the second signal.

Since the maximum amplitude of PWM is fixed, the integrated value of the amplitude over a certain number of cycles is proportional to the phase shift. Hence, an integrator circuit follows the PWM on APV Board. The integrator essentially delivers a low-pass filtered value of the PWM output.

Phase Resolution near 0 and 360°

The above discussion was based on the assumption that the output of a zero-crossing detector is a perfect square wave. In practice, the rising and falling edges of this signal have finite widths, so that the phase measurement based on a single PWM is not reliable near 0 and 360°.

Accurate measurement of phase shift over the entire range of 0–360° is accomplished in APV Board by using three-phase detectors; i.e. two

pulse-width modulators and one exclusive OR gate. The operation of the first pulse-width modulator (PWM1) is already discussed above. PWM1 is used only for measuring phase shifts in the range [90°–270°].

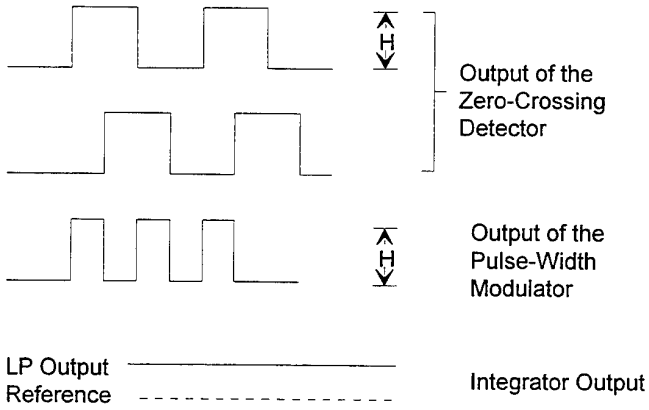

Figure 3: Pulse-width modulator and integrator

A second pulse-width modulator (PWM2) is used to measure the phase shift between the first signal and the inverse of the second signal, so that the output of PWM2 is shifted by 180° relative to PWM1. As illustrated in Fig. 4, PWM2 provides a stable output in the ranges [0°–90°] and [270°–360°]. Instabilities are encountered near 180°, as output of PWM2 switches from high to low.

To determine whether PWM1 or PWM2 should be used, a third phase detector is used, which performs the exclusive OR (XOR) function between the two signals and integrates the output. The integrated value is highest when there is a 180° phase shift between the signals, because either the first or the second signal is high all the time. As shown in Fig. 4, the integrated output of XOR decreases as the phase shift differs from 180° and reaches zero for phase shifts of 0° or 360°. As long as the XOR output voltage lies above a threshold V_C, the phase shift between the APV signals lies in the range [90°–270°] and PWM1 is used for phase measurement. As the output of XOR falls below V_C, PWM2 is used for phase measurement.

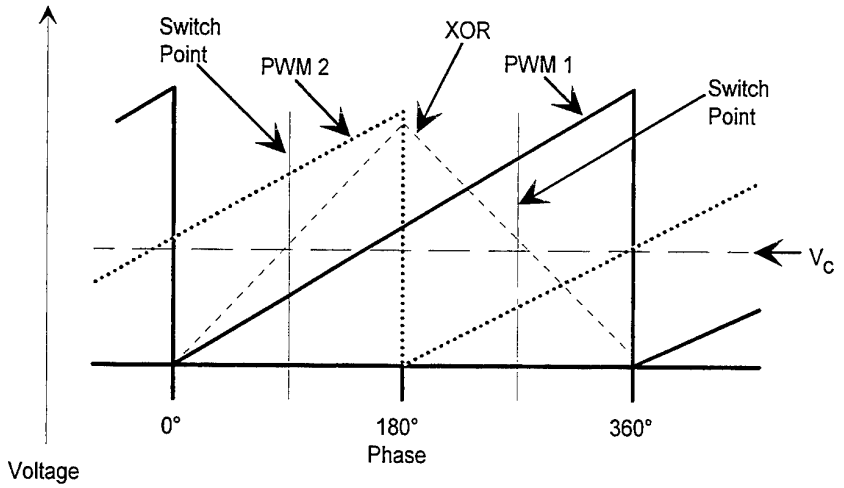

Figure 4: Detector voltages versus phase shift

Stabilizing the Pulse Height

Since the integrated amplitude is used for phase measurement, the accuracy of the measurement depends upon how well the amplitude of the PWM output is stabilized. The amplitude (H) must be invariant over frequency, temperature and time to obtain accurate values of the burst-averaged phase shift.

The output of the phase detectors show variations in the calibration if a large range of frequencies is involved. However, this uncertainty is eliminated in the APV Board by narrowing the frequency band to one octave prior to phase measurement.

Another proprietary technique allows to further stabilize the PWM output and makes it insensitive to variations in the operating temperature and supply voltage.

4. Experimental Evaluation

The APV Board was evaluated experimentally with signals of varying SNR. The SNR was defined as the ratio of the variance of the signal to the variance of the noise. It is understood that somewhat different definition of SNR may have been used in other studies. In order to compare the performance of APV Board with alternative techniques, a reference scheme of signal processing was also applied to the same signals that were processed by APV board. The reference measurements were conducted with a 4-bit FFT scheme as discussed by Host-Madsen (1995).

For generating noisy signals, the NoiseCom Model NC-6110 noise generator was used. This is a wideband (100 Hz – 1.5 GHz) white noise source. Phase shifted signals were generated on the Tektronix AFG2020 Synthesized Arbitrary Function Generator. The wideband (DC – 1.5 GHz) Mini-Circuits Model CAT-6 attenuators were used to achieve the various SNR levels. An oscilloscope was used to capture the data for the FFTs.

The test was performed on the 1–10 MHz filter range of the IFA 755. A TSI Model 1982 bandpass filter box was connected to the output of the noise generator and set to a 1–10 MHz bandwidth. This filter is a 5-pole LeGendre type and has much steeper cut-off than the APV Board's 3-pole Bessel filters. The use of this filter allowed more accurate calculations of actual SNR. The data used for the FFT calculations was *identical* to that used by the APV Board.

The signal frequency was 7 MHz, with phase set to 180° between the two channels. Since the oscilloscope was set to sample at 250 MHz, the number of samples per cycle for the FFT was 250/7 = 35.7.

The results are presented in Fig. 5 as standard deviation of error in the phase measurement versus signal SNR level. The FFTs were performed on 256-sample records and fifty different records were used to compute the standard deviation. All the quantization levels of the 4-bit sampler were used to cover the peak-to-peak variation in the signal amplitude.

For high SNR signals the APV Board provides a standard deviation of 0.83° which is better than the standard deviation of 1.26° (0.022 radian) reported for an alternative analog processor (Host-Madsen, 1995). Also, as compared to the reference case of 4-bit, 256-sample FFT, APV Board performs well with low SNR signals.

5. Conclusions

APV board for measuring phase shift between two burst-like signals is introduced. This device is compatible with the digital correlator (IFA series) that was introduced earlier for measuring frequencies of LDV signals. The combined system enables phase/Doppler measurements. The IFA signal processor uses a burst detector to determine the beginning and the end of the burst and to obtain the optimal sampling rate. The optimally-sampled *central portion* of the burst (with highest SNR) undergoes an auto-correlation for determining the signal frequency.

Simultaneously, each APV board performs a phase shift measurement between a pair of signals. The optimal sampling enables translation of all the signal frequencies to a single octave. This characteristic, combined with other innovative features, enables an accurate measurement of the phase shift. Experimental evaluation has shown that the performance of this device is at least comparable, and under some conditions, better than the alternative devices used for phase shift measurements in a phase Doppler system.

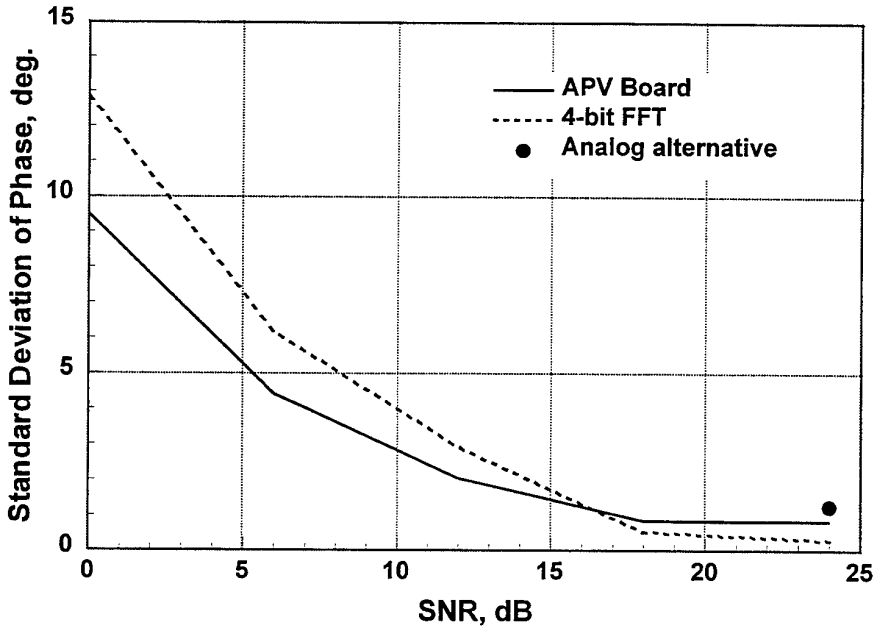

Figure 5: Effect of SNR on the standard deviation of the measured phase shift

References

Evenstad, J.: "Digital Burst Frequency Translator", US Patent Number 5,453,834 (1995).

Host-Madsen, A.: "Lower bounds for the accuracy of size measurement by phase Doppler anemometry", ASME FED-Vol. 229, Laser Anemometry, pp. 447–454 (1995).

Jenson, L. M.: "Coherent frequency burst detector apparatus and method", US Patent No. 4,973,969 (1990).

Jenson, L. M.: "LDV digital signal processor based on autocorrelation", Proc. 6th Intl. Symp. on Applications of Laser Techniques to Fluid Mechanics, Lisbon, paper 21.3, (1992).

Optimization of the shape of receiving aperture in a phase Doppler system

Amir A. Naqwi

TSI Inc.
St. Paul, MN, USA

Abstract

The *phase centroid* of an aperture used in a phase/Doppler velocimeter (PDV) is introduced. It is defined as the point detector whose phase response is identical to the finite-area aperture of PDV. The phase centroid is fixed only for certain aperture shapes and certain particle size ranges. Guidelines are provided to obtain a spatially invariant phase centroid.

It is also shown that displacement of the phase centroid with the particle size can be used to advantage, so as to extend the size range of a system without sacrificing its sensitivity to sizing small particles. Using special aperture shapes, the phase-diameter relationship may be made non-linear (even if the corresponding point detectors have a linear response), so as to have a high sensitivity for small particles and reduce it gradually to cover a large size range within 360° range of phase shift. This arrangement leads to a rather uniform percent-of-the-reading sensitivity of the system. Furthermore, the ambuiguity associated with the particle trajectory can be suppressed using shaped apertures.

1 The Basic Formulation

A receiving aperture with an arbitrarily varying width $w(x_A)$ is considered in Fig. 1, where x_A-axis is perpendicular to the scattered fringes and has its origin in the plane of symmetry of the phase Doppler system. The scattered light signal collected by a segment of thickness dx_A may be expressed as

$$dP_s = C_P\, w(x_A)\left[1+\cos\left(\omega_D t + \Delta\Phi\right)\right]dx_A\,, \qquad (1)$$

where C_P is a constant that has units of intensity. Assuming that the scattered fringe spacing s_f is uniform for a given particle diameter, the signal phase $\Delta\Phi$ is the phase shift for a point detector at x_A and is given as

$$\Delta\Phi = 2\pi x_A / s_f\,. \qquad (2)$$

The total scattered light signal is obtained by integrating Eq. (1) over the entire aperture, so that

$$P_s = P + F\cos\left(\omega_D t + \overline{\Delta\Phi}\right), \qquad (3)$$

where P and F are the *pedestal* and the *amplitude of fluctuation* respectively. These are given as

$$P = C_P \int_{x_{A\min}}^{x_{A\max}} w(x_A)\,dx_A \qquad (4)$$

and

$$F = C_P \sqrt{\left(\int_{x_{A\min}}^{x_{A\max}} w(x_A)\cos(2\pi x_A/s_f)\,dx_A\right)^2 + \left(\int_{x_{A\min}}^{x_{A\max}} w(x_A)\sin(2\pi x_A/s_f)\,dx_A\right)^2} \qquad (5)$$

In most of the PDV processors, the signals are *high-pass* filtered prior to measurement of phase shift and frequency, so that the signals can be represented by Eq. (3) without the first term on the right-hand side. Hence, the amplitude of fluctuation F represents the signal strength as seen by the processor.

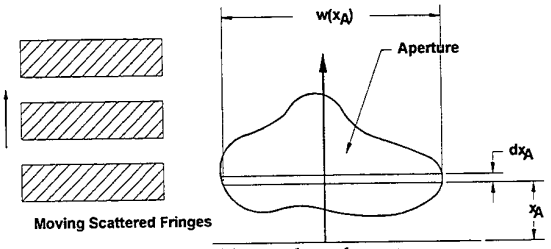

Figure 1: Arbitrary shaped aperture

The total phase shift $\overline{\Delta\Phi}$ is represented by

$$\sin\overline{\Delta\Phi} = \frac{C_P}{F}\int_{x_{A\min}}^{x_{A\max}} w(x_A)\sin(2\pi x_A/s_f)\,dx_A \qquad (6)$$

and

$$\cos\overline{\Delta\Phi} = \frac{C_P}{F}\int_{x_{A\min}}^{x_{A\max}} w(x_A)\cos(2\pi x_A/s_f)\,dx_A\,. \qquad (7)$$

The signal *visibility*, defined as the ratio of the fluctuation amplitude to the signal pedestal, may be expressed as

$$V = \frac{\sqrt{\left(\int_{x_{A\min}}^{x_{A\max}} w(x_A)\cos(2\pi x_A/s_f)\,dx_A\right)^2 + \left(\int_{x_{A\min}}^{x_{A\max}} w(x_A)\sin(2\pi x_A/s_f)\,dx_A\right)^2}}{\int_{x_{A\min}}^{x_{A\max}} w(x_A)\,dx_A} \qquad (8)$$

The phase difference between two symmetrically located receivers (see the preceding paper by *Evenstad et al.* in these proceedings) is given as

$$\Delta\Phi_{12} = 2\,\overline{\Delta\Phi}\,. \qquad (9)$$

For small values of phase angles, i.e. for large s_f or small particles,

$$\overline{\Delta\Phi} \approx 2\pi\bar{x}_A / s_f\,, \qquad (10)$$

where $\bar{x}_A$ represents the geometrical centroid of the aperture, given by

$$\bar{x}_A = \frac{\int_{x_{A\min}}^{x_{A\max}} w(x_A)\,x_A\,dx_A}{\int_{x_{A\min}}^{x_{A\max}} w(x_A)\,dx_A}\,. \qquad (11)$$

The phase-diameter relationship represented by Eqs. (10) & (11) is obtained by representing the tangent and sine

of small angles by the angles themselves and setting the cosine to 1. Similarly, using first two terms in the power expansion of sine and cosine functions the signal visibility may be expressed as

$$V = 1 - 2\left(\frac{\pi}{s_f}\right)^2 \left(\overline{x_A^2} - \bar{x}_A^{\,2}\right), \tag{12}$$

where

$$\overline{x_A^2} = \frac{\int_{x_{A\min}}^{x_{A\max}} w(x_A) x_A^2 dx_A}{\int_{x_{A\min}}^{x_{A\max}} w(x_A) dx_A}. \tag{13}$$

Clearly, visibility approaches 1 with decreasing particle diameter (i.e. increasing s_f) and narrowing aperture width along x_A-axis.

Comparing Eq. (10) with (2), the phase shift for the finite aperture is identical to that of a point detector at the centroid of the aperture. For small particles, the phase centroid of a finite aperture is represented by the geometrical centroid of the aperture regardless of its shape.

The phase-diameter curve is initially a straight line and is represented by a fixed point detector. However, according to Eqs. (6) & (7), location of the effective point detector may vary with the particle diameter for larger values of d_p. Equations (6)–(8) for phase and visibility are solved in the following sections for certain standard aperture shapes.

2 Rectangular Apertures

A rectangular aperture is characterized by the constant value of the width $w(x_A)$, so that the integrals in Eqs. (6)–(8) are easily evaluated. The results can be expressed as follows:

$$\sin\overline{\Delta\Phi} \propto \sin\left(2\pi\bar{x}_A/s_f\right)\sin\left(\pi\Delta x_A/s_f\right); \tag{14}$$

$$\cos\overline{\Delta\Phi} \propto \cos\left(2\pi\bar{x}_A/s_f\right)\sin\left(\pi\Delta x_A/s_f\right); \tag{15}$$

and

$$V = \frac{s_f}{\pi\Delta x_A}\left|\sin\left(\frac{\pi\Delta x_A}{s_f}\right)\right| = \left|\operatorname{sinc}\left(\frac{\pi\Delta x_A}{s_f}\right)\right|; \tag{16}$$

where

$$\Delta x_A = x_{A\max} - x_{A\min}. \tag{17}$$

According to Eqs. (14) & (15), phase shift can be given by an equation of the form (10), provided that the second factor, i.e. the common factor, on the right-hand side of Eqs. (14) & (15) has a positive sign. Otherwise, the phase is shifted by 180°; i.e.

$$\overline{\Delta\Phi} = 2\pi\bar{x}_A/s_f \quad \text{for} \quad 2ns_f \le \Delta x_A < (2n+1)s_f \tag{18}$$

and

$$\overline{\Delta\Phi} = \frac{2\pi\bar{x}_A}{s_f} - \pi = \frac{2\pi}{s_f}\left(\bar{x}_A - \frac{s_f}{2}\right) \quad \text{for} \quad (2n+1)s_f \le \Delta x_A < 2(n+1)s_f, \tag{19}$$

where $n = 0, 1, 2, \cdots$.

A *phase jump*, as pointed out by Naqwi & Durst (1991), occurs at the integer values of $\Delta x_A/s_f$. According to Eq. (16), the signal visibility vanishes at the point of each phase jump. For very small particles (or large s_f), the phase centroid is fixed and coincides with the geometrical centroid. It is shifted down abruptly by $s_f/2$ at $(2n+1)$th phase jump and shifted up at $2(n+1)$th jump.

With increasing particle diameter (i.e. decreasing s_f) the first phase jump occurs, when the scattered fringe spacing s_f reaches the thickness of the aperture Δx_A. Under this condition, the receiving aperture is continuously exposed to a complete scattered bright fringe and a complete dark fringe. Hence, the total amount of light collected by the receiver is unaffected by the motion of the scattered fringes. Consequently, the collected scattered light does not exhibit any oscillations, which is manifested as zero visibility.

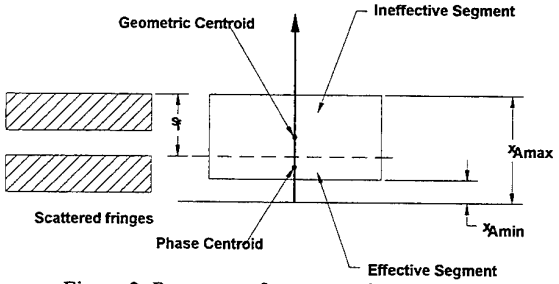

Figure 2: Response of a rectangular aperture

As the scattered fringe spacing reduces below the aperture height, the receiving aperture may be considered as being composed of two segments; i.e. the effective and the ineffective segments. The height of the ineffective segment equals the scattered fringe spacing, so that it does not contribute to the oscillations in the signal. The remaining aperture constitutes the effective segment, which is responsible for modulation of the signal. The geometrical centroid of the effective segment may be regarded as the phase centroid of the aperture, as shown in Fig. 2. Equation (19) is based on the assumption that the ineffective segment occupies the upper portion of the aperture, so that the phase centroid is shifted down after the phase jump. Alternatively, the ineffective segment could be considered as occupying the lower part of aperture. This would result in an upward shift in the phase centroid. The two alternative descriptions lead to phase-diameter relations that differ by a complete cycle, i.e. 2π radians.

After the second phase jump, a second ineffective segment may be identified. According to the formulation of Eqs. (18) & (19), an ineffective segment appears in the upper part of the aperture at each odd numbered phase jump and in the lower part at the even numbered phase jumps.

With decreasing s_f, a portion of the receiving aperture is "blinded" as it collects a fixed amount of light despite the motion of the scattered fringes. Such ineffective segments appear abruptly in the case of a rectangular aperture, because the shape of the aperture agrees with the shape of the scattered fringes. In the case of a non-rectangular aperture, the ineffective segments emerge gradually; i.e., the phase centroid is shifted gradually. Consequently, the signal visibility does not vanish completely.

In the case of a rectangular aperture, it seems most appropriate to design the aperture, such that the entire size range of interest lies in the first lobe of the visibility curve, so as to avoid the zero visibility condition. As a consequence, it suffices to treat the geometrical centroid as the phase centroid. In the earliest phase Doppler systems, the receiving apertures were nearly rectangular. This has been the reason for ignoring the shifts in the phase centroid in the early works on the technique.

As shown in the following section, the shifts in the phase centroid — in the case of non-rectangular apertures — may be substantial and may occur gradually with increasing particle diameter.

3 Trapezoidal Apertures

A trapezoidal aperture has the simplest shape that offers a variable width $w(x_A)$. Response of this aperture is examined to illustrate the gradual shifts in the phase centroid that may occur with increasing particle size.

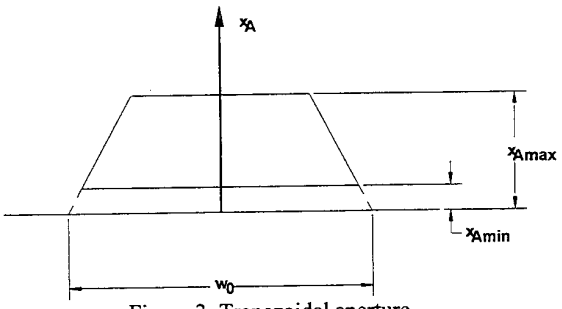

Figure 3: Trapezoidal aperture

The width of a trapezoidal aperture, as shown in Fig. 3, is given by

$$w(x_A) = w_0 - s_w x_A\,, \quad x_{A\min} \le x_A \le x_{A\max}\,, \tag{20}$$

where $x_{A\min} \ge 0$, $w_0 \ge 0$ and in the case of positive s_w, $x_{A\max} \le w_0/s_w$. In limiting cases this aperture may be reduced to a triangle or an inverted triangle with its vertex in the plane of symmetry.

Substituting Eq. (20) into Eq. (6), the following expression is obtained for the sine of the phase shift:

$$\frac{2\pi F}{C_P s_f}\sin\overline{\Delta\Phi} = w_0\left[\cos\left(2\pi x_{A\min}/s_f\right) - \cos\left(2\pi x_{A\max}/s_f\right)\right] + s_w\left[x_{A\max}\cos\left(2\pi x_{A\max}/s_f\right) - x_{A\min}\cos\left(2\pi x_{A\min}/s_f\right)\right] - \frac{s_w s_f}{2\pi}\left[\sin\left(2\pi x_{A\max}/s_f\right) - \sin\left(2\pi x_{A\min}/s_f\right)\right] \tag{21}$$

Similarly, by substituting Eq. (20) into Eq. (7), the cosine of the phase shift is expressed as

$$\frac{2\pi F}{C_P s_f}\cos\overline{\Delta\Phi} = w_0\left[\sin\left(2\pi x_{A\max}/s_f\right) - \sin\left(2\pi x_{A\min}/s_f\right)\right] - s_w\left[x_{A\max}\sin s\left(2\pi x_{A\max}/s_f\right) - x_{A\min}\sin\left(2\pi x_{A\min}/s_f\right)\right] - \frac{s_w s_f}{2\pi}\left[\cos\left(2\pi x_{A\max}/s_f\right) - \cos\left(2\pi x_{A\min}/s_f\right)\right] \tag{22}$$

The above relations can be reduced to Eqs. (14) & (15) for $s_w = 0$; i.e. a rectangular aperture.

For a trapezoidal aperture, the signal pedestal as given by Eq. (4) reduces to

$$P = C_P\left(x_{A\max} - x_{A\min}\right)\left[w_0 - s_w\left(x_{A\max} + x_{A\min}\right)/2\right]. \tag{23}$$

It may be noticed that the response of a trapezoidal aperture may be expressed in terms of three independent parameters; i.e. $2\pi x_{A\max}/s_f$, $x_{A\min}/x_{A\max}$ and $s_w x_{A\max}/w_0$. A triangular aperture may be defined by assigning the values of 0 and 1 to the second and third parameter respectively. The phase shift for this triangular aperture is examined below.

For the triangular aperture, Eqs. (21)–(23) are reduced to the following relations:

$$\frac{2\pi F}{C_P s_f w_0}\sin\overline{\Delta\Phi} = 1 - \operatorname{sinc}\left(3\pi d_p^*\right); \tag{24}$$

$$\frac{2\pi F}{C_P s_f w_0}\cos\overline{\Delta\Phi} = \frac{1-\cos\left(3\pi d_p^*\right)}{3\pi d_p^*}; \tag{25}$$

$$P = C_P\, w_0 x_{A\max}/2\,. \tag{26}$$

Using Eqs. (24)–(26), the signal visibility, as defined by Eq. (8), is expressed as

$$V = \frac{2\sqrt{9\pi^2 d_p^{*2} + 2\left(1-\cos 3\pi d_p^*\right) - 6\pi d_p^* \sin 3\pi d_p^*}}{9\pi^2 d_p^{*2}}, \tag{27}$$

where the non-dimensional particle diameter

$$d_p^* = \frac{2\bar{x}_A}{s_f}\,. \tag{28}$$

The symbol $\bar{x}_A$ represents the geometrical centroid of the triangular aperture, so that $\bar{x}_A = x_{A\max}/3$.

The non-dimensional diameter would be 1 for $\Delta\Phi_{12} = 360°$, provided that the phase centroid is fixed at the geometrical centroid, i.e. the initial slope of the phase-diameter curve is maintained. The size range $0 < d_p^* \le 1$ will be hereafter referred to as the *nominal size range*. As shown later, shaped apertures allow the

360° limit to be deferred to a larger value of d_p^*, such as 3.

According to Eq. (2), location of the phase centroid $\tilde{x}_A$ is given by

$$\tilde{x}_A = \frac{\overline{\Delta\Phi}}{2\pi} s_f = \frac{\overline{\Delta\Phi}}{3\pi d_p^*} x_{A\max} . \tag{29}$$

Since $\bar{x}_A = x_{A\max}/3$, the relationship between the phase centroid and the geometrical centroid may be expressed as

$$\frac{\tilde{x}_A}{\bar{x}_A} = \frac{\overline{\Delta\Phi}}{\pi d_p^*} . \tag{30}$$

Figure 4 shows the phase shift, visibility and the centroid location for the triangular aperture.

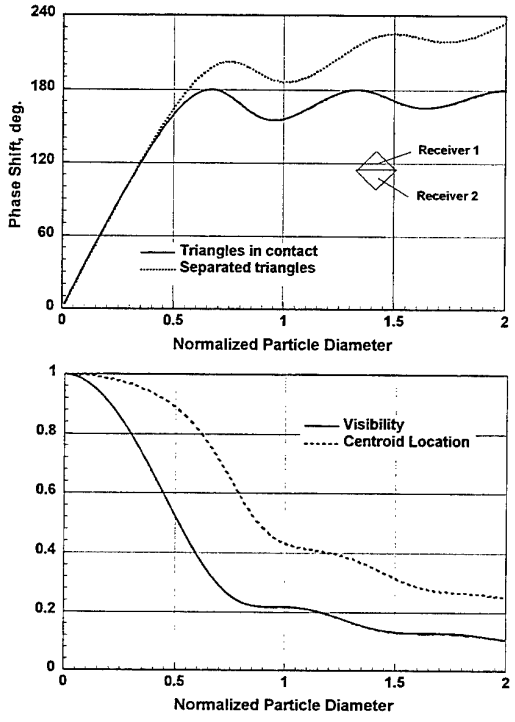

Figure 4: Response of the triangular apertures

The phase shift between a pair of triangular apertures saturates within the nominal size range and oscillates below 180°. As obvious from Eq. (25), $\overline{\Delta\Phi}$ is 90° for $d_p^* = 2/3, 4/3, 2, \cdots$, as the cosine of $\overline{\Delta\Phi}$ vanishes at these points. Consequently, $\Delta\Phi_{12}$ is 180° at the above values of d_p^*. It is also clear from Fig. 4 as well as Eqs. (24) & (25) that the limiting value of phase shift for very large diameters is 180°.

According to Fig. 4, signal visibility decreases gradually for a triangular aperture but does not vanish completely. The phase centroid is initially located at the geometrical centroid, i.e. $\tilde{x}_A/\bar{x}_A = 1$. It shifts towards the plane of symmetry with the increasing particle diameter.

Fig. 4 also includes the case of triangular apertures that are separated, so that $x_{A\min}/x_{A\max} = 0.03$, which corresponds to the experimental setup discussed in Sec. 6 below.

4 Aperture Shape for an Arbitrary Response Curve

The above discussion clearly shows that nonlinear phase-diameter relationships can be obtained using aperture shapes that are significantly different from a rectangle. Nonlinear response curves are desirable for the following reasons:

(i) To extend the size range, while maintaining a high sensitivity to small particles;

(ii) To obtain a uniform percent-of-the-reading sensitivity, i.e. an invariant value of

$$S_{por} = \frac{d\left(2\overline{\Delta\Phi}\right)}{100 d(d_p)/d_p} \tag{31}$$

for a pair of symmetric receivers;

(iii) To eliminate the 2π *ambiguity* by ensuring that the phase shift does not exceed 360°.

In order to meet the above requirements, one needs to solve the inverse problem, i.e. to calculate the aperture shape $w(x_A)$ for a given phase-diameter relationship $\overline{\Delta\Phi}(d_p)$. By multiplying Eq. (6) with $\sqrt{-1}$ and adding to Eq. (7), the integral can be expressed in the following form

$$\exp\left[i\,\overline{\Delta\Phi}(d_p^*)\right] = \int_{-\infty}^{+\infty} w^*(x_A^*)\exp\left(2\pi i d_p^* x_A^*\right) dx_A^* , \tag{32}$$

where the non-dimensional particle diameter is defined by Eq. (28). Furthermore, non-dimensional aperture width and height are introduced that are defined as below:

$$w^* = \frac{2\bar{x}_A C_P}{F} w , \tag{33}$$

$$x_A^* = \frac{x_A}{2\bar{x}_A} . \tag{34}$$

Note that the distance along x_A-axis is normalized with the spacing between the geometrical centroids of the two symmetrically located apertures. The above formulation allows one to treat the relationship between the aperture and the response curve as a *Fourier transform*.

In order for w^* to be real, the left-hand side of Eq. (32) must exist for both the positive and negative values of d_p^* and must satisfy the following relationship (see Press et al. (1986), Chap. 12):

$$\overline{\Delta\Phi}(-d_p^*) = -\overline{\Delta\Phi}(d_p^*) . \tag{35}$$

Negative particle diameter is a mathematical artifact that allows one to make use of the Fourier transform for

solving the inverse problem. Inverting the transform in Eq. (32),

$$w^*(x_A^*) = \int_{-\infty}^{\infty} \exp\left[i\overline{\Delta\Phi}(d_p^*)\right]\exp\left[-2\pi i d_p^* x_A^*\right] d(d_p^*). \quad (36)$$

It may be noticed that $w^*(x_A^*)$ is a delta function if the phase-diameter relationship is linear; i.e., the above formulation readily allows to recover the point detector arrangement.

For some phase-diameter relations, the corresponding function $w^*(x_A^*)$ may become negative for certain values of x_A^*, indicating that a realizable aperture shape does not exist. However, the exponential response curve, discussed below relates to a realizable aperture.

Various desirable features of a non-linear response curve discussed above are met closely by an exponential function of the following form:

$$\overline{\Delta\Phi} = \pi\left(1 - e^{-d_p^*}\right), \quad \text{for} \quad d_p^* \geq 0. \quad (37)$$

This function eliminates the 2π ambiguity by confining the phase shift to π for a single detector; i.e. the phase shift between two symmetric receivers would be restricted to 2π.

The percent-of-the-reading sensitivity for the above response curve is obtained by substituting Eq. (37) in Eq. (31), so that

$$S_{por}[\text{deg./\%}] = 3.6 d_p^* e^{-d_p^*}. \quad (38)$$

Although S_{por} is not constant, it varies slowly and remains above 0.5° per % in the range $0.2 \leq d_p^* \leq 3$. The largest value of S_{por} is about 1.32° per % and occurs at $d_p^* = 1$.

By extending the phase-diameter relationship of Eq. (37) to the negative diameters, in accordance with Eq. (35), a fast Fourier transform (FFT) algorithm could be used to compute the corresponding width function. The results are shown in Fig. 5. The aperture shape is fairly simple and may be approximated by a lognormal function.

Based on the above considerations, pairs of symmetrically located *lognormal apertures* are analyzed in detail in the following section.

5 Lognormal Apertures

It is understood that the response of the aperture in Fig. 5 would be unaffected if it is made symmetric by mirror imaging its contour about x_A -axis. The resulting aperture is shaped like an "onion" or a "tear drop", such as the shape depicted in Fig. 6. Such shapes can be implemented conveniently in practice. The lognormal apertures considered hereafter have symmetric onion-like shape.

A lognormal function has two independent variables. Four independent variables are needed if the coordinates of the lognormal function are shifted arbitrarily. Such a function may be expressed as

$$w = \frac{A_{lgn}}{(x_A + x_{A0})}\exp\left\{-\frac{1}{2\sigma_{lgn}^2}\left[\ln(x_A + x_{A0}) - \mu_{lgn}\right]^2\right\} - \Delta w,$$

for $x_{A\min} \geq x_A \geq 1$. (39)

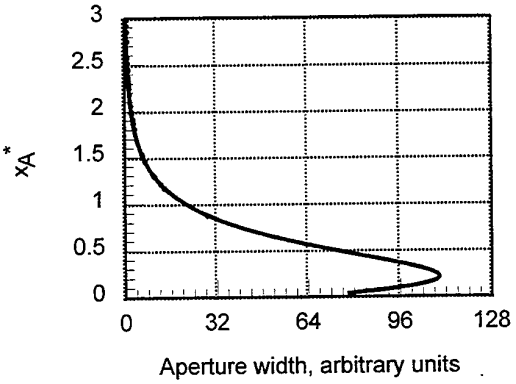

Figure 5: Aperture for an exponential response curve

The above aperture can be specified in terms of four parameters, i.e.

(i) $x_{A\min}$: the minimum value of normalized x_A, so that the maximum value is 1;
(ii) x_{A0}: the zero-shift of lognormal distribution along x_A -axis;
(iii) x_{Ap}: location of the maxima of the aperture width;
(iv) σ_{lgn}: width of the lognormal distribution.

Normalizing the maximum width of the aperture to 1, the parameters A_{lgn}, μ_{lgn} and Δw may be obtained from the relations:

$$\mu_{lgn} = \sigma_{lgn}^2 + \ln(x_{Ap} + x_{A0}); \quad (40)$$

$$\frac{1}{\Delta w} = (1 + x_{A0})\exp\left\{\frac{1}{2\sigma_{lgn}^2}\left[\ln\left(\frac{1 + x_{A0}}{x_{Ap} + x_{A0}}\right) - \sigma_{lgn}^2\right]^2 - \ln(x_{Ap} + x_{A0}) - \frac{\sigma_{lgn}^2}{2}\right\} - 1; \quad (41)$$

$$A_{lgn} = (1 + \Delta w)\exp\left[\ln(x_{Ap} + x_{A0}) - \frac{\sigma_{lgn}^2}{2}\right]. \quad (42)$$

Equations (6)–(8) were solved numerically for the above aperture shape. This numerical problem involves solution of integrals whose integrands are oscillating and may have many oscillations within the range of integration. For solution of these integrals efficient numerical schemes, provided by Stamnes (1986), were used.

Simulations show that it is important to minimize $x_{A\min}$ in order to significantly extend the nominal size range beyond 1. However, there are practical limits on the minimum gap between two symmetrically located apertures. Using a practically achievable value for the minimum gap, an optimal lognormal aperture can be

specified by the following combination of the shape parameters:

$$x_{A\min} = 0.04, \quad x_{A0} = 0.1, \quad x_{Ap} = 0.16, \quad \sigma_{\ln} = 0.65.$$

This shape is depicted in Fig. 6. The geometrical centroid of this aperture is located at $x_A = 0.3097$. The corresponding response curve, signal visibility and percent-of-the-reading sensitivity are given in Fig. 7. It can be seen that the size range is extended by a factor of three as compared to the nominal size range. Furthermore, the visibility is always non-zero and large enough to produce measurable signals. The sensitivity is such that over most of the size range, about 1° phase shift is obtained for 1% variation in the size.

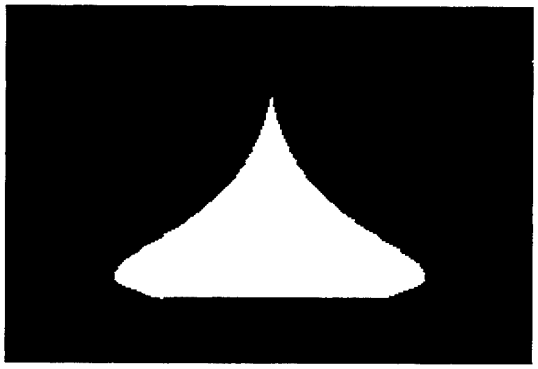

Figure 6: An optimal lognormal aperture

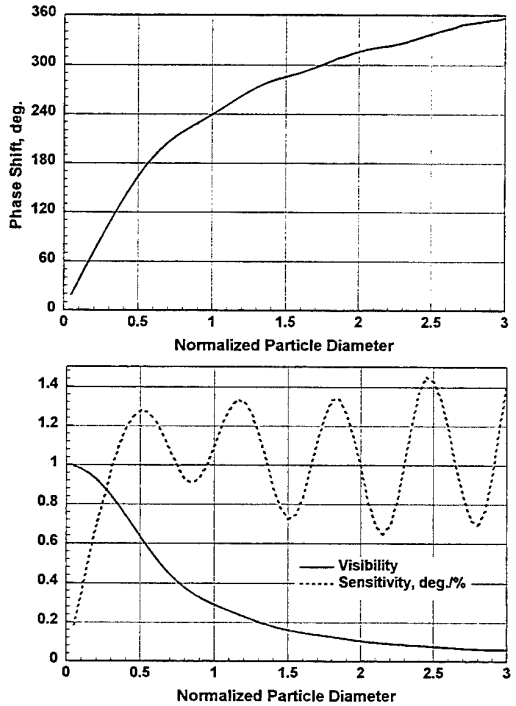

Figure 7: Response of the optimal lognormal aperture

Reduction in the signal visibility with increasing particle diameter is, in fact, a desirable feature of PDV. It is known that the signal strength increases with the square of the Mie parameter or particle diameter. However, due to decreasing visibility, the amplitude of fluctuation F would not increase so excessively. As explained in Sec. 1, parameter F represents the signal strength sensed by the signal processor. Uniform signal strength allows to obtain a uniform bit-resolution for the digitized signals, so that all the signals are processed with about the same precision. In the case of analog processors, the output of analog components varies with the signal amplitude. This source of uncertainty is suppressed if the signal amplitude is rather uniform.

Another adverse effect of large variations in the signal strength is discussed in Sec. 6, where effects of non-uniform illumination of the particle are taken into consideration. It is shown that the measurements are less prone to error if the signal strength is rather uniform over a wide range of particle diameters. The experimental results in the following section confirm that this objective can be achieved using lognormal apertures.

6 Experimental Results pertaining to Aperture Shape

The receiving optics of Adaptive Phase/Doppler Velocimeter (APV of TSI Inc.) allows to use external masks on the two receiving apertures, so that triangular apertures, similar to those described above, could be implemented. Measurements were taken with a spray of water, in which drop velocity correlates strongly with the drop size, i.e. larger drops move faster.

The measured phase shift versus velocity correlations are given in Fig. 8 for two sets of apertures, i.e. rectangular and triangular apertures. The triangular apertures were 36 mm high with $x_{A\min}/x_{A\max} \approx 0.03$ so that their response is expected to follow the curve for the separated receivers shown in Fig. 4. The rectangular receivers were matched with the triangular receivers in the location of the centroid as well as the cross-sectional area.

Figure 8 clearly shows that the phase response can be very different for two aperture sets with the same geometrical centroids. The rectangular receivers show an increase in the average velocity with increasing phase. Since phase increases linearly with drop size for rectangular apertures, this result illustrates the correlation between the drop size and drop velocity.

The triangular apertures exhibit a saturation of the phase response slightly above 180°, which verifies the theoretical result shown in Fig. 4.

In another set of experiments, the optimal aperture of Fig. 6 was used to measure a similar spray and the results were compared with the response of a pair of narrow rectangular apertures. Both the aperture shapes had the same geometrical centroids.

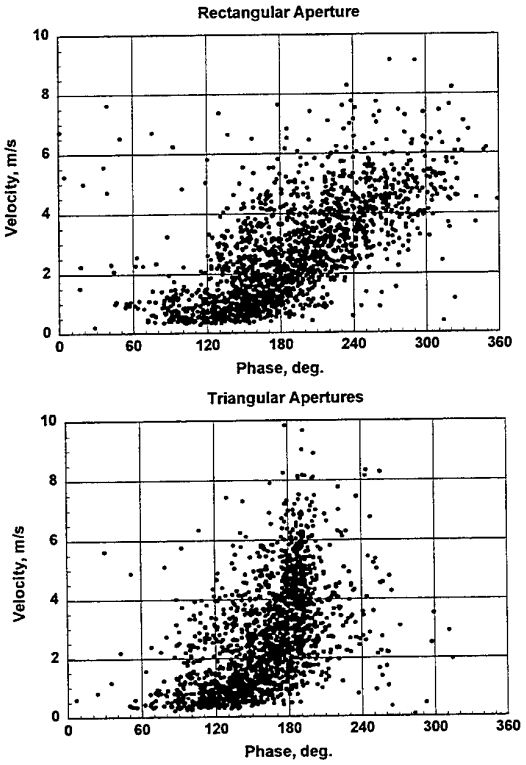

Figure 8: Phase-velocity correlations for rectangular and triangular receiver sets

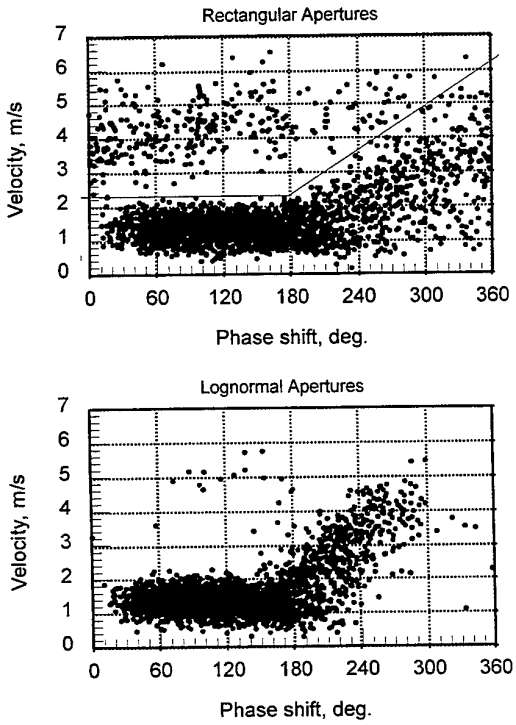

Figure 9: Phase-velocity correlations for rectangular and lognormal apertures

The phase-velocity correlations for the two aperture shapes are shown in Fig. 9. Clearly, the phase shift exceeds 360° in the case of rectangular apertures. The true phase shift for the data points above the dividing solid line in the upper plot of Fig. 9 is expected to be 360° in excess of the measured phase shift. After shifting the phases accordingly, the phase data were converted into the size distributions.

For the optical setup under consideration, the phase-to-diameter conversion factor of the rectangular apertures was 3.67°/μm; i.e. the nominal size range was 98.2 μm. This factor pertains to pure refraction and is based on the following optical parameters: beam half-angle, 3.94°; elevation angle, 2.11°; Wavelength of laser, 0.5145 μm; refractive index of the drops, 1.33 and off-axis angle, 74.74°. In the case of lognormal apertures, the correlation shown in Fig. 7 is used to convert the measured phase shifts into the normalized diameters, which are multiplied by the nominal size range to obtain the actual diameters.

The resulting size distributions are given in Fig. 10. The nominal size range is divided into 36 bins, so that each size bin is 2.73 μm wide. The vertical axis that represents the particle count in the corresponding bin is normalized, so that the total area under each curve is 100%.

According to Fig. 10, large drops are measured more frequently by the rectangular apertures, as the visibility of the corresponding signals is higher for the rectangular apertures. In the case of rectangular apertures, large drops generate measurable signals from a large portion of the fringe volume, including the outer regions where the intensity of illumination is low. Hence, the effective measuring volume is larger for large drops, provided that rectangular apertures are used. As shown by Saffman (1987), the r.m.s value of the burst length (which is defined as the product of particle velocity and the signal duration; both of these parameters were recorded) for a given size bin is a measure of the effective measuring volume for the corresponding drop size.

The r.m.s. burst lengths are plotted in Fig. 11 as a function of the drop size. For sizes exceeding 100 μm, there are very few drops in each size bin. Hence, large fluctuation are found in the r.m.s. burst length versus drop size relationship. Curve fitting with simple functions (using TableCurve 2D of Jandel Scientific) is used to estimate the stationary values of the r.m.s burst lengths.

According to Fig. 11, the effective measuring volume increases more significantly with the particle diameter for the rectangular apertures, as opposed to the lognormal apertures. In the case of lognormal apertures, the signal visibility decreases with the increasing particle diameter and hence, limits the strength of the filtered signals. As a result, the effective measuring volume diameter ceases to increase with the drop diameter.

The size distributions of Fig. 10 are corrected using the r.m.s burst length information from Fig. 11. The corrected temporal size distributions measured by the two aperture shapes are included in Fig. 10 and appear to agree well with each other.

It is known that signals from the outer regions of the measuring volume are undesirable as they may become dependent on the particle trajectory besides the size (see Gréhan et al., 1994 and the references therein). By eliminating such signals, the lognormal apertures also suppress the trajectory ambiguity associated with large drops.

7 Conclusions

Effects of the shape of receiving apertures on the response of a phase Doppler system are examined assuming uniform spacing between scattered fringes. It is shown that specially shaped apertures can be used to (i) extend the size range without sacrificing measurement sensitivity for small particles, (ii) obtain a uniform percent-of-the-reading sensitivity, (iii) suppress the 2π-ambiguity; i.e. keep the phase-shift smaller than 360° for a very wide range of particle diameters, (iv) obtain relatively uniform amplitude of filtered signals, by ensuring that the signal visibility decreases consistently with increasing particle diameters, (v) suppress the trajectory ambiguity associated with large particles.

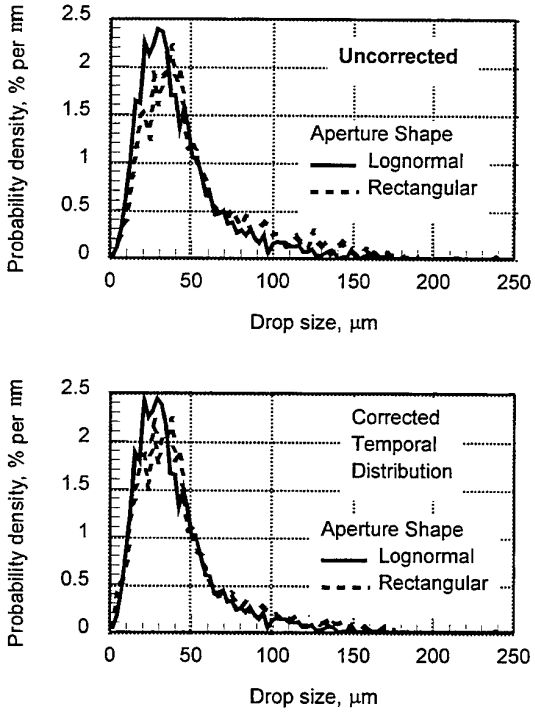

Figure 10: Size distributions measured by the lognormal and rectangular apertures

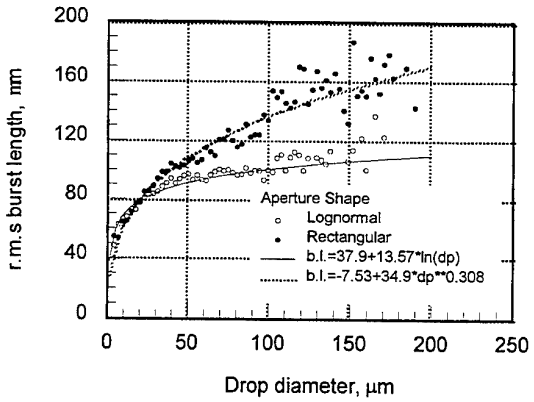

Figure 11: Root-mean-square burst lengths measured by lognormal and rectangular apertures

The above effects have been verified experimentally. Future work would involve rigorous simulations of the shaped apertures, using Mie scattering theory and the generalized Lorenz-Mie theory (see Gréhan et al., 1994 and the references therein).

References

Gréhan, G.; Gouesbet, G.; Naqwi, A. & Durst, F.: "Trajectory ambiguities in phase Doppler systems: study of a near-forward and a near-backward geometry", Particle and Particle System Characterization 11 (1994) 133–144.

Naqwi, A. & Durst, F.: "Constraints on the size and shape of receiving aperture in a phase Doppler system", Particle and Particle System Characterization 7 (1990) 113–115.

Saffman, M.: "Automatic calibration of LDA measurement volume size", Applied Optics 26 (1987) 2592–2597.

Stamnes, J. J.: "Waves in Focal Regions", Hilger, Bristol, 1986.

A NOVEL ARCHITECTURE FOR REAL-TIME PHASE MEASUREMENT

K.M. Ibrahim, and W.D. Bachalo

Aerometrics, Inc.
Sunnyvale, California
U.S.A.

Abstract:
The basic requirements for the implementation of a real-time phase measurement have been addressed in this paper. Both the analog and the digital approaches of implementation have been evaluated. For the digital approach, the effect of quantization has been thoroughly analyzed. For Phase Doppler (PDPA) applications, the amplitude dynamic range exceeds 1:2500. In order to digitally record and reproduce these signals, a 16-bit ADC (i.e 2^{16} quantization levels) should be used. It is shown that for accurate phase measurement, the efficiency of the sampler to encode (or represent) the signal phase information is far more important than the number of bits used in the analog-to-digital conversion (ADC). A novel sampling scheme using a 1-bit ADC is then developed and evaluated. It is shown that the performance of the developed scheme surpasses that of the conventional sampling methods with 1-bit and 8-bit ADC's. A practical implementation of the digital approach is described and its performance is evaluated. The implementation utilizes the innovative architecture provided by the Real-time Signal Analyzer (RSA).

1- Introduction::

For the early generations of PDPA signal processors, zero crossing counting methods have been used for both frequency and phase measurements. With these methods, the phase between two signals is measured by measuring the signal period and comparing it with the time between the positive slope zero crossings of the two signals. These methods are simple and accurate provided that the signal SNR is better than 10 dB and the signal bandwidth is less than 20 MHz. The need to work within progressively more difficult environments over larger frequency bandwidths necessitates the use of more powerful signal processing methods. It is well known in the literature that the Fourier analysis method provides the optimum performance. In fact; in many cases, this method proves to be the only method that provides reasonable results [1,2,3].

With the Fourier analysis method, the frequency is first estimated by computing the signal spectrum and extracting the frequency with maximum power. A reference sinusoidal signal is then generated. The frequency of the reference signal is set to the estimated signal frequency. The phase of each signal with respect to the reference signal is then computed by correlating each signal with the reference signal. The phase difference is then computed by subtracting the pairs of phase measurements. With this method, phase measurement accuracy is inversely proportional to the measurement time and the SNR. When sampled data is used, the variance of the phase is then given by [2]:

$$\mathrm{var}[\phi]=\frac{2(2N-1)}{\mathrm{SNR}N(N-1)} \qquad (1)$$

It is clear from the above equation that for a specified SNR, the only way to improve the phase measurement accuracy is by increasing the number of samples N. However, this will significantly complicate the hardware. Most of the increase in hardware complexity is associated with the frequency measurement as explained in the following paragraph.

For real time phase measurement, real time frequency measurement has to be performed prior to the actual phase measurement. In fact; the algorithm for phase measurement is divided into two parts. In the first part, the signal frequency is measured. The actual phase measurement is performed in the second part. It will be shown later that the complexity of the actual phase measurement is given by $\vartheta(N)$ (i.e. the number of the computations is proportional to the number of samples). The significant increase in the algorithm complexity is associated with the frequency estimation with an accuracy better than f_S / N. The Fast Fourier Transform (FFT) algorithm is one of the most efficient algorithms for this task and its complexity is given by $\vartheta(N \log N)$. This clearly shows that the complexity of frequency measurement algorithm is an order of magnitude greater than the complexity of the actual phase measurement algorithm.

The need to measure the frequency prior to phase measurement has been so far the main obstacle for the implementation of real time phase measurement. Moreover, the need to work over a wide amplitude and frequency dynamic range with transit times less than 1us has added to

the complexity of implementation. For example, to measure the size over a dynamic range of 1:50, the signal amplitude dynamic range can be well above 1:2500. Thus, if the digital approach is considered, the number of quantization levels needed to properly represent the signal should be more than 2500 levels. This corresponds to a 16-bit ADC. Such ADC's are not available at sampling frequencies exceeding 1 MHz.

In the following two sections, we will outline the essential elements of a Fourier analysis based signal processor for real-time phase measurement. In section 4, the effect of quantization is examined. These three sections provide a better understanding of the difficulties encountered with real time phase measurement. A practical implementation of a real time phase measurement scheme is described in section 5.

2- Basic Elements of a Real Time Phase Measurement Scheme:

With the Fourier analysis phase measurement, the frequency is first estimated. The frequency is measured by computing the signal spectrum and extracting the frequency where the signal has its maximum power. Let f_{es} be the estimated frequency. A reference sinusoidal signal is then generated. The frequency of the reference signal is set to f_{es} . The phase of each signal with respect to the reference signal is then computed by correlating the signal with the reference signal. The phase difference is then computed by subtracting the two measurements of phase.

When a quadrature (complex) signal is used, the signal *s(t)* can be represented as $s(t) = r(t) + jq(t)$ where

$$r(t) = A\cos\left(2\pi f_1 t + \phi\right) + n(t), \quad q(t) = A\sin\left(2\pi f_1 t + \phi\right) + \overset{v}{n}(t)$$

and $\overset{v}{n}(t)$ is the Hilbert transform of *n(t)*. With the Fourier analysis method the phase of the signal *s(t)* is computed using the following equation:

$$\phi_{es} = \tan^{-1}\left\{\frac{\frac{1}{T}\int_0^T\left\{-r(t)\sin\left(2\pi f_{es}t\right) + q(t)\cos\left(2\pi f_{es}t\right)\right\}dt}{\frac{1}{T}\int_0^T\left\{r(t)\cos\left(2\pi f_{es}t\right) + q(t)\sin\left(2\pi f_{es}t\right)\right\}dt}\right\} \quad \text{..... (2)}$$

where *T* is the time over which the phase is measured.

Examining the above equation, one may conclude that, any scheme for real time phase measurement requires the following:

1- A method for instantaneous frequency measurement using the Fourier analysis method. In section 3, we will present an analysis to determine how accurate the frequency should be resolved.

2 - A technique for instantaneous generation of variable frequency reference sinusoidal waves $\cos\left(2\pi f_{es}t\right)$ and $\sin\left(2\pi f_{es}t\right)$ For these signals, the amplitude should be constant and its frequency should be stable throughout the phase measurement time *T*.

3- Four multipliers and two integrators.

The signal phase is then measured by computing the inverse tangent of the ratio of the two integrator outputs.

The task of phase measurement is further complicated when PDPA applications are considered. For these applications, any practical implementation should allow measurements with the following signal conditions:

1- The signal amplitude dynamic range may exceed 1:2500. This requires special considerations in sampling and digitizing the signal when the digital approach of implementation is considered. This issue is discussed in section 4.

2- The frequency bandwidth may exceed 100 MHz. This poses serious difficulties in generating the reference sinusoidal waves when the analog approach is considered.

3- Quadrature signals should be used for accurate phase measurement. It will be shown in the section (3) that real signals will not provide accurate phase measurement.

The requirement for instantaneous frequency measurement has been so far the main obstacle for the implementation of real time phase measurement. Recently, the innovative architecture provided by the state of the art signal processor (RSA) allows real time frequency measurement at low SNR [4,5]. With this processor, the frequency of the Doppler signal is measured instantaneously. To apply this architecture for phase measurement, first we have to determine how accurate the frequency should be resolved for reasonable phase measurement accuracy. This is the subject of the following section.

3- Frequency Resolution Requirements for Phase Measurement:

As discussed earlier the implementation of the Fourier analysis phase measurement requires that the frequency be known. For PDPA applications, the frequency is unknown and it has to be estimated prior to phase measurement accuracy. This raises the question of how accurate the frequency should be estimated for reasonable phase measurement. For the simplicity of the analysis, clean signals will be first considered. The effect of noise is then examined. The analysis is then used to demonstrate the importance of using quadrature signals for accurate phase measurement.

Referring to Eq.(1) with *n(t)*=0 (i.e. clean signals), the estimated phase of the signal can be written as:

$$\phi_{es} = \phi + \lambda \quad (3)$$

$$\text{where, } \lambda = \tan^{-1}\frac{\int_0^T \sin\left(2\pi\Delta f t\right)dt}{\int_0^T \cos\left(2\pi\Delta f t\right)dt} \quad (4)$$

and $\Delta f = f_1 - f_{es}$ (i.e. the difference between the actual signal frequency and estimated frequency of the signal. Since the frequency of the Doppler signals can not be estimated with infinite precision, $\Delta f \neq 0$). It is clear from equation (3) that to measure the absolute phase of the signal, λ should be much smaller than one or $\Delta f T << 1$. In other words, the frequency has to be estimated with high precision. This means that complicated hardware for frequency measurement is required when the absolute value of the signal phase is considered. Fortunately, this is not the case for phase difference measurement. Using Eq.(3), the phase difference between two signals $s_1(t)$ and $s_2(t)$ is given by:

$$(\phi_d)_{es} = \phi_{es1} + \lambda - \phi_{es2} - \lambda = \phi_d \text{ = actual phase difference}$$

The above equation implies that for phase difference measurement of clean signals, there is no need to accurately estimate the signal frequency (any value for the frequency f_{es} can be used in Eq.(1)). However, when noise is added to the signal, Eq.(5) is reduced to:

$$\phi_{es} = \tan^{-1}\left\{\frac{\tan\phi + \lambda + \nu}{1 - \lambda\tan\phi + \mu}\right\} \qquad (5)$$

where, $\nu = \dfrac{\frac{1}{T}\int_0^T \left(n(t)\sin 2\pi f_1 t + \overset{v}{n}(t)\cos 2\pi f_1 t \right) dt}{\frac{1}{T}\int_0^T \cos 2\pi\Delta f t\, dt}$ and

$$\mu = \frac{\frac{1}{T}\int_0^T \left(n(t)\cos 2\pi f_1 t + \overset{v}{n}(t)\sin 2\pi f_1 t \right) dt}{\frac{1}{T}\int_0^T \cos 2\pi\Delta f t\, dt}$$

For optimum phase measurement, the noise effect should be minimized. This can be achieved by minimizing μ and ν. However, the numerator of μ and ν are characteristic of the noise. Therefore, minimizing μ and ν can only be achieved by maximizing the denominator ψ where:

$$\psi = \frac{1}{T}\int_0^T \cos(2\pi\Delta f t)dt = \frac{\sin(\pi\Delta f T)}{\pi\Delta f T} \qquad (6)$$

The maximum value of ψ is one and occurs when $\Delta f T = 0$ (i.e the frequency is estimated with infinite precision). Thus, maximizing μ and ν can be achieved by keeping $\Delta f T$ close to zero. This raises the question of how close the quantity ($\Delta f T$) to zero is enough. For $T\Delta f \leq 1/2$, ψ is greater than or equal to 0.65 and for $T\Delta f \leq 1/4$, ψ is greater than or equal to 0.9. This corresponds to a minimal loss in SNR of 1.5 dB (=10log(1/0.65) and 0.4 dB (=10 log(1/0.9)), respectively. These are key figures in the implementation of any scheme for Fourier analysis based phase measurement. When the digital approach is considered, these figures indicate that the frequency resolution required for optimum phase measurement is four times that attained with the DFT algorithm without interpolation. Simple interpolation algorithm can be used to provide this resolution. This is a feasible task and its implementation is discussed in section 5.

In the following, we will show that for accurate phase measurement, quadrature signals should be used. For the simplicity of the analysis, it is assumed that the noise is zero and the frequency is known with infinite precision (i.e $\Delta f T = 0$). Thus, the complex signal *s(t)* is given by $\cos(2\pi ft + \phi) + j\sin(2\pi ft + \phi)$ while the real signal *r(t)* is given by $\cos(2\pi ft + \phi)$. Using Eq.(2), it can be easily shown that for complex signals, the estimated phase is equal to the signal phase i.e:

$$\phi_{es} = \phi$$

However, for the real signal, the estimated phase is given by:

$$\phi_{es} = \tan^{-1}\left\{\frac{\frac{1}{T}\int_0^T \left\{-r(t)\sin(2\pi f_{es} t)\right\} dt}{\frac{1}{T}\int_0^T \left\{r(t)\cos(2\pi f_{es} t)\right\} dt}\right\} \qquad (7)$$

For clean signals and $f_{es} = f$, the above equation is reduced to:

$$\phi_{es} = \tan^{-1}\left\{\frac{\sin\phi + \frac{1}{T}\int_0^T \left(\sin(4\pi ft)\right) dt}{\cos\phi + \frac{1}{T}\int_0^T \left\{\cos(4\pi ft)\right\} dt}\right\} \qquad (8)$$

For the above equation, the factors $\alpha = \frac{1}{T}\int_0^T \left\{\sin(4\pi ft)\right\} dt$ and $\beta = \frac{1}{T}\int_0^T \left\{\cos(4\pi ft)\right\} dt$ are the source of considerable error. For accurate phase measurement, both α and β should be zero. This condition can only be guaranteed when the integration time T is a multiple integer of $1/f$. Figure (1) shows the error in the measured phase difference versus the integration time.

For this plot, two signals are used. The phase of the first signal with respect to the reference signal is zero. Two cases are considered for the second signal. For these cases, the phases of the second signal with respect to the reference signal are 30° and 60° respectively.

From this plot, it is clear that to measure the phase accurately, the integration should be performed over an integer number of cycles. This condition can be guaranteed only when the signal is clean and the zero crossings of the Doppler signal are well

defined. However, for noisy environments this task (i.e integration over an integer number of cycles) is difficult (if not impossible) to achieve. For these noisy environments, the only way to get reasonable phase measurement accuracy (say, error less than 2^{o}), is for the integration time to be greater than 10 cycles. Unfortunately, this limits the range of applications as the frequency dynamic range is affected. It should be pointed out that zero crossing based phase measurement methods suffer from this problem. With these methods, phase measurement is performed over an integer number of cycles. Accurate phase measurements cannot be attained at SNR less than 10 dB. Under these noisy conditions the location of the zero crossings is dominated by noise and not by the signal. Consequently, zero crossing methods fail to provide any meaningful results for noisy signals. These problems are not encountered when complex signals are used with the Fourier analysis method. Thus, for noisy environments, the Fourier analysis method and complex signals must be used for optimum phase accuracy.

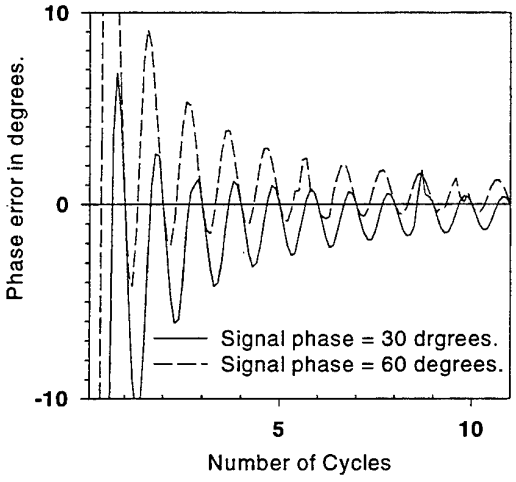

Fig. (1): Signal phase error in degrees vs. measurement time in terms of number of cycles.
Note: For complex signals, the phase error is zero everywhere except when the number of cycles (at this point the phase is undefined.

4- Effect of Signal Quantization on Phase Measurement Accuracy:

In section (2), it is stated that there are two approaches to implement Eq.(1) namely the analog and the digital approaches. The main obstacle for the implementation of the analog approach is the need to generate (within 100ns) stable quadrature sinusoidal waves over a bandwidth of 100 MHz. Furthermore, with the analog approach, careful calibration of both the input signal and the reference signal should be performed prior to any phase measurement. The calibration should include both the amplitude and the relative phase of the quadrature signals for both the input and the reference signals. These difficulties are not encountered with the digital approach. For these reasons the analog approach is less attractive and the focus in this paper will be on the digital approach. With this approach the phase is given by:

$$\phi = \tan^{-1}\left\{\frac{\sum_{i=0}^{K}\left(r(i)\cos\left(2\pi i k_s / N\right)+q(i)\sin\left(2\pi i k_s / N\right)\right)}{\sum_{i=0}^{K}\left(-r(i)\sin\left(2\pi i k_s / N\right)+q(i)\cos\left(2\pi i k_s / N\right)\right)}\right\} \quad \text{.....(9)}$$

where, $r(i)$ and $q(i)$ represent the in-phase (real) and quadrature (imaginary) components of the sampled signal $s(i)$, N is the number of samples used for phase measurement, and k_s is the frequency measured using the DFT algorithm.

A key figure in the implementation of the digital approach is the number of bits in the analog to digital conversion. Certainly, a 1-bit ADC provides the most efficient approach of implementation. The hardware complexity is proportional to the number of the bits. However, if the performance is compromised then higher resolution ADC's should be used. Figure (2) shows the performance of the 1-bit and error free quantization schemes. These results are compared with the Cramer-Rao bound for optimum measurement accuracy which is also plotted in this figure. It is clear from this figure that there is a minimal gain in using higher resolution ADC's. This gain does not justify the substantial increase in hardware complexity associated with higher resolution ADC's.

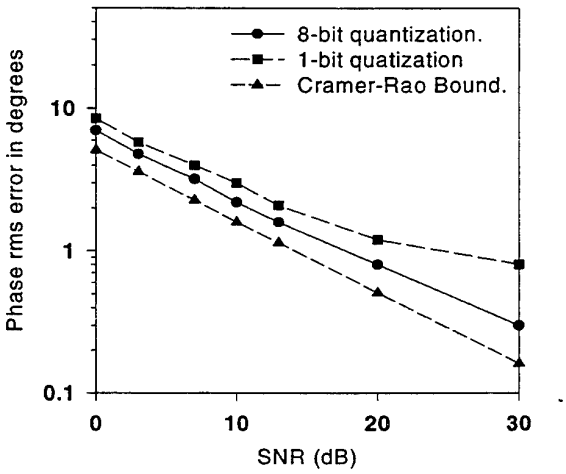

Fig(2): Phase rms error in degrees vs. SNR for N=128.

At this point, we will clarify two controversial arguments about the digital approach that have been discussed in recent literature. The first argument is related to the possibility of phase measurement at the frequencies $0, f_s/2$ and $3f_s/2$ (or $-f_s/2$). It should be pointed out that it is misguided to believe that the phase can be measured at these frequencies. In the vicinity of the frequencies $f_s/2$ and $-f_s/2$, due to aliasing of the sampled data, the frequency is ambiguous, so is the phase. Notice that, at these frequencies, the sampled data represents a signal alternating between two dc values and each signal period is represented by exactly two samples. Consequently the sampled data can represent sinusoidal waves with any phase values over the range $(0,\pi)$. At zero frequency, the signal is dc and hence the phase is meaningless. It should be pointed out that these conclusions are the same regardless of the ADC resolution used.

The second argument is related to the ambiguity in phase measurement that occurs at $f_s/4$ (same arguments follows for the frequency $3f_s/4 = -f_s/4$). This argument has been used to downplay the potential advantages in using 1-bit ADC's. It should be pointed out that even with high resolution ADC's, there is an ambiguity in phase measurement not only when the signal frequency equals to $f_s/4$ but also when the sampling frequency is exactly equal to a multiple integer (say *L*) of the signal frequency. At these frequencies, the effective number of samples used for the phase measurement will be reduced from *N* to *L*. This follows from the fact that the sampled data will repeat itself after L samples. It should be emphasized that this ambiguity occurs only at these exact frequencies and is encountered mostly with simulated signals. Surprisingly, the problem happens at high SNR (10 dB or higher). As more noise is added to the signal; the problem becomes less noticeable. One of the strategies that have been used to reduce the effect of this problem is to increase the number of samples or the sampling frequency or both. In some applications, these techniques are not effective due to the limitations posed by the signal transit time.

For a small signal amplitude dynamic range (less than 1:10), this ambiguity can be reduced by using higher resolution ADC's. However, for PDPA applications, the amplitude dynamic range may exceed 1:2500 (it is worth pointing out that due to visibility-size dependence and the effect of the trajectory, this range may be reduced by at the most a factor of 5 to 10 which is far from enough). For these applications, increasing the number of the quantization levels will not provide significant improvement over the much simpler approach using 1-bit ADC's. Figure (3) is used to illustrate this scheme. It shows the trajectory of the signal $s(t) = i(t) + jq(t) = A\left(\sin(2\pi ft) + j\cos(2\pi ft)\right)$ in the complex plain.

For the purpose of demonstration, let the signal dynamic range be 1:1000 (say the signal amplitude varies from 1mV to 1000 mV). Let an 8-bit ADC be used for signal quantization. To quantize small signals with reasonable resolution, each quantization level should be much smaller than 1 mV. If the quantization level is chosen to be 0.25 mV, the maximum signal that can be sampled accurately with the 8-bit ADC is 65 mV (or less than 7% of the input signal dynamic range. For actual PDPA applications this figure corresponds to less than 2% of the input signal dynamic range). If the signal *s(t)* is sampled at $f_s/4$, then it can be easily shown that the ambiguity in phase measurement can be as large as $90 - 2\sin^{-1} 0.25 = 61^\circ$. This example clearly demonstrates that using high resolution ADC's does not offer any significant improvement over the much simpler implementation using 1-bit ADC's. One may argue that this problem can be resolved by using a higher resolution (12-bit or 16-bit) ADC. However, such ADC's are very expensive and they are not available to cover signal bandwidths over 1 MHz.

From the above example, it is obvious that the solution to this problem can not be achieved by using higher resolution ADC's. However, this ambiguity can be resolved by using efficient sampling methods to encode the phase information more effectively. In ref. [6] , a highly efficient sampling scheme coupled with 1-bit ADC's is presented. Figures (4a), (b), (c) and (d) show the significant improvement in performance with this scheme over the conventional methods using both 1-bit and 8-bit ADC's. These figures represent the results for 1-bit and 8-bit ADC's compared with the modified 1-bit sampling scheme at the problem frequency $f_s/4$ for a realistic range of signal amplitude. In these figures, the number of samples *N* is equal to 128. Note that at low SNR, all of these methods show similar performance.

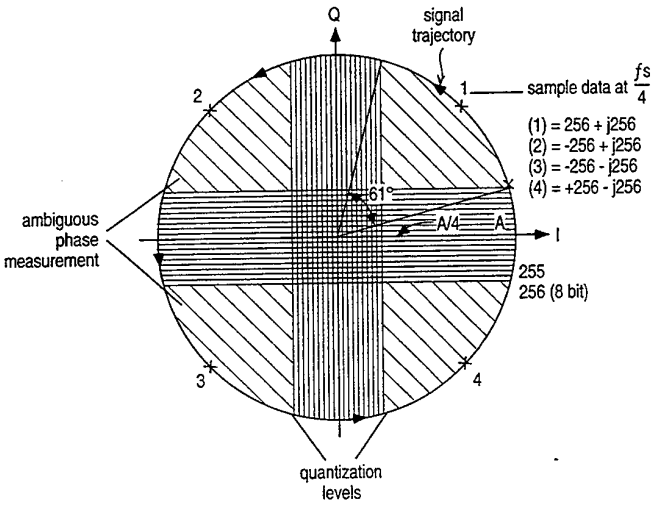

Fig.(3); Signal trajectory at $f_s/4$

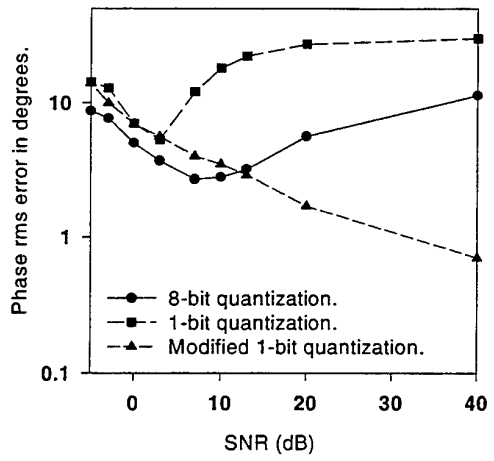

Fig (4a): Phase rms error in degrees vs. SNR for signal amplitude of 1 mV.

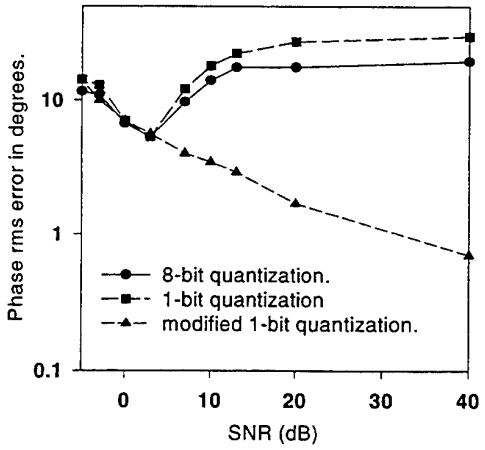

Fig(4c): Phase rms error in degrees vs. SNR for signal amplitude of 200 mV.

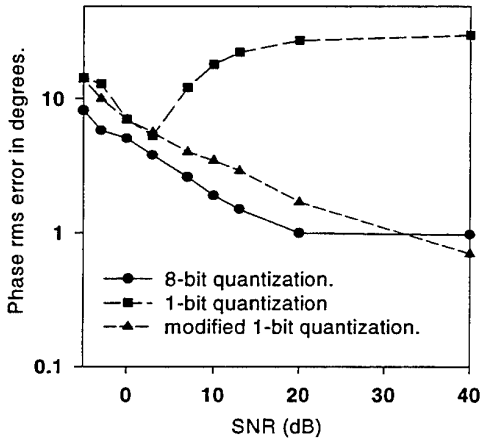

Fig(4b): Phase rms error in degrees vs. SNR for signal amplitude of 10 mV.

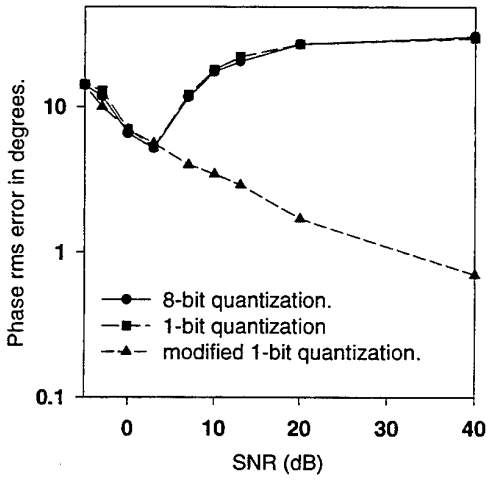

Fig (4d): Phase rms error in degrees vs. SNR for signal amplitude of 2V.

At low signal amplitude of 1 mV (Fig. 4a), the accuracy for the 1-bit ADC begins to deteriorate at 5 dB and decreases with increasing SNR to approximately 25°. The accuracy of the 8-bit ADC begins to deteriorate above 10 dB. The modified 1-bit sampling scheme shows a continuous improvement with increasing SNR. At 10 mV (Fig. 4b), 8-bit quantization provides a performance close to the optimum performance.

However at greater signal amplitudes of 200 mV and 2 V (Fig's (4c) and (d)), the 8-bit ADC has almost the same performance as the 1-bit ADC for the problem frequency $f_s / 4$. The modified scheme shows consistent performance over the range of signal amplitudes. This scheme is used in a practical implementation of a real time signal processor as described in the following section.

5- A Practical implementation of a Real Time Phase Measurement

The implementation of a Fourier transform based real time phase measurement is divided into two highly parallel processing parts. In the first part the frequency is measured using the innovative RSA architecture.

Figure (5) shows the block diagram of the RSA. It is comprised of an analog front end which performs high pass filtering, logarithmic amplification, quadrature mixing (to generate quadrature or complex signals) and low pass filtering to improve the SNR and to remove the high frequency component of the mixer output. The in-phase and the quadrature components are then applied at high speed Analog-to-Digital Converters (ADC) (equivalent to 320 MHz). The ADC outputs are applied to two units. These units are the Frequency Transform Burst Detector (FTBD) and the Parallel Processing Unit (PPU). The RSA uses a combination of time and frequency domain burst detection schemes. With the frequency burst detector the transform of the signal is computed at a rate of 20 million per second. A detailed description of this scheme is found in ref.[7].

The PPU contiguously processes and validates the incoming signal (irrespective of the presence or the absence of the Doppler signal) at a rate of 20 million measurements per second (this corresponds to 20 billion math operations per second or 200 times the computational power of the state of the art Digital Signal Processors). The PPU processes and validates the signal each time an updated packet of 8 complex samples are received from the ADC. Once the signal burst detector is triggered, the PPU starts storing valid frequency measurements in a circular 4-cell memory buffer. Figure(6) shows the RSA signal processing approach. Measurements with N= 64 are first used. Once the gate length corresponds to N> 128, the PPU switches automatically to perform frequency measurements with N= 128 and so on. The processing continues until four valid frequency measurements with N=512 are obtained. If the gate is shorter than that, the PPU sends whatever four validated measurements it has to the computer interface. Furthermore, the PPU sends the final frequency measurement to the phase measurement processing unit.

A second high speed parallel scheme is used to perform the phase measurement using Eq.(9). To implement this equation at the sampling frequency 160 MHz, the parallel processing scheme should be capable of performing 4 billion mathematical operations per second. The parallel processing architecture that is adapted with the phase measurement is different from that used for the frequency measurement. With the frequency measurement, the different processing units are working concurrently and the outcomes of these units are then combined to obtain the final result. With the phase processing, a pipeline parallel processing architecture is used. This means that the different processing units are working concurrently. However, the output of one processing unit (or section) is the input of the next processing unit. The pipeline used for phase measurement is divided into four sections. In the first section, the complex reference signal is generated and multiplied by the complex samples (i.e., $s(i)=r(i)+jq(i)$) to get:

$$\begin{aligned} A(J) &= -r(i)\sin\left(2\pi k_s i / N\right) + q(i)\cos\left(2\pi k_s i / N\right) \\ B(J) &= r(i)\cos\left(2\pi k_s i / N\right) + q(i)\sin\left(2\pi k_s i / N\right) \end{aligned} \qquad (10)$$

where, N is the number of samples used for each phase measurement and k_s is the signal frequency that is provided by the frequency processing board.

The numbers $A(J)$ and $B(J)$ are latched and fed to the second section of the pipeline. In this section the following is computed:

$$\begin{aligned} IM_{J+1} &= IM_J + A(J) \\ RE_{J+1} &= RE_J + B(J) \end{aligned} \qquad (11)$$

where IM_0=0 and RE_0=0. At the end of N computational cycles, the values of RE_N and IM_N are latched and fed to the third section of the pipeline. In this section, the phase of the channel c (c=1,2 or 3) based on current N samples is computed as follows:

$$\theta_{c,N} = \tan^{-1}\frac{IM_N}{RE_N} \qquad (12)$$

In the fourth section, the phase measurement is validated by computing the signal power at the Doppler signal frequency k_s. The signal power of the channel c during the time of the current phase measurement is given by:

$$P_{c,N} = \left(RE_N\right)^2 + \left(IM_N\right)^2 \qquad (13)$$

The signal power of each of the three channels is then compared with a software controllable threshold in the frequency domain. If all of them pass this threshold, the current phase measurement is latched and transferred to the I/O port.

Several tests have been conducted to evaluate the performance of the RSA for phase measurement. In the first test a tunable RF generator was used to modulate simulated Gaussian pedestal. Both the conventional and the modified sampling schemes were tested using clean signal. The ambiguity in the phase measurement was reproduced by careful tuning of the RF generator. Figure (7) shows the performance of these schemes over the processor bandwidth. With the conventional sampling, the rms error was 7° at $f_s / 4$. Using the modified sampling scheme, the rms error is reduced to less than 1°. It should be pointed out that the rms error (at $f_s / 4$) of the conventional sampling using the signal generator is much less that obtained with the computer simulation (presented in figures 4 a, b, c and d). This reflects the fact how difficult it is

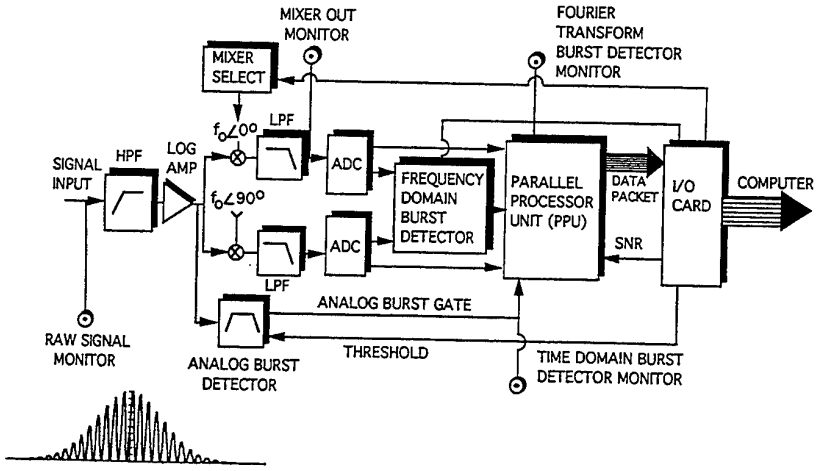

Fig.(5): Block diagram of the RSA.

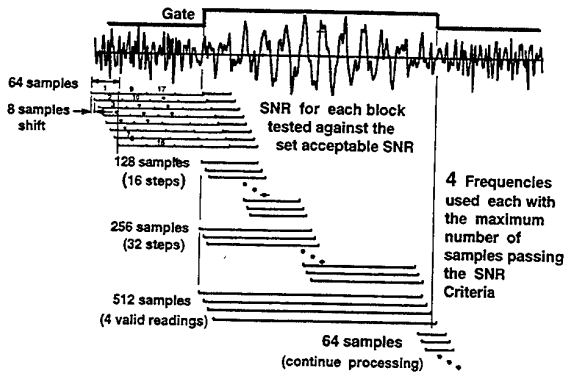

Fig(6): Schematic showing the RSA signal processing approach.

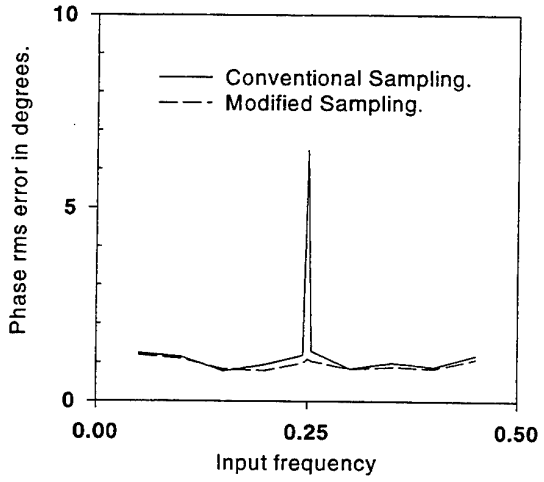

Fig(7): RSA phase error in degrees vs. input frequency normalized to the sampling frequency.

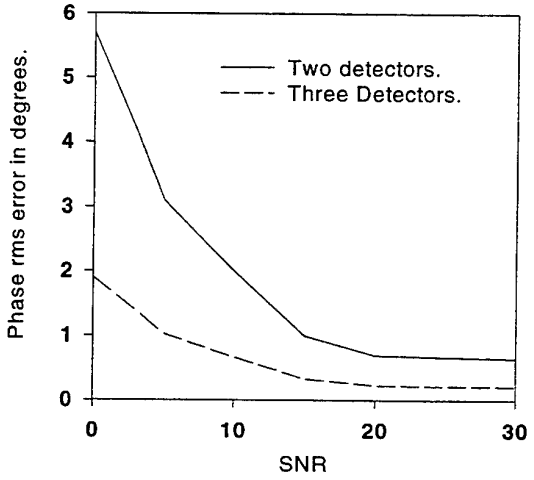

Fig(8): RSA phase rms error in degrees vs. SNR.

to reproduce the problem as we go from perfect computer simulated signals to real measurements using modulated Gaussian signals.

Figure (8) shows the performance of the RSA under different SNR conditions. By using three detectors (as described in ref. [8]), the effective phase rms error is reduced by a factor that is determined by the ratio of the detector separation between detector 1&3 to the detector separation 1&2. With the standard Aerometrics set-up, the rms error can be reduced by a factor of three. With this configuration, the rms error is less than 2° even at SNR of 0 dB. Moreover, the use of three detectors allows an additional validation method. With this method, the phase measurement from the three detectors should fall within a certain window. This proves to be powerful validation criteria for the detection of erroneous phase measurement results and to resolve the ambiguity in phase measurement around 0° and 360°. Without the use of this scheme small particles (with phase values close to 0°) may be interpreted as large particle (with phase values close to 360°).

6- Conclusion:

The essential elements for real time phase measurement have been defined in this paper. Both the analog and the digital approaches of implementation have been evaluated. For both approaches. It is shown that for accurate phase measurement, quadrature signals should be used with noisy environments. It is shown that the digital approach provides a practical scheme of implementation. With this approach, it is shown that the classical methods of sampling will not resolve the ambiguity that happens for phase measurements at $f_s / 4$ even if 8-bit ADC's are used. A novel sampling scheme is presented. With this scheme the ambiguity is resolved even with 1-bit ADC. This scheme coupled with the innovative RSA architecture is then used for the implementation of a real time signal processor for phase measurement.

Acknowledgment:

This work has been supported by NASA Lewis Research Center under Contract NAS3-27716 and US Army Tank Automotive and Armaments Command under contract DAAE07-96-CX014.

References:

[1] Wriedt T., Bauckhage K. A. and Schone, A., " Application of the Fourier Analysis to Phase Doppler Signal Correlated by Rough Metal Particles", IEEE trans. on Instrumentation and Measurement, Vol. 38, No. 5, Oct. 1989, pp. 984-990.

[2] Rife D.C. and Boortstyn R.R.' "Single Tone Parameter Estimation from Discrete Time Observations", IEEE trans. on Information Theory, Vol. 20, No. 5, 1974, pp. 591-598.

[3] Ibrahim, K.M., Werthimer, D. and Bachalo, W.D., " Signal Processing Consideration for Laser Doppler and Phase Doppler Applications", Fifth International Symposium on Applications of Laser Techniques, Portugal, pp. 291-316, July 1990.

[4] Ibrahim, K.M, and Bachalo W.B.,"Time-Frequency Analysis and Measurement Accuracy in Laser Doppler and Phase Doppler Signal Processing Applications", Seventh Int. Symp. on App. of Laser Techniques. Lisbon, July 1994.

[5]Ibrahim, K.M and Bachalo, W.D. "A Real time Fourier Analysis LDV Signal Processor", 41-st International Instrumentation Symposium, Denver, pp. 185-199, May 1995.

[6] Ibrahim, K.M. and Bachalo W.D.,"A Method and Apparatus for Low Signal to Noise Ratio Instantaneous Phase Measurement", US patent, pending.

[7] Ibrahim, K.M and Bachalo W.D, "The Significance of the Fourier Analysis in Signal Detection and Processing in Laser Doppler and Phase Doppler Applications", Sixth International Symposium on Applications of Laser Techniques, Lisbon, pp. 21.5.1-5, July 1992.

[8] Bachalo, W.D. and Houser, M.J.,"Phase Doppler Spray Analyzer for Simultaneous Measurements of Doppler Size and Velocity Distributions", Opt. Eng. Vol 23, 1983, 583-590.

The Influence of Flame on Phase Doppler Anemometry

Shoji TSUSHIMA, Fumiteru AKAMATSU, Masashi KATSUKI,
Yukio MIZUTANI and Yong-Dae CHO

Department of Mechanical Engineering, Osaka University
2-1 Yamada-oka, Suita, Osaka 565, Japan

ABSTRACT

The objective of the present study is to clarify the influence of flame on the phase-Doppler-anemometry (PDA) and to discuss quantitatively the accuracy of droplet size and velocity measurements using a known-size polystyrene particle and a Bunsen burner placed on the optical path of PDA to simulate the variation of refractive index of combusting field. It was found that the fluctuation of flame had significant influences on the measurement, especially on the size, and some scattering of measured data was observed, while the measured mean diameter obtained in these experiments had little difference depending on the existence of a flame in front of the PDA optics or not. Furthermore, we tried to elucidate the cause of errors by comparing the scattered data of size measurement with the displacement of incident laser beams. As a result, it was found that the displacement of the laser beams can be related to the degree of errors caused by the interference of flame on the optical path of PDA.

1. INTRODUCTION

Some of the characteristics of spray combustion are still unknown although it has long been used in industries. The structure of spray flames are affected by dispersion of fuel droplets which follow different trajectories depending on their diameter and the turbulence in flows. Since the phase-Doppler-anemometry (PDA) had been introduced into combustion researches as a powerful tool to measure spray fields, a number of intension applying the technique to the non-intrusive detection of droplet behavior in spray flames (Bachalo and Houser, 1984; Hardalupas et al., 1990; Qiu and Sommerfeld, 1992; Domnick et al., 1994; Akamatsu et al., 1994; Li et al., 1995) have been reported. In spite of the usefulness of PDA, the accuracy of the measurement in flames has not been discussed intensively. The measuring errors may possibly occur due to interaction of some influencing factors peculiar to combusting flows, such as, 1) the change of refractive index of droplets due to temperature rise during the passage through a combusting fields (Pitcher et al., 1990; Schneider et al., 1994), 2) the fluctuation and gradient of refractive index due to the existence of flames and fuel vapour along the optical path of PDA optics, hence a vibration of measuring volume or a change of crossing-angle of beams, 3) the deterioration of Doppler signal due to flame luminosity, 4) the size change of a droplet during the passage through the measuring volume due to vapourization.

In connection with the laser-Doppler-velocimetry (LDV), a number of researchers reported the influence of flame on LDV measurements (Hong et al., 1977, Buchhave and George, 1979). The influence of flame on PDA measurements, however, has not been reported yet with a few exceptions (Martin., 1992, Hirohata et al., 1995).

The objective of the present study is to clarify the influences of flame on PDA measurements and to discuss quantitatively the accuracy of droplet size and velocity measurements using a polystyrene particle of known diameter.

2. EXPERIMENTAL APPARATUS

Figure 1 shows the experimental set-up. A polystyrene particle of known diameter, measured with a microscope, was attached on a rotating disc driven by a motor. The whole rotating device was fixed on a 3-D micro stage having positioning resolution 0.01mm. The optics of PDA was carefully aligned so as the particle to cross cyclically the center of measuring volume of PDA. The position of the particle and the input voltage of receiving photomultipliers were adjusted for each experimental condition which was thought to have influences on the measurement. We used the receiving optics and the signal processor of PDA commercially available (DANTEC, 57X10 and 58N10), but adopted specially designed transmitting optics. The light source for the PDA transmitter was an Ar^+ laser (Spectra Physics, Stable 2017, wave length=514.5 nm). The specifications of the PDA system are shown in Table 1.

A Bunsen burner, inner and outer diameters of which was 13 mm and 16 mm, respectively, was placed on the optical path of the transmitter or on that of the receiver of the PDA to simulate the variation of refractive index of combusting field on PDA measurements. As seen in Figure 2 the burner was traversed horizontally or vertically between the object and the transmitter or the receiver to change the temperature and its fluctuation intensity profiles on the path. L_t and L_r denote the burner location from the transmitter or the receiver, respectively. H is the height from the burner port to the optical path. Adding that, two types of flames, a non-luminous premixed flame (the equivalence ratio ϕ =1.46, Reynolds number Re=1781) and a luminous diffusion flame (Re=95), were used to examine the influence of continuous emission of soot on the signal to noise (S/N) ratio of PDA signal. Figure 3 shows the mean temperature distribution and the distribution of temperature fluctuation measured with an electronically compensated Pt/Pt-13%Rh thermocouple of 25μm. It shows that the mean temperature of the non-luminous flame was higher than that of the luminous flame and the mean temperature gradually decreases while the temperature fluctuation increases along the burner axis.

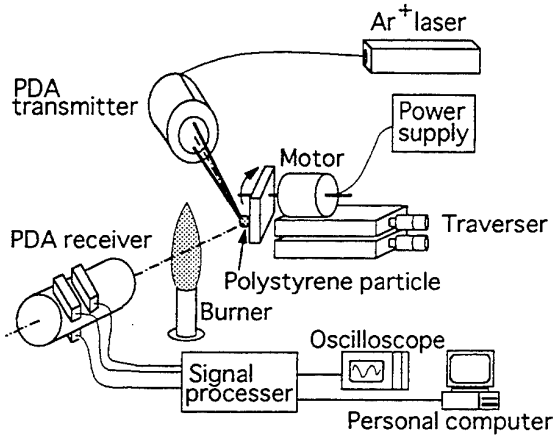

Fig.1 Experimental apparatus

Table 1 Specification of PDA sytem

Transmitting optics:		
Wavelength of laser beam	514.5	nm
Diameter of laser beam	1.34	mm
Focal length of front lens	500	mm
Beam separation	51.5	mm
Spot diameter	244.8	μm
Fringe spacing	5.0	μm
Fringe number	49	
Receiving optics:		
Off axis angle	63	degree
Focal length of receiving optics	310	mm
Width of spatial filter	100	μm
Range: Maximum diameter	254.0	μm
Maximum velocity	1.5	m/s
Minimum velocity	-0.5	m/s
Bandwidth of signal processor	0.4	MHz
Frequency shift	40	MHz
Sampling time	100	s

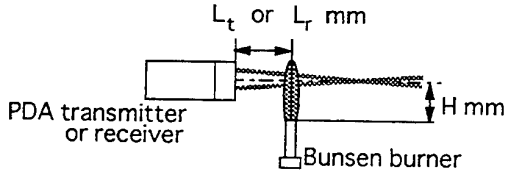

Fig.2 Burner traverse direction

3. RESULTS AND DISCUSSION

Figure 4 shows a series of measured velocity and size of the particle subjected to the interference of the flame. The diameter of polystyrene particle used in this experiment was 153μm. Figure 4(a), (b) and (c) correspond to the cases (a) without flame, (b) with non-luminous flame and (c) with luminous flame, respectively, placed at 150 mm in front of the transmitter lens and at H=50 mm. Almost precise diameters and velocities were obtained when there was not any flame interference. In contrast, some influences of flame were recognized. Both in velocity and size measurements, the rejection of data and the deviation of

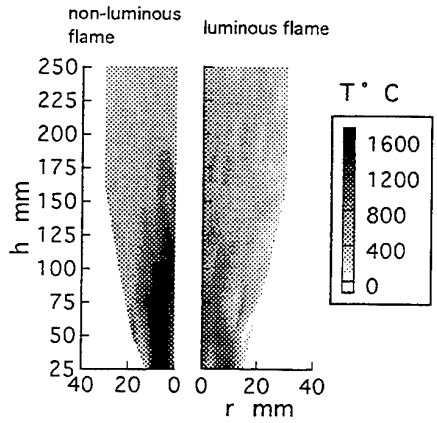

(a) Mean temperature

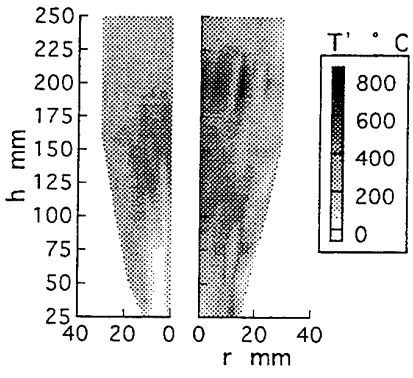

(b) Temperature fluctuation

Fig.3 Temperature distribution of Bunsen burner

measured values occurred occasionally due to the influence of flame. This facts suggest us that attention should be paid when we carry out a time series measurement with the PDA in a flame.

The probability distribution of measured velocities and sizes under the same condition are shown in Figure 5, as well as the mean and rms values of the distributions. Judging from these values and distributions, the influence of flame was not noticeable in velocity measurement, especially in terms of the mean value. In fact, the influence of flame was negligible in velocity measurement, and it will not be discussed further. The size measurement, on the other hand, showed noticeable influences of the flame. Though the derived mean diameter was almost unaffected, the more scattering of measured diameters due to flame was observed than in the case without flame.

In order to see the disturbance on which side of the object, on the transmitter-side or the receiver-side, is more influential on the measurement, the mean measured diameter D_{10} versus flame location is shown in Figure 6. During these experiments, the distance H between the optical path and the burner port was set 50 mm in order to keep the temperature profile and fluctuation intensities on the optical path constant. Regarding the measurement of mean diameter, the flame location showed little difference depending on which side or how far from the lens it was placed. It is clear that the biassing of obtained mean diameter did not occur. Figure 7 shows rms values D' plotted versus flame location, on the transmitter-side and the receiver-side, respectively. Some scattering of data in size measurement was produced by the existence of flame. The influence was more noticeable when the flame was placed on the receiver-side, and the nearer to the receiver the flame was placed, the more scattering of data was observed while the difference between luminous and non-luminous flames had only a negligible effect on signal to noise ratio.

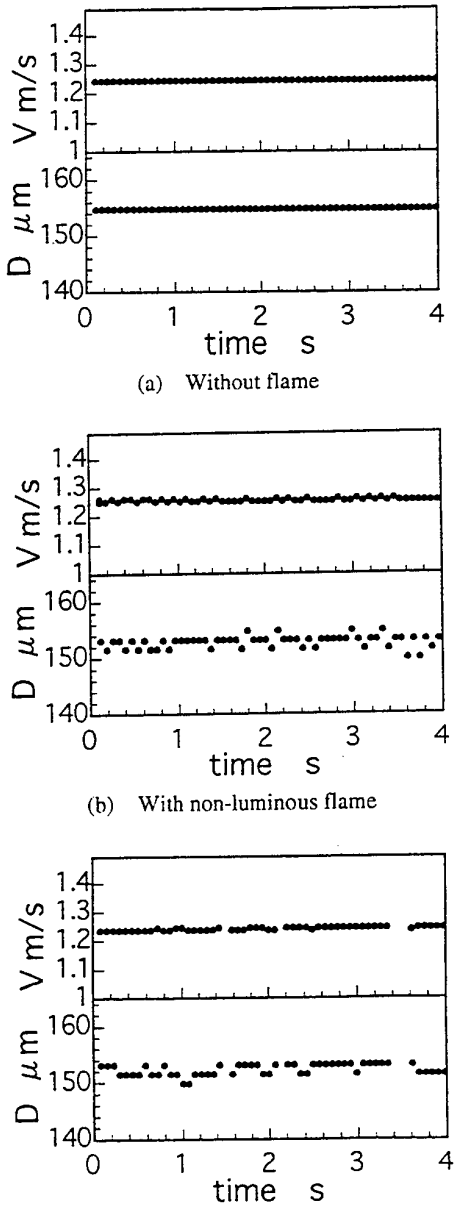

(a) Without flame

(b) With non-luminous flame

(c) With luminous flame

Fig.4 Time-series data of particle velocity and size

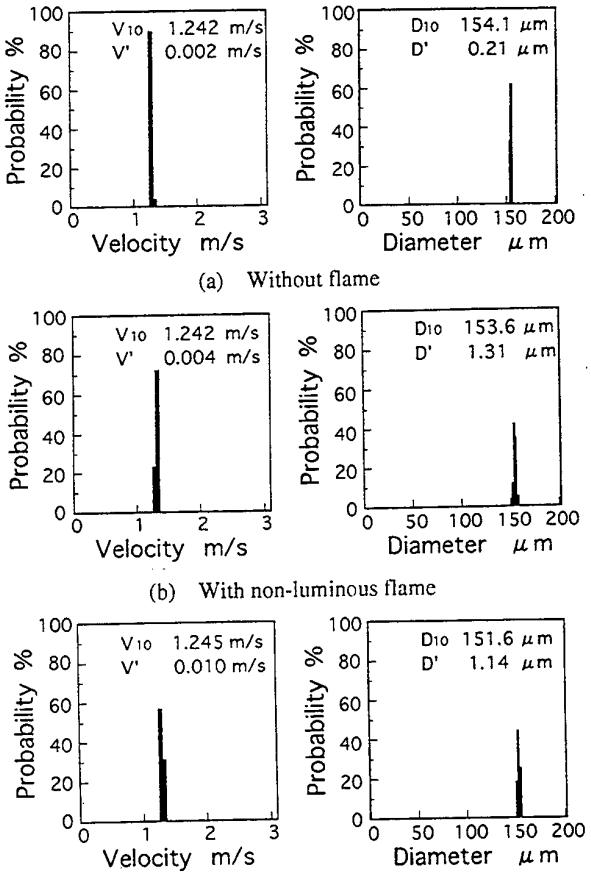

(a) Without flame

(b) With non-luminous flame

(c) With luminous flame

Fig.5 Probability distribution of the measured size and velocity

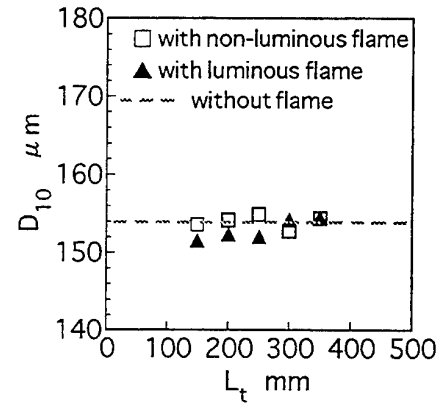

(a) transmitter-side

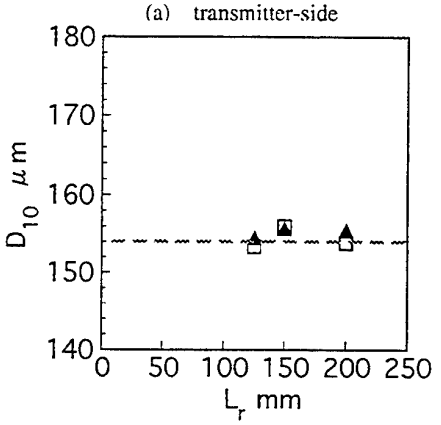

(b) receiver-side

Fig.6 Influence of flame location on the measured mean diameter

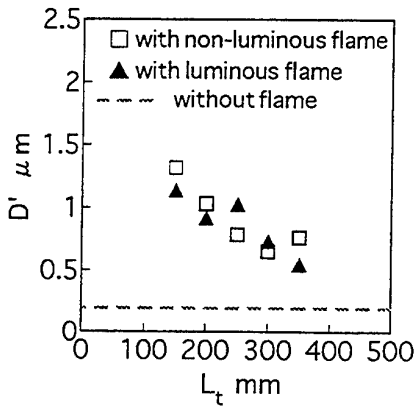

(a) transmitter-side

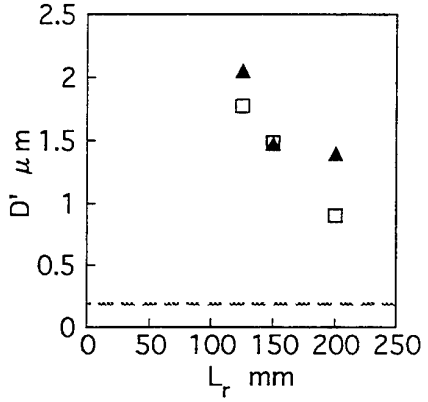

(b) receiver-side

Fig.7 Influence of flame location on the deviation of measured diameter

To discuss the cause of errors, we need to distinguish the flame effects on the transmitter-side from those on the receiver-side. In case of the flame placed on the transmitter-side, the change of refractive index affected by the flame may shift the refraction of two incident laser beams delicately resulting in the change of intersection angle, the change of distribution of laser intensity in the measuring volume, and the change of size and position of the volume. Therefore, the nearer to the transmitter the flame was placed, the more enlarged influences in the measuring volume might be produced, hence the larger variance of the data.

In case of the flame placed on the receiver-side, on the other hand, Doppler signals through the flame region are refracted depending on the change in refractive index and the deterioration of Doppler signals due to the flame is produced, which can be observed with an oscilloscope in practice. Furthermore, the focal point moves due to the flame effects. Accordingly, the phase detected by each photomultiplier is thought to be affected delicately.

In order to understand which factor, the mean temperature gradients or the temperature fluctuations on the optical path of PDA, was more influential on the accuracy, the burner was traversed vertically as well as horizontally, taking the measured distributions in Figure 3 into account. If we increase the height H, that is the distance from the burner port to the optical path, from 50 mm to 175 mm, the mean temperatures crossing the optical path decrease accompanying the increased temperature fluctuations. The diameter of the polystyrene particle used here was 153μm and the flame was the non-luminous premixed flame mentioned above. Figure 8 shows the mean measured diameter D_{10} plotted versus flame location including the change of height as a parameter, and the mean measured diameter exhibited little change in terms of the height. The derived rms values D' in Figure 9, on the other hand, showed some prominent increase with the increase of H, especially in the case of the burner placed on the receiver-side. However, the accuracy of PDA has been discussed so far in terms of L_t, L_r and H which denote the burner location relative to the optical path of PDA. These variables are not related directly to the physical quantities which define the accuracy of measurements. Therefore, we need to correlate these flame locations to some physical properties or indices which will yield general characteristics of the accuracy of the measurement.

When we place the flame on the transmitter-side, the principal cause of the observed errors brought by the shift of crossing angle, the change of the distribution of laser intensity in the measuring volume, and the size and position of the volume can be attributed to the movement or vibration of

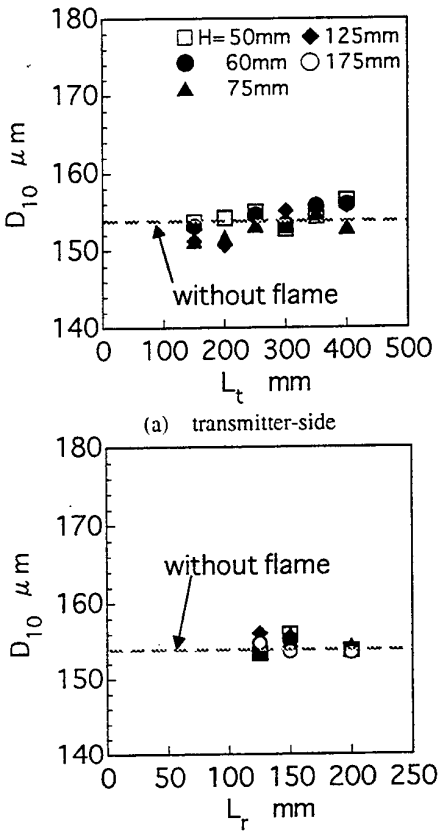

Fig.8 Influence of flame location on the measured mean diameter

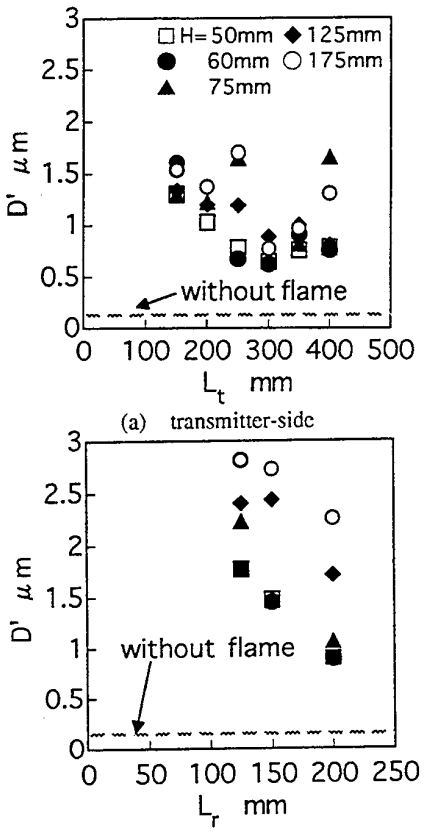

Fig.9 Influence of flame location on the deviation of measured diameter

incident laser beams due to the fluctuations of refractive index, hence temperature fluctuations. Thus we try to examine the relation between the observed deviation of the data and the measured temperature fluctuations shown in Figure 3.

The space variable η, having its origin at the crossing point of incident laser beams, is defined as shown in Figure 10. Then we can easily define the distributions of temperature fluctuation along the upper and lower laser beams as $T'_u(\eta)$ and $T'_l(\eta)$, respectively. Since the farther from the crossing point refraction may occur, the more enlarged displacement at the point is yielded, the influence of refraction at the crossing point is considered to be proportional to the product of the distance of refracting point from the crossing point and the temperature fluctuation intensity. Thus, the total influences of temperature fluctuations along laser beams at the crossing point is expressed as:

$$F_t = \int_0^{f_t} \eta T'_u(\eta) d\eta + \int_0^{f_t} \eta T'_l(\eta) d\eta \qquad (1)$$

where f_t is a focal length of the transmitter. Figure 11 shows the estimated distribution of F_t-values as a function of

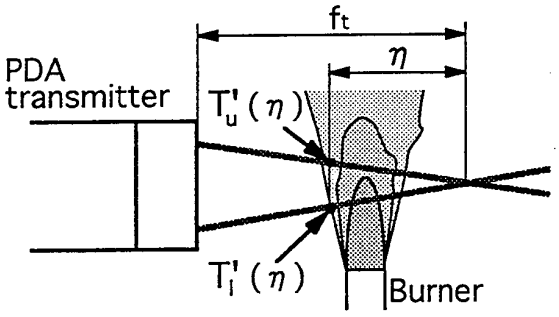

Fig.10 Definition of spacial distance along laser beams and the distribution of temperature fluctuation

L_t and H using the measured distributions in Figure 3. F_t-value increases with the increase of H and with the decrease of L_r. The tendency of F_t-value is similar to that of D'-value as seen in Figures 7(a) and 9(a).

When we place the flame on the receiver-side, the shift of phase in Doppler signal may occur as well as the delicate change of coincidence of the view of the receiver and the

measuring point as discussed for the transmitter-side. As shown in Figure 12 the former may be affected by the integration of temperature fluctuations in the view field as follows.

$$F_r = \int_V T' dV \qquad (2)$$

where V is the collection volume of receiving optics as shown in Figure 12. Figure 13 shows the estimated distribution of F_r-values as a function of L_r and H. F_r-value increases with the increase of H and with the decrease of L_r. The tendency

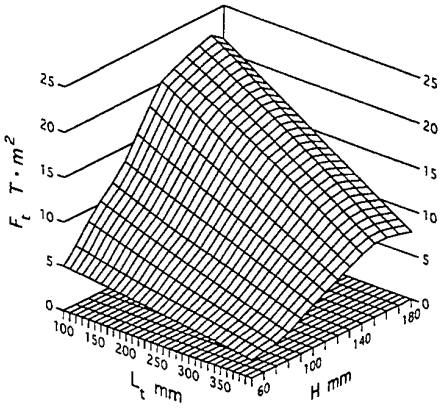

Fig.11 Distribution of F_t-value

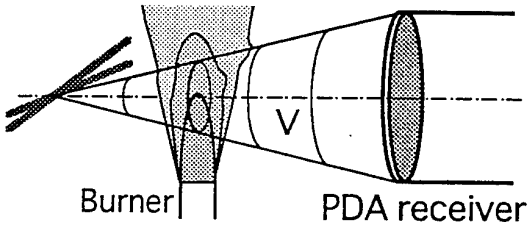

Fig.12 Solid view angle of receivng optics

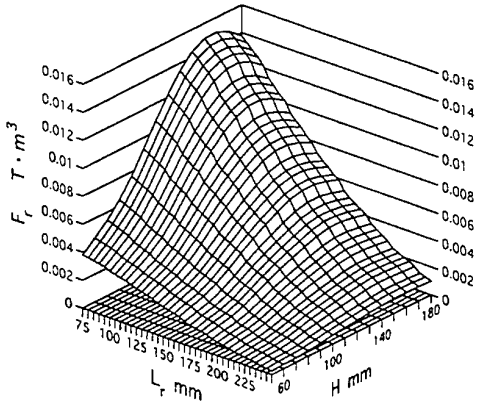

Fig.13 Distribution of F_r-value

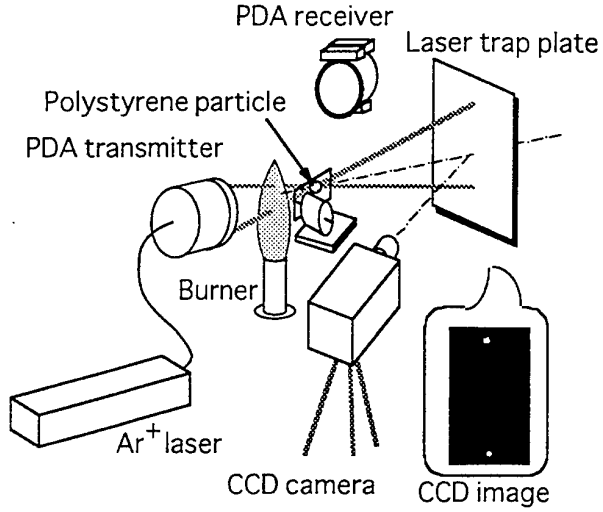

Fig.14 Experimental apparatus for laser beam displacement

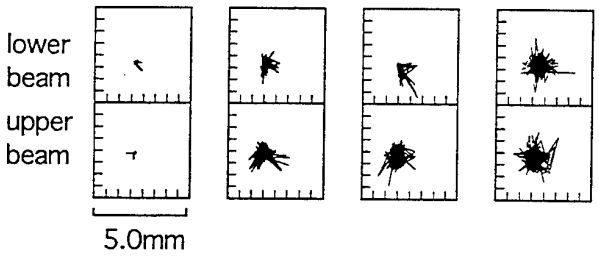

(a) Without flame (b) H=50mm (c) H=75mm (d) H=125mm

Fig.15 Loci of the two incident laser beams on the laser trap plate

of F_r-value is similar to that of D'-value as seen in Figures 7(b) and 9(b). Adding that, F_r changes more widely for the change in flame location compared with F_t, which was also observed in the experiments.

Thus, it is confirmed that the temperature fluctuation, hence the fluctuation in refractive index along the optical path of PDA is one of the most influential factors on the accuracy of PDA measurements.

However, it is not easy to know the profile of temperature fluctuations along the optical path in practical PDA measurements. Therefore, we try to evaluate the quantitative relationship between the variance of obtained data and the actual displacement of measuring point due to flame effects which is practically measurable in the measurement. Figure 14 shows the experimental apparatus used for the purpose. The loci of two incident laser beams projected on the laser trap plate located at L_p=1050 mm from the measuring volume and the velocity and size of droplets were obtained simultaneously by using a CCD camera and the PDA processor described previously. 300 frames for 10 seconds were recorded continuously by the CCD camera. In these experiments the diameter of the polystyrene particle used here was 105 μm and the non-luminous premixed flame

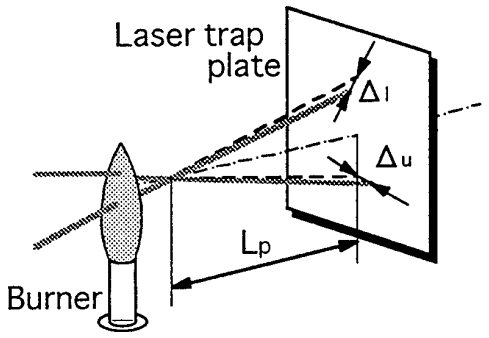

Fig.16 Definition of laser beam displacement

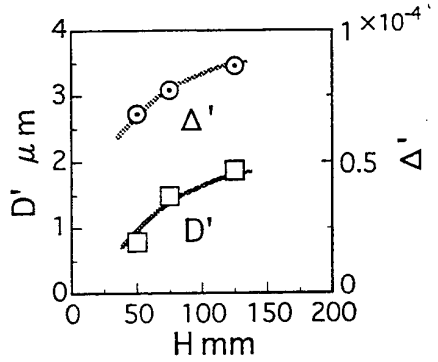

Fig.17 Comparison of the deviation of measured diameter with the laser beams displacement

was placed on the transmitter-side at L_t=150 mm and traversed vertically. The loci of the two beams on the laser trap plate are shown in Figure 15. As seen in the figure, the displacement of the loci were gradually increased with the increase of H. In order to evaluate the displacement of the loci quantitatively, we difined Δ' representing the deviation of the displacement of the measuring volume from the original position unaffected by the flame as shown in Figure 16. Practically, Δ' is given as follows.

$$\Delta' = \Delta'_u / L_p + \Delta'_l / L_p \qquad (3)$$

where Δ'_u and Δ'_l are rms values of each displacement of incident beams, upper and lower beams, respectively.

Comparison of rms values D' of measured diameters with the deviation of the displacement Δ' is demonstrated in Figure 17. The degree of error D' increases with the increase of H, which corresponds to the similar tendency of the displacement of the measuring volume. It is suggested that the simultaneous measurement of the displacement of laser beams in the PDA measurement is helpful in estimating the degree of errors caused by the existence of flame on the optical path of PDA.

Figure 18 shows the influence of laser intensity associated with flame effects on PDA measurements. The diameter of the polystyrene particle used here was 153μm and the non-luminous premixed flame was placed on the receiver-side at L_r=125 mm, H=50 mm and the intensity of the incident laser beam was adjusted to be 3, 5, 7 mW at the measuring volume, respectively. By comparing sample numbers obtained in three cases it is found that the rejection of datum due to flame effects was apt to occur for the lower laser beam intensity. As seen in the figures, when flame was on, the validation rates fell considerably with the low intensity laser beams, while the high rates were maintained by increasing the laser beam intensity. These facts indicate that the deterioration of Doppler signal occurs in flames and a powerful laser is needed for practical measurements in combusting flows. Furthermore, as shown in Figure 18(c), rms value D' in size measurement was increased by the flame effect although it seemed to be independent of the intensity of laser beam.

4. CONCLUSIONS

In order to elucidate the influences of flames on PDA

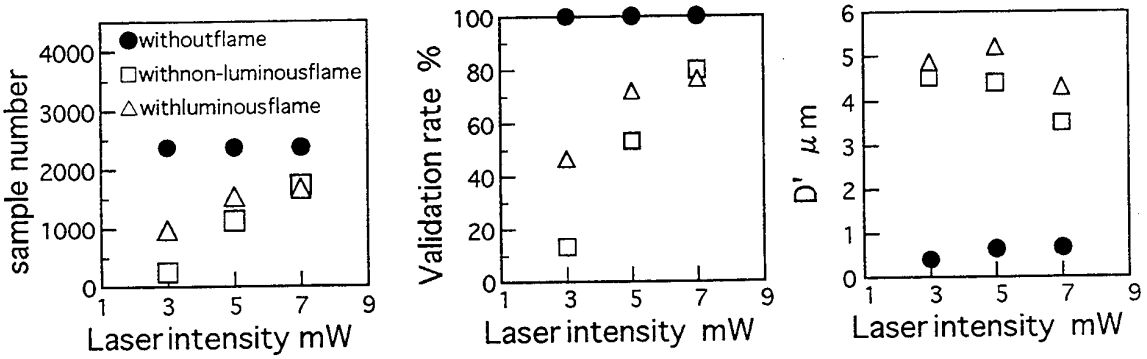

(a) sample number (b) validation rate (c) the deviation of measured diameter

Fig.18 Influence of the intensity of two incident laser beams

measurement in combusting flows, we measured the size and velocity of a polystyrene particle of known diameter which was disturbed by the existence of flame on the optical path of PDA. Furthermore, we carried out simultaneous measurement of PDA and the displacement of laser beams using a CCD camera to discuss the most influencing factors of the errors due to flames. The obtained results are summarized as follows:

(1) The occasional rejection of data may possibly occur by the existence of a flame on the optical path of PDA.
(2) The influence of flame is not noticeable in velocity measurements, especially in terms of mean values. However, some scattering of data occur in size measurements.
(3) Fluctuations of temperature, hence fluctuations of refractive index, are more influential as a cause of errors in PDA measurements than the mean temperature profile.
(4) The influence of flame is significant when it is placed on the receiver-side, and the nearer to the receiver it is placed, the more scattering of data is produced, while the difference between luminous and non-luminous flames has only a negligible effect on signal to noise ratio.
(5) The displacement of the laser beam can be related to the scattering of measured data caused by the influence of the flame placed in front of the PDA optics.

REFERENCES

Akamatsu, F., Nakabe, K., Katsuki, M., Mizutani, Y. and Tabata, T. 1994, Structure of Spark-Ignited Spherical Flames Propagating in a Droplet Cloud, Application of Laser Technique to Fluid Mechanics 7th Int. Symp., Lisbon, pp.212-223, Springer-Verlag.

Bachalo, W. D. and Houser, M. J. 1984; Phase/Doppler Spray Analyzer for Simultaneous Measurements of Drop Size and Velocity Distributions, Optical Engineering, Vol.23, no.4, pp.583-590.

Buchhave, P. and George, W. K. Jr. 1979, The Measurement of With the Laser-Doppler Anemometer, Ann. Rev. Fluid Mech, Vol.11, pp.443-503.

Domnick, J., Lindenthal, A., Tropea, C. and Xu, T.-H. 1994, Application of Phase Doppler Anemometry in Paint Sprays, Atomization and Sprays, Vol.4, pp.437-450.

Hardalupas, Y., Taylor, A. M. K. P. and Whitelaw, J. H. 1990, Velocity and Characteristics of Liquid-fuelled Flames Stabilized by a Swirl Burner, Proc. Roy. Soc. London, A, Vol.428, pp.129-155.

Hirohata, T., Kawahara, N., Ikeda, Y. and Nakajima, T. 1995, Error Estimation of PDA Measurement under the Influence of Flame, Combustion Symposium of Japan, pp.460-462. (in Japanese)

Hong, N.-S., Jones, A. R. and Weinberg, F. J. 1977, Doppler Velocimetry Within Turbulent Phase Doppler Boundaries, Proc. Roy. Soc. London, A, Vol.353, pp.77-85.

Li, S. C., Libby, P. A. and Williams, F. A. 1995, Turbrent Sprays in Stagnation Flows, Atomization and Sprays, Vol.5, pp.287-304.

Martin, J. K. 1992, Transients Diesels Sprays: Application of the Phase Doppler Analyzer for the Measurement of Liquid Droplet Characteristics, Combustion Research, No.91, pp.1-12.

Pitcher, G., Wigley, G. and Saffman, M. 1990, Sensitivity of Dropsize Measurement by Phase Doppler Anemometry to Refractive Index Changes in Combusting Fuel Sprays, Application of Laser Technique to Fluid Mechanics 5th Int. Symp., Lisbon, pp.227-247, Springer-Verlag.

Qiu, H.-H. and Sommerfeld, M. 1992, A Reliable Method for Determining the Measurement Volume Size and Particle Mass Fluxes Using Phase-Doppler Anemometry, Experimental in Fluids, Vol.13, pp.393-404.

Schneider, M. and Hirleman, E. D. 1994, Influence of Internal Refractive Index Gradients on Size Measurements of Spherically Symmetric Particles by Phase Doppler Anemometry, Appl. Opt., Vol.33, pp.2379-2388.

Determination of Effective Measuring Area in a Conventional Phase-Doppler Anemometry

Takeshi Maeda, Hiroshi Morikita†, Koichi Hishida and Masanobu Maeda

Department of Mechanical Engineering, Keio University
3-14-1 Hiyoshi, Kohoku-ku, Yokohama, 223, Japan

†current correspondence: Department of Mechanical Engineering, Imperial College
Exhibition Road, London SW7 2BX, U.K.

ABSTRACT

The paper presents a technique for particle mass flux measurements in dispersed two-phase flows by a standard phase-Doppler anemometry with an A/D converter based signal processor. The purpose was to improve the accuracy of mass flux measurements, which depends on the area size of the probe volume and signal processing technique. The area of probe volume was calculated by a geometrical optics approximation after considering two major error sources, called the 'trajectory ambiguity' and the 'slit effect'. The calculation results showed that the effective measuring area can be determined as a simple function of the probe diameter, size of the spatial filter and particle diameter when the 'phase validation' is applied. The amplitude of PDA signals determined the effective measuring area in the probe volume and ensured measurement in a higher signal to noise ratio region avoiding signals from particles crossing the edge of the probe volume. The flux measurement of a hollow-cone spray indicated that the error did not exceed 20%, at a volume fraction of 1.8×10^{-4}%.

1 Introduction

The determination of mass flux of the particulate phase is very important in order to investigate the flow characteristics of dispersed multi-phase flows, as well as the particle size and velocity. The phase-Doppler anemometry (PDA), which can provide size and velocity information of spheres, is one of the most well accepted techniques for this purpose and, several signal processing techniques have recently been achieved [e.g. Domnick et al., 1993; Kobashi et al., 1992; Bachalo et al., 1988].

The mass flux can be quantified from the total mass of particles passing across the measuring area per unit time. With regard to measurement accuracy, there are two major difficulties which still require attention: the first one is the accuracy in determining the size of the effective probe volume, and the second is the Doppler signals with poor signal to noise ratio (SNR) which may reduce the data rate.

There are a number of studies treating the first problem. At an early stage, the attention was focused on the particle size dependence of the probe volume [e.g. Saffman, 1987; Qiu et al., 1992; Higuchi et al., 1994]. Recently, however, two error sources were reported, namely trajectory ambiguity (TA) [Gouesbet et al., 1990; Sanker et al., 1992] and slit effect (SE) [Durst et al.,1994], which yield errors for both particle size and mass fraction due to the relatively strong magnitude of the reflected light to refracted light. Hence, minimising these error sources became an urgent topic for mass flux measurement. Although several techniques [Xu et al., 1994; Tropea et al., 1995, Aizu et al., 1993] were developed which overcome this problem, they require additional optical components which further complicate the alignment procedure and rule out their use in a standard PDA set-up.

The second major difficulty is the variation of SNR of Doppler signal. Since a laser beam has a Gaussian intensity distribution, signal amplitude is dependent on the particle trajectory even if the particle distribution is mono-disperse. Large variation of particle size makes the measurement even more difficult. For accurate mass flux measurements, all the particles passing through the measuring volume must be considered, and an appropriate technique must be introduced to minimise the ambiguity caused by the signal amplitude. In an effort to meet such a requirement, a signal processor based on an A/D converter was chosen, since it has been shown to be effective at processing signals with poor SNR [e.g. Qiu et al., 1992; Higuchi et al., 1994].

The purpose of the present study is to improve the accuracy of mass flux measurement with a standard PDA setup, by overcoming the two problems which may have combined effects on sizing. In order to minimise the error in the effective measurement area, the intensity of the scattered light by spheres was calculated with a geometrical optics approximation considering the combined error from both TA and SE as described in the following section. In section 3, the combined error caused by TA and SE, and the ability to reject the erroneous data in sizing by phase ratio validation scheme [Hardalupas et al., 1994] are discussed. The results of mass flux measurement in a dense water spray is described in section 3, which is followed by the conclusions of the present study in section 4.

2 Determination of the Effective Measuring Area

2.1 Calculation Method

In the standard configuration PDA, shown in Figure 1, only refracted light is needed for sizing because the refracted light is dominant compared to the other scattering modes. However, signals due to reflected light, which has a phase-diameter response curve with opposite slope to that of refraction, can have a comparable intensity if the scatterer is on the

farther side of the measuring volume relative to the receiving optics due to the Gaussian intensity distribution of the laser. This effect cause erroneous sizing and is the so called 'trajectory ambiguity' (TA). Similarly, the use of a spatial filter in the receiving optics can affect sizing because it blocks refracted light from reaching the collecting lens if the particle is on the edge.

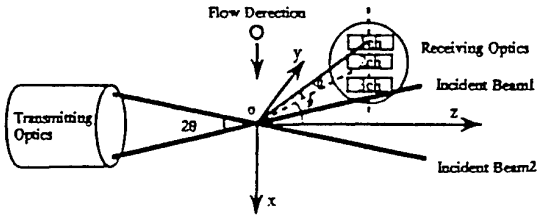

Fig. 1: A standard phase-Doppler arrangement and the coordinate system.

The area where a particle predominantly reflects the laser light must be excluded from the measurement region. Since the TA and SE yield complexity and incorrect measurement in the sizing, it is very important to determine the area in which the signal provides the correct particle size. Although the effects have been investigated independently, they may cause combined error of the measured size. For prediction of the correct measurement area size, a calculation based on the geometrical optics approximation was carried out.

The coordinate system for calculation is illustrated in Figure 1. Two beams form an ellipsoidal *probe volume* and the size of this volume is defined by three diameters, where intensity is $1/e^2$ of the maximum intensity at the centre, D_X, D_Y and D_Z. The centre of the *probe volume* corresponds to the origin *o*. The scattered light was collected by the receiving optics, which was equipped at an off-axis angle, ϕ, with a spatial limitation determined by the slit. And the volume limited by the spatial filter is referred to as the *measuring volume* . The size of the *detection area*, which is the cross-sectional area of the measuring volume, depends on particle size and the sensitivity of the instrument. And in the present study, the area in which a particle provides valid size information is defined as the *effective measuring area*, as shown in Figure 2. Note that the particle does not always give the correct size information in the detection area.

Scattered light intensity and phase were obtained by the same procedure as Hardalupas [1989]. The calculation domain of scattered light intensity and phase was limited to the plane *y-o-z* in Figure 2, while particles move perpendicular to the plane *y-o-z*. Rectangular grid with 1 μm pitch was employed along the *y-o-z* plane for particle locations, and the phase differences between three detectors were calculated as functions of the particle location and size. The range of particle size was varied up to the size of the slit image, and the particle refractive index remained constant at 1.33 for water droplets. Details of the calculated conditions are listed in Table 1.

2.2 Size of the Effective Measuring Area

Figure 3 (a) and (b) show the signal amplitude contours of 20 and 180 μm diameter particles with condition No.1 in Table 1. Since the signal processor used an A/D converter, the signal amplitude was normalised by 256 (8 bit), this level corresponded to the maximum measurable signal amplitude from a particle. The maximum particle diameter was the same as the slit width. The scattered light can be recognised only

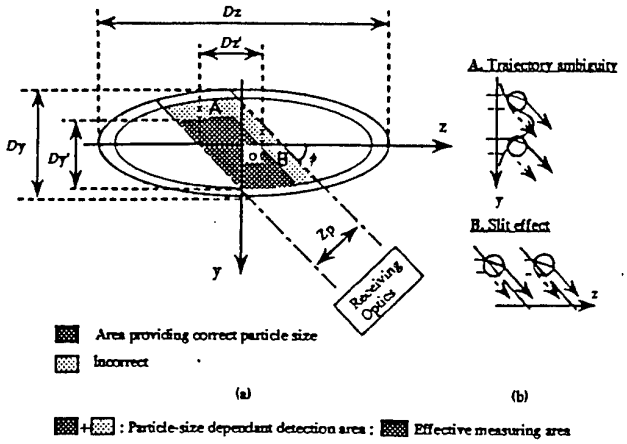

Fig. 2 : Definitions of the detection area and effective measuring area, and schematics of trajectory ambiguity and slit effect.

Table 1: Optical parameters used in the calculation

No.	Slit image width (Z_p) [μm]	Max.diameter (d_{pmax}) [μm]	Probe volume diameter (D_y) [μm]
1	200	200	180
2	400	400	180
3	400	400	350
4	200	200	250

Transmitting optics

Parameter	Unit
Wave length of the laser beam	514.5 nm
Beem inter section angle 2θ	4. 66°
Focal length of front lens	300 mm

Receiving optics

Off axis angle ϕ	30 °
Rotaion angle φ	1.699° (1-2ch), 3.932° (1-3ch)
Diameter to phase angle transfer function	0.731 ° / μm (1-2ch), 0.315 °/ μm (1-3ch)
Demensions of rectangular apertures	3 × 20 mm
Focal length of imaging lens	300 mm
Focal length of collimating lens	150 mm

when the signal amplitude is above the maximum amplitude resolution of the converter; thus the *detection area* was determined by this criterion and hence, there are no contour lines outside detection area as shown in Figure 3. In figure 3(b), the extra area was observed in negative *y* and positive *z* position due to SE and TA.

Since the erroneous measurement must be avoided, a validation scheme based on the phase ratio between phases 1-3 and 1-2 was applied [Hardalupas et al., 1994; Bachalo et al., 1995]. The tolerance of the validation has been defined as the

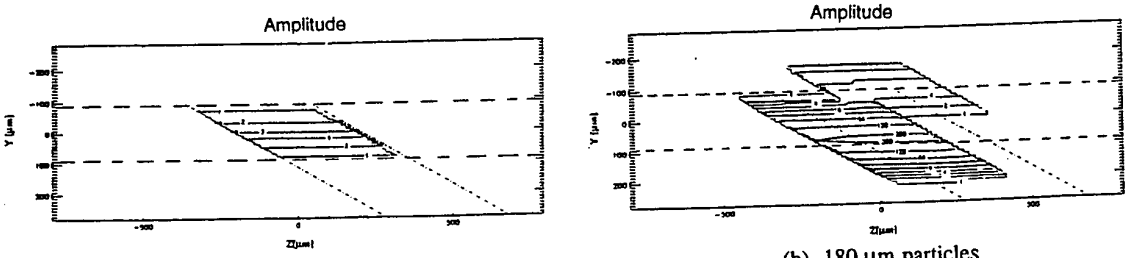

(a) 20 μm (b) 180 μm particles

Fig. 3: Contour of the signal amplitude in the measuring volume.

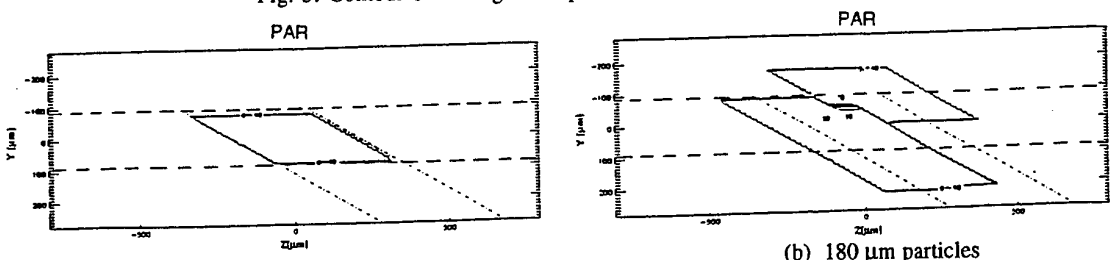

(a) 20 μm (b) 180 μm particles

Fig. 4: Contour of the phase acceptance ratio (PAR) in the measuring volume.

Phase Acceptance Ratio, PAR,

$$\mathrm{PAR} = \left(1 - \left(\left|d_{\mathrm{P1-2ch}} - d_{\mathrm{P1-3ch}}\right| / d_{\mathrm{P1-3ch}}\right)\right) \times 100 \qquad (1)$$

where $d_{\mathrm{p1\text{-}2ch}}$ and $d_{\mathrm{p1\text{-}3ch}}$ are the particle diameters calculated from the phase differences of two of the three detectors, respectably.

Figure 4 shows the PAR distribution. For a 20 μm particle, no sizing errors were observed whereas for a 180μm particle sizing errors were large in the extra area where the reflected light has relatively larger amplitude than refracted light. In this area, however, the signal amplitude was much smaller than at the centre of the detection area. The shape of the area is consistent with the result of the measurement by Willmann et al. [1994].

Figure 5 is the resultant average diameter over the *y-o-z* plane after phase validation and it shows the effect of the scheme. This figure denotes that the validation is effective to reject erroneous measurement and the correct sizing can be achieved with a phase acceptance rate over 90%; the PAR was therefore set constant at 90% in the experiments described below.

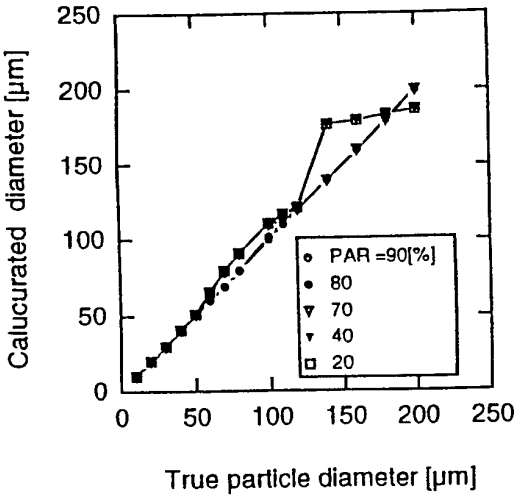

Fig. 5: Accuracy of size measurement with various phase acceptance ratio (validation tolerance).

The size of area and the *effective measuring area,* which was defined by the area includes validated particle locations, is different from the detection area, because signal form particles passing through reflection-dominant area can be rejected by the validation. Figure 6 compares detection area and effective measuring area. The extra area, where sizing errors were observed, increased with particle size and the difference reached 40% of the detection area at maximum. This difference was the primary reason for overestimation of the effective measuring area, and the error in flux measurement cannot be avoided unless appropriate validation of the signal, i.e. phase validation, was introduced.

Detailed dimensions of the effective measuring area along y and z axes are shown in Figure 7 (a) and (b), respectively. This figure denotes that y dimension of the effective measuring area, D_y' in Figure 2, consistently increases with the particle size. On the other hand, D_z' is preserved equal to the z dimension of the slit image, although the effective measuring area shifted toward negative z. These result suggest that the phase validation scheme can effectively eliminate the slit effect and it can be neglected if the PAR is set above 90%. Although trajectory ambiguity still remains, they do not produce any combined effects on the sizing.

2.3 Derivation of Approximated Equation of the Effective Measuring Area

For the different optical setup the same procedure was carried out for conditions No. 2, 3 and 4 as well as No. 1 (see Table 1 for further details). The correlation between the size

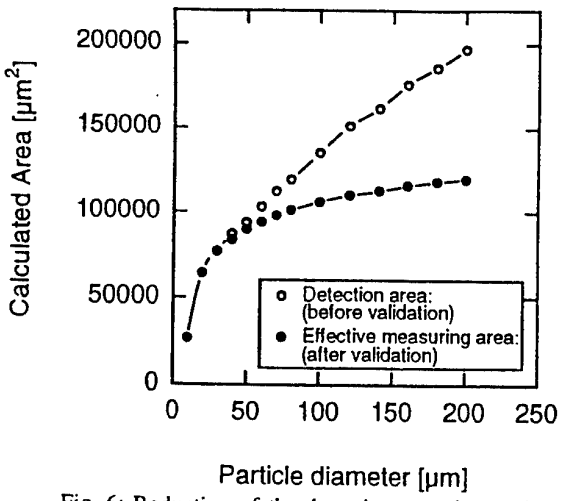

Fig. 6: Reduction of the detection area due to the trajectory ambiguity and the slit effect.

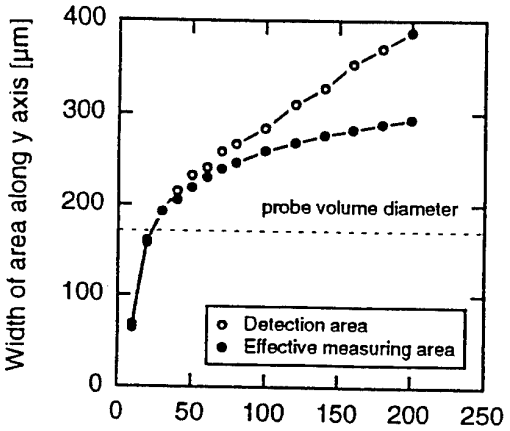

(a)

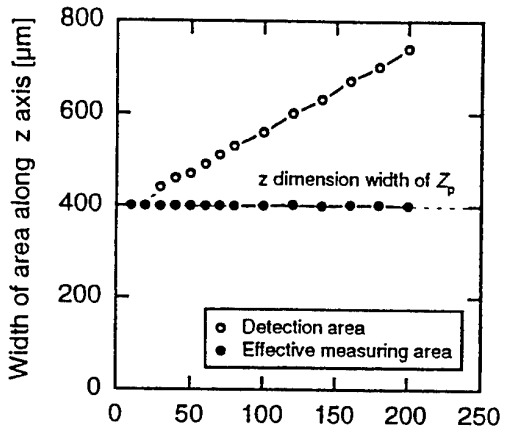

(b)

Fig. 7: The dimension of the detection area and the effective measuring area.(a: locations along the line parallel to the slit image, b: along the line parallel to the z axis.)

of the effective measuring area and the particle size showed similarity without obvious combined effect of SE and TA. Scattered plots in Figure 8 show area, normalised with the size of the cross sectional area limited by the slit image and measuring volume diameter, D_z, against particle diameter normalised by the slit width. The resultant normalised areas coincided well for all conditions. Scattered plots in Figure 9 show the area with various dynamic range of the A/D converter. The width, in which the signal amplitude is $1/e^2$ of the maximum amplitude, was equal to that of the measuring volume diameter for all the conditions. Hence, the size of effective measuring area can be determined as a function of the particle diameter, size of the slit and probe diameter.

The intensity of the incident rays depends on the spatial position; so that the incident intensity for the same particle size is given by

$$I = I_{max} \exp\left[-8\left(\frac{x^2}{D_x^2} + \frac{y^2}{D_y^2} + \frac{z^2}{D_z^2}\right)\right] \quad (2)$$

where I_{max} is the maximum intensity in the centre of the measuring volume. For the y dimension of the plane y-o-z, the incident intensity profile is given by

$$I = I_{max} \exp\left[-2(y/D_y)^2\right] \quad (3)$$

As predicted by geometrical optics, the scattered light intensity is proportional to the square of the particle diameter; hence, the amplitude of the unfiltered signal S becomes

$$S = C d_p^2 \exp\left[-2(y/D_y)^2\right] \quad (4)$$

where d_p and C are the particle diameter and a constant, respectively.

The maximum area size of a signal processor is dependent on its amplitude dynamic range (DR); using the maximum and minimum signal amplitude, $S_{max}(d_p)$ and S_{min}, the width of detection area in y direction can be determined as follows:

$$D_y' = D_y \sqrt{\frac{1}{2} \ln\left(\frac{S_{max}(d_p)}{S_{min}}\right)} \quad (5)$$

The maximum amplitude, $S_{max}(d_{pmax})$, is decided by maximum diameter d_{pmax} passing through the central region of the measuring volume. Then automatically, the minimum measurable amplitude, S_{min}, is determined as follows:

$$S_{min} = S_{max}(d_{pmax}) / DR \quad (6)$$

As described in Eq.(4), the maximum amplitude of the size d_p and d_{pmax} are related using constant C,

$$C = \frac{S_{max}(d_p)}{d_p^2} = \frac{S_{max}(d_{pmax})}{d_{max}^2} \quad (7)$$

Substituting eq. (4) with (5) and (6), D_y' yields

$$D_y' = D_y \sqrt{\frac{1}{2} \ln\left[DR\left(\frac{d_p}{d_{pmax}}\right)^2\right]} \quad (8)$$

On the other hand, the z dimension of the effective measuring area, D_z', is equal to the z dimension of the slit image, and becomes

$$D_z' = Z_p / \sin\phi \quad (9)$$

where ϕ and Z_p are off-axis angle and the width of the slit image, respectively. Hence, the size of the effective measuring area, is multiple of D_y' and D_z', given by

$$A = \frac{Z_p D_y}{\sin\phi}\sqrt{\frac{1}{2}\ln\left[\mathrm{DR}\left(\frac{d_p}{d_{p\max}}\right)^2\right]} \qquad (10)$$

Comparison of the results of calculations with Eq.(10) are shown in Figure 8 and 9 by solid lines. These figures show that Eq.(10) represents the size of the effective measuring volume, although underestimation is observed in small particle size ranges.

For practical mass flux measurements, the difficulty with using eq. (10) is the determination of the maximum particle size, d_{pmax}, since there exists determination errors resulting from poor statistics. Therefore, the methods such as 'weighting function' [Shöne et al., 1994] should be employed to overcome these difficulties. The weighting function procedure was performed by choosing a reference diameter dr, the size class with maximum number of particles. Once the maximum amplitude in the reference size class $S_{max}(d_r)$ was obtained, d_{pmax} could easily be determined with the aid the geometrical optics as follows. Using Eq.(10),

$$C = \frac{S_{max}(d_{Pmax})}{d_{Pmax}^{\ 2}} = \frac{S_{max}(d_r)}{d_r^{\ 2}} \qquad (11)$$

Here, the value of S_{max} corresponds to the maximum measurable amplitude of the A/D converter, hence, instead of Eq.(10), the size of the effective measuring area can be described as

$$A = \frac{Z_p D_y}{\sin\phi}\sqrt{\frac{1}{2}\ln\left[\frac{S_{max}(d_r)}{S_{max}(d_{pmax})}\left(\frac{d_p}{d_r}\right)^2\right]} \qquad (12)$$

With the aid of Eq.(12), mass flux F_n and volume fraction C_v are described as follows:

$$F_n = \frac{\pi}{6Ts}\sum_{i=1}^{n}\frac{\varrho N_i d_{pi}^{\ 3}}{A_i} \qquad (13)$$

$$C_v = \frac{\pi}{6Ts}\sum_{i=1}^{n}\frac{N_i d_{pi}^{\ 3}}{A_i U_i} \qquad (14)$$

where, ϱ, T_S, N and U are the density of the particle, total sampling time, particle number and the velocity perpendicular to the effective measuring area for each particle size class i, respectively.

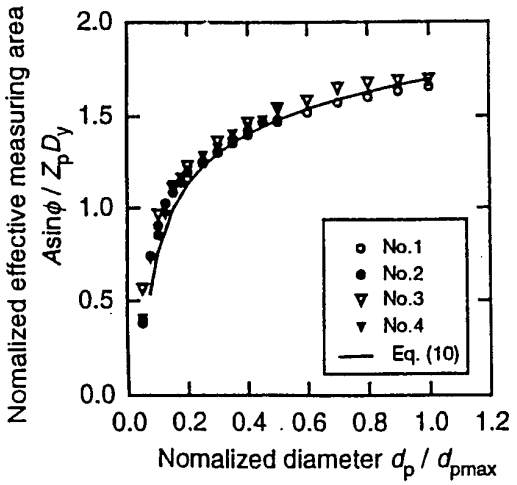

Fig. 8: Size of the effective measuring area with different optical conditions.

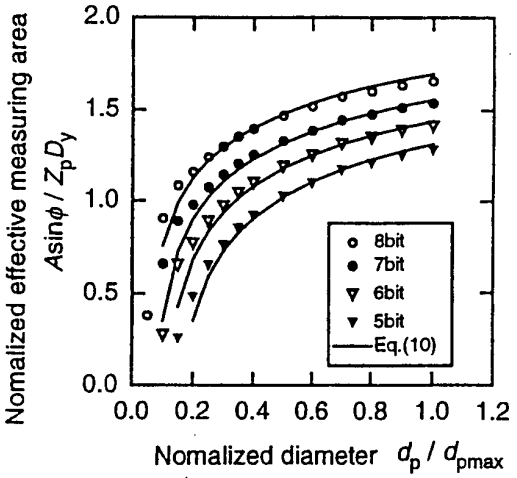

Fig. 9: Size of the effective measuring area with different dynamic range / trigger level of the signal processor, in comparison with equation 10.

3 Experiment

In order to examine the accuracy in area estimation presented in the previous section, two experiments were undertaken. The first test was conducted under idealised conditions with a low noise environment, such that the signal processing technique could be examined. The second test was mass flux measurement for the set of the system with the optimum setting decided in the first experiment and the accuracy was evaluated by measuring a radial profile of flux and estimating the flowrate after integration and comparing it to the true flow-rate.

3.1 PDA Setup

As the maximum diameter of the spray particle was known that 250 μm from the previous work, the probe diam eter was set at 250 μm: the condition was to yield trajectory ambiguity and slit effect. The size of the slit was set at 400 μm in the probe volume, which was larger than the maximum particle size. The rest of the optical parameters are presented in Table 1(b). Please note that validation PAR was set at 90% in all the experiments, in order to quantify correct size of the *effective measuring area.*

In order to calculate size and velocity, an FFT based signal processor [Kobashi et al., 1992; Higuchi et al., 1994] was employed, as shown in Figure 10. Doppler signals were transferred into a 2M byte transient recorder to retain the time-series data. Band-pass filters were not used to avoid the influence of poor signal visibility, because the visibility can often be smaller than unity in the real measurement. The FFT spectrum estimation was performed by a Digital Signal Processor (Motorola 56001), selecting the centre of the burst signal, in which the SNR is high (*centre-search function* [Higuchi et al., 1994]).

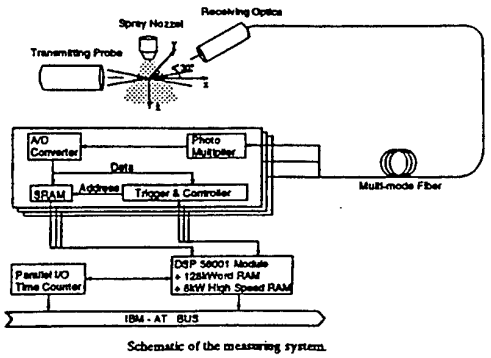

Fig. 10 Block diagram of the PDA system and the signal processor.

3.2 Optimisation of the Trigger Level

For mass flux/fraction measurements of droplets with a broad size distribution, e.g. spray droplets, the variation of scattered light intensity becomes considerably wide. Qiu et al. [1992] and Higuchi et al. [1994] have come to the same conclusion that employing *amplitude trigger* and *centre-detection function* was appropriate for the A/D converter based processors since they maximise the SNR, and SNR can be improved by 8 dB compared to that without the function [Higuchi et al., 1994]. In the method, the trigger level was set as low as possible to obtain low amplitude signals from small particles.

Even with the function, however, many signals are missed due to the poor SNR of very low amplitude signals of which the maximum signal amplitude is comparable to fixed trigger level. Such signals are mainly caused by two unwanted conditions: one is from small particles and the other is large particles passing through the edge of the measuring volume. Because of the Gaussian intensity profile of the measuring volume, the probability of signals with low amplitude from large particles is relatively high and these missed particles yield large underestimation of mass flux. Furthermore, at the extreme condition of fixing the trigger level such that it approaches 0 volts, erroneous measurements occur due to the small number of fringes in the signal.

In order to overcome the problems described above, some sets of flux measurements were performed with hollow-cone spray (Delavan type B, USA) to optimise the trigger level in signal processing diagnostics. Flow direction was normal to the interference fringes, and measurements were limited in a circular cross-section of the spray cone at 30 mm below the nozzle exit. Atomising pressure was set at 0.7 MPa, which provided a particle size range from 10 to 120 μm and a 68.7μm Sauter mean diameter over the circular cross-section. The stored signals were processed with various trigger levels and the resultant mass flow rates were compared with the true values; the true mass flow rate obtained by mass of water supplied to the nozzle was 0.32 mg/s. Measured flow rate was calculated by integrating the local mass fluxes measured over the cross-sectional circular plane. The mean volume fraction in the measured region was estimated at 1.8×10^{-4}%.

The area-averaged mass flux downstream of the spray cone is presented with open circles in Figure 11. Validation rate is also shown with blocked circles. The results are calculated from a series of stored data for all conditions. A local mass flux was obtained from Eq. (13). Trigger level was changed from 0.6% to 25% which corresponds to the amplitude resolutions from 7 bit down to 3bit. Figure 11 shows that by varying the trigger level, the accuracy changes by up to 81.3%. Since the normalised mass flux and validation rate coincided with trigger levels below 15% and the trigger level was too high to be affected by TA, the bias error was likely to be caused by multiple scattering and interruption of the optical path between the measuring volume and the receiving unit, by droplets. The error was relatively large when the trigger level was set below 7%, and this is due to poor SNR. In addition, this graph can justify the compensation procedure by validation rate to estimate true flux.

Figure 12 shows the inferred size distribution. Increasing the trigger level, validation rate was improved (see Fig. 12) due to the reduction of the effective measuring area and high SNR; however, at the same time, small particles were missed as shown in Figure 12. Since the small particles are not dominant in flux measurement, there is an optimum trigger level within the variation. In the present test, it is obvious that the best conditions was the 6.4 % trigger level which provided the maximum mass flux in Figure 11; thus, with the aid of appropriate trigger level, the bias errors of the flux measurement due to the limitation of the performance of the processor can be minimised. The optimum trigger level might change under different conditions, however, it should be around 6.4% for any bit resolution of the A/D converter when the spray has the typical size distribution.

3.3 Experimental Result of Mass Flux Measurement in Highly Dense Spray

Finally, mass flux measurements of a dense spray with wide size distribution, which could represent difficult measurement conditions for PDA, were performed. The geometrical arrangement of nozzle was identical to the previous experiment, however, the nozzle (IKEUCHI, Japan, atomising pressure was set at 0.25MPa) provided droplet sizes with wider distribution, from 20 μm to 250 μm, and Sauter mean diameter over the circular cross-section of 110.6 μm; with such a wide size distribution, large particles surely yield TA with the present optical set-up. Furthermore, the flow rate of the spray was about 80 times that of the former nozzle, 25.87 mg/s. Measurements were performed in four cross-sections of the spray cone at 20, 30, 40 and 60mm below the nozzle exit. For this flow condition, the appropriate trigger level was 6.4 %, as suggested in the previous experiment and, the measurement points were on radial direction in each circular plane. In addition, SNR validation [Kobashi et al., 1990] was introduced and the threshold value was set at -5 dB.

Figure 13 shows the total mass flow rate in each cross-sectional plane. For such a highly dense flow condition with the effects of TA and SE, the accuracy of the averaged mass flowrate measurement was about 72% at x=60 mm plane in which volume fraction was 0.6×10^{-3}%. The worst result was 56.5% at the plane 20 mm with estimated average volume fraction of 2.4×10^{-3}%. Most rejected signals were due to SNR, rather than phase ratio, and the measured mass flowrate remained constant downstream of 40 mm with almost the same accuracy as the dilute spray; these facts suggest that the bias error was due to the higher particle concentration rather than the TA and SE. As a consequence, the approximated equation of effective measurement area and the trigger level optimisation successfully improved the accuracy of flux measurement. The error was reduced by about 15% compared with our previous work.

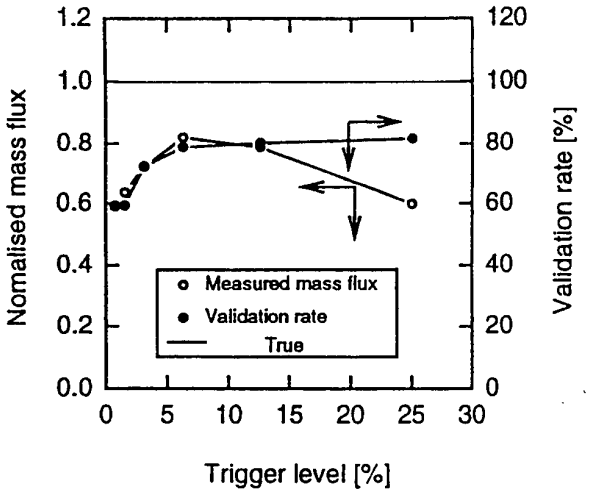

Fig 11 Mass flowrate (open circle) and validation rate (blocked) averaged over the cross section of the hollow-cone spray; the true value was determined by water mass added to the nozzle.

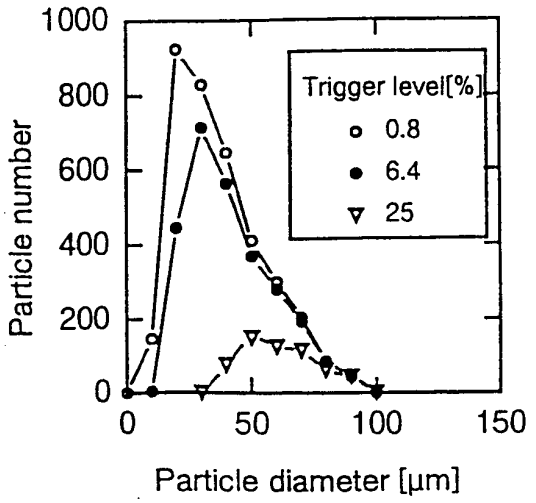

Fig. 12 Particle size distribution with various trigger level, relative to the maximum available signal amplitude.

4 Conclusion

An accurate technique to infer mass flux of droplets by a standard PDA with A/D converter based signal processor has been reported. In order to obtain the effective measuring area size, an approximate equation yielded by the geometrical approximation method was introduced and was found to be appropriate. The signal processing was improved by optimising the trigger level, which increased the data rate of the measurement.

The flux measurement of a dilute spray confirmed the effect of trigger level optimisation. The optimised trigger level was used for the measurement of dense spray and higher accuracy than the previous measurement.

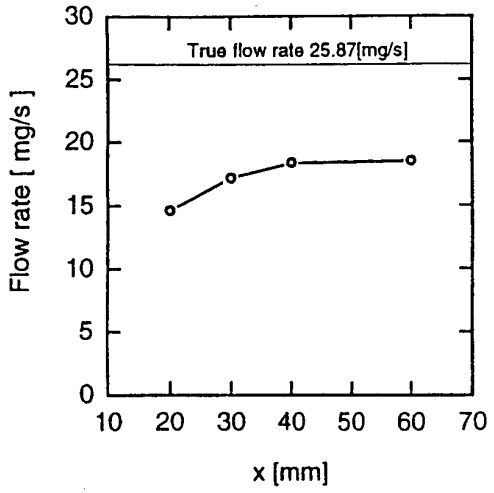

Fig. 13 Total mass flowrate of dense spray.

As a consequence, the results can be summarised as follows:

(1) The results of scattered light intensity calculation by the geometrical optics suggested the phase validation scheme is effective to remove erroneous measurements caused by the 'trajectory ambiguity', if the validation tolerance (PAR) is set above 90%.

(2) The 'slit effect' can be negligible if the phase validation is introduced, although the location of the effective measuring volume is shifted towards transmitting unit refereed to the area defined by the slit. The combined effect caused by the trajectory ambiguity and the slit effect was also negligible except when the particle size is comparable to the measuring volume.

(3) The size of the *effective measuring area* can be determined as a function of the probe diameter, the size of slit, particle diameter and the amplitude resolution of the signal processor. The approximate equation (Eq.10) was evaluated by the dilute spray measurements and was confirmed that the estimation error is 20% at maximum with a trigger level of 6.4%.

(4) In order to maximise the validation rate and to infer correct mass flux, the trigger level should be optimised. The level suggested by the present setup was 6.4% which is likely to be same for any A/D converter based signal processors.

(5) By the reliable determination of the effective measuring area size and the optimised trigger level, particles with low SNR were effectively removed. The improvement resulted in decreasing the measurement error and provided 56% of the true mass flux at the worst condition, which is 15% better than our previous work, with a dense spray with a volume fraction of 2.4×10^{-3}%.

Acknowledgement

The authors are grateful to Dr. Y. Hardalupas for providing the original computer code and Mr. M. Watanabe for his assistance on the experiments. H M would like to thank the Japan Society for the Promotion of Science for providing the Research Fellowship (Grant No.4927) which partly supported the project.

Symbols and Abbreviations

A	effective measuring area
C_v	volume fraction
d_p	particle diameter
d_r	reference diameter
D_y	probe diameter
F_n	mass flux
I	intensity of the incident beam
S	signal amplitude
Z_p	width of the image of the silt
ϕ	elevation angle
θ	beam intersection half angle
x, y, z	Cartesian coordinates
PAR	phase acceptance rate
SNR	signal to noise ratio
TA	trajectory ambiguity effect
SE	slit effect

References

Aizu, Y., Durst, F., Grehan, G., Onofri, F. and Xu, T., H., "PDA-system without Gaussian beam defects", 3rd Int. Cong. Optical Particle Sizing, Yokohama, Japan, 1993, pp. 461-470,

Bachalo, W., D., Rudoff, R., C. and Breña de la Rosa, "A mass flux measurements of a high number density spray system using the phase Doppler particle analyzer", AIAA 88-0236, 1988.

Domnick, J., Durst, F., Qiu, H. -H., Sommerfeld, M. and Ziema, M., "A new generation of phase-Doppler instruments for particle sizing and concentration measurements", 3rd Int. Cong. Optical Particle Sizing, Yokohama, Japan, 1993, pp. 407-414.

Durst, F., Tropea, C. and Xu, T.-H., "The slit effect in phase doppler anemometry", 2nd Int. Conf. on Fluid Dynamic Measurement and Applications, 1994, Beijing, China, pp. 38-43.

Gouesbet, G. and Gréhan, G., "Gaussian beam errors in phase-Doppler Anemometry and their elimination", Proc. 5th Int. Symp. Applications of Laser Anemometry to Fluid Mechanics, 1990, Lisbon, Portugal, 11.6., pp. 243-259.

Hardalupas, Y., "Experiments with isothermal two phase flows", Ph.D. Thesis, Imperial College, 1989.

Hardalupas, Y. and Taylor, A. M. K. P., "Phase validation criteria of size measurements for the phase Doppler technique", Exp. in Fluids, 16,1994.

Higuchi, M., Shirakawa, T., Morikita, H., Hishida, K. and Maeda, M., "Experimental study of multiple interacting sprays by phase doppler anemometry", 7th. Int. Symp. on Applications of Laser Techniques to Fluid Mechanics, Lisbon, Portugal, 31.2.1.

Kobashi, K. Hishida, K. and Maeda, M., "Measurement of fuel injector spray flow of I.C. engine by FFT based phase Doppler anemometer-An approach to the time series measurement of size and velocity", Applications of Laser Techniques to Fluid Mechanics, Springer-Verlag, 1990, pp268-287.

Kobashi, K. Hishida, K. and Maeda, M., "Multi-purpose high speed signal processor for LDA/PDA using DSP array", 1992, Sixth International Symposium Applications of Laser Techniques to Fluid Mechanics, 21.6.1-21.6.6

Qiu, H. -H. and Sommerfeld, M., "A reliable method for determining the measurement volume size and particle mass fluxes using phase-Doppler anemometry", Exp. in Fluids, 13, 1992, pp. 393-404.

Saffman, M., "Automatic calibration of LDV measurement volume size", Appl. Opt., 26,13, (1987a), pp. 2592-2597.

Sanker, S. V., Inenaga, A. and Bachalo, W. D., "Trajectory Dependent Scattering in Phase Doppler Interferometry: Minimising and Eliminating Sizing Errors", Proc. 6th. Int. Symp. of Appl. of Laser Tech. to Fluid Mechanics, LADOAN, Lisbon, 1992.

Sanker, S. V., Bachalo, W. D., and Robart, D. A., "An adaptive intensity validation technique for minimizing trajectory dependent scattering errors in phase Doppler interferometry", 4th Int. Congress Optical Particle Sizing, Nürnberg, Germany, pp. 1-14.

Schöne, F., Bauckhage, K. and Wriedt, T., "Size of the detection area of a phase-Doppler anemometer for Reflecting and Refracting particles", Part. Part. Syst. Charact., 11, 1994, pp. 327-338.

Sommerfeld, M. and Qiu, H. -H., "Particle concentration measurements by phase-Doppler anemometry in complex dispersed two-phase flows", Exp. in Fluids, 18, 1995, pp. 187-198.

Tropea, C. and Xu, T.-H., Onofri, F., Gréhan, G., Haugen, P. and Stieglmeier, M., "Dual mode phase Doppler anemometer", 4th Int. Congress Optical Particle Sizing, Nürnberg, Germany, pp. 287-296.

Willmann, M., Kneer, R., Eigenmann, L., Wittig., S and Hirleman, E., "Experimental investigations on the effect of trajectory dependent scattering on phase Doppler particle sizing with a standard instrument", 7th. Int. Symp. on Applications of Laser Techniques to Fluid Mechanics, 1994, Lisbon, Portugal, 18.1.

Xu, T.-H. and Tropea, C., "Improving the performance of two-component phase Doppler anemometers", Mess. Sci. Technol., 5, 1994, pp. 969-975.

MEASUREMENT UNCERTAINTIES OF PHASE DOPPLER TECHNIQUE DUE TO EFFECTS OF SLIT LOCATION, CONTROL VOLUME SIZE AND FLAME FRONT PRESENCE (IN APPLICATION FOR COMBUSTING SPRAY)

Yuji IKEDA, Toshiaki HIROHATA and Tsuyoshi NAKAJIMA

Department of Mechanical Engineering
Kobe University

Rokkodai, Nada, Kobe 657 JAPAN

ABSTRACT

Measurement uncertainties of phase Doppler technique in application for practical combusting spray was investigated. There are many error sources reported as Gaussian beam effect, trajectory effect and slit effect and so on. But in combustion further measurement uncertainty maybe yielded such as slit location shift effect, optical measurement volume size choice and flame front pressure effect. In this study, three factors have been examined.

It is found that the slit location shift effect can hardly be avoided in combustion and numerous error may be caused. The control volume size should be determined in consideration of velocity gradient in shear flow region. The flame front will change the optical path like slit location shift so as to have measurement error in the small diameter droplet.

1. INTRODUCTION

Over the past decade, phase Doppler measurement techniques (PDA / PDPA) have been developed and employed for practical spray studies and researches [*Bachalo, (1980); Bauckhage, (1985); McDonell, (1986); Durst, (1988); Edwards, (1990); Taylor, (1993) and so on*]. Numerous researches have been carried out using this phase Doppler technique in order to provide sophisticated data as each droplet velocity and diameter without disturbing the flow. Currently, many researches have been carried out by focusing on the next generation, that is, not just measurements of velocity and diameter but also investigations of droplet dynamics, drag coefficients, turbulence interaction, agglomeration, evaporation, group combustion, mass flux in practical combusting spray systems, and so on.

The error estimation [*Grehan, (1991); Sanker, (1992); Xu, (1994); Aizu, (1993)*], affecting factor analysis [*Bachalo, (1994)*] and measurement uncertainties of this technique have been highly required to be quantified both in experiment and theoretical analysis. But these conventional researches have been carried out mainly in a steady state and very simple experiment. The affecting factors of consideration are Gaussian beam effect [*Grehan, (1991); Sanker, (1992)*], scattering light analysis to reduce noisy phase information, refraction / reflection analysis, planer optical alignment analysis [*Tropea, (1995); Sanker, (1995)*], Rainbow effect [*Sanker, (1994)*], trajectory effect [*Scott, (1994); Sanker, (1995)*], slit effect [*Tropea, (1994)*], optimization of optical system [*Ikeda, (1990)*], set-up of processor, data number and data rate, liquid refractive index variation [*Brenn, (1994); Naqwi, (1991)*], and so on.

In application of this phase Doppler measurement system for practical combusting spray, additional uncertainty sources are raised up, which should be taken into account in a dynamics state.

The purpose of this study is to investigate these additional factors in dynamic state such as slit location effect, measurement volume size effect and flame-front induced data bias [*Ancimer, (1994)*]. Three kinds of experiment were curried out using two sets of PDA. A practical oil burner was used in the measurement under non-combusting condition.

2. SOURCES OF MEASUREMENT UNCERTAINTY

Besides of the conventional measurement uncertainty sources, there are mainly seven sources of measurement uncertainty in application of PDA systems for practical combusting spray measurements as illustrated in Fig. 1.

The first one is a phase shift wave front distortion at a flame front at the receiving optics due to refractive index changing. This error was examined in LDV [*Ancimer, (1994)*] well, but the distortion effect has not been investigated.

The second one is the slit location shift effect which is related to the first one. If there is a flame front and the refractive index changes, the optical path of receiving optics will shift. At the result, the slit location will shift. This slit location is normally adjusted empirically by manual at the center of the measurement volume. If this slit is not locating at the center, the measured data will be dramatically influenced and affected by Gaussian beam effect. This will be a big problem in obtaining mass flux. Furthermore, the slit aperture was defined as 100μm in an atmospheric pressure condition and room temperature. If the flame front is curved or not smooth such as distributed reaction zone [*Kuo, (1986)*], the slit width will differ from the defined one. This cause slit location shift and very much influence in calculating volume flux.

The third one is the measurement error associated with the liquid refractive index changing due to temperature changing. In combusting spray measurement, the refractive index of the fuel was changing due to combustion so that the assumption of PDA measurement, that is, the refractive index is constant will fail. Otherwise, the PDA can not measure the droplet diameter just from phase information without refractive index information. Because it is obvious that the refractive index of fuel changes with the temperature in combusting spray. The refractive index measurements were examined in order to show these effects but not so well quantified [*Brenn, (1994); Naqwi, (1991)*]. Then, we have to use the refractive index data of the fuel at standard condition. The temperature in combusting spray flame, the local temperature is not constant because the droplets travel. evaporate, and gasified flow travels, and high temperature gas flow are existing. The temperature is also varying. Even we can make measurement of the refractive index of the fuel, the temporal resolution should be very high which can be hardly achieved. This means that there are some uncertainties in diameter measurement, which can not be avoided.

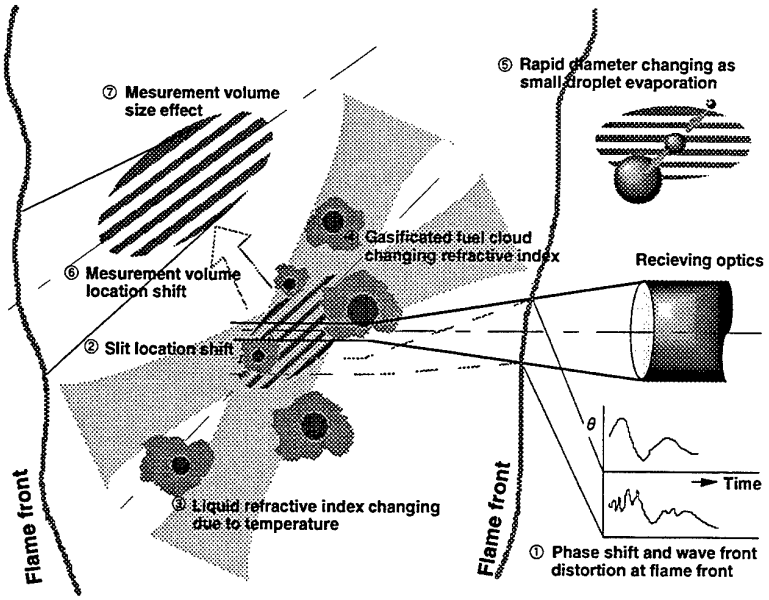

Fig. 1 Measurement uncertainty sources.

The fourth one is the refractive index changing around the droplet. The gasificated fuel forms a cloud in which the refractive index of this cloud also very. Theoretical evaluation of this effect will be discussed later paper.

The fifth one is the rapid droplet diameter changing like small droplet evaporation. The PDA measures the phase when the droplet travels through 5-8 fringes, so that the measurement cannot be performed if the droplet diameter changing time is faster than that measurement time, and this fact will cause error.

The sixth one is the measurement volume location shift effect, which is the same as the second one. The measurement volume will be formed at a different location due to the refractive index changing at the flame front and in the gasificated fuel cloud.

The seventh one is the measurement size effect. It is desirable to have long focal length both in transmitting and receiving optics for combusting spray measurements to prevent from fuel oil adhesion, soot and heat radiation. The long focal length makes larger measurement volume in which the fringe spacing is enlarged and the light intensity decreases (low SNR). The fringe spacing should be optimized in consideration of measurable ranges of velocity and diameter. The large measurement volume has to average the velocity and diameter within the large measurement volume, so that the characteristics of the large velocity gradient flow or strong shear flow region cannot be demonstrated well. This effect is an essential for LDV and PDA. If the measurement volume is too much small, which causes small fringe spacing and large fringe number. In PDA, the measurable diameter range is determined by these value, so that the optimization of the optics to the flow should be done before measuring the final data. The evaluation of the system is very important factor, but we have to say that this has been performed by experimentally and empirically.

These seven uncertainty sources can be classified into four groups in this story; flame-front effect(1), slit location shift effect (2,6,7), measurement volume size effects (5,7) and refractive index changing effect (2,4). In this study, these three measurement uncertainty sources will be investigated, that is, slit location shift, measurement volume size and flame front presence.

3. EXPERIMENTAL APPARATUS

A gun-type oil burner was used in this experiment as shown Fig. 2 as well as the flame picture [*Ikeda, (1995); Kawahara, (1996)*]. This oil burner is for 0.1 MW class boiler and furnace. An A-type fuel oil was pressurized at 0.7MPa and atomized by the hollow-cone nozzle (Danfos : H type) of 60 degree. The fuel rate used is 9.45×10^{-3} m³/h. The PDA setup is illustrated in Fig. 3. As signal processor, Dantec processor was used.

4. RESULTS

4.1 Slit Location Shift Effect

As explained in above section, the slit location shift will be happened due to flame front effects both on the transmitting and receiving optical paths. But we have to pay more attention to the measurement set-up at the initial stage. The slit location is normally adjusted by same one, which is empirical based one.

In order to examine the slit location shift effect, two measurement points were chosen. One (point A) is the dense spray region of large velocity gradient, the other (point B) is on the center axis of high data rate region as shown in Fig. 4 [*Kawahara, (1995)*]. Two dimensional velocities and the droplet diameter were measured. The sample number was 10,000. The size-classified [*Edwards, (1990); Presser, (1995); Seay, (1995); Ikeda, (1996)*] droplet velocity vectors are shown as well as slip velocity and fluctuation intensity. At point A, this point locates at the tail of recirculating flow region. This figure shows that the small droplet can follow to the reversing flow, so that the small droplet velocity was negative, while the large droplet penetrated into this recirculating flow region in which the larger droplet velocity was positive. The slip velocity vectors show the large shear stress region and their magnitude. The detailed flow characteristics were explained in the previous paper [*Kawahara, (1995)*].

Five slit locations were examined in the optical setup by manually. The measurement volume size was 0.19 × 4.09 mm and the slit width was about 100 μm. As shown in Fig.

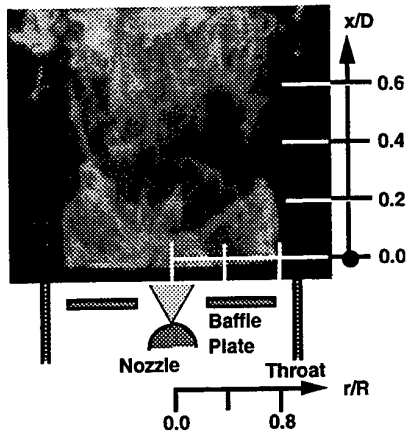

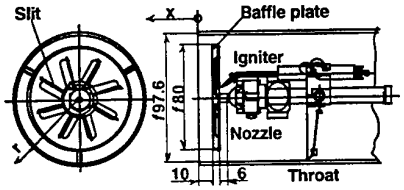

Fuel	A-type heavy oil 9.45×10^{-3} (m^3/h)
Heat release	0.103(MW)
λ	1.2
Spray type	Hollow corn spray of 60degree
O_2	4.7(vol%)
CO_2	10.8(vol%)
CO	0.0(ppm)
NO	58.4(ppm)

Fig. 2 Burner and flame photograph.

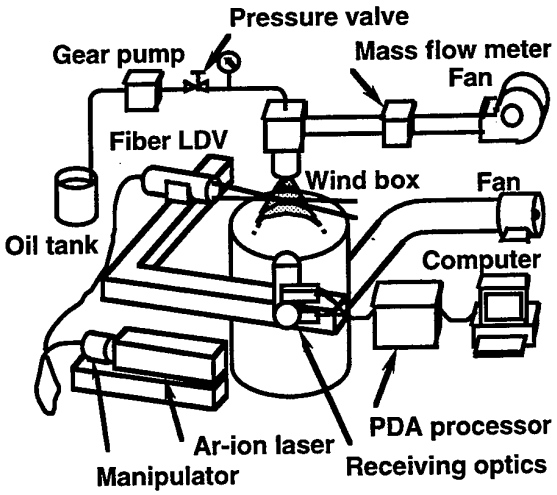

PDA optics
f = 400 mm
MV = 0.19× 4.09 mm
δf = 5.42 μm
Nf = 36
Velocity range: 16.2 - 48.8 (m/s)
Daimeter range: 2.7 - 230.1 (μm)

Fig. 3 Experimental apparatus.

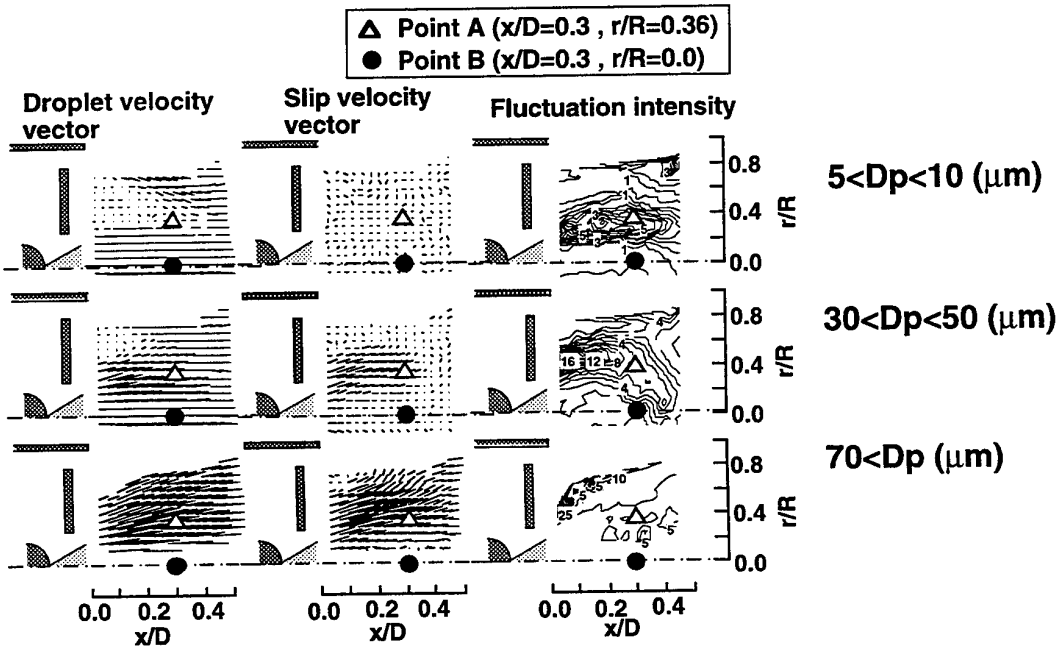

Fig. 4 Measurement points.

5, five sliced slit volumes are not the same, and the light intensity differences should be taken into account.

Figure 6 shows the raw data at two slit locations, #3(center) and #5(side end). As seen clearly, there are many discrepancies. For evaluating these data, the measured axial and radial mean velocities (U and V), and Sauter and Volume mean diameters (D_{32}) are shown in Fig. 7. The ratio of velocity and diameter were defined the ratio to that at the slit #3. The ratio 0.25 means that the velocity (diameter) is 25% larger than that measured at slit #3.

The point A is the recirculation flow tail. As shown in Fig. 6, these two measured data are not the same. The negative velocity was measured at slit #5 and the axial velocity profile was almost flat, while there was no negative velocity at slit #3 and the maximum velocity peak was about 4 m/s. Even in the diameter, the slit #5 could not measure the droplet less than 50 μm. But the slit #3 data is almost under 50μm. These two diameter is extremely different from each other. This point A is the strong shear flow region so that the difference of the slit location shows entirely different measurement point of different physics. The velocity different at these two location was over 30%.

The point B is on the center axis. The fuel was atomized at the hollow-cone angle of 60 degree so that there was residual and reversed droplet on the center axis. This point is less shear than point A. In the axial velocity distribution, the peak velocities are not so much different each other. But the diameter distribution are totally different.

In order to understand the difference and the error of the slit location in detail, Fig. 7 was used. In Fig. 7 at point A, the axial velocity at slit #2 to #4 are not so much different. The velocity ratio is under 10%. But the data at slit #1 and #5 are very much different, the velocity at slit #5 is 70% higher than that at slit #3 (center). At point B, the axial velocity at different locations are gradually increasing, but the discrepancies are less than 20%. The radial velocity was almost 0.3 m/s but the radial velocity changes are very large as shown in this figure.

For SMD at point A, the slit #3 shows 60 μm. The range of the measured diameter was almost 30 μm, which was about 30 %. At point B, the diameter ratio at different location was over 100%.

Here, we have to determine whether the measurement results were right or wrong. Those results are derived from the

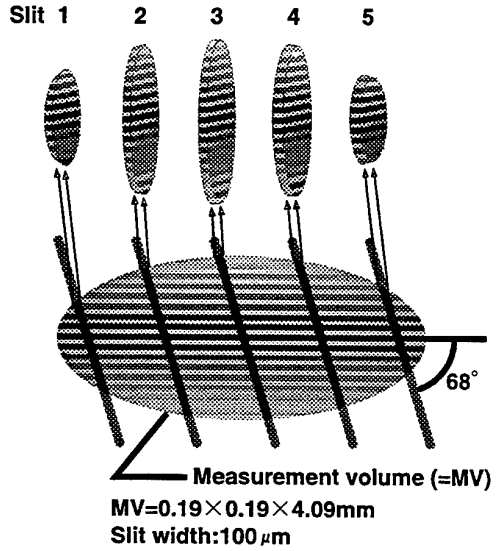

Fig. 5 Slit location.

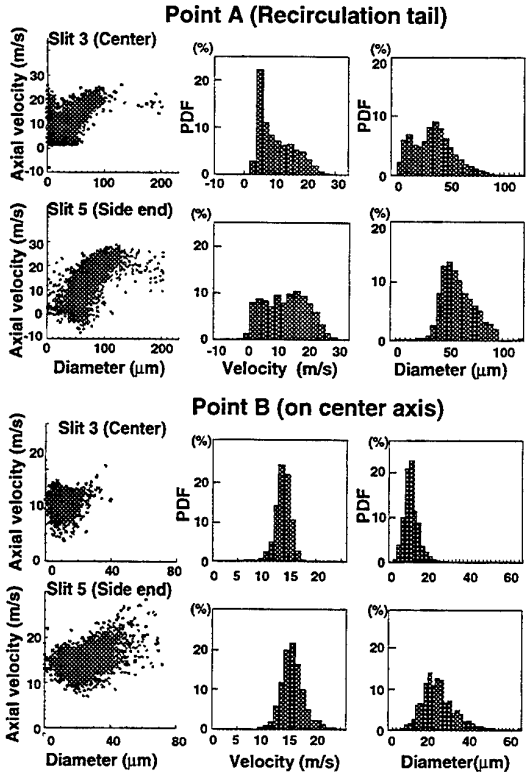

Fig. 6 Raw data at different slit location.

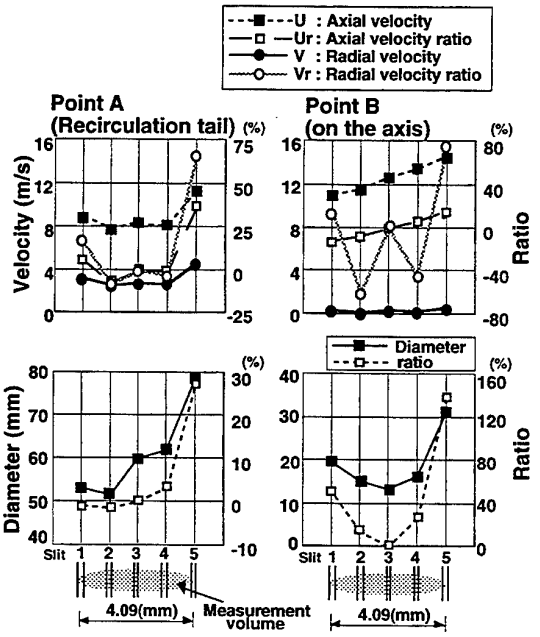

Fig. 7 Comparison of measured data coaxial mean velocity (U), radial mean velocity (V) and Sauter mean diameter D32.

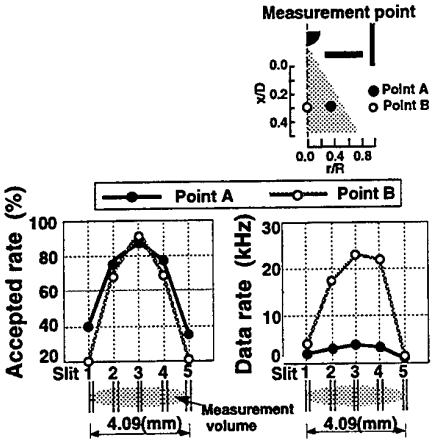

Fig. 8 Comparison of accepted rate and data rate.

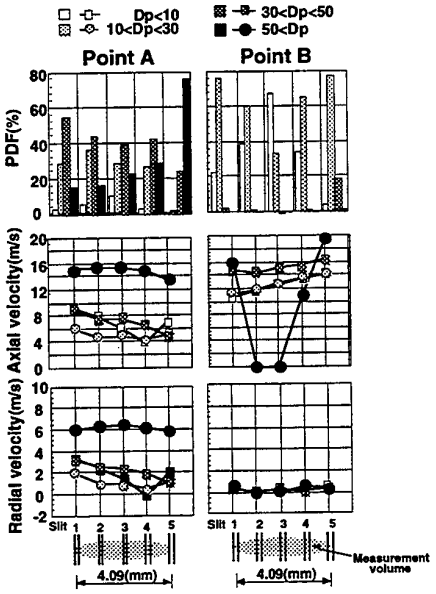

Fig. 9 Size-classified droplet distributions at points A and B.

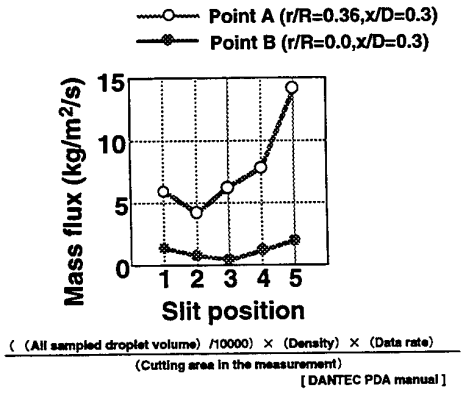

Fig. 10 Mass flux.

system set-up or from the physical issue. Then, these measurement status were evaluated with data rate, spherical rate and accepted rate as shown in Fig. 8 in order to find the optimal slit location.

Both in these points, the measurement at slit location #3 should be the best, which can be demonstrated in these three factors. At the side end of the measurement volume, #1 and #5, the accepted rate are lower both in two points, although the high spherical rate measured was over 98%. It is very difficult to say that the measured results at #1, 2 and 3 are right or wrong. Finally we have to say that the discrepancies in velocity and diameter at central three slit location do not derive from the measurement error, the measured results are accurate and appropriate in terms of measurement technique and system set-up. It should be emphasized the measurement uncertainty called "slit location shift effect".

When the measurement is carried out in a combusting spray, there is a flame fronts. The refractive indices at the flame fronts will cause the measurement volume location shift both on transmitting and receiving optical paths, which will cause this effect. Then the practical measurement results should be evaluated in this factor effected and show the uncertainty in quantitative value.

For further examination of the measured results, the PDF of size-classified droplet sample number and those velocities are shown in Fig. 9. It is found that this slit location shift effect can be seen in the larger droplet diameter. The axial velocities of small droplet have less difference than those of the larger droplet. The PDFs of droplet number show the same effect.

The one of the big advantage of the PDA technique is to be able to estimate a mass flux. The mass flux measurement errors have been evaluated in many researches [*Edwards, (1990); Sanker, (1995); Bachalo, (1994)*], but those are carrying out in the steady state. It should be noticed that the measurement of mass flux contains of large uncertainty due to the slit location effect in combusting spray.

As shown in Fig. 10, the mass flux at slit #5 is almost three times higher than that at slit #3 at point A. By taking that the large velocity gradient exists and droplet movements of large and small are different from each other into account, it is easy to assume that there is some uncertainties. But the value of three times higher is out of question. We have to take care of the initial optical set-up and uncertainty due to Gaussian effect [*Grehan, (1991); Sanker, (1992)*] and slit effect [*Tropea, (1995); Sanker, (1995)*], however the measured data might contain these error. There are many reports to obtain mass or volume flux by the phase Doppler technique. The key point is the slit aperture and its size. In combustion, the error due to slit location shift may be not such large. But it is highly required to consider the uncertainty and error in the measurements. The evaluation of the data as well as the system set-up is the only way to the eliminate these uncertainties.

4.2 Measurement Volume Size

For practical combusting spray measurements, it is desirable to have long focal length both in transmitting and receiving optics to prevent from oil adhesion, soot and heat radiation. But the long focal length causes the larger measurement volume which will have weak light intensity (low SNR) and volume averaging effect at a large velocity gradient region and large droplet diameter distribution region. In order to prevent from this volume averaging effect and abovementioned slit location effect, a small measurement volume is the one of the best solution. This is the trade-off relation. The smaller the measurement volume becomes, the higher the measurement accuracy becomes and the smaller the uncertainty becomes. But the measurable range of velocity and diameter decreases. An optimization of this effect is the quite important task for researcher before choosing the sys-

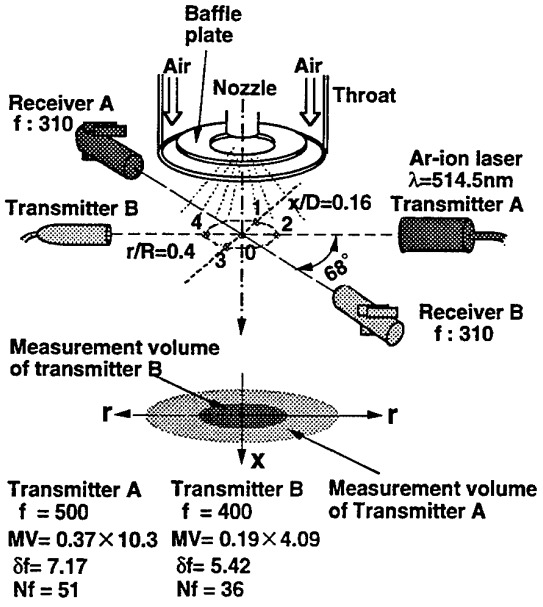

Fig. 11 Measurement under size effect.

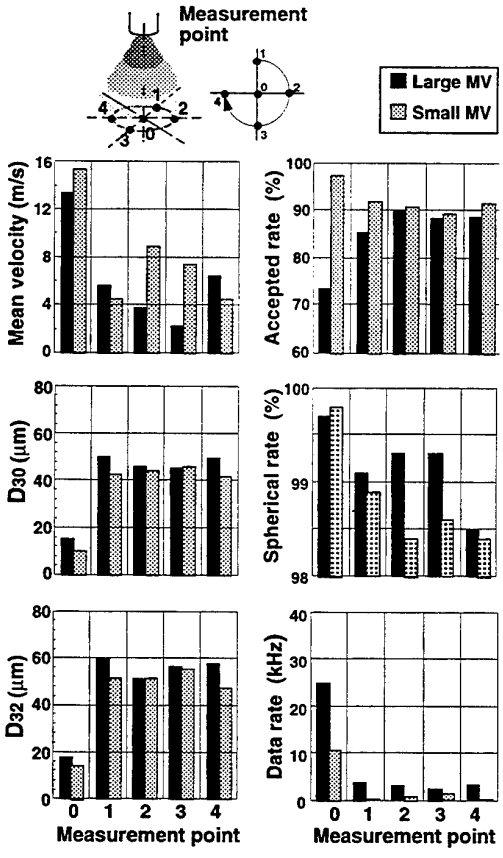

Fig. 12 Measurement volume size effect and measurement status evaluation.

tem set-up specification.

In this study, two measurement volumes were formed at the same location and overlapping each other and the measurements were carried out to show this measurement volume size effect as shown in Fig. 11. The larger measurement volume was 0.37×10.3 mm and the smaller was 0.19×4.09 mm. The measurement set-up was the same as the above-mentioned. Five measurement points were examined to show this effect at different conditions. One is on the axis #0, the others are four points in radius with 20 mm around the axis. The spray is a hollow-cone of 60 degree but an absolute axisymmetry was not achieved well. Figure 12 shows the comparisons of the measured data of axial mean velocity, D_{30} and D_{32} both in two measurement volume sizes. At the point #0, which is on the axial axis. The larger measurement volume results indicate the lower velocity and the larger diameter than those in the small measurement volume. This discrepancies came from the volume averaging effect. At the four radial locations, the discrepancies of D_{30} and D_{32} are not so large, but the velocity differences are not negligible.

Here, as evaluated in the above-mentioned as slit location shift effect, the measurement status was examined by data rate, spherical rate and accepted rate as shown in Fig. 12. At the point #0, the larger measurement volume can show the high data rate of 25 kHz but lower accepted rate of 73%. On the contrary, the small measurement volume cannot provide such high data rate but very high accepted rate of 97%. The spherical rate for both measurement volumes is over 99.7%. It is found that these two measurements were conducted at high level status having less error. For the status of the other four points, there are the same level and possible to identify that the measurement was very accurate.

The influence of measurement volume size on the droplet diameter distribution were examined as shown in Fig. 13. At

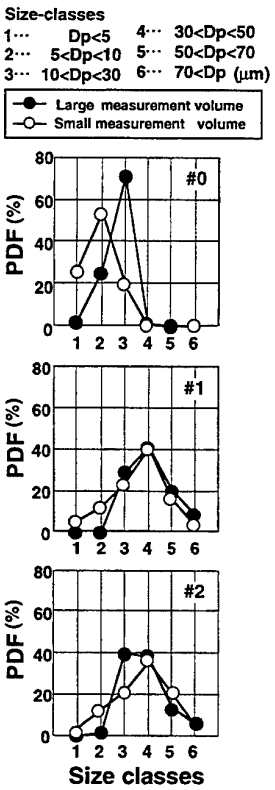

Fig. 13 Measurement volume size effect on size-classified droplet.

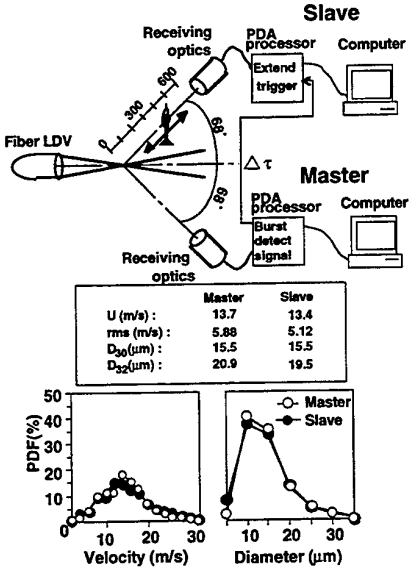

Fig. 14 Flame front presence effect.

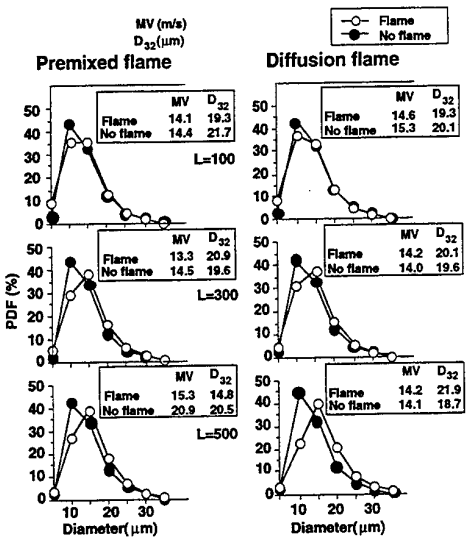

Fig. 15 Flame front location effect.

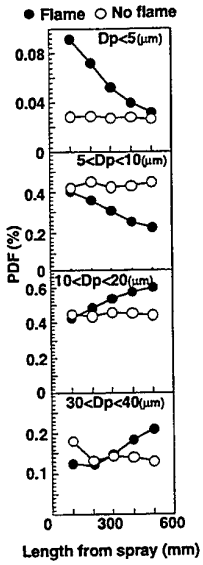

Fig. 16 Flame front location effect.

point #0 on the axis, the small measurement volume can detect large sample number of small droplet than those by the larger measurement volume. There are no differences for over 30 μm droplet. But the difference of PDF of 10-30 μm droplet is very remarkable. At the radial two points #1 and #2, the droplet diameter distributions are compared with each other. These two data show almost no significant difference. Then, it is found that the measurement volume size effect can be caused at the high data rate measurement.

4.3 Flame Front Presence Effect

At the flame front, the wave front of light scattered will have some distortion, which increases noise in data analysis. Furthermore, the presence of the flame front causes the measurement location shift and slit location shift as illustrated in Fig. 1.

In order to examine the effect of the flame presence on the receiving optical path as illustrated in Fig. 14, two receiving optics were implemented having the same reference angle of 68 degree. One processor was used as a master unit. When a burst signal was detected by the master processor, the burst detected monitor signal was used as a external trigger for the slave processor. The delay time of the start timing of these two units is less than several nano second. Since two receiving optics were applied for one measurement volume, there is some percentage of mis-matching of these two receiving points, in other words, the slit locations of these two receiving optics should be coincided each other. Furthermore, even for the coincided slit location, the measured values from these two processors should be extracted from the same droplet. This is the reason why the external trigger was needed.

The measured velocities and diameters both by the master and the slave were shown in the same figure. The discrepancies of these two measured data were 2% in mean velocity, 0% in D_{30}, and 6% in D_{32}. In consideration of the slit location effect and its uncertainty mentioned in the above section, this master / slave measurement location was proven to be the same, and these processors could detect the signals from the almost same droplet ($\fallingdotseq$5%).

Two small flames (premixed and diffusion) were chosen to examine the flame front presence effect on the measured results. Figure 15 shows the effect. In the figure, "flame" symbol denotes that there is a flame on the optical path of the slave receiver, "no flame" means the simultaneous measurement results both by two receivers without flame. The results indicate that the smaller droplet detection rate are strongly affected, especially when the flame is located close to the receiving optics. This result can be understood well as follows; if the flame front locates close to the receiving optics, the optical path length between the flame front and the measurement point becomes long and the measurement point shift even in a small refractive index changing at the flame front, the slit location shift effect can be found easily.

For further examination of this flame front presence effect, the sample number distributions of the size-classified droplet for different flame front locations on the receiving optical path were compared as shown in Fig. 16. It is found that the smaller droplets are much influenced than the larger droplet.

5. CONCLUSIONS

Measurement uncertainties of phase Doppler technique were investigated in three experiments. The effects of slit location shift, measurement volume size, and the flame front presence were examined. The results are summarized as follows:

The slit location shift effect causes a significant measurement uncertainty, especially in high data rate. The optical alignment of the slit location at the initial stage is the most important factors, and this slit location shift effect can be improved dramatically using two PDA receiving optics. The measurement uncertainty of the mass flux at low data rate yields large value. The measurement volume size effect can be seen in detection rate of small droplet at high data rate.

The flame front effect can be seen in the small droplet.

ACKNOWLEDGMENTS

This work was supported by the Grant-in Aid for Scientific Research, Ministry of Education, Science, Sports and Culture, Government of Japan.

REFERENCES

Durst,F.,et al., 1988, Proceedings of the Phase-Doppler Technique, Experiments in Fluids, vol.6.

Bachalo, W.D., 1980, Method for Measuring the Size and Velocity of Spheres by Dual-Beam Light Scatter Interferometry., Appl. Opt. vol.19,No.3,pp363-370.

Bauckhage, K., 1985, International Conference Laser Anemometry Advances and Application, Manchester, pp.261-278 .

Edwards, C.F., and Rudoff, R. C., 1990, Structure of a Swirl-Stabilized Spray Flame by Imaging, Laser Doppler Velocimetry, and Phase Doppler Anemometry, 23d Symp. (Int.) on Comb., pp.1353-1359.

Taylor, A.M.K.P., 1993, Instrumentation for Flows with Combustion, Academic Press.

McDonell, V.G.,et al., 1986, A Comparison of Spatially-Resolved Drop Size and Drop Velocity Measurements in an Isothermal chamber and a Swirl-Stabilized Combustor, 21st Symp. (Int.) on Comb., pp.685-694.

Grehan, G., et al., 1991, Evaluation of a Phase Doppler system using Generalized Lorenz-Mie Theory, Int. Conf. on Multiphase Flows '91, pp291-296.

Sankar, S.V., et al., 1992, Trajectory Dependent Scattering in Phase Doppler Interferometry: Minimizing and Eliminating Sizing Error, 6th Int. Symp. of Laser Tech. to Fluid Mech., Lisbon.

Xu.T.-H., Tropea, C., 1994, Improving the Performance of Two-Component Phase Doppler Anemometers, Meas. Sci. and Techn., 5, pp969-975.

Aizu, Y., et al., 1993, PDA Systems without Gaussian Beam Defects., 3rd Int. Conf. Optical Particle Sizing., Japan, pp.461-470.

Bachalo, W.D and Sankar, S.V, 1994, Factors Affecting the Measurement Resolution and Accuracy of the Phase Doppler Particle Analyzer, The Second Int. Conf. on Fluid Dynamics Meas. and Its Appl..

Tropea, C., et al., 1995, Dual Mode Phase Doppler Anemometer., 4th Int. Cong. Optical Particle Sizing, vol.4, pp287-296.

Sankar, S.V., and Bachalo, W.D., 1995, Performance Analysis of Various Phase Doppler Systems., 4th Int. Cong. Optical Particle Sizing, vol.4, pp407.

Sankar, S.V., et al., 1994, Simultaneous Measurements of Droplet Size, Velocity, and Temperature in a Swirl-Stabilized Spray Flame., 7th Int. Symp. of Laser Tech. to Fluid Mech., Lisbon.

Scott, A.S., et al., 1994, Theoretical analysis of the effects of particle trajectory and structural resonances on the performance of a phase-Doppler particle analyzer., Appl. Opt., vol.33,No.3,473-483.

Sankar, S.V., et al., 1995, An Adaptive Intensity Validation Technique for Minimizing Trajectory Dependent Scattering Errors in Phase Doppler Interferometry.,4th Int. Cong. Optical Particle Sizing, vol.4, p285.

Tropea, C., et al., 1994, Dual-Mode Phase Doppler Anemometer., 7th Int. Symp. of Laser Tech. to Fluid Mech., Lisbon.

Ikeda, Y., et al., 1990, A Compact Fibre LDV with a Perforated Beam Expander., Meas. Sci. and Techn., 1, 260-4.

Brenn, G., et al., 1994, Investigation of Polydisperse Spray Interaction Using an Extended Phase-Doppler Anemometry, 7th Int. Symp. of Laser Tech. to Fluid Mech., Lisbon.

Naqwi, A., et al., 1991, Two-Optical Methods for Simultaneous Measurement of Particle Size, Velocity, and Refractive Index., Applied Optics, 30, pp.4949-4959.

Ancimer, R.J and Fraser, R.A, 1994, Flame-Induced Laser Doppler Velocimetry Velocity Bias, Meas. Sci. and Techn., 5, pp83-92.

Kuo, K., 1986, Principles of Combustion, A Wiley-Interscience Publication.

Ikeda,Y., et al., 1995, Flux Measurements of O_2,CO_2 and NO in an Oil Furnace, Meas. Sci. and Techn., 6, pp.826-832.

Kawahara, N., et al., 1996, Size-Classified Droplets Dynamics of Combusting Spray in 0.1MW Oil Furnace, 8th Int. Symp. of Laser Techn. to Fluid Mech., Lisbon.

Kawahara, N., et al., 1995, Droplet Followability and Slip Velocity Analysis of Evaporating Spray on Gun-Type Oil Burner, 4th Int. Cong. Optical Particle Sizing, vol.4, pp593-602.

Edwards, C.F., and Rudoff, R. C., ﾒ Structure of a Swirl-Stabilized Spray Flame by Imaging, Laser Doppler Velocimetry, and Phase Doppler Anemometryﾓ, Twenty-Third Symposium on combustion, pp.1353-1359, 1990.

Presser, C., et al., 1995, Interpretation of Size-Classified Droplet Velocity Data in Swirling Spray Flames, AIAA Paper 95-0283.

Seay, J., et al., 1995, Atomisation and Dispersion from a Radial Airblast Injector in a Subsonic Crossflow, AIAA Paper 95-3001.

Ikeda, Y., et al., 1996, Spray Formation and Dispersion of Size-Classified Fuel Droplet of Air-Assist Injector, 8th Int. Symp. of Laser Techn. to Fluid Mech., Lisbon.

Edwards, C.F., et al., 1990, Measurement of Correlated Droplet Size and Velocity Statics, Size Distribution, and Volume Flux in a Steady Spray Flame, 5th Int. Symp. of Laser Tech. to Fluid Mech., Lisbon.

Bachalo, W.D., 1994, Injection, Dispersion, and Combustion of Liquid Fuels, 25th Symp. (Int.) on Comb., pp.333-344.

SESSION 3

Combustion I

INVESTIGATIONS OF TURBULENT JET DIFFUSION FLAMES BY SPONTANEOUS RAMAN SCATTERING AND LASER-INDUCED FLUORESCENCE

W. Meier, A.O. Vyrodov, V. Bergmann, U.E. Meier, W. Stricker

Institut für Physikalische Chemie der Verbrennung,
DLR, Pfaffenwaldring 38, D-70569 Stuttgart

ABSTRACT

An experimental arrangement for combined single-pulse Raman/LIF measurements of temperature, major species and NO concentrations was used to investigate turbulent N_2/H_2/air jet diffusion flames. Structural information about the reaction zone and the fuel jet were obtained by planar laser-induced fluorescence of OH and (doped) NO. Some fundamentals of the measuring system and the applied laser diagnostic techniques are described. The main goal of this paper is to demonstrate how these measuring techniques can be used to characterize the flames and to identify characteristic effects, like differential diffusion, the correlations between concentrations and temperature, and the flame structures in the near field of the jet. The transport mechanism of NO in this type of jet flames is discussed.

1. INTRODUCTION

In order to improve the understanding of turbulent combustion processes and to support the development of theoretical flame models, detailed experimental studies on well-chosen flames and combustors are of essential importance. Considering the complex interactions in turbulent flames, an approach focusing on the investigation of simple turbulent jet flames which provide a well-defined and rather simple flowfield seems to be suitable. Among the main problems that have to be treated are the interactions between the turbulent flow and chemical reactions in general and the formation of NO_x in particular. For the study of these processes, laser based measuring techniques have proven to be superior to sampling probes because they work non-intrusively, yield a high spatial resolution, and can be applied with single-pulse resolution for instantaneous measurements.

In "clean" particle-free flames, spontaneous pulsed Raman scattering allows the simultaneous determination of the major species concentrations and the temperature and yields, thus, an overall characterization of the chemical state within the flame. The potential of this technique and its contribution to a deeper insight in turbulent combustion has been demonstrated in a number of investigations on turbulent jet flames. However, for the detection of minor species concentrations as flame radicals or pollutants, laser-induced fluorescence (LIF) is far more sensitive and useful. The main difficulty in applying LIF is its relatively complicated signal evaluation in order to get absolute concentrations, because the fluorescence intensity depends on the relative population of the ground state (usually a Boltzmann distribution) and on collisional energy transfer processes. Thus, the quantitative data evaluation of LIF signals requires, in general, additional information about gas composition and temperature which can be obtained (on a single-pulse basis) by spontaneous Raman scattering, as demonstrated by Barlow et al (1990), Stårner et al (1990), Cheng et al (1992), and Schefer et al (1990).

The main topic of this paper are simultaneous Raman/-LIF measurements of temperature, major species and NO concentrations in turbulent H_2/air jet diffusion flames. The importance of NO as pollutant is well-known, and environmental concerns require strategies for combustors with low NO_x emission. In this context, fundamental investigations about NO formation mechanisms in turbulent flames are necessary, including an accurate determination of NO concentrations. Furthermore, the NO concentration is a critical parameter for the verification of mathematical flame models, because the NO formation depends strongly on temperature, radical concentrations, and residence time. An incorrect prediction of NO concentrations would therefore reveal shortcomings of the applied flame model. The combined Raman/NO-LIF technique was first applied by Barlow and Carter (1994) investigating a pure H_2/air and a helium diluted H_2/air diffusion flame. In the studies presented here, the H_2/air flames were diluted by N_2 in order to reduce heat loss by radiation, because this effect complicates the simulation of flames and especially of the NO emission. The goal of our investigations was the determination of accurate data sets from precisely defined jet flames which can serve as a test case for predictions from flame simulations. Currently, several groups of flame modelers are working with these data sets and first results of the comparison are available, e.g. by Sanders and Gökalp (1996). In addition to pointwise single-pulse Raman/LIF measurements, two-dimensional LIF images of OH and doped NO (added to the fuel) were recorded in

order to investigate the structures of the reaction zone and the mixing layer. These images provide helpful information for the understanding of the transport processes within these flames.

It is not the scope of this paper to present the complete data sets of the investigated flames. Instead it is intended to demonstrate how the applied measuring techniques were used to characterize the flames and to identify characteristic effects occuring in this type of jet flames, especially differential diffusion and the influence of the flame structures on NO and temperature distributions. More detailed information about the flames can be found in the paper of Meier et al (1996a) and readers interested in the complete data sets may get them on request.

2. EXPERIMENT AND DATA EVALUATION

The main components of the experimental setup, schematically shown in Fig.1, are a flashlamp-pumped dye laser for the Raman excitation, a Nd:YAG-pumped dye laser for NO LIF, a spectrograph for separating the different Raman signals, photomultiplier tubes (PMTs), electronic devices for signal detection, and burners for calibration and turbulent flames.

2.1 Burners

Calibration measurements for the Raman and NO LIF signals were performed in laminar premixed H_2/air flames stabilized on a flat flame burner (McKenna Products). The characteristics of this burner have been thoroughly studied by CARS, Rayleigh scattering, and flame calculations resulting in a set of 38 "standard flames" covering a range of temperatures from 1230 to 2180 K and of equivalence ratios from 0.3 to 2.0. A further extension of the temperature range down to about 700 K was achieved by using a stainless steel tube as a cooler for the exhaust gas. The operating conditions of the burner, as well as the temperatures and gas compositions of most of the "standard flames" can be found in the paper of Prucker et al (1994).

The burner for turbulent jet diffusion flames consisted of a 35 cm long straight stainless steel tube (i.d. 8 mm) with a thinned rim at the exit. The tube was surrounded by a nozzle (i.d. 140 mm) supplying co-flowing dry air at an exit velocity of typically 0.3 m/s. The burner could be translated in radial and axial directions to change the measuring location within the flame. The fuel and air flows were controlled by calibrated mass flow meters (Brooks Inc.). An identical burner is operated at the Technische Hochschule Darmstadt, Fachgebiet Energie- und Kraftwerkstechnik, where Neuber et al (1994) and Cheng et al (1995) have performed LDA, Raman, and CARS measurements on similar flames. In cooperation with that research group we are working on a library of complementary data sets of well-defined turbulent diffusion flames.

2.2 The Raman System

The Raman apparatus and the calibration and data evaluation procedure for the Raman signals are described in detail by Meier et al (1994 and 1996b) and only basic information will be given here. The flashlamp-pumped dye laser (Candela, LFDL-20) was operated with Coumarin 480 at a wavelength of 488 nm and a repetition rate of 5 Hz. Due to the relatively long pulse duration of 2-3 µs a quasi-intracavity configuration was used, i.e. the laser beam was reflected back into the dye cell after passing through the flame, yielding effective pulse energies of up to 4 J. To decrease the focal diameter to about 0.5 mm, the laser beam was expanded by a telescope (L1 and L2) to 80 mm. The scattered light from the focal region was collected by an achromatic lens (L4; f=160 mm, Ø=80 mm) and a spherical mirror (M2; f=200 mm, Ø=150 mm) and relayed to the entrance slit of a spectrograph (Spex 1802, f=1 m, f/8.4, dispersion ≈0.5 nm/mm). Corresponding to the magnification of the signal collection optics (approx. 3.2) and the width of the entrance slit of the spectrograph (1.8 mm) the observed

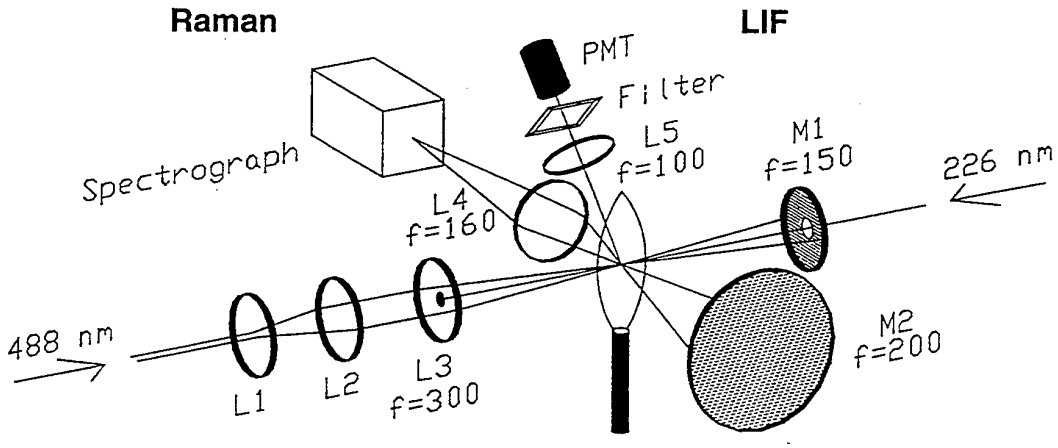

Fig.1: Schematic of the experimental arrangement. L: lenses; M: mirrors

volume had a length of 0.56 mm, which determines, together with the focus diameter (≈0.5 mm), the spatial resolution of the measurement. The dispersed Raman signals of O_2, N_2, H_2O, and H_2 were detected by photomultiplier tubes (Hamamatsu R928 and R3896), passed on to gated integrators (Stanford Research Systems SR250) and were finally stored and processed by a PC. The number density of each species was derived from the corresponding signal and a calibration factor, which was determined from measurements in the "standard flames". The temperature was calculated from the total number density using the ideal gas law. The precision of the temperature and concentration measurements, i.e. the shot-to-shot reproducibility, is typically 2% under flame conditions, the absolute accuracy is 3-5%, depending on the absolute density.

2.3 The LIF System

The LIF system and the data evaluation procedure for absolute NO concentration measurements have been previously described by Meier et al (1996a) and, therefore, only a condensed description will be presented here. NO was excited in the (0-0) band of the $A^2\Sigma^+$-$X^2\Pi$ transition at 226 nm, using a Nd:YAG-pumped dye laser operated with a mixture of DCM and Pyridine 1. The dye laser radiation at λ≈678 nm was frequency tripled by mixing the second harmonic (λ≈339 nm) with the fundamental in a BBO crystal yielding about 0.5 mJ at 226 nm in a pulse of 6 ns duration and a spectral width of 0.7 cm^{-1}. The beam was apertured to a circular shape and slightly focused through a hole (Ø=3 mm) in the mirror M1 into the measuring volume, where the beam diameter was approx. 0.5 mm. Saturation of the A-X transition was reduced to a small degree by attenuating the pulse energy to ≤ 0.1 mJ. The fluorescence, covering the spectral range from about 226 to 300 nm, was collected by a quartz lens (f=100 mm, Ø=100 mm) and detected by a solar blind photomultiplier (Hamamatsu R166 UH) with high quantum efficiency between 160 and 300 nm. To suppress stray light from the laser beam a long pass filter with a sharp edge at ≈230 nm was mounted in front of the PMT. The length and position of the measuring volume could be changed by a slit in the image plane of the detection optics in front of the PMT. To overlap the two laser beams at 226 and 488 nm and the measuring volumes of the Raman and LIF systems, a gas flow of H_2/NO from a capillary (Ø=0.4 mm) was used. The overlap was controlled and adjusted by translating the capillary in x, y, and z direction while monitoring the H_2 Raman and NO LIF signals. Hereby, the measuring volume of the Raman system was taken as fixed and that of the LIF system was adapted to it by adjusting the UV laser beam and the position and width of the slit in the image plane of the LIF detection optics. The time delay between the two laser pulses was ≈1 µs. A few percent of the UV laser beam were split off to monitor the relative pulse energy by a photodiode and to excite NO in a reference gas cell to control the stability of the UV laser wavelength. For the excitation of NO, the pair of lines $R_{11}(18.5)$ + $Q_{12}(18.5)$ was chosen because it is well isolated, it does not interfere with O_2 lines of the Schumann-Runge band, and yields a high signal level over a wide range of temperatures.

2.3 Quantitative Evaluation of NO LIF Signals

For the quantitative interpretation of the NO LIF data, the following influences on the signal strength have, in general, to be considered: Boltzmann fraction of the ground rotational state, vibrational and rotational energy transfer (VET, RET), line shift, line broadening, electronic quenching, and, in case, saturation. Beginning with the Boltzmann fraction, the relative population of the J=18.5 state was calculated from the temperature simultaneously determined by the Raman measurement. VET of the $A^2\Sigma^+$ v'=0 state of NO is slow in comparison to the electronic quenching rate, as determined by Cattolica et al (1989), and can be neglected in. RET changes the spectral composition of the fluorescence, but in case of broadband detection, as applied here, does not influence the detection efficiency by "spectral biasing". Furthermore, Raiche and Crosley (1990) and Drake and Ratcliffe (1993) showed, that electronic quenching cross sections do not vary significantly with rotational level so that RET does not change the overall fluorescence yield. Thus, RET can also be neglected for the for the quantitative data evaluation in our experiments.

Under these conditions and for weak excitation of a single transition, the detected fluorescence signal S_f per laser pulse can be written as:

$$S_f = C\, n_{NO}\, f_B\, E_p\, g\, A/(A+Q) \qquad (1)$$

where C is a constant including geometrical parameters, detection efficiency, size of the measuring volume, and the Einstein coefficient of absorption, n_{NO} is the NO number density, f_B is the Boltzmann population fraction, E_p is the laser energy per pulse, g is the line overlap integral, A is the Einstein coefficient of spontaneous emission, and Q is the electronic quenching rate. For the calculation of the line overlap integral between the molecular line shape (Doppler and collisional line shape) and the spectral laser profile, as well as for the calculation of the molecular line shift, information about temperature and collisional environment is necessary, which is in our case obtained from the Raman data. The temperature dependent broadening and shift coefficients for collisions of NO with N_2, H_2O, and O_2 used in our data evaluation program were taken from Chang et al (1992) and Di Rosa et al (1993). The variation of the overlap integral is small for typical flame conditions, but for gas densities at room temperature the value increases by about 30%. The effect of line shift leads to an additional change of the overlap integral of less than 2%.

The most important correction of the NO LIF signals concerns electronic quenching, which is typically two orders of magnitude faster than the spontaneous emission rate. The total quenching rate depends strongly on the gas composition and temperature, and, considering the conditions in our H_2/air flames, can vary by an order of magnitude. Therefore, an accurate knowledge of the quenching environment and reliable values of the quenching cross sections of the involved species are necessary in order to get correct NO concen-

trations. The quenching cross sections and their temperature dependence were measured for these species by Raiche and Crosley (1990) in the temperature range from 300 to 750 K and by Drake and Ratcliffe (1993) for 300-1570 K. Discrepancies between these data sets of up to 50% occur for the quenching cross section of H_2O for T > 300 K. We used the results of Drake and Ratcliffe because measurements in our calibration flames could only be interpreted consistently with their quenching cross section for H_2O. To extrapolate the measured quenching cross sections for temperatures above 1570 K (or 750 K for the data of Raiche and Crosley), the calculated values of Paul et al (1994) were taken. With these quenching cross sections and the temperatures and gas compositions from the Raman measurements, the total quenching rate was calculated as outlined by Paul et al (1994).

The calculation of the Boltzmann fraction and the corrections for quenching, line broadening, and line shift were included in our data evaluation program. The absolute quantification of the LIF signals was performed by calibration measurements in the standard flames doped with small amounts of NO (≤100 ppm). To ensure that doped NO is not consumed on its way from the flow meter to the measuring volume, e.g. in the reaction zone, the NO concentrations in the exhaust gas were measured using a commercial suction probe (Hartmann & Braun, Radas 1G). The measured NO concentrations in the doped calibration flames and in cold air/NO mixtures agreed within 5% with the concentrations deduced from the gas flow meters.

The small degree of saturation, which was applied in order to increase the LIF signal level, was not considered in the evaluation program. However, measurements in the calibration flames did not reveal a dependence of the degree of saturation on the gas composition or temperature within the measuring accuracy.

2.4 2D LIF Imaging

The 2D LIF imaging experiments were performed with a new laser system consisting of a Nd:YAG-pumped optical parametric oscillator with frequency doubler (Spectra Physics MOPO 730). For excitation of the OH radical the laser was tuned to the $Q_2(9)$ line of the $X^2\Pi(v=0) \rightarrow A^2\Sigma(v=1)$ transition at $\lambda \approx 283$ nm, for excitation of NO the same transition as in the point measurements was used. The pulse energies were on the order of 5 mJ. The UV laser beam was formed to a vertical light sheet of approx. 40 mm height and 0.2 mm thickness by a cylindrical lens (f=-19 mm) and a spherical lens (f=200 mm) and irradiated into the flame so that the sheet intersected the flame axis. The fluorescence was detected under 90° by an image-intensified CCD camera (PCO) equipped with a UV telephoto lens (Nikkor, f=105 mm, f/4.5), using a 100 ns temporal detection window.

Series of typically 25 single-pulse images were recorded at various downstream positions. The objective of the OH measurements was to get structural information about the position and thickness of the reaction zones. Imaging the fluorescence from (doped) NO was in this case used to visualize the structure of the H_2/N_2 jet. Because LIF on H_2 and N_2 is hard to perform under flame conditions, the fuel was seeded with 400 ppm of NO, so that the fluorescence from NO served, within certain limits, as an indicator for the fuel jet. The interpretation of these images will be treated in the discussion of the results.

3. RESULTS AND DISCUSSION

The Raman/LIF measurements were performed in a pattern of measuring locations at various radial and axial positions, r and x/d, respectively. At each point, probability density functions (pdf's) comprising 300 single pulses were recorded from which the mean values and fluctuations were extracted.

3.1 Mean Concentrations and Temperatures

In order to characterize the overall behaviour of this type of jet diffusion flames, radial profiles of the mean values are displayed in Fig.2 for the downstream positions x/d=5 and 40, recorded in a flame with Reynolds number Re=8800, fuel composition 75%H_2 + 25%N_2, and exit velocity v_{exit} =42.3 m/s. At x/d=5, combustion takes place in a region around r≈8 mm where the temperature and the concentrations of H_2O and NO have their maxima. The highest mean temperature is 2241 K which is close to the adiabatic flame temperature of T_{ad}=2264 K for this fuel composition.

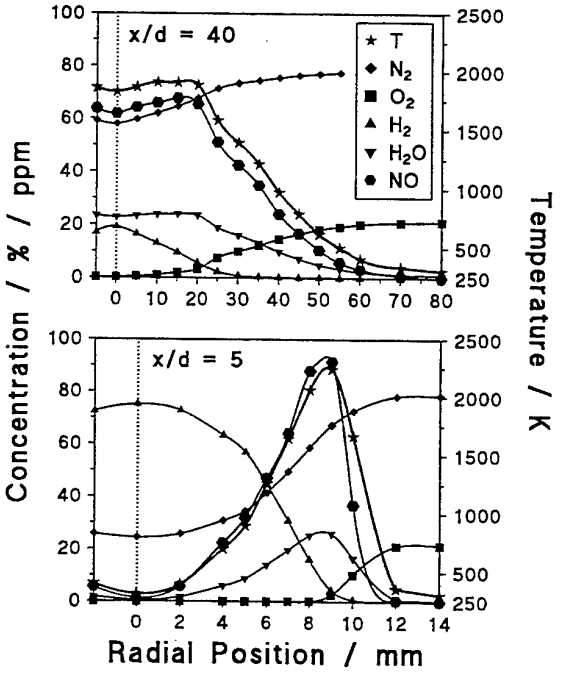

Fig.2: Radial profiles of mean concentration and temperature values from a H_2/N_2/air flame (Re=8800). Concentrations are given in % for major species and in ppm for NO. The symbols represent measured values and the solid lines are drawn as a guide line for the eye. The dotted line indicates the flame axis.

The corresponding mean NO concentration is 92 ppm. Near the flame axis, mainly unburnt fuel is present with a small amount of combustion products which have been transported by turbulent mixing from the reaction zone towards the center of the flame. Further downstream, the flame becomes broader and the regions of combustion reach the flame axis. At x/d=40, the H_2 concentrations have dropped below 20% and combustion is almost completed. The highest mean temperatures are around 1900 K and the maximum mean NO concentration is 68 ppm. At first sight, the drop in temperature and NO concentration is not plausible, because as long as the fuel is not consumed, heat is still released and NO should accumulate in the exhaust gas. Examining the single-pulse values (not displayed) confirms the observation that the temperatures at x/d=5 are considerably higher than farther downstream and exceed, for many single-pulse values, the adiabatic flame temperature. It will be shown in the next paragraph, that this deviation from adiabatic equilibrium is due to differential diffusion effects, leading to a temperature increase in the region around the reaction zone and an enhanced production of thermal NO. Above x/d=5, differential diffusion is less pronounced so that the temperature and the NO formation decrease. The net effect between further NO production and dilution of the initially high NO concentrations by downstream generated exhaust gas is, in this flame, a decrease of NO concentration. This effect is even more pronounced in a H_2/N_2/air jet flame of higher dilution by N_2 and lower Reynolds number, as shown by Meier et al (1996a).

3.2 Effects of Differential Diffusion

In a flow with fully developed turbulence, bulk transport by molecular diffussion is of minor importance and the concept of unity-Lewis-number, often used in turbulent flame models, is justified. However, it has been observed, e.g. by Drake et al (1986) and Smith et al (1995), that differential molecular diffusion, i.e. unequal diffusivity for different species, can play a significant role in turbulent jet flames fuelled with hydrogen. Our investigations in various H_2/N_2 jet diffusion flames have revealed that this effect is clearly pronounced in N_2-diluted H_2 flames, especially near the flame root.

The identification of differential diffusion effects in turbulent flows requires the simultaneous detection of all major species concentrations (on a single-pulse basis), because only in this way the correlations between the different species concentrations become obvious. A common way to identify differential diffusion is to compare the mixture fractions derived from different element mass fractions, as performed by Smith et al (1995) or Meier et al (1996a). However, in the examples given here, we want to restrict the presentation to the correlations between mole fractions and temperature (instead of mixture fractions) from which important indications for the transport processes in these flames can be deduced.

In order to investigate the influence of Reynolds number on the transport mechanisms, the exit velocity of the fuel jet (75%H_2 + 25%N_2) was varied stepwise from 14.1 to 56.4 m/s. Examplary results for the O_2-T and H_2O-T correlations at a downstream position close to the nozzle (x/d=5) are displayed in Fig.3 for v_{exit}=14.1 and 56.4 m/s (Re≈3000 and 12000). The symbols represent single-pulse values recorded at various radial locations between the flame axis and the periphery of the flame. The solid lines represent results from an adiabatic equilibrium calculation using the computer code of Gordon and McBride (1971). It is clearly seen that the measured values deviate markedly from adiabatic equilibrium (in contrast to the H_2-T and N_2-T correlations which are not displayed in the figure). To show that these deviations are partly due to differential diffusion effects, we make use of the results of Katta et al (1994) who investigated a laminar diffusion flame of similar composition. According to their definition, the local Lewis number, Le, of a species is the ratio of the conductive heat transport of the mixture to the mass transport of the species ($Le_i=\lambda/(\rho \cdot D_{i\text{-}N2} \cdot c_p)$ where λ is the thermal conductivity, ρ is the density, $D_{i\text{-}N2}$ is the diffusion coefficient of species i in N_2, and c_p is the specific heat of the mixture. For gas compositions and temperatures typical for our flames at x/d=5, O_2 has a Le number near unity, H_2 below 1, and H_2O has a Le number greater than 1 on the fuel side and little less than 1 on the air side.

Beginning with the almost laminar flame, v_{exit}=14.1 m/s, it is seen in Fig 3(a) that temperatures are measured which exceed the adiabatic flame temperature by several hundred K. The corresponding radial location is in or near the reaction zone. In that region of the jet (x/d=5, r≈10 mm), where the general flow direction is parallel to the flame surface and stretch effects are low, the mass diffusion rate from the flame zone is higher than the heat conduction rate (Le<1) and the temperature is increased above T_{ad}. Thus, the temperature increase is due to differential diffusion. On the fuel side of the reaction zone (rich branch), Le_{H2O} is much greater than 1, so that heat is faster transported away than H_2O leading to a temperature drop for this branch, in accordance with the experimental results. On the air side (lean branch) with $Le_{H2O}\leq 1$, only a little temperature increase is expected due to differential diffusion. The experimental results show, instead, quite high temperatures and/or low water concentrations in comparison to adiabatic equilibrium, indicating an additional influence on the H_2O-T correlation. The O_2-T correlation in Fig.3(b) shows high O_2 concentrations and /or high temperatures which can, again, not solely be explained by differential diffusion because the corresponding Lewis number is near unity.

For the more turbulent conditions (v_{exit}=56.4 m/s), where differential diffusion effects should be small, the maximum temperatures have dropped, but deviations from adiabatic equilibrium are still unexpectedly large. The O_2-T correlation and the "lean branch" of the H_2O-T correlation have not changed much, indicating that the transport processes on the air side of the flame are not affected markedly by the increase of the flow velocity. The "rich branch" in Fig.3(c) has, instead, changed its shape and moved closer to the equilibrium curve. Further downstream, e.g. at x/d=20 (not displayed), where the turbulence is well developed, all concentrations are in good agreement with adiabatic equilibrium.

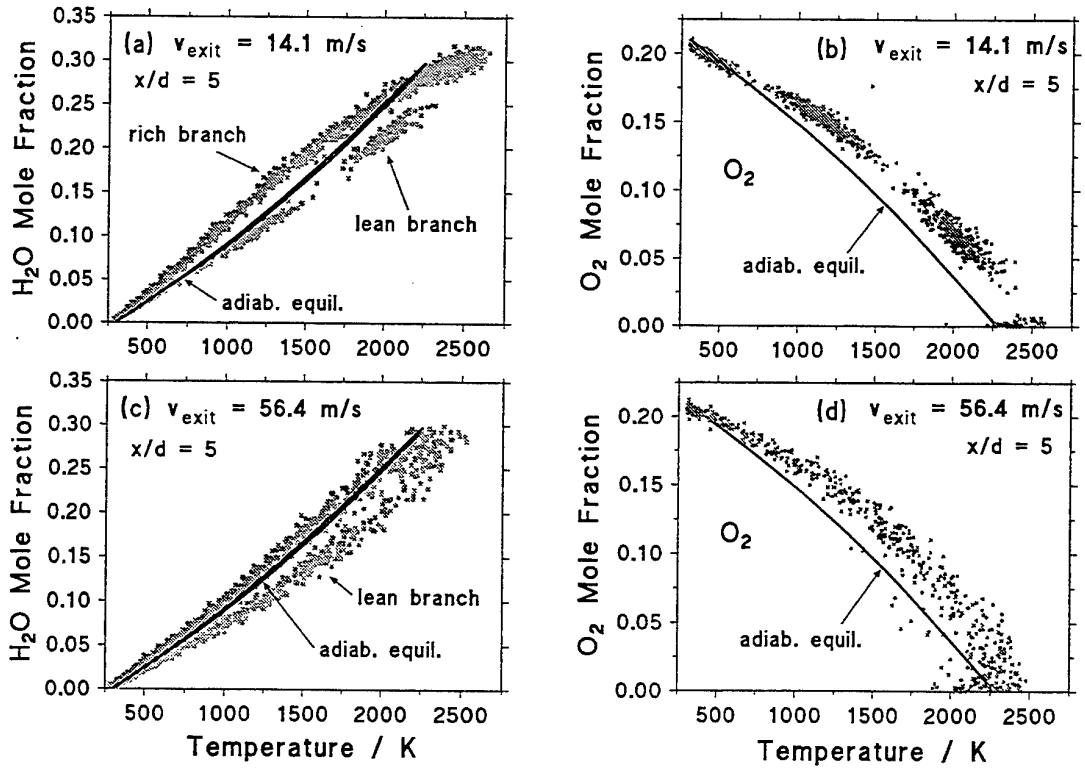

Fig.3: H_2O-T and O_2-T correlations showing the deviations between the experimental values (symbols) and adiabatic equilibrium at the downstream position x/d=5.

The results lead to the conclusion that differential diffusion plays a significant role in these flames, but that it is not responsible for all observed deviations from adiabatic equilibrium. To further illuminate the interaction between flow field and chemical state, the measured NO distributions are discussed now.

3.3 Correlation between NO and Temperature

Figure 4 displays the correlations between NO concentration and temperature for the same flames and positions as discussed in the previous paragraph. In this case, the single-pulse values were conditionally averaged, i.e. averaged within distinct temperature intervals, to yield a clearer identification of the relations. An essential difference between the flames is the level of NO concentrations which is more than 5 times higher for the slow jet. One reason for this difference is the longer residence time for the formation of NO at lower flow velocities. The other reason is the higher temperature level in the reaction zones of the slow jet, caused by differential diffusion, leading to a strong increase of thermal NO formation.

Another remarkable result is the splitting of the data into a "rich" and a "lean branch", i.e. NO concentrations measured on the fuel side of the reaction zone are considerably higher than those measured on the air side at the same temperature. At first sight, this effect is surprising, because in the near field of the jet, NO and heat are both produced

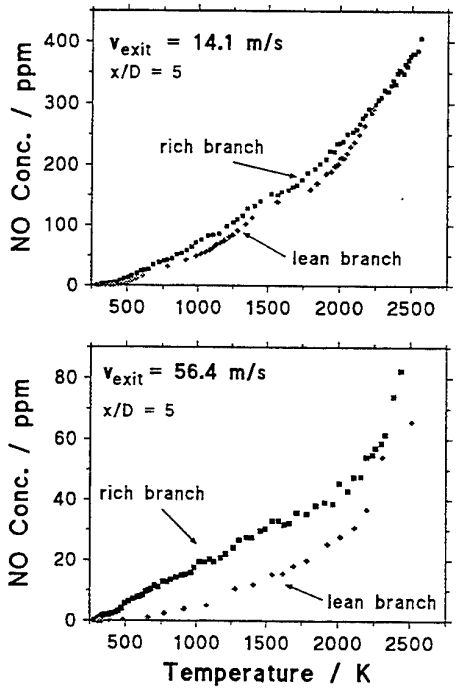

Fig.4: Correlation between NO and temperature. The single-pulse values were classified with respect to rich or lean gas compositions and conditionally averaged within distinct temperature intervals.

within the small spatial region of the reaction zone and the question arises, why they develop in a different way while being transported to the air or to the fuel side. The splitting is rather small for the slow jet with v_{exit}=14.1 m/s, most markedly pronounced for v_{exit}=42.3 m/s (not shown here), and begins to wash out for higher exit velocities. Furthermore, the splitting decreases with increasing distance from the nozzle. Combining these experimental results, this effect seems to be related to the structures and transport mechanisms within these flames. In order to get more information about the structure, 2D LIF imaging experiments were performed.

3.4 Structural Information from 2D LIF Imaging

Figure 5 shows two typical single-pulse 2D LIF images of OH and doped NO covering a field of view from x/d≈3 to 7 in a flame with v_{exit}=42.3 m/s and Re≈8800 (the same flame as in Fig.2). The OH distribution reflects the position and shape of the reaction zone, where high temperatures and superequilibrium concentrations of OH are present. It can be seen that the reaction zone is smooth and not wrinkled by turbulence. Further downstream (not displayed) the reaction zone becomes broader and more irregular and, finally, in the upper part of the flame the OH distribution is broad, indicating distributed reaction.

The fluorescence distribution from NO, seeded to the H_2/N_2 fuel jet, needs some explanation for the correct interpretation. In a pure H_2/N_2 mixture, NO fluorescence is very weakly quenched ($Q \approx 3 \cdot 10^7$ sec^{-1}) resulting in high signal levels. However, small admixtures of water enhance the quenching drastically, e.g. 2% water increase the quenching rate by an order of magnitude, leading to a rapid drop in LIF signal intensity. Thus, the bright regions in the NO LIF distribution in Fig.5 represent almost pure fuel, whereas the dark contours reflect the entrainment of water from the mixing layer, i.e. the region between the fuel side of the reaction zone and the fuel jet. From the fluorescence distribution it is seen that the flow field of the high-speed fuel jet and the mixing layer is highly turbulent exhibiting vortical structures from roughly 1 to 10 mm in dimension. Although the vortical structure of the inner core of the flame seems to be in contrast to the laminar shape of the reaction zone, this behaviour is not unusual. Investigations by Clemens and Paul (1995), Everest et al (1995), and some other research groups have revealed similar structures in jet diffusion flames. Due to the heat release in the reaction zone, the viscosity increases strongly, resulting in a decrease of Reynolds number and a laminarization of the flow in the region of the flame zone. In this way, the reaction zone forms a barrier for the vortices and the transport by turbulent diffusion. In the reaction zone and on the air side, the flow is laminar, at least in the near field of the jet. Further downstream the reaction zone is more and more broken up by turbulence and mass transport is finally dominated by turbulent diffusion.

With this picture of the flame, the results presented in the previous paragraphs, i.e. species-temperature correlations at x/d=5, can be qualitatively explained. In the reaction zone and on the air side, mass transport is dominated by molecular diffusion, whereas on the fuel side transport is dominated by turbulent mixing, except for the almost laminar flame with v_{exit}=14.1 m/s. NO molecules diffusing from the reaction zone to the fuel side are picked up and carried away by turbulent vortices in the mixing layer. To give an impression of the different time scales for molecular and turbulent transport, the large-eddy-turnover time, τ_t, taken as the measure for the turbulent time scale, is estimated according to Barlow et al (1990) as $\tau_t \leq 1$ ms at x/d=5. In the same time, a NO molecule covers a distance of about 1 mm by diffusion. Thus, the probability that NO molecules diffuse back from the fuel side into the reaction zone and further to the air side is rather low.

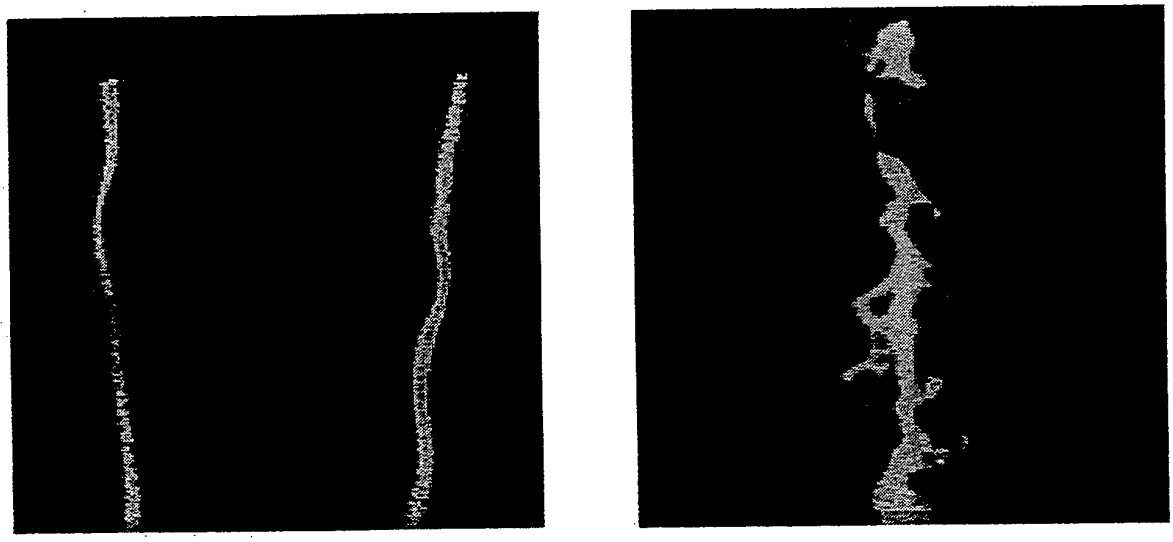

Fig.5: Single-pulse 2D LIF images of OH (left) and doped NO (right) recorded in the near field (x/d≈3-7) of a jet flame with v_{exit}=42.3 m/s. The width of each image corresponds to approx. 30 mm.

The turbulent vortices, being hindered from penetrating the reaction zone, neither can transport NO to the air side. Consequently, NO is, to some extend, trapped in the inner core of the jet. In the reaction zone and on the air side, NO is only transported by molecular diffusion and can move from the air side to the fuel side by random motion. In this way, the reaction zone acts quasi as a semipermeable wall for NO. For the transport of heat and temperature, the situation is somewhat different. While NO molecules have hardly enough time to diffuse from a fast moving vortex into the reaction zone, heat exchange between these regions is, due to the high collision rate, not suppressed. Considering the results from Fig.4, i.e. the splitting in the NO-T correlation, the described mechanism is fairly active for the turbulent jet with v_{exit}=56.4 m/s, but less pronounced for the nearly laminar jet with v_{exit}=14.1 m/s, where transport by turbulence is of minor importance. Further downstream, the splitting is washed out because the flow develops to a fully turbulent jet and transport by turbulent diffusion is the dominating mechanism on both, the air and the fuel side.

Some of the arguments also hold for the transport of H_2O, but with less consequences because H_2O has a higher diffusion coefficient and its formation is not temperature dependent. Nevertheless, it explains qualitatively the higher water concentrations on the fuel side observed in Fig.3.

4. CONCLUSIONS

A combined Raman/LIF apparatus for the simultaneous detection of temperature, major species and NO concentrations, and a 2D LIF imaging system have been presented. In investigations on various H_2/N_2/air jet diffusion flames the potential of these techniques for a detailed flame characterization has been demonstrated. A main advantage of simultaneous single-pulse measurements lies in the possibility to study the correlations between various quantities, which, in many cases, contain the key information for the understanding of the interaction between flow field and chemistry. It was shown that differential diffusion plays an important role in this kind of jet flames, especially near the flame root where the temperature is raised above T_{ad} and thermal NO formation is significantly enhanced. The experimental results further revealed different flow conditions in the near field of the jet: high turbulence on the fuel side of the reaction zone and laminar conditions within the reation zone. Based on the experimental results, a qualitative interpretation for the transport mechanism of NO has been given, which explains the higher NO concentrations on the fuel side in comparison to the NO concentrations on the air side at the same temperature.

ACKNOWLEDGEMENTS

We would like to thank Prof. Th. Just for his participation in our work and for helpful discussions. The financial support by the Ministerium für Wissenschaft und Forschung, Baden-Württemberg, within the TECFLAM research project is gratefully acknowledged.

REFERENCES

Barlow, R.S., Dibble, R.W., Chen, J.-Y. & Lucht, R.P. 1990, Effect of Damköhler Number on Superequilibrium OH Concentrations in Turbulent Nonpremixed Jet Flames, Combust. Flame, vol. 82, pp. 235-251.

Barlow, R.S. & Carter, C.D. 1994, Raman/Rayleigh/LIF Measurements of Nitric Oxide Formation in Turbulent Hydrogen Jet Flames, Combust. Flame, vol. 97, pp.261-280.

Cattolica, R.J., Mataga, T.G. & Cavolowsky, J.A. 1989, Electronic Quenching and Vibrational Relaxation of NO $A^2\Sigma$(v'=1 and v'=0) by Collisions with H_2O, J. Quant. Spectrosc. Radiat. Transfer, vol. 42, pp.499-508.

Chang, A.Y., Di Rosa, M.D. & Hanson, R.K. 1992, Temperature Dependence of Collision Broadening and Shift in the NO A ← X(0,0) Band in the Presence of Argon and Nitrogen, J. Quant. Spectrosc. Radiat. Transfer, vol. 47, pp.375-390.

Cheng, T.S., Wehrmeyer, J.A. & Pitz, R.W. 1992, Simultaneous Temperature and Multispecies Measurements in a Lifted Hydrogen Diffusion Flame, Combust. Flame, vol. 91, pp.323-345.

Cheng, T.-C., Früchtel, G., Neuber, A., Lipp, F., Hassel, E.P. & Janicka, J. 1995, Experimental Data Base for Numerical Simulations of Turbulent Diffusion Flames, Forschung im Ingenieurwesen-Engineering Research, vol. 61, pp.6-12.

Clemens, N.T. & Paul, P.H. 1995, Effects of Heat Release on the Near Field Flow Structure of Hydrogen Jet Diffusion Flames, Combust. Flame, vol. 102, pp.271-284.

Di Rosa, M.D., Chang, A.Y. & Hanson, R.K. 1993, Continuous Wave Dye-Laser Technique for Simultaneous, Spatially Resolved Measurements of Temperature, Pressure, and Velocity of NO in an Underexpanded Free Jet, Appl. Opt., vol. 32, pp.4074-4087.

Drake, M.C., Pitz, R.W. & Lapp, M. 1986, Laser Measurements on Nonpremixed H_2-Air Flames for Assessment of Turbulent Combustion Models, AIAA J., vol. 6, pp.905-917.

Drake, M.C. & Ratcliffe, J.W. 1993, High Temperature Quenching Cross Sections for Nitric Oxide Laser-Induced Fluorescence Measurements, J. Chem. Phys., vol. 98, pp. 3850-3864.

Everest, D.A., Driscoll, J.F., Dahm, W.J.A. & Feikema, D.A. 1995, Images of the Two-Dimensional Field and Temperature Gradients to Quantify Mixing Rates within a Non-Premixed Turbulent Jet Flame, Combust. Flame, vol. 101, pp.58-68.

Gordon, S. & McBride, B.J. 1971, Computer Program for Calculation at Complex Chemical Compositions, Rocket Performances, Incident and Reflected Shocks and Chapman-Jouget Detonations, NASA SP-273, NTIS N71-37775.

Katta, V.R., Goss, L.P. & Roquemore, W.M., 1994, Effect of Nonunity Lewis Number and Finite-Rate Chemistry on the Dynamics of a Hydrogen-Air Jet Diffusion Flame, Combust. Flame, vol. 96, pp.60-74.

Meier, W., Prucker, S. & Stricker, W. 1994, Species Concentration and Temperature Measurements by Single-Pulse Spontaneous Raman Scattering and 2D LIF Imaging in a Turbulent H_2/Air Flame, in Non-Intrusive Combustion Diagnostics, ed. K.K. Kuo & T.P. Parr, pp.40-51, Begell House, New York.

Meier, W., Vyrodov, A.O., Bergmann, V. & Stricker, W. 1996a, Simultaneous Raman/LIF Measurements of Major Species and NO in Turbulent H_2/Air Diffusion Flames, Appl. Phys. B., vol. 62.

Meier, W., Prucker, S., Cao, M.-H. & Stricker, W. 1996b, Characterization of Turbulent H_2/N_2/Air Jet Diffusion Flames by Single-Pulse Spontaneous Raman Scattering, Combust. Sci. Technol., accepted for publication.

Neuber, A.A., Hassel, E.P. & Janicka, J. 1994, Comparison of Turbulent Diffusion Flame CARS Temperature Measurements and Re-Stress Model Prediction, in Non-Intrusive Combustion Diagnostics, ed. K.K. Kuo & T.P. Parr, pp.432-440, Begell House, New York.

Paul, P.H., Gray, J.A., Duran, J.L. & Thoman, J.W. 1994, Collisional Quenching Corrections for Laser-Induced Fluorescence Measurements of NO $A^2\Sigma^+$, AIAA J., vol. 32, pp.1670-1675.

Prucker, S., Meier, W. & Stricker, W. 1994, A Flat Flame Burner as Calibration Source for Combustion Research: Temperatures and Species Concentrations of Premixed H_2/Air Flames, Rev. Sci. Instrum., vol. 65, pp.2908-2911.

Raiche, G.A. & Crosley, D.R. 1990, Temperature Dependent Quenching of the $A^2\Sigma^+$ and $B^2\Pi$ States of NO, J. Chem. Phys., vol. 92, pp.5211-5217.

Sanders, J.P.H. & Gökalp, I. 1996, Flamelet Based Analysis of Non Equilibrium Effects and NO-Formation in Turbulent Hydrogen Diffusion Flames, 32nd AIAA/ASME/SAE/ASEE Joint Propulsion Conf., Lake Buema Vista, Fl., AIAA 96-3033.

Schefer, R.W., Namazian, M. & Kelly, J. 1991, Simultaneous Raman Scattering and Laser-Induced Fluorescence for Multispecies Imaging in Turbulent Flames, Opt. Lett., vol. 16, pp.858-860.

Smith, L.L., Dibble, R.W., Talbot, L., Barlow, R.S. & Carter, C.D. 1995, Laser Raman Scattering Measurements of Differential Molecular Diffusion in Turbulent Nonpremixed Jet Flames of H_2/CO_2 Fuel, Combust. Flame, vol. 100, pp.153-160.

Stårner, S.H., Bilger, R.W., Dibble & R.W., Barlow, R.S. 1990, Some Raman/Rayleigh/LIF Measurements in Turbulent Propane Flames, Twenty-Third Symposium (International) on Combustion, pp.645-651.

APPLICATION OF PIV TO TURBULENT REACTING FLOWS

L. Muñiz, R.E. Martinez and M.G. Mungal

Department of Mechanical Engineering
Stanford University, Stanford, CA 94305-3032, U.S.A.

ABSTRACT

Particle Image Velocimetry (PIV) is used to measure the instantaneous velocity fields in the near and far field of an axisymmetric nitrogen-diluted methane jet (Re = 6000) issuing into a co-flowing air stream. Velocity measurements are taken under reacting and non-reacting conditions to determine the effects of heat release on flow structure and mixing. In addition, velocity measurements are made at the base of a lifted methane flame (Re = 4200) to examine the velocity criteria for flame stabilization. In each case, the jet and co-flow are seeded with nominally 0.3 μm alumina (Al_2O_3) particles to obtain planar, two-component (axial and radial) velocity data in the jet, flame zone and free stream. Measurement uncertainties are assessed for the current PIV configuration, and beam steering, image distortion and thermophoresis effects on reacting measurements are discussed.

INTRODUCTION

Established in the early 1980's, particle image velocimetry (PIV) is now routinely used by the experimental fluid mechanics community to measure the instantaneous two-dimensional velocity fields in a wide variety of complex flows (Adrian, 1991). While refinement of the technique continues through the improvement of accuracy and resolution (*e.g.* Westerweel, *et al.* 1996, Keane, *et al.* 1995), PIV is finding wider applicability through its extension into the combustion community. The non-intrusive laser diagnostics traditionally used in reacting flows have been planar laser-induced fluorescence, Raman scattering, Rayleigh scattering and laser Doppler velocimetry. To complement the planar techniques used to measure temperature and species concentration, PIV is becoming increasingly popular to measure velocity fields in reacting flows.

The non-uniform temperature fields associated with reacting flows add to the complexity of making PIV measurements because as the temperature rises across the flame front, the fluid density (thus seeding density) decreases. Early PIV studies in reacting flows had either no or sparse data in the hot post-flame gases due to the reduced seeding density (*e.g.* Reuss *et al.* 1989, Post *et al.* 1991 and Driscoll *et al.* 1993). Mungal *et al.* (1995) and Paone (1994) successfully reported velocity in the pre- and post-flame gases of laminar and turbulent premixed Bunsen flames by heavily seeding the pre-flame gases thus providing the full vector fields in the hot and cold regions of the flow simultaneously.

In the present study, a PIV investigation is underway to obtain planar two-component velocity data in reacting and non-reacting flows. The aim of the current study is to determine how turbulent mixing is affected by heat release and provide insights into the stabilization mechanism of lifted jet diffusion flames. Contributions to the assessment of PIV measurement uncertainty due to the high density gradients (such as beam steering, image distortion and thermophoresis) are also discussed.

EXPERIMENTAL SYSTEM

Flow Facility

The facility, shown in Fig. 1, is a vertical indraft wind tunnel with a 30 x 30 x 80 cm test section and 4:1 contraction inlet. Particle Image Velocimetry (PIV) is used to measure the velocity fields in the near and far field of an axisymmetric jet in co-flow at Re = 6000 under non-reacting and reacting conditions. The jet, comprised of methane diluted with 60% by volume nitrogen, has an exit velocity of 19 m/s and is surrounded by a co-flowing stream of air with a velocity of 0.5 m/s. Under reacting conditions, the nitrogen-diluted methane flame is stabilized by a hydrogen pilot with a volumetric hydrogen to methane flow rate ratio of 3%. The jet and pilot issue from two concentric copper tubes, 120 cm long, with a jet inner diameter of 4.8 mm (6.3 mm O.D.) and pilot inner diameter of 8.0 mm (9.5 mm O.D.). PIV measurements are also made at the base of a lifted methane flame; the flow configuration is the same as above except pure methane (99.0%) issues from the 4.8 mm jet and no pilot gas is used in the outer annulus. For both studies, the jet is seeded with nominally 0.3 μm alumina (Al_2O_3) particles, while the co-flow can be seeded with alumina or a micron-sized fog produced from a glycerol-water mixture. The fog, which is non-flammable, evaporates at elevated temperatures (80°C) and thus provides a useful means to mark the room-temperature free-stream fluid surrounding the hot flame jet. The alumina, however, survives flame temperatures and is used when making PIV measurements in flames. The fog is used primarily for flame-jet visualization.

PIV System

The seed particles are illuminated by a double-pulsed laser sheet at 532 nm, approximately 0.2 mm thick coincident with the jet centerline. The light source is a Nd:Yag, 400 mJ/pulse, Spectra-Physics PIV-400 laser containing two independent cavities. The pulse separation ranges between 5-50 μs provided by a delay generator (SRS Model DG 535). The scattered light from both laser pulses in a 5 cm x 5 cm region of the test section is collected with a 105 mm Nikkor lens at f#/5.6 onto a 2000 x 2000 pixel CCD array (Kodak Megaplus 4.2). The double-exposed image is processed by an IBM RISC 6000 workstation to yield the velocity field. The MKIV software package (written by FFD Inc., now sold through TSI) uses an autocorrelation technique to find the average particle displacement in each subregion of the image, which is converted into velocity based upon laser pulse separation. The images are processed with 60 x 60 pixel subregions in a 66 x 66 grid so that the overlap between two neighboring subregions is 50%, and each vector represents the average velocity in a 1.5 x 1.5 x 0.2 mm interrogation volume. To remove velocity ambiguity and increase dynamic range, the second particle image is shifted from the first by a known amount using a spinning mirror, and the bias is subsequently removed in post-processing. This CCD-based image acquisition system coupled with high-speed processing provides rapid data collection. The images can be collected at 2 Hz and processed at a rate of 50 vec/sec.

RESULTS AND DISCUSSION

Flow visualization

The three flows examined in this study are visualized in Fig. 2 by means of Mie scattering and flame emission. The photographs reveal the instantaneous (10 ns) large-scale jet structure and time-averaged (1/30 sec) flame shape. The jets are seeded with alumina in Figs. 2(a,b) and the co-flow is seeded with fog in Figs. 2(b,c). The non-reacting and reacting jet in co-flow (Re = 6000) are shown in Figs. 2(a,b). The flame in Fig. 2b is anchored to the burner by a hydrogen pilot. The outer flame jet structure (marked by fog) is similar to that of the non-reacting jet (marked by alumina), however, the flame does influence the inner (fuel) jet structure. The jet widths, characterized by the non-reacting jet visualization and the flame jet's influence on the free stream, are comparable. Figure 2c shows the pure methane lifted flame (Re = 4200). Fog, marker of the free-stream fluid, is shown being entrained into the jet upstream of the flame base location.

Heat Release

To examine the effect of heat release on turbulent mixing, PIV measurements are taken in a non-reacting and reacting jet at the same jet exit Reynolds number (Re = 6000). PIV data are taken at three axial locations (from jet lip to flame tip) centered at 7, 25 and 67 diameters downstream (see Muñiz & Mungal, 1995). Figure 3 shows side by side comparisons of the non-reacting and reacting case at 25 diameters downstream where the average flame length is 70 diameters. The upper PIV images (a,b) show the types of images captured on the CCD array. Note, the low seeding density regions on both sides of the centerline are the high temperature zones where the flame resides. Figures 3(c,d) show the velocity in the lab frame after removal of the bias velocity imposed by the spinning mirror. The reacting flow appears less turbulent, with the jet showing a zig-zag, meandering appearance. In Figures 3(e,f), large scale structures convecting downstream are visualized by performing a Galilean transformation to the reference frame convecting at one half the centerline minus co-flow velocity. The non-reacting flow shows a broad range of structures while the reacting flow shows a considerable reduction in vortical activity, and the meandering of the jet is readily apparent. Figure 4 shows the instantaneous centerline velocity decay for the reacting and non-reacting case. A factor of two increase in centerline velocity is seen under reacting conditions for axial distances greater than 10 diameters downstream. Since the jet conserves momentum, a less rapid decay in centerline velocity implies reduced entrainment of ambient fluid for the reacting case. Similar results for the hydrogen jet are reported by Takagi *et al.* (1981) using LDV measurements.

Lifted Results

PIV data are taken at the base of a lifted methane flame (Re = 4200) to determine what velocities the flame base can stabilize itself against. Figure 5 show a typical PIV image with the accompanying velocity field. The abrupt change in seeding density marks the thermal boundary of the flame base. This flame boundary is sketched on the velocity field. Since the flow is turbulent and unsteady, the flame base location moves up and down. Since PIV is an imaging technique, the velocity can be extracted at the flame base location even though the flame base is moving within the imaged region (see Muñiz & Mungal, 1996). Figure 6 shows the distribution of velocities at the instantaneous flame base location taken from 66 realizations. Note, the peak in the distribution is near 0.5 m/s. Figure 7 contrasts the instantaneous and average behavior. Figure 7a shows the instantaneous axial velocity as a function of axial distance along the centerline (filled symbols) and through the flame base on the left side (open symbols) of the image presented in Fig. 5. The meandering nature of the jet is seen in the centerline profile while the flame base profile shows the velocity decreasing just before being accelerated through the flame front. Similar profiles are seen in triple flame simulations by Ruetsch *et al.* (1995) where the triple flame is characterized by stratified premixed combustion at the base followed by a diffusion flame tail. The mean (from 66 images) profiles are shown in Fig. 7b. The smooth decay in centerline velocity is observed as well as the slow rise in velocity across the flame front.

UNCERTAINTY ANALYSIS

PIV measurement uncertainty due to temperature gradients is assessed by addressing beam steering, image distortion and thermophoresis. Before isolating these effects, the algorithm uncertainty is determined excluding the effect of out of plane motion and velocity variations

within a subregion which as has been studied by Keane & Adrian (1992).

Algorithm

The algorithm and imaging contribution to the PIV measurement uncertainty, which applies to non-reacting and reacting flow velocities, is assessed by performing an artificial shift experiment. A single-pulsed image of uniform co-flow seeding is captured on the CCD array. A double-exposed test image is generated by digitally adding the same single-pulsed image to itself shifted to the right by a specified number of pixels. Images of different offsets were generated and processed with different sized interrogation regions to estimate the uncertainty of the present PIV configuration excluding the effect of out of plane motion and velocity variations within a subregion. Figure 8 shows the relative measurement uncertainty for the above cases. Current PIV experiments are designed to have pixel displacements between 10 and 15, are processed with interrogation regions of 60 square pixels and contain 10 or more particle pairs yielding 0.8% pixel displacement uncertainty. These design criteria are consistent with those put forth by Adrian (1991), Lourenco *et al.* (1989) and Keane & Adrian (1992).

Beam Steering

To evaluate beam steering, a HeNe beam passes through the flame and terminates on a target 2 m away to measure the angular deflection. The angular deflection is 5.6×10^{-4} rad when the beam passes through the center of the Re = 6000 flame and is 2.3×10^{-3} rad when passing through the flame tangentially at x/d = 20. The angular deflection in the beam is caused by a density gradient in the direction perpendicular to the beam propagation (Holder & North, 1956) and is given by

$$\varepsilon_x = \frac{L}{\delta}\frac{n(T)-n_o}{n_o}$$

where ε_x is the deflection angle towards the region of highest density, L is the length of gradient along the beam axis and, δ is the width of the density gradient or flame thickness. The index of refraction as a function of temperature is given by

$$n(T) = K\frac{\rho(T)}{\rho_o} + 1 = K\frac{T_o}{T} + 1$$

where T_o equals 300K. Since the index of refraction of air at 300K equals 1.000298, K equals 0.000298 and the index of refraction at flame temperatures (2000K) equals 1.00199.

The measured deflections agree well with those calculated for L/δ = 1/3 and L/δ = 1 for center and tangential propagation of the beam through the flame. For L/δ = 1/3, the calculated angular deflection is 5.5×10^{-4} rad. For a laminar flame with circular cross-section, no beam steering would be expected since the density gradient is parallel (or flame surface perpendicular) to the beam propagation. However, for a turbulent flame, it is reasonable to expect the length of the flame surface parallel to the beam propagation to be about one third the flame thickness yielding L/δ = 1/3. When the beam is tangential to the flame, it is reasonable to expect L/δ = 1 yielding a calculated deflection angle of 1.6×10^{-3} rad. When making PIV measurements, the laser sheet passes through the center of the jet, and the sheet is expected to be deflected only 28 μm (less than one seventh of the sheet thickness) as it reaches far side of the imaged region. Therefore, the beam steering effect on PIV measurements in this study is negligible.

Image Distortion

To determine the extent of image distortion caused by the flame, a steel ruler is placed in the flow and imaged with the flow reacting and non-reacting. When in the flame, the ruler is imaged quickly before the ruler thermally expands. The image taken in the reacting flow is identical to the non-reacting ruler image down to the pixel as determined by their addition. Significant blurring and distortion occurs when the object plane is a substantial distance behind the density gradients, see Fig. 9. The image becomes increasingly blurred as L_1 increases while keeping $L_1 + L_2$ constant. In the present configuration, L_1 is essentially zero, and no blurring is seen. The camera lens (f = 105 mm) is approximately 25 cm away from the object plane (M = 0.36), the flame is 1.5 cm in front of the object plane at the center of the image and is coincident with the object plane on the sides. Since PIV measurements are taken in the flame and not far behind the flame, image distortion effects on the velocity measurements are found to be negligible.

Thermophoresis

Thermophoresis is phenomenon by which a particle suspended in a gas with a temperature gradient, will tend to drift down the gradient. Therefore, the particle velocity perpendicular to a flame surface will lag the fluid velocity as it approaches the flame, introducing an error to the PIV measurement. This lag in particle velocity due to thermophoresis is termed thermophoretic velocity. Thermophoretic velocities are estimated from the experimental and theoretical work of Sung *et al.* (1994) and Gomez & Rosner (1993). Sung *et al.* calculated and measured the thermophoretic velocity to be 15 cm/s for a 0.3 μm alumina particle traveling through a nitrogen-diluted methane/air, counterflow diffusion flame with a strain rate of 240 sec^{-1} . The calculation was done by solving the governing equation of the particle where F_{SD} is the Stokes drag, and F_{TP} is the thermophoretic force.

$$m_P\frac{dv_P}{dt} = F_{SD} + F_{TP}$$

$$F_{TP} \propto \frac{-\nabla T}{T}$$

In the calculations and LDV measurements, the particle velocity lagged behind the flow velocity in the preheat

zone where the gradients were high, and the estimated thermophoretic velocity accounted for this lag such that

$$v_F = v_P + v_{TP}$$

Gomez &Rosner (1993) calculated the thermophoretic diffusivity, I_P, by determining the thermophoretic velocity, v_{TP} from the following expression:

$$v_{TP} = (\alpha_T D)_P \cdot \left(-\frac{\nabla T}{T}\right)$$

where α_T is the dimensionless thermophoretic diffusion factor, D_P is the particle Brownian diffusivity, T is the local temperature and ∇T its local spatial gradient. The thermophoretic diffusivity of a TiO_2 particle with a diameter in the range between 2 nm and 0.4 μm was found to be 0.5μ/ρ. Sung *et al.* using Gomez & Rosner's results calculated the thermophoretic velocity of 0.3μm TiO2 particles for the case where k = 240 sec^{-1} with $(\nabla T)_{max} \approx$ 2000 K/mm at T ≈ 1300K to be 14 cm/s. From this, we took the thermophoretic diffusivity, hence velocity, of TiO_2 and Al_2O_3 to be approximately equal for diameters near 0.3 μm.

To evaluate the thermophoretic velocity in the current study, we needed to estimate ∇T. To this end, we examined the temperature field data of Everest *et al.* (1995) for a similar turbulent jet flame. The typical temperature gradients for methane/hydrogen jet flames at Re = 4000 and 8000, x/d = 42 were 1000 K/mm at T = 1300, yielding a thermophoretic velocity of 8 cm/s. In this study, PIV velocities measured on the air-side of the flame are 1 and 0.5 m/s (axial and radial respectively). The magnitude of error due to thermophoresis is estimated as 16 % of the radial component of velocity and 7% of the overall velocity. On the fuel side of the flame front, typical PIV velocities are 6 m/s (axial) and 0.5 m/s (radial) leading to a 1% error on the overall velocity and 16% error on the radial component. While these errors are not overwhelming for the velocity measurements themselves, they could have a serious impact on radial velocity gradient calculations. Since the nature of flame vortex interactions are complex in turbulent reacting flows, no attempt has been made to correct the PIV data for thermophoresis because the instantaneous temperature field is not known.

CONCLUSIONS

This experimental work provides instantaneous two-dimensional, two-component velocity fields in turbulent diffusion flames using particle image velocimetry. The non-reacting and reacting jet at Re = 6000 are compared and results suggest that heat release does affect jet behavior, namely increased centerline velocity and reduced turbulent activity. The results from the lifted methane jet at Re = 4200 show the flame base is anchored primarily in the low velocity regions of the jet. Measurement uncertainties related to high temperature gradients are assessed. While effects of image distortion and beam steering are found to be negligible, the radial particle velocity (thus PIV measurement) at the flame surface may be lagging the fluid's radial velocity by as much as 16% due to thermophoresis.

ACKNOWLEDGEMENTS

This work is sponsored by the Gas Research Institute, Contract #5093-260-2697, R. V. Serauskas, technical monitor. L. Muñiz is sponsored by AT&T Bell Laboratories Cooperative Research Program.

REFERENCES

Adrian R. J. (1991), "Particle-Imaging Techniques for Experimental Fluid Mechanics," Annu. Rev. Fluid Mech., 23, 261.

Driscoll, J. F., Sutkus, D. J., Roberts, W. L., Post, M. E. & Goss, L. P. (1993) "The Strain Exerted by a Vortex on a Flame - Determined from Velocity Field Images," AAIA-93-0362, 31st Aerospace Sciences Meeting, Reno, NV, Jan. 1993.

Everest, D., Driscoll, J. F. & Dahm, W. J. A. (1995), "Images of the 2-D Temperature Field and Temperature Gradients to Quantify Mixing Rates within a Non-premixed Turbulent Jet Flame," Combustion and Flame, Vol 101, n. 1-2, 58.

Gomez, A. & Rosner, D. E. (1993), "Thermophoretic Effects on Particles in Counterflow Laminar Diffusion Flames," Comb. Sci. & Tech., Vol 89, 335.

Holder, D. W. & North, R. J. (1956), Optical Methods for Examining the Flow in High-Speed Wind Tunnels: Part One - Schlieren Methods, AGARDograph, November 1956.

Keane, R. D., Adrian, R. J. & Zhang, Y. (1995), "Super-resolution Particle Image Velocimetry," Measurement Science & Technology, Vol 6, n. 6, 754.

Keane, R. D. & Adrian, R. J. (1992), "Theory of Cross-Correlation Analysis of PIV Images," Applied Scientific Research, Vol 49, 191.

Lourenco, L. M., Krothapalli, A. & Smith, C. A. (1989), "Particle Image Velocimetry," Lecture Notes in Engineering 45, M. Gad-el-Hak (editor), Advances in Fluid Mechanics Measurements, Springer-Verlag, 127.

Mungal, M. G., Lourenco, L. M. & Krothapalli, A. (1995), "Instantaneous Velocity Measurements in Laminar and Turbulent Premixed Lames Using On-Line PIV," Combust. Sci. and Tech., Vol 106, 239.

Muñiz, L. & Mungal, M. G. (1996), "PIV Study of Lifted Jet-Diffusion Flames: Low-Speed Stabilization and Evidence for Triple Flames," 26th Symp. (Int.) on Comb., The Combustion Institute, Work-in Progress Poster # 428.

Muñiz, L. & Mungal, M. G. (1995), "A PIV Investigation of Turbulent Diffusion Flames," WSS/CI-95F-206, Western States Section of the Combustion Institute, Fall Meeting, Stanford, CA.

Paone, N. (1994), "Velocity Measurements in Turbulent Premixed Flames: Development of a PIV Measurement System and Comparison with LDV," Seventh International Symposium on Application of Laser Techniques to Fluid Mechanics, 15.3.

Post, M. E., Goss, L. P. & Brainard, L. F. (1991), "Two-Color Particle-Image Velocimetry in a Diffusion Flame," Central States Section of the Combustion Institute, Spring Meeting, Nashville, TN.

Reuss, D. L., Bardsley, M., Felton, P. G., Landreth, C. C. & Adrian, R. J. (1989), "Velocity, Vorticity, and Strain-Rate Ahead of the Flame Measured in an Engine Using Particle Image Velocimetry," SAE Trans., Vol 99, n 3, 249.

Ruetsch, G. R., Vervisch, L. & Liñán, A. (1995), "Effects of Heat Release on Triple Flames," Physics of Fluids, Vol 7, n 6, 1447.

Sung, C. J., Law, C. K. & Axelbaum, R. L. (1994), "Thermophoretic Effects on Seeding Particles in LDV Measurements of Flames," Comb. Sci. & Tech, Vol 99, 119.

Takagi, T., Shin, H.-D. & Ishio, A. (1981), "Properties of Turbulence in Turbulent Diffusion Flames," Combustion and Flame 40:121-140.

Westerweel, J., Draad, A. A., van der Hoeven, J.G. Th. & van Oord, J. (1996), " Measurement of Fully-Developed Pipe Flow with Digital Particle Image Velocimetry, " Experiments in Fluids, Vol 20, n 3, 165.

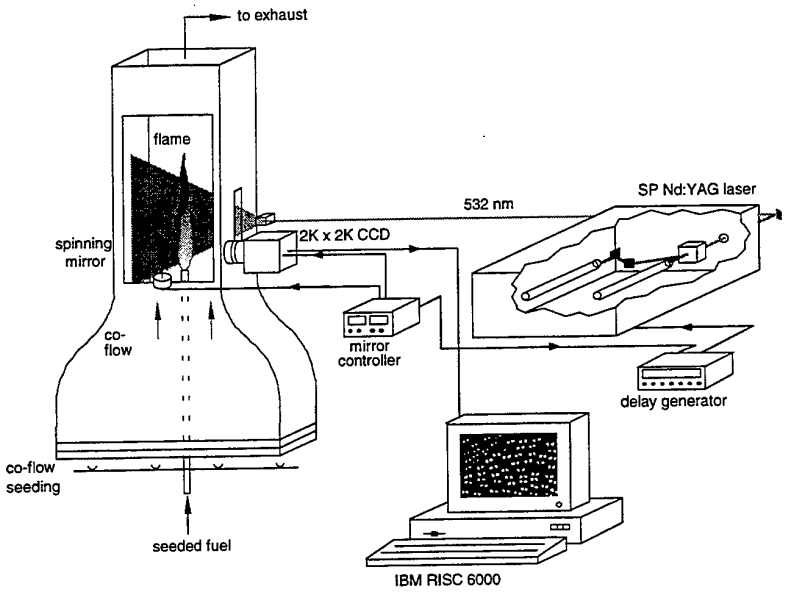

Figure 1: Experimental facility

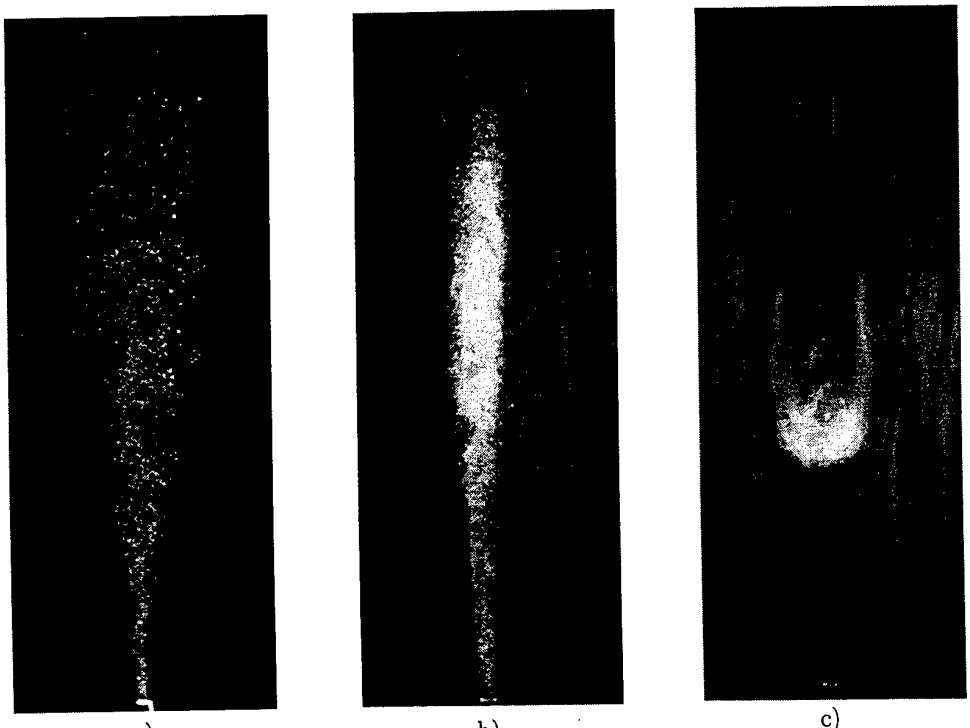

a) b) c)

Figure 2: a) non-reacting jet (Re = 6000); b) reacting jet (Re = 6000); c) lifted methane flame (Re =4200)

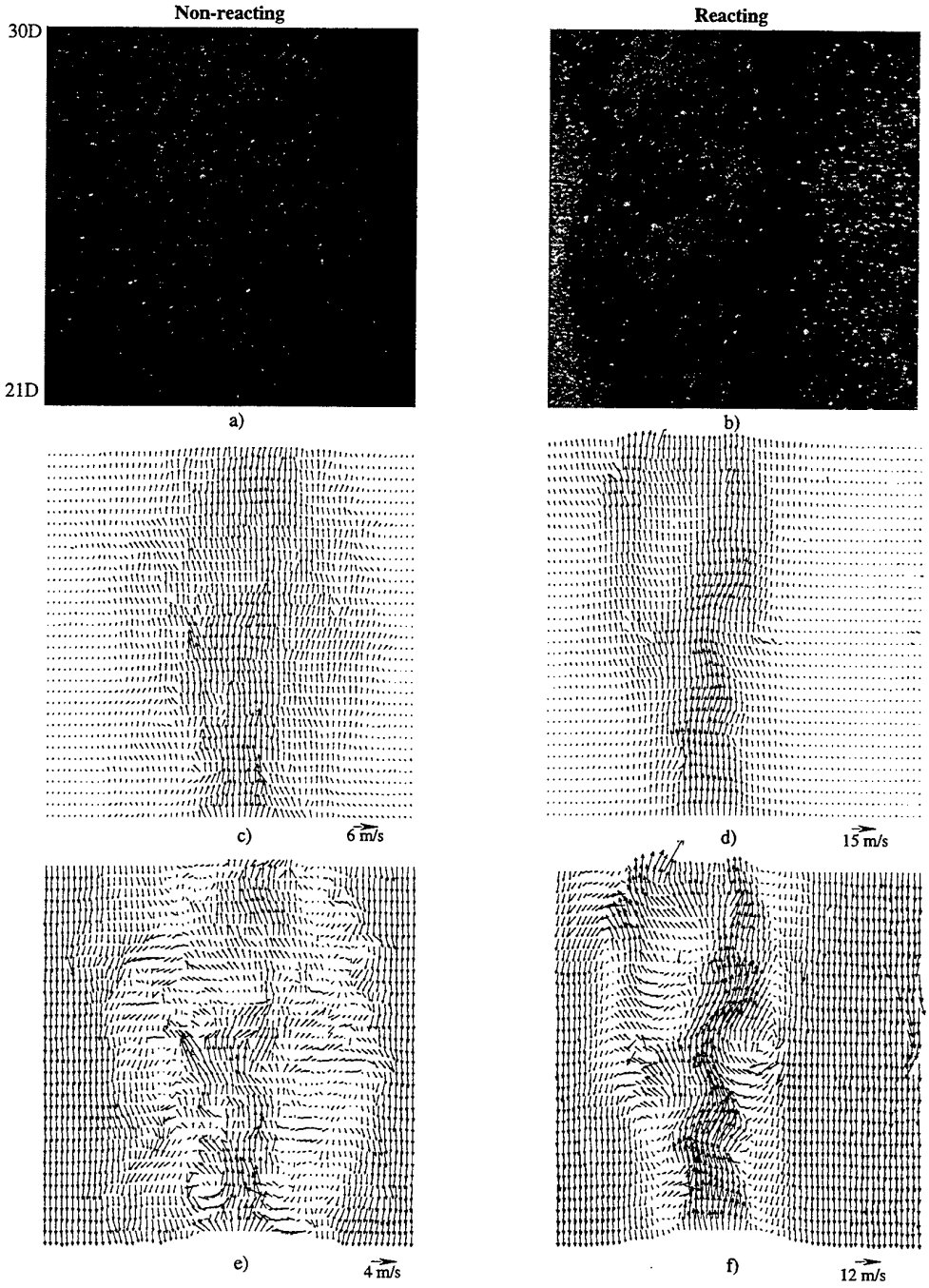

Figure 3: Non-reacting and reacting PIV images and velocity fields in lab frame and convecting frame at $x/d = 25$ and $Re = 6000$

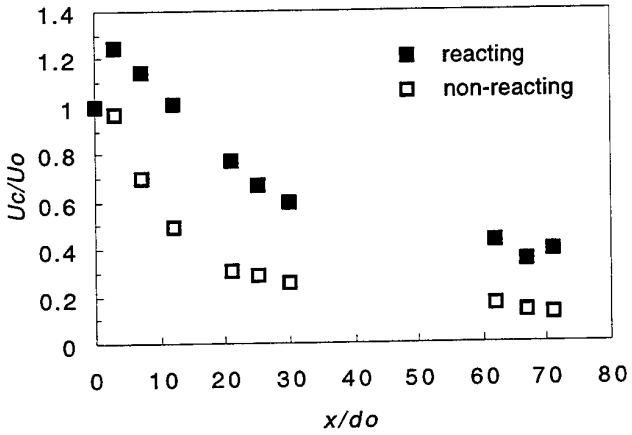

Figure 4: Centerline velocity decay

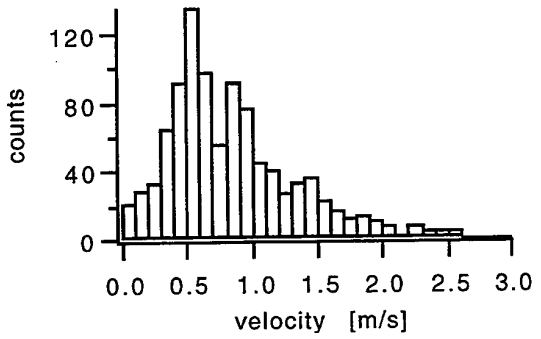

Figure 6: Velocity histogram at instantaneous flame base

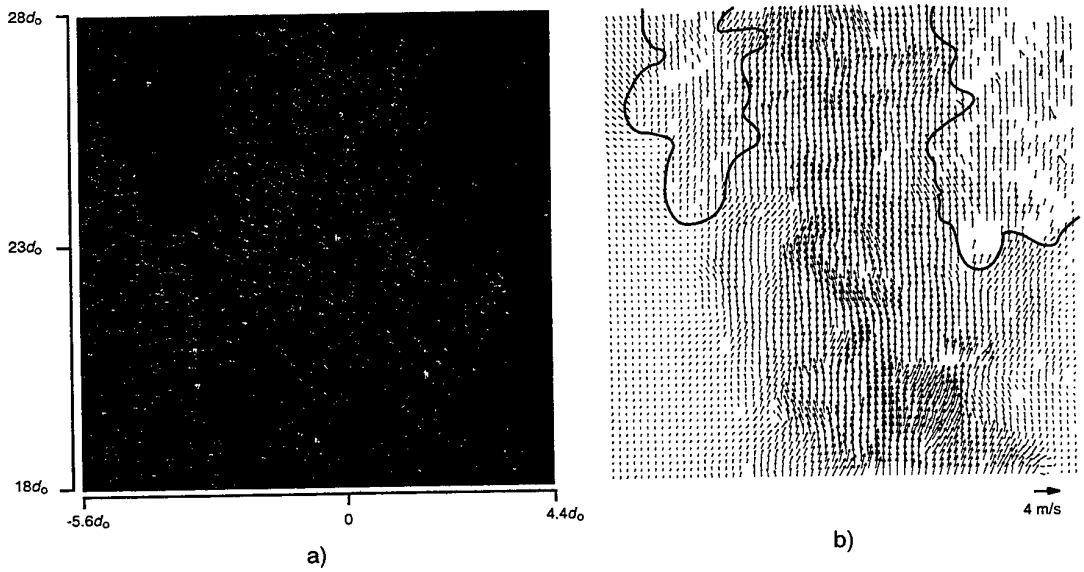

Figure 5: PIV image and instantaneous velocity field of lifted flame base

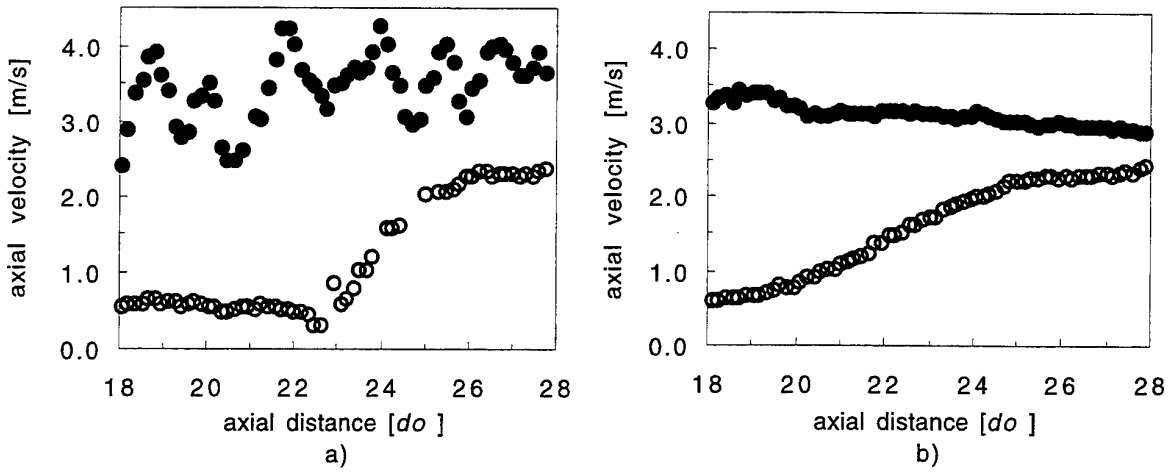

Figure 7: a) instantaneous and b) mean axial profiles (open symbols - through flame base; filled symbols - along jet centerline)

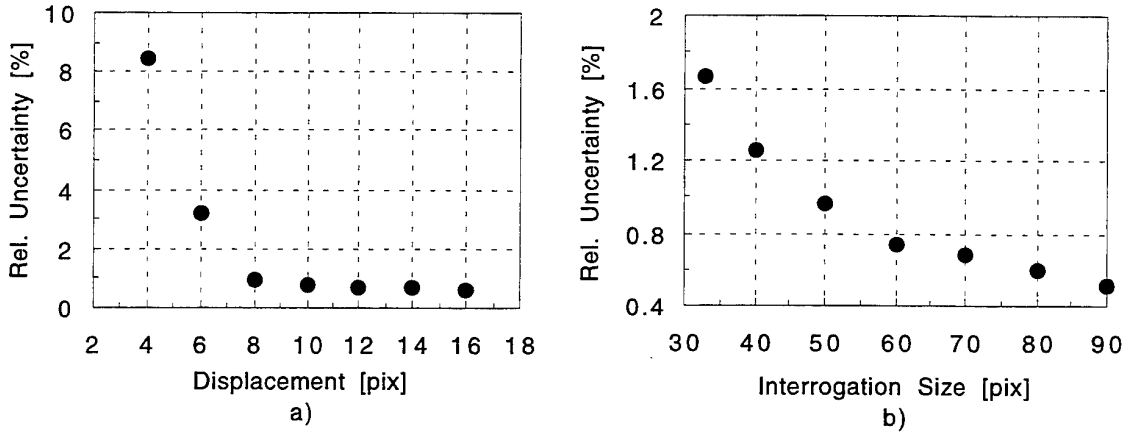

Figure 8: PIV measurement uncertainty in terms of processing parameters

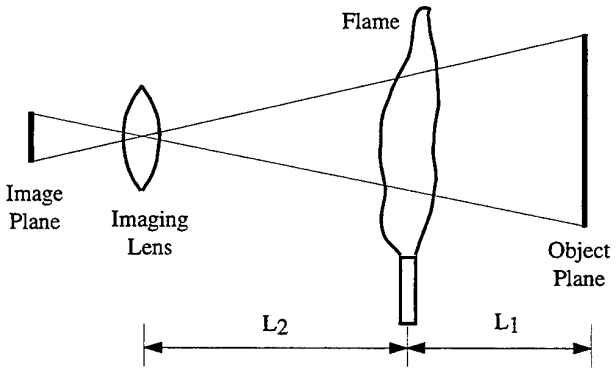

Figure 9: Schematic of imaging system with flame present

VELOCITY MEASUREMENT IN HIGH TURBULENT PREMIXED FLAMES BY A PIV MEASUREMENT SYSTEM

N. Paone*, G.M. Revel*, E. Nino**

*) Dipartimento di Meccanica, Università degli Studi di Ancona,
via Brecce Bianche, I-60131 Ancona, Italia
**) Dipartimento di Ingegneria e Fisica dell'Ambiente,
Università degli Studi della Basilicata, via della Tecnica 3, I-85100 Potenza, Italia

ABSTRACT

The application of a PIV system for measurements in high turbulent premixed flames is here presented. The system, based on photographic aquisition of images illuminated by a double oscillator Nd-Yag laser and on processing by a spatial autocorrelation algorithm, has been applied to seeded combusting flows in different conditions. The capability of the system to measure turbulent velocity fields has been tested on a cold non-reacting flow, where problems connected to seeding density are not present. Measurements have then been performed on premixed unconfined flames (at Re = 2355 and at Re = 3460) from a Bunsen burner, equipped with nozzles of different lenght and supplied with different commercial fuels, and on a larger CH_4 flames (Re=19200) confined in a trasparent combustion chamber. The results obtained from these tests are presented and discussed, with reference also to error sources occouring in PIV measurements applied to high turbulent reacting flow.
Maps of vorticity, strain rate and dilatation have been computed and analysed in order to obtain information about position and thickness of the preheat zone and of the flame front.

1. INTRODUCTION

It is well known that the combustion process is strictly connected to the fluidodynamic properties of the surrounding flow field; therefore, in order to completely understand important phenomena, such as heat release, mass transport, pollutant production and emission, it is necessary to quantitatively characterize physical quantities such as local velocity, turbulence, viscous strength, vorticity and strain rate and their interaction with chemical reactions acting in the flame. The possibility of experimentally determine these quantities is of paramount importance also to validate data and results from software programs for numerical simulation, where one of the main problems is the description of the turbulence pattern to be implemented.
PIV is presently one of the few techniques which can be usefully applied to measure a two-dimensional velocity field in combusting flows, providing instantaneous information about each point of the field. This is of great interest for the combustion process, because it is regulated by istantaneous gradients which are not obsevable by using traditional time avaraged single-point measurement techniques, such as LDV. For its istantaneous nature, PIV is suitable also for the study of unsteadiness phenomena, such as flame instability.
Many PIV applications have been already sucsessfully performed and described: Lewis et al. (1987), Reuss et al. (1989-1990), Armstrong et al. (1992), Nino et al. (1992), Mungal et al. (1994), Paone (1994). The latest works have shown that measurements in turbulent premixed flames can be realized both upstream and downstream of the flame front, by using sufficiently high particle seeding density; usually metal oxide particles (Al_2O_3, TiO_2, ZrO_2, etc.) have been employed, because of their capability to keep good scattering cross section at high temperatures. PIV has been applied also for measurements in the cylinder head of an engine (Reuss et al., 1990, Nino et al., 1992).
In this paper all the previous results are basically confirmed; the extension with respect to the earlier studies is the application of a traditional PIV system to flame with very high turbulence level (until Re = 19200) and rather large dimension (from 5.4×2.28cm to 17.97×7.95 cm), with the aim of measuring velocity vectors in the whole flow field, and not only in a single vortical structure or in the tip of the flame. Main difficulty and limitation in processing large images is related to limited spatial resolution and to its influence in resolving flows with large velocity gradients, whose effects in measurement uncertainty are addressed in the next paragraph. What is presented in this paper aims to the extension of PIV applications to large size flames

and large turbulence levels, step which is foundamental in order to apply the technique to industrial combustors.

2. THE PIV SYSTEM

The PIV measurement system used in this work is based on a double-oscillator Nd-Yag laser (Continuum, wavelenght λ=532 nm, energy 110 mJ/pulse, pulse duration 12 ns), triggered by a standard photografic camera (Nikon F-601, film 35 mm) by employing the camera flash contacts and a pulse generator for flash lamp and Q-swithc. The camera takes images by a 60 mm macro objective (Nikon, AF Micro-Nikkor) at its maximum opening f#2.8, with a narrow band interference filter (10 nm wide centered around 532 nm) used in order to remove undesired noise generated from flame radiation. Film is choosen to have resolution 100 line pairs/mm (Kodak T-MAX 400). Time delay between pulses is set according to velocity field and magnification ratio in the order of 80-160 μs. Different cylindrical and spherical lenses have been utilized to create a light sheet with minimum thickness (≈ 0.5 mm) and therefore maximum light intesity.

Metal oxide particles (TiO_2 and ZrO_2) with 0.7-1μm diameter have been employed as seeds for the flow; particles have been dispersed in ethylic alcohol with 5% weight ratio and injected in the primary air flow by an atomizer (TSI-Model 9306) which provides fine spray of liquid droplets. Alcohol has been choosen for this application because it forms very little droplets, avoiding agglomeration of solid particles and thus deviation of particles size in the reactant and the combustion products and generating seeding very similar to those from dry seeders; its flow rate has been set in such a way as not to modify significantly chemical reactions occuring within the flame. The pictures shown in this work put in evidence how uniform and suitable seeding density upstream and downstream the flame front is obtainable with liquid spray.

The interrogation system is based on a Nikon Coolscan LS-10E, able to scan a 35 mm positive or negative B/W or Color film with a resolution of 106.5 lines/mm. The driving software of the Nikon Coolscan allows the operator to select only a portion of the film to be scanned, rejecting all the regions without information. The digitized image is post-processed by a home made software able to import and to store in the extended memory of a 486 IBM compatible, and then to display on the monitor the whole PIV image. After this operation the software extracts a square sub-matrix of 128×128 pixels and perform an autocorrelation on this kernel, which therefore provides the digital dimension of the spatial resolution of the processing technique. A peak finding routine determines the pixel coordinate of the three highest peak locations, which represent the three most probable particle pair separation in the interrogation cell. The corrisponding velocity of the first peak is directly displayed on the monitor, in the same position in which the interrogation cell was extracted. The overlapping degree of the extracted sub-matrix can be selected by changing the distance in pixels between two consecutive sub-matrix.

The dimensions of the autocorrelation kernel, mapped on the physical image by multiplication by the magnification ratio and the scanner resolution, provide the size of the interrogation area. Autocorrelation avarages all velocity vectors within this region. If particle pairs are uniformely distributed across the region, the velocity gradient induced errors are minimized; but, in case of scarse seeding (as in the burnt gases), these errors may increase. In the worst case, which is unlikely to occur, a situation may arise in which only one particle pair is within the region, and it is at its borders, as sketched in Fig.1. In such a case, the resulting information regards only one point in the flow and therefore, if velocity gradient is high in the interrogation area, induced errors increase considerably.

After the whole images has been interrogated, the operator can select and display the second or the third peak if the first is not consistent with the neighborhood velocity vectors. All the mathematic operations and the image manipulations have been performed by means of digital a processor board PL 2500 (Eighteen Eight Laboratories).

Due to the dimension of the sub-matrix (128×128 pixels) and the precision (±1 pixel) in the find peak routine, the error in the velocity determination is about 1/64 (the velocity information are present only in half of the correlation domain) of the maximum measurable value, (i.e.≈ 1.5 % F.S.).

3. THE BUNSEN BURNER FACILITY

The Bunsen burner facility here used is schematically reported in Fig.2. The burner, here operating with LPG or with CH_4, is surrounded by a cylindrical settling chamber (200 mm diameter, 95 mm height), where primary air is injected; the nozzle is a pipe of 80 mm lenght and 17 mm internal diameter and is connected to a tube with the same diameter and lenght of 700 mm.

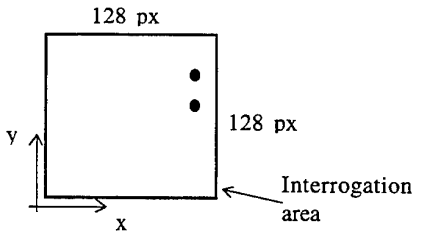

Fig.1 - Case with only one particle pair in the intorragion area: velocity gradient induced error increases.

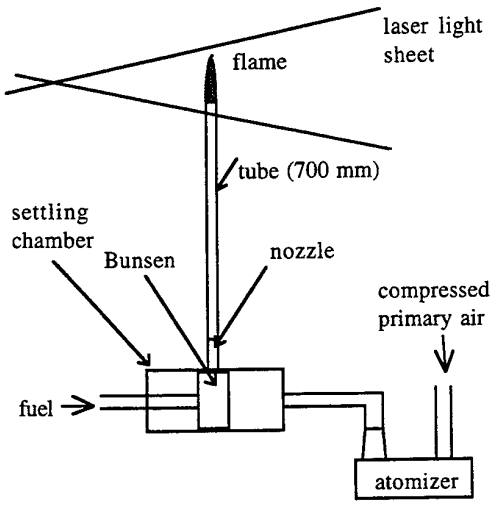

Fig.2 - Scheme of the Bunsen burner facility.

The air is seeded before entering the chamber by means of an atomizer and is then completely mixed with fuel along the pipe. Seeding density is set in the atomizer by using six jets, which discharge particles in the main air flow, and therefore is proportional to air flow rate from the jets.

4. MEASUREMENTS IN THE COLD NON-REACTING FLOW

Preliminary tests have been performed in the cold non-reacting flow jet coming out from the burner, in order to test the capabilty of the system to describe flows with vortical structures. CH_4 and air flow rates were respectively 2.78 l/min and 30.9 l/min (26 l/min primary air and 4.9 l/min secondary air from the seeding jets), with an avarage flow speed of 3.5 m/s (measured by LDV) corrispondig to a tube Reynolds number of 3460.
In this case TiO_2 particles have been employed and time separation between the two puslses was 100 μs.
Figure 3 shows an image of the flow with the computed velocity vectors superimposed.
The image has a dimension of 3134×1326 pixels, corresponding to a physical area of 55.3×23.4 mm. A grid of (55×22)= 1210 vectors has been used, with a spatial step of 0.95 mm. The interrogated sub-matrix has a physical size of 2.26×2.26 mm and the seeding density is about 20 pairs/mm^2.
The studied cold flow has the typical behaviour of a free jet formed when a fluid is discharged from a nozzle. At the pipe exit the velocity profile presents a maximum in the central axis, accordingly to the theoric parabolic shape. In the downstream direction the jet spreads out, its velocity decreases and it becomes turbulent and partly mixed with the sorrounding air. PIV measurement results agree with this behaviour and the velocity vectors describe vortical structures exactly; it can be seen in Fig. 4, where the relative velocity field, resulting from an ensamble-average velocity subtraction, is reported.
The only limitation of the system is due to the spatial resolution, which is a result of both the grid spacing (sampling frequency) and the interrogation sub-matrix size. The sampling frequency allows to resolve structures whose dimension is at least twice the grid spacing, while the average performed by the autocorrelation algorithm over the interrogation area may induce errors in velocity gradients computation.

5. MEASUREMENTS IN BUNSEN TURBULENT FLAMES

Many tests have been performed in the Bunsen turbulent premixed flame, at different Reynolds number and in different burner conditions, in order to verify the applicability range of the PIV system. Here the two more significant cases are reported. In the first one the burner, supplied with CH_4, is equipped in the same way as shown in Fig.2 and the flow presents Re = 3460; in the second, the tube of 700 mm lenght has been removed from the burner and therefore the flame came out directly from the nozzle (80 mm lenght, 17 mm internal diameter) at Re = 2355 and does not exhibit a fully developed profile. In this case LPG has been used as fuel.

5.1 Burner with the exit tube mounted

In this first case all the parametrs regarding the flow and the image acquisition and processing are the same as those descibed in Par.4 for the cold flow. Therefore the CH_4 flame presents an equivalence ratio $\phi = 1.16$ and a tube Reynolds number Re = 3460. PIV parameters have not been changed because the interrogation sub-matrix size is large enough to ensure that the processing software works correctly also with particles with higher velocity and acceleration (e.g. across the flame front).
Figure 5 shows a typical result. The seeding density is sufficient for processing data both upstream and downstream of the flame front, showing that TiO_2 particles maintain sufficient scattering cross section also after their passing through preheat and reacting zones. As described in other works (e.g. Mungal et al., 1994), the velocity vectors turn significantly at the sides of the flame, because the component normal to front flame increases significantly for the volume expansion associated with the combustion process, while the tangential component is conserved.
In the analysed condition the flame is near to blowout with any further increase in flow rate: it is confirmed from the image, where it is possible to note that flame angle is very small and the sides of the front are almost vertical. This behaviour is due to high flow speed with

respect to burning velocity and it is stressed in the axial streamtube, where flow seems to "open" the cone in the tip. In this region volume expansion is the dominant phonomenon and it is associated with heat release and significant increase of speed. Further to other research works (e.g. Mungal et al., 1994), we have found that velocity turns and increases only starting from the preheat zone, and therefore we suggest that combustion does not influence the unburned part of the flow, which seems to be very similar to the cold flow in Fig. 3.

It is interesting to note that vectors divergence and stretching occurs outside the heavier seeding density region: probably the reason is that heavier seeding decreases where the preheat zone begins (i.e. where volume expansion occurs), while vectors field strain appears in correspondance to the effective reacting zone. Therefore, it is possible to measure approximately the preheat zone thickness, which in Fig. 5 is about 0.9 mm at the sides and 2.3 mm at the tip. We note that this result may be affected by error due to low resolution, because interrogation area is larger than preheat zone.

In Fig. 6 the relative velocity field, resulting from an ensamble-average velocity subtraction, is reported; it clearly shows vortical structures generated from the combustion process.

Figures 7-8-9 represent the vorticity ($\omega_z = \delta v/\delta x - \delta u/\delta y$), the dilatation ($\nabla u = \delta u/\delta x + \delta v/\delta y$) and the strain rate fields ($S_{xy} = (\delta u/\delta y + \delta v/\delta x)/2$) respectively, computed from PIV data. Dilatation presents higher values in correspondance to the flame front and in the area past the flame tip, while vorticity and strain rate are distributed more uniformely, although they also evidently mark the reacting zone. However, these maps have to be considered with caution, because the limited spatial resolution does not allow accurate gradient computing.

In Fig. 10 another image in the same condition is reported, together with the dilatation field (Fig. 11). Here the flame appears more turbulent: in the central streamtube the flow speed is so high that combustion is not complete and unburned reactants are presents also outside the main flame front. Those zones (e.g. in the left part of the tip) are well marked in the dilatation map: in fact in their surronding air, combustion is still occurring and therefore heat release and volume expansion are presents.

5.2 Burner without the exit tube

In the second test reported the tube of 700 mm lenght has been removed from the burner; the flame, generated from LPG combustion, came out directly from the nozzle (80 mm lenght, 17 mm internal diameter) and therefore it is not a jet exhibiting a developed pipe flow profile. Figure 12 shows a processed image, where avarage flow speed at the exit is 2.05 m/s (Re = 2355) and the equivalence ratio is $\phi = 1.05$ (flow rates: 18.1 l/min air, 0.72 l/min LPG). Time delay between pulses is choosen to be 70 μs and a grid of (55×38) = 2090 vectors has been computed, corrisponding to a physical area of 79.8×55.2 mm, with a grid spacing of 1.35 mm and an interrogation area of 3.2×3.2 mm. TiO_2 particles have been employed as tracers.

From a combustion point of view Fig.12 is rather peculiar: the cusp structure of a typical premixed flame is not observable and the flame front results extremely corrugated. We think that this behaviuor occurs because the flow is not fully-developed and therefore the velocity field is different from those of typical jets. Furthermore, LPG and air seem to be not completly mixed and the flame is heavyly sooted since the fuel used is LPG.

Notwithstading this, PIV results are satisfactory. Looking the photogram by a microscope, it is possible to note that tracers are present more or less everywhere over the whole investigated area, with a density of about 50 pairs/mm^2 upstream of the flame front. PIV vectors follow vortical structures in the flow, confirming that combustion is occurring in a very complex way.

Vorticity maps (here not shown) report values significantly higher than the first case and more diffuse contours, but it has to be considered that here problems due to spatial resolution are more stringent.

Figure 13 shows the velocity field computed by avaraging 10 different images taken in the same condition. Vorticity results concentrated in the axial streamtubes, while at the sides and downstream of the flame front the flow appears more steady and regular.

6. MEASUREMENTS IN A PREMIXED CH_4 COMBUSTOR

Figure 14 shows the combustor facility used to verify applicability of PIV to large scale and high turbulent combusting flows. The burner, an induction type combustor, is operated at Re = 19200 and air and gas (CH_4) are mixed in a short diffuser, whose outlet diameter is 60 mm, at an equivalence ratio $\phi = 1.4$ (flow rates: 337.64 l/min air, 25.33 l/min gas; avarage flow speed at the exit: 5.5 m/s). A trasparent quartz combustion chamber (180 mm ID, 1000 mm lenght) is installed for optical access and fumes exit through a chimney. At an observer the flow appears highly turbulent, with a flame having a lenght in order of 300 mm, which develops horizontally.

PIV images are taken in an area of 179.7×79.5 mm (3056×1352 px) and interrogated with a step of 2.58 mm (corresponding to a grid of (48×18) = 864 vectors) and with an autocorrelation kernel of 7.52×7.52 mm. Time pulses separation has been set at 140μs and ZrO_2 particles have been used for seeding, whose density in the photograms is about 80 pairs/mm^2 upstream of the flame front.

Figure 15 reports one image with the measured velocity field. The flow field appears highly complex and not symmetric. Three dimensional structures should be present: the disconnected regions with uburnt gases may be related to fimger-like 3-D structures which cross the measurement plane at different positions.
Velocity vectors highlight this complexity. Velocity magnitude increases at flame front and along the elongated structure visible in the upper part of the flame, as if stretching of such structure is occurring. Although the image is complex, velocity vectors appear correlated to the image of the flame. Velocity gradients are large and recirculation zones are present, although sign ambiguity of autocorrelation may be misleading. Vorticity is high all across the flow field and the data allow an estimate of size of vortical structures, in the order of half exit pipe diameter.
In those conditions measurement uncertainty is rather large, mainly due to gradient induced errors, limited spatial resolution and 3-D motions.

7. CONCLUSIONS

In this work the applicability of PIV measurement technique to large scale and high turbulent flames has been demonstrated, both in the unburned mixture and the burned gases simultaneously by suitably regulating seeding density. Main limit is spatial resolution, which imposes a compromise between the dimension of the flame to be analysed and the maximum measurable velocity gradient. In order to overcome this problem it should be sufficient to reduce the interrogation area for images processing.
PIV data have been processed to measure derived quantities, such as vorticity, dilatation and strain rate fields, which are suitable to describe flame stretching. In particular, according to previous studies, dilatation seems to be the more useful to mark the reacting zone.
The results obtained allow to think that in the future PIV will be succesfully applied to large industrial combustor and then to better understand important phenomena like combustion energy production and pollutant production and emission.

8. ACKNOWLEDGMENTS

The authors would like to acknowledge ENEA for partly financing the research here presented.

9. REFERENCES

Armstrong N.W.H., Shand A.M., Bray K.N.C., Ereaut P.R., 1992, PIV applied to premixed turbulent flames. Optical Meth. & Data Proc. in heat & Fluid Flow. The Inst. of Mech. Eng. London.

Lewis G.S., Cantwell B.J., Leucona A., 1987. The use of particle tracking to obtain planar velocity measurements in an unsteady laminar diffusion flame. The Combustion Institute Western State Section, Spring Meeting, Paper No.87-35.

Logan P., Smith O., 1989. Particle Image Velocimetry in reacting flows. The Combustion Institute Western State Section, Fall Meeting, Paper No.89-56.

Mungal M.G., Lourenco L.M., Krothapalli A., 1994. Instantaneous Velocity Measurements in Laminar and Turbulent Premixed Flames Using On-Line PIV. Proc. 7th Int. Symp. on Laser Anem. in Fluid Mechanics, Lisbon, Portugal.

Nino E., Gajdeczko B.F., Felton P.G., 1992. Two-Color Particle Image Velocimetry Applied to a Single Cylinder Two-Stroke Engine, SAE paper N. 922309.

Paone N., 1994. Velocity Measurements in Turbulent Premixed Flames: Development of a PIV Measurement System and Comparison with LDV. Proc. 7th Int. Symp. on Laser Anem. in Fluid Mechanics, Lisbon, Portugal.

Reuss D.L., Bardsley M., Felton P., Landreth C., Adrian R., 1990. Velocity, vorticity and strain rate ahead of a flame in an engine using PIV, SAE paper N. 900053.

Reuss D.L., Adrian R., Landreth C., 1989. Two dimensional velocity measurements in a laminar flame using PIV, Comb. Sci. and Tech., vol.67 pp. 73-83.

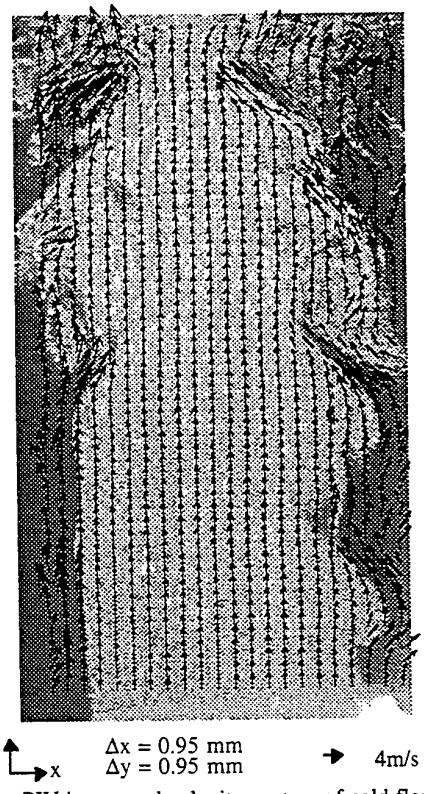

Fig. 3 - PIV image and velocity vectors of cold flow at Re = 3460.

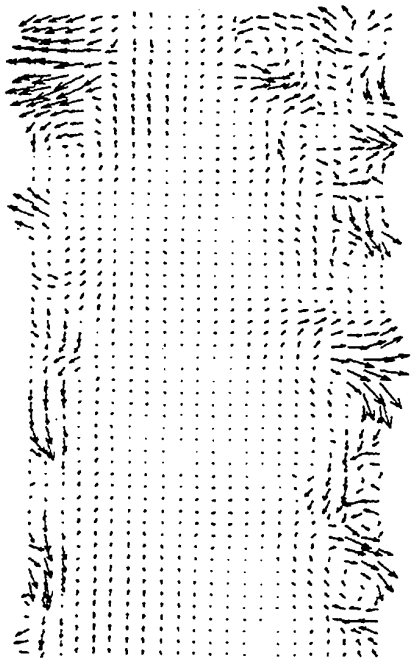

Fig. 4 - Relative velocity vectors computed from Fig. 3.

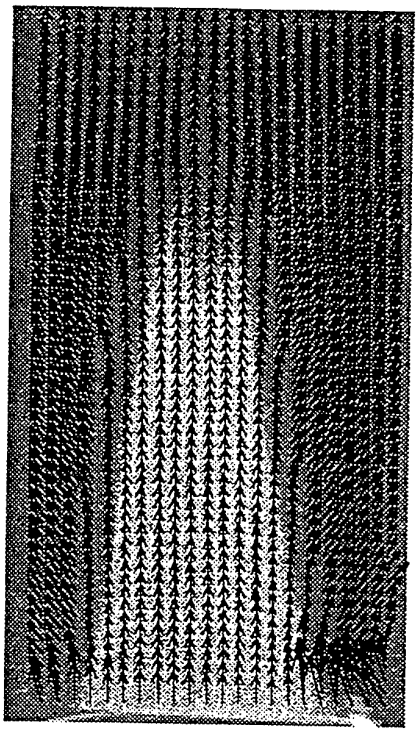

Fig. 5 - PIV image and velocity vectors of CH_4 flame at Re = 3460 (Bunsen with the exit tube mounted).

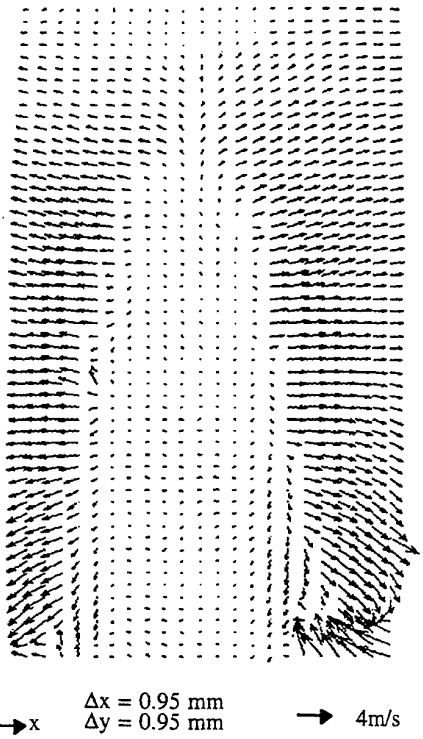

Fig. 6 - Relative velocity vectors computed from Fig. 5.

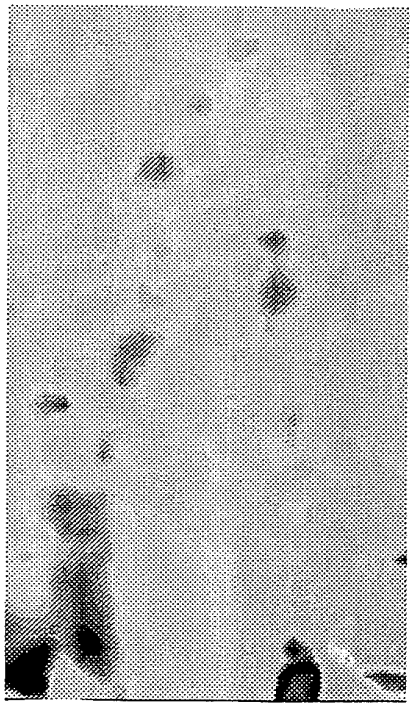

Fig. 7 - Vorticity computed from Fig. 5.

Fig. 8 - Dilatation computed from Fig. 5.

Fig. 9 - Strain rate computed from Fig. 5.

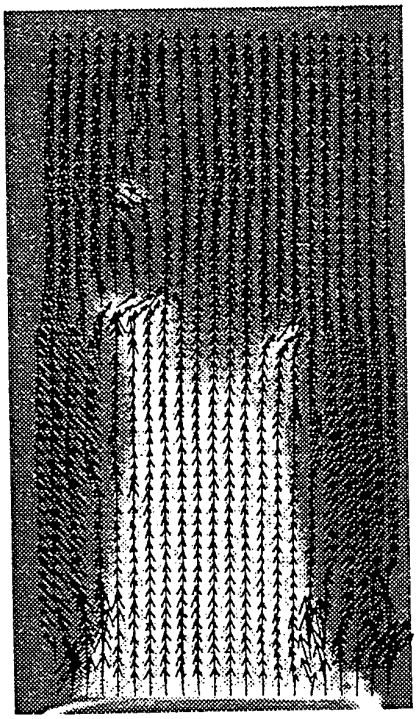

Fig. 10 - PIV image and velocity vectors of CH_4 flame at Re = 3460 (Bunsen with the exit tube mounted).

Fig. 11 - Dilatation computed from Fig. 10.

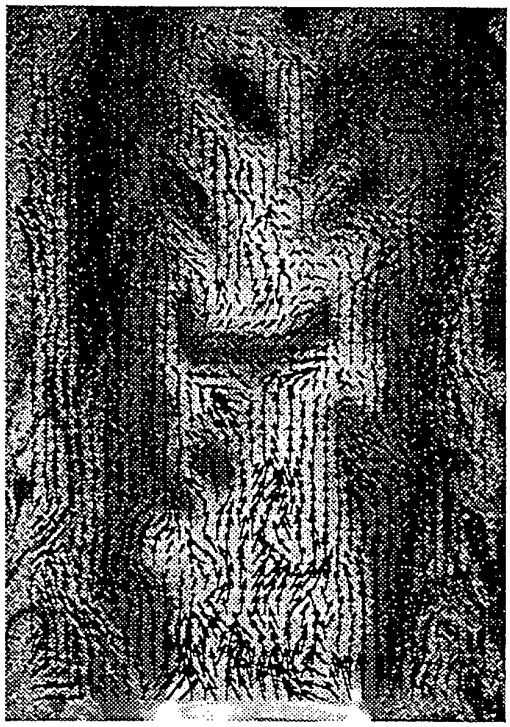

y ↑ x → Δx = 1.35 mm Δy = 1.35 mm → 2m/s

Fig. 12 - PIV image and velocity vectors of LPG flame at Re = 2355 (Bunsen without the exit tube mounted).

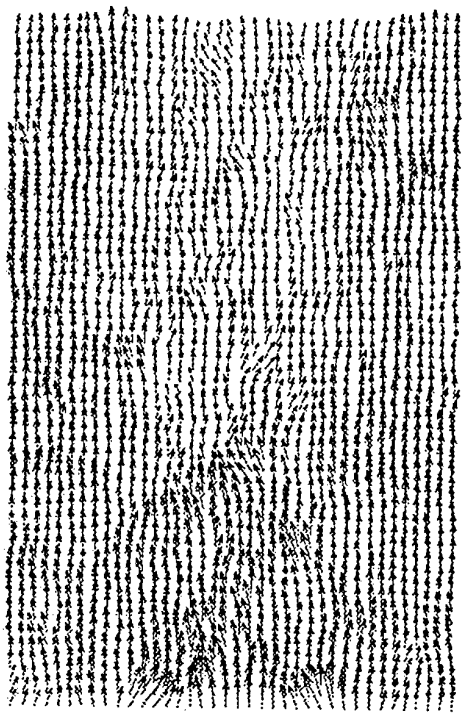

y ↑ x → Δx = 1.35 mm Δy = 1.35 mm → 2m/s

Fig. 13 - Velocity vectors computed avaraging 10 different images taken in the same condition as in Fig.12.

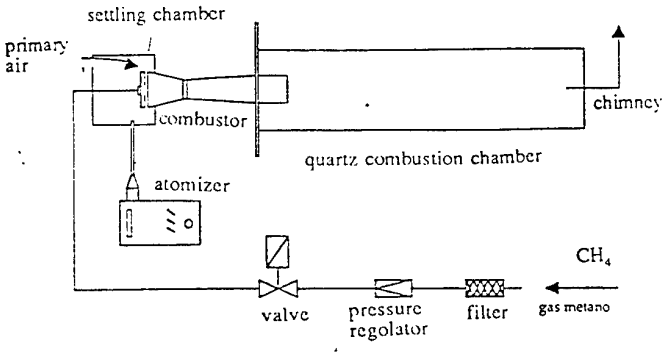

Fig. 14 - Scheme of the CH_4 premixed combustor.

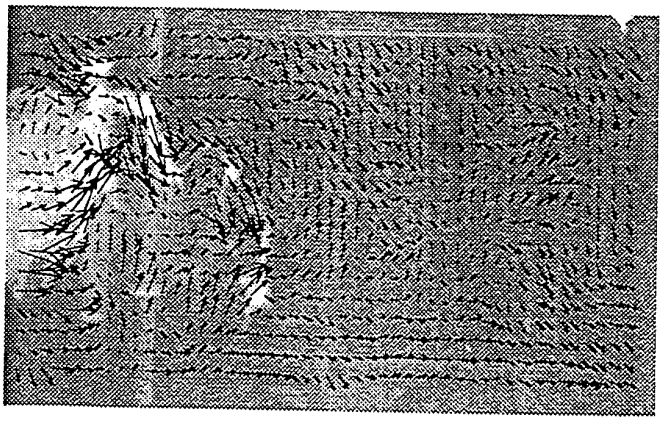

y ↑ x → Δx = 2.58 mm Δy = 2.58 mm → 8m/s

Fig. 15 - PIV image and velocity vectors of CH_4 flame at Re = 19200 from the premixed combustor.

FLAME SURFACE DENSITY MEASUREMENTS IN TURBULENT PREMIXED COMBUSTION

C. Martel, J. Piana, V. Liard, N. Darabiha and D. Veynante

Laboratoire E.M2.C. du CNRS et de l'Ecole Centrale Paris
92295 Châtenay-Malabry Cedex, France

ABSTRACT

The comparison between experimental and numerical data is an important step in model development and validation. The flamelet models assume that in premixed combustion, the flame is a thin interface between fresh and burnt gases. This assumption allows the definition of geometrical values for the flame surface topology. Tomography measurements applied on a 2D-burner provide quantitative values of flame surface topology. The objective of this work is to test and validate, by using synthetic front, the image processing techniques used to extract flame surface density, normal vectors to the flame front and flame front curvature. The optimum parameters of this procedure and its range of validity are determined.

1 INTRODUCTION

Numerical simulation is now used in many applied systems dealing with turbulent burning flows: rocket and jet engines, industrial furnaces, Diesel engines.... One of the major challenges in simulating such flows is to model the mean reaction rate. Since several years, many different turbulent combustion models have been derived. In all cases, systematic comparison with experimental data is an important step in model development and validation. Several recent works on turbulent combustion modeling are based on the flamelet concept. In such models, and under the fast chemistry assumption, the local instantaneous reactive flow is considered as a collection of laminar flame elements [(Marble & Broadwell, 1977), (Bray, Libby & Moss, 1984), (Candel & Poinsot, 1990)]. These flamelets are convected and distorted by turbulent motions. This approach is very attractive because it decouples the combustion problem from the description of the turbulent flow field.

In some flamelet models a flame surface density Σ is introduced to relate global flow description to local flamelet combustion. Then, the mean reaction rate of the mean progress variable $\tilde{c}$ may be expressed as a product of flame surface density Σ and the mean consumption rate per unit of flame area w_m, $\tilde{w} = w_m.\Sigma$. The chemistry effects are then described by w_m and the effects of the turbulent flow on the flame are taken into account through the flame surface density Σ.
The flame surface density may be obtained from an algebraic expression [(Bray, Champion & Libby, 1987)] or using a balance equation [(Marble & Broadwell, 1977), (Pope, 1988)]. Recent theoretical works have lead to an exact formulation for the Σ-equation. Splitting the velocity in Favre average and fluctuation $u = \tilde{U} + u''$, the Σ-equation may be written [(Trouvé & Poinsot, 1994)] :

$$\frac{\partial \Sigma}{\partial t} + \nabla.\tilde{U}\Sigma + \nabla.\langle u''\rangle_S\Sigma + \nabla.\langle wn\rangle_S\Sigma$$

$$= \langle A_T\rangle_S\Sigma + \langle a_T\rangle_S\Sigma + \langle w\nabla.n\rangle_S\Sigma$$

where n is the vector normal to the flame surface pointing towards the fresh gases, $\nabla.n$ the flame front curvature positive when convex towards the fresh gases and w the local propagation speed of the flame front. $\langle\rangle_s$ denotes the average along the flame surface. The last three terms on the left-hand side respectively represent, the convection by the mean flow, the turbulent diffusion and the flame propagation. The source terms on the right-hand side correspond respectively to the strain rate acting on the flame surface due to the mean flow field, turbulent strain rate and combined effects of flame curvature and propagation. The two strain rates are given by :

$$\langle A_T\rangle_s = \nabla.\tilde{U} - \langle nn\rangle_s : \nabla\tilde{U}$$

$$\langle a_T\rangle_s = \langle \nabla.u'' - nn : \nabla u''\rangle_s$$

Unfortunately, the Σ-equation remains unclosed and requires modeling assumptions (see (Duclos, Veynante & Poinsot, 1993)). The purpose of our study is to obtain experimental data on premixed turbulent flames allowing the quantitative analysis of flame surface density and some terms of the Σ-equation.
Measurements are based on flame front visualization by high speed tomography. We test here an experimental procedure to extract useful quantitative values on flame surface topology, such as the flame surface density (Σ), the normal vector (n) and the curvature ($\nabla.n$), presented in figure 1.
Section 2 presents the experimental setup and the diagnostic techniques. In section 3 the image processing procedure and validation tests are described. Finally, section 4 determinates the range of validity of the procedure.

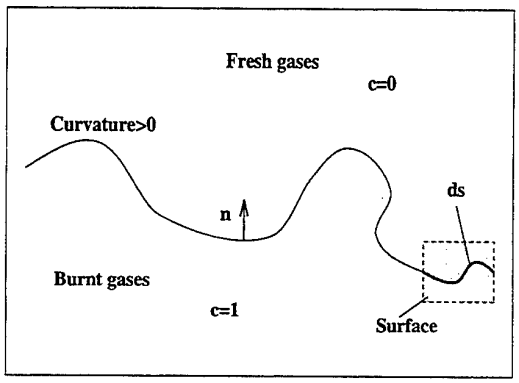

Figure 1: definition of parameters

2 EXPERIMENTAL SETUP AND DATA REDUCTION

The burner used in this study is presented in Fig.2. A mixture of air and propane at atmospheric pressure is injected into a two-dimensional burner through a grid (mesh size 2 mm). The height, depth and length of the combustion chamber are respectively 50, 80 and 300 mm. A V-flame is stabilized behind a small cylindrical rod of 3 mm diameter (6% blockage ratio). The lateral walls are transparent artificial quartz windows allowing the visualization of the whole chamber. The upper and lower walls are made of thick ceramic material including two narrow quartz windows permitting a laser sheet crossing.

Flame front visualization is obtained by tomography. A copper vapor laser (Oxford Inc., 15 W, 3-30 kHz, pulse duration 40 ns) is used to create a laser sheet. The laser beam is expanded through a concave cylindrical lens (f=-100 mm) and a spherical lens

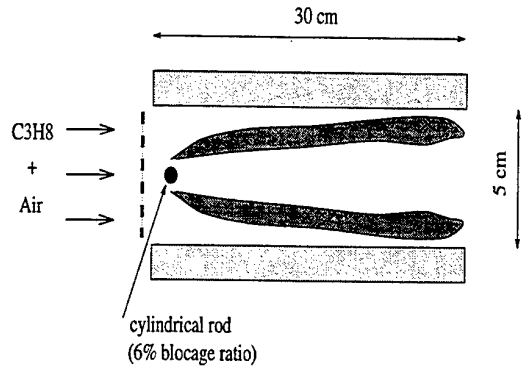

Figure 2: the 2D-burner

(f=500 mm, D=150 mm). The laser sheet is 100 mm wide and 1 mm thick in the burner. The laser is synchronized with a high speed 16 mm camera NAC E-10 operating up to 10 000 frames per second. An Ilford HP5-400 ASA film was used and developped at 800 ASA. The flow is seeded with oil droplets out of an ultrasonic atomiser. The diameter of droplets was found to be lower than 5 μm by previous PDA measurements. Due to their size, no droplet velocity slip with the gaseous phase has to be taken into account, and it may be assumed that droplets vaporize and burn rapidely and close to the flame front. Only fresh gases, including droplets, diffuse the laser light whereas burnt gases appear as dark areas.
Film images are digitized with a scanner operating at 2500 dpi (i.e. 100 pts/mm of film). This resolution of digitizing is close to the resolution of the film. Images appear as a set of pixels. Each pixel has a value between 0 and 255, and represents a surface of $(0.1) \times (0.1)\ mm^2$ in the real geometry. An example of digitized frame is displayed on fig. 3.
The frames are then binarized: each pixel receives the value of the corresponding progress variable c that is defined as $c = 0$ in the fresh gases and $c = 1$ in the burnt gases. The frames are first used to calculate the mean progress variable $\bar{c}$. c is averaged at each pixel upon all the binarized frames. As discussed further, various schemes may be used to extract the flame front coordinates defined as the interface between black ($c = 0$) and white areas ($c = 1$).

3 IMAGE PROCESSING PROCEDURE

3.1 Binarization

When plotting the histogram corresponding to gray-scale image of fig. 3, two peaks appear: one near 0 for the "black" area (burnt gases), and the other near 255 for the "white" area (fresh gases). A

threshold is chosen between these two peaks. If the gray-scale value of a pixel is lower than the threshold, the corresponding progress variable c is set to 1, otherwise, it is set to 0. On binarized images, isolated pixels are observed, either black pixels in white areas, or white pixels in black areas. This noise due to film resolution is removed using a median filter. Fig. 4 presents the final filtered binarized image corresponding to Fig. 3.

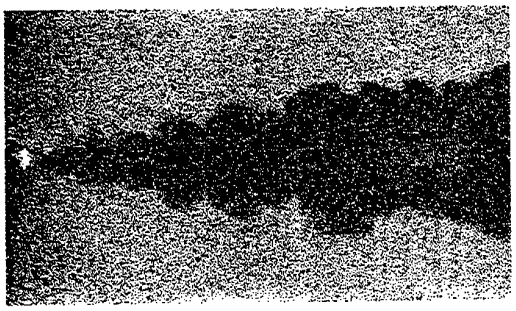

Figure 3: a gray-scale image

Figure 4: a binarized image

3.2 Front coordinates

For each instantaneous binarized frame, the flame front coordinates are determined considering the interface between black and white areas. Each frame is studied by lines and columns. In this case, the interface is the edge between two successive pixels having a different progress variable c. There are three ways to pick up the flame front coordinates relatively to this interface (see Fig. 5)

- The first way is to take the coordinates of the center of the pixel that is just before this change. Therefore, the front is set below and to the left of the interface whatever is the order of the change (fresh/burnt or burnt/fresh gases). Let us call it the "first front".
- the second way is to consider the coordinates of the center of the interface, called "edge front".
- The third way consists in keeping the coordinates of the center of the pixel which is at the interface, in the burnt gases ("black front").

It is clear that the "edge front" is the best one corresponding to our definition of the interface, but, as shown in section 3.4, it needs prohibitive computation times. The other two methods considerably reduce computation times but induce errors that will be discussed further.

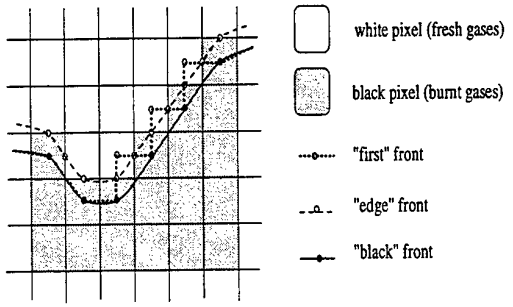

Figure 5: the definition of the three fronts

3.3 Smoothing and cubic-spline

The flame front is now represented by a set of points. In order to compute the flame parameters $(\Sigma, n, \nabla.n)$, the curvilinear abscissa and the first and second derivatives of the coordinates of the flame front are required. They are obtained using a cubic-spline function. When applied directly to the flame front coordinates, the cubic-spline gives blurried derivatives. For these reasons, smoothing is first applied to the front, and the process stands in four main operations :

- First, the front is smoothed using a local centered-moving-average on i_m points to reduce the sampling noise. This smoothing may be repeated i_r times.
- Secondly, an approximative cubic-spline is applied. It interpolates a C^3-function on a set of points, with a smooth factor S limiting the values of σ where σ are the residuals at each point (see fig.6). If $S = 0$, the spline is an interpolant, passing exactly at the specified points; if $S = \infty$ the spline is a straight line. This spline provides for each point the front arc length ds and the first and second derivatives leading to the normal vector and the curvature.

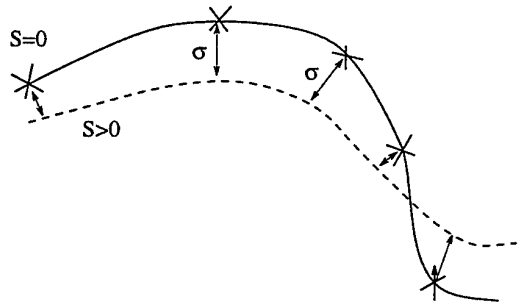

Figure 6: definition of the smooth factor S

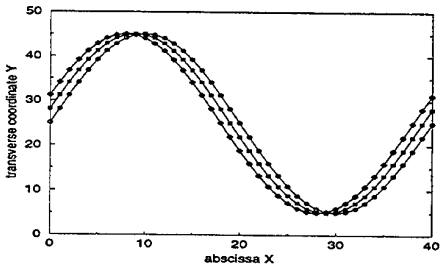

Figure 7: the first three images

- Then local quantities are averaged over $m * m$ pixel square boxes. The average are weighted by the front arc length ds:

$$\bar{\Phi} = \frac{\sum \Phi.ds}{\sum ds} = \langle \Phi \rangle_s$$

where Φ is, for instance, the curvature or the components of the normal vector. This averaging procedure corresponds exactly to the one used in the Σ-equation. The flame surface density is computed as the sum of the front arc lengths in the $m * m$ square box divided by the surface of the box.

- Finally, ensemble averaged quantities are achieved by averaging over all the instantaneous pictures.

In the following section, are tested the type of the front used ("edge", "first", "black"), the parameters of smoothing (i_m, i_r), the smooth factor S of the spline, and the heigth of boxes that less damage the results (m).

3.4 Testing procedure

Our image processing system is tested using synthetic sinusoidal fronts. The test is performed on T images simulating the displacement of a sinusoidal function of period T along X axis. Each image contains a sinusoid of period T pixels shifted of one pixel relatively to the previous one (see fig. 7). The burnt gases are located under the front, and the fresh gases are above the front. The scanner procedure is simulated as follow : a pixel is defined as black when 50% of its surface lies below the sinusoid. All the other pixels are white.

For any abscissa X, the average quantities, normal vector and curvature, depend only on the Y coordinate. These quantities are compared to exact values. The exact values are computed by simply considering the exact sinusoidal function : $f(x) = \frac{A}{2}.sin(\frac{2.\pi.x}{T}) + a$.

Determination of the front. We use 40 images of a sinusoid of period T and amplitude A equal to 40, centered on a=25, shifted of one pixel at each image. The parameters of smoothing are taken as $(i_m, i_r) = (3, 1)$.The smooth factor is taken to 1, and no box averaging is performed. On fig. 8, the three fronts ("edge", "first", "black") corresponding to one image are plotted . The "edge" front corresponds exactly to the interface black/white. The other two fronts are shifted half-a-pixel. The "black" front tends to sharpen the front when it is convex towards the fresh gases, and to flatten the front when it is convex towards burnt gases.

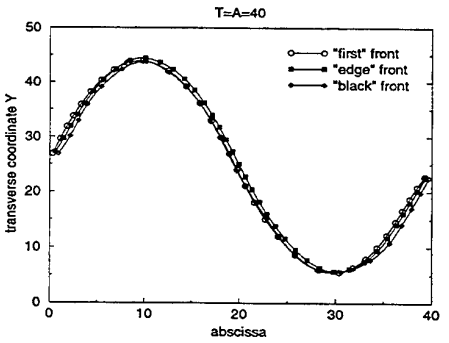

Figure 8: comparison of the three front extraction schemes

This results are confirmed when looking at the average normalized curvature $(pixel^{-1})$ obtained for the 40 images (Fig. 9).

At Y between 5 and 10 and Y between 40 and 45, stands the top and the bottom of the sinusoid, where the curvature reaches its maximum value. The curvature is negative for low values of Y, when the front is convex towards the burnt gases, and positive for high values of Y, when the front is convex towards the fresh gases. The three plots give the same general

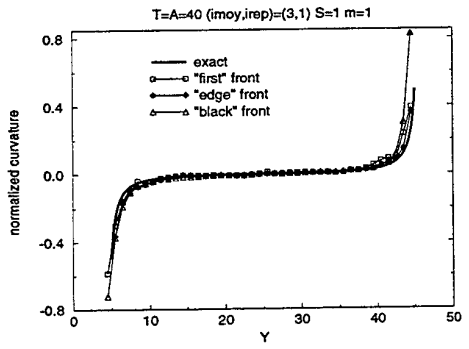

Figure 9: Mean curvature plotted as a function of the transverse location Y: comparison of the three front extraction schemes

trend. The "black" front gives greater absolute values than the exact values at Y around 5 and Y around 45. The fig. 10 represents the first component $M_1 = \langle n_1 \rangle_s$ of the average normal vector as a function of Y. Because of the succession of oblique fronts, and the direction of the normal vector, the average value of M_1 is zero at any Y. The average M_1 given by the "first" front is highly oscillating while the other two fronts give values close to zero, except Y around 5 and 45. Consequently, the "first" front will be not used.

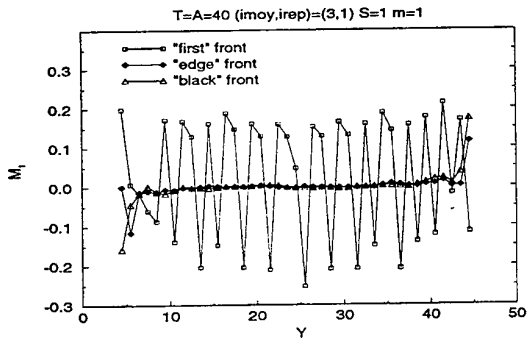

Figure 10: First component M_1 of the mean normal vector as function of the transverse location Y. Comparison of the three front extraction schemes

Figure 11 shows the second component $M_2 = \langle n_2 \rangle_s$ of the average normal vector to the front as a function of the transverse coordinate Y. Because of the direction imposed to the normal vector, M_2 is strictely positive at each Y. The two fronts seem to give similar results and close to the exact values.

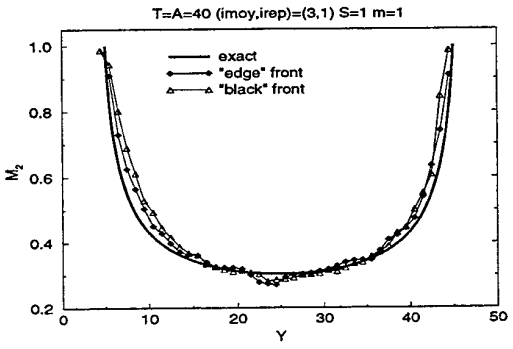

Figure 11: Second component M_2 of the mean normal vector as function of the transverse location Y. Comparison of the three front extraction schemes

The number of points contained in the "edge" front is generally twice the points contained in the "black" front. Therefore, the CPU time needed for the determination of the "edge" front is about twice the one needed for the "black" front. In the following, the "black" front is retained for image processing.

Smoothing. We consider 40 images of a sinusoid of period T and amplitude A equal to 40 pixels, centered on a=25. The smooth factor is set to S=1 and no box averaging is performed. Owing to the symetry of the results, the curvature, M_1 and M_2 are from now plotted for X between 25 and 50.

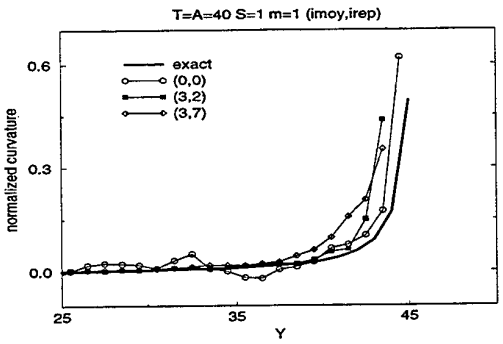

Figure 12: mean curvature plotted as function of the transverse location Y. Effect of front smoothing

On Figures 12 and 13 are plotted respectively the average curvature and the second component M_2 of the average normal vector as functions of the Y coordinate for different parameters ($i_m = 3, i_r =$

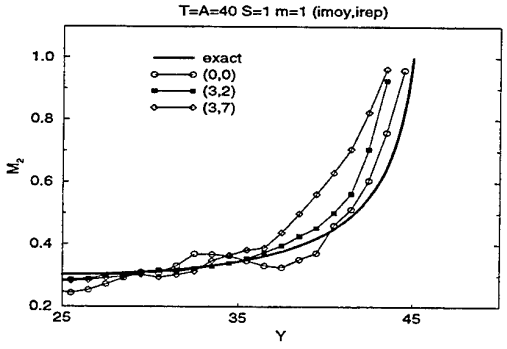

Figure 13: M_2 plotted as function of the transverse location Y. Effect of front smoothing

0, 2 *and* 7). It appears that the curve corresponding to no local averaging has too much noise. Therefore, a local averaging is needed. As one increases the number of repetition of local averaging, the result becomes smoother, but also moves away from the exact value. Similar observation can be done with $i_m = 5$. From now, the parameters ($i_m = 3, i_r = 2$) will be used.

Smooth factor. For this test, the smoothing is applied and the boxes are still 1×1 pixels. In figures 14, 15 and 16 are plotted respectively the curvature and the component M_1 and M_2 for different values of the smooth factor S as functions of Y. It can be observed that a smooth factor S greater than 0 is needed to avoid noise on curvature results. For high values of S ($S = 7$) the treatment induces too much errors in the results. A value of S between 1 and 3 seems to be satisfactory.

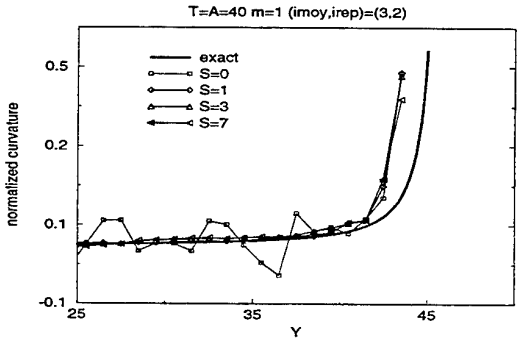

Figure 14: mean curvature plotted as function of the transverse location Y: influence of the smooth factor

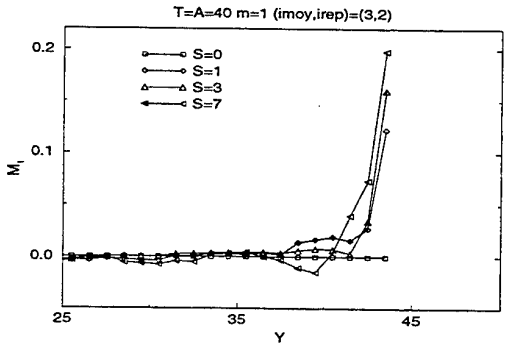

Figure 15: M_1 plotted as function of the transverse location Y: influence of the smooth factor

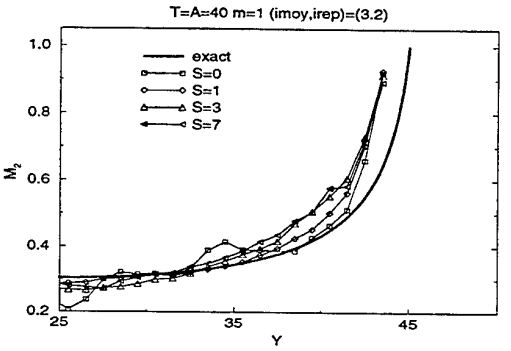

Figure 16: M_2 plotted as function of the transverse location Y: influence of the smooth factor

Box averaging . The box averaging is useful to attenuate the variations on curvature and normal components induced by the spline function or in processing of actual experimental data, but introduce a numerical diffusion. Their surface has two limits as it can be seen on Figures 17, 18 and 19 : if the boxes are too small, a noise remains on the averaged values. If the boxes are too large, they absorb effective variations of the front, and induce a too large diffusion. So the surface of the boxes has to be chosen relatively to the characteristic scales to be studied. Here if the boxes are greater than 5*5, the results are really altered.

4 RANGE OF VALIDITY

The important elements in our measurements are the flame surface density Σ, the normal vector n, and the curvature $\nabla.n$. Because it depends on the second derivatives of the front, the curvature is more

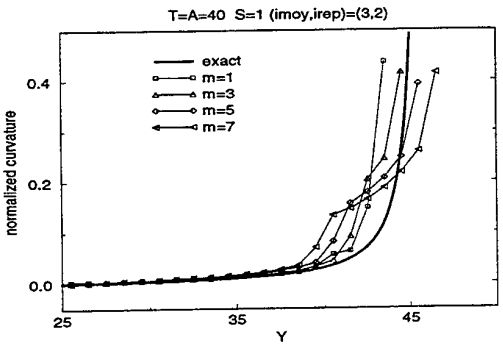

Figure 17: mean curvature plotted as function of the transverse location Y: influence of the box heigth

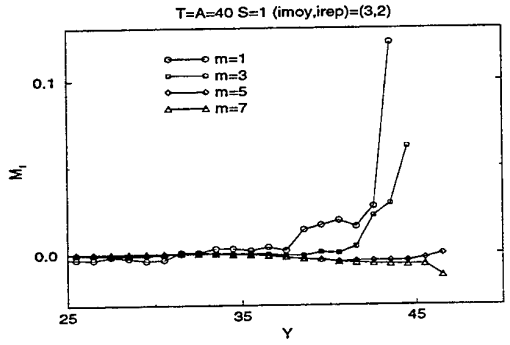

Figure 18: M_1 plotted as function of the transverse location Y: influence of the box heigth

sensitive to errors. The validity of the treatment is now tested only on the curvature, using images simulating a circle front. These images simulate a pocket of fresh gases separated from burnt gases by a circle shape front. Relatives errors on curvature are plotted as function of the angle. The smooth is defined by $(i_m = 3, i_r = 2)$, and a smooth factor $S = 1.5$. The values are computed with no box-averaging.

The scale of the variations of the front treated can induce some errors. Typically, small variations that can stand in a grid are not taken into account. Hereby, when the radius has a very small value, the circle is badly detected and an important error occurs. That limits our range of validity towards the small values of the radius. But large variations can be mis-interpreted. In our case, when the angle has the value of $-\pi, \frac{-\pi}{2}, 0, \frac{\pi}{2}, \pi$, the circle becomes parallel to the direction of the mesh and the front is then

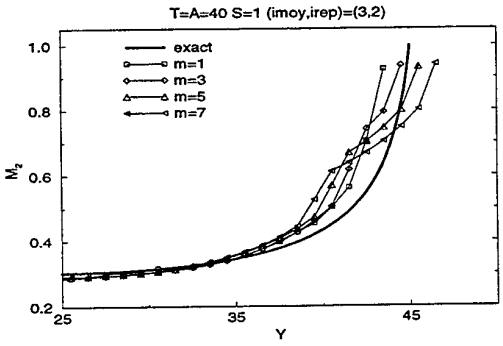

Figure 19: M_2 plotted as function of the transverse location Y: influence of the box heigth

detected as a straight line. Obviously, these parts of the front will create the most important errors on curvature and limit our domain towards great values of the radius. This phenomenon occurs in fig 20 where the error for two radii R=40 and R=42 is plotted as function of the angle. At $\theta = 0$ and $\theta = \pi$, the front is parallel to the transverse direction of the mesh and the error becomes important. An adaptative mesh that rotates around the flame in order to avoid this case would improve the results.

The maximum of the relative errors on curvature are plotted for different values of the radius R in Fig. 21. It shows that the numerical treatment gives a rather good accuracy (relative error smaller than 25%) on curvature, when the radius is between 15 and 40 pixels.

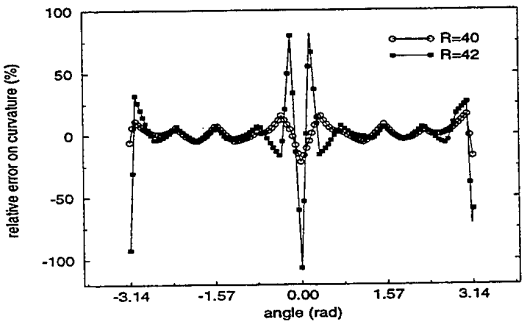

Figure 20: Relative errors on curvature plotted as function of the angle for circles of radius R=40 and R=42 pixels

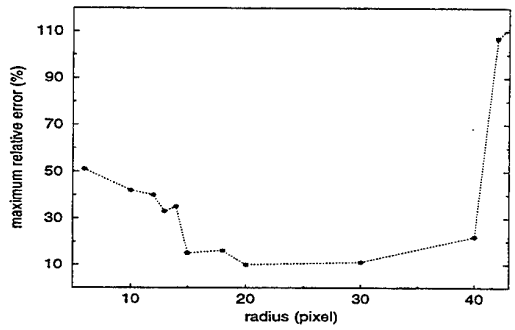

Figure 21: maximum relative errors on curvature as function of the radius of the test circle

5 CONCLUSIONS

Experimental data are now widely used for model development and validation. Tomography measurements coupled with high speed cinematography provide time resolved front visualization. The images are then digitized using a high resolved scanner and the accurate front tracking provides quantitative values on the flame surface topology. The image processing procedure detailed in this paper has been extensively tested and validated with synthetic signals. This procedure is now widely used to extract flame front characteristics from actual experimental images. Reliable comparisons between experimental and theoretical data are now possible (Veynante, Piana, Duclos & Martel, 1996).

ACKNOWLEDGEMENTS

The authors gratefully acknowledge Dr. F. Lacas for helpful discussions.

References

Bray, K., Champion, M., & Libby, P. (1987). The turbulent premixed boundary layer with enthalpy. *Combust. Sci. Technol., 55.*

Bray, K., Libby, P., & Moss, J. (1984). Flamelet crossing frequencies and mean reaction rates in premixed turbulent combustion. *Combust. Sci. Technol., 41*, 143–172.

Candel, S. & Poinsot, T. (1990). Flame stretch and the balance equation for the flame area. *Combust. Sci. Technol., 70*, 1–15.

Duclos, J., Veynante, D., & Poinsot, T. (1993). A comparison of flamelet models for premixed turbulent combustion. *Combust. Flame, 95*(1/2), 101–118.

Marble, F. & Broadwell, J. (1977). The coherent flame model of non-premixed turbulent combustion. Project Squid TRW-9-PU, Project Squid Headquarters, Chaffee Hall, Purdue University.

Pope, S. (1988). The evolution of surfaces in turbulence. *Int. J. Eng. Sci., 26*(5), 445–469.

Trouvé, A. & Poinsot, T. (1994). The evolution equation for the flame surface density. *J. Fluid Mech., 278*, 1–31.

Veynante, D., Piana, J., Duclos, J., & Martel, C. (1996). Experimental analysis of flame surface density models for premixed turbulent combustion. In *Twenty-sixth Symposium (International) on Combustion.* The Combustion Institute.

SESSION 4

3D Imaging Velocimetry

Dual-plane correlation for three-dimensional particle image velocimetry on planar domains

M. Raffel, A. Derville, C. Willert, O. Ronneberger, J. Kompenhans

Institut für Strömungsmechanik
Deutsche Forschungsanstalt für Luft- und Raumfahrt (DLR)
Bunsenstraße 10, D-37073 Göttingen, Germany

1 INTRODUCTION

Particle Image Velocimetry (PIV) allows the recording of a complete velocity field in a plane of the flow within microseconds. In PIV the velocity vector field is usually determined by subdividing the recordings of double exposed tracer particles into small interrogation areas and employing correlation methods for evaluation. The correlation methods are widely used, as they can easily be implemented into fast, reliable and fully automatic evaluation systems. Their theory is well known and described by various authors (Adrian 1988, Keane & Adrian 1990, 1992, Hinsch 1993, Westerweel 1993). The method described in this paper is based on the spatial cross-correlation of particle images stored on separate frames of each exposure as described by Willert and Gharib (1991). It is expanded by the analysis of the correlation peak heights. The correlation value depends on the portion of paired particle images, which itself depends on the out-of-plane velocity component, but also on other parameters such as background light, varying particle size and number, loss of pairs due to in-plane motion. To avoid problems arising from these other influences, images from a displaced light sheet plane, parallel to the first, are also recorded to perform a second correlation for normalization. This concept is referred to as 'dual-plane correlation technique' or 'dual-plane PIV' (Raffel et al. 1995, 1996). It has been shown by the aforementioned authors, that the recording of images of particles within a parallel light sheet on a third frame provides a number of advantages:

(1) the influence of the loss of image pairs due to the in-plane velocity on the out-of-plane velocity estimation can be reduced by normalization; (2) the directional ambiguity of the out-of-plane velocity component can be removed; (3) a larger out-of-plane velocity component can be tolerated compared to conventional PIV; and (4) a higher signal-to-noise ratio for the out-of-plane velocity estimation can be achieved. Progress in the mathematical formulation will be described in detail in this article. Equations will be given for the correlation peak height variance and the out-of-plane velocity component when using Gaussian laser beam profiles. The numerical implementation of the evaluation software will also be described. Software tools were implemented to perform simple numerical simulations in order to optimize the parameters for different experimental arrangements.

2 MATHEMATICAL FORMULATION

In this theoretical approach, the correlation of two frames of single exposed particle images is analysed. The equation necessary to compute the out-of-plane velocity component by using two correlations of three frames is derived taking Gaussian intensity profiles of the light sheets into account.

2.1 Particle images location

Typically, the recordings are subdivided into interrogation windows, also referred to as interrogation spots. The area within one interrogation spot on the first exposure is considered. The recording consists of a random distribution of N particle images. It corresponds to the following tracer pattern inside the flow:

$$\text{vector } \bar{\Gamma} = \begin{pmatrix} \bar{X}_1 \\ \bar{X}_2 \\ \vdots \\ \bar{X}_N \end{pmatrix}, \text{ in a } 3N\text{-dimensional space}; \quad \bar{X}_i = \begin{pmatrix} X_i \\ Y_i \\ Z_i \end{pmatrix} \quad (0)$$

$\bar{\Gamma}$ describes the state of the ensemble at a given time t. $\bar{X}_i$ is the position vector of the particle i at time t. Lower case letters refer to the coordinates in the image plane (Figure 1) such that

$\bar{x} = \begin{pmatrix} x \\ y \end{pmatrix}$ is the image position vector in this plane.

If the image plane is parallel to the light sheet, this position vector is related to the magnification factor M, such that:

$$X_i = x_i / M \text{ and } Y_i = y_i / M \quad (1)$$

if paraxial recording is assumed. For more details about the mathematical description, see Westerweel (1992).

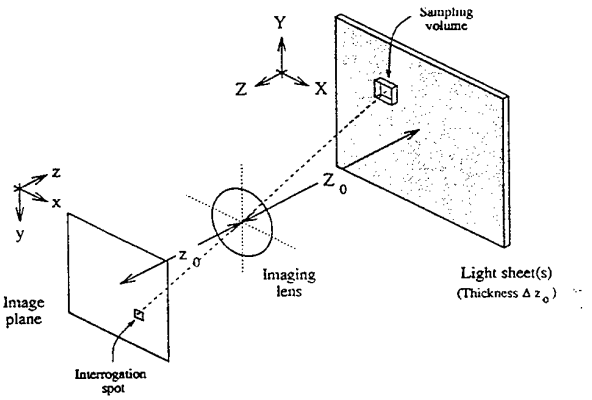

Fig. 1: Schematic representation of the set-up.

2.2 Image intensity field

In this section a mathematical representation of the intensity distribution in the interrogation plane is given. It is assumed that all the particles have the same transmissivity (light scattering profile) $t(\bar{x})$. The transmissivity of a particle image located at $\bar{x}_i$ is conveniently given by the convolution product of $t(\bar{x})$ with the Dirac delta-function shifted at the position $\bar{x}_i$:

$$t(\bar{x} - \bar{x}_i) = t(\bar{x}) * \delta(\bar{x} - \bar{x}_i) \quad \text{(see Appendix A1)} \quad (2)$$

Thus, the image intensity field of the first exposure may be expressed by:

$$I_1 = I(\bar{x}, \bar{\Gamma}) = t(\bar{x}) * \sum_{i=1}^{N} I_0(Z_i)\delta(\bar{x} - \bar{x}_i). \quad (3)$$

$I_0(Z) = I_Z \exp(-8Z^2 / \Delta Z_0^2)$ is the Gaussian intensity profile of the laser light sheet, with ΔZ_0 the thickness of the light sheet measured at the e^{-2} points. The intensity profile could also have a top hat distribution of thickness $\Delta Z_0 : I_0(Z) = I_Z$ if $|Z| \le \frac{\Delta Z_0}{2}$ (0 elsewhere).

The factor $I_0(Z_i)$ represents the amount of light received by the particle i inside the flow, and located at a position Z_i from the center plane of the laser light sheet.

Eq.(3) can alternatively be written as: $I(\vec{x},\vec{\Gamma}) = \sum_{i=1}^{N} I_0(Z_i)t(\vec{x}-\vec{x}_i)$.(4)

This expression of the image intensity field will be extensively used in the following sections.

2.3 Statistics of the intensity field

Given a particular distribution $\vec{\Gamma}$ of particles inside the flow, we first concentrate on the mean value μ_I and the variance σ_I of the intensity as a function of $\vec{x}$, as they are essential for the digital evaluation. The main equations used in the following are taken from Papoulis (1977) and Papoulis (1991).

The spatial average is defined as $\mu_I = \langle I \rangle = \frac{1}{S}\cdot\int_S I(\vec{x})d\vec{x}$, where S is the area of the interrogation spot.

Equation (4) yields : $\mu_I = \frac{1}{S}\cdot\int_S \sum_{i=1}^{N} I_0(Z_i)t(\vec{x}-\vec{x}_i)d\vec{x}$,

that is : $\mu_I = \frac{1}{S}\cdot\left(\sum_{i=1}^{N} I_0(Z_i)\cdot\int_S t(\vec{x}-\vec{x}_i)d\vec{x}\right)$.

Assuming that the particle image i is effectively located inside the area S, we have :

$\int_S t(\vec{x}-\vec{x}_i)d\vec{x} = \int_S t(\vec{x})d\vec{x}$,

since the diameter of a particle image is small compared to the size of the interrogation window. This assumption neglects the factor resulting from the difference $\int_S t(\vec{x})d\vec{x} - \int_S t(\vec{x}-\vec{x}_i)d\vec{x}$. However the arising error is negligeable: in case of a Gaussian transmissivity (see Appendix C), the amplitude of the error function is less than 5% at the e^{-2} point. Therefore, this approximation is commonly admitted. Because

$$\int t(\vec{x})d\vec{x} = t_0 \qquad \text{(see Appendix C1)} \qquad (5)$$

the mean intensity is given by $\mu_I = \frac{t_0}{S}\cdot\sum_{i=1}^{N} I_0(Z_i)$ (6)

The variance of the intensity may be calculated as follows:

$\sigma_I^2 = \left\langle (I-\mu_I)^2 \right\rangle = \left\langle I^2 \right\rangle - \langle I \rangle^2 = \mu_{I^2} - \mu_I^2$.

with $\left\langle I^2 \right\rangle = \frac{1}{S}\cdot\int_S I^2(\vec{x})d\vec{x}$. The derivation of $I^2(\vec{x})$ will be found in Appendix B:

$I^2(\vec{x}) = \sum_{i=1}^{N} I_0^2(Z_i)t^2(\vec{x}-\vec{x}_i)$.

Hence $\left\langle I^2 \right\rangle = \frac{1}{S}\cdot\sum_{i=1}^{N} I_0^2(Z_i)\int_S t^2(\vec{x}-\vec{x}_i)d\vec{x}$.

As before the integral can be expressed as follows:

$\int_S t^2(\vec{x}-\vec{x}_i)d\vec{x} = \int t^2(\vec{x})d\vec{x}$.

With $\int t^2(\vec{x})d\vec{x} = t_1^2$, (see Appendix C2) (7)

the mean value of the square of the intensity is:

$\left\langle I^2 \right\rangle = \frac{t_1^2}{S}\cdot\sum_{i=1}^{N} I_0^2(Z_i)$

Finally we obtain the square of the variance :

$$\sigma_I^2 = \frac{t_1^2}{S}\cdot\sum_{i=1}^{N} I_0^2(Z_i) - \frac{t_0^2}{S^2}\left(\sum_{i=1}^{N} I_0(Z_i)\right)^2 \qquad (8)$$

Assuming a Gaussian shape for the transmissivity (see Appendix C), yields the following relation between t_0 and t_1 : $t_1^2 = t_0^2 / S_\tau$. S_τ is the cross sectional area of the particle images. Thus Eq. (8) yields:

$$\sigma_I^2 = \frac{t_0^2}{S^2}\cdot\left[\frac{S}{S_\tau}\sum_{i=1}^{N} I_0^2(Z_i) - \left(\sum_{i=1}^{N} I_0(Z_i)\right)^2\right] \qquad (9)$$

In the following the ratio between the standard deviation and the mean value is derived. The previous equation combined with Eq. (6) yields:

$$\left(\frac{\sigma_I}{\mu_I}\right)^2 = \frac{S}{S_\tau}\frac{\sum_{i=1}^{N} I_0^2(Z_i)}{\left(\sum_{i=1}^{N} I_0(Z_i)\right)^2} - 1 .$$

In case the laser light sheet has a top hat intensity profile, we have : $I_0(Z_i) = I_Z$, $\forall i = 1...N$. Thus $(\sigma_I / \mu_I)^2 = S/NS_\tau - 1$.

If the particle images density is defined as $N_S = NS_\tau / S$ (10)

the ratio can be further reduced to : $\sigma_I / \mu_I = \left(\frac{1-N_S}{N_S}\right)^{1/2}$.

2.4 Cross-correlation function

As already mentioned before, PIV recordings are frequently evaluated locally by cross-correlating the two frames. In the following, the mathematical background of this technique is described.

A constant displacement $\vec{D}$ inside the flow is assumed and corresponds to a constant displacement $\vec{d}$ within the interrogation spot :

$$\vec{D} = \begin{pmatrix} D_X \\ D_Y \\ D_Z \end{pmatrix} \text{ and } \vec{d} = \begin{pmatrix} MD_X \\ MD_Y \end{pmatrix}.$$

The cross correlation function of two interrogation windows I_1 and I_2 can be written as:

$$R_{I_1I_2}(\vec{s},\vec{\Gamma},\vec{D}) = \sum_{i,j} I_0(Z_i)I_0(Z_j+D_Z)\int t(\vec{x}-\vec{x}_i)t(\vec{x}+\vec{s}-\vec{x}_j-\vec{d})d\vec{x} \qquad (11)$$

wherein $\vec{s}$ is the separation vector in the correlation plane. Assuming the Gaussian particle image transmissivity $t(\vec{x}) = K\exp(-8|\vec{x}|^2 / d_\tau^2)$ (Appendix C0) yields:

$$t(\vec{x}-\vec{x}_i)t(\vec{x}+\vec{s}-\vec{x}_j-\vec{d}) = K^2\exp\left[-8(|\vec{x}-\vec{x}_i|^2 + |\vec{x}+\vec{s}-\vec{x}_j-\vec{d}|^2)/d_\tau^2\right].$$

Given two vectors $\vec{a}$ and $\vec{b}$, it can be shown that $|\vec{a}|^2 + |\vec{a}+\vec{b}|^2 = |\vec{b}|^2/2 + 2|\vec{a}+\vec{b}/2|^2$. Hence:

$$t(\vec{x}-\vec{x}_i)t(\vec{x}+\vec{s}-\vec{x}_j-\vec{d}) = K^2\exp(-4|\vec{s}+\vec{x}_i-\vec{x}_j-\vec{d}|^2/d_\tau^2)\exp(-16|\vec{x}+(\vec{s}+\vec{x}_i-\vec{x}_j-\vec{d})/2|^2/d_\tau^2).$$

Consequently (11) may be rewritten as following :

$$R_{I_1I_2}(\vec{s},\vec{\Gamma},\vec{D}) = \sum_{i,j} I_0(Z_i)I_0(Z_j+D_Z)\exp(-4|\vec{s}+\vec{x}_i-\vec{x}_j-\vec{d}|^2/d_\tau^2)\cdot \cdot\int t^2(\vec{x}+(\vec{s}+\vec{x}_i-\vec{x}_j-\vec{d})/2)d\vec{x} \qquad (12)$$

By distinguishing the terms $i = j$ and $i \neq j$ yields :

$$R_{I_1I_2}(\vec{s},\vec{\Gamma},\vec{D}) = \sum_{i\neq j} I_0(Z_i)I_0(Z_j+D_Z)\exp(-4|\vec{s}+\vec{x}_i-\vec{x}_j-\vec{d}|^2/d_\tau^2) \cdot\int t^2(\vec{x}+(\vec{s}+\vec{x}_i-\vec{x}_j-\vec{d})/2)d\vec{x} + \sum_{i=1}^{N} I_0(Z_i)I_0(Z_i+D_Z)\exp(-4|\vec{s}-\vec{d}|^2/d_\tau^2)\cdot\int t^2(\vec{x}+(\vec{s}-\vec{d})/2)d\vec{x}$$

Following the decomposition proposed by Adrian (1988), we can write:

$R_{I_1I_2}(\vec{s},\vec{\Gamma},\vec{D}) = R_C(\vec{s},\vec{\Gamma},\vec{D}) + R_F(\vec{s},\vec{\Gamma},\vec{D}) + R_D(\vec{s},\vec{\Gamma},\vec{D})$.

$R_D(\bar{s},\bar{\Gamma},\bar{D})$ is the displacement correlation that gives the image displacement. It results from the component of the cross-correlation function that corresponds to the correlation of the particle images with their pair ($i = j$ terms):

$$R_D(\bar{s},\bar{\Gamma},\bar{D}) = \exp(-4\left|\bar{s}-\bar{d}\right|^2/d_\tau^2)\cdot\int t^2(\bar{x}+(\bar{s}-\bar{d})/2)d\bar{x}\cdot\sum_{i=1}^{N} I_0(Z_i)I_0(Z_i+D_Z).$$

The expression $\int t^2(\bar{x}+(\bar{s}-\bar{d})/2)d\bar{x}$ could further be simplified according to the assumption we already made to obtain Eq. (5) and (7). Hence it would yield to t_I^2. But as the variable $\bar{s}$ appears in this integral, we will rather write $\int t^2(\bar{x}+(\bar{s}-\bar{d})/2)d\bar{x} = t_1^2\cdot F_t(\bar{s}-\bar{d})$. However, it has to be kept in mind that $F_t \cong 1$. As a result, it can be obtained:

$$R_D(\bar{s},\bar{\Gamma},\bar{D}) = t_1^2 F_t \exp(-4\left|\bar{s}-\bar{d}\right|^2/d_\tau^2)\sum_{i=1}^{N} I_0(Z_i)I_0(Z_i+D_Z) \quad (13)$$

Hence, for a given distribution of particles inside the flow, the displacement correlation peak reaches a maximum for $\bar{s} = \bar{d}$. Therefore, - as a well known result - the localisation of this maximum yields the average in-plane displacement, and thus the X and Y component of the velocity inside the flow. Furthermore, it can be seen from Eq. (13) that the displacement correlation is a function of the N random variables $(Z_i)_{i=1..N}$. Consequently it is a random variable itself, for which the expectate value and the variance are calculated next to obtain information about bias and random errors.

2.5 Expected value of the displacement correlation

From (13), it follows:

$$E\{R_D\} = E\left\{t_1^2 F_t \exp(-4\left|\bar{s}-\bar{d}\right|^2/d_\tau^2)\sum_{i=1}^{N} I_0(Z_i)I_0(Z_i+D_Z)\right\}, \Rightarrow$$

$$E\{R_D\} = t_1^2 F_t \exp(-4\left|\bar{s}-\bar{d}\right|^2/d_\tau^2)\cdot E\left\{\sum_{i=1}^{N} I_0(Z_i)I_0(Z_i+D_Z)\right\}.$$

Defining $f_0(Z) = I_0(Z)I_0(Z+D_Z)$ yields:

$$E\{R_D\} = t_1^2 F_t \exp(-4\left|\bar{s}-\bar{d}\right|^2/d_\tau^2)\cdot E\left\{\sum_{i=1}^{N} f_0(Z_i)\right\}. \quad (15)$$

We proof in Appendix D1 that $E\left\{\sum_{i=1}^{N} f_0(Z_i)\right\} = N/\Delta Z_0\cdot\int f_0$,

where $\int f_0$ is the integral $\int f_0(Z)dZ$.

$$\text{Thus } E\{R_D\} = \frac{Nt_1^2F_t}{\Delta Z_0}\cdot(\int f_0)\cdot\exp -4\frac{\left|\bar{s}-\bar{d}\right|^2}{d_\tau^2}. \quad (16)$$

We can rewrite $\int f_0 = \int I_0(Z)I_0(Z+D_Z)dZ = I_Z^2\Delta Z'' F_0(D_Z)$,

with $I_Z^2\Delta Z'' = \int I_0^2(Z)dZ$, and $F_0(D_Z) = \dfrac{\int I_0(Z)I_0(Z+D_Z)dZ}{\int I_0^2(Z)dZ}$.

$F_0(D_Z)$ is interpreted as the out-of-plane loss of pairs (Keane & Adrian 1993). Finaly, (16) yields:

$$E\{R_D(\bar{s},\bar{D})\} = \frac{NI_Z^2\Delta Z''}{\Delta Z_0}\frac{4t_0^2}{\pi d_\tau^2}F_t F_0(D_Z)\exp(-4\left|\bar{s}-\bar{d}\right|^2/d_\tau^2) \quad (17)$$

2.6 Variance of the displacement correlation

The variance is given by: $\tilde{\sigma}_{R_D}^2(\bar{s},\bar{D}) = E\{R_D^2\} - E^2\{R_D$. (18)

For determination of $R_D^2(\bar{s},\bar{\Gamma},\bar{D})$, Eq. (13) is used to obtain:

$$R_D^2(\bar{s},\bar{\Gamma},\bar{D}) = t_1^4 F_t^2 \exp(-8\left|\bar{s}-\bar{d}\right|^2/d_\tau^2)\cdot\left(\sum_{i=1}^{N} f_0(Z_i)\right)^2.$$

We have $\left(\sum_{i=1}^{N} f_0(Z_i)\right)^2 = \sum_{i=1}^{N} f_0^2(Z_i) + \sum_{i\neq j} f_0(Z_i)f_0(Z_j)$.

The expected values of these terms are calculated in Appendix D:

$$E\left\{\sum_{i=1}^{N} f_0^2(Z_i)\right\} = N/\Delta Z_0\cdot\int f_0^2 \quad (D2)$$

$$E\left\{\sum_{i\neq j} f_0(Z_i)f_0(Z_j)\right\} = \frac{N^2-N}{\Delta Z_0^2}\cdot(\int f_0)^2 \quad (D3)$$

Finally we obtain:

$$E\{R_D^2\} = t_1^4F_t^2\exp(-8\left|\bar{s}-\bar{d}\right|^2/d_\tau^2)\cdot\left(\frac{N}{\Delta Z_0}\cdot\int f_0^2 + \frac{N^2-N}{\Delta Z_0^2}\cdot(\int f_0)\right) \quad (19)$$

Thus the variance of $R_D(\bar{s},\bar{D})$ is:

$$\tilde{\sigma}_{R_D}^2(\bar{s},\bar{D}) = t_1^4F_t^2\exp(-8\left|\bar{s}-\bar{d}\right|^2/d_\tau^2)\cdot\left(\frac{N}{\Delta Z_0}\int f_0^2 + \frac{N^2-N}{\Delta Z_0^2}(\int f_0)^2 - \frac{N^2}{\Delta Z_0^2}\cdot(\int f_0)^2\right)$$

This can be further reduced to :

$$\tilde{\sigma}_{R_D}^2(\bar{s},\bar{D}) = t_1^4F_t^2\frac{N}{\Delta Z_0}\left[\int f_0^2 - \frac{(\int f_0)^2}{\Delta Z_0}\right]\cdot\exp(-8\left|\bar{s}-\bar{d}\right|^2/d_\tau^2) \quad (20)$$

Finaly, we take the ratio of the variance and the expected value. Eq.(16) and Eq.(20) yield :

$$\frac{\tilde{\sigma}_{R_D}^2}{E^2\{R_D\}} = \frac{\Delta Z_0}{N}\frac{\int f_0^2 - (\int f_0)^2/\Delta Z_0}{(\int f_0(Z)dZ)^2} \quad (21)$$

This result has interresting aspects if a Gaussian intensity profile for the laser light sheet is assumed (see Appendix E):

$I_0(Z) = I_Z\exp(-8|Z|^2/\Delta Z_0^2)$. Hence:

$$f_0(Z) = I_0(Z)\cdot I_0(Z+D_Z) = I_Z^2\cdot\exp(-8Z^2/\Delta Z_0^2)\cdot\exp(-8(Z+D_Z)^2/\Delta Z_0^2)$$
$$= I_Z^2\cdot\exp(-4D_Z^2/\Delta Z_0^2)\cdot\exp(-16(Z+D_Z/2)^2/\Delta Z_0^2)$$

Using (A2), we may then calculate $\int f_0$ and $\int f_0^2$:

$$\int f_0(Z)dZ = I_Z^2\exp(-4D_Z^2/\Delta Z_0^2)\cdot\Delta Z_0\sqrt{\pi/16},$$

$$\int f_0^2(Z)dZ = I_Z^4\exp(-8D_Z^2/\Delta Z_0^2)\cdot\Delta Z_0\sqrt{\pi/32}.$$

Hence (21) yields :

$$\frac{\tilde{\sigma}_{R_D}^2}{E^2\{R_D\}} = \frac{1}{N}\cdot(4/\sqrt{2\pi}-1) = 0{,}596/N.$$

$$\frac{\tilde{\sigma}_{R_D}}{E\{R_D\}} = 0{,}772/\sqrt{N} \quad (22)$$

2.7 Results of the mathematical formulation

The derivation of the formula for the out-of-plane velocity component w as presented in literature (Raffel et al. 1995) was based on the assumption of a top-hat intensity profil of the light sheets in out-of-plane direction. However, the spatial intensity profil of the CW-laser can be approximated much better by a Gaussian curve. Therefore, the following equation for the out-of-plane w has been derived by substituing a Gauusian profile for I_0 in Eq.(13) in order to improve the results:

$$w = \alpha + \beta\cdot\ln(R_{D1,2}/R_{D0,1}) \quad (I)$$

with $\alpha = \dfrac{Z_2-Z_0}{2\Delta t}$ and $\beta = \dfrac{\Delta Z_0}{8\Delta t}\cdot\dfrac{\Delta Z_0}{Z_2-2Z_1+Z_0}$

$R_{D0,1}$ and $R_{D1,2}$ are the heights of the cross-correlation peaks of frames 0 and 1 and frames 1 and 2 respectively. Z_0, = Z_2 are the light sheet positions during first and third exposure, and Z_1 is the light sheet position during second exposure. ΔZ_0 is the light sheet thickness, and Δt the pulse separation time.

When using CW-lasers with a Gaussian beam profile the problem arises to define the light sheet thickness adequately. In theory this is usualy done considering the e^{-2} points. In praxis the light sheets thickness is influenced by many parameters like laser power, f-number of the lens, particle size, and others. Since a Gaussian intensity distribution of the light sheet yields

$$F_0(Z) = \exp(-4Z^2 / \Delta Z_0^2), \qquad \text{(II)}$$

for the out-of-plane loss, the recording of an image set of particles at rest can be used to determine the light sheet thickness ΔZ_0 more accurately by using the following equation:

$$\Delta Z_0 = \frac{2(Z_2 - Z_1)}{\sqrt{\ln(E\{R_{D0,1}\} / E\{R_{D1,2}\})}} \qquad \text{(III)}$$

The basic equations of the displacement correlation have been derived. In contrast to other authors, who were mainly interested in the location of the maximum, our main interest in this equation was directly the amplitude of the signal. This amplitude is clearly a function of the number of the effective number of particle images N. Assuming a random distribution of particles in the flow, random variable theory has been used to calculate the expected value $E\{R_D\}$ and the variance $\tilde{\sigma}_{R_D}$ of the displacement correlation amplitude. In order to analyse the random error contained in the out-of-plane velocity estimation given by Eq. (I), the correlation amplitude can be considered as $R_D = E\{R_D\} + \varepsilon$ with $\varepsilon = k\tilde{\sigma}_{R_D}$. It can be shown by substituting R_D in Eq. (I) that the uncertainty in the velocity estimation Δw, which is induced by the finite number of particles in the measurement volume N is $\Delta w = |\beta| \cdot \ln((1+\varepsilon_{1,2}) / (1+\varepsilon_{0,1}))$ and therefore (using a first order approximation for the logarithm):

$$\Delta w = |\beta| \cdot \bar{k}((1/\sqrt{N_{1,2}}) + (1/\sqrt{N_{0,1}})) \qquad \text{(IV)}$$

3 NUMERICAL IMPLEMENTATION

3.1 Simulation software

The traditional dual image cross-correlation method is generally associated with an in-plane measurement uncertainty but also contain distortions due to the perspective projection of the imaging lens and the out-of-plane velocity component. If planar flow is assumed this measurement error can be estimated by recording static (random-dot) particle image patterns which have been translated or rotated by known amounts. This method however is unsuited to assess the performance of a PIV system in three-dimensional flows and alternative techniques are required. One approach is to record images of known actual flow geometry as described in section 4. To gain full control over all involved parameters, numerical simulations are required. The aim of these Monte-Carlo simulations is to generate artificial particle images with a known underlying flow field, evaluate them with the existing analysis software and compare the result with the predicted values. Based on these simulations the application of the measurement technique to an actual flow field can then be optimized.

The core of the simulations consists of the generation of artificial particle images within a light sheet. The Mie-scattered light of the particle onto the rectangular sensor array is approximated by a circular intensity bell:

$$i(\bar{x}) = K \exp(-8|\bar{x}|^2 / d_\tau^2) \qquad \text{with } K = \frac{8 i_0}{\pi d_\tau^2}.$$

The center of the particle image has a peak intensity of $I_0(Z) \cdot K$, while the circular area of diameter d_τ centered at this point contains 95% of the light scattered by the particle (also known as the e^{-2} diameter). The factor K is a function of the scattering efficiency of the particle and depends on the location within the light sheet, which in itself has an intensity profile (see Figure 2). For the simulations the laser light sheet is assumed to have a Gaussian intensity profile with an e^{-2}thickness ΔZ_0:

$$I_0(Z) = I_Z \cdot \exp\left(-\frac{8Z^2}{\Delta Z_0^2}\right).$$

This profile closely resembles that of the Argon-ion laser beam used in the experiment, but other profiles may be imposed as well.

To generate a particle image, a random number generator specifies a location within a three-dimensional slab containing the light sheet (Fig. 2). The peak intensity I_0 is then calculated based on the intensity modulation given above. Using error functions (integral formulations of the Gaussian bell curve) the intensity distribution of the scattered light is computed over the discrete pixels which are assumed to be square and have an 100% active area. In the following exposures the particle locations in the three-dimensional slab are shifted by the imposed underlying flow field, generally a translation. For the generation of the third image frame the light sheet is offset in a parallel fashion by a known amount while the 'particles' continue to move. The placement of particles is repeated until a desired image density within the frame is reached.

In order to achieve a range of particle image sizes and intensities both the particle image diameter d_τ and scattering efficiency I_Z can be varied over a given statistical range. The image generation process is completed by quantizing the numerical image to a desired image depth (i.e. number of grey levels) and subjecting it to optional background noise, offset and gain factors.

In summary, a number of variable parameters exist for the generation of particle image alone:

- particle image diameter d_τ,
- particle image scattering efficiency I_Z,
- image quantization levels (number of bits),
- seeding density,
- background noise,
- gain factors,
- non-linearities in the quantization process,
- illumination beam profile,
- perspective distortion and other effects.

The underlying flow field is associated with a number of additional parameters such as particle image displacement, spatial and temporal gradients, particle path curvature and lag, and, of course, three-dimensional effects. Finally the interrogation parameters themselves enter: interrogation window, spacing and offset.

It is obvious that the parameter domain is far too complex to be studied in its completeness, so only selected parameters can be varied in order to assess the measurement errors in the triple frame PIV method. The aim is to generate particle images which closely match those obtained by digitization of video signals and concentrate on displacement fields with uniform (translational) profiles in three dimensions.

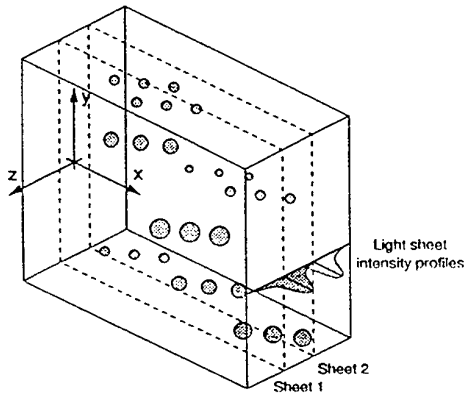

Fig. 2: Three-dimensional rendition of the particle image model used to generate artificial PIV images.

3.2 Evaluation software

The evaluation of the triple frame PIV recordings was performed by correlation analysis, similar to that described by Willert and Gharib (1991). This paper discusses the evaluation of two sequential, digital (video) PIV recordings containing single-exposed particle images by means of local cross-correlations. By applying a three-point Gauss fit through the correlation peak, the in-plane displacement vector can be reliably measured with sub-pixel accuracies down to the order of 0.01 to 0.05 pixels.

To adapt the dual image cross-correlation software to the triple image configuration described herein several modifications were necessary. In the new arrangement two correlation planes are computed by correlating the first image with the second and the second image with the third which is displaced from the first two. Thus the first correlation captures the in-plane particle motion while the second preferentially recovers particles moving normal to the light sheet in the direction of its displacement.

In the typical formulation the cross-correlation at a discrete point $\vec{s}$ is defined as a sum of products of the two grey level functions $I_1(\vec{x})$ and $I_2(\vec{x})$ representing the two interrogation windows:

$$R_{I_1 I_2}(\vec{s}) = \sum_{\vec{x}} I_1(\vec{x}) I_2(\vec{x}+\vec{s})$$

However to allow a comparison between the two correlation planes both need to be normalized to form correlation coefficient planes with a range from 0 to 1:

$$R_{1,2}(\vec{s}) = \frac{\sum_{\vec{x}} (I_1(\vec{x}) - \mu_1)(I_2(\vec{x}+\vec{s}) - \mu_2)}{\sqrt{\sigma_1 \sigma_2}}$$

where μ_1, μ_2 are the averages and σ_1, σ_2 the corresponding variances of the functions $I_1(\vec{x})$ and $I_2(\vec{x})$. In effect the cross-correlation coefficient function is defined as the ratio of the covariances of the image data divided by the product of the respective standard deviations.

The location of the highest correlation coefficient from both planes is associated with the mean, in-plane displacement vector. A second correlation coefficient is extracted from the adjacent correlation plane at the corresponding location of the displacement vector. These two correlation values are then used to recover the out-of-plane displacement component by taking the light sheet offset and intensity profile into consideration. In this arrangement only particles moving in the direction to the light sheet offset are captured. In an alternative configuration the second image is formed by a light sheet displaced from the first and the third which are at the same location. In this case both directions of out-of-plane flow can be recovered.

In terms of numerical implementation the cross-correlation coefficient summation was implemented using two-dimensional fast Fourier transforms (FFT's) to significantly increase the evaluation speed. Through the use of FFT's, the summations in the correlation expression given above reduce to point-wise, complex-conjugate multiplications in the spatial frequency domain. A further processing time reduction is achieved by applying the symmetry properties for Fourier transforms of real data. These properties allow two real data sets to be transformed to the spatial frequency domain using only one complex-to-complex FFT. Other optimizations included function in-lining of the platform independent C-source code, FFT's based on lookup table usage, as well as compiler specific optimizations. On a 90 MHz Pentium PC vector recovery rates exceeding 50 Hz are possible using a 32 x 32 px interrogation window allowing an image triplet to be processed in less than a minute (1500 vectors).

4 APPLICATION TO EXPERIMENTAL DATA

In a first experiment small tracer particles of approximately 3 µm diameter, which were randomly distributed in a transparent plastic block, have been illuminated by an argon-ion laser and recorded by a standard CCD camera. After each redording the position of the particles has been changed by 20 µm. In order to compensate for electronic noise, the frame grabber used for digitization was calibrated in such a manner that the average intesity of a frame recorded in a dark room was zero. Each recorded frame has been correlated with with the reference frame (light sheet position in the middle of the recorded range) after subdividing them into 88 independend interrogation windows of 64 x 64 pixels. The correlation peak height of each interrogation window has been found by analysing the shape of non-linear Gaussian fitting through the pixel of highest correlation intensity and its eight neighbours. The average and the standard deviation of the correlation peak height are shown in Fig. 3. The average values of the peaks heights can be interpreted as the experimental determination of the out-of-plane loss of correlation, which can be approximated by the autocorrelation function of the light sheet intensity profile. Assuming a Gaussian intensity profile the autocorrelation is also a Gaussian curve (see Eq. (II)).

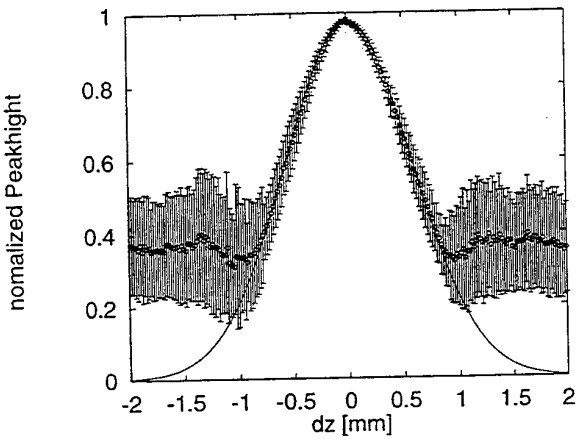

Fig. 3: Experimentally determined loss of correlation due to out-of-plane displacement of particles.

In a second experiment silver coated 10 µm glass-spheres were added to glycerine, which was filled in a glass cylinder. The particle motion due to the rotation of the cylinder was observed using a CCD-video camera, which recorded interlaced images at a frame rate of 25 Hz. Each frame of 752 x 582 px^2 was separated into two fields where the missing lines were linearly interpolated. The stepper motor driven cylinder (diameter 180 mm, angular speed: 3.1 rad/s) was mounted within a glycerine filled glass tank, to provide a plane liquid-air interface. The obtained measurement results could easily be compared with the solid body rotation. The particle motion contains both, positive and negative out-of-plane velocity components.

4.1 Experimental setup

The main elements of the experimental setup are shown in Figure 2. An argon-ion laser produced a continuous beam of about 1 Watt output power. A chopper disc containing three slits was driven by a stepper motor and controlled by a high precision signal generator. The rotational speed of the disc was adjusted to a light pulse frequency which was equal to the repetition rate of the video camera. It generated light pulses with a pulse length of t_e = 4 ms and a pulse separation time of Δt = 20 ms. A small glass plate was mounted on the disc and covered one of the slits (see Fig. 4). By placing the chopper disk at an angle, the beam passing through the glass plate is displaced sideways and thereby allows the generation of two alternating parallel light sheets.

A cylindrical lens was used to form a light sheet height approximately two times larger than the height of the observation field. The position of the light sheet location alternated after each capture of a field. Two subsequent full-frames containing two fields each were recorded. Thus the first and third field contain images of

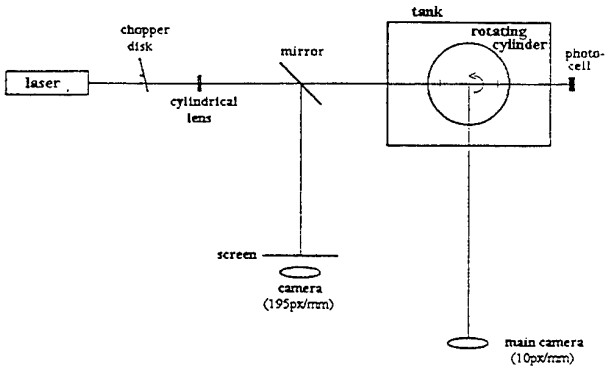

Fig. 4: Sketch of the main components of the rotating cylinder setup and the cameras used for PIV recording and light sheet displacement measurement.

tracer particles within the same light sheet oriented parallel to the axis of the disc (recorded at t_0 and $t_2 = t_0+2\Delta t$ respectively). The second field contains images of tracer particles within a light sheet slightly displaced with respect to both others (rec. at $t_1 = t_0+\Delta t$). The shift of the light sheet was $(Z_2 - Z_1) = 0.5$ mm resulting in an overlap of $O_z = 75$ % of the light sheet thickness ($\Delta Z_0 = 2$ mm).

4.2 Experimental results

In Fig. 5 the radial (u), axial (v), and azimuthal (w) velocity profiles of the particle motion are plotted. The radial velocity component (u) and the axial velocity component (v) are almost constant over the width of the observation field. The radial velocity component was greater than zero, since the light sheet was located 5mm out of the axis of rotation. It can be expected from theory, that the azimuthal velocity profile (w) of the rotating particles within the cylinder varies linearly over the radius; a trend that can also be observed in the present dual-plane PIV measurement. However, other features such as the oscillations of the azimuthal velocity profile (w) can be explained by the variance of the correlation peaks for a finite number of particle images per interrogation spot as derived in section 2.

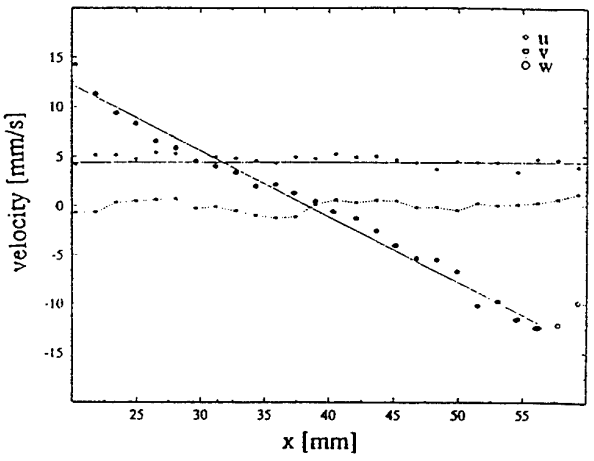

Fig. 5: Radial (u), axial (v), and azimuthal velocity profile (w) of the particles within the rotating cylinder along a line of the piv recording. The light sheet was located 5mm out of the cylinder axis (raw data without smoothing).

5 CONCLUSION

The analysis of the spatial averages has shown that the out-of-plane velocity distribution can be determined if the number of particle images is sufficient. The equation necessary to consider a Gaussian light sheet intensity profile has been presented. The evaluation software and the software necessary to perform numerical simulations to get insight into the optimal values for relevant experimental parameters has been developed. The experimental results allow to assess the performance of the dual-plane correlation technique. The presented evaluation system can now be used to test new modes of operation which allow to record images of different light sheets simultaneous. This is assumed to decrease the measurement noise. It could be experimentally done by quasi simultaneous recording of the second and third frame by means of a high-speed video camera and a multi-pulse laser, by coding the light sheets by different polarisation, or by image separation using a colour video camera and a colour coded light sheet as recently presented by Brücker (1996). However, first tests of the recording of small tracer particles in air with a two-colour pulse laser system and colour film already show, that the focal plane for green light can be displaced by up to 20 mm with respect to the focal plane for red light. Further experiments and numerical simulations are in progress.

6 APPENDIX

A. Useful mathematical results

(A1). For a real funtion f of the variable $\vec{x}$, and a given vector $\vec{x}_i$, we have:

$$f(\vec{x}-\vec{x}_i) = f(\vec{x})*\delta(\vec{x}-\vec{x}_i).$$

where $*$ is a convolution product and δ the Dirac delta function.

(A2). Given a real number α, we have :

$$\int_{-\infty}^{+\infty}\exp(-\alpha x^2)dx = \sqrt{\pi/\alpha} \text{ and } \int_{-\infty-\infty}^{+\infty+\infty}\exp(-\alpha|\vec{x}|^2)d\vec{x} = \pi/\alpha .$$

B. Square of the intensity

The image density field is given by equation (4):

$$I(\vec{x},\vec{\Gamma}) = \sum_{i=1}^{N} I_0(Z_i)t(\vec{x}-\vec{x}_i).$$

The determination of I^2 yields:

$$(I(\vec{x},\vec{\Gamma}))^2 = \left[\sum_{i=1}^{N} I_0(Z_i)t(\vec{x}-\vec{x}_i)\right]^2$$

$$= \sum_{i=1}^{N} I_0^2(Z_i)t^2(\vec{x}-\vec{x}_i) + \sum_{i\neq j} I_0(Z_i)I_0(Z_j)t(\vec{x}-\vec{x}_i)t(\vec{x}-\vec{x}_j)$$

Particle Image Velocimetry, in contrast to Laser Speckle Velocimetry, deals with a lower source density. Therefore, the average distance between the particle images is larger than the particle image diameter. The particle images density defined in (10) is such that $N_S << 1$. Thus, the particle images are isolated : they do not overlap.

As a result, we have : $\forall(i,j)/i\neq j$, $t(\vec{x}-\vec{x}_i)t(\vec{x}-\vec{x}_j) = 0$.

Hence the second sum cancel and we have :

$$(I(\vec{x},\vec{\Gamma}))^2 = \sum_{i=1}^{N} I_0^2(Z_i)t^2(\vec{x}-\vec{x}_i).$$

Moreover, according to (A1), we may write:

$t^2(\vec{x}-\vec{x}_i) = t^2(\vec{x})*\delta(\vec{x}-\vec{x}_i)$. Thus:

$$(I(\vec{x},\vec{\Gamma}))^2 = \sum_{i=1}^{N} I_0^2(Z_i)t^2(\vec{x}-\vec{x}_i) = t^2(\vec{x})*\sum_{i=1}^{N} I_0^2(Z_i)\delta(\vec{x}-\vec{x}_i)$$

C. Gaussian transmissivity

The transmissivity of the particle image (light scattering profile) is of Gaussian shape, as assumed by Adrian (1992):

$$t(\bar{x}) = K\exp(-8|\bar{x}|^2 / d_\tau^2) \qquad \text{with } K = \frac{8t_0}{\pi d_\tau^2}. \tag{C0}$$

From (A2), we find : $\int t(\bar{x})d\bar{x} = t_0$ (C1)

The square of the transmissivity is:

$$t^2(\bar{x}) = \left(\frac{8t_0}{\pi d_\tau^2}\right)^2 \exp(-16|\bar{x}|^2 / d_\tau^2).$$

Using (A2), we can write: $\int t^2(\bar{x})d\bar{x} = \left(\frac{8t_0}{\pi d_\tau^2}\right)^2 \cdot \pi d_\tau^2 / 16 = \frac{4t_0^2}{\pi d_\tau^2}$.

Hence we obtain $\int t^2(\bar{x})d\bar{x} = t_1^2 = t_0^2 / S_\tau$, (C2)

with $S_\tau = \pi d_\tau^2 / 4$ "area" of a particle image.

D. Some expected values

We have defined $f_0(Z) = I_0(Z)I_0(Z + D_Z)$ (equation (21)).
Here we will determine

$$E\left\{\sum_{i=1}^{N} f_0(Z_i)\right\},\ E\left\{\sum_{i=1}^{N} f_0^2(Z_i)\right\}, \text{ and } E\left\{\sum_{i\neq j} f_0(Z_i)f_0(Z_j)\right\}.$$

The three sums must be considered as functions of the N random variables $Z_1, Z_2 \ldots Z_N$. As the distribution of the particle inside the flow is assumed to be uniform, the probability density function of this N random variables depending function is $\rho = 1 / \Delta Z_0^N$. Hence:

$$\begin{aligned} E\left\{\sum_{i=1}^{N} f_0(Z_i)\right\} &= \int\int\cdots\int \sum_{i=1}^{N} f_0(Z_i)\Delta Z_0^{-N} dZ_1 dZ_2 \cdots dZ_N \\ &= N / \Delta Z_0^N \cdot \int f_0(Z_1)dZ_1 \cdot \int\int\cdots\int dZ_2 \cdots dZ_N \\ &= N / \Delta Z_0^N \cdot \Delta Z_0^{N-1} \cdot \int f_0(Z)dZ \end{aligned}$$

$$E\left\{\sum_{i=1}^{N} f_0(Z_i)\right\} = N / \Delta Z_0 \cdot \int f_0 \tag{D1}$$

The quantity $E\left\{\sum_{i=1}^{N} f_0^2(Z_i)\right\}$ is calculated in a similar way. We find:

$$E\left\{\sum_{i=1}^{N} f_0^2(Z_i)\right\} = N / \Delta Z_0 \cdot \int f_0^2 \tag{D2}$$

The last expected value $E\left\{\sum_{i\neq j} f_0(Z_i)f_0(Z_j)\right\}$ equals:

$$\begin{aligned} E\left\{\sum_{i\neq j} f_0(Z_i)f_0(Z_j)\right\} &= \int\int\cdots\int \sum_{i\neq j} f_0(Z_i)f_0(Z_j)\cdot\Delta Z_0^{-N} dZ_1 dZ_2 \cdots dZ_N \\ &= \frac{N^2 - N}{\Delta Z_0^N} \cdot \int\int f_0(Z_1)f_0(Z_2)dZ_1 dZ_2 \cdot \int\int\cdots\int dZ_3 \ldots dZ_N \end{aligned}$$

because the sum $\sum_{i\neq j}$ has $N^2 - N$ terms. Thus it results:

$$E\left\{\sum_{i\neq j} f_0(Z_i)f_0(Z_j)\right\} = \frac{N^2 - N}{\Delta Z_0^N} \Delta Z_0^{N-2} \left(\int f_0(Z)dZ\right)^2,$$

$$E\left\{\sum_{i\neq j} f_0(Z_i)f_0(Z_j)\right\} = \frac{N^2 - N}{\Delta Z_0^2} \cdot \left(\int f_0\right)^2 \tag{D3}$$

ACKNOWLEDGEMENT

The authors would like to thank Mr. Höfer for his help during the experiments. Prof. Klaus Hinsch's generous offer of his transparent plastic blocks containing randomly distributed tracer particles and stimulating discussions with him, Dr. Jerry Westerweel, and Dr. Thomas Roesgen are greatly appreciated. Special thanks also to Prof. Mory Gharib for good collaboration in the frame of CQV.

REFERENCES

R.J. Adrian: Statistical properties of particle image velocimetry measurements in turbulent flows. in *Laser Anemometry in Fluid Mechanics III.* R.J Adrian et al. Eds., Springer, 115-129, (1988).

J.S. Bendat, A.G. Piersol: *Random data - Analysis and measurement procedures.* Wiley-Intersience, New York, (1971).

C. Brücker: 3-D PIV via spatial correlation in a colour-coded light-sheet. to appear in Exp. Fluids as a Technical Note, (1996).

K. Hinsch: Particle image velocimetry. in *Speckle Metrology*, R.S. Sirohi Ed., Marcel Dekker, 235-234, New York, (1993).

R.D. Keane, R.J. Adrian: Optimization of particle image velocimeters. Meas. Sci. Technol. 1, 1202-1215, (1990).

R.D. Keane, R.J. Adrian: Theory of cross-correlation analysis of PIV images. Appl. Sci. Res. 49, 191-215, (1992).

A. Papoulis: *Signal Analysis.* Mc Graw Hill, New York, (1977).

A. Papoulis: *Probability, Random Variables, and Stochastic Processes.* Mc Graw Hill, New York, (1991).

M. Raffel, O. Ronneberger, M. Gharib and J. Kompenhans: Feasibility study of three-dimensional PIV by correlating images of particles within parallel light sheets. Exp. Fluids 19, 69-77, (1995).

M. Raffel, J. Westerweel, C. Willert, M. Gharib and J. Kompenhans: Analytical and experimental investigations of dual-plane PIV. to appear in Optical Engineering, July, (1996).

J. Westerweel: *Digital particle image velocimetry. Theory and application.* Delft University Press, Delft, (1993).

C.E. Willert, M. Gharib: Digital particle image velocimetry. Exp. Fluids 10, 181-193, (1991).

SPATIAL CORRELATION ANALYSIS FOR 3-D SCANNING PIV: SIMULATION AND APPLICATION OF DUAL-COLOR LIGHT-SHEET SCANNING

Ch.Brücker

Aerodynamic Institute, RWTH Aachen, Templergraben 55, 52062 Aachen, Germany

ABSTRACT

To obtain the out-of-plane velocity component in 3-D SPIV, a method on the basis of a color-coded light-sheet and a spatial correlation analysis was developed and applied for the study of vortex breakdown in a rotating tube flow. Therefore two overlapping light sheets of different color were recorded separately with a color CCD camera. A spatial cross-correlation analysis applied to the images in the overlapping planes allowed the determination of the out-of-plane velocity component from a three-point gaussian fit of the correlation maxima in the third dimension. The principal accuracy of the method was tested by a numerical simulation for three-dimensional generic flow fields. Using a scanning version of the color-coded light-sheet, experiments were carried out to obtain the three-dimensional time-dependent velocity field in the rotating tube flow.

1. INTRODUCTION

Today, PIV is a well suited technique for measuring the instantaneous velocity field in unsteady and three-dimensional flows. A large number of successful application of PIV have now been presented in the range of low speed water flows using video-technique up to high-speed supersonic flows in wind-tunnels with high-intensity puls lasers and photographic recording. However, classical PIV provides only the in-plane velocity field in a single slice in the flow. Thus, the feasability of quantitative investigation of highly three-dimensional flows to obtain the volumic distribution of quantities as, e.g., the vorticity is still a major subject of experimental research.

A practicable and now well tested whole-volume extension of PIV is 3-D Scanning-Particle-Image-Velocimetry (SPIV) which uses a scanning light-sheet that samples the flow in depth within a time smaller than the characteristic time scales of the flow (Brücker 1995a). However, 3-D SPIV still needs special techniques or algorithms to resolve not only the 2-D velocity field in the depth-sampled light-sheet planes but also the out-of-plane velocity component. Conventional 3-D PIV methods like stereoscopy or the use of two scanning light-sheets perpendicular to each other are well applicable for 3-D SPIV (Brücker 1995b) but either a second recording camera or even additionally a second scanning device is needed. This is often unpossible because of the high costs in High-Speed SPIV using rotating drum cameras or high-speed video technique. In principle, the concept of continuity allows the calculation of the 3rd component by integration of the continuity equation over the set of 2-D velocity fields in the parallel planes. This method has been tested for synthetic flow fields by Robinson and Rockwell (1992) and was applied by Brücker (1995a) to SPIV measurements of the development of starting flow behind a cylinder. Despite of the reliable results, one limitation is, that this method is only applicable for incompressible flows and since the 3rd component is a-priori known at the starting locations of integration, for example with a given symmetry condition, boundary condition etc. Further, the accuracy depends on the relation of the scanning width to the smallest scales in depth.

Unless using a calculation, just the temporal information of the particle images in two and more parallel light-sheet planes can be used for determination of the out-of-plane displacement. A dual-plane 3-D PIV method was proposed by Kimura and Kohno (1991) and is based on the correlation of particle patterns moving through two parallel light-sheet planes which they called „spatio-temporal correlation". The time-of-flight of certain particle clusters is obtained by finding the highest correlation peak over time in subregions of the simultaneous recordings of two parallel planes. With the known spacing between the light-sheet planes the out-of-plane velocity component is determined in addition to the in-plane components (from the in-plane correlation). Recently Raffel et al. (1995a) presented a similar method based on the normalization of the correlation peak height in a light-sheet which is shifted in a second position with the mean flow. A theoretical derivation of the correlation profile in depth allowed the determination of the out-of-plane velocity from only two correlations in three images.

When a large set of parallel planes is recorded with a high temporal repetition - this is the essential of SPIV - spatial correlation can be applied in each plane using the information of the particle images in the adjacent planes and the time-information in continuous recording. Therefore a certain spacing of the light-sheet planes according the maximum

expected out-of-plane flow is necessary and, on the other hand, the planes should be recorded approximately simultaneous with respect to the time-scales of the flow. However, this is already a basic requirement for application of SPIV and therefore no additional limitation. Figure 1 illustrates possible correlations of particle images in SPIV not only in the same plane as usual in conventional PIV but also in forward and backward direction in adjacent planes of the depth-sampled volume.

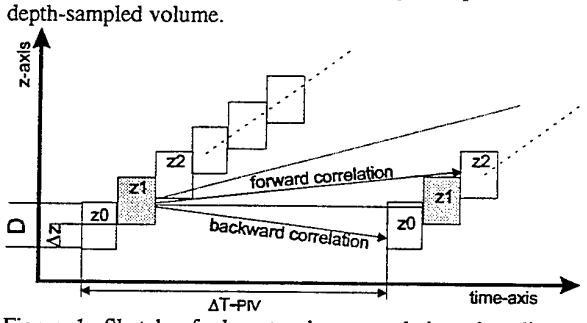

Figure 1. Sketch of plane-to-plane correlations in adjacent planes for spatial correlation in 3-D SPIV (light-sheet width D, light-sheet spacing Δz)

Direct spatial correlation was implemented by Gray and Greated (1994) for the three-dimensional velocity evaluation of holographic PIV recordings. Therefore, they scanned the reconstructed hologram of the flow in successive planes of depth using a camera mounted on a transverse table and applied a 3-D FFT algorithm to the volumic staggered images. From the result they determined the peak position in the correlation volume using curve fits of the correlation values in all three directions. Note, that in principle SPIV is the on-line counterpart of the hologram scanning procedure and thus the same algorithms for 3-D correlation are applicable assuming that the scanning time is much less than the time-scale of the flow and the light-sheet spacing is sufficiently small.

2. SPATIAL CORRELATION METHOD

For determination of the out-of-plane component the information of the local correlation profile in depth is needed. Even the in-plane correlation values contain this information by means of the loss of correlation due to the out-of-plane motion. Correlating particle images with a time-separation in the same plane yields the following relation between the image cross-correlation $R(r,s)$ and the loss-of-correlation due to the out-of-plane motion $F_0(DZ)$

$$R(r,s)=\tilde{R}(r-DX,s-DY)\cdot F_0(DZ) \qquad (1)$$

where $\tilde{R}(r,s)$ is the image self-correlation (for a more detailed discussion see Westerweel (1993) and Raffel et al. (1995b)). The functional relationship of the normalized correlation profile $F_0(DZ)$ in dependence on the out-of-plane motion DZ is determined by the light-sheet intensity profile $I_z(z)$:

$$F_0(DZ)=\frac{\int I_z(z)\cdot I_z(z+DZ)\cdot dz}{\int I_z(z)^2 dz} \qquad (2)$$

For example. in case of a gaussian function $I_z(z)$, which is a good approximation for the intensity profile of continuous wave lasers necessary for SPIV, the correlation profile in depth is a gaussian curve, too. To determine DZ in a single plane, there is the problem of directional ambiguity and the unknown image self correlation $\tilde{R}(r,s)$ from solely the one peak correlation value. Using the information of the particle images in two parallel light-sheet planes, the direction of out-of-plane flow is resolved and the displacement can be determined from two (Raffel et al. 1995) or more correlations (see Kimura and Kohno (1991). In two parallel planes with a spacing of Δz equation (1) becomes

$$R|_{\Delta z}(r,s)=\tilde{R}(r-DX,s-DY)\cdot F_0(DZ-\Delta z) \qquad (3)$$

With the assumption that the image self correlation remains approximately constant during the recording time - this means that there are no remarkable unsteady velocity gradients in that period - Raffel et al. were able to eliminate the unknown image self-correlation by peak normalization using eq. (1) and (3) with two correlations in a light-sheet shifted with the mean flow. In fact, a constant image self correlation yields analogue correlation profiles for spatio-temporal correlation and spatial correlation where the maximum position of correlation is shifted with the out-of-plane displacement which is illustrated in figure 2.

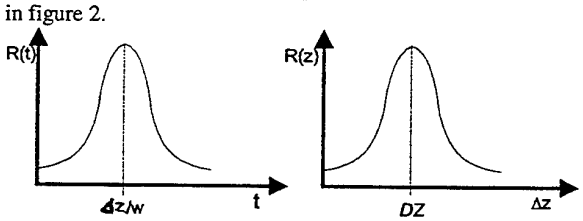

Figure 2: Correlation profile due to out-of-plane flow for gaussian intensity distribution of the light-sheet in depth; left: spatio-temporal correlation between two parallel light-sheets over time; right: spatial correlation in multiple planes by plane-to-plane correlation

To obtain an analytical solution for DZ from only two correlation values Raffel et al. used the approximation of a top-hat intensity profile of the light-sheet in depth. In comparison, SPIV with multiple planar images provides more than two independent correlation values in comparison to dual-plane PIV which enables improved detection of the maximum correlation location in depth. Similary, spatio-temporal correlation with a high temporal sampling rate yields a more detailed resolution of the correlation profile. For a gaussian profile we can use a curve fit of the obtained spatial correlation values to determine the maximum correlation position in depth wherefore we need at least three independent correlation values, see Brücker (1996). This is similar as done by Gray and Greated (1994) in their 3-D FFT results for holographic PIV. They could show, that a three-point curve fit of the local correlation values in depth to determine the maximum position improves the accuracy of the third component essential. These values can be obtained in SPIV

from correlating particle images in adjacent planes, see figure 1. In addition to the in-plane correlations we obtain the spatial correlation in forward and backward direction in depth approximately over the same time-span. To have correlating particle images in both directions the light-sheet planes should have an overlap and the light-sheet thickness should be adjusted so that the maximum out-of-plane displacement *DZ* is less than half of the overlap region. Then, with the spacing Δz of the light-sheet planes one obtains

$$\begin{aligned} R_{12}(r,s) &= \tilde{R}(r-DX, s-DY) \quad F_0(DZ-\Delta z) \\ R_{11}(r,s) &= \tilde{R}(r-DX, s-DY) \quad F_0(DZ) \\ R_{21}(r,s) &= \tilde{R}(r-DX, s-DY) \quad F_0(DZ+\Delta z) \end{aligned} \tag{4}$$

where the R-indexes indicate which of the planes are correlated.

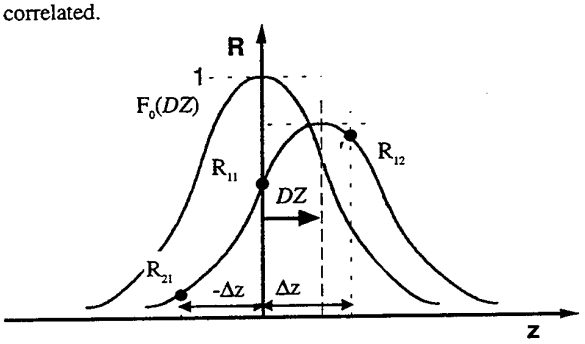

Figure 3: Correlation profile in case of two overlapping light-sheets with forward and backward correlation and an out-of-plane displacement of 60% of the light-sheet spacing

Now, the gaussian profile of the correlation function in depth, shifted to the center about the out-of-plane displacement *DZ*, can be determined from the three correlation values R_{12}, R_{11} and R_{21} with a three-point gaussian fit. Then, the out-of-plane displacement results from the maximum position to*:

$$DZ = \frac{\Delta z}{2} \cdot \frac{\log(R_{12}) - \log(R_{21})}{\log(R_{12}) - 2\cdot\log(R_{11}) + \log(R_{21})} \tag{5}$$

The assumption of a constant self-correlation $\tilde{R}$ in the three correlations obtained for different moments is only valid in first approximation for very short time-intervals which is fulfilled in SPIV with a high scanning frequency in comparison to the characteristic time scale of the flow. In praxis, SPIV has a bottleneck as discussed in Brücker (1995a) which is based on the mutual dependence of the total number of planes and the given temporal sampling frequency condition. Therefore sometimes a compromise has to be chosen unfavourable for the choice of a small scanning width. This may disable the application of the spatial correlation method for determination of the out-of-plane component.

* The maximum of both correlation values R_{11} and R_{22} in eq. (5) gives a higher accuracy in the simulation

A possible solution which makes the application of spatial correlation independent from the scanning width chosen is using a scanning light-sheet system with a color coded light-sheet which consists of two overlapping sheets of discernible colors as shown in figure 4 (Brücker 1996). Simultaneous recording using a color CCD camera and color splitting allowed the application of spatial correlation in each light-sheet plane to obtain the third component.

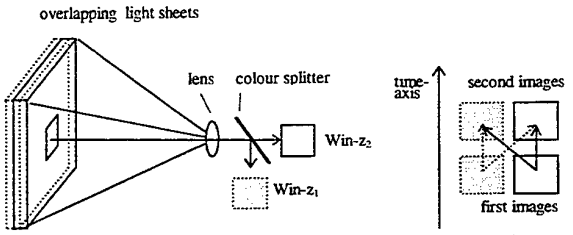

Figure 4. Color coded light-sheet system with two overlapping light-sheets of different color (the gaussian intensity profile of the light-sheets in depth is not indicated in the sketch for reasons of simplicity)

In this case, the possible correlation of *Win-*z_1;t_1 ⊗ *Win-*z_2;t_2 and *Win-*z_2;t_1 ⊗ *Win-*z_1;t_2. yields spatial correlation values in forward and backward direction which allows to use eq. (4) and (5), too. But here, the assumption of constant image self correlation is exactly fulfilled because the images are recorded over the same time-span.

In praxis, the determination of *DZ* in eq. (5) needs the calculation of two additional cross-correlations of the interrogation windows *Win-*z_1;t_1 ⊗ *Win-*z_2;t_2 and *Win-*z_2;t_1 ⊗ *Win-*z_1;t_2. With the assumption that the maximum out-of-plane displacement over the time separation between the recorded images is less than half of the overlap *OV* we can expect that the maximum of the three peak correlation values results from the in-plane cross-correlation, say at the location $(x,y)|_{max}$. The information of the forward and backward correlation result is only necessary at the same in-plane location $(x,y)|_{max}$. This allows to use an efficient algorithm for the forward and backward correlation because only one single correlation value has to be calculated at the previous determined location $(x,y)|_{max}$.

3. SIMULATION OF THE SPATIAL CORRELATION METHOD

The simulations were performed with synthetic generated particle images in overlapping planes with variation of the overlap *OV* and the out-of-plane velocity *DZ* using similar conditions as in the study of Raffel et. al (1995b). Randomly located particles were generated in a 768x768x512 voxel area with a density of 16 particles in subregions of 32x32x32 voxels. The particles were moved in space according to given generic flow fields. Assuming a gaussian intensity distribution of the particle's image with an e^{-2} width of 1.2 pixels and parallel projection on the image plane the pixel values were obtained by integrating the two-dimensional gaussian

intensity distribution over the pixel area. A gaussian light-sheet intensity profile was chosen with an e^{-1} width of 16 pixel units. The images were interrogated in 32x32 subimages with an overlap of 50%. The cross-correlations were normalized by subtraction of the mean values of the interrogation windows and by division by the autocorrelation peaks. As an example, figure 5 shows the particle images in the interrogation windows and the correlation fit of the peak values.

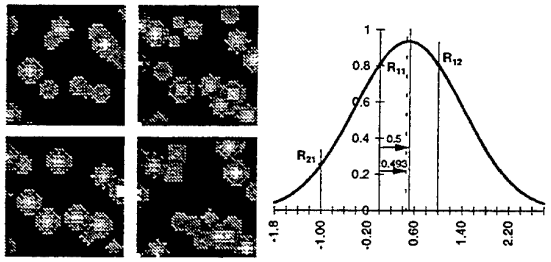

Figure 5. Left: simulated particle images in the window arrangement according to figure 4 when viewing from right (*OV*=50%, *DZ*=+0.5**OV*); right: Three-point gaussian fit in depth using the values of max(R_{11},R_{22}) and R_{12}, R_{21} at the location $(x,y)|_{max}$

First a parameter study similar to that of Raffel et al. was carried out which included variation of the overlap *OV* from 10% to 60% (in steps of 10%) and variation of the relative out-of-plane displacement *DZ/D* from 10% to 50% (in steps of 5%). We found that the most effective overlap value with the optimum combination of minimum error and maximum dynamic range is 50%.

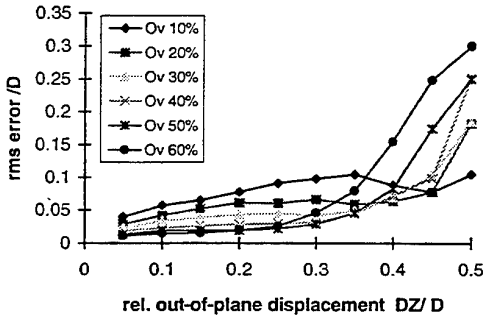

Figure 6: rms-error in simulation for different displacements and different overlaps

For an overlap value greater than 50% the error increases because of the increased assimilation of the correlation values and thus a broadening of the gaussian function. On the other hand, for a small overlap the uncertainty of one of the correlation values is over-influencing the general result. In conclusion the gaussian analysis in the third dimension gives results of less than 0.05 units of the light-sheet thickness for a given overlap of 50% which is shown by the simulation. Note, that the error increases if the out-of-plane displacement exceeds the value of 50% of the overlap region. Then the maximum correlation is not longer R_{11} and, for example in forward flow, there are no longer correlating particles in the backward correlation. This is by definition outside of the valid range for the gaussian curve fit. A comparison of the errors for the gaussian fit in the valid range with calculated values using the equation (20) given in Raffel et. al (1996) with a top-hat approximation is shown in Figure 7.

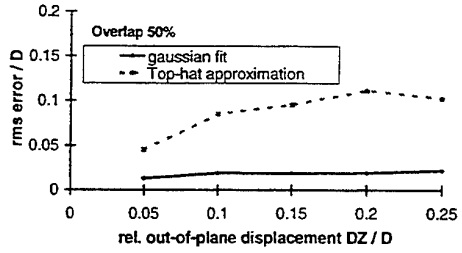

Figure 7: comparison of errors of spatial correlation results for gaussian fit and top-hat approximation for the optimum overlap condition and a maximum displacement of 0.5 OV

One can see, that the gaussian fit according to the correlation profile in depth increases the accuracy significantly in comparison to the top-hat approximation.

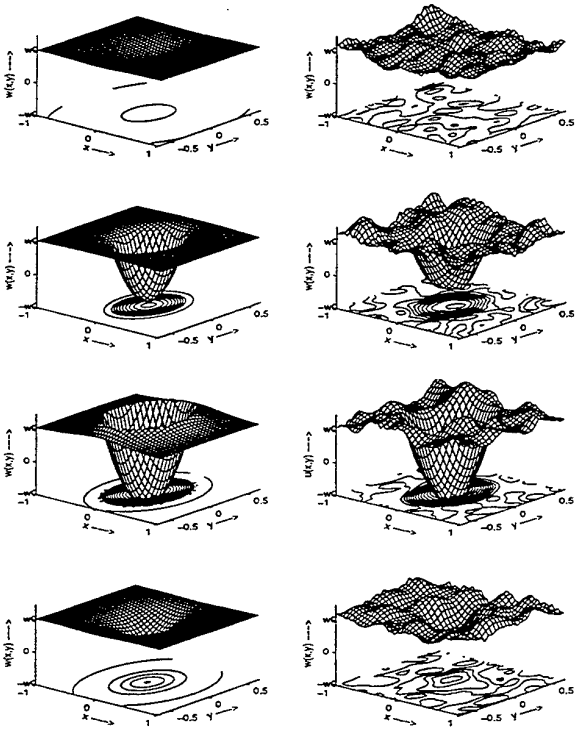

Figure 8: Comparison of surface corresponding to magnitude of out-of-plane component *w* evaluated in 4 planes; left: exact solution of a Hill vortex; right: results of spatial correlation

To simulate the spatial correlation method for application in SPIV, in a second simulation the volumic flow field of a Hill-type vortex (Radius *R*=175 pixel units, w_0=250 pixel

units/s) was generated and the particles (particle number density of 15 in a voxel of 32×32×32 pixel^3) were moved in a previous defined volume of $4R$×$4R$×$2.6R$ according to the analytically given velocity field (compare also the simulation by Robinson and Rockwell 1992). Ten sets of color-coded light-sheets perpendicular to the mean flow (gaussian intensity profile, D=32 pixel units, OV=50%) were placed with an equal spacing of $0.4R$ along the z-axis. Spatial correlation was carried out in subregions of 32×32 pixel^2 with an in-plane overlap of 50% to obtain the three-dimensional velocity field of the Hill-type vortex. Figure 8 shows the out-of-plane velocity field in 4 selected planes and Figure 9 displays on the top the three-dimensional reconstructed streamlines as well as an isosurface of the total amount of vorticity.

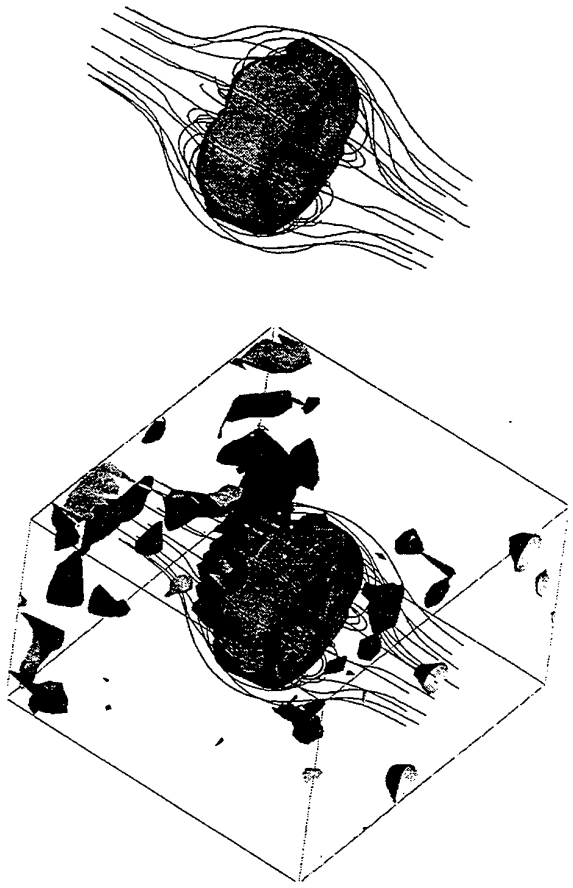

Figure 9: 3-D reconstruction of Hill-type vortex from SPIV simulation with 10 color-coded light-sheets (OV=50%, D=32 pixel units, w_0=250 pixel units/s) Top: reconstructed streamlines and isosurface of vorticity; bottom: regions of discontinuity with values larger than 1/10 of the maximum vorticity

Comparison of the results to the actual velocity values gave a volumic averaged RMS error of 16% of the out-of-plane component (related to the axial velocity w_0). Note, that the in-plane displacement in the radial planes through the Hill vortex is lower than one pixel unit (the in-plane components are determined only from subpixel analysis around zero value) and thus comparable relative errors were found for all three components. Although large individual errors of up to 30% are present in the results, the SPIV simulation provides a good presentation of the flow field. As already noted by Robinson and Rockwell, an average RMS error of 15% is high, but the distribution of these errors within the reconstruction domain can give acceptable overall image of the flow structure. The regions of discontinuity on the bottom in figure 7 give a hint on the distribution of the errors.

4. EXPERIMENTAL APPLICATION

The described color-coded light-sheet method was used for the study of the three-dimensional and unsteady velocity field in the breakdown region of an axially rotating tube flow. The set-up is shown in figure 10.

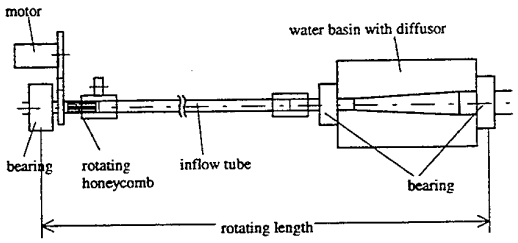

Figure 10: Experimental set-up with a rotating tube for study of vortex breakdown with 3-D SPIV in radial slices

For application of SPIV using a scanning dual-color light-sheet one needs a controllable stepwise parallel shift of the light-sheet system over a certain number of planes with exact repetition from scan to scan. This is obtained with a continuous rotating multifacet drum scanner (Brücker 1995c), see figure 11. The scanning drum consists of twenty 45° mirrors mounted in key-slots at the faces of the polygon (every two adjacent mirrors are arranged at the same position).

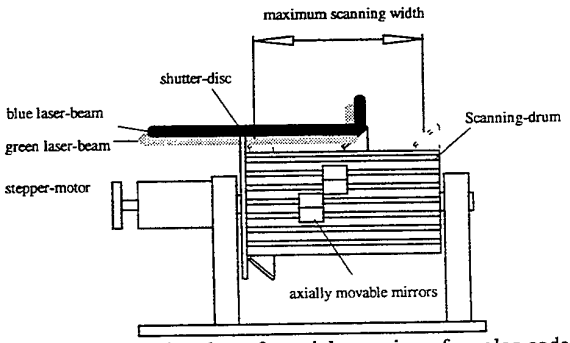

Figure 11: Scanning drum for axial scanning of a color-coded light-sheet

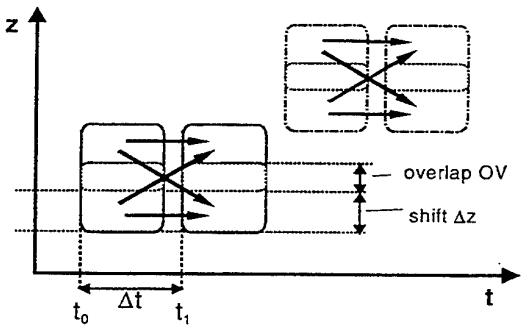

Figure 12: Space-time diagram of the scanning with a color coded light sheet and possible spatial correlations (shown here only for two light-sheet positions)

Figure 12 illustrates the space-time diagram of the scanning with the color-coded light-sheet. The laser beam of a 5 Watt multi-line Argon-Ion laser is splitted in its single wavelengths (512 nm, 488 nm) using dichroic plates to produce overlapping light-sheets (thickness 5mm and 50% overlap) of blue and green color. Using the scanning drum we recorded 10 successive radial planes with a scanning frequency of 2.5Hz along the axis of the tube in the region of the diffusor.

The images were recorded on two separate S-VHS recorder using the RGB output of a three-chip color CCD camera supplied with a color splitter and color filters (JVC KY17). The digitized images of the radial slices (Imaging Technology, 768x512 pixel) were processed by the spatial correlation in 64x64 subimages with a window overlap of 75%. Figure 13 shows the correlation results for evaluation of the out-of-plane displacement at one interrogation location in the images.

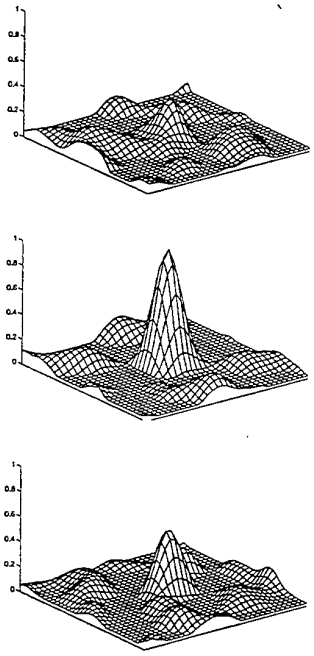

Figure 13. Correlation results for the backward, in-plane and forward correlation at one exemplary interrogation location

Figure 14 displays the reconstructed out-of-plane component in 4 planes which cover the breakdown bubble with an inner backflow region. A three-dimensional reconstruction of the streamlines including the surface of zero axial velocity are shown in Figure 15 which demonstrate a conical bubble-type breakdown form.

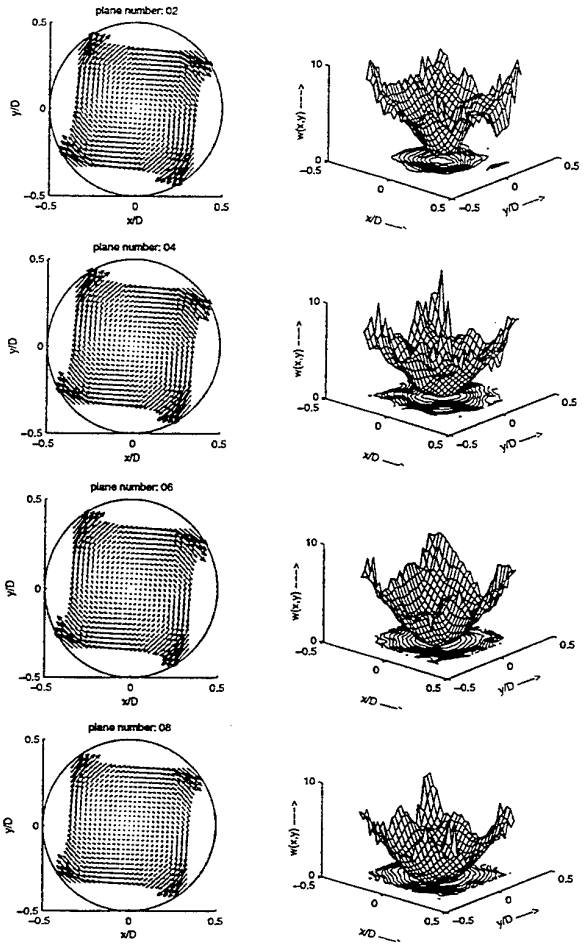

Figure 14: In-plane velocity field and surface presentation of the magnitude of out-of-plane velocity in 4 planes through the breakdown bubble (w_o=50mm/s,Re=4000, Ro=0.5).

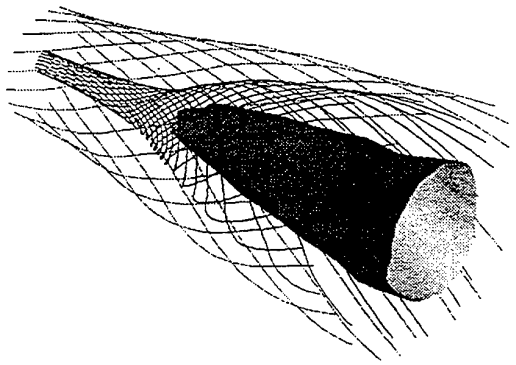

Figure 15: Three-dimensional reconstruction of streamlines and a surface of zero axial velocity for vortex breakdown in a rotating tube flow

5. CONCLUSION

The results show the feasibility of spatial correlation in multi-planar particle images as obtained from Scanning Particle-Image-Velocimetry. Plane-to-plane correlation of particle images in adjacent planes yields in addition to the in-plane correlation forward and backward correlation values in depth. This offers to use a three-point gaussian fit in depth for determination of the out-of-plane motion. The gaussian fit takes into account the general gaussian intensity profile of the light-sheet for continuous wave lasers useful in SPIV and the therefore gaussian profile of the correlation in depth. To be independent from the spacing of the light-sheet planes chosen in SPIV, also a color-coded light-sheet system is feasible for determination of the out-of-plane component in 3-D SPIV. This method using overlapping light-sheets of different color allows simultaneous recording of both planes on separate image planes using standard optical color separation. Hence, it enables to determine four spatial correlation values for the time-span of two successive exposures in each light-sheet plane. In principle, the accuracy can be further increased using a third simultaneous light-sheet with a separable color.

From a simulation, the RMS error was found less than 2% related to the light-sheet thickness in the valid range of out-of-plane displacement of less than 50% of the overlap region. The reason for this limit of the valid range is that we need correlating particle images in forward and backward correlation as well which restricts the out-of-plane displacement which can be obtained in positive and negative direction. The optimum value of overlap with respect to the accuracy and available dynamic range was found to OV=50%.Due to the chosen conditions of overlap and light-sheet thickness with respect to the maximum out-of-plane flow, the absolute maximum correlation value is found in-plane and its location determines the location where the spatial correlation has to be calculated. This allows to use fast correlation algorithms for determination of the spatial correlation values at these single locations.

The easy handling of the color-coded light-sheet method could be seen in the application for 3-D Scanning PIV where the overlapping beams were scanned through the volume. With the described spatial correlation method, reliable results were obtained in the simulation and the experiment of vortex breakdown in a rotating tube as well. In future studies, High-Speed video-technique will be used for recording in SPIV which allows to increase drastically the sampling frequency and the number of planes. This also opens the door for studies at higher Reynolds-numbers which were limited until now at order of Re=1000 due to the conventional video-technique used. To improve the spatial correlation results in 3-D SPIV, we intend to use the continuity equation for post-processing of the data. Because we obtain the complete velocity field in the scanned volume over time, equations can be derived on the basis of continuity to minimize the errors in the obtained velocity components. In conclusion, 3-D SPIV is a technique comparable to tomographic LIF (see Merkel et al. or Su & Dahm in this volume) but on the basis of correlating particle images. Therefore, well known processing algorithms can be used.

6. REFERENCES

Brücker, Ch. 1995a, Digital-Particle-Image-Velocimetry (DPIV) in a scanning light-sheet: 3D starting flow around a short cylinder, Exp. in Fluids 19, pp. 255-263

Brücker, Ch. 1995b, 3-D DPIV using a scanning light-sheet and stereoscopy: Study of the flow development around a spherical cap, FED-Vol 229, Laser Anemometry, pp. 497-503

Brücker, Ch. 1995c, Study of the 3-D flow in a T-Junction using a Dual-Scanning method for 3-D Scanning-Particle-Image-Velocimetry (3-D SPIV), Proc. 10th Symp. Turbulent Shear Flows, Penn State Univ., 14-16th Aug, 7-19 - 7-24

Brücker, Ch. 1996, 3-D PIV via spatial correlation in a color-coded light-sheet. Accepted for publication in Exp. in Fluids, March 1996

Gray, C. & Greated, C. A. 1994, Three-dimensional correlation analysis for particle field hologram velocimetry, IMechE Seminar „Optical methods and data processing", London, Mech. Eng. Publ., C485/008

Kimura, I. & Kohno, Y. 1991, Measurement of three-dimensional velocity vectors in a flow field based on spatio-temporal image correlation, 3rd. Int. Symp. FLUCOME, pp. 609-615

Raffel, M., Gharib, M., Ronneberger, O., Kompenhans, J. 1995a, Feasibility study of three-dimensional PIV by correlating images of particles within parallel light sheet planes, Exp.in Fluids 19(2), pp. 69-77

Raffel, M., Westerweel, J., Willert, C., Gharib, M., Kompenhans, J. 1995b, Analytical and experimental investigation of dual-plane PIV, SPIE Proc. 2546-13

Robinson, O. & Rockwell, D. 1993, Construction of three-dimensional images of flow structure via particle tracking techniques, Exp in Fluids 14, pp. 257-270

Schodl, R. 1986, Laser-Two-Focus-Velocimetry. AGARD CP-399, Philadelphia

Westerweel, J. 1993, Digital Particle Image Velocimetry. Theory and Application. Ph.D. thesis, Delft University Press, Delft

THREE DIMENSIONAL VELOCITY MEASUREMENTS USING HYBRID HPIV

Jingyi Zhang, Bo Tao and Joseph Katz

Mechanical Engineering Department
The Johns Hopkins University
Baltimore, MD 21218, USA

Abstract

A hybrid holographic particle image velocimetry system has been developed and implemented while studying fully developed turbulent flow in a rectangular channel. The system combines the advantages of both in-line and off-axis holography without having their drawbacks. It improves the signal to noise ratio of the reconstructed images, allows use of 3 - 15 μm particles in water at high density, and achieves large dynamic ranges both in velocity and space. An automated image acquisition system and correlation based software are used for analyzing data. In a sample volume of 47 x 47 x 42 mm^3 the data consist of 97 x 97 x 87 vectors. The success rate exceeds 80% of the total sample points. Sample results are provided.

1. INTRODUCTION

Holographic particle image velocimetry (HPIV) is a natural extension of the two dimensional particle image velocimetry (PIV) and it is based on the same principles. When double exposure images of a flow field seeded with small particles are recorded, the local velocities are determined by measuring the displacements of the particles. The advantages of HPIV over PIV is that it records data in a three dimensional (3-D) space and thus renders 3-D velocity distributions. Barnhart & *et al.* (1994), Hussain & *et al.* (1994) and other authors had reported successful 3-D flow measurements using HPIV systems developed in their labs.

The two common optical arrangements in HPIV are in-line and off-axis holography. An in-line scheme uses a single beam for both subject illumination (forward scattering) and a reference, which makes this approach simple to implement. However the reconstructed images are subject to speckle noise, mostly due to the overlap of the reference beam, real and virtual images (Collier & *et al.*,1971). In addition, the particle population in in-line holography is relatively low because the reference beam, which must maintain its coherence, passes through the interrogation volume. With increasing particle density the reference beam quality deteriorates. An off-axis holography system employs a separate reference beam. With proper design it eliminates the overlap of the reference and the two images and hence reduces the speckle noise substantially. The separate reference also allows higher population of seeding particles which yields higher spatial resolution. However, a typical off-axis scheme utilizes side-scattering of light from particles which is 2 to 3 orders of magnitude lower than forward scattering (depending on particle size and

scattering angle). Low scattering efficiency requires use of considerably larger particles, a setback as far as velocity measurements are concerned.

In a previous paper, Zhang & Katz (1994) proposed a hybrid optical system that combined the advantages of both in-line and off-axis holography without having their drawbacks. In this system, Fig.1, the subject beam is arranged for forward scattering. Two relay lenses are inserted in the path between the interrogation volume and the film drive. A spatial high pass filter (a small pin) is installed at the focus of the first relay lens, which blocks the undisturbed portion of the subject beam (DC components in the Fourier space - Goodman, 1968). However, light scattered from particles, AC components, can reach the film with minimum obstruction. A separate off-axis beam serves as the reference. The hybrid system eliminates the speckle noise associated with in-line holography, yet keeps its high efficiency of forward scattering (the zero-degree forward scattering is cut by the high pass filter). It allows an increase in the energy of subject beam without over exposing the film, since most of the beam is cut by the filter. This feature increases the intensity of light scattered from the particles - an advantage while using small particles. As a result, the signal to noise ratio (SNR) of the reconstructed images is greatly improved. Using this approach, images of flows seeded with dense population of particles in the range of 3 - 15 μm can be reconstructed successfully.

In the present study, the hybrid technique is further improved with the implementation of phase conjugate image reconstruction. A phase conjugate wave is used to illuminate the hologram from the opposite direction of the recording reference beam. The reconstructed wave front (real image of particles) propagates back through hologram that are located at the exact same

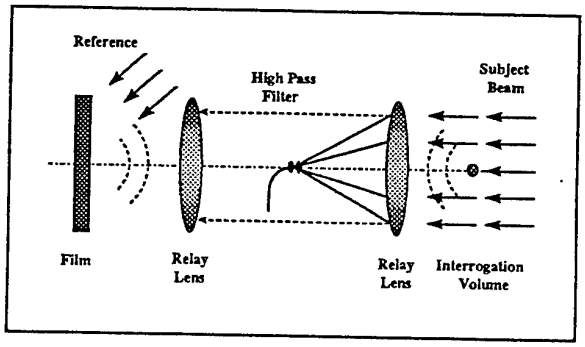

Fig. 1. The principles of the hybrid HPIV system. Solid lines indicate undisturbed subject beam. Dashed lines indicate scattered light from particle.

positions as in the recording setup. This modification eliminates the aberrations introduced by the relay lenses that cause severe distortions or even disappearance of particles located far from the optical axis in the reconstructed images. With conjugate reconstruction the images are aberration free and the sample volume with high image quality extends to the very edge of the subject beam. Thus, a large dynamic range in space is achieved.

Using the approach described above it is possible to determine the two velocity components perpendicular to the optical axis at a high accuracy (1~2%). However an attempt to determine the third, axial, velocity component by means of stereoscopy, i.e. by examining the reconstructed field with two cameras arranged at an angle (Meng and Hussain, 1995), has been unsuccessful. The main causes of the poor results are the relay lenses and the water-glass-air interfaces at the walls of the channel. The relay lenses allow only near forward light to pass and as a result, the cameras of the stereo system can only be arranged at a small angle, which adversely affects the accuracy of the axial velocity. The water-glass-air interfaces cause severe aberration during observations at angles exceeding a few degrees. Although in principle it can be corrected by using prisms, there are still many prohibitive practical

difficulties. Thus, in order to obtain all three velocity components at the same level of accuracy it is necessary to use two hybrid systems that intersect each other at a large angle (90° in the present study). Each system measures two velocity components and 3-D data are obtained by combining them together. As the next section shows, this dual system has been implemented successfully to measure fully developed, turbulent, channel flows.

2. EXPERIMENTAL SETUP

2.1 Test Facility

A schematic description of the test facility is shown in Fig. 2. The measurements are performed in a 57 x 57 mm^2, square vertical channel and the test section is located 2032 mm downstream of the entrance reducer. The wall of the test volume are made of flush mounted glass windows, that create an unobstructed interrogation volume of 57 x 57 x 50 mm^3. The entire loop is kept under low positive pressure to prevent bubbles formation.

The water is filtered and seeded with 15 μm diameter, polystyrene spheres that have a specific gravity of 1.06. Based on the experimental results, the seeding density in the test section varies between 1 - 8 particles/mm^3. The present measurements are performed at a mean velocity of 2.1 m/s. The corresponding Reynolds number is 1.04×10^5.

2.2 Optical Setup

A schematic description of the optical setup for recording the holograms is shown in Fig. 3. The light source is a ruby laser that has a wavelength of 694 nm, coherence length of about 1 m, pulse width of about 20 ns and

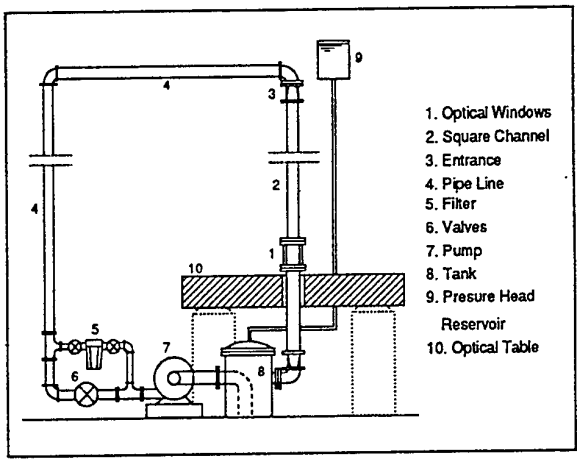

Fig. 2. Schematic description of the test facility.

energy level of 25 mJ per pulse. Only about 10% of this energy is needed for recording a hologram. This laser can generate multiple pulses during a single flash and the interval between pulses can be adjusted from about 20 to 500 μs. The delay between pulses while recording the present data is 40 μs.

The laser beam is pre-expanded by a lens pair and is split to two beams with the same intensity by the beam splitter B1. Each beam is further separated by splitters B2 or B3 that have transmission to reflection ratios of 90% to 10%. The two 90% transmitted subject beams are expanded to 70 mm diameter, collimated and directed to the test section at 90° to each other. The 10% reflected beams are spatially filtered, expanded, collimated and directed to the film drives at an angle of 15°. The holograms are recorded on AGFA, HOLOTEST 10E75, 70 mm film.

In each subject beam path, two identical achromatic doublet lenses, separated by twice their focal lengths, are inserted to form a relay. A 2 mm diameter, L-shaped pin, installed at the focus of the first relay lens, serves as a spatial, high-pass filter. Each set of relay

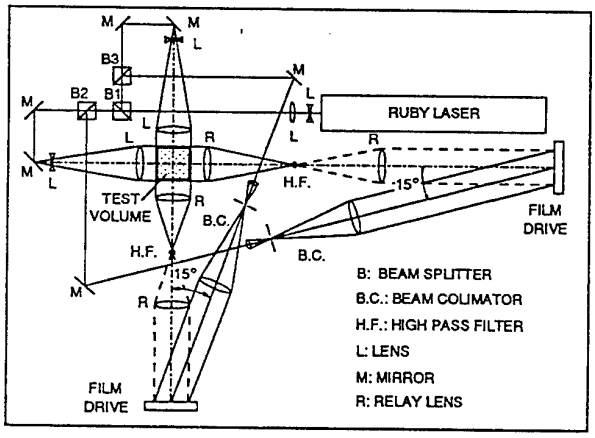

Fig. 3. Optical setup for recording holograms. The neutral density filters used to adjust the beam intensity are not shown.

lenses, high pass filter and film drive are mounted on a single rail. The entire unit is transported to another optical table during reconstruction.

2.3 Image Reconstruction

The image reconstruction system is shown schematically in Fig. 4. The light source is a 633 nm, 5 mW He-Ne laser, whose beam is spatially filtered, expanded and collimated.

To implement the phase conjugate image reconstruction, the relay lenses along with the film drive mounted on the rail are transferred to the reconstruction table. The film drive is removed and replaced by an adapter that ensures that the developed hologram is remounted at its exact location during exposures. The hologram is illuminated from a direction which is opposite to that of the recording reference (conjugate wave). The reconstructed wave-front propagates through the relay lenses and form a 3-D image in front of a video camera (Panasonic WV-BD400), that scans the image. The camera is equipped with an objective zoom lens, and is mounted on X-Y-Z translation stages driven by computer controlled stepping motors. A PC

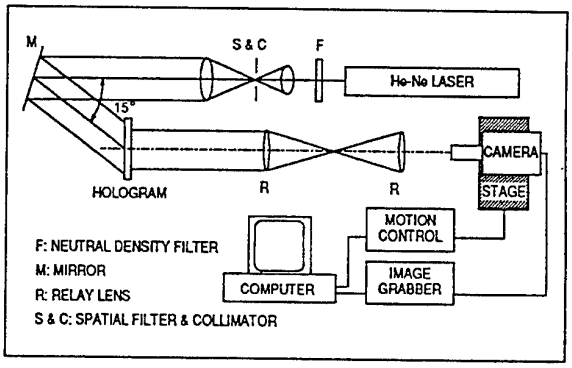

Fig. 4. Image reconstruction and data acquisition system.

based image grabbing system, CORECO OC-F/64 DSP, digitizes the images and saves them on a hard disk. The files are then sent via local network to a SGI Power Challenger for data analysis. The entire process of camera translation and image acquisition is automated.

2.4 Data Acquisition and Processing

In the present paper we present data on the turbulent flow outside of the immediate vicinity (5 mm) of the wall. The sample volume is 46.60 x 46.60 x 42.25 mm^3. Measurements very close to the wall require longer delays between exposures, denser seeding (allowing smaller windows), filtering of noise associated with imperfections or dirt on the glass windows and careful alignment of the beam relatively to the walls (to within 0.2°). These requirements can be satisfied with careful preparations, but they are not within the scope of the present paper that deals with the recording technique.

Each 640 pixel x 480 pixel image frame corresponds to a physical dimension of 3.11 x 2.35 mm^2. The camera scans an entire plane normal to the optical axis (that will be identified as a slice), changes its axial location and acquires the next slice. Each slice consists of 270 image frames, that are patched together. For convenience, the analysis is

performed using files that contain quarter slices. The images are enhanced and the velocity is computed using auto-correlation analysis adopted from two-dimensional PIV (Roth et al., 1995). The window size is 192 pixel x 192 pixel (0.93 x 0.93 mm^2) and the spacing between windows is 96 pixels (0.466 mm), i.e., a 50% overlap between windows. The entire interrogation volume contains 97 x 97 x 87 sample points, providing a total of 818,583 vectors. Using one processor of the SGI Power Challenger, it takes about 80 minutes to complete the processing of a single slice (8439 vectors), including frame patching, enhancement, auto-correlation (using look-up-table method instead of FFT), vector extraction and vector map patching. Each hologram generates 97 such slices. The final 3-D vector field is obtained by combining the two sets of data generated from two holograms. The redundant vectors in the main flow direction are used for precision matching of the two holograms and for evaluating the data quality.

3. RESULTS AND DISCUSSIONS

A sample reconstructed image obtained using the hybrid system is shown in Fig. 5. For comparison, Fig. 6 gives an image of a similar area recorded using in-line holography. It is evident that the background speckle noise that dominates Fig. 6 is essentially non-existent in Fig. 5. As a result, the characteristic SNR of Figure 5 is 12 dB compared to a mere 3 dB in Fig. 6. As noted before, the higher SNR of the hybrid scheme is achieved by eliminating the overlap of the reference, real and virtual images and by the introduction of high pass filter, which allows forward scattering with much higher intensity of the subject beam.

The entire imaging system has a lateral resolution of about 4.9 μm per pixel. The average measured particle diameter is around

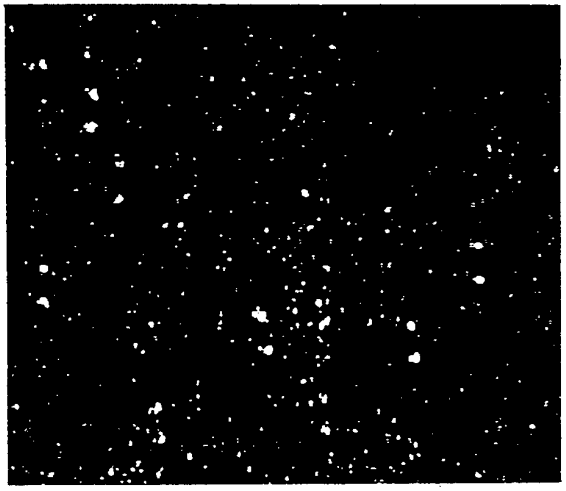

Fig. 5. Reconstructed image of 15 μm particles obtained with the hybrid system. Sharp particle pairs are in focus. The area covered is about 1.2 x 1.0 mm^2.

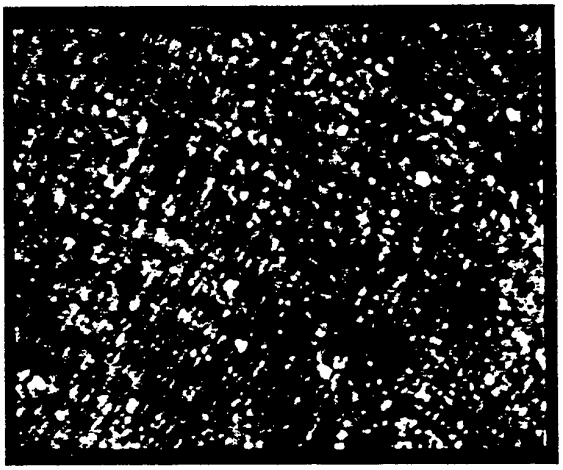

Fig. 6. Reconstructed image of particles obtained using in-line holography. The speckle noise is evident.

3 pixels, which is in good agreement with nominal size of the present particles, 15 μm. When a hologram is reconstructed particles show elongated shapes in the depth direction, a phenomenon known as the "depth of focus" (Barnhart *et al.*, 1994, Hussain *et al.*, 1994). The ratio of the elongated axial extent of particle image to its diameter ranges from

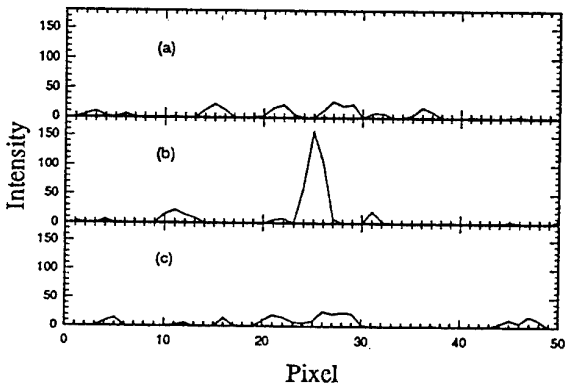

Fig. 7. Sample intensity distributions in adjacent slices separated by 0.93 mm. The plots are along lines with the same coordinates. In slice b the line crosses a particle. This particle does not leave any trace in slice a and c.

several hundreds in off-axis holography to over one thousand for in-line holography (Barnhart, *et al.*, 1994).

In the present setup, observations show that when the window size (0.93 mm) is used as the interval between adjacent slices, the majority of the particles appear only in one slice. This trend is illustrated in Fig. 7. There is only a very small fraction of large particles that appear on two, three or even more adjacent slices. Thus, for most of the data, successive slices contain different particles. This observation suggests that for most of the particles the elongation ratio is less than 62, which is smaller than results reported by Barnhart *et al.* (1994). A plausible (but speculative) explanation for the smaller ratio is the removal of the zero-degree forward scattered light from the particles by the inserted high pass filter. In in-line holography this zero-degree, forward scattered light is dominant, which may account for the associated high elongation ratio. Hussain *et al.* (1994), however, reported an elongation ratio of 15 - 20 using in-line holography. We could not achieve such a ratio using in-line holography in water.

Fig. 8 shows a sample 2-D velocity distribution of a single slice located at the center plane of the channel. The mean velocity in the channel (not in this plane in particular) is subtracted from each vector. As noted before, the data includes only the central 47 x 42 mm^2 of the sample volume (about 5 mm from the walls). Within this volume the characteristic displacement between exposures varies from 13 pixels at the edge to 21 pixels at the center (before subtracting the mean). The vector production rate, namely the fraction of the sampling nodes providing reliable data, exceeds 80%. Most of the windows with bad or no data do not contain any particles. At this stage we make no attempt to interpolate or filter the data. The decision on whether data is acceptable depends on the magnitude of the auto-correlation peak and limitations on the allowed difference in velocity between adjacent windows.

A 3-D vector field of the sample volume is presented in Fig. 9. The data are neither interpolated nor filtered. Clearly, the hybrid HPIV method allows us to map the three dimensional velocity distribution within water at a high Reynolds number. This data will be used mostly for turbulence modeling.

4. CONCLUSIONS

The hybrid HPIV system described in this paper is capable of measuring the three dimensional velocity distribution in liquid at high Reynolds numbers. It is characterized by a fairly simple optical setup. Its features include an off axis reference beam, the use of relay lenses together with high pass filters in the paths of the subject beams. This arrangement still allows forward scattering of light from the particles, more intense illumination of the sample volume (by an order of magnitude higher than in-line holography) and separations of the reference, real and

virtual images, which substantially reduces the speckle noise. Consequently, the SNR of the hybrid system is considerably higher than in-line holography. It allows to clearly resolve in water particles with diameters ranging from 3 to 15 μm. The depth of focus is reduced substantially. Wide dynamic ranges in both space and velocity are achieved. Combined with an automated image acquisition system and an existing correlation based data analysis software, this system has been used for measuring a three dimensional vector array containing almost one million vectors.

5. ACKNOWLEDGMENT

This work was supported in part by the Office of Naval Research under Contract Numbers N-00014-92-J-1109 and N00014-93-1-1359, and in part by National Science Foundation under contract No. OCE-9107564. The authors would also like to thank Professor Charles Meneveau for his close involvement and valuable discussions.

REFERENCES

Barnhart, D.H., Adrian, R.J. & Papen, G.C. 1994, Phase-conjugate holographic system for high-resolution particle-image velocimetry, Appl. Opt. vol. 33, pp. 7159-7170.

Collier, R., Burckhardt, C. and Lin, L. 1971, Optical Holography, pp. 74-78, Academic Press,

Goodman, J. W. 1968, Introduction to Fourier Optics, pp. 83-90, McGraw-Hill, New York.

Hussain, F., Meng, H., Liu, D., Zimin, V., Simmons, S. & Zhou, C. 1994, Recent Innovations in Holographic Particle Velocimetry, Proc. 7th ONR Propulsion Meeting, Eds. G. Roy & P. Givi, pp. 233-249.

Meng, H. and Hussain, F. 1995, Instantaneous flow field in an unstable vortex ring measured by holographic particle velocimetry, Phys. Fluids vol. 7, pp. 9-11.

Roth, G., Hart, D., Katz, J. 1995, Feasibility of Using The L64720 Video Motion Estimation Processor (MEP) To Increase Efficiency of Velocity Map Generation for PIV, Proc. of the ASME/EALA Sixth International Symposium on Laser Anemometry, FED vol. 229, pp. 387-396.

Zhang, J. & Katz, J. 1994, Off-axis HPIV with forward light scattering from particles, Proc. ASME Fluids Engineering Division Summer Meeting, Lake Tahoe, vol. 191 pp. 173-177.

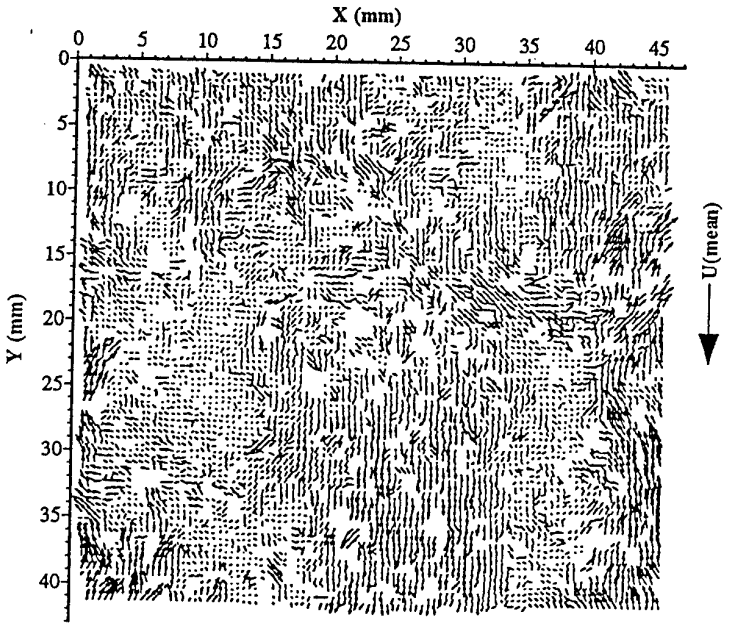

Fig. 8. The 2-D velocity distribution in the center slice after subtracting the mean velocity from each vector. The large arrow on right indicates the direction and magnitude of the mean velocity.

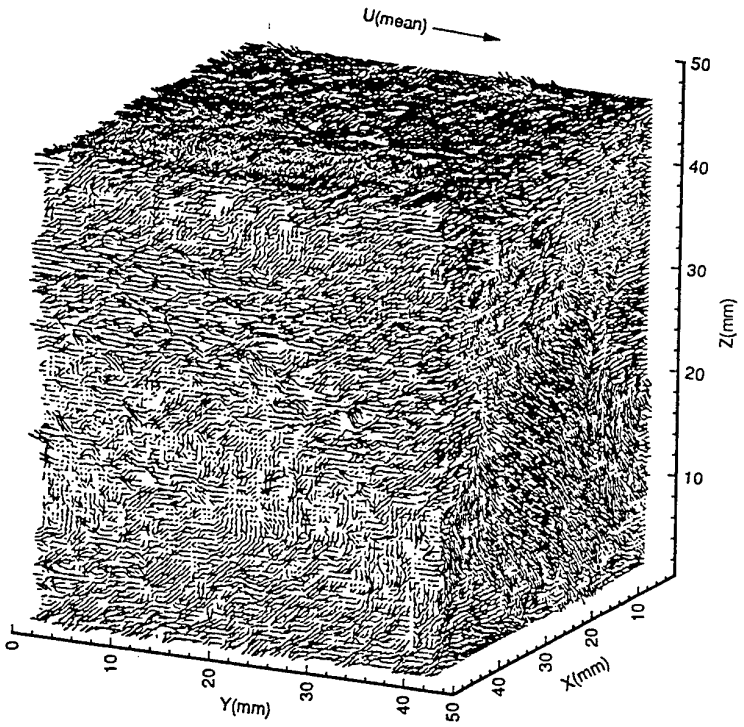

Fig. 9. A 3-D vector map of the velocity distribution within the channel. For clarity, only the data on the three surfaces of the sample volume are shown. The large arrow on top shows the direction and magnitude of the mean velocity which has been subtracted from each vector.

SOME STATISTICAL RESULTS FROM CONCENTRATION AND VELOCITY FIELD MEASUREMENTS USING LASER INDUCED FLUORESCENCE TOMOGRAPHY

G.J. Merkel, T. Dracos[1], F.S. Rys and P. Rys

Department of Industrial Chemistry & Chemical Engineering

[1] Institute of Hydromechanics and Water Resources Management

Swiss Federal Institute of Technology, Zurich, Switzerland

ABSTRACT

The work presented in this paper is a novel technique to measure 3-D velocity fields. It is based on an Adaptive Least Squares Correlation (ALSC) of grey level distributions in patches cut out of observation volumes, generated tomographically by Laser Induced Fluorescence (LIF). The method allows in addition to determine the vorticity vector and the rate of strain tensor without performing any differentiations.

A. INTRODUCTION

When the diffusion coefficient, D, of a solute is much smaller than the diffusion coefficient of momentum, i.e. the kinematic viscosity of the fluid ν and the Schmidt number is

$$Sc = \nu / D >> 10$$

the solute essentially marks the fluid particles and its dissolution is mainly due to turbulent mixing. Disodium Fluorescein is used as a conservative tracer to consecutively construct 3-D tomographic images of an observation volume by Laser Induced Fluorescence (LIF) (Merkel 1995, Merkel et al. 1995, 1996). Adaptive Least Squares Correlation (ALSC) of grey levels of a small cuboid inside a tomographic image at time t and its translated and deformed image at time $t + \Delta t$ are then used for the determination of its translation and deformation. Thereby the assumption is made that the deformation of the cuboid is affine, i.e. that straight lines and planes are conserved. Provided the cuboid is small, these quantities assigned to the centre of the cuboid at time t can be considered as point values.

B. TRACKING OF 3-D LIF TOMOGRAPHY PATTERNS BY ALSC

In the description of the method we follow the papers by Gruen (1985) and Maas et al. (1994). The basic principle of ALSC is: Given two LIF tomographic images of an observation volume at times t and $t + \Delta t$, take a small patch P_1, e.g. a small cube, in the first image and search for a corresponding patch P_2 in the second image so that the sum of the squares of grey level differences between the two patches becomes minimum. In the following we will call such patches conjugate. Let $g_i(x,y,z)$ $i = 1,2$ be discrete functions, e.g. voxel-wise given grey levels, describing the patches P_1 and P_2 and $e(x,y,z)$ as an error vector, the ideal correlation between the two patches is established if

$$g_1(x,y,z) - e(x,y,z) = g_2(x,y,z)$$

To express the geometric relationship between related patches at times t and t + Δt a 3-D affine transformation is used (more details are given in Dracos et al. (1995))

$$x_2 = a_0 + a_1x_1 + a_2y_1 + a_3z_1$$
$$y_2 = b_0 + b_1x_1 + b_2y_1 + b_3z_1$$
$$z_2 = c_0 + c_1x_1 + c_2y_1 + c_3z_1$$

The translation is determined with subpixel accuracy (1/20 to 1/30 of a pixel) and the convergence is usually fast. Less than 10 iterations are needed.

C. DETERMINATION OF THE FLOW PARAMETERS

ALSC gives for each patch selected in the tomographic image at time t the translation and deformation parameters. The vector (a_0,b_0,c_0) gives the translation of the centre of the patch during the time step Δt. The components of the translation velocity are determined by

$$u = \frac{a_0}{\Delta t}, \quad v = \frac{b_0}{\Delta t}, \quad w = \frac{c_0}{\Delta t}$$

Splitting a_i, b_i, c_i i=1,2,3 in a symmetric and an antisymmetric part and dividing by Δt yields the rate of strain tensor

$$\frac{1}{\Delta t}\begin{pmatrix} a_1-1 & \frac{1}{2}(a_2+b_1) & \frac{1}{2}(a_3+c_1) \\ \frac{1}{2}(a_2+b_1) & b_2-1 & \frac{1}{2}(b_3+c_2) \\ \frac{1}{2}(a_3+c_1) & \frac{1}{2}(b_3+c_2) & c_3-1 \end{pmatrix}$$

and the rotation tensor

$$\frac{1}{\Delta t}\begin{pmatrix} 0 & \frac{1}{2}(a_2-b_1) & \frac{1}{2}(a_3-c_1) \\ \frac{1}{2}(b_1-a_2) & 0 & \frac{1}{2}(b_3-c_2) \\ \frac{1}{2}(c_1-a_3) & \frac{1}{2}(c_2-b_3) & 0 \end{pmatrix}$$

Notice that the rate of strain tensor S_{ij} and the vorticity vector ω_i are directly determined without performing any differentiation (Merkel 1995).

D. EXPERIMENTAL CONDITIONS

The Schmidt number of the tracer used for marking the fluid must be large enough so that molecular diffusion can be neglected during the time step Δt. If the linear dimension of a voxel is l_v, the diffusion time t_D must be

$$t_D = \frac{l_v^2}{4D} = \frac{l_v^2}{4\nu}\mathrm{Sc} \quad >> \quad \Delta t$$

Turbulent diffusion has to be small during the time step Δt. This is achieved when

$$l_v < \lambda_\nu$$

with λ_ν as the viscous length. The resolution in z-direction had to be comparable to the resolution in the x,y-plane. The displacements of the x,y-observation planes in steps Δz must be equal to the length in object space imaged on a pixel. At least N = 50 plane cuts are needed for the tomographic generation of a representative volume. The time needed is

$$\Delta t = N\frac{1}{f_c}$$

where f_c is the number of images per second taken by the camera. This time is usually larger than the advection time t_A

$$t_A = \frac{l_p\, M}{\bar{u}_l}$$

with M as the mapping scale, l_p as the linear dimension of the pixel and $\bar{u}_l$ as the mean local advection velocity. To avoid distortion due to advection during the tomographic generation of the volume, the camera must be moved with $\bar{u}_l$. The 3-D grey level patterns in consecutive tomographic observations do not differ considerably. This condition is a consequence of the assumption that the deformation of conjugate patches is small. This implies:

$$\Delta t < \left(\frac{\nu}{\varepsilon}\right)^{1/2} = t_k$$

E. EXPERIMENTAL SET-UP

The observations are made in an axisymmetric nonbuoyant turbulent jet. It discharges through an orifice into a tank filled with water. The water entrained by the jet is supplied along the four edges of the tank and the sum of jet and entrained fluid is extracted at the end of the tank. Although the tank size is limited, this arrangement allows to run the jet under stable conditions for a long time (Merkel 1995).

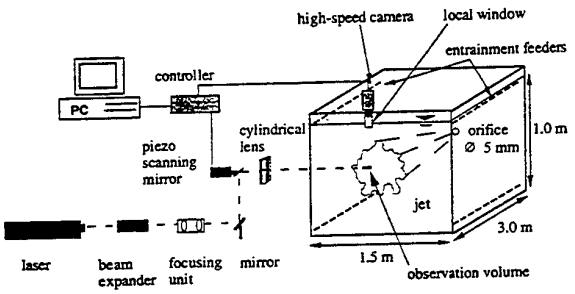

Figure 1 Layout of the optical arrangement

The light sheet was generated by an Argon Ion Laser as a light source and a appropriate optical system which includes a cylindrical lens and a piezo scanner mirror which stepwise moved the sheet parallel to itself in steps of 60 µm with the imaging frequency of the camera. A tomographic volume was generated by 50 individual images. Its thickness was 3 mm and the time needed for its generation was $\Delta t = 0.1$ s. The centre plane of this volume was located on a midplane of the jet and its centre nearly coincided with the inflection point of the mean velocity profile of the jet. At this location the maximum of turbulent production is expected to occur.

The optical arrangement including scanner mirror and camera was moved with the mean local advection velocity $\bar{u}_l = 9.5$ mm/s. The Schmidt number is $Sc = 2075$.

The viscous length at the observation location was $\lambda_\nu = 0.45$ mm and the Kolmogorov length $\lambda_k = 0.99$ mm. All conditions given in the mentioned equation chapter D are fulfilled. The time needed for the generation of a volume is about an order of magnitude smaller than the Kolmogorov time scale.

Table 1 Flow parameters

Orifice diameter	$d_o = 5$ mm
Velocity at orifice	$u_o = 0.85$ m/s
Reynolds number at orifice	$Re_o = 4275$
Reynolds number of the jet	$Re = u_m \delta \nu^{-1} = 6000$
Location of observation	$x/d_o = 280$
Mean center velocity of the jet	$u_m(x/d_o = 280)$ $= 19.4$ mm / s
Mean local advection velocity	$\bar{u}_l \approx 9.5$ mm/s
Kolmogorov length scale	$\lambda_k = 0.99$ mm
Viscous length scale	$\lambda_\nu = 0.45$ mm
Diffusion time	$t_D = 1.7$ s
Advection time	$t_A = 0.0063$ s
Imaging time	$\Delta t = 0.1$ s

F. EXPERIMENTAL RESULTS

Figure 3a shows the tomographically generated volumes, V_1 and V_2, at times t and t + Δt . In Figure 3b a cubic patch of 15 x 15 x 15 voxels, cut out of the volume V_1 at time t and the iterative determination of its conjugate patch at time t + Δt in volume V_2 are depicted. The iterated patches are transformed back to a cubic form for a better optical judgement of the grey level correlation. The translation and deformation of the original cubic patch are shown in Figure 5. The size of the volume in object space is 0.9 x 0.9 x 0.9 mm^3 and is of the order of λ_k^3.

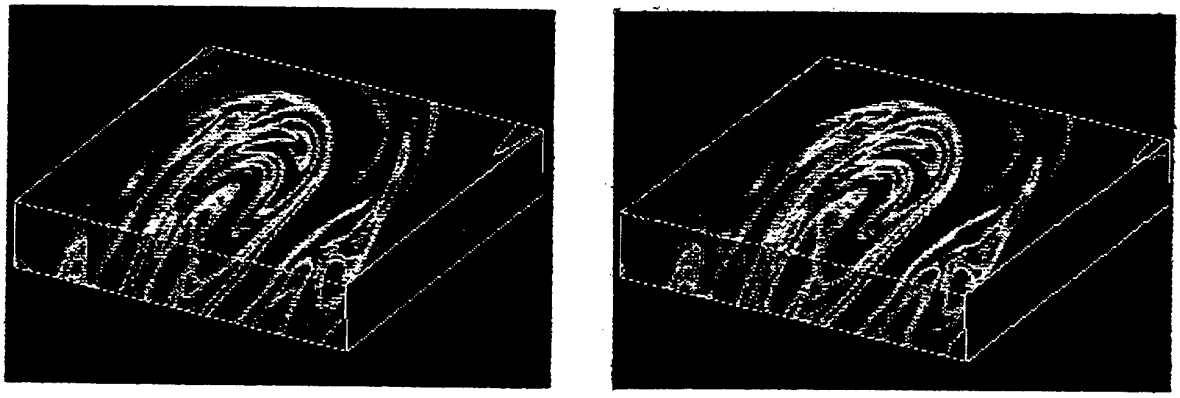

(a) V_1 V_2

(b)

P_1 P_2

Figure 3 (a) Two tomographic volumes V_1 and V_2 at times t and $t + \Delta t$

(b) Patch P_1 in V_1 and iterations of Patch P_2 in V_2

The velocity vectors located on the midplane of the volume V_1 are shown in Figure 4. In this figure one sees that in areas in which the grey level contrast is small the ALSC method fails. These are mainly areas in which engulfed, not yet mixed and not dyed ambient fluid is met. There is a very good correlation of neighbouring velocity vectors observed throughout the whole volume. This makes a postprocessing for screening wrong velocity vectors unnecessary and demonstrates the high degree of reliability of ALSC.

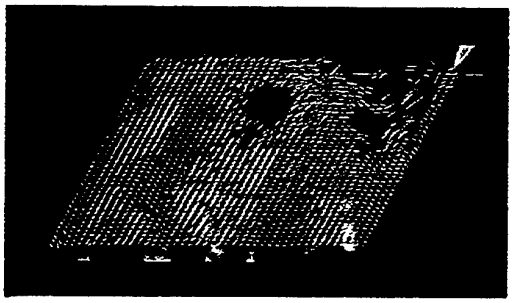

Figure 4 Velocity vectors in the midplane of V_1

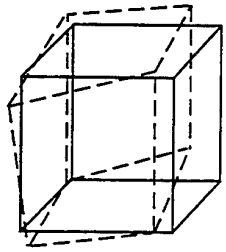

Figure 5 Conjugate patches P_1 (solid line) and P_2 in real coordinates

G. STATISTICAL RESULTS

(a) Incompressibility condition

To check the quality of the quantities depending on velocity derivatives, determined as mentioned in Section C, the mean value, root mean square, the correlation coefficient, flatness and skewness for the incompressibility condition

$$\frac{\frac{\partial u}{\partial x}+\frac{\partial v}{\partial y}}{\frac{\partial w}{\partial z}} = 1$$

were calculated. Table 2 shows these values.

Table 2 Statistical results

	mean	rms	correlation	skewness	flatness
$\left\|\frac{\frac{\partial u}{\partial x}+\frac{\partial v}{\partial y}}{\frac{\partial w}{\partial z}}\right\|$	0.99	0.25	0.97	0.19	5.95

The calculated mean value of the incompressiblity condition in the expermental data set is 0.991 with a correlation coefficient of 0.973. This coefficient is much higher than any found in measurements by multi-hotwire probes, which never exceed 0.7 (Tsinober et al. 1992, Ong 1992, Lemonis 1995). Figure 6 shows the correlation of $\left|\frac{\partial u}{\partial x}+\frac{\partial v}{\partial y}\right|$ with $\left|\frac{\partial w}{\partial z}\right|$.

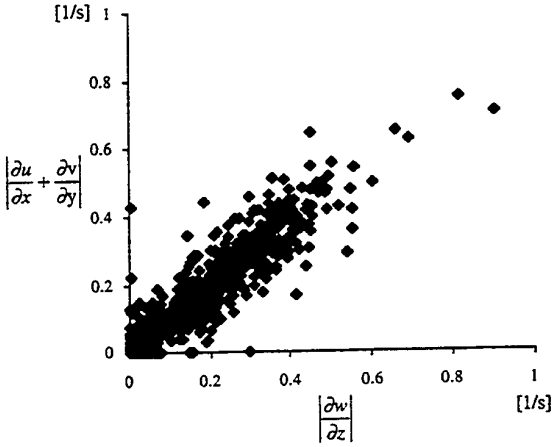

Figure 6 Correlation of $\left|\frac{\partial u}{\partial x}+\frac{\partial v}{\partial y}\right|$ with $\left|\frac{\partial w}{\partial z}\right|$

(b) Alignment properties

With the ALSC method we gain the translation and deformation parameters. These parameters give the rate of strain tensor and rotation tensor as shown in Section C. The vorticity vector can then easily determined. The orientation of the principal directions of compression and elongation and the orientation of the vorticity vector esspecially at high concentration gradient surfaces are of interest.

Figure 7 shows the pdf of the cosine of the angles formed between the vorticity vector $\vec{\omega}$ and the eigenvectors $\vec{e}_1$, $\vec{e}_2$ and $\vec{e}_3$. The preferred orientation for the principal direction of compression, $\vec{e}_1$, and elongation, $\vec{e}_2$, is for an angle of $\sphericalangle(\vec{\omega},\vec{e}_i)\approx 90^o$ or $\cos(\vec{\omega},\vec{e}_i)\approx 0$ (i=1,2). The orientation becomes more pronounced for large $\vec{\omega}$.

A very strong orientation is obtained for the vorticity vector and the intermediate eigenvector $\vec{e}_3$ for $\sphericalangle(\vec{\omega},\vec{e}_3)\approx 0^o$ e.g. 180^o or $\cos(\vec{\omega},\vec{e}_3)\approx 1$ e.g. -1. This alignment is very strong. Over 80% of 3500 considered values of the cosine $\cos(\nabla c,\vec{e}_3)$ are between $0.95<\left|\cos(\vec{\omega},\vec{e}_2)\right|<1$. This corresponds to the angle $\sphericalangle(\vec{\omega},\vec{e}_3)=\pm 18^o$. The alignment becomes more pronounced for large $\vec{\omega}$.

The pdf of the cosine of the angles formed between the concentration gradient ∇c and the eigenvectors $\vec{e}_1$, $\vec{e}_2$ and $\vec{e}_3$. shows a preferred orientation of ∇c and $\vec{e}_1$ for $\cos(\nabla c,\vec{e}_1)\approx 0.65$ e.g. -0.65. The corresponding angle for the cosine is $\sphericalangle(\nabla c,\vec{e}_1)\approx 50^o$.e.g. 130^o. The orientation becomes more pronounced for high concentration gradients.

When the diffusion of the scalar is negligibly small isoconcentration surfaces coincide with material surfaces and the gradient of the concentration is also normal to the latter.

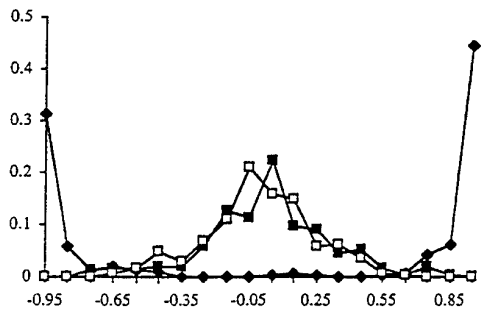

$\cos(\vec{\omega}, \vec{e}_1)$
$\cos(\vec{\omega}, \vec{e}_2)$ $\cos(\vec{\omega}, \vec{e}_3)$

Figure 7 Pdf of the cosine of the angle between vorticity vector $\vec{\omega}$ and eigenvectors $\vec{e}_1$ (elongation), $\vec{e}_2$ (compression) and $\vec{e}_3$ (intermediate).

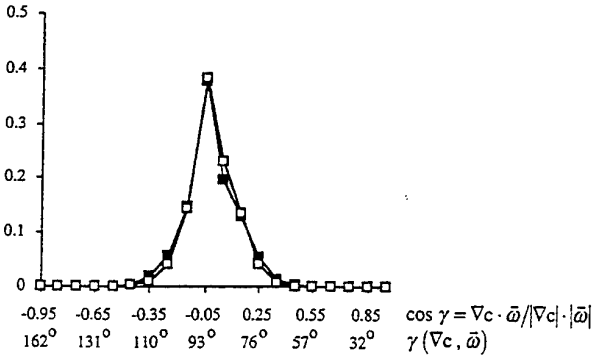

$|\nabla c| + |\omega|$
$|\nabla c| > |\overline{\nabla c}| + \nabla c_{rms} + |\omega| > |\overline{\omega}| + \omega_{rms}$

Figure 8 Pdf of the cosine of the angle between concentration gradient ∇c and vorticity vector ω_i.

Batchelor (1952) theoretically predicts in this case that the vorticity vector is perpendicular to the material surfaces and thus located in a tangential plane of this surfaces. The measurements performed allows to check these theoretical result. Figure 8 shows the pdf of the cosine of the angles formed between the concentration gradient , ∇c, and the vorticity vector $\vec{\omega}$. The corresponding angles are also given. The average is $\overline{\cos}(\nabla c, \vec{\omega}) = -0.001$ or $\sphericalangle(\nabla c, \vec{\omega}) = 90.06^\circ$. The root mean squares values are $\cos_{rms} = 0.125$ or $\sphericalangle(\nabla c, \vec{\omega})_{rms} = \pm 7.2^\circ$. The agreement with the theory is excellent. These values are not depending on the magnitude of the vectors ∇c and $\vec{\omega}$. In accordance with the numerical results of Ashurst et al. (1987) the vorticity vector is preferably aligned with the intermediate principal strain. This alignment becomes more pronounced for large $\vec{\omega}$.

The orientation of the concentration gradient ∇c, vorticity vector $\vec{\omega}$ and the principal directions of the rate of strain tensor (eigenvectors) at a point on a material surface is shown in Figure 9. The elongation of the surface is in direction of $\vec{e}_1$, the compression of the surface in direction of $\vec{e}_2$. The intermediate eigenvector and the vorticity vector are lying in the isoconcentration surface.

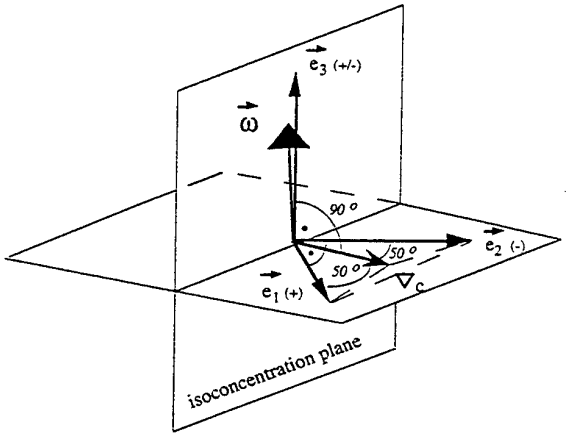

Figure 9 Orientation of concentration gradient ∇c, vorticity vector $\vec{\omega}$ and eigenvectors $\vec{e}_1$ (elongation), $\vec{e}_2$ (compression) and $\vec{e}_3$ (intermediate) at a point on a material surface.

CONCLUSIONS

The use of Laser Induced Fluorescence Tomography (LIFT) combined with Adaptive Least Squares Correlation (ALSC) is a novel and powerful technique for simultaneous determination of the three-dimensional concentration distribution, its gradient and of the three-dimensional velocity, vorticity and rate-of-strain fields. The accuracy of the method is at least as good as the one of well established one point measurement techniques, e.g. by hot-wires or LDA. The spatial resolution is very high with a satisfactory temporal resolution. With the affine transformation parameters gained by the ALSC method the rate of strain tensor and the vorticity vector can be directly determined without performing any differentiations. The compressibility condition is very good fulfilled. Alignment properties between the eigenvectors of the rate of strain tensor, the vorticity vector and the concentration gradient can be shown on a material surface in a fully developed self similar far field of a turbulent jet.

REFERENCES

Ashurst, W. T., Kerstein, A. R., Kerr, R. M. & Gibson, C. H. Alignment of vorticity and scalar gradient with strain rate in simulated Navier-Stokes turbulence. Phys. Fluids **30** (1987) 2343-2353.

Batchelor, G. K., 1952. The effect of homogeneous turbulence on material lines and surfaces, Proc. R. Soc. London, **A 213**, pp. 349 - 366.

Dahm, W. J. A., Southerland, K. & Buch, K. A. 1990: Four dimensional laser induced fluorescence measurements of conserved scalar turbulent flows. Proc. of 5th Int. Symp. on Application of Laser Techniques to Fluid Mechanics, Lisabon, Portugal

Dahm, W. J. A., Southerland, K. & Buch, K. A. 1991: Direct high resolution four dimensional measurements of the fine scale structure of Sc>>1 molecular mixing in turbulent flows. Phys. Fluids **A3,** 1115-1127.

Dracos, T., Merkel, G.J., Rys, F.S., Rys, P., Maas, H.-G., Grün, A. 1995: Velocity field measurements using Laser Induced Fluorescence tomography. Proceedings of Int. Workshop on PIV, Fukui, Japan, 7-15.

Gruen, A. W., 1985, Adaptive Least Squares Correlation: A powerful image matching technique, S. Afr. J. of Photogrammetry, Remote Sensing and Chartography, **14** (3), pp. 175 - 187.

Lemonis, G., 1995, An experimental study of the vector fields of velocity and vorticity in turbulent flows, Ph. D. thesis, Swiss Federal Institute of Technology, Zürich, Switzerland.

Maas, H.G., Stefanidis A., Grün A. 1994: From Pixels to Voxels: Tracking volume elements in sequences of 3-D digital images. Proc. of ISPRS Com. III Intercongress Symposium , Munich, Germany.

Merkel, G. J., 1995, Tomographie in einem turbulenten Freistrahl mit Hilfe von Ph-abhängiger Laser induzierter Fluoreszenz, Ph. D. thesis, Swiss Federal Institute of Technology, Zürich, Switzerland.

Merkel, G.J., Dracos, T., Rys, P. & Rys, F.S. 1995: Concentration and velocity field measurements using Laser Induced Fluorescence tomography. Proceedings of VII Int. Symposium on Flow Visualization, Seattle, USA, S. 504 - 509.

Merkel, G. J., Dracos, T., Rys, P., 1996, Two-dimensional and three-dimensional imaging of passive scalar fields in a turbulent jet, Progress in Visualization, **Vol. 2**, CRC Press (in print).

Ong, L., 1992, Visualization of turbulent flows with simultaneous velocity and vorticity measurements, Ph. D. thesis, Univ. of Maryland, College Park, USA.

Papantoniou, D., Bühler, J., Dracos, T., 1990, On the internal structure of thermals and

momentum puffs, Proceedings Int. Conf. on Physical Modelling of Transport and Dispersion, MIT, Aug. 7 - 10, Boston, USA

Tsinober, A., Kit E., Dracos, T., 1992, Experimental investigation of the field of velocity gradients in turbulent flows, JFM, **242**, pp. 169 - 192.

SESSION 5

Manufacturer's Technical Presentations

SESSION 6

Two-Phase Flows
Instrumentation II

CHARACTERISTICS OF A MINIATURIZED PROBE EMPLOYING THE PULSE DISPLACEMENT TECHNIQUE

Cecil F. Hess

MetroLaser, Inc.
Irvine, California, USA

ABSTRACT

This paper describes a miniaturized particle sizing velocimeter developed and built by MetroLaser to measure the spatial and temporal distributions of particle size and velocity. The instrument is the first of its kind to utilize the pulse displacement technique (PDT) to measure particle size. PDT is based on the detection of scattered refraction and reflection pulses which sweep past a detector at different times as a particle traverses a narrow laser sheet. In conjunction with Mie scattering and a time-of-fight velocity measuring technique, the instrument provides detailed distributions of particle size from 2 μm to 6000 μm in two optical configurations, and particle velocity from 0.5 m/s to 150 m/s. This paper summarizes the theoretical foundation of PDT which allows the calculation of particle diameter from various optical parameters such as refractive index and collection angle. An overview of the instrument is presented, followed by a brief description of the miniaturized optical probe. The processing of data is described and, lastly, the results of experimental studies are presented which verify the accuracy and versatility of the instrument.

1. INTRODUCTION

Commercially available single particle counters typically measure particle size over a limited range (e.g., 40 to 1). They utilize illuminating laser beams with dimensions of the same order of magnitude or larger than the size of the measured particles (see, for example, Bachalo and Houser (1984); Chu and Robinson (1977); Durst and Zaré (1975); Hess, C.F. (1984); and Holve (1980)). These features can present serious limitations in many two-phase flows which are characterized by a large size range and a high particle concentration.

The development and implementation of a new particle sizing technique, called the pulse displacement technique (PDT), addresses many of these limitations. In conjunction with a Mie scattering sizing technique called I_{max}, PDT forms the foundation of an optical probe designed to measure a size range from 2 μm to 6000 μm. In principle, this size range can be measured with a single optical configuration; however, in most applications small particles are present in large numbers while large particles are present in small numbers, creating incompatible probe volume requirements and number density constraints. For this reason, the instrument described here incorporates two optical configurations (referred to as the "small particle configuration" and "large particle configuration") which are easily selected through a combination of simple hardware and software choices.

PDT is implemented in the current instrument using a single off-axis receiver which measures the intensity of scattered light from a particle sequentially traversing two parallel laser sheets with wavelengths of $\lambda_1 = 0.5145$ and $\lambda_2 = 0.4880$ μm. This is shown schematically in Figure 1. The laser sheets have waists of 20 μm, smaller than the diameter of the particles being measured by PDT. As a particle traverses either sheet, a set of double pulses results when scattered laser light is first refracted and then reflected by the particle (or vice versa, depending on which side of the sheets the particle enters relative to the receiver), with one pulse separated in time from the other pulse. A second pair of pulses occurs when the particle traverses the second sheet. This is shown schematically in Figure 2 where the larger, refracted pulse occurs first. These light pulses are conducted to photodetectors by either two optical fibers or a fiber bundle, depending on the size range being measured, and are sorted according to wavelength, with λ_1 going to one detector and λ_2 going to a second detector. The detector outputs are then sent to two time-synchronized digital signal processing boards for digitization and data reduction. The temporal separation of either the two refraction pulses or the two reflection pulses (one of each wavelength) is proportional to the velocity of the scattering particle normal to the two sheets (this is a time-of-flight measurement). The temporal separation of the refraction and reflection pulses (each of the same color) is proportional to the diameter of the particle for a given velocity.

The second of the two techniques, the I_{max} technique, can measure particle diameters smaller than PDT. The I_{max} technique employs a laser beam elongated in one dimension to form a sheet where the intensity along the central portion of the sheet is approximately constant (this is compatible with PDT). Only light scattered from the central portion of the sheet is detected which allows the scattered intensity to be correlated with particle size using Mie scattering theory. For particles with diameters smaller than the laser sheet width, a single pulse of merged refracted and reflected light

is produced during each sheet traverse. As particle diameter increases beyond the laser sheet width, the refracted and reflected components become increasingly resolved. At a particle diameter ~1.5 times the sheet width, the pulses are separated and the I_{max} and PDT techniques overlap. As with the PDT technique, particle velocity is measured from the time-of-flight between the two sheets.

Combining PDT and I_{max} allows particle sizes to be measured which are both smaller and larger than the laser sheet width. In the current instrument, I_{max} is used to measure diameters from 2 μm to 45 μm and PDT is used for diameters greater than 45 μm. Note that particles smaller than 2 μm can be measured using I_{max} if sufficient laser power is available.

2. ANALYTICAL DESCRIPTION

This section presents basic analytical relationships governing PDT. More detailed analytical results are found in Hess and Wood (1993) and Hess and Wood (1994).

Following van de Hulst (1981), a light ray incident on a spherical particle or droplet may be separated into rays which are either refracted or reflected. Figure 3 illustrates this concept. R and L represent the points on the equator of a sphere which refract and reflect, respectively, incident light at an angle θ with respect to forward scatter. (E is the point of emergence of the refracted ray from the sphere). R and L are separated by a distance S(d). For a given refractive index and scattering angle, S(d) is a linear function of particle diameter, as derived below.

A particle traveling toward the left (as shown in Figure 3) will first refract light and then reflect light to a photodetector positioned at collection angle θ. The temporal separation of the two pulses received by the photodetector is S(d)/U, where U is the particle velocity normal to the direction of beam propagation. The determination of S(d) allows the calculation of the particle diameter, d.

As shown in Figure 3, τ_L and τ_R are the input angles of reflection and refraction, respectively, which cause incident light rays to be deflected by an angle θ. Specifically, the angle of reflection, τ_L, is given by:

$$\tau_L = \frac{\theta}{2}, \tag{1}$$

where $0 \le \theta \le \pi$. The angle of refraction, τ_R, is derived by applying Snell's law (i.e., $n_1 \sin\theta_1 = n_2 \sin\theta_2$) to a spherical particle or droplet with index of refraction n_2 scattering into a medium with index of refraction n_1. The resulting equation must be solved iteratively:

$$\tau_R = \cos^{-1}\left[\frac{n_1 \cos\tau_R}{n_2}\right] - \frac{\theta}{2}, \tag{2}$$

where $0 \le \theta \le \pi$. Equations 1 and 2 are valid when the distance between the spherical particle and the collecting lens is large compared to the spherical particle diameter (i.e., f >> d, where f is the distance from the particle to the collecting lens), which is usually the case in practical systems.

Referring again to Figure 3, the lateral displacements of points R and L from the vertical bisector of the spherical particle (line X-X) are designated as r_{ent} and ℓ, respectively. Analytical expressions for these displacements are derived from Figure 3:

$$r_{ent} = \frac{d}{2}\cos\tau_R, \tag{3}$$

$$\ell = \frac{d}{2}\cos\tau_L. \tag{4}$$

The spatial separation S(d) is then equal to:

$$S(d) = r_{ent} + \ell = \frac{d}{2}(\cos\tau_L + \cos\tau_R). \tag{5}$$

Rearranging the preceding equation gives the particle diameter, d, as a function of S(d):

$$d = \frac{2\,S(d)}{(\cos\tau_R + \cos\tau_L)}. \tag{6}$$

For example, for water (n_2 = 1.33) in air (n_1 = 1) scattering light at θ = 30°; τ_L = 15°, τ_R = 39.59°, and S(d)/d = 0.8683.

3. MINIATURIZED OPTICAL PROBE

This section presents a brief overview of the instrument and the miniaturized optical probe. A detailed description of each is presented in Wood and Hess (1994).

Figure 4 presents a schematic drawing of the miniaturized particle sizing velocimeter. The instrument consists of:

1. A miniaturized optical probe with integrated transmitter and receiver;
2. An argon ion laser with a laser-mounted fiber coupler;
3. Twenty-five meters of flexible, water-proof conduit containing optical fibers and a fiber bundle;
4. A rack-mounted electronic interface box (EIB) containing the photodetector assembly and probe heater controller;
5. An IBM-compatible personal computer containing two digital signal processing boards, monitor, and keyboard.

The instrument measures particle sizes in two ranges without the need for realignment. The first range, from 2 μm to 100 μm, utilizes PDT and I_{max} together. The second range, from 250 μm to 6000 μm, utilizes PDT only. (In principle, the instrument is capable of measuring particles from 100 μm to 250 μm; however, the current instrument was developed for an application devoid of particles in this size range.) When changing size ranges, the operator makes only simple changes at the optical probe (i.e., the insertion or removal of a diffusing screen and the installation of the appropriate aperture plates) and at the front panel of the EIB. The instrument will measure particle velocities from less than 0.5 m/s to more than 150 m/s.

The instrument employs a Lexel two-watt argon ion laser (model 95-2) operating in the multiline mode between 0.4579 μm and 0.5145 μm. 700 milliwatts of laser light is

launched into 25 meters of Fujikura single-mode optical fiber (type SM 48-P) using an OZ Optics laser-to-fiber coupler (model HPUC-23-500-P-1) mounted on the laser head. Approximately 300 milliwatts of laser power is delivered to the probe volume for an overall efficiency of ~ 40%.

The optical probe consists of an integrated transmitter and receiver. It is small enough to operate with negligible flow disturbance and is rugged enough to withstand harsh environments characterized by high ambient moisture levels, high noise and vibration levels, and wide swings in ambient temperature. The inner structure of the optical probe, containing all optics and mounting hardware, is constructed of Invar, an iron/nickel alloy with a low coefficient of expansion. The dimensional stability of Invar, along with thermocouple-controlled flexible heaters attached to the inside of the optical probe, ensures that the probe will operate from below 0°C to well above room temperature without realignment.

The transmitter optics produce two parallel laser sheets separated by 103 μm with wavelengths of λ_1 = 0.5145 μm and λ_2 = 0.4880 μm (see Wood and Hess (1994) for a detailed description). The sheets have waists of 20 μm located midway between the transmitter and receiver.

Light scattered by particles traversing the probe volume is collected by the receiver and focused onto a fiber bundle or individual multimode optical fibers (depending on the size range chosen) for transmission to a photodetector assembly located in the EIB. The design and use of the fiber bundle greatly simplifies the optical design of the receiver and allows the measurement of particle sizes from 2 to 6000 μm without significantly altering the optical configuration of the probe. The fiber bundle, composed of several thousand 50 μm glass multimode fibers together with a single 100 μm fused silica multimode fiber, provides a large field of view not achievable with a single glass fiber. At the termination within the probe, the 50 μm glass fibers are bundled into a 2 x 8 mm rectangular aperture with the 100 μm fused silica fiber positioned at the geometrical center of the rectangular aperture. At the end which feeds light to the photodetector assembly in the EIB, the 50 μm fibers and the 100 μm fiber are bifurcated from each other, allowing the fiber bundle and the 100 μm fiber to be mounted on separate photomultiplier tubes (PMTs) within the EIB.

The photodetector assembly consists of three Hamamatsu PMTs (model R-1784), each mounted on a custom preamp card. Two of the PMTs are fitted with 0.4880 μm interference filters and the third is fitted with an 0.5145 μm interference filter.

The output from the preamps is sent to a pair of Signatec digital signal processors (model DASP100A), housed within the system computer, for digitization and data reduction. The function of the digital signal processors is described in the following section.

The instrument is controlled by proprietary computer software which allows the operator to set important experimental and data acquisition parameters (sheet separation, size and velocity ranges, memory size, signal digitization rate, PMT high voltage levels, electronic threshold levels, etc.), and perform a wide range of data processing functions (calculate size/velocity/time correlations, liquid water content, etc.).

4. SOFTWARE ALGORITHMS

Critical to the success of the instrument was the development of robust and accurate algorithms to sort and identify all reflection and refraction pulses to minimize potential errors and data loss. This section describes the flow of data received in a typical Imax/PDT experiment and discusses how the instrument processes these data to arrive at accurate results.

Data collected with the miniaturized particle sizing velocimeter consists of two channels of digitized light pulses (one channel each for the 0.4880 μm and 0.5145 μm wavelengths) containing size, velocity, and arrival time information for each particle traversing the probe volume. The pulses vary in number, intensity, and temporal spacing depending upon the size and velocity of the particle. In addition, pulse intensity is a function of particle trajectory through the probe volume in the large particle configuration where PDT is used exclusively. As a result, each sheet traverse may generate one or two pulses to be analyzed by an Imax algorithm only or two pulses to be analyzed by a PDT algorithm only, depending upon the amplitude of the pulses. Because each particle must traverse two sheets to calculate velocity, one or two pulses are generated at each of two wavelengths for a total of two or four pulses per valid traverse. Furthermore, the reflection pulse generated by a particle larger than the sheet width is usually much less intense than the corresponding refraction pulse and must not be mistaken for the merged reflection and refraction pulse of a particle smaller than the sheet width. Lastly, trajectory effects may eliminate one or both pulses from one or both sheet traverses.

The particle sizing velocimeter uses two identical digital signal processors, designated DSP_1 and DSP_2, in a master/slave configuration. Depending upon the size range being measured, these processors are used with two of three PMTs to collect and process the pulses described above. The specific algorithms employed depend upon the size range being measured.

4.1 The Small Particle Configuration

In the small particle configuration (2 μm ≤ d ≤ 100 μm), scattered light is collected concurrently by a 300 μm signal fiber and a 100 μm validation fiber. The light from the 300 μm signal fiber is filtered at the photodetector assembly within the EIB to isolate λ_1 = 0.5145 μm and the corresponding PMT/preamp output is digitized by the master board, DSP_1 (channel 1). The light from the 100 μm validation fiber is filtered to isolate λ_2 = 0.4880 μm and the corresponding PMT/preamp output is digitized by the slave board, DSP_2 (channel 2).

The 100 μm and 300 μm fibers are focused concentrically at the probe volume (i.e., the field of view of the 100 μm fiber is fully contained within that of the 300 μm fiber). Although a detailed discussion is beyond the scope of this

paper, this concentric arrangement ensures that the 300 μm fiber will collect the full scattered light intensity without attenuation if scattered light is also received by the 100 μm fiber. Therefore, the scattered intensity from the 300 μm signal fiber at λ_1 = 0.5145 μm is used to calculate size in the I_{max} regime from d = 2 to 45 μm *if* it has been validated by the receipt of scattered light at λ_2 = 0.4880 μm from the 100 μm validation fiber.

The clocking circuitry on DSP_1 controls signal digitization on both boards. Using an "OR gate" on DSP_1, both digitizers are turned on or off simultaneously when the input to either board crosses a preset threshold voltage. Digitization ends after a preset time interval, called a time-out, following the return of the signal intensity below the threshold voltage. The contiguous sequence of digital intensity values, bounded in time by the initial upward threshold crossing and the end of the time-out, is called a record and is stored in on-board memory along with its respective start time. Both processors are quiet (i.e., no signal digitization occurs) between the end of a time-out and the next threshold crossing.

The digitizing clock frequency is set by the system software and is based on the maximum velocity, U_{max}, chosen by the instrument operator. Available clock frequencies are 100, 50, 25, 12.5, 6.25, 3.125, and 1.56 MHz.

When the allocated memory onboard either processor is full, data collection stops and the memory contents of DSP_1 and DSP_2 are analyzed. During analysis, each record is scanned from beginning to end to identify all intensity maxima and their corresponding time of occurrence. A record may contain one pulse if the particle was sufficiently small (i.e., the refraction and reflection pulses are merged) and was not followed by a second particle within the time-out period, or it may contain many pulses depending upon the size and number density of the particles in the flow. The following data is entered into a software table for each pulse: a) the maximum intensity, b) the start time of the record, and c) the offset time of the pulse centroid (i.e., the time at which half of the integrated pulse intensity has occurred relative to the start time of the record). A separate software table is created for each channel.

The next step is to correctly group the pulses from both channels. First, data is retrieved for the first pulse in the channel 1 software table. Then data is retrieved for the first pulse in the channel 2 software table with an arrival time greater than the channel 1 pulse. Depending on the peak intensity of the channel 1 pulse, the two pulses are either analyzed by I_{max} (where size is calculated from the channel 1 pulse intensity and the velocity is calculated from the temporal spacing between the channel 1 and 2 pulses) or data for additional pulses is retrieved for analysis by PDT. Although the exact PDT procedure employed for data analysis depends on the optical configuration used to collect data, the procedure used in the small particle configuration is fundamentally the same as described next for the large particle configuration.

4.2 The Large Particle Configuration

In the large particle configuration (250 μm ≤ d ≤ 6000 μm), scattered light of all wavelengths is collected by a 2 mm x 8 mm fiber bundle and transmitted to the photodetector assembly within the EIB. The individual 100 and 300 μm fibers are not used. The probe volume in the large particle configuration is defined by the 2 x 8 mm fiber bundle described above. The 30° collection angle, combined with the f/3 collection optics of the receiver, allow the measurement of particle trajectories from the surface of the transmitter aperture plate to ~5 mm in front of the receiver aperture plate. This is a total probe volume length along the laser sheets of ~15 mm. (The total gap between the transmitter and receiver is 20 mm.) The height of the probe volume is 2 mm as defined by the fiber bundle.

Within the EIB, a 50:50 beamsplitter directs half of the transmitted light to one PMT fitted with a λ_1 = 0.5145 μm interference filter and half to a second PMT fitted with a λ_2 = 0.4880 μm interference filter. Signal output from the first PMT (detecting light of λ_1 = 0.5145 μm) is digitized by the master board, DSP_1 (channel 1). Signal output from the second PMT (detecting light of λ_2 = 0.4880 μm) is digitized by the slave board, DSP_2 (channel 2). The functioning of DSP_1 and DSP_2 is the same as described for the small particle configuration, above.

PDT is used exclusively with the large droplet configuration because the refraction and reflection pulses are fully resolved in this size range and the large field of view relative to the dimensions of the laser sheets results in pulse intensities which are trajectory dependent, precluding the use of I_{max}.

In particular, the following steps are taken during data processing. Data for the first two pulses in channel 1 are retrieved from the channel 1 software table. Then data for the first pulse in channel 2 with an arrival time greater than the first channel 1 pulse is retrieved from the channel 2 software table along with data for the second pulse in channel 2. Data for these four pulses (two from each channel) are considered to represent a valid particle traverse if the following criteria are met:

a) The velocity calculated from the temporal spacing between the first pulses in each channel is equal to the velocity calculated from the temporal spacing between the second pulses in each channel to within a sufficiently small interval, ε_v, chosen by the instrument operator.

b) The diameter calculated from the temporal spacing between the two pulses in channel 1 is equal to the diameter calculated from the temporal spacing between the two pulses in channel 2 to within a sufficiently small interval, ε_d, chosen by the instrument operator.

c) The average velocity and diameter calculated in steps a and b, respectively, must fall between the minimum and maximum velocity and diameter selected by the operator (i.e., $U_{min} \le U \le U_{max}$ and $d_{min} \le d \le d_{max}$).

Note that if either criteria a or b are *not* met (i.e., if the temporal separation between the appropriate pulses is not equal), then the four pulses cannot belong to a single particle traverse. If all three criteria *are* met, the scattering

event is valid and the average velocity and diameter are stored.

5. EXPERIMENTAL RESULTS

This section describes the results of experimental studies performed with the instrument operating in both the small and large particle configurations. The results of measurements taken with a) a monodisperse droplet generator operating in both a continuous-stream mode and an induced spray mode, b) a humidifier, and c) glass spheres are presented and discussed.

All experimental results presented here were made at a laser power (all lines) of 280 mW at the point of measurement. In all cases, the laser sheets of $\lambda_1 = 0.5145$ μm and $\lambda_2 = 0.4880$ μm were separated by 103 μm; the sheet waists were 20 μm; the collection angle, θ, was 30°; and the collection f-number was 3.

6. SMALL PARTICLE RESULTS

The experimental results discussed in this section were obtained with the instrument in the small particle configuration using an electronic threshold of 5 mV.

Monodisperse results. Measurements were made on water droplets ($n_2 = 1.33$) generated with an Aerometrics monodisperse droplet generator (model MDG-100). The MDG-100 was operated with a 20 μm orifice, a water flow rate of 0.2 ml/minute, and was driven with a 20 volt peak-to-peak square wave at various excitation frequencies (depending on the desired droplet size). The MDG-100 head was mounted on a three-axis traverse to allow precise placement of the droplet stream during measurements. Actual droplet diameter, d_a, to which the measured droplet diameter was compared in each case, was calculated from the following relationship:

$$d_a = [6Q/\pi\nu]^{1/3}, \qquad (7)$$

where Q is the volume flow rate and ν is the excitation frequency applied to the 20 μm orifice.

Beginning with measurements made with PDT in the size range from 45 to 100 μm, Figure 5 shows the velocity and size histograms for a continuous droplet stream with d_a = 65.7 μm at ν = 22.5 kHz (n = 1000). The droplet stream was directed through the center of the probe volume for the entire test. Although the nearly exact match between the measured diameter (65.8 μm) and the actual diameter (65.7 μm) is fortuitous in this case, it is clear that the instrument is measuring nearly single bin velocities and diameters with excellent precision.

Measurements made with the I_{max} technique in the size range from 2 to 45 μm required a different approach. Although the MDG-100 can produce 40 μm droplets, well within the I_{max} size range, the spacing between adjacent droplets is too small, placing more than one droplet in the probe volume at all times. Therefore, the MDG-100 was operated under conditions identical to those used to produce Figure 5 (d_a = 65.7 μm at ν = 22.5 kHz) but the PMTs were operated at a lower gain. This resulted in channel 1 and 2 refraction pulse amplitudes of 2.8 ± 0.2 volts, equivalent to the amplitude of a droplet with d = 33.5 ± 1.2 μm. Thus, the reduction in PMT gains made the 65.7 μm droplet stream look artificially like a stream of 33.5 μm droplets, invoking the I_{max} algorithm during data analysis.

Figure 6 shows the velocity and size histograms taken with reduced PMT gains. Sample size was n = 34,464. The measured mean diameter of 32.70 μm is within the uncertainty for the measured amplitude of the refraction pulse.

Figure 7 shows the velocity and size histograms for a run taken under the same conditions used to obtain Figure 6 except that the droplet stream was traversed throughout the probe volume as the run progressed. Note that the mean velocity (9.74 m/s) is identical and the mean diameter (31.96 μm) is within 2% of the results shown in Figure 6.

To produce a spray of monodisperse droplets of known size, the droplet stream from the MDG-100 was diverted into the probe volume using a jet of canned tetrafluoroethane, resulting in random droplet trajectories. The MDG-100 was operated at ν = 33 kHz to produce droplets of d_a = 57.8 μm. This induced-spray method produced the results shown in Figure 8. The intermittent nature of the gas jet used to divert the droplets into the probe volume produced a broadened velocity distribution about a mean of 6.42 m/s (n = 200). The diameter distribution was also broadened (d_{rms} = 6.57 μm) due to possible droplet fragmentation and coalescence from the disruptive gas jet. However, 85% of the droplets sampled had measured diameters within 5% of the mean, and the mean diameter of d = 56.36 μm is only 2.5% less than the actual diameter of d_a = 57.8 μm.

Humidifier results. A spray of polydisperse droplets was produced using a commercial humidifier (Sunbeam Cool Spray Style 47) designed for use in the home. The effluent from the humidifier was directed into the probe volume using 1/4 inch diameter flexible tubing to create a higher velocity stream than is produced by the humidifier during normal use.

Figure 9 shows the results of the spray measurements. Although no independent data were obtained regarding the size distribution of droplets produced by the humidifier, such devices typically produce droplets with a mean diameter between 3 and 5 μm. The measured mean of d = 5.45 μm is just beyond this range possibly because measurements were truncated at 2 μm, the small diameter limit of the current configuration. Had the instrument been configured to measure sizes below 2 μm, Figure 9 indicates the measured mean may have been smaller.

Large particle results. The experimental results discussed in this section were obtained with the instrument in the large particle configuration using an electronic threshold of 100 mV.

Measurements were made using glass spheres ($n_2 = 1.51$) purchased from Duke Scientific Corp. Two diameters were used in the work reported here: 1016 ± 60.4 μm (catalog #438) and 2022 ± 127 μm (catalog #439). (The quoted size tolerances are ± 2 standard deviations from the mean as certified by Duke Scientific Corp.) The glass spheres were

attached to the perimeter of a 101.4 mm diameter disk with a minimum amount of liquid adhesive. The disk was spun at 29 ± 1 Hz to create particle velocities of 9.2 ± 0.3 m/s. The disk and motor were mounted on a three-axis traverse to allow the precise placement and movement of the particle trajectory throughout the probe volume during measurements. Note that the individual 1016 ± 60.4 μm and 2022 ± 127 μm glass spheres measured by PDT are referred to as 1000 μm and 2000 μm glass spheres, respectively, in the discussion to follow.

Figure 10 shows velocity and size histograms for a 2000 μm glass sphere traversing the probe volume midway between the transmitter and receiver (i.e., 10 mm from either) and centered on the 1.2 mm height of the laser sheets. Size (2118.4 μm), velocity (9.1 m/s), and data rate (30 Hz) fall within the uncertainties defined above for each parameter. The rms velocity and size are both 0.4% of their respective means.

Figure 11 shows the result of varying the rotational velocity of the spinning disk. Except for the variable velocity, the data shown in Figure 11 was collected under the same experimental conditions used to obtain Figure 10 (the same 2000 μm glass sphere was used in both cases). The velocity histogram shows a range of velocities from ~6 to 14 m/s with an rms velocity (2.18 m/s) equal to 21% of the mean velocity (10.32 m/s). In contrast, the size histogram depicts a much narrower size distribution with an rms diameter (22.8 μm) equal to only 1.1% of the mean diameter (2091.6 μm). In turn, this mean diameter is within 1.3% of the mean diameter measured at constant velocity (2118.4 μm, Figure 10).

Figure 12 shows the result of varying the trajectory of the 2000 μm glass sphere along the 2 mm height of the probe volume at a constant distance midway between the transmitter and receiver (i.e., 10 mm from either). Except for the variable trajectory, the data shown in Figure 12 were collected under the same experimental conditions used to obtain Figure 10 (the same 2000 μm glass sphere was used in both cases). Figure 12 shows that varying the trajectory of the glass sphere along the height of the probe volume broadened both the velocity and size distributions while keeping the velocity mode and diameter mode unchanged relative to Figure 10. Note, however, that the mean velocity *increased* 1.1% (9.19 m/s vs. 9.09 m/s) while the mean diameter *decreased* 4.9% (2014.6 μm vs. 2118.4 μm). As is clearly shown in Figures 10 and 12, the velocity distribution broadened nearly equally about the velocity mode while the size histogram broadened principally toward smaller sizes only. The measured sizes less than the mode in Figure 12 occurred only when the glass sphere was traversed through the edges of the elongated laser sheets.

Figure 13 shows the result of varying the trajectory of a 2000 μm glass sphere along the direction of propagation of the laser sheets from 1 mm in front of the transmitter to 5 mm in front of the receiver at a constant sheet height (i.e., through the central, most intense portion of the sheets). Note that data shown in Figures 13 were collected with a different 2000 μm glass sphere than was used to generate data shown in the other figures. For comparison, the same glass sphere was also measured at a constant trajectory through the center of the laser sheets, midway between the transmitter and receiver. (Histograms for the constant trajectory case are not shown.) Figure 13 shows a 4.8% increase in measured mean velocity (9.49 m/s vs. 9.06 m/s) and an 8.6% increase in measured mean diameter (2257.1 μm vs. 2079.1 μm) relative to the constant trajectory case. The higher means in Figure 13 are a result of higher velocities and sizes measured only when the glass sphere was traversed near either edge of the probe volume (i.e., near the aperture plates).

Lastly, Figure 14 shows the results of measuring both a 1000 μm and 2000 μm sphere attached to the same spinning disk. (The 2000 μm sphere is the same one measured in Figures 10, 11, and 12.) The trajectory was held constant and was set to traverse both spheres through the probe volume midway between the transmitter and receiver. Of the 1000 samples taken, 513 samples fell into bin 10 encompassing the size range from 987 to 1067 μm, 479 samples fell into bin 23 encompassing the size range from 2025 to 2105 μm, and eight samples fell into immediately adjacent bins.. (The unequal number of samples in bins 10 and 23 is an artifact of the 500 μm displacement in lateral trajectory, orthogonal to the direction of propagation of the laser sheets, taken by one glass sphere relative to the other because of their 500 μm difference in radius.) The resulting mean size was 1528.7 μm. The nearly single bin resolution for both the 1000 and 2000 μm spheres is clearly demonstrated.

7. SUMMARY AND CONCLUSIONS

This paper has described a miniaturized particle sizing velocimeter developed and built by MetroLaser to measure the spatial and temporal distributions of particle size and velocity. By combining PDT, the I_{max} particle sizing technique, and a time-of-fight velocity measuring technique, the instrument provides detailed distributions of particle size from 2 μm to 6000 μm and particle velocity from 0.5 m/s to 150 m/s. The instrument is small enough to fit in the palm of a hand and operates with negligible flow disturbance. It is rugged enough to withstand harsh environments characterized by high ambient moisture levels, high noise and vibration levels, and wide swings in ambient temperature.

PDT depends on a handful of parameters which are readily defined, allowing a fast and accurate calculation of size using analytical relationships presented in this paper. These parameters include index of refraction, collection angle, and particle velocity. Although the current instrument uses a two-color "time-of-flight" technique to measure velocity, PDT is also compatible with other velocity measuring techniques such as laser Doppler velocimetry.

As currently implemented, the lower size limit of PDT is ~1.5 times the laser sheet width which, in the present case, would anchor d_{min} at ~30 μm if PDT were implemented alone; however, the lower limit was successfully extended to 2 μm by combining PDT and the I_{max} technique.

The use of two multimode optical fibers and a fiber bundle has resulted in a receiver with unity magnification, allowing the measurement of particle sizes from 2 μm to 6000 μm in two ranges with only a minor change to the optical configuration of the probe.

The processing of PDT data is achieved quickly and accurately with commercially available computer hardware and digital signal processing boards, and the use of MetroLaser's proprietary software. All data collection and data processing parameters are defined by the operator via software.

Experimental results obtained with a droplet generator operating in both a continuous-stream mode and an induced spray mode, a humidifier, and glass spheres were presented and demonstrate the accuracy and versatility of the instrument.

8. REFERENCES

Bachalo, W.D. and Houser, M.J., 1984, "Phase/Doppler Spray Analyzer for Simultaneous Measurements of Drop Size and Velocity Distributions," Opt. Eng., vol. 23, no. 5, pp. 583-590.

Chu, W.P. and Robinson, D.M., 1977, "Scattering from a Moving Particle by Two Crossed Coherent Plane Waves," Appl Opt, vol. 16, no. 3, pp. 619-626.

Durst, F. and Zaré, M., 1975, "Laser Doppler Measurements in Two-Phase Flows," Proc. of the LDA-Symp, Copenhagen, pp. 403-429.

Hess, C.F., 1984, "Nonintrusive Optical Single-Particle Counter for Measuring the Size and Velocity of Droplets in a Spray," Appl. Opt., vol. 23, no. 23, pp. 4375-4382.

Hess, C.F. and Wood, C.P., 1993, "Pulse Displacement Technique to Measure Particle Size and Velocity in Large Number Density Applications," Laser Techniques and Applications in Fluid Mechanics, Durau, et al., Eds., Springer- Verlag, Berlin, pp. 131-144.

Hess, C.F. and Wood, C.P., 1994, "The Pulse Displacement Technique - a Single Particle Counter with a Size Range Larger than 1000:1," Particle and Particle Sys Char., vol. 11, pp. 107-113.

Holve, D.L., 1980, "In Situ Optical Particle Sizing Technique," Jrnl of Energy, Vol. 4, No. 4, pp. 176-183.

Van de Hulst, H.C., 1981, Light Scattering by Small Particles, Chpt 12, Dover Pub's, New York.

Wood, C.P. and Hess, C.F., 1994, "A Miniaturized Instrument Implementing Pulse Displacement to Measure Particles from 2 μm to 5000 μm," Seventh Intn'l Symp. on Applications of Laser Techniques to Fluid Mechanics, Lisbon, Portugal, July.

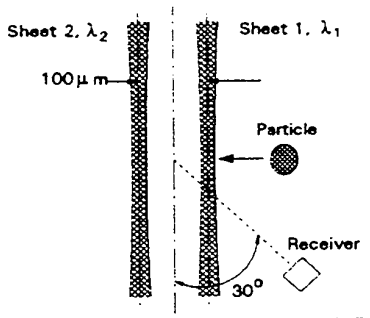

FIG. 1. SINGLE RECEIVER, DUAL WAVELENGTH CONFIGURATION.

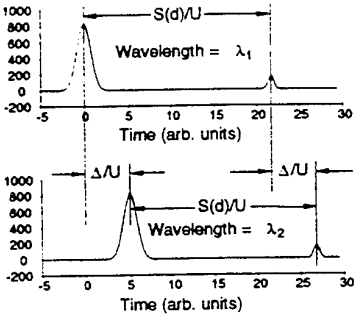

FIG. 2. SIMULATED REFRACTION AND REFLECTION PULSES. PARTICLE SIZE = 500 μm, SHEET SEPARATION = 100 μm.

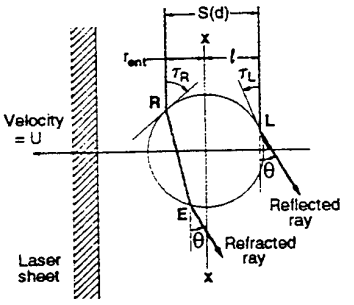

FIG. 3. DROPLET SCATTERING REFRACTED AND REFLECTED LIGHT INTO AN ANGLE θ.

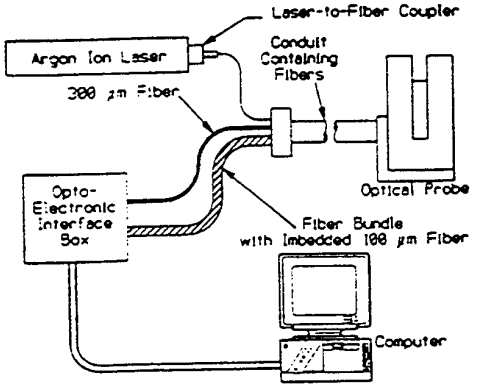

FIG. 4. SCHEMATIC OF MINIATURIZED PARTICLE SIZING VELOCIMETER.

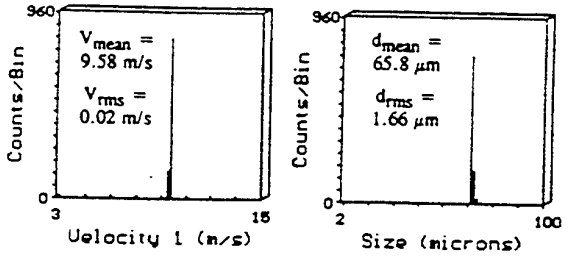

FIG. 5. VELOCITY AND SIZE HISTOGRAMS FOR 65.8 μm DROPLETS (CONSTANT TRAJECTORY).

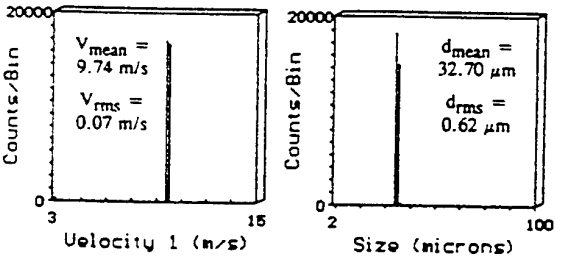

FIG. 6. VELOCITY AND SIZE HISTOGRAMS FOR SIMULATED 33.5 μm DROPLETS (CONSTANT TRAJECTORY).

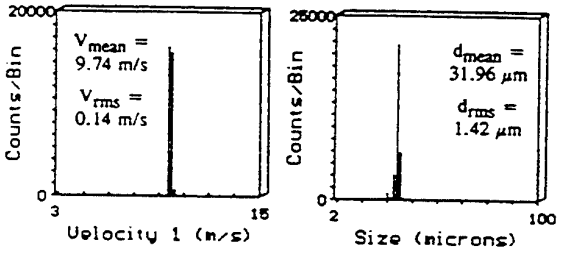

FIG. 7. VELOCITY AND SIZE HISTOGRAMS FOR SIMULATED 33.5 μm DROPLETS WITH VARIABLE TRAJECTORY.

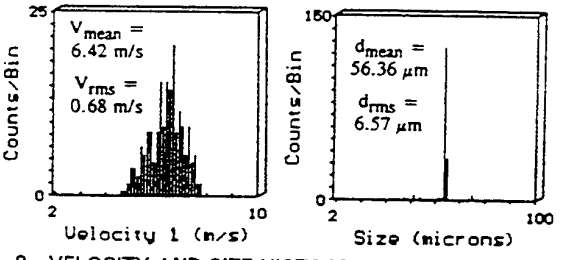

FIG. 8. VELOCITY AND SIZE HISTOGRAMS FOR A SPRAY OF 57.8 μm DROPLETS WITH RANDOM TRAJECTORIES.

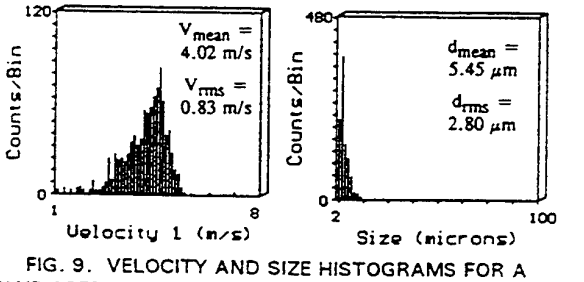

FIG. 9. VELOCITY AND SIZE HISTOGRAMS FOR A POLYDISPERSE DROPLETS PRODUCED WITH A HUMIDIFIER.

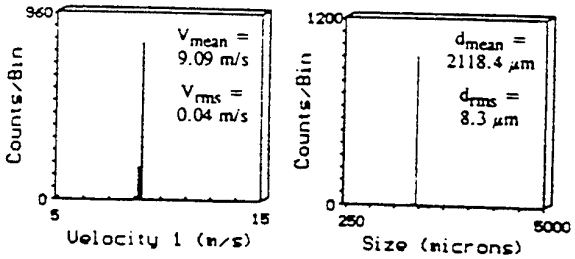

FIG. 10. VELOCITY AND SIZE HISTOGRAMS FOR A 2000 μm GLASS SPHERE (CONSTANT TRAJECTORY & VELOCITY).

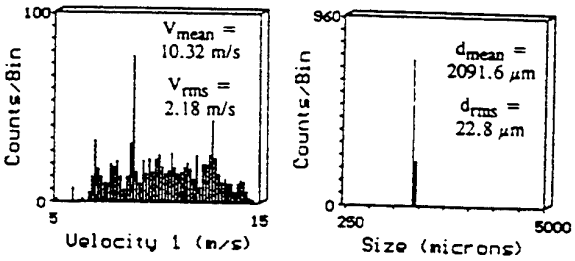

FIG. 11. VELOCITY AND SIZE HISTOGRAMS FOR A 2000 μm GLASS SPHERE WITH VARIABLE VELOCITY.

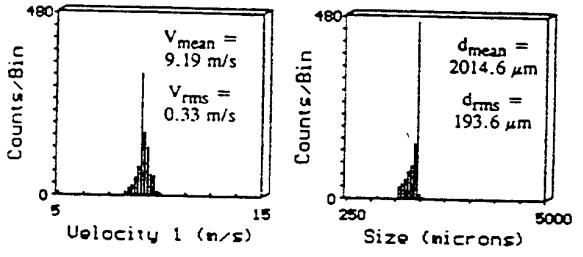

FIG. 12. VELOCITY AND SIZE HISTOGRAMS FOR A 2000 μm GLASS SPHERE WITH VARIABLE LATERAL TRAJECTORY.

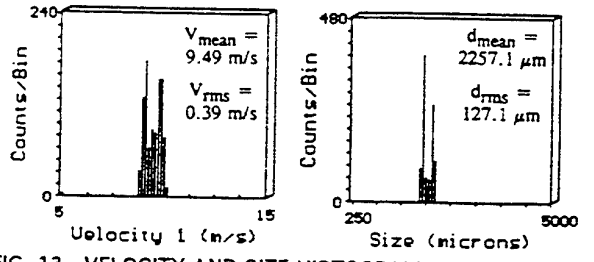

FIG. 13. VELOCITY AND SIZE HISTOGRAMS FOR A 2000 μm GLASS SPHERE WITH VARIABLE AXIAL TRAJECTORY.

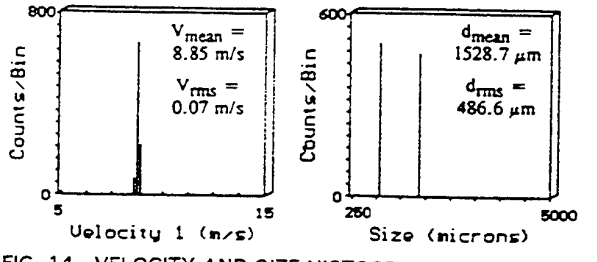

FIG. 14. VELOCITY AND SIZE HISTOGRAMS FOR 1000 μm AND 2000 μm GLASS SPHERES.

DETERMINATION OF SUBMICRONIC PARTICLE SIZE BY ANALYSIS OF LIGHT SCATTERED BY A GAS STREAM.

Laurent AZIZI* Philippe HERVE** Alain KLEITZ***

* LASUR, 119 bis rue de Colombes 92600 ASNIERES France
** Laboratoire d'Energétique et d'Economie d'Energie
University Paris X, 1 Chemin Desvallières 92410 Ville d'Avray France
*** Electricité de France - Direction des études et recherche - Département Machine
6 Quai Watier 78400 CHATOU France.

ABSTRACT

Determining the size distribution of a cloud of submicronic particles is a problem often encountered in combustion or fluid mechanics.
We are interested in putting into evidence the presence of condensation nuclei in the atmosphere, which generate water drops projected on gas turbines vanes at Mach 1. The condensation nuclei diameters range from 0.02 to 0.2 μm. The scattering figure of a polarized light through a cloud of particles depends on the wavelength used, the complex index and the particle diameters. The size parameter $\alpha = \pi D/\lambda$ is of utmost importance.

In the case of small particles, we have chosen to illuminate the cloud at a small wavelength in order to work within Mie's domain ($0.1 < \alpha < 5$) in which the scattering figure in polarized light depends on the particle diameters. An Argon laser provides a visible coherent light.

The particle velocity being very high (around 600 m/s), the picture must be taken very quickly (shutter opening time 100 ns).

The ratio between the perpendicular and parallel components of the energy received by the camera is a direct function of the diameter of the particles observed. The shutter opening time being very short, the energy received on the CCD matrix is very weak. An intensified camera is thus necessary to carry out this study. Despite the intensification which allows for counting the photons scattered by the particles almost one by one, the quantity are noisy because the number of photons scattered during the shutter opening time is around a few dozens and depends on a statistical distribution which, at first approximation, tends towards Poisson's law.

The results allow us to have a size distribution of a scene. We are at present trying to improve the signal/noise ratio in order to decrease the data acquisition time.

1. INTRODUCTION

The determination of submicronic particle size distribution is a problem often encountered in combustion and fluid mechanics.

An industrial application is to examine the influence of atmospheric particles on the icing of gas turbines. In some particular atmospheric conditions, these particles act as condensation germs and melt into liquid drops creating risks of icing at the first stage of the compressor. These nuclei generated by condensation are projected at MACH 1 speed on gas turbine blades.
Non intrusive measures are necessary to know the number and size of particles in the flow.

The diameters of these nuclei of condensation are between 0.02 and 0.2 μm as shown by Kleitz and Boulaud (1995). A scattered light diffusion picture through a particle cloud depends on the wavelength used, the complex refractive index and the diameter of particles. The main parameter is the size parameter $\alpha = \pi D/\lambda$. To use Mie's theory with those small particles, we chose to light up the cloud with a short wavelength. An ARGON laser provides a visible coherent light.

2. PHYSICAL PRINCIPLE

A light diffracted by a particle supposed to be spherical is scattered. At a given angle, the ratio of the parallel and perpendicular components of the energy received, or scattering ratio, depends on the particle size [9][10] and the refractive index.

2.1 Mie's theory recalls

The intensity scattered by a spherical particle on which an intensity *radiance* of I_o is sent in the spherical polar angles (θ,φ) is called $I_{diff}(\theta,\varphi)$.

The total scattered power in a solid angle $d\Omega$ is:

$$P_{Diff} = \int_{4\pi} I_{Diff}(\theta,\varphi) \cdot r^2 \, d\Omega$$

where r stands for the distance between the source and the detector.

A d diameter spherical particle with a complex refractive index n, located at the top of a direct trihedron, interacts with a plane wave which is propagated toward the positive (Oz), defined by the electrical field E = Ex ox, of wavelength λ. The scattered light is observed at point (P), at a distance r >> λ (Fig.1). It is made up of two components: one for which the electrical field vector vibrates in the plane formed by the OZ propagation direction and the OP observation direction; the other for which the electrical field vector vibrates in the perpendicular plane.

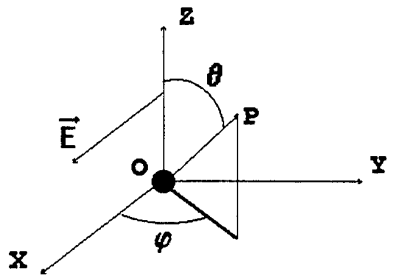

Fig 1: Scattered light by a spherical particle

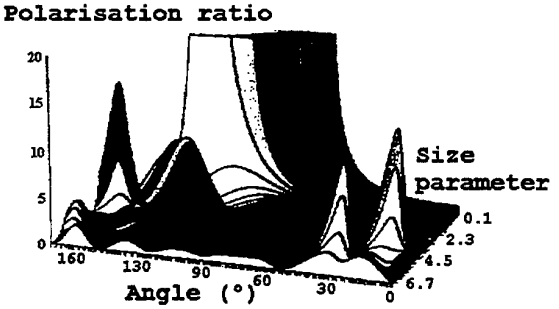

Fig 2: Polarisation ratio of scattered light versus size parameter and observation angle for a Nr=1.33+1e-5i particle

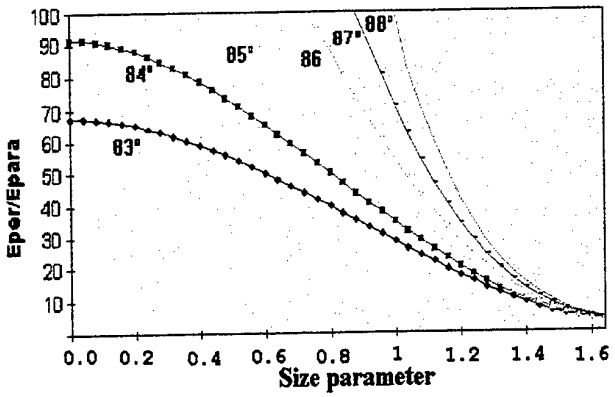

Fig 3: Scattering ratio versus size parameter and observation angle

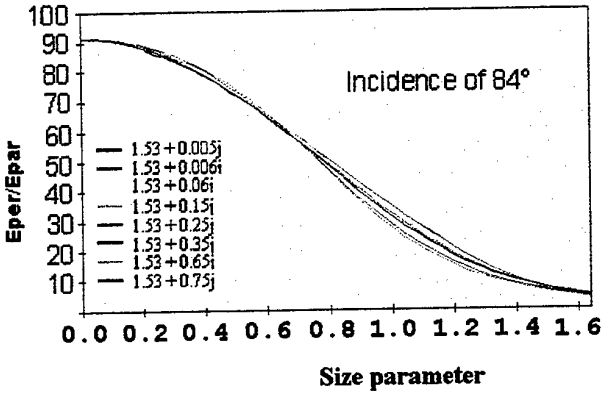

Fig 4: Scattering ratio versus size parameter and particle imaginary refractive index

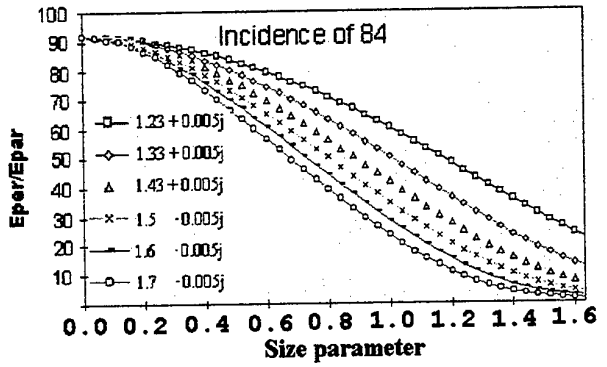

Fig 5: Scattering ratio versus size parameter and particle real refractive index

At wavelength 488 nm, the water particle complex refractive index value is about 1.530-0.005i (Fig.6) has been reported by Willeke and Baron (1992). The inaccuracy of this value is not really important as the scattering ratio little depends on it. The particle size can be then established without a doubt.

Refractive index		
Wavelength µm	Water-soluble	Dusklike
0.20000	1.530-0.070j	1.530-0.070j
0.25000	1.530-0.030j	1.530-0.030j
0.30000	1.530-0.008j	1.530-0.008j
0.33710	1.530-0.005j	1.530-0.008j
0.48800	**1.530-0.005j**	**1.530-0.008j**
0.51450	1.530-0.005j	1.530-0.008j
0.63280	1.530-0.006j	1.530-0.008j
0.69430	1.530-0.007j	1.530-0.008j
0.86000	1.520-0.012j	1.520-0.008j
1.06000	1.520-0.017j	1.520-0.008j
1.53600	1.510-0.023j	1.400-0.008j
2.00000	1.420-0.008j	1.260-0.008j
2.50000	1.420-0.012j	1.180-0.009j
2.70000	1.400-0.055j	1.180-0.013j
3.00000	1.420-0.022j	1.160-0.012j
3.20000	1.430-0.008j	1.220-0.010j
3.39230	1.430-0.007j	1.260-0.013j
3.50000	1.450-0.005j	1.280-0.011j
3.75000	1.452-0.004j	1.270-0.011j
4.00000	1.455-0.005j	1.260-0.012j
4.50000	1.460-0.013j	1.260-0.014j
5.50000	1.440-0.018j	1.220-0.021j

Fig 6: Complex index of atmospheric particles versus wavelength

2.2 Equipment

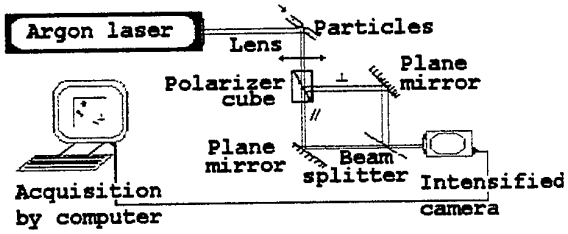

Fig 7: Experimental system

The observed zone is the intersection of the LASER beam (focused or not) and the zone aimed by the system shown on picture 7.
The particles speed is high, about 300m.s^{-1}, so the picture must be acquired very fast.

The polarisation ratio of the scattered light is a function of the particle diameter (Cf. fig 2, 3).

Aperture time of the camera is very short, so the energy which comes on the CCD is low. An intensified camera is necessary for this study. But if the camera allows for the counting of scattered photons almost one by one, the pictures are noisy because the few (about ten) scattered photons depend on a statistic distribution which seems, on first approximation, to follow Poisson's law. This technique has been patented by HERVE (1995).

Kaufman and Tekalp (1991) have shown the way to treat the picture before any interpretation. As the spectral density of the noise is a priori known, non parametric methods are usable as described by Kunt (1993).

3. RESULTS

3.1 0.451 μm diameter LATEX balls

We worked with monodispersed spherical LATEX particles of 0.451 micron diameter. By a direct measure of the histogram, we have calibrated the experiment. We have found a 0.35 μm diameter, and a spread size band. The precision of the measure is about 20 percent. We can optimize this precision by modifying the scattering angle and the sensitivity function.

3.2 particles in a gas stream

Tests have been carried out in the laboratory. Picture 8 represents the superposing of the parallel and perpendicular components, obtained by the system previously described. After applying convolution by different numeric filters (Average filter, Median filter, ...), we get a restored picture of the parallel component (in green) and the perpendicular component (in red), spatially shifted. A translation vector can be determined by maximizing autocorrelation function as shown by Draayer and Carhart (1994). It gives the way from the parallel component to the perpendicular one. The curve of the particle number versus the scattering ratio is given by the scanning of the picture. Then using the curve of figure 2, the size parameter is determined (Fig 10). Knowing the incident light wavelength, the distribution can be calculated (Fig 11 and 12).

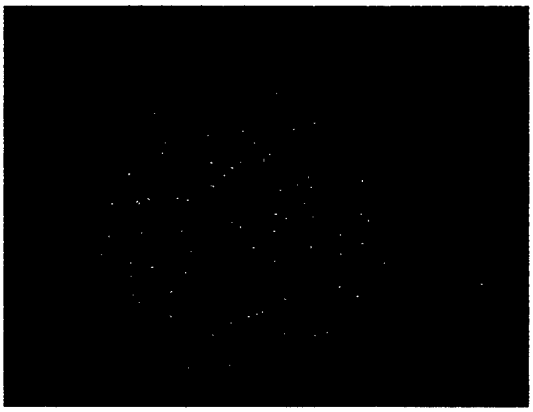

Fig 8: Brute picture before treatment

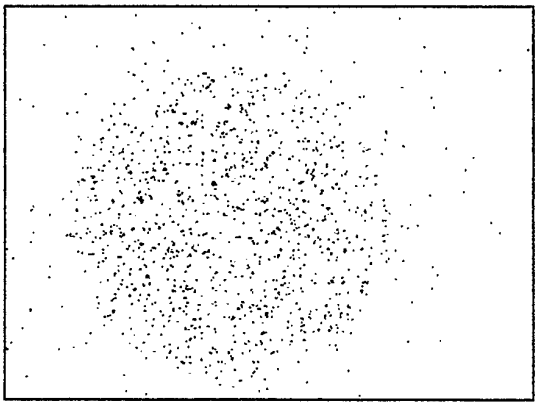

Fig 9: Restored picture.

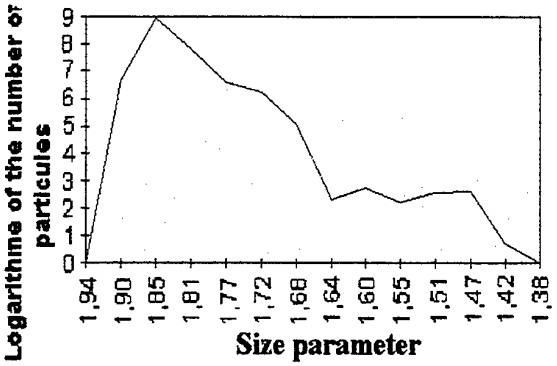

Fig 10: Number of particles *versus* size parameter.

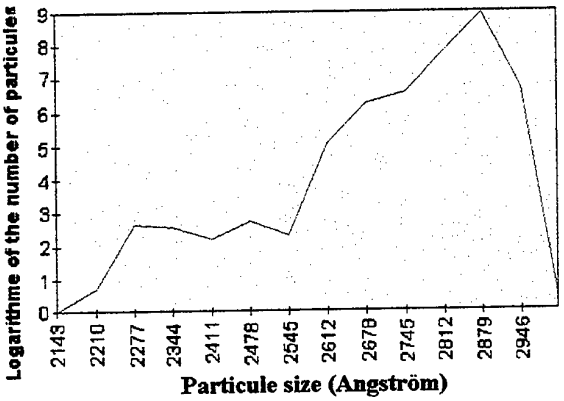

Fig 11: Particle size distribution.

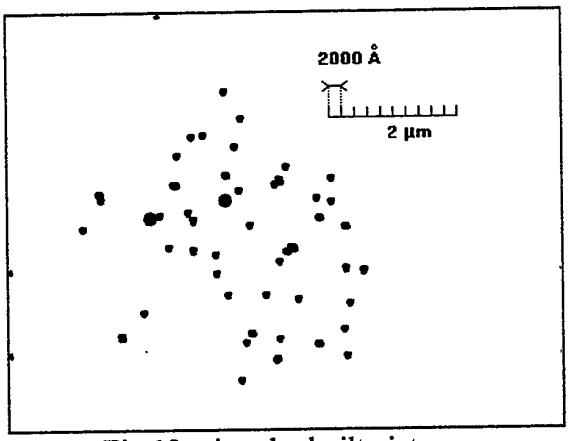

Fig 12: virtual rebuilt picture.

4. CONCLUSION

This system of measurement allows to get a spatial view of submicronic particle distribution. That is equivalent to an optical microscope with a resolution ability of about 100 Å, which is impossible because of the diffraction of light.
The lower limit of distribution size is, at present, about 200 Å.
If the angle of measurement is between 80° and 89°, it is possible to optimize the precision of measurements for a diameter range between 200 Å and 2000 Å. We work with a typical 20 percent precision.
Measurements carried out with laboratory atmosphere particles at scattered angle of 84°, show the presence of submicronic particles of 2800 Å size.
Fast data acquisition and treatment are in the process of development, to see the particle size evolution in real time. Conversely, we study the theory for cylindrical particles and axial symmetric particles for application to bacteria detection and identification.

NOMENCLATURE

$d\Omega$	Solid angle	(sr)
r, θ, φ	Spherical coordinates	(m,rad,rad)
X, Y, Z	Cartesian coordinates	(m,m,m)
P_{diff}	Scattered power	(W)
I_{diff}	Scattered intensity	(W/m^2 sr)
E	Electrical field	(V/m)
D	Diameter	(m)
λ	Wavelength	(m)
O	Origin	
α	Size parameter	

BIBLIOGRAPHY

(book)
Kunt, M. 1993, Traitement numérique des images. Presses polytechniques et universitaires romandes

(patent application)
Hervé, P. N° 9506365, 1995 « procédé et dispositif pour déterminer la taille de particules microniques ou submicroniques »

(Journal article)
Kleitz, A. & Boulaud, D. 1995, Granulométrie des particules en mouvement et des aérosols, Techniques de l'ingénieur, vol. 7, pp. 360-1-360-26

(Journal article)
Kaufman, H. & Tekalp, A.M. 1991, Survey of estimation techniques in image restoration, IEEE Control Systems Magazine, vol. 11, pp. 16-24

(book)
Willeke, K. & Baron, P.A. 1992, Aerosol Measurement Principles

ADVANTAGES OF UV LASERS IN LASER AND PHASE DOPPLER ANEMOMETERS FOR SUBMICROMETER PARTICLES

F. Durst, A. Melling and P. Volkholz

Lehrstuhl für Strömungsmechanik, University of Erlangen-Nürnberg, Cauerstr. 4
91058 Erlangen, Germany

ABSTRACT

For laser Doppler (LDA) and phase Doppler anemometry (PDA) measurements with submicrometer particles lasers with wavelengths between 240nm and 280nm have advantages over lasers that emit visible radiation. The main advantage is the higher signal-to-noise ratio (SNR) obtainable, since the scattered power is significantly increased at shorter wavelengths. Furthermore, for PDA the capability of making size class distinctions in the submicrometer size range is improved, as shorter wavelengths lead to steeper phase difference-to-diameter relationships. In particular, the use of ultraviolet (UV) laser light enables the size class distinction between 0.1μm and 0.2μm particles, that is not possible when using visible radiation. The feasibility of performing laser Doppler and phase Doppler anemometry measurements with ultraviolet laser light is confirmed by experiments.

1 INTRODUCTION

Laser Doppler and phase Doppler anemometers typically use He-Ne or argon ion lasers, i.e the wavelengths 633nm, 514nm, or 488nm. Laser diodes emitting at infrared wavelengths, e.g 820nm, are also frequently used. For particles larger than the wavelength, the scattering cross section C_{sca}, defined as the ratio of total scattered power P_s^{tot} to laser intensity in the probe volume I_0

$$C_{sca} = \frac{P_s^{tot}}{I_0} \tag{1}$$

is in approximation proportional to the square of the particle diameter d_p.

$$C_{sca} \propto d_p^2 \tag{2}$$

Therefore, for particles larger than about 1μm, only the output power, and not the wavelength, of a laser is relevant to the total scattered power. For particles smaller than the wavelength λ the scattering cross section becomes a function also of the wavelength and can be approximated by [1]

$$C_{sca} \propto \left(\frac{d_p}{\lambda}\right)^4 \tag{3}$$

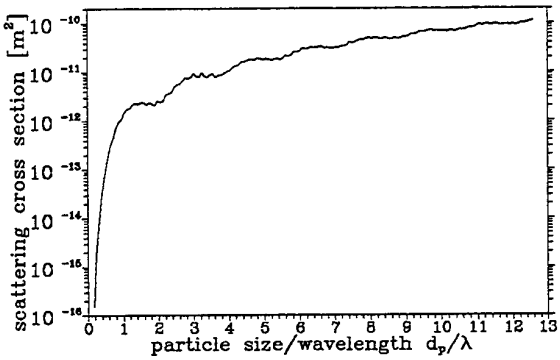

Figure 1: Scattering cross section C_{sca} as a function of the ratio particle size to wavelength d_p/λ (plotted for refractive index m=1.6)

This abrupt transition from $C_{sca} \propto (d_p/\lambda)^4$ to $C_{sca} \propto d_p^2$ at $d_p \approx \lambda$ is shown in fig. 1, where the scattering cross section is plotted logarithmically as a function of the ratio d_p/λ.

In the present work particles as small as 0.1μm are of interest. Fig. 1 makes clear that even when using a powerful argon ion laser at λ = 514nm, the scattered power from a 0.1μm ($d_p/\lambda = 0.2$) particle becomes very small, making a reduction of the wavelength necessary. This paper shows that the use of ultraviolet (UV) laser light is a logical and viable alternative.

The rest of the paper discusses the theory of UV-based LDA and PDA-systems and presents experimental results that demonstrate the feasibility of LDA and PDA with ultraviolet light.

2 THEORY OF LDA AND PDA FOR SUBMICROMETER PARTICLES; COMPARISON GREEN-UV

In this section a detailed analysis is given of how using UV (257nm) light for submicrometer particles will improve

1. the detectability, i.e. the SNR, of the Doppler signals.
2. the phase difference-to-diameter relationship, referred to as the phase-diameter relationship in the following.
3. the particle concentration at which PDA measurements can still be performed.

2.1 Improvement of the detectability of submicrometer particles using UV-light

For submicrometer particles down to 0.1μm, which are of interest in this paper, the scattered power and the SNR become so small, that it is very difficult to obtain processable Doppler signals.
The aim in this section is, therefore, to estimate theoretically the SNR of Doppler signals when using a photomultiplier (PM) [1] as a function of scattered power and signal frequency only. This is done by calculating the combined SNR due to quantum fluctuations in the light scattering process and due to the photomultiplier itself.

Theoretical SNR estimate for photomultipliers

The SNR of a photomultiplier (PM) can be estimated by dividing the mean signal current $\bar{i}_s$ by the root of the sum of mean square shot noise $\bar{i}_n^2$, mean dark count noise $\bar{i}_d^2$, and mean square thermal noise $\bar{i}_T^2$.

$$SNR_{PM} = \frac{\bar{i}_s}{\sqrt{\bar{i}_n^2 + \bar{i}_d^2 + \bar{i}_T^2}} \tag{4}$$

The mean signal current $\bar{i}_s$ produced by a Doppler burst is

$$\bar{i}_s = \frac{G}{\sqrt{2}} \cdot V \cdot \bar{i}_c \tag{5}$$

G: gain of PM
V: signal visibility.
The factor $1/\sqrt{2}$ accounts for the fact that the Doppler signal is an oscillating signal. $\bar{i}_c$ is the mean photocathode current and is given by

$$\bar{i}_c = \frac{P_s}{h \cdot \nu} \cdot \eta_Q \cdot e \tag{6}$$

[1] Avalanche Photodiodes (APD) are not considered here.

P_s: power scattered on to photocathode
h: Planck's constant
ν: laser light frequency
η_Q: quantum efficiency of photocathode
e: electron charge

The term $P_s \cdot \eta_Q/(h \cdot \nu)$ represents the number of photons detected per unit time.
The mean square shot noise $\bar{i}_n^2$ of a PM is given by

$$\bar{i}_n^2 = G^2 \cdot 2e \cdot \bar{i}_c \cdot \Delta f \tag{7}$$

Δf is the bandwidth of the electronics and is usually equivalent to the Doppler frequency f_D of the maximum velocity one wants to measure. Similarly, the mean dark count noise $\bar{i}_d^2$ is given by

$$\bar{i}_d^2 = G^2 \cdot 2e \cdot \dot{n}_d \cdot e \cdot \Delta f \tag{8}$$

$\dot{n}_d$: dark counts per second
The mean square thermal noise is given by

$$\bar{i}_T^2 = \frac{4k_B T}{R_L} \cdot \Delta f \tag{9}$$

where k_B is Boltzmann's constant, T the temperature, and R_L the load resistance.
Putting equations 5, 6, 7, 8, and 9 together, the SNR of a PM can be given as

$$SNR_{PM} = \frac{\frac{G}{\sqrt{2}} \cdot \frac{V \cdot P_s \eta_Q e}{h\nu}}{\sqrt{G^2 2e \left(\frac{P_s \eta_Q e}{h\nu} + \dot{n}_d \cdot e \right) \cdot \Delta f + \frac{4k_B T}{R_L} \cdot \Delta f}} \tag{10}$$

In eq.10 most values are the same for green and UV light. The exceptions are $P_s, \eta_Q, \nu, \Delta f$. How these four values differ for green and UV light will be discussed below.

Factors influencing the comparison green–UV

The main advantage of using UV-light is the increase in the scattered power P_s. According to eq.3, at 257nm wavelength, the scattered power is about 16 times larger than at 514nm up to $d_p \approx 0.5\mu$m, assuming equal light intensities in the probe volume. While this is a convenient assumption with which to start, it is unrealistic when comparing light scattering and detection of UV and green light relevant to LDA and PDA. The following factors, therefore, have to be taken into account:

1. Continuous wave (cw) laser sources generally deliver less power when emitting ultraviolet rather than visible radiation.
   The UV laser source considered in this paper, for example, was an argon ion laser with a built-in frequency doubling crystal [2] to convert radiation in the green line to UV. It produced about 10 times less output power at 257nm than at 514nm at equal plasma tube currents.

[2] Coherent Innova FReD 300

2. Since the fringe spacing Δx in the probe volume is given by

$$\Delta x = \frac{\lambda}{2 \cdot \sin(\alpha)} \tag{11}$$

halving the wavelength also halves the fringe spacing. Hence, the diameter of the probe volume can also be reduced by a factor 2 without reducing the number of fringes. At a particular laser output power P_0, the laser intensity in the probe volume I_0 can, therefore, be increased by a factor of 4 for a given number of interference fringes, when converting from green to UV-light.

3. According to the photocathode material, the quantum efficiency of a photomultiplier is wavelength dependent. The quantum efficiency of photomultipliers optimized for UV-light is generally 5 to 10 percent points higher than that of the best photomultipliers for green light.

4. The number of photons arriving at the detector per signal cycle is given by

$$n_{ph} = \frac{P_s}{h \cdot \nu} \cdot \frac{\eta_Q}{f_D} = \frac{P_s \cdot \lambda}{h \cdot c} \cdot \frac{\eta_Q}{f_D} \tag{12}$$

Since the Doppler signal frequency f_D is given by

$$f_D = \frac{1}{\lambda} \cdot v_\perp \cdot 2\sin(\alpha) \tag{13}$$

$v_\perp$: velocity component perpendicular to the probe volume fringes

eq. 12 predicts the following dependence:

$$n_{ph} \propto \lambda^2 \cdot P_s \tag{14}$$

This means that at equal scattered powers, using laser light at a wavelength of 257nm instead of 514nm reduces the number of scattered photons by a factor 4. The reduction of the probe volume size, that is possible using shorter wavelengths, therefore, does not increase the number of photons/cycle. However the SNR is increased, since the SNR $\propto 1/\sqrt{\Delta f}$ for the PM and the connected electronics.

These four points are taken into account in figure 2, where the number of detected photons per signal cycle is plotted versus particle size.

Despite the reduction in the photon rate with the wavelength and the 10 times lower power of the UV laser relative to the green laser, more photons are detected per signal cycle with UV-light than with green light for particles in the size range 0.1 to 0.6 μm. In the example calculated for fig. 2, there are 121 detected photons/cycle at 257nm and only 37 at 514nm for a $0.1\mu m$ particle.

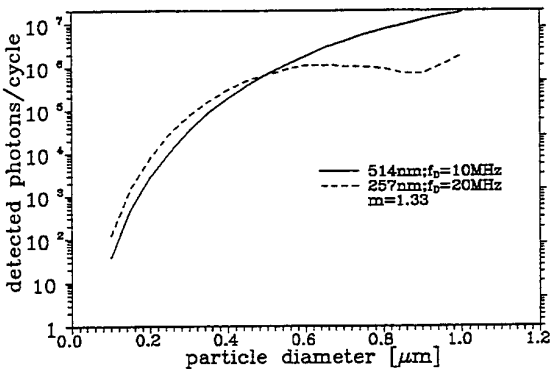

Figure 2: Detected number of photons per Doppler signal cycle versus particle size at the wavelengths 257nm and 514nm (output power at 257nm ten times less than at 514nm).

SNR due to quantum noise

The scattering process is a statistical process, i.e. the number of photons/cycle plotted in fig. 2 has to be seen as the expectation value. Hence, low numbers of photons/cycle lead to quantum noise, which can be quantified by the standard deviation σ_{ph} of the number of photons/cycle, approximately given by

$$\sigma_{ph} = \sqrt{n_{ph}} \tag{15}$$

The resulting relative error, i.e. the noise-to-signal ratio, is given by

$$\frac{\sqrt{n_{ph}}}{n_{ph}} = \frac{1}{\sqrt{n_{ph}}} \tag{16}$$

The signal-to-noise ratio due to quantum noise SNR_{QN} is therefore $\sqrt{n_{ph}}$. Returning to the example given above, 37 photons/cycle correspond to an SNR of 6, whereas 121 photons/cycle correspond to an SNR of 11.

Derivation of the combined SNR

In order to give a final estimate of the expected SNR of a Doppler signal produced by a 0.1 μm particle, as shown in figure 3, the combined SNR of the quantum noise and of the PM has to be obtained.
Relative random errors $\frac{\Delta l_i}{l_i}$ of measured quantities l_i add up to a combined relative error $\frac{\Delta R}{R}$ according to:

$$\frac{\Delta R}{R} = \sqrt{\sum_i \left(\frac{\Delta l_i}{l_i}\right)^2} \tag{17}$$

In our case, considering the noise-to-signal ratios, this translates to:

$$SNR_{tot} = \frac{1}{\sqrt{\left(\frac{1}{SNR_{QN}}\right)^2 + \left(\frac{1}{SNR_{PM}}\right)^2}} \tag{18}$$

Comparison green-UV of the combined SNR

With eq. 10, 16, and 18 a comparison of the SNR (in decibel) versus bandwidth for green and UV light is possible. This was done for a 0.1μm latex particle in air as shown in figure 3 again assuming that the UV laser is a factor 10 times weaker than the green laser. This plot shows that the total SNR using UV light is about 9 to 12dB larger than using green light, even when considering the fact that the Doppler frequency is doubled when the wavelength is halved. As an example, in fig. 3 one sees that the SNR using UV-light at 100MHz equals the SNR using green light at about 10MHz, i.e. it is possible to measure 10 times higher frequencies using UV-light, which, according to eq.13, converts to 5 times higher velocities, without a loss in SNR. Using a UV-based LDA-system can therefore be advantageous in transonic flows with submicrometer seeding particles. Further advantages from using UV laser light can be expected when using compact and portable lasers. Argon ion lasers are increasingly being replaced by frequency-doubled Nd:YAG lasers, which emit laser light at a wavelength of 532nm. The conversion efficiencies are about 50-60%, resulting in output powers of about 500mW. These Nd:YAG lasers can also be twice frequency-doubled producing a wavelength of 266nm. The conversion efficiencies from green to UV can be as high as 22% [2], which results in output powers of about 100mW. The estimated SNR's at 266nm and 532nm are shown in figure 4. Whereas the SNR at 266nm and 100mW is approximately the same as for 257nm in figure 3, the SNR at 532nm and 500 mW quickly drops to very low levels.

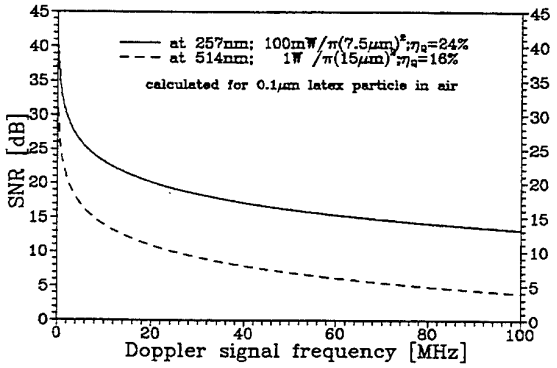

Figure 3: Estimated SNR of a Doppler signal produced by a 0.1 μm latex particle in air versus bandwidth

2.2 Phase difference-to-diameter relationship

In PDA, particle sizes are determined from the measured phase difference between the Doppler signals detected at two spatially separated detectors with the help of the so-called phase factor F:

$$\Phi_m = F(m, \alpha, ...) \cdot d_p \qquad (19)$$

For particles that are large compared to the wavelength, geometrical optics applies, and the phase factor is a constant for a fixed optical geometry [3]. For particles that are smaller than about 10 times the wavelength, geometrical optics no longer applies, and the exact Mie-theory [1] has to be used to predict the phase-diameter relationship. Figure 5 shows the phase-diameter relationship in the size range from 0.1 to 1μm using green and UV light with identical optical geometries.

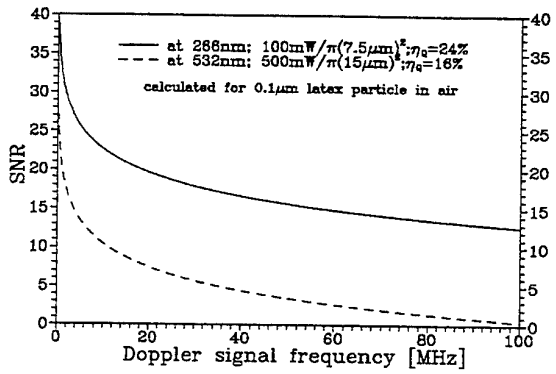

Figure 4: Estimated SNR of a Doppler signal produced by a 0.1 μm latex particle in air versus bandwidth

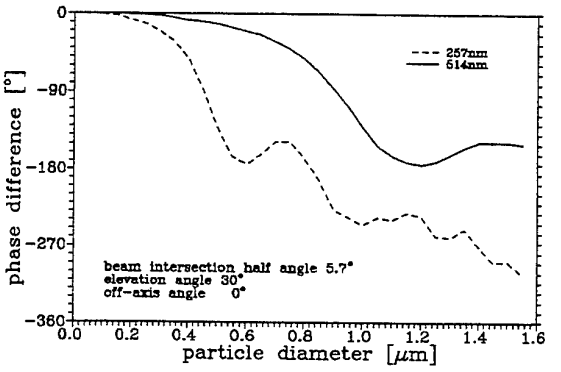

Figure 5: Comparison of the phase-diameter relationship using identical optical geometries

Firstly, it is important to note that the phase-diameter relationship is non-linear and non-monotonic. Secondly, the phase-diameter relationship is steeper when using UV light. To obtain a phase-diameter relationship with $\lambda = 514$nm that has an equally large phase factor F as with $\lambda = 257$nm at a certain size d_p larger beam intersection half angles are needed, thereby raising the signal frequency and reducing further the number of

photons per signal cycle as shown in fig. 2. Figure 6 shows such a phase-diameter relationship; although the relationship for $\lambda = 514$nm now has the same phase-difference at $d_p = 1.0\mu$m as for $\lambda = 257$nm, it is still not possible to differentiate between 0.1 and 0.2 μm particles with green light, since the phase-diameter relationship flattens off below 0.3μm.
Therefore, to differentiate the size classes 0.1 and 0.2μm, the utilization of UV-light becomes essential.

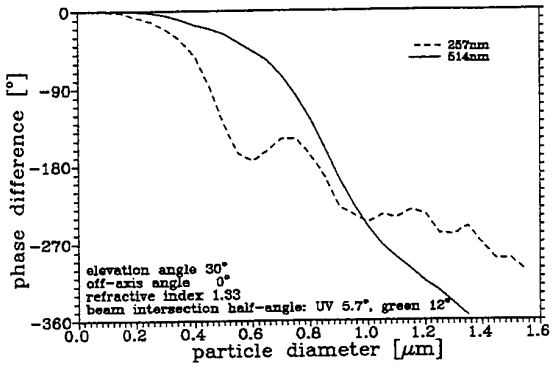

Figure 6: Comparison of phase-diameter relationships using green light and UV light. The beam-intersection half-angles α were chosen, so that the phase difference at $d_p = 1.0\mu$m has the same value for both $\lambda = 514$nm and $\lambda = 257$nm.

2.3 Probe volume and particle concentration

When considering submicrometer particles, relatively small volume fractions correspond to high particle concentrations. For example, a volume fraction of only $6.5 \cdot 10^{-7}$ corresponds to a particle concentration C of $10^7 \mathrm{cm}^{-3}$ for 0.5μm particles. Therefore, a submicrometer PDA has to be capable of performing PDA measurements at very high particle concentrations.
The prerequisite for performing valid PDA measurements is that only one particle is in the probe volume at a time. Assuming that particles in a fluid or spray are uniformly distributed in space, the probability p_k that k-particles are in the probe volume V_{PV} simultaneously is given by the Poisson-distribution:

$$p_k = \frac{(C \cdot V_{PV})^k}{k!} \cdot e^{-C \cdot V_{PV}} \qquad (20)$$

The probability P_2 that there are at least 2 particles in the probe volume simultaneously is then

$$P_2 = 1 - p_0 - p_1 \qquad (21)$$

Reducing the wavelength from green to UV by a factor of 2, allows the probe volume to be reduced by a factor of 8. Hence, according to eq. 20 and 21, the utilization of UV-light enables PDA measurements at 8 times higher particle concentrations without increasing the probability of there being more than one particle in the probe volume.

3 REALIZATION OF THE UVLDA-SYSTEM

3.1 Experimental setup and its components

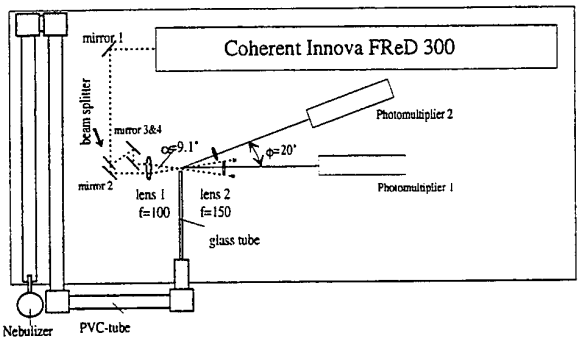

Figure 7: Experimental setup: overview

The experimental setup for the UVLDA is shown in figure 7. The cw UV laser light is redirected by mirror 1 and hits the beam splitter plate at an angle of 60°. The transmitted and reflected beams are made parallel by mirrors 2, 3 and 4 and focused into a probe volume by lens 1 with a focal length of $f_1 = 100$mm. At a distance of 200mm, lens 2 (focal length $f_2 = 150$mm) focuses the scattered light on to a 100 μm pinhole covering the photocathode of photomultiplier PM_1. The signal from the PM is first bandpass filtered, then digitized by a transient recorder and finally sent to a PC for processing. PM_2 is not used in the UVLDA.
The components of the system are the following:

1. UV-Laser: Coherent Innova FReD 300
   The Coherent Innova FReD 300 is a water-cooled argon ion laser, that uses a frequency doubling BBO-crystal to produce UV-light. All the visible lines of the argon ion laser can thereby be frequency doubled. In our case only the frequency doubling from $\lambda = 514$nm to $\lambda = 257$nm was used. The output power is 100mW, the conversion efficiency being about 20%.
2. Optics:
   - mirrors:
     257nm: UV-mirrors
     514nm: standard metal-coated mirrors

- lenses:
  257nm: UV-lenses (quarz)
  514nm: same lenses as for 257nm
- beam splitter:
  257nm: beam splitter plate for 250nm – 320nm (Melles Griot)
  514nm: path length compensated beamsplitter (Carl Zeiss Jena)

3. Photomultipliers:
   Photomultipliers selected for visible light, are not suited for the detection of UV-light [3]. A PM with a bialkali photocathode and a quantum efficiency of $\eta_Q = 24\%$ at $\lambda = 257$nm, the Thorn/EMI 9893QB100, was chosen. This PM has a very high gain of about max. $80 \cdot 10^6$ at its operating voltage of about $U_{PM} \approx 1.6$kV and a very low dark count of 20 Hz. Its suitability for the detection of UV-light is ensured by the use of a quarz-glass window. A special feature of this PM is that, due to internal focusing, only a 2.5mm in diameter large area on the photocathode is active. This reduces noise due to stray light, but makes the optical alignment very difficult.
4. Electronics:
   For the amplification and filtering of the raw signals, a PDA-Extension Box (Invent GmbH) was used. The signals were then digitized by a transient recorder (LeCroy 9424) and sent to a PC for further processing.
5. Particle generation:
   In order to generate an air flow seeded with submicrometer particles, monosized latex particles supplied by Bangs Laboratories, were dispersed in highly pure (99.8%) ethanol. This dispersion was then nebulized and passed through a 2.5m long PVC-tube with a diameter of 50mm, so that the ethanol evaporates. On the last 40cm, the ethanol/latex mixture was passed through a glass tube with a diameter of 10mm, which could be heated to several hundred °C, in order to ensure that the ethanol was completely evaporated, leaving only the latex particles. In such a way, seeded air flows with 0.1μm, 0.5μm, or with both 0.1μm and 0.5μm latex particles were obtained.

The main optical properties of the LDA-system are listed in table 1.

3.2 Verification experiments

Verification experiments were performed with UV-light to check that

1. LDA- and PDA-measurements are possible with UV-light

[3] The quantum efficiencies at wavelengths below $\approx$ 350nm are virtually zero, since the windows are UV absorbing.

Table 1: Optical parameters of the implemented LDA-system for both $\lambda = 257$nm and $\lambda = 514$nm

wavelength	257nm	514nm
beam spacing a	32mm	30mm
focal length transmitting lens f	100mm	110mm
beam-intersection half-angle α	9.1°	7.8°
fringe spacing Δx	0.81μm	1.89μm
number of fringes N	61	32
diameter of probe volume b_{MV}	50μm	60μm
focal length of receiving lens	150mm	170mm
distance probe volume – receiving lens	200mm	220mm
receiving-cone half-angle	6.8°	6.2°
magnification of receiving lens	1:3	1.3
pinhole diameter	100μm	100μm

2. improved SNR's can be obtained through the use of UV-light.

The LDA-measurements were performed in the seeded air flow described in section 3.1. In order to compare SNR's, LDA-measurements were performed with equal output powers for UV and green. Table 2 lists the measured SNR's, which were obtained for the following parameters:

- scattering angle: $\Theta = 20^0$
- particle size: d_p nominally 0.096μm; width of the size distribution about 20%
- velocity: $v \approx 1.3$ m/s
- operating voltage at the PM: $U_{PM} = 1550$V

Measurement of SNR value:

The SNR of each Doppler burst is determined by the signal processing software, which measures signal frequency and the phase difference between the two channels by computing the cross spectral density function (CSD) from the digitized data. From the CSD, the program determines the signal and the noise powers and calculates the SNR in dB according to:

$$SNR[dB] = 10 \cdot log_{10} \left(\frac{signal\ power}{noise\ power} \right) \qquad (22)$$

The SNR values listed in table 2 were obtained by evaluating several hundred Doppler bursts and forming the median SNR value of all bursts.
Using Mie-theory to calculate the scattered power P_s for 0.12μm latex particles, the expected SNR's were found from equation 18 and are also listed in table 2.
The data in table 2 show that the SNR with UV-light is significantly larger than with green light. Moreover, the probe volumes were of almost equal diameter. By exploiting the possibility with UV-light of halving the

[4] the visibility is taken to be 0.67 for the 60/40 UV-beam splitter.

Table 2: SNR comparison between UV and green

wavelength	257nm	514nm
output power	20mW	20mW
signal amplitude	150mV	20mV
signal frequency	0.94 MHz	0.63 MHz
visibility	0.67 [4]	1.0
SNR calculated	17.7dB	8.3dB
SNR measured	**17.1dB ± 0.5dB**	**9.4dB ± 0.5dB**
output power	20mW	-
signal amplitude	150mV	-
signal frequency	0.73 MHz	-
visibility	0.67	-
SNR calculated	18.8	-
SNR measured	**18.5dB ± 0.5dB**	-

probe volume diameter, without reducing the number of fringes, the same result could have been obtained with only 5mW of UV output power. Furthermore, the visibility at 257nm was only ≈ 0.7. A 50/50 beam splitter for UV-light would help to increase the SNR value at 257nm even more.
The calculated SNR values according to eq. 18 are very close to the measured values, confirming that the expected advantages in using UV-light as plotted in figures 3 and 4 can actually be achieved.

4 EXTENSION TO PDA MEASUREMENTS

4.1 Layout and main properties of the PDA-system

The setup shown in fig. 7 was extended to a PDA by including a second PM at a scattering angle of 20° to pick up a phase difference signal. To overcome the ambiguity of the phase-diameter relationship shown in fig. 5 and to enable the measurement of the refractive index, as well as the particle size and velocity, three detectors and an evaluation according to the "Joint Probability Method" would be necessary [4, 5]. In the presented series of measurements, however, a two detector system sufficed for the size range from 0.1μm to 0.6μm that was of interest. The results presented in section 4.2 show that

1. PDA-measurements can be performed in the submicrometer range with UV-light
2. the precision of the phase determination, i.e. the signal processing in general, at low SNR's has to be improved, especially with respect to determining the phase value 0°.

The phase-diameter relationship for the PDA-system of fig. 7 is shown in fig. 8 for refractive index values ranging from 1.6 to 1.7.

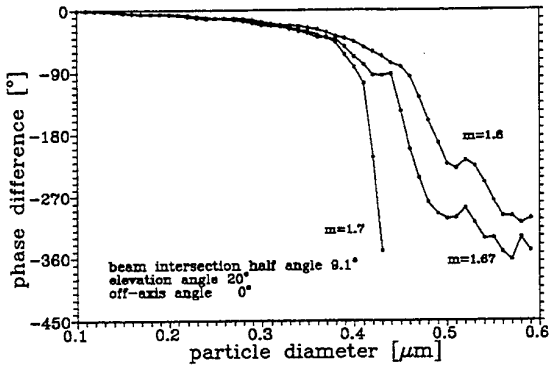

Figure 8: phase-diameter relationship for the implemented PDA, plotted for several refractive indices.

4.2 Verification experiments

Figure 9 shows an example of a measured phase difference distribution after seeding the air flow with 0.1μm and 0.5μm latex particles. Deducing the corresponding size distribution from fig. 9 was difficult for two reasons.

1. The refractive index of latex at $\lambda = 257$nm could not be found in the literature and had to be estimated. Starting from fig. 9, the peak of the phase difference distribution corresponding to 0.5μm latex particles was located at about 300°. Then phase-diameter relationships were computed for several refractive index values between $m = 1.6$ (the refractive index of latex at $\lambda = 514$nm) and $m = 1.7$. As shown in fig. 8, the best phase difference match for a diameter of 0.5μm was found for a refractive index value of $m = 1.67$.
   The size distribution corresponding to the phase-diameter relationship for $m = 1.67$ is shown in fig. 10. The widths of the size intervals in this figure are inversely proportional to the local gradient of the phase-diameter curve.
2. From the phase-diameter relationship in fig. 8, the phase distribution of the first peak in fig. 9 corresponds to a size range from 0.1 to 0.35μm in fig. 10. 0.1μm particles correspond to a phase value near 0°, where the accuracy of the phase difference measurement is lowest (at least with the CSD-method). The SNR-values are also lowest near 0.1μm, further reducing the measurement accuracy. Many particles in this size range were therefore evaluated as too large, although on the oscilloscope one could easily obtain signal pairs with no visible phase shift.
   Improvements in the amplification and filtering of the signals could increase the measurement accuracy. However, for the reliable measurement of the phase difference value 0°, which is vital in

submicrometer PDA, changes in the phase difference determination software near 0° will have to be made.

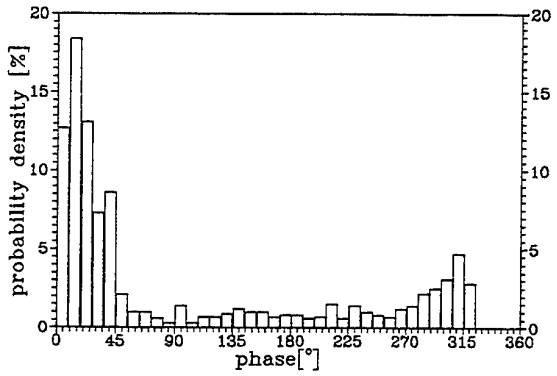

Figure 9: Measured phase difference distribution of the air-flow seeded with 0.1μm and 0.5μm latex particles

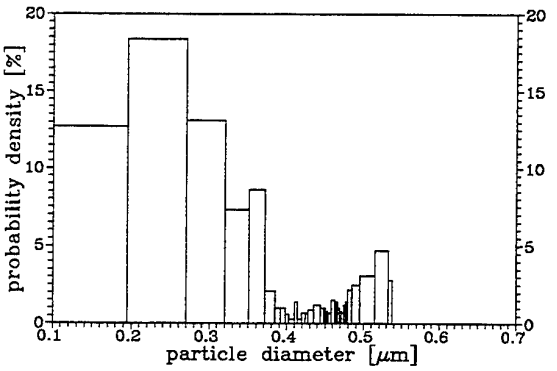

Figure 10: Size distribution determined by comparing fig.9 and fig.8

5 SUMMARY AND CONCLUSION

In this paper, it was shown that for LDA- and PDA-measurements in the submicrometer particle size range the use of UV-lasers is both possible and advantageous. The advantages have been demonstrated experimentally. They include

1. significant increases in signal-to-noise ratios, especially towards higher Doppler frequencies.
2. steeper phase-diameter relationships in the 0.1μm to 0.5μm region, permitting discrimination between 0.1μm and 0.2μm particles.
3. PDA measurements at up to 10 times higher particle concentrations.

With UV-light the SNR was increased by about 10dB relative to green light. To achieve a size measurement range from 0.1 μm up to several μm, including the measurement of the refractive index, it would be necessary to apply the "Joint Probability Method" to the evaluation of the phase differences from a PDA with three detectors.

6 ACKNOWLEDGEMENTS

The work presented in this paper is part of a research project funded by the Deutsche Forschungsgemeinschaft (grant Du 101/35-1).

References

[1] C. Bohren and D. Huffman. *Absorption and Scattering of Light by Small Particles.* John Wiley & Sons, Inc, 1983.

[2] L.Y. Liu, M. Oka, W. Wiechmann, and S. Kubota. Longitudinally diode-pumped continuous wave 3.5-W green lasers. *Optics Letters*, 19:189 – 191, 1994.

[3] K. Bauckhage. The phase-doppler-difference-method, a new laser-Doppler technique for simultaneous size and velocity measurements. *Part. Part. Syst. Charact.*, 5:16–22 – 66–71, 1988.

[4] A. Naqwi and M. Ziema. Extended phase Doppler anemometer for sizing particles smaller than 10μm. *J. Aerosol Sci.*, 23(6):613–621, 1992.

[5] F. Durst, A. Melling, and P. Volkholz. The extension of phase-Doppler anemometry to small particles. In *Proc. 4th Int. Congress on Optical Particle Sizing*, page 185, Nürnberg, 1995.

Scattering of a Gaussian beam by an infinite cylinder: Numerical results in GLMT-framework

K.F. Ren, G. Gréhan, and G. Gouesbet
LESP,
URA CNRS 230/CORIA,
INSA de Rouen, BP 08,
76130 Mont-Saint-Aignan, FRANCE

Abstract

The 3-D scattering of a Gaussian beam by an infinite cylinder is described. A particular attention is paid to the influence of the representation of the incident beam on the results.

1)Introduction

In light scattering theory and applications, most effort has been devoted to the study of spherical particles. Nevertheless, the interest for other particle shapes is warranted for fundamental as well as for industrial motivations.

Among all possible particle shapes, the infinite cylinder shape is particularly attractive because an exact solution of Maxwell's equations exists for an incident plane wave, and, during industrial processes, a lot of particles possess the shape of a cylinder. Such a situation has been at the origin of various devices. One of the more recent effort concerns the study of the potentiality of the phase-Doppler technique to characterize cylindrical particles (see Mignon et a. (1994), Onofri et a. (1995), Mignon et a. (S)).

This potentiality has been analyzed by assuming that the illuminating beam is a plane wave (Mignon et a. (1994), Onofri et a. (1995)) or by using geometrical-optics (Mignon et a. (S)). Nevertheless when compared to the size of the optical probe both the diameter and the length of the cylinder can be very large. Therefore the effect of a local illumination of the cylinder must be understood.

In Rouen, the analytical solution of Maxwell's equations when a Gaussian beam illuminates a cylinder has been obtained by using the distribution theory (see Gouesbet et Gréhan (1994), Gouesbet (1995a, 1995b, 1995c, S1), and references therein). The case of arbitrary shaped beam illumination has also been considered (Gouesbet S2).

This paper is then devoted to the presentation and to the discussion of numerical results obtained by using the above theory when an incident Gaussian beam is normal to the cylinder with the cylinder axis located at the beam waist center, with a particular approach to the beam description.

Section 2) is devoted to the incident beam description. In contrast with the case of a sphere, any inaccuracy in the description of the incident beam far from the beam axis is significant in the scattering process by the cylinder which has an infinite length. Then the scattered field can be accurately predicted only in a finite space domain, strongly depending on the quality of the beam description. Section 3) is devoted to the description of some scattering diagrams with a particular attention paid to the definition of the domain of validity depending on the beam description.

2)Incident beam

To mathematically represent the beam going out from a laser, we can choose between a beam description which perfectly agrees to Maxwell's equations in a framework relying on Davis Taylor expansions

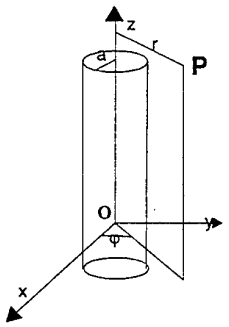

Figure 1: The geometry under study

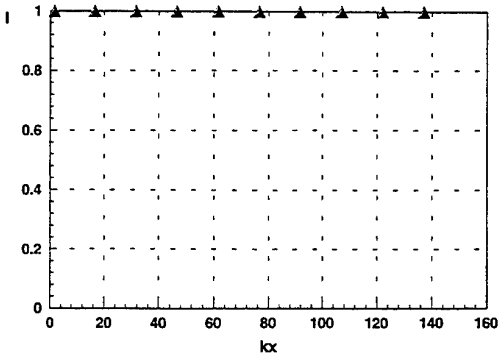

Figure 2: Intensity evolution along x-axis for a quasi-Gaussian beam.

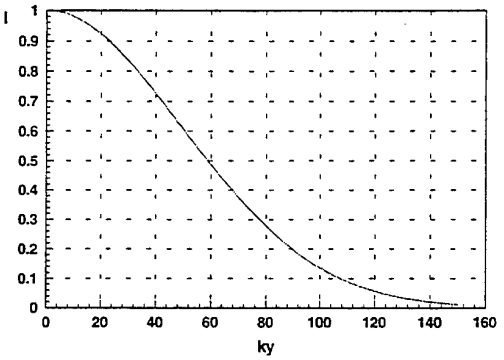

Figure 3: Intensity evolution along y-axis for a quasi-Gaussian beam.

or a beam description which exhibits the fast decrease of the intensity in transverse directions in a modified framework as explained later.

In the case of the representation of the impinging beam in a spherical coordinate system (scattering by a sphere), by using the Davis formulation (Davis (1979)), this issue has been studied in detail by Gouesbet and co-authors (Lock and Gouesbet (1994), Gouesbet and Lock (1994), Gouesbet et a. (1995)). In a cylindrical coordinate system, starting from the Davis formulation, three kinds of beam representation may be defined:

1. Standard beams constructed by using an infinite Davis-like expansion (see Gouesbet and Lock (1994) for details). Such beams exactly satisfy Maxwell's equations. They are said to be Maxwellian and Gaussian. Being at the present time numerically difficult to handle, they are not discussed in this paper.

2. Gaussian beams which are Maxwellian only up to $O(s^{2p})$, in which $s = \lambda/(2\pi w_0)$, with λ the wavelength and w_0 the beam waist radius, is the beam confinement parameter (used in Gouesbet (S1), Gouesbet (1995c), and references therein).

3. Quasi-Gaussian beams obtained from a remodelling of a first-order Davis beam. The handling of these beams would fit in the arbitrary shaped beam theory (Gouesbet, (S2)).

The incident beam propagates along the Ox axis, towards negative x's. The incident electric field polarization is perpendicular to the plane defined by the cylinder axis z and by the incident vector e_i. The incident beam is perpendicular to the infinite cylinder. The cylinder radius is a. The cylindrical coordinates (r, φ, z) are defined in Fig. 1.

2-1) Behaviour of a Quasi-Gaussian beam in cylindrical coordinates

From the (r, φ, z)-components of the electromagnetic field, the intensity is computed along x, y, and z axis. Fig. 2 plots I versus kx, Fig 3 plots I versus ky, and Fig 4 plots I versus kz. The beam confinement parameter is $s = 0.01$, which corresponds to a beam waist radius $w_0 \approx 7.9\,\mu m$ for an incident wavelength of $0.5\ \mu m$. The fast decrease of the intensity in transverse directions is observed (see Figs 3 and 4), while the intensity along the beam axis is founded nearly constant on a short distance (see Fig 2), as it should be.

To save room, the discussion is from now on limited to the intensity along the y-axis. The prop-

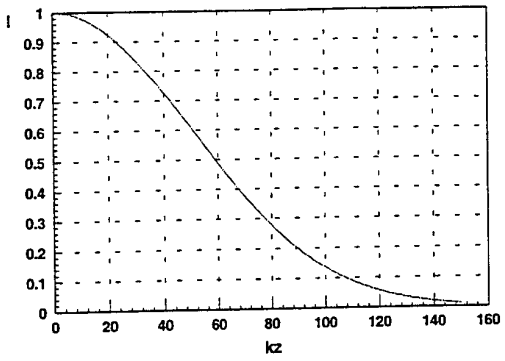

Figure 4: Intensity evolution along z-axis for a quasi-Gaussian beam.

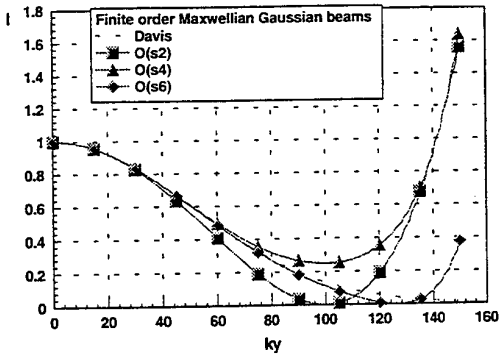

Figure 5: Comparisons between Maxwellian Gaussian beams at finite order and the first Davis beam.

erties discussed for that component are essentially true for the two others.

2-2) Behaviour of Maxwellian Gaussian beams of order s^{2p}

Gouesbet (1996) gives the expressions of the incident field in Cartesian coordinates up to $O(s^{10})$. From these expressions, the incident field in cylindrical coordinates (r, φ, z) is easily obtained. For example, H_z^i at order s^4 is given as:

$$\begin{aligned} H_z^i &= H_0 \exp(ikr\cos\varphi)\left\{-1+s^2\left[Z^2+\right.\right. \\ &\quad .\sin^2\varphi R^2+2i\cos\varphi R-E_{u000}^2\left.\right] \\ &\quad \left.+O(s^4)+..\right\} \end{aligned} \tag{1}$$

where E_{u000}^2 is a constant which depends on the beam description (Standard, Localized or Modified Localized). We use the coefficients E_{u000}^2 corresponding to a standard beam in that paper except in section 2.3. Similar expressions exist for E_z, E_r, E_φ, H_r, H_φ. Then the incident intensity components, obtained by applying the Poynting theorem to the incident field are computed.

Figure 5 compares the incident intensity along y-axis, described by a quasi-Gaussian beam and by a Maxwellian Gaussian beam at limited orders s^2, $s^4$and s^6.

For the three Maxwellian Gaussian beams at limited orders the general behaviour is the same: when ky increases the intensity decreases down to a minimum value and then increases up exponentially. For $ky < 130$, increasing the order of the Maxwellian Gaussian beam, the fit with the quasi-Gaussian beam is better and better, but in all cases

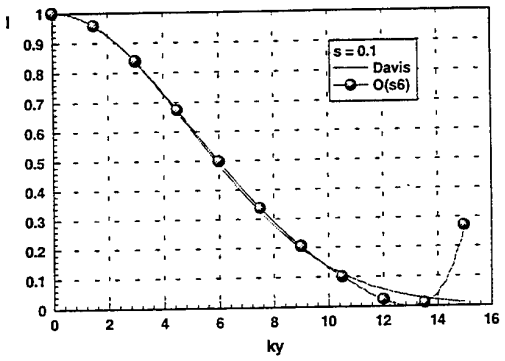

Figure 6: 0.8 μm beam waist radius.

when ky is larger than about 130, the Maxwellian Gaussian beam is characterized by an exponential increase of the intensity.

That behaviour is not improved when increasing the beam waist radius. Figures 6 and 7 display I versus ky with s as the parameter ($s = 0.1$ corresponds to a beam waist radius of about $0.8\,\mu m$, $s = 0.001$ to a beam waist radius of about $80\,\mu m$). The increase of the intensity is observed at kr values of about 13, 130 and 1 300 for s of 0.1, 0.01 and 0.001 respectively, (see Figs 6, 5 and 7), i.e. at equal values of ky when reduced by the values of w_0.

2-3) Comparison of S, MLA and LA descriptions at limited orders

The aforementioned divergence of the intensity I when ky is larger than the beam waist radius (about 130 for $w_0 = 8\,\mu m$) does not depend on the

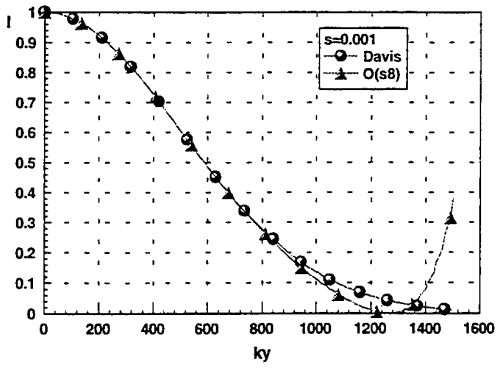

Figure 7: 80 μm beam waist radius

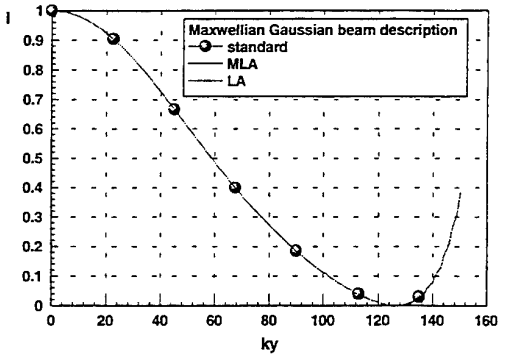

Figure 8: Comparison between Maxwellian Gaussian beam at order $O(s^2)$ for three kinds of beam (Standard, Modified Localized Approximation, Localized Approximation)

beam description at limited orders. In particular, if the value of the coefficient E^2_{u000} is taken as the one corresponding to the S (Standard), LA (Localized Approximation) or MLA (Modified Localized Approximation) cases, then the obtained curves cannot be distinguished (Fig 8). Here, the chosen order with respect to s is the main parameter. Beyond $O(s^{10})$ however, the required amount of algebra becomes prohibitive.

2-4) Reconstructed incident fields

From Gouesbet (1995b), the incident beam shape distributions $I_{m,TE}(\gamma)$ are defined by:

$$\left\langle I_{m,TE}(\gamma), (1-\gamma^2) J_m(R\sqrt{1-\gamma^2}) \exp(i\gamma Z) \right\rangle = \frac{1}{2\pi(-i)^m} \int_0^{2\pi} \left(\frac{H_z^i}{H_0}\right) \exp(-im\varphi) d\varphi \qquad (2)$$

Then the quality of the incident beam shape distributions directly depends on the quality of the description of the beam. In Gouesbet (1995b), the incident beam is assumed to be a Maxwellian Gaussian beam up to order $0(s^2)$ and the distribution is assumed to be under the form $\sum a_k \delta^{(k)}(\gamma)$. The incident magnetic field component H_z^i is given by:

$$H_z^i = H_0 \sum_{m=-\infty}^{+\infty} i^m \exp(im\varphi) \left\{ [-1+ \left[s^2(m^2+Z^2)\right] J_m(R) + s^2 R J_m'(R) \right\} \qquad (3)$$

Fig 9 displays the intensity I versus ky, the parameter being the number $m_{\max}$ of terms in the summation (Eq. 3). For $m_{\max}$ equal to or larger than 200, the reconstructed beam perfectly agrees to the Maxwellian Gaussian beam at order $O(s^2)$ as it should (see Fig 5).

Alternatively, in Eq. 2, we could assume that the distribution is under the form of:

$$\int_{-1}^{+1} I'_{m,TE}(\gamma') \, \delta(\gamma - \gamma') \, d\gamma' \qquad (4)$$

multiplying by $\exp(-i\gamma' Z)$, integrating on Z between -∞ and +∞, the beam shape distribution coefficients are obtained as:

$$I'_{m,TE} = \frac{i^m}{4\pi^2 (1-\gamma'^2) J_m\left(R\sqrt{1-\gamma'^2}\right)} \int_0^{2\pi} \exp(-im\varphi) \int_{-\infty}^{+\infty} \frac{H_z^i}{H_0} \exp(-i\gamma' Z) \, d\varphi dZ \qquad (5)$$

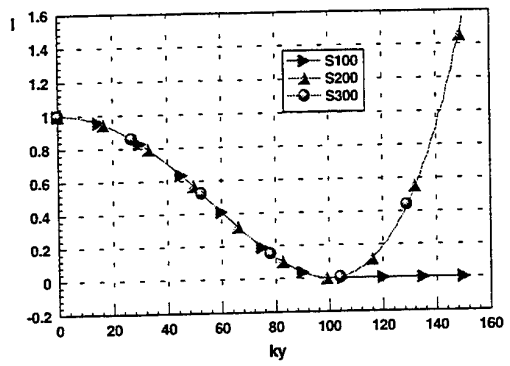

Figure 9: Comparison of I versus ky. The parameter is the number of terms $m_{\max}$ in the summation.

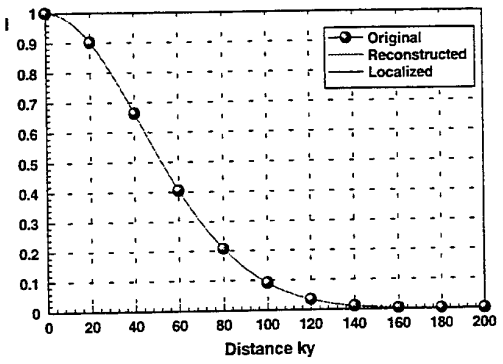

Figure 10: Comparison between the original, reconstructed from a quasi-Gaussian beam and reconstructed from a localized approximation incident fields for a quasi-Gaussian beam.

This expression is identical to the one obtained in the framework of plane wave spectrum.

As it should be, if in Eq. 5, the incident field H_z^i is given as a Maxwellian Gaussian beam at a finite order $O(s^n)$, the expressions of Gouesbet (1996) are reobtained.

If the incident field H_z^i is assumed to be a quasi-Gaussian beam, and numerically integrate the r.h.s. of Eq. 5 to compute the BSD, the reconstructed incident field perfectly agrees with the original quasi-Gaussian beam, as it should (Fig 10). Let us note that, in this process, a renormalization over z is also carried out in the same spirit than in Gouesbet et a. (S).

2-5) Reconstructed field with a localized approximation

The computation of the quadrature in Eq. 5 is time consuming. We now introduce an approximation to save computation time.

To compute the beam shape coefficients describing a Gaussian beam in spherical coordinates, the most efficient method is the localized approximation (LA) which deduces the beam shape coefficients from the incident field by applying an operator $\hat{F}$ to the E_r component. The operator $\hat{F}$ carries out the following transformation: $\left[r = (n+\frac{1}{2})\frac{\lambda}{2\pi}, \theta = \frac{\pi}{2}\right]$. This operator has been introduced by analogy to the van de Hulst approach without however any rigorous demonstration (Gréhan et a. (1986)), and later rigorously demonstrated (Lock and Gouesbet (1994)). The rigorous demonstration implies a small change $\hat{F} = \left[r = \sqrt{(n-1)(n+2)}\frac{\lambda}{2\pi}, \theta = \frac{\pi}{2}\right]$, leading to the Modified Localized Approximation (MLA). This modification has no effect when the beam is not extremely focused ($w_0 \approx \lambda$).

Without any mathematical demonstration, the localization operator to be applied in cylindrical coordinates is rewritten as $\hat{G} = \left[r = m\frac{\lambda}{2\pi}, \varphi = \frac{\pi}{2}\right]$, and applied to the field components E_z and H_z of a quasi-Gaussian beam to obtain the beam shape distributions in cylindrical coordinates. These beam shape distributions may be expressed in terms of beam shape coefficients reading as:

$$I_{m,TE} = \frac{1}{2\sqrt{2\pi}s} \exp\left[-m^2 s^2 - \frac{\gamma^2}{4s^2}\right] \qquad (6)$$

The numerical results obtained by using this localization approach are identical to the ones obtained by using quadratures with the quasi-Gaussian field components E_z or H_z as kernels. Such a comparison is displayed in Fig. 10.

This above rather extensive discussion concerning finite beam representations in cylindrical coordinates is necessary to understand the behaviour of computed scattered fields.

3) Scattered fields

In this section, the intensities scattered by a glass cylinder (M=1.5) of 1 μm diameter in air, are computed assuming that the incident beam is a Maxwellian Gaussian beam at order $O(s^2)$ or a quasi-Gaussian beam. A particular attention is paid to the behaviour of the scattered intensity when z and r are the parameters. As underlined in Gouesbet 1995b, scattered field evaluations for an $O(s^2)$ Maxwellian Gaussian beam may be ex-

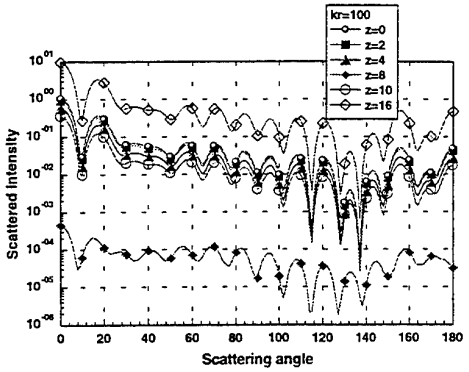

Figure 11: Evolution of the scattered intensity with z as the parameter for a Maxwellian Gaussian beam at order $O(s^2)$.

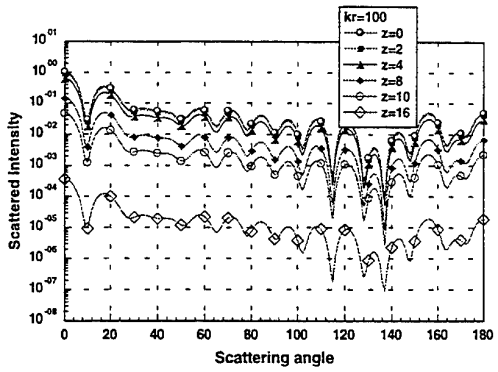

Figure 12: Evolution of the scattered intensity with z as the parameter for a quasi-Gaussian beam.

pected to be valid only essentially in a near-field zone, while a quasi-Gaussian beam should give realistic results for both the near-field and far-field zones.

3-1) Scattered fields versus z

Fig 11 displays the evolution of the scattered intensity predicted for a Maxwellian Gaussian beam at order $O(s^2)$. The distance kr is 100. The beam waist radius is 8 μm, and the incident wavelength is 0.5 μm. The scattering diagram at $z = 0$ μm fits well the plane wave prediction. The main behaviour is that, when the distance z increases, the scattered intensity decreases down to $z = 8$ μm, and, for z larger than 8 μm, the scattered intensity increases again. This increase of the scattered intensity is directly connected to the increase of the intensity in that kind of beam as described in Fig 5, and hence is an artefact of the beam description.

Fig 12 displays, for the same parameters as in Fig 11, the scattered intensity predicted for a quasi-Gaussian beam. Here the scattered intensity regularly decreases as z increases. For $z = 0$, the scattering diagram is identical to the one predicted for the Maxwellian Gaussian beam. But when z increases, the decrease of the scattered intensity is not so large as in Fig 11 when z is smaller than 8 μm. Then for z larger than 8 μm, the scattered intensity predicted in Fig 12 is smaller than the one predicted in Fig 11 for the same parameters. From Figs 3, 4 and 5, it is noted that in transverse directions at ky or kz equal to 100 ($z = 8\mu m$) corresponds the absolute minimum of the predicted intensity of an incident Maxwellian Gaussian beam

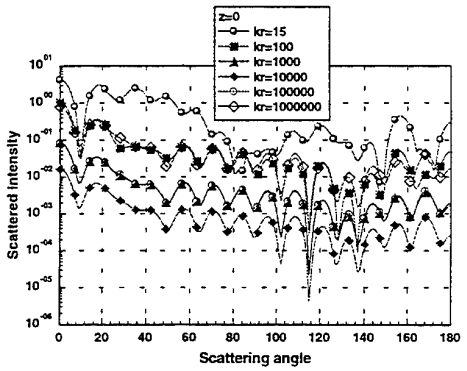

Figure 13: Evolution of the scattered intensity with the distance kr as the parameter for a Maxwellian Gaussian beam at order $O(s^2)$.

at order $O(s^2)$, then explaining this behaviour of the scattered intensity.

3-2) Scattered fields versus r

For the same particle and beams, Fig 13 displays the evolution of the scattered intensity at $z = 0$, with the distance from the cylinder kr as the parameter for an $O(s^2)$ Maxwellian Gaussian beam. As kr increases, the intensity of the scattered beam decreases down to $kr = 10000$ ($r \approx 800\mu m$). Then the intensity increases as r increases. Here again, the scattering is dominated by the exponential part of the Gaussian Maxwellian beam and is therefore an artefact of the beam description.

Conversely (Fig 14), for a quasi-Gaussian beam, the scattered intensity regularly decreases when r increases. Nevertheless, let us remark that for very

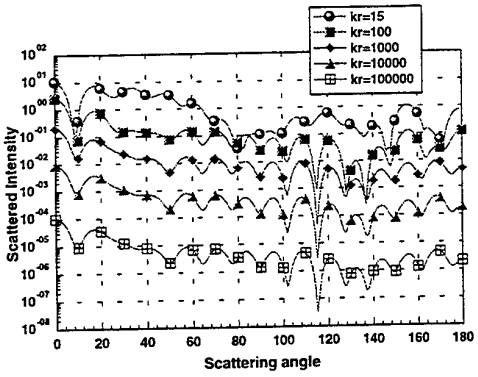

Figure 14: Evolution of the scattered intensity with the distance kr as parameter for a quasi-Gaussian beam.

small $kr = 10$, quasi-Gaussian beam predictions agree with Maxwellian Gaussian beam predictions when the full near-field formalism is used. For kr larger than 100, quasi-Gaussian beam predictions in the near-field and the far-field frameworks agree together. The agreement also exists with the Maxwellian Gaussian beam at order $O(s^2)$ when kr is smaller than about 10000. For larger values of kr, quasi-Gaussian beam predictions are difficult to carry out due to numerical difficulties in evaluating quadratures. It is strongly believed that these difficulties may be overwhelmed (current work).

3-3) Spreading of the scattered intensity

The spreading of the scattered field is an important phenomenon in a lot of applications as in phase-Doppler extension to the cylinder case (Mignon et a. (1994), Mignon et a. (1995), Mignon et a. (S)). This subsection is devoted to that issue.

Let us now repeat Figs 11 and 12 ($k = 100$) for $kr = 4000$ ($r \approx 320\mu m$), and consider from these families of curves the scattered intensity versus z for both values of kr. It is then possible to define a spreading of the scattered intensity. For the quasi-Gaussian beam, this spreading is found to agree with the spreading of the incident beam. Of course, such an agreement cannot be recovered in the case of Maxwellian Gaussian beams at $O(s^2)$ due to aforementioned artifacts in the beam description.

4) Conclusion

In this paper the implications of the beam representation on the scattering of a 3-D focused finite beam by an infinite cylinder has been explored. The advantages and limitations imposed by assuming that the incident beam is a quasi-Gaussian or a Maxwellian Gaussian beam at order $O(s^{2p})$ have been quantified, according to the transverse distance z and the distance from the axis r.

The next step of that work is to describe the scattering of a finite beam by an infinite cylinder of arbitrary orientation and arbitrary location, and to merge such a representation in a phase Doppler code.

References

L.W. Davis, 1979. Theory of electromagnetic beams *Physical Review A,* 19(3):1177-1179

G. Gouesbet and G. Gréhan, 1994. Interaction between shaped beams and an infinite cylinder, including a discussion of Gaussian beams. *Part. Part. System Charac.*, 11:299–308

G. Gouesbet and J.A. Lock, 1994. A rigorous justification of the localized approximation to the beam shape coefficients in the generalized Lorenz-Mie theory. II: off-axis beams. *JOSA A,* 11(9):2516–2525.

G. Gouesbet, J.A. Lock, and G. Gréhan, 1995. Partial wave representation of laser beams for use in light scattering calculations. *Applied Optics,* 34(12):2133–2143.

G. Gouesbet, C. Letellier, K.F. Ren and G. Gréhan (S), Discussion of two quadrature methods to evaluate beam shape coefficients in generalized Lorenz-Mie theory. To be published by Appl. Optics.

G. Gouesbet, 1996. Higher-order descriptions of Gaussian beams. J. of Optics, 27, 1, 35-50, 1996

G. Gouesbet, 1995a. The separability theorem revisited with application to light scattering theory. *J. of Optics (Paris),* 26(3):123–135.

G. Gouesbet, 1995b. Interaction between Gaussian beams and infinite cylinders, by using the theory of distributions. *J. of Optics (Paris),* 26(5):225–239.

G. Gouesbet, 1995c. Scattering of a first-order Gaussian beam by an infinite cylinder with arbitrary location and arbitrary orientation. Part. Part. Syst. Charact. 12, 242-256

G. Gouesbet, S1, Scattering of higher-order Gaussian beams by an infinite cylinder, Submitted to J. of Optics

G. Gouesbet, S2, Interaction between an infinite cylinder and an arbitrary shaped beam, Submitted to Applied Optics

J.A. Lock and G. Gouesbet, 1994. A rigorous justification of the localized approximation to the beam shape coefficients in the generalized Lorenz-Mie theory. I: on-axis beams. *JOSA A*, 11(9):2503–2515.

H. Mignon, G. Gréhan, G. Gouesbet, T.H. Xu, and C. Tropea, S. Measurements of cylindrical particles using phase Doppler anemometry. submitted to Applied Optics.

H. Mignon, F. Onofri, G. Gréhan, G. Gouesbet, and C. Tropea, 1994. Mesure de particules non sphériques par phase-Doppler: cas des cylindres et des particules irrégulières. In *Recueil des actes du 4^{eme} congrès francophone de vélocimètrie laser*, pages 1–4. Poitiers-Futuroscope, 26-29 septembre.

F. Onofri, H. Mignon, G. Gouesbet, and G. Gréhan, 1995. Phase-Doppler measurements of non-spherical particles: cylindrical and multilayer particles. In PARTEC, editor, *4th International Congress Optical Particle Sizing*, pages 275–284. Nürnberg, Germany, 21-23 March.

TIME DOMAIN SINGLE TONE ANALYSIS USING QUADRATURE ALGORITHM

V. Strunck, H. Müller, D. Dopheide

Laboratory for Fluid Flow Measuring Techniques
Physikalisch-Technische Bundesanstalt
Bundesallee 100
D-38116 Braunschweig

ABSTRACT

Processing a Laser Doppler signal usually requires high efforts to the data reduction system. But for the case of a single scatter centre in the measuring volume, the method proposed converts the sinusoidal output of a photodiode to a linear function in time of the position of the scatterer depending on its motion and to the Gaussian shape amplitude of the signal's envelope. The amplitude of the envelope reflects the presence of a scatterer and is a measure of the uncertainty of tracking its position. The position course of the scatterer allows by differentiation to evaluate velocity, acceleration and higher order moments at specified times inside the probe volume. The method exhibits the same accuracy as Fourier based methods operating at the Cramér-Rao bound, but it is time resolving and involves the possibility of being processed in real time because it performs in the time domain. Aspects of uncertainty, accelerating scatterer and phase Doppler application are outlined.

1. THEORY

The modulated part of a laser Doppler signal with frequency w and amplitude a is assumed to be a function of time t of the real part of $z(t) = a(t)\exp(i\omega t)$. For a continuos motion in direction of x of a scatterer with a velocity u the time t can be expressed as x/u and as $2\pi x/(\omega d)$ using fringe distance d, see Czarske et al (1993). The new description is a complex Doppler signal $z(x) = a(x)\exp(i2\pi x/d)$. Its amplitude $a(x)$ is a measure of the envelope of the measuring volume in space and its phase $\varphi = 2\pi x/d$ is linear in x and presents the position of the scatterer. The inconvenient sinusoidal shape of the signal in figure 1a has disappeared in favour of a simple relation in figure 1b.

The signal energy $a^2(x)$ will be used in the following as weight of the presence of the scatterer in the measuring volume. To calculate the momentary velocity, acceleration, etc., the position $x(t) = \varphi(t)\, d/(2\pi)$ can be differentiated with respect to time.

Particle sizing with Phase Doppler Anemometer requires to measure the phase difference of signals of two separated photo receivers. The phase difference $\Delta\varphi(t)=\varphi_2(t)-\varphi_1(t)$ obtained by quadrature signal analysis also allows to investigate dual burst signals as in the case of separable reflecting and refracting modes.

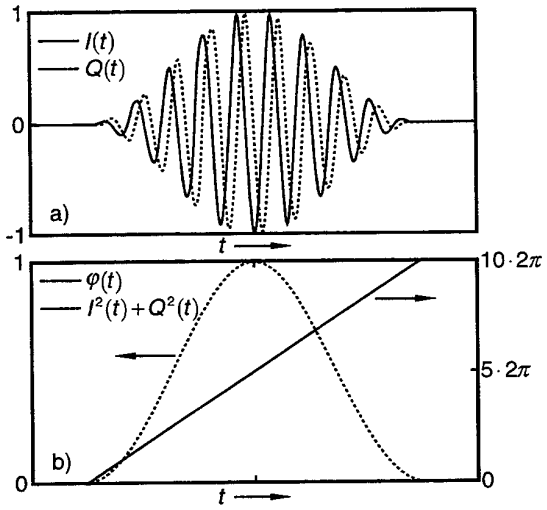

Fig. 1 a) Inline signal I and quadrature Q signal
b) Squared amplitude $a^2 = I^2+Q^2$ and phase signal φ

2. GENERATION OF QUADRATURE SIGNALS AND MEAN VALUE EVALUATIONS

All that has to be done to obtain a complex LDA signal is to use the inline signal and quadrature signal of a LDA, easily derived from sensors with frequency shift (Bragg cells, rotating gratings, ...) by downmixing the Doppler signal with the shift frequency itself giving the inline signal, and downmixing with the 90° phase shifted shift frequency, giving the quadrature signal, see Czarske et al (1993). The electrical components needed, all available on the market at low costs, are one 90° phase shifter and two multiplying mixers followed by two low pass filters specified for the shift frequency range. Common to frequency shift systems is the missing pedestal making the high pass filter useless. Moreover, in a quadrature system a high pass filter at the quadrature signal output would reject the information of zero velocities, because zero velocities generate DC quadrature signals, see Müller et al (1995).

If the LDA is not a frequency shift system and does not produce a quadrature signal, the quadrature signal must be generated. It has to be remarked that the quadrature signal generation method cannot supply directional information, because single Doppler signals have none, also zero velocities cannot be processed. But for single Doppler signals including some periods quadrature signals can be generated in real time by delaying the Doppler signal by a quarter of a period T or by differentiation. The delaying method needs to know a priori the Doppler frequency. The differentiation method also needs an estimation of the resulting Doppler frequency because of its influence as a factor on the amplitude of the differentiated signal. It will be shown how they perform with an assumed frequency f of 32 and with the exact frequency. The best method is using the Hilbert transform at the cost of two real fast Fourier transforms (RFFT), but it is far from being processed in real time. Whenever more signal information than simply the velocity is needed, the algorithm is faster than short time Fourier transforms (STFT) or Wigner-Ville time series analysis.

The methods investigated use the single Doppler signal I with the frequency f to generate the quadrature signal Q:

Delay method: $Q_j = I_{j+T}$ and $T=1/(4f)$

Differentiation: $Q_j = (I_{j+1}-I_{j-1})/(2\omega)$ and $\omega = 2\pi f$

Hilbert transform: $Q = \mathrm{RFFT}^{-1}(i\ \mathrm{RFFT}(I))$

The mean frequency f of the quadrature method best is calculated using a weighted linear regression. The squared amplitudes a_j comfortably can be used as weighting coefficients. To eliminate the noise floor, small amplitudes are set to zero.

The mean frequency f of the counter method was evaluated using a linear interpolation of zero crossing points of signal I at a moderate signal level and by counting the number of periods in the time interval to get the averaged period.

The mean frequency f of the Fourier method was obtained by determination of the centre of gravity of the Doppler peak in the spectra.

A computer simulation of Doppler signals with SNR = 20 dB has been performed to compare a simple counter processor model, the Fourier (FFT) and the quadrature methods using delayed, differentiated and Hilbert transformed signals. The sample burst fits completely due to its raised cosine shape into the observation window of 512 sample points, indexed in the upper equations by j, with a depth of eight bit. The frequency equivalent to the number of periods in the window was varied from 4 to 64. Figure 2 shows the averaged error curve of 6000 processed bursts for each method.

The Fourier method and the quadrature method using the Hilbert algorithm are in accordance with the Cramér-Rao bound, see Wriedt et al (1989). The quadrature method using a constant time delay of four sample points shows better results in a large range than the counter processing algorithm using interpolated zero crossings. Remarkable is the fact, that at a frequency of 4 the signal is not in a real quadrature, because the phase shift between the inline and quadrature signal is only 11,25°.

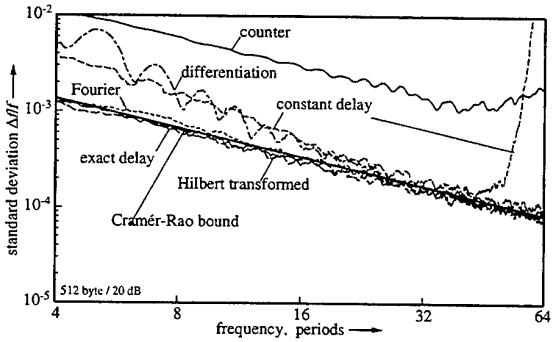

Fig. 2 Comparison of frequency uncertainties for several Doppler analysis methods

But the constant time delay method fails completely, when the phase difference between inline and quadrature signal is 180° at the frequency 64. Processing the constant time delay method twice, starting first with a delay of one sample point to get an estimate and a second time with the estimate for the accurate result, is shown if figure 2 as exact time delay method that also approaches the Cramér-Rao bound. However, buffering of a complete signal is needed for this reduction of uncertainty.

The differentiation method exhibits good results for high frequency, but at low frequency noise is increasing in the generated quadrature signal due to the differentiation process. Moreover, there is a misfit of the amplitudes between the inline and the quadrature signal, i.e. at a frequency of 4 the amplitude of quadrature signal Q is only one by eight of the inline signal amplitude.

Both constant delay and differentiation methods show better results in the mean frequency evaluation than the counter method due to the high tolerance of the quadrature algorithm on phase deviations and amplitude mismatch. Together with the linear regression using the signal energy as weighting factor these methods compensate for arising errors from phase and amplitude. In a real measurement the linear regression presents also a simple indicator to signal validation, the regression coefficient. Strong deviations from the linear behaviour of the phase course can easily be rejected by allowing only validations with a regression coefficient near to one. In the outlined computer simulation, the validation has been left out.

3. EVALUATION OF ACCELERATION IN THE MEASURING VOLUME

The quadrature analysis allows an easy access to the momentary location of a scatterer in the measuring volume. Differentiation versus time also gives the momentary velocity. By comparing the momentary velocity with the mean velocity, the mean acceleration is evaluable using again regression methods. To show the sensitivity of the method, a frequency change of 1% inside a Doppler signal with an overall SNR of 20 dB using constant white noise was generated and analyzed with the quadrature method and compared with the large-scale Wigner-Ville analysis, see Skerl et al (1994). Figure 3 depicts the momentary frequency (broken straight line) and the results of both

methods. In the middle of the signal where amplitudes and the SNR are high, both methods perform with a good accuracy. Because the quadrature analysis is faster and needs far less memory in a computer, it is a good instrument to improve the parallelity in the fringe system, or to measure tracer behaviour in shocks or gradients in reversing flows.

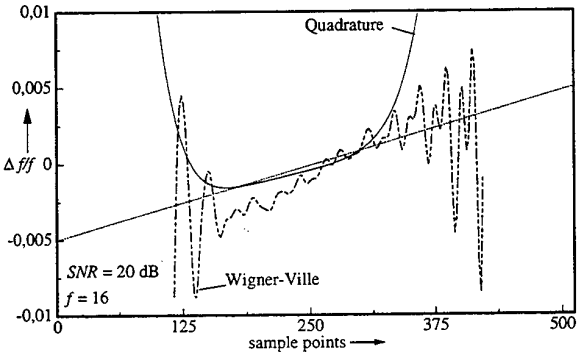

Fig. 3 Linear frequency change of 1% analyzed by Wigner-Ville and quadrature method

4. PHASE DOPPLER SIGNAL ANALYSIS USING QUADRATURE

The quadrature analysis can be an enrichment for phase Doppler data reduction systems. No correlation has to be calculated, only the phase curves of both quadrature signals simply have to be subtracted. Moreover, in the complicated dual burst system [5] when a reflected part of light is followed by a refracted one, no more special time resolving spectral methods are needed. Again, a simulation of two phase Doppler signals with an SNR of 20 dB and with a differential phase jump from -45° (reflection mode) to +15° (refraction mode) are exhibited in figure 4. Each double burst PDA signal consists actually of a pair of overlapping signals and is changing its phase smoothly in the middle of the figure, the first by 120° and the second by 60°. Both dual burst Doppler signals are shown in the upper part of the figure. The resulting phase difference can be seen in the lower part of figure 4. In general, the phase difference of phase Doppler signal should be between -180° and +180°, the modulo function eventually has to be used to keep the remainder of the phase difference inside this range. It has not been proofed that the phase analysis operates at the Cramér-Rao bound, but it promises that it does.

The amplitude maxima of the dual burst PDA signals denote supplementarily at which parts of the signals the phase difference of the reflection and of the refraction mode has to be evaluated. This additional information allows not only to measure the diameter of the scatterer but also its refraction index. The phase difference change in such type of PDA needs a survey on the velocity measurement. The phase change has influence on the velocity measurement because it deceives an acceleration that it not present in reality. In order to measure the velocity of a scatterer in a dual burst PDA, very similar to measure the surface velocity in vibrometer applications, the phase changing part of the signal has to be left out. One tool is the amplitude criteria exhibiting strong phase jumps inside a signal at places of a diminished amplitude. A second tool is to analyse the acceleration. When there is a sudden strong acceleration inside a signal of a scatterer, it is a phase change and this part has to be rejected.

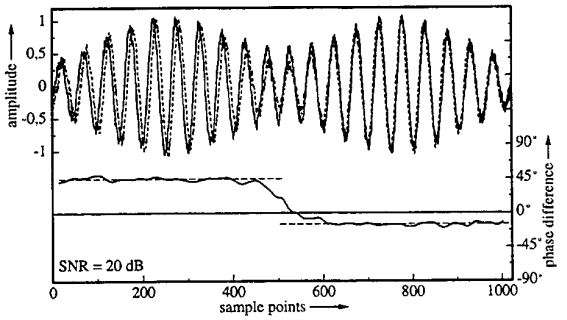

Fig. 4 Dual burst PDA signals and their phase difference curve

There are certainly a number of unnamed applications where quadrature analysis gives an easy and fast access to the solution. It has been the aim to recognize the LDA signal as a description of the scatterer's location in the measuring volume. The derivates versus time of the location allows to measure velocity and acceleration. Also the phase difference measurement in PDA applications can be understood as a distance measurement between two distinct parts on or in a scatterer. To put the algorithm in practice, a fast conversion method has been developed for use in computers and in a ASIC circuit in the following.

5. IMPLEMENTATION OF QUADRATURE ANALYSIS IN ASIC

To use the promising quadrature signal analysis for data reduction, a new type of processor was designed according to figure 5.

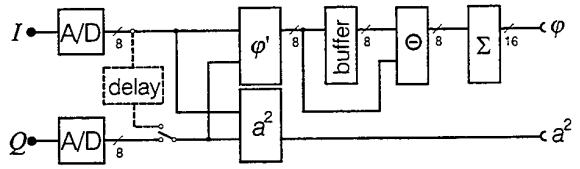

Fig. 5 Basic Doppler processor using quadrature signal analysis

Two Analogue to Digital converters (A/D) digitize the inline I and the quadrature signal Q. Without a quadrature signal, a substitute signal can be generated from the inline signal with a shift register or a differentiation circuit to obtain the missing signal. Instead of calculating the phase φ via the arcus tangent function from two eight bit values, a look-up table for φ of 64 Kbytes is easy and covers all combinations. One 64 Kbytes table gives the momentary value a^2 of the squared amplitude, the second table gives a phase φ '. Because the table with phase can only present values between $-\pi$ and $+\pi$ (modulo of 2π), two successive samples are differentiated. The phase differences again are integrated to yield the complete phase φ as shown in figure 1b.

Leaps in the change of φ ' from $-\pi$ to $+\pi$ and vice versa contradict the Nyquist theorem and are suppressed simply by neglecting the carry signal of the differentiating circuit ($\ominus$). The digitized output signals $a^2(t)$ and $\varphi(t)$ can now be easily processed by using subtractor, adder and multiplier and accumulator circuits to obtain velocity and acceleration mean values. A first approach to evaluate velocity has been performed in one field programmable gate array (FGA Xilinx 3000). To be operated at 100 MHz, the EPROMs for the arcus tangent and amplitude tables have been substituted by fast static RAM.

6. CONCLUSIONS

A method to investigate Doppler signals in the time domain using quadrature algorithm schemes has been outlined. It has been shown in the case of a single scatterer that this method stands out for a minimum of uncertainty of determining reduced data. The sinusoidal shape of the Doppler signal can be linearized in real time and also processed in real time. Not only velocity but also acceleration is measurable. The method allows to study without effort the momentary parameters of interest, as shown for the case of accelerating flows and more complicated dual burst PDAs. The implementation of the algorithm into hardware is possible without great requirements and leads to a highly miniaturized new type of LDA processor.

7. REFERENCES

Czarske, J., Hock, F. and Müller, H. 1993, Quadrature demodulation — a new LDV-burst signal frequency estimator, Proceedings of the 5th International Conference, Laser Anemometry — Advances and Applications, SPIE Vol. 2052, p. 79–86

Müller, H., Többen, H., Strunck, V., Arndt, V., Dopheide, D. 1995, Quadrature demodulation in novel frequency shift LDV systems as an alternative to fringe biasing, 6th EALA/ASME/JSME Laser Anemometry Conference, FED-Vol. 229, p. 455–458, South Carolina, USA

Onofri,F.; Gréhan, G.; Gouesbet, G.; Xu, T.-H.; Brenn, G.; Tropea, C., 1994, Phase Doppler Anemometry with dual burst technique for particle refractive index measurements. Proceedings of the 7th International Symposium on Applications of Laser Techniques to Fluid Mechanics, paper 21.4, Lisbon (Portugal)

Skerl, O., Schmidt, W., Specht, O., 1994, Wigner-Verteilung als Werkzeug zur Zeit-Frequenz-Analyse nichtstationärer Signale, Technisches Messen 61, 1

Wriedt, T., Bauckhage, K.A., Schöne, A., 1989, Application of fourier analysis to phase-Doppler-signals generated by rough metal particles, IEEE Transactions on Instrumentation and Measurement, Vol. 38, No. 5, p. 984–990

SESSION 7

Combustion II

TURBULENT PROPAGATION VELOCITY AND MEAN REACTION RATES OF PREMIXED TURBULENT FLAMES IN STAGNATION FLOWS

E. Bourguignon, Y. Michou and I. Gökalp

Centre National de la Recherche Scientifique
Laboratoire de Combustion et Systèmes Réactifs
1 C, Avenue de la Recherche Scientifique, 45071 Orléans, France

ABSTRACT

A new method to measure the burning rate of planar premixed turbulent flames stabilized in stagnation flow is explored. The principle is to determine the mass of reactants burned within a control volume that extends from pure reactants to the stagnation plane. The method is based on the balance of conditional mass fluxes in this control volume. Following this method, mean burning rates and turbulent flame speeds can be deduced from the measurements of the conditional reactant velocities and the reaction progress variable. This measurement technique is applied in this study to premixed turbulent flames in the opposed jet configuration and this paper describes the results of an initial parametric study.

1. INTRODUCTION

The determination of the turbulent flame speed and the mean reaction rate in premixed turbulent combustion is a fundamental problem for many energy systems. Many configurations and methodologies have been adopted to caracterize them. A few years ago, Cho et al. (1986) introduced the use of the turbulent stagnation flow configuration for fundamental studies of premixed turbulent flames. They demonstrated that, because of its planar configuration, the stagnation flame is useful to determine the propagation speed of turbulent premixed flames. Following previous studies by Wu et Law (1984) and Law et al. (1986) for laminar flames in this configuration, the turbulent burning velocity defined as the mean axial velocity at the upstream boundary of the turbulent flame brush. However, recent work by Shepherd and Kostiuk (1994) showed that the flow speed at the leading edge of a flame stabilized in a divergent flow cannot be used to determine the mean burning rate. In a more recent paper, Kostiuk and Shepherd (1996) have detailed the way to obain the turbulent flame speed based on the determination of the mean burning rate accross a flame brush. A technique for directly measuring the mean burning rate of steady turbulent flames in divergent flows has been proposed. The analysis is limited to the assumption of the wrinkled flame regime where the flame front is assumed to be a thin reaction zone. This technique is applied here to flames stabilized in opposed turbulent flows. The present paper describes the results of an initial parametric study.

2. EXPERIMENTAL SYSTEM

Figure 1 shows the experimental set-up. Two geometrically identical burners (30 mm diameter) are mounted on a computer controlled two-axe traverse system. The upper one is water-cooled. The burners are supplied with identical premixed methane/air mixtures. The nozzles are placed such that the generated opposed jet flowfield produces an axisymmetric free stagnation plane. The jets are surrounded by a co-flow of air (exit section 50 mm) that homogenizes the turbulence and reduces the buoyancy of the flames (Mounaïm and Gökalp, 1993). Thus, a uniform velocity profile for large radial distances is preserved. A perforated plate, placed at 40 mm upstream of the nozzle exit generates the turbulence. The perforated plates have 3 mm holes and a blockage ratio of 50%. The turbulence intensity at the exit of the nozzle is 10% with an integral length scale of 3.5 mm.

The laser diagnostic system provides one point information on both the dynamic and scalar fields. The flow velocities are measured by using a 2 color (green 514.5 nm and blue 488 nm), 2 component laser Doppler velocimeter. A 2 Watt beam from an argon-ion laser is focused in an optical fibre. The cyan color beam is separated into two beams; one cyan beam is then re-separated into a blue and a green beam. The beams are frequency shifted by a Bragg cell and a differential frequency of 5 Mhz is used for both components for removal of directional ambiguity. The axial velocity component is measured by using the cyan and the blue beams and the radial one is measured by using the cyan and the green beams.

Doppler bursts are collected by two photo-multipliers assembled with a color separator on an optical lens system placed in the forward scattering direction at approximately 15° from the optical axis. The signals are

analyzed by a TSI processor IFA 755 to determine the local flow velocity. The signals from the LDA processor are filtered (low pass filter 10 Mhz, high pass filter 1 Mhz) and amplified before computer storage for post-processing. The data are analysed to obtain the mean and rms fluctuations of the two conditional reactant velocity components. At each measurement position, 10240 pairs of validated velocity data points are stored. Seeding is provided by olive oil droplets with mean size less than 1 μm introduced into the flow by an atomizer. The disappearance of the droplets at the flame front provides an indicator function for the presence of reactants or products from which the reaction progress variable $\overline{c}$ may be readily determined.

The reaction progress variable $\overline{c}$ is obtained by collecting the Mie scattering intensity with another photomultiplier and lens assembly with a 514.5 nm interferential band pass filter placed also in the forward scattering direction at approximately 15° from the optical axis. The intensity of the signal from the multiplier is converted into voltage with a 20 kΩ resistor. The data acquisition system DAS-50 collects 10^6 points at a sampling rate of 375 kHz. The shape of the signal is insensitive to a sample rate above 100 kHz. The Mie scattering signal (figure 2) resembles a random telegraph signal with a sharp transition between signal levels representing the reactants and the products. A typical pdf of the Mie scattering signal in figure 3 shows two well-separated peaks. The products and the reactants are perfectly distinct. Consequently, the local value of $\overline{c}$ can be easily determined by specifying a threshold criterion near the mid range intensity and then by evaluating the percentage of time spent in the products. The local value of the progress variable is then:

$$\overline{c} = \frac{\bar{t}_p}{\bar{t}_r + \bar{t}_p}$$

where $\bar{t}_r$ and $\bar{t}_p$ are the mean passage times, of reactants and products, respectively.

3. EXPERIMENTAL METHODOLOGY

The method described by Kostiuk and Shepherd (1996) to estimate the burning rate of a flame is adapted here to flames stabilized in turbulent opposed jet flows. Consider the control volume shown in figure 4 which extends from pure reactants ($\overline{c} \approx 0$) to the stagnation plane ($\overline{c} \approx 1$) with a diameter D. The mass burned within the control volume is the difference between the mass flow of reactants into and out of the control volume. The mean burning rate is then given by

$$\int \overline{w} dz = \frac{\overline{\dot{M}}_{in} - \overline{\dot{M}}_{out}}{\pi D^2 / 4}$$

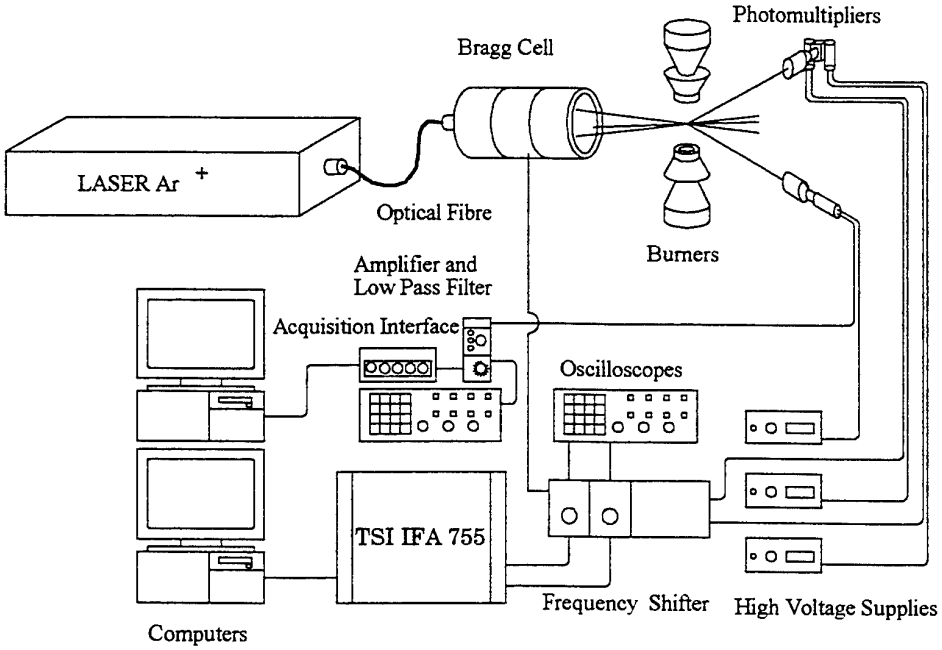

Fig. 1 Schematic of the experimental set-up

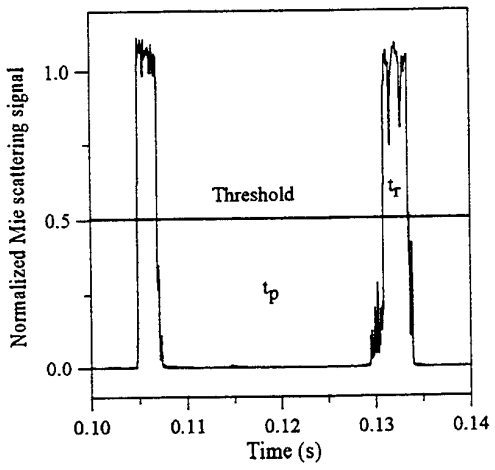

Fig. 2 Mie scattering signal and crossing times t_r and t_p

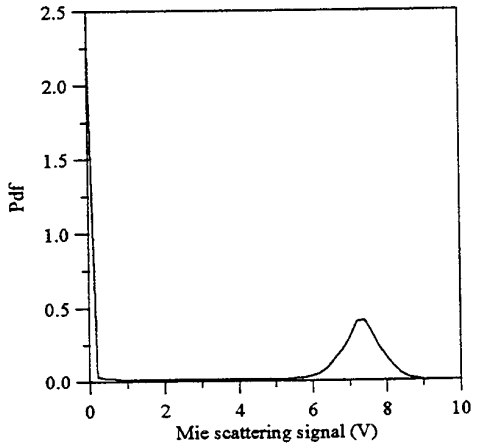

Fig.3 Pdf of a Mie scattering signal

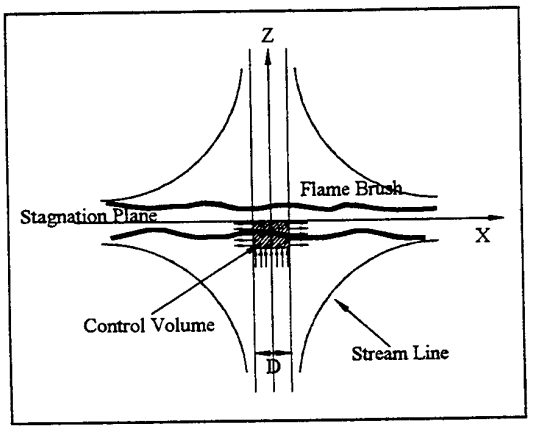

Fig.4 Schematic of the control volume

The mass flow of reactants into the control volume is:

$$\dot{\overline{M}}_{in} = \frac{\pi D^2}{4} \rho_r \overline{U}_{\overline{c}=0}$$

and the expression for the mass flow of reactants out of the control volume is:

$$\dot{\overline{M}}_{out} = \frac{\pi D \rho_r}{2} \int_{Z_{\overline{c}=0}}^{Z_{\overline{c}\approx 1}} \overline{V}_{r=\pm D/2} (1-\overline{c}) dz$$

Where $\overline{U}$ and $\overline{V}$ are the mean axial and radial velocities of the reactants respectively; ρ_r is the reactant density. The term $(1-\overline{c})$ represents the fraction of time the reactants spend in a given point of space. Dividing this burning rate by the reactants density leads to the mean turbulent burning velocity S_T

$$S_T = \frac{1}{\rho_r} \int \overline{w} dz$$

This mean turbulent burning velocity is different from the local flame propagation speed of a flame front relative to a turbulent flow. This speed measures the overall consumption rate of the turbulent flame brush.

4. EXPERIMENTAL RESULTS

The burning rate and the turbulent burning velocity are determined for various diameters D of the control volume. Measurements of the radial velocities and the progress variable are performed along traverses 8,10 and 12 mm from the stagnation Experimental measurements were made with a premixed methane/air mixture of equivalence ratio 1.0 and with an exit velocity of 5 m/s. The bulk strain rate defined by the velocity gradient at the upstream edge of the flame front is 225 s^{-1}. line.

For this first set of experiments, the flow conditions are chosen far from extinction. The two flames are well-separated and the mean progress variable $\overline{c}$ from the Mie scattering signal is equal to 1 in the region between the two flames.

As shown in figure 5, all curves of the mean progress variable $\overline{c}$ collapse on to one curve when $Z - Z_{\overline{c}=0.5}$ is normalized by the turbulent flame brush thickness δ_T, based on the relation

$$\delta_T = \left| Z_{\overline{c}=0.95} - Z_{\overline{c}=0.05} \right|$$

The behaviour of the progress variable obtained by Mie scattering measurements can also be correctly fitted

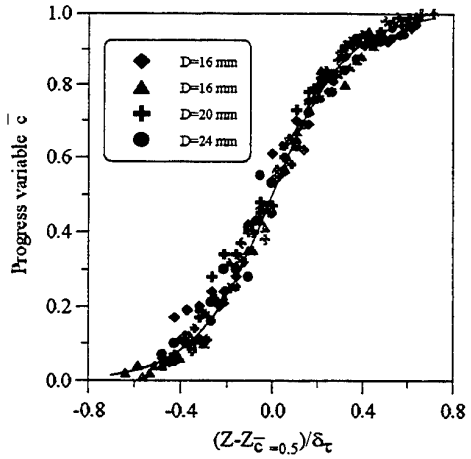

Fig.5 Progress variable versus a normalized distance

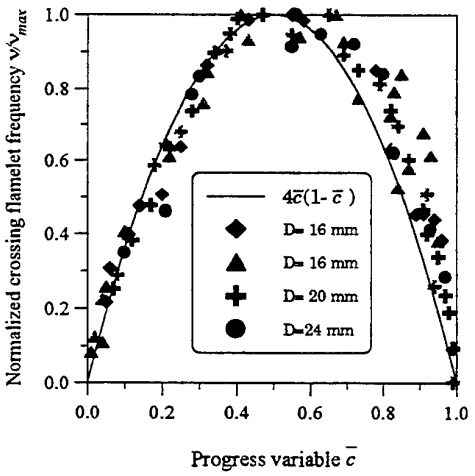

Fig.6 Normalized flamelet crossing frequency versus $\bar{c}$

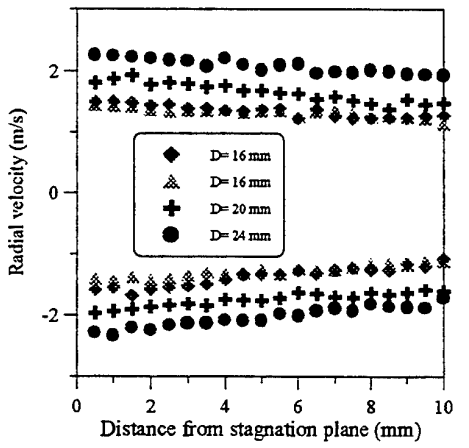

Fig.7 Radial velocity ot the reactants in the flame brush for different control volume diameters

with the expression given by Deschamps (1990) for conical flames and it agrees with the Rayleigh scattering measurements in opposed jet flames by Mounaïm-Rousselle (1993)

$$\bar{c} = \frac{1}{1+\exp\left(-6(Z-Z_{\bar{c}=0.5})/\delta_T\right)}$$

Figure 6 represents the flamelet crossing frequency ν normalized by its maximal value ν_{max}. The results are found to be in good agreement with those of Mounaïm-Rousselle (1993) using Rayleigh scattering measurements in a opposed jet configuration and with the BMCL model that predicts $\nu/\nu_{max} = 4\bar{c}(1-\bar{c})$ under the assumption of a constant integral time scale $\hat{T}$ of the scalar field (Bray et al. 1988). The characteristics of the flames in the opposed jet configuration obtained with Mie scattering measuements are comparable with Rayleigh scattering measurements that are directly representative of the temperature.

Figure 7 represents the behaviour of the radial velocity in the flame brush for different control volume diameters. The radial velocity is only slightly modified by the flame brush. The reactant flux out of the control volume is then obtained by weighting the radial velocity with the function $(1-\bar{c})$. An example of the variation with axial distance, for each side of the control volume around the symmetry axis, of the integrand on the right hand side of the equation for the mass flow of reactants out of the control volume, $\overline{\dot{M}}_{out}$, is shown in figure 8. The mass flow rate of reactants leaving the control volume is then subtracted from the axial mass flow rate of reactants at the cold boundary of the flame, $\overline{\dot{M}}_{in}$. The difference between the two fluxes gives the mass flow rate of reactants consumed in the control volume. Figure 9 shows the burning rate determined for each control volume diameters.

Dividing the burning rate by the unburned gas density, the mean turbulent burning velocity can be deduced (figure 10). The mean turbulent burning velocity is found to be independent of the size of the experimental control volume. Consequently, the flame is uniform near the stagnation streamline.

A second set of experiments is made with varying flow conditions in order to approach the extinction limits. The turbulence characteristics at the exit of the burner are here 9% with an integral length scale of 8 mm. The fixed equivalence ratio is 0.9.

In the oppposed jet configuration, the extinction limit for a flame at a fixed equivalence ratio is related to the imposed flame stretch. This stretch rate is a combination of the effects of flow divergence and turbulence. Moreover, in this configuration, the turbulence intensity and the bulk strain K are coupled. The bulk strain is estimated through the velocity gradient -dU/dz or it can be approach with the expression $2U_0/H$ where U_0 is the mean axial exit velocity and H the distance between the

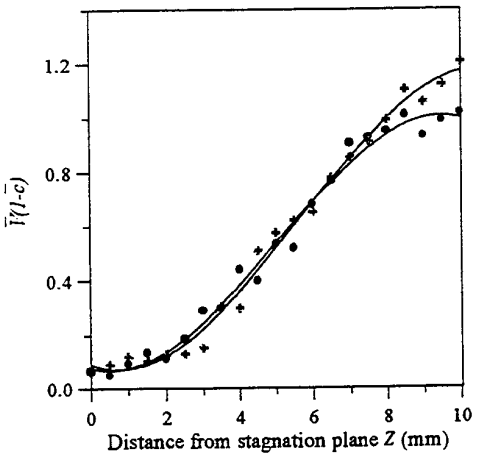

Fig.8 Variation of the radial reactant flux with axial distance

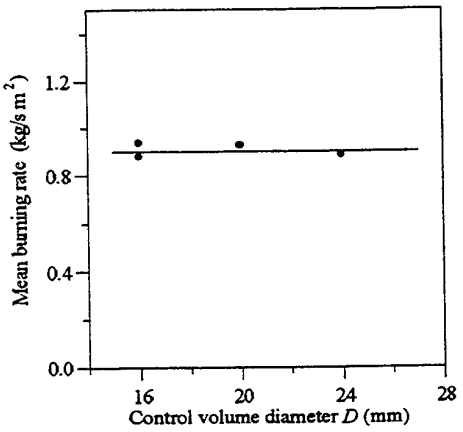

Fig.9 Burning rate for each control volume diameter

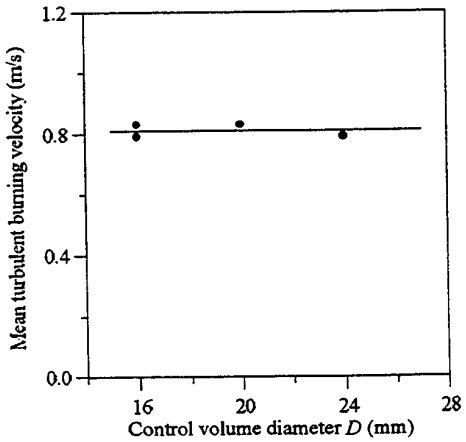

Fig.10 Turbulent velocity for each control volume diameter

two burners. Consequently, an increase of the mean axial velocity implies, at the same time, an increase of the bulk strain rate due to the divergence of the flow and an increase of the turbulent kinetic energy. When the stretch imposed upon the flame increases, the two flames move closer together until they visually appear as a single reaction zone. The maximum value of the progress variable $\overline{c}$ decreases below 1, and finally, global extinction occurs.

Figure 11 shows the variation of the mean burning rate as a function of the maximum value of the progress variable in the flame brush. The variation of the mean burning rate with kinetic energy at the leading edge of the flame front is presented in figure 12. In figure 13, the bulk strain K experienced by the flame during the experiments, given here by the axial gradient velocity -dU/dz, is shown. The burning rate initially increases with both turbulent kinetic energy and strain but subsequently decreases, as suggested in Bourguignon et al. (1996), when extinction is approached. Far from the extinction limit, the mean reaction rate is found to increase with the strain rate and the turbulent kinetic energy as long as the maximum value of $\overline{c}$ in the flame brush is approximatively between 0.95 and 1. Close to the extinction limit, the maximum value of $\overline{c}$ decreases (figure 11). The mean reaction rate, after reaching a maximum, decreases.

5. DISCUSSION

The mean turbulent burning velocity shown in figure 10 as determined by the present method can be compared to the classical definition used for flames in a stagnation point flow: the mean velocity at the cold boundary of the flame front. In the case of the opposed jet configuration, the mean axial velocity profile does not present a well-determined velocity minimum like for flames stabilized by a stagnation plate. Consequently, we here choose the mean axial velocity at the cold boundary of the flame front. This boundary is defined as the position where the progress variable is $\overline{c} = 0.05$, indicating the beginning of the flame brush. This definition gives us a mean turbulent propagation speed of 2.2 m/s. This latter value is 2.7 times larger than the value deduced from the mean reaction rate.

Therefore, the mean turbulent burning velocity, as determined here is different from the mean displacement velocity of the flame brush.

Consequently, the mean reaction rate determined by the classical method is overestimated compared to our direct measurements of consumed reactants. Indeed, as shown in figure 8, in divergent flows, a large part (about 65%) of reactants entering at the leading edge of the flame leaves the control volume without burning. The mean reaction rate estimated as the velocity at the leading edge of the flame brush do not take into account this fraction of reactants leaving the control volume without burning.

The normalization by the unstretched laminar burning velocity (S_{L0}=0.43 m/s) gives S_T/S_{L0}=1.9 instead of S_T/S_{L0}=5.1 with the classical definition. The turbulence

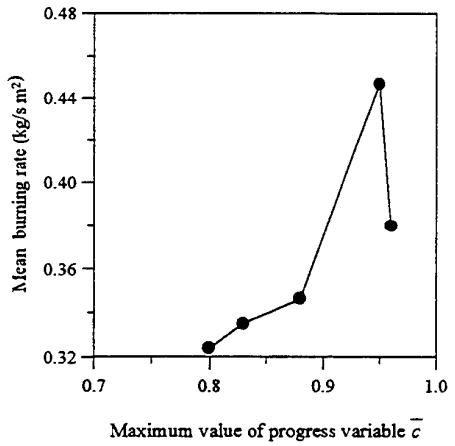

Fig.11 Variation of the mean burning rate with the maximum value of $\overline{c}$

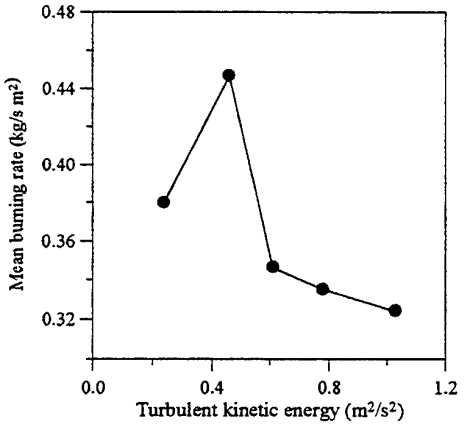

Fig.12 Variation of the mean burning rate with kinetic energy at the cold boundary of the flame brush

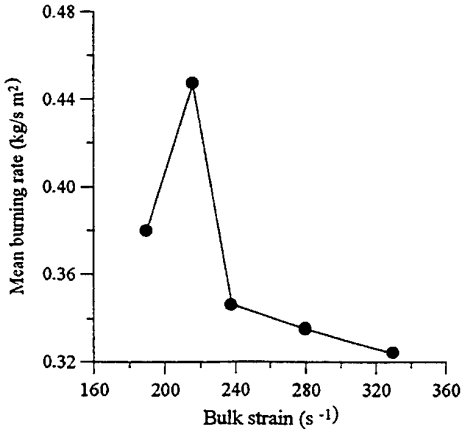

Fig.13 Variation of the mean burning rate with bulk strain due to the divergence of the flow

intensity was u'=0.8 m/s, i.e. u'/S_{L0}= 1.9. For comparison, the results of Cho et al. (1986) for turbulent methane/air flames stabilized by a stagnation plate give for u'/S_{L0}= 1.9 a set of experiments with a ratio S_T/S_{L0} between 3.5 and 4.

Some uncertainities in this comparison are due to the normalization of S_T with the unstretched laminar burning velocity. Normalization with the stretched laminar burning velocity would be helpful but there is still no consensus on the determination of the stretched laminar burning velocity(Tien and Matalon, 1991). Therefore, we do not know exactly to what extend the variation of S_T is caused by changes in the stretched laminar burning velocity S_L.

6. CONCLUSION

A measurement technique is used for turbulent premixed flames in the opposed jet configuration to measure the mean burning rate. The technique is based on the difference between the reactants mass flow in and out of a control volume.

The conditional reactants velocities are measured with a two-component Laser Doppler Velocimetry system in a flow seeded with oil. Simultaneous Mie scattering from L.D.V probe volume is used to measure the mean progress variable. The combination of velocity and progress variable allows the determination of the mean reactants flux.

Two sets of experiments were conducted in order to show that turbulent premixed flames in opposed jet configuration can be used to determine their mean burning rate and its behaviour at the approach of the extinction limit. The present investigation shows that the classical determination of the turbulent burning velocity defined as the axial cold boundary velocity leads to an overestimation of the mean burning rate because it does not take into account the radial flux of reactants. The mean burning rate is found to decrease when extinction is approached, with increasing strain rate and turbulent kinetic energy. It appears therefore that stagnation flames, because of their planar configuration and uniformity around the stagnation streamline, are a useful tool to determine the burning rate of turbulent flames.

To complement this study, it would be useful to conduct a set of experiments on stretched laminar flames in the opposed jet or stagnation plate configuration in order to determine the mean burning rate of stretched laminar flames by the present method. In this case, the normalization of S_T by the stretched laminar burning velocity S_L would take into account the effect of the bulk strain rate.

ACKNOWLEDGMENTS

This work is supported by the French Army Research Office, DRET, group 7, the Conseil Regional du Centre and the CNRS. The authors would like to thank Dr. L.W. Kostiuk for its helpful advices.

REFERENCES

Bourguignon E., Kostiuk L.W., Michou Y. & Gökalp I., 1996, Experimentally Measured Burning Rates of Premixed Turbulent Flames, Twenty-sixth Symposium (International) on Combustion, The Combustion Institute, Pittsburgh, accepted.

Bray, K.N.C., Champion M. & Libby P.A. 1988, Mean Reaction Rates in Premixed Turbulent Flames, Twenty-Second Symposium (International) on Combustion, The Combustion Institute, Pittsburgh, pp 763-769.

Cho, P., Law, C.K., Hertzberg, J.R. & Cheng, R.K. 1986, Structure and Propagation of Turbulent Premixed Flames Stabilized in a Stagnation Flow, Twenty-First Symposium (International) on Combustion, The Combustion Institute, Pittsburgh, pp 1493-1499.

Deschamps, B. 1990, Etude Spatiale et Temporelle de la Structure Dynamique et scalaire des Flammes Turbulentes Prémélangées de Méthane-Air, Ph. D. thesis, University of Orléans, France.

Kostiuk, L.W. & Shepherd, I.G. 1996, Measuring the Burning Rate of Premixed Turbulent Flames in Stagnation Flows, Combust. Sci. and Tech., Accepted.

Law, C.K., Zhu, D.L. & Yu, G. 1986, Propagation and Extinction of Stretched Premixed Flames, Twenty-First Symposium (Int.) on Combustion, The Combustion Institute, Pittsburgh, pp 1419-1426.

Mounaïm-Rousselle, C., 1993, Combustion Turbulente Prémélangée dans un Ecoulement à Jets Opposés, Ph. D. thesis, University of Orléans, France.

Mounaïm-Rousselle, C. & Gökalp I., 1993, Turbulent Premixed Flames in Counterflowing Streams- Influence of a Coflow, Annual Spring Meeting of the Western States Section of the Combustion Institute, Salt Lake City, OH.

Shepherd, I.G. & Kostiuk, L.W. 1994, The Burning Rate of Premixed Turbulent Flame in Diverging Flows, Combust. Flame, vol 96, pp 371-380.

Tien, J.H. & Matalon, M., 1991, On the Burning Velocity of Stretched Flames, Combust. Flame, vol 84, pp 238-248.

Wu, C.K. & Law C.K. 1984, On the Determination of Laminar Flame Speeds from Stretched Flames, Twentieth Symposium (International) on Combustion, The Combustion Institute, Pittsburgh, pp 1941-1949.

ON THE USE OF LASER RAYLEIGH SCATTERING TO STUDY THE AEROTHERMOCHEMISTRY OF RECIRCULATING PREMIXED FLAMES

F. Caldas, D. Duarte, P. Ferrão, M. V. Heitor and C. Poppe(*)

Instituto Superior Técnico
Dept. of Mechanical Engineering
Av. Rovisco Pais, 1096 Lisboa Codex
Portugal

(*) Imperial College of Science, Technology and Medicine
Dept. of Mechanical Engineering
Exhibition Road, London SW7 2BX
United Kingdom

ABSTRACT

The use of laser Rayleigh scattering, LRS, to study the thermochemistry of propane-air flames is shown to be accurate in the range of equivalence ratios $0.53 < \phi < 0.70$, making use of proper calibration procedures. The results have been analysed against thermocouple data and quantify the effect of flame luminosity on Rayleigh thermometry.

The measurements have been obtained in baffle-stabilised flames for Re = 150000 and the results are used to assess the effect of swirl, in the range $0 < S < 0.33$, on the aerothermochemistry of strongly sheared flames. To achieve these objectives, a previously reported LRS/LDV system was conveniently optimised and the results show that swirl attenuates the rate of turbulent heat transfer across the reacting shear layer, although it does not alter the existence of a large flame zone characterised by non-gradient scalar fluxes. The results have been evaluated against those obtained with the combination of LDV with digitally compensated thermocouples, which are shown to be attenuated by up to 50% mainly due to the lack of spatial resolution.

1. INTRODUCTION

Laser Rayleigh scattering, LRS, has been extensively used in laboratory flames to study the thermochemistry of non-luminous systems (e.g. Rajan et al., 1984; Namer and Schefer, 1985). Also, the results of Ferrão and Heitor (1996-a;-b) show that it can be conveniently combined with laser velocimetry and used, with adequate spatial and temporal resolution, to quantify the distribution of turbulent heat fluxes in recirculating flames, at least for lean flames (i.e., $\phi \leq 0.6$), see also the review of Ferrão and Heitor (1992) for details. Further, Almeida et al. (1995) have used a combined LRS/LDV system to analyse the effect of swirl on the structure of strongly-sheared baffle-stabilised flames. Nevertheless, the extent to which the technique can be used to study the details of the aerothermochemistry of flames with practical interest remains to be shown, mainly due to its limited application to luminous flames.

The work reported in this paper is intended to contribute to this discussion by providing experimental results on strongly-sheared recirculating propane-air flames as a function of equivalence ratio, in the range $0.53 < \phi < 1$.

Turbulent recirculating premixed flames stabilised downstream of baffles have been shown to be characterised by non-gradient scalar fluxes (e.g. Takagi et al., 1984; Takagi and Okamoto, 1987; Fernandes et al., 1994; Duarte et al., 1995), the extent of which appears to be particularly influenced by the magnitude of the mean pressure gradients associated with the streamline curvature or because of acceleration of gases across the flame front, Heitor et al.(1987), Ferrão and Heitor (1995), Duarte et al.(1995).

This paper provide further evidence of the process of turbulent mixing in recirculating flames and extends the results of Almeida et al. (1995) to improve the understanding of the interaction between gradients of mean pressure and density fluctuations. The effect of swirl on the aerothermochemistry of propane-air recirculating flames is particularly addressed, which has been possible due to the combination of laser Rayleigh thermometry and laser Doppler velocimetry.

The next section describes the experimental method and give details of the extent to which the LRS can be used in propane-air flames. Section 3 presents and discusses sample results and the last section provides the main conclusions of the work.

2. THE EXPERIMENTAL METHOD AND ACCURACY

2.1 The Flames Studied

The experiments reported in this paper were conducted in unconfined swirling and non-swirling premixed flames of air and propane, stabilised on a disk with D = 56 mm in diameter, which is located at the exit section of a contraction with 80 mm in diameter. The annular bulk velocity is equal to U_o = 42.4 m/s, resulting in a Reynolds number, based on the disk diameter, of 1.5 x 10^5. Swirl could be imparted to the premixed reactants by a set of curved blades, located upstream of the contraction, resulting in a swirl number of S = 0.33. The equivalence ratio was varied between 0.53 and 1, although most of the flames characterised in this paper correspond to lean flames, with ϕ = 0.55.

2.2. The Experimental Techniques

The instrumentation used throughout this work consists on a combined LDV/LRS system, which was based on a single laser light source (5 W argon-ion laser) as represented in figure 1. The system has derived from that described by Duarte et al. (1995) and Almeida et al. (1995), as the main data acquisition system includes a 16 bits analogue/digital converter, in place of the 12 bits data acquisition board previously used.

The velocimeter was based on the green light (514.5 nm) of the laser and was operated in the dual-beam, forward-scatter mode with sensitivity to the flow direction provided by a rotating diffraction grating. The calculated dimensions of the measuring volume at the e^{-2} intensity locations were 606 μm in length and 44 μm in diameter.

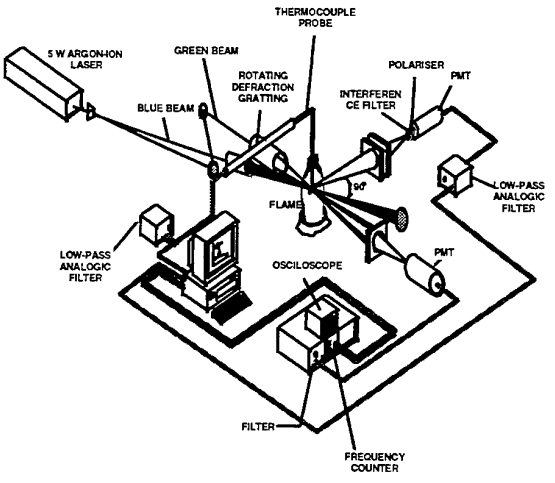

Fig. 1 Schematic diagram of the combined LDV/LRS system, together with thermocouple probe.

The Rayleigh scattering system was operated from the blue line of the same laser source, which was made to pass through a 5:1 beam expander. The light converged in a beam waist of 50 μm diameter was collected at 90° from the laser beam direction with a magnification of 1, and passed through a slit of 1 mm length. The collected light was filtered by a 1nm bandwidth interference filter and a polariser, in order to optimise the signal-to-noise ratio.

The signal was amplified and low pass filtered at 10 KHz before digitalisation. The temporal resolution of the system depends on the integration time associated with this filter which is quantified to be 50 μs. This value, associated with the typical flow velocities, give rise to path lengths up to 2 mm and, therefore, smaller than the integral length scales in the reaction shear layer. The resolution of the system was confirmed by the measured temperature distributions, which include instantaneous values close to either adiabatic or room temperature, confirming that the system is capable of resolving the temperature fluctuations associated with the premixed flames analysed in this work.

2.3. The Accuracy of LRS Thermometry

The amplitude of the LRS signal collected from a flame in the wavelength of the laser source, V, results from three main sources (e.g., Eckbreth, 1988):

i) The Rayleigh scattering process, as the electromagnetic radiation resulting from the elastic interaction between the incident electric field and the electric field of the molecules in the gas (with $d/\lambda \ll 1$, where d is the particle or molecule diameter and λ is the wavelength of the laser beam);

ii) The Mie scattering process, as the dispersion of the incident light caused by particles (i.e., $d/\lambda > 1$) present in the flame, including soot;

iii) The radiation emitted by different molecular species formed during the combustion reactions.

As the collecting optics cannot discriminate the different light sources, but just maximise the overall signal to noise ratio, dedicated signal processing and calibration techniques were used to extend the utilisation of the LRS technique. This is achieved by compensating for the so-called "non-Rayleigh" contributions (namely, ii and iii above) possible as long as they are not dominant and are uncorrelated with the LRS signal. The related assumptions essential for the calibration procedure are discussed bellow.

The Mie scattering signals (i.e., ii above) are detected by derivative and amplitude criteria as, at least for large particles with $d/\lambda \gg 1$, the light dispersed by a particle causes a significative distortion in the collected signal (see Ferrão and Heitor, 1996-a, for details). The molecular radiation (i.e., iii above), V_{Lum}, is considered to be a function of the equivalence ratio and is evaluated by measuring the amplitude of the signal in the absence of the laser source.

A calibration procedure based on these premises was implemented and sample results obtained in the propane-air flame considered in this paper were compared with measurements made using digitally-compensated fine-wire thermocouples (Ferrão and Heitor, 1996), in order to assess the limits of the utilisation of Rayleigh thermometry as a function of equivalence ratio.

The procedure was implemented making use of measurements made at the centre of the present recirculation zone, where gas analysis has shown complete combustion. In addition, reference conditions were established for a lean flame, namely close to extinction, for $\phi = 0.53$. The related Rayleigh signal, V_H, at the thermocouple-based temperature, T_H, and the corrected Rayleigh signal for the reactants at ambient temperature were then used to calibrate the technique. Further corrections for any equivalence ratio, ϕ, were derived from the following equations:

$$T = \frac{1}{a\,(V - V_{Lum}) + b} \qquad [1]$$

$$a = \frac{T_a - T_H}{T_a T_H\,(V_H - V_a)} \qquad [2]$$

$$b = \frac{T_H V_H - T_a V_a}{T_a T_H\,(V_H - V_a)} \qquad [3]$$

As the equivalence ratio is increased from $\phi = 0.53$, the Rayleigh signals V_a and V_H vary due to the modification in the composition of reactants and products, leading to different Rayleigh cross sections (e.g., Namer and Schefer, 1985; Ferrão and Heitor, 1996-a). Additionally, it should be noted that for different equivalence ratios, T_H do not represent the temperature of the products of combustion. Thus, two assumptions were considered as follows: i) The dependence of the Rayleigh cross section, σ, on temperature is taken as linear, as suggested by Rajan et al (1984) and Shepherd and Daily (1984); and ii) The ratio between the mean temperature in the centre of the recirculation zone (i.e., for complete combustion) and the adiabatic flame temperature for each value of ϕ is considered as constant. As a result, the values of the parameters used for the calculation of equations [2] and [3] for different equivalence ratios, are corrected according to table 1.

Figure 2 quantifies the relative contribution of the flame luminosity for the overall time-averaged signal collected along the centre line of the flame, as a function of equivalence ratio in the range $0.53 \le \phi \le 0.92$. The results clearly show that the "non-Rayleigh" contribution to the overall signal, as mentioned before, is important for $\phi > 0.70$ and precludes the utilisation of Rayleigh Thermometry. Figure 3 shows the related implications in terms of temperature data, by comparing the LRS results against thermocouple measurements at different locations within the flame. It is clear that for $\phi > 0.70$ the error associated with the Rayleigh measurements, namely due to contamination from flame luminosity, is larger than that expected to affect the thermocouple from radiation losses. Further, for $\phi > 0.80$, the error associated with Rayleigh thermometry is too large, that precludes the use of this technique in luminous flames.

It should be noted that the Rayleigh scattering measurements may be affected by the photomultiplier shot-noise, which results in an increase of the signal rms, according to the Poisson statistics (e.g., Ferrão and Heitor, 1996-a). This contribution is, for a given experimental set-up, quantified by:

$$\frac{rms_{shot}}{V} = \frac{k}{\sqrt{V}} \qquad [4]$$

where k was evaluated according to equation [5] for the voltage obtained by the PMT at ambient conditions, V_a, and the corresponding rate of photons at the cathode, R_p, considering a cut-off frequency of the system of $f_c = 5$KHz.

$$k = \sqrt{\frac{2 f_c V_a}{R_p}} \qquad [5]$$

The velocity-temperature correlations reported in this paper were not compensated for the shot-noise as it influences the temperature fluctuations, but it is not correlated with the velocity fluctuations in the flame.

Table 1 - Correction parameters for the calibration of the Rayleigh signal.

Values at $\phi = 0.53$	Corrected parameters for an arbitrary ϕ
V_a	$V_a \times \frac{\sigma_{react,\,\phi}}{\sigma_{react,\,\phi=0.53}}$
V_H	$V_H \times \frac{\sigma_{react,\,\phi} + \frac{(\sigma_{prod,\,\phi} - \sigma_{react,\,\phi})\,T_{ad,\,\phi=0.53}}{T_{H,\,\phi=0.53}\,T_{ad,\,\phi} - T_a\,T_{ad,\,\phi=0.53}}\,(T_{H,\,\phi=0.53} - T_a)}{\sigma_{prod,\,\phi=0.53}}$

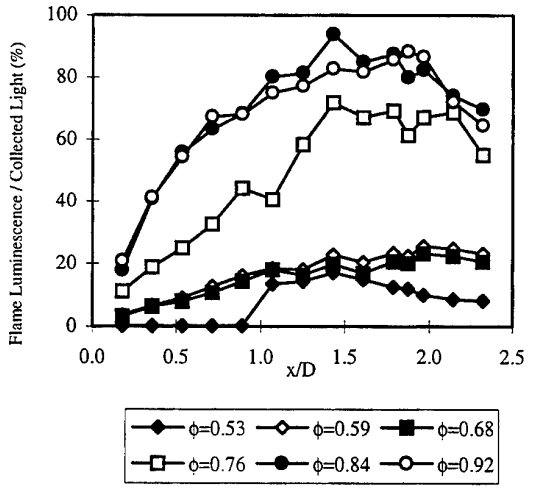

Fig. 2 - Contribution of flame luminosity for the overall time-averaged signal collected along the centre line of the flame, as a function of equivalence ratio.

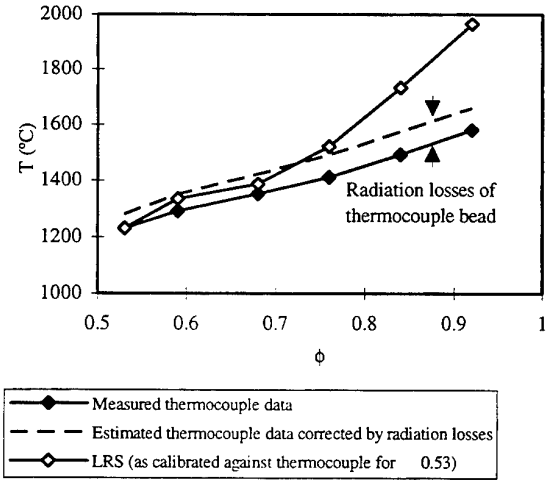

Fig 3 - Mean flame temperatures in the centre of the recirculation zone obtained by fine-wire thermocouples and calibrated LRS for different equivalence ratios.

3. RESULTS AND DISCUSSION

The analysis above has validate the use of Rayleigh thermometry to study non-luminous propane-air reacting mixtures for $\phi < 0.70$. We now turn to exemplify the use of the technique study two different recirculating flames with practical interest, namely with and without swirl. The results include those obtained by combining the Rayleigh signal with laser velocimetry in order to quantify the turbulent heat fluxes in the flames considered.

The most salient features of the mean flow characteristics of the two flames studied can be inferred from the streamlines represented in figure 4, together with

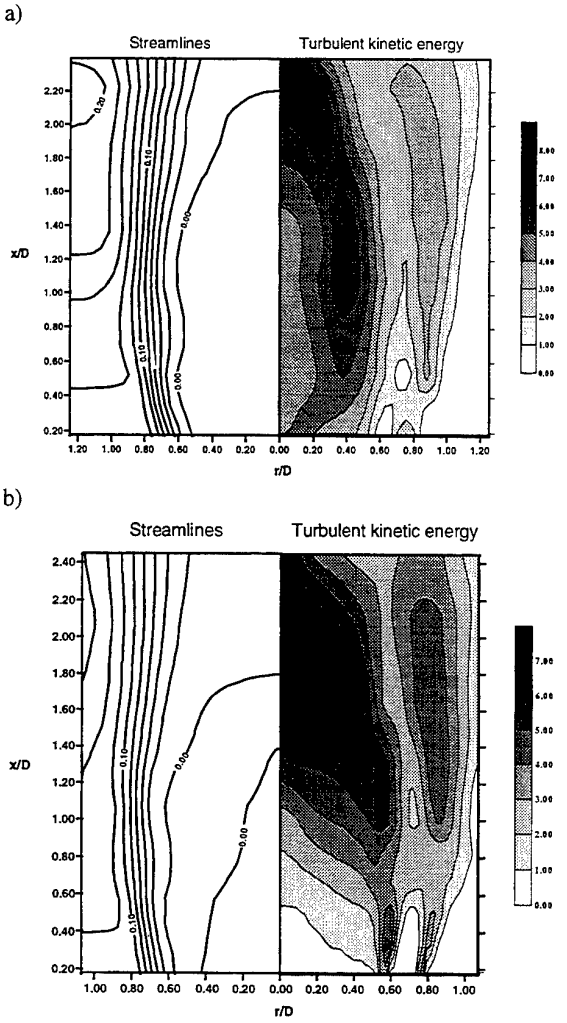

Fig. 4 Streamlines and distribution of turbulent kinetic energy along a vertical plane of symmetry:
a) Non-swirling flame. b) Swirling flame.

the distribution of turbulent kinetic energy. For the non-swirling flame (figure 4a) the results are similar to those found in other baffle-stabilised recirculating flames (e.g. Heitor et al, 1987; Ferrão and Heitor, 1995), in that they exhibit a recirculation region extending up to x/D = 2.21, where the fluid has a large and fairly uniform mean temperature, surrounded by annular region of highly sheared fluid where gradients of mean temperature are large.

The single recirculation zone of the unswirled flame is to be contrasted to that of the swirling flame, figure 4 b), which is shorter, wider and annular in shape, because it includes an inner annular vortex with positive velocities along the centreline (Almeida et al., 1995). The inner recirculation zone is associated with positive mean velocities along the centreline up to the first stagnation point and rotates in the opposite sense to the outer recirculation zone. This nature of the swirling flame is

characterised by a comparatively large inclination of the mean velocity vectors at the exit which, together with the aspects mentioned before, represents a direct consequence of the centrifugal forces associated with the swirl motion.

In general, the results quantify highly strained flames with maxima velocity fluctuations along the shear layer surrounding the recirculation zone. Turbulence is mainly generated by the interaction between shear strain and shear stress (Ferrão and Heitor, 1994), giving rise to a strongly anisotropic turbulent field with comparatively large axial velocity fluctuations. As the stagnation point is approached, the cross-stream turbulent components increase as a result of the augmented importance of the interaction between normal strains and normal stress in the conservation of turbulent kinetic energy, as in other recirculation flows with stagnation points.

Figure 5 shows profiles of the measured turbulent heat transfer rate of the two flames analysed, together with the corresponding mean velocity and the progress reaction variable.

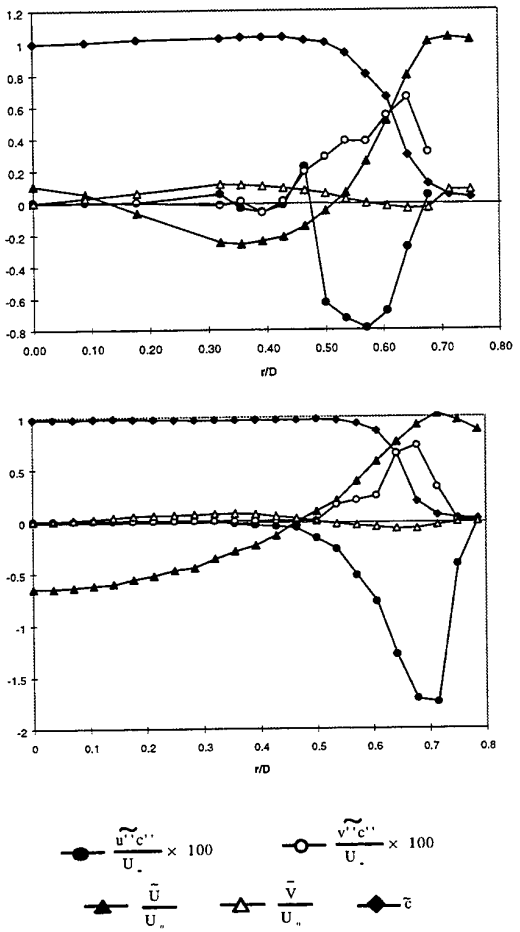

Fig. 5 - Radial profiles of the turbulent heat fluxes: a) Swirling flame at x/D = 1.04. b) Non-swirling flame at x/D = 1.09.

The results show that turbulent heat transfer is restricted to the reacting shear layers, where the temperature gradients are significative. Additionally, while in the non-swirling flame (figure 5 b), $\widetilde{u''c''}$ and $\widetilde{v''c''}$ do not change in sign, in the swirling flame (figure 5 a) the sign of both components of the turbulent heat fluxes change along the radius, as a result of the complex interaction between the pressure and temperature (or density) fields.

Prior to the analysis of the aerothermochemistry of the flames considered, it is convenient to discuss the accuracy of the results of figure 5, namely against those obtained by combining LDV with bare-wire thermocouples. Similar comparison in non-swirling flames (Ferrão and Heitor, 1996-b) has shown that the use of the thermocouple probes attenuates the measured velocity-temperature correlations mainly due to the lack of spatial resolution. The results of figure 6 extends this conclusion to swirling flames and shows that the results obtained from the two techniques are qualitatively in agreement, but the lack of spatial coincidence between the thermocouple bead and the LDV measuring volume leads to the underestimation of the values of the correlations obtained.

It is clear that the accuracy of the measured velocity-temperature correlations is also dependent upon the absolute accuracy of the time resolved measurements of the progress variable, which is analysed in figure 7 making use of sample results obtained with LRS and digitally compensated fine-wire thermocouples. The results show that the compensation of the LRS signal for the pmt shot- noise (as in Ferrão and Heitor, 1996-a) gives values in agreement with those obtained by digitally-compensated thermocouples and confirms the ability of the procedures used for temperature fluctuation measurements. In general, analysis has shown that the errors induced in the results due to the photomultiplier shot-noise depend upon the experimental conditions used, but the net effect is to increase the r.m.s. of the temperature fluctuations up to 10% of the measured values.

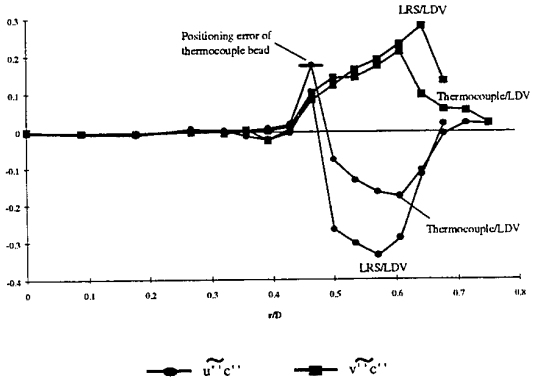

Fig. 6 - Radial profile of the turbulent heat flux components, measured by the combined LDV/LRS and LDV/thermocouple systems, for the swirling flame at x/D = 1.04.

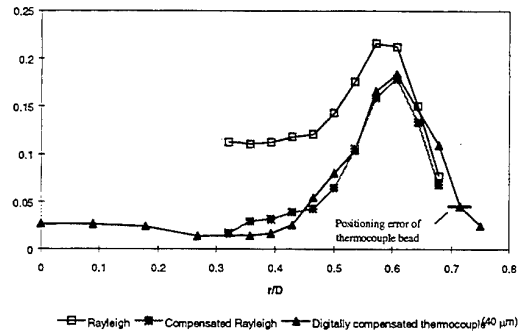

Fig. 7 - Radial profile of the rms of the fluctuations of progress reaction variable, measured by LRS and digitally compensated thermocouples, for the swirling flame at x/D = 1.04.

We now turn to the analysis of the turbulent heat flux in the flames considered and figure 8 shows that a large component of the related vectors is directed along the isotherms, rather than normal to them, as would be expected form gradient transport models (Ferrão and Heitor, 1995).

The new features provided by these results is that swirl decreases the magnitude of the turbulent heat fluxes due to the attenuation of the mean temperature gradients across the reacting shear layer.

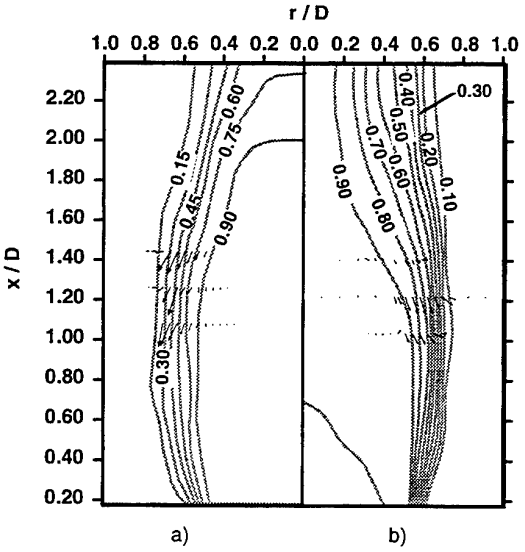

Fig. 8 - Turbulent heat fluxes superimposed on the isotherms: a) Non-swirling flame. b) Swirling flame.

The results for the non-swirling flame have been explained before in terms of the interaction between the mean pressure field and the density fluctuations , which are important in the process of turbulent transport typical of reacting flows. The present results confirm the evidence first given by Almeida et al. (1995) that this interaction is affected by the degree of swirl imposed on the flows. In general, the results confirm that the prediction of these kind of flames must be based on second moment, rather than on effective viscosity, turbulent model closures so as to capture the effects of the mean pressure field in the conservation of turbulent heat fluxes.

It has been shown in the literature that the process of "counter gradient" heat transport can be explained by the preferential deceleration of the products of combustion, relatively to the cold reactants (e.g., Heitor et al., 1987; Hardalupas et al., 1996), and here this is clearly shown throughout the joint probability density function (pdf) of axial velocity and temperature of figure 9.

The change in sign of the axial turbulent heat flux across the reacting zone at x/D = 1.04 is explained in terms of the mean pressure distribution across the double recirculation zone associated with the swirling flame (see figure 4b), which results in the change of the patterns of the distributions of figures 9 a) and 9 b). In the zone of its curved flame front, where the flow is characterised by an adverse pressure gradient (as at x/D = 0.57, figure 9 a), the hottest "pockets" of fluid are associated with the lowest velocities. However, the radial heat flux is always positive, as previously shown for non-swirling flames. This is the expected direction of the heat flux in baffle-stabilised flames, which is not altered by the swirl motion. In summary, the evidence is that the net turbulent scalar flux is particularly dependent on the mean pressure distribution in the flow and occurs along directions in which the mean scalar gradient is not large.

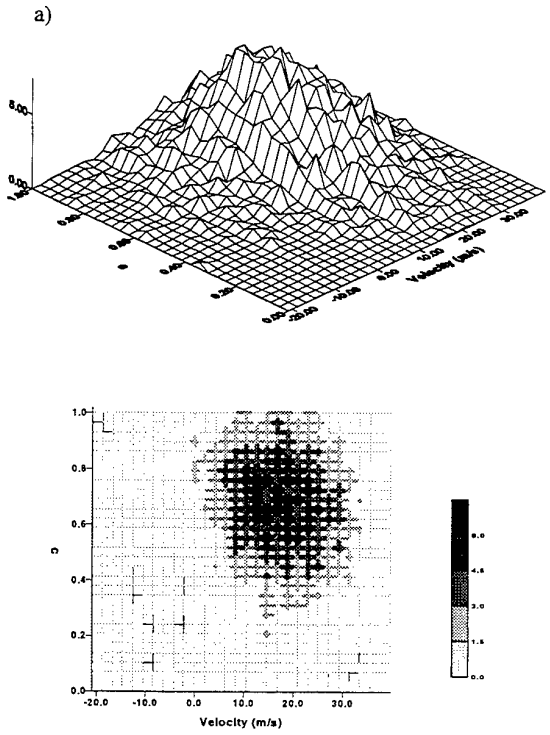

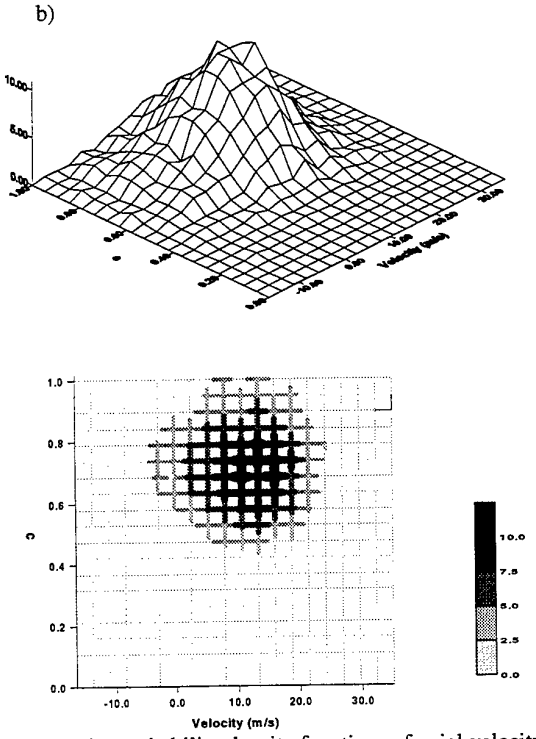

Fig. 9 - Joint probability density functions of axial velocity and temperature fluctuations, for the swirling flame at x/D = 1.04.
a) r/D = 0.57 b) r/D = 0.46

4. CONCLUSIONS

The use of laser Rayleigh scattering, LRS, to study the thermochemistry of turbulent premixed propane-air flames is shown to be accurate for equivalence ratios smaller than 0.70, if adequate calibration procedures are used.

The results quantify the effect of flame luminosity on the accuracy of Rayleigh thermometry and are extended to those of combined velocity-temperature correlations.

The shot noise associated with the photomultiplier used to collect the Rayleigh signal do not affect the turbulent velocity-temperature correlations obtained by the combined LDV-LRS system, which also avoids the limitation previously found associated with the lack of spatial resolution of combined LDV-thermocouple system.

Swirl alters the main aerodynamic features of the baffle-stabilised flames, in that it generates two annular counter rotating recirculation zones. The results give evidence of zones of non-gradient scalar fluxes which are associated with preferential deceleration of the combustion products relatively to the cold reactants. In general, the net turbulent scalar flux occurs along directions in which the mean scalar gradient is not large and is mainly determined by the mean pressure field associated with the flames studied.

5. REFERENCES

Almeida, P., Ferrão, P. and Heitor, M.V., 1995, The effect of swirl on the interaction between pressure gradients and density fluctuations in baffle-stabilised premixed flames, Proc. of 10th Symposium on Turbulent Shear Flows, Vol. 2, pp. 16-7 to 16-12.

Chandran, S.B.S., Komerath, N.M., Grissom, W.M., Jogoda, J.I. and Strahle, W.C., 1985, Time resolved thermometry by simultaneous thermocouple and Rayleigh scattering measurements in a turbulent flame, Combust. Sci. and Tech., Vol. 44, pp. 47-60.

Dibble, R.W. and Hollenbach, R.E., 1981, Laser Rayleigh thermometry in turbulent flames, Proc. of 18th Symposium (Intl.) on Combustion, The Combustion Institute.

Duarte, D., Ferrão, P. and Heitor, M.V., 1996, Flame structure characterisation based on Rayleigh thermometry and two-point laser Doppler measurements, in: Developments in Laser techniques and application to Fluid Mechanics, Eds. Adrian et al, Springer Verlag, pp. 185-249.

Eckbreth, A.C., 1988, Laser Diagnostics for Combustion Temperature and Species, Abacus Press.

Fernandes, E.C., Ferrão, P., Heitor, M.V. and Moreira, A.L.N., 1994, Velocity-temperature correlations in recirculating flames with and without swirl, Experimental Thermal and Fluid science, Vol. 9, pp. 241-249.

Ferrão, P. and Heitor, M.V., 1992, Probe and optical techniques for simultaneous scalar-velocity measurements, in: Combustion Flow Diagnostics, Durão et al., pp. 169-231.

Ferrão, P. and Heitor, M.V., 1995, Turbulent mixing and non-gradient diffusion in baffle-stabilised flames, in: Turbulent Shear Flows - 9, Eds. Durst et al, Springer Verlag, pp. 427-437.

Ferrão, P. and Heitor, M.V., 1996-a, Measurements of velocity and scalar characteristics in premixed recirculating flames, part 1: probe and optical diagnostics, Submitted to Experiments in Fluids.

Ferrão, P. and Heitor, M.V., 1996-b, Measurements of velocity and scalar characteristics in premixed recirculating flames, part 2: simultaneous measurements, Submitted to Experiments in Fluids.

Hardalupas, Y., Tagawa, M: and Taylor, A.M.K.P., 1996, Characteristics of counter-gradient heat transfer in a non-premixed swirling flame, in: Developments in Laser Techniques and Applications to Fluid Mechanics, ed. Durst et al.., Springer Verlag, pp. 159-184.

Heitor, M.V., Taylor, A.M.K and Whitelaw, J.H., 1987, The interaction of turbulence and pressure gradients in baffle-stabilised premixed flames, J. Fluid Mechanics, Vol. 181, pp. 387-413.

Namer, I. and Schefer, R.W., 1985, Error estimates for Rayleigh scattering density and temperature measurements in premixed flames, Experiments in Fluids, Vol. 3, pp. 1-9.

Rajan, S., Smith, J.R. and Rambach, G.D., 1984, Internal structure of a turbulent premixed flame using Rayleigh scattering, Combustion and Flame, Vol. 57, pp. 95-107.

Shepherd, I.G. and Daily, J.W., 1984, Rayleigh scattering measurements in a two-stream free mixing layer, Proc. of The Combustion institute, Western States (USA), W98/CI, paper #84-15.

Takagi, T. , Okamoto, T. , 1987, Direct measurement of the turbulent transport of momentum and heat in the swirling flame, in: Laser Diagnostics and Modelling of Combustion, Eds.Iinuma, K. et al., pp 273-280, Springer Verlag, Berlin.

Takagi, T. , Okamoto, T. , Taji, M. and Nakasuji, Y. ,1984, Retardation of mixing and counter-gradient diffusion in a swirling flame, Proc. 20th Symposium (Intl.) on Combustion, pp. 251-258. The Combustion institute, Pittsburgh.

A PIV INVESTIGATION IN AN AXISYMETRIC NON PREMIXED BLUFF BODY BURNER FLAME

SUSSET A.
Institut National des Sciences Appliquées de ROUEN
76130 Mont Saint Aignan Cedex, France

JAFFRE D., PERRIN M.
Gaz de France, Research and Developement Division, CERSTA
BP 33, 93211 La Plaine St Denis Cedex, France

GRAY C., RICHON J.B.
Optical Flow System
Mayfield Road, Edinburgh, Scotland

ABSTRACT

Velocity measurements by PIV are made in a turbulent non pre-mixed methane/air flame stabilised by the wake effect of an obstacle. The experimental choices made for this study resulted in a PIV bench which was very simple of use. The seeding concentration and the energy balancing of the laser shots were determined by luminance methods. To exploit quantitatively the instantaneous velocity fields, all the components of the experimental chain are calibrated. The optical aberrations of the lens optics, the non-linearity of the CCD sensor, the clock fluctuations on the image capture card were all investigated separately in order to estimate their respective effects on the correlation computations. The accuracy on the computation of the correlation peak position is calibrated using synthetic images. We compare the velocity measured by PIV to that measured using LDV. The PIV vector fields converge after 250 images towards the fields obtained by LDV. Analysis of the fluctuating velocity components in the PIV measurements reveals differences with LDV results which are mainly caused by the limited spatial resolution of the PIV method. The exploitation of PIV-specific information, i.e. the spatial correlation of measurements, makes it possible to quantitatively study the coherent structures present in the flow.

1 - INTRODUCTION

The knowledge of dynamic fields in a turbulent flow is a key asset for the understanding and modelisation of complex phenomena which govern turbulence in industrial natural gas flames. For the last few years, the development of PIV (Gray, 1992) has been heralding genuine advances in the quantitative study of vortical structures and the complex flows they generate.

The bluff-body model burner is a simplified geometry version of an industrial burner exploiting the wake effect of an obstacle to stabilise a turbulent non-premixed flame. It replicates the operating conditions of a full-scale burner while simplifying its study (axisymmetric geometry). It is a valuable tool for the investigation of the influence of the conditions of the methane/air mixture on the characteristics of the flame (stability, length, temperature, polluting emissions). Until now the imaging techniques applied to bluff-body studies have been essentially species concentration measurements by Raman scattering and PLIF (Namazian et al, 1988, Kendrick et al, 1996) or by Mie scattering (Mokkadem et al., 1996).

The processing of simultaneous LDA velocity and temperature measurements (Neveu et al, 1994) highlighted the shedding of hot gas "packets" from the recirculation zone. The visualisation of the flow by high-speed imaging (Kendrick et al, 1996) also allows the capture of instantaneous structures such as vortices. These two techniques both have shortcomings. The former requires a fastidious set-up and heavy post-processing, while the latter only brings forth qualitative information. For velocity measurements, PIV is an efficient solution to the two problems above since it provides at the same time the benefit of a simple set-up, and that of instantaneous visualisation of the coherent structures present in the flow via the velocity field.

In the following study, we present PIV measurements made on the bluff-body burner for one given flow case. The effect of each of the components of the acquisition system on the correlation calculation is evaluated, in order to underline the weakness of the Signal-to-Noise Ratio as a vector validation criterion. The comparison of average velocity fields obtained by PIV and LDV makes it possible to validate experimental choices and confirm the efficiency of the PIV method. A last approach based on the spatial correlation of the vectors shows the quality of the information provided by PIV.

2 - EXPERIMENTAL SETUP

2 - 1 Description of the burner

Several geometries have been already the subject of numerous studies (Perrin et al, 1990, Namazan et al, 1995). Their characteristics can be defined by several non-dimensional quantities :

- The obstacle ratio $Ro = D_J / D_B$
- The blockage ratio $Rb = (D_B / D_A)^2$

Figure 1 shows the geometric characteristics of the burner. The blockage ratio is high (0.83). The case studied corresponds to a flow velocity of 21 m/s in the central methane jet, and 7.5 m/s in the annular jet of air. This case was studied with and without flame, without any confinement. The Reynolds Numbers found in the methane and air jets are 7000 and 3300 respectively.

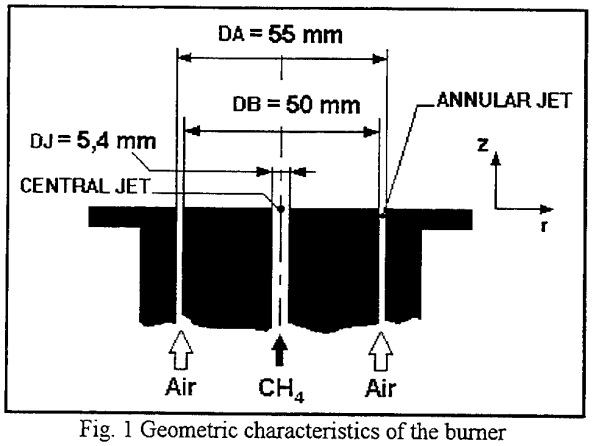

Fig. 1 Geometric characteristics of the burner

2 - 2 Processing Method

The axial velocity histogram for the whole of the flow (from z = 0 to z = 60 mm) is shown in Figure 2. The variation of velocities between the central methane jet (35 m/s maximum) and the recirculation zone (zero and near-zero velocities) imposes to resolve a large dynamic range. Such a resolution is only possible with cross-correlation processing, where zero and reversing displacements can theoretically be measured.

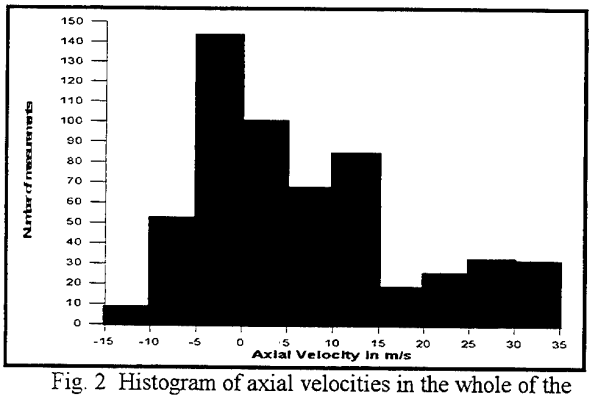

Fig. 2 Histogram of axial velocities in the whole of the reactive flow.

Figure 3 is an instantaneous image of the flow seeded with Micron-sized particles of Zirconium Oxide.The presence of zones with large seeding concentrations in the vicinity of each of the jets adds another limitation to the use of an auto-correlation technique (Trinité et al, 1993).

We therefore selected the cross-correlation image analysis technique. The technical problems inherent to this technique are linked to the necessity to obtain independent images separated by very short time (35 µs).

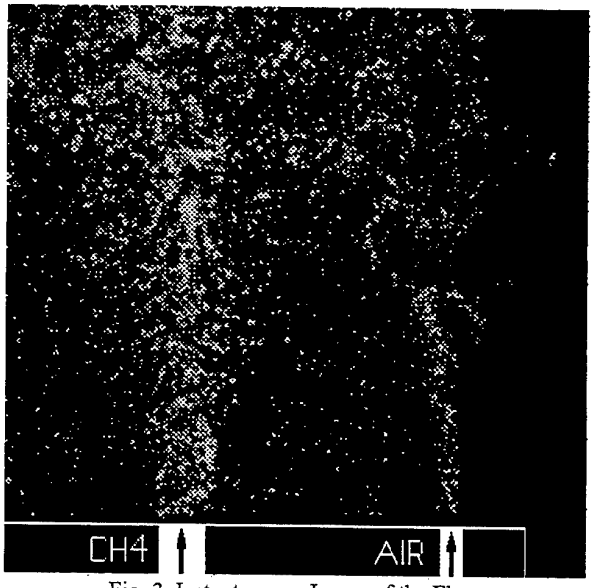

Fig. 3 Instantaneous Image of the Flow

2 - 3 Set-up and Synchronisation

The synchronisation timing diagram is presented in Figure 4.The CCD camera (LH510 from LHESA Electronique) operates in field mode, at a frequency of 25Hz (Lecordier et al, 1994). The camera drives a Quantel YG585 Nd-YAG Laser via a pulse generator (Stanford Research DG535) triggered by the odd/even signal of the VD/2 field.

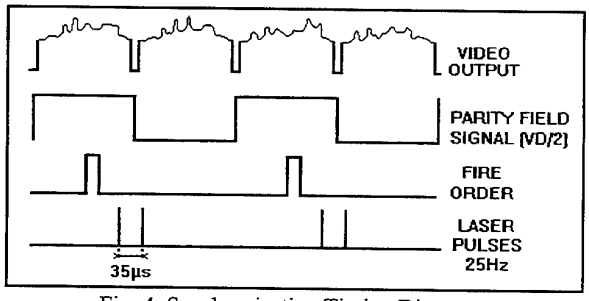

Fig. 4 Synchronisation Timing Diagram.

The set-up is presented in Figure 5. The field of view covers a 60x58 mm area, seen through a f:1.2/50 mm lens (Nikon) set at f:2. Each series of 250 images is digitised over 8 bits (Matrox Magic Color) then stored in PC RAM at video rate, with a resolution of 512x512 pixels.

The exposure control being limited to the odd field in triggered mode, the CCD sensor is operated in un-shuttered mode. However, to improve the quality of the recorded signal, an interferential filter is used (532 nm center wavelength, with 10 nm bandwidth), with the effect of eliminating most of the radiation from the flame and the hot particles.

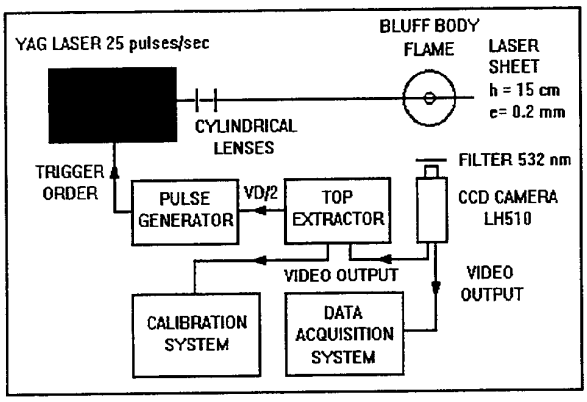

Fig. 5 PIV Set-up.

The calibration system is composed of a TV monitor and a video recorder. This system enables on one hand simple adjustment of the time of each laser shot in relative to the CCD sensor integration by visualisation of a flickering of the TV image, and on the other hand to evaluate by eye the energy balance of the laser shots by comparison of the two recorded image fields.

The rate of seeding is first evaluated theoretically from the mass concentrations in particles in each of the two gases. These calculations take into consideration neither the accumulation of particles in the body of the burner, nor the diverging thickness of the Laser sheet over the field of view.

The settings are therefore refined by use of a luminance method. The average grey level of two interrogation areas located at the exit of each jet. Considering that 100% of the particles are present in these zones, the luminance ratio will indicate the corrections required to the theoretical rate of seeding to minimise the seeding bias.

The energy fluctuations of the two beams are controlled after image field separation by comparing the average grey level in the two fields belonging to the same frame. As it was found that for a luminance difference greater than 10%, the smallest particles located in the recirculation zone were lost, the field pairs not meeting this threshold were rejected.

3 - CALIBRATION OF THE PIV RIG

Figure 6 shows how the information flows across the elements of the acquisition system.

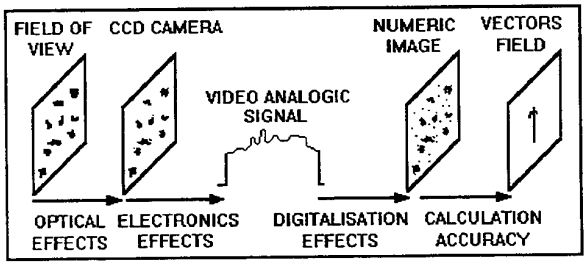

Fig. 6 Information flow across the components of the acquisition system.

3 - 1 Optical Effects

The aberrations of the recording optics which noticeably affect the images are mainly geometric distortion and vignetting. These two effects, commonly encountered in imaging, are corrected for during an image pre-processing phase.

To attenuate the vignetting, images of a uniformly lit object plane are recorded at different stops of the recording optics. The resulting images serve as correction files for the PIV images.

The geometric distortion is directly corrected by built-in functions in the OPTIMAS image processing software.

3 - 2 Electronic effects.

Following the principle of the photoelectric effect, the number of electrons stripped from a semi-conductor medium is proportional to the incident light intensity. The response of each pixel on the CCD sensor to uniform lighting is not in itself uniform, therefore it is necessary to construct a correction file to counter this effect.

The sensor without its optics is exposed to different light levels cast on a uniform plane. For each light level an averaged image is produced. By performing a linear regression on the whole of the averaged images, the regression coefficient, slope and zero ordinate are determined for each pixel.

The displacement changes resulting from the non-linearity corrections are not significant. If during a batch analysis we apply vector filtering using the Signal to Noise Ratio of the correlation computation, the number of vectors left intact by the filter at one given point of the analysis grid can vary by as much as 6% for a 1.18 SNR threshold. The SNR is a parameter far too sensitive to image definition to be adopted as main vector validation criterion.

3 - 3 Digitisation Effects

Image defects induced by the synchronisation and the digitisation of the video signal are mainly caused by line jitter and pixel jitter.

To evaluate these jitters we numerically synthesise a ramp going from 0.3V to 1V. The function generator (Stanford Research DS345) is capable of generating any waveform. A synthesised video line is synchronised on the Horizontal Drive (HD) signal and output at the HD frequency (15.625 kHz) to the image acquisition card. Figure 7 shows the synthetic ramp video signal.

For different rates of climb of the ramp, the images captured by the card are analysed by lines and by columns.

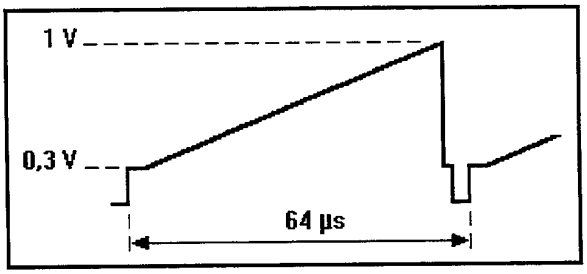

Fig. 7 Synthetic ramp video signal

The line jitter is a randomly fluctuating deviation from complete synchronicity between the frame grabber internal line reset and the HD video signal generated by the camera. The direct effect of this, i.e. a horizontal shift of the digitised lines, can be observed on the fluctuations of the grey levels in an image column. The effect of this shift on a vector field has been shown by Rouland (Rouland et al, 1994). Images of a target with randomly set white spots were taken to assess the accuracy of zero velocity measurements. An accuracy better than 0.04m/s was found with our set-up.

The pixel jitter corresponds to a small random fluctuation in the digitisation time of a pixel. This fluctuation can reach 7% of the digitisation time (15 MHz pixel clock). Whenever the video signal exhibits a gradient over a line, this effect can cause a significant jump in the grey level associated with an image pixel. The shape of the analogue signal corresponding to the scatter image of a particle obeys a gaussian distribution. The jumps in pixel grey level will then be more important on the edges of the particles. The line analysis of the digitised synthetic video ramp image demonstrates that this fluctuation can reach 5 grey levels for the steepest gradients. The incidence of this jitter on the accuracy of the correlation computations is quantified using synthesised digital images . The accuracy of the displacement measurements is not significantly modified (about 5%). This fluctuation of the particle edge definition mainly degrades the SNR.

3 - 4 Calculation Accuracy

We seek to determine the accuracy on the localisation of the maximum of the correlation peak. The interpolation of the correlation peak by a gaussian function leads, in ideal conditions, to a maximum theoretical accuracy near 1/100th of a pixel (Willert et al, 1991).

The accuracy of the calculation is calibrated with synthetic images. The particle image size distribution in the flow images is used as a guide for choosing the shape and the grey level intensities of the synthesised particles. The concentration in particles is also determined from real flow images. In the range of measured displacements, i.e. from 0 to 8 pixels, the accuracy on the determination of the correlation peak position is 0.08 pixel.

4 - RESULTS AND DISCUSSION

4 - 1 Comparison with LDV

A PC-based analysis software with batch processing facility (VidPIV 2.09, Optical Flow Systems) is used to obtain the instantaneous velocity fields (see Figure 8). The size used for the interrogation areas is 32x32. Each instantaneous field is filtered by an SNR threshold of 1.18 and by thresholding of each velocity component.

The calculation of a field composed of 854 vectors takes 70 seconds on a 130 MHz Pentium. The addition of a DSP card would at least double the processing rate.

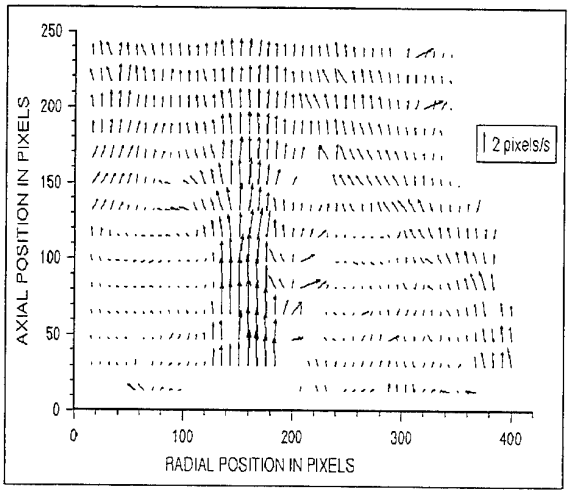

Fig. 8 Instantaneous velocity field for a non-reacting flow

The convergence of the cross-correlation PIV measurements towards a field average over 480 vector files is presented in Figure 9. We calculate the difference between partial averages and total averages, weighted by the value of the average velocity at the point of interest.

In order to eliminate the coupling between the instant at which images are recorded and certain natural frequencies of the flow, the convergence calculations are repeated after shifting the analysis window.

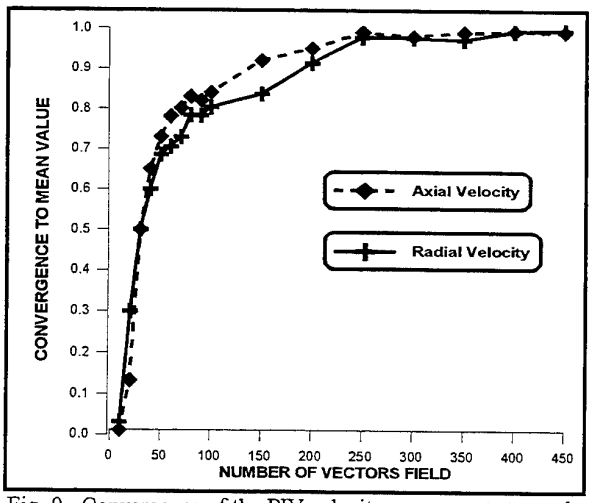

Fig. 9 Convergence of the PIV velocity components towards the average velocity field.Non-reactive flow.

The convergence towards the average dynamic field is very quick, as illustrated by Figure 9. We consider that a set of 250 vector fields, i.e. 10 seconds worth of video imaging, is sufficient to obtain a good representation of the average vector fields in the flow. For the LDV measurements (Neveu et al, 1994), the average velocity at one point is obtained in about 3 seconds, i.e. about 3000 particles crossing the measurement volume. For the PIV images, we count in average around 30 particles per grid cell in the recirculation zone, i.e. 7500 particles for the convergence towards the average dynamic field.

Figure 10 shows the average fields resulting from LDV and PIV measurements. The original LDV measurement grid is of much finer step than that for PIV measurements,

therefore an interpolation of the LDV measurements to the PIV grid is performed. The average velocity field in the recirculation zone shows the existence of two vortices : a first one rotating clockwise, which is driven by the air flow, the second one, smaller, is located at the root of the methane jet, and rotates counterclockwise.

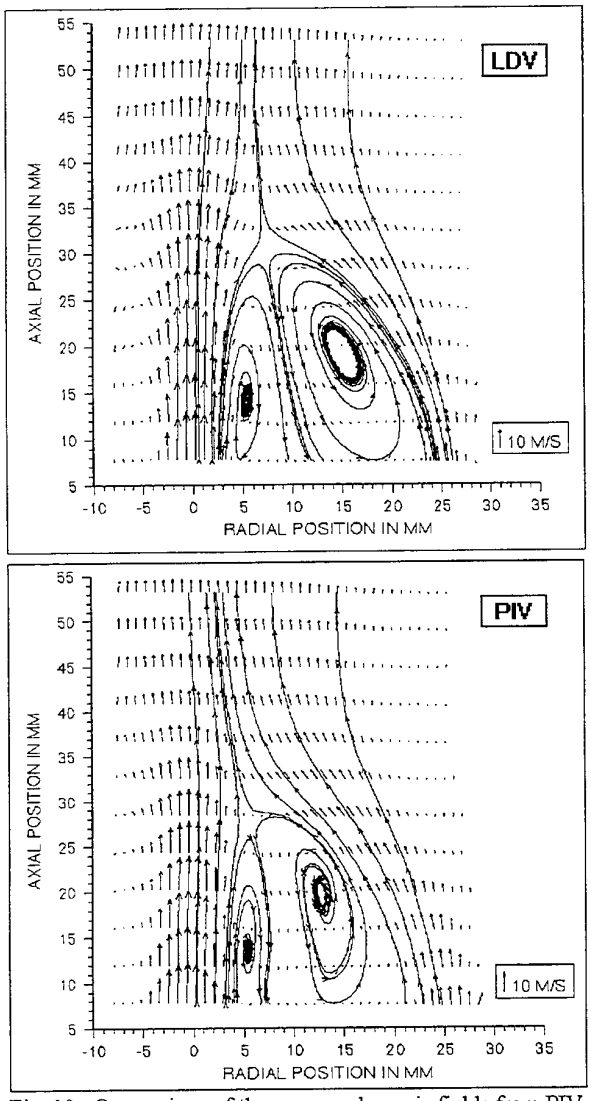

Fig. 10 Comparison of the average dynamic fields from PIV and LDV. Non-reacting flow.

The overall structure of the average dynamic field, which consists in the different zones of interaction between the two jets, is similar for the two methods. We think that the main difference seen in the central fuel jet and in the recirculation zone may be due to a fuel flowrate control drift.

Figure 11 shows the radial velocity profile at a height of 5.6 mm. The profiles have similar features. The main difference has to do with the value of the methane flow velocity.

The amplitude difference at the location of the methane jet is due to a flowrate control drift. The profiles obtained by PIV are wider in the region of the jets. This effect is the consequence of the coarse spatial resolution of PIV and of the large overlap of the interrogation windows in the radial direction (75%). The lack of spatial resolution of PIV is mostly felt in the air jet, where the interrogation window (3.2 mm in the x - direction) is larger than the jet (2.5 mm).

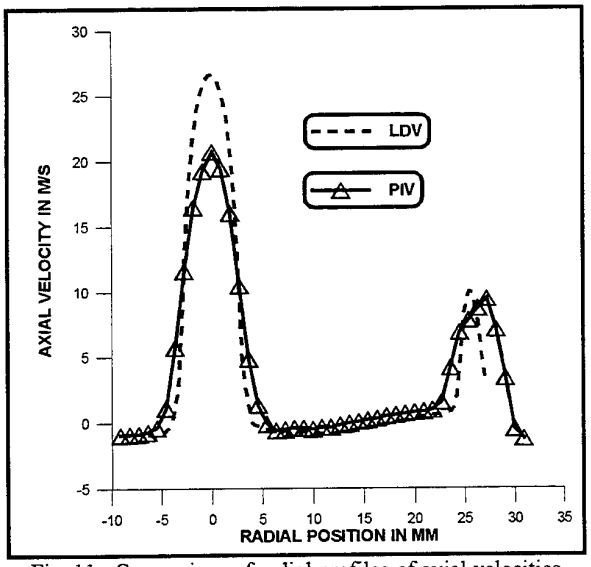

Fig. 11 Comparison of radial profiles of axial velocities (z = 5.6 mm).
LDV: 95 measurement points. PIV : 45 measurement points.

The axial profile of axial velocities is shown in Figure 12. The profiles are in overall agreement over the height of flow under study. It is difficult to interpret the velocity differences because of the error on the methane flowrate, hence the use of normalised variables for the comparison.

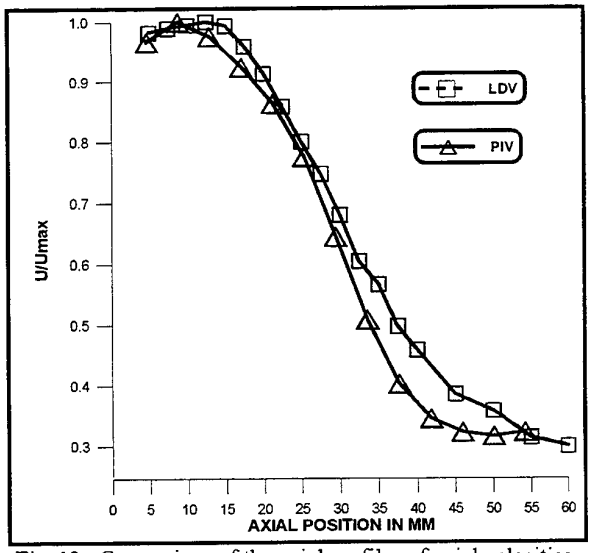

Fig. 12 Comparison of the axial profiles of axial velocities. Non-reacting flow.

The comparative fluctuation profiles are shown in Figure 13. The same general trend is found in both axial RMS profiles. The amplitude differences and the absence of a double maximum are due to the lack of spatial resolution of PIV compared to LDV. Recently, algorithms have been devised to bring a solution to the loss of information in the analysis window (Okamoto et al, 1995). Such algorithms allow in theory the identification of rotation, expansion and shear in the analysis window by linking each particle by a

fictitious spring and then analysing the deformation of these systems from one image to the next. This technique, which is based on the identification and tracking of particles, could be applicable in PIV in the recirculation zone.

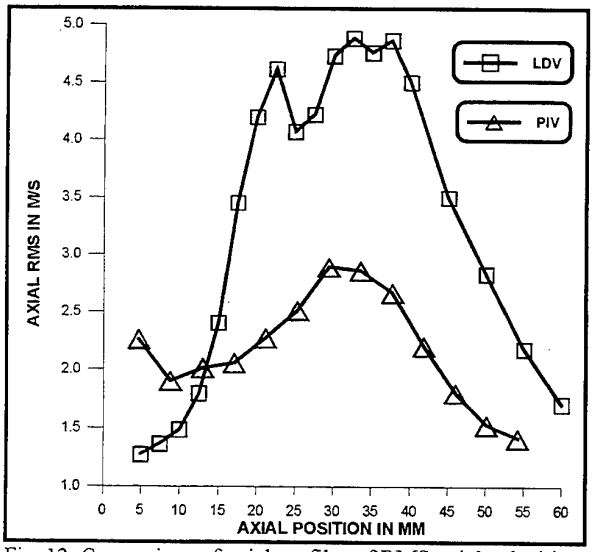

Fig. 13 Comparison of axial profiles of RMS axial velocities. Non-reacting flow.

The 3 first points of the RMS profile of the axial component, as obtained by PIV, show greater velocity values than LDV. For the first point, it is the position of the analysis window in the image which is mainly responsible for the high RMS value. Indeed, the edge of the Laser sheet is located a few mm above the burner, causing half of the first interrogation area to be empty of particle images for the analysis grid chosen. As SNR filtering is used, some erroneous vectors computed in this interrogation window are not eliminated by the filtering operation. If the SNR threshold is increase to 1.4, the number of vectors drops from 350 to 250 out of a total of 480.

The position of the 3 first points corresponds to the plateau of high velocities (see Figure 11). For these velocities, the calculated displacement in the 32x32 pixel interrogation area is about 6 pixels, which reduces the useful area for the calculation. The SNR of these 3 first points is 25% less than the average SNR over the vector field. It is then difficult to appreciate the incidence of erroneous vectors on the value of the fluctuation.

In the first part, the comparative study of the two methods has mainly enabled us to validate the PIV measurements. The following section is based on an aspect which is specific to PIV, i.e. the spatial correlation of vectors, which makes it possible to identify in the flow coherent structures such as vortices.

4 - 2 Vortex Identification

Figure 14 is an instantaneous image of the reactive flow. Two different structures can be identified in the eddy driven by the air jet in the recirculation zone.

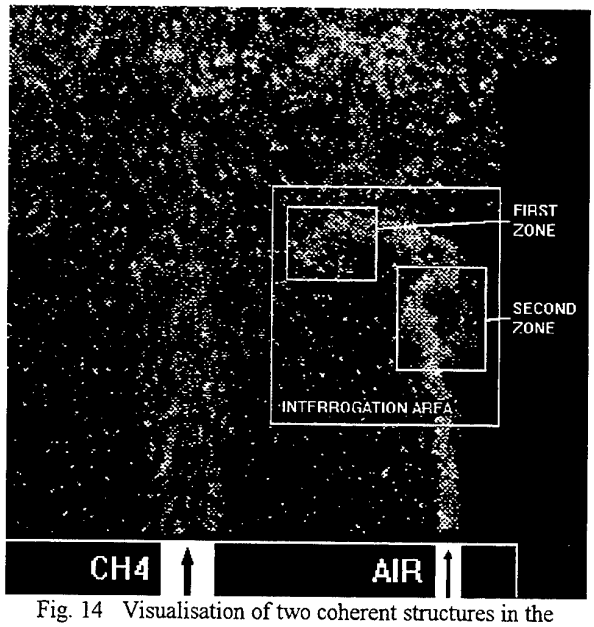

Fig. 14 Visualisation of two coherent structures in the reacting flow.

Figure 15 presents the vector field calculated over the interrogation area shown in Figure 14.

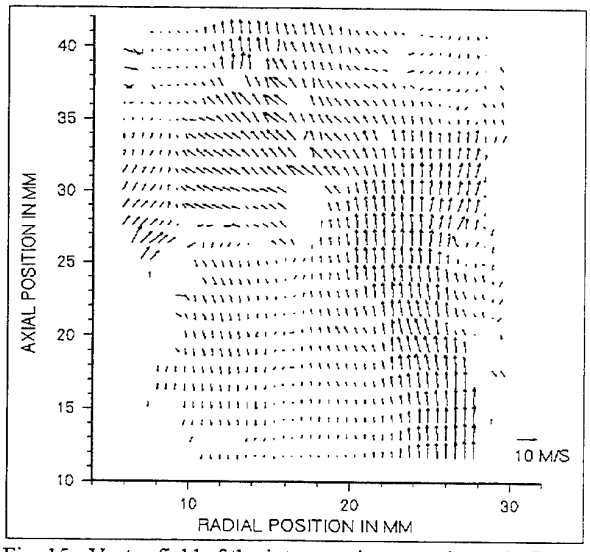

Fig. 15 Vector field of the interrogation area shown in figure 14. Reacting flow.

The first structure identified in Figure 14 is directly visible on the vector field, without post-processing. We see a set of vectors which have a group velocity with an orientation differing from that of the surrounding velocity vectors. The second structure in the image in Figure 14 is not apparent in the raw vector field.

Simultaneous measurements by fine wire thermocouple and LDV (Neveu et al, 1994) have shown that hot gas "packets" were ejected from the recirculation zone for two distinct velocity values corresponding each to a specific gas temperature (Tg = 900K and Tg = 1700K). Figure 16 shows the two velocity values at r = 17.5mm and z = 30 mm.

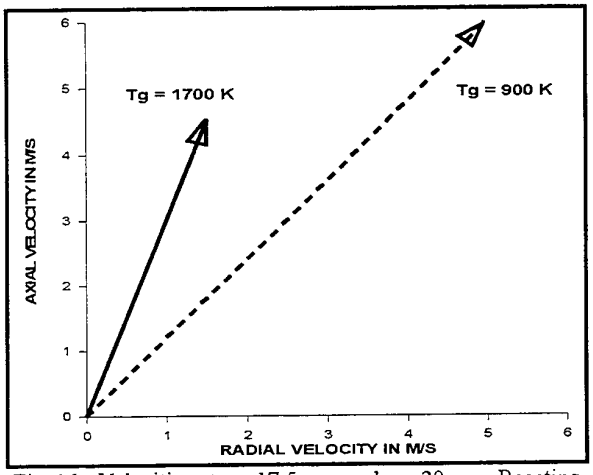

Fig. 16 Velocities at r = 17.5 mm and z = 30 mm. Reacting flow.

The bimodal nature of the joint velocity distributions at this point explains the intermittent behaviour of the flow in the the recirculation zone area, this behaviour being driven by the radial velocity component (Scheffer et al, 1987).

Figure 17 shows a colour-coded plot of the radial velocity component for the visualised field.

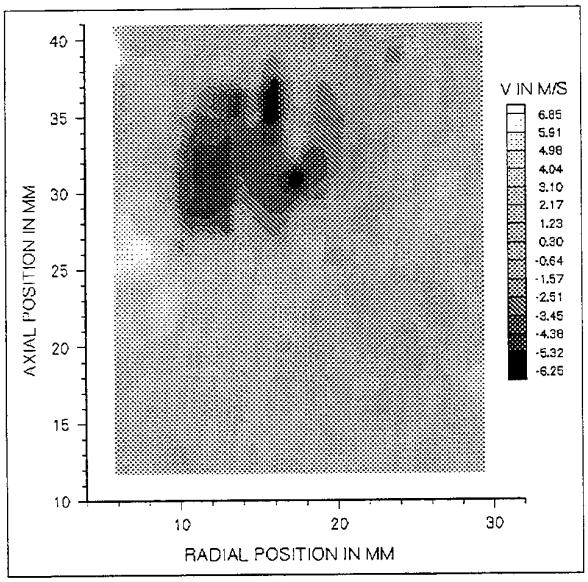

Fig. 17 Radial velocity component for the dynamic field visualised in figure 15.

One sees clearly a zone with a group velocity breaking the continuity of the surrounding values. This set may correspond to the hot gas "packet" ejected out of the recirculation zone. The measurements of velocity and position of this structure corroborate this assumption, as the results obtained with PIV are identical to that obtained with LDV (900K component). In the near future, experiments will be conducted in order to correlate the velocity measurements with the position of the flame front. We emphasise that the observed structure has mainly a translation component, since the subtraction of the average entrainment velocity does not produce a vortical velocity field.

The second structure seen on the image bears resemblance to the shedding of a vortex. A first processing pass is performed on the image, then an average velocity value corresponding to the entrainment velocity of the structure is subtracted from the vector field. The final result is presented in Figure 18. A vortical velocity distribution is clearly visible.

The difficulty in this type of processing is to locate the structure in the image to calculate its average entrainment velocity. A systematic study over the whole image could be undertaken if the characteristic dimensions of the structure were known, but the associated processing would be time-consuming and the smaller-scale structures would be missed. In our case we could take advantage of the presence of a strong concentration in particles in the vortex to define a skeleton the size and location of which would serve as starting point for the calculation of the vector field.

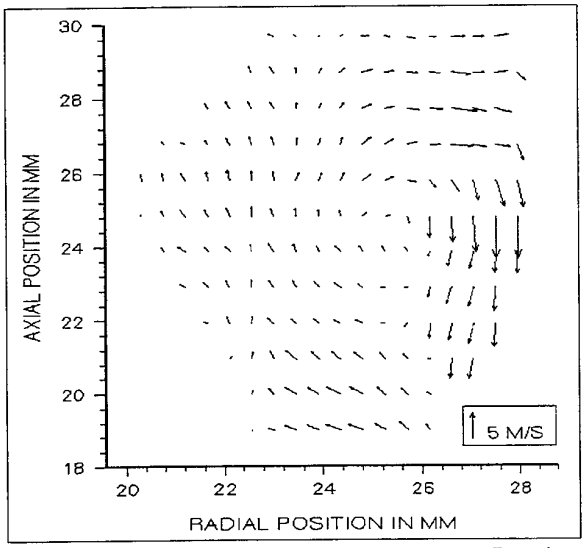

Fig. 18 Velocity field inside the second structure. Reacting flow.

5 - CONCLUSION

The analysis of PIV data has shown that the production of an average dynamic velocity field was much faster than with LDV, while the fluctuating component bandwidth and the spatial resolution are inferior. A convergence criterion cannot be the only guarantee of integrity of the PIV method. The knowledge of the accuracy on the correlation calculations for each point of the interrogation grid, as well as the vector validation methods still remain key parameters for the quantitative use of PIV measurements.

While currently available spatial resolution and imaging rate limit the ability of PIV to produce temporal flow statistics, it is the only measurement method allowing the spatial correlation of velocity data across a two-dimensional region.

The development of post-processing algorithms based on instantaneous velocity fields, such as the identification and tracking of coherent structures in the flow, is the next challenge to overcome in order to systematise the use of PIV as a velocity measurement technique.

ACKNOWLEDGEMENTS

We thank K. Mokkadem (CNRS EM2C) and J. Imbach (GDF) for their advice on experimental matters. We also thank R. Grossiord, student at the Institut National des Sciences Appliquées of Rouen for the development of PIV post-processing software.

REFERENCES

Gray C, "The evolution of Particle Image Velocimetry", IMechE Optical Methods and Data Processing in Heat and Fluid flow, Londres, pp 19 - 35, 1992.

Kendrick D. W., Mokaddem K., Scouflair P., Rolon J. C., Jaffre D., Perrin M., "Simultaneous PLIF and Mie Imaging of a Turbulent, Non-Premixed CH4/Air Flame", 26th International Symposium on Combustion, Naples, 1996.

Lecordier B., Mouqallid M., Vottier S., Rouland E., Allano D., Trinité M., "CCD recording method for cross-correlation PIV development in unstationnary high speed flow", 7th International Symposium on Applications of Laser Techniques to Fluid Mechanics, Lisbon, 1994.

Mokaddem K., Kendrick D., Rolon J-C, Jaffre D., Perrin M., "Methane concentration by Mie scattering imaging technique in axisymetric non premixed bluff body flames", 8th International Symposium on Apllication of Laser Techniques to Fluid Mechanics, Lisbon, 1996.

Namazian M., Kelly J. T., Scheffer R. W., 1988, "Near Field Instantaneous Flame and Fuel Concentration Structure", 22th International Symposium on Combustion/The Combustion Institute, pp 627-634.

Namazian M., Kelly J. T., Scheffer R. W., Perrin M., 1995, "Effects of Confinement and Bluff-body Burner Recirculation Zone and Flame Stability", IGRC, Cannes, 1995.

Neveu F., Corbin F., Perrin M. et Trinité M., "Simultaneous velocity and temperature measurements in turbulent flames obtained by coupling LDV and numerically compensated finewire thermocouple signals", 7th International Symposium on Application of Laser Techniques to Fluid Mechanics, Lisbon, 1994.

Neveu F., "Mesures simultanées de la température et de la vitesse dans une flamme turbulente non prémélangée méthane-air stabilisée par un brûleur de type bluff-body", Thèse Rouen, 1994.

Okamoto K., Hassan Y.A., Schmidl W. D., 1995, "New tracking algorithm for particle image velocimetry", Experiments in Fluids, Vol 19, pp 342-347.

Perrin M., Namazian M., Kelly J. and Scheffer R.W., "Effect of confinement and blocage ratio on non-premixed turbulent bluff-body burner flames", 23th International Symposium on Combustion, Orléans 1990.

Rouland E., "Etude et developpement de la technique de vélocimétrie par intercorrélation d'images de particules et application aux écoulements en tunnel hydrodynamique", Thèse Rouen, 1994.

Trinité M., "La vélocimétrie par Intercorrélation d'Images de Particules, Séminaire Européen, Le laser outil de Diagnostic en Milieu Industriel, GDF, La Plaine Saint Denis, 1993.

Scheffer R.W., Namazian M. and Kelly J., "Velocity measurements in a turbulent nonpremixed bluff-body stabilized flame", Combustion Science and Technology, Vol. 56, pp 101-138, 1987.

Willert C.E. and Gharib M., "Digital particle image velocimetry", Experiments in Fluids, vol 10, pp 181-193, 1991.

METHANE CONCENTRATION BY MIE SCATTERING IMAGING TECHNIQUE IN AXISYMETRIC NON PREMIXED BLUFF BODY FLAMES

MOKADDEM K., KENDRICK D.,W., ROLON J. C.
Laboratoire EM2C, CNRS, Ecole Centrale de Paris
92295 Chatenay Malabry Cedex, France

JAFFRE D., PERRIN M.
Gaz de France, Research and Developement Division, CERSTA
BP 33, 93211 La Plaine St Denis Cedex, France

ABSTRACT

This paper presents an experimental investigation of a turbulent, non premixed, methane/air flame, produced by an axisymetric bluff body burner. Little experimental data exists on time and spatially resolved fuel concentration on such reacting flows, despite their interest for a better understanding of combustion processes, modelling and numerical calculations in turbulent combustion.

The aim of this work is to provide these experimental data by using instantaneous, multiple point and spatially resolved measurements of species concentration of methane on the above mentionned type of flames. Planar MIE scattering is used on a non premixed CH4/Air flame.

Two dimensional planar Mie scattering is undertaken on a non premixed CH4/air flame in order to derive the field of methane concentration. Several tracer particles such as silicone oil, Calcium Hydroxyd, Zirconium Oxyd and Teflon are used. Results for both reacting and non reacting cases are compared to those obtained elsewhere from Raman scattering and probe measurements of methane concentration.

The Teflon marker is revealed to be the more efficient methane tracer in flow as it is capable to follow the aerodynamical flow fluctuations and to characterize the zones corresponding to CH_4 consumption in the flame by identifying the mean identical decomposition temperature of CH_4 molecules and Teflon particles. In this work we show that Mie scattering on Teflon particles is an accurate tracer in both reactive and non reactive flows as it gives informations on methane concentration and flame structure

1 - INTRODUCTION

Instantaneous, multiple point and spatially resolved measurements of species concentration in combustion gases are needed to guide the formulation and testing of models describing the interaction between chemistry and fluid mechanics.

Bluff Body burners provide a useful tool for the study of fuel-air mixing processes and flame stabilization that are present in industrial burner. There have been several 2D flow visualisation techniques employed for quantitative and qualitative measurements in flames. Lorenz/Mie scattering, for exemple were used in cold flows (Sheffer and al), Raman scattering or Planar Laser Induced Fluorescence were used for concentration measurements and flow imaging in Bluff Body stabilised flames (Namazian and al).

Mie scattering yields signal strengths many orders of magnitude greater than Raman or PLIF techniques. However, these latter methods provide a more faithful representation of reacting flow fields with respect to the finer scales of turbulent flow. In non reacting turbulent flows, Mie scattering has been widely used to characterise the temporal evolution of concentration fluctuations (Bilger and al). In reacting flow fields, the seeding particles must visualize regions having physical significance to the combustion process. For this purpose, oil droplets (Hanson) or $TiCl_4$ particles (Chen and Roquemore) have been generally used for the qualitative study of the structure and shape of the flame front.

In the current study, turbulent, non premixed methane-air flames are investigated using Planar Mie scattering to render 2D maps of the methane concentration. Different tracers are compared and new markers studied. The experimentally averaged data of methane concentration in the non reacting case is then compared to 2D Raman data of methane molecules. This last method is not easily quantitative in turbulent flames. Therefore the reacting case is compared to probe measurements of fuel concentration

2 - EXPERIMENTAL SET UP

2 - 1 Burner description

A schematic view of the axisymmetric, unconfined burner is shown in Figure 1. Methane is supplied through the center of the Bluff Body at a velocity of 21 m/s with a corresponding Reynolds number (based on the fuel jet diameter) of 7000. Air is supplied through a coaxial jet surrounding the Bluff Body at a velocity of 7.5 m/s (case L) or 25 m/s (case N) with a Reynolds number (based on the Bluff Body diameter) of 3300 (case L) and 11000 (case N).

The flows created by this burner are characterized by the interaction of the air and the central jet which forms a slower moving, yet intense recirculating zone condusive to flame stabilisation.

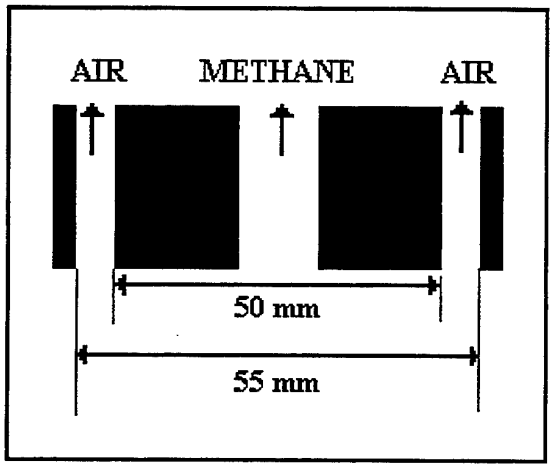

Figure 1 : Schematic view of the Bluff Body Burner

2 - 2 Imaging apparatus

The optical arrangement is shown in Figure 2. A Nd : Yag laser (Quantel) is used for Mie scattering off particles seeded in the methane jet. The YAG laser beam is doubled at 532 nm with a pulse duration of about 10 ns. An energy of 150 mj/pulse was obtained at frequency of 25 Hz. The beam is formed into a 0.2 mm thick parallel light sheet of light by a 150 mm diameter, 600 mm focal lenght cylindrical lens. The scattered light is then focused onto an intensified, CCD camera (Proxitronic HF1) which is triggered by the laser pulses .

In order to suppress the spontaneous emission, the camera is gated at 1 ms and an interferential filter centered at 532 nm and 10 nm bandwidth is added. Sequences of 250 images are directly acquired and numerised at the video frequency in the computer's RAM with a resolution of 512 x 512 pixels and 8 bits ADC depth. Imaging processing is performed over an ensemble of 1000 images.

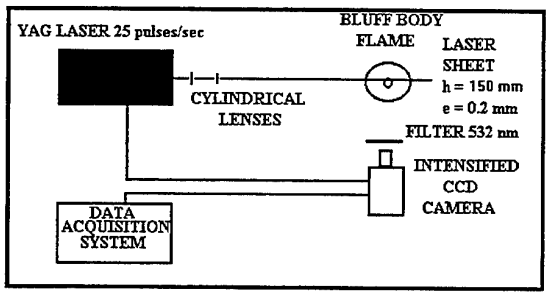

Figure 2: Optical arrangement for the Mie Scattering technique experiment

2 - 3 Resolution of the experiment

The CCD camera, having a resolution of 780 x 590 pixels, provides a measurement volume of 0.15 x 0.15 x 0.2 mm3. This resolution is determined by the field of view dimensions and the need to have sufficient particles in the measure volume so as not to invalidate the assumption of marker continuum and to reduce the marker shot noise. This latter effect is due to the finite number of particles in measurement volume. To minimise this uncertainty, it is desirable to have as many particle as possible in each sampling volume. If the flow is seeded too densely, however, secondary scattering will become important and the three dimensional nature of the flow will introduce an unknown attenuation error in the two dimensional concentration profile. In addition, for heavily seeded flows, the particles may affect the fluid's density and viscosity. A simple test for the absence of multiple scattering is to double the concentration of the particles at the exit of the jet (maximum of particle density) (Van de Hulst) and see if the signal luminance is also doubled showing that only single scattering is significant.

The Nyquist sampling theorem states that the maximum observable spatial frequency is half the sampling frequency. The size of the smallest detectable structures is two pixels or 0.3 mm which should be compared to the Kolmogoroff length. In this experiment (case L), the microscale has the approximate value of 0.03 mm (see Perrin). The experimental resolution is a factor 10 larger than the Kolmogoroff scale and well below the larger flow scales which vary between 5 and 25 cm. This results in flow scales being filtered below 0.3 mm.

This is not critical since the Kolmogroff scale is characterised by molecular diffusion processes. In this microscale, Mie scattering lead to important inaccuracies induced by the fact that particles effective diffusivity is completely different from that of methane.

2 - 4 Data reduction and error analysis

The CH_4 concentration data is obtained by correcting each image for CCD spatial non uniformities, non uniformity of the laser sheet, aberrations and "vignetting" of the optics (Mokaddem, Rolon, Perrin and al for more details on the camera calibration).

Each image is rescaled so that the maximum intensity measured at the base of the jet potential core corresponds to 100% methane concentration and the minimum signal intensity out of the flow corresponds to 0 % of methane concentration. This correction takes into account the shot to shot variations in laser power.

Random errors have been estimated by recording the laser sheet illumination in an uniformly seeded volume. The calculated rms value of the error has a maximum value of 2% of the maximum dynamic range. This random error takes into account the fluctuations in the seeding density, the shot noise, electronic noise of the camera and frame grabber. These effects are negligibles in the calculations of average methane concentration.

The bias errors which depend on the spatial coordinates are corrected by using a reference image taking into account the spatial non uniformities and non linearity of the CCD response, non uniformity of the laser sheet and the optics' aberrations. The rms value of the error was found to have the maximum value of 2% of the maximum dynamic range.

Statistical errors are introduced on the calculation of the statistical quantities over a finite ensemble of images. For an estimated mean value x and variance s^2 of N samples, the 1 - a confidence interval, the true mean μ and variance s^2 (calculated over an infinite ensemble of images) are given by the following equation (Manoukian or Newlang):

$$-\frac{s^2}{\sqrt{N}} t_{N-1,\alpha/2} \le x-\mu \le \frac{s^2}{\sqrt{N}} t_{N-1,\alpha/2}$$

$$\frac{(N-1)s^2}{\chi^2_{\alpha/2,N-1}} \le \sigma^2 \le \frac{(N-1)s^2}{\chi^2_{1-\alpha/2,N-1}} \}$$

t denotes the Student Distribution and c the Chi-Square distribution. 1000 images (N=1000) and a 90% confidence interval (1- a = 90%) are chosen. Using tabulated values for t and c, one can calculte the mean and variance of methane concentration with the relations below :

$$\left|\frac{x-\mu}{\mu}\right| \le 3\%$$

$$\left|\frac{\sigma^2-s^2}{\sigma^2}\right| \le 8\%$$

The estimated mean concentration has, therefore, a probability of 0.9 to have a relative statistical error inferior to 3%. The variance has a probability of 0.9 to have a relative statistical error inferior to 8%. If we combine bias and statistical errors, the uncertainties obtained in the mean concentration data are about 5%.

3 - THE DIFFERENT MARKERS

3 - 1 Aerodynamic study of the particles' response

A conceptual model for the dispersion of particles is the entrainement of particles by the vortex structure and ensuing centrifugal effects as the particle rotate within the organised structures (Crowe and al). This model is accurate in Bluff Body flames since the role of large scale structures widely determines the mixing and mass transport in these flows.

The Stokes number is an important parameter which affects the particles spreading in organised structures. It is defined as :

$$S_t = \frac{\tau_p}{\tau_f}$$

where tp is the aerodynamic response of the particle and tf the time associated with the motion of large scale structures.

$$\tau_p = \frac{\rho_p d_p^2}{18\mu_f}$$

r_p is the density of the particles, d_p the diameter and m_f the dynamic viscosity of the carrier fluid. The flow time response is modelled as :

$$\tau_f = \frac{\delta}{U}$$

where d is the size of the structures and U the mean velocity of the flow.

If St<<1, the particle will faithfully follow the fluid path lines. If St~1, the particles will trend to be centrifuged by the structure. For St>>1, the particle will have insufficient time to respond to changes in the fluid and will continue along a near rectilinear path. Figure 3 provides a summary of these effects.

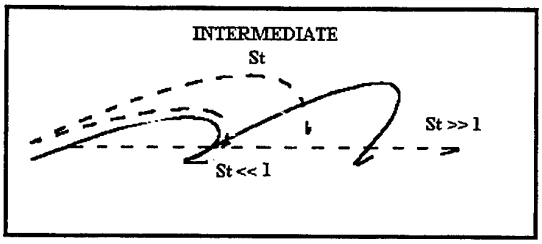

Figure 3 : Effect of the Stokes number on the aerodynamic response of a particle

The particles used in this work are silicone oil, zirconium oxide and new markers such as Teflon and calcium hydroxide. Figure 4 gives the time response of these tracers in comparison the flow time macroscale response (cold case L). It shows that the particles will follow the fluctuations of the large scale motions with an accuracy depending on the Stokes number.

Particle	Diameter (μm)	Stockes Number
Silicone Oil	5	0.02
Teflon	3	0.003
Calcium Hydroxyd	10	0.2
Zirconium Oxyd	between 1 and $30\ 10^{-3}$	between $1.3\ 10^{-4}$ and $1.2\ 10^{-7}$

Figure 4: Time response and diameter of the particles used in this study

3 - 2 Chemical study of the particles

In the Mie scattering experiment, the particles are injected with the fuel jet flow. In the cold flow experiment, the presence of the seeded particles is correlated with the methane presence within the volume domain. In order to extract the methane concentration from the images of flames, the particle must yield information on regions corresponding to the methane reaction zones and the seeding quantities must be sufficiently low to have little effect on the chemistry of the combustion process. It is known that CH_4 molecules dissociates at 400°C. Two possibilities have been therefore explored :

- the use of particles disappearing before or at 400°C such as silicone oil or a new particle such as Teflon,

- the use of particles that generate a noticeable decrease in signal luminance above 400°C by a decrease in their molecular dimensions. A new particle such as calcium hydroxide which losses a H_2O molecule at this temperature satisfies this criterion.

These particles used herein are compared to an inert reference : zirconium oxide.

4 - RESULTS AND DISCUSSION

4 - 1 Mean CH4 concentration : case L

Mie scattering is demonstrated using several particles such as silicone oil, Teflon, calcium hydroxide and zirconium oxide. Figure 5 shows the average methane concentration in a cold, Bluff Body flow using Teflon particles. This Figure reveals the symmetry of the flow and the weak penetration of the entrained air within the central jet. These results qualitatively agree with LDV velocity data discussed in Neveu and al.

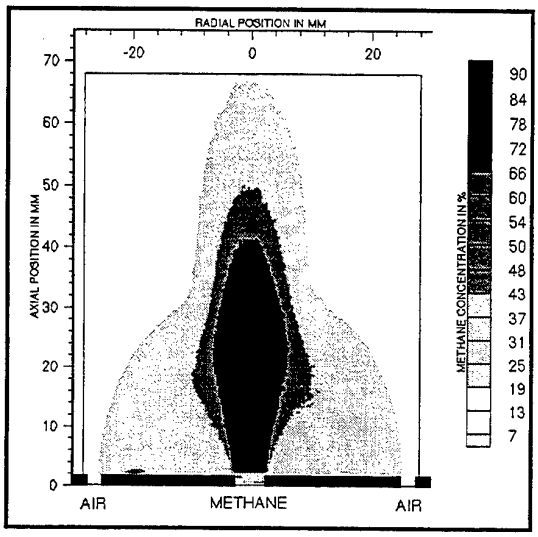

Figure 5: Mean value of methane concentration in a Bluff Body cold flow (case L) by Mie scattering off Teflon particles

Figure 6 presents the mean value of methane concentration profile along the axial direction of the fuel jet. The data from Mie scattering are compared with those (Prwzeswa and Albert) obtained from probe measurements (horizontal probe, 4 mm in diameter). In this experimental method, the absolute uncertainties in the mean CH_4 concentration are about ±1%. The results show good agreement between the two experimental methods for cold flows.

The differences noticed in the particles' behavior are due to their time response. The corresponding Stokes number for each particle indicates that centrifugal effects will be important for hydroxide calcium. This effect, coupled the inhomogeneities in the seeding particle diameter, also explains the fluctuations in the mean axial profile for hydroxide calcium.

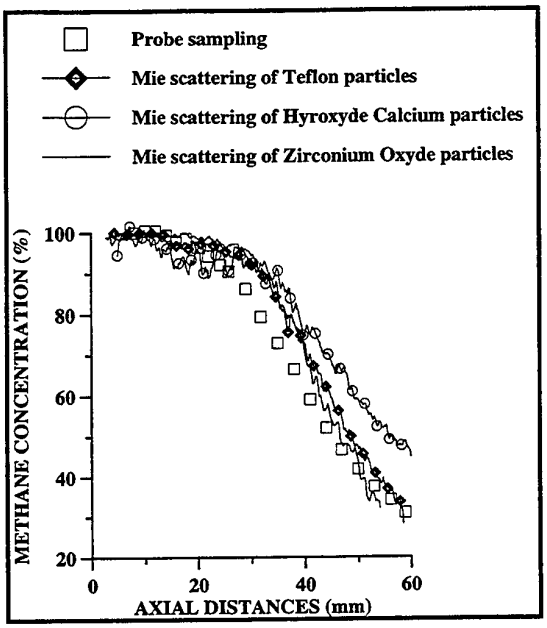

Figure 6: Mean axial methane concentration in a Bluff Body cold flow (case L) by Mie scattering off different particles

Figure 7 presents the mean methane concentration, 20 mm from the burner and shows good agreement between both the probe and Mie measurements. The mixing of the fuel into the recirculating zone is evident, indicating that this region consists of a nearly uniform mixture of fuel and air.

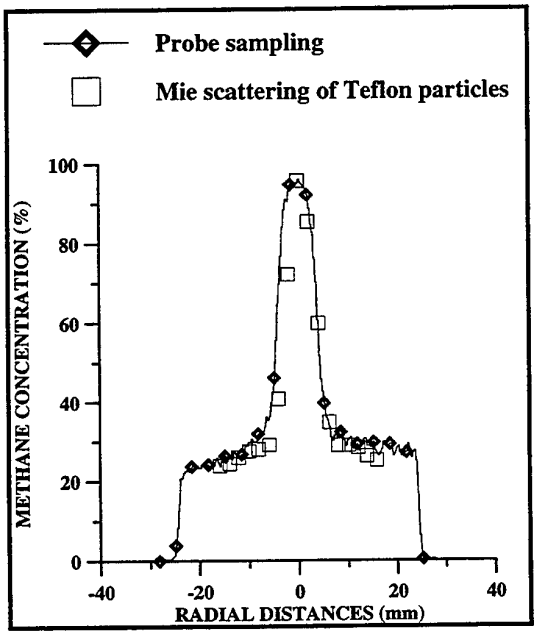

Figure 7: Mean radial methane concentration in a Bluff Body cold flow (case L, 20mm from the base of the burner) by Mie scattering off different particles

Figure 8 reveals the mean CH_4 concentration for the combusting case using Teflon particles. One sees that the methane concentration, in the recirculating zone, is beyond 0.5% (theoretical limit of detectability by Mie scattering). This result shows that this region corresponds to a reacting zone where the fuel is being consumed.

It is also apparent that there is no penetration of the ambient recirculating air into the potential core of the fuel jet.

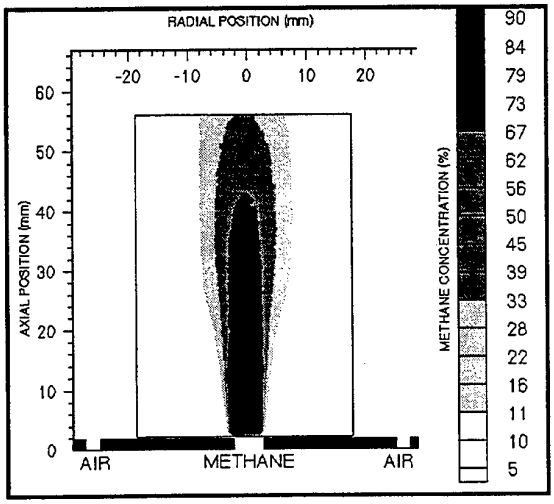

Figure 8: Mean methane concentration in a Bluff Body flame (case L) by Mie scattering off Teflon particles

Figure 9 depicts the axial methane concentration by Mie scattering using different particles. Together with these results, the mean temperature profile at the same locations from fine wire thermocouple measurements is also presented (Neveu and al). This graph shows that Teflon particles are able to depict the mean CH_4 concentration until a height of 50mm from the basis of the burner. Oxide zirconium particles which act as an inert, provide methane concentrations measurements below the values obtained for a jet seeded with Teflon particles jet. This effect, which was not observed in the cold case, is most likely due to changes in the optical properties with temperature.

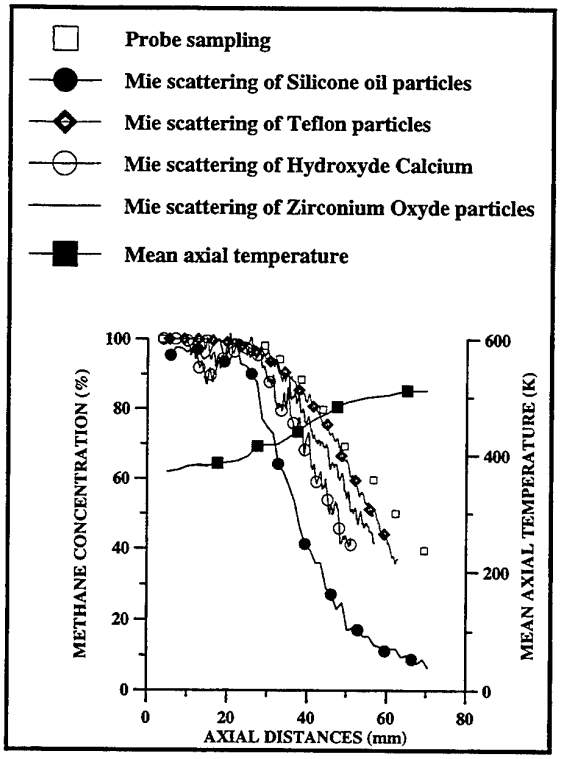

Figure 9: Mean axial methane concentration and temperature in a Bluff Body flame (case L) by Mie scattering off several particles

Figure 10 shows that above 50 mm from the base of the burner, Mie scattering off Teflon particles yield methane concentration data below the probe measurements. In this low velocity region, the effects of molecular diffusion are more pronouced and thereby explain the difference in behavior between the particle and the CH_4 molecules.

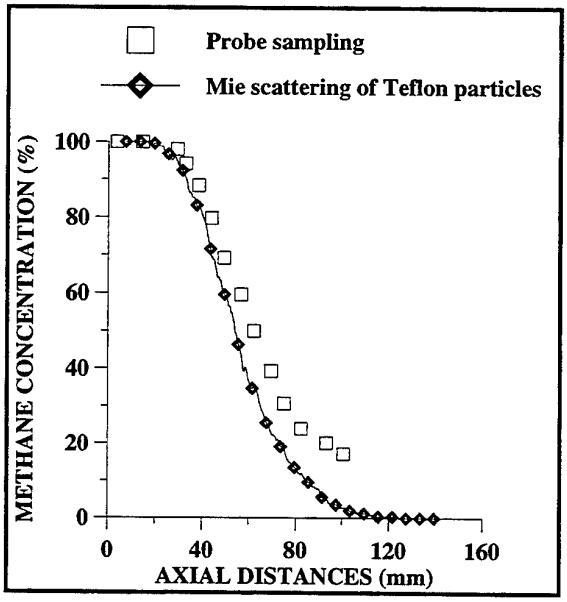

Figure 10: Mean axial methane concentration in a Bluff Body flame (case L) by Mie scattering off Teflon particles

A radial concentration profile at 20 mm from the burner's base (Figure 11) shows the accuracy of the Teflon particles in comparison with the probe measurements. The difference observed at the edge of the fuel jet between the Teflon measurements and the probe data is probably due to the intrusive effect of the latter method. During combustion, methane is consumed at the edge of the fuel jet. In this region, the horizontal probe generates a recirculation zone that increases the fuel air mixing and hence the combustion, thereby under estimating in the CH_4 concentration. This effect, however, does not exist with Mie scattering.

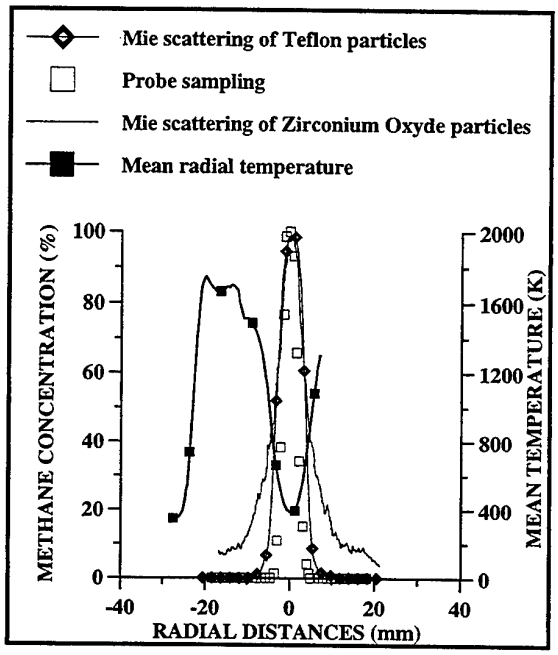

Figure 11: Mean radial methane concentration and temperature in a Bluff Body flame (case L) by Mie scattering off several particles

4 -2 Mean methane concentration : case N

This cold flow case is characterised by an axial stagnation point resulting from the fuel jet penetrating into the recirculating zone. Here, only Teflon particles are used to follow the methane behavior. The Mie scattering data are compared to correspond Raman results which uses the emission of light off the fuel molecules.

More information about the Raman experiments conducted at Sandia National Laboratories (Livermore USA) can be found in Namazian and al.

The spontaneous Raman scattering from CH_4 is observed at 514 nm for a 444 nm excitation. The beam from the Research facility's flash lamp pumped dye laser (1.8 microsecond pulse duration) is formed into a 0.3 mm thick sheet of light by a multipass cell. The spatial resolution is 300 x 500 pixels. Calibration in a flow of pure CH_4 at room temperature and pressure allowed the CH_4 signal to be converted to number density and then to a relative methane concentration. The absolute uncertainties in the mean CH_4 concentration by Raman scattering are about ±1% .

Figure 12 presents the mean CH_4 concentration by Mie scattering of Teflon particles. For this case, the stagnation zone is located at 30mm from the basis of the burner. The results agree with corresponding LDV measurements (Neveu).

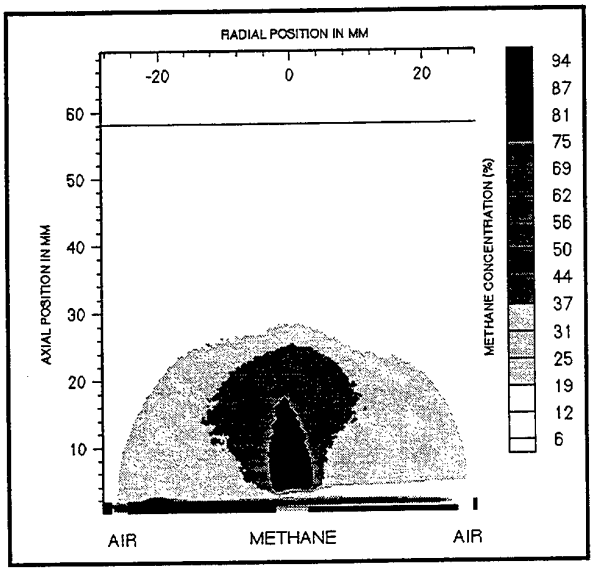

Figure 12: Mean methane concentration in a Bluff Body cold flow (case N) by Mie scattering off Teflon particles

The axial profiles of CH_4 concentration are shown in Figure 13 along with corresponding axial velocity profiles. Mie scattering is in good agreement with the data from Raman diffusion until an axial distance of 30 mm which corresponds to the stagnation zone. In this region where the velocity drops to near zero, the flow becomes highly unstable and is characterised by large scale fluctuations.

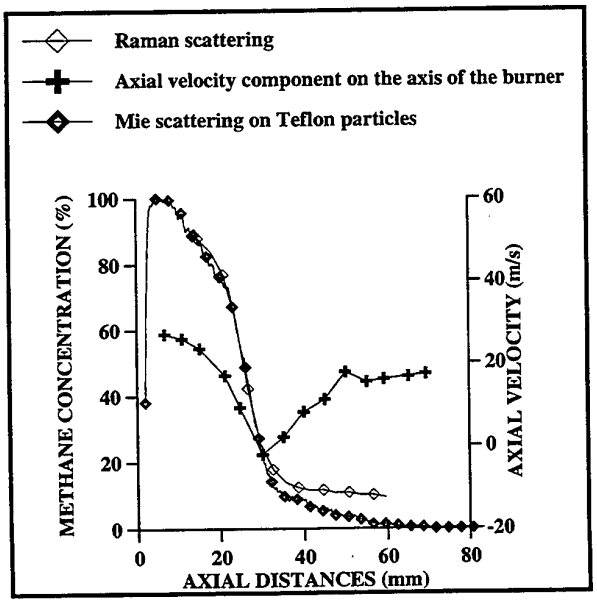

Figure 13: Mean axial methane concentration and axial velocity in a Bluff Body cold flow (case N) by Mie scattering off Teflon particles

Particles tend to move by inertial effects in the recirculation zone which reveals a lack of signal downstream of the stagnation zone.
In addition, above 30mm, the signal/noise ratio becomes less important leading to higher uncertainties in this zone.

Figure 14 presents a radial concentration profile at 20mm from the burner. It is seen that Mie scattering on Teflon particle overestimates the methane concentration in the recirculation zone which is a direct result of a large movement of particles from the fuel jet into the recirculating zone.

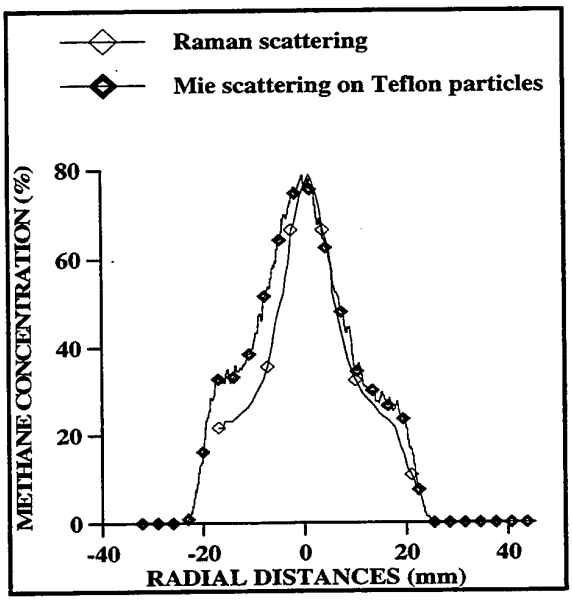

Figure 14: Mean radial methane concentration and axial velocity in a Bluff Body cold flow (case N) by Mie off Teflon particles

The position of the maximum CH_4 concentration and the general trend of the profile is, however, in good agreement with the scattering data.

5 - CONCLUSION

The data obtained by Mie scattering indicates the accuracy of Teflon particles as a methane tracer in both reactive and non reactive flows. Due to the difficulties in using Raman diffusion technique in reacting turbulent flows, Mie scattering on Teflon particles is a complementary diagnostic technique for studying turbulent flames. The images resulting from Mie scattering on Teflon particles provide information on the CH_4 concentration, the flame structure, the recirculating zone and the stagnation regions. This method is capable of producing future quantitative results of rms methane concentration fluctuations, probability density functions and spatial correlations. Futhermore, the 25 Hz recording rate should also provide in sight into the temporal development of large scale motions in similar flowfields. Finally, Mie scatering technique on Teflon particles is an non intrusive method which can be easily used in an industrial context and does not request a large investement compared to Raman experiment.

ACKNOWLEDGEMENTS

Thanks should be given to P. Mahé from Gaz de France R&D for his technical support during the experiments, Albert S. who performed the probe measurements, F. Neveu and M. Trinité who performed the fine thermocouple measurements at Gaz de France R&D, M. Namazian, J. Kelly and R. W. Scheffer who performed the Raman scattering experiments on CH4 molecules at the Sandia Laboratories in the framework of a joined research of the Gas Research Institute and Gaz de France.

REFERENCES

Chen L. D., Roquemore W. M., 1986, "Visualisation of Jet Flames", Combustion and Flame, Vol 39, pp 321-323.

Crowe C. T., Chung J. N., Troutt T. R., "Particle Mixing in Free Shear Layers", Prog. Energy Combust. Sci., Vol 14, pp 171-194, 1988.

Long M. B., Starner S. H., Bilger R. W., 1993, "Differential Diffusion in Jets Using Joint PLIF and Lorenz/Mie Imaging", Combustion Science and Technology, Vol 92, pp 209-224

Manoukian E. B., "Guide de Statistiques Appliquées", Hermann Collection, 1975

Mokaddem K, Perrin M. Y., Rolon J. C., Perrin M., Levinsky H., "Flame Front Visualization by C2 Spontaneous Emission and OH LIF in Axisymmetric Laminar Methane Air Premixed Flames", 7th International Symposium on Application of Laser Techniques to Fluid Mechanics, Lisbon, 1994.

Namazian M., Kelly J. T., Scheffer R. W., 1988, "Near Field Instantaneous Flame and Fuel Concentration Structure", 22th International Symposium on Combustion/The Combustion Institute, pp 627-634.

Newlang D. E., "An Introduction to Random Vibrations and Spectral Analysis", Longman Scientific and technical, 1975.

Neveu F, Corbin F., Perrin M.and Trinité M.,"Simultaneous velocity and temperature measurements in turbulent flames obtained by coupling LDV and numerically compensated fine wire thermocouple signals", 7th International Symposium on Application of Laser Techniques to Fluid Mechanics, Lisbon, 1994.

Perrin M., Kelly J. T., Namazian M.and Sheffer R. W., 1990, "Effect of Confinement and Blockage Ratio on Non Premixed Turbulent Bluff Body Flames", 23th International Symposium on Combustion, Orleans.

Perrin M.,1993, "Mesures de Conditions Aerodynamiques Initiales dans un Brûleur Bluff Body ", GDF Internal Report, Ref: M.CERSTA-Bcn N° 931060, 1993.

Prwzeswa M., Albert S., 1991, "Mesures de Concentration de méthane dans un Brûleur Bluff Body ", GDF Internal Report, Ref: M.CERSTA-Bcn N° 931000.

Scheffer R. W., Namazian M., Kelly J, 1989, "Comparison of Turbulent Jet and Bluff Body Stabilized Flames", Combustion Science and Technology, Vol 67, pp 123-146.

Van de Hulst H. C., "Light Scattering by Small Particles", Dover Publications Inc, New York, 1957.

NON-INTRUSIVE SPECTROSCOPIC MEASUREMENTS WITH A TUNEABLE EXCIMER LASER IN AN ATMOSPHERIC COMBUSTOR WITH PREMIXING AND PREVAPORIZATION

R. Lachner, D. Theisen, H. Kettl, R. Hönig[#], D. Rist, G. Kappler[#], and A. Schmid[#]

Munich University of Technology, Department of Flight Propulsion
[#] BMW Rolls-Royce AeroEngines, Dahlewitz

ABSTRACT

Non-intrusive spectroscopic measurements with a tuneable excimer laser were performed in an atmospheric combustor with premixing and prevaporization. Mixing shells and film layers are used to inject the fuel (n-heptane), to mix it with air, and to stabilize the flame in the rectangular combustion chamber equipped with silica quartz windows allowing laser-based investigations in the UV regime.

A qualitative distribution of fuel vapour is obtained measuring the intensity of laser-induced (ArF laser; $\lambda \approx 193\,\text{nm}$) fluorescence from pyrolized hydrocarbons (UHC); this emission is mainly caused by multi-photon dissociation (MPD) of acetylene. The hydroxyl radical (OH) is detected using 248 nm KrF laser to excite $A(v'=3) \leftarrow X(v''=0)$ transition.

Averaged images of UHC and OH reflect the visible shape of the flame characterized by two regions where the main combustion processes occur and which are located near the header plate giving a short combustion zone. Single shots of OH reveal a high turbulence level in the flame.

1. INTRODUCTION

During the last decade, non-intrusive laser-based imaging techniques have been applied in numerous experiments to gaseous reactive flows (Allen et al. (1993)) and spray flames (Koch et al. (1993), Hönig et al. (1994)). High-power excimer or pulsed dye lasers are employed for the determination of temperature, velocity, or pressure, and, furthermore, for the selective detection of single species, e.g. CH, OH, NO, and O_2, or the visualization of liquid and gaseous fuel. Most experiments were conducted at atmospheric pressure; recently, investigations were extended to high-pressure combustion (Allen et al. (1994), Allen et al. (1995), Locke et al. (1995)).

As lean premixed prevaporized combustion is one of the concepts proposed for gas turbine combustors with low nitric oxide emissions, an atmospheric combustor with premixing and prevaporization was investigated in this work. A new double shell concept is employed to atomize the fuel (n-heptane) and to stabilize the flame. Using a tuneable excimer laser at ArF transition ($\lambda \approx 193\,\text{nm}$), intensities of broadband emission from unburned hydrocarbons (UHC) are measured. This fluorescence light stems mainly from multi-photon dissociation (MPD) of acetylene (C_2H_2) as reported by Allen and Hanson (1986), McDonald et al. (1978), and Jackson et al. (1978). Operating the laser at KrF transition ($\lambda \approx 248\,\text{nm}$), the distribution of the hydroxyl radical (OH) is obtained with the LIPF (laser-induced predissociative fluorescence) method described by Andresen et al. (1988) and Koch et al. (1993).

2. COMBUSTION CHAMBER

The premix/prevaporizer duct is built inside the atmospheric combustor, as drawn in Figure 1. The fuel is injected through two film layers onto a double shell serving as an airblast-atomizer. About 4% of the air stream $\dot{m}_{air}$ flows into the atomizer and the adjacent prevaporizer duct with a length of about 100 mm. Into the air/fuel mixture leaving the prevaporizer duct, additional air ($\approx$ 16% of $\dot{m}_{air}$) is injected through a mixer; subsequently, the "new" mixture passes a second double shell entering the rectangular part of the combustor (height $\approx$ 101 mm, width $\approx$ 124 mm), in which the flame is stabilized . One part of the remaining air ($\approx$ 20% of $\dot{m}_{air}$) cools the header plate, the other one ($\approx$ 60% of $\dot{m}_{air}$) enters the rectangular part of the combustor through slits along the four walls as one measure to protect the walls against thermal loading; another measure is described below. Three sides of the combustor are equipped with fused silica quartz windows, the fourth side is a metal plate in which the ignitor is placed. About 65 mm to 70 mm behind the header plate, a restrictor plate, which has an orifice of 40 mm times 80 mm (vertical x horizontal dimension) and which is protected by a ceramic fibre sheet, is mounted to enhance recirculation. The combustor is supplied with electrically heated air ($T_{air,max} \approx 650\,\text{K}$). Additional air (ambient temperature; mass flow rate up to

150 g/s) is used for the cooling of the windows and the metal plate. This cooling air flows in eight small ducts along the combustor edges from which slits branch off creating two cooling films for each side of the combustor. These ducts start at the beginning of the combustion chamber and are blocked at the end. Therefore, the cooling air mostly leaves the duct in the second half of the combustor, thus only slightly influencing the combustion processes which take place in the first half of the combustor.

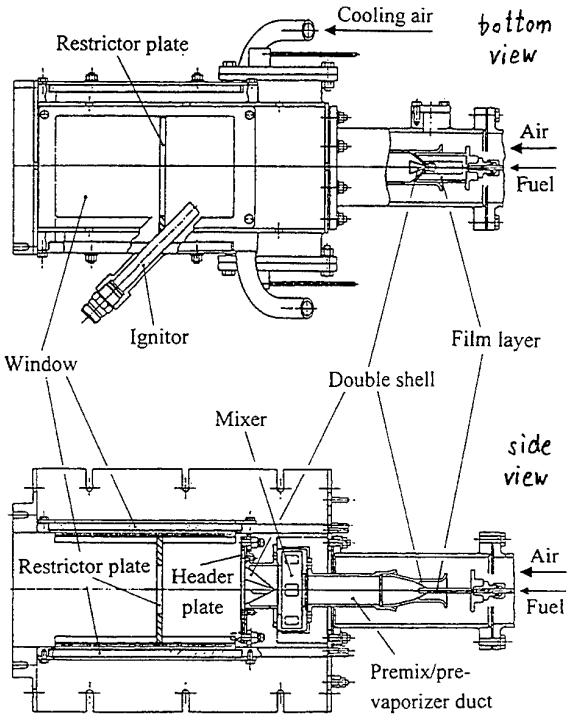

Fig. 1: Drawing of the premix/prevaporizer duct built in the rectangular combustor; bottom and side view

The air stream flowing into the combustor is measured with a metering orifice, the cooling air with a vortex flowmeter. The amount of fuel is determined with a mass flowmeter utilising the phenomenon of the Coriolis force. N-heptane ($n-C_7H_{16}$) is used as fuel because it is nearly transparent for UV laser radiation and its properties are similar to those of kerosene. The temperature of the air entering the combustor is measured with a NiCr-Ni thermocouple (type K) positioned about 300 mm in front of the header plate. The distribution of the air in the inlet section of the combustor is derived from experiments in which various parts in this section are blocked and the dependence of the reduced air mass flow on the pressure loss is determined. For the measurements described in this report, the pressure loss is adjusted to about 4 % corresponding to an air mass flow of $\dot{m}_{air} \approx 42\,g/s$ to $56\,g/s$ in the investigated temperature range of 400 K to 630 K.

3. EXPERIMENTAL SET-UP FOR LASER MEASUREMENTS AND EXCITATION/DETECTION STRATEGY

A scheme of the experimental set-up used for the non-intrusive spectroscopic measurements with detection system and laser beam path is drawn in Figure 2. A tuneable excimer laser (1) (Lambda Physik EMG 150 T-MSC) is operated at ArF transition ($\lambda \approx 193\,nm$) or at KrF transition ($\lambda \approx 248\,nm$). The specifications of the laser are listed in Table 1.

Tab. 1: Laser specifications

Laser medium	**ArF**	**KrF**
Wavelength [nm]	193	248
Tuning range [nm]	1	1
Pulse energy max. [mJ]	100	250
Average power max. [W]	6	20
Repetition rate max. [Hz]	80	80
Bandwidth [nm]	0.005	0.001
Pulse width [ns]	13	17
Beam shape, v x h [mm x mm]	21 x 4	21 x 5

The laser beam passes a calibration section (2) and several mirrors (3) and is formed to a sheet of about 27 mm x 1 mm through cylindrical lenses (4) and a slit (5). The laser sheet (6a, 6b) penetrates the combustor (7) from bottom to top.

Natural or laser-induced fluorescence light leaves the combustor through a side window. The signals sometimes filtered with transmission filters or dielectric mirrors (8) are imaged onto a photometric digital camera (9) (LaVision Flamestar II) via a Nikkor UV lens (105 mm, F/# 4.5) (10). The Flamestar camera system consists of a UV sensitive high gain image intensifier (S20 photocathode, P20 phosphor) fibroptically coupled with the CCD chip (Thomson TH7863). The intensifier is gated so that the camera records only a short period (50 to 500 ns) during and after each laser pulse. The resulting grey scale pictures are digitized and stored in a computer (11). The computer with an external camera multiplexer (12) triggers the laser and the photometric cameras and controls both the stepmotor to tune the laser frequency and the position of a translation stage moveable in the two dimensions of the horizontal plane. The detection system and the optics guiding and forming the laser beam are mounted on this stage.

Measurements were performed with two different configurations regarding the plane of interest. On the one hand, the laser sheet (6a) is passed through the combustor along the main flow direction and the camera is positioned in an angle of 90° to the laser sheet (see Figure 3 top). One image in a plane along the flow direction comprises four or five laser sheets. Co-ordinate "y" starting off at the middle of the combustor denotes the position of a plane. Looking downstream, a minus sign corresponds to the left hand side of the combustor, a plus sign to the right hand side. A dark bar in each image taken in a plane along the flow direction is a space which has to be omitted due to the restrictor plate. The images start at about 7 mm downstream of the header plate.

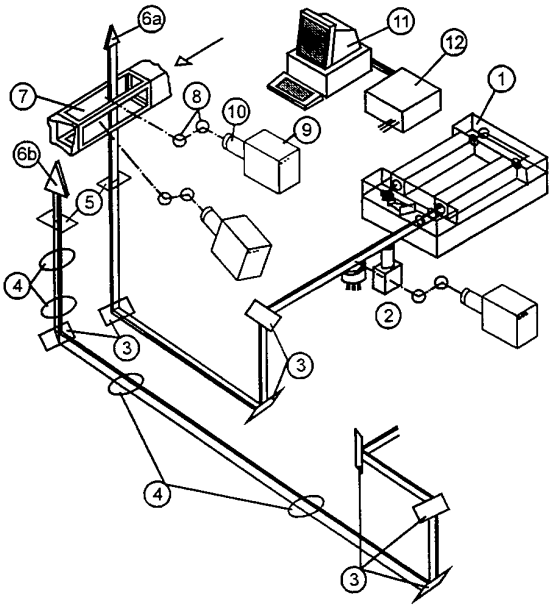

Fig. 2: Sketch of the experimental set-up with detection system and laser beam path

On the other hand, the laser sheet (6b) is perpendicular to the flow direction and the camera detects the signals in an angle of about 20° with regard to the plane of the laser sheet (see Figure 3 bottom). Single pictures are rotated with the aid of the computer giving a view of 90° on the plane of interest. Each of those planes perpendicular to the flow direction is made up of three laser sheets; the position of a plane is indicated by co-ordinate "x" starting from the header plate. Due to the camera position, the resulting images represent a view against the main flow direction. At certain positions (x = 47, 57, 61 mm), signals are totally blocked by the restrictor plate or can only be detected through the orifice of that plate (vertical dimension: 40 mm).

For the detection of gaseous unburned hydrocarbons (UHC), the laser is used at ArF transition ($\lambda \approx 193\,\text{nm}$) and

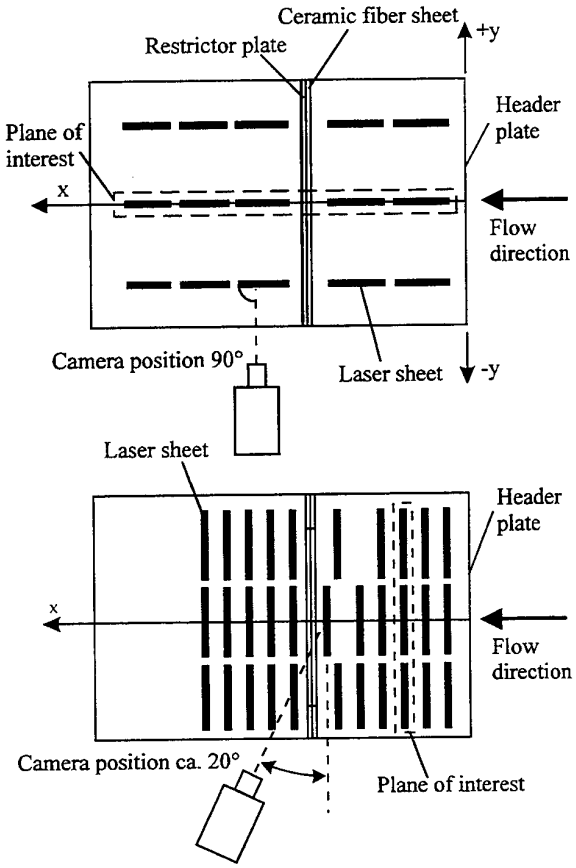

Fig. 3: Scheme of the two configurations regarding the plane of interest in which measurements are performed; top: plane along flow direction; bottom: plane perpendicular to flow direction

tuned to a wavelength off-resonant to O_2 and NO (Allen and Hanson (1986), Hönig et al (1994)). Subsequent broad-band emission, which may be dominated by emission from excited states of CH and C_2 caused by photodissociation of small hydrocarbons (Jackson et al. (1978), McDonald et al. (1978), Craig et al. (1982)), is detected in a range of about 250 nm to 400 nm (UG 11 filter). To give an example for this emission, the high flux of the UV laser allows non-resonant two- or three-photon absorption by acetylene yielding mainly electronically excited C_2 (McDonald et al. (1978)). The fact that the emission from UHC is initiated by a non-resonant process explains why this fluorescence phenomenon is independent of the excitation wavelength.

Hydroxyl radicals (OH) are detected using KrF excimer laser ($\lambda \approx 248\,\text{nm}$) to excite the $P_2(8)$ line ($\nu = 40248.48\,\text{cm}^{-1}$, Andresen et al. (1988)) of the vibrational transition $3 \leftarrow 0$ in the $A^2\Sigma^+ \leftarrow X^2\Pi$ absorption band. The upper state of this transition predissociates with a rate of about $10^{10}\,\text{s}^{-1}$ (Gray and Farrow (1991)); yet, the quenching

rate in hydrocarbon flames at atmospheric pressure is about $0.5 \cdot 10^{-9}\ s^{-1}$ (Schwarzwald et al. (1987), Köllner et al. (1990)). Hence, the fluorescence light of the excited OH molecules, detected through a UG 11 filter, is only slightly influenced by quenching processes. Interpreting the OH measurements in a quantitative manner, one has to keep in mind that the population density of the ground state depends on temperature. For the considered transition of OH, however, this dependence is small over typical flame conditions (Koch (1992), Koch et al. (1993), Hönig et al. (1994)). Furthermore, transition from $v' = 3$ to lower vibrational states $v' = 2, 1, 0$, which do not predissociate, takes place (Koch (1992), Andresen et al. (1988)). The vibrational energy transfer in the excited state accounts to about 5 %; yet, the intensities of the direct ($v' = 3$) and indirect ($v' = 2, 1, 0$) emission appear to be almost equal (Koch (1992)). Therefore, it is recommended to detect only the emission via the 3-2 band in the range of 295 to 305 nm, the main transition in the fluorescence of the directly excited state of OH ($v' = 3$). Unfortunately, this detection strategy for OH could not be realized in this work.

For the selective detection of OH, images are taken with the laser tuned on- and off-resonant to an appropriate absorption line; subsequently, the off-resonance signals are subtracted from the on-resonance ones to make sure that the resulting images trace back solely to the species under investigation.

The laser-induced fluorescence signals are imaged onto the CCD-chip with an exposure time of 0.2 - 0.5 µs (single shot picture). To get a residence probability or averaged spatial distribution of the species investigated, images are taken with "sequence summing", i.e. 50 shots are added up "on chip" and this procedure is repeated 10 times before storing the data.

4. RESULTS

The shape of the flame could be seen through the quartz windows. Photos and video records have been taken. They reveal that two regions exist in which the main combustion processes occur, one directed to the upper left corner of the combustor and one to the lower right one if one looks downstream. These two "clubs" of the flame stay at a relatively large angle to the main flow direction, i.e. they are positioned quite near to the header plate giving a short combustion zone. Regarding the visible shape of the flame, it turned out - for a given air-fuel ratio - that it was almost the same with and without restrictor plate. Therefore, the restrictor plate is not necessary to achieve a stable flame.

In both cases, the flame burned stably only under very rich conditions ($2 \leq AFR_{prevapour} \leq 3$, $10 \leq AFR_{flame} \leq 15$). Although the double shell failed in achieving stable lean combustion, it works well as atomizer. Images obtained with the Mie scattering technique show that, if the inlet temperature exceeds a certain limit, only a small amount of liquid fuel is present in the flow. This is consistent with the observation that no droplets are visible in the flame. Liquid fuel is mainly detected around the vertical symmetry plane of the combustor (-15 mm < y < 15 mm).

The capability of the prevaporizer is also demonstrated in Figure 4 showing the distribution of signal intensities of gaseous pyrolized fuel (UHC) at different inlet temperatures. Using ArF laser ($\lambda \approx 193\,nm$) tuned off-resonant to O_2 and NO, 10 single shots (exposure time $\approx 0.4\,\mu s$) are summed up measuring in a plane along the flow direction (y = - 25 mm).

$T_{in} = 410$ K

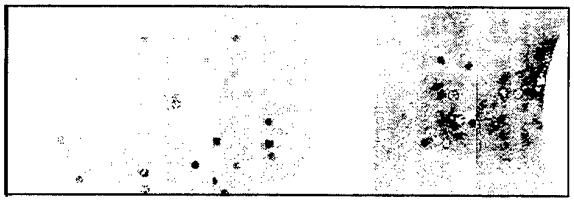

$T_{in} = 615$ K

Fig. 4: Distribution of gaseous fuel (UHC) intensities at varying inlet temperature, detected with multi-photon dissociation method (ArF laser, $\lambda \approx 193\,nm$) in a plane along flow direction (y = - 25 mm); flow from right to left; excitation wavelength off-resonant to O_2 and NO; sum of 10 single shots (exposure time ≈ 0.4 µs); imaged area: 46 mm x 112 mm (height x length); filtering: UG 11 filter, i.e. range of detection about 250 - 400 nm; $\dot{m}_{air} \approx 45 - 56 g/s$; $\dot{m}_{fuel} \approx 1.3 - 1.35 g/s$; grey scale: black: max.; white: min. intensities;

The transmission filter (UG 11 Schott glass) used to detect the broad-band emission from small pyrolized hydrocarbons does not totally block the elastically scattered light (Mie scattering). Hence, fuel droplets are observable in Figure 4. Obviously, the focusing of the camera was not perfect in these experiments as the fuel droplets appear slightly blurred.

UHC measurements performed in several planes along the flow direction indicate that pyrolized hydrocarbons can be found along the central line of the combustor and in the two "clubs" of the flame, described above. Furthermore, the images of UHC reveal that gaseous fuel is burned rapidly, but it is obviously distributed unequally, as far as this can be inferred from qualitative measurements. The UHC images and the distribution of LIPF-OH signal

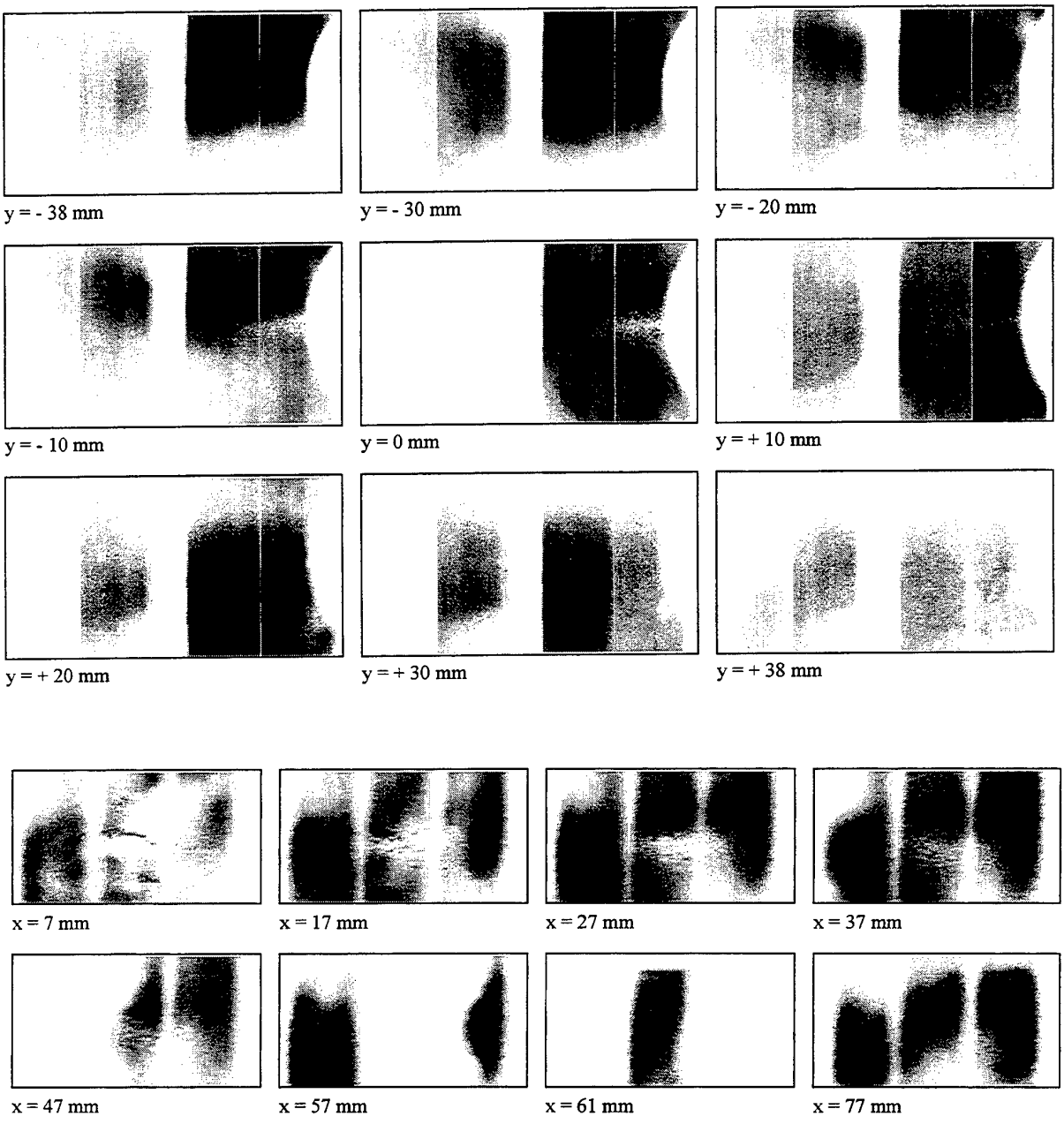

Fig. 5: Distribution of hydroxyl radical (OH) detected with LIPF-method (KrF-laser, $\lambda \approx 248$ nm); excitation wavelength: $P_2(8)$ line of the vibrational transition 3←0 in the $A^2\Sigma^+ \leftarrow X^2\Pi$ absorption band ($\nu = 40248.48\,cm^{-1}$); off-resonance signals subtracted; "sequence summing", 10 times 50 shots (exposure time ≈ 0.25 µs); filtering: UG 11 filter, i.e. range of detection: about 250 - 400 nm; $\dot{m}_{air} \approx 42-44\,g/s$; $T_{in} \approx 560-635\,K$; $\dot{m}_{fuel} \approx 1.05\,g/s$;
grey scale: black: max.; white: min. intensities;
top: 9 planes along flow direction; flow from right to left; imaged area: 62 mm x 116 mm (height x length);
bottom: 8 planes perpendicular to flow direction; view against flow direction; imaged area: 45 mm x 73 mm (height x width);

intensities in Figure 5 unveil a region, located in the right bottom corner of the combustor between x = 0 mm and about x = 25 mm, where, evidently, the vaporization dominates over the oxidation processes as high signals from UHC, but low ones from OH are detected.

OH is investigated in 9 planes along and in 8 planes perpendicular to the flow direction. All images in Figure 5

are derived with "sequence summing" (10 times 50 shots), i.e. adding up 500 shots, and by subtraction off- from on-resonance signals. Koch et al. (1993) report that, using KrF laser, unfiltered emission from pyrolized hydrocarbons is stronger than the fluorescence of OH. Although in this work

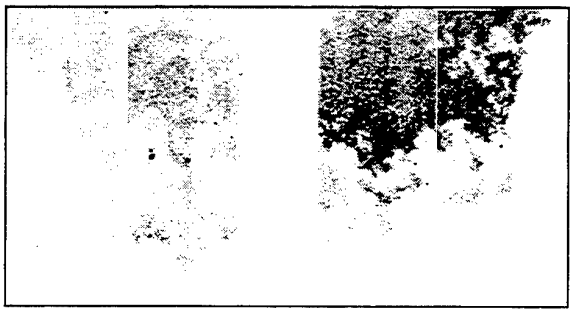

y = - 20 mm

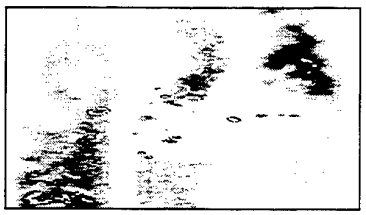

x = 27 mm

Fig. 6: Distribution of hydroxyl radical (OH) detected with LIPF-method (KrF-laser. $\lambda \approx 248$ nm); excitation wavelength: $P_2(8)$ line of the vibrational transition $3 \leftarrow 0$ in the $A^2\Sigma^- \leftarrow X^2\Pi$ absorption band ($\nu = 40248.48 cm^{-1}$): single shot: exposure time ≈ 0.25 µs; filtering, inlet conditions, and imaged areas cf. Fig. 5;
grey scale: black: max.; white: min. intensities;
top: plane along flow direction;
bottom: plane perpendicular to flow direction;

no selective filtering of the emission induced by KrF laser is employed, the on-resonance signals are more intense than the off-resonance ones, in contrast to the experiences made by Koch et al. (1993) in liquid-fuelled spray flames of commercial oil burning furnaces using also n-heptane as fuel. The distribution of OH in Figure 5 resembles the visible shape of the flame described above.

Figure 6 displays two single shot images of OH, one in a plane along and one perpendicular to the flow direction. No off-resonance signals are subtracted as on- and off-resonance signals cannot be detected simultaneously. Therefore, in regions where still large amounts of gaseous fuel are present, as mentioned above, the results of single shot measurements without selective detection of the OH emission ought to be viewed cautiously. In those regions, intensities of off-resonance signals can be in the same order as that of on-resonance emission. In the OH single shot image in a plane along the flow direction (Figure 6 top), one can see the typical structure of a turbulent flame. In small bright regions, where the flame front is located at the moment of detection, hot products encounter and ignite fresh fuel-air mixtures thus starting and supporting the combustion processes. Beside the bright spots, larger fields of lower brightness are visible where combustion products can be found. The convoluted flame front indicates a high turbulence level. Allen et al. (1994) report on similar structures observing the inner flame front of a spray flame at 0.1 MPa using a solid cone nozzle. The high turbulence, obviously caused through the vortices induced by the double shell, associated with a large strain rate of the flame, might be one reason for the blow out of the flame at quite rich conditions.

Furthermore, the examination of several single shots of OH reveals relatively large fluctuations of the flame. The same feature is perceptible in images of the natural fluorescence, taken with an exposure time of 100 µs. Checking the fuel supply concerning irregularities, this source can evidently be excluded for causing the fluctuations of the flame.

In single shots of OH taken in planes perpendicular to the flow direction, one example is given in Figure 6, the fine-scale structure in the turbulent flame is almost totally blurred because of the steep angle at which the camera detects the signals induced by the laser sheet resulting in a deterioration of spatial resolution.

5. CONCLUSIONS

An rectangular combustor was investigated at atmospheric pressure employing a new double shell concept for fuel atomization and flame stabilization. Silica quartz windows allowed laser-based imaging measurements.

Lean stable combustion could not attained with the double shell. Yet, good atomization and vaporization was observed. Almost no droplets are visible in the flame and, respectively, are detected using Mie scattering techniques. Multi-photon dissociation measurements of UHC show a rapid consumption of gaseous fuel. Averaged LIPF-OH images reflect the visible shape of the flame characterized by two regions where the main combustion processes take place. These regions are situated near to the header plate thus resulting in a short combustion zone. Single shot images of OH reveal a high turbulence level and quite large fluctuations of the flame, probably responsible for blow out at relatively rich conditions. Further work will concentrate on an improved concept for the stabilization of the flame.

ACKNOWLEDGEMENT

This work was funded by the Commission of the European Union through the Brite-EuRam II project "Low Emissions Combustor Technology, Phase II".

REFERENCES

Allen, M. G. and Hanson, R. K. 1986, Digital Imaging of Species Concentration Fields in Spray Flames, Twenty-first Symposium (International) on Combustion, pp. 1755-1762.

Allen, M. G., Parker, T. E., Reinecke, W. G., Legner, H. H., Foutter, R. R., Rawlins, W. T., and Davis, S. J. 1993, Fluorescence Imaging of OH and NO in a Model Supersonic Combustor, AIAA Journal, vol. 31, No. 3, pp. 505-512.

Allen, M. G., McManus, K. R., and Sonnenfroh, D. M. 1994, PLIF Imaging Measurements in High-Pressure Spray Flame Combustion, 30th AIAA/ASME/SAE/ASEE Joint Propulsion Conference, AIAA 94-2913.

Allen, M. G., McManus, K. R., and Sonnenfroh, D. M. 1995, PLIF Imaging in Spray Flame Combustors at Elevated Pressure, 33rd Aerospace Sciences Meeting and Exhibit, AIAA 95-0172.

Andresen, P., Bath, A., Gröger, W., Lülf, H. W., Meijer, G., and ter Meulen, J. J. 1988, Laser-induced fluorescence with tunable excimer lasers as a possible method for instantaneous temperature field measurements at high pressures: checks with an atmospheric flame, Applied Optics, vol. 27, No. 2, pp. 365-378.

Craig, B. B., Faust, W. L., Goldberg, L. S., and Weiss, R. G. 1982, UV short-pulse fragmentation of isotopically labeled acetylene: Studies of emission with subnanosecond resolution, J. Chem. Phys., vol. 76, No. 10, pp. 5014-5021.

Gray, J. A. and Farrow, R. L. 1991, Predissociation lifetimes of OH $A^2\Sigma^+(v'=3)$ obtained from optical-optical double-resonance linewidth measurements, J. Chem. Phys., vol. 95, No. 10, pp. 7054-7060.

Hönig, R., Kappler, G., Andresen, P., and Brehm, N. 1994, Multi Species Detection in a Liquid Fuelled Model Combustor using Tunable Excimer Lasers, Combust. Sci. and Tech., vol. 102, pp. 255-272.

Jackson, W. M., Halpern, J. B., and Lin, C.-S. 1978, Multiphoton Ultraviolet Photochemistry, Chemical Physics Letters, vol. 55, No. 2, pp. 254-258.

Koch, A. 1992, Verbrennungsanalyse in turbulenten und laminaren Flammen mit schmalbandigen Excimerlasern, Ph.D. Thesis, Universität Göttingen.

Koch, A., Chryssostomou, A., Andresen, P., and Bornscheuer, W. 1993, Multi-Species Detection in Spray Flames with Tunable Excimer Lasers, Appl. Phys. B, vol. 56, pp. 165-176.

Köllner, M., Monkhouse, P., and Wolfrum, J. 1990, Time-Resolved LIF of OH ($A^2\Sigma^+$, $v'=1$ and $v'=0$) in Atmospheric-Pressure Flames Using Picosecond Excitation, Chemical Physics Letters, vol. 168, No. 3/4, pp. 355-360.

Locke, R. J., Hicks, Y. R., Anderson, R. C., Chun, K. S., Ockunzzi, K. A., and North, G. L. 1995, Two-Dimensional Imaging of OH in a Lean Burning High Pressure Combustor, 33rd Aerospace Sciences Meeting and Exhibit, AIAA 95-0173.

McDonald, J. R., Baronavski, A. P., and Donnelly, V. M. 1978, Multiphoton-Vacuum-Ultraviolet Laser Photodissociation of Acetylene: Emission from Electronically Excited Fragments, Chemical Physics, vol. 33, pp. 161-170.

Schwarzwald, R., Monkhouse, P., and Wolfrum, J. 1987, Picosecond Fluorescence Lifetime Measurement of the OH Radical in an Atmospheric Pressure Flame, Chemical Physics Letters, vol. 142, No. 1/2, pp. 15-18.

SESSION 8

Aerodynamic and Rotating Machines I

LDA-INVESTIGATIONS ON TURBULENT SHEAR STRESS IN A FULL SCALE CENTRIFUGAL PUMP

Martin Lutz, Viktor Denk, Antonio Delgado

Lehrstuhl für Fluidmechanik und Prozeßautomation
Technische Universität München, D-85350 Freising, Germany

1. ABSTRACT

In this work, the flow through a radial centrifugal pump has been examined. With a two-component Laser-Doppler-Anemometer (LDA), the velocity distributions and the profiles of the turbulent shear stress have been measured in impeller and casing of the pump. Investigations at different rotational speeds and flow rates showed some main influences on the transport conditions, especially the advantage of speed-controlled operation compared to throttling control.

2. INTRODUCTION

Shear forces due to fluid motion can cause severe product destruction on shear sensitive media in applications in food- and biotechnology. Agglomeration of milk fat bubbles /Hinrichs (1994)/, the negative influence on beer wort contents /Denk (1995)/, or shear induced damage to cells /Cherry & Kwon (1990)/ or enzymes /Tirrel & Middleman (1975)/ in bioreactors have been reported in literature. Typical values for the critical shear stress for such destruction in long term experiments are in the order of magnitude of 50 Pa /Hinrichs (1994), Denk (1995)/.

Due to the fast rotating impeller and the energy input in a pump, shear forces considerably higher than this level can be expected. But the typical operating behaviour, the good possibility for cleaning and sterilising, connected with comparatively low cost make radial centrifugal pumps very widespread in the food- and biotechnological industry. In this work the profiles of the mean flow and the turbulent shear stress have been investigated in a standard industrial pump at different rotational speeds and flow rates to find the main influences on the transport conditions in the pump. To support these LDA measurements in regions close to walls, wall shear rate measurements at the impeller of the pump have been performed with the limiting current electrodiffusion technique which are reported elsewhere /Lutz et al. (1996)/.

These examinations shall lead to recommendations for the operation of centrifugal pumps and, with further investigations, to improved pump geometries for the transportation of shear sensible liquids.

3. EXPERIMENTAL

3.1 Pump and Test Rig

For the investigation, a full scale radial centrifugal pump with an open stainless steel impeller was used. The impeller (diameter d = 150 mm) has seven backward bounded blades (height s = 20 mm) of simple two dimensional design. The pump has a toroidal casing (gap width l = 30 mm) with a planar front cover which provides good accessibility for the optical measurements. This front cover has been replaced by a plate of acrylic glass, but the overall geometries of casing and impeller have not been changed (Fig. 1).

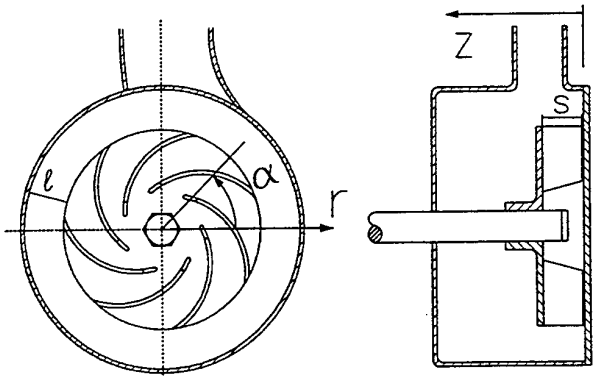

Fig. 1 Schematical sketch of the pump geometry and the used coordinate system.

The pump is run with a speed-controlled motor in a closed pipe circulation. The speed of the pump, temperature, head, and the flow rate are measured. To realise different flow rates at one rotational speed, a throttle was used. Fig. 2 schematically shows the test rig. The Net Positive Suction Head (NPSH) of the plant is 1.5 m, thus rotational speeds n up to 1650 revolutions per minute (rpm) and flow rates up to

$\dot{V} = 26\ m^3/h$ were possible until cavitation occurred. All experiments were carried out with demineralised water at a temperature of T = 20°C, mostly at n = 1450 rpm, which corresponds to a standard four-pole asynchronous motor at a mains frequency of 50 Hz. The specific speed n_q of the investigated pump at its point of best efficiency is $n_q \approx 22\ min^{-1}$.

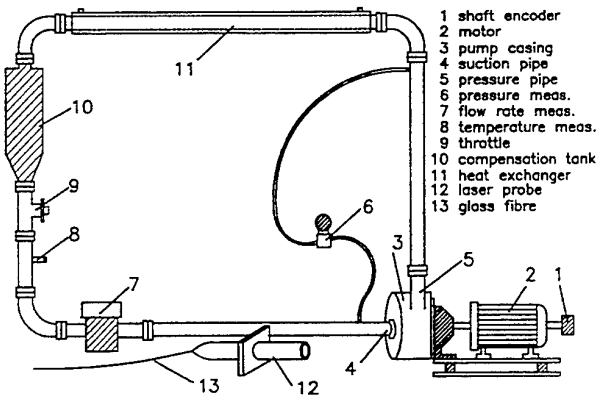

Fig. 2 Sketch of the pump test bed.

3.2 Measurement of the Velocity

For the velocity measurements, a standard two-component Laser-Doppler-Anemometer (LDA) with backscattering technique is used. It consists of a 100 mW Ar-Ion-Laser and the green and the blue line were used for coincidence measurement of the radial and circumferential velocity component. The LDA-system works with bragg-cell frequency-shifting, photo-multipliers, and two counter-processors. The laser beam is lead in a fibre optic cable to the non-corotating probe that is mounted on a three axis traverse table in front of the pump. Because the central entering suction pipe and its connection to the pump did not allow to position the laser probe very close to the pump, a focusing lens with a focal length of 349.8 mm had to be used. This led to a diameter of the measurement control volume (MCV) d ≈ 85 µm.

The diameter of the probe volume is large compared to the smallest length scales occurring in the flow. The Kolmogorov microscale of length η can be estimated to /Tennekes & Lumley (1972), Delgado (1986)/

$$\eta = l \times \mathrm{Re}^{-3/4} \approx 60\ \mathrm{mm} \left(\frac{0.15\ \mathrm{m}\ 10\ \mathrm{m/s}}{10^{-6}\ \mathrm{m^2/s}} \right)^{-3/4} \approx 1.4\ \mu\mathrm{m}\,, \quad (1)$$

with the distance between two blades at the outer radius of about 60 mm as typical integral length scale and a velocity scale in the order of 10 m/s. But usually a MCV of 3-5 η is recommended for LDA-measurements /Tropea (1996)/, which would mean a possible resolution of the configuration used in this work of about 85 µm/5 = 17 µm. Therefore the smallest turbulent motions in the present case could not be resolved. But because most of the energy in a turbulent flow is associated with the large scale motion /Schlichting (1982), Tennekes & Lumley (1972)/, the spatial resolution of the measurements is sufficient for characterization of the shear stress profiles in the pump.

Due to the planar cover of the pump casing (Fig. 1), an intersection of the two MCVs inside the pump was possible and coincidence measurements could be performed. With the simultaneous measurement of two velocity fluctuations u',v', one component of the turbulent stress tensor can be calculated according

$$\tau_{u,v} = -\rho \left(\overline{u'v'} \right). \quad (2)$$

Because purified water and a backscattering arrangement was used, seeding particles were needed to obtain satisfying data rates. These were latex-spheres with a mean diameter $d_p = 12\ \mu m$ and a density $\rho_p = 2.6\ g/cm^3$. A possible estimation for the slip velocity of the particles $|v_p - v_f|$ relative to the fluid can be made following /Adrian (1991)/

$$\left| v_p - v_f \right| = \frac{\rho_p\, d_p^2}{\rho_f\, 36\upsilon} \left| \dot{v} \right|. \quad (3)$$

In the present investigation, with an acceleration of $\dot{v} \approx v^2/r$, a particle slip velocity of about 7 mm/s can be expected, which is below 0.1% of the mean velocity.

The number of measured data points required for a given error ε of the mean velocity can be estimated with the relation /Tropea (1996)/

$$\varepsilon_{max}^2 = 2.58 \frac{Tu^2}{N}. \quad (4)$$

To achieve a maximum error ε_{max} for the measurement of 1 % (99 % confidence interval), the number of necessary data points at a turbulence intensity Tu ≈ 20 - 40 % inside the impeller is N ≥ 4000 statistically independent velocity data points.

3.3 Angular Resolution

For a detailed description of the flow inside the impeller, it is necessary to correlate the velocity data of the LDA to the angular position of the impeller. For that purpose, a shaft encoder is connected to the motor shaft (the impeller is mounted directly on the motor shaft, see Fig. 2). With every valid velocity measurement of the LDA, self-developed electronics supply the signal of the shaft encoder to the LDA-processor and the actual position of the impeller is saved. The shaft encoder works with a resolution of 6000 increments per revolution ($\Delta\alpha = 0.06°$).

In Fig. 4, a typical distribution of the measurement data at one position of the laser probe over the angular position of the shaft encoder is shown. The seven blades of the impeller, where no valid data points occur, are clearly visible. After the measurement, the data was sorted on the PC according to its angular position.

Because 6000 positions per revolution with the accuracy mentioned above would require a measurement time per position of about 70 hours, the angular resolution had to be reduced. A resolution of $\Delta\alpha = 1.0°$ was found to be sufficient for the detection of local shear stress maxima. That refers to an averaging of the velocities over an arc length of ($0.6 \le s \le 1.3$) mm which is similar to the length of the MCVs ($l \approx 1.2$ mm). The velocity profiles and of course the turbulent shear stress as well, show some differences in the various

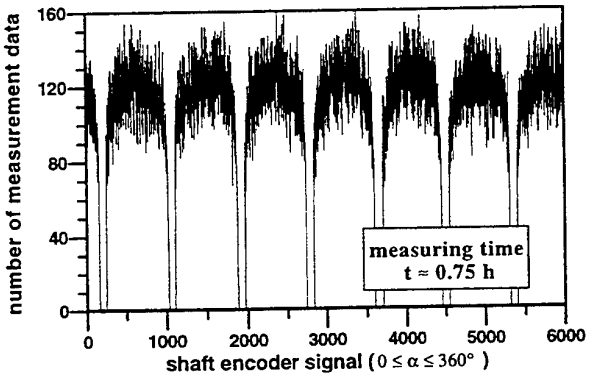

Fig. 4 Distribution of measurement data vs. angular position of the impeller.

impeller channels, due to manufacturing tolerances (Fig. 5). But these differences (typically: $\Delta\bar{v} \le 3\,\%$, $\Delta\tau_t \le 15\%$) did not justify, for our purposes, the much bigger amount of data to be collected, if all passages would have been analysed separately. Therefore, the angular positions of all seven passages were superpositioned relative to the preceding blade. Thus the measurement time for one position of the laser-probe was reduced to about 35 minutes. After the measurement, the data was sorted according to the angular positions and analysed.

To get statistically independent data, there should be at least a time of two integral time scales t_i of the flow between

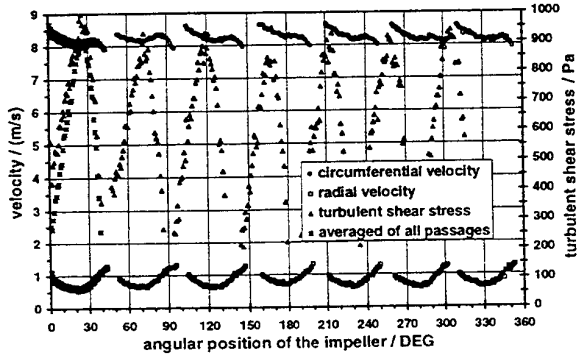

Fig. 3 Absolute velocities and turbulent shear stress data in the seven impeller passages. (Separately and superpositioned).

two succeeding measurements. But because of the rotating impeller and the described method of angular resolution with a fixed probe volume, there must be at least one turn of the impeller until the same position can occur again. Therefore, every measurement at one specific angular position comes from another turn of the impeller and is not correlated to the preceding measurement.

Even with the reduction of the angular resolution to $\Delta\alpha = 1°$, the averaging time t_a in one passage becomes about $t_a \approx 0.1$ ms for one turn of the impeller. At the used measurement frequencies of $f \approx 500$ Hz no problems with statistically dependent data occurred.

4 RESULTS AND DISCUSSION

A main interest in this work was to detect for the pump geometry under consideration the magnitude of the apparent turbulent shear stress for different operating conditions (rotational speed and flow rate) of the pump. The areas where the highest shear forces occur and possible ways to reduce the stress for the fluids and their ingredients should be found. This shall lead to an optimization of this pump system for the transportation of shear sensitive media.

Fig. 3 shows the absolute value of the measured Reynolds stress $|\tau_t|$ on a straight line in the midheight of the blades from points near the blades inlet edge ($r = 40$ mm) to the casing ($r = 102$ mm). The "toroidal area" describes the gap between

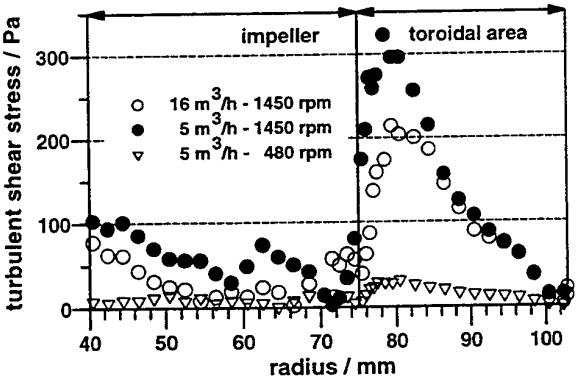

Fig. 5 Turbulent shear stress τ_t in the pump ($\alpha = 0°$) Comparison of throttling control and speed control.

the impeller and the casing wall (In Fig. 1 referred to as l). In this graph, the measurement data is averaged over the whole perimeter and is not resolved according to the angular position of the impeller (probe position $\alpha = 0°$). The three curves refer to three different operating conditions of the pump: two lines at a standard rotational speed of $n = 1450$ rpm, but at different flow rates of $\dot{V} = 16$ m³/h (head $H = 2.8$ m) and, with the throttle closed, 5 m³/h ($H = 5.4$ m). That refers to a dimensionless delivery coefficient

$$\varphi = \frac{\dot{V}}{n\,d^3} \qquad (5)$$

of $\varphi = 0.055$ and $\varphi = 0.017$ respectively. Another possibility to operate the pump at the reduced flow rate is the adjustment of the impeller speed to about n = 480 rpm, indicated in the third line ($\varphi = 0.049$). For every measuring point, 10000 samples have been collected.

At 1450 rpm and $\dot{V}$=16 m³/h, the turbulent shear stress has values below τ_t = 100 Pa inside the impeller, with a slight increase at the inlet edge, where the fluid has to change its flow direction by 90°. But the highest values occur in the coupling zone where the accelerated fluid leaves the impeller ($\bar{v} \approx 9$ m/s) and enters the comparatively slow flow ($\bar{v} \approx 5$ m/s) in the toroidal casing. With a reduced flow rate due to throttling control (1450 rpm, $\dot{V}$=5 m³/h), the pump is operated at part-load conditions and the efficiency of the pump decreases. This results in higher shear forces in the impeller and especially in the coupling zone. The fluid velocity in the casing decreases ($\bar{v} \approx 4$ m/s) because of the lower flow rate, and due to the higher relative velocities of impeller and casing flow, the turbulent shear stress reaches values above τ_t = 300 Pa (Tu ≈ 50 %). In the case of the speed controlled pump, the velocity difference of impeller and casing flow becomes smaller and this can be observed at the much lower values of the Reynolds stress, too.

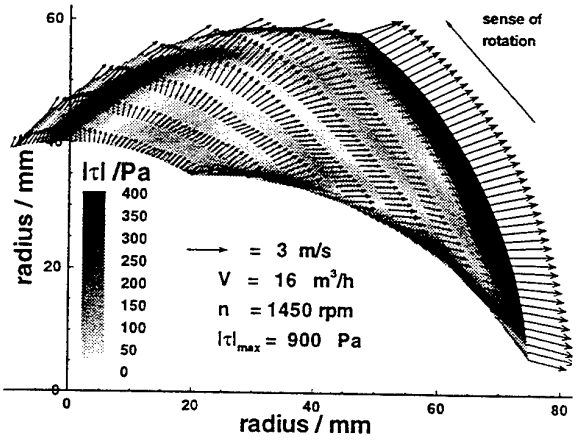

Fig. 6 Turbulent shear stress τ_t contours and relative velocities in the impeller passage ($\alpha = 45°$, $\varphi = 0.055$).

A detailed presentation of the shear stress conditions and the relative velocities in the passages of the impeller is given in Fig. 6 and Fig. 7 (here measured at an angle of $\alpha = 45°$). As mentioned above, a fixed laser probe and a shaft encoder for the angular resolution were used. All measuring points on one radius in these graphs are therefore sampled at the same point inside the pump (with respect to the casing), but distributed along an arc for the graphics. In this kind of graphics, the data shows more a resolution in time, relative to the preceding blade, than in space.

The shear stress contours again show the effect of the slow casing flow which evokes high values at the edge of the impeller. But areas alongside the blades with high turbulent shear forces were found, too. For example, an area of separation is visible at the suction side of the blade close to the inlet. But for the main flow in the passage, τ_t is below 100 Pa (Fig. 6). In case of the throttling-control to 5 m³/h, the area of high shear forces at the border of the impeller enlarges, and the maximum of τ_t and of the shear stress value in the main flow increases. This is due to an operation of the pump at part-load conditions and low efficiency (Fig. 7).

All results above refer to a mid-height plane of the blades with a distance from the front cover of z = 9 mm. In Fig. 9 the circumferential velocities inside the impeller and the casing at different depths of the blades is presented. At the inlet of the blades, where the axial entering fluid is forced to change its direction by 90° (mean velocity in the pipe just before the pump is $\bar{v} \approx 7$ m/s), the flow does not follow the blades close to the bottom. High velocities, even higher than the circumferential velocity of the blades, were measured to a depth z = 7 mm, but were significantly lower for parts closer to the bottom. This seems to be an effect of bad suction conditions because of a small inlet pipe upstream of the pump. This size was chosen to improve the accessibility for the laser-probe.

With increasing radial position, the flow gets more and more distributed over the whole cross section of the passage. Near the outlet edge of the impeller ($r \geq 63$ mm) the same mean velocity was measured over the whole channel.

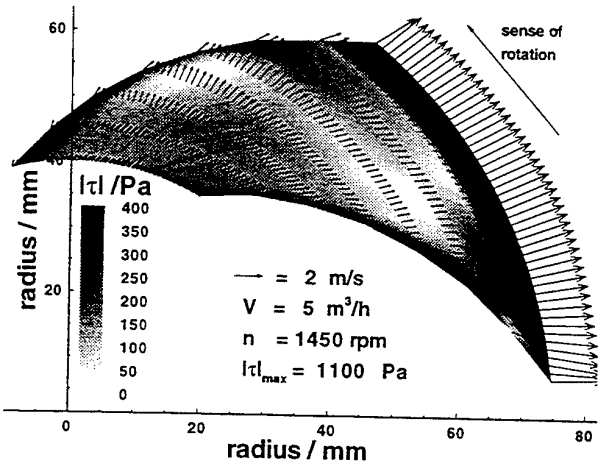

Fig. 7 Turbulent shear stress τ_t contours and relative velocities in the impeller passage ($\alpha = 45°$, $\varphi = 0.017$).

In the toroidal area of the casing close to the impeller, the fluid becomes decelerated to the mean velocity of the rotating main fluid in the casing $\bar{v} \approx 5$ m/s and the velocity gradients become steeper if positions closer to the bottom of the impeller are reached. Because there is still a length of about 65 mm from the bottom of the impeller to the backside of the casing (Fig. 1), there is a lot of slowly rotating fluid that decelerates the fast fluid leaving the impeller. The lines at z = (23 and 27) mm refer to positions in the casing behind the impeller.

In Fig. 8 the turbulent shear stress in a section through the casing at $\alpha = 45°$ is shown from the front cover to points behind the impeller. Clearly visible are the areas where high velocity gradients occur next to the impeller. Again, the highest shear stress is measured where the fast flow leaving the impeller is rapidly decelerated close to the bottom of the impeller.

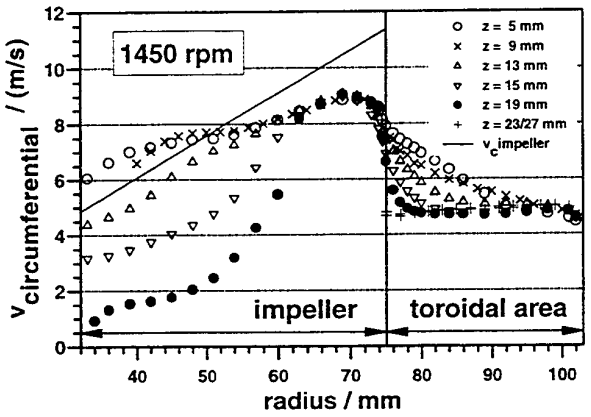

Fig. 8 Absolute circumferential velocity $\bar{v}_c$ at different depths of the impeller. ($\alpha = 0°$, $\varphi = 0.055$).

5 CONCLUSIONS

In this work velocity and shear stress profiles in a radial centrifugal pump of standard industrial design have been shown. They have been investigated inside the impeller and the casing for different operating conditions of the pump. The highest shear forces were detected in the coupling zone where the accelerated flow leaving the impeller hits comparatively slow flow regimes in the casing. These areas of high shear stress conditions enlarge, if the pump is operated at part load conditions and low efficiency.

It is a typical problem in industrial applications that *one* pump with a certain rotational speed is used for various flow rates. One main task was to evaluate the effect of obtaining a certain flow rate by means of throttling control or speed control. The examinations showed that a reduced impeller speed and therefore lower velocity gradients between impeller- and casing flow lead to a great reduction of the turbulent shear stress in the pump. For shear sensitive media, speed controlled pumps should therefore be preferred to reduce the damage to the

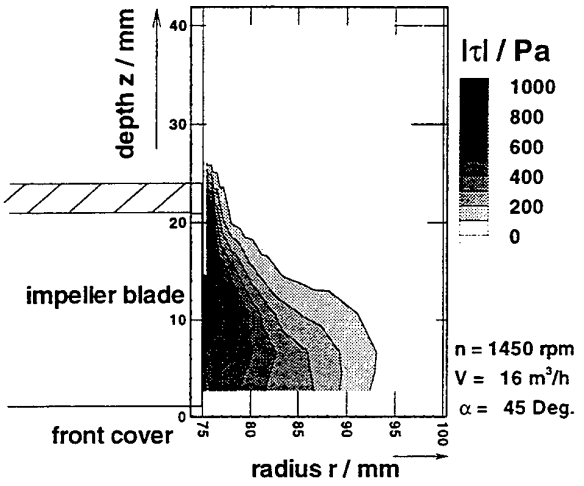

Fig. 9 Turbulent shear stress τ_t contours in the toroidal area beside and behind the impeller ($\alpha = 45°$, $\varphi = 0.055$).

fluids or their contents. Of course it must not be forgotten that the head of the pump decreases with the rotational speed *n* to the power of two. It has to be assured that the operating point of the pump at reduced speed has still to fit the requirements of the plant.

All investigations presented in this paper have been carried out with one pump and impeller geometry. Further investigations with other impeller types (closed impellers, number and geometry of the blades) and casings have already been started. This shall lead to the optimization of centrifugal pumps for the transport of shear sensitive media.

6 REFERENCES

1. Adrian, R.J. 1991, Particle-imaging techniques for experimental fluid mechanics, Annu. Rev. Fluid Mechanics 23, pp. 269-279. Quoted after: Visser, F.C.; Jonker & J.B. 1995, Laser Doppler Velocimetry Flow Measurements in the Rotating Frame inside the Passage of a Low Specific Speed Model Centrifugal Pump Impeller, FED-Vol. 229, Laser Anemometry, ASME.
2. Cherry, R. S. & Kwon, K.-Y. 1990, Transient Shear Stresses on a Suspension Cell in Turbulence. Biotechnology and Bioengineering, Vol. 36, pp. 563-571
3. Denk, V. 1995, Die Wirkung von Schubspannungen auf die Würzeinhaltsstoffe. European Brewery Convention, Proc. of the 25th Congress - Brussels, pp. 267-276, Oxford Press.
4. Delgado, A. 1986, Untersuchung der turbulenten Strömung von Polymerlösungen in einem zweidimensionalen Kanal mittels Laser-Doppler-Anemometrie. Ph.D. thesis, Universität-Gesamthochschule-Essen, Essen, Germany.
5. Hinrichs, J. 1994, Die mechanische Stabilität von Fettkugeln mit kristallinem Fettanteil im Strömungsfeld -

Verfahrenstechnische Einflußgrößen und technologische Veränderungen, Ph.D. theses, VDI-Verlag, Düsseldorf.
6. Lutz, M., Wichterle, K., Sobolík, V., Denk, V., 1996 Wall shear rate measurements in a centrifugal pump. Proc. of the 4th International Workshop on Electrochemical Flow Measurements - Fundamentals and Applications, Lahnstein, Germany.
7. Schlichting H. 1982, Grenzschicht-Theorie.. Karlsruhe Germany
8. Tennekes, H., Lumley, J.L. 1972, A First Course in Turbulence. p. 21, MIT-Press, London 1972
9. Tropea, C. 1996, Lecture during the Kurzlehrgang LDA und PDA, Erlangen, Germany
10. Tirrel, M. & Middleman, S. 1975, Shear Modification of Enzyme Kinetics. Biotechnology and Bioengineering, Vol 17, pp.299-303

7 SYMBOLS

head	H	[m]
sampling frequency	f	[s^{-1}]
diameter	d	[m]
length	s,l	[m]
radius	r	[m]
number	N	[-]
rotational speed	n	[s^{-1}]
power	P	[W]
flow rate	$\dot{V}$	[m^3/s]
temperature	T	[K]
time	t	[s]
turbulence intensity	Tu	[%]
velocity	v	[m/s]
angle	α	[DEG]
error	ε	[%]
kolmogorov length	η	[m]
delivery coefficient	φ	[-]
density	ρ	[kg/m^3]
shear stress	τ	[Pa]
dyn. viscosity	υ	[m^2/s]
Indices:		
average	a	
circumferential	c	
integral	i	
fluid	f	
particle	p	
radial	r	
turbulent	t	

8 SUPPORT

The authors gratefully acknowledge the following grants and support:

- Arbeitsgemeinschaft industrieller Forschungsvereinigungen (AIF), No.: 10423N, Köln
- Wissenschaftsförderung der Deutschen Brauwirtschaft e.V., Bonn
- Philipp Hilge GmbH, Bodenheim/Rhein

VELOCITY MEASUREMENT IN THE IMPELLER AND IN THE VOLUTE OF A CENTRIFUGAL PUMP BY PARTICLE IMAGE DISPLACEMENT VELOCIMETRY

M. Oldenburg and E. Pap

Institut für Strömungstechnik und Thermodynamik
Otto-von-Guericke-Universität Magdeburg, Germany

ABSTRACT

For improving the design of radial turbomachines there is a great interest to understand the flowfield in impeller and casing. The paper shows the first results of measurements of velocity distribution in a purpose made centrifugal pump of plexiglass by particle image displacement velocimetry (PIDV).

1. EXPERIMENTAL TECHNIQUE

PIDV is a whole field method, which allows the measurement of a two dimensional velocity field at one time. For this a slice of seeded flow field is double illuminated by a pulsed laser. The images of the particles are captured by a CCD-recorder placed at right angle to the light sheet. Using correlation techniques a vector velocity map is formed by calculating the displacement of particles in the time between two laser flashes.

For our measurements we used the DANTEC FlowMap System with a double pulsed Nd:YAG laser with a wavelength of 532 nm and an output energie of 200 mJ/pulse. A flexible light guide with a cylindrical lens at its end brings the pulsed laser light sheet with about 1 mm thickness savely in the test pump. Images of the particles in the flow are captured by a CCD-recorder with a resolution of 1024 x 1024 pixels. Fig. 1 shows the test stand schematically. We got the best results by seeding the flow with hollow glass spheres of 10 µm diameter and with the same density as water.

Because of the two dimensional light sheet and in order to avoid problems in capturing the images and in calculating the scale we used an especially made test pump. Impeller and volute were produced of plane plates of plexiglass. The vanes of impeller are cylindrical curved, therefore the impeller flow becomes approximately two dimensional. The diameter of the impeller is 250 mm and its speed is 600 rpm. The pump has a purpose constructed inlet, making it possible to see the whole impeller through its back shroud (Fig. 2).

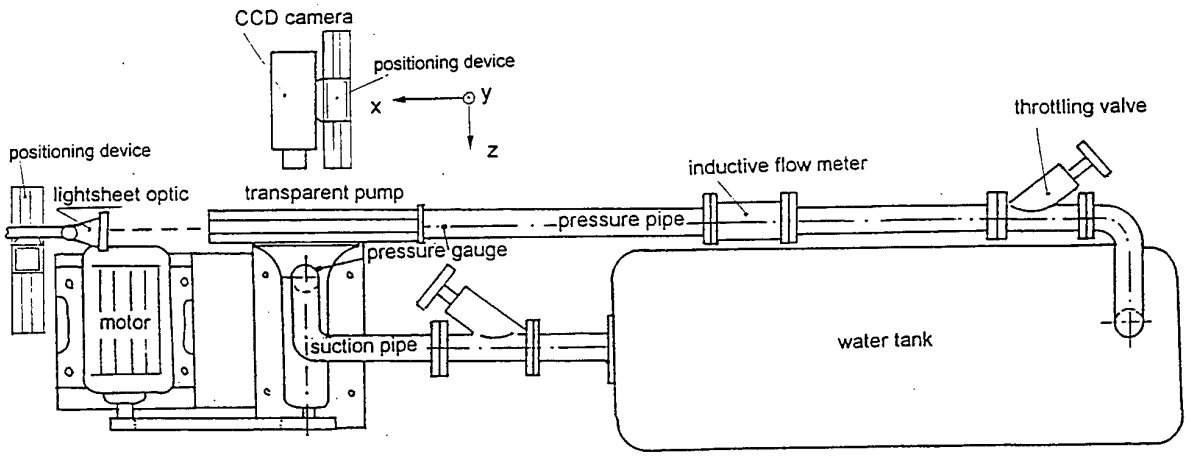

Fig. 1 Test stand

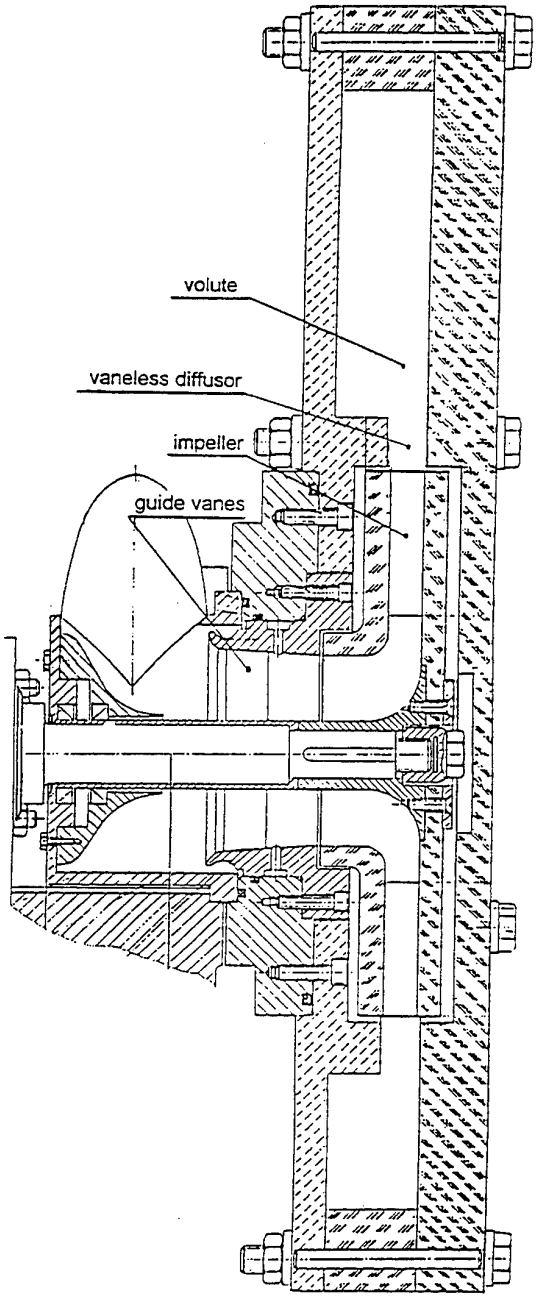

Fig. 2 Test pump

For moving the CCD-camera and the light sheet in three directions (x, y, z) there are two computer controlled positioning devices (Fig. 3). So the light sheet can illuminate the test pump from the upper side or from the right side by changing the y-position, or it illuminates a slice of the whole pump (great x-position) or only a little cross section . The movement of the CCD-camera in z-direction is limited by focusing. In its nearest position to the pump a flow field of 40x40 mm in size can be

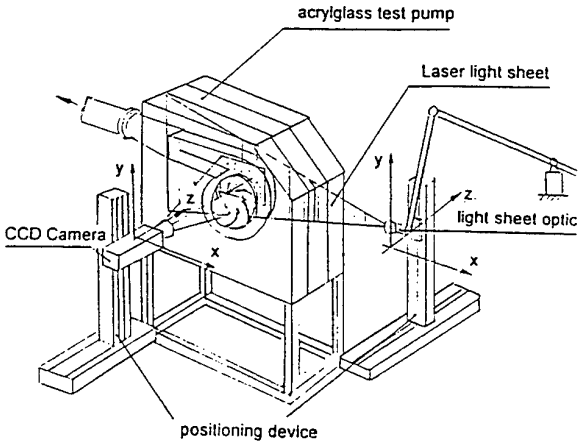

Fig. 3 Experimental arrangement

reproduced. The CCD-camera must be focused to the light sheet inside the pump. If that was done both the light sheet optic and the CCD-camera computer controlled can be moved together in z-direction without changing the distance between them. So it is possible with this light sheet tomographie to study the flow field in the test pump between front shroud and back shroud. An important condition is that the flow field in each light sheet is two dimensional (no z-componente of velocity) so that the particles in the time between the two light flashes can not leave the light sheet of only 1 mm thickness.

The intention of this teststand is both, to study the flow inside the pump in order to verify modern codes of flow calculation and to study the interaction between impeller and volute especially at off design mass flow too. We assume, that our results found in a two dimensional flow field can be converted on to a three dimensional velocity field, too.

In addition, this teststand is also design to measure two phase flow (water-gas) and cavitation phenomena.

2. FIRST RESULTS

To study the flow inside of the impeller at first the lightsheet was positioned normal to the shaft of the pump in the middle between the back shroud and the front shroud of the impeller. Fig. 4 shows a typical image of a part of the rotor gained by CCD-camera. You can see two vanes and the double illuminated particles in the flow. The rotation of the rotor is anticlockwise. The black shaddow at the inlet of the middle vane shows the direction of the laser light. At the upper corner on the left side of the picture you see a little piece of the tongue of the volute.

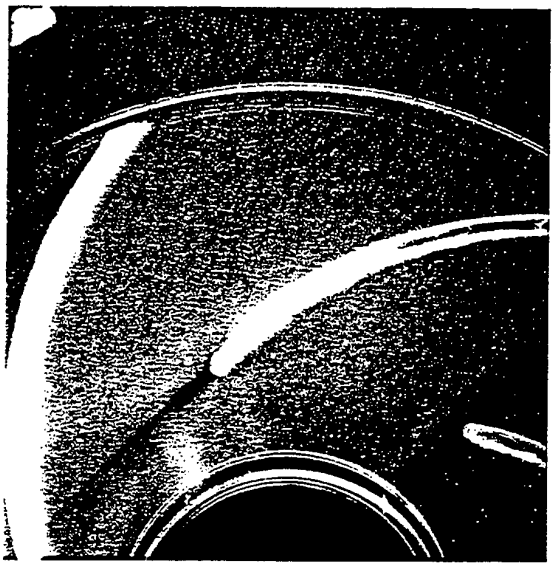

Fig. 4 Image of the invested part of the rotor

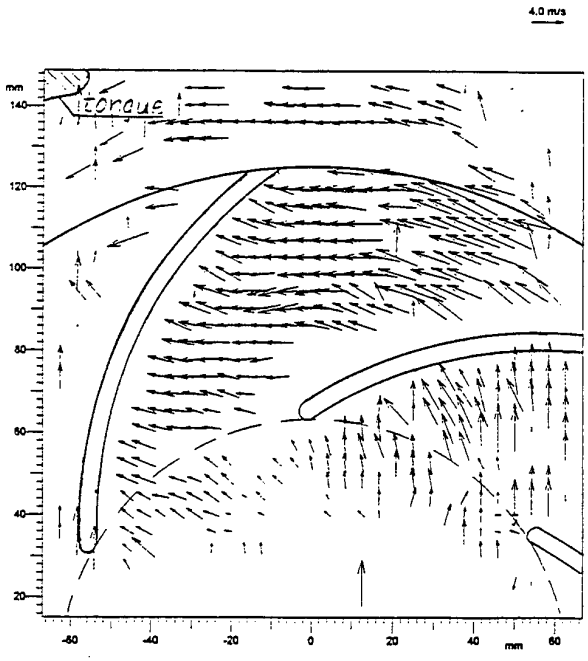

Fig. 5 Vector map of absolute velocity

The vector map of velocity calculated by autocorrelation technique is shown in Fig. 5. Scattering light at the surfaces of plexiglass causes the defect of vectors near the vanes and near the circumference of the rotor. Later on we hope to avoid this by painting black color on the critical points. By PIDV you can only measure the absolute velocity c. But inside of the impeller it is more descriptive to know the relative velocity with regard to impeller vanes. Therefore it is necessary to compute the relative velocity w in the impeller blade channel by addition of the vector c and the vector u of the circumferential speed. At Fig. 6 you see the flow velocity relative to the rotor inside of the impeller and the absolute velocity outside of the impeller.

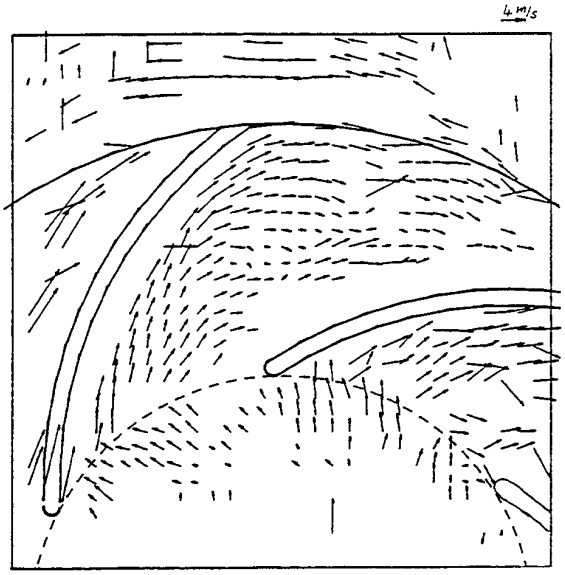

Fig. 6 Relative velocity field between the impeller vanes

The flow field of the relative velocity looks like there is no shockless entrance flow to the impeller vanes. There may be different reasons for that. At first Fig. 6 shows that the flow at the impeller inlet is not irrotational as assumed for calculation of the pump, but there is a prerotation. So the angel of relative velocity becomes greater than the inlet angel of the impeller vanes.

A second reason may be the influence of the volute and its tongue to the impeller flow. If the dimensions of the casing are correct at the design capacity the pressure distribution around the outlet of the impeller is rotationally symmetrical. Therefore the flow between two vanes and the capacity of this channel must be unchanged while one revolution of the rotor. For studying the flow in the channel and for nearly calculation of its capacity there were made additional images with a light sheet near the front shroud and an other sheet near the back shroud of the impeller. So it is possible to calculate the radial componente of velocity on a cross section at $r = const$ between front shroud and back shroud and between two vanes.

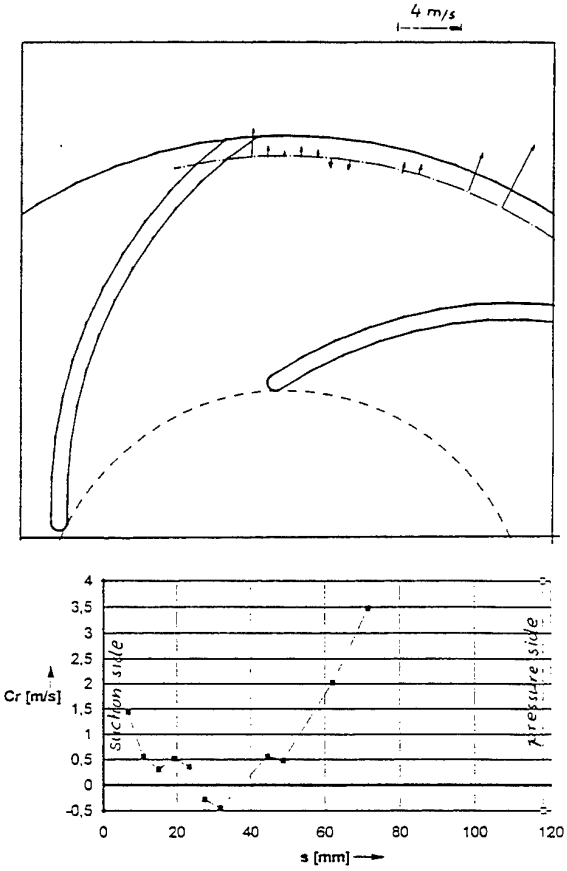

Fig. 7 Radial velocity c_r on a cross section of a impeller channel at $r = const = 120\ mm$

(Fig. 7) shows the graet differences of c_r across the area of channel. Integrating the radial velocity into this area we got the flow rate of the channel. If all 6 channels would have the same flow rate the pump capacity must be sixtimes this flow rate. For the measured pump capacity was greater than that, there must be an unsymmetrical pressure distribution in the volute around the impeller which influences the operation point of the impeller channels while one revolution. Therefore the channel was measured in three different positions relativ to the tongue of the volute. The positions of the left vane exit were: at the tongue, 23 degrees before and 40 degrees before (Fig. 8). You see the influence of the volute to the flow pattern inside of the impeller. Later on this phenomena will be investigated more precisely. The classical streamline theory of turbopumps assumes, that the direction of relativ velocity is the same as the vane direction. Only near the exit is a difference caused by the so called slip factor. Fig. 9 shows the vectors of the relativ velocity along three vane congruent lines from entrance to outlet of the impeller. You see, that the direction of relativ velocity is only along short distances the same as that of vanes. Later on we will study how that will be influenced by the flow rate of the channel. For important is not the flow rate of the pumps but the flow rate of the channel.

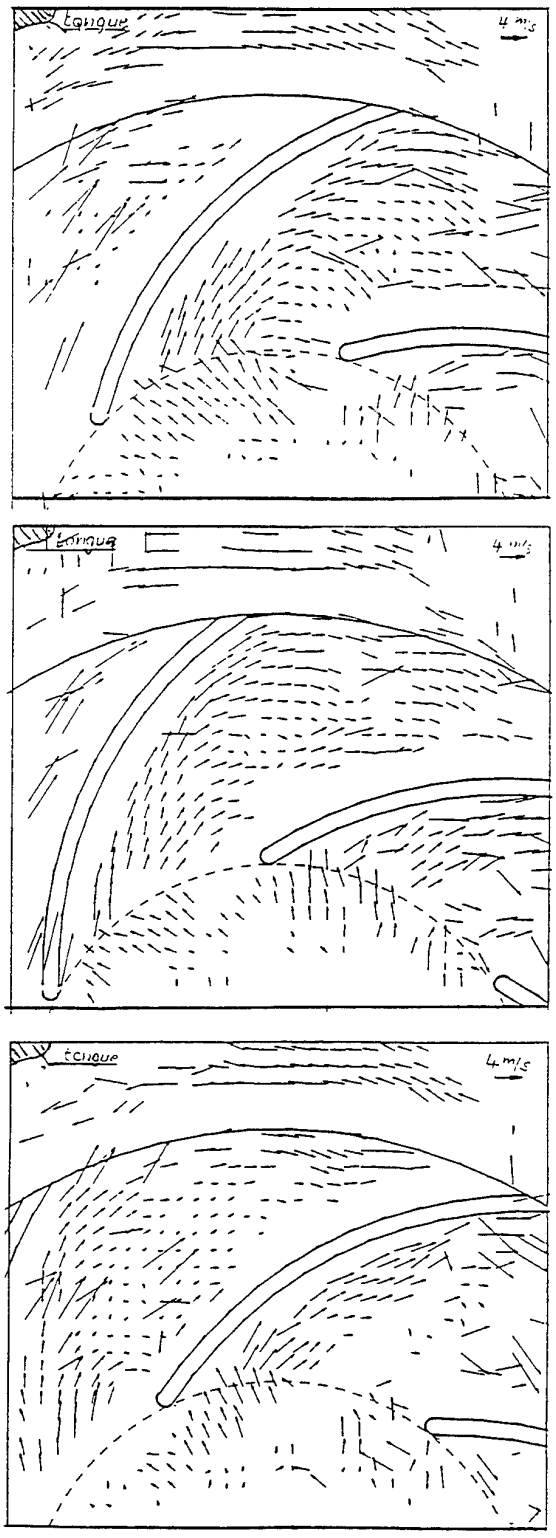

Fig. 8 Impeller flow pattern in three different positions relativ to the tongue of volute

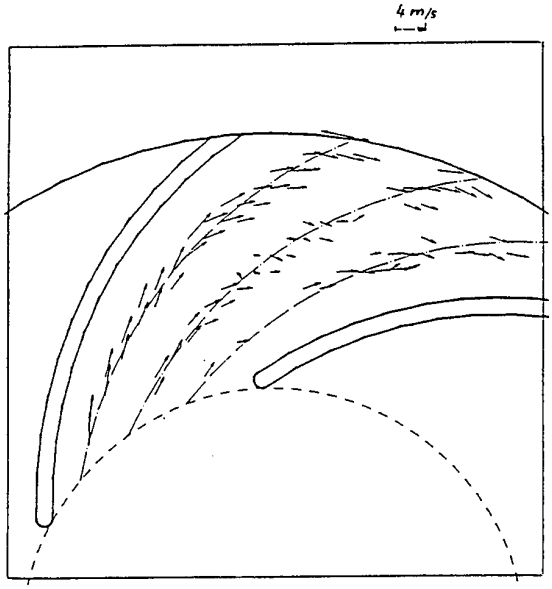

Fig. 9 Relativ velocity along vane congruent lines from impeller inlet to outlet

3. SUMMARY

The first results of measurements of velocity distribution in a centrifugal pump by particle image displacement velocimetry (PIDV) was shown. For the condition of two dimensional flow pattern there must be a purpose made pump with transparent parts. By PIDV you get the absolut velocity field on a light sheet inside the pump. By light sheet tomography it is possible to study the flow field in greater cross sections. First exampels of matematical postprocessing show how to calculate quantitativ results for valuation the vector maps.

For interpretation of PIDV measurements you must notice, that the images are only a snapshot of unsteady velocities.

In next time therefore we will improve the mathematical postprocessing especially for flow investigations in turbopumps in order to verify modern codes of flow calculation.

The investigations are sponsored by Deutsche Forschungsgemeinschaft (DFG) Bonn.

MEAN AND TURBULENT FLOW CHARACTERISTICS OF SINGLE HYPERBOLOID IMPELLER STIRRED VESSELS

F. M. Piqueiro, M. F. Proença
Departamento de Engenharia Civil, Faculdade de Engenharia
Rua dos Bragas, 4099 Porto Codex, Portugal

F. T. Pinho
Departamento de Engenharia Mecânica e Gestão Industrial
Faculdade de Engenharia, Rua dos Bragas, 4099 Porto Codex, Portugal

A. M. Santos
Instituto de Engenharia Mecânica e Gestão Industrial, Unidade de Térmica Industrial
Rua do Barroco 174, 4465 S. Mamede de Infesta, Portugal

ABSTRACT

Detailed angle resolved measurements of the mean and rms velocities were carried out in a stirred vessel driven by a low power hyperboloid impeller with 8 shear ribs and 48 transport ribs at $1/10^{th}$ clearance from the bottom of the vessel.

In the turbulent flow regime the hyperboloid stirrer required only one fifth of the energy of more conventional agitators. In most in the vessel the fluid was found to flow axially downwards, with a velocity of around 5% of the tip velocity, and it raised close to the vessel walls reaching a maximum velocity of 15% of the tip velocity.

The turbulence was isotropic, with normalised rms values of 2% in the core of the vessel and growing up to 4% as the wall was approached. Flow periodicity was detected only at the vicinity of the impeller, in a region representing less than 5% of the whole volume of the tank, with rms velocities reaching maxima of 15% of the tip velocity.

1. INTRODUCTION

The search for energy savings and increased performance in stirred vessels has lead to the development of new impeller shapes, as is the case of the low power hyperboloid stirrer developed by Höfken *et al* (1991), a device that was designed for mixing sludges where the nitrification and oxigenation are important steps of the bacteriological digestion process.

The assessment of the quality of a mixing process requires a detailed knowledge of the flow characteristics within the stirred vessel and the quantification of some parameters, such as the local energy dissipation rate. Such information is especially important in the vicinity of the impeller, as shown by the research carried out over the years around the conventional Rushton impeller by Cutter (1966), Mujumdar *et al* (1987) and Laufhütte and Mersmann (1985) amongst others, and are required, for instance, for the proper development of computer codes.

Reed *et al* (1977) and Popiolek *et al* (1987) have measured the radial jet coming out of the Rushton impeller plane, colliding with the vessel wall and forming two wall jets. The latter authors characterised the large vortical structures coming out from behind the impeller blades into the bulk flow, above and below the impeller disc, with their angle-resolved measurements and have shown that not considering this flow periodicity would overpredict turbulent quantities by as much as 400%. The interaction between turbulence and the kinetics of aggregates in vessels stirred by Rushton turbines was investigated by Kusters (1991). Other investigations on the two- phase flow behaviour of the Rushton stirred vessel flow were those of Nouri and Whitelaw (1992).

Other standard impeller geometries, such as the pitched blade impeller, were also thoroughly investigated, as by Hockey (1990). He analysed in detail the flow characteristics of Newtonian and weakly elastic non- Newtonian fluids and quantified the distribution of the inputed energy into its various components, as a function of fluid rheology and impeller type.

Similar studies must obviously be performed with the new type of agitator, if it is to be well understood. Nouri and Whitelaw (1994) carried out some detailed velocity measurements with the hyperboloid impeller at the standard configuration of 1/3 clearance from the bottom, and conducted an overall assessment of the flow characteristics as a function of the impeller size and clearance. Their impeller included 8 shear ribs on the agitator upper surface, and they concluded that in terms of particle suspension effectiveness, the $1/10^{th}$ clearance impeller performed better than the 1/3 clearance impeller. The measured power consumption of the hyperboloid stirrer was at least 20 times lower than that of the Rushton impeller, although its Zwietering parameter was not so good. They demonstrated the advantage of mounting the impeller close to the bottom, with a $1/10^{th}$ clearance, but did not investigate in detail the flow characteristics of the hyperboloid stirrer with this low clearance, rather with the typical 1/3 clearance of conventional stirrers.

Some mixing processes require aeration, which for this impeller is usually introduced from its conical bottom surface, Höfken *et al* (1991). Their investigations on aerated systems led to an improved design of the impeller, with the incorporation of 48 transport ribs at the edge of the bottom surface, necessary for breaking up the gas bubbles. An efficient aeration from below the impeller also required it to be located close to the bottom of the vessel, in order to aerate the whole flow. So, for a number of reasons the $1/10^{th}$ clearance seems to be more adequate than other configurations and should be the object of research.

The objective of this work is the characterization of some of the mean and turbulent flow features in the stirred vessel powered by this low clearance hyperboloid agitator, having both the shear and transport ribs.

In the next section, the experimental facility, the instrumentation and the measuring programme are described. This will be followed by the presentation of the results and its discussion, and the paper will end with a summary of the main conclusions.

2. EXPERIMENTAL RIG

The stirred vessel had a diameter of 292 mm and the fluid height to vessel diameter ratio (H/T) was equal to 1. The hyperboloid stirrer was close to the bottom, at a clearance to vessel diameter ratio (C/T) of 1/10 and its diameter was equal to 100 mm, roughly corresponding to 1/3 that of the vessel diameter.

The vessel was mounted inside a square trough filled with the same liquid, in order to reduce optical refractions and help maintain a constant temperature in the bath, and the trough standed directly on top of a 3-D milling table for easy traversing.

Four 25 mm wide and 4 mm thick baffles were mounted inside of the tank, at 90° intervals, to avoid solid- body rotation of the fluid. They were not directly attached to the vessel wall, but were fixed to small triangular connectors, which separated them by 6 mm from the wall, thus eliminating the dead zones normally appearing behind the baffles. The bottom of the tank was flat and had a bearing embedded to support the drive shaft. A schematic representation of the vessel and the coordinate system used throughout this paper are shown in figure 1.

The hyperboloid stirrer was provided by Invent GmbH, according to its patented design and had 8 transport and 48 shear ribs on its top and bottom surfaces, respectively. The transport and shear ribs are small rectangles welded to the impeller surface at regular intervals, along their longer dimension. The transport ribs were 5.9 mm by 3.6 mm in shape and were mounted every 5°, and the shear ribs were 10 mm by 3.8 mm, and were mounted every 45°. The ribs were not aligned along

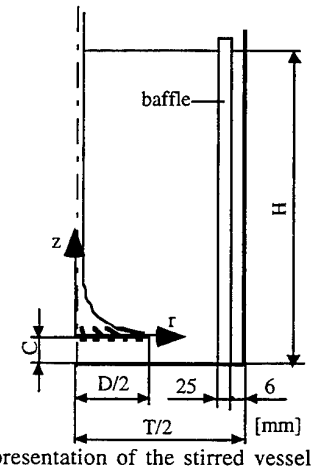

Figure 1- Representation of the stirred vessel and of the coordinate system.

diametral planes of the impeller, but had a 45° inclination in the horizontal plane. The construction was not perfect and there were rib to rib differences, especially with the transport ribs. More details on the construction can be found in Höfken and Bischof (1993). The stirrer was driven by a 600 W DC Servomotor controlled by a variable power supply unit, and the speed could be kept constant within 1 rpm, which corresponded to an uncertainty of less than 0.5%.

A one component Laser- Doppler anemometer from Dantec was used in forward scatter, whenever possible and in backscatter otherwise. The beam from the 100 mW Ar-ion laser, operating in multimode, passed through a series of optical elements before the Bragg cell, where a frequency shift of 0.6 MHz was imposed. To improve the alignment of the optics and reduce the size of the control volume, a pinhole section and beam expander, with an expansion factor of 1.95, were put before the 600 mm front lens.

The scattered light was collected by the photomultiplier (PM) before which stood an interference filter of 514.5 nm. The signal from the PM was processed by a TSI 1990 C counter operating in the single measurement per burst mode, with a frequency validation setting of 1% with 10/16 cycle comparison, after being band- pass filtered. A 1400 Dostek card interfaced the counter with a 80486 based computer, which provided all the statistical quantities, via a purpose built software.

For the angle resolved measurements, a mechanical encoder mounted on the shaft of the hyperboloid and connected to the counter, was used to discriminate the velocity measurements in 1° windows.

Due to the low velocities and high turbulence of this type of flows and in order to reduce the measuring uncertainties, a sample size of 30,000 realizations was selected for measurements taken far from the impeller, where the flow was not angle dependent. Close to the impeller, a total sample of 600,000 events was used, thus defining an average sample size of more than 1650 points per degree. In this region, weight average values of the mean and rms velocities were also calculated from the 1° angle-resolved data, to allow a proper visualisation of the mean flow field. These weight-average mean and rms values were calculated using equations 1 and 2, respectively.

$$\overline{U} = \frac{\sum_{\theta=1}^{360} U_\theta N_\theta}{\sum_{\theta=1}^{360} N_\theta} \qquad (1)$$

$$\overline{u'^2} = \frac{\sum_{\theta=1}^{360} \overline{u'^2}_\theta N_\theta}{\sum_{\theta=1}^{360} N_\theta} \qquad (2)$$

where U_θ, $\overline{u'^2}_\theta$ and N_θ represent local angle- resolved values of the mean velocity, variance of the velocity and sample size, respectively.

Table 1 lists the main characteristics of the LDA system, and an assessment of the various contributions to the overall uncertainty of the mean and rms velocities

Table 1- Main characteristics of the Laser- Doppler anemometer in air at e^{-2} intensity.

Laser wavelength	514.5 nm
Measured half angle of beams in air	3.65°
Dimensions of measuring volume in air	
major axis	2.53 mm
minor axis	162 μm
Fringe spacing	4.041 μm
Frequency shift	0.6 MHz

gave the following results: for the 360° ensemble average measurements taken far from the impeller, the overall uncertainty of the mean velocity is thus less than 1.2% for a 100% turbulence intensity and of about 5% for the rms velocity, in regions of high turbulence. Close to the agitator, with the average sample size of 1650 points per degree, the overall uncertainty was less than 3.5% and 5% for the mean and rms velocities, respectively, also under conditions of 100% turbulence intensity.

3. RESULTS AND DISCUSSION

Figure 2 compares the power consumption of the hyperboloid stirrer with that of the Rushton and pitched blade impellers, over the laminar and turbulent flow regimes. There is a clear energy advantage of the hyperboloid stirrer for Reynolds numbers above 50, because of the early transition to turbulence and flow separation of the Rushton and pitched blade impellers. However, for lower Reynolds numbers the flow is not separated and the hyperboloid impeller requires more power, because of the friction over its larger surface area. These observations are well documented and explained in Piqueiro *et al* (1995).

Most of the current practical applications of the hyperboloid stirrer are for turbulent flow conditions, hence a Reynolds number of 50,000, where the power curve has stabilised, was selected for the detailed flow field investigation reported here.

Next, the mean flow characteristics are presented and discussed and are followed by those of the turbulent flow field. After this overall picture, the paper moves on to discuss the periodic flow near the impeller and the bottom of the vessel. All the velocities were normalised with the impeller tip velocity and the values of the radial locations by the impeller radius. The axial coordinate was left in [mm], because we felt it was easier to visualize the flow in this way. We remind the reader that the vessel height is 300 mm, the impeller radius is 50 mm and the shear rib height is 5 mm.

The vertical cut through a radial plane in figure 3 shows a vector plot of the mean axial and radial velocity components, whereas figures 4 a), b) and c) and figures 5 a), b) and c) show radial profiles of the mean axial, radial and tangential velocity components. These figures were made from the measured 360° ensemble-average data taken far from the impeller and weighted averages calculated from the angle resolved measurements close to the impeller.

The flow is predominantly a downward axial flow, with an average magnitude of about 5% of the tip velocity, occupying over 70% of the radius of the vessel. Then, mass conservation requires a rather strong upwards

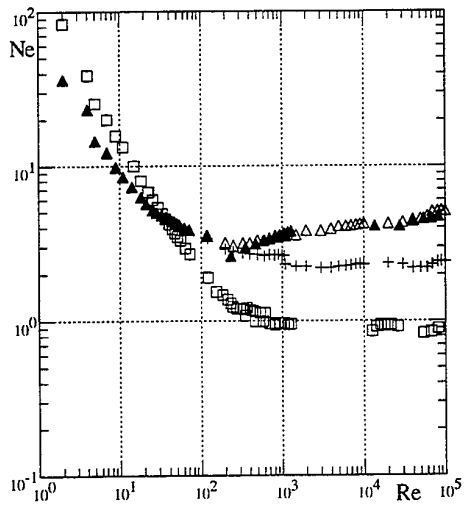

Figure 2- Newton number versus Reynolds number for H/T=1 and D/T=1/3. Comparison with the literature. This work: □ hyperboloid; ▲ Rushton. From Hockey (1990): △ Rushton and + pitched blade.

axial flow close to the vessel side wall, reaching a maximum of 15% of the tip velocity. Near the tip of the impeller, the long vectors show that the velocities are very intense because the flow is being pushed directly by the ribs.

A radial velocity component is acquired only very close to the impeller surface, and especially at the bottom of the vessel. On the upper half of the vessel (z> +140 mm) the fluid moves slowly towards the shaft, with a magnitude of about 2% of the tip velocity, whereas the outwards radial flow between z= +20 to z=+90 mm is also of about 2% of the tip velocity. Further down, close to the bottom, in a region also influenced by the agitator, the radial velocities are higher than above, reaching maximum values of about 10% of the tip velocity, and at the impeller, where the fluid is being pushed by the shear ribs, of 20 to 30% of the tip velocity.

The vortex defined by the circulating flow pattern just described is centred at around r/R = 2.4 and z/R = 1.75.

Close to the free surface (z> +190 mm), but especially above z = +240 mm, the measured axial and radial velocity components tend to zero, i.e., the fluid is almost motionless.

The mean tangential velocity component has magnitudes similar to the mean radial velocity component, except near the impeller. Far from the agitator the fluid slowly rotates in the same direction of the impeller, with magnitudes between 1 to 4% of the tip velocity. It is below the impeller that the rotational velocities are higher because of the transport ribs, but they decrease very quickly with the radius, dropping from over 40% of the tip velocity at r/R= 1.08 to less than 10% at r/R=1.4.

Below the impeller the rotation of the fluid is always positive but not above its base plane. Here, starting at about r/R= 1.5 and up to the vessel side wall, the fluid rotates in the opposite direction to the impeller, with the higher negative velocity, of around 2.5% of the tip velocity, occurring close to the wall. This counter-rota-

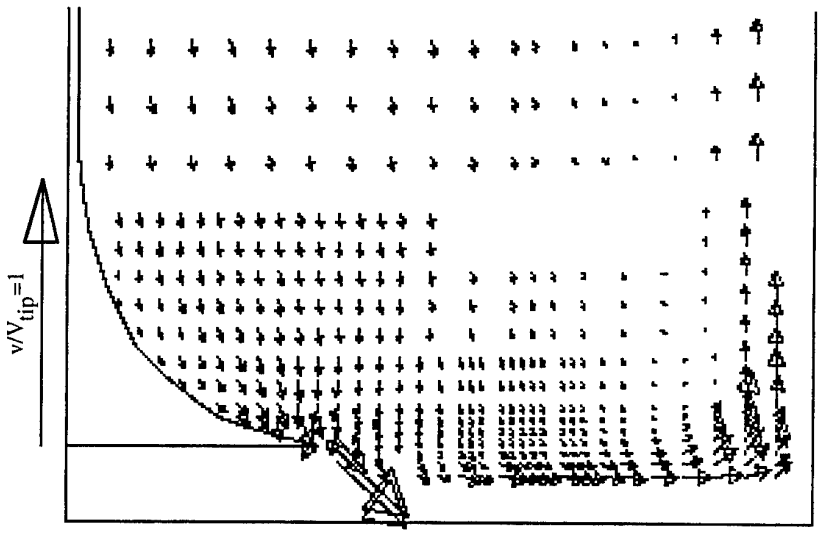

Figure 3- Vector plot of the mean axial and radial velocity components in a diametral vertical plane in the vicinity of the bottom of the vessel and impeller.

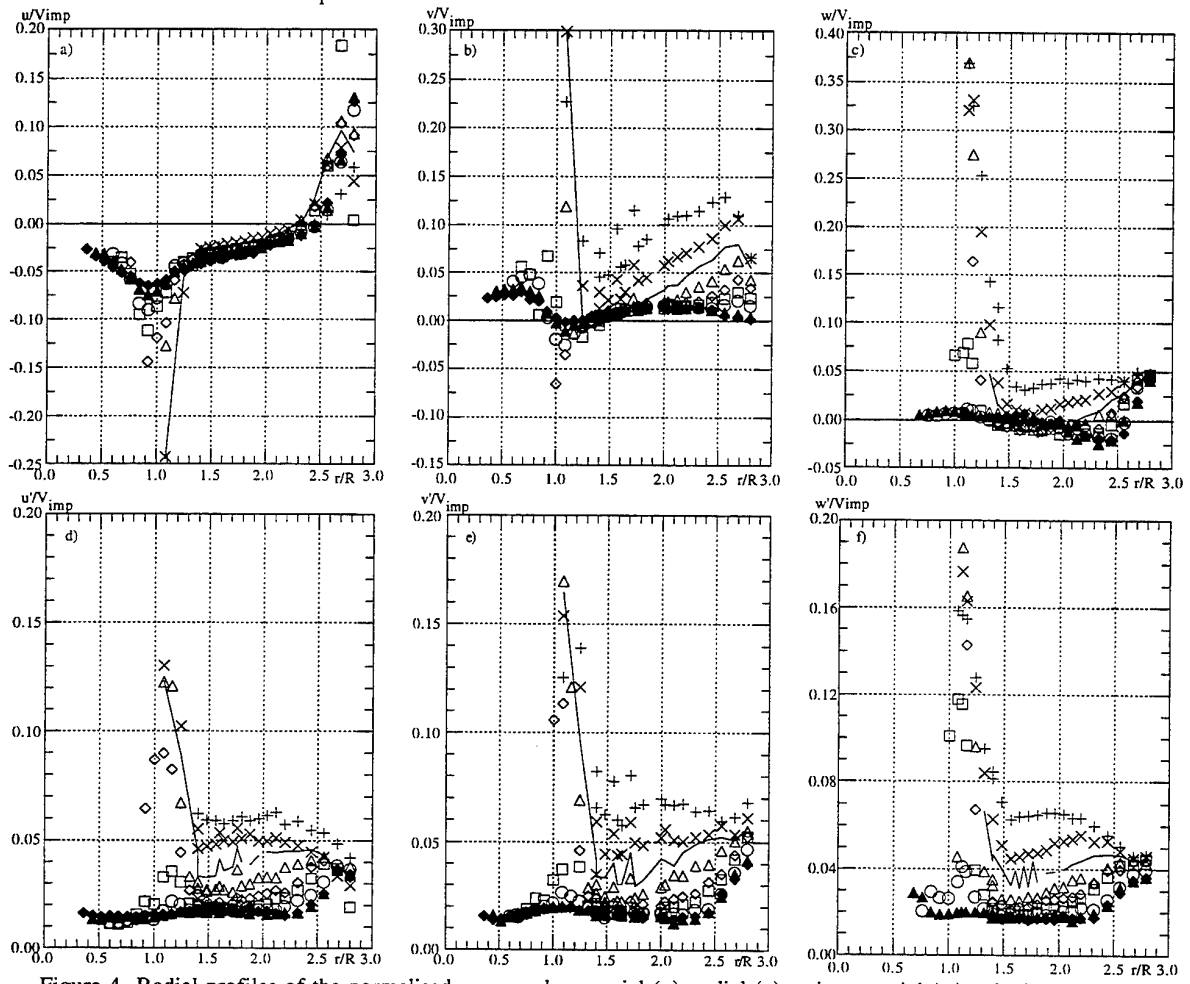

Figure 4- Radial profiles of the normalised mean and rms axial (u), radial (v) and tangential (w) velocity components at different heights. + z=-5, x z=-3, — z=-1, Δ z=+1, ◊ z=+3, □ z=+5, o z=+7, ▲ z=+11, ◆ z=+15.

ting flow disappears for heights above 60 mm from the impeller base plane, and could be due to the simultaneous influence of the baffles and a low pressure created by the high speed jet at the bottom.

Figures 4d), e) and f) and figures 5 d), e) and f) represent radial profiles of the normalised rms of the axial, radial and tangential velocity components at different heights. As far as the turbulence is concerned two different zones are distinguished. Above z=+7 mm the turbulence is isotropic and remains fairly constant, regardless of the vessel height, at about 2% of the tip velocity in the center of the vessel, growing to 4% near the side walls.This higher turbulence is due to turbulence production on the side wall jet, plus a contribution of transported turbulence by this jet, which originated from the high turbulence radial flow at the bottom of the vessel. Near the free surface, the slow velocities reduce the turbulence to values of about 1 to 1.5% of the tip velocity.

Below z=+7 mm the turbulence continues to be rather isotropic, but here it is high because of the proximity of the impeller and of the bottom of the vessel. At the impeller the high shear rates created by the passage of the ribs are an important contribution to the production of turbulence, whereas at the bottom of the vessel the turbulence is produced at the boundary-layer created by the radial disharge jet.

The 8 shear ribs located above the impeller base plane (z=0) create local flow reversals relative to the mean vectors plotted in figure 3, and a strong periodic flow emanates from that region. However, this periodicity is rather short- lived in comparison to that in more typical agitators, such as the Rushton and pitched-blade impellers of Hockey (1990).

Note also, that a strong radial flow does not exist at the impeller base plane, but below it. Unfortunately, due to difficulties in measuring close to the bottom, detailed velocity measurements have not yet been carried out here, but the increase in the magnitude of the vectors in the radial direction at the lowest measured horizontal plane, as one approaches the vessel side walls, suggests that closer to the bottom the radial velocities could be even stronger, with a boundary-layer type flow growing to the outside.

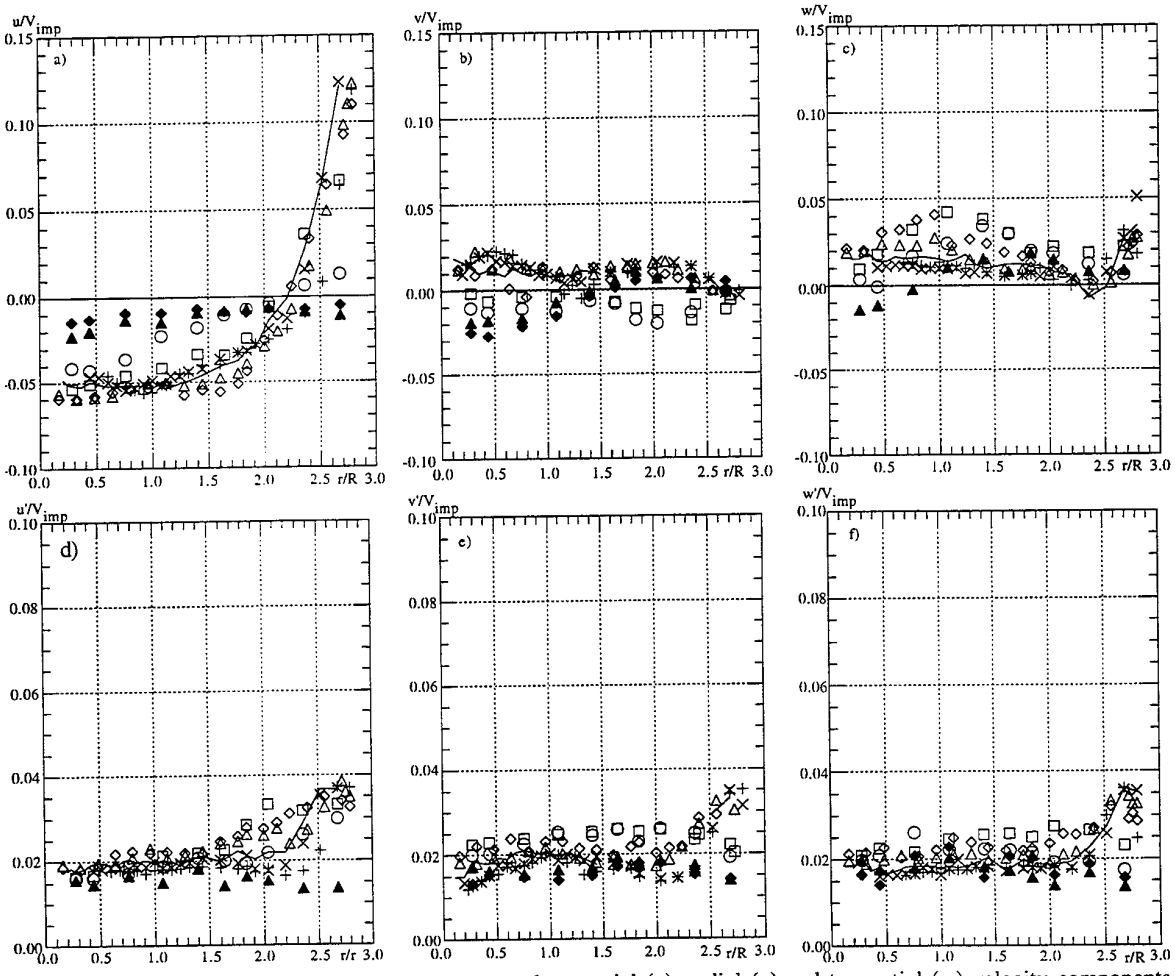

Figure 5- Radial profiles of the normalised mean and rms axial (u), radial (v) and tangential (w) velocity components at different heights. + z=+20, x z=+25, — z=+40, Δ z=+60, ◊ z=+90, □ z=+140, o z=+190, ▲ z=+240, ◆ z=+270.

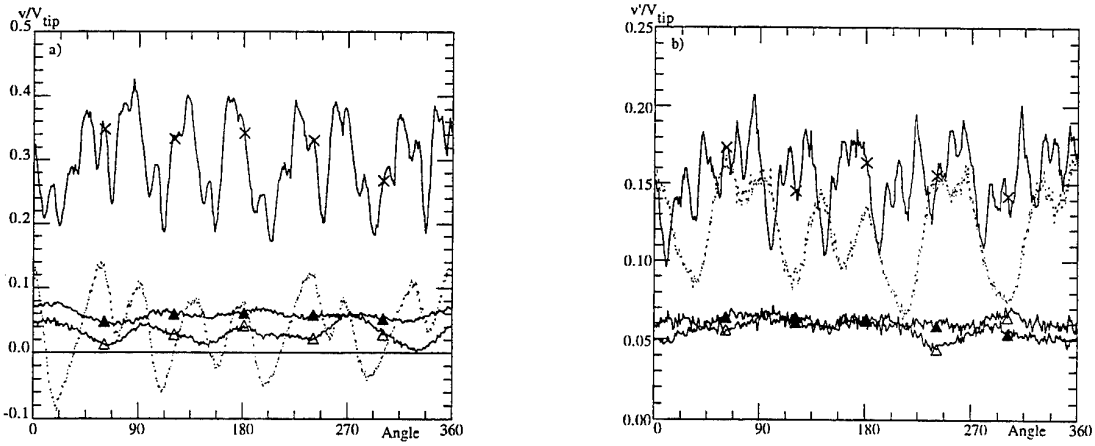

Figure 6 a) and b) Mean and rms radial velocity component at z= -3 mm as a function of the angular position and at radial locations: r/R= 1.08 -X-, r/R= 1.24 ----, r/R= 1.4 -Δ- and r/R= 1.76-▲-.

The most interesting flow features are those near the impeller tip, where the periodicity imposed by the shear and transport ribs is felt. In terms of periodicity three different flow patterns are identified, corresponding to three different regions, one below the impeller base plane and two above.

Below the impeller base plane, the flow is affected by both the 8 shear ribs and the 48 transport ribs, with this combination imparting a rather chaotic flow behaviour, as one of the angular plots of figure 6 shows. This figure presents four different profiles of the radial velocity component at four different radial locations pertaining to the same horizontal plane, located below the impeller. The eight major cycles at r/R = 1.08 are disturbed by the strong tangential flow created by the 48 ribs, which tend to smooth out the periodicity imposed by the shear ribs, a more clearly noticed effect in the rms velocity profile than in the mean velocity profile. Moving away from the impeller the effect of the ribs is reduced, so that at r/R= 1.24 the eight cycles still exist with a lower amplitude and especially with less "noise", from the transport ribs.

Farther away from the agitator, the reduction of the flow periodicity occurs through a pairing process, which led to the formation of only four low- amplitude cycles at r/R = 1.4. The curves pertaining to r/R= 1.08 and 1.24 are also seen to decay, on the average, to values of about 5% of the tip velocity, as we move into a zone of stronger axial flow. At a higher radius (r/R = 1.76) the periodicity has been reduced to a small single cycle, an effect which we attribute to the small wobbling of the impeller.

Above the impeller base plane, at the plane touching the upper edge of the shear ribs, the flow exhibits a strong eight- cycle periodicity, with the observed cycle to cycle differences always taking place at the same location, i.e., they seem to be attributed to imperfections in the positioning of the ribs on the impeller upper surface.

Figure 7 shows a typical 360° angular profile with such cycle-to-cycle differences. The eight measured cycles were averaged into a single 45° cycle and this average profile was reproduced to the full 360° in the figure, for assessing the magnitude of the cycle- to- cycle differences. These differences are more intense in the 5th and 6th cycle, and in the rms of the velocity than in the mean velocity, being at most of 30% and 20% in the magnitude, respectively. The stronger effect upon the rms is expected, because of its strong dependence of the shear

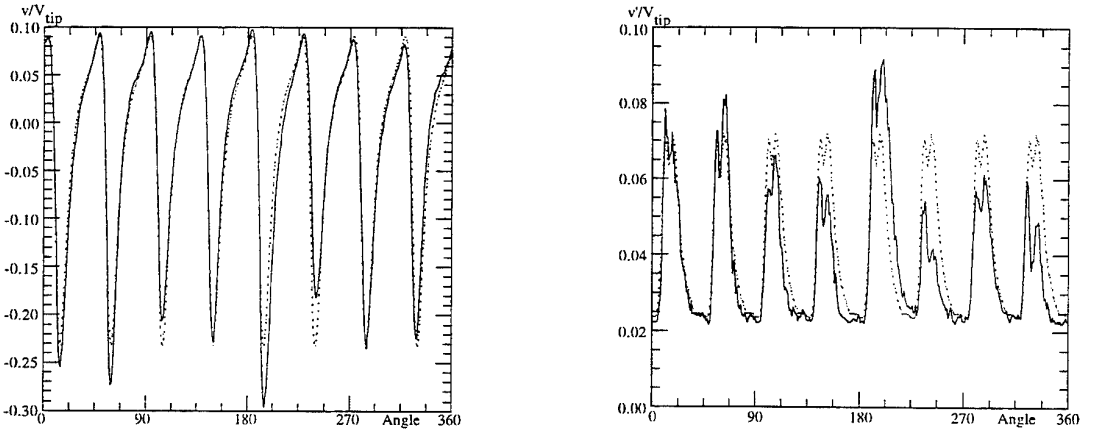

Figure 7 a) and b) Angular profiles of the mean and rms normalised radial velocities at z=+ 5 mm and r/R= 1.08. Solid line: measured profile. Broken line: calculated average cycle.

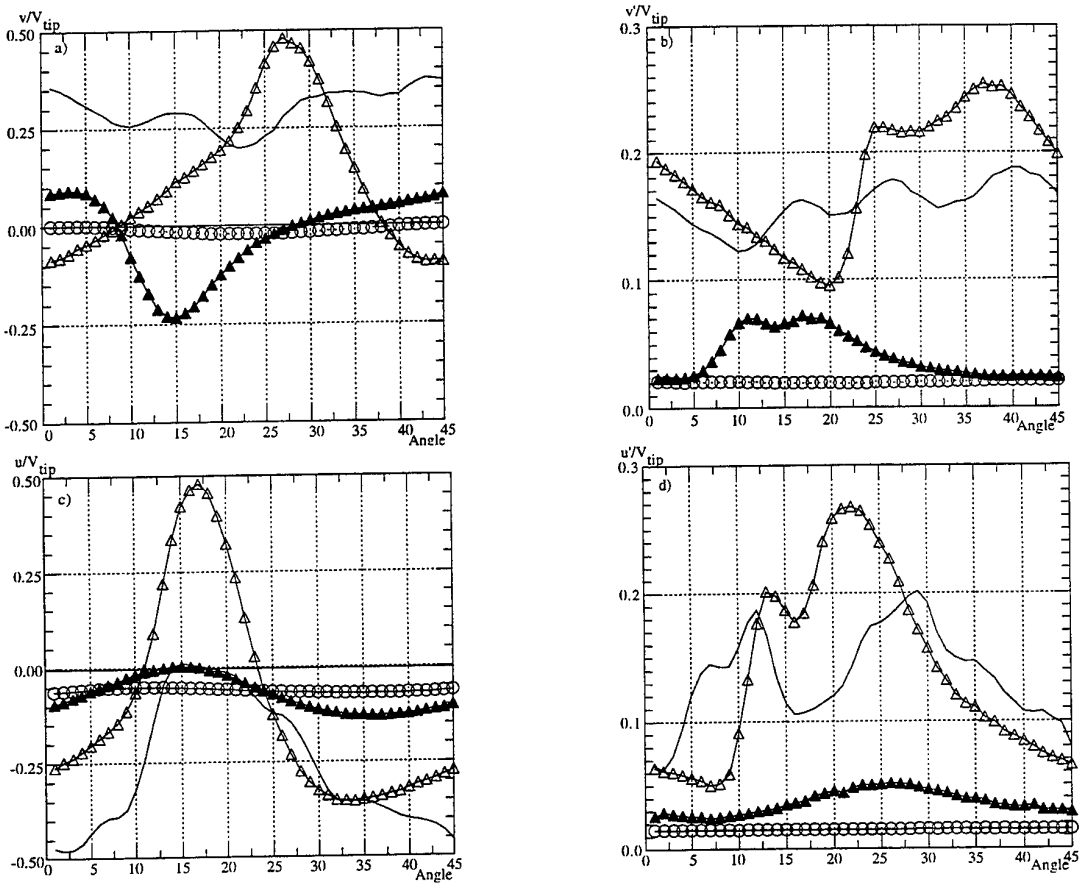

Figure 8 Angular profiles of the mean and rms radial (v) and axial (u) velocity components at z= -3 mm (——), z= +1 mm (Δ), z= +5 mm (▲) and z= + 11 mm (O), for a constant r/R= 1.08.

rates. Since the amplitudes of the mean velocity cycles are large, slight imperfections in the construction change the maximum shear rate and thus the rms of the velocity value.

Close inspection of the impeller showed that the 6th shear rib, located at 225°, was slightly bent forward rather than being perpendicular to the impeller surface and could be responsible for the two different cycles which stand between 180° and 270°. The gentle wobble of the impeller motion and other minor imperfections could then be behind the other smaller variations.

In the remaining of the paper, the description of some of the characteristics of the periodic flow is based on the calculated 45° average cycle rather than on the fully measured 360° angular profile.

In figure 8, angular profiles of the radial and axial mean and rms velocity components, pertaining to points at the same radial location r/R= +1.08, but to different heights, below and above the impeller base plane, are plotted. The figure confirms that below the impeller, the outwards radial velocity is fairly constant, because of the smoothing effect of the strong tangential flow induced by the transport ribs, whereas above the agitator the periodicity is better defined.

The strong periodicity introduced by the shear ribs is not only found in the angle dependence, but also in the vector direction. Comparing the mean velocity profiles pertaining to z= +1mm (aligned with the root of the rib) and z=+5 (aligned with the upper edge of the rib) four dif-

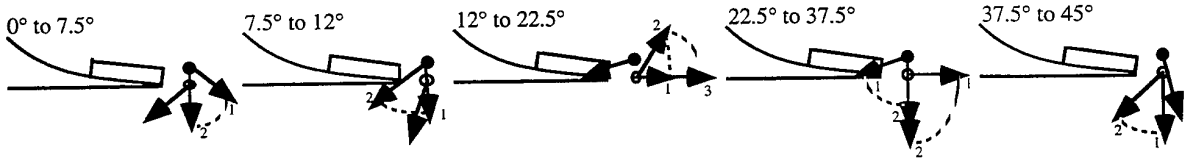

Figure 9- Qualitative sketch of the radial and axial mean flow pattern close to the ribs, as a function of the angular location. θ= 0° and θ= 45° are the locations of consecutive tips of shear ribs.

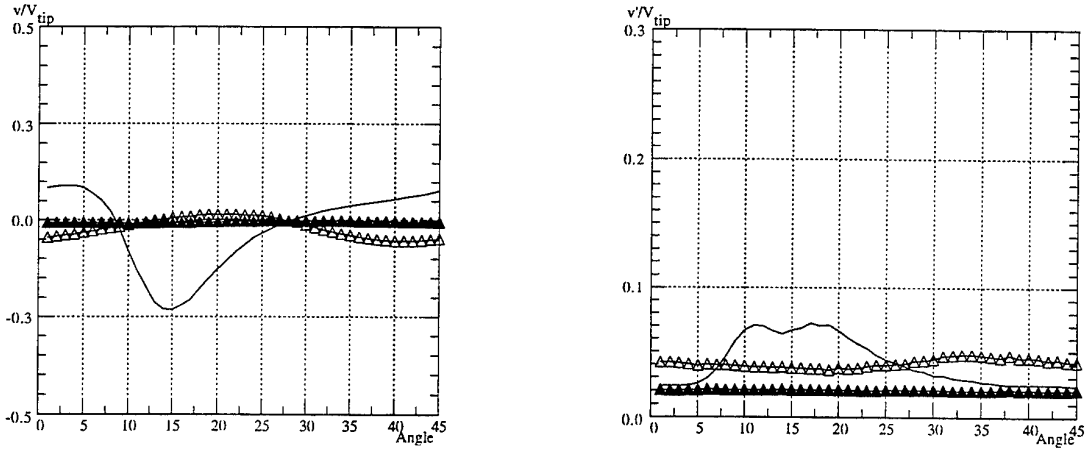

Figure 10 a) and b) Mean and rms radial velocity component at r/R= 1.08 (—), r/R= 1.24 (Δ) and r/R= 1.4(▲) as a function of the angular position at z= +5 mm.

ferent types of behaviour are identified, which are qualitatively sketched in figure 9. The flow has been described on average as going down axially and outwards radially, but close inspection of figure 8 shows that in between the ribs, there are instances when the fluid flows the other way around, i.e., upwards and towards the impeller, rather than away from it.

Figure 10 shows angular profiles of the normalised radial component of the velocity at different radius and at a constant height of z= +5 mm, and together with figure 8 it allows the assessment of the extent of the zone of influence of the rib- induced periodicity. Since the flow is on the whole an axial downwards flow, it is not surprising to observe that above the impeller the region affected by the ribs is very limited, and that at r/R= 1.4 the flow remains independent of the angle.

From data not presented here, we observed that the vertical influence was also rather limited to about three rib heights, i.e., at z=+15 mm the periodic flow was barely noticed. Obviously, considering the mean flow patterns presented and discussed above, the region of periodic flow below the impeller is longer, going up to about r/R= 1.76. Thus, the volume of fluid experiencing periodic effects above and below the impeller base plane account for less than 5% of the total volume of the vessel.

4. CONCLUSIONS

Detailed angle- resolved measurements of all three components of the mean and rms velocities in a stirred vessel, powered by a low consumption hyperboloid stirrer, were carried out using laser- Doppler anemometry, after measurements of the torque allowed the definition of the power consumption curve.

The hyperboloid stirrer was found to require only one fifth of the energy of conventional stirrers (Rushton and pitched blade) for Reynolds numbers above 1 000, but was less efficient for Reynolds numbers under 200.

The flow field was mainly axial, with a downwards velocity of about 5% of the tip velocity in the central part of the tank, and a wall jet up the side walls with a maximum mean velocity of around 15% of the tip velocity. In the same regions the turbulence was isotropic with an intensity of about 2% and growing up to 4%, respectively. The flow was three-dimensional, but quite uniform in all components, without strong shear rates except in the close vicinity of the shear ribs. However, this and other parameters still need to be quantified for comparison with those of conventional agitators. No dead zones were encountered within the vessel, making this impeller adequate for applications were a full gentle motion of the fluid, without excessive local deformation rates, is required.

Periodicity in the mean and turbulent flow fields was limited to less than 5% of the volume of the tank, and was found only close to the impeller and at the bottom of the vessel. The main periodicity was introduced by the 8 shear ribs on the upper surface of the impeller, whereas the 48 transport ribs at its bottom surface were mainly responsible for increasing the turbulence at the bottom, inducing a strong tangential flow and smearing the strong 8- cycle periodic flow, thus introducing a rather chaotic flow behaviour. Within this region, maximum values of the rms velocity of around 25% of the tip velocity were measured.

Further analysis of the data is required to extract various other useful quantities needed for assessing the performance of this impeller, such as the pump discharge coefficient and the distribution of the energy input into its various forms.

ACKNOWLEDGEMENTS

The authors wish to thank the European Commission and Junta Nacional de Investigação Científica e Tecnológica for financing this work through contracts JOU 2-CT9-0127 and PEAM/C/TAI/265/93, respectively. Special thanks are due to Mrs. Manuela Lemos for her assistance and valuable comments and to Mr. Jerónimo de Sousa for his technical support.

REFERENCES

Cutter, L. A. 1966. Flow and turbulence in a stirred tank. AIChEJ, vol. 12, pp. 35- 45.

Durst, F., Melling, A. and Whitelaw, J. H. 1981. Principles and Practice of Laser- Doppler Anemometry. 2nd Edition, Academic Press.

Hockey, R. M. 1990. Turbulent Newtonian and non-Newtonian flows in a stirred reactor. PhD Thesis, University of London, London.

Höfken, M., Bischof, F. and Durst, F. 1991. Novel hyperboloid stirring and aeration system for biological and chemical reactors. ASME FED- Industrial Applications of Fluid Mechanics, vol. 132, pp.47- 56.

Höfken, M. and Bischof, F. 1993. Hyperboloid stirring and aeration system: operating principles, application, technical description. Invent GmbH report, version 1.1, August 1993, Erlangen.

Kusters, K. A. 1991. The influence of turbulence on aggregation of small particles in agitated vessels. PhD Thesis, Technical University of Eindhoven.

Laufhüttle, H. D. and Mersmann, A. B. 1985. Dissipation of the power in stirred vessels. 5th European Conference on Mixing, Würzburg, West Germany, 10- 12 June, Paper 33, pp 331- 340.

Melling, A. 1975. Investigation of Flows in Non-Circular Ducts and Other Configurations by Laser-Doppler Anemometer. PhD Thesis, Imperial College, University of London.

Mujumdar, A. S., Huang, B., Wolf, D., Weber, M. E. and Douglas, W. J. M. 1970. Turbulence parameters in a stirred tank. Can. J. Chem. Eng.,vol. 48, pp.475- 483.

Nouri, J. M. and Whitelaw, J. H. 1992. Particle velocity characteristics of dilute to moderately dense suspension flows in stirred reactors. Int. J. Multiphase Flow., vol. 18, pp. 21-33.

Nouri, J. M. and Whitelaw, J. H. 1994. Flow characteristics of hyperboloid stirrers. Can. J. Chem. Eng., vol. 72, pp. 782- 791.

Piqueiro, F. M., Valente, J. T. and Pinho, F. T. 1995. Power consumption and flow pattern of the mixing vessel flow with single and double hyperboloid stirrers. Internal report, Deps. Civil and Mech. Eng., Faculty of Engineering, University of Porto, Portugal.

Popiolek, Z., Yianneskis, M. and Whitelaw, J. H. 1987. An experimental study of steady and unsteady flow characteristics of stirred reactors. J. Fluid Mech., vol. 175, pp. 537- 555.

Reed, X. B., Princz, M. and Hartland, S. 1977. Laser-Doppler measurement of turbulence in a standard stirred tank. Proc. 2nd Euro Conf. Mixing, Cambridge, UK, paper B1, 1.

T. S. I. 1988. Manual of the 1990 C counter, TSI Incorporation, Minneapolis.

Vafidis, C. 1985. Aerodynamics of Reciprocating Engines. PhD Thesis, Imperial College, University of London.

Yanta, W. J. and Smith, R. A. 1973. Measurements of Turbulence- Transport Properties with a Laser- Doppler Velocimeter. 11th Aerospace Science Meeting, Washington, AIAA paper 73, pp. 169-180 .

DETAILED LDV-MEASUREMENTS FOR VISUALIZATION OF THE FLOW-FIELD WITHIN A RUSHTON TURBINE

Marcus Schäfer, Marcus Höfken and Franz Durst

Department of Fluid Mechanics
Friedrich-Alexander-University of Erlangen-Nuremberg, Germany

ABSTRACT

The work at hand presents the results obtained during investigations carried out on a multifunctional stirrer test rig which was established at the Department of Fluid Mechanics at the University of Erlangen-Nuremberg. Main objective of the research work was to generate a reliable data basis for the validation of numerical simulations of the flow-field in stirred tank reactors. For the measurements advanced Laser Doppler Velocimetry including full refractive index matching and automated data acquisition was used. The flow-field in this case was induced by a Rushton turbine which was made of transparent material in order to create access to the important flow-field within the turbine.

The presentation of the large-scale flow-field approves the results known from previous publications, however a higher resolution was realized. The turbulent length scale L was found to be about half the blade height. Maximum velocities found in the jet stream in the direct vicinity of the Rushton turbine were up to $0.85U_{tip}$, the maximum local energy dissipation rates were about 25 times higher than the average energy dissipation.

Due to the total access to the flow-field also the formation and path of the trailing vortices was determined in detail. These results are shown graphically in the paper.

1 INTRODUCTION

Stirring processes have always played an important role in industry. In practically every branch of the chemical industry, food industry, biotechnology and environmental technology, stirred tank reactors (STR) are an important component in processing plants.

As befits this importance, they were subjected to comprehensive experimental investigations in the past. These often concerned the design of stirrers for special applications with the specific power input at the center of the observations. Integral investigations for selected stirrer/vessel combinations were used to derive stirrer-related scaling rules for the design of stirrers.

In more recent times, the emphasis has been on the development of numerical computation techniques (CFD) for the purposes of establishing accurate and low-cost design and dimensioning methods for stirrers. These are based on finite volumes, finite differences or finite element methods that can be introduced into the basic equations of fluid mechanics. These methods can only be implemented for these tasks, however in conjunction with precise, detailed experimental methods, which are required to validate the calculations and in further development the turbulence models. Laser Doppler Velocimetry (LDV) was used here almost exclusively.

Until now, investigations with this measurement technique have been concerned with determining the average velocity of flow, turbulence variables and energy dissipation rates (e.g. Patterson and Wu (1985), Laufhütte and Mersmann (1985), Yianneskis et al. (1987, 1993, 1994), Kresta and Wood (1992)). Despite this work, there is still a lack of detailed data concerning the flow-field, partly because the resolution of the measurements was insufficient for the validation of numerical simulations of STR flows and also because the flow-field has never been thoroughly investigated (e.g. within the stirrer elements). There is a particular need for a more precise description of the local energy dissipation throughout the STR because this is the coupling variable between fluid mechanics and reaction technology.

During fast reactions, mixing processes on a molecular scale have to be taken into account in reaction technology, and are described by so-called micromixing models. Energy dissipation is one of the basic variables in these models, and therefore it is essential to determine precisely and reliably the distribution of this variable throughout the STR using experimental methods.

The objective of this paper is to present a method for obtaining precise, detailed and comprehensive experimental results and to show how they can be used for the above mentioned purposes through appropriate graphical presentation. This is described here on the basis of the example of investigations on a Rushton

turbine, but the procedure described can be applied analogously to any type of stirrer. It is recommended that this should be carried out for all types of stirrer in common use in order to establish a secure basis for numerical simulation.

Progress in modern computation techniques leads to the expectation that the computing power that is required for reliable calculations of flow in STR's will soon be available. These developments will be supported by the detailed experiments discussed here.

2 EXPERIMENTAL

Laser Doppler Velocimetry has proved to be more precise and reliable in the measurement of flow-fields in STR's than any other technique (e.g. Pitot probes, hot wire anemometers), due to (a) providing reliable flow information even in non-steady-state and highly turbulent flow areas as well as in the return flow areas of the STR and (b) operating without fluid contact. A standard LDV system only supplies flow information at a single point, so the entire flow-field can only be determined rapidly, precisely and in detail if measured data acquisition is automated. In the vicinity of the stirrer element, the rotating stirrer blades cause periodic variations in the flow variables that can increase the turbulent variables considerably, if steady-state LDV measurements are used (up to a factor of 4, according to Yianneskis et al. (1987)). Angle resolved measurements allow for taking into account the periodic variations in the flow-field by assigning each single velocity value to the corresponding angle.

No quantitative information is available from any of the previous investigations for the flow-field within the Rushton turbine investigated here. Taking into account the fact that up to 20% of the total energy input to the STR is dissipated within the stirrer element, integral balances can be supplemented by the incorporation of this area to arrive at a deeper understanding of the functioning of the stirrer. Through complete adaptation to the refractive index of the implemented fluid in every main section of the measurement circuit, as was carried out in these investigations, this important area between the blades of the Rushton turbine can also be investigated using the LDV measuring technique.

Taking all these aspects into account, at the Department of Fluid Mechanics (LSTM) within the framework of several research projects, a multifunctional stirrer test rig has been developed (see Höfken (1994)). The structure of the test rig is shown in Figure 1. The basic structure comprises three substructures, the measuring circuit, the traversing equipment and the LDV measurement system. Further details on the test set up were described by Höfken (1994). The semiconductor LDV measuring system used has been described in detail by Stieglmeier and Tropea (1992).

In the investigations described here, a Rushton turbine is used as the stirrer (see Figure 2), with the

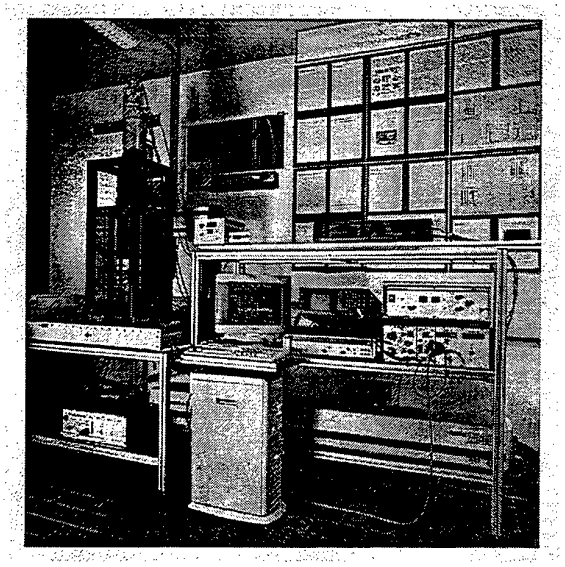

Fig. 1: Test set up

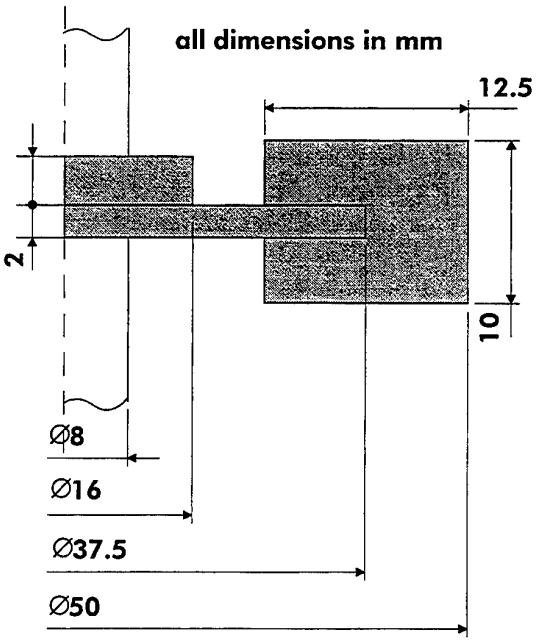

Fig. 2: Rushton Turbine Model

dimensions D = T/3, H = D/5, W = D/4 and a clearance of T/3 in a cylindrical and baffled STR with a tank diameter of T = 150 mm.

The entire measuring circuit was refractive index matched, i.e. the STR walls and the stirrer blades were constructed from transparent material that has the same refractive index as the model fluid (n = 1.473). In addition, the STR was suspended in a rectangular

container filled with the model fluid, in order to eliminate the distorting effect of the rounded surface of the STR on the path of the laser beams.

The results presented below were obtained from measurements that were carried out at a stirrer speed of N = 1200 rpm. With the characteristic values for the fluid, this resulted in a turbulent Reynolds number of Re = $1.2^{*}10^{3}$.

3 RESULTS

3.1 Large-Scale Flow

For the purpose of clarifying the flow relationships existing throughout the STR, the complete flow-field was measured with high resolution at an axial and radial step width of 4 mm. As the baffle positions influence the flow-field significantly, several measuring traverses were carried out at different baffle positions relative to the blade positions of the stirrer.

Figure 3 illustrates the locations of the planes which are presented here (15°, 45° and 75° in front of the baffles), by way of example. In Figures 4 to 9, the average flow-field and the distribution of the energy dissipation are presented for these planes. The diagrams correspond to a momentary picture of the flow, i.e. the flow events are related to the depicted angular position (0°) of the stirrer element with respect to the plane of stirring. At a greater distance from the stirrer element, the flow events can, however, be viewed as steady-state so that the flow-field here remains almost identical during one complete revolution of the stirrer element.

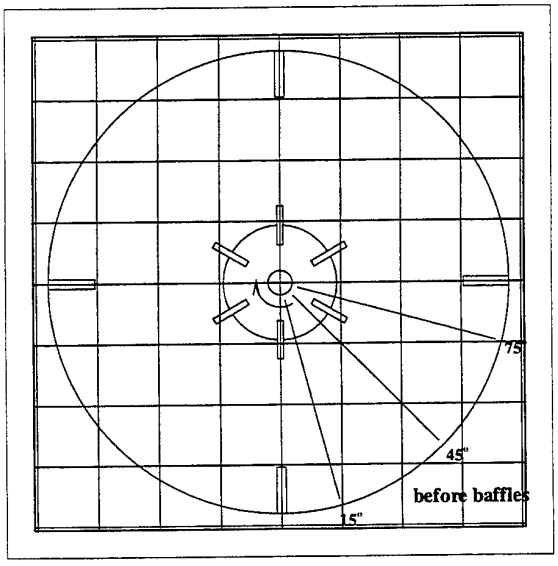

Fig. 3: Positions of presented planes

The flow-fields presented show the typical mode of operation of the Rushton turbine. The liquid is drawn into the stirrer element axially, deflected in a radial direction, and ejected again in the form of a radial jet stream. The fluid jet ejected at flow velocities of up to $0.85U_{tip}$ splits at the vessel walls and is diverted upwards and downwards. The tangentially propelled fluid at the level of the stirrer element meets the baffles close to the vessel walls and is also deflected axially here. Two large-scale ring vortices are formed, one above and one below the area of radial flow at the level of the stirrer blades. The mounting height of the stirrer element at 1/3 of the liquid level means that the upper ring vortex is only able to form over a section of the upper vessel volume, whereas the lower ring vortex spans the entire lower vessel area, ensuring excellent macro-mixing there.

The center of the upper ring vortex moves further towards the central plane as the distance from the baffles increases. At the plane located at 15° in front of the baffles, a secondary vortex is generated that is able to maintain minimal macro-mixing in the uppermost area of the STR.

Furthermore, the intensity of the lower ring vortex is significantly stronger, a fact that is confirmed by the considerably higher velocity of axial flow moving into the stirrer element (up to $0.25U_{tip}$ as opposed to $0.15U_{tip}$ above the stirrer element).

For the purposes of determining the local energy dissipation (Figures 7 to 9), a statement from Brodkey (1975) was referred to that was based on a dimensional analysis and resulted in the following equation:

$$\varepsilon = A \cdot \frac{u'^3}{L} \cdot$$

where u' represents a characteristic turbulent velocity and L represents a characteristic length scale of the flow. The constant of proportionality A can be set to A = 1 in jet flows according to Batchelor (1953). It was therefore possible to determine the characteristic length scale via an energy balance calculation throughout the STR (see, for example, Höfken (1994)). A length scale of L = 5.74 mm was determined for the Rushton turbine flow in this case, corresponding to about half the height of the stirrer blades. This length scale was then inserted in the above equation for calculating the local energy dissipation distribution in each separate volume element of the entire STR.

The results obtained via LDV measurement techniques show that the highest values for local energy dissipation are found in the area of the outwardly flowing radial jet. Values were obtained in this area of $\varepsilon = 20 - 25\varepsilon_{tot}$, compared with values in the other areas of less than $0.5\varepsilon_{tot}$, which constitutes an increase of between a factor of 40 and a factor of 200. The higher values for local energy dissipation in the outward flow area can be traced back to the trailing vortices detached by the edges of the stirrer blades that have already been described by

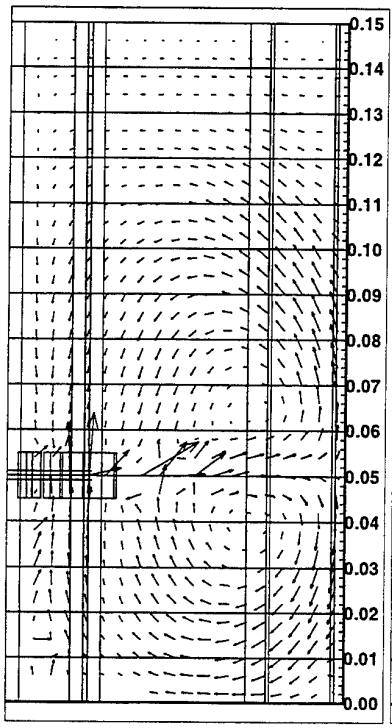

Fig. 4: Average velocities in the r,z-plane at 15°

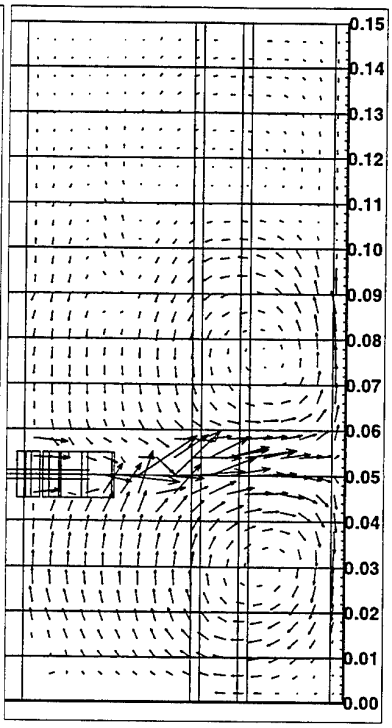

Fig. 5: Average velocities in the r,z-plane at 45°

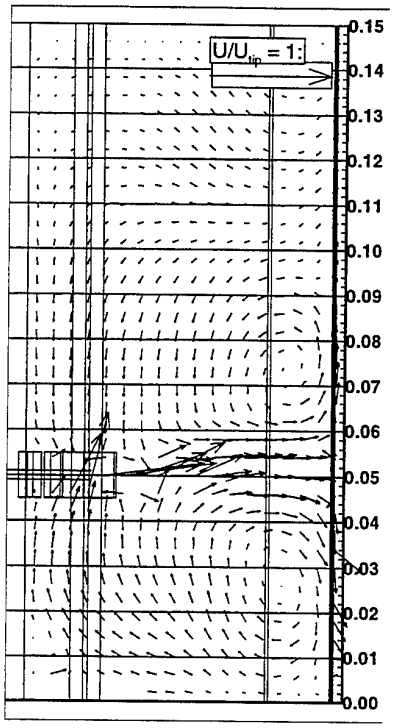

Fig. 6: Average velocities in the r,z-plane at 75°

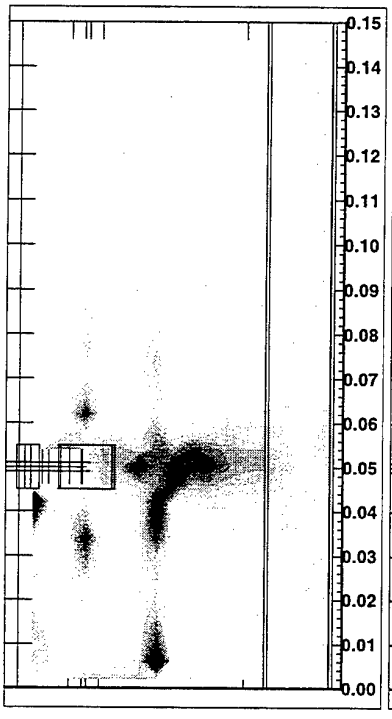

Fig. 7: Energy dissipation distribution in the r,z-plane at 15°

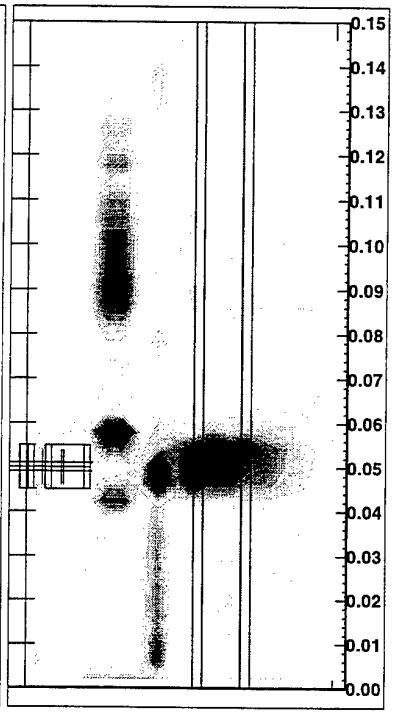

Fig. 8: Energy dissipation distribution in the r,z-plane at 45°

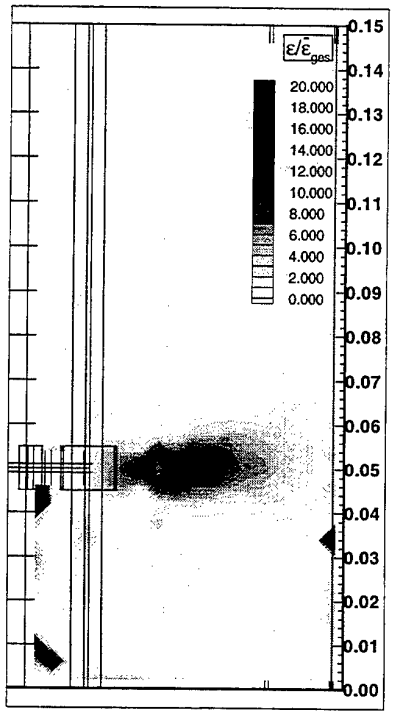

Fig. 9: Energy dissipation distribution in the r,z-plane at 75°

van't Riet and Smith (1973) and Yianneskis et al. (1994) as well as being analyzed in detail in the following section. The collapse of these detached vortices in the outer flow-field beyond a certain distance from the stirrer element leads to a further increase in the local energy dissipation, as can be clearly seen in figures 7 to 9.

3.2 The Area within and in the Vicinity of the Stirrer

In the inner area of the stirrer and within the outward flow area, the highest values for local energy dissipation are found which account for approximately 80% of the total energy dissipated in the STR. A detailed explanation of the flow conditions especially with respect to the trailing vortices arising here requires even higher resolution of the measuring grid. Outside the stirrer element, an axial and radial step width of 2 mm was specified for this purpose that was reduced to 1 mm within the stirrer.

The results given here were obtained with a baffle position of 45° relative to the measuring plane in angular coordinates. The following figures comprise a selection of two-dimensional presentations of the velocity field from different perspectives that give a complete picture of the flow-field. In figures 10 and 11 the locations of the presented planes within the entire STR are shown. Figures 12 to 17 depict r,θ planes for z = 48, 50 and 52 mm. An additional perspective is obtained via the θ,z plane depicted in figures 18 and 19 for r = 20 mm. This is located just behind the central disc of the stirrer, as can be seen clearly from figure 11. A third perspective is provided by the r,z planes which are shown in figures 20 to 25 for θ = 6°, 30° and 54°.

The velocity field depicted at θ = 6° shows the mode of operation of the Rushton turbine extremely clearly. The fluid stream is sucked into the stirrer element axially and deflected into a radial path along which the fluid leaves the stirrer element. In this plane, the inflowing velocities reach values of up to $0.25U_{tip}$ whereas in the plane for θ = 30°, only a minimal inflow with axial velocity values of $0.05U_{tip}$ can be determined. Just before the subsequent stirrer blade at θ =54° inflow does not exist; there is even some axial outflow that works against the stirring mechanism as such. Taking into consideration the velocity fields in the r, θ plane for z = 48 mm, the clearly defined direction of the velocity vectors points to a pronounced area of low pressure that is located just behind the stirrer blades and without which the fluid could not be sucked in. It can be deduced from this that the major proportion of the circulated fluid only flows into the stirrer element in a limited area that is characterized by the low-pressure area.

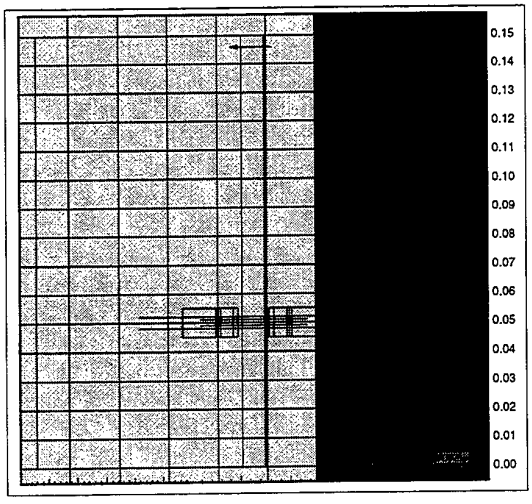

Fig. 10: Positions of the r,θ planes considered

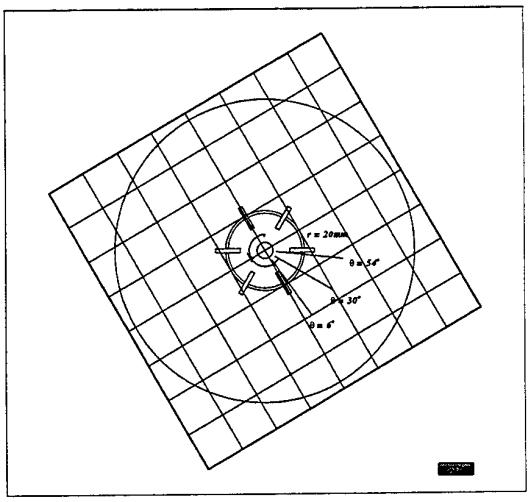

Fig. 11: Positions of the θ,z and r,z planes considered

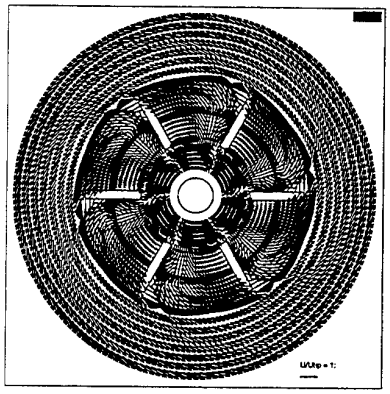

Fig. 12: Average velocities in the r,θ plane at 48 mm

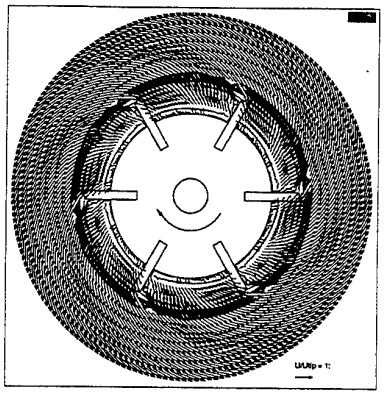

Fig. 13: Average velocities in the r,θ plane at 50 mm

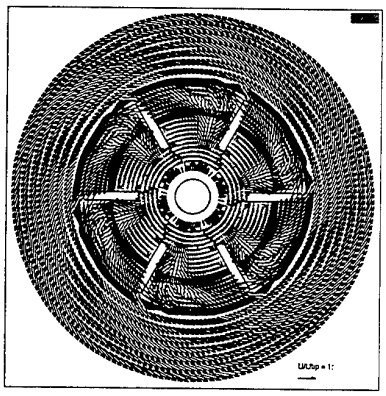

Fig. 14: Average velocities in the r,θ plane at 52 mm

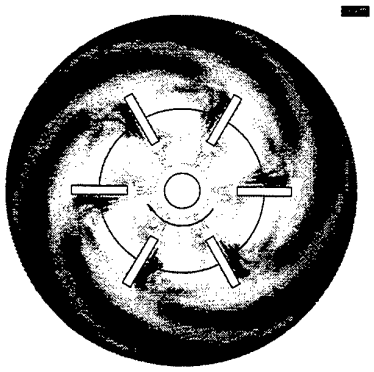

Fig. 15: Energy dissipation distribution in the r,θ plane at 48 mm

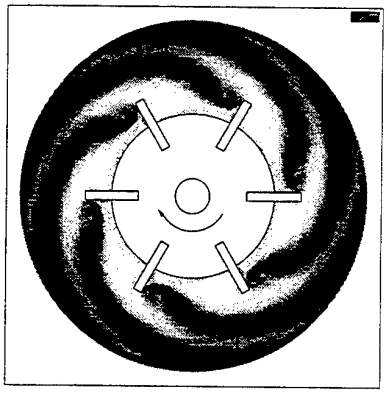

Fig. 16: Energy dissipation distribution in the r,θ plane at 50 mm

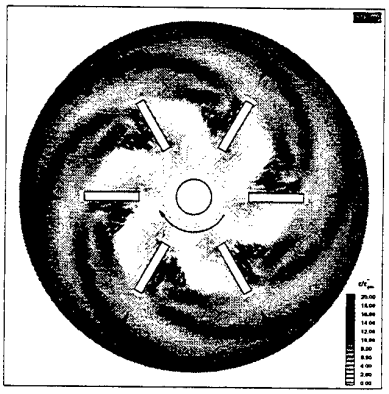

Fig. 17: Energy dissipation distribution in the r,θ plane at 52 mm

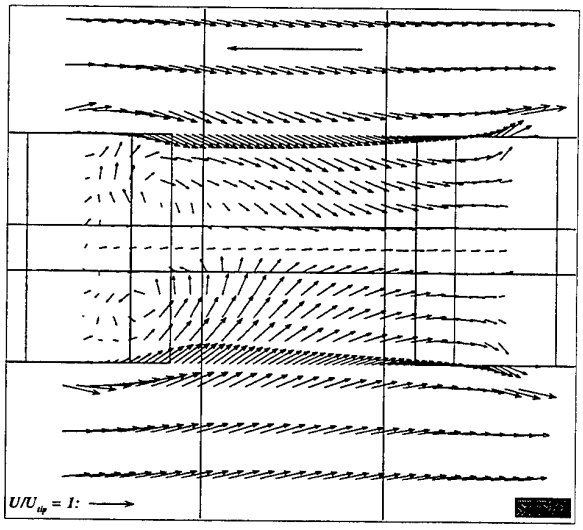

Fig. 18: Average Velocities in the θ,z - plane at 20mm

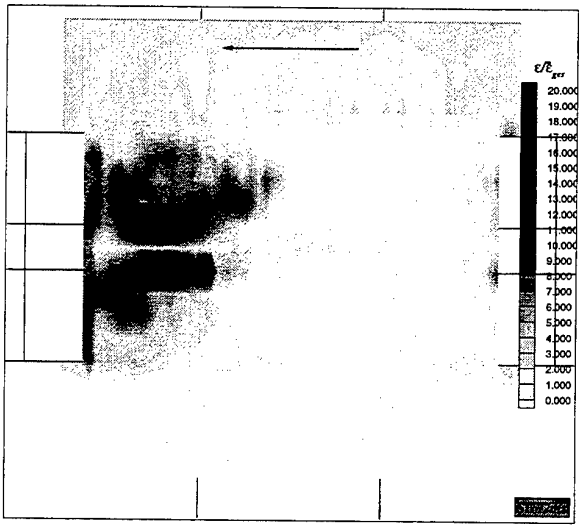

Fig. 19: Energy dissipation distribution in the θ,z - plane at 20mm

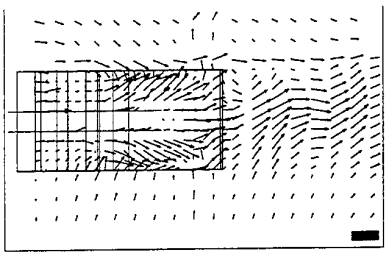

Fig. 20: Average Velocities in the r,z - plane at 6°

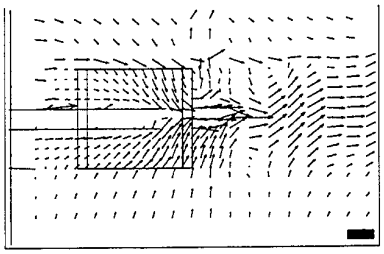

Fig. 21: Average Velocities in the r,z - plane at 30°

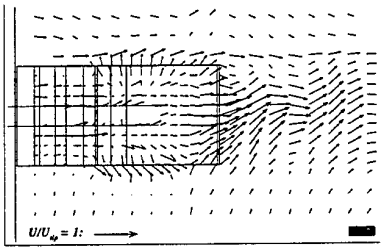

Fig. 22: Average velocities in the r,z - plane at 54°

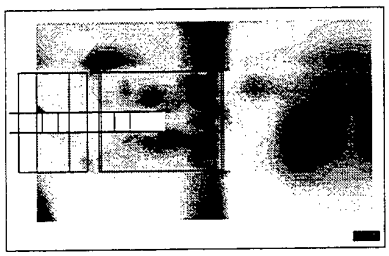

Fig. 23: Energy dissipation distribution in the r,z - plane at 6°

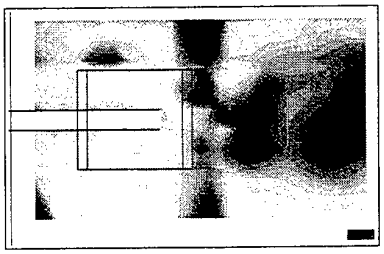

Fig. 24: Energy dissipation distribution in the r,z - plane at 30°

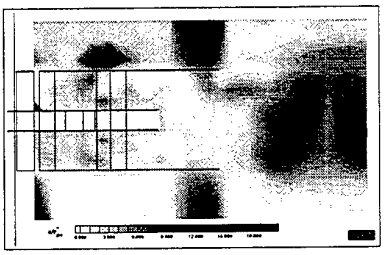

Fig. 25: Energy dissipation distribution in the r,z - plane at 54°

Within the stirrer, owing to the forced rotation of the fluid located within the stirrer, two vortices are formed above and below the central discs and driven as depicted in the θ,z plane at r = 20 mm. These move with the main flow along the stirrer blade outwards and detach themselves from it just before reaching the outer blade end. These trailing vortices cause increased turbulence values, which is why the local energy dissipation in this area increases significantly. The highest energy dissipation values are obtained between the two vortices at the point where they influence each other. With reference to the distribution of the local energy dissipation in the r,θ planes (figures 15 to 17), the trailing vortex path can be followed precisely. After being detached from the rear edge of the stirrer blade, the trailing vortices are deflected into a tangential path. After exiting the stirrer, the vortex centers in the outer flow-field move along a path such that with increasing distance they move further away from the stirrer and move further into alignment with a tangential path. The vortices are, however, no longer being driven in the outer flow-field so they collapse slowly until they completely disappear. The beginning of this dissolution causes a further increase in turbulence or energy dissipation which occurs, for example, in the r,θ plane at z = 48 mm (figure 15) at approximately the level of the following stirrer blade. This behavior can be approximated to the turbulence behavior of a free jet flow for which high turbulence values only arise within the free jet beyond a certain distance from the outlet opening.

4 SUMMARY

The results presented here show that the flow-field induced by a stirrer can be precisely characterized using the described methods. In particular, it is possible to prepare a precise, detailed description of the distribution of the local energy dissipation at the points where the highest energy dissipation is found, which can supply valuable information especially for the calculation of two-phase and multi-phase flows. Energy dissipation rates can therefore now be inserted in the basic equations for modeling reaction processes to contribute towards more reliably designed reactions and reaction equipment. In two-phase flow, the optimal entry point for the second phase often has to be found, in which case the designer will find the depicted presentation of the energy dissipation distribution within the STR extremely useful.

Furthermore, the described methods show, for the first time, a method for optimization and further development of stirrers on the basis of detailed investigations. A stirring element can only be optimized with respect to a specific stirring task using numerical methods when a precise knowledge of the flow conditions, turbulence parameters and energy dissipation is available.

List of symbols

n	[-]	Refractive index
N	[rpm]	Stirrer speed

r, θ, z	[m]	Cylinder coordinates
u'	[m/s]	Characteristic turbulent velocity
A	[-]	Constant of proportionality
W	[m]	Width of the stirrer blade
D	[m]	Diameter of the stirrer
H	[m]	Height of the stirrer blade
L	[m]	Integral length value
U_{tip}	[m/s]	Stirrer tip velocity
T	[m]	Diameter of the STR
ε	$[m^2/s^3]$	Energy dissipation
ε_{tot}	$[m^2/s^3]$	Average energy dissipation referred to the total input energy

References

Batchelor, G. K., 1953, The Theory of Homogeneous Turbulence, Cambridge Univiversity Press, Cambridge.

Brodkey, R. S., 1975, Turbulence in Mixing Operations, Academic Press, New York - San Francisco - London.

Höfken, M., 1994, Moderne experimentelle Methoden für die Untersuchung von Strömungen in Rührbehältern und für Rührwerksoptimierungen, Ph.D. thesis, Institute of Fluid Dynamics, Friedrich-Alexander-Universität Erlangen-Nuremberg.

Kresta, S. M. & Wood, P. E. 1992, The Flow-field Produced by a Pitched Blade Turbine: Characterization of the Turbulence and Estimation of the Dissipation Rate, Chem. Eng. Sci., vol. 48, pp. 1761-1774.

Laufhütte, H. D. & Mersman, A. B. 1985, Dissipation of Power in STR's, presented at the 5th European Conference on Mixing, Cranfield, UK.

Patterson, G. K. & Wu, H. 1985, Distribution of Turbulence Energy Dissipation Rates in Mixers, presented at the 5th European Conference on Mixing, Cranfield, UK.

Riet van't, K. & Smith, J. M. 1973, The Trailing Vortex Systems Produced by Rushton Turbine Agitators, Chem. Eng. Sci., vol. 28, pp. 1031-1037.

Riet van't, K. & Smith, J. M. 1975, The Trailing Vortex Systems Produced by Rushton Turbine Agitators, Chem. Eng. Sci., vol. 30, pp. 1093-1105.

Stieglmeier, M. & Tropea, C. 1992, Mobile Fiber-Optic Laser Doppler Anemometer, Applied Optics, vol. 31, no. 21, pp. 4096-4105.

Wu, H., Patterson, G. K. & Doorn van, M. 1989, Distribution of Turbulence Energy Dissipation Rates in a Rushton Turbine Stirred Mixer, Experiments in Fluids, no. 8, pp. 153-160.

Yianneskis, M., Popiolek Z. & Whitelaw J.H. 1987, An Experimental Study of the Steady and Unsteady Flow Characteristics of Stirred Reactors, J. Fluid Mech., vol. 175, pp. 537-555.

Yianneskis, M., Whitelaw J.H. 1993, On the Structure of the Trailing Vortices around Rushton Turbine Blades, Trans. IChemE, vol. 71, Part A, pp. 543-550.

Yianneskis, M., Rutherford K. & Lee K. C. 1994, The Interaction of the Trailing Vortex Streams from Rushton Turbine Blades, Seventh International Symposium on Applications of Laser Techniques to Fluid Mechanics, Lisbon, Portugal, vol. 1, pp. 10.2.1-10.2.7.

THE DECAY OF THE TRAILING VORTICES FROM IMPELLER BLADES

N J Fentiman, N A Borrett, K C Lee and M Yianneskis

Department of Mechanical Engineering
King's College London
Strand, London WC2R 2LS
United Kingdom

ABSTRACT

The flow in the vicinity of the Rushton impeller in stirred vessels is strongly periodic due to the crossing of the individual impeller blades and the associated trailing vortex structure. Earlier investigations (Popiolek et al (1984), Yianneskis et al (1987), Yianneskis and Whitelaw (1993), Stoots and Calabrese (1994)), have reported in detail the structure of the flow around a Rushton impeller and have identified the main features of the mean flow and turbulence fields.

The present study is concerned with the decay of the trailing vortices with increasing distance from the blades of the impeller. Angle-resolved and time-resolved LDA measurements of the three mean velocity components and of the corresponding turbulence levels were made in a $T = 100$ mm diameter fully baffled stirred vessel with a Rushton impeller of diameter $D = T/3$ and located at a clearance of $C = T/3$ above the flat bottom of the vessel.

It is shown that the vortices maintain their identity for only a short distance from the blade. Spectral analysis of the time-resolved data and comparisons of the distributions of the axial, radial and tangential turbulence levels indicated that the turbulence might be considered anisotropic near the impeller blade, and becomes increasingly isotropic with distance from the blade.

1. INTRODUCTION

A pair of trailing vortices are produced by a rotating Rushton impeller as the flow passing each blade above (and below) the impeller disc interacts with the tangential velocity imparted on the flow by the impeller. This flow combines to form a pair of trailing vortices, one above and one below the disc rotating in opposing directions. This is shown schematically in Figure 1. The presence of a large periodic component in the flow in the vicinity of the impeller, was first reported by Mujumdar et al (1970), with a time scale equal to the number of blades multiplied by the rotational speed and an amplitude decreasing with distance from the impeller. The corresponding energy spectra showed a peak at this frequency. It was estimated that the turbulence intensities were up to five times larger that the true value due to this periodicity. Van't Riet and Smith (1973, 1975) reported the existence of trailing vortices behind each impeller blade, which maintained their identity for 2–3 blade lengths. They found the vortex axis to be nearly horizontal. Günkel and Weber (1975) showed that the pair of trailing vortices between two successive blades gave rise to anisotropic turbulence in the impeller stream. Van't Riet et al (1976) suggested that most of the velocity fluctuations, originated from the periodicity of the flow in the impeller region and the accompanying vortex structure and coined the term pseudo-turbulence for such fluctuations. Van der Molen and van Mannen (1978) observed that the periodic component reached near-zero values at two thirds of the tank radius and thereafter decayed into random turbulence. LDA measurements averaged over 1° intervals were performed by Popiolek et al (1984), Yianneskis et al (1987), Stoots and Calabrese (1995) and Yianneskis and Whitelaw (1993). It was found that the turbulence levels were overestimated by up to 400% when ensemble-averages were obtained over 360° compared with 1° intervals. Popiolek et al (1984) found the velocities in the vortices were of the order of $0.25V_{tip}$ and the maximum kinetic energy of turbulence was $0.19V_{tip}^2$ at around 20° behind each blade. The fluctuating quantities measured indicated strong anisotropy of the turbulence in the impeller

stream. Yianneskis et al (1987) found the axis of the trailing vortex to be nearly horizontal, hence the effect of periodicity was not seen to extend far above or below the impeller. The trailing vortices merged with the bulk flow at 25°–30° behind each blade.

In this study the decay of the trailing vortices with increasing radial distance from the impeller has been investigated. This has been achieved through LDA measurements and subsequent spectral analysis of the results.

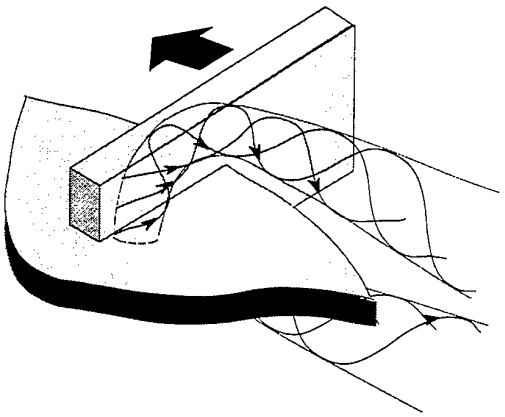

Figure 1. Schematic diagram of a pair of trailing vortices generated by a Rushton impeller blade.

2. FLOW CONFIGURATION AND MEASUREMENT TECHNIQUES

Experiments were performed in an acrylic cylindrical fully-baffled vessel agitated by a single 6-bladed Rushton turbine. The vessel configuration is shown Figure 2 and was of internal diameter (T) 100 mm and 4 baffles of width $T/10$ were located on the periphery of the tank. The vessel was located inside an acrylic square trough, and the space between the vessel and trough was filled with distilled water fed from a constant temperature water bath, in order to remove the heat generated by the impeller and to minimise refraction effects. The Rushton impeller was of diameter (D) $T/3$ and located at an off-bottom clearance (C) of $T/3$. The working fluid inside the vessel was distilled water and the tank was filled to a height $H = T$. A lid was placed at this height, to avoid air entrainment in the flow. The impeller shaft was driven by a bi-directional variable speed DC motor. The rotational speed, N, was set to 2165 ± 10 rpm for all experiments; this corresponded to a tip velocity (V_{tip}) of 3.77 m/s and a Reynolds number of 40 000. The origin of the co-ordinate system was taken to be the centre of the base of the vessel and all positions are described in terms of polar co-ordinates in the axial (z), radial (r) and tangential (θ) directions. For the angle resolved measurements, the measuring volume location is expressed in terms of polar co-ordinates relative to the impeller, viz. r, z and ϕ, where ϕ is the angle measured from the centre of a reference blade. All measurements were performed in the plane located halfway between two adjacent baffles ($\theta = 0°$). The impeller shaft was coupled to an optical shaft encoder that provided a train of 1999 pulses and one marker pulse per revolution. From this the rotational speed of the impeller could be determined and each velocity result could be angle-stamped with respect to the impeller position.

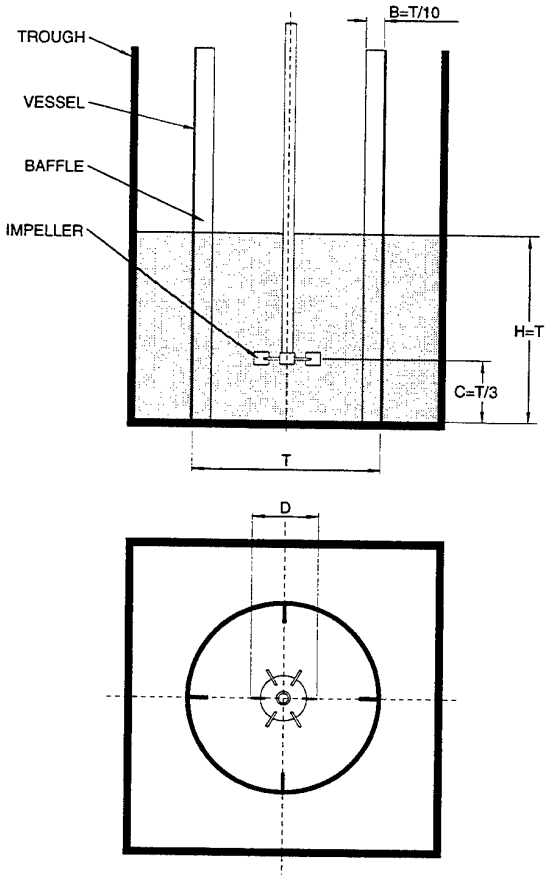

Figure 2. Vessel configuration.

Time-resolved data were acquired by measuring all validated Doppler signals arriving over a predetermined number of impeller revolutions. Angle-resolved data were acquired by ensemble-averaging the velocity measurements between two particular adjacent blades, i.e. over a 60° interval, and sorted into 1° bins. This was performed over a number of revolutions until sufficient data had been acquired for each 1° interval of the 60° band.

Time-resolved and angle-resolved velocities were measured using an LDA system operating in the dual beam, forward scatter mode. The beams from a 10 mW Helium-Neon laser entered the flow field from either the base or the side of the tank, depending on the velocity component being measured. A radial diffraction grating was used for splitting and frequency shifting of the two first order laser beams. The fluid inside the vessel was seeded with neutrally buoyant particles of 3 μm mean diameter. Scattered light from the particles crossing the measuring volume created by the two beams was collected using a photomultiplier tube. The Doppler signals were processed using a frequency counter for the angle-resolved and a burst spectrum analyser (BSA) for the time-resolved measurements. The counter and BSA data were processed to obtain the quantities of interest with a microcomputer and a VAX mainframe computer respectively. The measuring volume length and diameter were 370 μm and 46.5 μm respectively. The errors in the mean velocities were estimated to be 1–5% and in the rms velocities 5–10%.

3. RESULTS AND DISCUSSION

3.1. Angle-Resolved Measurements

For the angle-resolved measurements at least 500 samples were taken for each 1° blade angle interval to achieve statistically independent results. The mean velocities in the axial, radial and tangential directions are denoted by $\overline{U}$, $\overline{V}$ and $\overline{W}$ respectively. The rms velocities in these three directions are denoted by u', v' and w' respectively.

In Figure 3, the contours of the kinetic energy of turbulence normalised with the tip speed squared, V_{tip}^2, are shown in the $\phi = 0°$, 15°, 30° and 45° planes. The presence of the trailing vortices is indicated by the regions of high k/V_{tip}^2 values. For all ϕ planes, k/V_{tip}^2 levels greater than 0.02 are found within a region bounded by $z/T = 0.29$ and 0.40, i.e. a cylindrical region of around 1.5 blade heights. In the $\phi = 0°$ and 15° contours, two regions of high k/V_{tip}^2 values can be discerned: the first is associated with the vortices generated by the leading blade, the centre of which is on the $\phi = 0°$ plane, and the second with the vortices from the preceding blade.

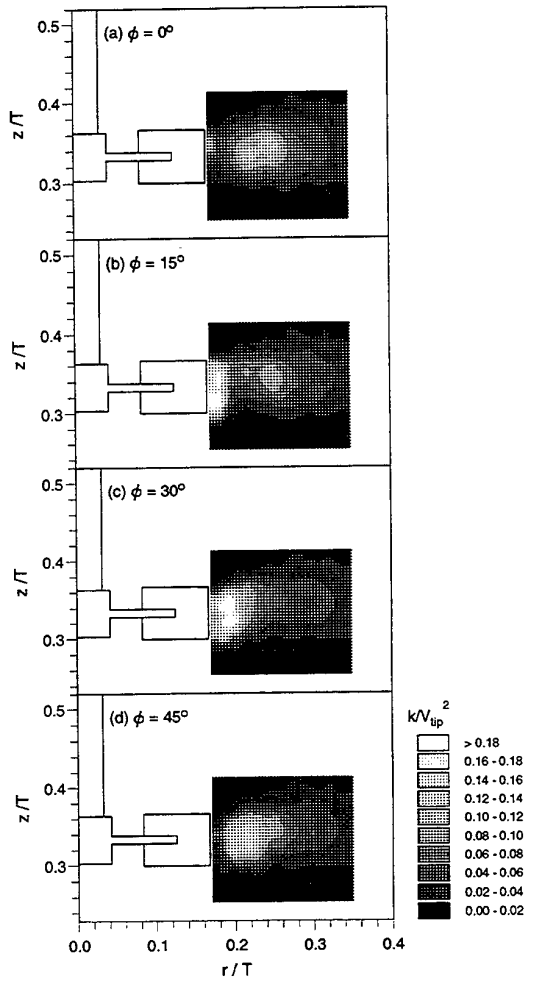

Figure 3. Normalised turbulence kinetic energy contours in the $\phi = 0°$, 15°, 30° and 45° planes.

At $\phi = 0°$ the vortex pair from the preceding blade is centred just above the impeller disc at $r/T \approx 0.23$ and $z/T \approx 0.34$, while in the $\phi = 15°$ plane the corresponding region (where $k/V_{tip}^2 = 0.08$–0.10) is centred at $z/T \approx 0.34$ and $r/T \approx 0.25$. By the time the impeller has moved to the $\phi = 30°$ and 45° planes, the trailing vortices produced by the preceding blade can no longer be discerned, but most probably contribute to the elongated shape of the 0.04–0.06 contour in these plots.

The trailing vortex pair from the leading blade in the $\phi = 0°$ plane is indicated by the region of $k/V_{tip}^2 = 0.08–0.10$ just above the impeller disc at the edge of the impeller blade. At $\phi = 15°$, the vortices are located in the area near the blades where k/V_{tip}^2 is greater than 0.10. A corresponding region of high k levels exists in the $\phi = 30°$ and 45° planes, but is seen to move away from the impeller blade as ϕ increases. This illustrates that the trailing vortex pair behind the impeller blade moves radially outwards.

Figure 4 shows the turbulence kinetic energy contours normalised with V_{tip}^2 in the $z/T = 0.33$ plane. The impeller is rotating in a clockwise direction. The region of high k behind the leading blade indicates the presence of the trailing vortex pair streaming radially outwards. The second region of high k corresponds to the trailing vortex pair generated by the preceding blade (not shown on the Figure).

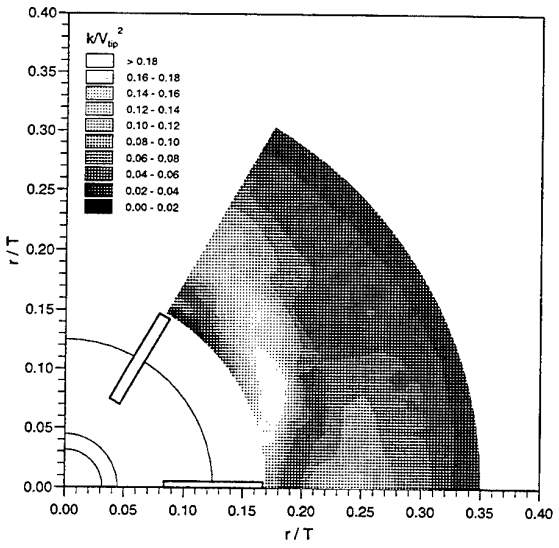

Figure 4. Normalised turbulence kinetic energy contours in the $z/T = 0.33$ plane.

In order to assess the isotropy of turbulence in the impeller stream, the values of the turbulence levels in the three co-ordinate directions were compared. As values of u'/v' and w'/v' may give an erroneous assessment of isotropy in regions where these levels are low, it was found more appropriate to consider the distribution of $|u' - v'|/V_{tip}$ and $|w' - v'|/V_{tip}$ instead.

Figures 5 and 6 show contours of $|u' - v'|$ and $|w' - v'|$ normalised with V_{tip} in the $\phi = 0°$, 15°, 30° and 45° planes.

Turbulence can be considered to be isotropic where the contour values tend to zero. In all ϕ planes in Figure 5, the highest values of $|u' - v'|/V_{tip}$ are found near the impeller blades. At the edge of the measured area the contour values are very low, 0–0.02 as the turbulence is becoming more isotropic. In Figure 6, the highest values of $|w' - v'|/V_{tip}$ are again in the vicinity of the impeller blades and the lowest at the edge of the measurement region. These distributions indicate that the turbulence might be considered to be isotropic away from the blades, while near the impeller it is largely anisotropic. This finding has important implications for CFD predictions of the flows employing turbulence models such as the k-ε, which are based on an implicit assumption of isotropic turbulence.

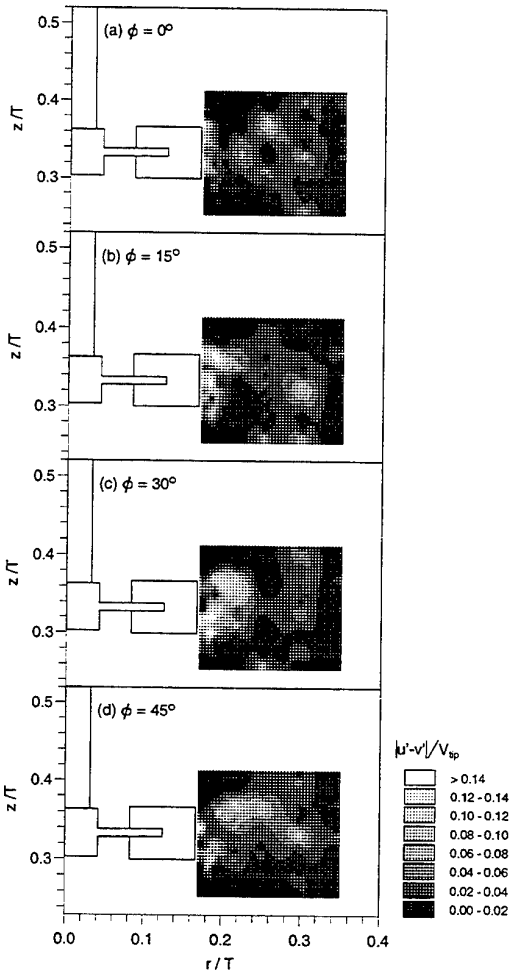

Figure 5. $|u' - v'|/V_{tip}$ contours in the $\phi = 0°$, 15°, 30° and 45° planes.

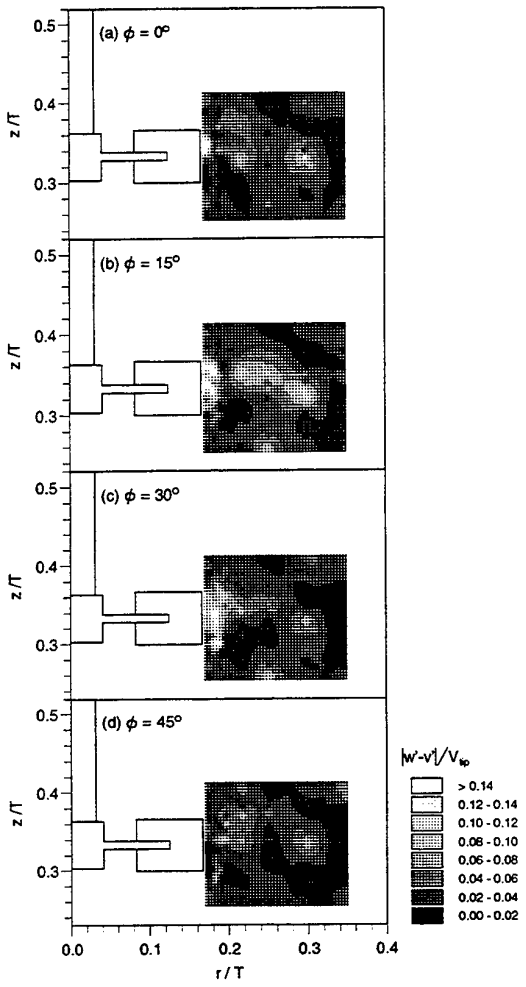

Figure 6. $|w' - v'|/V_{tip}$ contours in the $\phi = 0°$, 15°, 30° and 45° planes.

3.2 Time-resolved Measurements

Time-resolved measurements of the instantaneous radial velocity over a number of impeller revolutions, were made at a series of radial locations. This serves to highlight the periodicity at a certain point in the flow field, due to the action of the blade passages and the associated trailing vortices. It is thus possible to ascertain how far radially outwards from the impeller this periodicity is felt and where the periodic component decays and the associated trailing vortices dissipate into the main ring vortices in the bulk flow. Figures 7(a)–(d) show the instantaneous radial velocity, V, normalised with the impeller tip speed V_{tip} in the $z/T = 0.33$ plane (through the centre of the impeller disc), at a series of radial locations: $r/T = 0.17$, 0.18, 0.22 and 0.25 respectively. At the two radial locations closest to the impeller: $r/T = 0.17$ and 0.18, a cyclic variation of velocity is observed. Six cycles can be clearly seen for each complete impeller revolution, corresponding to the number of blade passages, as was also reported by Popiolek et al (1984). Further out at $r/T = 0.22$ there is still some periodicity, which decays even further by $r/T = 0.25$.

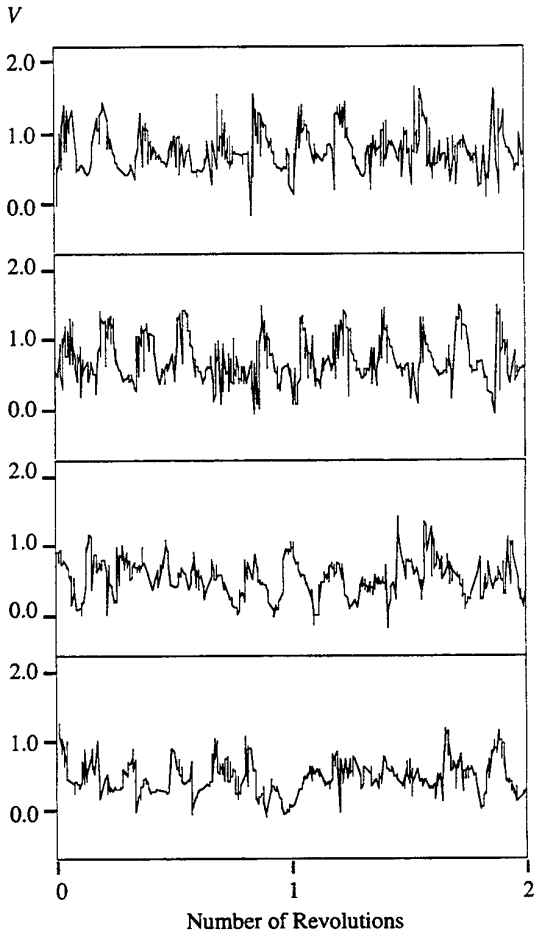

Figure 7. Normalised instantaneous radial velocity recordings made in the $z/T = 0.33$ plane at (a) $r/T = 0.17$; (b) $r/T = 0.18$; (c) $r/T = 0.22$ and (d) $r/T = 0.25$.

In order to quantify the changes in strength of the frequency components along the impeller stream, normalised energy spectra were calculated from the instantaneous velocity traces in Figure 7. This also serves to highlight discrete frequencies in the flow. Normally, when calculating energy spectra, data should be sampled at equal time

intervals, however, during the time-resolved measurements data were acquired at random intervals. For the spectral analysis of unevenly sampled data the Lomb method was adopted and applied in a manner described by Press et al (1992). The normalised energy spectrum function, $P(f)$ is given by:

$$P(f) = \frac{E'(f)}{v'^2}$$

where $E'(f)$ is the energy spectrum function calculated from unevenly spaced data using the Lomb method and v' is the rms value of the recorded radial instantaneous velocities which includes both the 'real' and 'pseudo' components of turbulence.

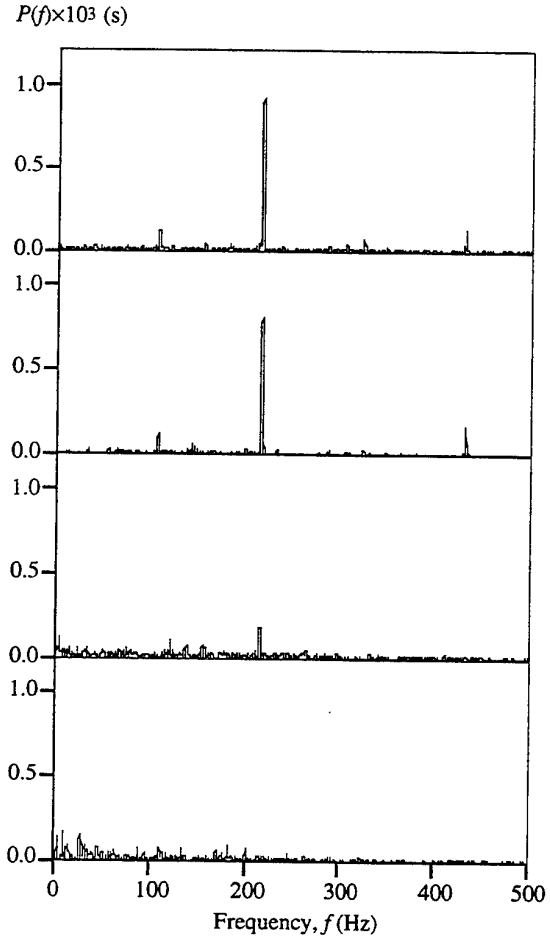

Figure 8. Normalised instantaneous radial velocity recordings made in the $z/T = 0.33$ plane at (a) $r/T = 0.17$; (b) $r/T = 0.18$; (c) $r/T = 0.22$ and (d) $r/T = 0.25$.

Figures 8(a)–(d) show the distributions of $P(f)$ against frequency on the $r/T = 0.33$ plane at the radial positions of $r/T = 0.17$, 0.18, 0.22 and 0.25 respectively. At the radial location closest to the impeller, $r/T = 0.17$ in Figure 8(a), the highest peak is at 216 Hz, corresponding to the blade passage frequency. The smaller peak at 432 Hz represents a harmonic of this frequency. The peak at the dominant frequency is seen to decrease slightly in Figure 8(b) as the radial distance from the impeller increases to $r/T = 0.18$. Further out still at $r/T = 0.22$ (Figure 8(c)), the magnitude of $P(f)$ at the dominant frequency has fallen to 20% of its value in Figure 8(a). At $r/T = 0.25$ in Figure 8(d), no peaks and hence no periodicity in the flow can be distinguished. This indicates that trailing vortices start to decay at around $r/T = 0.22$ and by $r/T = 0.25$ have completely broken down into random turbulence. These results agree with the observations of Mujumdar (1970) who observed that 80–90% of turbulence intensities measured close to the impeller blade were due to the periodic component and that at 0.66 of the tank radius, the periodic component rapidly decayed to a negligible value.

In order to obtain the energy spectrum of the real turbulence, it is necessary to remove the periodic component present in the flow. A number of methods can be used to obtain the real turbulence velocity component, for example, by subtracting the 1° ensemble-averaged mean velocities from the instantaneous velocities, or by estimating the instantaneous mean velocities using a moving-window averaging technique. However, the former method generally does not yield a zero-mean velocity fluctuation due to cycle-to-cycle variations (see, for example, Yianneskis and Whitelaw, 1993), while the latter acts as a high-pass filter and thus information on low-frequency turbulence will be lost. Therefore, a band-stop frequency filtering technique was employed. However, frequency filtering requires equi-spaced data in the velocity time traces. To achieve this, the data was re-sampled with a number of sampling intervals, and the most appropriate one was selected by comparing the normalised energy spectra of the re-sampled traces with those of the raw data.

With equi-spaced data, the energy spectrum $E(f)$ can be obtained through a Fast Fourier Transform (FFT) of the autocorrelation function coefficient $R(\tau)$, which is given by:

$$R(\tau) = \frac{\overline{v_t \, v_{t+\tau}}}{v'^2}$$

where τ is the correlation time.

The solid line in Figure 9 shows the energy spectrum of the re-sampled radial velocity recording made at $r/T = 0.17$ and $z/T = 0.33$, plotted in log-log scale. It can be observed that there is a peak at the blade passing frequency. The periodic component of the velocity trace was removed by band-stop filtering the FFT of the re-sampled velocity trace, and then performing an inverse FFT. The resulting energy spectra is shown by the dotted line. It can be seen that at frequencies below around 800 Hz, $E(f)$ is much higher for the spectrum with the periodic component. This is due to the pseudo-turbulence contribution, mentioned earlier. At frequencies above this, the two spectra, with and without the periodic component, are identical.

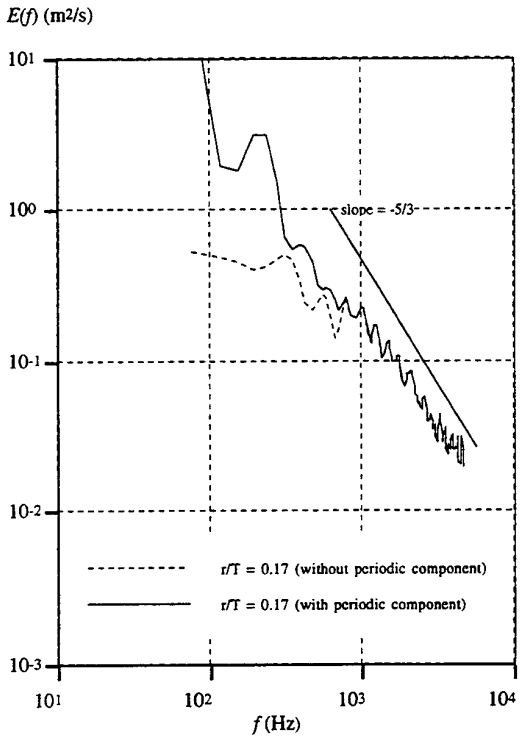

Figure 9. Energy spectra of the radial velocity fluctuations at $r/T = 0.17$, $z/T = 0.33$, with and without the periodic component.

An indication of isotropy can be obtained from Kolmogorov's isotropic turbulence theory: for the inertial subrange, the energy distribution is given by a straight line of slope -5/3. This is shown in Figure 9 on the log-log graph. Figure 10 shows several energy spectra of the radial velocity, all with the periodic component removed with a band-stop filter. A straight line of slope -5/3 representing isotropic turbulence is again shown on the Figure. At $r/T = 0.17$, the spectra do not exhibit a -5/3 slope at frequencies below 1 kHz. At frequencies above this the slope is around -1.4, indicating some anisotropy in this region. Further away from the impeller, at $r/T = 0.27$, there is a fairly good match with the -5/3 slope at frequencies above 1 kHz while at $r/T = 0.35$ the spectra show a -5/3 slope for frequencies above 200 Hz. Therefore the $E(f)$ distributions might be considered to indicate that the flow is becoming more isotropic with increasing distance from the impeller.

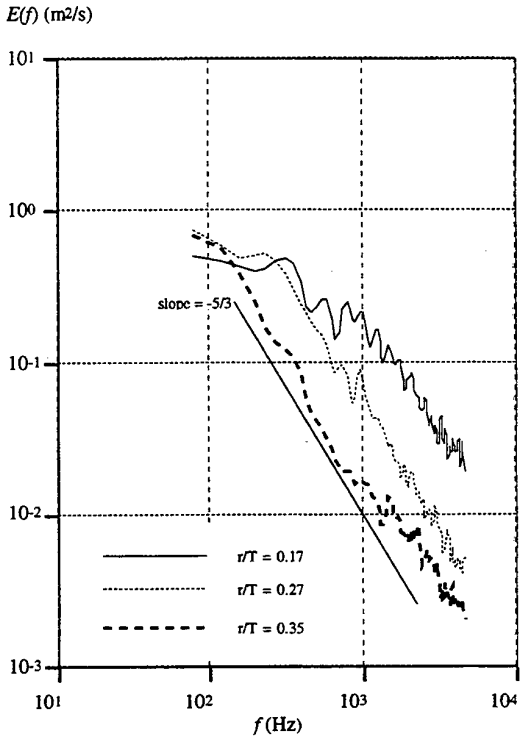

Figure 10. Energy spectra of the radial velocity (with the periodic component removed) at $r/T = 0.17$, 0.27 and 0.35, $z/T = 0.33$.

4. CONCLUDING REMARKS

1° ensemble-averaged LDA measurements were made around a Rushton impeller to determine the mean flow and turbulence characteristics between two successive blades. The turbulent kinetic energy values are highest in the vicinity of the impeller and are associated with the presence of the trailing vortices. Comparison of the three turbulence level

component distributions indicated that the turbulence in this region might be considered anisotropic.

Time-resolved measurements of the radial velocity have indicated strong periodicity in the flow in the impeller region, resulting from the impeller blade passages and the associated trailing vortices. Energy spectra show a distinct peak at the blade passing frequency which decreases in magnitude with distance from the impeller. Energy spectra plotted in log-log scale indicate that the turbulence becomes isotropic further from the impeller.

REFERENCES

Günkel A. A., Weber M. E. 1975, Flow Phenomena in Stirred Tanks, Part I. The Impeller Stream, AIChEJ, vol. 21, No. 5, pp. 931–948.

Mujumdar A. S., Huang B., Wolf D., Weer M. E. & Douglas W. S. M. 1970, Turbulence Parameters in Stirred Tank, Can. J. Chem. Eng., vol. 48, pp. 475 –483.

Popiolek Z., Whitelaw J. H. & Yianneskis M., Unsteady Flow over Disk Turbine Blades, 1984, Proc. 2nd Intern. Symp. of Laser Anemometry in Fluid Mechanics, Lisbon, pp. 17.1.1–17.1.6.

Press W. H., Flannery B. P., Teukolsky S. A., Vetterling W.T. 1992, Numerical Recipes, the Art of Scientific Computing, Cambridge University Press.

Stoots C. M. & Calabrese R. V. 1995, The Mean Velocity Field Relative to a Rushton Turbine Blade, AIChEJ, vol. 41(1), pp. 1–11.

Van der Molen K. & van Maanen H. R. E. 1978, Laser Doppler Measurements of the Turbulent Flow in Stirred Vessels to Establish Scaling Rules, Chem. Eng. Sci., vol. 33, pp. 1161–1168.

Van't Riet K., & Smith J. M. 1973, The Behaviour of Gas - Liquid Mixtures Near Rushton Turbine Blades, Chem. Eng. Sci., vol. 28, pp. 1031–1037.

Van't Riet K., & Smith J. M. 1975, The Trailing Vortex System Produced by Rushton Turbine Agitators, Chem. Eng. Sci., vol. 30, pp. 1093– 1105.

Van't Riet K., & Smith J. M. 1976, Real and Pseudo-Turbulence in the Discharge Stream From a Rushton Turbine, Chem. Eng. Sci., vol. 31, pp. 407– 412.

Yianneskis M., Popiolek Z., & Whitelaw J. H., 1987, An Experimental Study of the Steady and Unsteady Flow Characteristics of Stirred Reactors, J. Fluid Mech., vol. 175, pp. 537–555.

Yianneskis M. & Whitelaw J. H., 1993, On the Structure of the Trailing Vortices Around Rushton Turbine Blades, Trans. I.Chem.E, vol. 71, Part A, September 1993, pp. 543– 550.

Particle Tracking Velocimetry Measurements in a Radial Pump With Particle Pair Detection Using the HOUGH transform

C ROTHLÜBBERS[1], T SCHEFFLER[2], R ORGLMEISTER[1], H SIEKMANN[2]

[1]Institute of Electronics, Sec. EN-3,Technical University Berlin, Germany

[2]Institute of Hydraulic Turbomachinery and Fluid Dynamics, Sec. K2,
Technical University Berlin, Germany

1 Abstract

A new technique based on the HOUGH transform is presented to analyse single frame double exposure particle tracking velocimetry images (PTV). High particle concentrations are possible by this evaluation method. The technique is applied to a single blade pump. Several optical components between measuring plane and camera decrease image quality, so that measurements using particle image velocimetry (PIV) are unsatisfactory. Therefore the PTV technique is used which is independent of particle size.

2 Introduction

The digital particle image velocimetry (DPIV) (Willert, 1991; Adrian, Yao, 1985) and the PTV (Malik et al., 1993; Hassan, Canaan, 1991) are useful methods for measuring the flow velocities in hydraulic turbomachinery. Both digital techniques are useful for measuring velocity fields correlated to a rotating angle of an impeller. The PTV is advantageous compared with DPIV in the case of test facilities, where optical components like a window, a casing and a disk reduce the quality of the imaging process by blurring the image diameter of the particles. In addition, different refraction indices caus images of particles out of focus for one frame (Figure 1). Furthermore, a particle concentration, which is required for DPIV measurements, reduces the signal to noise ratio if the distance between the measurement plane and the window is too big. Additionally the need of measuring velocity fields in an area of approximately 1100 cm^2 implies a high energy laser. On the other hand, quantitative investigations of the behavior of macroscopic particles are only possible with PTV. Single frame double exposure PTV measurements were done with a dual-Nd:YAG-laser and a ccd-camera. Single frame double exposure PTV measurement requires a low particle concentration, which is extremely time consuming for investigations in rotating machinery.

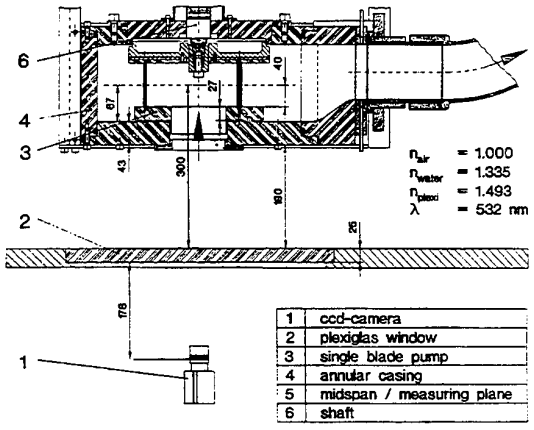

Figure 1: Investigated single blade pump and its related geometry referring to the refraction indices

The necessity of investigations by PTV based on single frame double exposure pictures motivated to search for an evaluation method suitable for particle concentrations as high as possible.

3 HOUGH transform

In general image processing tasks the HOUGH transform is useful for edge detection. The purpose of the present application is the particle pair detection based on single frame double exposure PTV images.

A straight line at a distance d_1 and an orientation α_1 can be represented by

$$d_1 = x \cos\alpha_1 + y \sin\alpha_1 . \qquad (1)$$

As shown in Figure 2, the HOUGH transform of a line in the (x, y) plane is just a point in the (d, α) plane, the so-called HOUGH space.

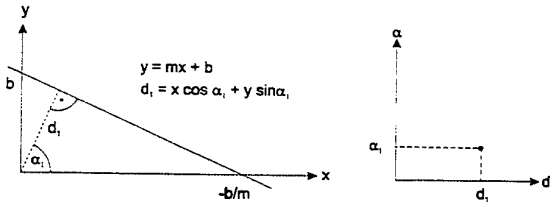

Figure 2: Straight line and the related HOUGH transform

On the other hand, transforming a single point generates a sinusoid in the HOUGH space, as shown in Figure 3. Each point along this sinusoid corresponds to the (d, α) values for a single line passing the original point. So transforming a single point in the real space means transforming all possible straight lines crossing this point.

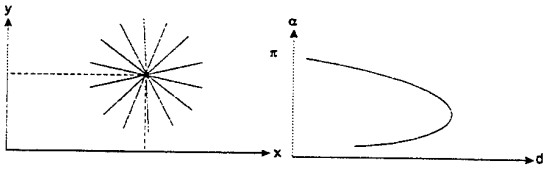

Figure 3: All straight lines crossing a single point and their representations in the HOUGH space

Two single points in the (x, y) plane representing a particle pair in PTV (Figure 4) are transformed into two different sinusoids in the HOUGH space (Figure 5). The intersection of these curves determines the connecting straight line of the two single points in the (x, y) plane.

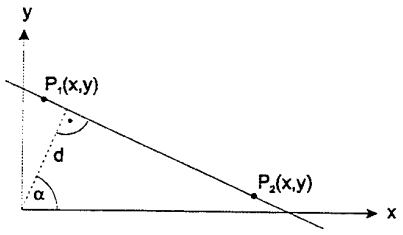

Figure 4: Two points on a straight line

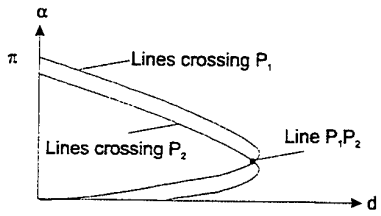

Figure 5: Identification of the connecting line in Figure 4 due to an intersection in the HOUGH space

Velocity field analysis based on real PTV measurements requires a particle concentration as high as possible which effects in ambiguous particle pair detection. Figure 6 shows an example.

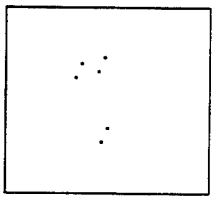

Figure 6: Ambiguous particle distribution

Figure 7 shows the corresponding HOUGH space.

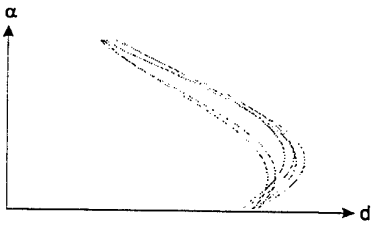

Figure 7: HOUGH space of Figure 6

As shown before, each intersection between two sinusoids represents a straight line connecting two

particles. Using the nearest neighbour method to connect particle pairs must fail because of the mentioned ambiguity. Obviously, the presence of a main displacement direction is known to a human observer, so that a manual connection would be a simple task. The main displacement direction corresponds to the angles α_{Di} (Figure 8).

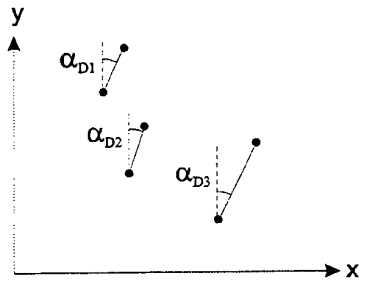

Figure 8: Different particle-pair angles α_{Di}

In the HOUGH space, the main displacement direction corresponds to a maximum of intersections referring to an angle α_D. Because the real displacement vectors do not match exactly, the counting of intersections according to an angle α has to be extended to a region $\alpha_D \pm \beta$ (Figure 9).

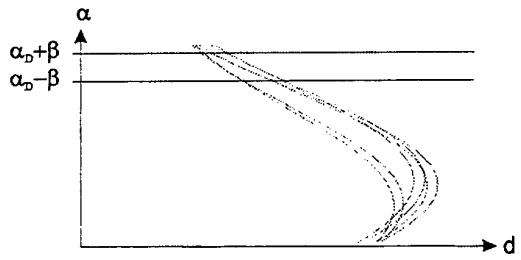

Figure 9: Search area $\alpha_D \pm \beta$ in the HOUGH space

The angle of a potential connection of two particles in the (x, y) plane is proved by the extended displacement direction $\alpha_D \pm \beta$.

In summary, the analysis of the HOUGH space uses only the information of the angle $\alpha_D \pm \beta$. Evaluations using the HOUGH transform were performed on computed test images of randomly distributed particle pairs as shown in Figures 10 to 15.

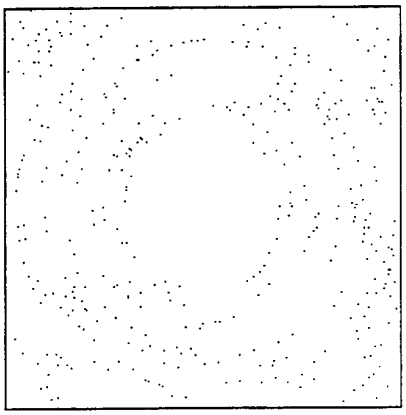

Figure 10: Circle distribution

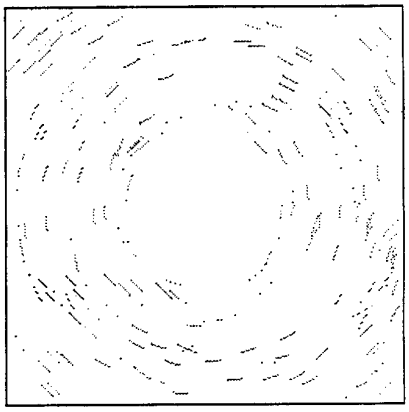

Figure 11: Detection result of circle distribution

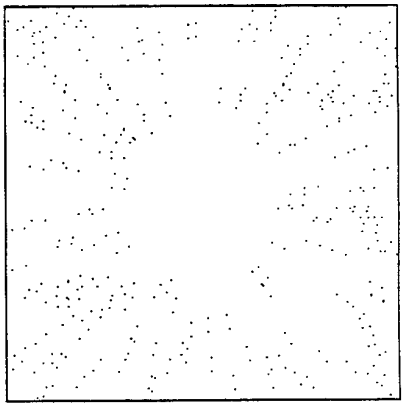

Figure 12: Star distribution

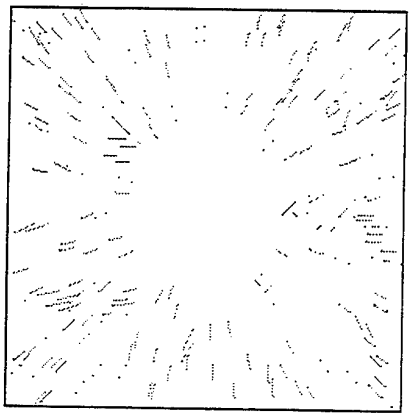

Figure 13: Detection result of star distribution

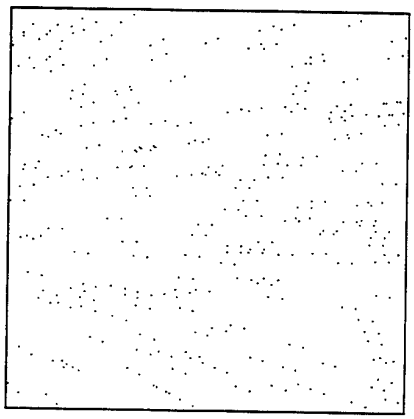

Figure 14: Fan-shape distribution

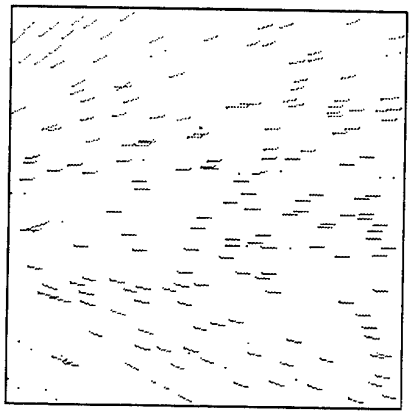

Figure 15: Detection result of fan-shape distribution

These examples show the possibilities of the HOUGH transform for particle pair detection.

4 Experimental Setup

Figure 16 shows the test facilities for the measurements of the velocity fields in the investigated radial single blade pump (Pos. 1) with PTV. The single blade pump is characterised by the following parameters:

Capacity	145 m^3/h
Head	8 m
Nominal speed of rotation:	1450 min^{-1}
Specific speed	51 min^{-1}
Diameter of annular casing	380 mm
Single blade diameter	240 mm
Pipe diameter	DN 100
Drive: 10 kW, closed loop	

Casing and single blade are made of plexiglas, the test basin (Pos. 2) has windows (Pos. 3) for optical access. During the PTV measurements the test basin has to carry out light dense.

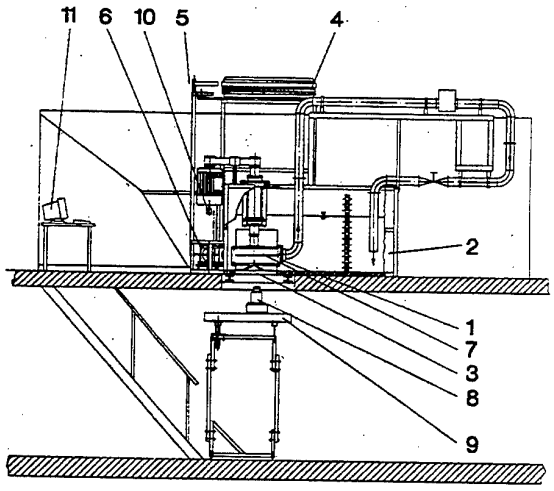

Figure 16: Test facilites

The light source for the measurements is a 15 Hz dual-Nd-YAG-laser (Pos. 4) with a puls energy of 200 mJ each. The laser beam is set with mirrors (Pos. 5) to the light sheet optics (Pos. 6), which is implemented with cylindrical lenses. The light sheet is positioned in the midspan of the pump (Pos. 7). The midspan of the pump is shown in Figure 17. A ccd-camera (Pos. 8) with a resolution of 1024 x 1024 pixels is positioned under the pump on a x-y-traverse (Pos. 9) for scanning the velocity field. For adjustment of the ccd-camera to the pump markers are adapted to the casing. The velocity fields have to be correlated to the rotating angle and the revolution

of the impeller. Therefore, an incremental encoder (Pos. 10) is adapted to the drive. A personal computer controls the dual-Nd:YAG-laser, the ccd-camera and realises the measurement of the rotating angle by a plug-in timer board. Due to measurements correlated to the rotating angle a huge amount of data has to be stored and evaluated. For that reason, the computer is linked to a Pentium based MIMD parallel computer via the local network of the Technical University of Berlin. To get a single frame double exposure PTV picture, the dual-Nd:YAG-laser operates continously and the ccd-camera is synchronized by an external trigger asynchronously. Due to a delay of 12 ms between the external trigger and the opening of the shutter of the ccd-camera, the external trigger is set between two pulse pairs of the laser. The shutter opens for a period of 10 ms. The first pulse of the laser starts counting the increment signals up to the reference signal of the encoder.

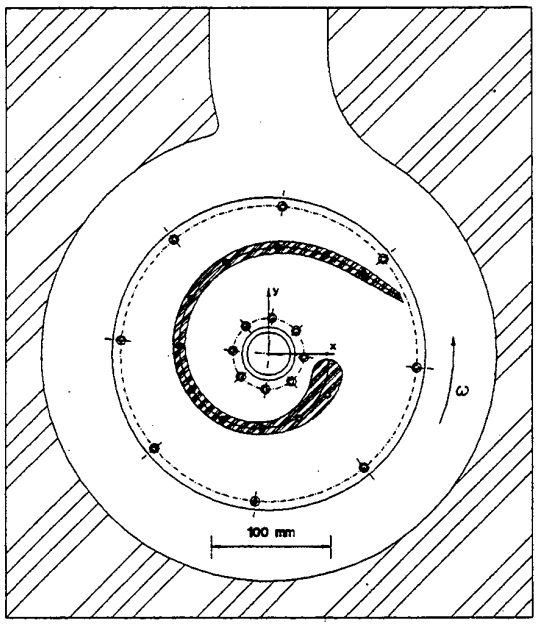

Figure 17: Midspan of the investigated single blade pump

5 Evaluation method

Figure 18 depicts the sheme of the evalution of PTV images using the HOUGH transfom. Under the condition that data only consists of particle information, images of the measurement area are taken before particles are given into the fluid. These images are used to eliminate the contours of the impeller. Therefore the superposition of all images, preprocessed with morphological operations (Jain, 1989) to connect the whole contour, is used as a look-up table. In the region of the impeller particle identification is inhibited. On the other hand, the calculation of the magnification factor is done by these images. The use of the HOUGH transfom includes the need to reduce the particle images to one pixel. Therefore the PTV images are converted to a binarized pixel based image.

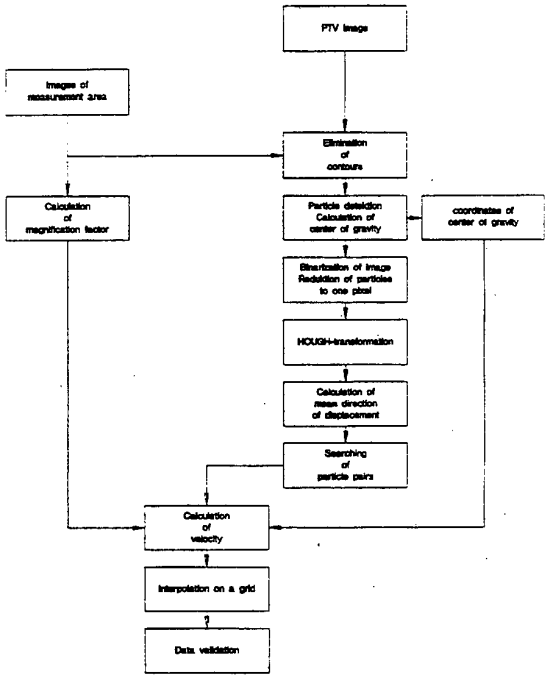

Figure 18: Evaluation method

To improve the accuracy of the calculated velocities, the coordinates of gravity are stored for further calculations. The next step in the evaluation is the HOUGH transform and computation of the main direction of displacement. A parameter which limits the maximum displacement of particles is needed during the search of particle pairs. The results of pair detection are combined with the real particle coordinates and the magnification factor to calculate the velocities. Due to post processing, the randomly distributed vectors have to be interpolated to a grid. Then different images are superimposed to increase the number of detected velocity vectors in the investigated area. The validation of data based on a local mean operator (Raffel et al., 1992) analyses each velocity vector in its nearest neighbourhood to reject incorrect vectors.

6 Results

Figure 19 and Figure 20 show the absolute flow field and the relative flow field nearby the outled edge of the single blade. The origin of the coordinate system is located in the shaft of the pump and the graph shows the part marked in Figure 17.

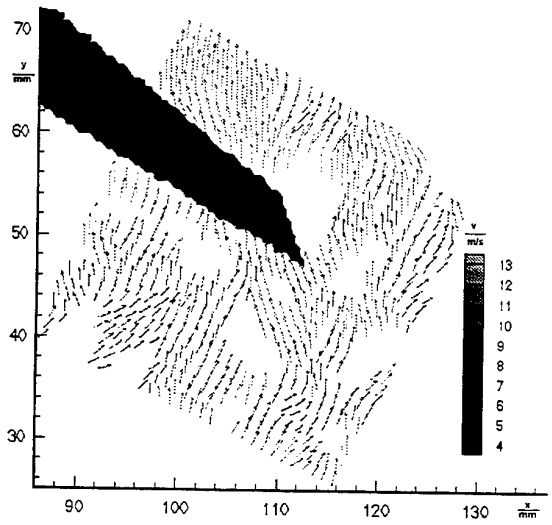

Figure 19: Absolute flow field nearby the outled edge of the single blade

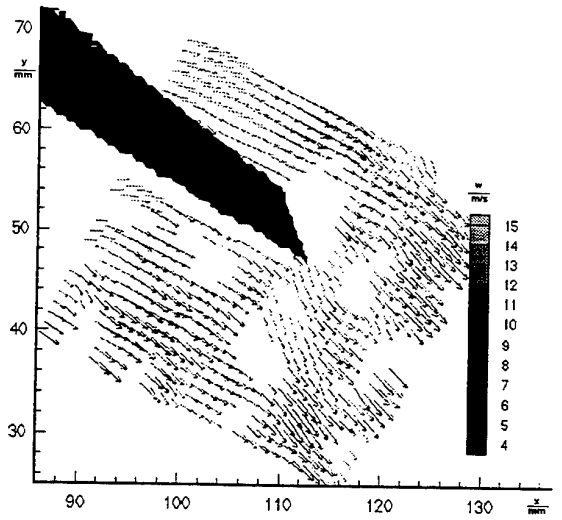

Figure 20: Relative flow field nearby the outled edge of the single blade

Both graphs show the ability of measuring in rotating machinery using the HOUGH transfom instead of conventional methods e.g. laser DOPPLER velocimetry and correlation techniques as the particle image velocimetry. Due to the fact of a high particle concentration referring to PTV only a few measurements are needed.

7 Conclusions

A new PTV technique has been discussed. Advantages are the ability of operating with a high particle concentration using the same equipment employed by standard PIV measurements. Basic investigations on computed particle distributions using the HOUGH transform show respectable results. Also the extension to measurements in a single blade pump has been satisfactory. To inprove image quality, particle detection and post-processing, further investigations have to be done.

Literature

[1] Willert, C. E., Gharib, M. 1991, Digital particle image velocimetry, Experiments in Fluids, No.10.

[2] Adrian, R. J., Yao, C. S. January 1985, Pulsed Laser Technique Application to Liquid and Gaseous Flows and the Scattering Power of Seed Materials, Applied Optics, vol. 24, No.1.

[3] Malik N. A., Dracos Th., Papantoniou D. A. 1993, Particle tracking velocimetry in three-dimensionnal flows, part 2. particle tracking, Experiments in Fluids No. 15, pp. 279-294.

[4] Hassan, Y. A., Canaan, R. E 1991, Full-field bubbly flow velocity measurements using a multiframe particle tracking technique, Experiments in Fluids, No. 12, pp. 49-60.

[5] Hough, P.V.C. 1962, Method and Means for Recognizing Complex Patterns, U.S. Patent 3069654.

[6] Duda, R. O. & Hart, P.E. 1973, Pattern Classification and Scene Analysis, Wiley and Sons, New York.

[7] Jain, A. K. 1989, Fundamentals of Digital Image Processing, Prentice-Hall, New Jersey.

[8] Raffel, M., Leitl, B., Kompenhans, J., 1992, Data Validation for Particle Image Velocimetry, Proc. 6th Int. Symposium Applications of Laser Techniques to Fluid Mechanics.

SESSION 9

Two-Phase Flows
Instrumentation III

A SINGLE-BEAM VELOCIMETER BASED ON RAINBOW-INTERFEROMETRY

J.P.A.J. van Beeck and M.L. Riethmuller

von Karman Institute for Fluid Dynamics, Chaussée de Waterloo 72,
B-1640 Rhode-Saint-Genèse Belgium
Fax: +32 2 3582885 E-mail: vanbeeck@vki.ac.be

ABSTRACT

A velocimeter which consists of one laser beam and one photomultiplier is proposed. The instrument is based on the monochromatic rainbow interference-pattern created by a transparent particle illuminated by a laser beam; this rainbow moves in front of a photomultiplier when the particle traverses the laser beam. Frequency analysis of the recorded signal leads to the droplet size and to one component of the velocity vector. Validation experiments have been carried out using a spherical glass bead. To improve the measurements with water droplets, a nonsphericity detection is proposed by adding another photomultiplier.

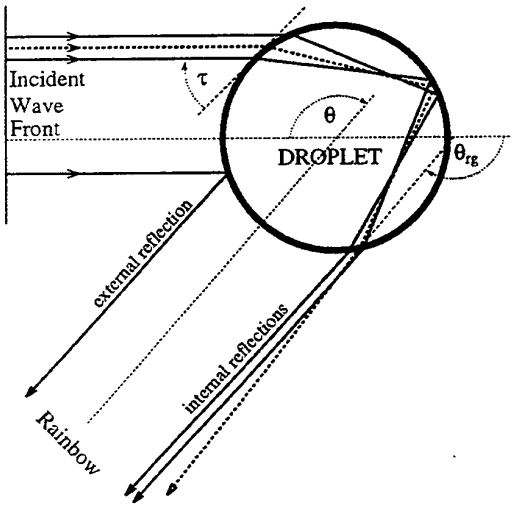

Fig. 1: The dominant geometrical rays that form the first-order rainbow.

1. INTRODUCTION

In 1988, the rainbow was introduced as a non-intrusive measurement technique to determine the refractive index, i.e. the temperature, of droplets. The initiators N. Roth, K. Anders and A. Frohn (1990, 1991) directly applied the technique to droplet combustion. Shortly after, Sankar et a. (1993, 1994) integrated the rainbow technique with the Phase Doppler technique in order to determine simultaneously the droplet size, velocity and temperature.

The rainbow that is used for the technique is created by a single droplet scattering laser light. The technique is based on the first-order rainbow which can be explained geometrically by once-internally reflected rays for which the scattering angle θ goes through an extremum with respect to the incidence angle τ; this yields the characteristic high intensity of the rainbow near the extremum which is called the geometrical rainbow angle θ_{rg} (see figure 1). From figure 1 one can understand that this high intensity pattern consists of fringes because for scattering angles larger than θ_{rg} there exist two parallel rays that interfere at infinity; from the resulting so-called Airy fringes the droplet size can be deduced (J.P.A.J. van Beeck and M.L. Riethmuller (1995)). Moreover, externally-reflected rays interfere with internally-reflected rays to form a ripple structure superimposed on the Airy fringes. Frequency analysis of both the ripple structure and the Airy fringes indicates the degree of nonsphericity of the scattering particle (J.P.A.J. van Beeck and M.L. Riethmuller (1996)); this is necessary to know as the droplet temperature and diameter derived from the rainbow highly depend on the nonsphericity.

In the present paper another application of the rainbow as a measurement device is proposed, i.e. the measurement of one component of the velocity vector of a moving droplet. This application is also based on frequency analysis of the Airy fringes and the ripple structure. Therefore, the detection of the droplet nonsphericity has to be carried in an alternative manner.

2. DETECTION OF THE MONOCHROMATIC RAINBOW WITH A PHOTOMULTIPLIER

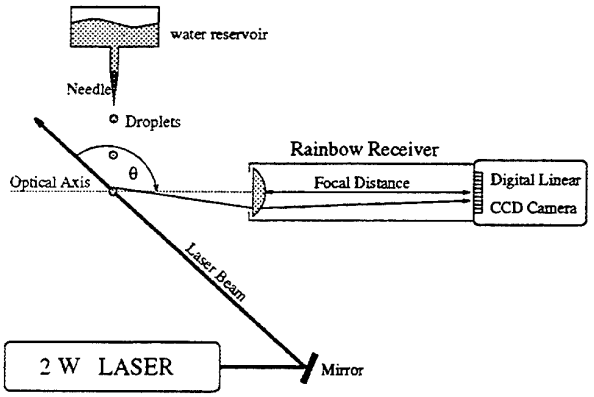

Fig. 2: Sketch of the setup to detect the rainbow pattern with a linear CCD-camera.

The conventional way to detect a rainbow interference-pattern coming from a single droplet is to use a linear CCD-camera placed at focal distance of a positive lens (figure 2). Each pixel of the linear CCD-array corresponds to a certain scattering angle. This means that the position of the rainbow pattern on the array is independent of the position of the droplet in the laser beam.

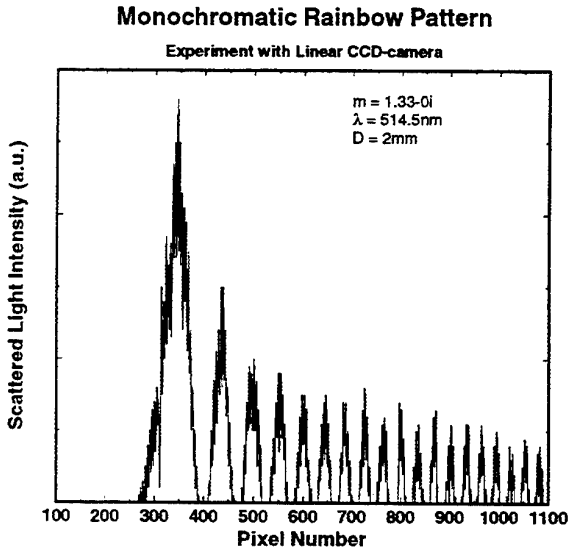

Fig. 3: Typical rainbow signal recorded with a linear CCD-camera. The low-frequency pattern resembles the Airy fringes on top of which a ripple structure is superimposed. The light-scattering droplet measured about $2\,mm$.

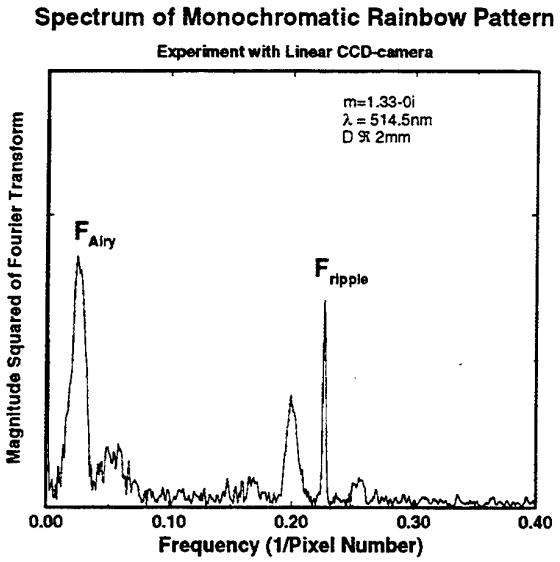

Fig. 4: Spectrum of the rainbow pattern in figure 3.

Figure 3 shows a typical rainbow signal recorded with the CCD-camera. Figure 4 depicts the spectrum. The indicated peak F_{Airy} originates from the low frequency interference pattern, i.e. the Airy fringes. F_{ripple} corresponds to the ripple structure. Both F_{Airy} and F_{ripple} yield a droplet diameter; if F_{Airy} equals F_{ripple} then the droplet is spherical. Only then a reliable temperature can be determined from the angular position of the main rainbow maximum. The detailed procedure has been described by Van Beeck and Riethmuller (1996).

Because of the limited sensibility of the CCD-camera to the scattered-light intensity, it was decided to study the possibility of using a photomultiplier for the detection of the rainbow signal. When a single falling droplet is concerned, a pin-hole in combination with a photomultiplier is sufficient to constitute a rainbow receiver (see figure 5). The idea is that the fringes in the rainbow pattern move in front of the pin-hole when the droplet traverses the laser beam. If the pin-hole is much smaller than the smallest fringe spacing then a rainbow pattern in time can be detected. The actual amount of fringes traversing the pin-hole depends on the diameter D of the light-scattering particle, the diameter ω of the laser beam and on the distance l between the pin-hole and the particle.

A simulation of the photomultiplier signal, made with the help of the Generalized Lorenz-Mie theory (G. Gouesbet et a. (1988)), shows how the rainbow pattern is modulated with the Gaussian intensity profile of the laser beam (figure 6). The simulation was carried out with the following parameters: $D = 1\,mm$,

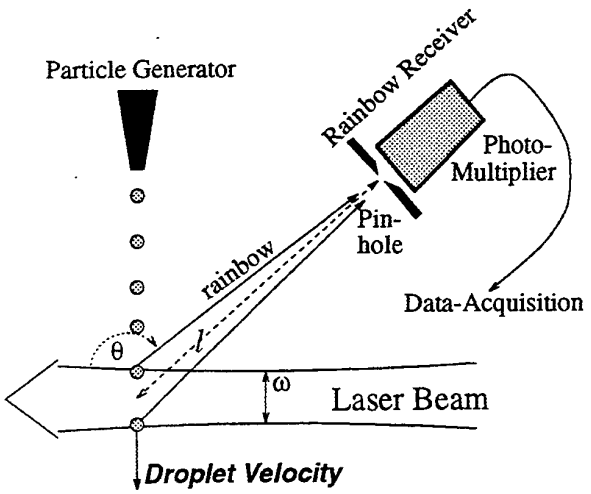

Fig. 5: Outline of the setup, containing a photomultiplier, to detect the rainbow pattern coming from a single scattering transparent particle. ω is the diameter of the laser beam and l is the distance between the pin hole and the particle in the center of the beam.

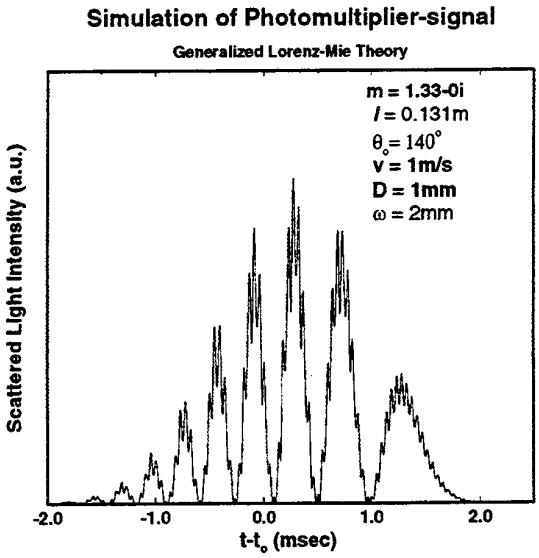

Fig. 6: A simulation of a photomultiplier signal concerning the setup of figure 5. θ_o is the scattering that corresponds to the time t_o at which the droplet is positioned at the center of the laser beam. ($D = 1\,mm$, $\omega = 2\,mm$, $l = 0.131\,m$, the wave length of the laser light $\lambda = 514.5\,nm$, the refractive index $m = 1.33 - 0i$ and the droplet velocity $v = 1\,m/s$.)

$\omega = 2\,mm$, $l = 0.131\,m$, a wave length of the laser light $\lambda = 514.5nm$, a refractive index $m = 1.33 - 0i$ and a velocity $v = 1\,m/s$. Figure 7 shows both the spectrum and the spectrum of the derivative of the rainbow pattern. Similar peaks as in figure 4 can be identified. However, the difference is that the spectrum of figure 7 not only depends on the droplet diameter (and weakly upon the refractive index) but also on the droplet velocity. This implies that the detection of the rainbow pattern with the photomultiplier-setup (figure 5) leads to the possibility to determine the droplet velocity from this setup. This will be explained in the following section.

The main difference between the spectrum and the spectrum of the derivative is that in the latter the peak at $0\,kHz$ has disappeared which makes the Airy frequency F_{Airy} easier to identify. It is important to recognize that the positions of the peaks in both spectra are exactly similar.

3. DETERMINATION OF THE DROPLET VELOCITY FROM THE RAINBOW PATTERN

As suggested in the previous section, the photomultiplier-setup of figure 5 can be used to determine the velocity of a moving light-scattering particle. The signal recorded with the photomultiplier reveals clearly the Airy fringes (with the angular Airy frequency F_{Airy}) and the ripple structure (with ripple frequency F_{ripple}) which are so characteristic for the rainbow (figure 6). Both interference structures depend on diameter and velocity. Therefore, the droplet diameter has to be known a priori. In order to determine the droplet size, the ratio F_{ripple}/F_{Airy} can be used because it only depends on this parameter. When applying the Airy theory close to the main rainbow maximum, the following expressions for this ratio can be found (van Beeck and Riethmuller (1996)):

$$F_{ripple}/F_{Airy} = 1.089\,(\frac{D}{\lambda})^{\frac{1}{3}} + \frac{1}{2} \quad \text{for m=1.333-0i,} \qquad (1)$$

$$F_{ripple}/F_{Airy} = 0.6112\,(\frac{D}{\lambda})^{\frac{1}{3}} + \frac{1}{2} \quad \text{for m=1.517-0i.} \qquad (2)$$

Knowing the diameter, the velocity can be obtained from either the Airy frequency (in Hz):

$$v = l \cdot F_{Airy} \cdot 1.777(\frac{D}{\lambda})^{-\frac{2}{3}} \quad \text{for m=1.333-0i,} \qquad (3)$$

$$v = l \cdot F_{Airy} \cdot 1.304(\frac{D}{\lambda})^{-\frac{2}{3}} \quad \text{for m=1.517-0i,} \qquad (4)$$

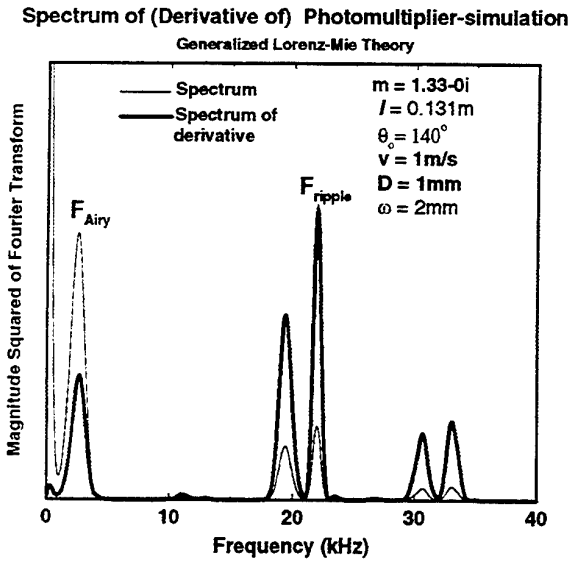

Fig. 7: Spectrum and spectrum of the derivative of the rainbow pattern in figure 6.

or the ripple frequency (also expressed in Hz):

$$v = l \cdot F_{ripple} \cdot \frac{1}{0.613(\frac{D}{\lambda}) + 0.281(\frac{D}{\lambda})^{\frac{2}{3}}} \quad \text{for m=1.333-0i,} \qquad (5)$$

$$v = l \cdot F_{ripple} \cdot \frac{1}{0.469(\frac{D}{\lambda}) + 0.383(\frac{D}{\lambda})^{\frac{2}{3}}} \quad \text{for m=1.517-0i,} \qquad (6)$$

where l is the distance between the pin-hole and the location in the laser beam where the droplet passes. As the Airy theory is used, the validity of above expressions is limited to droplet diameters larger than $100\,\mu m$ (Van Beeck and Riethmuller (1994)); if measurements in the micrometer range are desired, the set of equations should be based on the Lorenz-Mie theory.

Finally, it is important to realize that the component of the velocity vector, which is measured, lays in the scattering plane and is perpendicular to the optical axis of the rainbow receiver. Therefore, it is not the laser beam but the optical axis of the rainbow receiver that has to be perpendicular to the velocity component that one studies.

4. EXPERIMENTAL RESULTS AND DISCUSSION

The rainbow technique, used as velocimeter, was compared to the conventional laser Doppler technique. The setup is depicted in figure 8. It contains two crossing He-Ne-laser beams. The Doppler signal is created

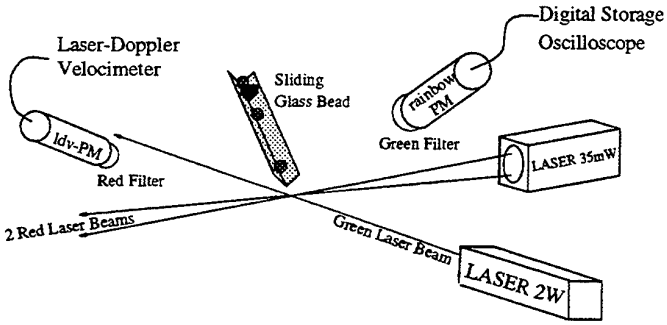

Fig. 8: Schematic of the optical system that served to validate the rainbow technique concerning the velocity measurement.

when a particle passes the cross-over region (i.e. the probe volume); the signal is detected by the photomultiplier "ldv-PM" which is placed after a red filter. Frequency analysis yields the particle velocity, v_{ldv}, which denotes the vertical component of the velocity vector.

An expanded green laser beam ($\pm 10\,mm$) crosses the probe volume and is perpendicular to both red laser beams. It generates a rainbow pattern that moves in front of the photomultiplier "rainbow-PM" which is mounted at the geometrical rainbow angle. A green optical filter prevents the Doppler-signal from reaching the photomultiplier. The rainbow signal is recorded by a digital storage oscilloscope that is connected to a personal computer. As explained in the previous section, the rainbow pattern in time provides the droplet size D and the velocity component, $v_{rainbow}$, perpendicular to the optical axis of the rainbow photomultiplier.

Validation of the rainbow-technique has been performed with a spherical glass bead (D=5.9 mm, m=1.517-0i). The bead was sliding down in an inclined tube having a squared cross-section; the position of the tube could be adjusted in the horizontal plane. The inclination was such that the velocity vector of the bead while passing the probe volume was perpendicular to the optical axis of the "rainbow-PM" and was laying in the scattering plane of this photomultiplier. Therefore, the velocity measured with the rainbow technique, $v_{rainbow}$, equals the absolute value of the velocity vector. A removable catch inside the tube made the bead velocity to be repetitive.

Figure 9 shows an experimental signal detected by the photomultiplier. The pin-hole had a circular aperture of $50\,\mu m$ and was positioned at a distance of $0.83\,m$ from the probe volume. The Airy fringes are clearly visible and on some of them the ripple structure can be observed. The spectrum (figure 10) has

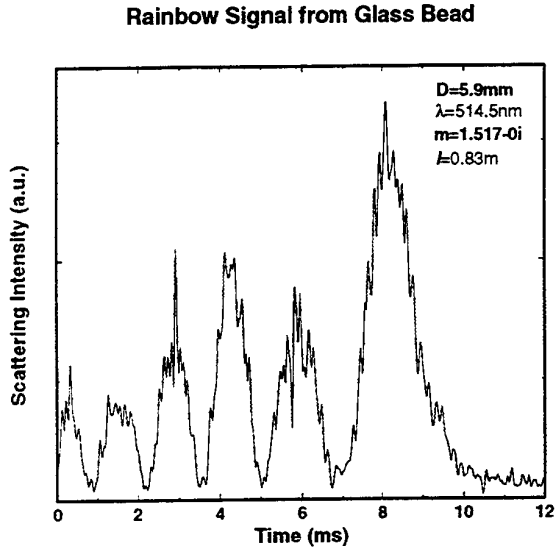

Fig. 9: Experimental rainbow signal obtained with the rainbow receiver ("rainbow-PM"). The scattering particle was a glass bead.

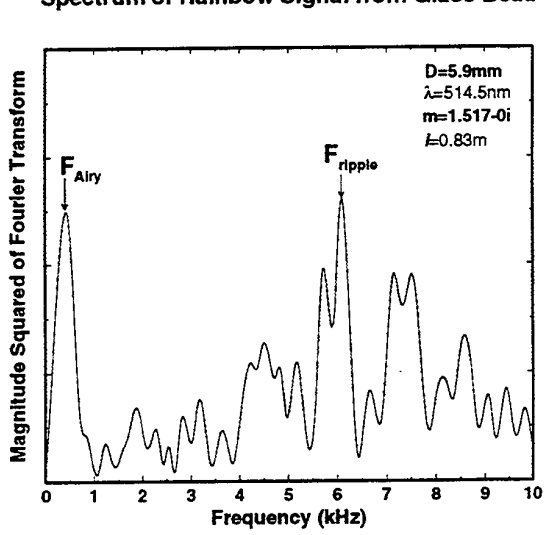

Fig. 10: Spectrum of the derivative of the rainbow pattern of figure 9.

been taken from the derivative of the rainbow pattern to better resolve the Airy frequency F_{Airy} (see section 2). The ratio F_{ripple}/F_{Airy} gives a diameter of $6.2 \pm 0.5mm$ according to equation 2. This compares rather well to the geometrically measured value of $5.9 \pm 0.1\,mm$. Relationship 4 yields the rainbow velocity based on the Airy frequency: $v_{rainbow} = 0.89 \pm 0.02\,m/s$. In order to obtain the vertical component, $v_{rainbow}$ has to be multiplied with $\cos 22°$, i.e. the angle between the velocity vector and the vertical; this results in a velocity of $0.82 \pm 0.05 m/s$. If relationship 6 is used then the rainbow measurement is based on the ripple structure and yields a vertical velocity component of $0.85 \pm 0.02 m/s$. With the laser-Doppler velocimeter a velocity of $v_{ldv} = 0.85 \pm 0.01 m/s$ was measured which agrees perfectly with value obtained with equation 6.

While performing measurements with the rainbow technique it is important to recognize that the laser beam has to be as collimated as possible. For the present setup, a beam divergence of $1\,mrad$ would already have resulted in a velocity bias of $-6\,\%$. Furthermore, from figure 1 one understands that the diameter of the laser beam has to be larger than the droplet size in order to create the entire rainbow structure. Yet, looking to figures 9 and 10, it is clear that it is not easy to detect the ripple structure because of the rather high level of noise. Therefore, a proper detection of the rainbow requires a high signal to noise ratio. This ratio is determined by the photomultiplier-voltage, the laser power, the size of the droplet, the size of the pin hole and the distance l between droplet and probe volume. A clear ripple structure is necessary, not only in order to obtain the droplet diameter but also because the uncertainty in the determination of the ripple frequency is smaller than the uncertainty in the Airy frequency (see e.g. the spectrum in figure 10). This is why the rainbow velocity derived from equation 6 was more accurate than the rainbow velocity based on the Airy frequency.

5. NONSPHERICITY DETECTION OF DROPLETS WITH PHOTOMULTIPLIER-SETUP

Figure 11 shows a rainbow signal detected with the setup depicted in figure 8. The scattering particle was a single falling water droplet of about $6\,mm$ in diameter and having a velocity of $v_{ldv} = 2.6\,m/s$ while passing the probe volume. The ratio F_{ripple}/F_{Airy} results in a droplet diameter of only $D = 356\,\mu m$. If with this erroneous diameter the velocity is calculated, then equation 3 would yield $v = 44 \pm 3\,m/s$ and equation 5 $v = 42 \pm 1\,m/s$. A large free falling droplet at about $37\,cm$ from the needle-exit is oscillating, thus only temporarily sufficient spherical to obtain reliable physical quantities from the technique rainbow (Van Beeck & Riethmuller (1995)). The nonsphericity detection method using the CCD-camera compares the diameter from the Airy frequency with the diameter obtained from the ripple frequency (section 2). For the photomultiplier-setup of figure 5 this method can not

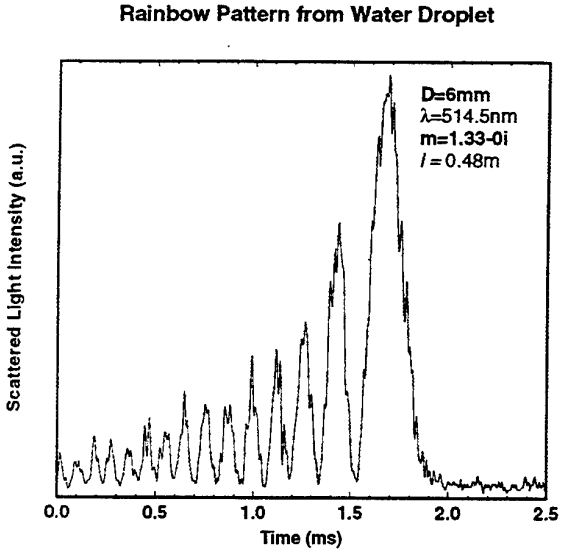

Fig. 11: Rainbow pattern coming from a single falling water droplet.

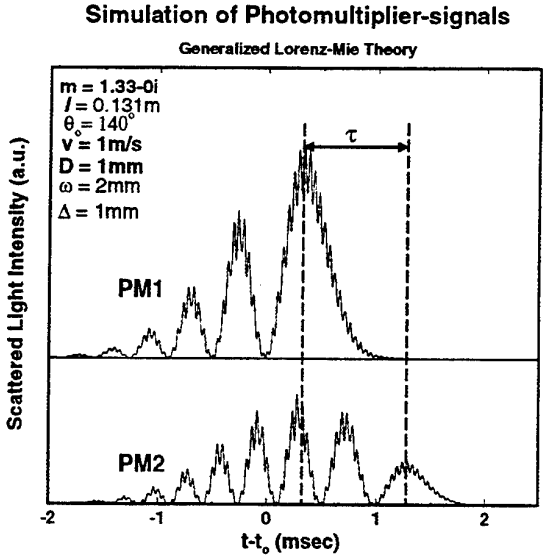

Fig. 13: Simulation of the photomultiplier-signals in the setup of figure 12 using the generalized Lorenz-Mie theory (Gouesbet et a. (1988)).

be applied as only one diameter is obtained from the ratio of both frequencies F_{ripple} and F_{Airy}. Therefore a modification of the setup is presented in figure 12.

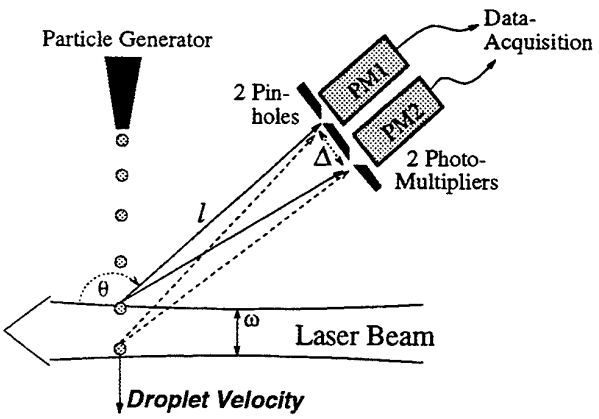

Fig. 12: Modification of the photomultiplier-setup of figure 5 in order to detect the nonsphericity of the scattering particle.

It consists of two photomultipliers instead of one, separated by a distance $\Delta = 1\,mm$. Figure 13 shows a simulation of the signals as recorded by the two photomultipliers PM1 and PM2; the set of parameters is the same as the simulation of figure 6. Both photomultipliers are placed such that they observe the main rainbow maximum and several supernumerary Airy fringes. Due to the distance Δ, the rainbows are shifted by a time τ and are modulated in a different way by the Gaussian laser beam intensity profile. The velocity can directly be deduced from τ and Δ:

$$v = \frac{\Delta}{\tau} \,. \tag{7}$$

Then one diameter D_{Airy} can be found based on the Airy and another D_{ripple} based on the ripple frequency applying respectively equation 3 and equation 5. When the diameters mismatch, the droplet is nonspherical. This method to detect the droplet nonsphericity can be applied to the signal in figure 11 using the velocity obtained by the laser Doppler velocimeter, $v_{ldv} = 2.6\,m/s$. It results in $D_{Airy} = 25\,mm$ and $D_{ripple} = 8\,mm$. Subsequently, the droplet was nonspherical. It is very interesting to notice that, unlike the diameter, the droplet velocity obtained from equation 7 is probably independent of the droplet nonsphericity as the velocity is not derived from the Airy theory which is only valid for spherical particles. This statement deserves certainly further study because it would mean that with the photomultiplier-setup of figure 12 also reliable velocity measurements can be made in a medium with only nonspherical scatterers.

6. CONCLUSIONS

A velocimeter based on rainbow-interferometry has been proposed. The instrument can be used to measure simultaneously the velocity and the size of droplets. The detection of the rainbow is performed by a photomultiplier. The validation of the instrument has been demonstrated for spherical glass particles by comparing it with the performance of the established laser Doppler velocimeter. The detection of the nonsphericity of water droplets was proved to be necessary in order to obtain reliable quantities from the rainbow technique. A promising method to select spherical droplets has been proposed making use of an additional photomultiplier.

ACKNOWLEDGEMENTS

The authors are grateful to J-Ph. Pages for his contributions to the experiments presented in this paper.

REFERENCES

Roth, N., Anders, K. & Frohn, A. 1990,
Simultaneous Measurement of Temperature and Size of Droplets in the Micrometer Range,
Journal of Laser Applications, vol. 2, number 1.

Roth, N., Anders, K. & Frohn, A. 1991,
Refractive-index Measurements for the Correction of Particle Sizing Methods,
Appl. Opt., vol. 30, pp. 4960-4965.

Sankar, S.V., Ibrahim, K.H., Buermann, D.H., Fidrich, M.J. & Bachalo, W.D. 1993,
An Integrated Phase Doppler/Rainbow Refractometer System for Simultaneous Measurement of Droplet Size, Velocity, and Refractive Index,
Proc. of The Third International Congress On Particle Sizing, Yokohama, Japan.

Sankar, S.V., Buermann, D.H. & Bachalo, W.D. 1994,
Simultaneous Measurements of Droplet Size, Velocity, and Temperature in a Swirl-Stabilized Spray Flame,
Seventh International Symposium on Applications of Laser Techniques to Fluid Mechanics, Lisbon, Portugal.

van Beeck, J.P.A.J. & Riethmuller, M.L. 1995,
Non-intrusive Measurements of Temperature and Size of Raindrops, Applied Optics, vol. 34, number 10, pp. 1633-1639.

van Beeck, J.P.A.J. & Riethmuller, M.L. 1996,
Rainbow Phenomena applied to the Measurement of Droplet Size and Velocity
and to the Detection of Nonsphericity,
Accepted for publication in Applied Optics.

Gouesbet, G., Maheu, B. & Gréhan, G. 1988,
Light Scattering from a Sphere Arbitrarily Located in a Gaussian Beam using a Bromwich Formulation,
J. Opt. Soc. Am. A, vol. 5, number 9, pp. 1427-1443.

van Beeck, J.P.A.J. & Riethmuller, M.L. 1994,
Simultaneous Determination of Temperature and Size of Droplets from the Rainbow using Airy Theory,
Seventh International Symposium on Applications of Laser Techniques to Fluid Mechanics, Lisbon, Portugal.

SIZE INSENSITIVE RAINBOW REFRACTOMETRY: THEORETICAL ASPECTS

N. Roth, K. Anders, A. Frohn

ITLR Institut für Thermodynamik der Luft- und Raumfahrt
Universität Stuttgart
Pfaffenwaldring 31, D-70550 Stuttgart, Germany

ABSTRACT

The evaluation of the intensity distribution of light scattered by droplets in the region of the rainbow gives information on size and refractive index of the droplets. Three different evaluating techniques for obtaining the refractive index are compared with each other. All three techniques give an angle characterizing the angular position of the rainbow, which is related to the refractive index of the droplet. The first technique uses the maximum value of the intensity distribution as rainbow position. The second technique uses the maximum value of a filtered intensity distribution. For this purpose the original intensity distribution is filtered with a digital low pass filter in order to obtain intensity distributions without ripple structure. The third technique, which is new, assumes a maximum of the derivative of the filtered intensity distribution as rainbow position. The position of this maximum is the position of the point of inflection in the increase of the filtered intensity distribution up to the main maximum of the rainbow. In the comparison it was found that the third new technique is insensitive to droplet size in a wide range of droplet diameters, whereas in both other techniques the droplet size has to be taken into account for determining the refractive index. With this new techniques a rainbow position is obtained, which is very close to the rainbow position according to the theory of Descartes, which uses ray optics to determine the rainbow position and which is size independent.

1 INTRODUCTION

Rainbow refractometry is an optical and therefore non-intrusive measuring technique to determine the refractive index of droplets as presented by Roth et a. (1988) and further developed by Roth et a. (1991, 1992, 1994) and Anders et a. (1993, 1995). This techniques has been adopted by several other groups as for instance by Sankar et a. (1993), van Beek and Riethmüller (1994), Massoli et a. (1993), Kai et a. (1993), Schombacher and Bauckhage (1996). A rainbow may be observed in the backward hemisphere of the scattered light if for instance raindrops are illuminated by sunlight. The rainbow observed is multicolored and is produced by many drops. If a single droplet is considered rainbow phenomena can be detected in the angular intensity distribution of the scattered light. The scattering angle θ_R at which these phenomena are observed is measured relative to the forward direction of the incident light. As this angle depends on the color or the wavelength of the light the white sunlight is splitted into the colors of the rainbow. For large droplets in the range of millimeters like raindrops the intensity maxima observed as rainbow phenomena are rather sharp and their angular position is practically independent of droplet size. Therefore a well defined rainbow can be observed in nature, despite the rainbow is produced by many raindrops of different size. A theory by Descartes predicts the angular position θ_R of the rainbow without taking the droplet size into account. In this theory the position of the rainbow depends only on the refractive index of the droplet. The refractive index depends on the properties of the droplet material and on the wavelength of the light. If the light is monochromatic the refractive index can be determined by measuring the angular position of the rainbow according to Descartes' theory. This theory holds only for very large droplets. In technical systems, however, much smaller droplets have to be considered. For smaller droplets the position of the rainbow depends significantly on droplet size. This influence has been taken into account by Airy. In this paper a formula given by Walker (1976), which is based on Airy's theory has been used for calculations of the rainbow angle θ_{RA}. For determining the refractive index the droplet size has to be measured in addition to the angular position of the rainbow. Here a new method is described, which allows to determine the refractive index without size measurements even for rather small droplets.

2 RAINBOWS AT DIFFERENT DROPLET SIZES

Scattered light intensities according to Mie's theory can be calculated using for instance the computer code published by Bohren and Huffman (1983). A dimensionless representation of the intensities leads to gain factors as defined by van der Hulst (1981). Here the gain factors, which are proportional to the intensity in the plane perpendicular to the polarisation of the incident light are used as a measure for the scattered intensities. Angular distributions of the gain factor in the region of the rainbow maximum are shown in Fig. 1 for three droplets with different sizes. In all three diagrams a ver-

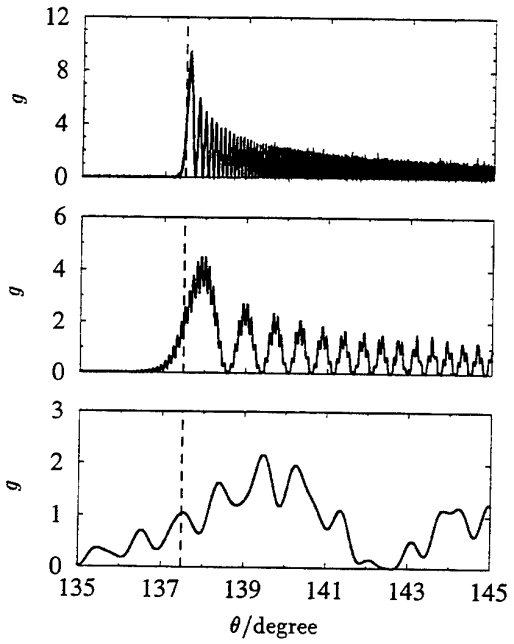

Figure 1: Gain factors g as a function of scattering angle θ representing the intensity distribution of the scattered light in the region of the first rainbow. Shown are results for three different droplet diameters d_T. The diameters are from top to bottom d_T = 5000 μm, 500 μm, and50 μm. The refractive index was in all cases $m = 1.33$

tical dashed line indicates the result for the rainbow position according to Descartes. The refractive index was $m = 1.33$ in all cases. In the top diagram the result for a rather large droplet with the diameter $d_T = 5$ mm is shown. As can be seen the main maximum of the rainbow is rather sharp and very close to the result according to Descartes. If the droplet is ten times smaller the main maximum has broadened and the position has shifted to larger angles as can be seen in the diagram in the middle of Fig. 1. In addition a ripple structure becomes visible. The angular distance between neighbouring maxima of the ripples is a measure for droplet size as shown by Anders et a. (1993). If the droplet size is decreased furthermore the main maximum is broadened and shifted further away from Descartes' results as shown in the last diagram of Fig. 1 for a droplet with $d_T = 50\,\mu$m.

3 FILTERED INTENSITY DISTRIBUTIONS

According to Airy's theory the position of the main maximum of the rainbow depends on droplet size. However, the ripple structure found is not explained by Airy's theory. Therefore the position of the maximum found in experiments or in Mie calculations is not necessarily in agreement with the position derived from Airy's theory. The ripple structure with its high frequency can be eliminated using an appropriate digital filter. The characteristic of such a filter is shown in

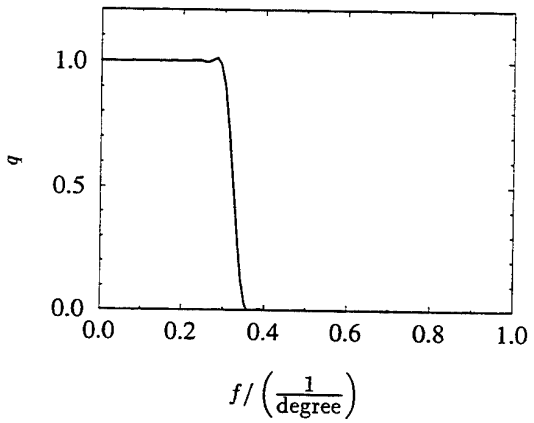

Figure 2: Characteristic of a digital filter used to filter the intensity distributions in the region of the rainbow. For $q = 1$ the corresponding frequencies will still be found in the filtered distributions and for $q = 0$ the frequencies will not be found there.

Fig. 2. The value of q indicates how much a selected frequency f within the initial intensity distribution is influenced by the filter. For $q = 1$ there is no influence of the filter and for $q = 0$ the frequency is filtered totally and cannot be found in a Fourier transform of the filtered intensity distribution. The filter used here is rather sharp. It is a low pass filter, which filters the original intensity distribution in such a way, that the high frequency ripple strutcure found in the intensity distribution disappears in the filtered distribution. An example of the effect of the filtering process is shown in Fig. 3. In the top diagram of Fig. 3 the intensity distribution in the region of the rainbow is shown for a droplet with the diameter $d_T = 99.92\,\mu$m and the refractive index $m = 1.33$. The dashed line indicates the rainbow position according to Descartes whereas the dotted line represents Airy's result. As can be seen Airy's result seems to be a better estimation of the position of the

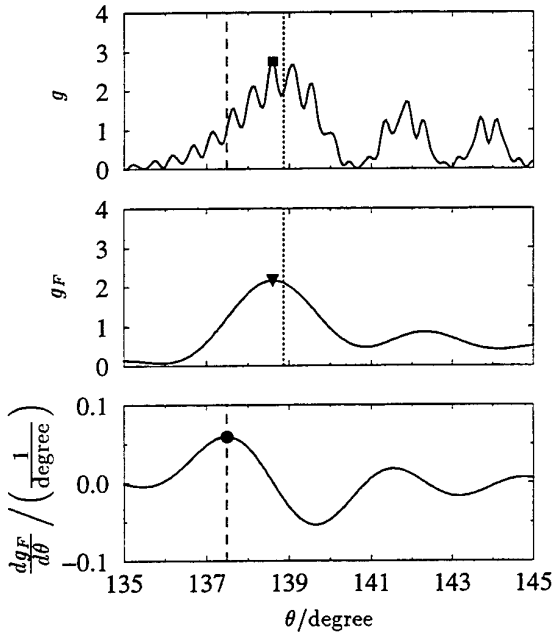

Figure 3: Shown are three diagrams which demonstrate the evaluation techniques applied to the intensity distributions in the rainbow region. In the diagram at the top the gain factor representing the intensity distribution itself is shown for the refractive index $m = 1.33$ and the droplet diameter $d_T = 99.92\,\mu$m. The squared symbol indicates the maximum of the distribution. In the diagram below the filtered intensity distribution is shown. The triangled symbol indicates the maximum of the filtered distribution. In the diagram at the bottom the derivative of the filtered intensity distribution is shown. The circled symbol indicates the maximum of the derivative of the filtered distribution. The vertical dashed lines lines mark the results for the rainbow angle according to Descartes' formula. The vertical dotted lines lines mark the results for the rainbow angle according to Airy.

main maximum of the rainbow but it is not identical with the maximum of the intensity distribution. If the ripple structure is eliminated using a digital filter the diagram in the middle of Fig. 3 is obtained. The maximum of the filtered intensity distribution is taken as rainbow position. This maximum is close to the rainbow position according to Airy. The derivative $dg_F/d\theta$ of the filtered distribution is shown in the diagram at the bottom of Fig. 3. Extrema of this derivative indicate points of inflection of the filtered distribution. As can be seen in the diagram one maximum is close to the rainbow position according to Descartes. This maximum is related to the point of inflection of the filtered intensity distribution found at the increase up to the main maximum. As this point of inflection is close to the results according to Descartes it may be insensitive to droplet size. The influence of droplet size on this inflection point is discussed in the next section.

4 RAINBOW POSITION AND DROPLET SIZE

Calculations of the scattered intensity where performed for scattering angles $120° \leq \theta \leq 170°$ for droplets with diameters $10\,\mu\text{m} \leq d_T \leq 300\,\mu\text{m}$. As described above there are different ways to define rainbow positions of each intensity distribution in order to determine the refractive index. As shown above different rainbow positions are obtained for different evaluation techniques. The simplest way is taking the position θ_{RM} of the absolute intensity maximum in the region of the rainbow. Results are shown for the refractive index $m = 1.33$ as a function of droplet diameter d_T in Fig. 4. The resulting rainbow positions θ_{RM} are close to the rainbow position according to Airy. This rather simple evaluation technique leads, however, to large fluctuations of the rainbow position θ_{RM}. These fluctuations are partly caused by the ripple structure of the intensity distribution. The evaluation of the filtered distribution gives obviously better results as can be seen in Fig. 5. In this figure the positions of the maxima of the filtered intensity distribution are shown as a function of the droplet size. The resulting rainbow positions θ_{RFM} are again close to results of Airy's formula. Most values found are smaller than Airy's results. The amplitude of the fluctuations decreases with increasing droplet size. A closer look at the fluctuations shows a regular structure as can be seen in the enlarged view. More about these fluctuations is found in papers of Ashkin and Dziedzic (1971) or Roth et a. (1994). The positions of the maxima of the filtered intensity distribution are size sensitive like Airy's results. Finally the positions θ_{RFW} of the point of inflection as described above were calculated. The

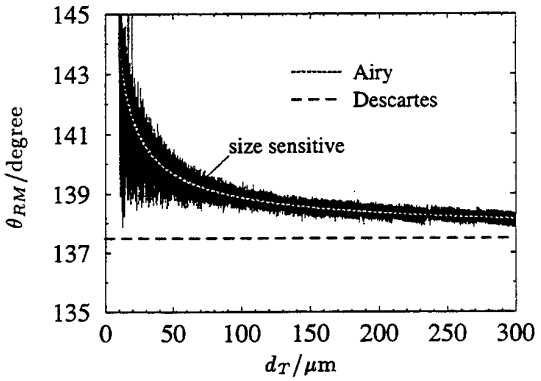

Figure 4: Position θ_{RM} of the maximum of the intensity distribution in the rainbow region as a function of droplet diameter d_T. The refractive index was $m = 1.33$. Comparisons are made with the theories of Descartes and Airy.

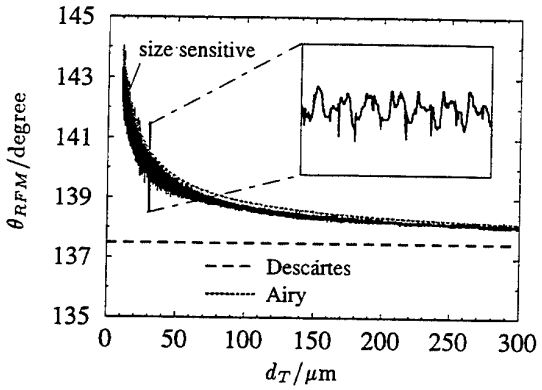

Figure 5: Position θ_{RFM} of the maximum of the intensity distribution in the rainbow region as a function of droplet diameter d_T. The refractive index was $m = 1.33$. Comparisons are made with the theories of Descartes and Airy. In the enlarged view the regularity of the oscillations can be recognized.

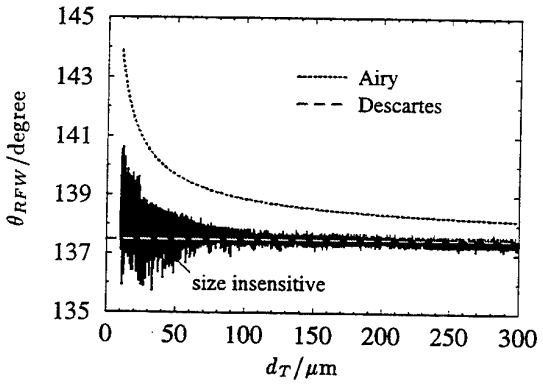

Figure 6: Position θ_{RFW} of the maximum of the intensity distribution in the rainbow region as a function of droplet diameter d_T. The refractive index was $m = 1.33$. Comparisons are made with the theories of Descartes and Airy.

results are shown in Fig. 6. The positions θ_{RFW} of the point of inflection are apart from minor fluctuations size insensitive and are found to be close to the rainbow angle obtained by Descartes' theory. These fluctuations of θ_{RFW} found by varying the droplet size are similar to the fluctuations of the position θ_{RFM} of the maximum of the filtered intensity distribution. Their amplitudes, however, are slightly smaller. They increase if the droplet size decreases. The regularity of these fluctuations may still be recognized, but it can not be seen as clearly as the regularity of the fluctuations of θ_{RFM}.

The fluctuations may be considered in this context as statistical fluctuations as their period is very short as shown by Roth et a. (1994). Even changes in droplet diameter of less than 200 nm result in positions θ_{RFM} and θ_{RFW} within the whole range of the amplitudes of the fluctuations around the considered diameter. To perform a statistical evaluation of results as shown in Fig. 6 mean values $\bar{\theta}_R$ and standard deviations σ_R of the positions θ_{RM}, θ_{RFM} and θ_{RFW} were calculated within small intervals Δd of the droplet diameter. The width Δd was 10 % of the diameter at which the mean values and standard deviations were calculated. This means that for a droplet diameter of $d_T = 30\,\mu$m for instance the positions of the rainbow at diameters $28.5\,\mu\text{m} \leq d_T \leq 31.5\,\mu\text{m}$ were taken into account for the calculations. Results of these calcula-

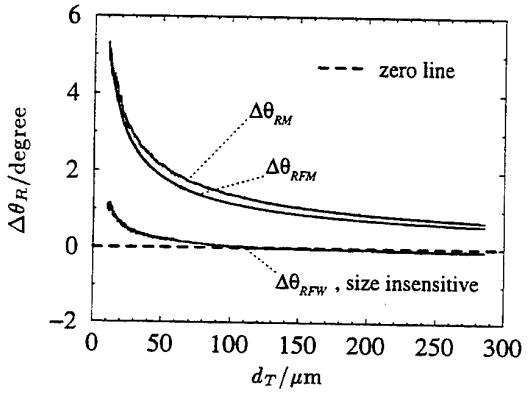

Figure 7: Differences between the rainbow angle θ_{RG} according to Descartes and the mean rainbow angles $\bar{\theta}_{RM}, \bar{\theta}_{RFM}$, and $\bar{\theta}_{RFW}$ obtained by different evaluation techniques of the intensity distributions near the rainbow angle as a function of droplet size. The refractive index was $m = 1.33$.

tions are shown in Fig. 7. In this diagram the differences between the mean values and the size independent rainbow position θ_{RG} according to Descartes are plotted over the droplet diameter. The results for the position of the maxima of the non-filtered intensity distribution $\Delta\theta_{RM} = \bar{\theta}_{RM} - \theta_{RG}$ and of the filtered intensity distribution $\Delta\theta_{RFM} = \bar{\theta}_{RFM} - \theta_{RG}$ show even at a droplet diameter of $d_T = 300\,\mu$m a significant difference to the dashed marked zero line. For smaller droplets this difference increases monotonically. This behaviour shows clearly the size sensitivity of the positions θ_{RM} and θ_{RFM}. The results for the position $\Delta\theta_{RFW} = \bar{\theta}_{RFW} - \theta_{RG}$ of the inflection point is very close to the zero line except for rather small droplets. This shows, that the new method, which characterizes the intensity distribution in the rainbow region by the position of the inflection point as described above is size insensitive in a large range of droplet diameters. In experiments only the rainbow has to be evaluated then. Without knowing the droplet size the refractive index can be determined using Descartes' formula. A measure or estimation for the amplitudes of the fluctuations around the mean values of the rainbow angle

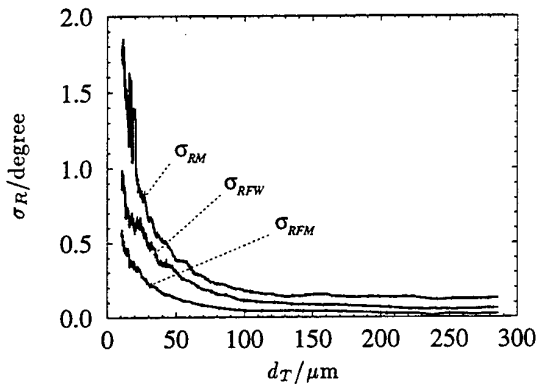

Figure 8: Standard deviations $\sigma_{RM}, \sigma_{RFM}$, and σ_{RFW} obtained by different evaluation techniques of the intensity distributions in the rainbow angle as a function of droplet size. The refractive index was $m = 1.33$.

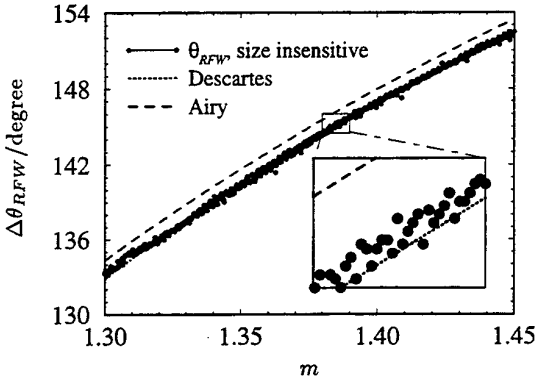

Figure 9: Size insensitive rainbow angle θ_{RFW} as a function of refractive index m compared with the theories of Airy and Descartes. The droplet size was $d_T = 100\,\mu$m.

give the standard deviations σ_R shown in Fig. 8. Shown are standard deviations obtained by all three evaluation techniques, where σ_{RM} is derived from the maxima of the intensity distribution, σ_{RFM} from the maxima of the filtered distribution, and σ_{RFW} from the inflection point of the filtered distribution. As can be seen the smaller the droplet diameter the larger the standard deviation. It has to be noticed, that the standard deviation of the size insensitive method σ_{RFW} is approximately twice as large as σ_{RFM}. However, σ_{RM} reaches up to four times larger values as σ_{RFM}. If the refractive index has to be determined with a higher accuracy the amplitude of the fluctuations should be low. Therefore the rainbow angle θ_{RFM} with the lowest amplitudes has to be determined. But in this case the droplet size has to be measured in addition. This causes a more complex experimental setup and additional evaluation time. As the rainbow angles θ_{RM} and θ_{RFM} are close but not exactly equal to Airy's results experimental or theoretical calibrations have to be performed. Instead of the calibrations an empirical method may be developed to model the difference between Airy's results θ_{RA} and θ_{RM} or θ_{RFM}. For faster evaluation by omitting the filtering process just the position θ_{RM} may be determined if a very low accuracy is acceptable. The main advantage of using the rainbow angle θ_{RFW} is, that no size measurements have to be performed while the results have medium accuracy.

If the refractive index is varied results of the size insensitive evaluation technique remain still close to the rainbow angle obtained by Descartes. In Fig. 9 the size insensitive rainbow angle θ_{RFW} is shown as a function of the refractive index m for droplets with the diameter $d_T = 100\,\mu$m. These results are compared with results according the theories of Airy and Descartes. In the enlarged view it can clearly be seen, that θ_{RFW} is close to the rainbow angle according to Descartes. A lot of additional calculation not shown here give the same results.

5 CONCLUSIONS

It was shown, that different droplet sizes show different intensity distributions of the scattered light in the rainbow region. Three different evalution techniques were discussed to determine a rainbow position for an intensity distribution. Two techniques are size sensitive and therefore the droplet diameter has to be measured in addition if the refractive index is to be determined. One method uses the position θ_{RM} of the absolute maximum of the intensity distribution. This evaluation is rather fast but results in a low accuracy for smaller droplet diameters. The other size sensitive method is to filter the intensity distribution and to determine the position θ_{RFM} of the maximum of the filtered distribution. This method results in the highest accuracy but the evaluation time is longer. Both size sensitive methods need a calibration process in advance to perform a correlation to the results according to Airy's formula. If the position θ_{RFW} of the inflection point of the filtered intensity distribution is taken as rainbow angle it was found, that in a large range of droplet diameter this position is insensitive to droplet size. Therefore a size measurement is not necessary and the size independent formula of Descartes can be applied to determine the refractive index. The accuracy, however, is not as good as with the maximum of the filtered function. The main advantage is the size insensitivity. In many cases the size measuring method is sensitive to the refractive index. Then in a first step the refractive index has to be determined in measuring θ_{RFW}. In a second step the droplet size can be determined using the refractive index already measured. If a higher accuracy in the refractive index is desired the droplet diameter may be used to get a better result. In future work these theoretical investigations should be applied in experiments to get accurate measurements of droplet size and refractive index in a fast and convenient way.

REFERENCES

Anders, K., Roth, N. & Frohn, A. 1993, Light Scattering at the Rainbow Angle: Information on Size and Refractive Index, Proc. 3rd Int. Congr. on Optical Particle Sizing, Yokohama, pp.183-187.

Anders, K., Roth, N. & Frohn, A. 1996, Influence of Refractive Index Gradients within Droplets on Rainbow Position and Implications for Rainbow Refractometry, Part. Part. Syst. Charact., vol.13, (in press).

Ashkin A. & Dziedzic J.M. 1971, Optical levitation by radiation pressure, Appl. Phys. Lett., vol.19, pp.283-285

Bauckhage, K. & Schombacher, H. 1996, Private Communication.

van Beeck, J.P.A.J. & Riethmüller, M.L. 1994, Simultaneous Determination of Temperature and Size of Droplets from the Rainbow Using Airy Theory, Proc. 7th Int. Symp. on Applications of Laser Techniques to Fluid Mechanics, Lisbon, pp.21.5.1

Bohren C.F. & Huffman D.R. 1983, Absorption and Scattering of Light by Small Particles, John Wiley & Sons, New York.

van de Hulst, H.C. 1981, Light Scattering by Small Particles, Dover Publ. Inc., New York.

Kai L., Massoli P. & D'Alessio A. 1993, Studying Inhomogeneities of Spherical Particles by Light Scattering, Proc. 3rd Int. Congr. on Optical Particle Sizing, Yokohama, pp.135-143.

Massoli P., Beretta F. & D'Alessio A., Lazzaro M. 1993, Temperature and Size of Single Transparent Droplets by Light Scattering in the Forward and Rainbow Regions, Appl. Opt., vol.30, pp.3295-3301.

Roth N., Anders K. & Frohn A. 1988, Simultaneous Measurement of Temperature and Size of Droplets in the Micrometer Range, Proc. 7th Int. Congr. on Optical Methods in Flow and Particle Diagnostics ICALEO 88, L.I.A., Sunnyvale, vol.67, pp.294-304.

Roth N., Anders K. & Frohn A. 1991, Refractive-Index Measurements for the Correction of Particle Sizing Methods, Appl. Opt., vol.30, pp.4960-4965.

Roth N., Anders K. & Frohn A. 1992, Simultaneous Determination of Refractive Index and Droplet Size Using Mie-Theory, Proc. 6th Int. Symp. on Application of Laser Techniques to Fluid Mechanics, Lisbon, pp.15.5.1

Roth N., Anders K. & Frohn A. 1994, Examination of the Rainbow Position of Optically Levitated Droplets for the Determination of Evaporation Rates of Droplets, Proc. 7th Int. Symp. on Applications of Laser Techniques to Fluid Mechanics, Lisbon, pp.21.2.1

Sankar S.V., Ibrahim K.M., Buermann D.H., Fidrich M.J. & Bachalo W.D. 1993, An Integrated Phase Doppler/Rainbow Refractometer System for Simultaneous Measurements of Droplet Size, Velocity and Refractive Index, Proc. 3rd Int. Congr. on Optical Particle Sizing, Yokokama, pp.275-284.

Walker J.D. 1976, Multiple Rainbows from Single Drops of Water and Other Liquids. Am. J. Phys., vol.44, pp.421-433.

ACKNOWLEDGEMENT

This work has been sponsored by Deutsche Forschungsgemeinschaft (DFG).

AN ADVANCED RAINBOW SIGNAL PROCESSOR FOR IMPROVED ACCURACY IN DROPLET TEMPERATURE MEASUREMENTS

S.V. Sankar, D.M. Robart, and W.D. Bachalo

Aerometrics, Inc.
Sunnyvale, California
U.S.A.

ABSTRACT

A virtual rainbow signal processor has been developed to increase the reliability and accuracy of the in-situ droplet refractive index measurement, and hence the temperature measurement, in reactive and non-reactive sprays. The virtual processor makes use of the Airy theory to accurately extract both droplet size and refractive index information from fully digitized rainbow signals. Several signal parameters are measured, and a data validation logic is used, to establish confidence in the measurements. When used in conjunction with a phase Doppler system, the redundant size measurement provided by the rainbow refractometer serves to minimize refractive index measurement errors that could result from droplet non-sphericity and droplet inhomogeneity. The virtual signal processor has been applied to rainbow signals obtained from a stream of monodisperse water droplets generated by a vibrating orifice droplet generator as well as from polydisperse droplets in a water spray. The results show that the post-processing approach used yields refractive index and temperature measurement accuracies that are about 3-4 times better than that achievable with the peak-detection based real time rainbow signal processor.

1. INTRODUCTION

The availability of the phase Doppler instrument has permitted simultaneous measurement of droplet size and velocity of fuel droplets in complex spray flames [Edwards and Rudoff, 1990; Presser et al., 1990]. These studies have contributed to an increased understanding of the behavior of droplet dynamics and other droplet-gas phase interactions in spray flames as well as the effect of fuel properties on the structure of swirling spray flames. However, in order to obtain a better understanding of the complex droplet heating and evaporation process in spray flames, it is also necessary to measure the fuel droplet temperatures.

Recently, Sankar et al. (1993) completely integrated a rainbow refractometer to a conventional phase Doppler system yielding a single diagnostic for the simultaneous measurement of droplet velocity, size, and refractive index in spray environments. Rainbow refractometry takes advantage of the fact that the main rainbow angle is a function of the refractive index of the droplet. Therefore, by measuring the location of the main rainbow with a linear array detector, such as a CCD, the refractive index of the droplet can be determined (Roth et al., 1990). For particles less than about 150 μm in diameter, the rainbow location exhibits a dependence on the droplet size as well as on the droplet refractive index. However, by independently measuring the droplet size with a phase Doppler instrument, the size dependence can be properly accounted for. The feasibility of using this integrated diagnostic instrument for droplet size, velocity, and temperature measurement has also been demonstrated by Sankar et al. (1994a).

The rainbow refractometer/thermometer used in the studies by Sankar et al. incorporated a rainbow signal processor that basically performs a real-time peak detection on the CCD output to locate the main rainbow location. In addition to the rainbow location, the signal amplitude at that location is also digitized. The drawback with this signal processor is that it works well only for clean, noise-free rainbow signals. The inherent presence of high frequency oscillations on the rainbow signature, droplet non-sphericity, droplet inhomogeneity, false gating, and multiple droplets all give rise to noisy or distorted rainbow signatures which cannot be detected and rejected by a peak detection based system.

This paper describes the development of an advanced rainbow signal processor which provides improved measurement accuracy when compared to the peak detection based real-time rainbow signal processor. The newly developed processor performs real time peak detection, but at the same time, digitizes and saves the entire rainbow signal for each droplet in the onboard memory of the processor. During post-processing, various digital filtering and validation criteria are implemented to clean the signal and to reject the bad signals. As a result, the droplet temperature measurement accuracy is significantly improved. The improved processor has been applied to process rainbow signals obtained from monodisperse droplet streams as well as in a water spray. The general details of the advanced processor and the results obtained from the experimental measurements are presented in this paper.

2. RAINBOWS

The occurrence of rainbows can be understood with the help of the simple geometrical optics based theory proposed by Descartes several hundred years ago (Nussenzveig, 1977). Using geometrical optics assumptions, the scattering of light by spherical particles can be described as a combination of diffraction, external reflection, refraction, and refraction occurring after multiple internal reflections. Furthermore, adopting van de Hulst's (1957) notation, $p=0$ refers to externally reflected light, $p=1$ refers to refracted rays, $p=2$ refers to rays that emerge from the droplet after undergoing one internal reflection, and so on. For each order scattered ray, the scattering angle bears a definite relationship to the incident angle. The location of the primary rainbow can then be understood to correspond to that scattering angle at which the angular relationship for $p=2$ goes through an extremum. At the rainbow angle, the scattered intensity achieves a local maximum. To one side of the rainbow angle is a shadow region into which no rays emerge and to the other side is a lit region. Similarly, the secondary rainbow corresponds to the scattering angle extremum for $p=3$ rays. For example, for water droplets, the primary and the secondary rainbows occur at scattering angles of 137.9^{o} and 128.8^{o}, respectively. The dark region between the primary and the secondary rainbow is historically known as Alexander's dark band. Rainbows of order greater than $p=3$ can also be present, but in general, are very weak in intensity.

Several characteristics of the rainbow cannot be adequately explained with the geometrical optics based theory, for example, the presence of supernumerary arcs on the lighted side of the primary and secondary rainbows. The occurrence of supernumerary arcs was explained by Young as resulting from interference (Nussenzveig, 1977). They occur as a result of interference between two different rays of the same order emerging in the same direction. Thus, at any given angle slightly greater than the rainbow angle, the scattered light includes rays that have followed two different paths through the droplet. To further complicate the situation, the interference of the internally reflected rays with externally reflected ($p=0$) rays gives rise to high frequency intensity oscillations that are superimposed upon the supernumerary fringes. The pattern of the supernumerary arcs and the high frequency oscillations are therefore a function of the droplet size.

Both the Descartes and Young rainbow theories predict that the rainbow angle is independent upon the droplet size and that the intensity is infinite at the rainbow angle. In the geometric analysis of Descartes, intensity is infinite at the rainbow angle but it declines smoothly (without supernumerary arcs) on the lighted side and falls off abruptly to zero on the dark side. Young's theory predicts supernumerary arcs but retains the sharp transition from infinite to zero intensity.

Subsequently, Airy (1838) made use of Huygen's wave propagation principle to describe the intensity of the scattered light in neighborhood of the rainbow. The Airy theory does not reach an infinite intensity at any point. Also, the Airy theory, unlike Descartes and Young theories, predicts that the maximum intensity of the rainbow falls at an angle somewhat greater than the Descartes rainbow angle. Furthermore, the Airy rainbow angle is a function of droplet size. However, at the Descartes rainbow angle (or geometric rainbow angle), the intensity predicted by the Airy theory is approximately 45% of the main maximum (van de Hulst, 1957).

The Airy theory is strictly asymptotic, i.e., its valid only for drops very much larger than the wavelength of light. On the contrary, the Lorenz-Mie light scattering theory provides an exact description of the rainbow for droplets of all sizes (van de Hulst, 1957). This theory provides a rigorous analytic solution of the scattering of light by a homogeneous sphere of any size and refractive index, and therefore, provides a detailed description of the rainbow produced by a spherical droplet. Figure 1 presents the computed variation of the scattered light intensity in the neighborhood of the primary and secondary rainbows. The computations were performed using the Lorenz-Mie theory for a water droplet (m=1.33) having a diameter of 150 μm. The wavelength of the illuminating light source was assumed to be 514.5 nm. The important rainbow characteristics such as the locations of the primary and secondary bows, the dark band, the supernumerary fringes, and the high frequency oscillations that ride on the low frequency oscillations have been identified in Fig. 1.

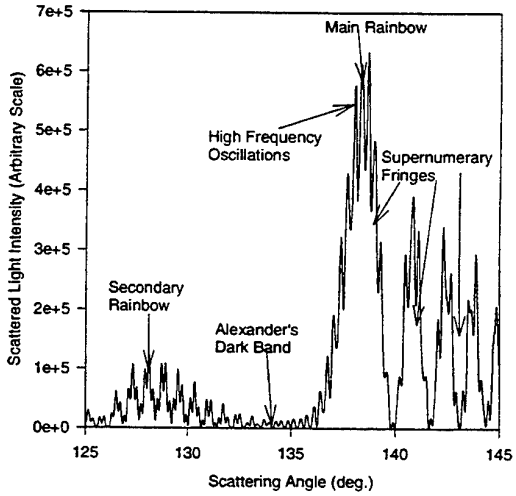

Figure 1: Computed variation of the scattered light intensity in the neighborhood of the primary and secondary rainbows for a water droplet (m=1.33) having a diameter of 150 μm and illuminated by a light source having a wavelength of 514.5 nm.

Certain transformations of the Mie series lead to the Airy formulas for the rainbows. Wang and van de Hulst (1991) have made direct comparisons between the more rigorous Lorenz-Mie computations and the asymptotic Airy theory to determine the particle size limit at which deviations become visible. Their study has shown that, contrary to what has often been thought, the Airy theory starts to be useful at relatively small droplet sizes. For droplets as small as 20 μm, the Airy approximation is still useful in identifying the main rainbow peak for refractive indices greater than 1.33. This finding justifies the use of the Airy theory for droplet refractive index and size measurement (for particles greater than about 20 μm) in rainbow refractometry.

3. INTEGRATED DIAGNOSTICS

The details of the integrated phase Doppler/rainbow refractometer that has been developed for the simultaneous measurement of droplet size, velocity, and refractive index (temperature) for spray applications have been provided by Sankar et al. (1993, 1994). The optical system basically consists of a single transmitting module, a phase Doppler receiver, and a rainbow receiver as shown in Fig. 2. The optical transmitter provides the necessary laser beams for conducting phase Doppler interferometry and rainbow thermometry. The phase Doppler receiver is placed in the forward scatter direction at a scattering angle of about 30°. The rainbow receiver is placed diametrically opposite to the phase Doppler receiver at a scattering angle of about 150°. The receiver module of the phase Doppler system is identical to that used conventionally. On the other hand, the optical rainbow receiver basically consists of a system of lenses for imaging the rainbow pattern onto a linear CCD array.

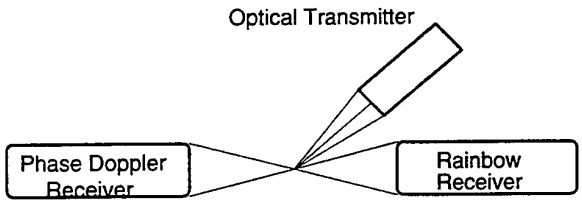

Figure 2: Optical configuration of the integrated diagnostics.

The major components of the electronics/opto-electronics system includes a CCD based imaging board, a gate control system, data acquisition/signal processing board for real-time processing of the rainbow signals, and a frequency domain based signal processor for processing the Doppler signals. The CCD output is sampled and digitized by a dedicated real-time rainbow signal processor. As discussed earlier, the rainbow signals contain high frequency components which would be undesirable if the rainbow peaks are to be determined directly. However, the rainbow signal processor contains a digital filter for minimizing the adverse effects of the high frequency oscillations. The rainbow peak location and intensity of the rainbow are available for transfer to the data acquisition computer for further analysis and post processing.

The real-time rainbow processor based instrument has been applied to a variety of applications such as the temperature measurement of isolated, burning n-heptane droplets in motion (Sankar et al., 1994b), droplet temperature measurement in a swirl-stabilized kerosene spray flame (Sankar et al., 1994a), and the study of liquid-liquid mixing in sprays (Sankar et al., 1995). The major advantage of the real-time rainbow processor is the speed; it can process the data at a speed of 10 KHz. While the real-time rainbow processor performs well with ideal signals, such as from a stream of monodisperse droplets, the measurement uncertainty is high when it is applied to complex sprays where the presence of multiple particles in the probe volume, random trajectories through the probe volume, non-spherical particles, oscillating droplets, inhomogeneous droplets, and noise can give rise to distorted rainbow signatures.

Figures 3-5 show typical rainbow signals that were obtained in a water spray. Figure 3 is an example of a rainbow signal with good SNR whereas Fig. 4 shows a distorted rainbow signal which could be due to droplet non-sphericity or multiple droplets in the probe volume, and Fig. 5 shows a rainbow signal with low SNR. In each of these cases, the real-time rainbow processor would yield a rainbow location which would be grossly different from the actual rainbow location. To overcome the limitations of the real-time processor, an advanced signal processor is required which can reliably identify good rainbow signals and improve the accuracy of the refractive index and temperature measurements.

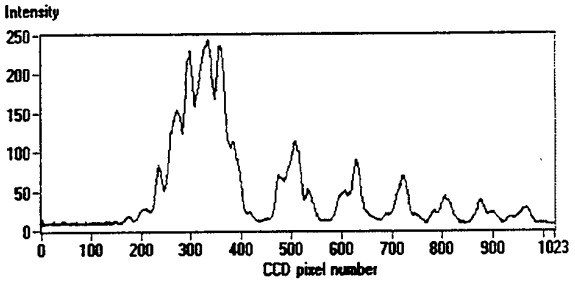

Figure 3: Typical rainbow signal with good SNR obtained in a water spray. The droplet diameter as measured by the PDPA is 68.26 μm.

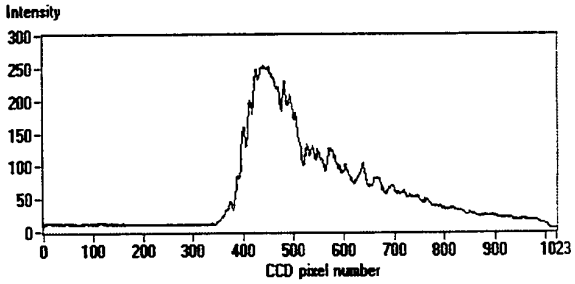

Figure 4: Example of a distorted rainbow signal that was obtained in a water spray. The distortion could be due to multiple droplets in the probe volume or droplet non-sphericity. The droplet diameter reported by the PDPA is 14.13 μm.

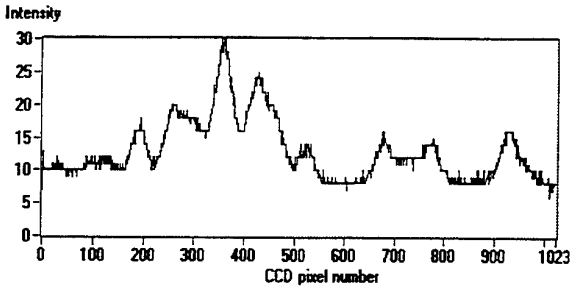

Figure 5: Typical rainbow signal with a low SNR obtained in a water spray. The droplet diameter as measured by the PDPA is 26.45 μm.

4. VIRTUAL RAINBOW PROCESSOR

In order to perform detailed processing of the rainbow signal, it is necessary to capture and save the entire rainbow signal for each droplet in a spray application. During post-processing, various digital such as those based on the FFT can be applied to remove the high frequency oscillations and noise, correlation techniques can be used to recognize the characteristic rainbow signature, and sophisticated peak fitting algorithms can be applied for increasing the measurement accuracy. Though time consuming, the reliability and accuracy of the rainbow refractometer/thermometer measurements can be significantly improved using this approach. A hardware system capable of digitizing and saving the 8-bit, 2048 pixel output of the CCD for each droplet has been developed. This system runs in parallel with the real-time peak detection system. The hardware system has on-board memory for recording several thousand rainbow signals per run. At the end of each run, the digitized rainbow data is saved as a TIFF image.

A virtual signal processor has also been developed for analyzing the digitized rainbow signals. We call it "virtual" because it is a software simulation of something that could be done much faster in hardware or using a dedicated DSP sub-system. Each rainbow signal is processed, and the refractive index and droplet diameter information is inferred purely from the rainbow signal making use of the Airy theory. As a final validation, the "rainbow diameter" is compared to the "PDPA diameter". If the two answers do not agree to within an acceptable tolerance, the data is rejected. The rejection criteria is believed to be effective in eliminating erroneous measurements resulting from droplet inhomogeneity, droplet non-sphericity, false gating, multiple particles in the probe volume, and noise.

The most important components of the virtual rainbow processor are the adaptive filtering module, the computational module, and the data analysis module. The adaptive filtering module implements a FFT based filtering technique to remove the high-frequency oscillations of the rainbow signal as well as the noise. Additionally, the power spectrum is used to compute a signal-to-noise ratio (SNR) for the digitized waveform, and this provides a means for eliminating any waveform which does not meet this criteria.

The FFT based low-pass filter is not adequate to handle the cases where the signal has been clipped by exceeding 255 (the 8-bit limit). In such cases, invariably one of the rounded corners is higher than the other and the estimate finds a peak that is not well centered. The raw signal is therefore examined to detect any "clipping" of the signal. For clipped signals, peak detection scheme is abandoned in favor of a centroid detection technique wherein the location of the sides at some prespecified value (like 200) is determined and the half-way point between these points is used as an estimate for the rainbow location.

The computational module performs the important function of both analyzing the filtered waveform and also detecting if the waveform is a valid rainbow waveform based upon certain rules derived from the Airy theory. If the digitized waveform passes these rules then it is assumed to be a valid rainbow signal and is further processed to extract both the droplet size and refractive index information.

As mentioned earlier, the virtual processor makes use of the Airy theory to estimate the droplet size and refractive index. The Airy theory defines an angle α which is a normalized angular deviation from the geometric rainbow angle θ_{rg} (van Beeck and Riethmuller, 1995):

$$\alpha = \left(\theta - \theta_{rg}\right)\left(\frac{16\,D^2}{\lambda^2 \cos\tau_{rg}}\right)^{1/3} \sin\tau_{rg} \qquad (1)$$

where λ is the wavelength of the incident light, D is the droplet diameter, θ_{rg} is the size-independent geometric (Descartes) rainbow angle, and τ_{rg} is the incident angle between the external droplet surface and the incident ray which gives rise to the scattering angle θ_{rg}. The relationship for θ_{rg} and τ_{rg} are as follows:

$$\theta_{rg} = -2\tau_{rg} + 4\cos^{-1}\left(\frac{1}{m}\cos\tau_{rg}\right) \qquad (2)$$

$$\sin\tau_{rg} = \left(\frac{m^2-1}{3}\right)^{1/2} \qquad (3)$$

Furthermore, the scattered intensity at a normalized angle α can be computed using the Airy or rainbow integral:

$$F(\alpha) = \int_0^{\infty} \cos\frac{1}{2}\pi\left(\alpha t - t^3\right) dt \qquad (4)$$

By computing the intensity values for a range of α values, a universal rainbow pattern can be established. Furthermore, the α values corresponding to the first and second maxima in this universal rainbow signature have been computed by van de Hulst (1957) to be $\alpha_1 = 1.08$ and $\alpha_2 = 3.47$. Also, it can be observed from Eq.(1) that when $\alpha = 0$ then $\theta = \theta_{rg}$. For $\alpha = 0$, Eq.(4) yields that $F(\alpha) = 0.454$. This observation implies that

the size-independent geometric rainbow angle can be obtained from the digitized rainbow signal by low-pass filtering the signal, measuring the intensity at the first maxima, and finding a point on the filtered rainbow signal where the intensity is 45.4% of the first maxima. This directly yields the geometric (Descartes) rainbow angle θ_{rg} which can be used along with Eqs. (2) and (3) for determining the droplet refractive index. This approach could be treated as a size-independent means of determining the droplet refractive index from rainbow signals. The practical problem in implementing this technique is that an unknown DC shift is present in each digitized rainbow signal. Therefore, our approach for measuring the geometric rainbow angle has been to measure the locations of the first and second maxima, θ_1 and θ_2, from the low-pass filtered signal. From Eq.(1) we get

$$\frac{\alpha_1}{\alpha_2} \equiv \frac{1.08}{3.47} = \frac{(\theta_1 - \theta_{rg})}{(\theta_2 - \theta_{rg})} \qquad (5)$$

which can be solved to yield the size-independent geometric rainbow angle, θ_{rg}, which can be used to compute the refractive index, m. Having determined θ_{rg} and m, the droplet size can be determined using Eq.(1). A similar method for droplet size and refractive index measurement from the rainbow signature has been proposed by van Beeck and Riethmuller (1995). This is the approach used in the virtual processor for droplet size and refractive index measurement from the digitized rainbow signatures.

The final function of the virtual rainbow processor is to provide the results and the associated statistics. Various user controllable data acceptance/rejection criteria are made available from the control panel. This includes ability to set maximum and minimum acceptance limits on the measured droplet diameter, peak rainbow location, peak intensity level, covariance factor (obtained by cross-correlating the acquired rainbow signal with a theoretical signal that is generated based upon the measured droplet size and refractive index), and SNR. Only signals that pass all these validation criteria are accepted as valid data. This implies that a signal can pass all the acceptance criteria except one and still be rejected. To overcome this binary acceptance logic, fuzzy logic based acceptance criteria are currently being evaluated and will be implemented in the future.

As a final criteria, the droplet size inferred from the rainbow signature is compared with that provided by the phase Doppler system. If the two diameters do not agree to within a preset tolerance, the data is rejected. It is believed that any significant disagreement between the "rainbow diameter" and the "PDPA diameter" is an indication that the droplet might be non-spherical or inhomogeneous. van Beeck and Riethmuller (1995) have observed that even a 1% deviation from sphericity can cause significant errors in the refractive index measurements. It is postulated that the PDPA will not have the same sensitivity to droplet non-sphericity (Bachalo and Sankar, 1994) and therefore the difference in the response characteristics of the two sizing techniques can be exploited to recognize droplet non-sphericity. The same logic is applied to the detection and rejection of droplets exhibiting radial inhomogeneity. Schneider and Hirleman (1994) have shown that a PDPA configured to size in the forward scatter direction is not very sensitive to the presence of droplet radial inhomogeneity, and yields sizing errors of the order of 5%. However, it has also been shown by them that the rainbow pattern (or PDPA sizing at backscatter angles) is more sensitive to droplet inhomogeneity than PDPA sizing in the forward scatter angle. Therefore, it is believed that the "rainbow diameter" for inhomogeneous droplets will be different from the "PDPA diameter" providing a means for detecting droplet inhomogeneity. Research is currently being undertaken to satisfactorily address these issues.

5. RESULTS

The integrated diagnostic, along with the newly developed virtual rainbow processor, has been applied to analyze rainbow signals acquired from monodisperse water droplets generated by a vibrating-orifice generator, and also from polydisperse droplets in a water spray.

5.1 Monodisperse Droplets Measurements

Typical refractive index and size histogram obtained for the monodisperse droplet case (123.3 μm in diameter) are presented in Figs. 6, 7, and 8, respectively. The results are excellent with a data acceptance rate of 100%. The measured mean refractive index is 1.3332 and the standard deviation is only 0.00054. The full scale measurable range for the chosen optical configuration is 1.28 to 1.38. This shows that for the monodisperse droplets, the uncertainty in the measured refractive index can be as low as 0.55% (of full scale range). Since refractive index and temperature bear a nearly linear relationship, the temperature measurement uncertainty is also 0.55%. The mean droplet size measured with the PDPA is 124.5 μm and the standard deviation is 0.4 μm, Fig.7. In comparison, the mean droplet diameter obtained from the rainbow signatures is 122.3 μm and the standard deviation is 1.7 μm, Fig. 8. Figure 9 shows the measured "rainbow" and

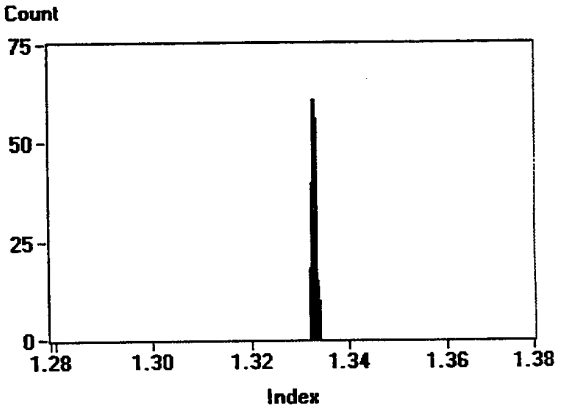

Figure 6: Measured refractive index histogram for monodisperse droplets of size 123.3 μm.

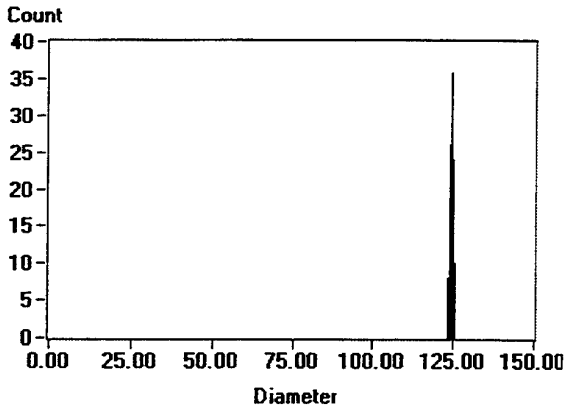

Figure 7: PDPA measured size histogram for monodisperse droplets of size 123.3 μm. The mean diameter measured is 124.5 μm and the standard deviation is 0.4 μm.

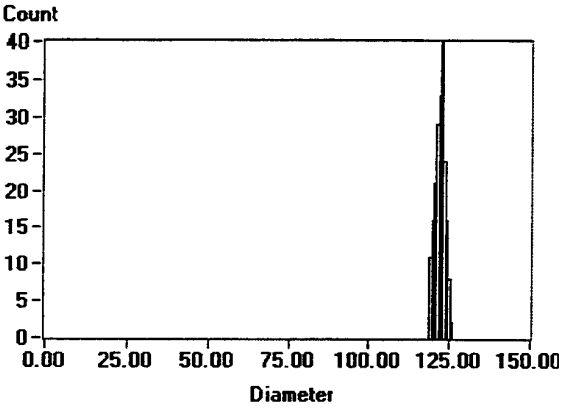

Figure 8: Rainbow refractometer measured size histogram for monodisperse droplets of size 123.3 μm. The mean diameter measured is 122.3 μm and the standard deviation is 1.7 μm.

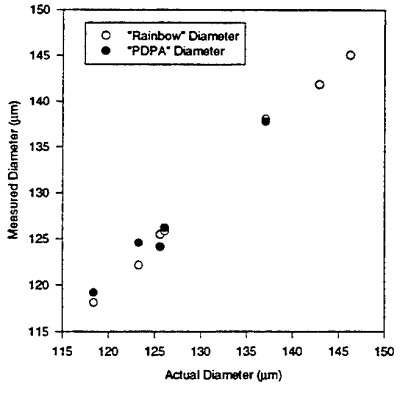

Figure 9: Comparison of the mean droplet diameters measured from the rainbow signals and by the PDPA. Monodisperse droplets of known size were generated with a vibrating orifice droplet generator.

"PDPA" mean diameters versus the actual diameters for a range of droplet diameters generated by the monodisperse droplet generator. The agreement is excellent.

5.2 Water Spray Measurements

A typical raw signal obtained in a water spray is presented in Fig. 10. The low pass filtered signal is also presented in Fig. 10. In Fig. 11 the theoretical rainbow signal generated with the Airy theory is presented along with low pass filtered signal showing good agreement between the two. The measured "PDPA" and "rainbow" diameters are 54.8 μm and 58.2 μm, respectively, and the measured refractive index is 1.3340. Similar results are presented in Figs. 12 and 13 for a 24.9 μm droplet. The "rainbow diameter" is 25.4 μm and the refractive index is 1.3339.

Figure 14 presents a typical histogram of the measured droplet refractive index in a water spray using the real-time peak detection technique. The measured mean and standard deviation are 1.3335 and 0.0074, respectively. The measurement uncertainty based upon the standard deviation is about +/- 4.38% of the full scale range (1.26 - 1.43). The only data validation criteria available with the real-time processor are limits on the peak intensity and peak location. Applying this criteria we were able to validate 87.7% of the 200 rainbow signals. Figure 15 presents a histogram of the refractive index after processing the same data with the newly developed

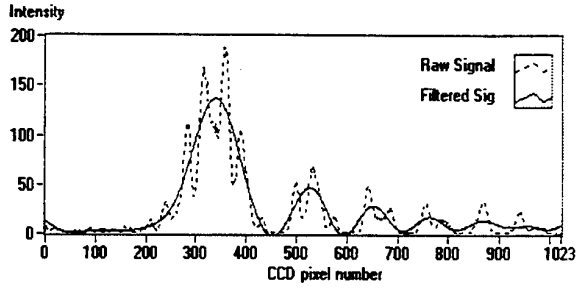

Figure 10: Raw signal and low-pass filtered rainbow signal for a 54.8 μm (measured by the PDPA) droplet in a water spray.

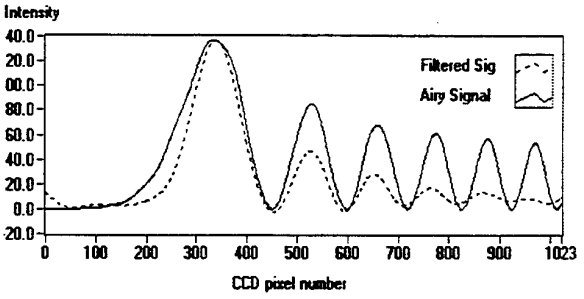

Figure 11: Low-pass filtered rainbow signal (shown in Fig. 10) compared with the Airy signal for a 58.3 μm droplet having a refractive index of 1.3340.

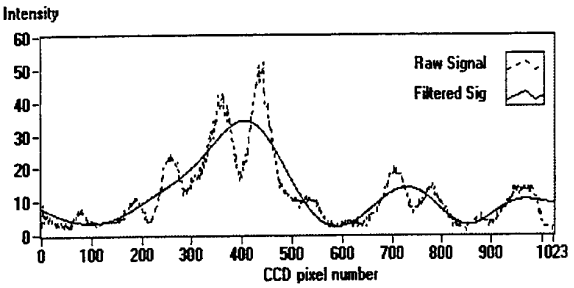

Figure 12: Raw signal and low-pass filtered rainbow signal for a 24.9 μm (measured by the PDPA) droplet in a water spray.

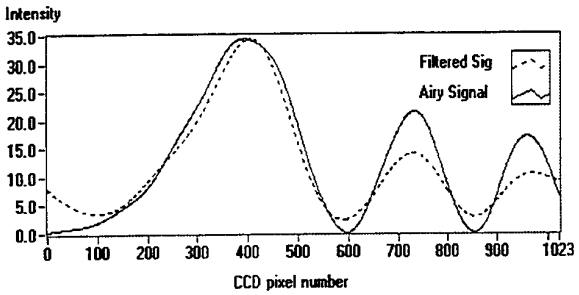

Figure 13: Low-pass filtered rainbow signal (shown in Fig. 12) compared with the Airy signal for a 25.4 μm droplet having a refractive index of 1.3339.

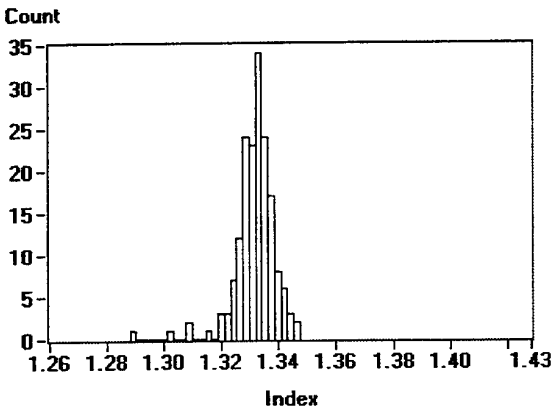

Figure 14: Histogram of the droplet refractive index measured using the real-time peak-detection based rainbow processor.

virtual processor. For this case, the measured mean refractive index is 1.3335, the standard deviation is 0.0029, and the data acceptance rate is 82.6%. The measurement uncertainty based upon the standard deviation is +/- 1.71% (of full scale range). This already shows an improvement in the measurement uncertainty by a factor of about 2.5 without significantly altering the data validation rate.

As mentioned earlier, the final validation step is to compare the "PDPA diameter" with the "rainbow diameter"

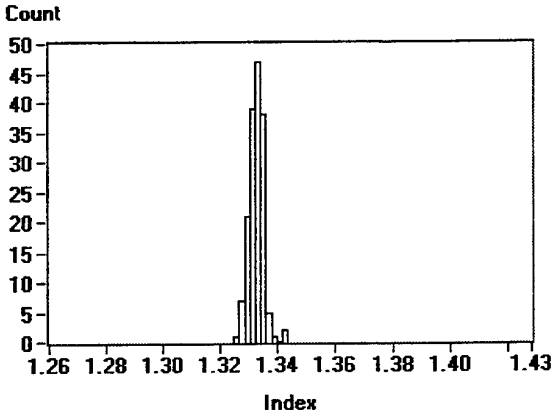

Figure 15: Histogram of the droplet refractive index measured using the rainbow post-processor.

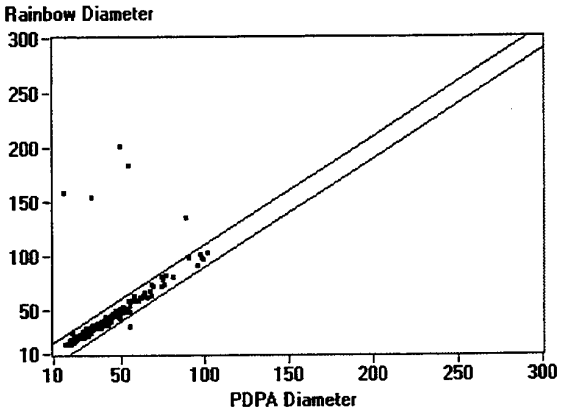

Figure 16: Comparison of the droplet diameters (in microns) as measured by rainbow refractometer and the PDPA.

and to reject data that do not agree to within a preset tolerance. Figure 16 presents such a comparison. The two straight lines shown in Fig. 16 represents the acceptance band; data for which the two diameters are different by more than 10 μm lie outside the acceptance band. Size histograms corresponding to the data lying within the acceptance band are presented in Figs. 17 and 18. Figure 17 shows the size histogram measured by the PDPA with a mean diameter of 40.4 μm and a standard deviation of 17.1 μm. The corresponding size histogram obtained with the rainbow refractometer is presented in Fig. 18. The measured mean diameter for this case is 40.9 μm and the standard deviation is 17.5 μm. The agreement between the "PDPA" and the "rainbow" diameter histograms is excellent. It is interesting to observe that the diameter standard deviation measured by the rainbow refractometer agrees very well with that measured by the PDPA even though a similar comparison for the monodisperse case showed that the "rainbow diameter" standard deviation was greater than that obtained with the PDPA. This is because the measurement uncertainty for each size class is spread into the neighboring size classes. It can also be observed that the histograms do not show the presence

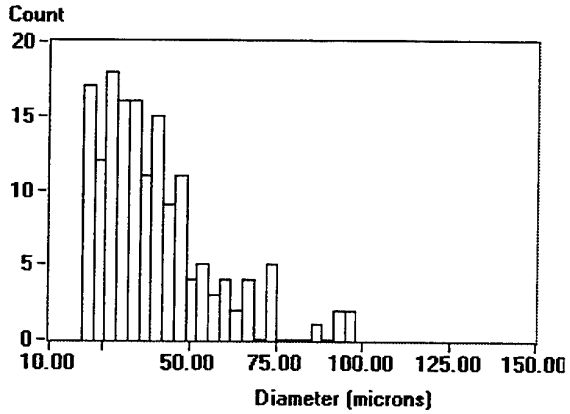

Figure 17: Size histogram measured by the PDPA. The mean diameter is 40.4 μm and the standard deviation is 17.1 μm.

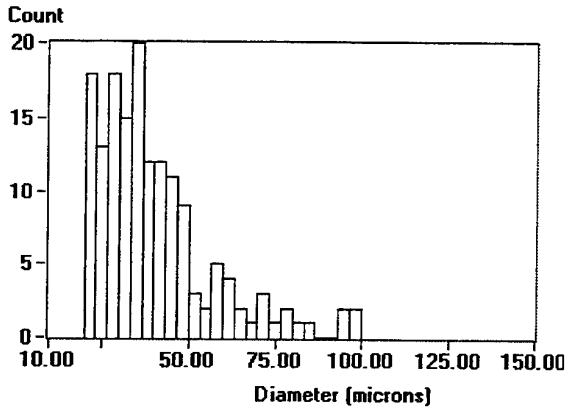

Figure 18: Size histogram measured by the rainbow refractometer. The mean diameter is 40.9 μm and the standard deviation is 17.5 μm.

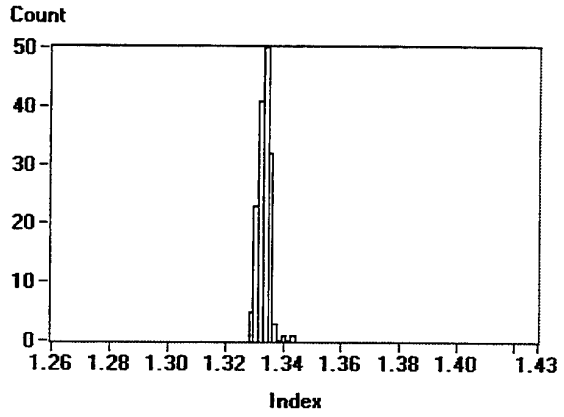

Figure 19: Histogram of the droplet refractive index after rejecting data for which the difference between the "PDPA" diameter and the "rainbow" diameter is greater than 10 μm.

of any particles less than 20 μm. This is due to the lower size limit imposed by the rainbow refractometer. In general, these results suggest the possibility of using the rainbow refractometer for sizing particles greater than about 20 μm (in addition to refractive index measurement).

Figure 19 shows the computed histogram of the droplet refractive index after applying this validation criteria. This results in a mean refractive index of 1.3334, a standard deviation of 0.0023, and a data acceptance rate of 80%. The measurement accuracy is now +/- 1.34% which is about 3.3 times better than what was achievable with the real-time processor.

Finally, comparing the results of the water spray and the monodisperse droplets, we find that the measurement uncertainty in a spray is about 2-3 times worse than that achievable with a stream of water droplets. The major reason for this discrepancy is attributed to the fact that a range of particle trajectories are possible in a spray causing a lateral displacement of the rainbow signatures. These errors are expected to be eliminated in the new optical design for the rainbow receiver that has just been completed.

6. CONCLUSIONS

A virtual rainbow processor has been developed to yield improved accuracy and reliability in droplet refractive index and temperature measurement. It has been shown that the measurement accuracy achievable with this processor is 3-4 times better than that achievable with a real-time peak detector. Because the virtual processor makes use of the Airy theory, it has the potential for detecting and rejecting data resulting from non-spherical and inhomogeneous droplets, as well as from multiple droplets and noise. In the future, the algorithms used in the virtual processor will be used to code a DSP or even in the development of a dedicated hardware processor.

7. ACKNOWLEDGMENTS

The authors would like to acknowledge the consulting services provided by Dr. William Mayo in this effort, and the exceptional support provided by our engineering team members, Mr. Alex Kindwall, Mr. Mehyeddine Alayleh, and Ms. Lien-Chun Chin.

8. REFERENCES

Airy, G.B., 1838, "On the Intensity of Light in the Neighbourhood of a Caustic," *Trans. Camb. Phil. Soc.*, Vol. 6, pp. 379-402.

Bachalo, W.D. and Sankar, S.V., 1994, "Factors Affecting the Measurement Resolution and Accuracy of the Phase Doppler Particle Analyzer," *2nd International Conference on Fluid Dynamics Measurement and its Applications*, Beijing, China.

Edwards, C.F. and Rudoff, R.C., 1990, "Structure of a Swirl-Stabilized Spray Flame by Imaging, Laser Doppler Velocimetry, and Phase Doppler Interferometry," *Proceedings, 23rd Symposium (Intl.) on Combustion,* Orleans, France, The Combustion Institute, pp.1353-1359.

Nussenzveig, H.M., 1977, "The Theory of the Rainbow," *Scientific American*, Vol. 236, pp. 116-126.

Presser, C., Gupta, A.K., Avedisian, C.T., and Semerjian, H.G., 1990, "Fuel Property Effects on the Structure of Spray Flames," *Proceedings, 23rd Symposium (Intl.) on Combustion,* Orleans, France, The Combustion Institute, pp.1361-1367.

Roth, N., Anders, K., and Frohn, A., (1990), "Simultaneous Measurement of Temperature and Size of Droplets in the Micrometer Range," *Journal of Laser Applications,* Jan./Feb, pp. 37-42.

Sankar, S.V., Ibrahim, K.M., Buermann, D.H., Fidrich, M.J., and Bachalo, W.D., 1993, "An Integrated Phase Doppler/Rainbow Refractometer System for Simultaneous Measurement of Droplet Size, Velocity, and Refractive Index," *3rd International Congress on Optical Particle Sizing,* Yokohama, Japan, August 23-26.

Sankar, S.V., Buermann, D.H., and Bachalo, W.D., 1994a, "Simultaneous Measurements of Droplet Size, Velocity, and Temperature in a Swirl-Stabilized Spray Flame," *7th Intl. Symp. on the Appl. of Laser Techniques to Fluid Mechanics,* Lisbon, Portugal, July 11-14.

Sankar, S.V., Buermann, D.H., Ibrahim, K.M., and Bachalo, W.D., 1994b, "Application of an Integrated Phase Doppler Interferometer/Rainbow Thermometer/Point-Diffraction Interferometer for Characterizing Burning Droplets," *25th Symposium (International) on Combustion, The Combustion Institute,* pp. 413-421.

Sankar, S.V., Buermann, D.H., Bachalo, W.D., and Robart, D.M., 1995, "Nonintrusive Characterization of Liquid-Liquid Mixing in Sprays," AIAA 95-0138, *33rd Aerospace Sciences Meeting and Exhibit,* Reno, Nevada, January 9-12, 1995.

Schneider, M. and Hirleman, E.D., 1994, "Influence of Internal Refractive Index Gradients on Sizez Measurements of Spherically Symmetric Particles by Phase Doppler Anemometry," *Applied Optics,* Vol. 33, No. 12, pp. 2379-2388.

van Beeck, J.P.A.J. and Riethmuller, M.L., 1995, "Nonintrusive Measurements of Temperature and Size of Single Falling Raindrops," *Applied Optics,* Vol.34, No.10.

van de Hulst, H.C., 1957, *Light Scattering by Small Particles,* Dover Publications, Inc., New York.

Wang, R.T. and van de Hulst, H.C., 1991, "Rainbows: Mie Computations and the Airy Approximation," *Applied Optics,* Vol. 30, No. 1, pp. 106-117.

Investigations on Accuracy and Resolution of Refractive Index Measurements with an Extended Phase-Doppler Anemometer

G. Brenn, C. Tropea, T.-H. Xu
Universität Erlangen-Nürnberg, Lehrstuhl für Strömungsmechanik
Cauerstraße 4, D-91058 Erlangen, Germany

ABSTRACT

Detailed computations on the performance of an extended phase-Doppler anemometer using Generalized Lorenz-Mie Theory were carried out to investigate the sources of deviations of measured refractive indices from the correct values. A clear effect of the drop trajectory through the probe volume was found, leading to deviations of up to -8% for $65\mu m$ water drops with a $60°/30°$ system (circular receiving apertures). Trajectories on the measurement volume side of the receiving units yield correct measurements for particles larger than $37\mu m$. Rectangular receiving apertures yield results which depend on the aperture orientation in space. Additional FLMT computations show that, for all considered particle sizes and scattering angles used, the first order refracted light dominates, but the intensity of reflected light increases considerably for drop trajectories on the probe volume side opposite from the receivers.

1 INTRODUCTION

Since the first works by *Naqwi & Durst (1990)*, *Pitcher et al. (1990)* and *Naqwi et al. (1990)*, the extended phase-Doppler anemometry (EPDA) has been the subject of detailed studies evaluating its potential for the measurement of the refractive index of scattering particles. Furthermore, *Naqwi et al. (1992)* pointed out that an EPDA setup may be used for fine particle sizing using the method of joint probability density functions (JPDF) for data processing. *Brenn & Durst (1995)* quantified the resolution of the EPDA both experimentally and by computations based on Geometric Optics. Experimental results showed large scatter of the refractive index measurements in polydisperse sprays, while the statistical reliability of the measurements was one order of magnitude better in monodisperse drop streams. In order to improve the accuracy of the refractive index measurements, *Qiu & Hsu (1995)* proposed an asymmetric arrangement of the four photodetectors and carried out computations on the error in the refractive index measurements caused by the Gaussian Beam Defect and the scattered light intensity for four selected drop sizes as a function of the location of the particle trajectory relative to the probe volume center. These authors used the ratio of two phase shifts measured with one of the receiving optics units to control the accuracy of the refractive index measurement.

In existing literature, detailed computations on the accuracy of the refractive index measurement with a standard EPDA cannot be found. The present paper fills this gap by providing results of computations based on Generalized Lorenz-Mie Theory (GLMT) (*Gouesbet 1994*) on accuracy and resolution of the standard EPDA. Section 2 summarizes the present state of development of the EPDA technique. In Section 3, the results of computations with different receiving aperture shapes and the role of different scattering modes are described and discussed; Section 4 compares some of these results with experimental data obtained in monodisperse drop streams and in polydisperse sprays. The paper ends with conclusions and suggestions for improvements of the system.

2 STATE OF DEVELOPMENT OF EPDA

Since some years, the potential and limitations of the EPDA technique have been subject of extensive experimental investigations. Experiments with a setup such as the one shown in Fig. 1 have shown that, for monodisperse drops, the refractive index measurements may be very accurate and exhibit narrow distributions. Typical results of measurements in monodisperse drop streams of water ($d_{p,w} = 72.1\mu m$, $m_w = 1.334$) and ethanol ($d_{p,e} =$

$86.3\mu m$, $m_e = 1.361$) are shown in Fig. 2. The achieved accuracies and normalized standard deviations of the distributions are (−0.6%, 0.8%) and (−1.26%, 0.92%) respectively. However, the uncertainty of the refractive index measurements increases drastically in polydisperse sprays, as shown in Fig. 3. The deviation of the measured refractive index from the correct value is again small ($\bar{m} = 1.352$, normalized deviation 1.3%), but the standard deviation of the measured distribution is about eight times as large as in the monodisperse case (6%).

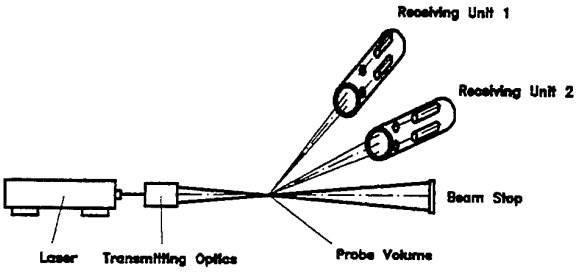

Figure 1: Optical configuration of a standard EPDA. The two receiving units are placed at different scattering angles.

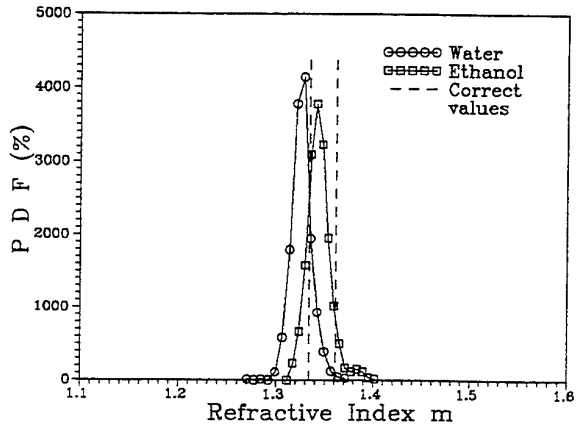

Figure 2: Probability density distributions of refractive index measurements of monodisperse streams of water and ethanol. The fluctuations of the drop size in the data sets are less than ± 0.7%. The measured values are $\bar{m}_{w,m} = 1.326$ and $\bar{m}_{e,m} = 1.344$ respectively.

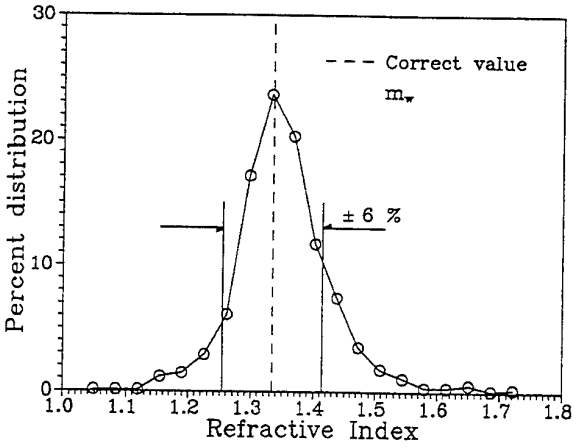

Figure 3: Probability density distribution of the refractive index measured in a polydisperse water spray. The number mean drop size at the point of measurement (90mm downstream the spray nozzle, center of the spray) was $D_{10} = 51.6\mu m$.

Presently, the sources of these errors are still unidentified, and it is the purpose of this paper to provide quantitative computational results which clarify the reasons for the broadening of the refractive index distribution in polydisperse sprays.

3 COMPUTATIONAL INVESTIGATIONS

For the computational simulations of the EPDA system shown in Fig. 1 (data in Table 1), the Generalized Lorenz-Mie Theory (GLMT) was used (*Gouesbet 1994*). This theory provides a complete descrip-

Table 1: Geometrical configuration of the standard EPDA system simulated by GLMT.

Laser wavelength	632.8 nm
Beam crossing half-angle α	1.69°
Probe volume diameter b_y	279 μm
Off-axis angle ϕ_1	60°
Off-axis angle ϕ_2	30°
Elevation angles ψ of detectors	±3.69°
Receiving cone half angle of circular aperture	2.77°

tion of light scattering by spherical particles including effects arising from the non-uniform illumination of the particle ("Gaussian Beam Defect"). The computations were carried out for drop sizes within the measurement range of the two PDA systems at

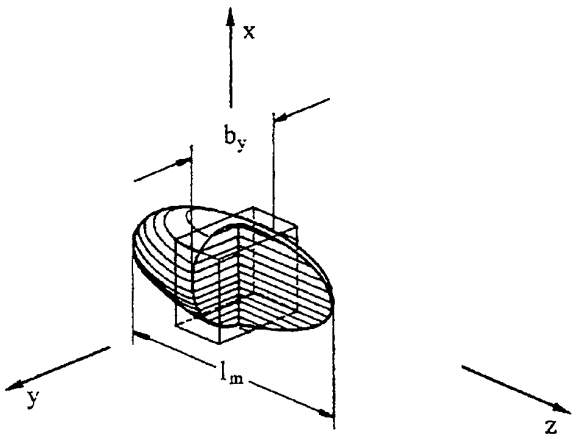

Figure 4: Geometry of the probe volume and coordinate system. The laser beams establish the x/z plane, the receivers are located in the half-space with positive y.

$60°$ and $30°$ with a stepwidth of $\Delta d_p = 0.1\mu m$. This fine size resolution was necessary to achieve sufficient resolution of refractive index fluctuations within each size class given by the PDA size measurements. Different particle locations y with a stepwidth $\Delta y = 20\mu m$ were investigated (for coordinate system refer to Fig. 4). The main direction of motion of the drops is the x direction. The coordinates x and z of the particle were set to zero, as preliminary investigations showed that a variation of these coordinates had no significant influence on the results. The computations were carried out for water.

One further influencing parameter of the system is the shape of the receiving aperture. Circular and rectangular apertures were simulated, where the orientation of the rectangular aperture was set parallel and perpendicular to the interference fringes.

The computations yielded scattered light power, half phase angle and visibility as a function of the particle size for the two scattering angles $60°$ and $30°$. From these results, phase shift ratios were computed and used for the refractive index computation using the equation (*Brenn & Durst, 1995*)

$$m = -\frac{1}{2}\frac{\sqrt{f_2} - A\sqrt{f_1}}{A-1} + \sqrt{\left(\frac{1}{2}\frac{\sqrt{f_2} - A\sqrt{f_1}}{A-1}\right)^2 - 1}\ , \tag{1}$$

where

$$f_1 = 2\,(1 + \cos\alpha\cos\psi_1\cos\phi_1)$$

$$f_2 = 2\,(1 + \cos\alpha\cos\psi_2\cos\phi_2)$$

$$A = \left(\frac{\Phi_1}{\Phi_2}\frac{\sin\psi_2}{\sin\psi_1}\right)^2 \frac{f_1}{f_2}\ .$$

The quantity Φ_1/Φ_2 is the phase shift ratio. This equation was derived from Geometric Optics and it is commonly used for determining the refractive index from measured phase shift ratios in processing software.

In the following sections, the computational results for the different receiving apertures are presented and discussed.

3.1 Circular Receiving Aperture

The computational results obtained with a circular receiving aperture for the above EPDA system are shown in Fig. 5. The diagram depicts the refractive index computed from the ratio of the computed phase shifts at the two scattering angles as a function of the drop size. The varied parameter is the y coordinate of the drop location in the probe volume. The curves give detailed information about the behaviour of the EPDA system.

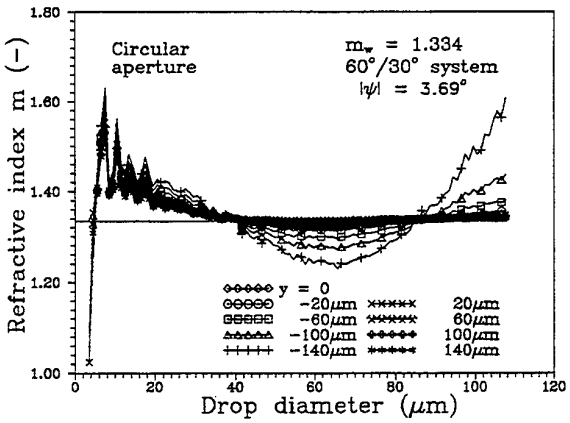

Figure 5: Simulated refractive indices as a function of the drop size for varying coordinate y_p of the particle position (circular receiving aperture, $x_p = z_p = 0$).

- The Gaussian Beam Defect causes the refractive index measurement of large drops located in the probe volume opposite from the detectors ($y < 0$) to be incorrect by up to -8% ($d_p = 65.5\mu m$) and $+21\%$ ($d_p = 108\mu m$). The deviations are all negative for drop sizes between $40\mu m$ and $87\mu m$, and positive outside this range (except for some small sizes below $10\mu m$).

- The curves for $y > 0$ show that these drop locations in the probe volume yield correct refractive index measurements for drop sizes larger than $37\mu m$. The correct value $m_w = 1.334$ is given by the horizontal solid line in the graph.
- All curves together exhibit two node points at $d_{p1} = 40\mu m$ and $d_{p2} = 87\mu m$. These drop sizes differ from the node points of the detectors at $30°$ ($d_{n1,30} = 48.3\mu m$ and $d_{n2,30} = 96.5\mu m$) and $60°$ ($d_{n1,60} = 78.4\mu m$ and $d_{n2,60} = 156.9\mu m$), which are defined by equality of the phases from refracted and reflected light. The observed node points of the EPDA are lying closer to those of the $30°$ detectors than to the $60°$. This means that the higher intensity of reflected light at $30°$ dominates the location of the EPDA node points. Note that the refractive index at the node points is not only equal for all trajectories, but also correct.
- The deviations between the curves vanish almost completely for drop sizes less than $12\mu m$. Above this size, the Gaussian Beam Defect leads to an influence of the drop location on the refractive index measurements (except the node points).
- The large deviations of the curves from the correct value for drop sizes less than $36\mu m$ were also predicted by LMT computations (*Brenn & Durst, 1995*). They are due to the light scattering process which is characterized by a very fine lobe structure of the scattered light for small particles (Mie parameter less than 178).

The conclusion from these results is that, even for monodisperse drops, refractive index measurements may be significantly wrong if the drops pass through the probe volume on a trajectory in x direction opposite from the detector units.

Due to the size resolution of $0.1\mu m$ in the computations, 10 computational results on the refractive index are available in every size class with a width of $1\mu m$. These values were treated statistically to get information about the fluctuations of the refractive index measurements caused by the physics of the light scattering process. The standard deviations of the refractive index distributions inside each size class of width $1\mu m$ are shown as error bars on the curves in Fig. 6. For clarity, only the curves for $y = \pm 140\mu m$ are shown. The error bars show regions of fluctuations, within which the refractive index measurements for drops of given size may lie. The y coordinate which leads to correct refractive index measurements exhibits small fluctuations. This

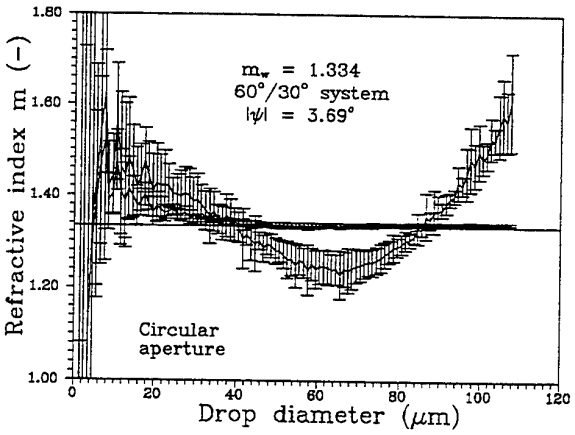

Figure 6: Fluctuations of the refractive index within each size class of 1 μm width as a function of the drop size for $y = \pm 140\mu m$. The curve with the large fluctuations belongs to $y = -140\mu m$.

gives a first estimate of uncertainties in the refractive index measurements which must be expected from the physical properties of the light scattering process and, therefore, cannot be avoided. Additional uncertainties are due to the limited resolution of the EPDA caused by the uncertainty of the phase shift measurement. This will be discussed later when experimental data are compared with the theoretical results.

3.2 Rectangular Receiving Aperture - Horizontal

In commercially available PDA systems, the receiving apertures are more or less rectangular in shape with the orientation of the longer side of the rectangle parallel to the interference fringes of the probe volume ("horizontal"). Such an aperture, with half-angles of $\delta_x = 2.77°$ and $\delta_y = 0.277°$ was also simulated computationally. The results for various y locations of the particle in the probe volume are depicted in Fig. 7. The behaviour of the curves as a function of the particle size with varying y coordinate of the particle position is similar to the curves obtained with circular aperture. The node points of the curves occur at the same drop sizes, and the deviations of the "measured" refractive index from the correct value have the same orders of magnitude. Only in the range of small particle sizes the computed refractive indices may take far larger values in some cases than with the circular aperture. This, however, does not affect the behaviour of the EPDA, as in the small particles range, the fluctuations of the

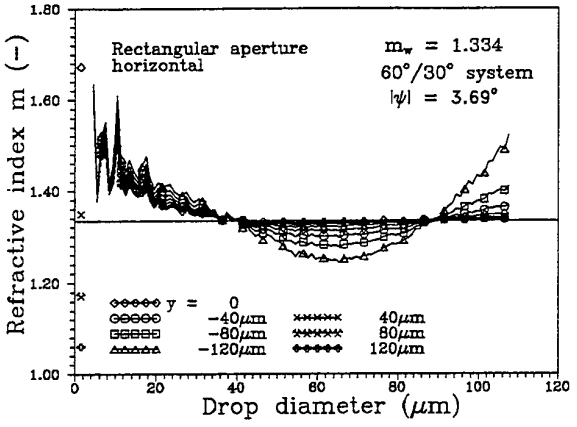

Figure 7: Simulated refractive indices as a function of the drop size for varying y coordinate of the particle position (rectangular receiving aperture, orientation horizontal).

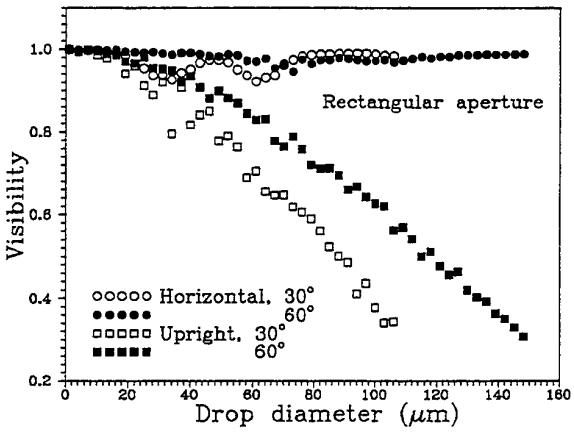

Figure 9: The visibility of the particles for the different rectangular apertures as a function of the particle size.

refractive index with varying particle size are large anyway. It is furthermore worth noting that, with this aperture, the trajectory $y = 0$ yields deviations of the refractive index from the correct value larger than with the circular aperture.

3.3 Rectangular Receiving Aperture - Upright

In addition, the effect of a rectangular aperture rotated by 90° on the refractive index was examined ($\delta_x = 0.277°$ and $\delta_y = 2.77°$). Without computations it can be forecast that this leads to a decrease of the visibility of the particles, since with this orientation of the receiving aperture many fringes are visible on the detector owing to the longer side of the rectangle being orientated rectangular to the fringes ("upright aperture").

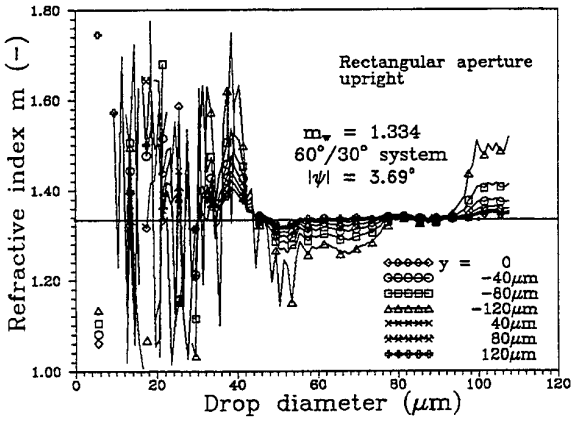

Figure 8: Simulated refractive indices as a function of the drop size for varying y coordinate of the particle position (rectangular receiving aperture, upright).

The results of these computations are shown in Fig. 8. The curves show smaller errors in the refractive index for drop sizes between the node points than the horizontal aperture. The node points are shifted to $44\mu m$ and $85\mu m$ (with a range of particle sizes between $85\mu m$ and $92\mu m$ where the curves coincide), but large fluctuations and errors of the refractive index measurement occur for particle sizes less than $40\mu m$. Figure 9 shows the comparison of the visibility of the particles for the two rectangular apertures discussed here. From the strong decrease of the visibility with increasing drop size for the upright aperture we can conclude that the advantages of this aperture orientation regarding the refractive index measurements may be negated by the low visibility which causes practical problems.

3.4 The Role of Different Scattering Modes in the Refractive Index Measurements

Using the FLMT technique developed by *Albrecht et al. (1994)*, our colleagues at Rostock University investigated for us the contributions of different scattering modes to the scattered light. These computations were carried out in order to find physical reasons for the behaviour of the EPDA in refractive index measurements. Computations were carried out

for the three particle sizes $40\mu m$, $64\mu m$ and $87\mu m$, i.e., at the node points of the curves obtained in the GLMT computations for circular receiving aperture and at one intermediate size. The influence of the x and y coordinates of the particle position in the probe volume was investigated.

The FLMT computations yield the following results:

- For all treated particle positions, scattering angles and particle sizes, the scattered light intensity of first order refraction is higher than the intensity due to reflection. The scattered light detected by the receivers is therefore dominated by first order refracted light, but for drop sizes above $40\mu m$ (except the node points) the contribution of reflection influences the measured phase angle and therefore the refractive index computed from the phase shift ratio. For $\phi = 30^o$, the intensity ratio reflection/first order refraction is $6.5 \cdot 10^{-2}$ at $y = -100\mu m$ and $6.8 \cdot 10^{-3}$ at $y = +100\mu m$, i.e., one order of magnitude higher at the negative y location than for positive y, indicating the stronger influence of reflection at $y < 0$.

- The phase difference between the detectors at the elevation angles $\psi_{i,1} = -3.69^o$ and $\psi_{i,2} = +3.69^o$ for both scattering angles i is constant for varying particle coordinate x, i.e., during the transit of the particle through the probe volume. The phase differences at 60^o and 30^o exhibit ratios which yield the refractive indices obtained from the GLMT computations with only slight deviations.

- From the FLMT computations, the phase for purely reflected light is obtained. Using these values for the computation of the refractive index, results are obtained which are smaller than the correct value. This clearly identifies the effect of reflected light on the refractive indices obtained for drop sizes between $40\mu m$ and $87\mu m$, leading to too small values.

3.5 Resolution of the EPDA

The resolution of the EPDA considered here is the difference of two values of the refractive index, between which the system can distinguish reliably. The resolution varies with the drop size, as has been shown quantitatively by *Brenn & Durst (1995)* using Geometric Optics. The present GLMT data enable the resolution of the EPDA to be computed more realistically.

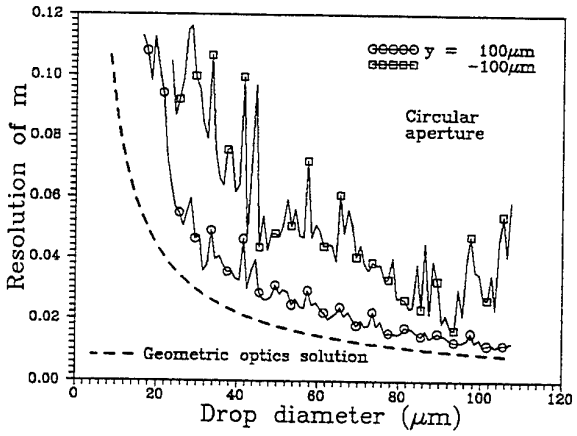

Figure 10: Resolution of the EPDA system with 60^o / 30^o as a function of the drop size. The dashed line represents the results of the geometric optics computation by *Brenn & Durst (1995)*.

The resolution is influenced by two different effects. First, fluctuations of the refractive index within each size class (here of constant width $1\mu m$) are caused by the light scattering, which represent one component of the resolution (or measurement uncertainty). Second, the phase shift measurement of the EPDA system is subject to an uncertainty which, for the present system, may be estimated to be $\pm 1^o$. Due to this effect, an additional uncertainty is introduced which must be added to the above uncertainty. Results of the computation of this composed uncertainty are shown in Fig. 10. For comparison, the dashed line in the diagram represents the results of the Geometric Optics computations. It can clearly be seen that the resolution in reality is worse than predicted by Geometric Optics. For positive y both results converge with increasing drop size. These results confirm the experimental result indicating that, for drop sizes below $40\mu m$, the difference between the refractive indices of two spray components should be larger than 0.06 in order to obtain reliable discrimination between the components.

4 COMPARISON OF EXPERIMENTAL AND COMPUTATIONAL RESULTS

Diagrams with computational results as in Figs. 5 through 7 suggest a comparison with results from refractive index measurements in monodisperse drop streams and polydisperse pure-liquid sprays. Such measurements were carried out by *Brenn & Durst*

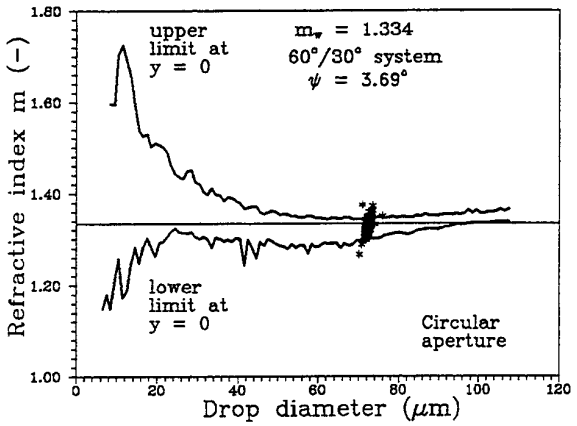

Figure 11: Comparison of experimental data obtained in a monodisperse water drop stream with the computed uncertainty range in the refractive index for $y = 0$.

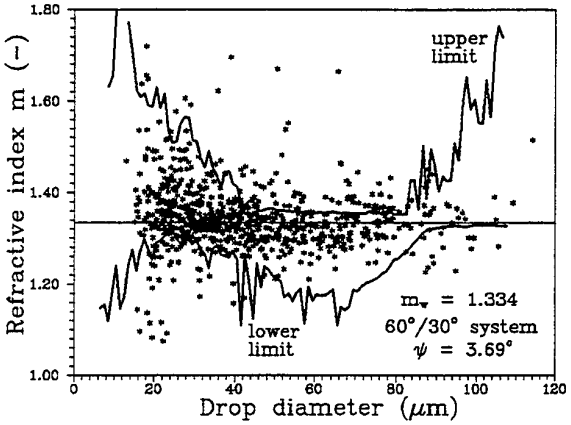

Figure 12: Comparison of experimental data obtained in a polydisperse water spray with computed uncertainty ranges in the refractive index for $|y| \leq 140\mu m$.

(1995) with a 60°/30° EPDA (circular apertures). The data are used here for comparison.

The range of scatter in the measured refractive indices is expected to be at least as large as the computed range. The range is limited by an upper and a lower curve as a function of the drop size. These curves were computed by adding to the maximum and subtracting from the minimum occuring computed refractive index in each size class the resolution of the instrument obtained from the Geometric Optics computation (*Brenn & Durst 1995*). Measurements in monodisperse water drop streams exhibit narrow refractive index distributions and even narrower drop size distributions. The data set for the water drops shown in Fig. 2 is depicted in Fig. 11 as a cloud of data points (asterisks). The upper and lower curves in the diagram are computed with the refractive index fluctuations obtained for the trajectory $y = 0$. The experimental data cloud is very narrow in both directions and exceeds the expected range of refractive indices only slightly. The drop sizes were computed with the known (and correct) refractive index $m_w = 1.334$.

The same comparison was carried out with a data set from measurements in a polydisperse water spray. For this case, the limiting curves were computed taking all trajectories $|y| \leq 140\mu m$ into account. The data are shown in Fig. 12. The scatter of the data points in the drop diameter direction reflects the drop size spectrum at the point of measurement in the polydisperse spray; the scatter in the refractive index exceeds the range predicted by the computations only slightly in some regions. The vast majority of the data coincide with the computed range. This indicates that most of the measurement deviations from the correct value are caused by the physics of the light scattering process and, therefore, cannot be avoided with circular receiving apertures.

5 CONCLUSIONS

Detailed computational investigations on the performance of a standard EPDA system for refractive index measurements were carried out. The results quantify the reliability of the measurements as a function of the drop size. For drops smaller than $37\mu m$, the computations indicate large fluctuations in the refractive index, regardless of the drop trajectory. For sizes above $37\mu m$, drop trajectories with positive y coordinate yield correct refractive index measurements, but errors depending on the drop size occur for negative y_p.

The computations show that the errors depend on the shape of the receiving aperture. Circular apertures and rectangular apertures with the long side of the rectangle parallel to the interference fringes exhibit the above described behaviour. For the rectangular aperture, however, the drop trajectory at $y = 0$ still leads to refractive index errors, while the results are correct with the circular aperture. Computations for a rectangular receiving aperture rotated by 90° ("upright" orientation) yield different results which indicate advantages for the refractive index measurements. Computations with FLMT allowed to quan-

tify the role of reflected light for the refractive index measurement errors.

Comparisons of experimental data with the computations show that most of the refractive index fluctuations obtained with monodispersed drops are due to the light scattering process itself (as these drops have a constant trajectory). The fluctuations of refractive index data obtained in polydisperse sprays also compare well with the computational results. The correlation of drop size and refractive index covers the area limited by two curves computed with GLMT.

For further developments it seems to be necessary to suppress the reflected light completely, as it disturbs the refractive index measurements considerably. A step towards this solution is to choose larger scattering angles, which, however, reduces the resolution of the system (*Brenn & Durst 1995*). Another solution may be the use of a rectangular receiving aperture for sprays with large drop sizes. The orientation of the aperture is crucial, and for large drops the low visibility of the upright aperture may be acceptable because of high signal intensity. One measure to suppress reflected light completely may be the use of a planar EPDA.

ACKNOWLEDGEMENT

The support from our colleagues at Rostock University and TechnoTrans e.V., especially from Mr. Nils Damaschke, by carrying out the FLMT computations, is gratefully acknowledged.

REFERENCES

Albrecht, H.-E., Bech, H., Damaschke, N. & Feleke, M. 1995, Berechnung der Streuintensität eines beliebig im Laserstrahl positionierten Teilchens mit Hilfe der zweidimensionalen Fouriertransformation, Optik, vol. 100, pp. 118 ff.

Brenn, G. & Durst, F. 1995, Refractive Index Measurements Using the Phase-Doppler Technique, Atomiz. and Sprays, vol. 5, pp. 545 - 567.

Durst, F. & Naqwi, A., 1990, Optical Methods for Studies in Multiphase Flows, Proc. 2nd Int. Cong. Optical Particle Sizing, Tempe, Arizona (USA).

Gouesbet, G. 1994, Generalized Lorenz-Mie Theory and Applications, Part. Part. Syst. Charact., vol. 11, pp. 22 - 34.

Naqwi, A., Durst, F. & Liu, X.-Z. 1990, An Extended Phase-Doppler System for Characterization of Multiphase Flows, Proc. 5th Int. Symp. on Appl. of Laser Techn. to Fluid Mech., Lisbon (Portugal), paper 24.4.

Naqwi, A., Ziema, M. & Durst, F. 1992, Fine Particle Sizing Using an Extended Phase-Doppler Anemometer, Proc. 5th Europ. Symp. Particle Characterization (PARTEC), Nürnberg (Germany), pp. 267 - 279.

Pitcher, G., Wigley, G., & Saffman, M. 1990, Sensitivity of dropsize measurements by phase-Doppler anemometry to refractive index changes in combusting fuel sprays. Proc. 5th Int. Symp. on Appl. of Laser Techn. to Fluid Mech., Lisbon (Portugal), paper 14.4.

Qiu, H.-H. & Hsu, C.-T. 1995, Optimization of EPDA Parameters for Accurate Material Recognition in Multiphase Flow, Proc. 2nd Int. Conf. Multiphase Flow, Kyoto, Japan, vol. 1, paper IN-1.

PHASE-DOPPLER PARTICLE SIZING WITH OFF-AXIS ANGLES IN ALEXANDER'S DARKBAND - A PROMISING APPROACH FOR COMPLEX TECHNICAL SPRAY SYSTEMS

M. Willmann, A. Glahn and S. Wittig

Institut für Thermische Strömungsmaschinen
Kaiserstraβe 12
76128 Karlsruhe, Germany

ABSTRACT

A promising optical layout for standard phase-Doppler particle sizing instruments for use in complex technical two-phase flows is presented. Applied to turbine oil of variable temperature ($1.40 <= n <= = 1.46$) the layout procedure leads to several suitable off-axis angle configurations. From these a backscatter angle of $F = 125°$ is chosen due to geometrical restrictions. Although this angle lies in Alexander's darkband and the intensities are low, the theoretical analysis indicates that this configuration is extremely insensitive to Gaussian-beam defects, which usually aggravate backscatter applications.

Monosized droplet experiments confirm the application of the layout and show an acceptable accuracy of the measurements. Experiments in a bearing chamber test rig give reliable results and for the first time allow insight into the flow phenomena of this highly complex technical two-phase flow.

1. INTRODUCTION

Detailed investigations of complex technical two-phase flow phenomena which are required for many practical applications often suffer from severe geometrical constraints as well as from extremely difficult thermo-physical boundary conditions. With respect to droplet sizing and velocimetry in aero-engine bearing chambers, which is necessary in order to analyse heat to oil transfer problems and efficiency losses of jet engines, the phase Doppler Particle Analyzer (PDPA) is expected to be the only measuring device capable of the backscatter application demanded in rotating machinery. However, problems may occur due to temperature dependent fluid properties, i.e. the index of refraction, and the superimposition of low reflective light intensities with higher orders of refraction typical for the near backscatter range. Therefore, prior to measurements in this system a careful analysis of the performance characteristics of the instrumentation setup is strongly required.

The present paper deals with a general strategy to account for these effects. As a result, it will be shown that detailed simulation of light scattering is absolutely necessary for the design of a reliable measuring setup.

2. SCATTERING CHARACTERISTICS

Exposed to elevated temperatures, which are typical for jet-engine bearing chamber applications, turbine oils show refractive index values ranging from $n = 1.40$ to $n = 1.46$. Measurements with a Abbe-refractometer for temperatures up to 70°C are illustrated in Fig. 1 and can be continued to higher temperatures.

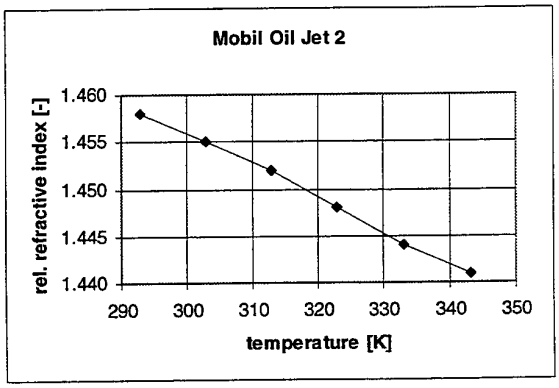

Fig. 1: Refractive index of turbine oil

From these values, the scattering behaviour of spherical droplets is calculated by means of the models from geometrical optics as suggested by van de Hulst (1981). The scattering diagram for the extreme case of very hot oil ($T = 450$ K, $n = 1.41$) is plotted in Fig. 2. In this diagram the gain for individual scattering modes is plotted versus the off-axis angle. In contrast to most other publications, the individual scattering modes are divided into submodes (e.g. $p = 2a, 2b$). These submodes result from scattered light rays of the same scattering mode but from different zones of the incident laser beam. The

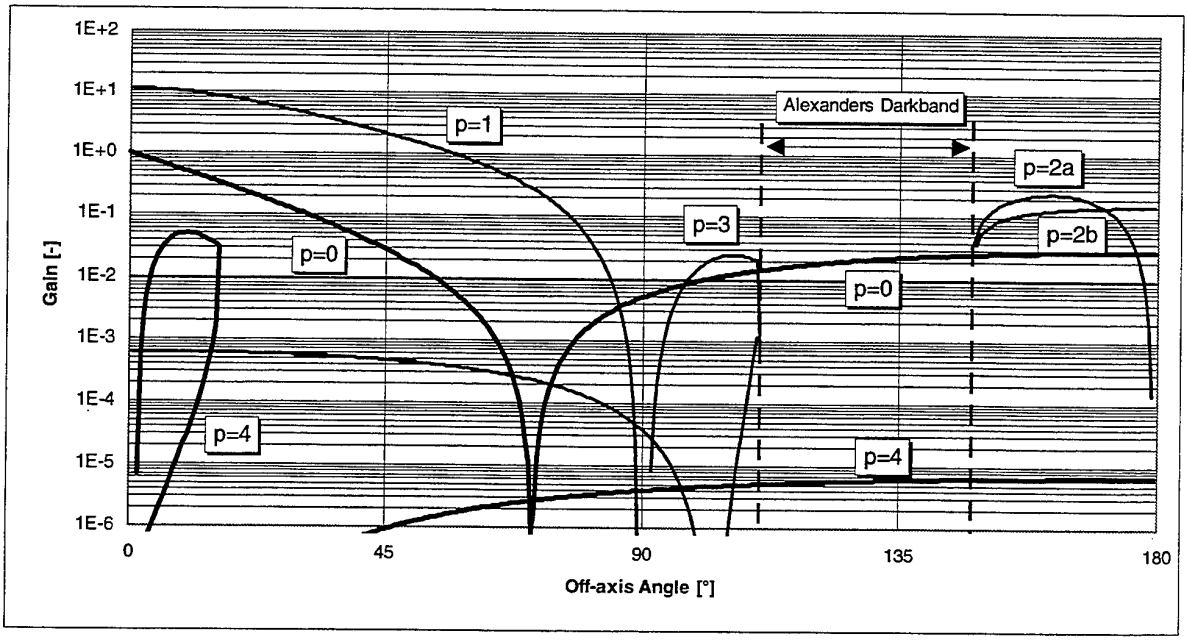

Fig. 2: Scattering characteristic, hot turbine oil (n=1.41), parallel polarization

actually scattered light results from a superimposition of all submodes with respect to their individual phase. From the geometrical optics point of view, each mode or submode produces an individual interference pattern on the detector plane when interfering with the light of another mode or submode of the same or another laser beam. It is well known, that proper phase-Doppler particle sizing is only possible, when one single mode or submode is dominant in intensity. In that case, the interference pattern is dominated by one single scattering mode of the two incident laser beams. The distance between the dominant and the following modes determines the sensitivity to errors caused by the Gaussian beam defect [Grehan et al. (1994), Willmann et al. (1994)].

3. THEORETICAL ANALYSIS

As a typical feature of fluids with high refractive indices, Alexander's darkband, the region between the two first rainbow angles, is widely extended between $\Phi = 110°$ and $\Phi = 145°$ off-axis. In this range, scattered intensity is very low and particle sizing requires rather high incident intensities. On the other hand, the reflected light ($p = 0$) is dominant in intensity resulting in linear phase-diameter correlations. In addition, since pure reflected light is used for sizing, measuring in that range is independent to refractive index changes or gradients inside the droplet. The selection of the detectors off-axis angle in the range between the two rainbow angles depends on two limitations: First, the angular distance between the outer edge of the detector and the rainbow angle should be as large as possible. This is due to idealizations made in geometrical optics resulting in sharp rainbow angles, where in reality a broad angular range for the rainbow is observed. From comparisons with Mie calculations performed with the 'STREU'-Code of Naqwi et al. (1991) it is clear, that this angular distance should be at least DF = 5°. As a second limitation, changes in the refractive index have to be accounted for, since they influence the overall scattering behaviour. Therefore, for all possible refractive indices in the two-phase flow under investigation Alexander's darkband must be wide enough to provide an additional angular range of about Dq = 10° for the detector plane, necessary to sample the low intensity light signals.

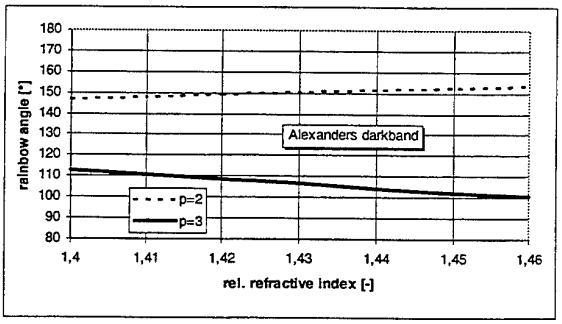

Fig. 3: Width of Alexander's darkband

From Fig. 3 it is obvious, that a mean off-axis angle of about F = 130° follows both above mentioned constraints for particle sizing in Alexanders darkband. With this off-axis configuration measurements are possible in the range from n = 1.4 up to n = 1.46 for the refractive index. For lower refractive indices, sizing in Alexander's darkband gets more and more difficult, due to the decrease of the distance between the two rainbow angles. Because of additional geometrical restrictions of the test rig, this angle

had to be reduced to $\Phi = 125°$ for the following investigations.

The calculated phase-diameter correlations in Fig. 4 for this off-axis configuration shows the expected linear behaviour and confirms the suitability of this configuration for phase-Doppler particle sizing.

From the work of Grehan et al. (1994) or Willmann et al. (1994) it is well known, that trajectory depending scattering may cause significant measurement errors when using a standard instrument. Furthermore, it is also well known that rejection algorithms using scattered intensities, as suggested by Bachalo et al. (1988) may fail especially in near backscatter applications, since scattered intensities of correct and erroneous signals do not differ significantly. One reason for this is the low distance between different scattering submodes as illustrated on the right hand side of the rainbow angle (p = 2a, 2b) in Fig. 2.

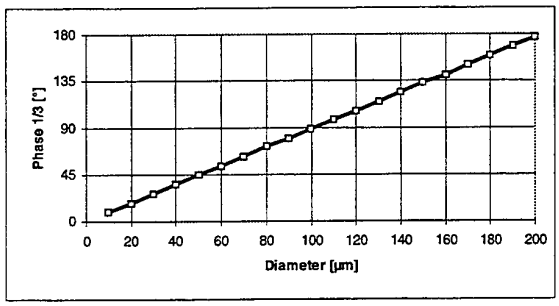

Fig. 4: Phase-diameter correlation (125° off-axis)

To avoid any of these trajectory dependent scattering effects for the configuration selected here, calculations were performed with the geometrical optics code PDCALC developed at the 'Institut für Thermische Strömungsmaschinen' at the University of Karlsruhe. The computer program, which is based on geometrical optics, simulates phase-Doppler configurations up to any desired order in the scattering mode. In addition to Gaussian beam effects, the code also allows to calculate slit-aperture effecs as discussed by Xu and Tropea (1994), which may cause serious errors, too. The program is validated with the generalized Lorentz Mie theory data of Grehan et al. (1994). The optimized structure of the code makes PDCALC to a powerful and efficient layout tool for phase-Doppler configurations.

The program was used to analyze the chosen off-axis angle configuration of $\Phi = 125°$. For these calculations a single, spherical droplet was virtually traversed in the scattering plane of the standard phase-Doppler instrument. Typical results are Fig. 5 and Fig. 6, which show the map of scattered intensities and the map of phase differences, respectively. The axis of these maps correspond to the middle of the traversed droplets. The calculations are based on a droplet diamter of d = 150 µm in a probe volume of d = 200µm, using a slitwidth of l = 200 µm. This configuration causes significant errors due to trajectory dependent scattering in typical forward scattering configurations.

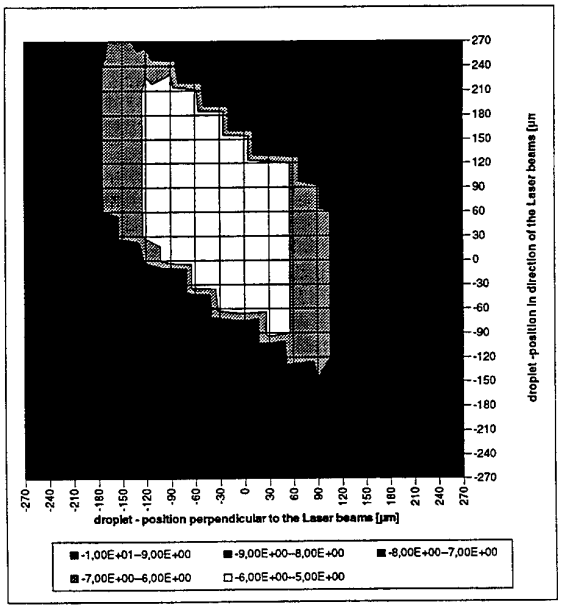

Fig. 5: Map of intensities (exponents)

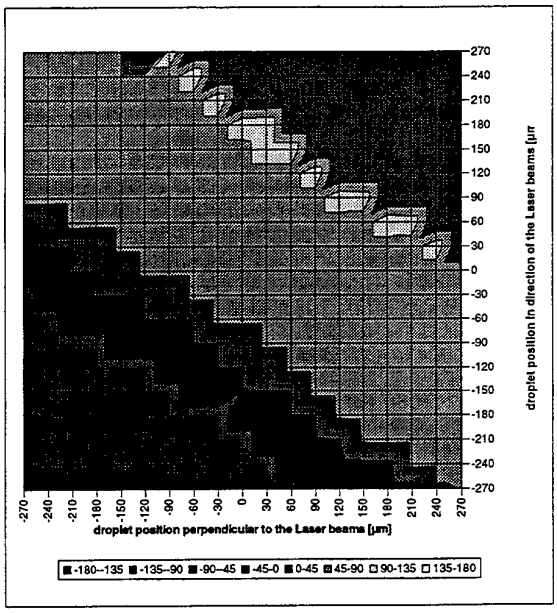

Fig. 6: Map of phase differences

The map of intensities shows the characteristic shape of the phase-Doppler probe area. It should be noted, that the legend shows the exponent of the scattered intensities. The two laser beams are directed vertically in a plane perpendicular to the plotted diagram and intersect at the position x = 0, y =0. The detectors observe the probe area from the lower right side. The maximum of intensity is observed at a particle position y = 30µm, which is due to the measuring volume displacement as described in Albrecht (1995). Intensity decreases continously to the left and right side due to the Gaussian intensity profile in the beam.

The diagonal bounds of the measuring volume in the other direction results from the slit-aperture effect as observed by Willmann et al. (1994) and described in detail by Xu and Tropea (1994). Additionally, a displacement from the center of the coordinate system is observed, resulting from similar effects as observed perpendicular to the laser beams.

However, it is obvious from this diagram and the corresponding data, that in directions perpendicular to the virtual slit-aperture the intensity distribution has a sharp edge where intensity decreases drastically by several decades over less than some microns of traversing.

As expected from the light scattering diagram in Fig. 2 no sensitivity to Gaussian beam effects is observed for this configuration. Across the probe area, in direction of the axis of the receive no significant change of the phase is observed. Nevertheless, phase changes occur when traversing in direction of the laser beams due to the slit-aperture effects. But the sharp edges in the intensity distribution shown in Fig. 5 suppress any phase errors. A detailed comparison clearly indicates, that scattered intensities at positions of 'erroneous' phase are lowered to values which are out of the intensity dynamic range of any common detector system. These observations have been confirmed up to droplet diameter values of about d = 1mm.

4. VALIDATION OF PHASE-DOPPLER SETUP

In order to justify this setup which has been solely derived from a numerical study, different off-axis configurations have been tested on a laboratory level using a single droplet generator in a well defined and calm environmental atmosphere.

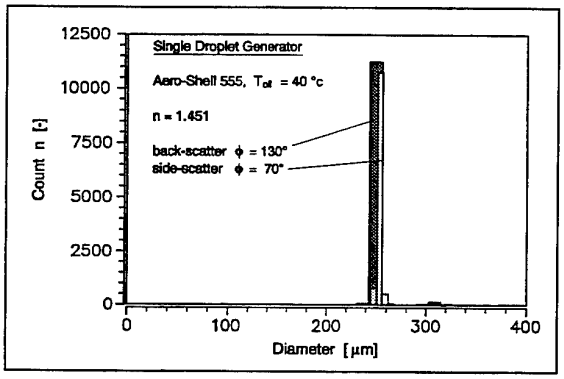

Fig. 7: Comparison of forward and backward scattering configurations

The comparison between the measurements at F = 70° and F = 125°, plotted in Fig. 7, indicates that both, the forward and the backward configuration show a satisfying agreement. These results confirm the chosen off-axis configuration, especially since no trajectory dependent scattering effects were observed in the monosized droplet experiments.

5. APPLICATION TO AERO-ENGINE BEARING CHAMBERS

5.1 BACKGROUND AND RIG ADAPTION

The assessment of phase-Doppler particle sizing setups in Alexander's darkband as described above has been initiated by some of the demands given in the design of aero-engine bearing chambers. Today, a major task within the calculation of flow rates required in lubrication systems of jet-engines is the proper matching of heat transfer to the oil. Besides friction inside the bearings, one has to deal with several other heat transfer phenomena such as oil film convective heat transfer at the housing walls, heat transfer from the sealing air to the disperse phase and churning processes inside the bearing chamber.

Obviously, the latter topics require a sufficient knowledge of droplet flow characteristics. Unfortunately, correlations for droplet sizes and velocities in bearing chambers are not available up to now. In order to overcome the severe drawbacks arising from this lack of data, the bearing chamber test rig available at the 'Institut für Thermische Strömungsmaschinen', which is capable to simulate aero-engine operating conditions given by high rotational shaft speeds of $n_s = 16000$ rpm and enhanced temperatures of $T_{max} = 200°C$, has been adapted to the PDPA measurement technique. Design considerations and a description of the rig and its facility components are given elsewhere [e.g. Wittig et al. (1994), Glahn and Wittig (1995), (1996)]. However, some comments referring to the measuring conditions and the PDPA adaption requirements should be included here.

A cross-sectional view of the test rig is shown in Fig. 8 for a co-axial plane located at a circumferential position of $\varphi=45°$ measured counter-clockwise from the horizontal. The roller bearing under investigation is located between the two bearing chambers signed with 'I' and 'II'. Droplet flows that are generated by atomization of lubrication oil in the roller bearing have been investigated in bearing chamber II at a distance of $\Delta r=3.25$ mm from the rotor and $\Delta z=4.1$ mm from the bearing, respectively. The chamber is pressurized to $p_n \approx 3$ bar by the sealing air entering through a three-fin labyrinth in chamber II and discharged through a vent at the top ($\varphi=90°$). Oil emanating from the bearing is carried by the air flow through the vent system or scavenged from the bottom of the chamber by pumps, respectively.

The adaption of the measuring technique is reflected by additional efforts in order to establish an optical access for the transmitting laser beams and the receiving optics. Special window configurations have been designed in order to avoid droplet containment on glas surfaces in the optical path. As shown in Fig. 8, they consist of conical tubes that are purged by compressed air, which is supplied as a cleaning air film over the inner side of the window by tangential nozzels. Any droplets emanated from the chamber into the window unit are driven radially outwards due to the swirl of the purge flow. Mixtures of air and small quantities of oil then are discharged through radial holes at the root of the tube. In order to minimize any reaction of the cleaning air flow on the bearing chamber atmosphere, a series of reference

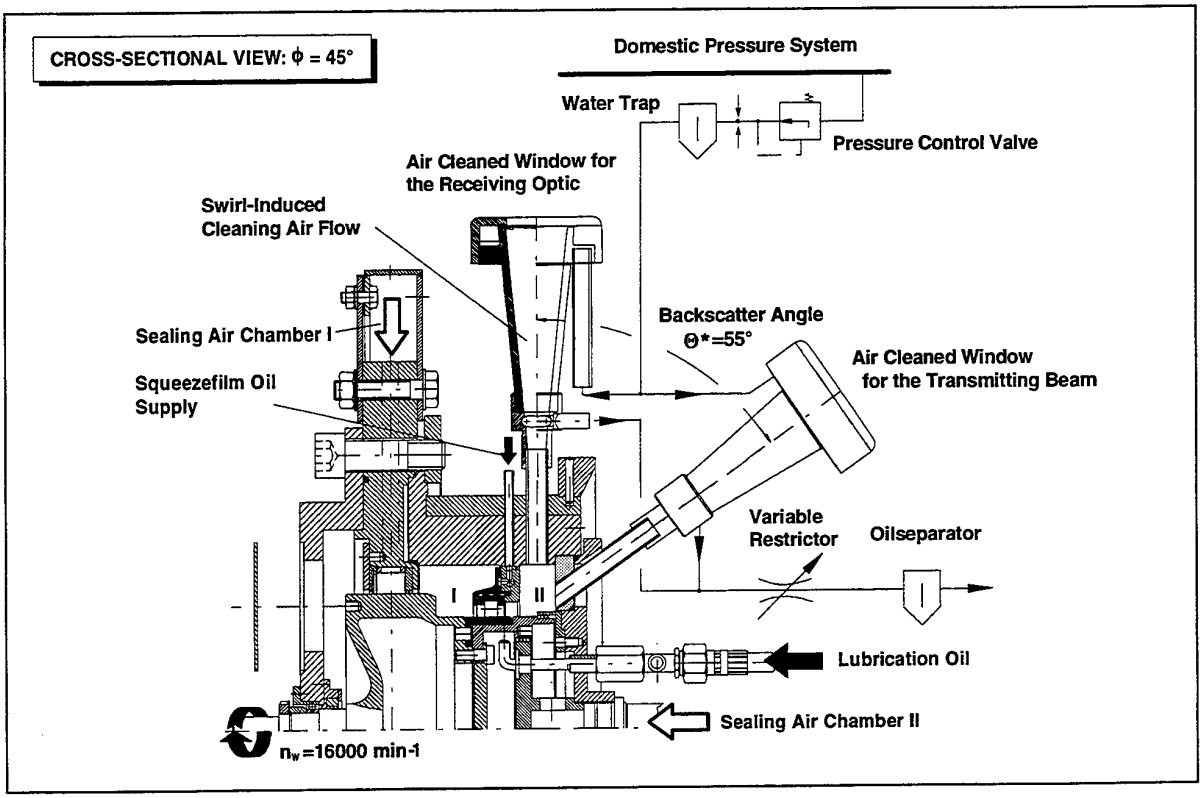

Fig. 8: Rig adaption

measurements has been performed prior to the phase-Doppler adaption, which includes bearing chamber pressures and air flow balances for operating conditions such as rotational speed and flow rates. The purge air which impacts on the bearing chamber flow has been assessed to be negligible in the event that the same pressure and air balances have been obtained for both setups, i.e. with and without phase-Doppler window-unit adaption.

5.2 DROPLET FLOW IN BEARING CHAMBERS

The objective of the present paper is to show a general strategy for an adaption of phase-Doppler sizing techniques to complex technical spray systems. Therefore, results of our bearing chamber flow investigations presented in this subsection are of exemplary nature. However, Fig. 9 shows distributions of diameter and velocities for typical bearing chamber conditions give by flow rates of $\dot{m}_{II}$ = 10 g/s and $\dot{V}_{II}$ = 100 l/h and a speed of n_s = 12000 rpm as they are reduced from individual diameter/velocity correlations by use of the standard data acquisition system.

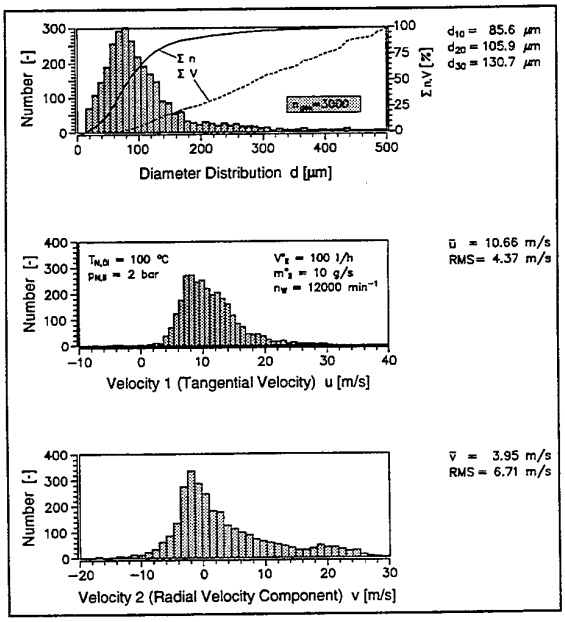

Fig. 9: Diameter and velocity distributions for typical aero-engine bearing chamber conditions

Obviously, the droplet flow in bearing chambers can be characterized by a large number of droplets in the range of 20 µm < d_d < 180 µm with a maximum at approx. d_d = 80 µm and, in addition, by larger droplets up to d_d < 500 µm which are less frequent but must not be neglected, since they represent a large amount of the overall liquid mass flow.

In technical flow systems as given in bearing chambers, mean and RMS values are not suitable parameters to give representative information about complex flows which often show multi-modal distributions. In order to overcome any misinterpretation, a reduction of measured data is performed only, when the probability density distributions are well known mono-modal functions.

For a more sophisticated examination of two-phase flows the postprocessing program ANAPDPA was developed at the 'Institut für Thermische Strömungsmaschinen'. It allows a detailed analysis of data obtained with a AEROMETRICS counter based equipment. In Fig. 10, results are plotted in terms of droplet size class velocities in tangential, u(d), as well as radial, v(d), direction. Oil and air flow rates are the same as for Fig. 9 but shaft speeds have been varied up to n_{max} = 16000 rpm.

The data represent mean values for the size classes d_d = 50, 100, 150, and 200 µm. It can be readily concluded from the figure, that the droplet flow is strongly influenced by the circumferential velocity of the rotor. In general, the radial velocity of the droplets is decreasing, whereas the tangential velocity component strongly increases with an increase in shaft speed. Thus, it can be concluded that the droplet flow angle is changing from a radial to a tangential direction, reflecting a dominant effect of air flows to the vent at low speed and dominant influences of rotating core flows inside the chamber at high speed conditions, respectively. With the exception of the highest speed of n_{max} = 16000 rpm this is more significant for small droplets. Larger droplets are accelerated by rotation, but keep a radial velocity component even for the high speed conditions due to their inertia.

In order to classify the measured velocities, a comparison can be made against the shaft velocities which range between 20 m/s < u_s < 104 m/s corresponding to the shaft radius of r_s = 62 mm and the rotational speed given in the figure. Ratios of droplet velocity to shaft velocity are between 0.1 < u(d)/u_s < 0.2 which seems to be very low. An explanation may be given based on the consideration of the measuring position which is shown again in the upper part of Fig. 10. Measurements have been performed close to the shaft as well as close to the bearing. However, it may be possible as drawn schematically by projections of possible trajectories that droplets flying through the measuring volume are not only original droplets emanating

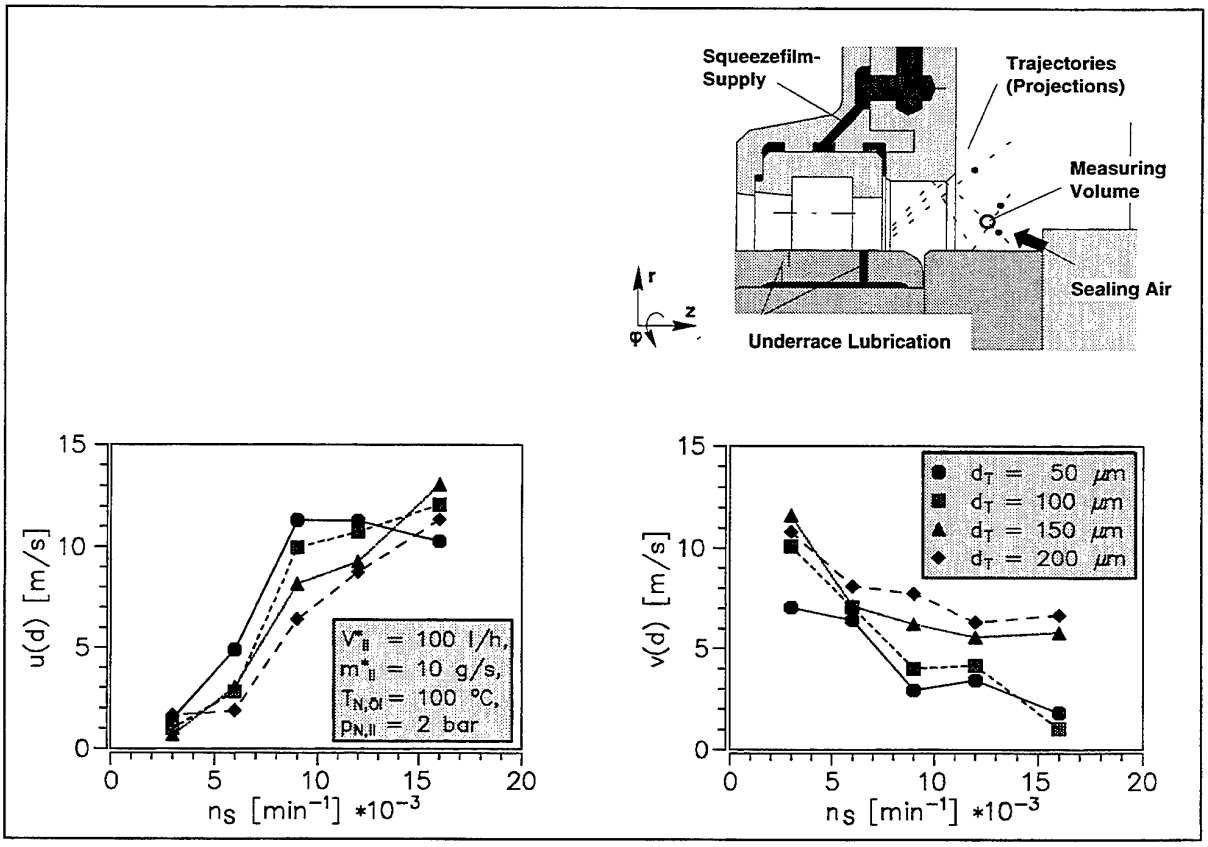

Fig. 10: Individual diameter dependent velocities

from the bearing but particles which are torn from a wall film on the bearing support or reflected from the support, respectively. Therefore, they would pass the measuring volume with a low but negative velocity and may be accelerated again if they hit the high speed rotating shaft. However, evidence for such an attempt of explanation cannot be concluded from mean velocity values.

At this point, further refinement of data analysis is definitely necessary. Fig. 11 demonstrates the potential of the advanced postprocessing software offering scope for individual correlations of diameters and corresponding velocities. As an example, the droplet size class $d_d = 80\ \mu m$ has been chosen and each individual measurement resulting in an appropriate diameter is drawn in the figure according to its velocities. Therefore, this figure is a two-dimensional probability density function with high number densities indicated by dark colours. Cumulated two-dimensional histograms are included for both related velocity distributions. Due to its Gaussian character the velocity distribution for the tangential component fits fairly well to the mean values discussed before (Fig. 10).

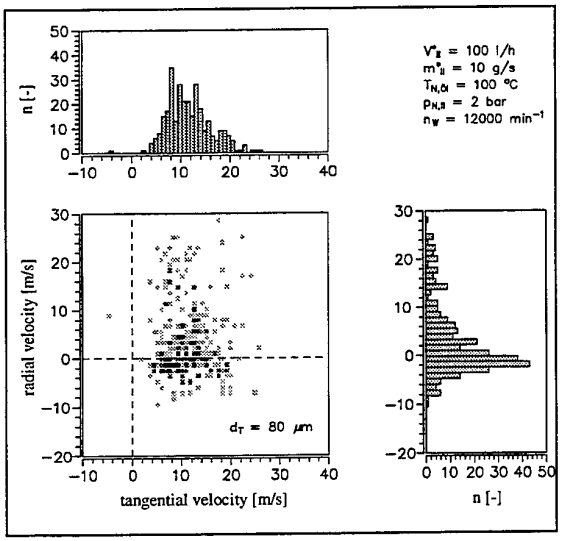

Fig. 11: Correlations of velocities (d=80µm)

In difference to this, it is obvious, that the distribution of radial velocity components has a maximum in the range of $-2\ m/s < v(d) < 0\ m/s$ which would not be reflected by averaged values because an additional range with high velocities exists at $12\ m/s < v(d) < 24\ m/s$. However, the distributions shown here can be treated as a confirmation of local droplet flow interpretation given above.

CONCLUSIONS

The systematic, comprehensive analysis of phase-Doppler configurations for fluids in the range of n=1.4 up to n=1.46 in refractive index indicates that besides the usual standard applications in near forward configurations, backward scattering phase-Doppler particle sizing gives suitable results when an off-axis angle in Alexander's darkband is chosen. Even if the intensity is low in that angular range, theory as well as measurements indicate, that these positions are suitable configurations for sizing in technical sprays, which often are limited in optical access due to geometrical restrictions.

Special emphasis was put on the comprehensive analysis of the phase-Doppler configuration including several sources of errors. This analysis includes a general systematic layout and a detailed study of Gaussian beam and slit effects. The main advantage of the chosen configuration in comparison to extreme near backward scattering applications is, that Gaussian beam effects as well as slit effect are negligible.

As a typical application of this configuration, an extremly complex aero-engine bearing chamber two-phase flow has been investigated. It shows the typical restrictions of complex technical flows drastically restricted in optical access under extreme boundary conditions. First results of these measurements show important effects and improve the understanding of this complex flow.

ACKNOWLEDGEMENT

The experiments described in this paper were funded partially by Rolls-Royce, Bristol, and Motoren- und Turbinen-Union, MTU, München. Thanks are due to R.M. Coleman and H. Zimmermann. Special thanks are due to K. Anders of Stuttgart University, who lend us the monodroplet generator which was necessary for a relevant part of this work.

REFERENCES

Albrecht, H.E., Borys, M., Wenzel, M. (1995): PDA-Meßvolumeneffekte und ihr Einfluß auf die Teilchengrößenmessung bei der Auswertung der Phasen- und Zeitverschiebung von PDA-Signalen, GALA, Rostock.

Bachalo, W.D., Brena de la Rosa, A., Rudoff, R.C. (1988): Diagnostics Development for Spray Characterization in Complex Turbulent Flows, 88-GT-241, ASME-paper

Glahn, A. and Wittig, S. (1995): Two-Phase Air/Oil Flow in Aero Engine Bearing Chambers – Characterization of Oil Film Flows, ASME Turbo Expo `95, Houston, Texas, USA, June 5-8, 1995, Paper 95-GT-114.

Glahn, A. and Wittig, S. (1996): Two-Phase Air/Oil Flow in Aero Engine Bearing Chambers – Assessment of an Analytical Prediction Method for the Internal Wall Heat Transfer, The 6th International Symposium on Transport Phenomena and Dynamics of Rotating Machinery, Honolulu, Hawaii, USA, February 25-28, 1996.

Grehan, G., Gousbet, G., Naqwi, A., Durst, F. (1994): Trajectory Ambiguities in Phase Doppler Systems: Study of a near-Forward and a near-Backward Geometry, Part. Part. Syst. Charact. 11, pp.133-144

Naqwi, A.A., Durst, F. (1991): Light Scattering Applied to LDA and PDA Measurements. Part 1: Theory and Numerical Treatment, Part. Part. Syst. Charact. 8.

van de Hulst, H.C. (1981): Light Scattering by Small Particles, Dover Publications, Inc., New York

Willmann, M., Kneer, R., Eigenmann, L., Wittig, S. (1994): Experimental Investigations on the Effect of Trajectory dependent Scattering on Phase Doppler Particle Sizing with a Standard Instrument, 7th Int. Symp. on Application of Laser techniques to fluid mechanics, Lisboa, 1994, Paper 18.1

Wittig, S.; Glahn, A.; Himmelsbach, J. (1994): Influence of High Rotational Speeds on Heat Transfer and Oil Film Thickness in Aero Engine Bearing Chambers, Transactions of the ASME: Journal of Engineering for Gas Turbine and Power, Vol.116, pp.395-401.

Xu, T.H., Tropea, C. (1994): Improving the performance of two-component phase-Doppler anemometers, Meas. Sci. Technol. 5, pp. 969-975.

SESSION 10

Combustion III

THE DEVELOPMENT OF SPARK IGNITED TURBULENT FLAMES.

R.A. Hicks, M. Lawes, C.G.W. Sheppard and R. Woolley

The Department of Mechanical Engineering,
The University of Leeds, U.K.

ABSTRACT

A high speed sequential laser sheet imaging technique has been used to investigate the development of spark ignited explosions in the Leeds fan stirred bomb. A good correlation was found to exist between the development of flame wrinkles and the 'effective' rms turbulent velocity. This highlighted the important role played by the turbulence energy spectrum in flame development following spark ignition.

1. INTRODUCTION.

The development of spark ignited turbulent flames, such as those in a gasoline engine, undergo an interesting evolution. Initially, the high spark energy propels a thermal and radical wave forward and, after overcoming high geometric stretch, laminar flame propagation will begin. As the small kernel grows and the influence of geometric stretch is superseded by aerodynamic strain, the flame is, at first, wrinkled by only the smallest scales of turbulence – larger length scales merely convecting the kernel bodily. However, as the kernel continues to grow it becomes progressively wrinkled by larger length scales until the size of the kernel is sufficient for it to experience the entire turbulence spectrum. The influence of turbulence (embodied in the rms turbulent velocity, u') on flame wrinkling and the turbulent burning velocity is then fully developed (Abdel-Gayed *et al.* (1987)). To quantify the degree of turbulence affecting the growing flame, the concept of an "effective" rms turbulent velocity, u'_k, has been proposed (Abdel-Gayed *et al.* (1987) and Bradley *et al.* (1996)). The variation of u'_k with dimensionless time from ignition (expressed in terms of a non-dimensional wavenumber, $\bar{k}$) was obtained by integrating the dimensionless power spectral density of turbulent energy, $\bar{S}(\bar{k})$ (derived from laser Doppler velocimetry measurements) up to a dimensionless wavenumber, $\bar{k}_k^{-1}$. The manner in which the normalised "effective" rms turbulence velocity, u'_k/u', varied with $\bar{k}_k^{-1}$ is shown in Fig. 1.

First, experiments are described in which the turbulence characteristics of the Leeds fan stirred bomb were determined. Then, sequential high speed laser sheet flame images are presented and used to characterise the nature of turbulent flame development in the bomb. Finally, a comparison is made between turbulence and flame characteristics. The important role of the turbulence spectrum in influencing the growth of a turbulent flame following spark ignition is clearly demonstrated.

2. APPARATUS.

Premixed iso-octane - air mixtures were exploded in a high pressure/high temperature spherical fan stirred combustion vessel at an initial pressure and temperature of 1 bar and 358 K, respectively. The 380 mm diameter stainless steel vessel had extensive optical access via 3 pairs of orthogonal windows of 150 mm diameter. Turbulence was generated by four fans, each driven by an independently controlled electric motor up to a maximum speed of 10 000 rpm. For all experiments, the combustible pre-mixture was ignited by a spark electrode which was located in the centre of the bomb. An average ignition energy of 23 mJ was supplied to the spark gap.

The turbulent flow field was calibrated for different fan speeds using laser Doppler velocimetry (LDV). A single velocity component, argon-ion laser LDV system was used with signal processing being performed with a Dantac 57N20 Enhanced Burst Spectrum Analyser (BSA). Directional ambiguity in the velocity measurements was removed by the adoption of a 40 MHz frequency shift to one of the beams. At each condition, 20 000 Doppler bursts were collected, at a typical rate of 10 kHz. Alumina (Al_2O_3) particles, with a nominal diameter of 0.3 μm, were used to seed the airflow. Measurements indicated that, within the region of optical access (150 mm diameter), the turbulent velocity flow field was nearly isotropic with very small mean velocities. The rms

turbulent velocity was found to vary linearly with fan speed, f_s, such that u'(m/s) = 0.0012f_s (rpm).

The turbulent integral length scale, L, was found directly from a spatial correlation. For these measurements, a second LDV system and BSA processor were borrowed from Dantec. Simultaneous velocities were measured at two points within the bomb. The centre of the bomb was taken as one fixed measurement point whilst the second point was at variable horizontal distances away from the centre. The longitudinal integral length scale, was then calculated from the two point correlation function. With the exception of the lowest fan speeds, L was independent of fan speed and found to be 20 mm, as shown in Fig. 4.

To assess the temporal development of spark ignited turbulent flames, a high speed laser sheet imaging technique was employed. An Oxford Lasers high repetition rate copper vapour laser was used to generate a series of sequential laser sheets. The 510.6 nm pulsed laser beam was formed into a 0.5 mm thick laser sheet using suitable optics. The laser sheet was located vertically, just in front of the spark electrode and Mie scattered from tobacco smoke particles of sub-micron size (Ziegler *et al.*, 1988). The scattered light was recorded using a Kodak EktaPro HS Motion Analyser (Model 4540) at a framing rate of 4.5 kHz. To block extraneous light, a 510.6 nm bandpass (10 nm FWHM) interference filter was placed directly in front of the camera lens. Digitised flames contours, with a spatial resolution of 1 mm, were extracted from the video images using the hand tracing procedure adopted by Bradley *et al.* 1994.

The digitised flame contours were expressed as a series of amplitudes, a_j, given by the distance of the local flame front from the mean flame front (Hicks *et al.* 1994). From this data, a power spectral density (psd) function was obtained to characterise flame wrinkling. The rms amplitude of flame wrinkling, a'_k, representative of the turbulent flame brush thickness, was derived from the psd function via:

$$(a'_k)^2 = \int_0^{k_{max}} S(k)dk \qquad (1)$$

where $S(k)$ is the spectral coefficient at wavenumber k, (= 1/l), l is the length of wrinkling and k_{max} is the maximum wavenumber of wrinking and is given by the reciprocal of the circumference of the mean flame front. In addition, values of a_j were spatially autocorrelated to yield an integral scale of flame wrinkle, L_{ak}, given by $L_{ak} = \overline{a(l)a(l+\Delta l)}$.

3. RESULTS AND DISCUSSION.

Shown in Fig. 2 are sequential flame contours extracted from laser sheet images of stoichiometric iso-octane - air mixtures at a value of u' of 0.56 m/s (fan speed = 500 rpm). At this low rms velocity the flame front was continuous and approximately circular in cross section. However, at higher turbulence (fan speed), as shown in Fig. 3, the flame front was, in general, non-circular and significantly more wrinkled. At higher turbulence, appreciably more unburnt gas was observed within the flame boundary and there was a significant increase in the appearance of gaseous "islands" ahead of and behind the flame contour. Previous studies in spark ignition engines (Hicks *et al.* 1994, Mantzarras *et al.* 1988) have suggested that, at turbulence levels similar to those being considered here, these "islands" are associated with sections through 3D eddy structures at the leading edge of the flame.

During the early stages of development, the flame kernel experienced increasing random convection away from the spark electrode. This can be seen in Fig. 5, where the velocity of the centroid of the flame is plotted against elapsed time from ignition. At decreasing elapsed times the convecting speed from explosion to explosion ranged from 0 to 3u', (~ 10m/s in Fig. 5) and the average value was close to the mean speed of turbulence which is given by $(8/\pi)^{0.5}u'$ (Akindele *et al.* (1982), Abdel-Gayed *et al.* (1987)). This supports the idea, discussed in Section 1, in which a developing turbulent flame kernel will sense a growing spectrum of turbulent scales. Those scales greater than its instantaneous size will merely convect rather than wrinkle it. However, with greater lapsed time, the growing kernel encompasses a larger range of eddy sizes, such that the average convective velocity falls towards the expected mean of zero as also is shown in Fig. 5.

Shown in Figs. 6 and 7 are the temporal developments of the wrinkling parameter a'_k and L_{ak} for three different turbulence velocities. The more rapid increase in the magnitude of both parameters with an increase in turbulence is a consequence of the flame growing more quickly into the low frequency, large scale, part of the turbulent spectrum. The 'shot to shot' variations at each fan speed highlights the stoichastic nature of early flame development as the flame kernels experienced 'shot to shot' variations in the local turbulence spectrum. An important consequence of the variation in the flame brush thickness (as quantified by a'_k) as the flame develops is that there can be an appreciable and changing proportion of unburnt gas within the mean flame front. Consequently, measurements of the progress of a visible or schlieren flame front can lead to over-estimation of the burn rate.

Set out in Figs. 8 and 9 are the same data expressed in terms of the mean flame radius. Here, the influence of turbulence is less clear cut. At mean flame radii less than ~ 15 mm, the rate of increase of both wrinkle parameters is similar for all three turbulence velocities. However, at larger radii, the rate of increase in a'_k and L_{ak} with radius is not so obvious. The lack of any consistant trend with turbulence and radius is probably a result of the non-linear developing nature of turbulent burning velocity and flame thickness. It would appear, from Figs. 8 and 9, that the level of wrinkling experienced by a growing flame kernel is a stronger function of the kernel's size than of time from ignition. The slower rate of development in the lower turbulence case than in the other caes might be associated a degree of turbulence intermitency as indicated by the high value of flatness in the measured velocity pdf at low

turbulence. However, further work is required to establish the relative importance of elapsed time and flame radius on flame development.

The solid curves in Figs. 10 and 11 show the variation of u'_k/u', for values of u' of 2.2 and 4.5 m/s (2000 and 4000 rpm). They were obtained by the method used to derive Fig. 1. The symbols show the variation in a'_k for the same conditions. For a flame radius equal to the turbulent integral length scale, L, (20 mm), it can be seen that when $u' = 2.2$ m/s, the effective turbulence velocity is only about 40% of its fully developed value, and at the largest measured mean flame radius of 70 mm it is about 65% of its fully developed value. Indeed, a flame would need to be of the order of $20L$ to experience 90% fully developed turbulence (Bradley *et al.* (1996)).

For both fan speeds, and up to the maximum measured radius, the rate of development of a'_k is similar to that for u'_k/u'. A limitation of Figs. 10 and 11 is that the fully developed flame thickness, a', is unknown and, hence, the more logical parameter, a'_k/a' could not be determined. However, if as is anticipated from Figs. 10 and 11, the developments of u'_k/u' and a'_k/a' similar, then the right hand axis also could be used as an indicator of the extent of development of a'_k/a'.

4. ACKNOWLEDGEMENTS

The authors would like to thank Dantec Measurement Technology for the loan of LDV equipement for the spatial correlation and the EPSRC for supplying the high speed video camera and copper vapour laser. This work was undertaken as part of CEC JOULE II programme, contract JOU2-CT 92-0162.

The advice and assistance of Prof. Derek Bradley FRS at Leeds is gratefully acknowledged.

5. REFERENCES

Abdel-Gayed, R.G., Bradley, D. and Lawes, M. 1987 Turbulent burning velocities: a general correlation in terms of straining rate, Proc. R. Soc., Lond. A414, p.389.

Akindele, O.O., Bradley, D., Mak, P.W. and McMahon, M. 1982 Spark ignition of turbulent gases, Combustion and Flame , vol. 47, pp. 129-155.

Bradley, D., Lawes, M., Mushi, E.M.J. and Scott, M.J. 1994 Afterburning in spherical premixed turbulent explosions, 25th Symp. (Int) on Comb., The Comb. Inst., Pittsburg.

Bradley, D., Lawes, M. and Scott, M.J. 1996, Characteristics of isotropic turbulence in a fan stirred vessel: generalised power spectral densities and strain rate PDF's, to be published.

Hicks, R.A., Lawes, M., Sheppard, C.G.W. and Whitaker, B.J. 1994, Multiple laser sheet imaging investigation of turblent flame structure in a spark ignition engine, SAE paper 941992.

Mantzarras, J., Felton, P.G. and Bracco, F.V. 1988, Three-dimensional visualization of premixed-charge engine flames: islands of reactants and products; fractal dimensions; and homogeneity, SAE paper 881635

Ziegler, G.F.W., Zettlitz, A., Meinhardt, P., Herwig, R., Maly, R. and Pfister, W. 1988, Cycle-resolved two-dimensional flame visualization in a spark-ignition engine, SAE paper 881634

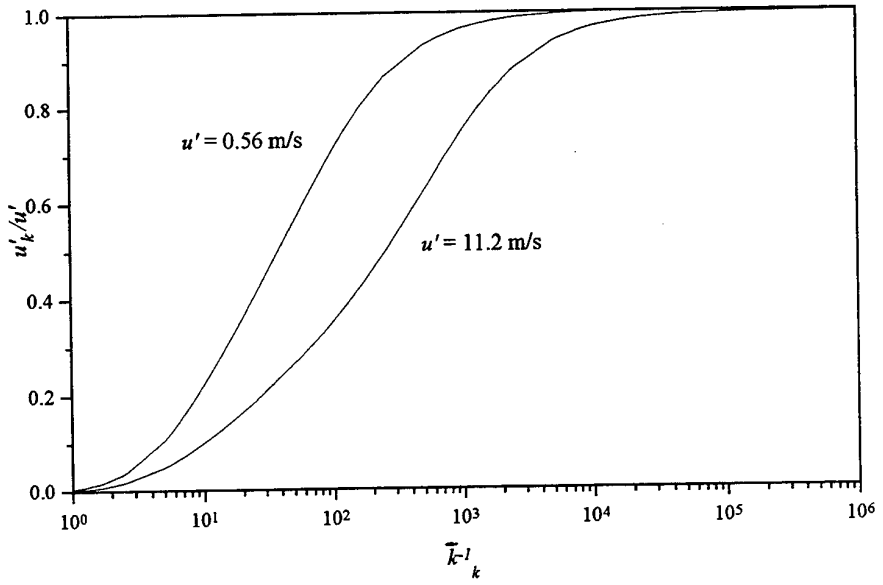

Fig. 1. Variation of the dimensionless effective r.m.s. velocity u'/u'_k with $\overline{k}_k^{-1}$ over the rms velocity range available in the bomb, from u' of 0.56 m/s (500 rpm) to 11.2 m/s (10,000 rpm).

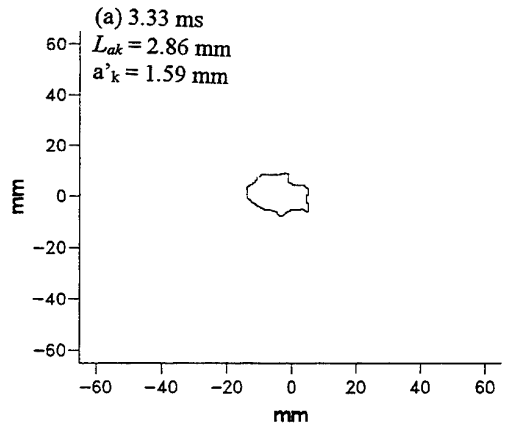

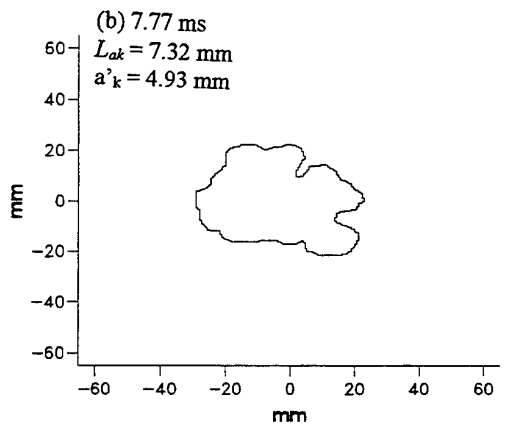

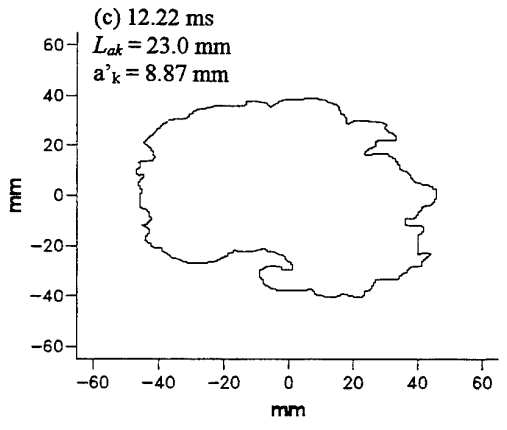

Fig. 2. Sequential flame contours stoichiometric iso-octane - air flames at u' = 0.56 m/s (500 rpm). Initial temperature = 358 K; initial pressure = 1 bar. Elapsed time from ignition idicated on diagrams.

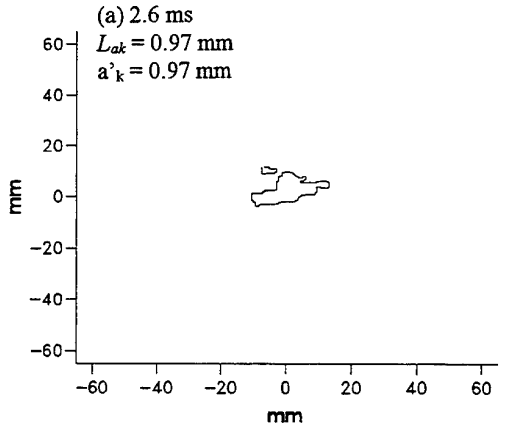

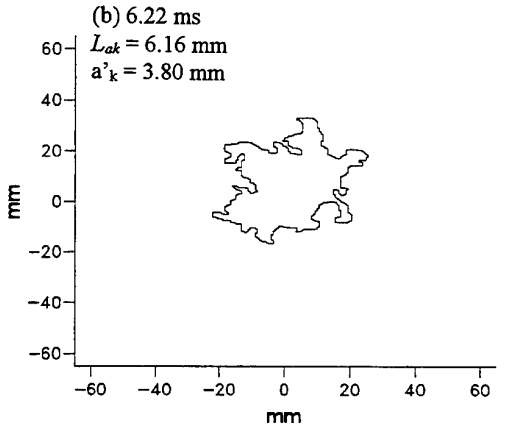

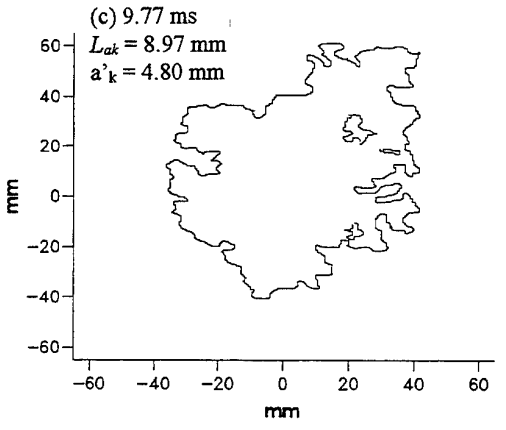

Fig. 3. Sequential flame contours stoichiometric iso-octane - air flames at u' = 2.2 m/s (2000 rpm). Initial temperature = 358 K; initial pressure = 1 bar. Elapsed time from ignition idicated on diagrams.

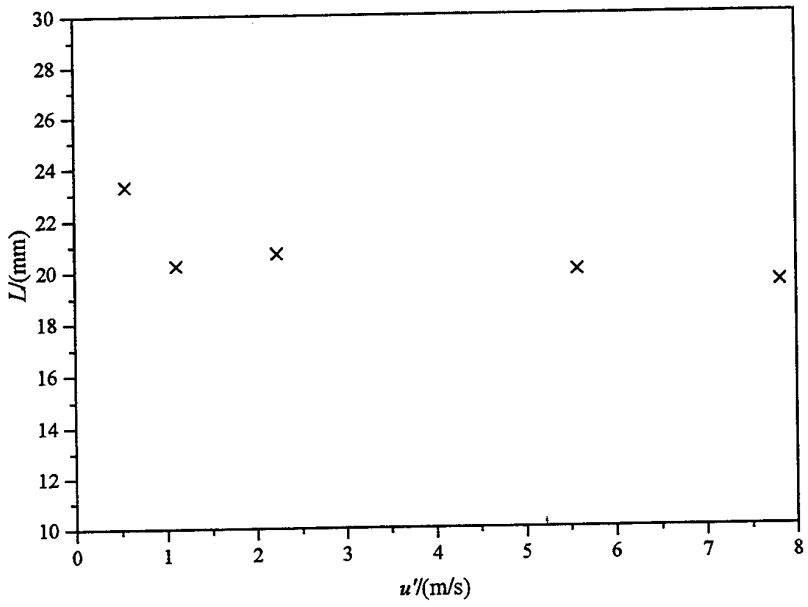

Fig. 4. Variation of the integral length scale, L, with u'.

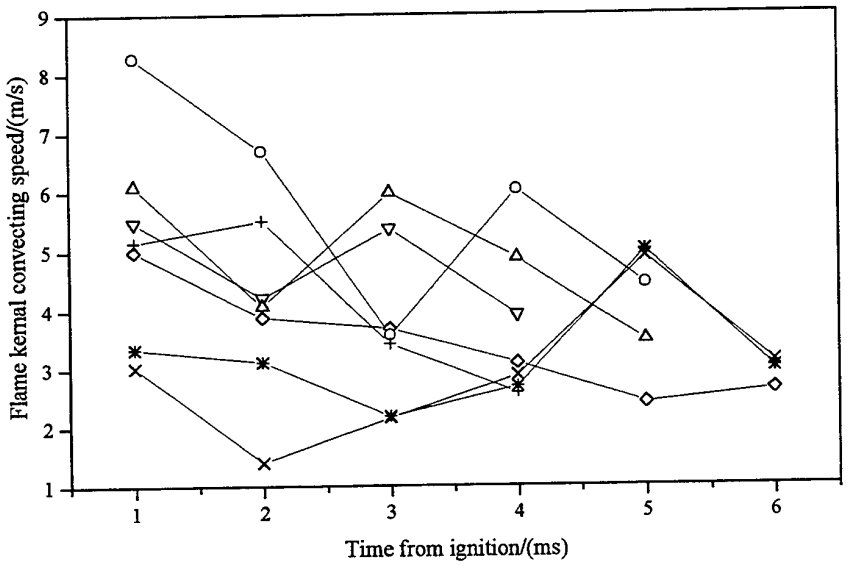

Fig. 5. The variation of the flame kernel convection speed with time for u' = 3.4 m/s . Each line represents a single flame.

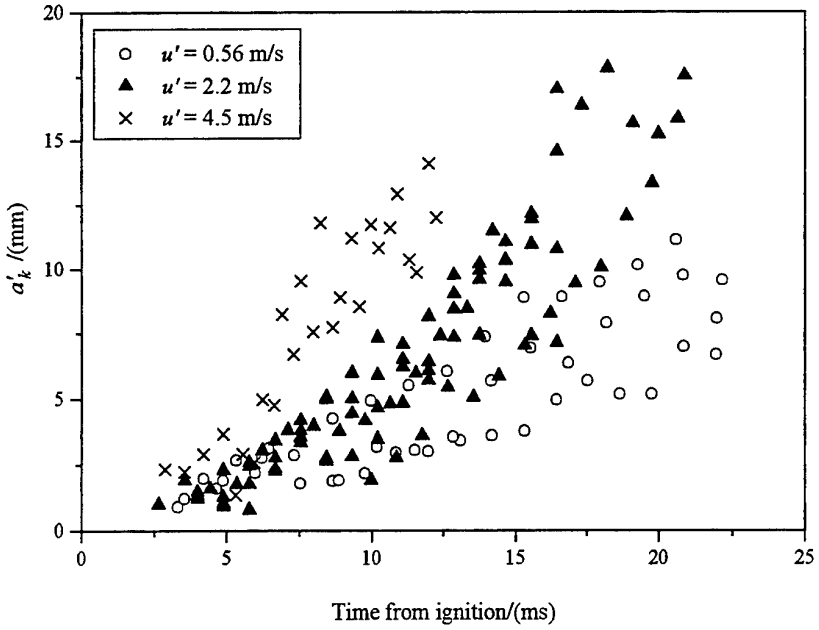

Fig. 6. Variation of a' with time from ignition for Mie scattered images. Stoichiometric iso-octane - air mixture, initial temperature = 358 K, initial pressure = 1 bar. u' = 0.56 m/s - data from 3 explosions, u' = 2.2 m/s - data from 6 explosions and u' = 4.5 m/s - data from 2 explosions.

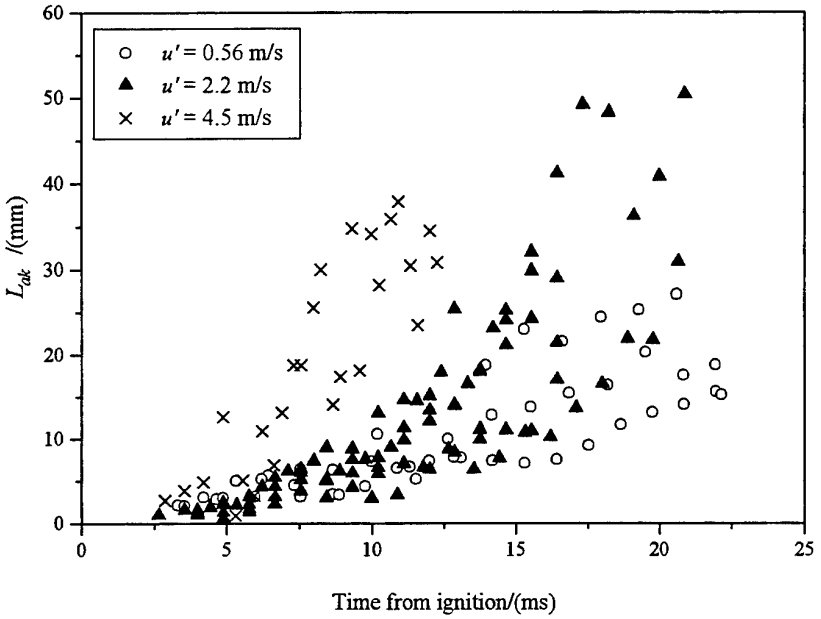

Fig. 7. Variation of L_a with time from ignition for Mie scattered images. Stoichiometric iso-octane - air mixture, initial temperature = 358 K, initial pressure = 1 bar. u' = 0.56 m/s - data from 3 explosions, u' = 2.2 m/s - data from 6 explosions and u' = 4.5 m/s - data from 2 explosions.

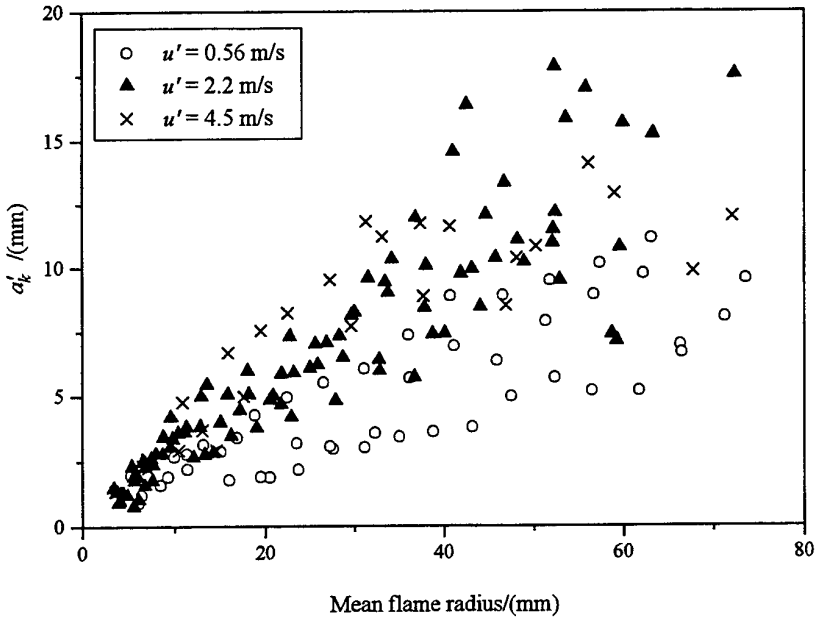

Fig. 8. Variation of a' with mean radius from ignition for Mie scattered images. Stoichiometric iso-octane - air mixture, initial temperature = 358 K, initial pressure = 1 bar. u' = 0.56 m/s - data from 3 explosions, u' = 2.2 m/s - data from 6 explosions and u' = 4.5 m/s - data from 2 explosions.

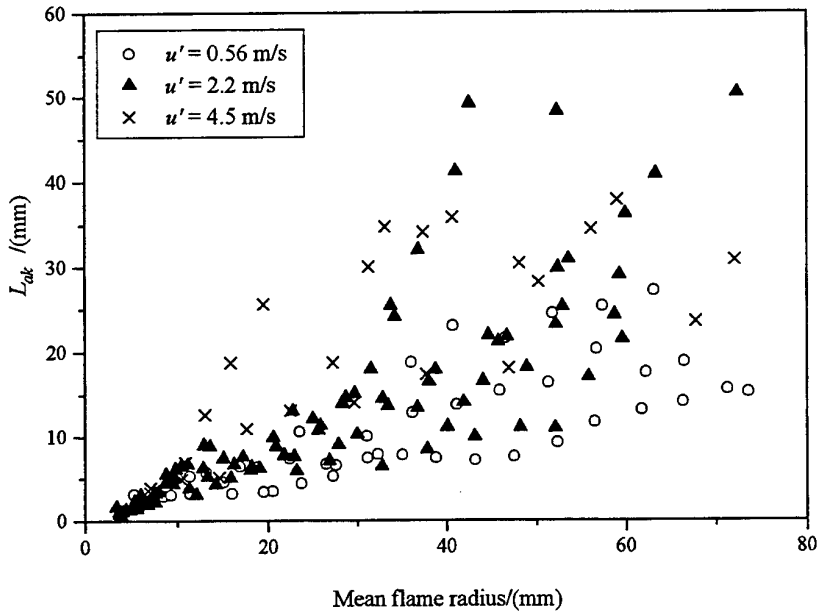

Fig. 9. Variation of L_a with mean radius from ignition for Mie scattered images. Stoichiometric iso-octane - air mixture, initial temperature = 358 K, initial pressure = 1 bar. u' = 0.56 m/s - data from 3 explosions, u' = 2.2 m/s - data from 6 explosions and u' = 4.5 m/s - data from 2 explosions.

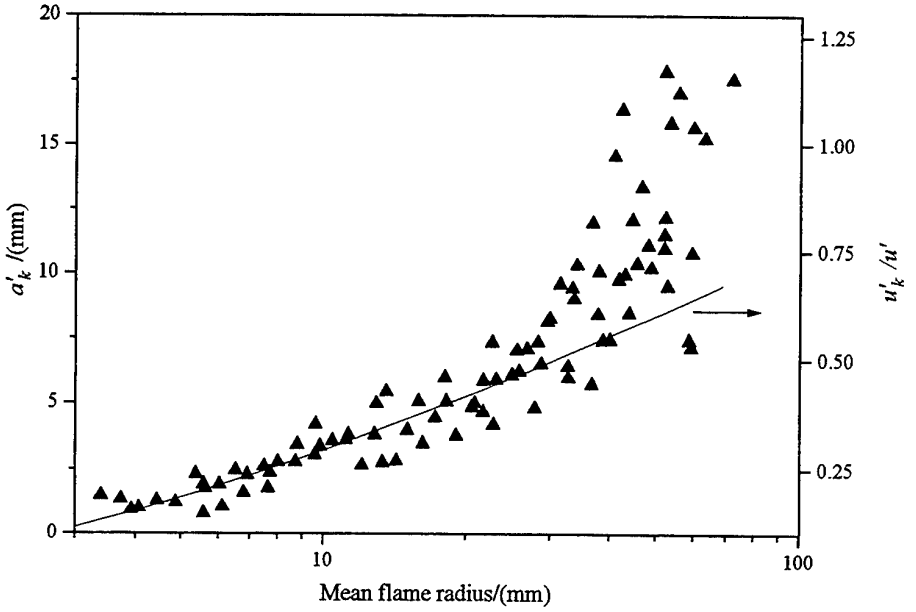

Fig. 10. Comparison of the development of a' with u'_k at u' = 2.2 m/s (2000 rpm). The experimental results consists of data from 6 explosions

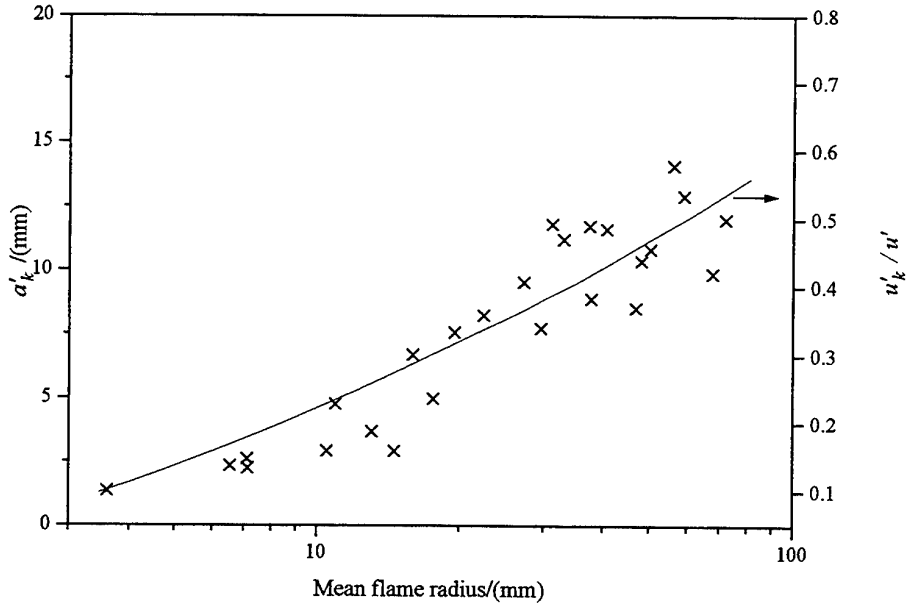

Fig. 11. Comparison of the development of a' with u'_k at u' = 4.5 m/s (4000 rpm). The experimental results consists of data from 2 explosions.

AERODYNAMIC FLOW CHARACTERISATION OF A SWIRL BURNER

Bertrand Poireault, Jean-Michel Most
Laboratoire de Combustion et de Détonique
UPR 9028 au CNRS - Université de Poitiers - ENSMA
BP109 - Site du Futuroscope
86960 FUTUROSCOPE Cedex

Jean-Imbach
Gaz de FranceDirection de la recherche
CERSTA-Division Combustion et Piles à combustible
361 Avenue du Président Wilson
93211 La Plaine Saint Denis

ABSTRACT

An aerodynamic characterisation of a high confined swirl flame is developed, using a Laser Doppler Velocimeter. It allows us a better understand of the flame stabilisation processes, optimisation of combustion efficiency and reduction of pollutant formation. Detailed measurements of mean and fluctuating velocity fields are made to characterise the effects of swirl number upon central recirculation zone stability and turbulent mixing. The exit of the 40Kw swirl burner is equipped with a 25° diverging quarl opening in a hot wall furnace. Two laser velocimeter heads are used perpendicularly (one of them is water cooled) to measure three velocity components on the confined reactive flow. We seek the influence of the swirl intensity on the mean aerodynamic field, on the capacity of the rotation to improve the formation and stability of a recirculation zone, and on the behaviour of the combustion. Turbulence and Reynolds shear stresses are determined to get complete data fields for a numerical modeling. The turbulent fluxes are evaluated to give assumptions on turbulent exchanges between the central recirculation zone and the main flow. At last, a scenario for the flame stabilisation process is proposed.

1. INTRODUCTION

Swirl burners are currently used for their capacity to stabilised high intensity flames, optimise combustion efficiency and reduce pollutant formation. The design of such a burner requires a perfect knowledge of the flow structure and flame stabilisation processes. For many years, different aspects of the swirling combustion have been extensively studied, including flow structure and transport mechanisms [1, 2, 3], flow instabilities [4, 5], mixing and flame stability [6, 7]. These studies are developed on various burner geometries (degree and shape of the confinement), combustion types (premixed or non-premixed flame, staged combustion), scale and thermal output power (model burner to large complex industrial systems). Moreover, the obtained results are generally strongly dependant of the characteristics of the studied burner and any generalisation to an other burner type becomes hazardous.

The design or the optimisation of a burner requires the development of numerical tools validated with experimental data, that's why, complementary studies are still necessary to describe phenomena involved in the flow structure and combustion processes.

2. EXPERIMENTAL SET-UP AND MEASUREMENT METHODS.

2.1. Experimental Apparatus.

In the present work, a vertical model swirl burner is investigated. The thermal output of the non-premixed methane-air flame is 40kW that corresponds to an intermediate scale between laboratory flames and the 500kW half-industrial burner studied by the Combustion Research Group of Gaz de France. The burner (Fig. 1) is an axial plus tangential air type. Both air flows are supplied by an air compressor. Methane is supplied through a central pipe nozzle with an axial injection exit located at the base of the quarl enter. During cold flow tests, methane is injected but not ignited. All gas mass flow rates are controlled and adjusted by mass flow meters. The swirl number (axial to tangential momentum ratio) is experimentally determined from velocity measurements at the burner enter using the definition gives by Gupta and al (22).

$$S = \frac{\int_0^{R_0} \overline{\rho u w} r^2 dr}{R \int_0^{R_0} \overline{\rho}[\overline{u}^2 + (\overline{w}^2 - \overline{w}_m^2)/2] r dr}$$

w_m : Maximum swirl velocity at x/D=0.09
R_0 :Radius of the burner exit

A quarl is added to the burner used for the previous study [8]. The combustion is confined in a 0.55m diameter and 0.8m height hot wall furnace installed at the quarl exit. Two main motivations explain the choice of this configuration: to stay close to industrial burners and to get well known boundary conditions for future numerical modeling.

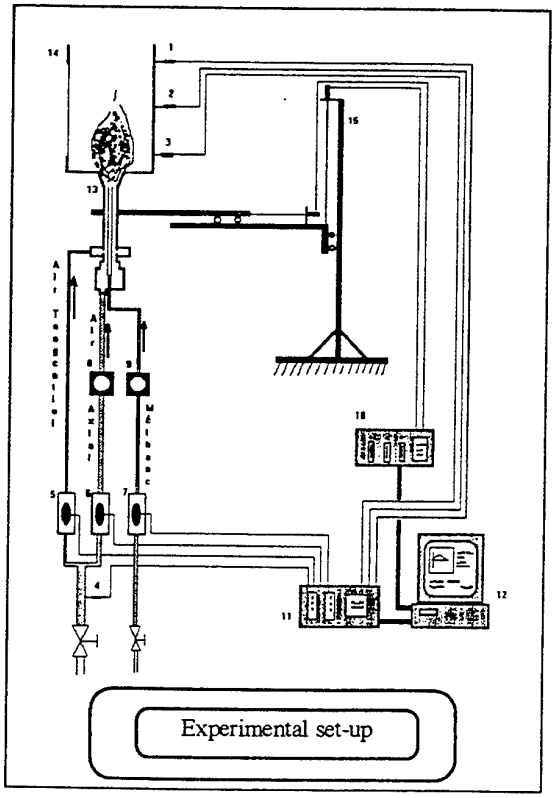

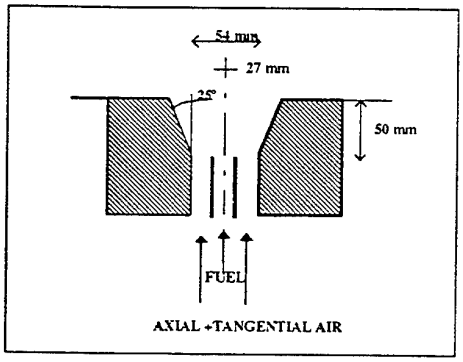

Fig. 1. Schematic diagram of burner arrangement and detailed dimensions.

The image processing of flame spontaneous emission and the flame stability diagram are used to determined the aerodynamic conditions leading to stable and efficient flames. Three sets of working parameters, corresponding to three swirl number conditions are selected keeping constant the global gas/air equivalent ratio and thermal output power (Table 1). The lowest swirl number is determined from Fricker et al [10] criteria for the flame blow-off limits.

Swirl number S	Q_{axial} (m^3/h)	Q_{swirl} (m^3/h)	Thermal output (kW)	equivalent ratio ϕ	Reynolds number at burner exit
0.1	55	4.4	40	0.7	17100
0.4	45	13.5	40	0.7	17100
0.82	38	21	40	0.7	17100

Table 1
Operating conditions for swirl stabilised flames

2.2 Experimental techniques.

Published data base of swirl flow velocity fields are generally imperfect to validate physical models or numerical codes, the mesh of data points being not sufficient to accurately evaluate mean flow streamlines or velocity gradients. Moreover, optical measurements are difficult inside quarl and furnace.

In this work, three dimensional Laser Doppler Velocimetry (L.D.V.) measurements are realised with a two-dimensional system including 5W Argon Ion laser, two optical fiber L.D.V. probes, and Burst Spectrum analysers. Narrow windows are installed in the quarl and furnace wall in order to get axial U and tangential W velocity components in the perpendicular plane of the optical axis of the first L.D.V. head. The radial velocity component is generally determined by moving the L.D.V. head radially to the burner axis. Unfortunately such an operation becomes impossible with confinement. In this work, we use the original technique derived from the intrusive method developed few years ago [8]. It consists to introduce a water cooled L.D.V. probe vertically inside the furnace (Fig. 2). The complete L.D.V. system is fixed and the burner is moved with a two-dimensional table. In order to minimise the intrusive probe perturbations, the focal length of this second L.D.V. head is 60cm, then, the tip of the probe is located outside the flame (external diameter of the jacket: 16cm). The influence of the water cooled probe on measured datarate quality is evaluated before measurement (Fig. 3). The light intensity attenuation at the L.D.V. control volume by the water cooled probe has been estimated at around 15% in the full input power range. The main limitation of this techniques appears in datarate fall with the water cooled system in front of the laser probe. For the same working conditions, we notice the lost of more than 70% on the datarate in backward -scattered mode.

In order to be sure of the coincidence of the two measurement volumes, tests are made by receiving with the first L.D.V. head, the light scattered by particles illuminated by the second head. Unfortunately this arrangement provides a low Doppler signal datarate: the scattered light at 90° is not optimised (Mie theory) and temperature gradients between the probes and measuring volume induce fluctuations of the two measurements points reducing the coincidence time.

This technique is only used for cross correlation measurements.

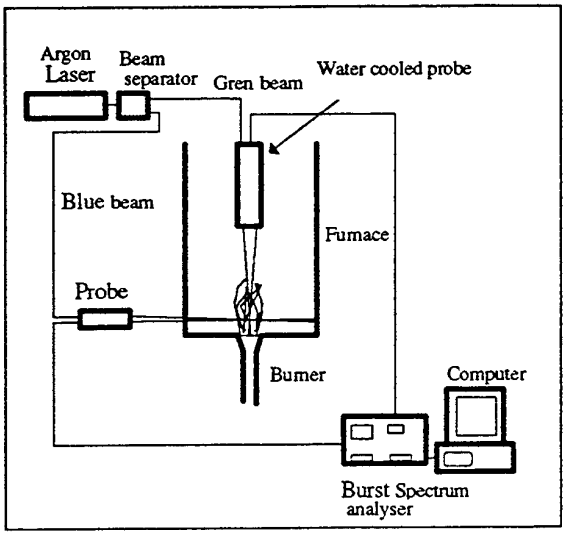

Fig. 2 : Schematic diagram of the instrumentation for the two L.D.V probes measurement.

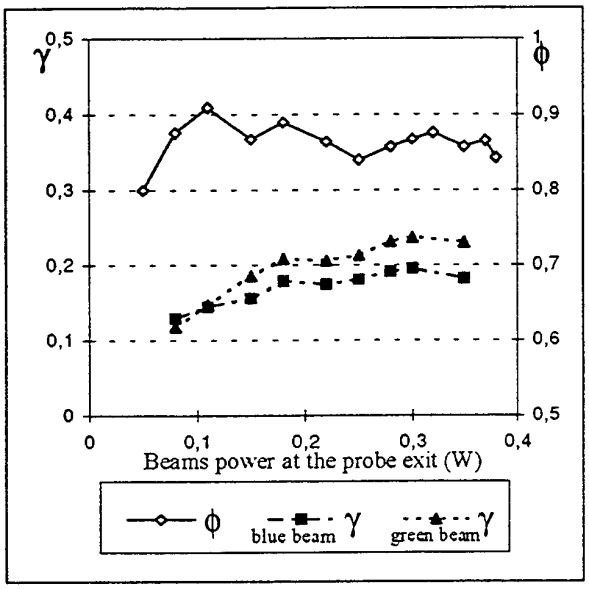

$$\phi = \frac{\text{Power.with.water.cooled.probe}}{\text{Power.without.water.cooled.probe}}$$

$$\gamma = \frac{\text{datarate.with.water.cooled.probe}}{\text{Datarate.without.water.cooled.probe}}$$

Fig. 3: Influence of water cooled probe on the quality of the LDV signal.

A thin thermocouple, whose the thermal inertia is numerically compensated, is used to determined the mean and fluctuating temperature fields. The stable chemical species concentrations are measured by an on-line gas analyser system. Then, the local mean density can be deduced from these quantities using the perfect gas state law.

The mean and fluctuating velocity fields are determined with a radial step of 5mm in quarl and 10 mm in the furnace. For inert flow conditions, methane is injected but not ignited.

3. RESULTS AND DISCUSSION

3.1 Mean Flow Characterisation

The depression region, induced by air rotation, can inflect the flow stream lines. When the swirl number S becomes sufficient, an central recirculating zone (RZ) is created. A second RZ (lateral RZ) is detected outside the main flow at the quarl exit due to sudden radial expansion of the confinement.

In the cold weak swirl number case, any RZ is observed, but, after ignition, for the same flow conditions, a RZ is formed, as observed by Shen [8] for a straight exit burner. The combustion process seems to favour the stabilisation of the central recirculation zone. This phenomenon can be interpreted by a decrease of the gas density with combustion leading to an increase of the adverse pressure gradient $(\partial p/\partial r)_{r=0}$, which generates the reverse flow zone [14, 15]. The strength of the adverse pressure gradient is also observed for the two other swirl number conditions (i.e.: S=0.4 and S=0.82) with an increase of the RZ surface, a modification of the shape of the RZ upper zone, and a downstream displacement of its recirculation zone bottom (Fig. 4).

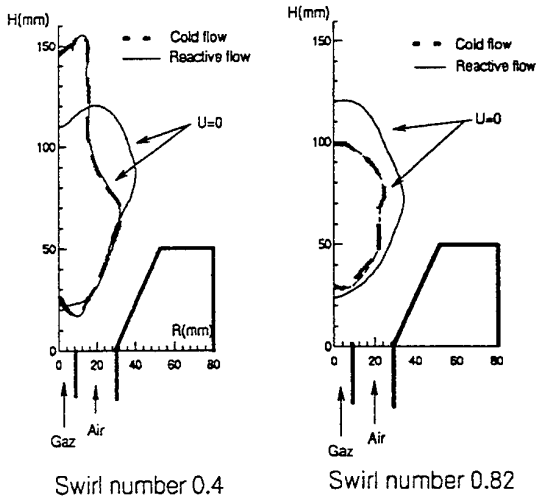

Fig. 4: Zero axial line velocity for cold and reactive flows.

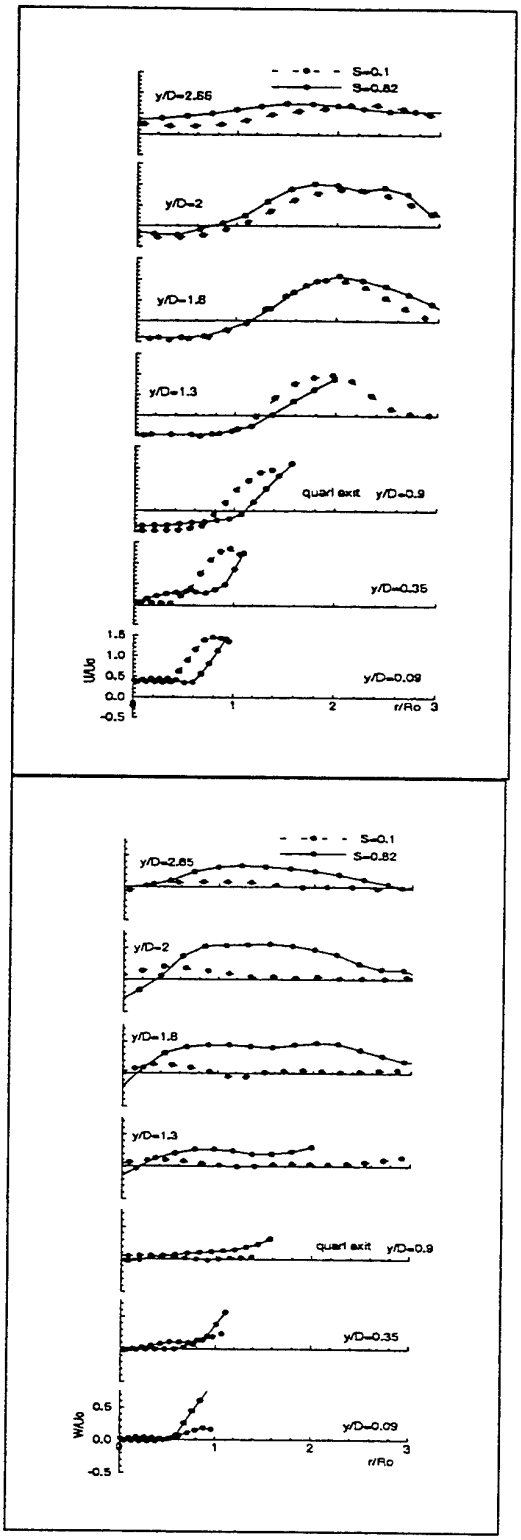

Fig. 5: radial profile of mean axial U and tangential velocities

In the reactive flow, the stability limits and combustion efficiency of swirl flame are widely dependant of the characteristics of the RZ. Then, the presented results are focused on the swirl number effects upon the reverse flow zone for the cold and reactive cases.

Flame spontaneous emission study shows an appreciable decrease in the flame height when increasing the swirl number (up to 20 % between the two extreme swirl cases). The present objectives are to determine if modifications in the aerodynamic field can induce the observed flame height variation.

Fig. 5 illustrates radial evolution of nondimensional axial and tangential velocity measurements at different stages inside the quarl and furnace (reactive flow). The increase of the swirl intensity moves the axial velocity maximum towards the quarl edge. This result contrasts with Shen's observations [16] with a straight exit burner. The diverging quarl and furnace wall acts here as a physical frontier which limits the sudden radial transport of the upstream rotating air to the environment even for high rotation intensities. The negative tangential velocities observed in the RZ for the highest swirl number values can be interpreted as the location of the processing vortex core centre (PVC) [9, 18, 20] near the geometric system centre. This particular location of the vortex core has been also encountered by Yazbadi et al [21] in a cyclonic flow with bend angled and by Tangirala [14] in a quarl exit burner.

In order to study the rotation intensity influence upon the velocity field structure, the Strokes stream functions are calculated from the local measured mean axial velocity component and gas density, using the equation:

$$\psi = 2\pi \int_0^r \overline{\rho u} r dr$$

normalised by the burner exit stream function:

$$\psi_o = \left[2\pi \int_0^{R_0} \overline{\rho u} r dr \right]_{x/D=0.09}$$

R_0 is the recirculation zone radius.

The density is determined from previous measurements of local mean temperature and species composition. The small dubiousness, around 7%, of the mass flow rate determined either with mass flow meter or $\rho u r$ integration calculated at x/D=0.09, is attributed to velocity measurement and integration errors near the quarl edge where the property gradients are large.

As observed by Chigier et al [16] and Hillesmans et al [17] the zero streamline encompasses the central recirculation zone outside the quarl burner (Fig. 6). Like Syred and al [3] results for a straight exit burner, the "eye" of the recirculation vortex seems to be located on the edge of the reverse flow zone.

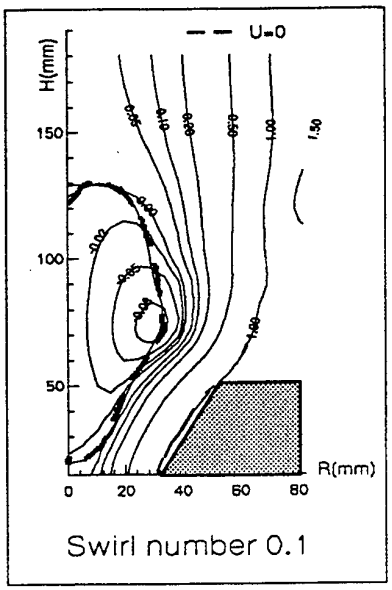

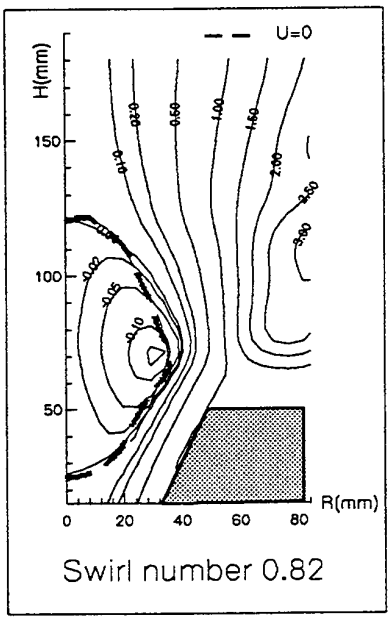

Fig. 6: Spatial distribution of streamlines (ψ/ψ_0)

The maximum deflection of streamlines occurs at the quarl exit, around the recirculation vortex "eye". The location of the measured radial velocity maximum confirms the radial expansion at the quarl exit whereas it stays constant inside the confinement. When the swirl number value increases, the two characteristics lines (i.e.: U=0 and ψ=0) become closer implying a diminution of the mean exchange surface between the RZ and the main flow. Moreover, both inflection of the streamlines and air entrainment increase downstream the RZ.

The modifications in size and shape of the RZ do not show a remarkable alteration with the swirl intensity. This observation is consistent with Tangirala et al results[14] for 30° quarl exit burner. For the highest swirl number value (S=0.82), the length of the reverse flow zone decreases and becomes a little bit wider, but less than Syred and al [19] or Shen and al [8] observations with a straight exit burner. The calculated RZ surface decreases about approximately 9% between the extreme studied swirl number settings (Fig. 7).

The value of the nondimensional calculated recirculated mass flow rate M_r is commonly used as a measure of the RZ strength.

$$M_r / M_0 = \int_0^{R_{rz}} \rho \bar{u} r dr \Big/ \int_0^{R_0} \rho \bar{u} r dr$$

R_{rz} : Recirculation zone radius

M_0 is the mass flow rate at the burner exit. Due to the complex dependence of the reverse flow zone shape on the experimental set-up and working parameters, Hillesmans et al [17] normalise the maximum of the recirculated mass flow rate by the maximum RZ width. Fig. 7 does not show appreciable variation of the recirculated mass flow rate ratio with the swirl number value.

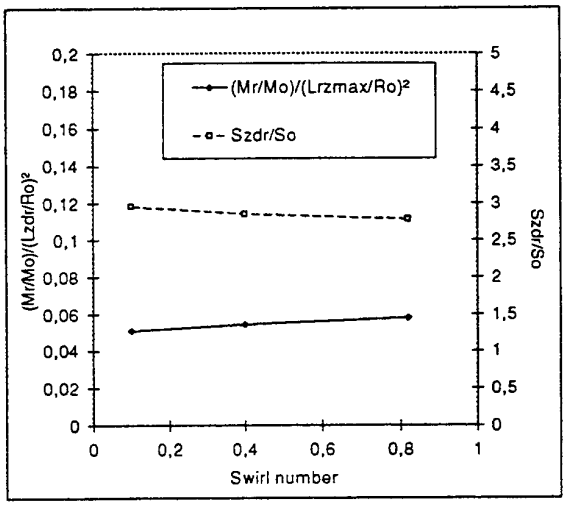

Fig. 7:Normalised mass flow rates and recirculation zone surfaces as a function of swirl number.(M_0 mass flow rate at the burner exit, S_0 Surface of the burner exit ,R_0 radius burner, L_{RZ} maximum RZ radius)

The general trends observed on the RZ are both a decrease of the RZ surface and an increase of the recirculated mass flow rate. Nevertheless a generalisation is hazardous in regard to these relatively small variations.

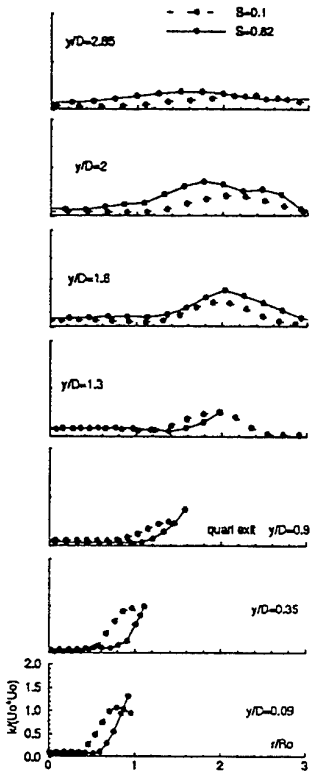

Fig. 8: Turbulent kinetic energy k in the reactive flow

The last macroscopic feature observation concerns the spatial invariability of the fuel breaking point against the RZ with swirl number variation (i.e.: x/D=0.35). This result differs from those of number of authors observations (Syred et al [18], Shen et al [8], Bach and Gouldin [19], with straight exit burners). They obtain a displacement of the location and the modification in shape of the RZ with the swirl intensity, fuel and air injection velocity or overall equivalence ratio. With a straight exit, a competition exists between the central jet inertia which pushes up the RZ, and the adverse pressure gradient, related to S, which pushed down it. With quarl, as soon as the swirl intensity becomes sufficient, the RZ is formed and stays invariant in position.

3.2. Turbulence

Turning now to the turbulence characteristics analysis, the turbulent kinetic energy k is calculated from $k = \frac{1}{2}\left(\overline{u'^2} + \overline{v'^2} + \overline{w'^2}\right)$ (Fig. 8). Both k and U_{max} maximums are observed at the same location, any characteristic influence of the swirl number on the absolute maximum value of k is observed (Fig. 8). For the lowest swirl number case (S=0.1), the axial one-dimensional turbulence $\overline{u'^2}$ (Fig. 9)increases at the quarl exit whereas a constant decrease is observed for the highest swirl number (S=0.82). At the fuel jet breaking point (x/D=0.35) for S=0.82, we observe an increase of $\overline{u'^2}$. Goulding and al [20] has obtained the same behaviour. From a spectral analysis of axial velocity data, he put into evidence a low frequency oscillation of the RZ not observed in cold flow or weak swirl conditions. So, in the present work, we can interpret the high intensity level of $\overline{u'^2}$ as an axial fluctuation of the RZ. The two $\overline{u'^2}$ maximums downstream the quarl exit, also observed by Durao and al (11), are located respectively on the RZ frontier, and in the shear layer between main flow and lateral RZ.

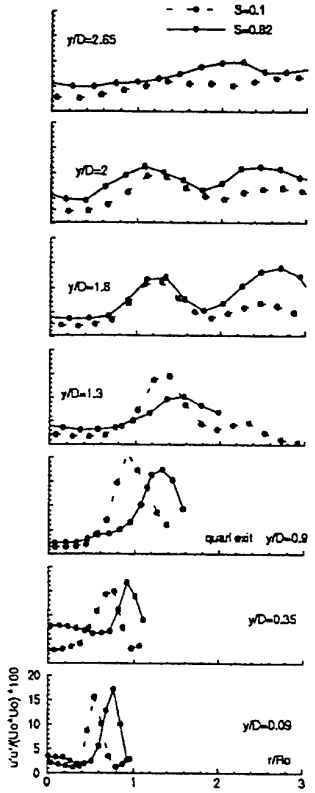

Fig. 9: Axial turbulent velocity u'^2 in the reactive flow

The behaviour of tangential $\overline{w'^2}$ and radial $\overline{v'^2}$ normal stresses are qualitatively similar according the following relationships $\overline{w'^2} = 3.\ \overline{v'^2}$. An important increase of $\overline{v'^2}$ and $\overline{w'^2}$ is measured at the top and downstream the RZ. The maximum of the velocity fluctuations are not located at the maximums of velocity gradients.

3.3. Reynolds Stresses

The diagram of the Reynolds shear stress $\overline{u'w'}$ (Fig. 11) shows the high dependence of the swirl number upon its distribution and maximum value. The increase of the swirl intensity leads to an appreciable increase of $\overline{u'w'}$ around and downstream the RZ limits. The negative $\overline{u'w'}$ values

observed on the external radius can be attributed to the shear strain generated by the lateral RZ.

This result shows an improve of turbulent momentum flux through the RZ envelop with the swirl number. This observation is corroborated by the observation of the increase of the cross correlation $\overline{u'T'}$ (turbulent heat flux) at the RZ edge.

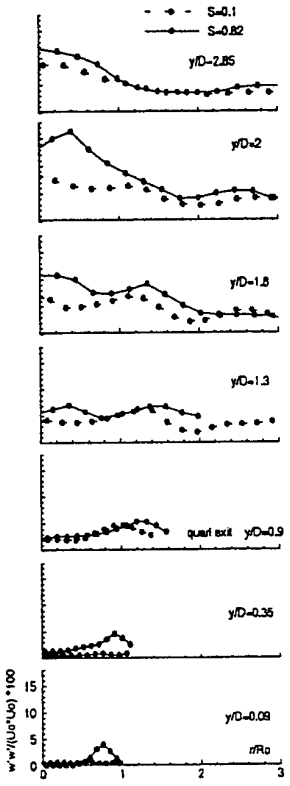

Fig. 10: Tangential turbulent velocity $\overline{w'^2}$ in the reactive flow

3.4. Assumptions on the Flame Stabilisation Processes

The RZ acts as an obstacle for the swirl flow which passes around. Reactants are preheated by this hot body and burn out side it. The combustion products flow along it, only a small mass flow rate of them (less than 12%) recirculates inside the RZ. The increase of the swirl number, improve turbulent heat and mass exchange with the RZ. This phenomenon can explain the observed decrease of the flame height with the rotation intensity and an increase of the chemical production rate. The complete study including temperature and species concentration measurements should indicate if such a turbulent exchange improve the combustion efficiency.

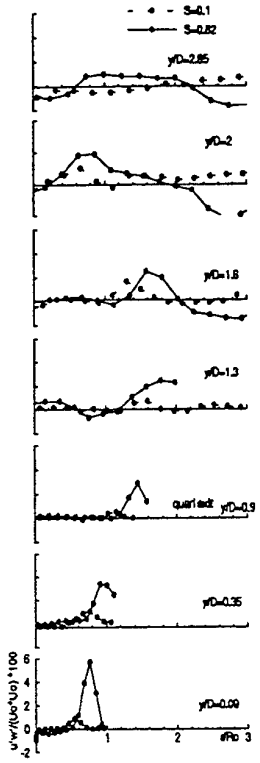

Fig. 11: Reynolds shear stress $\overline{u'w'}$ in the reactive flow

4. CONCLUSION.

Velocity measurements inside quarl and furnace are made to describe the aerodynamic structure of a confined swirl flame flow.

The study of the mean flow field shows that combustion can improve the strength of an central recirculation zone (RZ) not observed for inert flow and weak swirl values.

For reactive flow, when increasing the swirl number, the RZ surface decreases but the recirculated mass flow rate stays constant. Nevertheless, these modifications stay relatively small in regard of the influence of the other working conditions (i.e.: overall equivalence ratio, geometry, fluid velocity injection) studied by many authors. In opposition to straight exit burner study, quarl and furnace confinement limits radial jet expansion, even for high swirl numbers. The streamline inflection downstream the central recirculation zone lightly increases with the swirl intensity that can explain the decrease of the flame height. The RZ zone acts as an obstacle where reactants and combustion products flow around

The main effect of swirl number appears in the turbulent characteristics of the flow. Though the lower part location of the RZ inside the quarl and the fuel jet breaking point

stay independent of the swirl number, an increase of the rotation intensity leads to axial fluctuation of the bottom of the central RZ.

The results of the aerodynamic study of this swirl flame give a lot of important informations on the swirl flow behaviour related to the combustion processes (trajectory of reactants and products, heat and mass transfer,...). Complementary measurements of temperature and specie concentrations are made and under processing to locate the reaction zone and pollutant formation regions. A better knowledge of such a combustor system should help the designer to optimise future industrial burners and the modeler to validate numerical codes.

REFERENCES

1. Chen, Driscoll (1988) *22^{sd} Int Symposium on Combustion*, pp 531.

2. Lilley, (1977), *AIAA Journal*, Vol 15, n°8, pp 1063.

3. Syred, Chigier, Beer, (1967), *13th Int Symposium on Combustion*, pp 489.

4. Rawe, Kremer, (1977), *18th Int Symposium on Combustion*, pp 667.

5. Feikema, Chen, Driscoll, (1991), *Comb. and Flame*, Vol 86, pp347.

6. Leuckel, Fricker, (1976), *Journal of the Institute of fuel*, pp103.

7. Feikema, Chen, Driscoll (1990), *Comb. and Flame*, Vol 80, pp183.

8. Shen D., Most J-M., Joulain P. (1994), *Comb. Sc. and Tech*, Vol 100, pp203.

9. Froud D., O'Doherty, Syred N., (1995), *Comb. and Flame*, Vol 100, pp407.

10. Fricker, Leuckel, (1976), *Journal of the institute of fuel*, pp152.

11. Durao, Fernandes, Heitor, Moreira, Simoès, (1992), *6 th Int. Symp. on Applications of Laser Techniques to Fluids Mechanics*, pp 22-2-1.

12. Ferrao, Heitor ,(1992), *6 th Int. Symp. on Applications of Laser Techniques to Fluids Mechanics*,pp34-1-1.

13. Neveu, Corbin, Perrin, Trinité, (1994), 7th International Symposium on Applications of Laser Techniques to Fluids Mechanics,pp 2.4.1.

14. Tangirala, Chen, Driscoll, (1987), *Comb.Sci. and Tech.* , vol51, pp75.

15. Gouldin, Depsky, Lee, (1985),*AIAA Journal*, vol 23, pp95.

16. Chigier Dvorak, (), *15 th Int. Symp. on Comb.*, pp573.

17. Hillesman, Lenze, Leuckel, (1986), *21th Int. Symp. on Comb.*, pp1445.

18. Syred, Beer, (1974), *Comb. and Flame*, vol 23, pp143.

19. Bach, Vu, Gouldin, (1981), *AIAA Journal*, vol 19, n°5,pp642.

20. Gouldin, Halthore, Vu, (1984), *20th Int.Symp. on Comb.*,pp269.

21. Yazdabadi, Griffiths, Syred, (1994), *11th Int. Symp. on Application of Laser Anemometer to Fluid Mechanics*, pp19-4-1.

22. Gupta, Lilley, Syred, (1984),*"Swirl Flows"*. Abacus Press.

MIXING PROCESSES AND COMBUSTION OF A GAS JET FLAME SURROUNDED BY A SHROUD OF COMBUSTION AIR

by

P. X. Tran, M. P. Mathur, and J. M. Ekmann

Pittsburgh Energy Technology Center
P. O. Box 10940, MS 84-340
Pittsburgh, PA. 15236, USA

ABSTRACT

The present work reports an experimental study on the behavior of a jet flame which is surrounded by a shroud of combustion air. Measurements focussed on the flame length and on the emissions of NO_x, total unburned hydrocarbon, CO_2 and O_2. Four different fuel flow rates (38.33, 78.33, 138.33, and 166.6 cm^3/s), air flow rates up to 2500 cm^3/s and four different air injector diameters (0.079 cm, 0.158 cm, 0.237 cm, and 0.316 cm) were used. The results showed that a substantial shortening of the flame length occurred by increasing the air injection velocity keeping fuel rate fixed or conversely by lowering the fuel flow rate keeping air flow rate constant. NO_x emissions ranging from 5 ppm to 64 ppm were observed. NO_x emissions decreased strongly with the increased air velocity and the emission of NO_x was described well using the ratio of air to fuel Reynolds number as well as with the ratio of air to fuel velocity. On the contrary, the emission of the total hydrocarbon increased with the increased air velocity or with the decreased fuel flow rate. At the ratio of air to fuel velocity of about 1 the emissions of NO_x and of the total hydrocarbon were found to be under 10 ppm.

1. INTRODUCTION

The fuel-air mixing plays an important role in combustion. It has a strong effect on the combustion efficiency, flame length as well as the composition of the combustion products. Poor mixing produces zones of fuel rich and fuel lean within a combustor leading to a long, unstable and incomplete burning flame and unwanted exhaust gases. The mixing problem becomes even more important for high speed combustion application and for the development of super-lean and low NO_x burners where ultra fast mixing of fuel and oxidant is required.

The present work reports an experimental study on the behavior of a jet flame which is surrounded by a shroud of combustion air. The shroud of combustion air serves as a source for recirculation. We have two major objectives. The first one is to study the role of the shroud of combustion air in improving the fuel to air mixing rate. It is known that fuel-air mixing rate can be improved significantly by introducing internal recirculation flow (Chen and Driscoll (1988), Philipp et al (1992), Masri et al (1992)) or acoustically modulating the exit velocity of a coflowing jet, Lewis et al (1988). Chen and Driscoll (1988), in a study of the role of the recirculation vortex in improving fuel-air mixing within swirling flames, concluded that the vortex recirculation governs the mixing process of a swirling flame and that the flame length of a swirling flame follows a different scaling trend than that of a simple jet flame as fuel flow is increased. They found that, as fuel flow is increased, the length of a simple turbulent jet flame remains unchanged, yet the length of a swirling flame increases linearly.

Although acoustic excitation of isothermal jets produces significant increase in the near field spreading and entrainment rates, the far field remains essentially unchanged for small perturbation amplitudes. Large amplitudes and high frequencies, are, therefore, required to affect the far field significantly, Johari and Motevalli (1993).

Attempts have been also made to improve fuel-air mixing rate by burning of fuel puffs. It has been shown that individual fuel puffs have a considerably higher mixing rate as opposed to

steady jets in both quiescent media, Johari and Motevalli (1993), and as well as a transverse flow, Eroglu and Breidenthal (1991) and Vakili et al (1991). Johari and Motevalli (1993) reported that burning of small, well-separated fuel puffs in a quiescent air created intense and compact blue-colored flames as opposed to larger, closely-coupled puffs which were mainly yellow in color in the later case. They measured the flame length of a burning fuel puff and found that the flame length of individual puffs scales with the initial volume of the puff in the limit of small duty-cycles. As the duty-cycle increases for a specific flow condition, the flame length reduction stops due to the interaction among neighboring puffs. Eroglu and Breidenthal (1991) and Vakili et al (1991) discussed that introduction of fuel puffs into a quiescent media or in a cross flow, results in a totally different flow pattern and features which could be of a considerable value in increasing the diffusion and entrainment. For example, a train of puffs in a cross flow has a deeper penetration depth in comparison with steady jets, which may sweep through the surrounding gases and increase the mixing rate.

The second objective of our study is to investigate how an improved mixing rate effects the emission of NO_x from a steady gas jet flame. The Zel'dovich chain mechanism of the thermal NO_x has been assumed to be a dominant NO_x formation process in the combustion of natural gas. However, compared to the combustion process, it occurs at rather high temperature and at a slow rate, spread over a few milliseconds. Thus, to control the NO_x exhaust, both the combustion temperature and the combustion time need be reduced. Present-day burners usually involve with low oxidant excess combustion such as partially aerated and slotted burners, with flame cooled by water injection, by ceramic or metal rods placed in the flame, or with radiating surfaces such as ceramic or metallic fiber burners. Although these burners can reduce the NO_x exhaust to some degree, many disadvantages still remain. For example, reducing the excess oxidant prolongs the flame length and might result in the formation of carcinogenic products of incomplete combustion of benzopyrene type; flame cooled by metallic rods or by radiating surfaces reduces the overall thermal output.

The most effective way to reduce NO_x emissions from natural gas burners is to create a reverse flow of the combustion products into the flame before it reaches its maximum temperature. Recirculation can be introduced either externally by employing a recirculation device (such as a swirl, a central bluff body etc.) or internally by the dynamic action of the fuel and air flowing out of the burner in the furnace.

Peters and Donnerhack (1981) studied the NO_x production in a turbulent diffusion flame and observed a Reynolds and a Froud number dependence of the NO_x emissions. A theoretical formula was developed to predict the influence of the kinetics, the residence time and the flame length on the NO_x emission index (defined as NO_x production rate normalized by the fuel mass flow rate). When the influence of the nozzle diameter was considered a $Re^{-0.66}Fr^{0.33}$ dependence was proposed for scaling the NO_x-emission index.

Chen and Driscoll (1990) studied the effects coaxial air velocity, Reynolds number, and Damkohler number on the total nitric oxide emissions of a hydrogen diffusion flame. They reported a significant reduction of NO_x by forcing coaxial air into the flame. By using the ratio of air velocity to fuel velocity (V_a/V_f), together with the fuel gas Reynolds number they were able to predict successfully the reduction of the NO_x with the increased V_a/V_f. For methane flames with coaxial air flow, however, the NO_x emission levels did not decrease for V_a/V_f up to 0.15 and the decrease of NO_x emission was expected to occur for larger values of V_a/V_f.

Tomeczek et al (1994,1995) studied the NO_x emissions from large scale natural gas flames. They concluded that to attain successful NO_x abatement it is necessary to guarantee a good mixing of the flue gases with the combustion air. A reduction of NO_x up to 70% with only 15-20% flue gas recirculation was reported. The influences of air and fuel velocity, air swirl angle, air preheating temperature, furnace wall temperature etc. on NO_x emissions were investigated. The ratio of the coaxial air to fuel velocity was found to be an important parameter determining NO_x emissions and its effect on NO_x emissions showed a similar trend to that reported by Chen and Driscoll (1990). The influence of gasdynamics on NO_x emission was described very well using the ratio of the coaxial air to fuel velocity and the ratio of the coaxial air to fuel momentum density together with the air preheating and the wall temperature.

The influence of mixing on the flame characteristics and the formation of NO_x in semi-industrial scale oxy-natural gas flames was investigated by Hedley et al (1995). They reported that the mixing angle and increased oxygen

injection velocity results in increasing strength of the recirculation and hence reduced NO_x.

Since the properties of a diffusion flame depend strongly on both fuel and air flow conditions, for this objective, the present work will study the NO_x emissions of a natural gas flame for a variety of fuel and air flow conditions. The aim is to develop a NO_x scaling which could be useful for burner design. It will be shown later that an increase of the air velocity shortens the flame length and forces the jet flame to exist closer to the nozzle tip where the velocities are larger. This reduces the local residence time and the combustion zone volume. It is, therefore, that the reduction of NO_x by increasing the air velocity may affect the emissions of other unwanted species such as the unburned hydrocarbon. Thus it is also of equal importance to investigate the emissions of the unburned hydrocarbon for a variety flow conditions in order to identify a crossover condition that can benefit both NO_x and THC reduction.

2. EXPERIMENTS

The experimental apparatus used in the study consisted of a combustion chamber, a gas nozzle unit, and a gas handling system coupling with a gas mixer and an electrical heater.

The combustion chamber was a pyrex glass tube of 20 cm diameter and 70 cm long. At one end, the chamber was attached to a base that was designed to house a gas/air injection unit at its center and to have ports for temperature monitoring and ignition source. The other end was fitted with gas lines for on-line NO_x, unburned hydrocarbons, CO_2 and O_2 monitoring. The air/gas injection unit had a cylindrical shape with an inside diameter of 2.5 cm, an outside diameter of 5 cm and a length of 2 cm. It was made out of brass. Its end, facing the chamber, attached to a brass orifice plate while two gas supply lines were fitted into the other end. The plate had 19 holes of equal size. The gas nozzle unit had a contoured nozzle, a solenoid valve with the associated electronic control circuit. The nozzle was made from stainless steel with the inlet diameter of 2.5 cm and the exit diameter of 0.158 cm. It was situated inside the gas/air injection unit. The solenoid valve had an opening diameter of 0.65 cm and maximum operating frequency of about 15 Hz. Opening and closing the solenoid valve was done by a solid state relay which was controlled by a digital output board (DAS-08). The frequency and duration of the injection was determined by a software controlling the board to produce square non-symmetrical waveforms.

Methane, (density ρ = 0.652 kg/m^3, and viscosity $\mu = 1.1 \times 10^{-5}$ kg/m-s), from a high pressure cylinder was used in the present study. The pressure was regulated and set at 160 kPa throughout the tests. Steady flow rates were maintained constant between 38 to 170 cm^3/s for methane and 300 to 2800 cm^3/s for air. For the "pulsed" jet flame, the frequency was varied between 0 to 5 Hz and fuel injection times were varied between 60 to 200 ms. Combustion experiments were supported by several on-line total hydrocarbon, oxygen NO_x, CO_2, and O_2 analyzers. A high speed digital imaging system was used for visualizing the flow pattern and the mixing process.

3. RESULTS AND DISCUSSIONS

Our observations showed that without air injection, the flame was lazy and yellow indicating the presence of soot. When air was injected a stagnation point region was formed on top of the flame that marked the farthest penetration of the fuel jet. The stagnation region then acted like an obstacle to reverse the flow of both fuel and air back to the nozzle creating a strong recirculation zone at the flame base. This flow pattern increased dramatically the fuel to air mixing process. For a given fuel flow rate, as air flow rate was increased, the stagnation point region moved toward the nozzle and the recirculation became stronger. As a result, the flame was seen to burn closer to the nozzle tip. The flame was noisy, compact and so intensely blue that the flame was visible only when the laboratory was darkened. For a fixed air flow rate, as fuel flow rate was increased, the stagnation contour was deformed and moved upward weakening the recirculation zone. Further increasing the fuel flow rate the fuel jet penetrated through the stagnation contour and air entrained into the flame along its axis. The flame completely reverted from a short, intensely blue and noisy to a longer and jet-like premixed flame.

Flame lengths were measured for a wide range of fuel flow rates (Q_f), air flow rate (Q_a), air injection momentum, etc. For a given test, the desired fuel flow rate and flame length for a steady jet diffusion flame were determined first. With the solenoid valve being activated to fully open for about 5 min, the flow rate was determined by

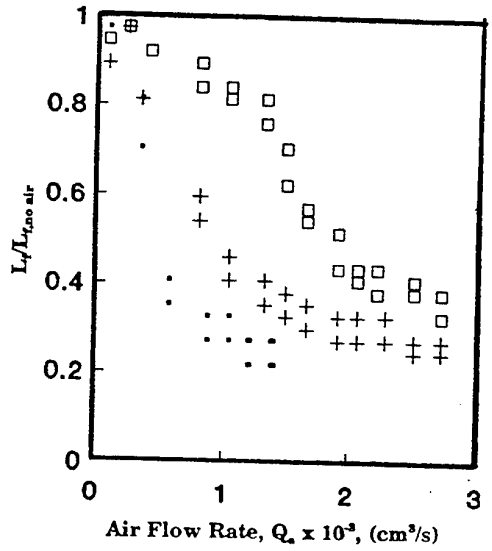

Figure 1. Flame Length with air injection normalized by the flame length without air injection as a function of air flow rates (Fuel flow rate: 43.33 cm^3/s; d_f: 0.158 cm; d_a: ▪: 0.079 cm; +: 0.158 cm; □: 0.316 cm)

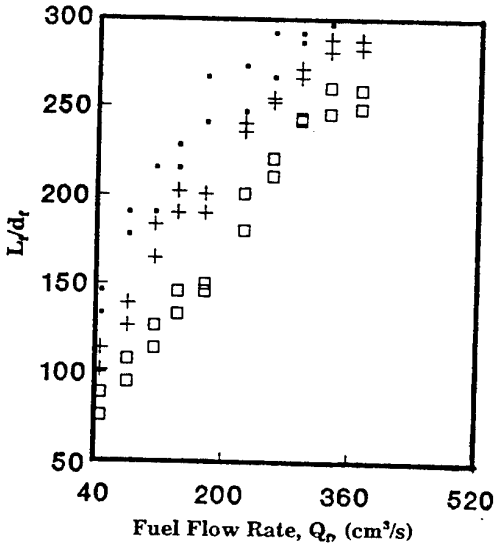

Figure 2. Flame Length normalized by nozzle diameter as a function of fuel flow rates (d_a: 0.237 cm; d_f: 0.158 cm; air flow rates: ▪: 1317 cm^3/s; +: 1678 cm^3/s; □: 2450 cm^3/s)

adjusting the control valve of the flowmeter on the gas control panel. When the fuel flow rate was set, combustion air was introduced via the combustion air ring. The air flow rates were increased and the flame length was recorded using two high speed digital video cameras.

Typical data showing the effects of fuel flow rate, air flow rate, and air injection velocity on the flame length were given in Figs. 1 and 2. In general, the flame length with air injection was five to six times shorter than that of a simple flame in a quiescent air. A substantial reduction of the flame length occurred by increasing the air flow rate, keeping fuel flow rate fixed or conversely by lowering the fuel flow keeping air flow rate fixed. A substantial shortening of the flame length also occurred by increasing the air injection velocity while both fuel and air flow rates were kept constant. The present results are similar to the observations made by Chen and Driscoll (1988), in a study of the role of the recirculation vortex in improving fuel-air mixing. They concluded that the vortex recirculation governs the mixing process and of a flame and that the flame length decreases substantially with the increased air velocity.

To investigate the effect of the air injection on NO_x emissions, measurements were carried out for a wide range of fuel and air flow conditions. Four different fuel flow rates (38.33, 78.33, 138.33, and 166.6 cm^3/s), air flow rates up to 2500 cm^3/s and four air injector diameters (0.079 cm, 0.158 cm, 0.237 cm, and 0.316 cm) were used.

For such a variety of flow conditions we observed NO_x emissions ranging from 5 ppm to 64 ppm and a significant dependence of NO_x emissions on fuel flow rates, air velocity and air mass flow rates. As shown in Fig. 3, for a fixed fuel flow rate, as the air flow velocity increased the NO_x emission significantly decreased and leveled off at a constant value which was from 5 ppm to about 15 ppm depending on the fuel mass flow rate. Such a substantial decrease in NO_x emissions also occurred by lowering the fuel flow rate keeping air velocity rate constant. The reduction of NO_x presented in these figures is caused by the recirculation of the combustion products into the flame. This is because the

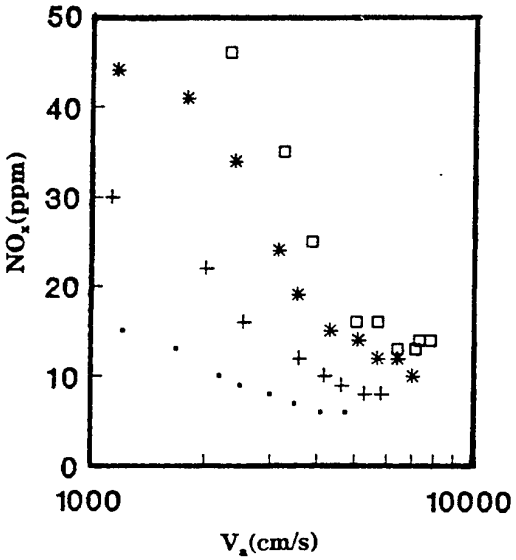

Figure 3. NO_x emissions as a function of air velocity: Effects of fuel flow rate (d_a = 0.158 cm; d_f = 0.158 cm; fuel flow rate: ■: 38.33 cm^3/s; +: 78.83 cm^3/s; *: 138.33 cm^3/s; □: 166.6 cm^3/s)

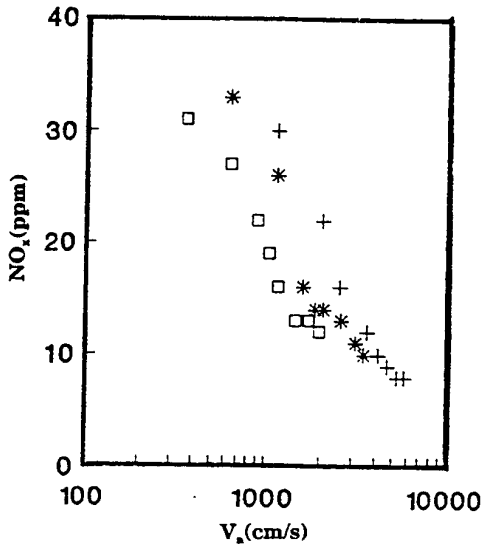

Figure 4. NO_x emissions as a function of air velocity: Effects of air mass flow rate (d_f = 0.158 cm; fuel flow rate: 138.33 cm^3/s; +: d_a = 0.158 cm; *: d_a =; 0.237 cm; □: d_a = 0.316 cm)

conditions for the recirculation of the combustion products into the flame are determined almost entirely by the air injection momentum as observed by our present experiments.

The effect of the air mass flow rate on NO_x reduction can be investigated using Fig. 4 which showed data on NO_x emissions versus the air velocity, at three different air injector diameters. It is clear that the reduction of NO_x also occurred by increasing the air mass flow rate while both fuel flow rate and air injection velocity were kept constant. However, the effect of the air mass flow rate on NO_x emissions was much less significant than the effect of air velocity or of fuel mass flow rate.

In practice, it is of interest to relate the NO_x emission to both fuel and air flow conditions in order to obtain the NO_x scaling which could be useful for burner design. For a simple jet diffusion flame in a quiescent air the amount of NO_x emission has been related to the fuel gas Reynolds number by Peters and Donnerhack (1981). Chen and Driscoll (1990) used the ratio of air velocity to fuel velocity to correlate NO_x emissions from coaxial air-hydrogen diffusion flames. For industrial flames the NO_x scaling is more difficult because of the complex shape of the air and fuel nozzle of the burner. Available data, however, show that NO_x emission decreases when air velocity increases, Tomeczek et al (1994,1995). Our data confirm such a behavior as shown in Fig. 5 and 6 where data on NO_x emissions were plotted against the ratio of air to fuel velocity,(V_a/V_f), and the ratio of air to fuel Reynolds number ratio, (Re_a/Re_f), respectively. The present data showed a significant decrease of NO_x for V_a/V_f less than 1 and for larger values of the air velocity to fuel velocity ratio the reduction of NO_x was much less significant. In these figures, the solid lines, which were calculated using an equation similar to the one proposed by Tomeczek et al (1995), agreed very well with the measured data. Thus it is clear that there is an excellent correlation between NO_x emissions and these ratios and the NO_x emissions can be predicted using either one of these three ratios.

Since the properties of a diffusion flame depend strongly on both the fuel and air flow conditions the reduction of NO_x by increasing the air velocity or by lowering the fuel flow velocity may also affect the emissions of other unwanted species such as the unburned hydrocarbon. Thus

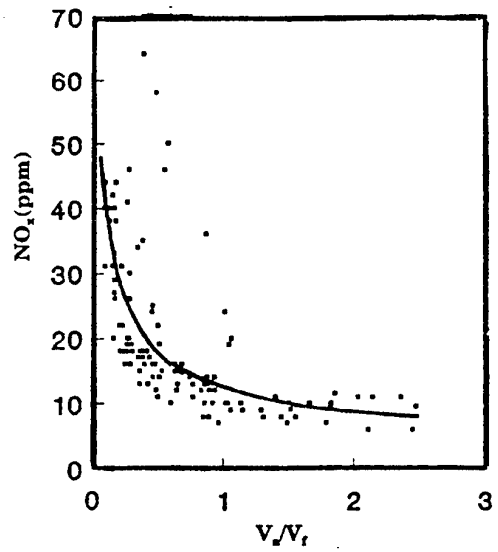

Figure 5. Effect of V_a/V_f on NO_x emissions (■: measured; the solid line calculated from $NO_x(ppm) = 12.43(V_a/V_f)^{-0.5}$)

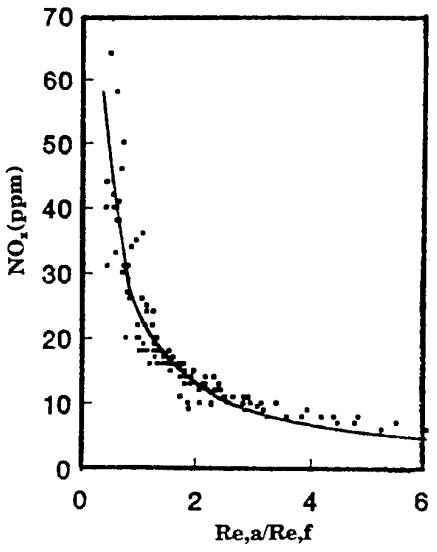

Figure 6. Effect of Re_a/Re_f on NO_x emissions (■: measured; the solid line calculated from $NO_x(ppm) = 24.24(Re_a/Re_f)^{-0.9}$)

it is of importance to investigate the emissions of the unburned hydrocarbon for a variety flow conditions in order to identify a crossover condition that can benefit both NO_x and THC reduction.

Data in Figs. 7 and 8 showed the total unburned hydrocarbon in the exhaust gases for a variety of fuel and air flow conditions. It is clear that, for a fixed fuel velocity the unburned hydrocarbon emissions increased substantially as the air velocity increased. For a given air velocity a substantial increase of the total unburned hydrocarbon emissions also occurred when the fuel velocity decreased.

For a given fuel velocity, if air velocity is not high enough to form a stagnation contour on top of the flow, the flame is long and intense with air rapidly entraining into the flame along its axis. As a result the flame temperature is high leading high NO_x emissions. Since the flame is long the fuel has enough time to burn resulting in high CO_2 and low THC emissions. For example, at air velocity of 2396 cm/s, an increase of the fuel velocity from 6909 cm/s to 8425 cm/s resulted in an increase of NO_x emissions from 34 ppm to 46 ppm and a decrease of the unburned hydrocarbon from 7 ppm to 1 ppm. The decrease of the THC emissions indicated that more fuel was burned in the combustion zone as indicated by the increase of the CO_2 concentration in the exhaust gases from 4.2% to 5.1% and the decrease of oxygen concentration from 13% to 11% respectively. If the air velocity is high enough the stagnation contour is formed creating a strong recirculation zone near the nozzle tip where fresh fuel and air intensely mix with the combustion products. As a result, the flame temperature is low and NO_x emissions are reduced. Because the flame length is short the jet flame is forced to exist closer to the nozzle where the velocities are larger. This reduces the local residence time as well as the reaction zone. Thus there may exist a situation that the combustible mixture slip over the combustion zone before it has enough time to burn completely. Thus this results in high unburned hydrocarbon in the exhaust gases. For example at fuel velocity of 1938 cm/s an increase of the air velocity up to 9973 cm/s led to a decrease of the NO_x emissions from 44 ppm to less than 2 ppm while the total unburned hydrocarbon increased from 8 ppm to 750 ppm.

The above results indicate that the shroud of the combustion air has a strong effect on the flame length, NO_x formation and the total unburned hydrocarbon emissions. The reduction of NO_x always is associated with the increase of the

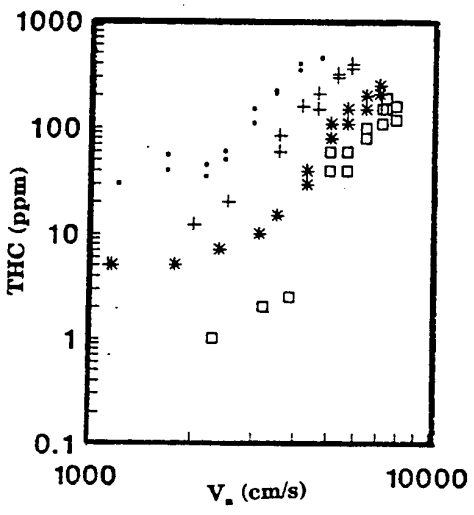

Figure 7. THC emissions as a function of air velocity: Effects of fuel flow rate (d_a = 0.158 cm; d_f = 0.158 cm; fuel flow rate: ■: 38.33 cm^3/s; +: 78.83 cm^3/s; *: 138.33 cm^3/s; □: 166.6 cm^3/s)

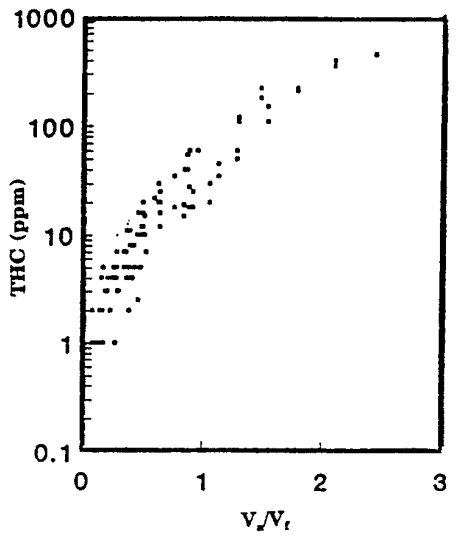

Figure 8. THC emissions as a function of V_a/V_f

unburned hydrocarbon. A crossover condition that benefits both NO_x and unburned hydrocarbon must be identified. With the conditions used by the present work it was found that NO_x and unburned hydrocarbon emissions were both less than 10 ppm at the ratio of air to fuel velocity of about 1.

4. CONCLUSIONS

A experimental apparatus has been developed for studying the combustion characteristics of a steady-jet flame which is surrounded by a shroud of combustion air. From these preliminary observations, it is clear that the shroud of air has a strong effect on the flame length, NO_x and unburned hydrocarbon emissions. The NO_x emission is correlated very well with either the ratio of air to fuel velocity or the ratio of the air to fuel Reynolds number.

REFERENCES

1. Chen, H. R., and Driscoll, J.F. 1988, The Role of the Recirculation Vortex in Improving Fuel-Air Mixing Within Swirling Flames, Twenty-Second Symposium (International) on Combustion, The Combustion Institute, Pittsburgh, pp. 531-540.

2. Chen, R.H., and Driscoll, J. F., 1990, Nitric Oxide Levels of Jet Diffusion Flames: Effects of Coaxial Air and Other Mixing Parameters, Twenty-Third Symposium (International) on Combustion, The Combustion Institute, Pittsburgh, pp. 281-288.

3. Eroglu, A., and Breidenthal, R. E., 1991, Effects of Periodic Disturbances on Structure and Flame Length of a Jet in a Cross Flow, AIAA paper 91-0317.

4. Hedley, J., T., Pourkashanian, M.m Williams, A., and Yap, L. T. 1995, NO_x Formation in Large-Scale Oxy-Fuel Flames, Combustion Science and Technology vol. 108, pp. 311-322.

5. Johari, H., and Motevalli, V. 1993, Flame Length Measurements of Burning Fuel Puffs, Combustion Science and Technology, vol. 94, pp. 229-244.

6. Lewis, G.S., Cantwell, B.J., Vandsburger, U., and Bowman, C.T. 1988, An Investigation of The Structure of a Laminar Non-Premixed Flame in an Unsteady Vortical Flow, Twenty-Second Symposium (International) on Combustion, The Combustion Institute, Pittsburgh, pp. 515-522.

7. Masri, A. R. Dibble, R.W. and Barlow, R.S.1992, The structure of Turbulent Nonpremixed Flames of Methanol Over a Range of Mixing Rates, Combustion and Flame, vol. 89, pp. 167-185.

8. Philipp, M. Hoffmann, S. Habisreuther, P. Lenze, B. and Eickhoff, H. 1992, Experimental and Numerical Study Concerning Stabilization of Strong Swirling Premixed and Nonpremixed Flames, Twenty-Fourth Symposium (International) on Combustion, The Combustion Institute, Pittsburgh, pp. 361-368.

9. Peters, N., and Donnerhack, S. 1981, Structure and Similarity of Nitric Oxide Production in Turbulent Diffusion Flames, Eighteen Symposium (International) on Combustion, The Combustion Institute, Pittsburgh, pp. 33-42.

10. Tomeczek, J., Goral, J., and Gradon, B. 1995, Gasdynamic Abatement of NO_x Emission from Industrial Natural Gas Jet Diffusion Flames, Combustion Science and Technology vol. 105, pp. 55-65.

11. Tomeczek, J., Goral, J., and Gradon, B. 1994, Influence of Gasdynamics on NO_x Emission from Large Diffusion Natural Gas Flames, Twenty-Fifth Symposium (International) on Combustion, The Combustion Institute, Pittsburgh, pp. 1035-1041.

12. Vakili, A. D., Chang, Y. K., and Wu J. M. 1991, Vortex Rings in Uniform Cross-Flow, AIAA Paper 91-0522.

Visualisation of Coherent Structures in a Highly Turbulent Swirling Flame

W. Fick, A. J. Griffiths and T. O'Doherty

University of Wales, Cardiff
Division of Mechanical Engineering & Energy Studies
PO Box 917, Cardiff CF2 1XH, GB

1. ABSTRACT

Experimental characterisation of highly turbulent flows in swirl burners has revealed complex three dimensional structures. Advanced diagnostic tools with the aid of the phase averaging technique has made it possible to experimentally evaluate the complex flow patterns and to explain the combustion principles.
The use of phase averaging is limited when dealing with highly turbulent swirling flows. Fine structures in the flow might not be detected and the interpretation of combustion principles governing the rotating flame incomplete.
The aim of this research was to correlate flow visualisation techniques to the results obtained using phase averaged analysis. An additional vortex in the rotating flame was found. The effect of this vortex on the combustion process is advantageous and correlates very well with the main vortices previously found.

2. INTRODUCTION

A considerably driving force for research into the characteristics of swirl burners has been the industrial desire to combust poor quality fuels efficiently, particularly gaseous fuels with low calorific value (Gupta et al (1984) and Froud et al (1995a). Swirl Burners are particularly useful for combusting difficult carboneous materials and poor quality gases.
They are of simple geometrical construction, although the aerodynamics are extremely complex due to the high levels of turbulence. Hence flame stabilisation and emissions are the main problems arising from a lack of fundamental understanding of the interaction between the aerodynamics and thermal characteristics within the swirling flame.
Sensitive to both the geometry as defined by the geometric swirl number and flow, a breakdown phenomenon occurs at a condition where a three dimensional time dependent flow is generated. This phenomenon is called the Precessing Vortex Core (PVC). Discovered 20 years ago by Gupta et al (1984), it is only recently, with the advancement of laser diagnostics and high speed photography that any detailed analysis has been successfully undertaken.

The physical appearance of the PVC in swirling flames reduces the flame length and generates a high emissivity flame. It creates large pressure variations within the flame such that to stabilise the flame a closed loop feed back system is established. This feedback manifests itself as a Reverse Flow Zone (RFZ) within the structure of the flame.
It is this RFZ that stabilises the flame and allows the mixing and re-mixing of the reactants, such that efficient combustion takes place. It has also been noticed that the PVC is present many burner exit diameters downstream within the exhaust region of the flow (Yazdabadi et al (1994)).
Phase averaged Laser Doppler Anemometry (LDA) measurements at Cardiff University by Froud et al (1994 and 1995b) revealed the highly complex flow structures and funded the basis for further investigations. The same phenomena has been investigated with similar techniques by Yazdabadi et al (1994) and isothermal results from cyclone dust separators are available for comparison. Lucca-Negro and O'Doherty (1996) are currently modelling the isothermal flow in an industrial scaled swirl burner and the three dimensional time dependent predictions are in good qualitative and quantitative agreement when compared to LDA measurements.
As a non intrusive technique High Speed Photographic flow visualisation under combustion conditions was used to characterise the swirling flow. A 16 mm high speed camera, synchronised with the laser, was used to photograph the flow highlighted by the laser sheet when seeded with suitable discrete particles.
Additional coherent structures were found associated with the PVC but resolution limitations of the high speed photography did not allow further investigations, PTV (Particle Tracking Velocimetry) images under isothermal conditions were obtained to further characterise the flow.
The experimental set-up was similar to that of the highspeed photography. A controller was used instead of continuous synchronisation to trigger a still camera and the laser to fire pulses at a certain frequency simultaneously. This results in multiple exposed single frame images.

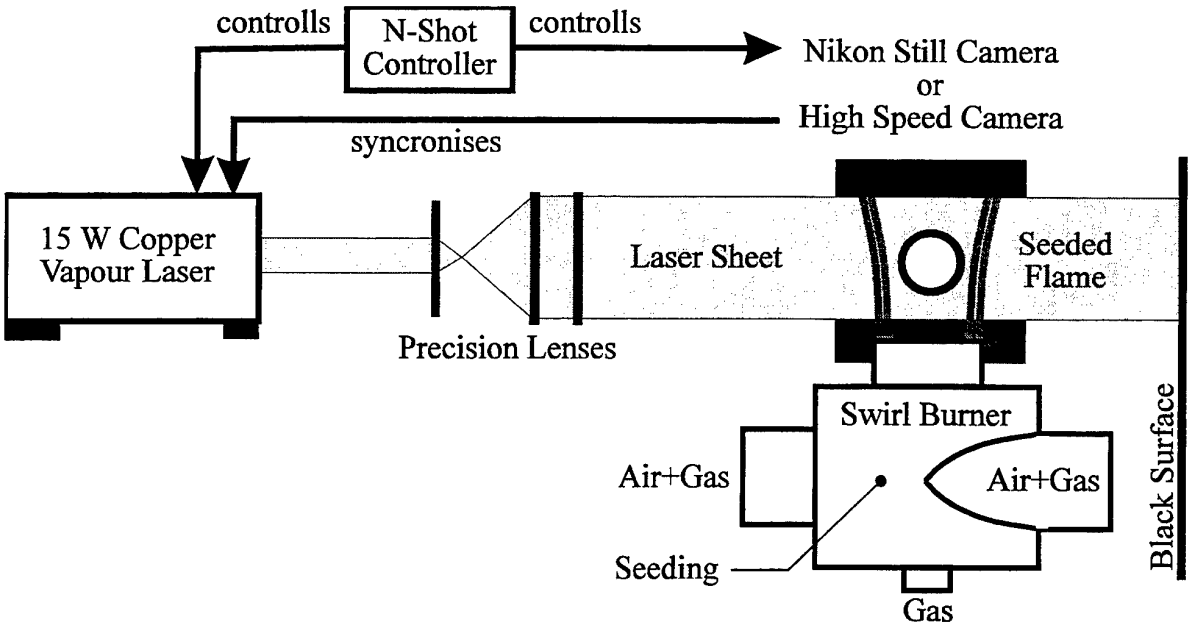

Figure 1: Experimental Set-Up

3. APPARATUS AND EXPERIMENTAL CONDITIONS

The results presented in this paper were obtained under isothermal as well as combustion conditions. For isothermal conditions PTV was used and for combustion conditions high speed photography was used to visualise the flow.

Test Rig

A 150 kW model swirl burner was used. It is of simple design and a 1/4 scale model of a large scale 2 MW swirl burner. The furnace was removed to allow complete access for flow visualisation. The tangential inlets were reduced by 50 % in cross-sectional area by the use of inserts, hence the geometric swirl number increased. By varying the tangential inlet area the geometrical swirl number could be varied between 0.8 and 4. In this particular case 90 % of the gas was premixed in the two tangential inlets of the burner, and the final 10 % added axially to the bottom of the swirl burner. This corresponds to a volumetric mixture ratio of 1.4, hence 40 % excess air was present in this particular configuration. The geometrical swirl number S of the burner was 1.5 for all the experiments described in this paper.

Seeding:

Two types of discrete particles were used to seed the flow for both isothermal and combusting flow. In the case of combustion the flow was seeded with submicron titanium dioxide particles of a size of 0.1-1 μm to enhance the self illuminating effect of the rotating flame and to visualise the flow around it. For the isothermal case spherical glass balls of a measured mean diameter of 30 μm were used. They followed the strong swirling flow very well and provided excellent reflection characteristics to visualise the same area of the flow as under combustion conditions. This could not be achieved with titanium dioxide particles since the amount of light reflected by the particles and the sensitivity of the film could not be matched.

Illumination-System:

As a light source a CU10-A Copper Vapour Laser from Oxford Lasers Ltd was used. The laser produces light at a wavelength of 510.6 nm at burst frequencies ranging from 2 to 30 kHz and with a typical power output of 9 mJ per pulse. One cylindrical lens and two spherical lenses to produce a constant light sheet of 1.5 mm thickness. Figure 1 shows the two operation modes used for the experiments. For high speed photography the laser was directly synchronised by the high speed camera. For PTV the laser was operated by a controller to modulate the burst pulses determined by the controller (Fick et al (1996a)).

Still Camera:

To record multiple pulses on single frame a Nikon F-801s still camera was used. High sensitive colour 35 mm film (ISO 1600) was used to record multiple exposed PTV images. The film was specially developed to enhance the resolution. The images were digitised with a high resolution scanner.

High Speed Camera:

A Photec high speed cine photography system was used to record single exposed high speed film sequences. 16 mm RAR Kodak film was used for the camera. Developing solutions and speeds were chosen to maximise the contrast of the developed film.

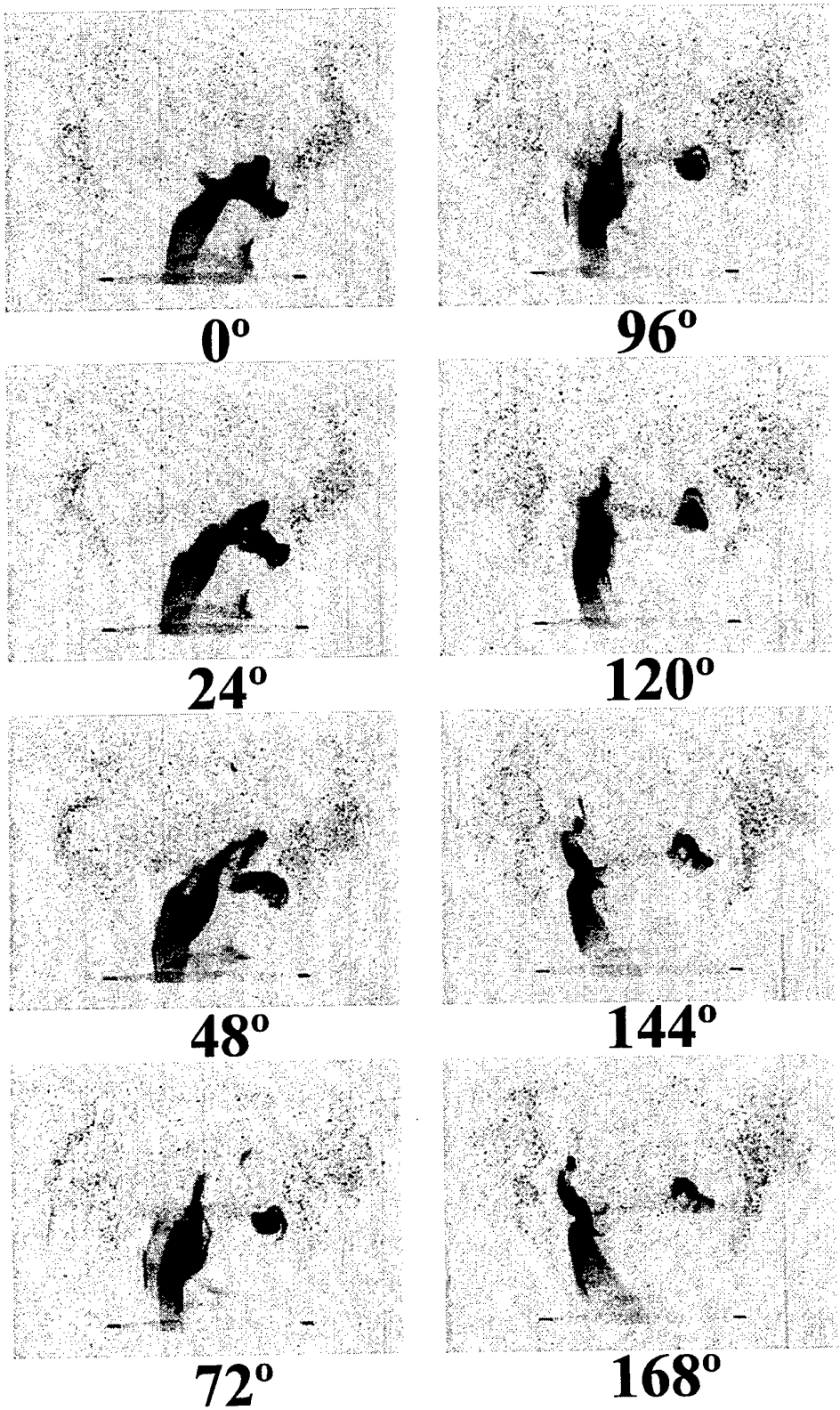

Figure 2: Side View High Speed Sequence of the PVC

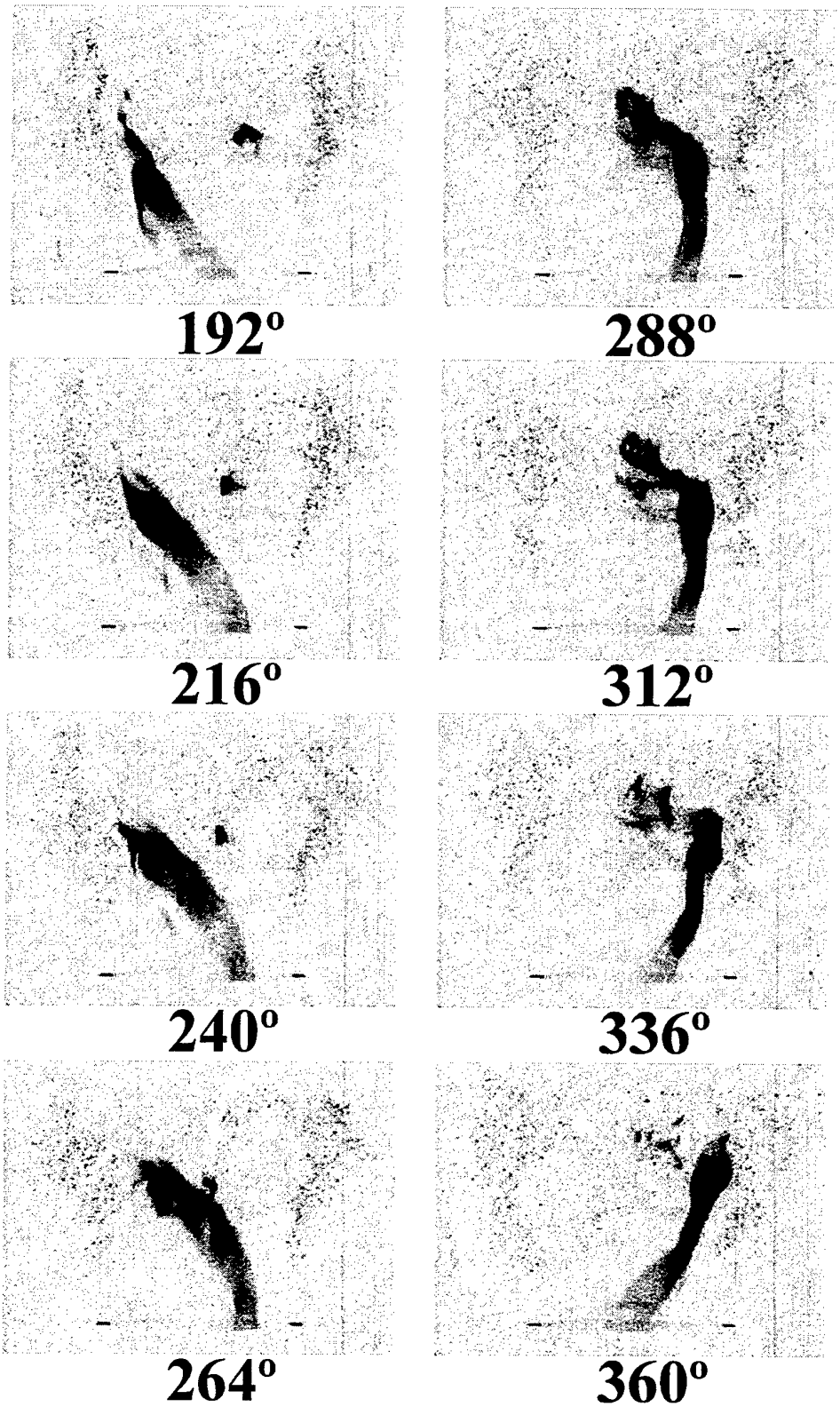

Figure 2: Side View High Speed Sequence of the PVC (continued)

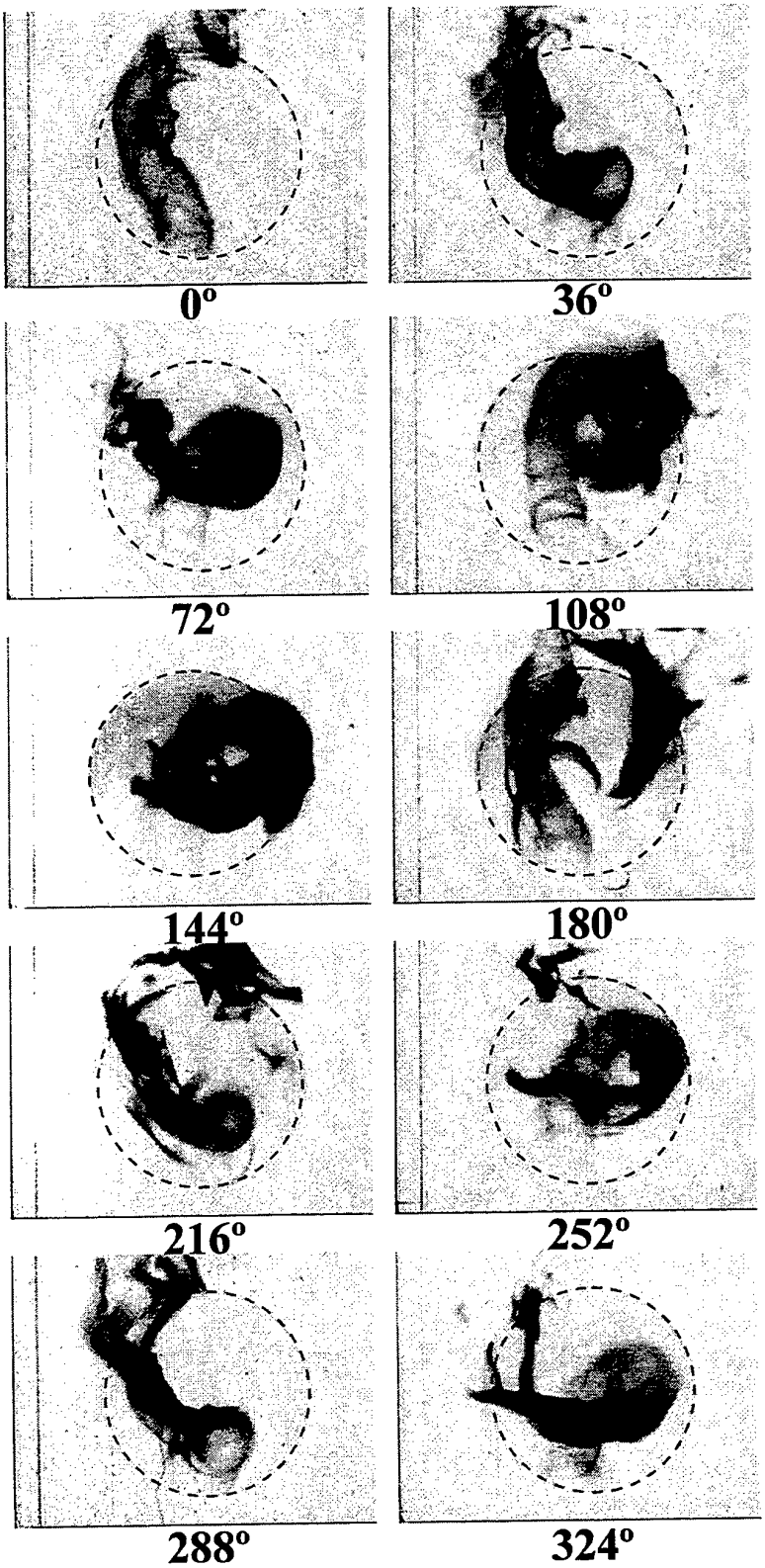

Figure 3: Plan View High Speed Sequence of the PVC

Figure 4: Isothermal PTV Image of Flow

Figure 5: High Speed Snap Shot under Combustion Conditions

4. VISUALISATION TECHNIQUES

The main objectives of this work were to visualise the PVC and the flowfield associated with the aid of laser based techniques to further explain the complex aerodynamics caused by this phenomena and to determine its impact on the combustion characteristics. For both High Speed Photography and PTV analogue recording media were used.

Recording Media	Photographic Resolution	Resolution Digitised Image
16 mm Film	780 × 1070 pixels	240 × 320 pixels (Real Time Frame Grabber Card)
35 mm Film	2400 × 3600 pixels	2400 × 3600 pixels (High Resolution Scanner)

Table 1: Resolution Limits of Recording Media

The photographic resolution limits are based on the resolution of conventional film. This is generally 100 lines per mm. Due to more advanced lenses and better film quality of the 35 mm technique the resolution is estimated to be considerably higher as described in Table 1. Therefore the use of High Speed Photography with a pulsed laser source does not resolve fine enough to investigate fine structures in an isothermal flow.

High Speed Photography

High Speed Photography was used under combustion conditions in this case to visualise the rotating flame. Figure 1 shows the experimental set-up. The self illuminating effect of the rotating flame was enhanced by the seeding and the laser light. The surroundings were highlighted by the laser sheet showing the varying boundaries of the flame.

Two different speeds were chosen to photograph the flow. 2000 fps (frames per second) for the plan view and 3000 fps for side view. At those speeds the power output of the laser and the sensitivity of the high speed film could be matched to give the best results. With an approximate frequency of the PVC of 100 Hz this results in 20 or 30 frames per revolution respectively.

The images were transferred to VHS video tape. A VHS video recorder connected to a real time video capture card mounted in a PC was then used to digitise images for presentation.

Since an absolute starting point of the PVC on the high speed sequences is hard to determine, the positions on Figures 2 and 3 do not mark the absolute position of the PVC in a particular cycle, but show various positions in a cycle relatively to each other.

PTV

PTV images as shown in Figure 4 in this case were obtained under isothermal conditions to be compared to the results obtained under combustion conditions as shown in Figure 5. High Speed Photography did not prove as successful in this case due to resolution limits of the recording media.

5. RESULTS AND DISCUSSION

Research in this area has been directed to investigate high levels of swirl in inert as well as reacting flows. LDA measurements carried out previously by Froud et al (1994 and 1995b) described the occurrence of the PVC in swirl burners with rotating velocity fields, the dissipation of energy in swirling reactors is described by O'Doherty et al (1992) and temperature characterisation of the rotating flow by Fick et al (1996b and 1996c).

The insight gained via flow visualisation is expected to correlate previous findings and to fund the basis for further applications of optical techniques.

The occurrence of the PVC and its associated structures are considered to be of paramount importance for the combustion of low calorific value gases. The high levels of mixing caused by the PVC and the presence of an associated rotating large off centre RFZ are substantial to the combustion of low calorific value gases in swirl burners under premixed conditions.

The Vortex Breakdown, the PVC and the RFZ

Figure 2 shows a side view high speed photographic sequence for one revolution of the PVC in steps of 24°. The two black dashes at the bottom of each picture mark the burner exit. The PVC shows the typical curved and bent structure as found in previous work (Froud et al (1995b) and Fick et al (1995b)). The PVC in this case rotates clockwise and is bent anticlockwise against the direction of the rotating flow. Four subsequent pictures of each column in Figure 2 confirm how the PVC bents after 90° in a cycle. At 120° (which corresponds to about 180° in an absolute cycle) the PVC moves towards the back and at 312° (0° in an absolute cycle) the PVC moves towards the front.

Some important features of the PVC are clearly visualised in Figure 2.

- The PVC continuously changes its shape and appearance, even several times within a single cycle.
- The breakdown of the PVC (i.e. the breakdown of the flame) at about one burner exit diameter downstream is not clearly defined and occurs in an irregular way over 1 complete cycle.
- The flamefront breakdown is essential to the RFZ, it feeds the RFZ and hence increases the residence time of hot (and unburned) combustion reactants.
- The boundaries of the flame are dependent on the PVC and subsequently axisymmetric.

Fick et al (1996b) found that two types of flames were identified in the rotating temperature fields. This is now confirmed with the high speed sequences. The outer flame is stabilised by premixing and surrounds the PVC. The inner flame is stabilised by diffusive mixing and the RFZ. As can be seen in Figure 2 the flamefront breakdown does not only supply hot combustion reactants but as well active combustion species. At 24° a part of the tip of the flamefront breaks off and combustion of this fragment is maintained till about 264°. This provides reignition for the reactants in the RFZ and proves the fuel rich nature of the RFZ. Also the recirculation zone plays an important role in flame stabilisation by providing a hot flow of recirculated combustion products and a reduced velocity region where flame speed and velocity can be matched and allow efficient combustion to take place.

Figure 3 shows a plan view high speed sequence of the PVC. The dashed cycles on each picture mark the burner exit. Again, it evidently shows the highly turbulent nature of the PVC and the flamefront breakdown that partially directly feeds the RFZ. Figure 3 at 180° actually shows that the "fireball" remaining behind the PVC in Figure 2 is not spherical, but crescent in shape. This corresponds very well to crescent shaped regions of high and low tangential and axial velocity regions found 180° opposite to each other in rotating velocity contour plots by Froud et al (1995). The same is reflected in the phase averaged temperature contour plots by Fick et al (1996) where a crescent shaped region of high temperatures was found to lag the PVC by 180°.

The Vortex Breakdown and the Outer RFZ

Figure 4 shows an isothermal PTV image. The PVC is situated at 180° in absolute co-ordinates, 180° opposite to the vortex on the right in Figure 4. This isothermal PTV image corresponds very well to Figure 5, which is a frame taken from a high speed sequence under the same inlet flow conditions. In both pictures the PVC is at the same position and a second vortex appears geometrically opposite.

Not only does the PVC leave a low pressure region behind where the RFZ forms towards the geometric centre of the system, the kinetic energy extracted from the system by the PVC and the RFZ generates a second vortex. This vortex is three dimensional as the PVC itself and the RFZ.

O'Doherty et al (1992) show that the overall pressure drop of the system with respect to the average exhaust velocity can be represented as:

$$\Delta P_e = \Delta P_v + \Delta P_{rfz} + \Delta P_{pvc} = \varepsilon_e \frac{\rho}{2} U_e^2$$

where:

ΔP_v = *pressure drop across the swirling flow*
ΔP_{rfz} = *pressure loss across the exhaust nozzle*
ΔP_{pvc} = *system pressure drop caused by the PVC*
ε = *Euler number*
ρ = *density*
U = *mean axial velocity*
Subscript e = exhaust

The driving of the PVC absorbs significant quantities of energies which is reflected in an increased system pressure drop (O'Doherty et al (1992)).

It is mainly due to ΔP_{pvc} that an additional vortex structure opposite the PVC can originate. It directs part of the axial and tangential flow towards the geometric centre where premixed gas and air sustain the RFZ. Figure 4 shows that a flame is maintained around this vortex which has its own feedback mechanism as the reactants follow the circular motion or join the flow as the PVC appears 180 ° later in a cycle.

The effect of the outer recirculation zone is expected to be enhanced under confined conditions where a low pressure region is typically present between the burner rim and the furnace wall.

Figure 6 shows averaged temperature profiles under confined conditions. Stick formed R-type thermocouples were used for these measurements. 10000 samples were taken at a speed of 1 kHz and averaged.

The experimental conditions were the same as for High Speed Photography under unconfined conditions.

The attachment point of the flame to the wall was at about x/De=1 which is the same height as the flamefront

breakdown in Figures 2 and 5. At x/De=0.4 and x/De=0.8 the fluctuations are highest. This marks the border of the PVC. At x/De=0.4 in particular there is even an increase in temperature from the furnace wall to r=45mm before the temperature substantially decreases at r=40mm (burner exit radius). This indicates an outer reverse flow of hot combustion reactants towards the bottom of the furnace. The aerodynamics governing this flow is the outer RFZ visualised in Figures 4 and 5.

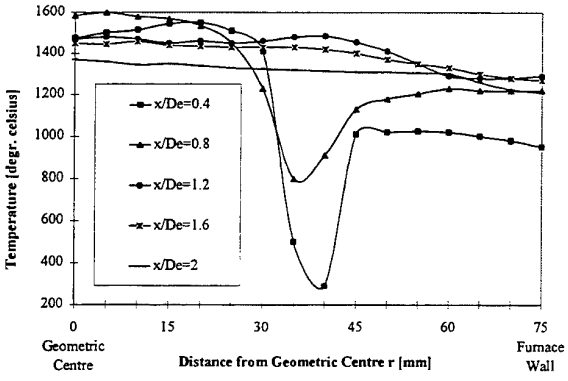

Figure 6: Average Temperature Profiles under Confined Conditions

Regions of high and low seeding density areas in Figures 4 and 5 show how the PVC squeezes the coherent flow resulting in an acceleration of both tangential and axial velocities.

No evidence of this structure has been found in other previous measurements (Froud et al (1995b) and Fick et al (1996b)).

It is hoped that the application of PIV will reveal more details of these complex flow structures and therefor allow even better interpretation of the combustion principles. A validation of time resolved measurements with PIV and flow visualisation is expected to fully explain the occurrence of the PVC in swirl burners.

6. CONCLUSIONS

The results of the visualisation emphasise the importance of reverse flow regions as feedback mechanisms for an efficient combustion of low calorific value gases.

The additional vortex structure found correlates very well with the occurrence of the PVC and the RFZ and manifests their existence in the flame.

The averaged temperature profiles under confined conditions strongly indicate an outer reverse flow region which is validated through the existence of a vortex recirculating hot reactants in the opposite direction of the main flow and outside the main area of the flow.

Another important area in this research is the investigation of the flamefront breakdown phenomenon. The results showed that it appears very irregular but has an impact on the flame shape and hence the combustion process.

The results presented here allow more insight into the turbulent nature of a flowfield governed by the PVC. They have proved to be of considerable benefit in so much that they have collaborated the previous findings in using optical techniques.

It is envisaged that PIV measurements will detail flow patterns in specific areas of the flame. The overall knowledge of the flow regime is of paramount importance for such studies.

Emission measurements were carried out recently on an industrially sized swirl burner and the results will be available soon.

7. REFERENCES

1. Fick W., Griffiths A. J., O'Doherty T. and Syred N., PIV Measurements in a Highly Turbulent Swirling Flame, Joint Meeting of the Portuguese, British, Spanish and Swedish Section of the Combustion Institute, Madeira, 1996a
2. Fick W., Griffiths A. J., O'Doherty T., Syred N. and Froud D., Phase Averaged Temperature Characterisation in Swirl Burners, in print, IMechE, Part A, 1996b
3. Fick W., O'Doherty T., Griffiths A. J. and Syred N., Thermal Characterisation of Swirl Burners, Energy and Environment towards the year 2000, Capri, 1996c
4. Froud D. Y., Fick W., Bowen P. J., O'Doherty T. and Syred N., Characterisation of Industrial Swirl Burners for Efficient Combustion of Low Calorific Value Gases, Proceedings of The Institute of Energy Conference held in London, UK, London, 1995a
5. Froud D., O'Doherty T. and Syred N., Phase Averaging of the Precessing Vortex Core in a Swirl Burner under Piloted and Premixed Conditions, Combustion and Flame 100, 407-412, 1995b
6. Froud D., O'Doherty T. and Syred N., The Interaction of the precessing vortex core and reverse flow zone in the exhaust of a swirl burner, Proc. Instn Mech Engrs, Part A, 1994, 208, 27-36
7. Froud D., O'Doherty T., Bates C. J. and Syred N., Characteristics of a Power Station Boiler, Proc. Instn Mech Engrs, Part A, 1992, 208, 89-101
8. Gupta A. K., Lilley D. G. and Syred N., Swirl Flows, Abacus Press 1984
9. Lucca-Negro O. and O'Doherty T., Prediction of the Precessing Vortex Core, The 6th International Symposium on Flow Modelling and Turbulent Measurements, Tallahassee, 1996
10. O'Doherty T., Biffin M. and Syred N., The use of tangential offtakes for energy savings in process industry, Proc. Instn Mech Engrs, Part E, 1992, 206, 99-109
11. Yazdabadi P., Griffiths A. J. and Syred N., Investigations into the Precessing Vortex Core Phenomenon in Cyclone Dust Separators, Proc. Instn Mech Engrs, Part E, 1994, 208

SIZE-CLASSIFIED DROPLETS DYNAMICS OF COMBUSTING SPRAY IN 0.1 MW OIL FURNACE

Nobuyuki Kawahara, Yuji Ikeda, Toshiaki Hirohata, and Tsuyoshi Nakajima

Department of Mechanical Engineering
Kobe University
Rokkodai, Nada, Kobe 657 JAPAN

ABSTRACT

The purpose of this study is to investigate the relation between droplet dynamics and spray combustion characteristics near a burner where the flame is held by recirculating flow. Firstly, three-dimensional measurements of velocity and gas concentration measurements of O_2, CO_2 and NO near the burner were carried out to understand the flame-holding mechanism and fluctuation characteristics. Secondly, measurements of the aerodynamic characteristics of combusting spray made in a small industrial oil burner were carried out by a phase Doppler anemometer to study the effect of the presence of droplets in turbulent flow. The size-classified technique is used with the relative Reynolds number and recombined two-dimensional size-classified droplet velocity.

The results show that a two-dimensional behavior of spray flame can be demonstrated. The size-classified droplet technique can provide very useful information on droplet aerodynamics and dispersion. The follow / penetration characteristics of spray can be understood very well in consideration of the features of classified droplets. Larger droplets had larger mass and inertia, and thus could penetrate through the recirculation flow region. Consequently, larger droplets formed a large, luminous flame. On the other hand, smaller droplets were entrained by the turbulent air flow and played the role of flame-holding. In addition, the interaction between the fuel droplets and air flow is a process that significantly affects the flame-holding mechanism of spray flames.

1. INTRODUCTION

The performance of spray combustion in an oil burner is associated with fuel atomization, fuel droplet dispersion, evaporation, mixing of fuel vapor with air, and group combustion [*William (1985), Lefebvre (1989)*]. Recently, quantitative measurement of the droplet size distribution, dispersion, and velocity has been made by laser techniques such as the top-hat system, phase Doppler anemometer (PDA) [*Saffman, et al. (1984), Bauckhage (1985), Rudoff, et al. (1987),* and so on.] The PDA techniques have been applied to gas turbine combustors [*McDonell, et al. (1986), McDonell and Samuelsen (1988), Cameron, et al. (1988)*] and swirl burners [*Edwards (1988), Edwards and Rudoff (1990), Edwards and Marx (1991)*], but these studies have paid little attention to the detailed spray features near the nozzles and the gas-droplet interaction in turbulent flow. Little is currently known about the coupling problems of mass, momentum, and energy transfer phenomena between fuel liquid phase and its surrounding flow field with chemical reaction, which are indispensable to modeling the aerodynamic characteristics of spray combustion.

Moreover, the regulation of NOx emission from oil burners has been established, for example, 70 ppm for small industrial oil furnaces and boilers in Tokyo 1991, so that the oil burner characteristics should be understood to achieve low NOx combustion.

An analysis of a two-dimensional gas-droplet flow field incorporating the effect of gas-droplet mass and momentum coupling has been made by Crowe et al. [*Crowe, et al. (1977)*]. The model treated the droplets as the source of mass,momentum, and energy of the gaseous phase and hence is known as the particle-source-in-cell (PSI-Cell) model. But experimental data are currently insufficient to be used as inlet conditions or proved data for modeling.

The authors have carried out this stusy in order to understand the spray combustion characteristics and droplet dynamics in a spray flame. Firstly, the authors carried out both experimens and simulations in order to characterize the aerodynamic features of spray, and repoted on fuel droplet dispersion and turbulent mixing [*Kawahara, et al. (1995)*]. Secondly, the flow velocity measurements and flux measurements of the gas species (O_2, CO_2 and NO) in an oil furnace were carried out. Consequently, the generated gas species in the flame and their convection outside the flame were discretized, and the application of flux in spray combustion research was found to be very useful and effective [*Ikeda, et al. (1995)*]. Moreover, the time-scale of turbulence as well as CO and CO_2 gas variation were compared in order to investigate the flame-holding mechanism in a transparent evaporating region. The comparison results show that the time-scale of turbulence and chemical species fluctuation were of the same order.

The purpose of this study is to investigate the relation between droplet dynamics and spray combustion characteristics near a burner where the flame is held by recirculating flow. Firstly, three-dimensional measurements of velocity and gas concentration measurements of O_2, CO_2 and NO near the burner was carried out to understand the flame-holding mechanism and fluctuation characteristics. Secondly, measurements of droplet velocity, mass fraction and dispersion were made by the PDA to study the effect of the presence of spray in a turbulent reacting flame. Moreover, the study focuses on turbulent structure, and follow / penetration criteria using size-classified droplet data [*Presser, et al. (1995), Seay, et al. (1995)*], the relative Reynolds number, and recombined two-dimensional size-classified droplet velocity vector.

2. EXPERIMENTAL APPARATUS

2.1 Gun-Type Burner and Furnace

The experimental set-up and the oil burner used are illustrated in Fig. 1. This furnace was designed for the oil burner to be traversed (space resolution : 100 μm) for obtaining detailed data near the burner, so that the optical misalignment occurring when the optical unit was traversed might be prevented. The oil burner itself was traversed because a PDA system consists of transmitting optics and receiving optics which have different off-axis locations. This type of oil burner [*Ikeda (1995)*] is commercially available for small industrial furnaces (< 0.3 MW) and boilers, and has a baffle plate for flame holding and reducing soot formation by providing several slits in the plate. The burner used type A fuel oil (Japanese Industrial Standard : JIS). The fuel oil was pressurized to 0.7 MPa in a gauged gear pump and atomized by a hollow-cone nozzle (Danfos : type H) of 60 degrees. There were eight slits in the baffle plate which reduce soot formation and prevents the plate from melting by the cooling effect of by-pass air.

Figure 2 is a direct picture of the flame [*Ikeda, et al. (1995)*]. It can be seen that there are three main regions: one is the flame-holding region near the baffle plate, the second is the transparent region in which the fuel droplets are evaporating, and the last one is the main combustion region with much luminescence from soot.

Figure 3 shows an illustration of droplet behavior in our previous experiments [*Kawahara, et al. (1995)*] under isothermal conditions. It was experimentally found that droplets under 30 μm in diameter tended to follow the reversing flow in the flame-holding region, while droplets over 50 μm penetrated the reversing flow.

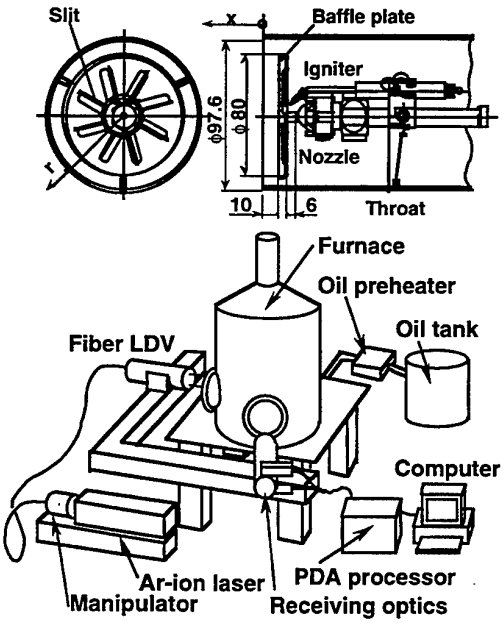

Fig. 1 Schematic layout of the furnace and the gun-type burner.

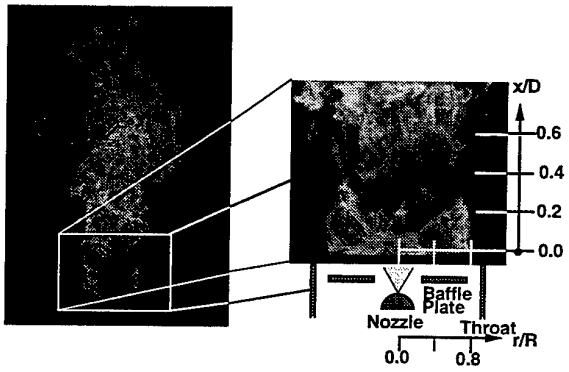

Fig. 2 A photograph of the flame.

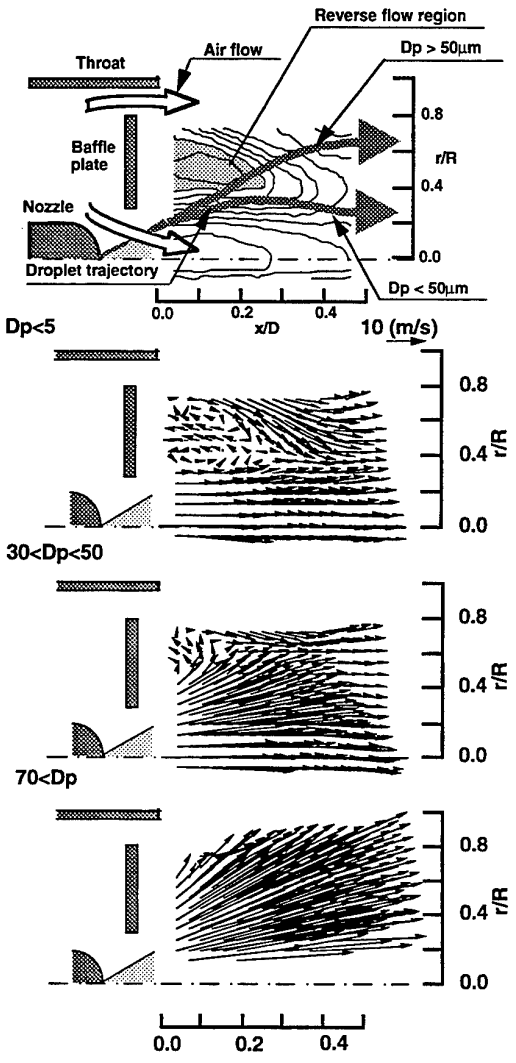

Fig. 3 Schematic droplet behavior in isothermal conditions.

2.2 The Laser Doppler Velocimeter Optics

For gas velocity measurements, the laser Doppler velocimeter developed by the authors [*Ikeda, et al. (1995),*] and a Burst Digital Correlator (BDC : Ono Sokki) were used. The measurements were carried out in the backscattering mode and a data rate of over 8 kHz was achieved near the burner nozzle.

2.3 Temperature and Gas Species Measurement

For temperature measurements, an R-type thermocouple (Pt/Pt-13% Rh) was used. The wire diameter was 0.5 mm without sealing. A coating was provided to avoid catalytic effects. In the temperature measurements, no corrections for radiation, heat conduction, and droplet sticking were made.

In gas species measurements, a water-cooled sampling probe was used. For O_2 measurement, the magnetic method (Shimazu POT101) was used. For CO_2, the NDIR method (Shimazu CGT101A) was used and for NO, the chemiluminescence method (Shimazu NOA-305A) was used. The probe diameter was 1.6 mm at the intake and 10.0 mm at the main body. The sucking speed effect was taken into account, so that a damping chamber was inserted in the gas flow line.

2.4 Fuel Droplet Diameter and Velocity Measurement

For fuel droplet diameter and velocity measurements, phase Doppler anemometer (PDA : 57×12, 58N10: Dantec) was used. An optical-fiber linked-phase Doppler anemometer was designed and mounted on the horizontal bench as shown in Fig. 1. The performance of the PDA is given in Table 1. The dimensions of the measurement volume were 0.422 × 4.02 mm. The measurable droplet diameter was less than 321.1 μm. The laser power at the measurement volume was 200 mW. The focal length of the transmitting optics was 600 mm, while 600 mm for the receiving optics.

In application of the phase Doppler measurement technique to practical combusting spray measurements, uncertainty factors are considered, which should be taken into account in a dynamic state. The affecting factors of consideration are (1) the phase shift at the receiving optics due to refractive index changes and the wave front distortion at the flame front, (2) the measurement error associated with the liquid refractive index changes due to temperature changes, (3) the refractive index changing around the droplet, (4) the rapid droplet diameter changes due to small droplet evaporation, and so on. The authors were estimated these errors [*Ikeda, et al. (1996)*], which are caused by application of this phase Doppler measurement system to practical combusting spray measurements.

Table 1 Performance of FLDV probe for PDA system.

Focal length (mm)	600
Spot diameter(μm)	442
Fringe spacing(μm)	8.56
Fringe number	52
Maximum measurable diameter(μm)	321.1
Maximum measurable velocity(m/s)	77.0
Minimum measurable velocity(m/s)	-25.7
Where	
Focal length of receiving optics	: 600 mm
Wave length of laser beam	: 514.5 nm
Bandwidth of signal processor	: 12 MHz
Frequency shift	: 40 MHz

2.5 Experimental Conditions

The fuel rate in the experiment was 9.45×10^{-3} m³/h. The fuel temperature was maintained at 25℃ by an oil heater. An excess air ratio of 1.2 was used. The various gas concentrations at the furnace exit were [O_2]=4.7 vol%, [CO_2]=10.8 vol%, [NO]=58.4 ppm (at [O_2]=0 vol%), and [CO]=0 ppm, and the NOx index was 2.97 g/kg of fuel.

Ten thousand data were taken at each measurement point. Acceptable measurement criteria were more than 80 % in accept rate, 1 kHz in data rate, and 90 % in spherical rate.

3. RESULTS

3.1 Spray Combustion Characteristics near the Burner

In a direct picture of the flame shown in Fig. 2, it can be seen that the recirculation flow region is formed and holds the flame. From x/D=0.02 to 0.04, where D is the diameter of the burner's throat and R is the radius of the burner's throat, the flame became narrow. In this region, the fuel spray travels, aggregates, collides, separates and evaporates. In the previous paper [*Ikeda , et al. (1995)*] , the three components of velocity near the burner were measured by the developed LDV with a BDC processor (Ono Sokki). Figure 4 shows

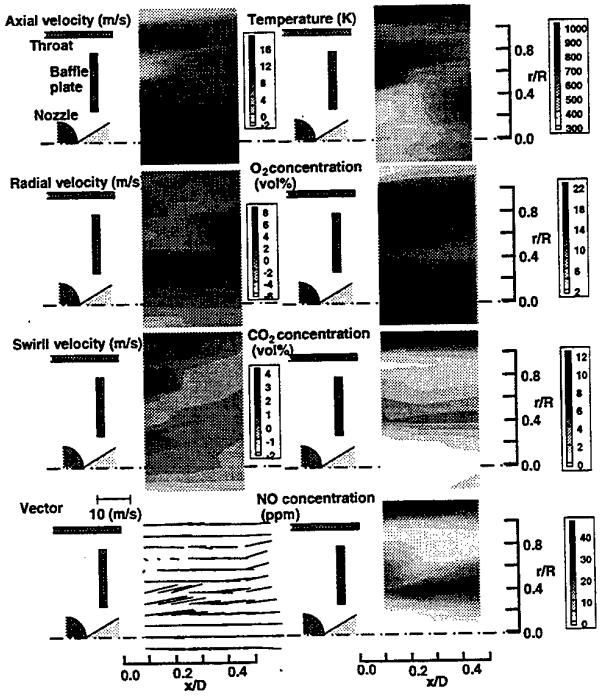

Fig. 4 Contours of O_2, CO_2 and NO concentration, together with gas flow field and temperature.

the contours of O_2, CO_2 and NO concentrations, together with the gas flow field and the temperature in order to understand the spray combustion characteristics.

Firstly, the temperature distribution showed a lower value (about 500 K) along the spray cone, which had a 60° hollow cone angle, but it indicated a higher value (about 1200 K) both outside and near the center axis. Behind the baffle plate, a high temperature region (about 800 K) was formed. The main reason was that the flame-holding region was formed in the recirculation region behind the baffle plate. But it was necessary to understand that the temperature was estimated lower than actual in the spray cone, because fuel adhesion occurred.

Secondly, when the authors took note of flow field, it was found that there were a pair of reverse flows. High velocity at r/R=1.0 in the axial direction was due to the flow passage between the baffle plate and the burner's throat. The maximum temperature was observed at the point where a pair of reverse regions collided with each other. But it was found that the inner and outer reverse flows rotated in opposite directions at swirl velocity. This phenomenon was due to the eight slits in the baffle plate. At downstream positions, neither the inner reverse flow nor the outer reverse flow was observed, but it was found that there were two vortices (w<0) in the swirl direction. This flow remained up to x/D=0.5, and had a relation to the flame-holding and entrainment flow.

In the distributions of O_2, CO_2, and NO concentrations, an active combustion region was formed at x/D=0.3, r/R=0.4, and inside the spray cone, where O_2 concentration was low, and CO_2 and NO concentrations were high. It was found that an active combustion process occurred at the point where two reverse flow regions collided with each other (x/D=0.3, r/R=0.4).

It was not possible to directly compare the velocity vector shown in Fig. 4 with the gas velocity because the fuel droplet was also traveling within the inner reverse region. In this study, the authors took note of the relation between droplet dynamics and spray combustion characteristics near the burner, where an active combustion region and the flame-holding region were formed. The fuel droplet diameter and its velocity were measured, using the PDA technique.

3.2 Droplet Size and Velocity

First of all, in order to observe the droplet dispersion, the correlation between droplet diameter and velocity was calculated as shown in Fig. 5. Near the center axis, there were many small droplets less than 30 μm in diameter. On the other hand, at the spray cone (x/D=0.23, r/R=0.41; x/D=0.34, r/R=0.82), droplets were distributed over 100 μm. This figure indicates that larger droplets over 70 μm traveled along the spray cone, but there were relatively smaller droplets near the center axis. Near the center axis, it was found that the droplets had the same velocity. On the other hand, at the spray cone (x/D=0.34, r/R=0.82), small droplets had low velocity, but large droplets had high velocity distribution. Consequently, small droplets were affected by the recirculation region and decreased their velocity. But large droplets penetrated straight into the recirculation region.

The spatial distribution of the Sauter mean diameters (SMD) and their velocity vectors are presented in Fig. 6. The vectors indicated that fuel droplets were traveling at a hollow-cone angle of 60 degrees. The mean droplet velocity was about 25 m/s, and the droplets traveled at almost the same velocity. The SMD contour indicated the spreading of the spray with increasing axial distance downstream of the

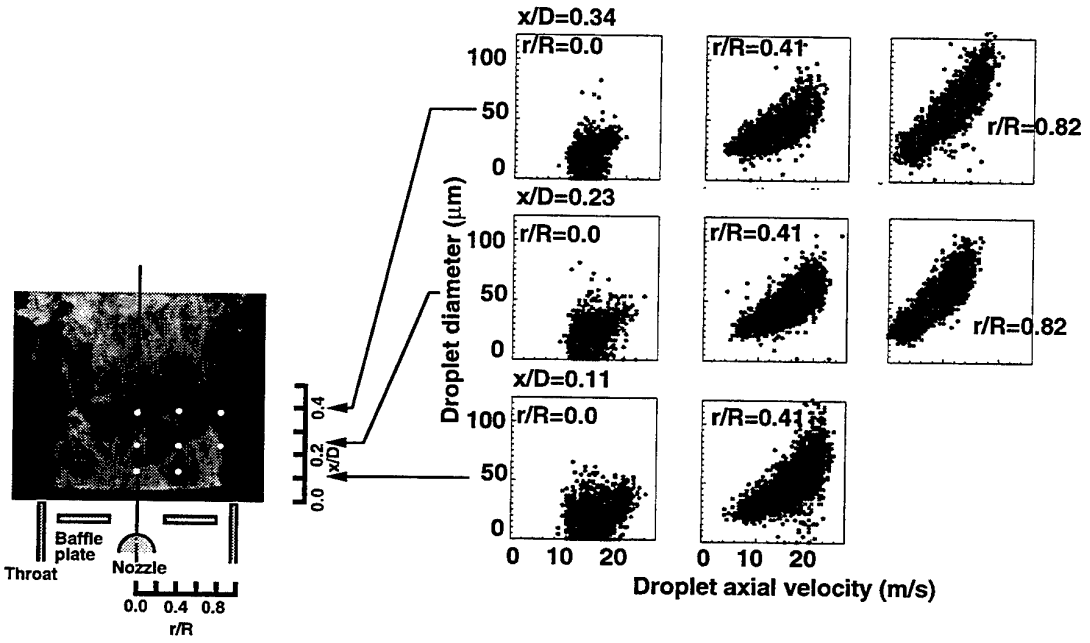

Fig. 5 Correlation of droplet diameter and velocity.

nozzle exit. Smaller values of the SMD were found near the center axis. The maximum value of the SMD increased with increasing axial distance along the hollow-cone angle. The reason was that small droplets followed the reverse air flow and played the role of flame-holding. On the other hand, large droplets survived as they flew downstream regardless of the high temperature region.

However, it was difficult to understand the dispersion of droplets and the interaction between the turbulent air and spray by the SMD analysis. It was clearly found that the difference in droplet size had another velocity distribution.

In the present study, the behavior of droplets was thus classified by droplet diameter. The mean value and dispersion of the classified droplets were treated as representative values.

The size-classified droplet velocities at x/D=0.13, 0.22, 0.34, and 0.43 are shown in Fig. 7. Each plane in the figure indicated the inside of the recirculation flow, the transparent region and their midpoint as shown in the direct picture of the flame (Fig. 2).

At x/D=0.13, the all droplets traveled at the same velocity in comparison with gas velocity. The difference of velocity could not be observed by the effect of the droplet diameter. With increasing axial position, larger droplets showed higher velocity, and thus larger mass and inertia. At x/D=0.34, the droplets less than 30 μm in diameter showed a sudden decrease in velocity behind the baffle plate. Smaller droplets under 30 μm were affected to decelerate by the recirculation flow. On the other hand, larger droplets over 50 μm penetrated the recirculation flow along the spray cone with large initial velocity. In radial velocity , same tendency were observed. At x/D=0.13, the droplets indicated same velocity profile and formed hollow cone distribution. However, at x/D=0.34, smaller droplets under 30 μm decelerated and indicated reverse velocity to the center axis. The reason was that gas flow through outside of the baffle plate entrained smaller droplets. On the other hand, larger droplets had large velocity , so that larger droplets had a large mass and inertia. Consequently, small droplets were greatly affected by the recirculation vortex and evaporated, contributing to flame-holding. On the other hand, larger droplets penetrated straight along the spray cone and formed an active combustion region.

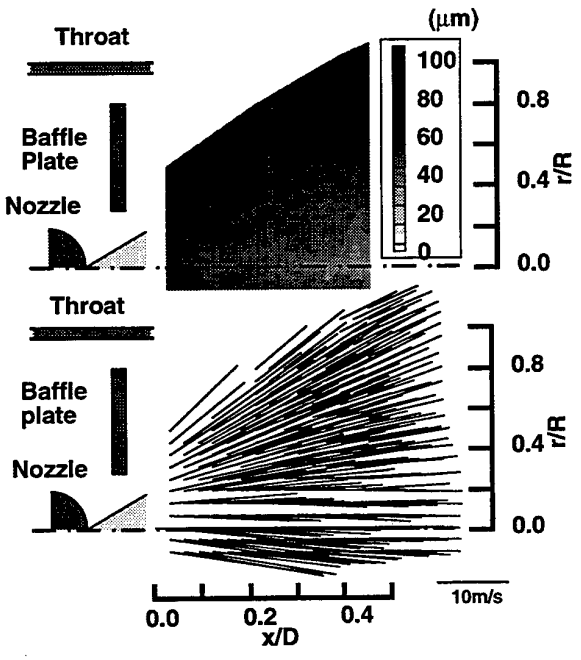

Fig. 6 Spatial distribution of the SMD and velocity vector for all size classes.

3.3 Aerodynamic Features of Spray

In order to further understand the gas-droplet interaction, the particle Reynolds number was calculated from the droplet size and the relative velocity of the droplet to the air flow as shown in Fig. 8. The particle Reynolds number is defined by Equ. (1).

$$R_{ep} = \rho \frac{|u_a - u_d| D_p}{\mu} \qquad (1)$$

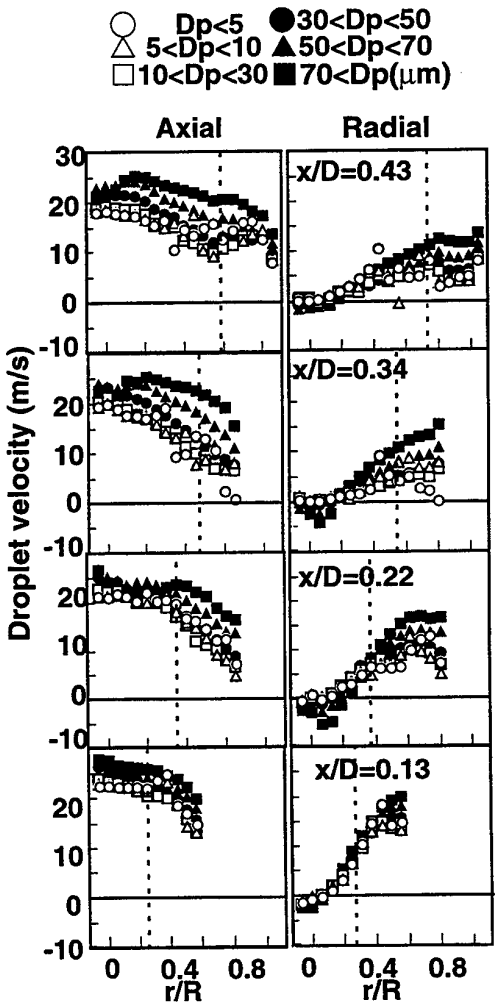

Fig. 7 Droplet velocity distribution for different droplet sizes.

where r is the density, Dp is the fuel droplet diameter, u_a is the gas velocity, and ud is droplet velocity.

The particle Reynolds number for small droplets showed a low and flat distribution. Since these droplets followed the air flow well, their relative velocities (slip velocities) were very small. On the other hand, large droplets had a peak in the radial distribution. A large Reynolds number means a large relative velocity or a large droplet size. Large droplets were affected by the turbulent air flow and penetrated the re-circulation flow. However, we must keep in mind that the gas flow velocity cannot be completely measured, because small droplets less than 5 μm evaporate quickly

The lifetime of a droplet in high temperature region is defined as follows:

$$\frac{D_o^2}{\tau} = const. = C_o \qquad (2)$$

where Do is the initial droplet diameter, τ is the lifetime of droplet in high temperature region, and Co is the combustion rate constant. Where the temperature of the region was 1000 K, Co was 0.67 (mm^2/s). Therefore, droplets less than 5 μm existed for 37.3 ms in this condition. In this experiment, the diameter of the control volume was 442 μm. If the velocity of droplets less than 5 μm was 10m/s, the transit time through the control volume was 44.2 ms. Droplets less than 5 μm were completely gasified while passing through the control volume and were less detectable. Hence, the PDA cannot measure the gas flow velocity by assuming that the droplet less than 5 μm in diameter can completely follow the air flow.

But the particle Reynolds number indicates a difference in spray behavior, droplet size of 30-50 μm being the boundary. In order to understand the gas-droplet interaction, the particle Reynolds number is useful and effective.

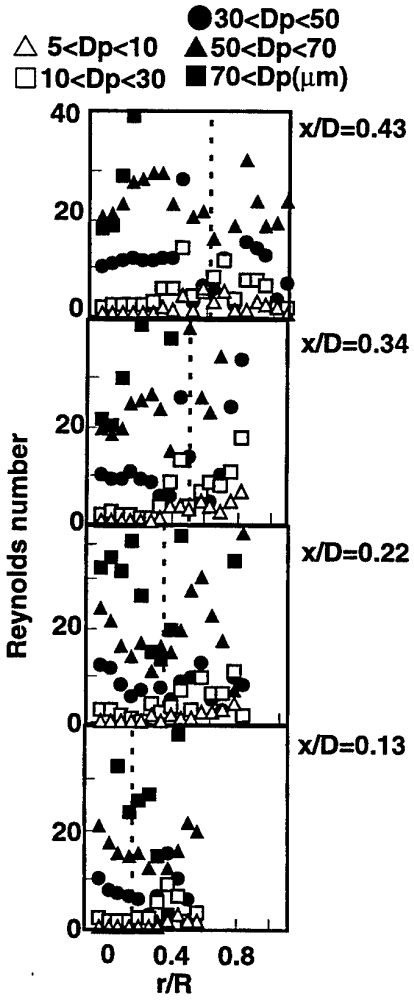

Fig. 8 Droplet relative Reynolds number distribution.

3.4 Turbulence and Dispersion of Droplet Velocity

The turbulent kinetic energy which is defined by Equ. (3) is shown in Fig. 9.

$$\sigma = \frac{u'^2 + v'^2}{2} \qquad (3)$$

This value means the turbulent kinetic energy for the air flow and the velocity fluctuation for the droplets. At x/D=0.13, larger droplets fluctuated inside the spray cone and smaller droplets fluctuated greatly outside the spray cone. Large droplets had a large slip inside the spray cone, and small droplets had a large slip outside the spray cone. In this

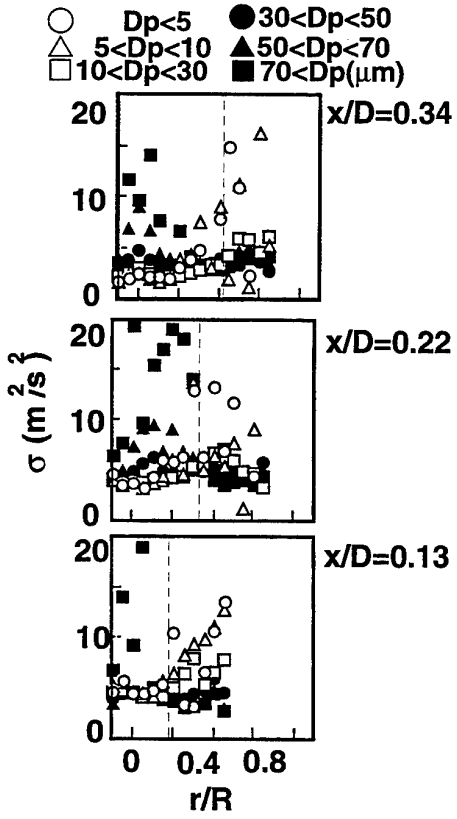

Fig. 9 Dispersion of droplet velocity.

region, there were a pair of vortices in the swirl direction. At x/D=0.34, large droplets had no slip near the center axis, but small droplets fluctuated along the spray cone. Hence, in the region where the gas flow outside the baffle plate collided with the spray cone, small droplets greatly fluctuated and were suddenly decelerated. On the other hand, large droplets had a large inertia and penetrated straight at the high-shear layer which is formed by the spray cone and the gas flow.

3.5 Droplet Behavior

In the previous section, it was pointed out that small droplets could trace the turbulent air flow but that large droplets penetrated the recirculation flow. Figure 10 shows two-dimensional velocity vectors, velocity fluctuation, and number density profiles. Velocity fluctuation means the turbulent kinetic energy of the air flow and the velocity fluctuation of droplets. Number density was calculated from the sample number and the elapsed time during measurement. However, it was necessary to take the decrease in number density into account, which was caused by droplet evaporation and detection error of scattering light.

Larger droplets over 70 μm penetrated in radial trajectories. On the other hand, small droplets under 50 μm followed the air flow inside the baffle plate and were found near the center axis. In addition, it was found that the velocity fluctuation of droplets under 30 μm was large but that of those over 50 μm was small. The reason is that small droplets were greatly affected by the air flow outside the baffle plate, but large droplets penetrated the air flow. The spray with droplets larger than 70 μm in diameter formed a hollow-cone distribution, which induced a shear flow along the spray. Consequently, it was found that the follow/penetration criterion was 30-50 μm for droplet behavior in the turbulent flow region. Near the center axis, there existed mainly droplets between 10 and 30 μm, while 30-50 μm droplets were detected behind the baffle plate. The reason that small droplets remained near the center axis was that the air flow outside the baffle-plate pushed them towards the center axis. On the other hand, large droplets had a large mass and inertia, and penetrate straightly along the spray cone.

3.6 Spray Combustion Model

An illustration of the flow field with droplets and combustion characteristics near the burner is shown in Fig. 11. The peaks of the number density for two droplet sizes, shown in Fig. 10, are indicated by black arrows in Fig. 11. This illustration summarizes the above discussion of the interaction of droplet behavior and combustion characteristics. Small droplets flow near the axis but large droplets flow outward owing to large inertia. Large droplets over 50 μm in diameter penetrated through the recirculation flow region and formed a large luminous flame. On the other hand, small droplets near the axis formed an active combustion region, and small droplets inside the recirculation flow played the role of flame holding. The separation region coincided with the high shear stress region. Consequently, the recirculation flow enhanced the droplet dispersion and contributed to a steady main flame.

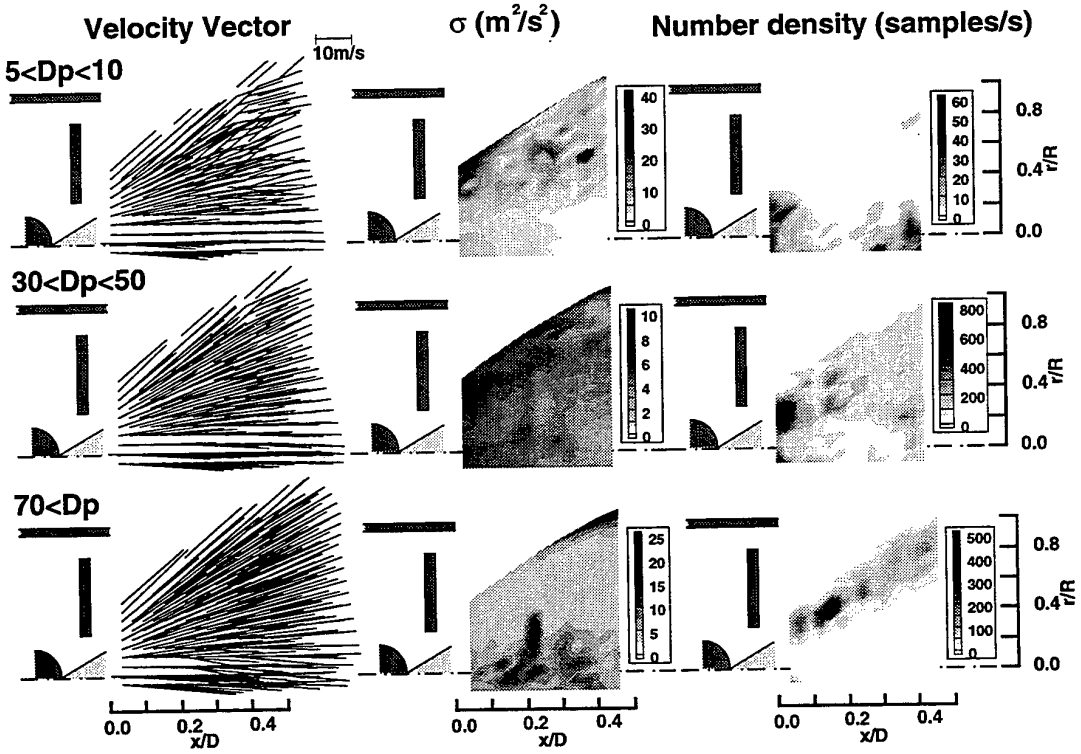

Fig. 10 Two-dimensional velocity vector and velocity fluctuation with number density.

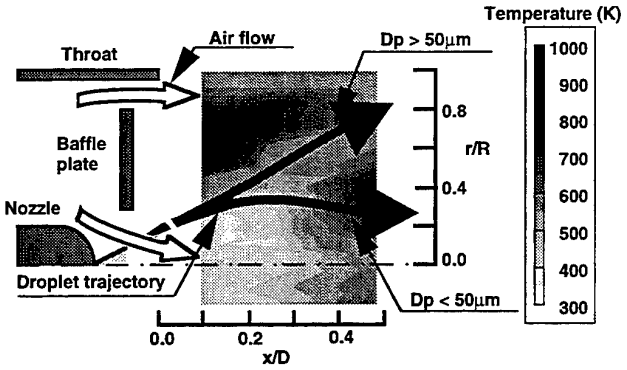

Fig. 11 Illustration of flow field with droplets and combustion characteristics near the burner.

4. CONCLUSIONS

The measurement of the aerodynamic characteristics of fuel droplets made in a small industrial oil burner was carried out by a phase Doppler anemometer. The flow field and the droplet behavior as well as the interaction of momentum transfer were investigated.

The obtained knowledge on the aerodynamics of the spray is summarized as follows:

(1) The recirculation flow enhanced the droplet dispersion.

(2) Size-classified techniques were effective to understand the gas-droplet interaction

(3) Small droplets under 30 μm in diameter were taken into the recirculation flow region and played an important role of flame holding. On the other hand, large droplets over 50 μm in diameter penetrated the recirculation flow region and formed a large luminous flame.

(4) Droplets less than 5 μm were completely gasified in the control volume. Therefore, the PDA cannot be used to obtain the gas flow velocity by assuming that droplets less than 5 μm in diameter can completely follow the air flow.

ACKNOWLEDGMENTS

This work was supported by the Grant-in Aid for Scientific Research, Ministry of Education, Science, Sports and Culture, Government of Japan, and the authors thank lecture K. Hiroshima of Kobe University for his technical advises.

REFERENCES

Bauckhage, K. 1985, International Conference Laser Anemometry Advances and Application, Manchester, pp.261-278.

Cameron, C.D., et al., 1988, A Model Gas Turbine Combustor with Wall Jets and Optical Access for Turbulent Mixing, Fuel Effects, and Spray Studies, 22nd Symp. (Int.) on Comb.

Crowe, C. T. et al. 1977, Trans. ASME, Ser.I, 99-2, 325.

Edwards, C.F. 1988, ASME Paper HTD-Vol. 104, pp.99-110.

Edwards, C.F., et al., 1990, Measurement of Correlated Droplet Size and Velocity Statics, Size Distribution, and Volume Flux in a Steady Spray Flame, Fifth International Symposium of Laser Techniques to Fluid Mechanics, Lisbon.

Edwards, C.F., and Rudoff, R. C. 1990, Structure of a Swirl-Stabilized Spray Flame by Imaging, Laser Doppler Velocimetry, and Phase Doppler Anemometry, 23rd Symp. (Int.) on Comb., pp.1353-1359.

Edwards, C.F., and Marx, K.D. 1991, Application of Poisson Statistics to the Problem of Size and Volume Flux Measurement by Phase-Doppler Anemometry, Fifth International Conference on Liquid Atomization and Spray system, ICLASS.

Ikeda, Y., et al., 1995, Flux Measurements of O2,CO2 nad NO in An Oil Furnace, Meas. Sci. Techn., 6, 826-832.

Ikeda,Y., et al., 1996, Measurement Uncertainties of Phase Doppler Technique Due to Effects of Slit Location, Control Volume Size and Flame Front Presence (in Application for Combusting Spray) ,8th Symposium on Application of Laser Measurement on Fluid Mechnics, Lisbon.

Kawahara,N., et al., 1995, Droplet Followability and Slip Velocity Analysis of Evaporating Spray on Gun-Type Oil Burner, 4th Internatinal Congress Optical Particle Sizing, vol.4, pp593-602.

Lefebvre,H., 1989, Atomization and Sprays, Hemisphere Publishing Corporation.

McDonell, V.G., et al., 1986, A Comparison of Spatially-Resolved Drop Size and Drop Velocity Measurements in an Isothermal chamber and a Swirl-Stabilized Combustor, 21st Symp. (Int.) on Comb., pp.685-694.

McDonell, V.G., and Samuelsen, G.S., 1988, Application of Two-Component Phase Interferometry to the Measurement of Particle Size, Mass Flux, and Velocities in Two-Phase Flows, 22nd Symp. (Int.) on Comb., pp.1961-1971.

Presser,C., et al., 1995, Interpretation of Size-Classified Droplet Velocity Data in Swirling Spray Flames, AIAA Paper 95-0283.

Rudoff, R.C., et al., 1987, AIAA 25th Aerospace Sciences Meeting, Nevada, AIAA-87-0062.

Saffman, M., et al., 1984, The 2nd International Symposium on Application of LDA to Fluid Mechanics, Lisbon, pp.8.1.

Seay, J., et al., 1995, Atomisation and Dispersion from a Radial Airblast Injector in a Subsonic Crossflow, AIAA Paper 95-3001.

William,F.A., 1985, Combustion Theory, 2nd ed., 446, The Benjamin/Cummings Publishing Company, Inc.

SESSION 11

Doppler Global Velocimetry and Interferometry

EVOLUTION OF DOPPLER GLOBAL VELOCIMETRY DATA PROCESSING

James F. Meyers

NASA Langley Research Center
Hampton, Virginia
United States

ABSTRACT

The development of data processing techniques and algorithms for Doppler Global Velocimetry is presented. The discussion begins with the fundamental calculation of the velocity dependent transfer function of Iodine vapor, and proceeds through laboratory and wind tunnel investigations to develop insight into the physics of the technique. The knowledge gained through this process provided the basis for the development of algorithms to correct for optical distortions, electronic noise, and camera misalignment.

1. INTRODUCTION

For the past six years, Doppler Global Velocimetry (DGV) has been under development at the NASA Langley Research Center. This technology can provide three-component velocity measurements of a flow as it passes through a selected measurement plane defined by a laser light sheet. Its ability to measure velocity within broad areas of the flow field, while maintaining cubic millimeter spatial resolutions in large wind tunnels, is of great interest to NASA. The increased productivity provided by DGV helps reduce the cost of aerodynamic testing. It is also an ideal measurement technology for validation of Computational Fluid Dynamics since it is capable of providing measurement grids equivalent to the computational grids. Further, the use of video technology provides real-time quick-look capability to view the velocity field as run conditions are changed, allowing adjustment of test parameters to optimize flow field conditions.

Although the basic principles were very simple, implementation of DGV technology as a flow diagnostics tool for routine wind tunnel application has proven somewhat difficult. Early investigations confirmed that an optical absorption line in Iodine vapor could be used to obtain images with velocity dependent amplitudes. However, it was also apparent that the images did not have sufficient quality to provide quantitative data with acceptable accuracy. The effort to enhance this technology and develop a usable system with acceptable measurement accuracy has included wind tunnel investigations along with laboratory studies. The five year program has included velocities ranging from low subsonic to Mach 4.6, in various wind tunnels from the 1-x 1-meter Basic Aerodynamic Research Tunnel at Langley to the 40-x 80-foot National Subsonic Tunnel at NASA Ames. Although the basic optical hardware configuration has changed little, the data processing algorithms have undergone considerable development. The following is a description of that evolution along with example results from the various test programs.

2. THE BEGINNING

Komine, reference 1, devised Doppler Global Velocimetry when he used the light absorption characteristics of Iodine vapor to determine the absolute frequency of Doppler shifted laser light scattered by small particles passing through an Argon ion laser beam. This concept was a spin-off of his work with laser spectroscopy where an Iodine vapor cell was used in a feedback loop to stabilize the optical frequency of an Argon ion laser operating at 514.5 nm. The cell was used as the sensor in the feedback loop since the Iodine vapor transfer function provided optical frequency discrimination. The transfer function was found by passing a small portion of the laser beam through the cell, and determining the ratio of laser powers before and after the cell. By monitoring the power ratio while frequency tuning the laser, the characteristics of the absorption line were determined, figure 1. The laser frequency was then tuned to a point midway along the side of the absorption line, figure 1, and the laser power ratio electronically monitored. If the laser frequency, and thus the power ratio, changed, the feedback electronics adjusted the laser etalon temperature, and thus its length, to return the laser frequency to the set value. This principle, in an open loop version, was fundamental to the concept behind Doppler Global Velocimetry. With the laser frequency tuned to the midpoint of the absorption line as above, Doppler shifted scattered light would pass through the Iodine vapor with greater (or less, depending on the direction of the Doppler shift) absorption, thus establishing a fundamental relationship between the scattered light power ratio and velocity.

The implementation of this new technology uncovered characteristics that would make Doppler Global Velocimetry a uniquely capable flow diagnostic measurement system. Unlike other laser velocimetry systems, this technology did not require

the optical resolution of individual seeding particles, since the velocity measurement was based on the fraction of collected scattered light absorbed by the Iodine vapor. Thus, the source of the scattered light was immaterial. Further, the direct measure of optical frequency eliminated the problems of signal interference from multiple scatterers inherent in standard laser velocimetry. These characteristics allowed the laser beam to be expanded into a light sheet, and the laser power detectors replaced with Charge Coupled Device (CCD) video cameras, figure 2. In this configuration, each pixel element of the CCD became, in effect, a single detector collecting scattered light originating from the small volume within the light sheet imaged on that pixel. The ratio of the video output signals from the two cameras yielded images whose amplitude information was directly related to velocity.

These concepts were first demonstrated in the laboratory by Komine, *et al* at the Northrop Research and Technology Center, reference 2. Further development at the NASA Langley Research Center resulted in the first wind tunnel measurements, references 3 and 4. Additional studies at Northrop, under contract to NASA, found that a pulsed, injection seeded, frequency doubled Nd:YAG laser could be used as the laser source to obtain instantaneous velocity flow field mappings, reference 5.

3. ON TO THE DATA IMAGES

Since the optical frequency dependent transfer function imposed by the Iodine vapor was obtained by dividing the output (signal camera) image by the input (reference camera) image, figure 3, data processing was expected to be straight forward. Both the Northrop, references 2 and 5, and NASA, reference 3, efforts used analog dividers to normalize the RS-170 signal camera output with the reference camera signal as the images were transmitted from their respective cameras. Although the normalized images of a small supersonic jet, reference 2, and the vortical flow above a delta wing, reference 3 and figure 4, showed the expected velocity dependencies, the images were very noisy and the velocity structures were not well defined.

3.1 Phase I – Image Alignment

A laboratory investigation was conducted at NASA to determine the reason for the noise and poorly defined images. A test target, figure 5, was viewed by the receiver optical system and the cameras carefully aligned to overlap the pixels. If the alignment was perfect, the normalized image would be a flat gray since the transfer function remained constant throughout the image. Unfortunately, the edges of the dots on the test target were clearly visible with overall patterns indicative of optical differences between the signal and reference optical paths, figure 6. Adjusting camera position, pan, tilt, and magnification improved the normalized image, but perfect alignment was never achieved. The inability to obtain the proper alignment was traced to minor imperfections in the receiver optical elements. One potential solution was to replace the optics with components built to tighter specifications. However, a more cost effective solution was to remove the distortions using image processing techniques. After using the analog circuitry to obtain the best physical alignment, the electronics were disconnected and the signal and reference images acquired by computer in sequence by a video frame grabber. Since the target was composed of a grid of evenly spaced dots, dewarping algorithms in a commercial software package were used to remove the distortions. While the resulting dewarped images appeared to be square, the normalized image still showed the dot edges, indicating that the distortions were not totally removed. Further investigation found that the commercial packages could remove linear variations such as perspective, but were incapable of removing the effects of minor nonlinear distortions originating from optical imperfections in the receiver optics. These packages used a single first, second or third order equation to describe the entire horizontal and vertical directions respectively. While this process might be acceptable for visual applications, it was inadequate for image normalization.

Since the laboratory investigation identified minor optical imperfections as a cause of measurement error, and the commercial image processing software provided insight into a potential solution, a development program to obtain the needed image processing algorithms was undertaken. The resulting method was to use piecewise, bilinear warping procedures to subdivide the target image into sections sufficiently small to correct for the minor optical distortions, reference 4. In practice, a grid of 20 by 20 sections, defined by the dot centroids in the test target, appeared to yield sufficient correction. Dewarping figure 5 with this method yielded figure 7. An improvement in image alignment was found when the dewarped images were normalized, figure 8.

3.2 Phase II – Noise Reduction

The vortical flow field above the delta wing was again measured, and the acquired images dewarped before normalization, reference 4. Additionally, the Gaussian intensity profile of the light sheet was flattened to lessen occurrences of pixel saturation in the center of the light sheet and insufficient scattered light at the edges. The flat intensity profile was obtained by replacing the cylindrical lens with a high-speed galvanometer scanner. Scattering angle and polarization dependent Mie scattering intensity variations were also reduced by placing a quarter-wave plate in the laser output optical path to circularize the laser light polarization, reference 7.

Although aerodynamic symmetry was not present, as shown by laser light sheet flow visualization in figure 9, the normal and burst vortical flow field above the delta wing was clearly detected, figure 10. In spite of the vast improvement in the data image, it was still noisy and contained unrealistic values at the edges of the smoke plume. An analysis of CCD video camera operation revealed several characteristics that could be responsible for these anomalies. These characteristics included dark current, variations in pixel sensitivity, charge transfer noise, modulation transfer function, and field interlacing. The characteristics, the effects on the data image, and the correcting procedures are described below:

Dark current - CCD video cameras, in the manner of other photo-electronic detector systems, occasionally produce spurious photoelectrons without the stimulation of triggering photons. The collected charge represents an offset in the pixel amplitude that must be removed before normalization calculations are performed to determine the correct Iodine vapor transfer function.

Variations in pixel sensitivity - Minor imperfections in the photo-electronic sensor result in variations of pixel-to-pixel

quantum efficiency. The effect is random noise superimposed on the acquired image. Since the quantum efficiency is constant, the pixel-to-pixel variations can be removed through calibration of pixel sensitivity. The calibration is typically obtained by illuminating the CCD sensor with flat field light at two intensities, and determining the sensitivity slope or quantum efficiency for each pixel. Flattening the CCD sensitivity response then consists of simply multiplying the data images by the average quantum efficiency divided by the quantum efficiency for each respective pixel.

Charge transfer noise - Once the photoelectrons have been acquired during field acquisition, the field image is transferred from the CCD by moving the charge packets from capacitor to capacitor until they reach the output port. As each charge packet leaves a capacitor, there is a possibility that one or more electrons may be left behind, or electrons left by previous packets, added. These random charge variations become a white noise component in the output signal, and thus a superimposed random noise on the acquired image. The best method to reduce the effect of charge transfer noise is to low pass filter the image by convolving the image with a 5x5 top hat kernel. Since this kernel matches the measured modulation transfer function of the camera system, only high frequency charge transfer noise is removed, while the data information is maintained. With industry standard RS-170 video cameras, the remaining noise is estimated to be 1-percent of full scale, or a velocity uncertainty of ±2 m/sec.

Modulation Transfer Function - The Modulation Transfer Function (MTF) is a measure of spatial frequency limit or sharpness factor of the imaging optics and CCD camera. For example, a photograph taken with an f16 lens opening produces a sharper image than the same photograph taken with an f2 lens opening. The MTF of a CCD video camera is related to electronic charge leakage between adjacent pixels. The combined lens/camera MTF is measured by imaging a spatial step change in light intensity, and determining the kernel needed to match the measured response. A typical industry standard RS-170 video camera has an MTF that matches a 5x5 top hat kernel.

Field interlacing - Industry standard RS-170 video cameras are interlaced devices which acquire photons in the even pixel rows while transferring the previously acquired image in the odd pixel rows out of the camera. During the next acquisition cycle, the newly acquired even row image is transferred out while the odd rows acquire the next image. Standard video devices reconstruct the video frame by combining the two interlaced images. Since the interlaced or field images are acquired at different times, motion within the viewed scene adds distortion to the combined image. This effect can be seen as a series of horizontal lines that indicate a change of scattered light caused by variations in the smoke cloud and/or a change in the velocity flow field occurring between the acquisition of the two video fields. Thus the two fields are separated and the missing rows interpolated to yield a field image that is then dewarped and processed.

Calibrations and procedures were developed to account for the CCD video camera characteristics outlined above. Dark current images were acquired and saved for use during data processing. Each video camera system, including video amplifiers, signal processing electronics, and computer frame grabber, were calibrated for pixel sensitivity. The MTF for each camera was determined and found to be equivalent to a 5x5 kernel. Finally, data processing algorithms were developed to subtract dark current contributions from the data images, flatten the effects of pixel sensitivity variations, low pass filter the data images, and separate the video fields and interpolate the missing rows.

3.3 Phase III – Optical Difficulties

Following completion of the data processing software, the DGV system was installed in the Langley Unitary Plan Wind Tunnel and used to investigate the vortical flow above a delta wing at Mach 2.8. This investigation presented the opportunity to determine the measurement characteristics from submicron diameter water condensation particles. The uniform illumination, shown in the photograph of the laser light sheet visualization in figure 11, eliminated potential measurement uncertainties related to variations in smoke density. The visualization showed three distinct scattered light intensity levels: free stream, behind the cross flow shock, and the vortex. The velocity image, figure 12, did not yield the expected change in velocity at the intensity boundaries. This anomaly was traced to the inclusion of background light in both the signal and reference images. The background light level included contributions from the camera dark current discussed above, reflected laser radiation from tunnel and model surfaces, and ambient lights. The influence of ambient light was reduced by placing a green photographic filter in front of each camera. The remaining background light was measured by acquiring images under run conditions, but without particles in the flow. These background images were then subtracted from the signal and reference data images, respectively, prior to normalization.

Closer examination of the measured velocity images revealed unexpected velocity patterns, especially in the constant velocity free stream portion of the image. Since the condensation scattered light in a uniform manner, the origins of the velocity patterns were traced to the receiver optical system. An overall velocity bias was found to originate from a mismatch in optical transmission between the signal and reference paths. The transmission differences were caused by the characteristics of the beamsplitter, windows in the Iodine vapor cell, neutral density loss through the Iodine vapor, and mismatch in electronic signal amplification. Spatially dependent biases were caused by dirt on the optics, bending of the beamsplitter and Iodine vapor cell windows, and polarization effects from the interaction of Mie scattered laser light with the beamsplitter. The bias and spatially dependent transmission effects were isolated by adjusting the laser output frequency to place the Doppler shifted frequency outside the Iodine absorption line and acquiring data normally. The resulting normalized images were inverted and averaged to obtain a transmission correction image for multiplication with the normalized data images prior to velocity conversion.

4. MOVING TO THE THIRD DIMENSION

Although the several wind tunnel investigations using the single-component DGV, reference 6, provided insight into various aerodynamic flows, the primary interest of aerodynamicists was three-component velocity measurements in standard U, V, and W component directions. Two receiver optical systems were added to the DGV system and laboratory

tests conducted on a rotating wheel to develop three component measurement capability.

4.1 Phase I – The Laboratory

The three-component DGV optical system was placed about a rotating wheel, with a receiver set on the left, right and above with a 30° angle to the plane of the wheel. The wheel was illuminated with a cone of laser light propagating in the horizontal plane, and inclined by 45° to the wheel. The view from each receiver of the calibration card is shown in figure 13. The perspective and optical distortions were removed using the normal piecewise bilinear warping software. The number of rows and columns extending from the central dot were matched for the three images. The resulting warped views are also shown in figure 13. Thus, the images had the proper overlay to not only determine the A, B, and C velocity components, but also determine the standard U, V, and W velocity components using triangulation procedures for each pixel location.

The wheel was spun and the velocity data acquired. The measured and converted velocity images are shown in figure 14. As expected, the U component was nominally 0 m/sec, and the V and W components had the appropriate profiles for a solid body of revolution, with the proper 90° phase difference between components.

4.2 Phase II – The Tunnel Test

The first wind tunnel application of three-component DGV served as a demonstration of the Langley-designed system for the 40-x 80-foot National Subsonic Wind Tunnel at the NASA Ames Research Center, reference 8. The system orientation for the measurement of the jet flow exiting from a High Speed Civil Transport engine model is shown in figure 15. The investigation yielded resolved U, V, and W velocity components of a 0.22 m diameter jet, operating at temperatures up to 700° C with velocities over 500 m/sec. An example image, figure 16, of the streamwise velocity component obtained within a plane normal to the jet axis, 0.25 jet diameters downstream from the exit, clearly shows the velocity deficit caused by the conical central body. The spatial measurement grid capability of the technique, even at focal distances up to 15.5 m, is shown by the X-Y plot of the measured velocities obtained from a single row of pixels, with a resolution of 1.25 mm, along the diameter of the jet.

This investigation revealed two additional problems. Vibration in large wind tunnels, coupled with the need for long focal distances, placed unrealistic requirements on the maintenance of optical alignment. The other concern was the large measurement uncertainty at the edge of the smoke. As with earlier obstacles, system misalignments that occurred during wind tunnel testing were corrected using image processing techniques. The dewarped signal and reference images were cross correlated to determine their spatial misalignment. The signal image was then shifted to realign the two images before normalization. The reference images from each component were also cross correlated to determine their spatial misalignment. Again, two components were shifted to align the images before conversion to the standard U, V, and W velocity components. It is noted that only the reference images were correlated to insure the absence of velocity dependencies induced in the signal images by the Iodine vapor that would influence the correlation results.

As the smoke density dissipated at the edge of the plume, the acquired signal and reference amplitudes decreased, thus increasing the uncertainty of the corresponding normalized results. Additionally, since the plume moved and changed with time, reduced scattered light levels influenced a greater spatial area when sequential velocity images were averaged, thus increasing overall measurement uncertainty. By raising the acceptable threshold levels, measurement uncertainties were reduced. Additionally, a band of four pixels along the smoke plume edges was removed in each normalized image to negate the low frequency rolloff induced by the spatial low pass filter described above.

5. THE CURRENT TECHNOLOGY

Wind tunnel entries continued with the three-component investigation of a wing tip vortex, and its interaction with a trailing model in the Langley 30-x 60-foot Full Scale Wind Tunnel, figure 17. Although this facility was smaller than the NASA Ames 40-x 80-foot National Subsonic Wind Tunnel, it had an open test section making installation of the optics more difficult. Two of the receiving optical systems were installed in pods placed on the test section floor, figure 17, at focal distances of 7.5 m, and the third was placed on top of the test section inlet at a focal distance of 18.25 m. The 5-cm diameter vortical flow was measured with the upstream airfoil set to 2- and 10-degree angles of attack. Averaging the cross-flow velocity data images produced the results shown in figure 18. While these images gave an indication of the vortex motion, they provided little information about the vortex structure. Using the cross correlation procedure described above, the vortex structures became clear, figure 19.

The latest entry was the investigation of the flow entering a powered helicopter model tail rotor in the 14-x 22-foot Subsonic Tunnel. The three velocity components indicated that the flow moved downward at 45 degrees in a uniform manner, figure 20. The measurements showed the influence of the main rotor flow, but the expected rotor tip vortices were not found. The lack of evidence from tip vortex passage was traced to flow field averaging by the video cameras. During the 17 msec video field acquisition of scattered light, the main rotor rotated 240 degrees which moved at least two vortices through the light sheet. Further complications included the comparatively large measurement uncertainty, ±2 m/sec, attributed to charge transfer noise, and the inability to maintain a constant temperature in the Iodine vapor cells because of the -5° C ambient temperature.

The implications of these investigations have led to major modifications in the current DGV optical system. These modifications will increase measurement capabilities along with measurement accuracy. The Argon ion laser is being replaced with a pulsed single-frequency, frequency-doubled Nd:YAG laser to provide the capability to measure unsteady flow fields. Further, the 10 nsec pulse width will provide measurement images with full turbulent bandwidth allowing the measurement of turbulence intensity and turbulence power spectra using spatial domain techniques. The industry standard RS-170 video cameras are being replaced with 10-bit digital cameras to increase velocity measurement resolution. The remaining modification is the enclosure of each Iodine vapor cell in an insulated container to provide better temperature stability. All Iodine vapor cell stem and body temperatures are

measured for each set of three-component data images acquired. These temperatures are then used to theoretically determine the Iodine vapor cell transfer function for each corresponding data image. This yields greater measurement accuracy than would be obtained using calibrated transfer functions for a few selected temperatures.

5. CONCLUDING REMARKS

The development program conducted at NASA Langley Research Center has shown that Doppler Global Velocimetry is a robust and versatile technology that can provide global three-component velocity measurements of an aerodynamic flow. Its evolution included laboratory and wind tunnel testing to develop a basic understanding of the technology, the nature of Mie scattered light, and the characteristics of the elements comprising the DGV system. Example test results were presented and characteristics identified which triggered advances in data processing algorithms. The results also showed a progressive improvement in data quality as the new algorithms were included during processing. The measurement envelope increased during the development program from single-component measurements of low-speed flows in a small wind tunnel to the measure of a Mach 2.8 flow using submicron water condensation, and three-component investigations of a 22-cm diameter hot jet in a 40-x 80-foot wind tunnel and a 5-cm diameter tip vortex measured at a focal distance of 18.25 m.

6. REFERENCES

1. Komine, H. 1990, System for Measuring Velocity Field of Fluid Flow Utilizing a Laser -Doppler Spectral Image Converter, US Patent 4 919 536.

2. Komine, H., Brosnan, S. J., Litton, A. B., and Stappaerts, E. A. 1991, Real-time Doppler Global Velocimetry, AIAA 29th Aerospace Sciences Meeting, Reno, NV, paper 91-0337.

3. Meyers, J. F. 1991, Review of Typical Applications - Wind Tunnels, in von Karman Institute for Fluid Dynamics, Lecture series 1991-08, Brussels, Belgium, Laser Velocimetry.

4. Meyers, J. F. 1992, Doppler Global Velocimetry – The Next Generation?, AIAA 17th Aerospace Ground Testing Conference, Nashville, TN, Paper 92-3897.

5. Komine, H., Brosnan, S. J., Long, W. H., and Stappaerts, E. A. 1994, Doppler Global Velocimetry Development of a Flight Research Instrumentation System for Application to Non-intrusive Measurements of the Flow Field, NASA Report CR-191490.

6. Meyers, J. F., Usry, J. W., and Miller, L. S. 1994, Assessing the Capability of Doppler Global Velocimetry to Measure Vortical Flow Fields, Journal of Aerospace Engineering, part G, vol. 208, pp. 99-105.

7. Mie, G. 1908, Optics of Turbid Media, Ann. Phys. Vol 25, pp. 377-445.

8. Meyers, J. F. 1994 Development of Doppler Global Velocimetry for Wind Tunnel Testing, AIAA 18th Aerospace Ground Testing Conference, Colorado Springs, CO, paper 94-2582.

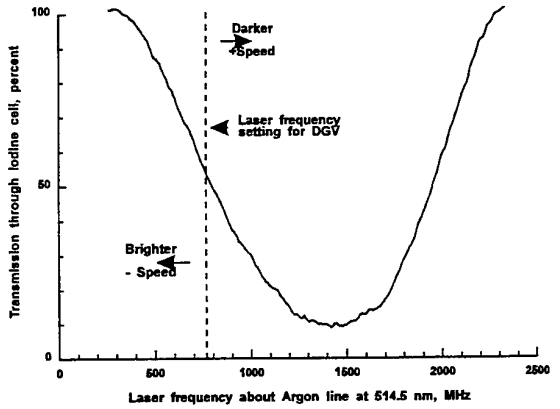

Fig. 1. Transfer function of the Iodine vapor cell.

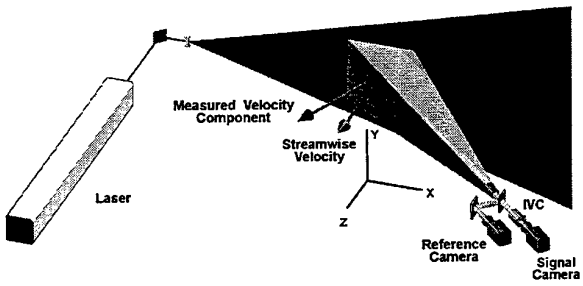

Fig. 2.- Pictorial view of the Doppler Global Velocimeter used in the Basic Aerodynamics Research Tunnel to measure the flow above a 75° delta wing.

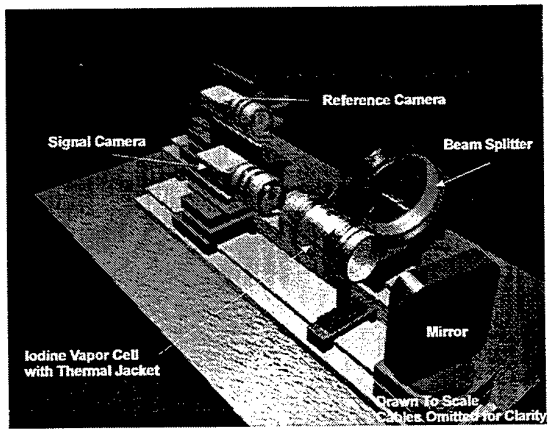

Fig. 3.- Pictorial view of the receiver optical system.

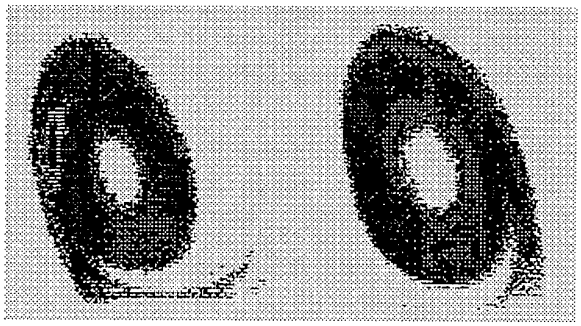

Fig. 4.- DGV data image for the near cross-flow component of the vortical flow above a 75° delta wing at an angle of attack of 20.5 °.

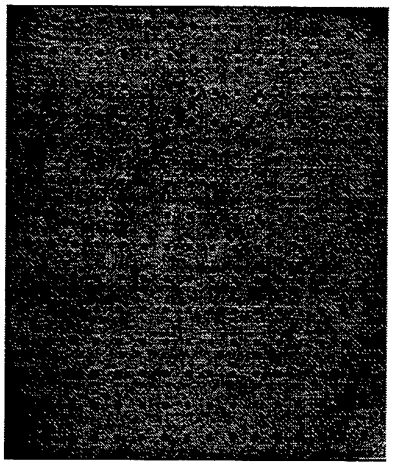

Fig. 5.- View of equally spaced dots on a flat card placed in the laser light sheet position.

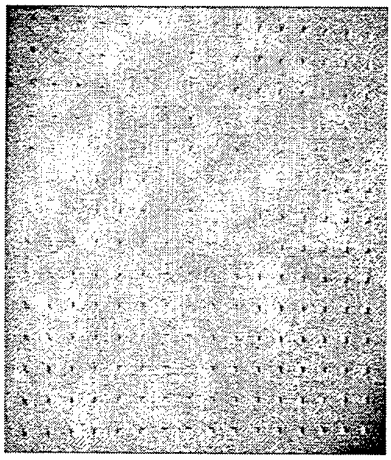

Fig. 6.- Normalized image based on the dot card image shown in Fig. 5.

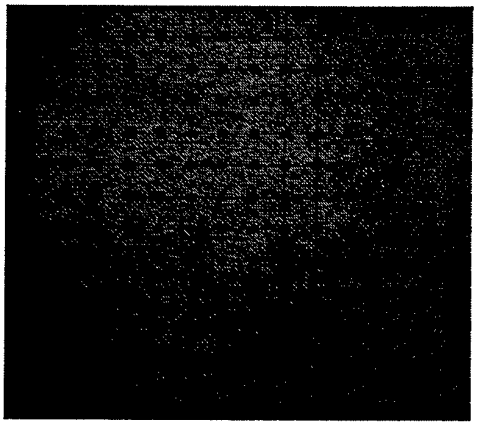

Fig. 7.- Dewarped dot card image.

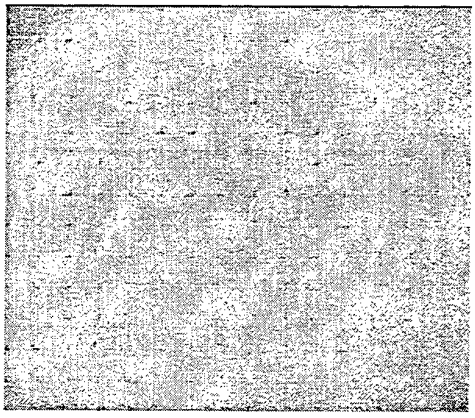

Fig. 8.- Normalized image based on the dewarped dot card image shown in Fig. 7.

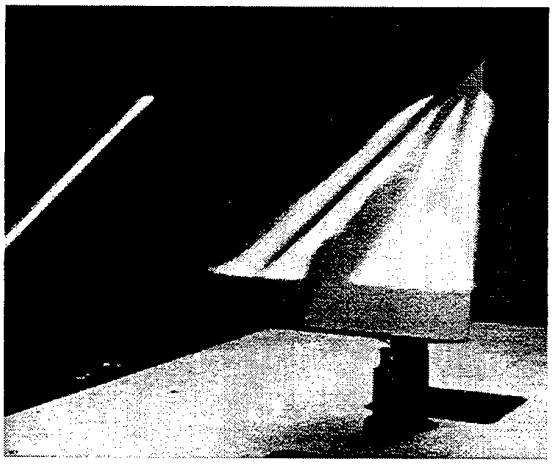

Fig. 9.- Flow visualization of the vortical flow above a 75o delta wing at an angle of attack of 20.5 °.

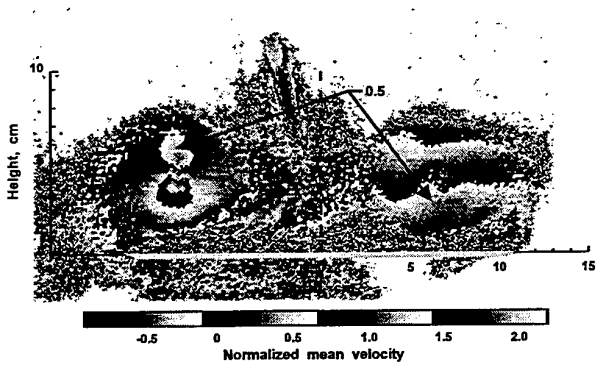

Fig. 10.- DGV data image for the near cross-flow component of the vortical flow above a 75o delta wing at an angle of attack of 20.5 °.

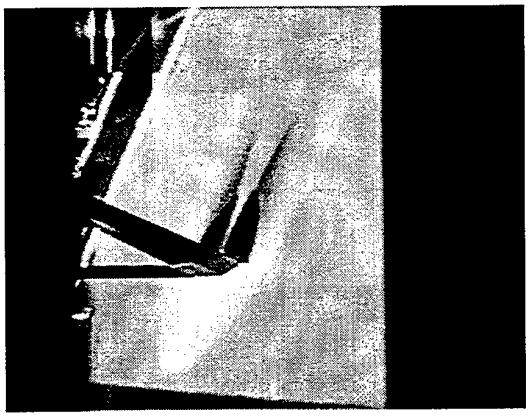

Fig. 11.- Photograph of the laser light sheet above a 75° delta wing at the 95% chord location at Mach 2.8.

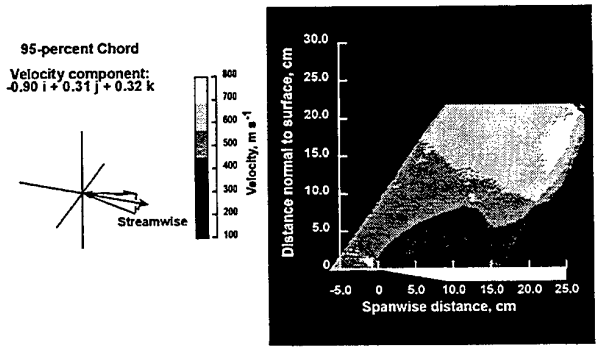

Fig. 12.- Map of the velocity flow measured by the DGV system of the vortical flow above a 75° delta wing at the 95% chord location at Mach 2.8.

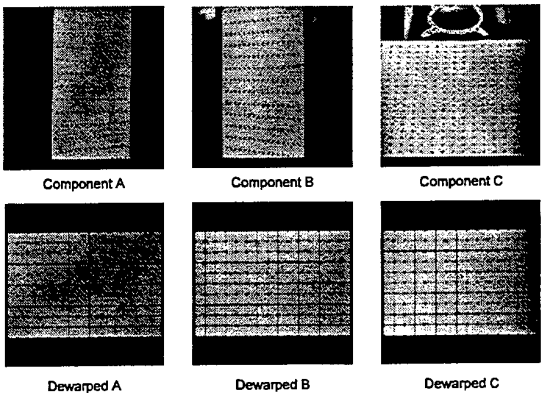

Fig. 13.- Views of equally spaced dots on a flat card from the left, right, and above with an inclination of 30° from the card plane before and after warping.

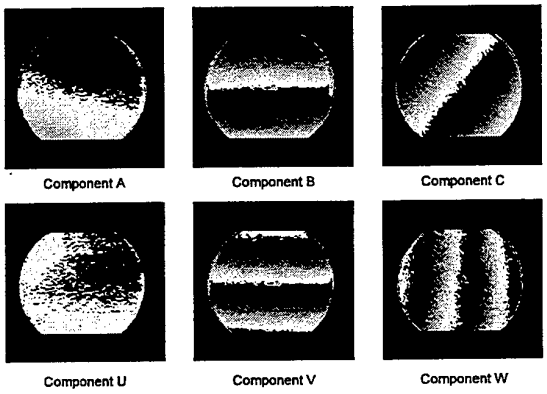

Fig. 14.- Original and resolved U, V, and W velocity component images of a rotating wheel obtained from the three views shown in Fig. 13.

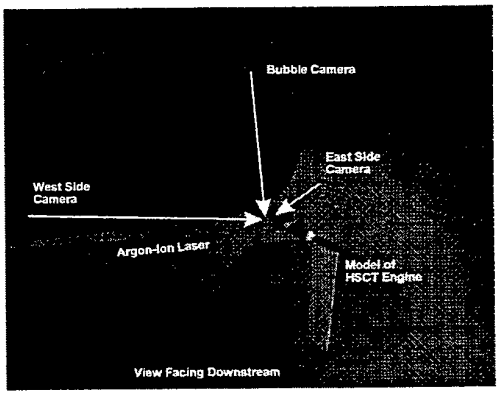

Fig. 15.- Configuration of the three-component DGV optical system in the NASA Ames Research Center 40-x 80-foot National Subsonic Wind Tunnel.

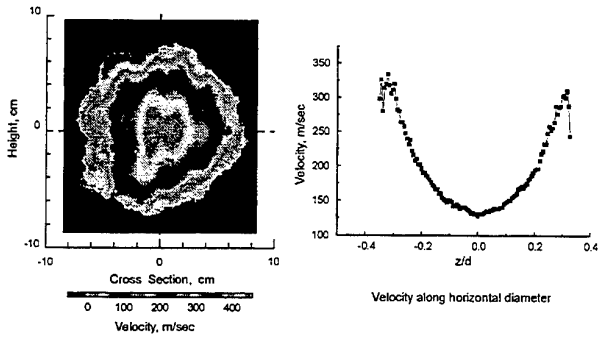

Fig. 16.- Resolved streamwise component of velocity from the high-speed jet flow operating at 463° C at a free stream Mach number equal to 0.15.

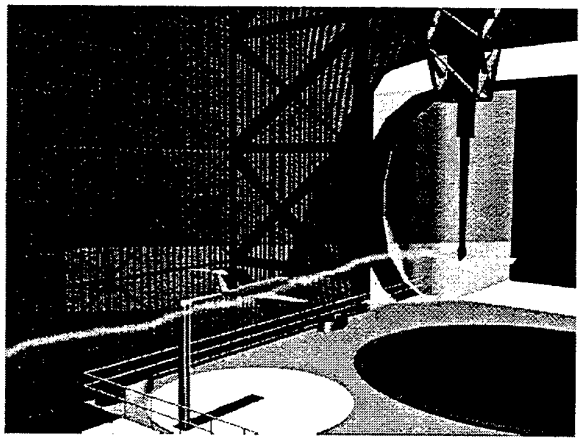

Fig. 17.- Pictorial view of the wing tip vortex interaction investigation in the Langley 30-x 60-foot Full Scale Wind Tunnel.

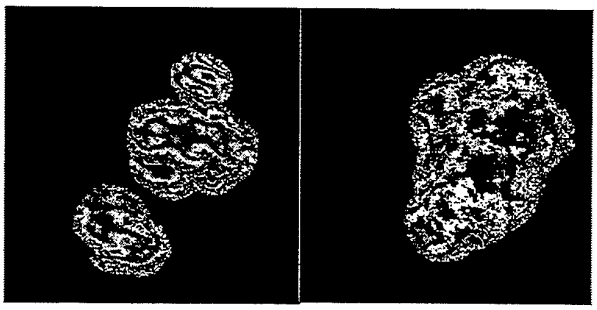

Fig. 18.- Cross flow component velocity mapping of the wing tip vortex, normal average.

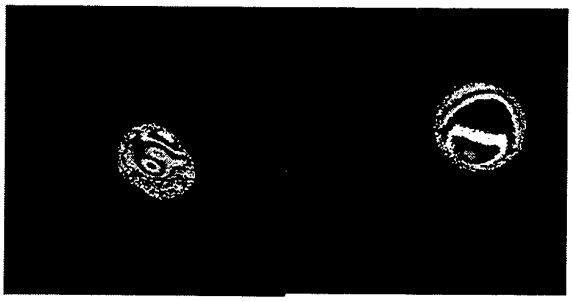

Fig. 19.- Cross flow component velocity mapping of the wing tip vortex, spatially correlated average.

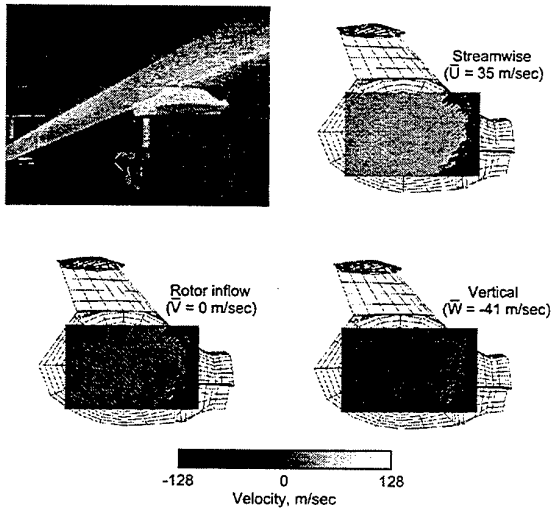

Fig. 20.- Velocity measurements of the inflow to the tail rotor of a powered helicopter model in the 14-x 22-foot Subsonic Tunnel.

DEVELOPMENT OF DOPPLER GLOBAL VELOCIMETRY FOR TURBOMACHINERY APPLICATIONS

H.D. Ford and R.P. Tatam

Optical Sensors Group, Centre for Photonics and Optical Engineering
School of Mechanical Engineering, Cranfield University, Cranfield, Bedford, MK43 0AL, UK.

ABSTRACT

A Doppler Global Velocimetry system has been developed based around a cw Argon-ion laser and a fast digital image-processing system, with the eventual aim of using the technique for measurement of flow velocities in turbomachinery. In this paper the influence of the laser source, the cameras and the absorption cell on the velocity resolution are considered and initial results are presented from tests in an 8-inch high-speed air flow duct. These indicate that a velocity resolution of 2.5 ms^{-1} is attainable with the current system. The limiting factor on the resolution at present is the signal-to-noise performance of the cameras.

1. INTRODUCTION

Doppler Global Velocimetry (DGV) is an optical technique for the measurement of fluid flow velocities. It detects the Doppler shift experienced by light scattered from moving seed particles entrained in a flow. A single image provides a two-dimensional array of flow velocity measurements, typically containing several hundred thousand velocity vectors, and DGV can therefore be considered to be the extended-field analogue of Laser Doppler Velocimetry (LDV). DGV was first demonstrated by Komine *et al* (1991) and Meyers and Komine (1991), and has since been developed in the USA, by Meyers (1995) of NASA, for full three-dimensional mapping of flow vectors in wind tunnel tests.

Unlike LDV, which uses an interferometric method to measure the optical Doppler shift, DGV employs a cell containing an absorbing vapour, typically molecular iodine at an elevated temperature, as a highly sensitive edge filter (Quinn and Chartier (1993)). The laser light source, which must have a linewidth at least an order of magnitude narrower than the width of the absorption line, is tuned to the approximately linear region centred on the 50% absorption level of the chosen line. Scattered light from the seeded flow passes through the absorption cell, where the optical Doppler shifts are transduced into intensity variations. Directional discrimination is automatic; if positive flow vectors result in increased absorption of the scattered light, then negative vectors will result in decreased absorption, and vice versa.

The Doppler shift $\Delta\nu$ is given by the equation

$$\Delta\nu = \frac{\nu(\mathbf{u}-\mathbf{k}).\mathbf{V}}{c}$$

where ν is the initial laser frequency, $\mathbf{k}$ and $\mathbf{u}$ are unit vectors in the illumination and viewing directions respectively, $\mathbf{V}$ is the velocity vector and c is the free-space speed of light. The velocity component detected is thus that in the direction perpendicular to the bisector of the illumination and viewing vectors (Figure 1).

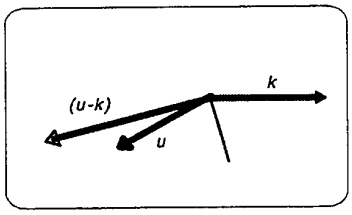

Figure 1: DGV geometry showing directions of viewing vector **u**, illumination vector **k** and measured velocity component **u-k**.

The ability of DGV to measure velocity vectors over an extended region from a single image greatly reduces the time required to map a flow. This offers a considerable advantage when investigating large test rigs, for which running costs can be high. The precision and dynamic range of DGV velocity measurements, however, are inferior to those for point LDV, and the lowest measurable speed is limited to values of the order of one metre per second. The velocity range extends up to several hundred metres per second in the direction of the measured component.

DGV is directed at the same type of measurement as the more established technique of particle image velocimetry (PIV). Both aim to detect velocities in a region within the flow defined by a laser light sheet. However, there are significant

differences between the two techniques. PIV usually detects the component of motion in the plane of the light sheet, although other components are available from double sheet (Prenel *et al* (1989)) or holographic (Hinsch (1995)) implementations of PIV. The signal processing requires time-intensive particle tracking or image correlation, although recent advances have enabled state-of-the-art PIV systems to produce several flow maps per second (McCluskey (1995)). DGV can measure any velocity component by appropriate choice of system geometry, and is tolerant of a wider range of seeding conditions than PIV.

Velocities experienced in turbomachines are typically in the range of tens to hundreds of metres per second, appropriate for measurement using the DGV technique. DGV offers the capability of measuring either time-averaged or instantaneous measurements, depending on whether the source is a cw or a pulsed laser. Detector integration times are typically 40 ms, but can be increased up to several seconds for cooled cameras. PIV uses a pulsed source and inherently measures near-instantaneous velocity. Most CFD codes at present produce time-averaged flow models, for comparison with which DGV data may prove more appropriate than those obtained using PIV.

Access is more restricted in turbomachinery than in wind tunnels or free flows. However, DGV using cw lasers is amenable to optical fibre delivery for difficult access problems. The DGV signal processing in its simplest form is a straightforward ratio operation between the images on two cameras, although additional image warping in software, to improve pixel-to-pixel matching between the two images, is required to obtain improved accuracy in flows with high spatial velocity gradients. DGV works well at high velocities, above 100 ms^{-1}, where the very short inter-pulse time necessary in PIV becomes more difficult to achieve. The differing attributes of PIV and DGV suggest that in many situations they are complementary, rather than competing, techniques.

In this paper, the development of a one-dimensional DGV system at Cranfield is described, with emphasis on the design of the optical system for optimal velocity resolution of the technique.

2. OPTICAL SYSTEM

The optical arrangement used is similar to that of Meyers (1992). Light from a frequency-stabilised Argon-ion laser (Spectra Physics Beamlok 2060) is expanded into a sheet using a combination of two spherical lenses followed by two cylindrical lenses, in a double telescope configuration. The light sheet intersects the flow in the measurement region. In the viewing system, shown in figure 2, the first element is a zoom camera lens, which forms an image of the light sheet a few centimetres behind the back surface of the lens.

A transfer lens then re-images the light sheet onto a CCD camera at a distance of 36 cm from the first image. This allows the iodine absorption filter to be interposed between the transfer lens and the camera. Intensity variations appear across the camera image for reasons other than absorption by the iodine, including variation of the light-sheet power due to the Gaussian profile, variations in seeding level, and imperfections of the optics. Temporal variations in illumination level may also occur. To correct for all these variations, the image beam is amplitude-divided by a beamsplitter following the transfer lens, and this light forms an image on a second camera in a reference arm from which the iodine cell is omitted.

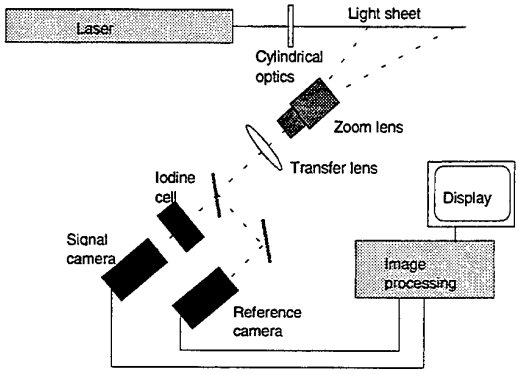

Figure 2: Schematic of the DGV optical arrangement.

A 40 MHz digital image-processing system (Imaging Technology 150/40 board) is used, which comprises acquisition, display, and computational modules. This sytem enables simultaneous capture of images from the reference and signal cameras, and calculation and display of the normalised intensity map in pseudo-real time, at an update rate of 25 Hz. The real-time capability greatly eases the process of camera alignment, since adjustments can be performed interactively, while viewing the normalised image. Quantitative information is obtained from post-processing.

Spatial resolution, for high seeding density, is a function of the number of elements in the camera array, the quality of optical components in the imaging system and the area of the measurement region in the flow. For low seeding densities, averaging less than one seed particle imaged per pixel during the integration time, seeding may be the limiting factor in spatial resolution.

Velocity resolution depends upon the performance of several elements of the optical system, including laser frequency stability, temperature stability of the heated iodine cell, and camera noise. The images on the two cameras are assumed to be identical in everything but intensity, so the degree of pixel-to-pixel matching obtained and any difference in response of individual camera pixels will also influence the overall system performance, as will aberrations introduced into the signal beam by its passage through the iodine cell. A recent publication by Manners *et al.* (1996) suggests that pixel

matching to better than one twentieth of the pixel dimension is required in order to obtain optimum accuracy in difficult regions of flows such as shocks. The effect of each individual system component upon the total performance of the DGV system is considered in more detail in following sections of the paper.

3. IODINE CELL

The iodine cell must be large enough in diameter to encompass the signal beam, and must be of sufficient length to ensure appreciable absorption at readily attainable iodine vapour pressures. A fused silica cell, 50 mm long and 30 mm in diameter, was used in these experiments. A small amount of solid iodine was introduced into the cell, which was subsequently evacuated using a high-vacuum pump and sealed. Heating of the cell was necessary to obtain good visibility in the signal image. Some solid remained in the heated cell, therefore the vapour concentration was fixed by the saturation vapour pressure of iodine.

The type of cell described above is said to be saturated, whereas if no solid remains, the cell is called an unsaturated, or starved, cell. The absorption varies approximately linearly with vapour pressure in either case and, in an unsaturated cell, the fractional variation in temperature is equal to the fractional variation in vapour pressure. However, the temperature dependence is much stronger for a saturated cell (Fredin-Picard (1989)). The fractional vapour pressure variation is about twenty-five times greater for the same fractional temperature variation. An unsaturated cell may be preferred for this reason, but it has certain disadvantages; the relatively low vapour pressure results in a reduced dynamic range, and the cell can become optically saturated for high levels of scattered light. A saturated cell was therefore chosen for the Cranfield system.

Temperature stability to about 0.1 K is required to maintain the absorption fluctuations below one grey level (about 0.5%) for an 8-bit system. The velocity variation (which is a maximum for the full backscatter geometry) will then be below about 1 ms^{-1}. Much attention was given to the design of the oven for heating the cell, since both stability of the cell temperature with time, and constancy of temperature throughout the body of the cell were expected to be crucial to the performance of the system.

Initial trials, using a design in which the cell was surrounded by heated air, did not provide sufficiently even heating. Modifications were made, and a second oven was constructed using the design shown in figure 3. The cell was coated with heat-sink compound, and closely surrounded by a copper jacket, which was in contact with the cell wall. A thermocouple sensor was cemented to the copper jacket, and heating cable was wound around the jacket, completely covering it.

Where the side-arm and tap protruded from the cell, a small gap was unavoidable. Finally, the entire structure was enclosed in a close-fitting, thick-walled plastic tube, which provided thermal insulation. Entrance and exit holes were provided for the heating cable, and the anti-reflection-coated optical windows were sealed into the ends of the plastic tube. The substantial electrical insulation around the heating cable also provided additional thermal insulation. The copper jacket, heating coil and tube extend beyond the cell by about 3 cm at each end. This minimises temperature gradients in the cell by ensuring that air in the gap between cell and oven windows, the least well insulated part of the enclosure, is heated by contact with the copper jacket, reducing the temperature gradient between the two sets of windows as much as possible.

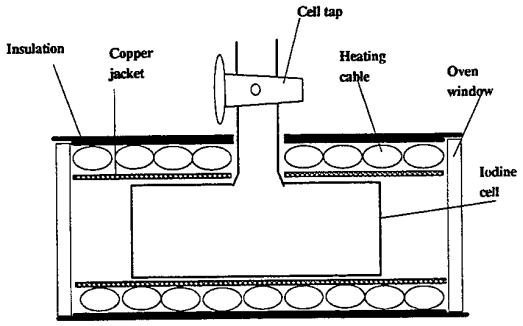

Figure 3: Schematic of DGV heating oven.

The heating cable used was of the type which has a cool lead section, thus avoiding unnecessary heating around the cameras in the DGV head. The cable was attached to a Proportional/Integral-type temperature controller. This type of controller provides heat at a rate proportional to the difference between actual measured temperature and set point temperature, and also compensates for any discrepancy between the set and final temperatures due to differences in the heat supply and heat loss rates. The controller was programmed to bring the temperature to the operating point as rapidly as possible without overshoot, and subsequently to maintain the sensor temperature to within 0.1 °C. Due to the large thermal mass inside the oven, the temperature stability of the cell itself was expected to be better than this.

The performance of the cell oven was tested by mounting the oven on a translation stage with continuous transverse adjustment and stepwise height adjustment. The output from the argon-ion laser, strongly attenuated using neutral density filters, was directed to pass through the cell, parallel to its axis. Software was written to sum the intensity values recorded over all the pixels of a CCD camera, which was thus used as a large area detector for the laser beam, behind the oven.

The laser frequency was set to a point on the side of the iodine absorption line, and the transmission was recorded as the laser beam passed through different positions across the cell aperture. The experiment was repeated with the laser tuned off

the absorption line, and these values were used to normalise the first set of measurements. The positions where measurements were made, and the measured transmission values are shown in figure 4. The standard deviation is 3.5%, attributed largely to errors in translating the cell to exactly corresponding positions for both sets of measurements. No systematic variation in absorption is detectable across the cell aperture.

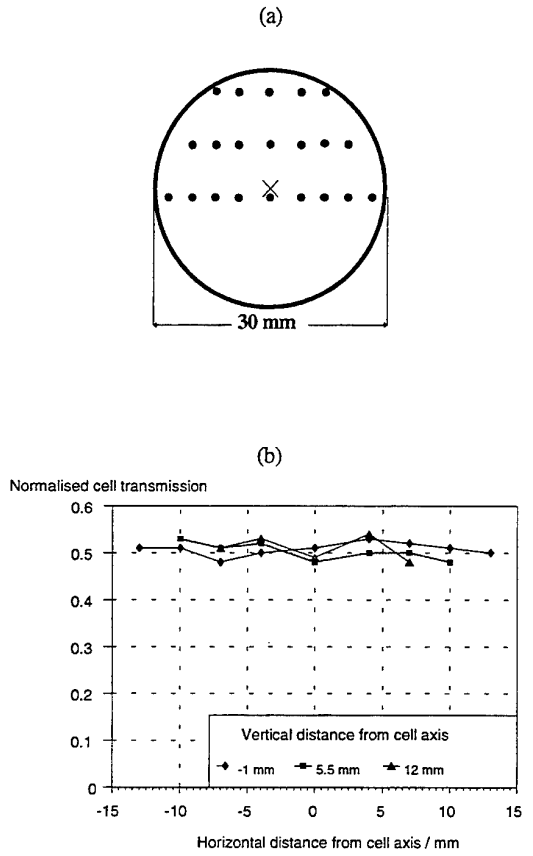

Figure 4: (a) Positions in cell where transmission measurements were made, (b) Normalised transmission curves for the three rows of measurements.

Calibration curves for the cell were obtained by scanning the laser frequency slowly across the region of the iodine absorption line. Curves for operating temperatures of 40 °C and 60 °C are shown in figure 5. The intensity variation is 71% of the maximum at 40 °C, increasing to 90% at 60 °C.

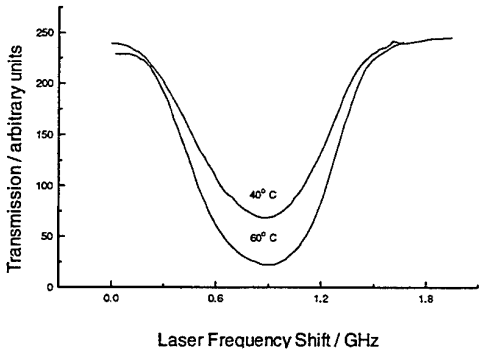

Figure 5: Transmission curves for iodine cell, as a function of laser frequency.

4. LASER SOURCE

The Spectra Physics Beamlok Argon-ion laser used with the Cranfield DGV system contains a temperature-stabilised etalon for single-line operation. It provides a maximum of about 2.5 W of optical power at 514.5 nm, when the etalon temperature is tuned so that its minimum attenuation coincides with the centre of the laser gain curve. The linewidth is about 3 MHz and a combination of frequency-stabilisation circuits limits the jitter of the centre frequency to about 2 MHz over a frequency range from 10-500 Hz. Drifts of several hundred MHz can occur in the centre frequency over longer time periods if the ambient temperature changes, but mode-hopping is almost completely eliminated unless drastic and sudden changes of ambient temperature are experienced.

Particularly for instantaneous (pulsed) DGV measurements, it is important that the jitter on the centre frequency be as small as possible, and that the position of this centre frequency relative to any point on the iodine absorption line is either stable, or is tracked as the two drift relative to one another. A combination of stabilisation and tracking is the most practical solution. For time-averaged measurements, the effect of the jittter will be less than for the pulsed case due to averaging. The linewidth of the laser, while it should be as narrow as possible, is not as crucial as the stability of the centre wavelength. Provided that the laser frequency is positioned in the approximately linear region of the iodine line, small errors from frequencies above the centre value are cancelled by small errors from frequencies below the centre value, permitting rather large laser linewidths to be tolerated with little error. This would be particularly helpful when using short-pulsed lasers for DGV, since transform-limited linewidths are usually at least an order of magnitude greater than linewidths for cw lasers.

5. CAMERAS

The cameras used were COHU 4910 series analogue cameras, with an array size of 752 (H) x 582 (V) elements giving an interlaced resolution of 560 (H) x 450 (V) TV lines. The signals were digitised to 8 bits (256 grey levels) by the image-processing board. The frame rate was 25 Hz, and synchronisation for simultaneous reference and signal image acquisition was achieved using a pulse output from the image processing board via a signal splitter box which sent the trigger pulse to both cameras simultaneously. It was found in early DGV tests with the system that the signal-to-noise performance of the cameras was rather poor; with the gain adjusted to the minimum possible value, the maximum variation in the output of any one pixel was measured to be about 4 grey levels in 256, or 2 bits of noise, while at maximum gain the variation was as much as 20 grey levels, or more than 4 bits of noise. Acceptable performance, without the necessity for averaging over large numbers of frames, was therefore only achieved with the camera gains set close to the minimum value. This greatly increased the seeding level required to produce reasonable signal levels when making measurements on a flow, as discussed later.

The noise levels experienced appear to be typical for this type of inexpensive analogue camera. Similar performance was measured from a Pearpoint 800 analogue camera. Improved signal-to-noise would be expected from a better quality analogue camera or, preferably, an 8 or 10-bit digital camera. A cooled chip would allow much longer integration times and thus improve performance still further for steady-state flows, with low scattered light levels.

6. EXPERIMENTAL MEASUREMENTS

The DGV system was initially tested in the laboratory, viewing a rotating perspex disc 15 cm in diameter, coated with reflective paint. The rotation speed of the disc, which was about 45 ms^{-1} at the circumference, was calibrated against a strobe mark, using a point photodetector, and the DGV illumination and viewing vectors were arranged to lie in a horizontal plane, so that a horizontal velocity component only was detected. The horizontal velocity varies linearly along a vertical line throught the centre of the wheel. Pixel intensities on this line were averaged over 40 frames, and the velocity of the wheel was correctly measured to a velocity resolution of about 1 ms^{-1}.

To allow measurement under normal room lighting conditions, the entire viewing system was enclosed in a light-tight case, and a narrowband (2 nm FWHM) bandpass filter for the laser wavelength of 514.5 nm was positioned behind the front zoom lens. This was not always required in laboratory testing, but was essential during later wind-tunnel tests, which were made under conditions of direct sunlight.

Following the successful tests on the rotating disc, experiments were subsequently performed on an 8-inch diameter high-speed flow duct, equivalent to a miniature wind tunnel. Due to work on other rigs, testing was often carried out with external doors open, so that the DGV system was exposed to large, rapid temperature fluctuations and direct sunlight. The narrowband line filter was always required under these conditions. The air flow in the duct could be varied in speed from zero to more than 100 ms^{-1}. Titanium dioxide particles of about 0.5 μm diameter were used as a solid seeding agent. The flow speed in the duct was calibrated against Pitot tube measurements.

The DGV geometry used is shown in figure 6. The laser was mounted on a table beside the test rig, and the light-sheet optics on a small optical table close to the duct entrance. Mirrors were used to direct the beam, through the light-sheet optics, directly down the centre of the duct in the direction of flow. The DGV head viewed the light sheet, which was slightly divergent and measured about 10 cm in height in the region imaged, through a 5 cm diameter perspex window in the side of the duct. Thus the illumination and viewing directions were perpendicular, and the velocity component measured was at 45° to the flow direction.

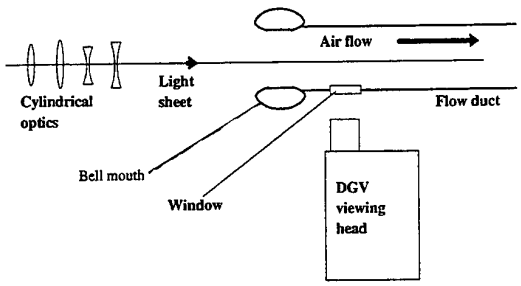

Figure 6: DGV illumination and viewing geometry used for flow duct measurements.

The cell temperature was set to 60 °C to obtain a large dynamic range, and the cameras were used on near-minimum gain to maximise the signal-to-noise ratio (S/N).The black level (zero offset) was adjusted for each camera separately with no light entering the DGV head, and the camera gains were adjusted to give identical outputs for a laser frequency just off the low-frequency side of the iodine absorption line. The laser frequency was then set to a point in the linear region on the negative-gradient side of the iodine line. It was found that, under these conditions, with a collection aperture of about f/4 and with the laser providing about 1.5 W of power, sufficient seeding to use the full dynamic range of the cameras was obtained only immediately after switching on the seeder, when a particularly concentrated burst of seeding was obtained. The camera gains could have been increased, but only at a cost of reduced S/N, and capture of image frames was therefore restricted to the duration of the initial seeding bursts.

7. RESULTS

The flow was adjusted to a range of different speeds and DGV images were captured under each condition. Averaging

was performed over a square block of 36 pixels near the centre of the normalised image, thus reducing the expected signal variation due to camera noise from about 6 grey levels to about 1 grey level. The zero-flow intensity value was re-checked between measurement of each velocity point. The DGV measurements of velocity, calculated form the averaged pixel intensity in the normalised image, are plotted against independent Pitot tube velocity measurements in figure 7, for one such experiment. The two sets of symbols correspond to two different series of measurements and the solid line shows the expected velocity as given by the Pitot tube measurements. A fit to the DGV results gives a gradient which differs from the expected gradient of 1 by about 7%. This could be due to a slight deviation from 90° of the angle between the illumination and viewing directions. The 90° configuration is particularly sensitive to angular errors, such that an error of just 1° in the viewing angle can introduce a velocity error of 2%, and an angular error of 5° can introduce a velocity error of 9%. In future experiments, the 90° viewing angle could be more carefully set up using reflections of the beam from a right-angled prism, provided that there is sufficient access to the beam at the intersection of the viewing and illumination directions. Another solution would be to mount the illumination and viewing equipment on a large-scale angular positioning system.

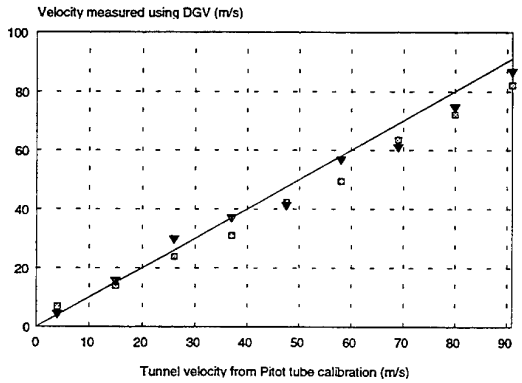

Figure 7: Graph of tunnel velocity measured using DGV plotted against velocity calculated from Pitot tube measurements.

The standard error for the velocity measurements shown in figure 7 is 2.5 ms^{-1}, under these relatively favourable conditions of unidirectional flow, strong seeding and little or no velocity gradient within the image. The S/N deteriorates towards the top and bottom edges of the normalised images, where the seeding is less concentrated and the full dynamic range of the cameras is not available.

These results were obtained under reasonably stable ambient temperature conditions (variation of less than 3 K during the course of the measurements), and the laser frequency drifted by a velocity-equivalent of no more than 50 ms^{-1} during the measurements. The drift was corrected for using the zero-velocity calibration checks between each measurement. With the test-house doors open, the laser frequency can change by several hundred MHz within half an hour or so, and very frequent calibration checks at zero velocity must be made if meaningful results are to be obtained. Mode hops can also occur under these conditions.

A prototype additional feedback stabilisation circuit, designed to lock the laser to a point on the iodine cell absorption line, has been successfully tested in the laboratory (figure 8). Without the circuit, the laser remained close to the switch-on frequency after warm-up, and drifted slightly during the day as the laboratory temperature changed by about 2 K. With the stabilisation circuit on, the laser can be brought to an appropriate frequency for DGV, at about the 50% absorption level, and remains at this frequency, to within 1% absorption variation, despite similar drifts in ambient temperature. The circuit is currently being packaged appropriately to allow its use with the portable DGV head in field testing.

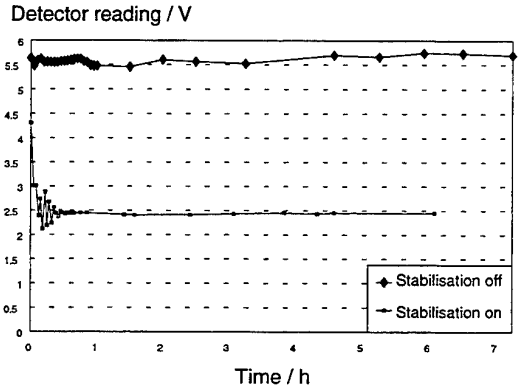

Figure 8: Transmission of laser through iodine cell with and without stabilisation feedback circuit in operation.

8. CONCLUSIONS AND FUTURE WORK

In the current programme, all the major instrumentation issues important to the optimisation of velocity resolution in a DGV system have been investigated. A velocity resolution of 2.5 ms^{-1} has been achieved in a relatively straightforward flow with low spatial velocity gradients. This is currently limited by the poor signal-to-noise ratio of the cameras, and would be expected to improve immediately by a factor of at least four if better cameras were substituted which gave true 8-bit performance.

A more stringent test of the system requires large velocity gradients to be present within the image region. Improved pixel-to-pixel matching will certainly be necessary to allow our system to operate satisfactorily under these conditions. At present, pixel matching is achieved to better than the pixel dimension, but further experiments are needed to determine more accurately and to improve upon the degree of pixel matching. A short series of experiments is planned in the current programme to make preliminary measurements on more difficult flows, including shocks.

9. ACKNOWLEDGMENTS

This work was supported by grant no. GR/J46555 from the Engineering and Physical Sciences Research Council.

10. REFERENCES

Fredin-Picard, S., 1989, A Study of Contamination in $^{127}I_2$ Cells using Laser-induced Fluorescence, Metrologia, vol. 26, pp. 235-244.

Hinsch, K.D., 1995, Three-dimensional Particle Velocimetry, Meas. Sci. Technol. vol. 6, pp. 742-753.

Komine, H., Brosnan, S.J., Litton, A.B. and Stappaerts, E.A., 1991, Real-time Doppler Global Velocimetry, 29th Aerospace Sciences Meeting, Reno NV, Paper AIAA-91-0337..

Manners, R.J., Thorpe, S.J. and Ainsworth, R.W., 1996, Image Processing Techniques for Doppler Global Velocimetry, Optical Methods and Data Processing in Heat and Fluid Flow, London, Paper C516/041/96.

McCluskey, D.R. (Dantec MT), 1995, Obtaining High-Resolution PIV Vector Maps in Real-Time, Int. Workshop on PIV, Fukui, Japan.

Meyers, J.F. and Komine H., 1991, Doppler Global Velocimetry: A new way to look at Velocity, ASME 4th International Conference on Laser Anemometry, Advances and Applications, pp. 289-296.

Meyers, J.F., 1992, Doppler Global Velocimetry: The Next Generation, 17th Aerospace Ground Testing Conference, Nashville, TN, Paper AIAA-92-3897.

Meyers, J.F., 1995, Development of Doppler Global velocimetry as a Flow Diagnostics Tool, Meas. Sci. Technol., vol. 6, pp. 769-783.

Prenel, J.P., Porcar, R. and El Rhassouli, A., 1989, Three-dimensional flow analysis by means of sequential and volumic laser sheet illumination, Exp. Fluids, vol. 7, pp. 133-137.

Quinn, T.J. and Chartier, J.-M., 1993, A new type of Iodine Cell for Stabilized Lasers, IEEE Transactions on Instrumentation and Measurement, vol. 42, no. 2, pp. 405-406.

AN IMPROVEMENT IN DOPPLER GLOBAL VELOCIMETRY THE USE OF A CW DYE LASER

by
B. Leporcq, J.F. Le Roy
Institut de Mécanique des fluides de Lille
Office National d'Etudes et de Recherches Aérospatiales
5, Boulevard Paul Painlevé, 59045 Lille cedex
FRANCE

B.Pinchemel, C. Dufour
Laboratoire de Dynamique Moléculaire et Photonique
Centre d'Etudes et de Recherches Lasers et Applications
Université de Lille 1
59655 Villeneuve d'Ascq cedex
FRANCE

ABSTRACT

The Doppler Global Velocimetry (DGV) is a non intrusive optical technique yelding to a vizualization of the flow and to the whole instantaneous associated velocity field. In the plane of a laser sheet, the Doppler shift of the light scattered by the moving particles seeding the flowfield, is detected through an iodine frequency discriminator.

The improvement of this method consists in using a narrow bandwidth tunable dye laser. The purpose of this study is to characterize the enhancement in the DGV method induced by such a dye laser.

NOMENCLATURE

B_v, rotational energy of the J level for the v vibrational level
c, light velocity
E(v), vibrational energy
FGH(J), hyperfine structure coefficient
$f_1(T)$, Boltzmann fraction at temperature T
f_r, rotational fraction
f_v, vibrational fraction
h, Boltzmann constant
$\vec{I}$, unity vector in the laser direction
J, rotational level
J_{opt}, optimal rotational level
k, Boltzmann constant
m, molecular mass of the species,
$\vec{O}$, unity vector in the observation direction
P, pressure
T, temperature
u, velocity component
v", vibrational level of the fundamental X state
V, velocity
$\Delta\nu_D$, Doppler shift
ν, laser frequency

1. INTRODUCTION

Sophisticated calculation methods which may be used to study complex vortices have to be validated against refined experimental measurements including accurate local velocities. In the same way, advances in aerodynamics in military aircraft performances require a better experimental knowledge of complex three-dimensionnal vortical flows occuring especially at high angles of attack. The study of vortical flows are also of interest for civilian applications such as lift induced drag reduction for cruise flight or vortex wake attenuation in take-off or landing configuration.

For many years, aerodynamic measurements have been obtained from intrusive probes such as hot wires or anemoclinometers. These conventionnal techniques are very easy to use, but their main disadvantages lie in the perturbations they induce to the local velocity field.

Various non intrusive techniques have been developed to qualify the flows [1]. These techniques are based on the physical properties of the fluid in motion or on a well-defined seeded flow. Usual non intrusive measurements are well suited for very small probe volume typically a few 10^{-3} mm^3.

Non intrusive optical techniques include interferential laser velocimetry and two-focus laser velocimetry [2]. They give access to the velocity measurement at one point and are not convenient for very unsteady flows because they require a finite avaraging or integration time.

In the investigated range of vortical flows, the Doppler Global Velocimetry is of interest because this non-intrusive method yields a whole instantaneous velocity field in a short time, which is compatible with an unsteady flow. Developments of this method are compatible with tests performed on an airplane model in motion or with static tests in wind tunnel.

2. DOPPLER GLOBAL VELOCIMETRY

2.1. Principles of Doppler Global Velocimetry

Early DGV experiments started in the U.S.A. in 1992 and have been described by J. F. Meyers *et al* [3, 4]. They rely on Doppler shift measurements of light scattered by a seeded flow illuminated by a laser sheet. The previous works used an Argon ion laser operating at 514.5 nm, in axial single mode, which fortuitously is tuned on the unresolved P13-R15 (43-0) absorption line of molecular iodine. A camera records the images of the particles seeding the flow when illuminated by a laser sheet. Particles moving at velocity V, may be considered successively as receptors in motion then as moving sources. Thus the scattered light is at a frequency $\nu + \Delta\nu$, where ν is the frequency of the illuminating laser and $\Delta\nu$ is the Doppler shift given by :

$$\Delta\nu = \frac{\nu_0(\vec{o}-\vec{i})}{c}\vec{V}$$

The velocity measurements are simultaneously taken at any point in the observation field. Then viewed through an iodine cell, any Doppler shift is readily translated into an absorption variation. The entire image of the laser light sheet recorded through the iodine cell is numerically digitalized. This method gives access to a velocity map of the seeded flow at a speed depending only on the recording device.

2.2. Experimental Set Up

A typical experimental D.G.V. set up has shown in figure 1 involves five parts :

- the flow and the seeding system ;
- illuminated slice of the flow by a laser at the wavenumber ν_0 tuned to an iodine absorption line ;
- a frequency discriminator built from an iodine cell with parallel windows located in front of a camera ;
- a recent improvement in the optical design suggested by Chan *et al* [5] and Thorpe *et al* [6] allows the use of only one camera which records two images of the same object : the first one is the reference image while the second is discriminated through the iodine cell ;
- a computer for the numerical handling of the data.

The ratio between the two images gives access to the local velocity measurement with a significant reduction of the noises induced by the inhomogeneous seeding of the flow and intensity variations of both the laser light and the scattered light.

3. ADVANTAGES OF A CW DYE LASER IN DGV

In the previous works, no flexibility is allowed by the narrow tunability range (< 10 GHz) of the laser line ; nor the absorption conditions neither the line profile can be chosen. The strong temperature dependance of the P13-R15 (43-0) absorption lines requires the thermal calibration of the iodine cell to be very carefully monitered at better than 0.1 K. On the contrary a narrow bandwidth 500 KHz CW dye laser line can be tuned from 500nm to 700 nm allowing a great flexibility to select any well resolved iodine line. At il will be discussed later, this characteristic will overcome the rigidity of the use of a fixed-frequency laser.

3.1. Laser Emission

The best monochromatic light is achieved with a longitudinal single mode laser. Such a laser line is about 10^{-3} more narrow than the iodine line.The laser emission yielded by a dye laser is tunable and can be turned single mode. The active part is an organic dye which absorbs the light of a pump argon-ion laser and can emit on a large wavelength range, typically 50 nm. The dye is selected to fulfil the expected spectral range where the laser can be continuously tuned with a Lyot filter. The most commonly used dyes are rhodamines 110 and 6 G. Yield of these dyes is about 20% of the argon pump laserin a single mode operation.

In order to optimize the tunability and the single mode operation, active frequency stabilization is achieved through piezo-electric mounted mirrors. Under these conditions a 500 kHz wide line can be obtained.

A commercial ring dye laser, COHERENT 899-29 pumped by a COHERENT INNOVA 100 Argon-ion laser is driven by an AUTOSCAN device which determines the exact wavelength and allows continuous scans on several nanometers and records the experimental data.

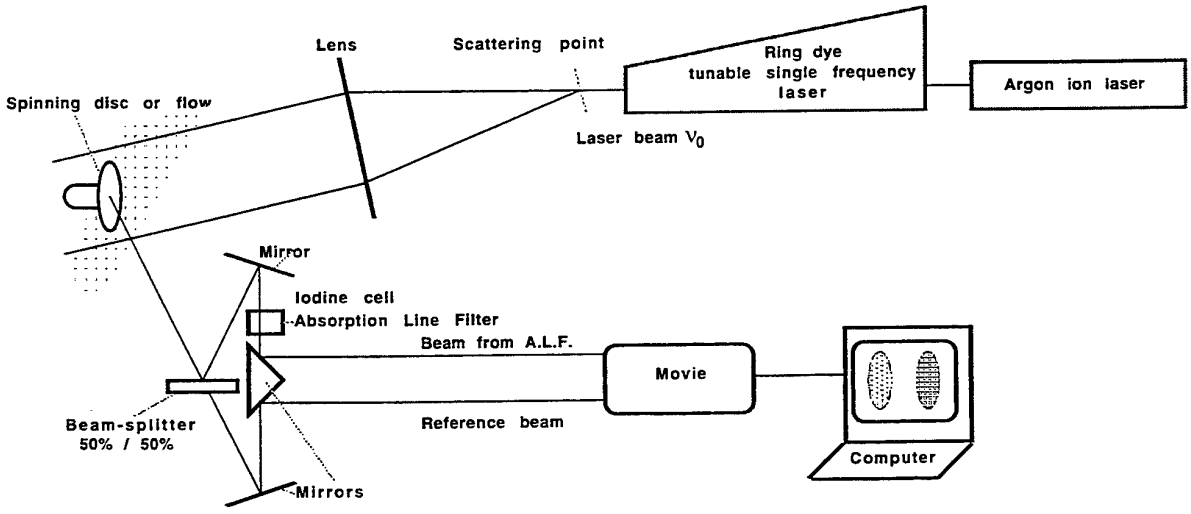

fig.1 Experimental D.G.V. set up

One of the criterious requested by DGV is the accurate determination of the laser frequency ν_0 and the reproductibility of the location of the laser line in the selected absorption iodine profile. The internal frequency device of the COHERENT AUTOSCAN provides the signals of two Fabry-Pérot etalons which can be recorded simultaneously with the iodine absorption line. Relative positions of the three signals are quite independant of the experimental conditions, as a consequence a confident assigment of the laser frequency can be achieved with a great accuracy at least equal to those given in reference [7].

3.2. Selection of an Iodine Absorption Line

A strong absorption associated to a linear Doppler profile on 1 to 3 GHz is generally required. the profile of the line must match the studied speed range. For velocity range between 150 m/s to 450 m/s. The magnitude of the Doppler shift for usual observation angles is about 0.3 GHz. For low velocities less than 50 m/s, an iodine absorption lines exhibiting a sharp slope Doppler profile should be chosen. For iodine molecules, the number of hyperfine components 15 or 21 allows such a choice. To minimize the temperature dependance and to make easy the thermal stabilisation of the iodine cell, it is necessary to study the Boltzmann fraction. The population fraction of the molecules in the absorbing level (v, J) can be described by the product of the fraction f_v of molecules in the fundamental vibrational level v"= 0 and rotational fraction f_r in the rotational level J":

$$f_1(T) = f_v.f_r = \frac{e^{-\frac{E(v)\,hc}{kT}}}{Q_v} \frac{2(2J+1)\,e^{-\frac{B_v.h.c.\,J.(J+1)}{kT}}}{Q_r} FGH(J)$$

The possibility to minimize the temperature dependance of the Boltzmann fraction is based on the appropriate choice of the fundamental rotational level J", which is provided by an analysis of the partial derivative of the rotational fraction f_r versus T. The optimal rotational level can be expressed as :

$$J_{opt} = 0{,}83 \sqrt{\frac{T}{B_v(cm^{-1})}}$$

The evolution of the Boltzmann fraction for several rovibrational absorbing levels (v"=0, J") versus temperature is well known [8, 9]. The choice of the optimal rotational level J" is very important first to minimize temperature effects in the Boltzmann fraction, secondly for the level of the total population at a given temperature which is directly proportionnal to the intensity of the fluorescence signal. According to the previous considerations, the tunability of the laser makes possible to select a rovibrationnal iodine line which is almost insensitive to the temperature fluctuation inside the absorption cell. For this purpose we selected the rotational quantum number J" close from 70. For a temperature of the iodine cell equal to 340K, the operable temperature range is plus or minus 5K.

3.3. Iodine Cell

After being evacuated a 6 cm-diameter and 3cm-thick cell is filled at the vapor pressure corresponding to a temperature of 328K and is then sealed. The equilibrium pressure between solid and gaseous Iodine is monitored by temperature following Dewar law[11] :

$$\log(P(mmHg)) = 10{,}0392-(3137/T)$$

The cell is set in a thermalized water bath at a temperature of 340K. This allows to prevent the iodine deposit, and keep constant the pressure and as a consequence the absorption profile of the lines.

3.4. Light Absorption of Iodine

The main electronic transition of I_2 molecule occurs between the ground X state and the excited B state which are separated by about $16000 cm^{-1}$. Between these two state numerous ro-vibrational transitions are observed inducing a large number of lines in the spectral range 14000 to 20000 cm^{-1}.

For pressures in the iodine cell, less than 1500 Pa, the main broadening is due to Doppler broadening which originates from the thermal motion of molecules. This Doppler width measured at half height of the line is :

$$\Delta\nu D = \sqrt{\frac{8\,k\,T\,\ln 2}{m\,c^2}}$$

Another kind of broadening arises from the hyperfine structure (HFS) of I_2 which originates from the coupling between the rotational and the nuclear angular momenta. As previously mentioned, each rotational level with even quantum number is split into 15 HFS components while an odd rotational level includes 21 HFS sub-levels. HFS leads to an inhomogeneous broadening of the lines. Both Doppler and HFS effects induce a non symmetrical and erratic profile of the lines. As a consequence, the choice of an Iodine line for the D.G.V will be of importance. This gives a definite interest to the frequency tunability of the single mode dye laser.

4. D.G.V. MEASUREMENTS

Experimental studies have been performed with a spinning disc of 8 cm in diameter, the speed of which can be adjusted from 5000 and 30000 rpm and is controlled by a tachymeter.

The spinning disc is illuminated by a parallel light beam arising from a scattering light originated from the focus point of a 10 cm-diameter lens. Great care has been taken in order to obtain a uniform density of the light on the horizontal diameter of the spinning disc. The recent improvement suggested by Chan *et al* [5] has been used in this experiment.

4.1.Absorption Calibration Versus Laser Frequency

First of all, it is necessary to calibrate the absorption curve of iodine versus laser frequency. The selected P 71 (22-0) line is frequency-scanned by the laser. A set of images is recorded and digitalized in order to determine the absorption level as a function of the laser frequency on the spinning disc , where the Doppler shift is equal to zero. As observed in figure 2, it is possible to assign an accurate frequency to an absorption level ranging from

7% to 80%. From the calibration it is possible to determine a frequency from the experimental absorption level.

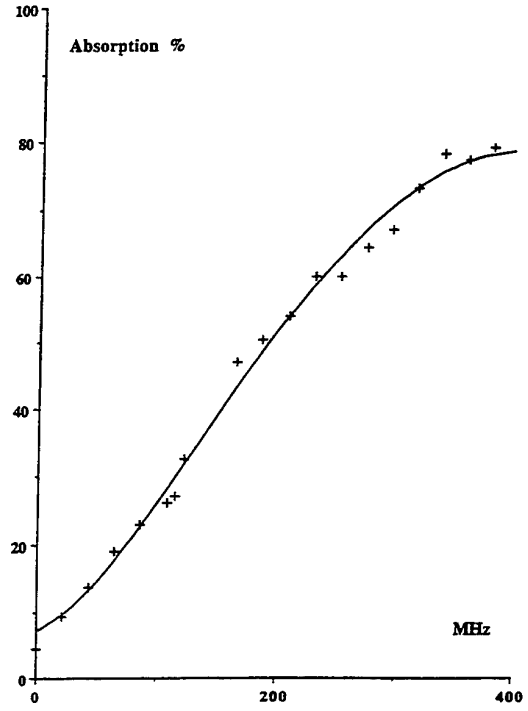

Fig.2 Variation of absorption versus frequency

4.2. Velocity Determination at Stationary Laser Frequency

The laser frequency is now tuned at a level of absorption close to 40% of the selected side of the P 71 (22-0) line. The variation of absorbed intensity is determined by digitalization on the vertical diameter of the spinning disc (figure 3) for various speeds of the disc.

The experimental set up allows an easy comparison between the two images, respectively the reference and Absorption Line Filter signals. A superposition pixel to pixel of the two images is necessary. This is achieved with the help of three fixed enlighted points and geometrical considerations. The mathematical processing, following a vertical mirror symetry, includes a translational, rotational and homothetical transformations. After these operations, the two images are perfectly identical in size and position. The signal to noise ratio is enhanced when dividing the ALF signal by the reference one. This allows to cancel the inhomogeneities due to the scattered light and the disc reflectivity.

For each intensity the calibration curve (figure 2) allows the assigment of a Doppler shift which can be linked to a given velocity and compared to that given by the tachymeter. The agreement is good for the vertical diameter of the spinning disc i.e. for velocity included in the range -130 m/s to 130 m/s (figure 4). On this figure, are reported the experimental data collected from pictures performed at different speeds between 4150 to 27500 RPM. The linear velocities have been measured on the edge of the disc.

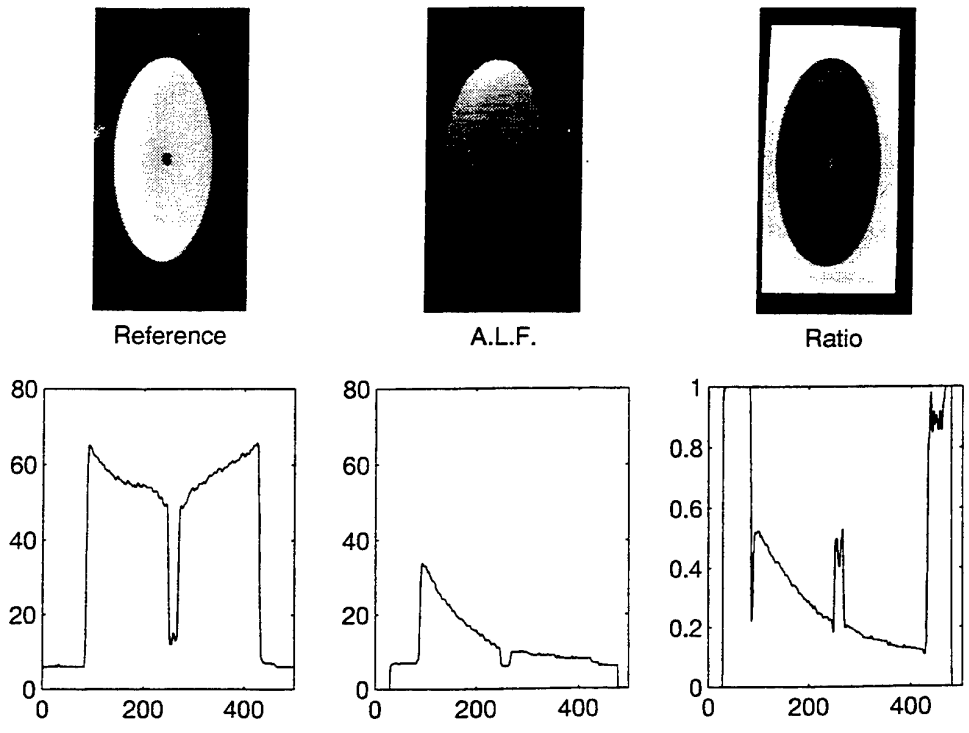

Fig. 3 Evolution of absorption on a vertical diameter of a spinning disc

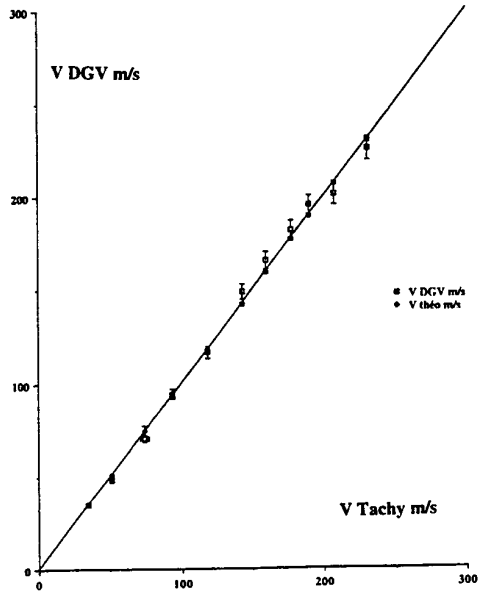

Fig 4 Comparison of velocities determined by dgv and tachometry

5. CONCLUSION AND PROSPECTS

DGV is a technique which is of interest in fluid mechanics and more particularly for the measurement of the field of an aerodynamic flow.

The first description of the method in 1992, referred to the use of a single mode argon-ion laser which fortuitously fits the P13 et R15 (43-0) absorption lines of molecular iodine. The improvement described in this paper is based on the use of a single mode dye laser which generates a narrow width line. The most important feature is the tuning ability which makes it possible to select an iodine line which satisfies the following needs : a well-resolved shape, a linear side profile, whose slope depends on the HFS distribution which contributes to the sensitivity and the selection of the vibrational and rotational quantum numbers. These in turn are of importance for absorption intensity and temperature dependence. The easy tunability of the laser allows the calibration of absorption and consequently permits a straightforward conversion from the absorption measurements to the velocity determination. We expect this technique to be usable in a wide velocity range (10 m/s to 1500 m/s). The versatility of the dye laser gives the opportunity to use different molecules as a discriminating frequency filter. Bromine could be a good candidate for such an application. Bromine molecules include less HFS components than iodine, that leads to a more narrow profile which can be expected to increase the sensitivity.

ACKNOWLEDGMENTS

The authors thank Miss M. Eleaume, Mr. X. Lefebvre and Mr. J.-P. Bourez for assistance in the experimental part of this work.

REFERENCES

[1] R.L. McKenzie - Progress in laser spectroscopic techniques for aerodynamic measurements : an overview. AIAA Journal, Vol. 31, N.3, March 1993

[2] A. Boutier - Vélocimètrie laser. Les techniques de l'Ingénieur, R2161, p. 35-43

[3] J. W. Usry, J. F. Meyers, L. Scott Miller - Doppler Global Velocimeter Measurements of the Vortical Flow Above A Thin Delta Wing. AIAA 92-0005, January 1992

[4] J. W. Lee, J. F. Meyers, A. A. Cavone, K. E. Suzuki - Doppler Global Velocimeter Measurements of the Vortical Flow Above an F/A-18. AIAA 93-0414, January 1993

[5] V. S. S. Chan, D. I. Robinson, J. T. Turner, A. L. Heyes - A simplified Doppler Global Velocimeter. FED-Vol.229, Laser Anemometry. ASME 1995

[6] S. J. Thorpe, R. W. Ainsworth, R. J. Manners - The development of a Doppler Global Velocimeter and its application to a free jet flow. FED-Vol.229, Laser Anemometry. ASME 1995

[7] Gerstenkorn, P.Luc - Atlas du spectre de la molécule d'iode de 14800 à 20000 cm-1. Editions du CNRS5, Edition Masson et cie.

[8] F.Lemoine - Thèse de Doctorat de l'Université de Paris VI , 1993 . Application de la fluorescence induite de l'iode par laser à la mesure de pression. Extension aux principes de la mesure de vitesse.

[9] F. Lemoine, X. Lefebvre, B. Leporcq - Pressure and velocity measurements in a compressible flows using iodine fluorescence induced by a single mode laser. ASME95

COMBINED TECHNIQUES OF HOLOGRAPHIC INTERFEROMETER AND PARTICLE TRACK LASER SHEET TO STUDY FLAME SPREAD OVER LIQUIDS

Ghassan Tashtoush, Akira Narumi, Akihiko Ito, Kozo Saito, and Clifford Cremers

Department of Mechanical Engineering, University of Kentucky
Lexington, KY 40506

ABSTRACT

Detailed temperature measurement of the condensed phase is important for the study of flame spread over liquid fuels. The measurement requires high spatial resolution near the interface between the liquid and gas, where a steep temperature gradient is formed that controls the heat-transfer interaction between the two phases. Conventional thermocouple techniques have limitations on the accuracy of measurement in this sensitive location because the presence of the thermocouple bead significantly distorts the surface motion that is due to the thermocapillary effect, this disturbance in the region alters the original temperature structure near the interface. To avoid such interference, we developed a holographic interferometer (HI) technique that is non-intrusive and is capable of detecting nearly simultaneously a sudden and minute temperature change occurring over a distributed area. The thermo-optical coefficients of liquids are two orders of magnitude higher than those of gases. Therefore, if an interferogram is obtained simultaneously for the interface region between a gas and a liquid, the gas-phase hologram would be two orders of magnitude less sensitive than the liquid-phase hologram. We avoided this by employing a dual wave-length hologram To enhance the sensitivity in the gas phase.

In addition to these HI measurements, we developed a laser-sheet particle-track flow visualization system (LSPT) combined with a high resolution video camera. We applied it to the measurement of transient velocity profiles in the liquids by seeding the liquids with small particles to visualize their convection patterns. All these measurements were conducted simultaneously in order to obtain detailed velocity and temperature profiles in the liquid and to accurately determine the location of the flame leading edge. Using these simultaneous measurements, we are able to study the mechanism of pulsating flame spread over liquid fuels, a phenomenon that is currently not well understood.

Major findings from this study include: (1) The HI technique was proven to be a very effective tool for nearly simultaneously obtaining a detailed and temporal temperature map over a distributed area about the fuel-gas interface for studying both flame spread and pool-fire phenomena. (2) The liquid motion ahead and underneath the flame was visualized by the LSPT technique and temperature profiles in that area were measured by HI with a visible flame location.

These results support our earlier interpretation that the principal mechanism of the pulsating flame spread is by liquid convection, driven by both surface tension and buoyancy. We also found another flow circulation beneath the sub-surface convection. It flows close to the surface of the liquid fuel, going from upstream to downstream. The return path has not yet been determined. The existence of this flow can explain previously observed experimental results shows that spread-rate changes with decreasing depth of the fuel layer.

1. INTRODUCTION

The study of flame ignition and spread across liquid-fuel pools is a problem of interest both for purely scientific reasons and for its relevance to many practical fire safety situations according to Ross (1994). Experimental studies were performed to understand the mechanism of flame spread over alcohol and the factors influencing this mechanism and the flame speed. Four distinct regimes of flame spread were observed over a rang of temperature about the flash point. These are:

(a) Pseudo-uniform, sub-flash, $T_{liquid} << T_{flash}$.
(b) Pulsating, sub-flash , $T_{liquid} < T_{flash}$.

(c) Uniform, near-flash, $T_{liquid} < T_{flash}$.
(d) Uniform, super flash, $T_{liquid} > T_{flash}$.

The pioneering studies of the flame spread over liquids were published by Kinbara (1930 through 1942) in Japan, He identified the dependence of flame spread on the initial fuel temperature .

During the period 1955-1980 extensive experimental studies were conducted in England, USA, and Japan to determine the controlling mechanism of flame spread.

The study of flame spread over liquids and liquid-pool fires requires detailed temperature measurement with precise resolution near the interface between liquid and gas. These measurements were commonly conducted in the past by the use of thermocouples for repetitive tests, e.g. Glassman and Dryer (1980). Because of the invasive nature of this kind of measurement, optical techniques are presently taking its place. Hirano et al. (1980) measured the induced air velocity above a methanol surface using high speed schlieren photography and their unique hot gas trace device, and varying the initial liquid temperature between -5 and 30 °C. Miller and Ross (1994) at NASA used rainbow schlieren deflectometry (RSD) which had not been applied previously to flame spread over liquid fuel pools. RSD basically depends on the gradient of refractive index. Ito et al. (1989-1994) applied HI for the measurement of the temperature distribution in the liquid phase during flame spread over liquid fuel. In this technique both the objective beam and the comparison beam travel across the same objective space. Therefore, high optical quality of the setup is not required. HI analysis is based on refractive index change in the sample caused by temperature variation.

Research in the period 1955-1980 showed that there was a liquid-phase convection prior to ignition and during flame spread at pool temperatures below the flash point. Ito et al. (1991) conducted an experimental study to gain understanding of the uniform regime near the flash point temperature. If heat were transferred to the liquid ahead of the flame leading edge from either the gas phase or liquid phase, a temperature gradient would have to exist in the liquid phase which would generate subsurface liquid convection. This liquid-phase convection is driven by thermocapillary (surface tension) and buoyancy forces and to a much lesser degree by thermal expansion. Buoyancy effects might be small. However, both buoyancy and thermocapillary forces are inherently coupled. Ross (1994).

We conducted this study by using an HI technique connected to photographic or video recording systems that can instantaneously detect sudden and minute temperature changes occurring in a distributed area. The conventional thermocouple point by point measurement technique is incapable of satisfying these requirements because of the effect of the wire disturbance on the flow and the limited spatial resolution of the thermocouple.

2. HOLOGRAPHIC INTERFEROMETRY (HI) EXPERIMENT

Temperature in flames is often measured by a thermocouple, but insertion of the thermocouple alters the conditions of the experiment and the spatial resolution of transient temperature measurements is generally limited by the actual number of thermocouples that can be installed. Conversely, optical methods have a unique advantage: they do not disturb the temperature field, and because there is no inertial error in this method, rapidly changing processes can be accurately recorded.

The most common optical methods used in the past were Mach-Zender and Michelson interferometry as well as various Schlieren and shadowgraph methods. In 1949 Gabor invented a new optical recording technique, called holography that allows the recording and reconstruction not only of the amplitude but also of the phase distribution of wave fronts.

In HI both the object and comparison waves travel across the same objective space. Therefore, high optical quality of the setup is not required. The requirement for this technique is only transparency of the medium and availability of data on the thermooptic coefficient of the material with temperature.

There are few studies that report the application of HI to measure temperature distributions in the liquid phase. Walter and Mayinger (1974) and Chen and Mayinger (1984) measured the temperature distribution around a single bubble in water. Olsuji (1981) used the method to visualize forced convection boiling. Kashiwagi et al. (1985) measured the concentration distribution in an aqueous solution. Ito et al. (1989 and 1991) started to apply the HI technique for measuring the transient temperature distribution of liquid fuel under spreading flame conditions. Ito et al. (1993) also reported a series of HI measurements in order to improve understanding of the mechanism of pulsating flame spread over n-propanol.

Fig. 1 shows an optical setup for the holographic interferometry used in this study The tray is 30 cm long, 2 cm deep, and has three different widths (0.5,1, 2 cm). The two long sides of the tray were made of Pyrex of 0.15 cm thickness. Since 1-Propanol was used by NASA's microgravity experiment and by Ito (1989 and 1991), this will provide a good data - base for comparison. A 20 mw He-Ne laser (632.8 nm) was used as light source and real time HI was used to obtain the temperature profile in the liquid phase.

The reference condition interferogram for each exposure was photographed with 1/125 s exposure time, while the interferogram for the spreading flame was recorded with a video camera or a regular still photo camera. The temperature of the liquid phase was measured by a copper-constantan thermocouple and the spatial resolution for the interferogram was determined to be 30 μm.

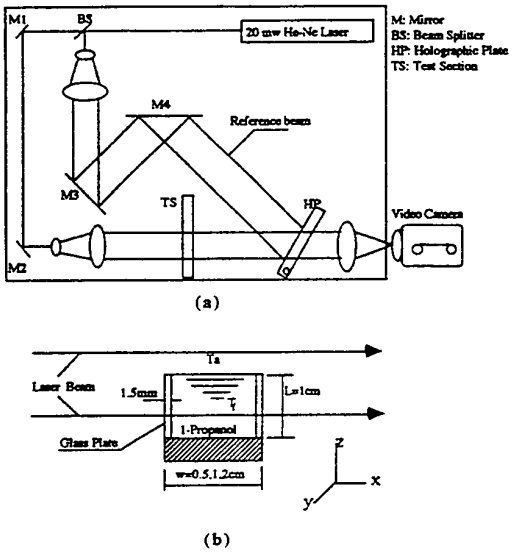

Fig. 1(a) Schematic diagram of the optical setup and (b), test section.

3. FRINGE INTERPRETATION

Fringe analysis is dependent on the availability of the thermooptic coefficient for the liquid. For alcohol fuel the magnitude of the thermooptic coefficient is 4-6 times that of water. Table 1 shows results reported by Hauf and Grigull, and Ito et al. for the thermooptic coefficients at a wave length of 632.8 nm at 25 °C and temperature range 2-80 °C respectively.

Table 1 Thermooptic coefficient (- dn/dT $^{o}C^{-1}$) of water and liquid fuel at wave length 632.8 nm.

Liquid fuel	Hauf & Grigull 1870, 25°C	A. Ito et al. 1991 (2-80) °C
Water	0.985×10^{-4}	$(3.6+0.256T)\times10^{-5}$
Methanol	4.0×10^{-4}	$(3.7+0.0105T)\times10^{-4}$
Ethanol	4.0×10^{-4}	$(3.8+0.0106T)\times10^{-4}$
Iso propanol	4.15×10^{-4}	----------
n-Propanol	----------	$(3.8+0.0137T)\times10^{-4}$

Assuming that the liquid is initially at a uniform temperature, and the variation of temperature along the y direction (laser direction) is negligible so the change of refractive index is only in the z direction, the relation between temperature and fringe number can be given by

$$\Delta\phi = \int_0^L \left\{ \int_{To}^{T} \frac{dn_l}{dT} + \int_{To}^{T} \frac{dn_g}{dT} dT \right\} dz \quad \ldots\ldots\ldots (1)$$

Where $\Delta\phi$ is the optical path length and equal to $N\lambda$, λ is the wave length of the laser (632.8 for He-Ne), n is the refractive index of the medium, N=1,2,3,4,5.....etc. for bright fringes, and N=0.5,1.5,2.5,3.5....etc. for dark fringes.

The first integral dn_g/dT in equation 1, is the change of the optical path length due to the different refractive index of glass plate. This has a magnitude of less than 2%, if the thickness of the glass plate is one order of magnitude smaller than the width of the tray. The second integral dn_l/dT is the change of the optical path length due to the different refractive index of the liquid fuel.

The integration $\int_0^L dz = L$ is the length in z direction. Then equation 1 can be written as

$$N\lambda = \int_{To}^{T} \frac{dn_l}{dT} dT \quad \ldots\ldots\ldots\ldots\ldots\ldots (2)$$

By entering the order of the fringe, N, from the photograph into equation 2 and knowing dn_l/dT for the liquid used in the experiment from Table 1, the temperature distribution (isothermal lines) can be calculated as shown in fig. 2 and 3.

4. PARTICLE TRACK LASER SHEET

We developed a laser-sheet particle-track flow-visualization by using a 25 mw He-Ne laser source with wave length of 632.8 nm. The laser sheet with a 1 mm thickness and 10 cm length was formed by using two cylindrical lenses. The sheet passed through the surface of the liquid at the centerline. The results were recorded simultaneously with the HI technique by using a video camera aimed perpendicularly at the light sheet to receive the deflected light from the HI plate and the scattered light from the particles at the same time.

Aluminum particles, 20-70 μm in diameter were mixed with the propanol in a 50 mg per 250 ml mixing ratio. This was good enough to scatter the light and allow the visualization of the liquid movement in the tray.

To analyze the data qualitatively, a regular video camera and a multi frame (4 frame/sec) photo camera were used to record the particle motion in the liquid.

5. RESULTS AND DISCUSSION

Simultaneous measurement of temperature of both phases and the velocity of the liquid was used to investigate and better understand the flame-spread phenomenon. It was thought previously, based on the temperature measurement only, that there are two vortices in the liquid phase ahead of the flame. Whereas by combining the temperature and the velocity measurements, it was found that the isothermal line cannot be used as a stream line in the liquid phase. So we introduced a technique that combined both temperature HI and particle tracking flow-visualization PTV techniques. This made it possible to observe both the temperature and velocity maps simultaneously over a region about the fuel-gas interface.

Fig. 2 and 3 Show both the simultaneous liquid movement and temperature distribution in the liquid phase under a flame front. The liquid temperatures were 14.5 °C (Pulsating) and 19.3 °C (Uniform) respectively.

Fig. 4 shows the flame spread mechanism in the pulsating region where the flame first decelerates to heat the fluid ahead of the flame and vaporize it fig. 4(a). Because of the coupling effect of the surface tension and buoyancy forces, the hot liquid starts to move far away from the flame front and then go deep into the cool liquid via the vortex motion as can be seen clearly in fig. 4(b, and c). At the end, the fuel-air mixture over the liquid reaches the flammability limit. The flame then accelerates as a premixed flame and consumes all the ready mixture over the liquid surface. Then the flame has to stop or decelerate again to start another cycle.

As can be seen from these results the combined HI and PTV technique was proven to be a very effective tool in obtaining more detailed temperature and velocity maps in the liquid phase ahead of the flame. Both the transient liquid temperature and movement profiles can be accurately detected and compared to the point by point thermocouple measurement, which has a limitation due to its spatial resolution.

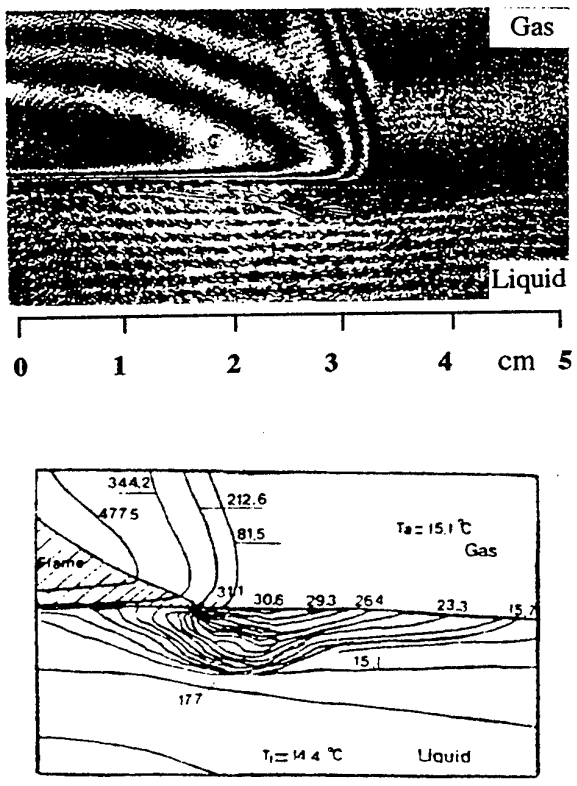

Fig. 2 Hologram and particle velocity for flame spread over liquid propanol at a temperature of 14.4 °C (Pulsating).

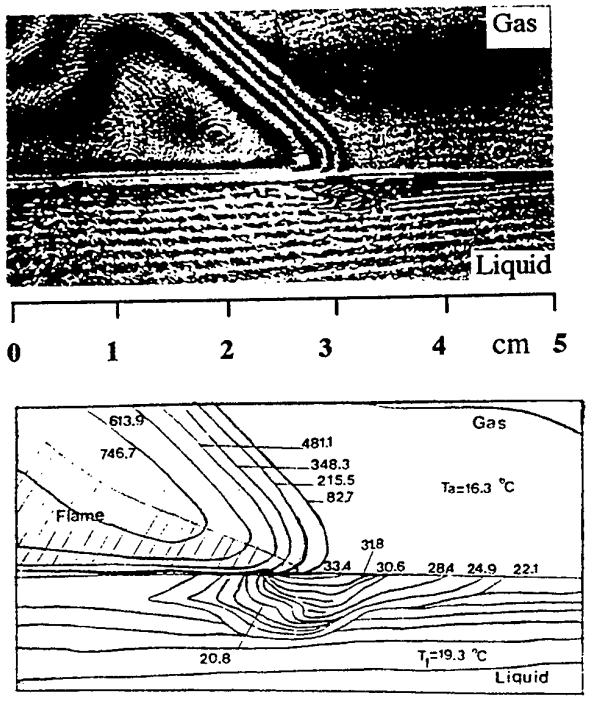

Fig. 3 Hologram and particle velocity for flame spread over liquid prpanol at a temperature of 19.3 °C (Uniform).

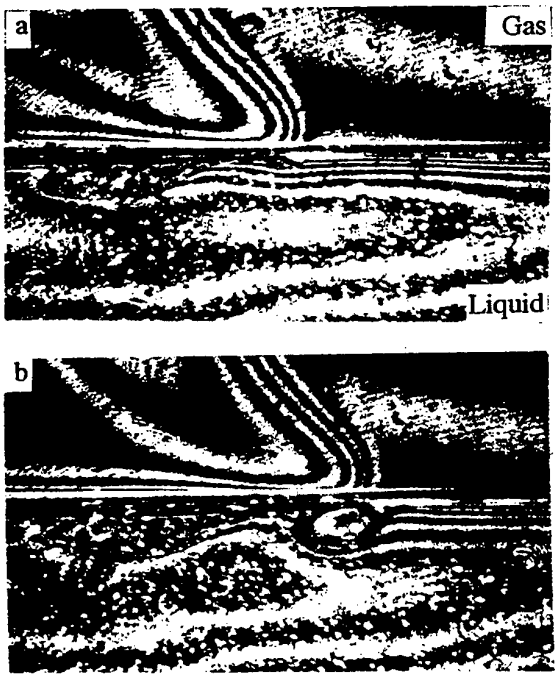

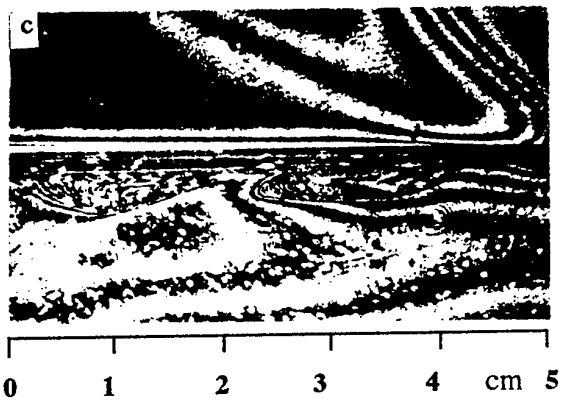

Fig. 4 Hologram for flame spread over liquid at a temperature of 14.4 °C (Pulsating).

Fig 5 shows the mechanism of the flame spread in the uniform region at a liquid temperature 19. 3 °C. The flame heats the liquid ahead of it. Then the hot liquid starts to move because of both the buoyancy and surface tension effects and then circulates in a vortex motion to keep providing enough fuel vapor to the flame to keep it spreading uniformly.

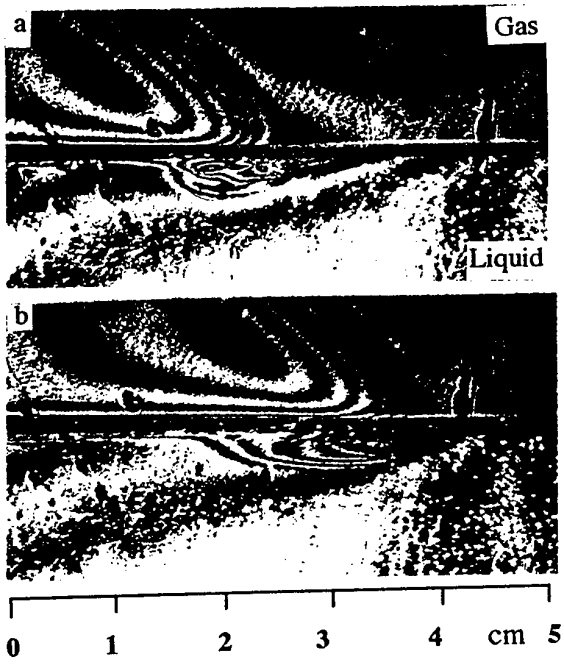

Fig. 5 Hologram for flame spread over liquid at temperature 19.3 °C (Uniform).

ACKNOWLEDGMENTS

We wish to acknowledge H. Ross and F. Miller of NASA Lewis Research Center for valuable technical discussions on flame spread and particle tracking system. This study was in part supported by the Kentucky NASA EPSCoR Program (NCCW-60), and in part by the Center of Manufacturing System of the University of Kentucky.

REFERENCES

1- Glassman, I. & Dryer, F.L. 1980/81, Flame Spreading Across Liquid Fuels, Fire Safety Journal, vol. 3, pp. 123-138.

2- Ito, A. et a. 1995, Temperature Measurement in Liquids by Holographic Interferometry, 8th International Symposium on Transport Phenomena in Combustion. San Francisco, CA.

3- Ito, A. et a. 1991, A Technique for Measuring an Unsteady Temperature Distribution in a Liquid using Holographic Interferometry, JSME International Journal. Series II, Vol. 34, No. 2.

4- Ito, A. et a.. 1994, Pulsating Flame Spread over Liquid, Fire Safety Science-Proceeding of the Fourth International Symposium, pp. 445-456

5- Ito, A. et a. 1991, A Study of Flame Spread Over Alcohol Using Holographic Interferometry, Combustion and Flame. Vol. 83, pp. 375-389.

6- Mayinger, F. 1993, Advanced Optical Method in Transient Heat Transfer and Two-Phase Flow, 6th Int. Symposium on Transport Phenomena in Thermal Engineering, Seoul, Korea..

7- Miller, F. & Ross. H. 1994, Temperature Field During Flame Spread over Alcohol Pools, Measurements and Modeling.

8- Murad, R.J. et a. 1970, A Study of Some Factors Influencing the Ignition of a Liquid Fuel Pool, Combustion and Flame, vol. 15, pp. 289-298.

9- Ross, H. 1994, Ignition of and Flame Spread over Laboratory-Scale Pool of Pure Liquid Fuels, Prog. Energy Combustion and Science, Vol. 20, pp. 17-63.

SESSION 12

Two-Phase Flows
Instrumentation IV

USAGE OF THE SPATIAL FILTER METHOD FOR MEASUREMENTS OF LOCAL PARTICLE VELOCITIES IN CIRCULATING FLUIDIZED BEDS

O. Fiedler[1], N. Labahn[2], J. Kumpart[3], and K. Christofori[4]

[1]Department of Electrical Engineering, University Rostock, Germany
[2,3]Department of Measurement Engineering, Technical University Hamburg-Harburg, Germany
[4]ASTECH GmbH, Rostock-Warnemünde, Germany

ABSTRACT

Spatial filters provide a method of measuring velocities optically. Application of this method for particle velocity measurement in two-phase systems with high solids loadings requires the use of a probe to reach different positions inside the flow. After a short comparison with other methods, a new realization of spatial filter velocimeters is presented. Our approach involves the use of a CCD line sensor (CCD – charge coupled device). The circuit design contains a new, all-electronical way for direction recognition. The principle of this method, a phase orthogonal differential grating, is explained. The design of the probe for measurements inside a circulating fluidized bed riser with a diameter of 0.4 m is discussed. Results of measurements are presented, which prove the usefulness of the spatial filter probe for the desired application.

1. INTRODUCTION

During recent years, the use of circulating fluidized bed technology has been steadily increasing. Such systems work as chemical reactors as well as combustion units in power plants, see Werther et al. (1993). Recently they have become interesting for the thermal treatment of waste and sewage sludges.

Despite its broad application, there is no generally accepted mathematical model for the description of all parts of a circulating fluidized bed (CFB). This means that there are many problems with the scale-up and start-up of industrial systems. To overcome these problems, many investigators have strived to develop better models for the description of the processes in a CFB, for instance Werther et al. (1992), Horio et al. (1988) or Leckner and Karlsson (1993).

For verification of such models, the knowledge of different parameters is necessary. In the turbulent and circulating fluidized bed, local parameters are especially important, see Werther et al. (1993). In addition to the local solid volume concentration, the local particle velocity distribution is required for the calculation of the mass flux at different locations inside the fluidized bed.

In recent years, various methods for measurements of local particle velocities have been published. Tracer methods are often used to provide an improved signal to the measuring system for a better understanding of the structure of the process, see Fiedler (1992). They give the possibility to measure the velocity in a direct way, but they may be disruptive. This may be acceptable for many basic investigations at pilot scale systems, but is often not suitable for use with industrial-scale reactors.

Optical systems do not exhibit this disadvantage. They measure the velocity of particles or particle clusters in a direct way and inject only light into the process. Optical systems can be divided into time-of-flight and spatial filter methods. The time-of-flight methods are mainly used with a cross-correlation for the determination of the time for the measured quantity to pass between two sensors. One kind of these methods is the laser two-focus method, see Albrecht et al. (1993). It is used for the measurement of very small particles and high velocities. Another kind has been succesfully employed by Werther et al. (1993). It works with a pair of optical fibres. A problem with the use of correlation methods in systems with fluctuating solid velocities is the correct determination of the length of the integration period of the short-time cross-correlation, because it has a substantial influence on the accuracy of the measurement. For higher degrees of turbulence in the flow, the two detectors have to be placed at a short distance. This is also

desirable because the measuring volume should be small for local measurements.

The second optical method is the spatial filter. Laser-Doppler anemometry is one application of this method that is well known. However, this technique is only suitable for low solid concentrations, such as in the upper freeboard of bubbling fluidized beds, see Berkelmann and Renz (1991). Another class of spatial filtering techniques works with incoherent (white) light and uses a reticle placed in front of a photodetector or a grating-like structured detector. This is the most modern technique of active spatial filters. Such systems have the following advantages: the optical device is very simple, the system needs no adjustment, and it is robust against variations of the basic light level.

2. SPATIAL FILTER METHOD

2.1 Principle

The basis of all spatial filter methods is the evaluation of spatial light distributions by grating-like structures. The basic principle can be seen in Fig. 1. An illuminated or luminous moving object (1) is projected onto a grating (3) by a focusing lens (2). All light passing through the grating is collected on a photo detector (5) by a collecting lens (4). If the object moves, the output of the photo detector will change with the rhythm in which the image of the object falls onto the opaque and transparent lines of the grating. If the object moves faster, the change will be faster, and the frequency of the output signal will be higher. The equation for the evaluation of the velocity v of the moving object from the frequency f in the output signal $s(t)$ is:

$$v = \frac{f \cdot g}{\beta} \qquad (1)$$

g – grating constant, distance between two equal lines of the grating
β – image scale

One problem is the correct determination of the corresponding frequency f in the output signal. As can be seen in Fig. 1 (b), the signal contains a dc component, often called the pedestal component. Because the method measures not only an object which behaves as one bright point in front of a dark background as is shown as an example in Fig. 1 (a) but also on rough surfaces with stochastic brightness distributions, the dc component may be up to 100 times higher than the ac component containing the frequency of interest f, see Christofori (1990). Because it is desirable to establish a wide measuring range, it may be necessary to measure very low frequencies generated by slowly moving objects. However, it is rather difficult to separate the dc and ac components by use of a high-pass filter in this case.

A very useful method for solving this problem is the use of a differential grating. That means, the light is not only blocked by opaque lines of the grating, but is also guided to a second photo receiver. The signals of both receivers are electrically subtracted by an operational amplifier. Because the dc components of both parts of the grating are equal, they complement each other to zero. The output contains only the ac component.

To realize such a differential grating, several arrangements have been investigated in the past. One possibility is the use of a beam splitter with two normal transmission gratings and two photo receivers behind it, see Aizu and Asakura (1987). A disadvantage of this approach is the relatively complicated optical system which needs a lot of adjustment. The same is valid for a system using a lenticular grating, see Ushizaka et al. (1986), or a prism grating, see Aizu and Asakura (1987).

Another way is possible by use of optical fibres, see Hayashi and Kitagawa (1982). The ends of optical fibres are arranged in one line. The other ends are separated into two groups and bundled onto two photo receivers. If light falls onto the ends of the fibres, the arrangement realizes the same function like a differential grating. Because the fibres accept light from a wide angle, it is often possible to omit the focusing lens. If the object moves very near in front of the ends of the fibres the effect of the spatial filter comes into operation and a measurement is possible. In this case the measuring arrangement is very simple and it is easy to design a probe for measurements in two-phase flows, see Morikawa et al. (1986).

Another possibility is the use of a structured receiver, see Ogiwara and Ukita (1975). The principle is shown in Fig. 2. A number of photo receivers are arranged in one line with equal distances. This arrangement combines the function of the grating with that of the receiver. But an additional task on the electrical side is the summation over the receiver areas for both groups. The advantage of this method is the simplification of the optical system in comparison with the transmission grating system. The photo receiver may be solar cells or photo diodes. In the case of solar cells, the summation can

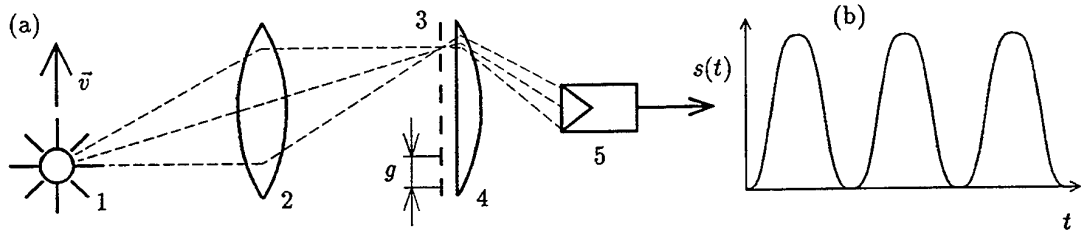

1 – illuminated or luminous object, moving with velocity $\vec{v}$
2 – focusing lens
3 – grating with constant g (distance between two equal lines)
4 – collecting lens
5 – photo receiver

Figure 1: Spatial filter method, (a) Basic principle, (b) Output signal $s(t)$

be carried out by simply switching all cells of one group together directly on the chip.

Another differential grating design involves the use of a CCD line sensor. The advantage over the above mentioned solar cell array is that such CCD-chips are commercially available, because they are widely used in fax devices and scanners. Several well known possibilities exist to carry out the summation. Either integration amplifiers are used or the digitized output of the CCD is processed by the computer, see Yamasaki et al. (1988).

The new approach is to use a special clock regime for the CCD-chip. This possibility was introduced by Schulz and Fiedler (1985) and is used for measurements of particle velocities for the first time in the present work. The special clock regime involves that the summation is carried out in the sliding register of the CCD itself. This means less expense for the signal processing and allows the measurement of higher velocities.

An additional advantage of the use of a CCD line sensor is the high accuracy of the grating constant g. As may be seen from equation 1, the grating constant has direct influence on the determination of the velocity v. Any error in the determination of the grating constant is also found in the velocity. While CCD sensors are built with microelectronic processes, the production of the fibre optic spatial filters, for example, has to be done manually. It is rather impossible to ensure the same accuracy in the latter case.

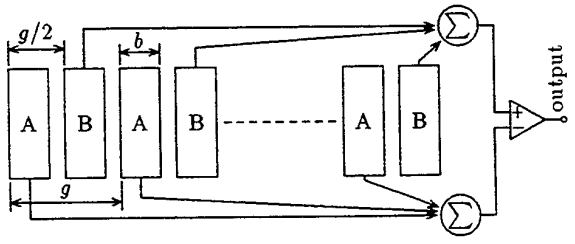

Figure 2: Spatial filter using a structured receiver

Irrespective of which system acts as the spatial filter, one common task is to determine the correct frequency from the output signal. Mainly two methods have been used: fourier analysis and period measurement. Especially in case of measuring in turbulently flowing media, the period measurement has the advantage that it can separate objects with different velocities by using a plausibility check.

2.2 Direction Recognition

The demand of a simultaneous detection of velocity and direction arised because in nearly all parts of circulating fluidized beds there are changes of the basic direction of particle motion. While measuring velocity and length of moving solid or liquid surfaces with the spatial filter camera, the detection of direction is of minor importance because the basic direction is usually known. In contrast the direction recognition is indispensable in order to determine particle velocity distributions as a profile over the cross-section of a circulating fluidized bed. In nearly all areas of CFB risers particles are moving up and down with rapid changes in sign and magnitude of velocity. Thus the determinations of particle velocity and direction must be performed simultaneously.

Common suggestions to the recognition of direction are based on carrier modulation methods. The modulation of the filter output signal is achieved by moving the grating. When this signal is compared to the carrier frequency a statement about the directon can be made. This has been realized by e.g. a rotating prism grating, see Arzt and Ringelhan (1978). Another possibility would be an oscillating structured receiver stimulated by piezo-

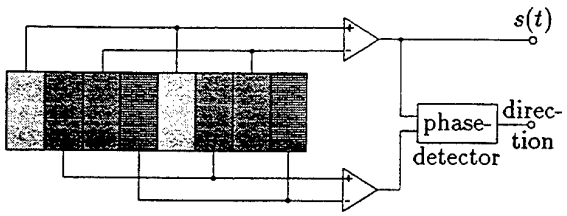

Figure 3: Structure of phase orthogonal differential gratings

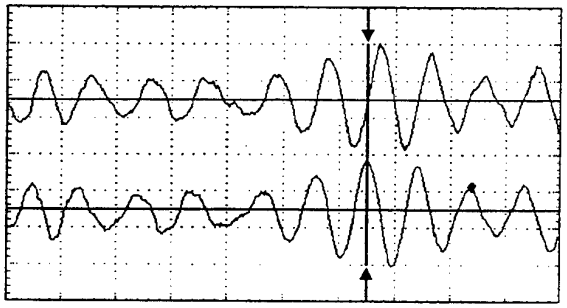

Figure 4: Measured output signals of both differential gratings

electric effects. Both cases require high mechanical efforts to achieve exact synchronism, as instability would influence the measurement result.

A new all-electronical way of detecting the sense of direction by CCD spatial filters could avoid these problems. A method using phase shift evaluation between the elements of the grating is explained as follows:

Differential gratings, which can be considered as two single gratings 180° out of phase, do not allow to detect the sense of direction. When the elements of the grating are split up into three groups as it is known from electrical three-phase systems a phase displacement of ±120° allows to detect the sense of direction whereas common mode rejection is impossible.

A new structure is the arrangement of two differential gratings that are grouped in quadrature, see Richter et al. (1994). The phase displacement of the output signals of both gratings is ±90° depending on the moving sense of the particles. Figure 3 shows the structure of this arrangement. Even and odd pixels are combined separately to two differential gratings. The direction information is obtained in a phase detector whereas the velocity can be obtained from one of the differential gratings.

In Fig. 4 the phase displacement of 90° between the two differential grating outputs can be seen clearly.

2.3 Circuit Design

Figure 5 shows the block circuit diagram of the realized spatial filter sensor VLM 200. It consists of two parts. First there is a module carrying the CCD line sensor and its direct control devices. This module is directly combined with the focusing lens and the tube probe described later on. The second part, called sensor electronic device, is operated separately. It contains the clock generator (5) for delivering different clock regimes to the CCD line sensor (3), suitable drivers (4), a differential amplifier (6) for compensation of the clock signal CS in the output signal OS, sample & hold devices (7) for recording the signals of the four channels of the two differential gratings, operational amplifiers (8) for producing the differential signals, low-pass filters (9) to form the output signals, a period measurement device determining the frequency of interest f in the spatial filter output signal by zero crossing principle with plausibility check and a phase detector which delivers the direction information. A controller supervises all parts of the spatial filter sensor and establishes the connection to a PC via serial link. It also computes the velocity value from the measured frequency f and combines it with the direction information from the phase detector.

In on-line mode the controller may preprocess the velocity data, for instance compute the gliding mean value, and transmits it to the PC for further use, for instance control purposes. In off-line mode the controller stores all velocity values during a certain time together with the direction information and the number of periods in the spatial filter output signal which led to the respective velocity value. Afterwards these data can be transfered to the PC where storage and further data processing like statistical analysis, graphical output etc. can be carried out.

3. PROBE DESIGN

The spatial filter sensor itself is suitable for velocity measurements on solid surfaces. For measurements of local particle velocities in two phase flows a special probe is necessary. The design of this probe is influenced by the conditions given by the used experimental setup. For tests of our spatial filter measuring system this was the pilot scale circulating fluidized bed cold model unit ZWS 400 at

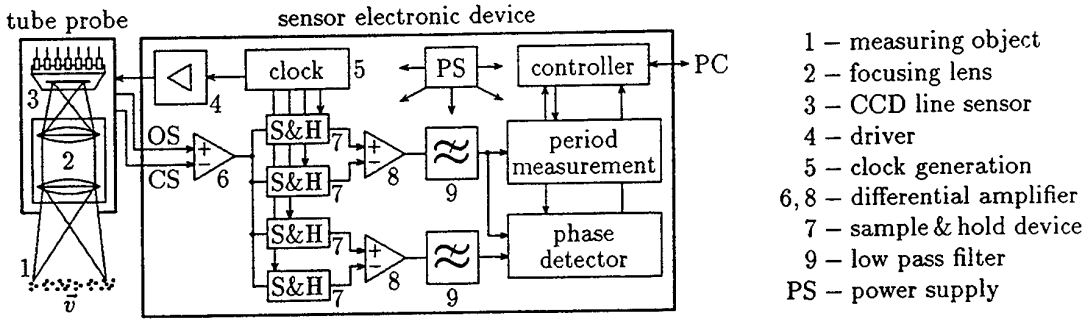

Figure 5: Block circuit diagram of the spatial filter sensor VLM 200

the Technical University Hamburg-Harburg. The design of this unit is shown in figure 6. It has a riser inner diameter of 400 mm and a total height of 15.6 m. This equipment is used for investigations of the fluid dynamics and is operated at ambient temperature. The solids is quartz sand and air is used as fluidizing medium. The riser is equiped with a lot of measuring holes in various heights.

Summarized, the probe for measurements of local particle velocities in circulating fluidized beds

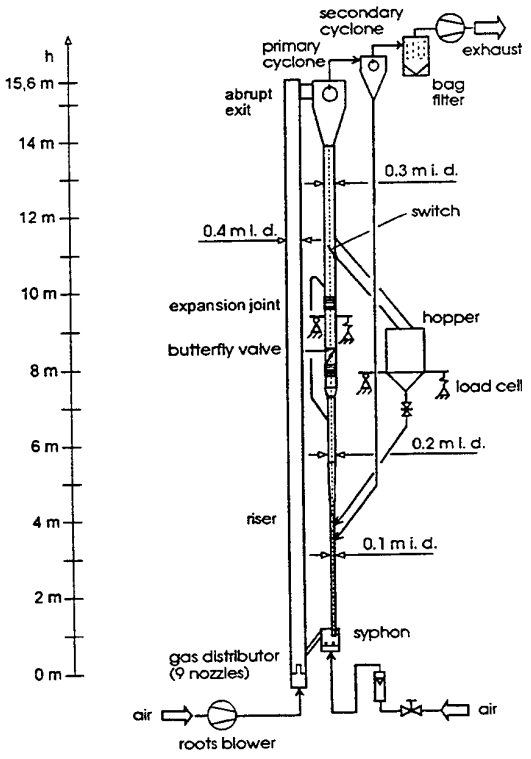

Figure 6: Pilot scale circulating fluidized bed cold model unit ZWS 400

by use of the CCD spatial filter sensor had to solve the following problems:

- Put the measuring volume into various radial positions of the CFB, that means to guide light to the measuring volume and to give the possibility to observe the measuring volume by the CCD spatial filter sensor.
- As low as possible disturbance of the flow to be measured.
- Stability against vibrations of the CFB unit.
- Protection against pollution or erosion of the optical window by the solid in the CFB.
- Registration of particles with the given size distribution.

Figure 7 and 8 show the construction principle of this probe. On the left hand side of Fig. 7 the module of the CCD spatial filter sensor with the CCD line sensor and the focusing lens can be seen.

The probe itself consists of a tube made from high grade steel, a special prism made from silica at the tip and a shank, which secures the connection to the focusing lens and takes up the connecting piece for the light guide cables. The tube has an outer diameter of 8 mm. This dimension has been chosen based on the diameter of the available measuring holes at the pilot scale CFB unit ZWS 400. This is a good compromise between the disturbance to the flow and the relation between the effective grating constant and the number of grating lines which take place in signal generation. The tube consists of several parts. The outer sections contain optical fibres which guide light to the tip of the probe. In the front is placed a special prism, which deflects the light into the measuring volume, see Fig. 8. The inner part of the prism acts as an optical window. Light scattered by particles in the measuring volume passes the inner section of the tube and reaches the focusing lens and the CCD line sensor.

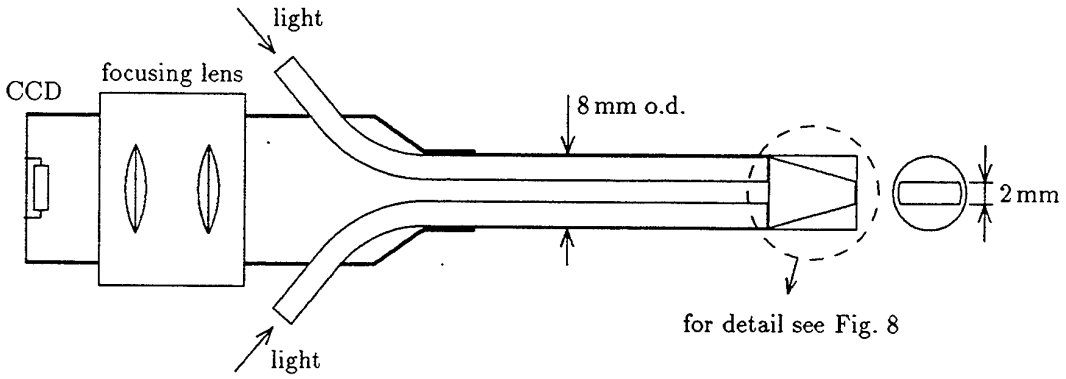

Figure 7: Probe for the CCD spatial filter sensor: Principle of construction

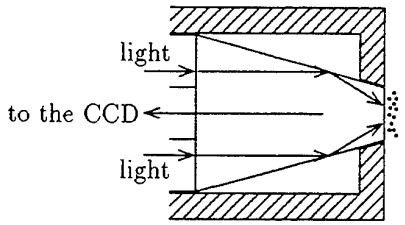

Figure 8: Probe for the CCD spatial filter sensor: Probe tip in detail with light path inside

4. MEASURING RESULTS

Tests of the developed measuring system consisting of the spatial filter sensor VLM 200 and the tube probe have been carried out to prove the usefulness for the desired purpose, the measurement of local particle velocity distributions in circulating fluidized beds. These measurements took place at the above mentioned pilot scale CFB unit ZWS 400. The fluidized solids were quartz sand with a particle size distribution between 20 and 500 μm. The mean diameter of the particles was 181 μm. The fluidized bed was working with a superficial gas velocity $u = 4$ m/s and a solids circulation rate $G_S = 15$ kg/(m^{2}s). The spatial filter probe was put into the riser through a measuring hole in a height of 6.43 m above the gas distributor.

Figure 9 shows distributions of particle velocities at various radial positions. Position $r = 0$ mm means, the tip of the probe and consequently the measuring volume has been at the middle axis, $r = 185$ mm at a distance of 15 mm from the wall and $r = 195$ mm 5 mm from the wall. The axis on the left hand side shows the scale of the number density $q_0(v)$ in m^{-1}s and the axis on the right hand side the scale of the normalized cumulative

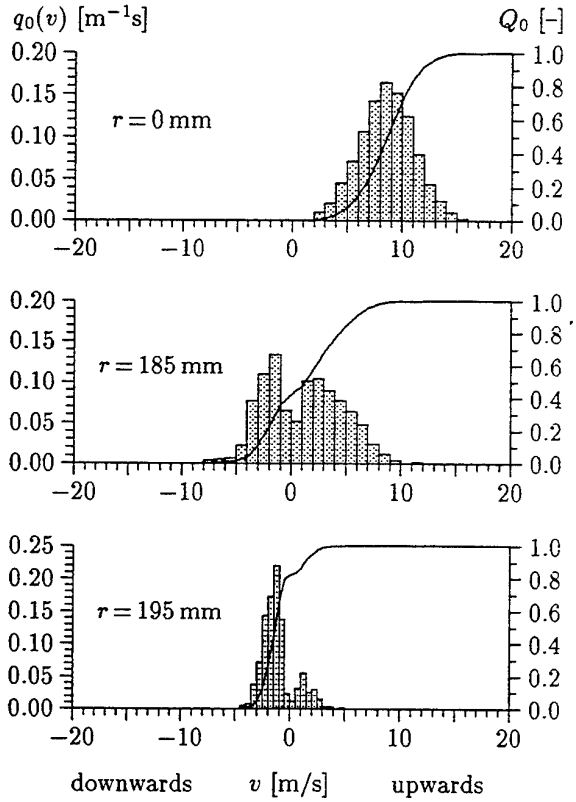

Figure 9: Distributions of particle velocities at various radial positions in the riser of the ZWS 400 at the height 6.43 m, $u = 4$ m/s, $G_S = 15$ kg/(m^{2}s), solid: quartz sand

number density Q_0. It can be seen, that at the middle axis all particles move upwards, but the velocity distribution is very broad and symmetrically with a mean value near the double of the superficial gas velocity. In the transition zone nearly the same

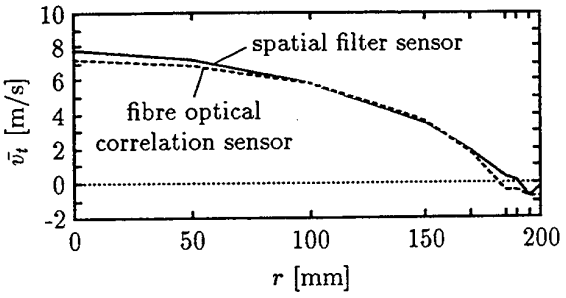

Figure 10: Profile of temporal mean of local particle velocities in the ZWS 400 at the height 6.43 m, $u = 4\,\mathrm{m/s}$, $G_S = 15\,\mathrm{kg/(m^2 s)}$, solid: quartz sand; comparison between the results of the spatial filter sensor and the fibre optical correlation sensor according to Hartge et al. (1989)

number of particles move upwards and downwards and the distribution is broad and unsymmetrically. The mean value is near zero. Near the wall most of the particles move downwards and the distribution is narrow.

The shown distributions base on a number of single velocity values that differs between 509 and 4490. These values have been measured in 2 min in each case. That means, the developed measuring system is able to provide statistically reliable information about the flow in circulating fluidized beds in a short time.

A comparison between the profiles of temporal mean of local particle velocities, which has been measured with the spatial filter sensor and the fibre optical correlation sensor according to Hartge et al. (1989) can be seen in Fig. 10. The radial measuring points are marked at the abszissa. The comparison shows a very good conformity of the profiles. The remaining differences are explained by the basic differences of both measuring systems. While the fibre optical correlation sensor is primarily measuring the velocity of particle clusters and seldom of single particles, it is at the spatial filter vice versa.

As it was mentioned above the profile in Fig. 10 shows the temporal mean of particle velocities. These values result from the single velocity values by weighting them at the computation of mean value to compensate the different probabilities for the appearance of a special value. This biasing correction is necessary at all measuring systems, which get its data according to events and not in a fixed time raster, for instance also at LDA measurements, see Fiedler (1992). Without this correction the ensemble mean is calculated, which is higher than the temporal mean, because higher velocities may be measured more often than lower ones in the same time. Because the fibre optical correlation sensor determines the temporal mean directly and this value is necessary for the determination of flow parameters, the correction has to be done for the values from the spatial filter sensor.

An additional parameter for the valence of a single measuring data is at measurements with spatial filters and evaluation with a period measurement device the number of periods p_i in the spatial filter output signal, which have led to a measuring value. This value has been determined by the period measurement device during measurement and is part of the output. The more periods in one burst fulfil the period condition, the more reliable is the velocitiy value and the longer the measuring object took part in the generation of the output signal. Consequently the correction value is:

$$c_i = \frac{p_i}{|v_i|} \tag{2}$$

Accordingly the temporal mean is determined by

$$\bar{v}_t = \frac{\sum_{i=1}^{N} c_i v_i}{\sum_{i=1}^{N} c_i} = \frac{\sum_{i=1}^{N} \frac{p_i}{|v_i|} v_i}{\sum_{i=1}^{N} \frac{p_i}{|v_i|}} \tag{3}$$

5. CONCLUSIONS

The applicability of a spatial filter sensor for the measurement of local particle velocity distributions in circulating fluidized beds has been investigated. The CCD-based spatial filter sensor developed in the present work could prove its usefulness for the desired purpose, if a special designed tube probe was used. The circuit design of the sensor contains a new, all-electronical way for direction recognition, called phase orthogonal differential grating method. Results of tests of the CCD-based spatial filter probe have shown, that a high measuring rate can be achieved, i.e. meaningful velocity distributions may be collected in less time. The comparison with results obtained with another measuring system, the fibre optical correlation sensor, shows a good conformity.

The tube probe described in this paper, which connects the CCD-based spatial filter sensor with the CFB, can only be used at temperatures up to 70°C because of its design. Meanwhile a new probe

has been developed, which will allow measurements under high-temperature conditions, see Labahn and Kumpart (1995).

6. ACKNOWLEDGEMENT

This work was supported by the *Deutsche Forschungsgemeinschaft, DFG* within the *Sonderforschungsbereich 238*. This support is gratefully acknowledged.

REFERENCES

Aizu, Y. & Asakura, T. 1987, Principles and development of spatial filtering velocimetry, Appl. Phys. B: Photophys. and Laser Chem., vol. 43, no. 4, pp. 209-224.

Albrecht, H.-E., Borys, M. & Hübner, K. 1993, Generalized theory for the simultaneous measurement of particle size and velocity using laser doppler and laser two-focus methods, Part. & Part. Systems Char., vol. 10, no. 3, pp. 138-145.

Arzt, R. & Ringelhan, H. 1978, Optical sensors for non-contact and slip free length and velocity measurements at land vehicles (in German), Feinwerkt. & Meßt., vol. 86, no. 2, pp. 69-71.

Berkelmann, K.-G. & Renz, U. 1991, Gas and solid flow in the freeboard of a fluidized bed combuster, Pow. Tech., vol. 68, pp. 271-280.

Christofori, K. 1990, CCD sensor system for non-contact velocity measurements in the automation technique (in German), Ph.D. thesis, Department of Electrical Engineering, University Rostock, Germany.

Fiedler, O. 1992, Flow measurement techniques (in German), R. Oldenbourg Verlag, München Wien.

Hayashi, A. & Kitagawa, Y. 1982, Image velocity sensing using an optical fiber array, Appl. Opt., vol. 21, no. 8, pp. 1394-1399.

Horio, M., Morishita, K., Tachibana, O. & Murata, N. 1988, Solid distribution and movement in circulating fluidized beds, Proc. of Circ. Fluid. Bed Tech. II, pp. 147-154.

Hartge, E.-U., Rensner, D. & Werther, J. 1989, Fibre-optical measuring system for determining local solids concentrations and velocities in gas/solids flow of higher concentration (in German), Chem. Ing. Tech., vol. 61, no. 9, pp. 744-745.

Leckner, B. & Karlsson, M. 1993, Emissions from circulating fluidized bed combustion of mixtures of wood and coal, 12th Int. Conf. on Fluid. Bed Comb., ASME, vol. 1, pp. 109-115.

Labahn, N. & Kumpart, J. 1995, Measurement of local particle velocity distributions in multiphase flows by using spatial filters - a new area for CCD line image sensors (in German), 4. Conf.: Laser methods in flow measurement, German Association for Laser Anemometry GALA e.V., pp. 25.1-25.3.

Morikawa, Y., Tsuji, Y. & Tanaka, T. 1986, Measurements of horizontal air-solid two-phase flow using an optical fiber probe, Bulletin of JSME, vol. 29, no. 249, pp. 802-809.

Ogiwara, H. & Ukita, H. 1975, A speckle pattern velocimeter using a periodical differential detector, Jap. J. of Appl. Phys., vol. 14, pp. 307-310.

Richter, A., Labahn, N. & Christofori, K. 1994, Semiconductor spatial filter sensor for measurement of local particle velocities in two phase flows (in German), DGLR year book, German air and space travel congress, vol. I, no. 94-B2-033, pp. 273-280.

Schulz, K.-P. & Fiedler, O. 1985, Velocity measurement based upon spatial filter principle using CCD line camera (in German), Preprint of 1st Int. Cong. 'Autom. Image Proc.' (CAIP), Berlin, Germany.

Ushizaka, T., Aizu, Y. & Asakura, T. 1986, Measurements of velocity using a lenticular grating, Appl. Phys. B: Photophys. and Laser Chem., vol. 39, pp. 97-106.

Werther, J., Hartge, E.-U. & Kruse, M. 1992, Radial gas mixing in the upper dilute core of a circulating fluidized bed, Pow. Tech., vol. 70, pp. 293-301.

Werther, J., Hartge, E.-U. & Rensner, D. 1993, Measuring techniques for gas/solid fluidized bed reactors, Int. Chem. Eng., vol. 33, no. 1, pp. 18-27.

Yamasaki, H., Oka, K. & Yamaguchi, K. 1988, An adaptive intelligent velocity sensing system, J. of the Fac. of Eng., Univ. of Tokyo, vol. A-26, pp. 38-39.

FREQUENCY RESPONSE OF SOLID PARTICLES IN OSCILLATING FLOWS

G. Tedeschi[(1)] and R.K. Menon[(2)]

[(1)] I.S.I.T.V. - L.E.P.I., Av. G. Pompidou, B.P. 56, 83162 La Valette, France
[(2)] TSI Inc., PO Box 64394, S[t] Paul, MN 55164-0394, USA

ABSTRACT

The frequency response of solid spherical particles in a oscillating flow is determined. Drag laws taking into account rarefaction around particles and inertial effects are used. Results are compared to two previous studies. The influence of various flow and particles parameters is studied in the context of LDV measurements. As expected, large and heavy particles respond poorly to high flow fluctuation frequencies. It has been found that in very low density flows, the particle size has a lesser impact on particle behaviour. Another result found is that only high amplitudes of flow velocity fluctuations increase particle response. On the other hand, low amplitudes do not influence particle behaviour.

1. INTRODUCTION

In Laser Doppler Velocimetry (LDV) scattering particles are the source of the signal. In addition, the flow velocity is obtained by measuring the velocity of the particle. In a few measurement situations, particles naturally present in the flow are sufficient to provide good signal quality. But, in majority of the measurement situations seeding particles are added to the flow to get better signal quality and higher measurement rates. Hence, the selection of these seed particles is of great importance and need to be done systematically. Several criteria exist in order to select the proper seeding for a given configuration (Menon and Lai (1991)). One of the most crucial parameters is the particle size, but the selection of the size is influenced by conflicting requirements. On the one hand, particles have to be large enough to obtain a sufficient scattered light intensity which will provide good signal quality and high data rate. On the other hand, particles have to be small enough to follow accurately the flow fluctuations.

In turbulent flows, the use of inappropriate particle sizes can lead to the cut-off of high frequency fluctuations and hence loss of information on the turbulent kinetic energy spectrum. The focus of this study is to provide a systematic approach to help experimentalists select suitable seed particles based on fluid dynamic considerations.

Various studies have been carried out on particle transport in turbulent flows, but not necessarily applied to the influence of particle behaviour on LDV measurements. Among recent works, Kulick *et al.* (1994) studied particle response in turbulent flow by LDV, and modification of flow turbulence generated by the presence of large particles (around 70 μm diameter). LDV was here only an instrument and not a subject of the study. Numerical simulations have been done to study particle dispersion in turbulent flows (for example MacInnes and Bracco (1992), Schaeffer *et al.* (1993) and Wang and Squires (1996)). Some of them still use the simple Stokes (1851) drag law. This last point will be discussed later in this paper.

A simple way to calculate the response of particles (considered spherical) to high flow frequencies is to use an oscillating one-dimensional flow. The ratio between maximal velocity fluctuations for particle and flow $\Delta u_p/\Delta u$ is used to estimate ability of the particle to respond to flow frequencies f.

A new expression to solve the problem of particle motion has been developed earlier by one of the authors (Tedeschi *et al.* (1993)). Cunningham's (1910) expression has been extended to high velocities and high rarefaction flows. This expression can cover the various flow regimes. Comparison of some of the results using this approach with two other works, (Maxwell and Seasholtz (1974) and Feller and Meyer (1975)) is provided. A detailed parametric study is conducted to examine the influence of various parameters on the response of particles.

2. THEORETICAL ANALYSIS

2.1 Simplified Flow Model

The aim of the present paper is to determine behaviour of particles present in a fluctuating flow and not to study directly the turbulent flow. The best approach would have been to make a direct numerical simulation of a turbulent flow, with a particle cloud inside. The flow

around each single particle would have to be calculated exactly to take into account all interaction effects between fluid and particles. Such calculation, interesting as it might be, does not allow a systematic investigation of the influence of various parameters. It would be particularly useful to understand the fundamental physics of flow-particle interaction. But this kind of calculation requires so much computer time that it is not possible for a LDV user to employ this as a useful tool. On the contrary, if numerous calculations must be done over a wide range of parameters, a simplified model has to be employed.

In this study, we focus particularly on the ability of particles to respond to high frequencies of turbulent flows. The simplest model for an oscillatory (one-dimensional) flow is :

$$u = \overline{u} + u' = \overline{u}\left\{1 + u_c \sin\left(\frac{2\pi f}{\overline{u}} x\right)\right\} \qquad (1)$$

where $\overline{u}$ is the mean fluid velocity, u' represents the oscillating part of velocity (by analogy with turbulent flows), x is the abscissa and u_c is a constant. Assuming Taylor's hypothesis (time t corresponds to abscissa x through the mean velocity), it is easy to calculate the mean of the oscillating velocity and the turbulence intensity I :

$$\overline{u'} = 0, \; I = \frac{\sqrt{\overline{u'^2}}}{\overline{u}} = \frac{u_c}{\sqrt{2}} \qquad (2)$$

In order to satisfy the mass-conservation equation, the fluid density ρ should not be constant for an one-dimensional flow. Nevertheless, we will assume a constant density in this study, as compressibility only occurs in very high velocity flows. Moreover, particle behaviour is more influenced by velocity fluctuations than by density fluctuations. So, the density will be considered as constant, as well as fluid temperature T and pressure p. These three physical quantities will be connected by the ideal gas law.

2.2 Particle Drag Law

When studying particle motion in fluids, the most important parameter is the drag coefficient C_D. As the form of the particle is often unknown, it is usually considered as apparently spherical (i.e. the particle reacts as if it were a sphere, with a certain diameter d). Then, the drag coefficient is related to the drag force F exerted on the sphere by the fluid by the expression :

$$C_D = \frac{8\,F}{\rho\, u^2\, \pi\, d^2} \qquad (3)$$

Numerous theoretical or empirical expressions of the drag coefficient have been developed since Stokes (1851) formulated :

$$C_D = \frac{24}{Re} \qquad (4)$$

where the Reynolds number Re is based on sphere diameter and the relative velocity between fluid and particle. This expression, although widely used, is only valid for $Re \ll 1$ and for continuum flow (where Knudsen number, based on diameter d, $Kn \ll 1$). It has been pointed out that in atmospheric air conditions, diameters below 1 µm lead to a rarefied flow regime around the particle. Moreover, the condition $Re \ll 1$ will not be satisfied for relative velocities higher than 0.5 m/s.

Many expressions for the drag coefficient take into account only one of these phenomena. In this study, we will use two different laws valid over a wide range of Reynolds and Knudsen numbers. The first one has been developed by Carlson and Hoglund (1964) :

$$C_D = \frac{24}{Re} \frac{\left(1+0.15\,Re^{0.687}\right)\left[1+e^{-\left(\frac{0.427}{Ma^{4.63}}+\frac{3}{Re^{0.88}}\right)}\right]}{1+\frac{Ma}{Re}\left(3.82+1.28e^{-\frac{1.25\,Re}{Ma}}\right)} \qquad (5)$$

where Ma is the Mach number based on relative velocity. The second expression has been developed by the first author ((Tedeschi (1993), Tedeschi *et al.* (1993)) in extending Cunningham's (1910) expression to high velocities and high rarefaction :

$$C_D = \frac{24}{Re} k\left[1 + 0.15\,(k\,Re)^{0.687}\right]\xi(Kn)\,C \qquad (6)$$

where :

$$\xi(Kn) = 1.177 + 0.177\,\frac{0.757\,Kn^{1.16} - 1}{0.757\,Kn^{1.16} + 1} \qquad (7)$$

$$C = 1 + \frac{Re^2}{Re^2 + 1}\, e^{-\frac{0.225}{Ma^{2.5}}} \qquad (8)$$

and k is the solution of the equation :

$$a_1 k^{1.687} + a_2 k - 1 = 0 \qquad (9)$$

where :

$$a_1 = \frac{9}{4}\,0.15\,\frac{Kn}{\varepsilon}\,Re^{0.687} \qquad (10)$$

$$a_2 = 1 + \frac{9}{4}\,\frac{Kn}{\varepsilon} \qquad (11)$$

$$\varepsilon = \frac{3}{8}\sqrt{\pi}\,\frac{1+S^2}{S}\,\mathrm{erf}(S) + \frac{1}{4}\,e^{-S^2} \qquad (12)$$

$$S = \sqrt{\frac{\gamma}{2}}\,Ma \qquad (13)$$

This law, less empirical than Carlson-Hoglund expression, is valid for the whole range of Kn (continuum to highly rarefied flow), $Re < 200$ and $Ma < 1$, and is thus relevant to applications of LDV.

The motion equation of a particle will be (for constant values of flow parameters such as density, pressure, viscosity) :

$$M_p \frac{du_p}{dt} = F(u_p, u) \qquad (14)$$

where M_p is the particle mass. The force F depends explicitly on relative velocity through Mach and Reynolds numbers, and thus implicitly on abscissa x and time t through the fluid velocity u. In an earlier study (Tedeschi *et al.* (1992)), additional terms such as added mass and Basset (1888) history term were found to be negligible for particle motion in air, except for conditions of very strong acceleration (across shock waves, for example) and ratio $\rho_p/\rho < 100$.

2.3 Criterion for Comparisons

As the sign of the relative velocity acts directly on the sign of particle acceleration, particle velocity will increase each time fluid velocity becomes higher and particle velocity will decrease each time fluid velocity becomes lower. Therefore, the frequency of the particle velocity will be the same as the fluid velocity. The difference with particle behaviour will appear in the amplitude of velocity variations and thus in turbulent intensities measured by LDV. With the right choice of particle size, fluid and particle amplitudes will be close, otherwise particle amplitudes will be very low compared to the fluid. In real experimental measurements, the proper criterion would be the ratio of turbulence intensities of the flow and the particles. Unfortunately, this requires knowledge on the fluid flow proper, as a Laser Doppler Velocimeter does not measure the turbulence intensity of flow directly but rather that of the particles. In our case, we replace the previous criterion with $\Delta u_p/\Delta u$, the ratio of maximum velocity fluctuations of particle and flow. The measurement of the maximum velocity fluctuation of the particle, Δu_p, is made when the particle motion is stationary (after three cycles of velocity oscillations). These two criteria are equivalent for sinusoidal velocity profiles.

The parameters with the greatest influence are frequency f, maximum velocity amplitude Δu, density ρ for the fluid, radius r and density ρ_p for the particles.

3. COMPARISONS WITH PREVIOUS STUDIES

Comparisons are made between our calculations and results obtained in two previous studies. Maxwell and Seasholtz (1974) studied velocity lag of solid particles in oscillating gases. They used Carlson-Hoglund expression (5) for the drag coefficient of particles. Feller and Meyer (1975) used a criterion based on the solution of the equation of motion of a particle in an oscillating flow. By using Stokes drag law, it is found analytically that :

$$\frac{\Delta u_p}{\Delta u} = \frac{1}{\sqrt{1 + (2\pi f \tau)^2}} \qquad (15)$$

where τ is Stokes time constant :

$$\tau = \frac{d^2 \rho_p}{18\eta} \qquad (16)$$

This expression is only valid for $t \geq 4\tau$. Evidently, as it is based on Stokes drag law ($Re \ll 1$, $Kn \ll 1$), this expression can only be used in LDV applications in very restricted cases. However, it is simple and very convenient to use, and allows the direct determination of the ratio of the amplitude of particle and flow velocity fluctuations. Moreover, the expression can be inverted to obtain, within a given error band, the maximum frequency response. If we fix a minimum value for the ratio R_{min}, we can easily obtain the maximum frequency allowed :

$$f_{max} = \frac{1}{2\pi\tau}\sqrt{\frac{1}{R_{min}^2} - 1} \qquad (17)$$

or expressed in deciBel :

$$f_{max}(\mathrm{x\ dB}) = \frac{1}{2\pi\tau}\sqrt{10^{\frac{x}{10}} - 1} \qquad (18)$$

For example, the maximum frequency within 3 dB will be :

$$f_{max}(3\ \mathrm{dB}) = \frac{1}{2\pi\tau} \qquad (19)$$

A comparison is made between results obtained in those studies and our calculations, with parameters used by Maxwell and Seasholtz, in figure 1.

For $r = 2$ µm ($Kn = 0.01$), we have continuum flow around particles and for $r = 0.5$ µm ($Kn = 0.04$), we obtain slip flow (light rarefaction). Results obtained by Maxwell and Seasholtz and the ones calculated in the present study are comparable. Feller and Meyer expression (15) tends to under-estimate the response of particles at low frequencies and to over-estimate it at high frequencies.

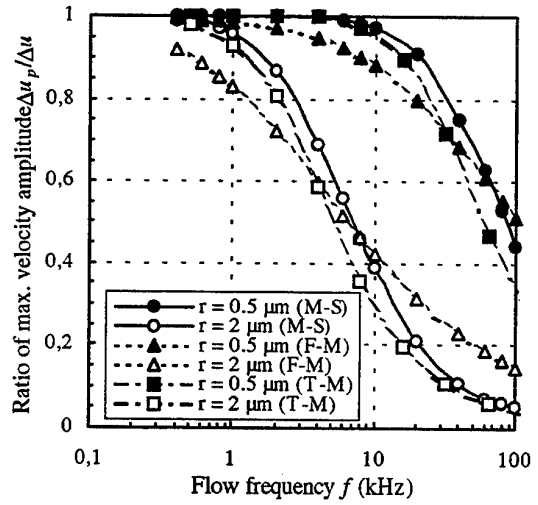

Fig. 1 Comparison between ratio of maximum velocity amplitude of particle and flow, obtained by Maxwell-Seasholtz, Feller-Meyer and Tedeschi-Menon. Δu = 15.2 m/s, ρ = 1.22 kg/m^3, ρ_p = 1000 kg/m^3.

4. COMPARISONS BETWEEN DIFFERENT DRAG LAWS

Three different drag laws are compared : Stokes expression (4) because it is the most well known and often used, Carlson-Hoglund (5) and Tedeschi (6) expressions because they are valid in extended conditions. The aim of this comparison is to show clearly that in certain conditions

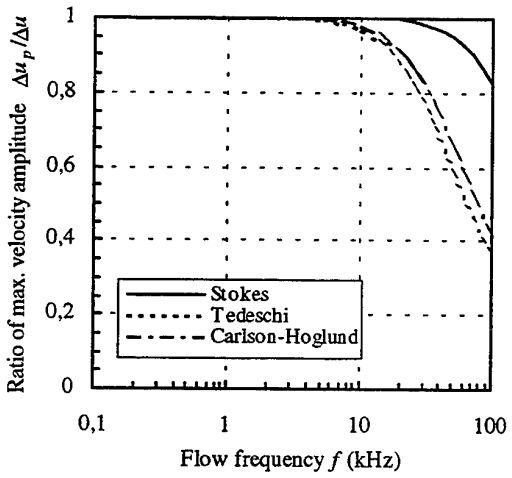

Fig. 2 Comparison between ratio of maximum velocity amplitude of particle and flow, calculated with Stokes, Tedeschi and Carlson-Hoglund drag laws, for rarefied flow conditions (Kn = 0.9). Δu = 10 m/s, r = 0.25 µm, ρ = 0.12 kg/m^3, ρ_p = 1000 kg/m^3.

associated with LDV measurements, Stokes law does not predict sufficiently accurately the cut-off of high frequencies. The two examples covered here are representative of experimental measurement conditions which can occur, although not frequently.

The first one implies rarefaction conditions. If particles of small sizes are used, the flow around these particles can be rarefied, even if the flow itself (in a wind tunnel for example) is a continuum. It is sufficient that the diameter d is of the same order as the mean free path $\overline{\lambda}$, which is the case here (Kn = 0.9). It can be seen in figure 2 that Stokes expression indicates too high values of $\Delta u_p/\Delta u$ as it does not take rarefaction effects into account, while Tedeschi and Carlson-Hoglund expressions give similar results.

The second case presented implies high relative Reynolds numbers, or more exactly implies that the condition Re « 1 is not satisfied. Here, the maximum value (based on the maximum velocity amplitude of fluid Δu) of Reynolds number is equal to 25. This value will not be reached, but if the particle lag is important, the relative velocity will be of great importance, as well as the relative Reynolds number. Thus, its effect will be increased and Stokes law will be less valid. Graphs in figure 3 shows this phenomenon. On the contrary, Carlson-Hoglund and Tedeschi expressions give same results.

5. PARAMETRIC STUDY

The influence of the main parameters are analysed in this section, using equation (6) for the drag force exerted

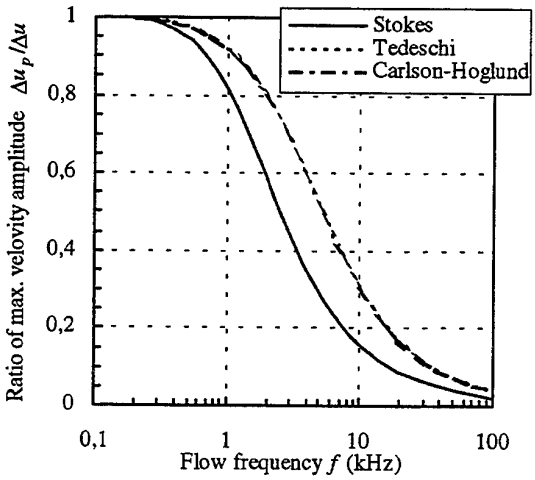

Fig. 3 Comparison between ratio of maximum velocity amplitude of particle and flow, calculated with Stokes, Tedeschi and Carlson-Hoglund drag laws, for high relative Reynolds number conditions. Δu = 50 m/s, r = 2.5 µm, ρ = 1.22 kg/m^3, ρ_p = 1000 kg/m^3.

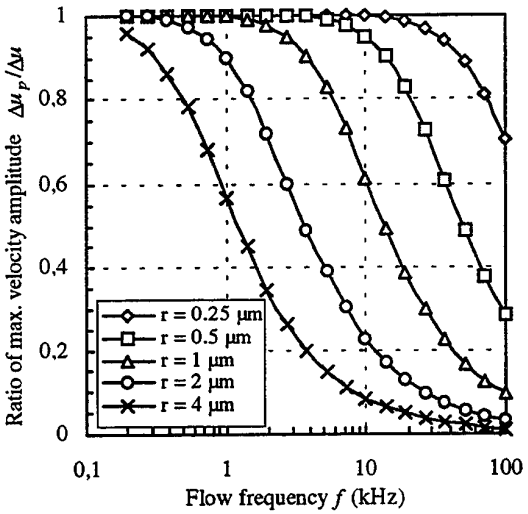

Fig. 4 Ratio of maximum velocity amplitude of particle and flow, for normal flow density conditions. $\Delta u = 5$ m/s, $\rho = 1.22$ kg/m^3, $\rho_p = 1050$ kg/m^3.

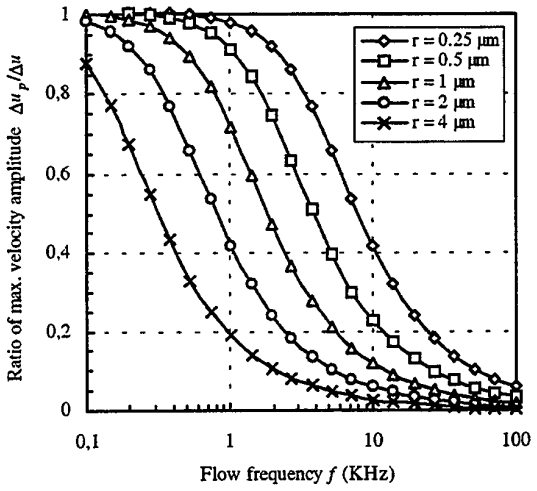

Fig. 5 Ratio of maximum velocity amplitude of particle and flow, for very low flow density conditions. $\Delta u = 5$ m/s, $\rho = 0.012$ kg/m^3, $\rho_p = 1050$ kg/m^3.

on particles. For each period of particle velocity oscillation, calculations have been carried out for at least 100 time steps. For smallest particles, this number has been increased to avoid numerical divergence. The ratio $\Delta u_p/\Delta u$ is calculated after four cycles, when the particle motion is fully stationary.

5.1 Influence of Particle Size

The most important parameter is of course the size of particles. Figure 4 presents results of calculations corresponding to atmospheric conditions for the flow, which induce light rarefaction around particles ($0.006 < Kn < 0.09$). As expected, large particles are less able to respond to high frequency fluctuations. For example, a 4 µm radius particle can respond to flow frequencies within 80 % until 0.5 kHz, while a 0.25 µm radius particle can correctly respond until 75 kHz. The particle density employed for this calculation corresponds to latex particles.

5.2 Effect of Flow Density

Figure 5 shows the results of calculations similar to those presented in figure 4, but for a very low density flow ($\rho = 0.012$ kg/m^3). Knudsen numbers are between 0.6 and 9, which indicates a high rarefaction. The influence of particle size is less important here than for a normal density flow. For a response of particles within 80 % of the maximum velocity amplitude, the previous calculations indicated a ratio of 150 between the maximal frequency obtained by 0.25 and 4 µm radius particles (respectively 75 and 0.5 kHz). In a very low density flow, this ratio falls to 30 (f_{max} = 3.4 and 0.12 kHz for r = 0.25 and 4 µm, respectively). Hence, although large particles are not able to follow high frequency fluctuations, the requirement of using them to obtain sufficient scattered light could become of greater importance here, compared to the previous case. This phenomenon will be increase in case of high rarefaction around particles. Theoretically, the acceleration exerted on a sphere by the flow depends on the inverse of the radius square with Stokes law (continuum flow). In a highly rarefied flow, this acceleration depends only on the inverse of the radius. Figure 6 shows clearly that, for a given frequency, when the flow density ρ decreases, the

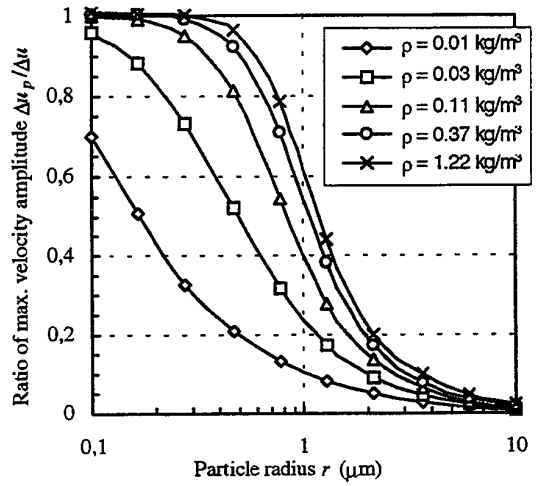

Fig. 6 Ratio of maximum velocity amplitude of particle and flow as a function of particle radius, for various flow density conditions. $\Delta u = 5$ m/s, $f = 10$ kHz, $\rho_p = 1050$ kg/m^3.

ratio $\Delta u_p/\Delta u$ is less dependant on the particle radius. For ρ = 1.22 kg/m^3, the drop in particle response becomes noticeable around r = 0.5 µm and is steep, while for very low densities the gradient is less steep but the decrease appears for smaller sizes.

5.3 Influence of Particle Density

Results of calculations using different particle densities are presented on figure 7. A density ρ_p equal to 250 kg/m^3 is representative of microballoons, while ρ_p = 1000 kg/m^3 corresponds to latex balls and ρ_p = 4000 kg/m^3 to titanium dioxide (TiO_2). These kinds of particles are calibrated and, for this reason, employed for LDV measurements. Thomas and Bütefisch (1993) used titanium dioxide particles to measure flow velocities and rms values across a shock wave. As expected, heavy particles are less responsive to high frequency fluctuations. For example, a particle of 0.5 µm radius can follow frequencies within 80 % up to 100 kHz for ρ_p = 250 kg/m^3, 24 kHz for ρ_p = 1000 kg/m^3 and only 6 kHz for ρ_p = 4000 kg/m^3.

5.4 Influence of the Amplitude of Flow Velocity Fluctuations

It would seem natural to assume that when flow velocity fluctuations increase, the particle is less able to follow them. However, the opposite phenomenon occurs. When fluctuation amplitudes are high, particles are more sensitive to relative velocity and the drag force increases. This can be seen from the factor given below (Schiller and Neuman (1933)) :

$$1 + 0.15\, Re^{0.687} \qquad (20)$$

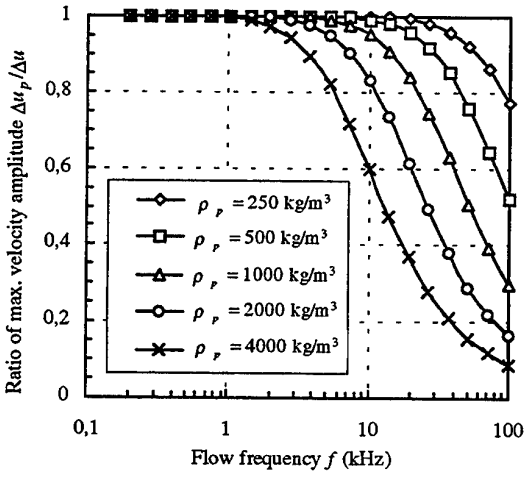

Fig. 7 Ratio of maximum velocity amplitude of particle and flow, for various particle densities. Δu = 5 m/s, ρ = 1.22 kg/m^3, r = 0.5 µm.

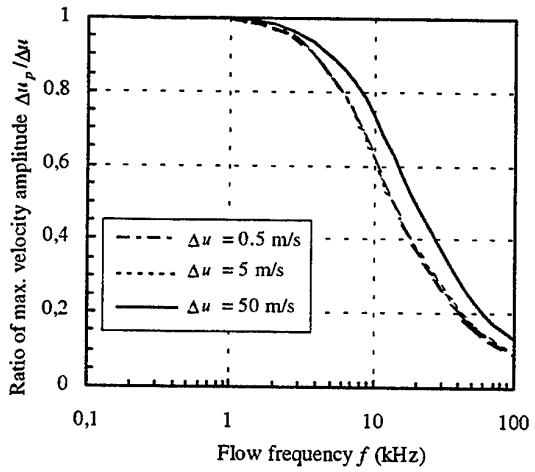

Fig. 8 Ratio of maximum velocity amplitude of particle and flow, for various maximum velocity amplitude of fluid. ρ = 1.22 kg/m^3, ρ_p = 1050 kg/m^3, r = 1 µm.

which is used to multiply the drag force exerted on the particle. Figure 8 shows that for low fluid velocity fluctuations (Δu = 0.5 and 5 m/s) no modification appears in particle behaviour, but for high fluid velocity fluctuations (Δu = 50 m/s) particle velocity fluctuations are higher.

The dependence of $\Delta u_p/\Delta u$ with the maximum velocity amplitude of fluid Δu, for given frequencies, is shown in figure 9. It appears that values of $\Delta u_p/\Delta u$ increase for Δu higher than 5 m/s. This phenomenon is less evident for low and high than moderate frequencies. For f = 2 kHz, fluid and particle velocities are almost equal. For f = 128 kHz, the increase of $\Delta u_p/\Delta u$ occurs more slowly because the flow frequency is too high and particles move across fluc-

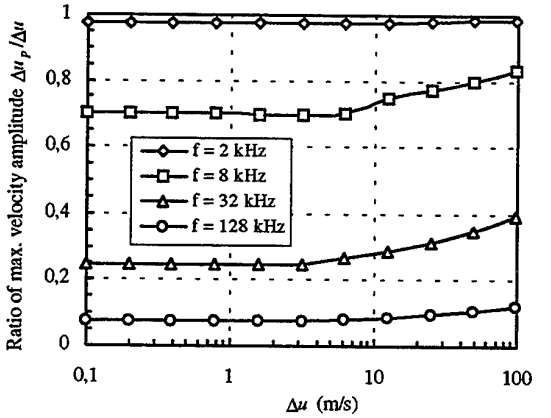

Fig. 9 Ratio of maximum velocity amplitude of particle as a function of maximum velocity amplitude of fluid, for various flow frequencies. ρ_p = 1050 kg/m^3, ρ = 1.22 kg/m^3, r = 1 µm.

tuations without sensing them.

Hence, it appears that for low and moderate velocities, the parameter Δu is not important for the frequency response of particles, but it can have an influence for high velocities. This last remark is made assuming constant values for other parameters. It must be noted that supersonic flows are generally associated with low densities. Therefore, the increase in particle response due to high velocities will, in this case, be counter-balanced by the decrease due to low flow density.

6. CONCLUSION

The response of particles in oscillating flows has been studied in order to determine their ability to respond to high frequencies. An expression developed by the first author and valid in ranges of flow occurring for LDV applications has been used. Results have been compared to results obtained in two previous studies. It has been shown that Stokes law used for calculation of particle drag may provide values that are not valid for certain conditions. A more detailed parametric study than previous ones taking into account rarefaction effects has been carried out. It has been shown that the size of particle has a great influence on particle response and an example is given for normal flow conditions. This phenomenon is reduced in the case of low density flows. The influence of particle density has been also studied. It appeared that the amplitude of flow velocity fluctuations has an influence over 5 m/s.

This study can help experimentalists determine the proper size of the seed particle for use in Laser Doppler Velocimetry or in Particle Image Velocimetry (P.I.V.) measurements as a function of flow conditions and frequencies expected. Using this information, proper choice of seed particles that provide strong signal quality can be made. It can be especially useful in difficult flow situations where experience of using seed particles is lacking, or to improve actual measurements by using as large a particle as possible.

ACKNOWLEDGEMENT

The first author wishes to thank TSI Inc. (Saint Paul, USA) for the support of this study.

REFERENCES

Basset, A.B. 1888, Treatise on Hydrodynamics, vol. 2, chap. 22, Deighton Bell, Cambridge.

Carlson, D.J. & Hoglund, R.F. 1964, Particle Drag and Heat Transfer in Rocket Nozzles, AIAA Journal, vol. 2, n°11, pp. 1980-1984.

Cunningham, E. 1910, On the Velocity of Steady Fall of Spherical Particles through Fluid Medium, Proc. of The Royal Soc. of London, Series A, vol. LXXXIII, pp. 357-365.

Feller, W.V. & Meyers, J.F. 1975, Development of a Controllable Particle Generator for LV Seeding in Hypersonic Wind Tunnels, Minnesota Symposium on Laser Anemometry, pp. 345-357.

Kulick, J.D., Fessler, J.R. & Eaton, J.K. 1994, Particle Response and Turbulence Modification in Fully Developed Channel Flow, J. Fluid Mech., vol. 277, pp. 109-134.

MacInnes, J.M. & Bracco, F.V. 1992, Stochastic particle dispersion modeling and the tracer-particle limit, Phys. Fluid A, vol. 4, n°12, pp. 2809-2824.

Maxwell, B.R. & Seasholtz, R.G. 1974, Velocity Lag of Solid Particles in Oscillating Gases and in Gases Passing through Normal Shock Waves, NASA TN D-7490, March.

Menon, R. & Lai, W.T. 1991, Key Considerations in the Selection of Seed Particles for LDV Measurements, Fourth Int. Conf. on Laser Anemometry, Cleveland, Ohio, USA.

Schaeffer, T., Aouina Y., Huilier, D. & Burnage, H. 1993, A Numerical Model for the Prediction of Water Droplets in a Turbulent Jet-Grid Flow, 2pd Int. Symp. on Exper. and Computational Aerodynamics of Internal Flows, Prague, Czech Republic, July.

Schiller L. & Nauman A. 1933, Z. Ver. Deut. Ing., vol. 77, n°318.

Stokes, G.G. 1851, On the Effect of the Internal Friction of Fluids on the Motion of Pendulums, Trans. Cambridge Phil. Soc., vol. 9, n°2, pp. 8-27.

Tedeschi, G. 1993, Etude Théorique et Expérimentale du Comportement de Particules à la Traversée d'une Discontinuité de Vitesse (Onde de Choc), Ph.D. thesis, Université Aix-Marseille II, Marseille, France.

Tedeschi, G., Elena, M. & Gouin, H. 1993, Particle Motion through an Oblique Shock Wave, Laser Anemometry : Advances and Applications, Proc. SPIE, vol. 252, pp. 273-278.

Tedeschi, G., Gouin, H. & Elena M. 1992, Solution of the Equation of Particle Motion across a Shock Wave, La Recherche Aérospatiale, vol. 6, pp. 1-9.

Thomas, P.J. & Bütefisch, K.-A. 1993, An Investigation of the Influence of the Size Distribution of Seeding Particles on LDA Velocity Data in the Vicinity of a Large Velocity Gradient, Phys. Fluids A, vol. 5, n°11, pp. 2807-2814.

Wang, Q. & Squires, K.D. 1996, Particle Transport in a Nonuniformly Seeded Mixing Layer, 34th Aerosp. Sciences Meeting & Exhibit, Reno, Nevada, U.S.A., January.

COMPARISON BETWEEN VELOCITY MEASUREMENTS BY LDA TECHNIQUES AND DOUBLE FIBER OPTIC SENSORS IN TWO PHASE JETS

M. Gasparetti*, G.L. Rossi*
A. Campi°, R. Onori°

*Dipartimento di Meccanica, Università di Ancona, Via Brecce Bianche, 60131 Ancona, Italy
°Teuco Guzzini SpA, Recanati (MC), Italy

ABSTRACT

Flow velocity measurements in a horizontal submerged two phase air-water jet flowing inside a Plexiglas water tank has been performed by a two component laser Doppler anemometer and by a measurement system based on a double fiber optic sensor. Performances and limits for the applicability of the two measurement methodologies, a question not entirely settled yet.

1. INTRODUCTION

Measurement of void fraction and bubble velocity is of great interest in many technological applications: steam generators, cooling systems, transport of fluids with gaseous and liquid phases, air jets into liquids, etc.

The use of a laser Doppler anemometer (LDA) to analyse the subject requires the volume taken up by the liquid fluid not to be outnumbered by that of the gaseous phase. If so the laser beams can hardly reach in a correct way a measurement point in the core of the stream. On the contrary a fiber optic probe with two sensing elements inserted into the flow, as the one experimented, can operate well in the whole two phase flow field if the bubbles are many and big, because only in this case the probability that a bubble hits both the fiber tips is satisfactory.

In this study the two measurement techniques are compared to evaluate their possibility of success: the comparison is accomplished in a submerged air-water jet.

The use of LDV techniques in two phase flow has been previously proposed by many authors [1, 2, 13, 14]. The problems we met with [12] when analysing air water jets with a ratio close to 0.5 between the air volume flow rate and the water volume flow rate are due to a reduction of the signal to noise ratio and of the data rate and data valid for the laser Doppler anemometer when the measurement volume is inside the flow. In this condition the laser beam cannot penetrate the bubble stream, the measurement volume does not exist or it is heavily distorted and so the measurement technique cannot be applied [12, 15].

A further problem is represented by the signal analysis, related both to bubbles and to little solid particles suspended in water. Some authors proposed the use of the "oversize rejection" parameter of the LDA systems in order to reject the larger bubble signals. With this option it is theoretically possible to evaluate only liquid phase velocity. Other authors state that it is possible to evaluate only bubble velocity by disabling the "oversize rejection" parameter and setting to a low value the photodetector supply and the laser power. In this way in fact only the grater bubbles generate a good signal to noise ratio and can be detected by the LDA processor. With the above mentioned techniques it is possible to measure the velocity of both liquid and gas phases. In our tests, by using those techniques, the same bubble and water velocities have been found in the analysed flow sections, so it was possible to consider a homogeneous model.

2. THE DOUBLE FIBER OPTIC PROBE

A double fiber optic sensor for local measurements in multi-phase flows is illustrated in figure 1.

For each sensing element a light source is coupled with an optic fiber that, through a coupler and a connector, guides the light to the end of the fiber. If its tip is inside a bubble of air, the light is mainly back reflected because of the high difference in the refraction coefficients between the fiber and the air. If the tip is inside water, the light is mainly transmitted because of the nearly equal refraction coefficients. The back reflected light is guided through the coupler to a photodiode that converts the intensity of the received light to an electric signal.

Different tip shapes have been proposed for single fiber optic sensors, in order to increase sensitivity (conically shaped fiber tip), robustness (sapphire tip coupled to the fiber end face), and to reduce intrusivity (limited dimensions of the sensing element) [1, 2, 3, 4, 6, 7, 8, 9, 10, 11, 16].

A pulse with low peak value can also occur when a bubble passes near the fiber tip due to light reflection at the bubble-liquid interface.

When a series of bubbles passes near or on the fiber tip, the electric signal consists in a series of pulses (fig. 2). The pulse width increases with bubble diameter and decreases with bubble velocity. Different techniques have been proposed to calculate, with only one sensing element, the local void fraction a_l. The most common method is based on the determination of a single threshold level S from which the local void fraction can be calculated as the ratio of the sum of the intervals Δt_i during which the signal is above the threshold level to the total time T of the acquisition

$$a_l = (\Sigma \Delta t_i) / T. \qquad (1)$$

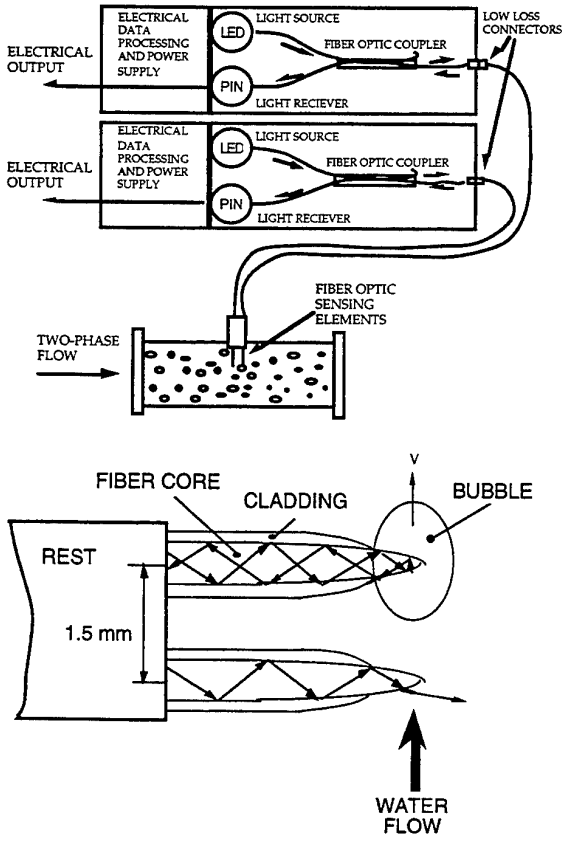

Figure 1. Components of a double fiber optic sensor for bubble velocity measurements in multi-phase flows.

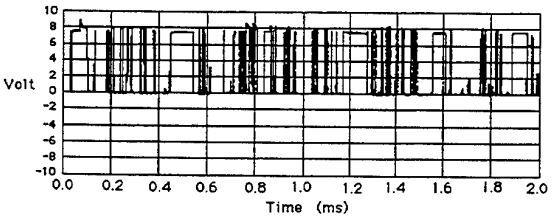

Figure 2. Signal from each sensing element.

With two fiber optic sensing elements, spaced by a Δs distance, it is possible to obtain an estimate of the bubble velocity. In fact if t_{1i} and t_{2i} are the initial instants of the two pulses related to the i-th bubble, we can calculate bubble velocity with the formula:

$$v_i = \Delta s / (t_{1i} - t_{2i}). \qquad (2)$$

In this work data processing of the two signals has been performed by using a cross-correlation function to obtain a mean value of the time shift (t_1-t_2) between the two series of pulses and to obtain a mean value of velocity, during the acquisition time of the two series of pulses.

Complex three phase interfacial phenomena at the probe tip, deformation of the bubble when touching the sensing elements, deformation of the sensing elements when invested by the flow, disturbance of the flow, require a calibration of the sensor and of the whole associated measurement chain [15], including the data processing methods.

3. THE TEST SET-UP

The experimental rig arranged for the tests is illustrated in figure 3. An air-water jet discharges the flow inside a Plexiglas tank with constant level and dimensions of 0,4 x 0,4 x 1,5 meters. Water flow rate in the mixing device is measured by an electromagnetic flow meter and can be regulated by a valve, air flow is controlled with a valve and evaluated by a thermal mass flow meter (TSI).

The device used for air water mixing is a classical ejector (fig. 4): the air is inspired by the depression in the suction section. The device has been designed in order to generate an annular jet flow. Flow rates up to 60 l/min of water and up to 40 l/min of air have been used for the tests.

The double fiber optic sensor is introduced in the tank from high.

The LDA system is composed by a two component backscatter fiber optic probe, a 4 W max Argon-ion laser source, two Burst Spectrum Analysers. The air-water jet area is accessible through the transparent side walls of the tank by a probe front lens with 310 mm focal length, that produces a 0.146x2.39 mm measurement volume.

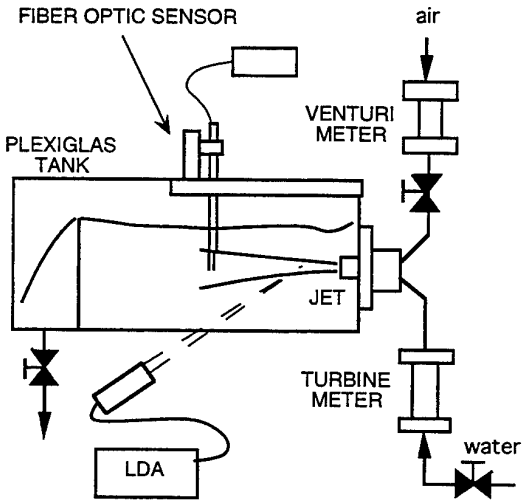

Figure 3. Test rig.

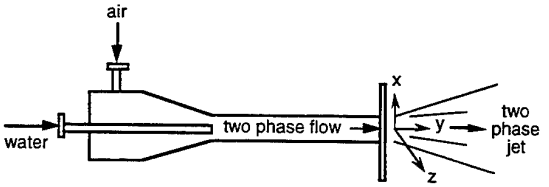

Figure 4. Air water mixing device.

4. PERFORMED TESTS

Measurements have been previously accomplished in six sections of the two phase jet, along a vertical line, at distances from the outlet section of 20, 50, 70, 120, 150 and 200 mm (y co-ordinate). Water flow rate was 40 l/min and air flow rate was 20 l/min. On each section profiles composed by 11 to 19 points with different spacing between them have been measured. By the LDA system 10000 two component velocity samples have been acquired for each point. From the double fiber optic sensor, calibrated in advance by following the procedure described in [15] a data file of 10000 samples has been obtained for each sensing element with a sampling rate of 50 kHz.

A comparison between the axial component of mean velocity measured by the laser Doppler anemometer and by the fiber optic sensor in the section at 20 mm is illustrated in figure 5.

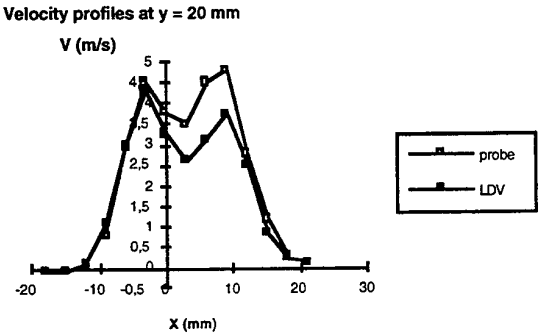

Figure 5. Comparison between LDA and double fiber optic sensor measurements in the section at 20 mm from the jet outlet.

It can be observed the annular character of the flow, as previously stated, that confirms that the LDV takes data in the measurement volume. It can also be observed that the fiber optic sensor overestimates the higher velocity values. Another comparison between the mean velocity values is illustrated in figure 6.

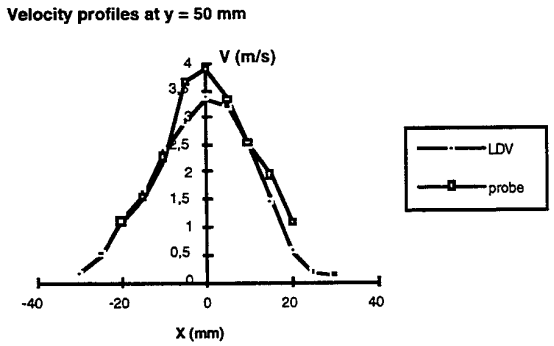

Figure 6. Comparison between LDV and double fiber optic sensor measurements in the section at 50 mm from the jet outlet.

The annular character of the flow cannot be observed any longer while it can be noticed again that the fiber optic sensor overestimates the maximum velocity values.

From both figures 5 and 6 it can also be deduced that it was not possible to analyse the acquisition of the double fiber optic sensor signals taken to the edges of the jet because of the low bubble concentration. On the contrary it was possible in this region to easily take measurements with the laser Doppler anemometer, since no bubble stream exists through the laser beams producing the measurement volume.

Then a series of tests has been performed with the double fiber optic sensor and the LDA system measuring velocity in the same point at different values of water and air flow rate. The examined point is at a distance of 50 mm from the jet outlet in the middle of the bubble stream.

The signals of the double fiber optic sensor have been acquired at a sampling rate of 250 kHz for time intervals including 500 samples.

In the same point and at the same time the acquisition of 5000 two component velocity samples has been performed by the LDA system with the oversize rejection option enabled and disabled.

In table 1 all the examined experimental conditions and the LDA measurements of the gaseous and liquid phase axial velocity are listed.

Water flow rate (l/min)	Air flow rate (l/min)	Air/ water ratio	Bubble velocity (m/s)	Water velocity (m/s)	Bubble rms (m/s)	Water rms (m/s)
30	1.7	0.06	1.3	1.31	0.43	0.34
35	1.1	0.03	1.46	1.43	0.36	0.34
35	4.8	0.14	1.55	1.71	0.44	0.46
35	12.4	0.35	2.86	2.9	0.77	0.77
40	1.1	0.03	1.63	1.6	0.47	0.40
40	4.8	0.12	1.83	1.77	0.54	0.45
40	12.5	0.31	2.97	3.04	0.93	0.89
45	1.1	0.02	2.04	1.92	0.55	0.48
45	4.8	0.11	2.07	2.08	0.61	0.53
45	14.0	0.31	3.41	3.48	1.03	0.99
50	1.1	0.02	2.29	2.28	0.61	0.57
50	4.8	0.10	2.17	2.12	0.61	0.57
50	18.6	0.37	4.36	4.32	1.25	1.25
60	1.1	0.02	2.76	1.44	0.76	0.37
60	24.4	0.41	5.04	5.18	1.65	1.51

Table 1. Experimental conditions and LDA results.

For each condition the time-lag between the signals coming from the two sensing elements of the fiber optic probe has been calculated by averaging the results of ten cross correlation procedures applied to windows containing only one peak in the right sequence.

Figure 7 shows the bubble velocities monitored by the double fiber optic sensor and by the laser Doppler anemometer (axial component only). The data show a significant dispersion in the region of low air/water ratio, probably due to the inaccuracy of the fiber optic probe in a measuring condition not favourable for its operation. The coincidence of the results improves at higher values of air/water ratio, with two exceptions that may derive from the vibrations induced by the flow, very rough in those situations, in the mounting rod of the fiber optic sensing elements.

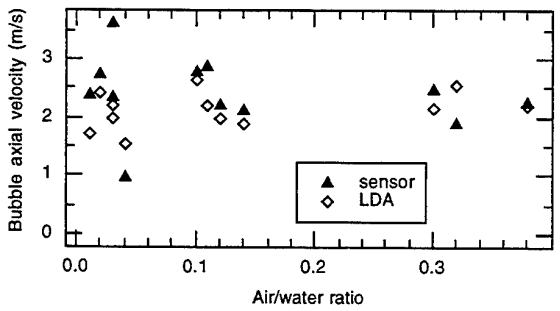

Figure 7. Comparison between LDA and double fiber optic sensor measurements at different air/water ratios.

The average overestimate of the velocity value determined by the fiber probe reduces from low to high air/water ratio (fig. 8).

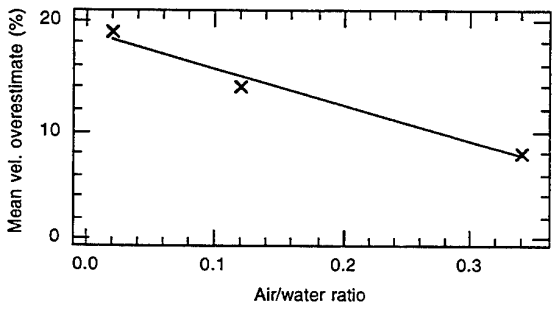

Figure 8. Overestimate of the velocity value determined by the double fiber optic sensor with regard to the LDA measurement.

In figure 9 the reduction of validation in the LDA measurements with the increase of the air/water ratio is illustrated. The data rate, which depends also from velocity, has a more undefined behaviour. In the graph only the higher values of validation and data rate obtained for each region of air/water ratio are reported. The trend of the data rate is described by a fitting curve too.

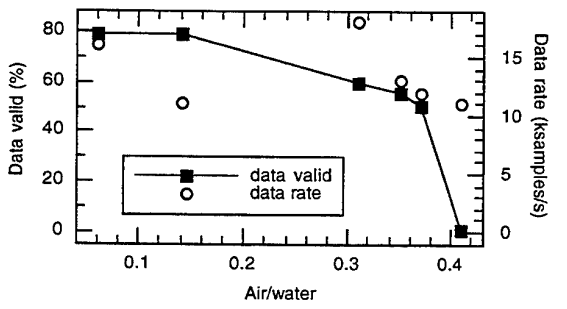

Figure 9. Data rate and validation for the LDA measurements at different air/water ratios.

5. CONCLUSIONS

The performed tests have confirmed that to evaluate the characteristics of two phase flows produced by air/water jets, the use of LDA systems is recommended for points with low void fraction, while double fiber optic probes work well in flows with high air/water ratios.

In highly turbulent streams the inaccuracy of fiber optic sensors, generally about 10 % [12, 15], can be increased by the oscillations to which the fiber tips and their mounting rod are subjected.

REFERENCES

[1] Multi-Phase Flow Measurement, 1985, Cranfield Ins. of Technology, London 17-18 June.

[2] Hetsroni G., 1982, Handbook of Multiphase Systems, McGraw-Hill.

[3] Danel F. & Delhaye J.M., 1971, Sonde optique pour mesure du taux de presence local en ecoulement diphasique, Mes. Regulation Autom., pp. 99-101.

[4] Galaup J.P., 1975, Contribution à l'ètude des méthodes de mesure en ecoulement diphasique, Ph.D. thesis, Univ. Scientifique et Médicale de Grenoble, Ins. Nat. Polytechnique de Grenoble.

[5] Krohn D.A., 1988, Fiber Optic Sensors - Fundamentals & Applications, Instrument Society of America.

[6] Berti M., 1983, Optical reflection probe for the measurement of local void fraction, bubble velocity, bubble size and for the identification of flow regime, Ph.D. thesis, Wuerenlingen Eidg. Inst. Reakt.

[7] Danel F., 1978, Local measurement in two phase flow - recent optical probe design, Houille Blanche, n. 5, pp. 351-355.

[8] Delhaye J.M. & Jones O.C., 1975, Measurement techniques for transient and statistical studies of two phase gas liquid flows, ASME paper 75-HT-10.

[9] Annunziato M., Giammartini M., Presaghi S. & Sica M., 1988, Catena di misura con sonda a fibra ottica per il rilievo della frazione di vuoto, Termotecnica, vol. 42, n. 5, pp. 63-69.

[10] Clark N.N., Seiss R. & Turton R., 1992, Probe measurements in gas-liquid systems, Flow Measurement and Instrumentation, vol. 3, n. 1.

[11] Delhaye J.M., 1979, Optical methods in two-phase flow, Proc. Dynamic Flow Conference.

[12] Paone N., Rossi G.L. & Tomasini E.P., 1992, Caratterizzazione sperimentale di tecniche di misura ottiche per lo studio di flussi bifase, 47° Convegno ATI, Parma.

[13] Sun T-Y. & Faeth G.M., 1986, Structure of turbulent bubbly jets - I. Methods and centerline properties, Int. J. Multiphase Flow, vol.12, n.1, pp. 99-114.

[14] Sun T-Y. & Faeth G.M., 1986, Structure of turbulent bubbly jets - II. Phase property profiles, Int. J. Multiphase Flow, vol.12, n.1, pp. 115-126.

[15] Rossi G.L., 1996, Error analysis based development of a bubble velocity measurement chain, Flow Measurement and Instrumentation, to be published in July 96.

[16] Cartellier A., 1990, Optical probe for local void fraction measurements: characterization of performance, Review of Scientific Instruments, n. 61.

THE LOCUS OF CENTRES METHOD FOR LDA AND PDA MEASUREMENTS

Th. Panidis[1] and M. Sommerfeld[2]

[1] Laboratory of Applied Thermodynamics, Mechanical Engineering Department, University of Patra, GR 265 00 Patra-Rio, Greece
[2] Institute fur Mechanische Ferfahrenstechnik und Umwltscutztechnik, Martin-Luther-Universitat Halle-Wittenberg, D-06099 Halle (Saale), Germany

ABSTRACT

A new method is introduced for the analysis of LDA and PDA optical setups, especially suited for larger particles. The properties of an optical setup are studied, for a specific particle size, in an effective control volume defined as the Locus of the Centres of the particles producing interference signals. The effect of the particle size on the size and position of such a control volume are evaluated and discussed. The convenient description using control volume fringes is adapted to suit larger particles and used to derive the equations of LDA and PDA measurements. The method sets new standards for the estimation of the active control volume as a function of the particle size, for dispersed two phase flows measurements.

1. INTRODUCTION

The non intrusive character of the Laser Doppler Anemometer and the its sizing counterpart Phase Doppler Anemometer in addition to their measuring performance have established them among the most advanced techniques for fluid flow research. A great deal of work has been done in the last two decades and significant contributions have advanced the physical understanding of the techniques. The use of geometrical optics gives a very good overview of the technique and satisfactory results for most of the applications. Furthermore the development of more accurate tools based on Lorenz-Mie theory (LMT) has significantly improved our understanding and capability to optimise demanding optical setups.

In the last years research in dispersed two phase flows has greatly benefited from the advances in the PDA technique. The ability of PDA to measure simultaneously the velocity and size of the dispersed phase has been extended to concentration and particle flux measurements while new capabilities seem to be on the way. On the other hand the demand to understand the influence of larger particles has increased For this task geometrical optics is used with satisfactory results. Lorenz-Mie calculations are used for setup optimization mainly for medium particle sizes since large particles demand significant computational power. Moreover for large particle most of the scattering phenomena can be included in geometrical optics models. In the frame of geometrical optics analysis the present work is aiming to improve our understanding of the effect that larger particles have on the measuring parameters of LDA and PDA.

It is common practice measurements of the dispersed phase properties in two phase flows to be attributed to the individual particle present in the measuring volume. Therefore it is reasonable to map the measuring volume to a corresponding volume that is defined by the Locus of the Centres (LoC) of the sensed particles. In the present work this methodology is applied to LDA and PDA measuring volumes revealing some aspects not readily observable in previous derivations.

Geometrical optics is used to analyze the properties of the Locus of Centres (LoC) volume in flows with reflecting or transparent spherical particles. Reflection and first order refraction are considered.

In comparison with the conventional geometrical optics analysis the present work incorporates the same level of accuracy to a more convenient scheme. Of course it lacks the accuracy of LMT methods but this drawback is not considered important for larger particles for which the presented method is more suitable.

Throughout this work boldface letters are used to indicate vectors. Uppercase letters, unless explicitly specified otherwise, are used for position vectors initiating at point **O**, that is the centre of the co-ordinate system, while lowercase letters stand for unit vectors.

2. LOCUS OF CENTRE OF A RAY

2.1. Reflecting particles

Consider a Laser beam of parallel rays with direction unit vector **k** and a photodetector (PD) located at point **P** (figure 1). A reflecting spherical particle of radius r_p is reflecting only one ray to the PD from point **X**. The unit vector in the direction of **X-P** is **m**. The centre of the particle is located at point **Q** at distance r_p from **X** on the bisection of the transmitted and the reflected ray, that is in direction **n**.

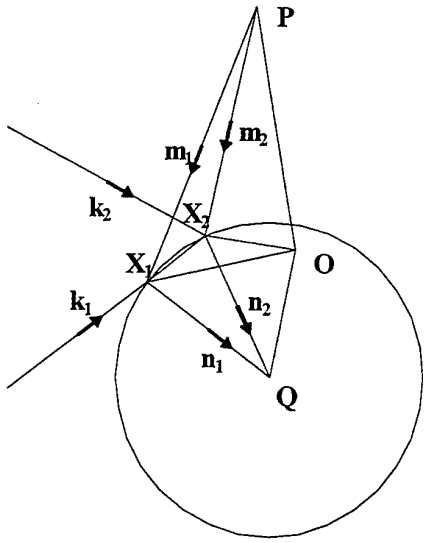

Figure 1. Reflection on a sphere

$$\mathbf{Q}=\mathbf{X}+r_p\,\mathbf{n} \tag{1}$$

with

$$\mathbf{n}=\frac{\mathbf{k}+\mathbf{m}}{|\mathbf{k}+\mathbf{m}|} \tag{2}$$

The line consisting of all points **Q** corresponding to all points **X** along the ray is the ray Locus of Centres (LoC) corresponding to this particle size.

2.2. Refracting particles

In figure 2 refraction of a ray through a sphere is studied. The upper part of the figure is referring to refraction through a particle with refractive index n_2 smaller than the refractive index n_1 of the surrounding medium and the lower part to the inverse case. Simple geometrical considerations

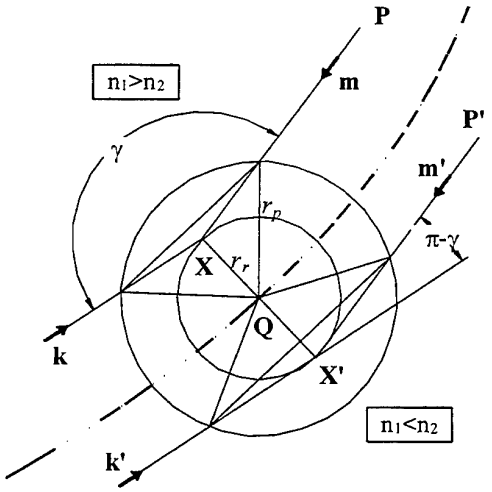

Figure 2. Refraction through a sphere

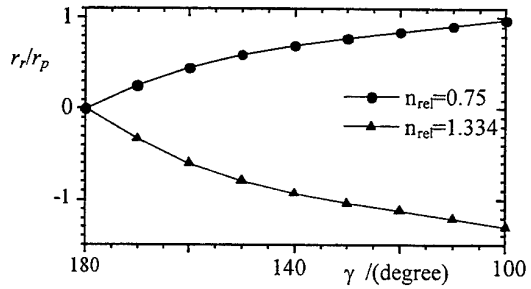

Figure 3. Radius correction for refraction

show that the centre of a sphere of radius r_p refracting a ray of unit vector **k** towards direction **-m**, is located at the same point as the centre of a sphere of radius r_r reflecting the same ray towards the same path. The reflection takes place either on the convex (for $n_1>n_2$), or on the concave (for $n_1<n_2$) surface of the sphere. If γ is the angle between direction vectors **m** and **k** then:

$$r_r = r_p \frac{\sin\left(\arctan\left(\dfrac{n_{rel}\cos(\gamma/2)}{1-n_{rel}\sin(\gamma/2)}\right)\right)}{\sin(\gamma/2)} \tag{3}$$

where $n_{rel}=n_2/n_1$.

Positive values of r_r indicate reflection on a convex surface and negative ones on a concave. In this way the vector $r_r\mathbf{n}$ always points from the apparent reflecting point to the centre of the sphere. According to this derivation the LoC of rays refracted through spherical particles can be obtained in the same way as with reflected ones on the bisection of the incident and the reflected or refracted ray at distances which for given angles will be proportional to the particle size. In figure 3 the evolution of r_r/r_p is given for water droplets in air ($n_{rel}=1.334$) and for air bubbles in water ($n_{rel}=0.75$). For angles less than 97.1° total reflection either at the outer surface ($n_{rel}=0.75$) or at the inner surface ($n_{rel}=1.334$) prevents the transmission of this kind of rays. This limit corresponds to $r_r=r_p$ for $n_{rel}<1$ and $r_r=r_p\,n_{rel}$ for $n_{rel}>1$. This means that the apparent reflecting sphere is larger for $n_{rel}>1$, or equal for $n_{rel}<1$ to the real one near total reflection angle. For larger angles γ, that is in the forward direction, the size of the apparent reflecting sphere is decreasing to zero.

In figure 4 the displacement of the LoC for reflected or refracted rays, nondimensionalised with the particle radius, is given as a function of the intersection angle γ, on the ray-receiver plane. Co-ordinate z is in the direction of ray propagation and y is normal to it. The photodetector is located in the side of negative y. In this co-ordinate system the displacement is calculated from the vectors $r_r\mathbf{n}$ with

$$\mathbf{n}=\sin(\gamma/2)\mathbf{y}+\cos(\gamma/2)\mathbf{z} \tag{4}$$

where **y**, **z** are the unit vectors in the corresponding directions.

For forward reflection ($\gamma=180^o$) the LoC is at distance

r_p normal to the ray, indicating grazing reflection on the particle surface. For backward reflection ($\gamma=0^o$) the ray is reflected at normal incidence on the particle surface and the LoC is on the ray at distance r_p behind the reflecting point. For refraction the LoC is departing mostly from the apparent reflecting point on the ray just before total reflection limit. It has to be noted that since refraction for $n_{rel}>1$ is equivalent to reflection on the concave surface of a sphere the LoC for reflection and refraction depart from each other for $n_{rel}>1$ especially near the total reflection angle. On the contrary for $n_{rel}<1$ the LoC for reflection and refraction are almost the same near total reflection angle.

3. DUAL BEAM LDA SETUP

A conventional dual beam LDA optical setup is shown in figure 5. Two laser beams, with half angle $\vartheta/2$, are propagating on the zx plane towards positive z. Their waists are centred at point **O**. The photodetector is located at point **P** at an elevation angle ψ from the yz plane. The off axis angle φ is measured on this latter plane. The planar configuration of the preceding section corresponds to $\vartheta=\psi=0^o$.

3.1. LoC Control Volume

Following the same line of reasoning the LoC of the two beams can be defined. It is obvious from figure 4 that the LoC of a beam is not geometrically similar to the beam itself. Assuming though that the distance l from **O** to **P** is very large, angle γ will be constant in the vicinity of the beam intersection. In that case the LoC of a beam section in the vicinity of **O** is geometrically similar to the beam section itself and parallel displaced from it in the direction **n** at distance r_r (in the following we will use r_r implying that $r_r/r_p=1$ for reflection). According to equation (2) and using the notation of the LDA setup the unit vectors $\mathbf{n_1}$ and $\mathbf{n_2}$ for beams 1 and 2 are:

$$\mathbf{n}_1=\frac{\sin(\vartheta/2)-\sin\psi}{f_m}\mathbf{x}+\frac{\cos\psi\cos\varphi}{f_m}\mathbf{y}+\frac{\cos(\vartheta/2)-\cos\psi\cos\varphi}{f_m}\mathbf{z} \quad (5)$$

$$\mathbf{n}_2=\frac{-\sin(\vartheta/2)-\sin\psi}{f_p}\mathbf{x}+\frac{\cos\psi\cos\varphi}{f_p}\mathbf{y}+\frac{\cos(\vartheta/2)-\cos\psi\cos\varphi}{f_p}\mathbf{z} \quad (6)$$

where **x**, **y**, **z** are the unit vectors in the corresponding directions and

$$f_m=\sqrt{2}\left(1-\sin(\vartheta/2)\sin\psi-\cos(\vartheta/2)\cos\psi\cos\varphi\right)^{1/2} \quad (7)$$

$$f_p=\sqrt{2}\left(1+\sin(\vartheta/2)\sin\psi-\cos(\vartheta/2)\cos\psi\cos\varphi\right)^{1/2} \quad (8)$$

The LoC of the two beams are evolving in different directions as the size of the particle increases and for large particles they may depart completely from each other. In the frame of the present analysis a particle transmits only one ray from each beam to the PD, for every mode of transmission (reflection and refraction). In order to have interference from the two beams at the PD, a particle centre should be in the intersection of the LoC of the two beams. Moreover the apparent reflecting points should be viewed by the PD.

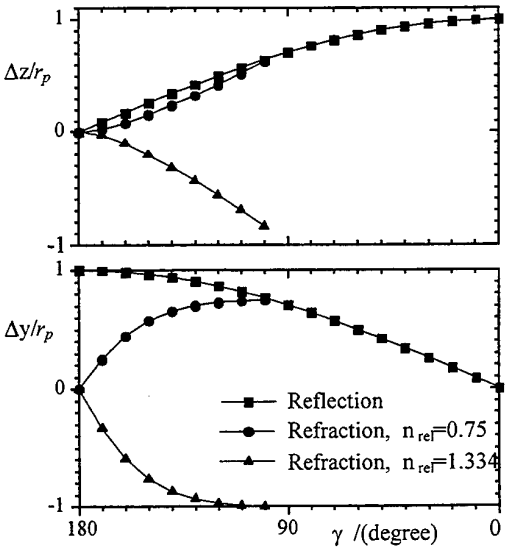

Figure 4. Nondimensional distance of the LoC points

The difference of the four vectors $r_{r1j}\mathbf{n_1}$ and $r_{r2j}\mathbf{n_2}$ (subscripts 1 and 2 are referring to beam 1 and 2 while j is used to indicate reflection and refraction) give the information concerning the intersections of the four LoC of the beams.

$$\mathbf{D}_{jk}=r_{r1j}\mathbf{n}_1-r_{r2k}\mathbf{n}_2=\Delta_{xjk}\mathbf{x}+\Delta_{yjk}\mathbf{y}+\Delta_{zjk}\mathbf{z} \quad (9)$$

There are four vectors $\mathbf{D}_{jk}$ (these are not position vectors) which describe how the beams' LoC intersect with each other. Usually we are interested in intersections of the same type beams' LoC, that is either for reflection or for refraction. Discrepancies though may occur due to the

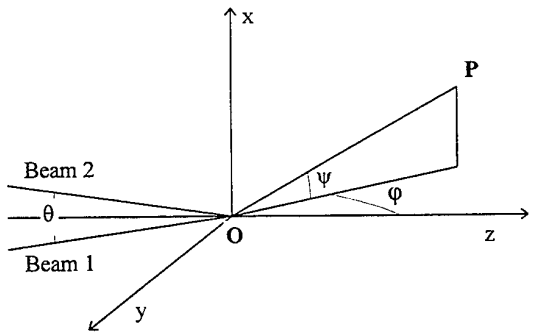

Figure 5. LDA setup

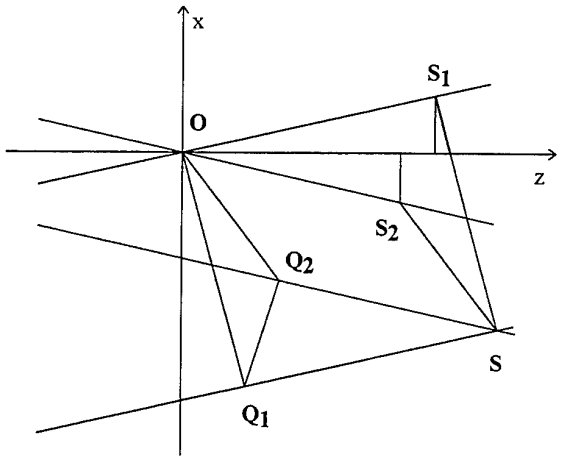

Figure 6. Intersection of the beams' LoC

intersection of different type of beams' LoC, as the Gaussian beam effect discussed in the next section.

Differences in y components indicate reduction of the effective control volume as the LoC for the beams are no longer on the same plane. If the y component of the difference is larger than the beam diameter no interference is possible. Differences in the x and z components reveal changes of the point of intersection. In figure 6 the beam intersection point **O** corresponds to points $\mathbf{Q_1}$ and $\mathbf{Q_2}$ on the LoC of beam 1 and 2 respectively. The intersection of the LoC of the beams is at **S**, which corresponds to point $\mathbf{S_1}$ on beam 1 and $\mathbf{S_2}$ on beam 2. This means that interference signals will be produced when a particle centre is at **S** and the PD is viewing points $\mathbf{S_1}$ and $\mathbf{S_2}$. Geometrical considerations show that:

$$\mathbf{S_1} = -\frac{\Delta_x + \Delta_z \tan(\vartheta/2)}{2}\left(\mathbf{x} + \frac{1}{\tan(\vartheta/2)}\mathbf{z}\right) \qquad (10)$$

$$\mathbf{S_2} = -\frac{\Delta_x - \Delta_z \tan(\vartheta/2)}{2}\left(\mathbf{x} + \frac{1}{\tan(\vartheta/2)}\mathbf{z}\right) \qquad (11)$$

3.2. Locus of "Fringes"

The understanding of the LDA method is significantly facilitated with the introduction of the control volume fringes produced due to the interference of the Laser beams. This fringes are the result of the arrival of the incident rays of the two beams at the control volume points with phase difference which is varying in the x direction. Since a point scatterer is assumed this phase difference is sensed by the PD which acts as an optical integrator. This concept is not suited for larger particles and the corresponding analysis usually concentrates at the spatial fringe pattern scattered by a particle to the far field.

In the LoC control volume approach we can define, for a specific particle size and PD location, Locus of "Fringes" (LoF). When a particle centre is in a LoF the two reflected (or refracted) rays of the two beams arrive at the PD with a phase difference of 180°. Following van de Hulst (1981) and Bachalo (1987) the optical path length of a light ray through a sphere of diameter d relative to a reference ray deflected at the centre of the sphere can be expressed as

$$\eta = \frac{2\pi n_1 d}{\lambda}(\sin\tau - p\,n_{rel}\sin\tau') \qquad (12)$$

where λ is the laser wavelength in vacuum, p=0 for reflection and p=1 for refraction, and τ and τ' are the angles between the surface tangent and the incident and refracted rays respectively.

The rays from each beam are incident upon the sphere at different angles and therefore reach the PD by different optical paths. Neglecting the phase shifts at reflection and focal lines, the phase difference of the two rays is,

$$\delta = \frac{2\pi n_1 d}{\lambda}\left(\left(\sin\tau_1 - \sin\tau_2\right) - p\,n_{rel}\left(\sin\tau_1' - \sin\tau_2'\right)\right) + \delta_0 \qquad (13)$$

where the subscripts (except in n_1) represent beam 1 and 2 and δ_0 is the phase difference of the reference rays at the centre of the sphere. Since the angles τ are fixed by the geometry of the setup the first term in the right hand side of the above equation will be constant for a given diameter d. The second term, δ_0, is the phase difference of the incident beams responsible for the fringe pattern in the classical LDA analysis. This means that the LoC fringes will have the same spacing as the normal fringes, that is,

$$d_f = \frac{\lambda}{2n_1\sin(\vartheta/2)} \qquad (14)$$

and they will be displaced by

$$d_x = \frac{d}{2\sin(\vartheta/2)}\left(\left(\sin\tau_1 - \sin\tau_2\right) - p\,n_{rel}\left(\sin\tau_1' - \sin\tau_2'\right)\right) \qquad (15)$$

When a particle centre is crossing the LoC intersection, that is the LoC control volume, normal to the fringes, the photodetector is seeing the familiar Doppler burst.

3.3. Effective Control Volume

The effective control volume for a certain particle size is the LoC control volume corresponding to the beam sections viewed by the photodetector. For an optical setup focused on the beam intersection centre the effective control volume is the intersection of the two beam' LoC corresponding to the part of the control volume viewed by the PD. In figure 7 the displacement of the LoC of the xy cross section of a control volume is shown for reflecting particles of diameter 0.5 and 1.0 mm (ϑ=1.77°,ϕ=80°, ψ=2° and beam waist radius w_o=49μm). The effective control volume for a photodetector focused to a slice of the control volume at z=0, would be significantly reduced for the larger particles. The control volume is decreasing by the volume corresponding to the "rectangle" ABCD in figure 7. An estimate of this volume is the product of the absolute value of the corresponding vector $\mathbf{D}_{jk}$ multiplied with the cross sectional area of the control volume, cut by a plane normal to $\mathbf{D}_{jk}$ at midpoint. As it will be further discussed in the last

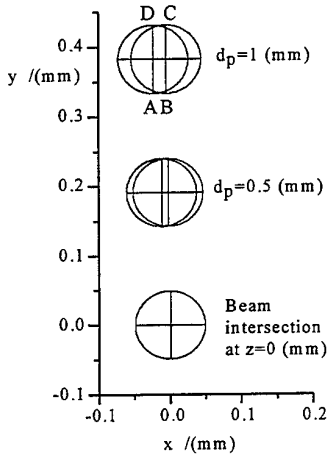

Figure 7. Displacement of the XY cross section of LoC control volume for reflecting spheres of d_p=0.5 and 1.0 mm. (ϑ=1.77°, φ=80°, ψ=2°, w_o= 49μm)

part of this work, the original size of the control volume, for this size class, could be restored if the photodetector was focused about 1mm from the beam intersection centre at the expense of reduced effective control volume for smaller size classes.

3.4. PDA

The spatial displacement of the LoC fringes is used for the evaluation of particle sizes in PDA. A second photodetector at a slightly different position than the first is viewing the LoC fringes displaced by a different distance d_x'. A cross section of the two LoC control volumes and the corresponding LoC "fringes" is shown in figure 8. The spatial distance of the fringes results in a phase difference between the two photodetectors which is

$$\Delta\phi = 2\pi\frac{d_x - d_x'}{d_f} \tag{16}$$

Equation (15) for two photodetectors placed symmetrically about the yz plane at elevation angles $\pm\psi$, leads to the well-known phase difference equations for reflecting and refracting particles (Bauckhage 1988).

$$\Delta\phi = \frac{2\pi d\, n_1}{\lambda}\beta \tag{17}$$

where

$$\beta = \sqrt{2}\left[\left(1+\sin(\vartheta/2)\sin\psi - \cos(\vartheta/2)\cos\psi\cos\varphi\right)^{1/2} - \left(1-\sin(\vartheta/2)\sin\psi - \cos(\vartheta/2)\cos\psi\cos\varphi\right)^{1/2}\right] \tag{18}$$

for reflection and

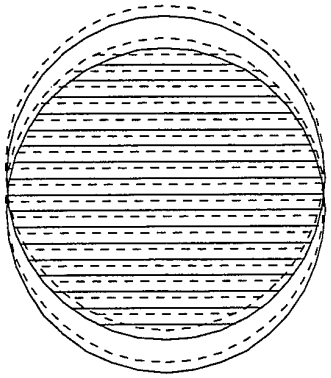

Figure 8. Locus of "fringes" for LDA and PDA

$$\beta = 2\left[\left(1+n_{rel}^2-\sqrt{2}\,n_{rel}\left(1+\sin\frac{\vartheta}{2}\sin\psi+\cos\frac{\vartheta}{2}\cos\psi\cos\varphi\right)^{1/2}\right)^{1/2} - \left(1+n_{rel}^2-\sqrt{2}\,n_{rel}\left(1-\sin\frac{\vartheta}{2}\sin\psi+\cos\frac{\vartheta}{2}\cos\psi\cos\varphi\right)^{1/2}\right)^{1/21}\right] \tag{19}$$

for refraction

The LoC control volume for PDA measurements is the intersection of the two LDA LoC control volumes viewed by the two photodetectors.

4. APPLICATIONS OF THE LOC METHOD

In this part of the work some optical setups are briefly discussed using the LoC methodology. The diagrams used are projections of the LoC of the beams on the zx and zy planes. Sometimes two diagrams are used for the zx plane to allow for the appropriate resolution. Three types of line are on these diagrams, as indicated in the legend of figure 9. The light continuous line is defining the boundaries of the laser beam. The heavy continuous or dashed lines correspond to the boundaries of the beams' LoC for reflection or refraction respectively.

4.1. Forward scatter LDA in water-air bubble flow.

In figures 9,10, the projections of the beams' LoC on the zx and zy planes are shown for a forward scatter LDA measuring in a water-air bubble flow, for bubble size r_p=1mm. The optical setup is described by the parameters ϑ=11.5°, φ=ψ=0°, w_o= 50μm. The projections on the zy plane indicate that the LoC of the beams remain on the beam plane. The intersection points though change significantly as the zx projections indicate. For reflection the LoC of the beams intersect at z=-10 mm and the interference of the transmitted rays is impossible due to the separation of the reflecting cross sections (indicated by vertical line segments on the beams). Refraction gives an effective LoC control

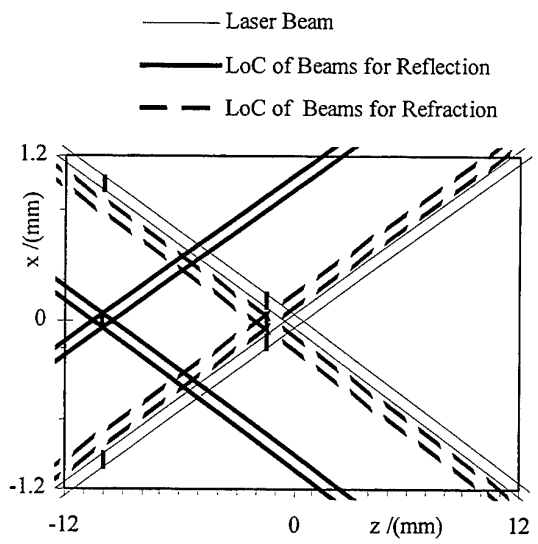

Figure 9. Projections of the beams' LoC on the zx plane for the forward scattering case

volume with maximum cross section at z=1.5mm, not overlapping with the beam intersection control volume. Careful adjustment of the depth of field with the receiving aperture and focusing on the ordinary control volume can be used to eliminate signals from bubbles with radius larger than 1mm. In this way discrimination of phases is achieved and the continuous phase velocity field can be measured using small particles for seeding.

4.2. Increase of the effective volume

The beams' LoC projections of figure 11 are for 1mm diameter bubbles measurements with an optical setup defined by ϑ=1.77°,ϕ=80°, ψ=2° and w_o=49μm. It is the same setup presented in 3.3(figure 7). The zy diagrams show that although the beams' LoC depart from the y=0 plane they remain all on the same plane. The zx diagrams indicate that the intersection of the beam' LoC correspond to scattering cross sections at z=-0.8mm. This means that the original size of the maximum cross section area can be restored for the measurement if the PD is focused at the beams at z=-0.8mm. At this point the beam intersection area is smaller and thus smaller sized particles will be measured with a smaller effective control volume. In fact the effective control volume as a function of particle size will have its larger value for 1mm particles. The usual procedure of aligning the PD in the final stages for maximum data rate may lead in similar situations the focusing to the cross section most suited to the particles in the flow. Of course the real life procedure does take into account the higher scattering effectiveness of large particles which we have left outside the present analysis.

4.3. Gaussian Beam Effect

The setup described by Grehan et al.(1994) is analysed with the LoC method. The setup used for r_p=20μm droplet calculations is described by the parameters ϑ=1.8°, φ=30°, ψ=4.1°, w_o= 40μm. The LoC of the beams projections diagrams are presented in figure 11. The projections on the zx plane show very small changes in x and z coordinates of

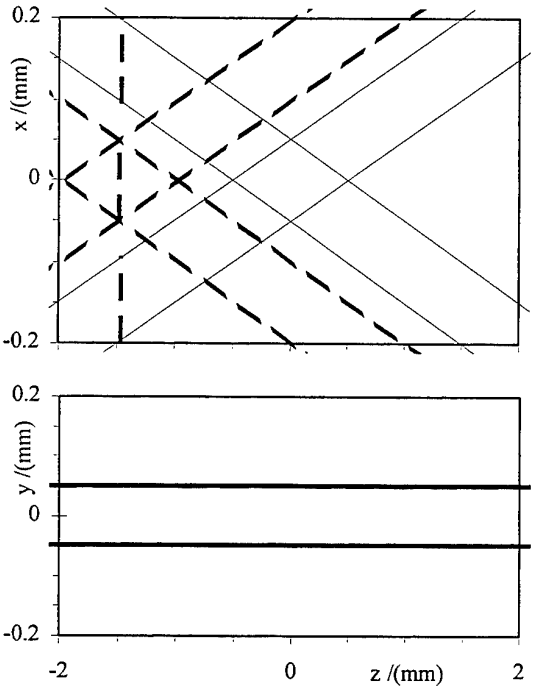

Figure 10. Projections of the beams' LoC on the zx and zy planes for the forward scattering case

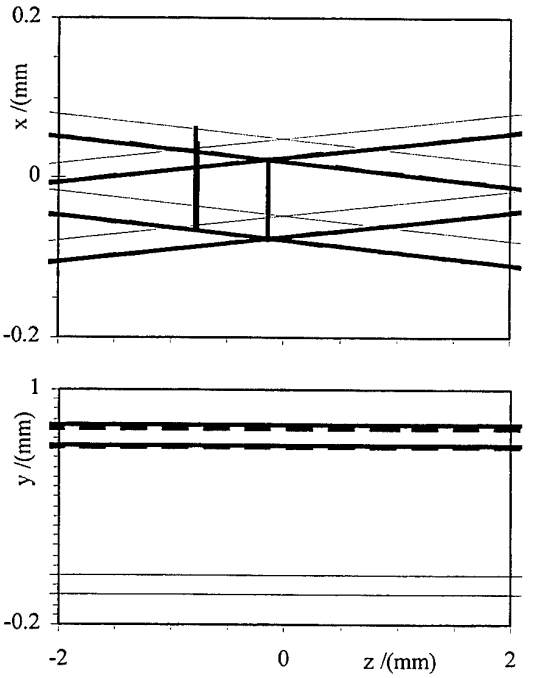

Figure 11 Projections of the beams' LoC on the zx and zy planes for case 4.2

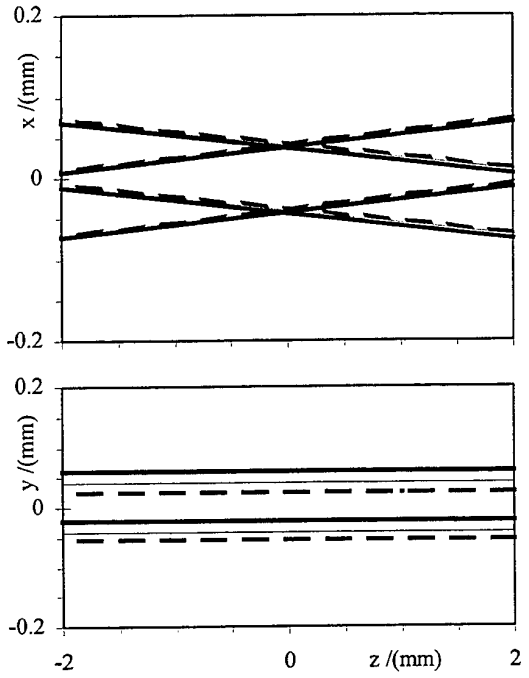

Figure 12 Projections of the beams' LoC on the zx and zy planes for the gaussian beam effect case (droplets).

the LoC. Significant changes are shown though in the y direction. The LoC control volume for reflection is displaced towards positive y, contrary to that for refraction which is displaced towards negative y. This behaviour results in a larger effective control volume formed by the union of the refraction and reflection control volumes. In the intersection of the reflection and refraction LoC control volume the location of the LoF is depending on the interference of four rays thus becoming a function of the relative amplitudes as well as of the phase differences. Although the reflection is weaker at this angle, due to the gaussian distribution of the intensity in the beams the high intensity regions of the reflection LoC control volume corresponding to the low intensity regions of the refraction LoC control volume are responsible for significant discrepancies in phase difference in this region.

In bubble flow the gaussian effect is not so pronounced (Grehan et al. 1994). The setup used for r_p=20μm bubble calculations is described by the parameters ϑ=1.35°, φ=30°, ψ=4.1°, w_o= 40μm. The projections in figure 12 show that this is due to the fact that for n_{rel}<1 the LoC of the beams are displaced in the same direction for reflection and refraction. In this way the relative magnitude of the reflection and refraction components remains almost constant throughout the effective control volume and the phase difference is mainly due to the interference of the refracted rays. The gaussian beam effect is expected to be significant though if the two loci depart, that is if the beam waist radius is decreased or the particle size increased as the ratio r_r/r_p for γ=150° in figure 3 indicate.

4.4. Planar PDA

The planar PDA was suggested as a solution to the

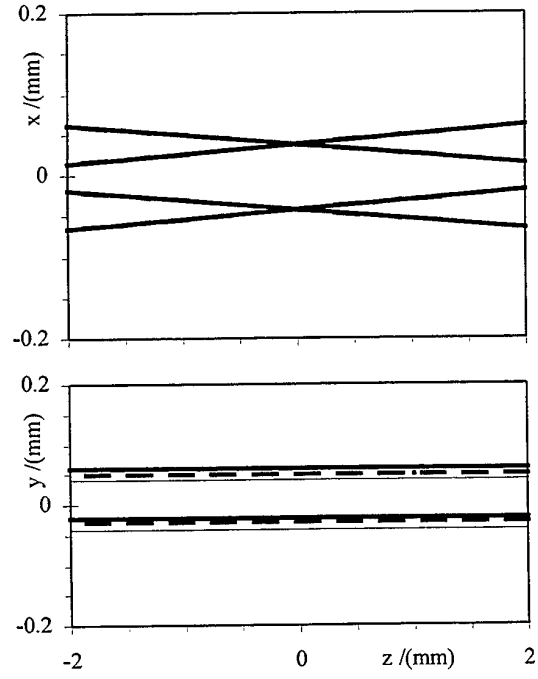

Figure 13 Projections of the beams' LoC on the zx and zy planes for the gaussian beam effect case (bubbles).

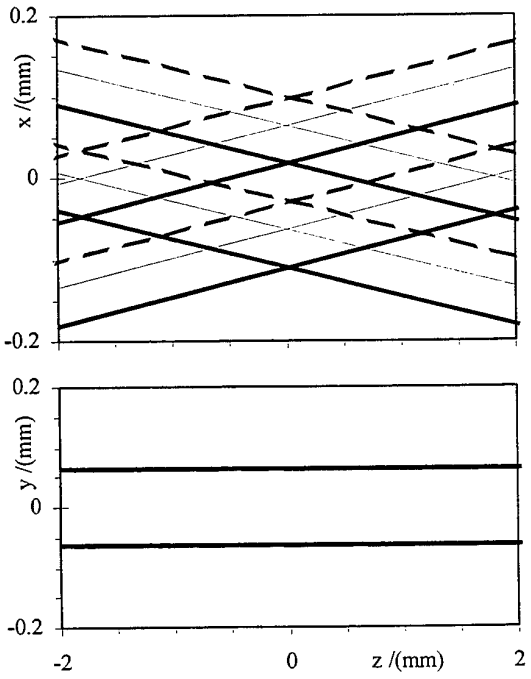

Figure 14 Projections of the beams' LoC on the zx and zy planes for the planar PDA, d_p=95μm.

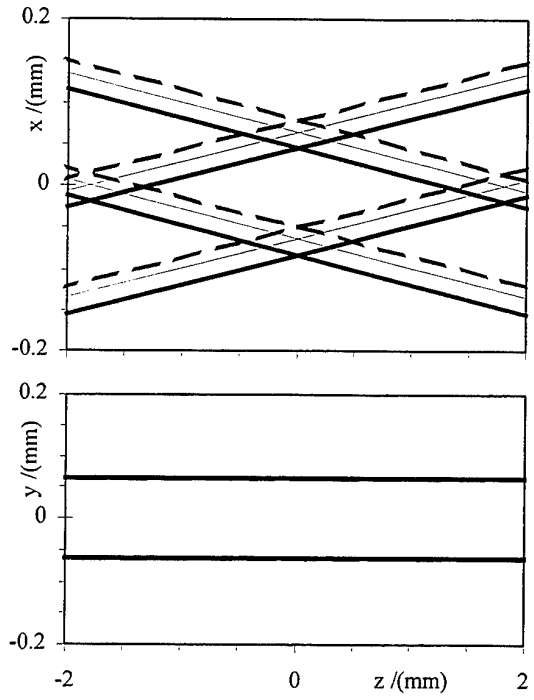

Figure 15 Projections of the beams' LoC on the zx and zy planes for the planar PDA, d_p=40μm.

gaussian beam effect by Aizu et al.1994. The optical setup used is described by the parameters $\vartheta/2$=2.04°, φ=0°, ψ=26.31°, w_o=64μm, and the particles were droplets with d_p=95μm. As the projections of the beam' LoC in figure 14 show, the two LoC control volumes for refraction and reflection are barely overlapping at the edge. The main LoC control volume is that of refraction, due to the higher intensities of refraction at this angle. Adjacent to it is a reflection LoC control volume responsible for the low amplitude second burst appearing in the experiments. For smaller particles the problem of gaussian effect was not alleviated. The projections shown in figure 15 for the same setup and d_p=40μm droplets suggest that the refraction and reflection LoC control volumes overlap significantly. Due to this fact high intensity regions of the reflection LoC control volume destroy the fringe pattern of the low intensity region of the more important refraction LoC control volume. Following the analysis of the first part of the present work it can be calculated that the distance between LoC control volume centres for γ=150° is $1.8r_p$. That is for r_p=20μm, the distance of the centres is 36μm and since the waist radius is w_o=64μm the two LoC control volumes can not be separated.

5. CONCLUSIONS

The LoC method presented in this work seems to be promising in the analysis and optimisation of LDA and PDA optical setups for measurements with larger particles. More specifically:

- It gives a good physical overview of the techniques without being overcomplicated
- It allows a global quantitative understanding of the effects of larger particles on the control volume properties. In this way the choice of the optical setup can be done with the help of soundly based rules.
- It simplifies the investigation of erroneous setups associated with velocity or size measurements due to the distortion of the normal fringe pattern seen by larger particles.
- It sets new standards in the estimation of the active control volume as function of the particle size, which is very important in concentration and particle flux measurements

ACKNOLEDGMENT

The authors gratefully acknowledge the support of the European Union for the presented work.

REFERENCES

Aizu, Y., Durst, F., Grehan, G., Onofri, F. & Xu, T.H. 1993, PDA-System without Gaussian Beam Defects, 3rd Intl. Conf. Optical Particle Sizing, Yokohama, Japan, pp.461-470.

Bachalo, W.D. 1987, The Evolution of Particle Size and Velocity Measurement Technology, 2nd Intl. Conf. on Laser Anemometry-Advances and Applications, Strathclyde, UK, pp. 79-99.

Grehan, G., Gouesbet, G., Naqwi, A. & Durst, F. 1992, On Elimination of the Trajectory Effects in Phase Doppler System, 5th Eur. Symp. Particle Caracterization, Nurnberg, Germany, pp. 309-318.

Grehan, G., Onofri, F., Cirasole, T., Gouesbet, G., Durst, F. & Tropea, C. 1994, Measurements of Bubbles by Phase Doppler Technique and Trajectory Ambiguity, 7th Intl. Symp.on Applications of . Laser Techniques to Fluid Mechnanics, Lisbon, Portugal, vol. 1, paper 18.2.

Van de Hulst, H.C. 1981, Light Scattering by Small Particles, Dover, New York.

A FOURIER OPTICS METHOD FOR THE SIMULATION OF MEASUREMENT-VOLUME-EFFECT BY THE SLIT CONSTRAINT

H. -H. Qiu and C. T. Hsu

Department of Mechanical Engineering
Hong Kong University of Science and Technology
Kowloon, Hong Kong

ABSTRACT

A new method was introduced to analysis the accuracy of sizing large particles in two-phase flows by using a phase-Doppler anemometry (PDA). This method is based on Fourier Optics Theory (FOT) and Geometrical Optics Theory (GOT) to calculate the intensity ratio of refractive and reflective lights scattered by a sphere with a slit constraint. To insure the accuracy of Geometrical Optics method for calculating the light intensity, the calculated results were compared with the results from the simulation based on the Generalized Lorenz Mie Theory (GLMT). The phase jump due to the slit constrain has been found by using this method. This method can also be used to simulate the performance of the dual model phase Doppler anemometry.

1. INTRODUCTION

Laser Phase-Doppler Anemometry (PDA) is nowadays widely used for velocity measurement and particle sizing in experimental studies of dispersed two-phase flows. The new extensions in dynamic range, signal processing and particle property recognition have made PDA one of the most versatile and accurate techniques available today. However, the initial development of the PDA technique was based on the assumption of an uniform intensity in laser beams which is preliminary valid when the particle diameter is small compared with the beam waist. As a result, it suffers from error for sizing large particle due to nonlinearity in the phase/diameter relationship because of non-uniformity in beam intensity. This nonlinear effect is usually called as the Gaussian beam defect. The Gaussian beam defect has been demonstrated by several authors using Geometrical Optics Theory (GOT) (Saffman, 1986; Bachalo and Sankar, 1988; Sankar et al., 1992; Qiu and Hsu, 1995a,b) and Generalized Lorenz Mie Theory (GLMT) (Grehan et al., 1991). For better understanding the trajectory ambiguity and Gaussian beam defect, several numerical tools have been successfully developed for GOT (Sankar et al., 1992; Qiu and Hsu, 1995b) and GLMT (Grehan et al., 1991). Various solutions to minimize the trajectory ambiguity have been proposed for classical geometry (Grehan et al., 1991) or using more original designs such as the planar geometry (Aizu et al., 1993), dual mode geometry (Tropea et al., 1994) and spatial frequency geometry (Qiu and Hsu, 1995). For the effect of the slit image in the measurement volume, previous studies focused on the effect due to intensity distribution, i.e. the vignetting effect from receiving optical aperture and slit (or pinhole) to the effective measurement volume size. However, recent experimental studies by Durst et al. (1994) found that the nonuniform illumination effect due to image boundary of the spatial slit filter in the receiving optics is even more critical than the Gaussian beam defect in the particle sizing. Furthermore, local particle concentration is one of the most important properties for the characterization of two-phase flows. The difficulty for the measurement of particle mass flux and concentration results from the fact that both the particle size and the particle size dependent cross-section of the measurement volume have to be determined accurately. Several methods (Bachalo et al., 1988; Saffman, 1987; Qiu and Sommerfeld, 1992; Sommerfeld and Qiu, 1995) have been introduced to measure these properties by using phase-Doppler anemometry in complex two-phase flows. Nevertheless, these methods are still limited by the nonlinearity in the phase/diameter relationship due to nonuniform incident intensity across the particle surface, when the particle size is not small compared to the focused beam diameter. Apparently, the Measurement Volume Effect (MVE) consists of the Gaussian beam defect and the slit effect, which greatly hinder the accuracy in particle sizing, as well as the particle flux and concentration measurements. There exists no methods to simulate the slit effect so far. Because the magnitude of the MVE depends on the optical geometry and particle trajectory, a better understanding of the mechanism of particle scattering by slit constraint is needed to minimize the nonuniform illumination effect.

2. GEOMETRICAL OPTICS APPROACH

The schematic of a conventional phase-Doppler system is shown in Fig. 1, where the receiving optics consists of a two-detector system. The phase difference ϕ between the two receiving detectors can be determined from the two Doppler signals (see Fig. 1).

If we assume the scattering light as being dominated by refraction, from the geometrical consideration the relation

between the phase and the particle size can be described as following:

$$\phi = C_1 \cdot D \qquad (1)$$

where D is the particle diameter. The phase conversion factor C_1 can be written as (Bauckhage, 1988):

$$\begin{cases} C_1 = \dfrac{4\pi}{\lambda}\left\{\begin{matrix}\sqrt{1+m^2-m\sqrt{2(1+K)}} \\ -\sqrt{1+m^2-m\sqrt{2(1-K')}}\end{matrix}\right\} \\ K = \sin\frac{\theta}{2}\sin\psi + \cos\frac{\theta}{2}\cos\psi\cos\varphi \\ K' = \sin\frac{\theta}{2}\sin\psi - \cos\frac{\theta}{2}\cos\psi\cos\varphi \end{cases} \qquad (2)$$

where m is the particle refractive index and the angles, θ, φ and ψ, are defined in Fig. 1.

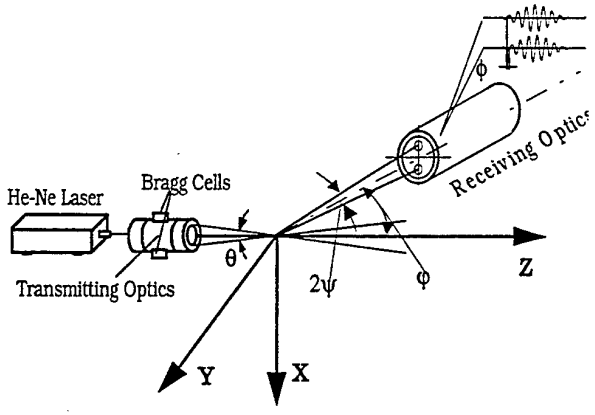

Fig. 1: Geometry of PDA System

Equation (1) is true only when the scattering is dominated by the refractive light. When the particle size is not small in comparison with the laser beam diameter in the measurement volume, the light dominance and then the phase-size relation depend on the particle location. This effect is called *Gaussian beam effect* or *trajectory ambiguity*, as documented by Sankar et al. (1992), Gréhan et al. (1991), Qiu and Sommerfeld (1992), Qiu (1994), and Qiu and Hsu (1995).

The Gaussian beam effect is due to the Gaussian distribution of laser beam intensity in the measurement volume. When the particles pass through a focused beam on different trajectories, it can cause a change in balance between the reflected and refracted lights.

When the particle is at the position A as shown in Fig. 2, light of higher beam intensity will be reflected from a point on the surface of the particle to the receiver whereas light of lower intensity will be deflected by refraction. The reverse situation occurs if the particle is in the position B. When a particle moves from position A to position B, the ratio of the two scattering components changes continually and depends also on the sphere diameter to beam diameter ratio D/w_0. In the general case of PDA, D/w_0 *is* less than one. Therefore, it may be considered as parallel light scattering since the reflection and refraction lights reach the detector at the same time. If $D/w_0 > 1$, the dominant light occurs sequentially depending on the two scattering mechanisms. In either case, the trajectory dependence can lead to significant errors. For example, when the scattering light is dominated by reflection, the phase conversion factor can be written as (Bauckhage, 1988):

$$C_0 = \frac{2\pi}{\lambda}\sqrt{2}\left\{\sqrt{1+K'} - \sqrt{1-K}\right\} \qquad (3)$$

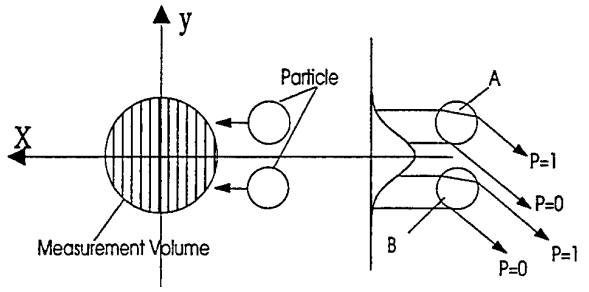

Fig. 2: Demonstration of Gaussian Beam Effect

Because the reflective fringe pattern moves in the opposite direction to that of the refractive pattern, the phase and size relation for the receiving optics is described as:

$$2\pi - \phi = |C_0| \cdot D \qquad (4)$$

Therefore, the detection of the wrong scattering component will occur, leading to the misrepresentation of mid-range size particles as being very large. This has a significant effect on the refractive index measurement.

In fact, because the scattering light from a particle is contributed from a mixture of the refracted and reflected lights, i.e.:

$$I = I_0 + I_1 \qquad (5)$$

the phase and size relations for the receiving optics (see Fig. 1) can be modified as following:

$$\begin{aligned} \phi &= arctg\left(\frac{I_1\sin(C_1D) - I_0\sin(C_0D)}{I_1\cos(C_1D) + I_0\cos(C_0D)}\right) \\ &= arctg\left(\frac{\sin(C_1D) - \frac{I_0}{I_1}\sin(C_0D)}{\cos(C_1D) + \frac{I_0}{I_1}\cos(C_0D)}\right) \end{aligned} \qquad (6)$$

where the conversion factors C_1 and C_0 for the refraction and reflection have been described in Eqs. (2) and (3) respectively. Assuming that the incident beams are in the parallel polarization and have the uniform illumination, the amplitudes of scattering lights as calculated by using the geometrical optical method (Saffman, 1987) are

$$S_0 = \frac{\pi D}{\lambda} \cdot \frac{m^2 \sin\frac{\varphi}{2} - \sqrt{m^2 - \cos^2\frac{\varphi}{2}}}{m^2 \sin\frac{\varphi}{2} + \sqrt{m^2 - \cos^2\frac{\varphi}{2}}} \qquad (7)$$

and

$$S_1 = \frac{\pi D}{\lambda} \cdot \left[1 - \left(\frac{\left(1+m^2\right)\cos\frac{\varphi}{2} - 2m}{\left(m^2-1\right)\cos\frac{\varphi}{2}}\right)^2\right] \times \sqrt{\frac{m^2\left(m\cos\frac{\varphi}{2}-1\right)\left(m-\cos\frac{\varphi}{2}\right)}{4\cos\frac{\varphi}{2}\left(1+m^2-2m\cos\frac{\varphi}{2}\right)^2}} \qquad (8)$$

Considering the trajectory effect as resulted by the Gaussian intensity distribution, the intensity of the scattering light can be written as:

$$I_1 = |S_1|^2 \exp\left(-2\left(\frac{Dm\sin\frac{\varphi}{2}}{2\sqrt{1+m^2-2m\cos\frac{\varphi}{2}}} - y\right)^2 \Big/ \left(\frac{w_0}{2}\right)^2\right) \qquad (9)$$

and

$$I_0 = |S_0|^2 \exp\left(-2\left(\frac{D}{2}\cos\frac{\varphi}{2} + y\right)^2 \Big/ \left(\frac{w_0}{2}\right)^2\right) \qquad (10)$$

$$\frac{I_0}{I_1} = \frac{|S_0|^2 \exp\left(2\left(\frac{Dm\sin\frac{\varphi}{2}}{2\sqrt{1+m^2-2m\cos\frac{\varphi}{2}}} - y\right)^2 \Big/ \left(\frac{w_0}{2}\right)^2\right)}{|S_1|^2 \exp\left(-2\left(\frac{D}{2}\cos\frac{\varphi}{2} + y\right)^2 \Big/ \left(\frac{w_0}{2}\right)^2\right)} \qquad (11)$$

Combining Eqs. (7-11), one obtains

$$\phi = f(m, \theta, \psi, \varphi, D, y) \qquad (12)$$

Hence, for a given sphere, the signal phase is not only proportional to the particle size but also dependent on the particle trajectories. As the particle trajectories are unable to measure, unacceptable errors occur, when Eq. (1) is used for calculating directly the particle diameter without taking the Gaussian beam effect into account.

Besides the Gaussian beam effect, the slit effect was reported as another error source in size, flux and concentration measurements with a conventional phase Doppler anemometer (Durst et. al 1994). The slit effect can be explained by Fig. 3, which describes the slit effect qualitatively.

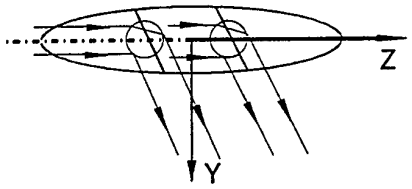

Fig. 3: Schematic Representation of the Slit Effect

The refractive light and the reflective light take different paths. Thus, light will be detected even when the particle center is outside of the slit aperture image. It is also obvious from Fig. 3 that the region of particle center locations allowing the refractive light to be received, is not symmetric with respect to the measurement volume center, but is shifted to the left. When the particle is at a positive z location as shown in Fig. 3, the refractive light is blocked by the slit but the reflective light can still be detected. Since the phase of the reflective light (Eq. 4) is different from that of the refractive light (Eq. 1), the size measurement is incorrect. When the particle is at the negative z location outside the slit window, only the refractive light can be detected as the reflective is blocked by the slit. In this case, the signal phase will be correct. However, as the diffraction by the slit and the finite receiving cone angle due to the non-zero receiving aperture size, the situation is more complicated. As shown in Eq. 11, the ratio of the reflective light to the refractive light will vary according to the position of the particle. The slit effect has been observed experimentally by Durst et al. (1994). A more exact theoretical analysis of this effect is, however, difficult at present since existing programs for computing light scattering, either Mie or GLMT, do not allow for such a slit aperture. To solve this problem, a Fourier optics method for analyzing the slit effect is developed.

3. FOURIER OPTICS METHOD

In this study Fourier Optics Theory (Goodman, 1968) was used to analyze the single-particle scattering model for PDA's receiving optics by considering the slit constraint. To simplify the analysis process, only two-detector system was used and the rectangular receiving aperture was considered. The sharpness of the image strongly depends on the receiving optics aperture size which in this case is given by the width of the rectangular apertures in the mask mounted behind the receiving lens (Fig. 4). This mask is used to determine the elevation angle of the PDA-optics and has slits of width l_y and height l_x. In order to demonstrate the optical transform function of the receiving aperture and the slit, calculations based on Fourier optics theory were performed. Assuming the complex field on object plane (scattering plane) being $t_0(x_0,y_0)$, the complex field across the focal plane behind the lens can be calculated by

$$U_f(x_f, y_f) = \frac{A\exp\left[j\frac{\pi}{\lambda f_1}\left(1-\frac{d_0}{f_1}\right)\left(x_f^2+y_f^2\right)\right]}{j\lambda f_1} \times \int_{-\infty}^{+\infty}\int_{-\infty}^{+\infty} t_0(x_0,y_0)\exp\left[-j\frac{2\pi}{\lambda f_1}\left(x_0x_f + y_0y_f\right)\right]dx_0dy_0 \qquad (13)$$

where λ is the wave length, f_1 the focal length of the receiving lens, and d_0 the distance from the scattering plane to the receiving lens.

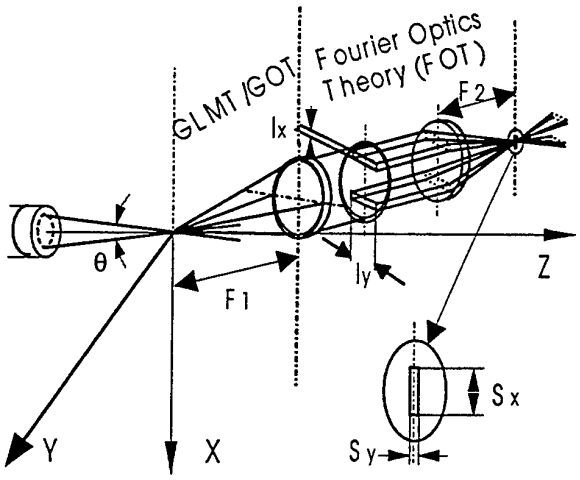

Fig. 4: Optical lay-out of the PDA-system

To include the effects of the receiving aperture we assume the measurement volume length as compared to the focal length is sufficient small and the scattering object is deeply within the region of Fresnel diffraction for the receiving aperture. Such an assumption is an accurate one for a practical PDA configuration. Therefore, the complex field with the lens aperture limit can be described by

$$U_f(x_f,y_f)=\frac{A}{j\lambda f_1}\int_{-\infty}^{+\infty}\int_{-\infty}^{+\infty} t_0(x_0,y_0)P(x_0+x_f,y_0+y_f)\times$$

$$\times\exp\left[-j\frac{2\pi}{\lambda f_1}(x_0x_f+y_0y_f)\right]dx_0dy_0 \qquad (14)$$

where $P_f(x_f,y_f)=\mathrm{rect}(x_f/l_x)\cdot\mathrm{rect}(y_f/l_y)$ is the function of rectangular receiving aperture. The complex field across the slit plane then can be determined by

$$U_2(x_2,y_2)=\frac{A\cdot P_2(x_2,y_2)}{j\lambda f_2}\int_{-\infty}^{+\infty}\int_{-\infty}^{+\infty} U_f(x_f,y_f)\times$$

$$\times\exp\left[-j\frac{2\pi}{\lambda f_2}(x_1x_f+y_1y_f)\right]dx_fdy_f \qquad (15)$$

where $P_2(x_2,y_2)=\mathrm{rect}(x_2/S_x)\cdot\mathrm{rect}(y_2/S_y)$ is the transform function of the slit.

By using inverse Fourier transformation for Eqs. 13-15, the image of the slit can be determined as shown in Fig. 5 and 6.

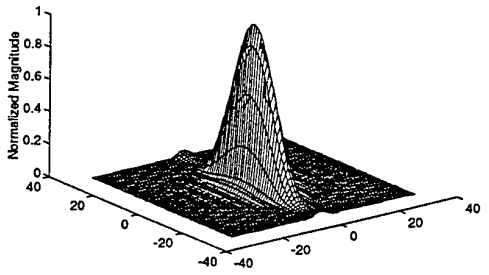

Fig. 5: The Fourier spectrum of a slit through a rectangular receiving aperture

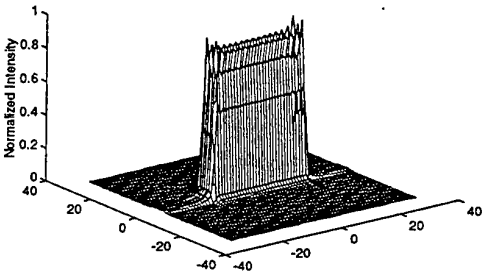

Fig. 6: The image of a slit in the measurement volume

To include the receiving cone angle and the diffraction effects, following geometry will be considered for this study as shown in Fig. 7.

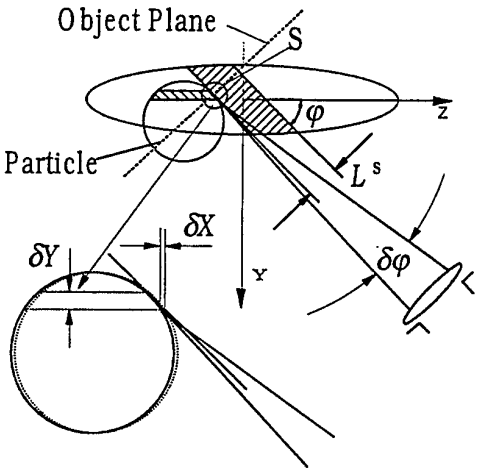

Fig. 7: Enlargement of the effective length of the measurement volume due to the finite size of aperture and the particle

As the length of measurement volume in receiving angle direction is much smaller than the focal length of the receiving lens, the object plane was always assumed on the focal plane, i.e. $d_0=f_1$. By substituting the Eqs. 7-11 into Eqs. 13-15, one can calculate the refractive and reflective light intensities

received by photodetectors separately. Thus, the signal phase of the scattering light can be determined from Eq. 6.

To evaluate the phase accuracy by using Eq. 6, the calculation was compared with GLMT using without slit constraint situation. The GOT method is to determine the phases based on Eqs. 6-11, where only the first order refraction and the reflection are considered. The simulated results obtained from this geometrical optical method and the GLMT method are shown in Fig. 8. The dash line in Fig. 8 represents the received light intensities when a particle is moving along Y direction. The simulation results show that the geometrical optical method is in good agreement with the GLMT method but the calculating speed of this method is about 200 times faster than the speed of the GLMT method. This will give user the possibility to "on-line" optimize the parameters of EPDA.

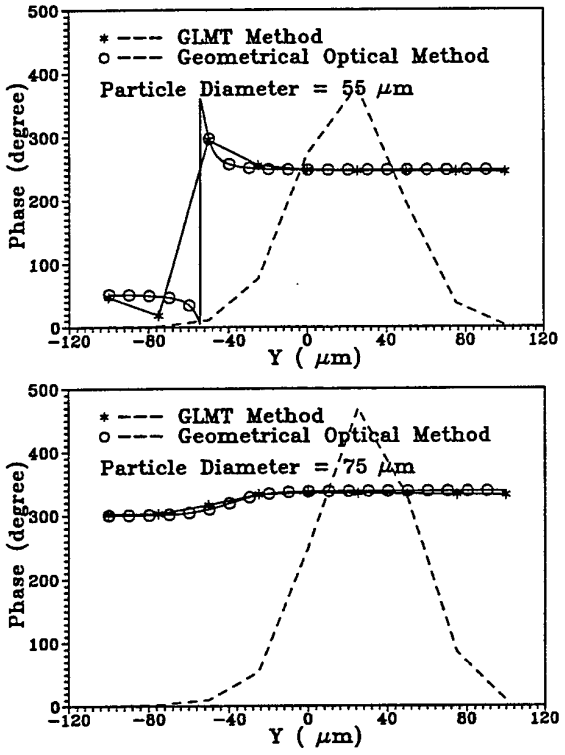

Fig. 8 Comparison of the geometrical optics method and the GLMT method

Furthermore, these results also demonstrate that only the first order refraction and the reflection should be considered. This can greatly simplify the trajectory effect for a better understanding of the physics phenomena such as using the vector diagram (Qiu H. H. and Hsu C. T., 1995). In this study, only geometrical optics method was used.

4. RESULTS OF SIMULATIONS

The parameters of the system geometry as shown in Fig. 4 for the simulation is given in Tab. 1.

Wavelength	0.5145	μm
Beam Waist	100	μm
Transmitting Angle	2.309	degree
Receiving Elevation Angle	3.54	degree
Off-Axis Angle	70	degree
Refractive Index	1.33	
Receiving Aperture 1 ($l_x \cdot l_y$)	10×60	mm
Receiving Aperture 2 ($l_x \cdot l_y$)	10×15	mm
Slit Width	100	μm

Tab. 1 Optical parameters

Different size of the receiving apertures were used to analyze the MVE. To analysis the slit effect, droplets with the diameters of 50 and 80 μm have been simulated along different trajectories when passing through the measurement volume. Two images of the slit for different receiving aperture sizes are shown in Fig. 9.

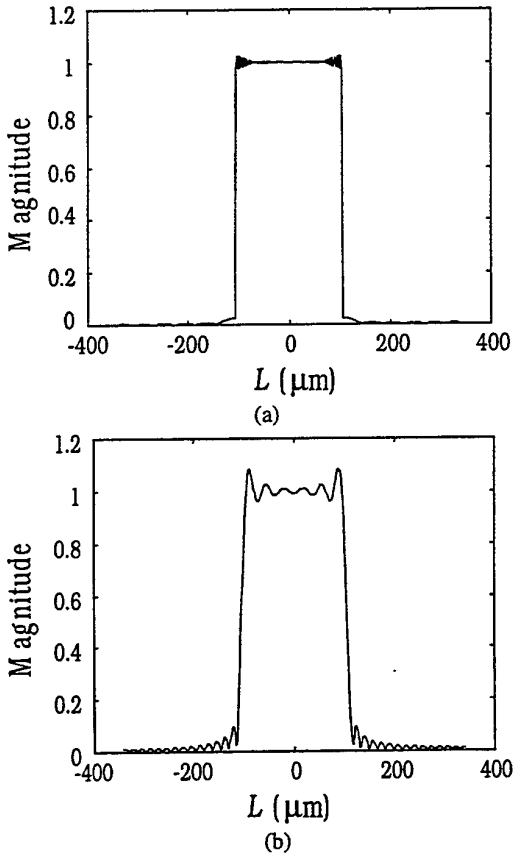

Fig. 9: Image of the slit for different size of receiving apertures

The geometry of measurement volume and the different droplet trajectories are shown in Fig. 10. The simulated results are shown in Fig. 11-15. In Figs. 11 and 12, the 50 μm droplets parallel to the Y-axis pass through the measurement volume along Z = 16. Figures 11 and 12 are for large and small apertures respectively. The same for Figs. 13 and 14,

respectively except that they are for 80 μm droplets passing the measurement volume along z = 5 μm. From these results, the differences in the phase are significant although the signal amplitudes changes only slightly for the cases with and without slit,. It is clear that the phase nonlinearity (phase jump from refraction to reflection) will occur near the center of measurement volume in the case with slit constraint, i.e., the uncertainty due to silt effect not only result from the measurement volume size, but also from the particle size. As the receiving aperture for Figs. 11 and 13 is relative larger than the one in Figs. 12 and 14, the image of the slit in large aperture case is much close to an ideal rectangular window. By comparing Fig. 11 with Fig. 12, Figs. 13 with 14, the signal phase with slit constraint is different from that without slit. However, the effect of receiving aperture size is hardly observable for both particles of 50 and 80 μm as shown in Figs. 11 to 14. It seems to be more critical for large particles as both in Fig. 13 and 14 show the large difference between with and without slit cases.

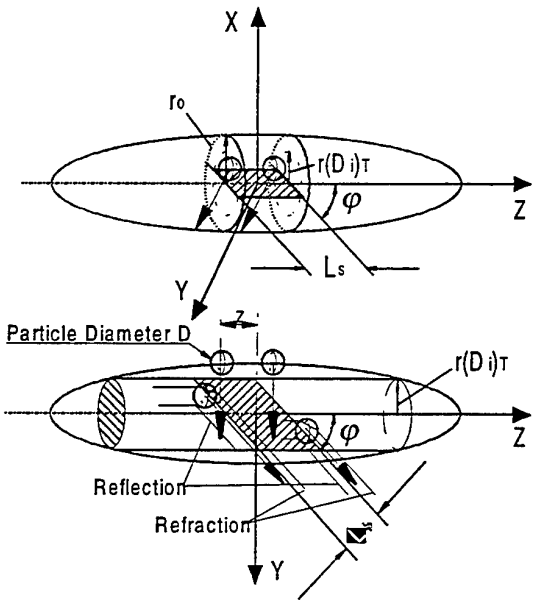

Fig. 10: Geometry of measurement volume and particle scattering model with slit constraint

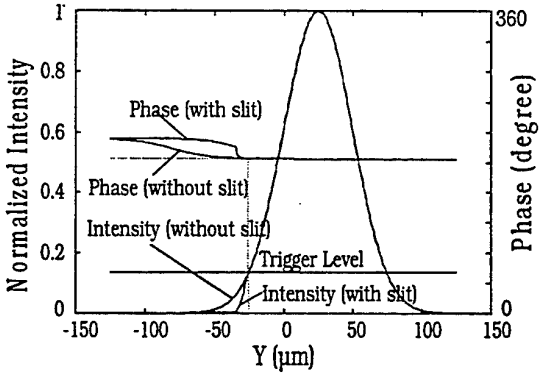

Fig. 11: Comparison of the phase uncertainty with and without slit (Large Aperture Case 10×60, Z=16μm, D=50μm)

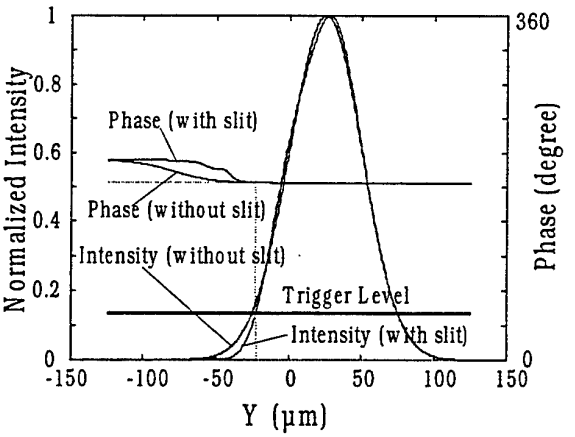

Fig. 12: Comparison of the phase uncertainty with and without slit (Small Aperture Case 10×15, Z=16μm, D=50μm)

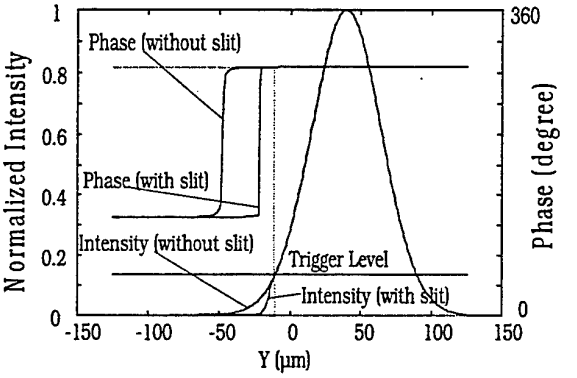

Fig. 13: Comparison of the phase uncertainty with and without slit (Large Aperture Case 10 × 60) Z=5μm, D=80μm)

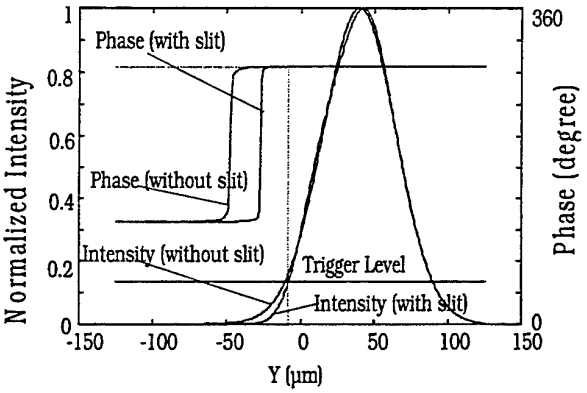

Fig. 14: Comparison of the phase uncertainty with and without slit (Small Aperture Case 10 × 15) Z=5μm, D=80μm)

Fig. 15 shows the results when 80 μm droplets pass through the measurement volume in three trajectories of different Z. The simulated results show that for the particle moving in Z=50+Y/tan(φ) direction (case c), only the reflective light can be received due to the slit effect. Therefore, the phase depends only on the reflection. If the particle is moving in Z= -50+Y/tan(φ) direction (case a), the received light will be dominated by the refraction which consequently determine the phase. For the case b of Z= Y/tan(φ), the signal amplitude and

phase are not affected by the slit. The results shown above demonstrate that the signal phase is trajectory dependent when a slit is used.

5. CONCLUSIONS

Investigation towards the use of a Fourier optics method to analysis measurement volume effect for PDA is conducted. The simulations using this newly developed FOT model can not only yield the better understanding the particle scattering with the slit effect and the Gaussian beam defect, but also the numerical solution for the optical parameter design in minimizing the Measurement-Volume-Effect. The same principle developed here can be also used to simulate the performance of a dual model PDA system.

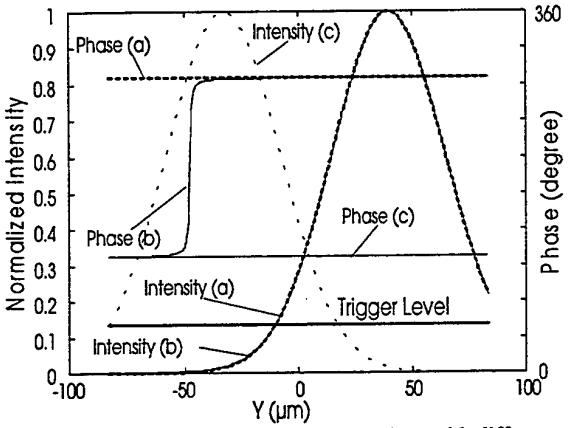

Fig. 15: Comparison of the phase uncertainty with different particle trajectories
(a: Z= -50+Y/tan(φ); b: Z= Y/tan(φ); c: Z=50+Y/tan(φ); D = 80 μm, Slit = 100μm)

6. REFERENCE

[1] Saffman, M. 1986: "The use of polarized light for optical particle sizing", *Proc. 3rd Int. Symp. on Applications of Laser Anemometry to Fluid Mechanics*, Lisbon.

[2] Bachalo, W. D. & Sankar, S. V., 1988: "Analysis of the light scattering interferometry for spheres larger than the light wavelength", *Proc. 4th Int. Symposium on Applications of Laser Anemometry to Fluid Mechanics*, Lisbon paper 1.8.

[3] Sankar, S. V., Inenaga, A.S., and Bachalo, W. D. 1992: "Trajectory Dependent Scattering in Phase Doppler Interferometer: Minimizing and Eliminating Sizing Errors", *Proc. 6th Int. Symp. on Applications of Laser Anemometry to Fluid Mechanics*, Lisbon.

[4] Qiu, H. -H. and Hsu, C. T. (1995a): "Optimization of EPDA Parameters for Accurate Material Recognition in Multiphase Flow", *2nd Int. Conf. on Multiphase Flow* '95-Kyoto, IN1-IN9.

[5] Qiu, H. -H. and Hsu, C. T. (1995b): "A New Spatial Frequency Method For Sizing Large Particles in Laser Anemometry", *ASME Fluids Engineering Summer Meeting and 6th Int. Conf. on Laser Anemometry*, South Carolina, vol. FED 229, 81-88.

[6] Grehan, G., Gouesbet, G., Naqwi, A. and Durst, F.1991: "Evaluation of Phase Doppler System using Generalized Lorenz-Mie Theory", *Proc. Int. Conf. on Multiphase Flows* '91-Tsukuba, 291-294.

[7] Aizu Y, Durst F, Gréhan G. Onofri F, Xu T-H (1993): "PDA systems without Gaussian beam defects", *Proc. 3rd Int. Conf. Optical Particle Sizing*, Yokohama, pp461-470.

[8] Tropea C., Xu T.-H., Onofri F., Gréhan G. and Haugen P. 1994: " Dual Mode Phase Doppler Anemometry", *Proc. 7th Int. Symp. on Applications of Laser Techniques to Fluid Mechanics*, Lisbon, pp18.31-18.3.7.

[9] Durst F., Tropea C. and Xu T.-H. 1994: "The Slit Effect in Phase Doppler Anemometry", *2nd. Int. Conf. on Fluid Dynamic Measurement and Its Applications*, Beijing, 38-43.

[10] Bachalo, W. D., Rudoff, R. C. and Brenda de la Rosa, A. 1988: "Mass flux measurements of a high number density spray system using the phase Doppler particle analyzer", *AIAA Paper* 88-0236.

[11] Saffman,M. 1987: "Automatic calibration of measurement volume size", *Applied Optics*, 26, 2592-2597.

[12] Qiu, H.-H. and Sommerfeld M. 1992: "A reliable Method for determining the measurement volume size and particle mass fluxes using phase-Doppler Anemometry", *Experiments in Fluids* 13, 393-404.

[13] Sommerfeld M. and Qiu, H.-H. (1995): "Particle Concentration Measurements by Phase-Doppler Anemometry in Complex Dispersed Two-Phase Flows", *Experiments in Fluids*, 18, 187-198.

[14] Goodman J. W. 1968: "Introduction to Fourier Optics", *McGraw-Hill.*

SESSION 13

Engines

TURBULENT FLOW FIELD CHARACTERISTICS IN A RECIPROCATING ENGINE: APPROPRIATE CUT-OFF FREQUENCIES FOR CYCLE-RESOLVED TURBULENCE, AN ANALYSIS OF CO-INCIDENT 3-D LDV DATA BASED ON COMBUSTION-RELATED DIMENSIONAL-ARGUMENTS.

P. Dimopoulos*, K. Boulouchos* and G.Valentino**

*) Swiss Federal Institute of Technology (ETH), Zurich, Switzerland

**) Istituto Motori, CNR, Naples, Italy

ABSTRACT

We have performed a cycle-resolved analysis of coincident 3-D LDV data acquired in a motored, single-cylinder, transparent engine. We have thereby used filtering techniques for separating the high frequency ('true' turbulence) from the low-frequency (believed to be mainly due to cycle-to-cycle variation or deterministic phase mismatch of the engine flow field) part of the fluctuations of all three velocity components at selected engine speeds and measurement locations in the combustion chamber.

For that purpose appropriate 'cut-off' frequencies for the filtering processes have been elaborated on the basis of characteristic time scales associated with important sub-processes of turbulent combustion in I.C. engines. Premixed flame propagation in S.I. engines as well as evaporation of a droplet ensemble and chemical ignition delay in diesel engines have been considered as examples of such relevant phenomena.

Results of this analysis show that the frequency distribution of the velocity fluctuations is different for the three velocity components, suggesting a 'second order' anisotropy as opposed to the isotropicity observed with the ensemble averaged quantities. Engine speed dependence of the turbulent intensity relevant for either the S.I. flame propagation or the diesel droplet evaporation is not necessarily linear, as would be suggested by the ensemble averaged values. Conditions of low and high swirl exhibit different behaviours in that, for all frequencies important to engine combustion strong swirl (together with tumble) is associated with higher turbulent intensities, while low swirl yields more low frequency (<100Hz), rather combustion-irrelevant flow motion. The trend of the ensemble averaged quantities is reversed also here with concern to the high frequency part of turbulence. Finally the ensemble power frequency distribution of the turbulent kinetic energy shows a decaying turbulence eddy structure during late compression and early expansion; it moreover suggests that the whole inertial subrange is relevant for the engine combustion processes considered in this study.

NOMENCLATURE

Quantity	Symbol
mean piston speed	c_p
droplet diameter	d
'cut-off' frequency	f_{co}
engine stroke	H
pressure	p
Reynoldsnumber	Re
laminar flame speed	s_L
turbulent flame speed	s_{tf}
temperature	T
apparent activation temperature for the fuel autoignition process	T_A

Greek Symbols

Quantity	Symbol
apparent diffusivity for the fuel evaporation	β
laminar flame thickness	d_f
engine rotating frequency	ν_{eng}
fuel-air-equivalence ratio	Φ

Subscripts

Quantity	Symbol
relevant properties to diesel fuel droplet evaporation	evap
relevant properties to chemical ignition delay in diesel engines	ig.d
relevant properties to premixed engine combustion	S.I.

1. INTRODUCTION

Further improvement of I.C. engines in terms of energy conversion efficiency and environmental compatibility will primarily depend on the ability to control combustion in the appropriate way. For this goal a deeper understanding of the interaction between fluid mechanics and chemical kinetics in the combustion chamber is necessary.

Given the complexity of the hydrocarbon combustion chemistry on one hand and the very high Reynolds numbers of the flow field on the other, memory and CPU requirements of direct flow and combustion computations for real engines exceed the available computer capabilities by several orders of magnitude. Even though further progress in reduction techniques of complex reaction systems is expected and computational costs keep decreasing, turbulence poses a clear limit on what is feasible for practical applications today and the foreseeable future.

In the past 10 to 15 years experimental non-intrusive diagnostic techniques have provided substantial development in our understanding of the turbulent flow features during compression and expansion under mostly motored engine conditions. Together with CFD k-ε based computations at least qualitative information on flow parameters have been acquired, despite the fact that the shortcomings of this model are obvious with respect to anisotropy as well as unsteadiness and non-periodicity of the flow field, that prevail in I.C. engines.

The latter characteristics of the flow field lead to some additional difficulties in the interpretation of experimental data. The turbulent component of a flow parameter cannot be simply defined as the departure from its time-averaged value, as usually done in statistically steady flows. In periodic flows, the concept of phase averaging has proven to be useful. In this approach, a quantity is measured within a small crank angle window around the same crank angle over many cycles. The average over many cycles is the phase (or ensemble) average and the difference between the instantaneous values and the ensemble average is the turbulent fluctuation of that quantity. Under this definition turbulence will not necessarily relate to the random high frequency fluctuations in space or time that exist in every single cycle. Following one of the main conclusions of reference 12: ‚In reciprocating engines features of turbulence must be cycle resolved and the separation into turbulence and bulk motion is relative to the process observed and influenced by the flow'.

In order to overcome these difficulties procedures for cycle-resolved data analysis have been developed in the past years. A common feature of these techniques is the necessity of choosing a more or less arbitrary cut-off scale for distinguishing true turbulence from other low frequent fluctuations of the flow field (like for example cycle-to-cycle fluctuations of the mean flow field, deterministic motions that are not in phase with the piston motion etc.).

In this work we present cycle-resolved analysis of coincident three-dimensional Laser-Doppler-Velocimetry measurements in the combustion chamber of a motored reciprocating engine. We therefore propose appropriate cut-off frequencies (for the first time according to our knowledge) related to

- characteristic time-scales of premixed engine combustion,
- typical time-scales for injected fuel-droplet evaporation in diesel engines as well as to
- characteristic ignition time-scales under diesel conditions.

The paper is organised as follows: We describe first the experimental setup and the signal processing techniques used in this investigation. Then we work out the selection of the relevant 'cut-off' frequencies based on physicochemical arguments. Next we present and comment on the results of our cycle-resolved analysis and finally we summarise with the conclusions.

2. EXPERIMENTAL SETUP

The measurements were carried out in a motored single-cylinder, four-stroke, two-valve engine similar to commercial engines with a flat piston and a flat cylinder head. The optical access was provided through a fully transparent quartz ring forming the upper part of the cylinder liner and simultaneously through the quartz piston crown, which was mounted on an elongated piston-cylinder assembly. A shrouded intake valve in combination with various inlet port configurations allowed for a wide variation of the in-cylinder flow pattern (variation of swirl intensity, while in some cases a tumbling motion was also created). The engine main parameters are summarised in Table 1.

Spatially and temporally coincident three-dimensional Laser-Doppler-Velocimetry (LDV) measurements have been carried out at 600, 1000 and 1500 rpm. This was enabled by modifying a commercial LDV-System using three laser beam pairs and the three main wavelengths of an Argon-Ion Laser (514.5nm, 488nm, 476.5nm). The system operation in the off-axis crossscatter mode assured coincidence of the three signals and resulted also in high signal quality. The effective probe volume dimensions were $70x70x70\mu m^3$. The LDV-signals were processed by three Burst-Spectrum-Analyzers.

A detailed description of the engine and the LDV-System can be found in previous work see references 2, 3.

Table 1: Principal Engine Data

Bore	85 mm
Stroke	92 mm
Compression Ratio	8.0
Combustion Chamber	Pancake, flat piston
Swirl Number	0. - 5.0
Intake Valve Close	220 c.a.d.
Exhaust Valve Open	490 c.a.d.
Engine rpm	600, 1000, 1500
Shaft Encoder Resolution	0.2 c.a.d.

3. DATA PROCESSING

The complex nature of the three dimensional flow field within engines is due to the non-stationary conditions imposed by piston and valves motion. This makes necessary to employ data reduction techniques that should extract parameters of the flow, such as mean motion, turbulence intensity, and temporal as well as length scales, that are required for development and validation of turbulence sub-models in engines. During the last 15 years, two basic approaches have emerged for computing the mean velocity and turbulence: ensemble and cycle-resolved analyses. Data

processing in engines uses the Reynolds decomposition in which the instantaneous velocity is split into a mean (time varying), $\underline{U}(\vartheta, j)$, and a random fluctuating component, $u(\vartheta, j)$:

$$U(\vartheta, j) = \underline{U}(\vartheta, j) + u(\vartheta, j) \qquad (1)$$

where ϑ is the crank angle and j is the engine cycle. For in-cylinder flows, in which the air motion is time-dependent, the mean velocity can be defined using an ensemble-averaged procedure and the turbulence intensity is given by the root mean square (rms) of the fluctuations about the ensemble mean velocity, ref. 2. This definition of turbulence includes all fluctuation frequencies, therefore, cycle-by-cycle variations and any low-frequency instability phenomena are included in the computed turbulence, ref. 4. Efforts have been undertaken to estimate an in-cycle mean velocity and remove the effect of cycle-to-cycle fluctuation from turbulence; All of them rely on the selection of a cut-off frequency , ref. 5, 6, 7, 8, 9, which however up to now has been defined based on rather arbitrary concepts.

Even if this frequency is known, the separation of the mean motion from the effective turbulent flow component requires some careful thought with concern to the validity of the procedure to be used. If for example the flow is on average non-stationary the Fourier-transformed-time series of the considered interval within the engine cycle will not exactly correspond to the turbulent kinetic energy spectrum, but will still include some lower frequency components. For this reason, the phase intervals used in the present work have been selected for each velocity component in such a way, that the temporal variation of the mean motion therein is very small.

Furthermore, in order to estimate the individual cycle mean velocity, $\tilde{U}(\vartheta, j)$, a low-pass digital filter, in the time domain, has been used with a moving-window average shifted through the whole cycle, ref. 10. The length of this window, given by the choice of the cut-off frequency, is used to estimate $\tilde{U}(\vartheta, j)$ by taking a weighted sum over $2L+1$ input values of the instantaneous velocity $U(\vartheta, j)$, at equally spaced angular intervals of $\Delta\vartheta = 0.2°$. The mean velocity of the *j-th* cycle, $\tilde{U}(\vartheta, j)$ using a rectangular weighting function $h(K) = 1/(2 \cdot L + 1)$, is computed as:

$$\tilde{U}(\vartheta, j) = \sum_{k=-L}^{L} U(\vartheta - K, j) \cdot h(K) \qquad (2)$$

Triangular weighting functions have also been used, but they didn't lead to any significant differences in the results. As it can be noted by equation *(2)*, the filtering of the instantaneous velocity data requires that in each crank angle interval ($\Delta\vartheta = 0.2°$) at least one instantaneous velocity value has been acquired. In practice, there are some windows, where either no data at all have been obtained, or the ones acquired have been subsequently rejected for various reasons during data processing and reduction. In order to fill those empty intervals, a cubic spline function has been used to interpolate missing values. For example data whose deviation from the ensemble mean velocity was more than three times the standard deviation (corresponding to the 95% confidence limit of a Gaussian distribution) were rejected. Furthermore, the arithmetic mean were taken for these single intervals ($\Delta\vartheta = 0.2°$) with more than one measurement obtained. The high frequency fluctuation u'_{hf}, referred to the filtered turbulence intensity, has been computed as the rms deviation of the instantaneous velocity about the cycle-resolved mean velocity:

$$u'_{hf}(\vartheta, j) = \left[\frac{1}{N} \sum_{j=1}^{N} \left(U(\vartheta, j) - \tilde{U}(\vartheta, j) \right)^2 \right]^{1/2} \qquad (3)$$

where N is the number of engine cycles. Similarly, the low frequency fluctuation intensity, related to the unsteady mean motion, can be computed as the rms deviation of the cycle-resolved mean velocity from the ensemble mean velocity.

The main contribution of this paper refers to the elaboration of appropriate 'cut-off' frequencies for the filtering method, that are based on characteristic scales of physical or chemical processes, which are of interest in a concrete situation (diesel or S.I. engine combustion). In other words, what is in each case considered to be turbulence or low frequency motion depends on the time scale of the process to be observed and analyzed (ignition, flame propagation, droplet evaporation etc.).

The next section deals with the method of determination of such appropriate 'cut-off' frequencies.

4. DEFINITION OF APPROPRIATE 'CUT-OFF' FREQUENCIES

Key thermal or chemical subprocesses relevant to turbulent engine combustion exhibit a rich variety of modes of interaction among themselves as well as with the flow-field in the combustion chamber. Correspondingly, the range of time, length and velocity scales associated with those interactions usually extends over several orders of magnitude.

In this section we will exemplarily investigate three phenomena important for combustion in engines and work out their characteristic frequencies in order to use them in the cycle-resolved analysis described previously. Those phenomena are simply chosen as representative of many others; they nevertheless allow to make clear the basic concept we employ and the way we use to quantify the characteristic frequencies each time.

The method will be applied to a) the flame propagation through the combustion chamber of S.I. engines, b) the evaporation of large droplets in diesel engine sprays and c) the chemical ignition delay under compression ignition conditions. In principle, characteristic times related to the reaction zone structure in premixed laminar flamelets (i.e. scaling with d_f/s_l) would be also of importance for this investigation. They are however very short ($\sim 10^{-5}$s), so that they might interact, if at all, only with the very high frequency part of the turbulent power spectrum (close to the Kolmogoroff scales). Therefore they are not of interest in

the context of separating low-frequency fluctuations from 'true turbulence', since moreover the LDV system is, due to various reasons, not capable to capture frequencies far beyond the 10kHz range.

Premixed flame propagation in S.I. engines. The characteristic frequency of this process corresponds to the reciproce of the time required for the flame to propagate through the combustion chamber. The idea is that all turbulent eddies with life times larger than the flame propagation time will certainly experienced by the flame front not as locally and instantaneously acting turbulence but rather as a sort of convective, bulk flow motion. Hence:

$$f_{COS.I.} \approx \frac{s_{t_f}}{x_c} \approx \frac{A \cdot u'_{rms}}{x_c} \qquad (4)$$

Typical values of A are around 4 and assuming that $u'_{rms} \approx \frac{1}{2} c_p \approx H \cdot \nu_{eng}$ as well as that combustion is usually terminated during early expansion stages $x_{C\min} \approx H/5, H \approx B$ it can be obtained that

$$f_{COS.I.} \approx 20 \cdot \nu_{eng} \qquad (5)$$

Evaporation of large droplets in diesel engine sprays. Approximate evaporation times of single droplets are given by the following equation

$$t_{evap} \approx d^2/\beta \;, \qquad \beta = \beta_0 (1 + 0.25 \cdot \mathrm{Re}^{1/2}) \quad ....(8)$$

where the effective diffusivity under diesel-engine-TDC conditions is about $4 \cdot 10^{-7} m^2/s$. Reynolds-numbers for the droplets are between 100 and 1000. Sauter-mean droplet diameters of roughly 10μm are typical for diesel sprays on average but the largest droplets (corresponding to 5%-volume percent) are reported to be twice as large, ref. 14. Thus a conservative estimate for the appropriate 'cut off' frequency for the case considered here (largest droplets in the spray yields

$$f_{COevap.} \approx 500 \; s^{-1} \qquad (9)$$

Chemical ignition delay under diesel-engine TDC conditions. Reaction kinetics involved in ignition of hydrocarbons at temperatures between 750K and 1000K are extremely complex and no single characteristic time scale can be deduced from fundamental studies thereabout. Based on both shock tube as well as rapid compression machine experiments however there is considerable agreement in the diesel engine research community that chemical ignition delay times can be approximated, even for multicomponent fuels by an expression of the following type (see refereces 14, 15).

$$t_{ig.d.} \approx A_0 \cdot p^{-n} \cdot e^{T_A/T} \cdot f(\Phi) \quad (10)$$

Using typical values for fuels with appropriate Cetane-Numbers for compression ignition engines we finally get $f_{COig.d.} \approx 1000 \; s^{-1}$.

Thus, we conclude that for the engine combustion subprocesses considered here the relevant 'cut-off' frequencies are all between 200 and 1000Hz. For small high-speed S.I. engines as well as for small, high-duty diesel engines with high compression ratio this range can be extended to about 2000Hz. at the most. Interestingly enough, of the processes that we have looked in this section, only for the flame propagation in S.I. engines does f_{co} depend on engine speed; obviously this is so due to the coupling between the turbulent flame speed and the engine-speed-dependent turbulence intensity. Results of the analysis that we present in the next section refer therefore to 'cut-off' frequencies of 200, 333 and 500Hz (for S.I. combustion, the latter also for droplet evaporation) as well as 1000Hz (for ignition delay and or higher engine speeds).

5. RESULTS AND DISCUSSION

In this paragraph results of radial, axial, and tangen

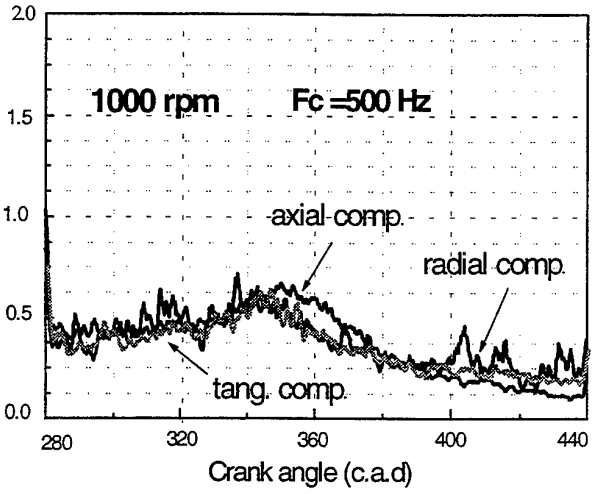

Figure 1. Filtered turbulence intensity [m/s] vs. crank angle at 1,000 rpm for the high swirl condition.

tial ensemble-rms and filtered-rms velocity traces, obtained from sets of data at different engine speeds (600, 1000, 1500 rpm) and two swirl ratios will be presented. 'Cut-off' frequency selection depending on the power spectrum analysis and relevant physical or chemical processes for engine combustion (flame front passage for S.I. engines, ignition delay for D.I. diesel engines and, largest droplet evaporation time in a diesel spray) will be considered. The discussion will be focused on the measurement point located at *r=16 mm* from the cylinder axis and *h=6.5 mm* from the engine head along a diameter located between the intake and exhaust valve, see reference 3.

Radial, Axial and Tangential Turbulence. Figure *1* reports the filtered turbulence intensity of all three velocity components at 1000 rpm, for the high swirl case. For all components the turbulence intensity increases gradually during compression, and reaches a peak at

$\vartheta \approx 350°$, decreasing after that continuously until late expansion.

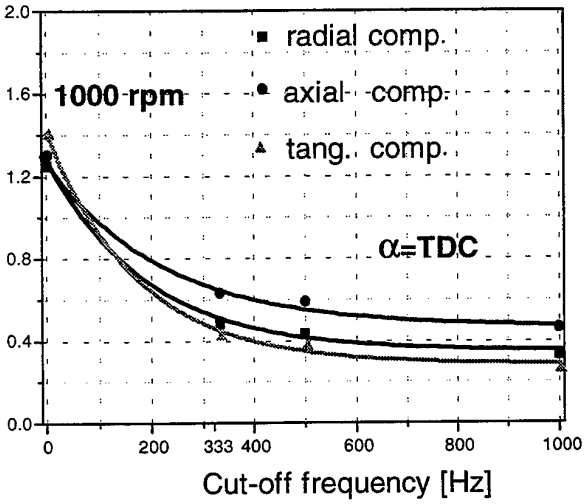

Figure 2. Radial, axial and tangential turbulence intensity [m/s] vs. cut-off frequency at TDC and 1,000 rpm for the high swirl condition.

The peak shortly before TDC is probably due to breakup of tumbling vortices (analysis of mean flow patterns, not shown here, suggests that for these intake conditions substantial tumble is generated and sustained throughout the compression stroke). The temporal trend is almost the same for the three components (radial, axial, tangential), but some degree of anisotropy is apparent around TDC, where the axial turbulence intensity is higher than the radial and tangential and from 400° to 440° c.a. where the radial turbulence intensity is higher than the axial and tangential. The ensemble turbulence intensities however exhibit a different behavior. The trend is highlighted in Fig. 2, that shows the turbulence intensity of all three components as a function of the 'cut off' frequency at TDC. At $f_{co}=0$, (ensemble turbulence intensity) the tangential component is of higher magnitude than the axial and radial ones. However, for all f_{co} relevant for the engine processes examined and taken into account (i.e. $f_{co}=333\text{-}1000s^{-1}$), the axial filtered turbulence intensity is higher than the other two. This result highlights the component-specific contribution of the low frequency cycle-to-cycle ariation to the ensemble turbulence. The latter is therefore not necessary an appropriate measure for the 'true' turbulence with concern to engine combustion.

Influence of Engine Speed. Figure 3 shows the dependence of the radial turbulence intensity on the cut-off frequency f_{co}, at different engine speeds. Although, the dependence of swirl flow and ensemble turbulence intensity on engine speed has been reported frequently in the past, see references 11, 12, 13, it is interesting to specifically observe here the effect of f_{co} on u'_{hf}. The results refer to the low swirl condition at TDC and show an almost linear increase with engine speed for the ensemble turbulence intensity ($f_{co}=0$). For the filtered intensities ($f_{co}>200Hz$) on the other hand, the trend is different in as much as the curve for 1000rpm is collapsing to the one for 600rpm at higher f_{co}'s. For the specific example of the flame propagation in S.I. engines therefore (curve denoted with (*)), no linear dependence of u'_{hf} on engine speeds holds.

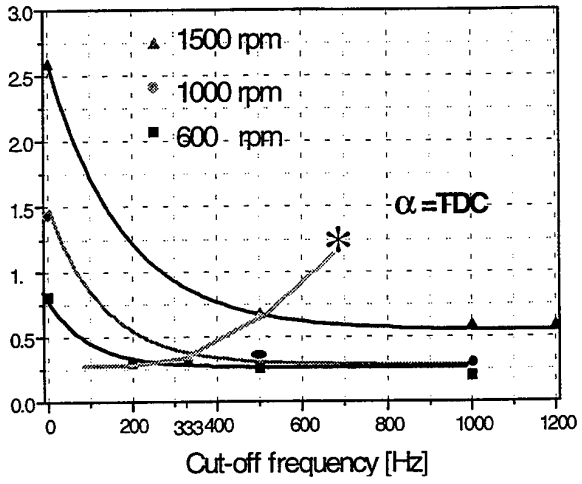

Figure 3. Dependence of radial turbulence intensity [m/s] at TDC on cut-off frequency for the low swirl condition. (*) denotes $f_{co}=f(rpm)$ for flame propagation in S.I. engines.

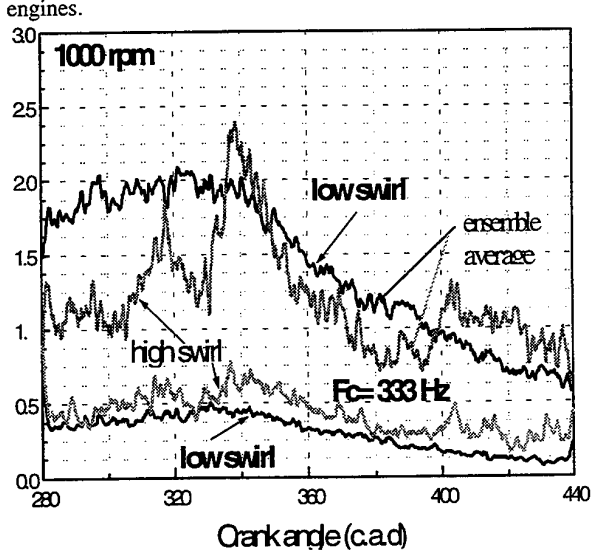

Figure 4. Radial filtered turbulence intensity, [m/s], vs. crank angle at 1,000 rpm for the low and high swirl conditions.

Low and High Swirl. In Fig. 4 we plot the ensemble and high frequency fluctuation intensities oftheradial turbulence intensity, at 1000 rpm. The ensemble turbulence

intensity at the high swirl condition is generally lower than for low swirl and shows an increase for both components (upper curves) during compression and a peak around 345°. This seems to have its origin in the strong radial mean flow component prevailing at that time as is apparent from Fig. 5. At low swirl ratio, on the other hand, there does not exist a significant radial mean flow component and the ensemble-rms velocity shows a monotonic decay from 340° c.a. on.

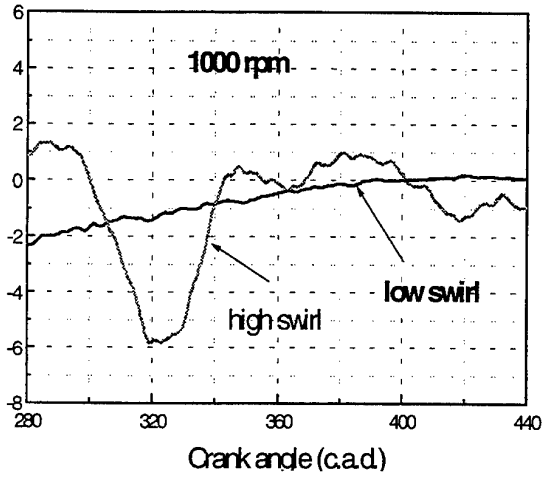

Figure 5. Ensemble mean velocity [m/s], vs. crank angle at 1,000 rpm for the low and high swirl conditions.

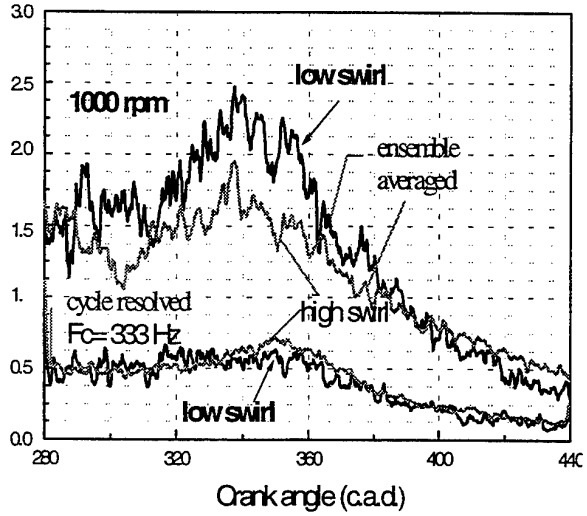

Figure 6. Axial ensemble and filtered turbulence intensities [m/s] vs. crank angle at 1,000 rpm for the low and high swirl conditions.

Interestingly enough the filtered turbulence intensities shown in the lower part of Fig. 4 and corresponding to $f_{co} = 333Hz$, exhibit a different behavior. First the turbulence intensities u'_{tf} are higher with high swirl than in the low swirl case; second, the sharp increase of the high-swirl ensemble turbulence intensity around 335° is not observed for the filtered intensity. This can be interpreted, as indicative of low-frequency radial velocity fluctuations in the high-swirl and tumble case, which is probably associated with phenomena like phase-mismatch and/or axis precession of the tumbling motion for the location investigated. Except for this small crank angle interval however, the general finding according to Fig. 6 is that high swirl tends to homogenize and stabilize the flow pattern in the combustion chamber (i.e. to reduce low-frequency fluctuations) for most of the part of the engine cycle.

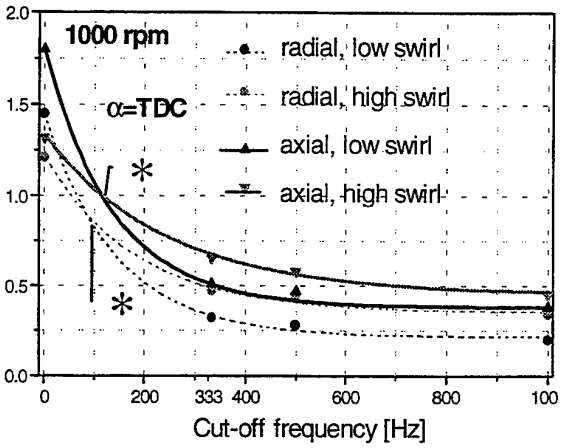

Figure 7. Dependence of radial and axial turbulence intensity [m/s] at TDC on cut-off frequency at 1,000 rpm

Figure 7 is quite interesting in this context too. For both the radial and axial flow components the filtered turbulence intensity is, in contrast to ensemble intensities, higher at the high swirl case. The trend reversal, i.e. the intersection (denoted by (*)) of the high- and low-swirl curves occurs for both components around 100Hz, which for the given engine speed of 1000rpm corresponds to 60° c.a. In any case the u'_{tf} relevant for all considered S.I. and diesel engine processes (i.e. between 200 and 1000Hz) are consistently about 20%-60% higher with high swirl than with low swirl. Beyond this, Fig. 7 suggests that a certain anisotropy of the turbulence intensities between the flow components exists throughout the frequency range (0-1000Hz) investigated.

Another issue of importance and interest in technical flows is the frequency distribution of the turbulent kinetic energy at a certain time and location in the flow field. In Fig. 8 we show the ensemble power spectrum of the instantaneous axial velocity at 1000rpm for the high swirl condition. Four crank angle intervals around TDC (each being 40 c.a.d. wide) have been considered and the associated power spectra are plotted as separate curves for each interval.

Keeping in mind that an important restriction for relevance of power spectra is the stationarity of the underlying process and that this condition is in our case even for

every one of those rather short crank angle intervals only approximately fulfilled, some very interesting features can be observed in this figure.

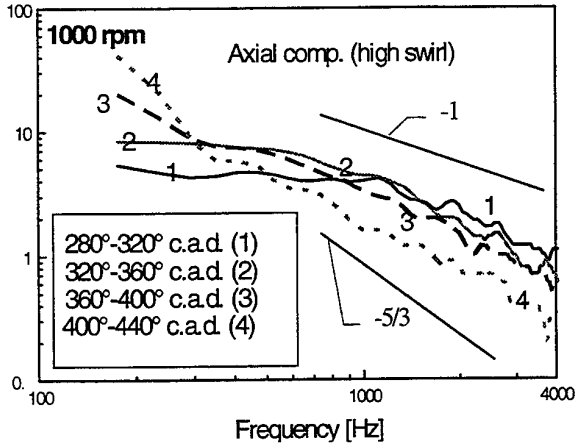

Figure 8. Ensemble power spectrum of the axial instantaneous velocity computed over four adjacent crank angle sectors each of width $\Delta\vartheta = 40°$ c.a., at 1000 rpm for the high swirl condition (TDC=360° c.a.).

First, the frequency distribution of kinetic energy is quite different for the four intervals considered. Energy containing eddies seem to be predominant late during the cycle (intervals (3) and (4)), while in the early intervals more kinetic energy is contained in the high frequency range. In view of the fast dissipation of small, high frequency eddies, this behavior is quite reasonable, since in combustion chamber geometries like the ones investigated, turbulence is generated very early in the engine cycle, i.e. during intake and early combustion. Thus, later on in the expansion stroke mostly large low-frequency, long living structures are expected to dominate the frequency distribution of the turbulent kinetic energy of the flow.

Second, the slope of the power spectrum over frequency is nevertheless similar for all 40° c.a. intervals considered, and lies, plotted in double-logarithmic scale, between -5/3 and even closer to -1. It is interesting to notice, that, while for homogeneous, stationary turbulence with $u' < \overline{U}$ the -5/3 dependence can be shown to be valid for the kinetic energy distribution not only over the wavelength but over frequency of the turbulent eddies too (see reference 6), for the engine case considered here, where the Taylor Hypothesis is not expected to be justified, a slope of -1 is obtained from dimensional arguments.

Finally, as all characteristic frequencies associated with important engine combustion processes have been shown to be not higher than about 1kHz (with the exception of time scales relevant for the inner structure of laminar flamelets or perhaps tiny droplet evaporation), from the power spectrum of Fig. 8 it appears that, at least for the engine speed and the high swirl conditions considered, the whole internal subrange of the turbulent kinetic energy distribution is relevant for turbulent engine combustion.

6. CONCLUSIONS

The main findings of the work carried out so far can be summarized as follows:

- The high frequency spectrum of the velocity fluctuations is different for the three velocity components, while the ensemble averaged fluctuations are rather isotropic.
- The relevant high frequent turbulence intensity for the engine processes taken into account in this study, increase, however not linearly, with increasing engine speed. Though the intensity of the fluctuations about the ensemble averaged mean velocity shows linear dependence on engine speed.
- When high swirl prevails in the cylinder there is a significant increase of the high frequent part of turbulence.
- The ensemble power spectrum shows a decaying turbulence eddy structure during late compression and early expansion.
- A relevant 'cut-off' frequency for premixed engine combustion is about 20 times the engine frequency while for diesel fuel droplets evaporation is of the order of 500Hz. A characteristic 'cut-off' frequency for chemical ignition delay in diesel engines lies around 1000Hz.

7. REFERENCES

1. Bracco, F. V., *International Symposium COMODIA, pp. 1-14*, 1985
2. Dimopoulos, P., and Boulouchos, K., *International Energy Agency, TLM*, 1994
3. Dimopoulos, P., and Boulouchos, K., *SAE Paper 950725*, 1995.
4. Reynolds, W.C., *Combustion Modeling in Reciprocating Engines*, Plenum Press, 1980.
5. Fansler, T.D., and French, D.T, *SAE Paper* 880377, 1988.
6. Fansler, T.D., *SAE Paper 930479*, 1993.
7. Fraser, R.A., and Bracco, *SAE Paper 880381*, 1988.
8. Arcoumanis, C., Enotiadis, A.C., and Whitelaw, *J.H., Proc. I. Mech. E., 205D:177-184*, 1991
9. Bertoli, C., Corcione, F.E., Police, G., and Valentino, G., *International Symposium COMODIA, pp.273-283*, 1985
10. Hamming R.W., *Digital Filters*, Prentice-Hall International, 1989
11. Ikegami, M., Shioji, M., and Nishimoto, K., *SAE Paper 870372*, 1972.
12. Corcione, F.E., and Valentino, G., *Combustion and Flame 99:387-394 (1994).*
13 Margary, R., Nino, E., and Vafidis, C., *SAE Paper 900057*, 1990
14. Heywood, J.B., Combustion Engine Fundamentals, *Mc Graw Hill, New York*, 1988
15. Boulouchos, K., and Kellenberger, M., *FVV-Workshop, Frankfurt a.M.*, 1992

LIF VISUALIZATION OF LIQUID FUEL IN THE CYLINDER OF A SPARK IGNITION ENGINE

Peter O. Witze and Robert M. Green

Combustion Research Facility
Sandia National Laboratories
Livermore, California 94551 USA

ABSTRACT

Laser-induced fluorescence (LIF) has been used to investigate the presence and location of liquid fuel films on the combustion chamber walls of a port fuel-injected engine. A frequency-tripled, Nd:YAG laser provided full-field illumination of the combustion chamber through a window in the piston crown. LIF from liquid-phase gasoline was imaged onto a gated, intensified solid-state camera, and recorded in real-time, synchronous with the engine, on video tape. The technique has been demonstrated on a production, four-valve head, comparing open and closed-valve injection timing. A cold start was simulated by motoring the engine at constant speed before enabling injection and ignition. For open-valve injection, liquid fuel was observed on and around the exhaust valves during the first injected cycle, and combustion occurred by the fourth cycle. For closed-valve injection, a detectable fuel film was seen near the intake valve seat by the fifth cycle, and combustion began by the eighth cycle.

1. INTRODUCTION

In order to meet future, ultra-low emission vehicle (ULEV) regulations in California, significant reductions will need to be achieved in unburned hydrocarbon (UHC) emissions during cold start. Typically, more than 60% of the UHC emissions measured during the Federal Test Procedure occur in the first two minutes when the catalyst is not yet hot enough to efficiently convert the UHC in the exhaust. Also during this period, the temperatures of the port walls, intake valve(s), and combustion chamber surfaces are too low to fully vaporize the liquid fuel. As a result, even for closed-valve, port fuel injection (PFI), liquid fuel can enter the cylinder during intake, and exist in the combustion chamber both as droplets and films on the walls and in crevices. While it is believed that all liquid that remains suspended as an aerosol during compression does vaporize, it has recently become apparent that a significant portion of the liquid film on the walls survives compression heating, and exists there at the time of ignition. Perhaps even more surprising, the thicker of these liquid films appear to survive combustion. Thus, although it is well known that crevices are the main source of exhaust UHC under steady, operating conditions, it is likely that the diffusion-controlled burning of liquid-fuel films is a major contributor to UHC emissions during a cold start.

Three related, yet distinctly different areas for investigation are evident. The first is droplet sizing and dynamics, for which PDA and direct imaging have been widely used in the past few years to study droplets in both the intake port and cylinder. The second is the measurement of film thickness. Based on earlier work on the measurement of cylinder-wall oil-film thickness by Smart and Ford, (1974) and Hoult et al. (1987), Le Coz et al. (1994) and Almkvist et al. (1995) used LIF to measure liquid-fuel film thickness in the intake port, both at a single point and along a line excited by a laser sheet.

The third area of interest is the location of liquid-fuel films, which has been investigated using a number of direct-imaging techniques. Shin et al. (1994) performed high-speed digital-video recordings (1000 fps) of liquid films on the flat head and quartz walls of a square-piston engine. They used indirect lighting to observe the evolution of the films from a 20°C cold start until the cylinder wall temperature approached 100°C (after approximately 2 minutes). The resulting visualizations led them to characterize the in-cylinder liquid film distribution according to the three mechanisms by which they are believed to have formed: 1) A thick film on the valve face and around the seat, formed by a liquid film flowing from the port side of the valve; 2) A thin film on the combustion chamber surfaces from impingement of the droplet stream created by strip-atomization off the valve seat area; 3) Isolated puddles formed by the accumulation of splashed drops created by the intake-valve closing process (literally a squeezing of the liquid in the seat area as the valve closes). The interpretation of the results indicates that the latter two film-types disappear quickly (within one cycle) during the combustion process, even in the early cycles, while the first film-type persists for up to one minute. Because of the low compression ratio of this engine, 6.07, there is some question as to applicability of the results to a more realistic engine with a pent-roof geometry. The fuel used in these tests was indolene, the engine speed was 1000 rpm, and the manifold pressure was 50-60 kPa.

Fry et al. (1995) performed a similar study using a copper-vapor laser as the light source, and a high-speed movie camera to visualize liquid fuel in direct backscatter through a window in the piston crown. They found it necessary to polish the combustion chamber walls, so the liquid fuel would appear as dark shadows. During induction, they determined that wall films formed in the apex area of the wedge-shaped chamber and in the crevices around the intake and exhaust valves. These films remained in these locations during compression and combustion, and then were scavenged from the wall during the exhaust blowdown period, where the liquid was carried directly into the exhaust ports.

Both of these studies used direct, visible-wavelength illumination of the liquid fuel. This can be rather difficult, since the thin fuel films are essentially transparent, and thus their detection is dependent on scattering properties different from those of the surrounding walls of the combustion chamber. Saito et al. (1995) solved this discrimination problem by using fluorescence induced by full-field illumination with mercury lamps. They observed liquid fuel on the walls of a quartz cylinder liner. A high-sensitivity, conventional-speed video camera was used to record the images, implying a framing rate of either 30 or 60 Hz, depending on whether full-frame or single-field recording was used. They were only able to observe films on the cylinder wall; neither the head nor the piston crown were in the field-of view. Their results show considerably greater wall-wetting for open-valve injection (OVI) as compared to closed-valve injection (CVI), and greater wall-wetting for a conventional injector as compared to an air-assisted injector. During the compression stroke, the fuel that was deposited on the cylinder wall during induction is scraped off by the top ring and forced into the top-land crevice. As top-dead-center (TDC) is approached and combustion occurs, the increased pressures force liquid fuel into the second land, where it mixes with oil. With the beginning of the expansion stroke, the liquid fuel in the top-land is laid-down on the cylinder wall as a thin film, with far greater area than it occupied during induction. The authors note that this thin film is not consumed by combustion, but rather that it vaporizes as unburned HC when the pressure falls in the exhaust stroke.

Felton, et al. (1995) used a similar approach to observe liquid-fuel films on the walls of the intake port. They used a frequency-tripled Nd:YAG laser as the excitation light source, which entered the intake port through a quartz periscope. A small lens expanded the laser beam to illuminate the back walls of the port. The LIF signal was collected with a fiberscope and imaged onto an intensified CCD camera. Because of the slow framing rate of the camera, a single image was obtained each engine cycle, recorded either directly onto video tape or into computer memory. The results obtained for a cold start from 20°C showed a continual increase in the liquid area indicated by the fluorescence image for about 30 seconds. By integrating the intensity of the LIF signal over a selected region of each image, a semi-quantitative curve of signal intensity versus time was obtained. This curve reached a maximum at about 2 minutes, and then fell to about 60% of the maximum at about 4 minutes; it stayed constant at this value until 8 minutes, when it fell again to a value of 10% of maximum at 11 minutes. No explanation of the plateau at 60% is given, but it may represent a condition where the wall temperature in 40% of the integration region has exceeded the high-end boiling point of the fuel.

The significance of the results obtained with this technique, together with its simplicity and ability to clearly discriminate liquid-fuel films from dry surfaces, inspired us to apply it to image liquid films on the combustion chamber walls, as observed through a window in the piston crown. Of particular interest are differences in the amount and location of liquid-fuel films during a simulated cold start for CVI versus OVI.

2. ENGINE FACILITY

The engine configuration, shown in Fig. 1, consists of an extended cylinder with transparent piston for optical access from below. The piston is unlubricated and uses a bronze-loaded Teflon® rider ring to prevent it from directly contacting the cylinder wall. The top ring is a sealing ring made of Vespel®, a graphite-filled polyimide material. The sapphire window in the piston provides optical access to 80 percent of the cylinder. The head is a complete, unmodified 1994 General Motors Quad-4, with the #3 combustion chamber aligned with the single cylinder block, and the compression ratio is 9.5. Both the coolant and oil systems are active along the entire length of the head, but all fluid passages that would normally mate with the block are plugged,. A closed-loop system maintains the coolant temperature to a preset value, within a few degrees. Finally, an uncooled piezoelectric pressure transducer is installed, flush with the combustion chamber wall.

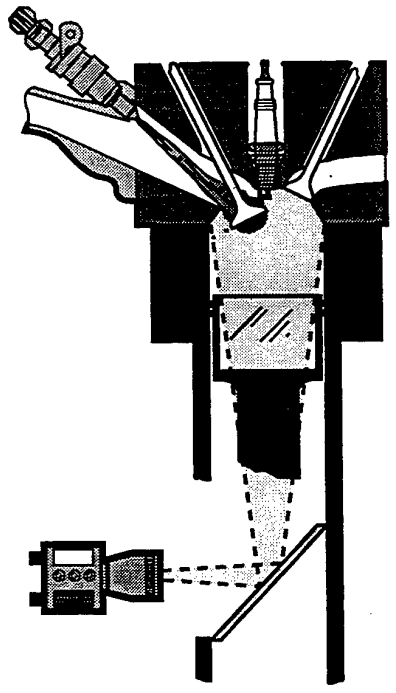

Fig. 1 Single cylinder engine with extended piston for optical access. The camera and laser illumination share the same field-of-view via a dichroic mirror.

The engine was fueled with commercial, 87 octane gasoline injected through a standard, single-spray fuel injector (with a nominal 12° cone angle). As opposed to the stock fuel rail, we used a 'once-through' system, where the fuel was supplied from a one-liter vessel pressurized with nitrogen to 270 kPa.

The cold start simulation consisted of motoring the engine at a constant speed, and then initiating fuel injection and ignition. A 300 rpm, wide-open-throttle condition was used in the current work for ease of implementation and demonstration of the new diagnostic techniques we are using. With the exception of engine speed, all engine and data acquisition events are controlled by a dedicated PC. An absolute-position, shaft encoder attached to the intake camshaft, with one crank-angle-degree (CAD) resolution, provides the crankshaft position for the engine controller. Start-of-fuel-injection, ignition, laser firing, and image-grab timing are all performed in the crank-angle domain, as determined from the shaft encoder. End-of-fuel-injection, however, and thus injection duration, is controlled by a timing board in the computer. This is done to assure that the same amount of fuel is injected each engine cycle, irrespective of instantaneous changes in engine speed that occur when combustion first begins, and when combustion is unstable due to misfires and slow or partial burning cycles.

While it is straightforward to record LIF images directly into computer memory using a standard frame-grabber interface board, the large number of images involved in a typical cold-start test sequence make the use of real-time video-tape recording preferable. One image is obtained by the frame grabber each engine cycle, and is continually output to tape at normal video framing rates until the next image is grabbed. We have found that the playback of the video recording is much more useful if it is annotated with the cycle number of each image and the combustion chamber geometry, showing the location of valves, spark plug, and squish areas. We therefore have developed a software package that utilizes an overlay-plane capability with the frame-grabber board (Coreco Oculus TCX) that, in effect, creates a mask that overlays the LIF images. Only the portion of the mask that corresponds to the clear aperture of the window in the piston is transparent, permitting display of the LIF image. This blocks all irrelevant parts of the image outside the field-of-view through the window. The mask consists of a line drawing of the combustion chamber and is positioned and scaled to align with the actual head configuration.

3. OPTICAL SETUP

The optical system we used for the LIF imaging experiments is illustrated schematically in Fig. 2. The light source for excitation was a frequency-tripled, Nd:YAG laser operating at 10 pulses/sec and 30 mJ at 355 nm. The laser pulses were synchronized to the engine crank-angle via the shaft encoder and engine controller. The laser output beam was expanded into a light field by lens L_1, a spherical, plano-concave lens with a focal length of -100 mm. This expanding light field was then directed into the engine cylinder through the window in the piston by mirrors M_2 and M_3, such that the laser light completely filled the window aperture to thecombustion chamber. The fluorescence emission retraced the same optical path

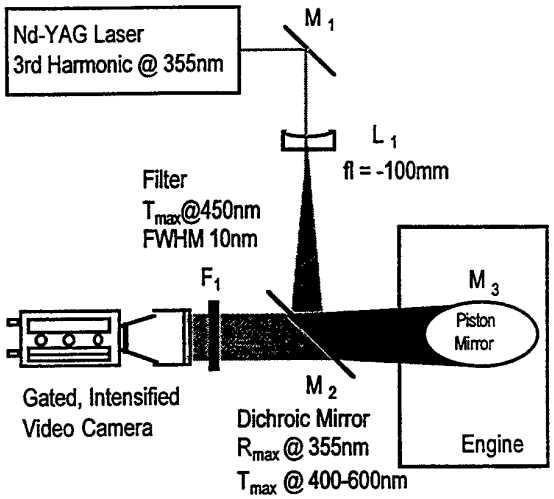

Fig. 2 Optical setup for full-field LIF imaging of the combustion chamber.

as the laser beam until it reached the dichroic mirror M_2, where it passed directly through to the video camera.

The dichroic mirror M_2 was coated for maximum reflectance at 355 nm to reflect the incident laser light field, and for maximum transmittance between 400 and 600 nm to transmit the fluorescence emission. The piston mirror M_3 was coated with UV-enhanced aluminum having a reflectivity of 90% at 355 nm. This coating is adequate because the energy density of the laser light is reduced by the expansion of the field to a level below the damage threshold. Between 400 and 600 nm this coating has a reflectance of 90 to 95%, which is quite acceptable for reflecting the fluorescence emission. The light entering the camera lens was passed through a narrow band-pass filter to reject extraneous background. The maximum transmission of the filter was at 450 nm, with a FWHM of 10 nm.

The intensified video camera captured the image on a 340 by 480 CCD array with a 105 mm, f/2.8 camera lens. The intensifier was gated synchronously with the laser Q-switch signal, and the LIF images were obtained with a PC-based video frame grabber also synchronized to the engine by the engine controller.

4. FLUORESCENCE CHARACTERIZATION

A variety of compounds have been used to observe LIF from fuel films in engines, with the choice generally depending on the application. For quantitative measurements of fuel-film thickness, Almkvist et al. (1995) doped isooctane with 3-pentanone, selected for its close match with the boiling point of this single-component fuel (99°C). Le Coz et al. (1994) performed a comprehensive study of the liquid/vapor phase equilibrium of isooctane and six potential dopants, and showed that it is not adequate simply to match the boiling points, since when mixed with isooctane at low concentrations, the effective boiling point of the dopant is reduced. They obtained their best results using dopants with boiling points of about 130°C.

For multicomponent fuels, it is far more difficult to perform quantitative LIF because of the different boiling temperatures. However, if the fluorescing molecule has a boiling point near the high-temperature end of the fuel distillation curve, then it can be argued that LIF can be used to measure the shape and area of liquid films. In addition, if the area of the liquid film is always growing during the period of measurement, then a dopant with an even higher boiling point can be used, although it might be necessary to clean surfaces of residue between tests. Saito, et al. (1995) used Xanthene dye added to an unspecified fuel to distinguish it from oil films. Xanthene has a melting point of 102 °C and a boiling point of 310 °C, which suggest that it will leave a residue if it is not consumed by combustion. Felton et al. (1995) used Unocal RF-A test fuel, which for visual identification purposes contains Oil Purple M Liquid dye. They found that the fuel fluoresced strongly when excited by UV light, and speculated that the dye was the source of the fluorescence. For the dye concentration used in RF-A, they observed no residual fluorescence signal from intake port walls after complete evaporation of the fuel. Because their experiment to observe liquid-fuel film was quite simple and yet successful, we chose to investigate the use of this dye as a fluorescing dopant for regular grade gasoline.

In order to understand better the fluorescence characteristics of the various liquids that might be encountered in the combustion chamber of our engine, we made use of a luminescence spectrometer. This device allows the investigation of fluorescence characteristics of liquid samples under tightly controlled conditions. Spectral excitation scans can be run at a fixed emission wavelength; or spectral emission scans can be run at a fixed excitation wavelength. For the purposes of the current work, we performed emission scans at an excitation wavelength of 355 nm to examine isooctane, a single-component, straight-chain, paraffinic fuel; 87 octane gasoline (direct from the pump), a multicomponent fuel containing various, unknown additives; 10w-30 motor oil, a potential, in-cylinder contaminant of liquid fuel films; and Oil Purple M Liquid dye, a fuel additive used to provide color for visual identification of special fuels, and a substance that has been suspected of yielding strong fluorescence emissions when excited with UV light.

We chose to examine isooctane because it is a pure, single component liquid known to have a weak fluorescence response. This is confirmed in Fig. 3, where we have plotted the emission scans for pure isooctane, isooctane with enough dye added to create an obvious purple tint, and isooctane with a small quantity (<5%) of motor oil dissolved in it. The pure isooctane exhibits only a weak fluorescence emission between 360 and 600 nm, with a small peak near 395 nm. The addition of the dye caused a small but insignificant increase in the amplitude of the fluorescence emission, and the spectral characteristics were unchanged. On the other hand, oil dissolved in the isooctane caused an order-of-magnitude increase in the amplitude of the signal, along with a change in the spectral characteristics. Note that the isooctane peak at 395 nm can still be observed along with the strong oil peak at 390 nm.

Having obtained the isooctane results described above as a reference, we next performed the same series of tests with 87 octane, "pump" gasoline. These results are

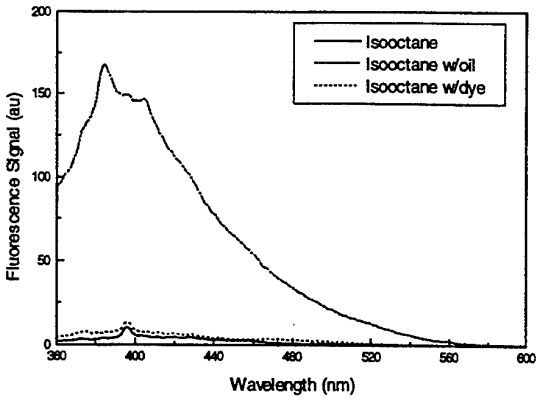

Fig. 3 Fluorescence signal of pure isooctane and with oil and dye added.

illustrated in Fig. 4, where the fluorescence from straight gasoline (without oil or dye) is seen to be many times stronger than that from pure isooctane. The spectrum exhibits a double-peaked behavior, with a minor peak at 410 nm and a major peak at 450 nm. Notice also that the peak fluorescence signal from gasoline is a factor-of-two stronger than that from isooctane with oil dissolved in it, and at 450 nm the ratio of their signals is about six. However, the most interesting aspect of these data is that the dissolution of small amounts of dye or oil (the same amounts as used with the isooctane) only has the effect of reducing the magnitude of the fluorescence emission. The fact that the characteristics of the fluorescence emission spectra are similar indicates that the oil or dye dissolved in the gasoline only absorbs the excitation light at 355 nm (reducing the excitation of the gasoline), and does not absorb or trap the LIF, since the latter would be wavelength dependent. Furthermore, while Fig. 3 showed fluorescence due to oil and dye dissolved in isooctane in the spectral region from 360 to 600 nm, Fig. 4 indicates that it is insignificant compared to the fluorescence from gasoline alone.

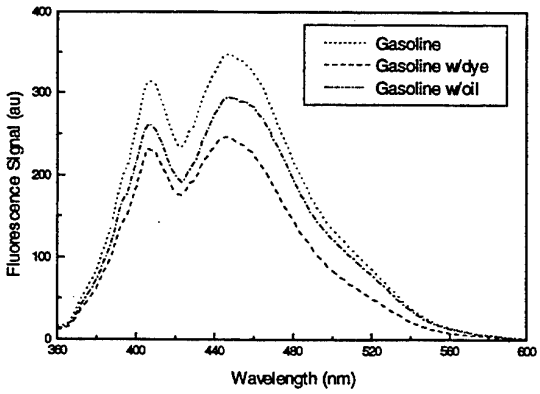

Fig. 4 Fluorescence signal of pure 87 octane gasoline and with oil and dye added.

The above observations lead us to conclude that gasoline alone will provide a good fluorescence signal to locate the presence of liquid inside the engine intake port or combustion chamber, without the need to add dopants. Furthermore, if the fluorescence emission is high-pass filtered above 440 nm, the major peak of the gasoline fluorescence should be observed without serious conflict with fluorescence from engine oil that is either pure or dissolved in gasoline.

Finally, we performed two simple studies in controlled environments to examine the fluorescence from residue left behind after the evaporation of gasoline. In the first test, we placed several drops of liquid on thin quartz disks and allowed the liquid to evaporate by leaving the disks in an oven at 75 °C for 15 hours. We tested three liquids - gasoline, pure isooctane and isooctane with enough dye added to give the liquid a slight purple tint - with the objective of identifying how the residues respond to excitation from laser light at 355 nm. The results revealed that the residues from pure isooctane and isooctane with dye produced insignificant fluorescence, while the residue from gasoline fluoresced enough to suggest that it could confuse interpretation of images of liquid fuel films.

In the second test, we simulated the repeated wetting and evaporation of gasoline from a valve. We placed a production valve in a holding device with the valve face oriented upward. A liberal amount of gasoline was applied to the valve face, and then the valve was placed in an oven at 170 °C. As soon as the valve reached a temperature that evaporated the fuel, a second film of fuel was applied. This was repeated three times, and then the valve was baked for 20 minutes. We then exposed the valve to 355 nm laser light, and observed fluorescence from the polished surfaces of the valve face; a yellowish film was also visible to the unaided eye. Somewhat to our surprise, the unpolished, rough-casting region in the center of the valve did not fluoresce except in one small region. This result is consistent with the observation of Felton et al. (1995), who found that they did not need to clean the intake port walls between cold start tests using LIF.

5. CONTROLLED SIMULATION

Before beginning the LIF experiments in the operating engine, we decided it would be useful to set up a benchtop simulation for evaluation and refinement of the technique under controlled conditions. To this end, we positioned a cylinder head on an optical bench and used the optical system described above to look at several different aspects of the problem under static conditions, without the complications of the transparent piston, periscope mirror and an operating engine.

The first issue we addressed was the primary background signal. This includes elastic scattering of laser light and broadband LIF from combustion chamber surfaces. The image illustrated in Fig. 5a is a typical example of these sources of background, where the two intake valves are at the top. The brightest areas in the image are the smooth, machined surfaces of the squish region between the intake valves, the apex of the pent-roof head, and the sparkplug. The source of this light is most probably a combination of reflected laser light and LIF from deposits and soot. To create Fig. 5b, we placed a narrow bandpass filter (maximum transmission (T_{max}) at 450 nm, with 10 nm FWHM) in front of the camera, which effectively rejected most of the extraneous background signal. The remaining signal seen in Fig. 5b is due to oil that enters the ports through the valve guides and collects around the valve seats. Prior to performing these experiments, we carefully cleaned the intake valve seat in the upper left of the image to verify the cause of this effect. The total lack of signal from the clean valve seat indicates that

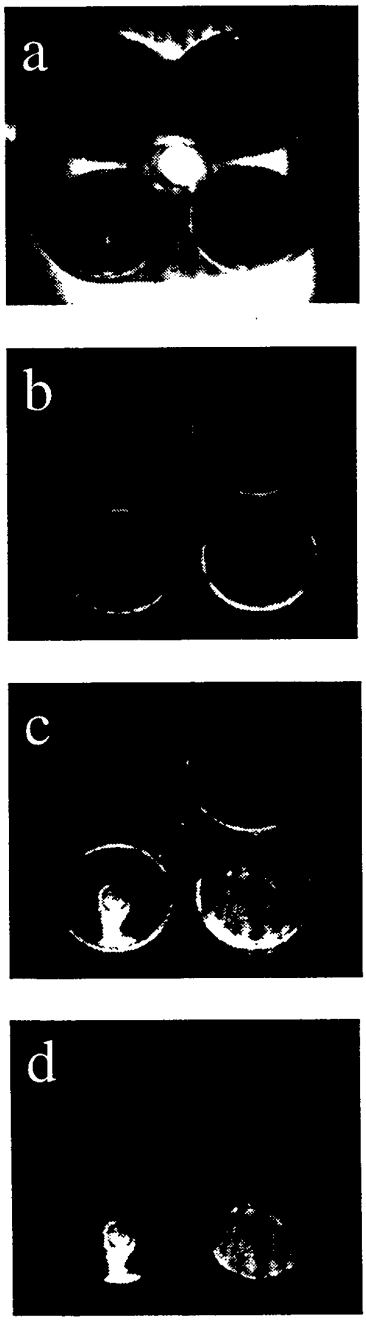

Fig. 5 Effects of band-pass filtering and background subtraction

oil and/or other contaminants do, indeed, cause background in the images. From these results, we concluded that the filter would remove most of the primary background signal, but we would still have to use background subtraction to remove the secondary background signal and further enhance the quality of the images.

In order to verify that background subtraction could reduce the secondary background signal without seriously affecting the desired data, we created a simulation of liquid films on two of the valves and recorded an LIF image. We placed several drops of oil on the lower left valve and several drops of gasoline on the lower right valve. Due to the high surface tension of the oil, it formed a thick, localized film on the face of the valve, while the lower surface tension of gasoline allowed it to form a thin film that spread over most of the lower half of the valve face. The LIF image of these films is shown in Fig. 5c, and illustrates a strong signal from the thick oil film along with a somewhat weaker signal from the thinner gasoline film. We removed the background from the liquid-film image by simply subtracting the image in Fig. 5b from the image in Fig. 5c. The result is shown in Fig. 5d. Clearly, the background subtraction procedure has enhanced the data without any serious detrimental effects.

6. ENGINE RESULTS

LIF images were obtained for two test sequences involving OVI and CVI of a stoichiometric mixture. End-of-injection was at 440 CAD and 700 CAD, respectively, where 720 CAD is TDC of compression. We recorded the cylinder pressure and used it to compute the gross, indicated-mean-effective-pressure (IMEP). These results, which are summarized in Fig. 6, indicate first-measurable heat release in cycle #4 with OVI, while with CVI this did not occur until cycle #8 or 9. The large negative IMEP in cycle #11 for CVI is the result of flashback into the intake port that occurred when the intake valve first opened. Combustion in cycle #10 was probably complete, but somewhat slow, leading to residual gas that was severely underexpanded and unusually hot at the time of valve overlap. This resulted in ignition of the fresh charge in the intake port, leading to low-density products filling the chamber in cycle #11. This was followed by very good combustion in cycle #12, probably due to better fuel vaporization in the port caused by the flashback. Cycle #13 had a null IMEP, for unknown reasons, followed by another good burn because of a high level of fresh charge in the residual gas.

By cycle #20, combustion has stabilized and the IMEP's for OVI and CVI are nearly the same. We chose not to present results past this point, because after cycle #30 there is a considerable accumulation of soot clearly visible on the piston window. On first thought, one might expect soot to block the laser excitation and/or fluorescence, causing extinction of the LIF signal. However, the signal clearly persists, leading us to conclude that the soot traps the heavy-ends of the fuel and/or fuel additives and oil, creating a fluorescing mixture of residual gunk. Because this would no longer be representative of a pure liquid-fuel film, we will leave study of it to another day.

LIF results for CVI and OVI are shown in Figs. 7 and 8, respectively. The numbers in the upper left-hand corner

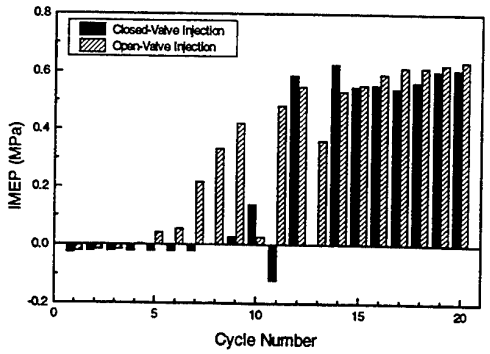

Fig. 6 Gross IMEP for the first 20 cycles of a simulated cold start, comparing OVI with CVI.

are the cycle number of the image, where the particular frames shown were selected as a good representation of the evolution of the fuel film for the two cases presented. The largest circle in the superimposed mask of cylinder features corresponds to the cylinder bore, and the smaller circle represents the clear aperture of the window in the piston. The triangular tip of the squish region between the two intake valves on the left side is visible in the field-of-view, whereas the exhaust side squish region cannot be seen.

For the CVI case shown in Fig. 7, liquid fuel can be observed in the intake-valve seat crevices by cycle #5, and perhaps even in cycle #2 as well (for the two earliest images in this sequence, it would have been better not to include the valve diagram in the mask, since it hides low levels of LIF from within the crevice). As the sequence progresses, this fuel film propagates away from the intake valve seat crevice and across the head surface; we believe it is on the head, and not the piston, because it flows around the spark plug and does not cover the faces of the exhaust valves.

A liquid-film first appears in the squish region on the intake-valve side in cycle #10. Because the film follows the contour of the squish area, it is definitely on the head, and not the piston. It would appear that liquid fuel stripped off the intake valve strikes the near-vertical wall leading to the squish area, distinctly marking its contour. By cycle #15, this squish area is totally covered by liquid, and the film has also grown to cover a significant portion of the intake-valve faces. We can only speculate as to the location of these later films, but because we can visually see fuel residue on the piston in these areas when we stop a test, and do not see similar amounts of residue on the valves and head, we are reasonably certain that they reside primarily on the piston.

For the OVI case shown in Fig. 8, liquid fuel is clearly evident in the first cycle. Because this image in not spatially resolved along the optical path, we can only speculate as to whether the fuel is on the piston, head or both. However, we believe that the large spot on the exhaust valve side is most likely located on the piston, and that the small spot under the upper intake valve is located on the valve face. This latter spot, and the analogous one that first appears on the lower intake valve in cycle #2, we find interesting. These regions grow as near semi-

circles, with a significantly thicker film near the film's leading edge (based on the LIF intensity). Recalling that the injector used produces a single spray aimed at the septum dividing the two intake-valve ports, these semi-circular films appear to be the result of fuel that has impacted the back of the valve and moved along the surface around the valve seat and onto the face. Note also that by cycle #5 a liquid film is visible along the entire intake valve crevice, similar to what we saw for CVI. We believe that the film in the seat crevices is from the flow of liquid films collecting initially on the port side of the valves, and that the semi-circular films on the intake valve faces are from direct impingement of the spray on the back of the valve seat during OVI.

For OVI, the film is slower to develop in the squish region on the intake side than it did with CVI. Note, however, that in cycle #15 the film in this region clearly follows the contour of the valve seat, with this trend continuing into cycle #20, suggesting that the observed LIF is due to fuel that is on the head. However, as was the case with the CVI, post-test visual inspection reveals a residual film on the piston in this region. We suspect that liquid films exist on both the piston and head in this region, but the LIF from the film on the head dominates the image, while the sapphire window in the piston retains a larger post-test residue than the head and intake valves.

It is interesting to note that the film under the upper exhaust valve does not significantly change in size or shape from cycle #5 through #20. In fact, the amount of film on the exhaust-valve side of the chamber continually decreases after cycle #5, and is unexpectedly asymmetric, with very little fuel ever visible over the face of the lower exhaust valve. Similarly, the area of the film on the head between the exhaust valves is largest in cycle #2, and is gone by cycle #15, except for very close to the spark plug; this behavior may be indicative of a rapid heating of the head surface between the exhaust valves.

Finally, for cycles #1-10 there is a bright fluorescence spot on the spark plug at about 10 o'clock. This is from liquid fuel on the ground strap. When we wrote the software for the engine-configuration mask, we thought it would be an unnecessary detail to bother aligning the ground strap of the mask with the actual orientation of the spark plug; the results presented here would suggest that this was a mistake, and that knowledge of the orientation of the ground strap is important for understanding LIF images of in-cylinder liquid films.

7. CONCLUSIONS

We have demonstrated the LIF imaging of liquid-fuel films on the combustion chamber walls of a production engine head for common-grade gasoline without the need of dopants. Excellent image clarity was achieved using a frequency-tripled Nd:YAG light source expanded into a light field and an intensified CCD camera; background subtraction was used to enhanced the image quality by removing unfiltered, elastically-scattered light and

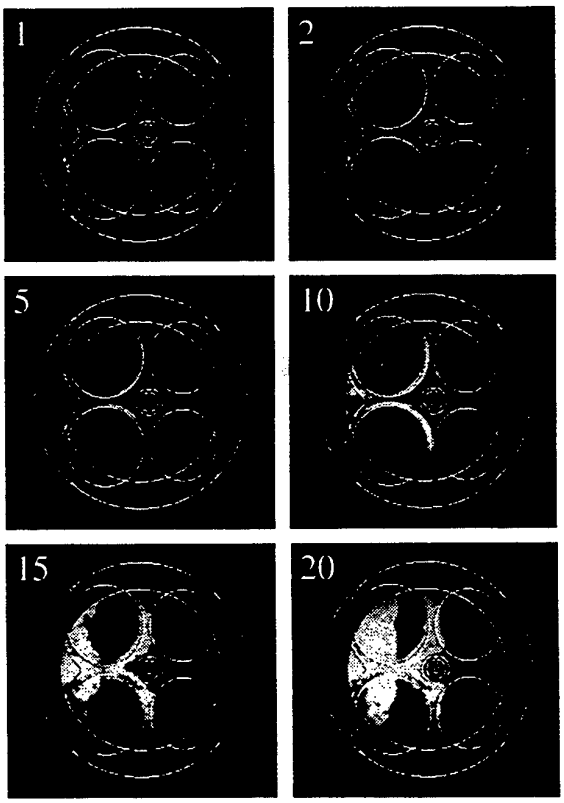

Fig. 7 Liquid-fuel fluorescence for closed-valve injection.

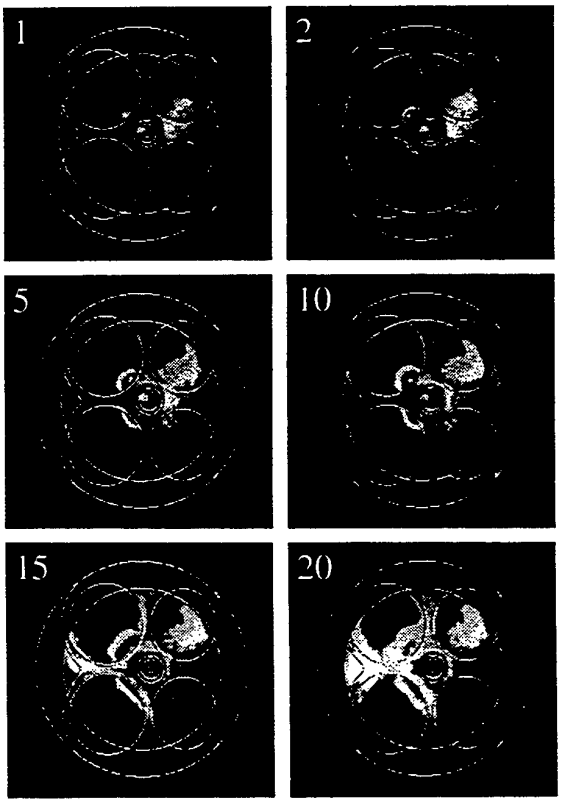

Fig. 8 Liquid-fuel fluorescence for open-valve injection.

fluorescence due to contaminants on the combustion chamber surfaces. We learned that gasoline, and, to a lesser degree, oil, leave a residue that requires the cleaning of all surfaces between tests. Because commonly-used oils will fluoresce in the same spectral regions as gasoline, this potential interference should be carefully monitored. We also found it useful to employ an overlay feature of the frame-grab interface board to create a diagram of the combustion chamber geometry directly on the LIF images.

For closed-valve injection, liquid fuel is first observed in the intake valve crevices by cycle #2, but the amount is not significant until about cycle #10; the first measurable IMEP occurred in cycle #9. This film grows to fill the regions of the head surfaces between the intake and exhaust valves, but does not grow in size over the intake valves themselves. Liquid fuel is also observed in the squish region between the intake valves beginning at about cycle #10, from whence it continues to grow until it covers more than half of the valve-face area by cycle #20. Liquid fuel is never seen on the exhaust-valve side of head.

For open-valve injection, liquid fuel is seen under one of the exhaust valves in the very first cycle; the first measurable IMEP occurred in cycle #4. This particular film does not change in size or shape from cycles #5-20. Significant liquid fuel is never observed under the other exhaust valve, revealing an unexpected asymmetry. In a manner similar to closed-valve injection, liquid fuel is seen to accumulate in the intake valve crevices. However, additional semi-circular pools of liquid form on the intake valves in the region near the spark plug. This appears to be due to fuel that has impacted the back of the valve, and flows around the valve seat to the valve face. These pools grow fairly large, and appear to be much thicker along theleading edge. Finally, while a liquid film does form in the squish area between the intake valves, it is considerably smaller than the one observed for closed-valve injection.

ACKNOWLEDGMENT

The authors wish to acknowledge the efforts Duane Sunnarborg in the design and assembly of all mechanical aspects of this work. This work was performed at the Combustion Research Facility of the Sandia National Laboratories, and was funded by the U.S. Department of Energy, Office of Transportation Technologies.

REFERENCES

Almkvist, G., Denbratt, I., Josefsson, G. & Magnusson, I. 1995, Measurements of Fuel Film Thickness in the Inlet Port of an S.I. Engine by Laser Induced Fluorescence, SAE Paper No. 952483.

Felton, P. G., Kyritsis, D. C. & Fulcher, S. K. 1995, LIF Visualization of Liquid Fuel in the Intake Manifold During Cold Start, SAE Paper No. 952464.

Fry, M., Nightingale, C. & Richardson, S. 1995, High-Speed Photography and Image Analysis Techniques Applied to Study Droplet Motion within the Porting and Cylinder of a 4-Valve SI Engine, SAE Paper No. 952525.

Hoult, D. P., Lux, J. P.,Wong, V. W. & Billian, S. A. 1988, Calibration of Laser Fluorescence Measurements of Lubricant Film Thickness in Engines, Trans. SAE, vol. 97, sec. 3, p. 576.

Le Coz, J-F., Catalano, C. & Baritaud, T. 1994, Application of Laser Induced Fluorescence for Measuring the Thickness of Liquid Films on Transparent Walls, Seventh International Symposium on the Application of Laser Techniques to Fluid Mechanics, Lisbon, p. 29.3.1.

Saito, K., Sekiguchi, K., Imatake, N., Takeda, K. & Yaegashi, T. 1995, A New Method to Analyze Fuel Behavior in a Spark Ignition Engine, SAE Paper No. 950044.

Shin, Y., Cheng, W. K. & Heywood, J. B. 1994, Liquid Gasoline Behavior in the Engine Cylinder of a SI Engine, SAE Paper No. 941872.

Smart, A. E. & Ford, R. A. J. 1974, Measurement of Thin Liquid Films by a Fluorescence Technique, Wear 29, p. 41.

INVESTIGATION OF THE STRUCTURE OF INJECTION SPRAYS IN DIESEL ENGINES BY MEANS OF A LIGHT SCATTERING TECHNIQUE

K. Prescher; A. Astachow; G. Krüger; J. Henße; D. Potz *

Institut für Thermische Maschinen und Anlagen, Universität Rostock
* Robert Bosch GmbH, Stuttgart

ABSTRACT

A laser light-scattering method is used to investigate the structure of diesel injection sprays. Temporal and local droplet size distributions were measured as well as geometric parameters of the spray. To analyze heavy fuel sprays with different optical properties a technique has been developed to simultaneously record the scattered-light amplitude and the image of the droplet. Investigations were carried out varying nozzle hole diameter, injection pressure and kinematic viscosity of the fuels.

1. INTRODUCTION

Knowing the dynamic structure of diesel injection sprays the injection process can be controlled deliberately in order to obtain a mixture formation and combustion that matches the present demands for a reduction in exhaust gas emission, a decrease in fuel consumption and an increase in the performance, respectively. In the end the combustion process is a result of the temporal and local distribution of the fuel concentration in the combustion chamber during the spray formation and development and the droplet distributions, which are considered a measure of the quality of the process, formed under the influence of several injection accompanying parameters.

The development of optical laser-based techniques for the diagnostics of two-phase flows gives new potential for the investigation of the transient injection under the conditions of modern diesel engines. Basically, the methods can be divided into local and global ones. Local methods which are used to investigate very small measurement volumes include for instance LDA/PDA-techniques /1,2/, techniques based on the evaluation of the amplitudes of scattered light /3/, CARS /4/ or Raman-Spectroscopy /5/. With other techniques such as the Fraunhofer diffraction-based MALVERN /6/ a small part of the injection spray is analyzed. The complete fuel spray can be detected with high-speed cinematographic techniques /7,8,9/ holography /10,11/, schlieren fotography /12/, laser-induced fluorescence /13/ or interferometry /14/. Nowadays temporal resolutions up to 200 MHz are possible. The local stochastic techniques provide quantitative information about single positions of the spray while the global techniques give the complete momentary figure of the spray, however, both techniques have their advantages and disadvantages. Therefore, only by analyzing both quantitative local parameters of the atomization process and global geometric parameters of the spray development comprehensive statements about the dynamic structure of fuel sprays can be derived /15,16/.

Main objective of experimental investigations is to quantify the influence of various injection parameters on the spray geometry and the distribution of the liquid phase in the combustion chamber. As significant parameters, for example, the effect of the injection pressure /17/, the nozzle hole diameter /18/, the nozzle opening pressure /19/, the conditions in the combustion chamber /20/ and the physical fuel properties /21/ have been investigated.

To characterize the atomization of diesel sprays a laser-based scattered-light technique is described in this report. Temporal and local droplet size distributions were measured varying the nozzle geometry, the injection pressure and the kinematic viscosity of the fuels /22/. The atomization of high-viscosity fuels which is of great importance for engineers designing and operating large-size diesel engines has not found significant consideration in research so far. The temporal alteration of the spray geometry is recorded by a CCD-camera to connect local droplet distributions to the complete process of the spray development.

2. MEASUREMENT PRINCIPLE

To estimate the temporal and local droplet distributions in an injection spray the measurement principle shown in figure 1 is used which was described by Beljaew /23/,for example, and technically applied by Dibelius and Funcke /3/. The identical emitting and receiving optics arranged in an angle of 90° form a measurement volume (MV) with side lengths of 50 µm. Crossing the MV the fuel droplet scatters the light of an Ar^+-laser. The intensity of the

scattered light is a function of the optical arrangement, the intensity and polarity of the laser light, the droplet size and the optical properties, that is the complex refractive index of the fuel used.

As generally known for optical diagnostics of aerosols (/23,24,25/) a uneven distribution of light intensity in the MV may occur as it did in the research work presented here. In order to estimate the influence of the light intensity distribution in the MV on the droplet size distributions numerical investigations were carried out. Known droplet distributions were send through measurement volumes characterized by pre-defined intensity distributions. As results distributions were obtained containing both information about the original droplet distribution and the influence of the intensity distribution in the MV. By means of these simulated measurements a correction program was developed which calculates the real droplet size distribution from the measured distribution provided that the intensity distribution in the MV is known (figure 2).

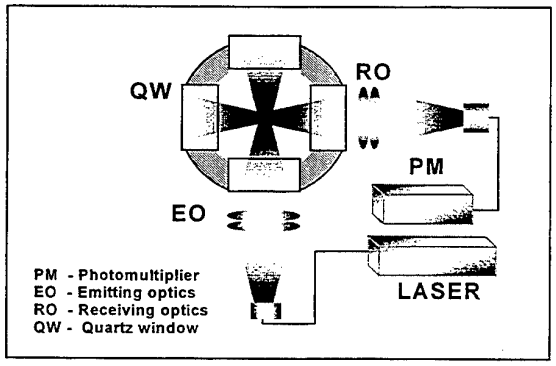

Figure 1 Measurement principle

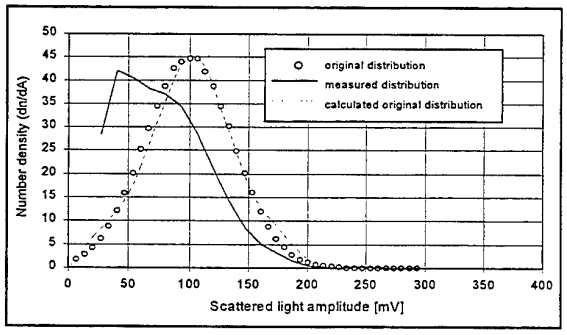

Figure 2 Example of the results of the correction algorithm for a known intensity distribution in the MV : **original distribution** - numerically generated; **measured distribution** - simulates the original distribution randomly passing the MV; **calculated distribution** - correction of the influence of the light intensity distribution in the MV

First, measurements of the real light intensity distribution in the MV were carried out using model particles (a 16 µm glass bead and a glycerine aerosol with a known size distribution) crossing the MV at defined positions and later real fuels were used. From the analysis of the signal amplitudes measured at the same position related to the centre of the MV the dependence of the signal amplitude on the crossing position in the MV could be obtained and an approximation function $I/I_0 = f(x,y)$ was derived.

3. INFLUENCE OF THE OPTICAL PROPERTIES

The scattered light detected by means of a photomultiplier (PM) is dependent on the complex refractive index *m* of the fuel. The real part defines the phase shift of the electro-magnetic wave interacting with the particle material and the imaginary part estimates the extinktion of the signal amplitude. The experimental investigations of the dependence of the scattered light intensity on the optical fuel properties were conducted by means of a technique to simultanously detect the scattering signal and the image of the droplet momentarily located in the measurement volume. The droplet distributions of fuels with different properties were generated with an ultrasonic atomizer. While passing the MV the light scattered by the droplet is detected by a PM and used to trigger both the apparatus for the scattering measurements and a CCD-camera. The droplets undergo a multiple ilumination by a high-speed flash light in order to get an image of the droplet trajectory from which the diameter can be derived with a micro-scale (figure 3).

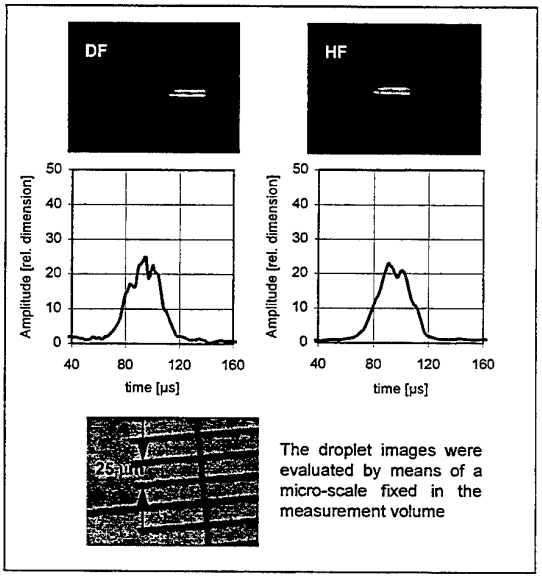

Figure 3 Comparison of scattered light signals from 6 µm droplets of diesel fuel and heavy fuel

Thus, each measurement provides information about size, position in the measurement volume and scattered light

amplitude of the droplet. The analysis of that information results in a signal distribution along the coordinate x for each droplet size class. The maximum signal amplitude of a droplet size class corresponds to the amplitude generated by a droplet of this size crossing the centre of the measurement volume.

4. EXPERIMENTAL SYSTEM AND CONDITIONS

A schematic drawing of the experimental apparatus is shown in figure 4. An optically accessible pressure chamber which can be heated up to 500°C is used. Besides the measurements of the light intensity scattered by the fuel droplets shadow fotographs of the sprays were recorded by means of a CCD-camera during different stages of the injection process. The evaluation of the CCD images provides the spray tip penetration, spray angle and the velocity of the spray tip.

The injection system applicable to high-viscosity fuels consists of a Bosch high pressure injection pump of the type PFR 1 CY (210/485), a pressure pipe and DLLA type nozzles (Bosch). For the investigations single hole nozzles with a concentric hole were used with the exception of the so-called button hole nozzle having four holes which are all directed into the same direction (see figure 5).

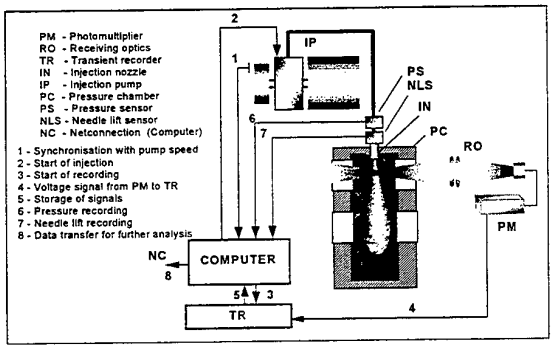

Figure 4 Experimental apparatus

The investigations described later were carried out at ambient temperatures (25°C) and chamber pressures of 20 bar, thus, preventing the influence of evaporation. Injection pressure and needle lift were recorded for each measurement. In order to prevent the quartz windows from contamination through liquid fuel the chamber was continuously scavenged by an air stream with a velocity of approx. 0.1 m/s.

In the following chapters the results of two measurement series comprising the variation of nozzle hole diameter, injection pressure and kinematic viscosity of the fuels are represented. The conditions of the series are shown in figure 5.

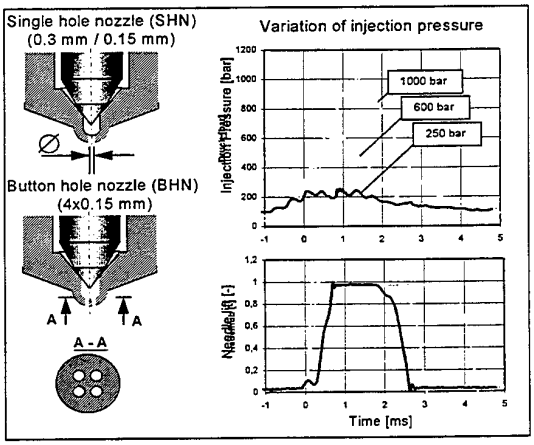

Variation of the physical fuel properties:

Property	DF	HF3	HF1	HF2
Viscosity at 27°C [mm²/s]	4	10	20	30
Density at 27°C [kg/m³]	842	910	945	965

Measurement conditions for all investigated fuels:

- Chamber pressure 20 bar
- Air temperature 298 K
- Single hole nozzle 0.3 mm
- Injection pressure 600 bar

Figure 5 Measurement conditions

5. RESULTS

5.1 Structure of Transient Injection Sprays

The specific features of the injection spray structure shall be demonstrated for the example of the single hole nozzle with 0.3 mm diameter at a maximum pressure of 600 bar. During the injection duration of approx. 3 ms the pressure in the nozzle hole bore alters from chamber pressure (20 bar) at closed needle to the maximum pressure of 600 bar. About 1 ms after the start of injection the fuel volume flow reaches the maximum and subsequently decreases with increasing acceleration. From the CCD-images shown in figure 6 a relatively large increase in spray penetration can be observed during the first millisecond. Afterwards the spray increasingly expands radially because of the turbulent mixing of droplets and air.

The number of droplets registered show different temporal and local distributions. For example in a distance of 70 mm from the nozzle orifice a larger radial expansion of the spray can be seen. At about 1 ms after the start of injection the first droplets arrive at this measurement position and for prolonged periods after the end of injection significant amounts of droplets still pass the position. Furthermore, a distinct maximum in the number of droplets can be observed in the spray tip. Figure 6 represents a clear difference in the proportions of different droplet size classes depending on the time in two distances (20 and 70 mm) from the nozzle orifice. Consequently, the mean diameters also vary with time and position. The differences in the mean diameters at these two positions are

in the same order of magnitude as those caused by a variation of the injection parameters, as described later.

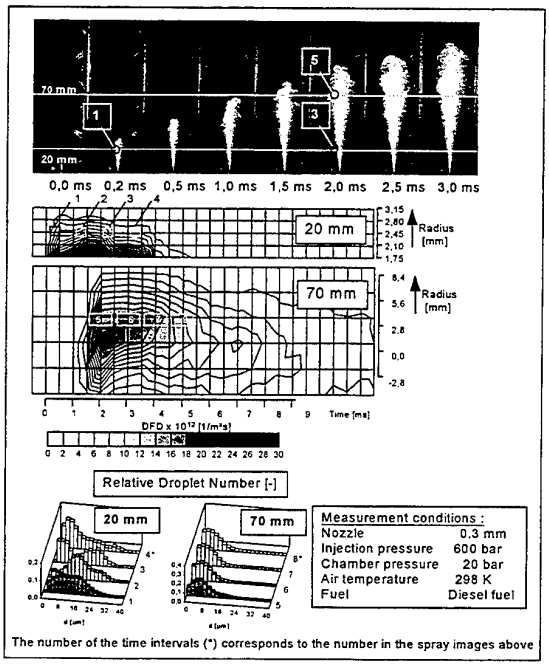

Figure 6 Example for the recorded data of the spray

At each distance the spray is scanned systematically by radially shifting the measurement volume. As a side effect the spray centre is defined and fields in the inner part of the spray are detected where reliable measurements cannot be realized because of the falsifying influence of extinction and multiple scattering. The droplet flow density (DFD) with the dimension (-/m²s) is used as basic information for further analysis which includes the estimation of temporally and/or locally averaged characteristic values of the distributions.

5.2 Variation of nozzle hole diameter

For this measurement series the three nozzles described in figure 5 were used. The single hole nozzle with a diameter of 0.15 mm (SHN015) can be considered to correspond to a hole of a four hole nozzle with the same effective cross-section as the 0.3 mm diameter single hole nozzle (SHN03). The investigation of the button hole nozzle (BHN) should demonstrate which influence the interaction of four separately generated but together as one spray acting fuel sprays has on the spray structure compared to the single spray of the EHN015. The comparison of EHN03 and BHN will show whether and if yes, which influence the atomization mechanisms in the nozzle bore channel have got on the spray structure.

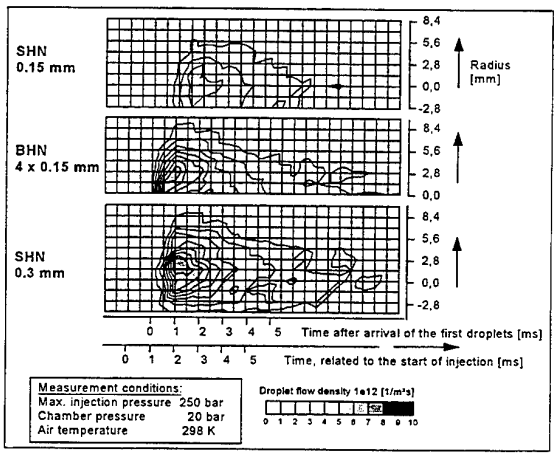

Figure 7 Droplet flow density as a function of spray radius and time

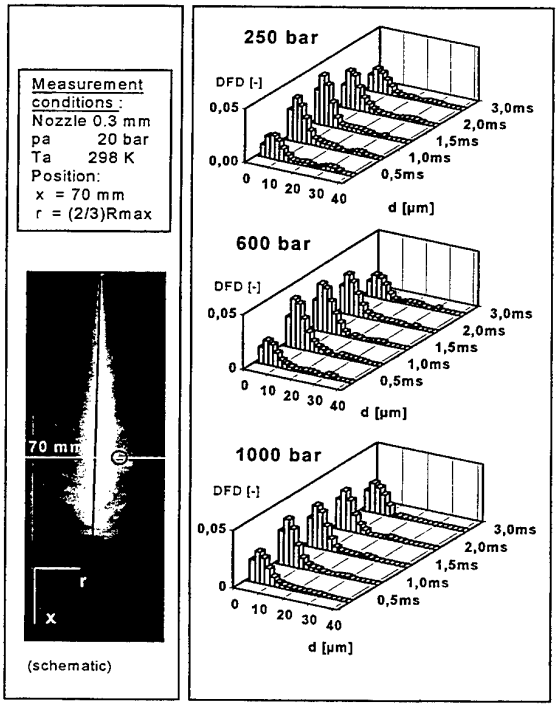

Figure 8 Droplet distributions for the variation of injection pressure

The diagrams in figure 7 represent the droplet flow density distributions versus radius and time averaged over time periods of 0.5 ms. A qualitative comparison of the distributions shows that the maximum spray radius for the injection with EHD015 is smaller than that of ELD03 and BHN. Furthermore, it becomes visible that the absolute values of the DFD in the case of the SHN015 are

significantly smaller, too. The maximum of DFD for the two nozzles with equal effective cross-sections was measured beyond the axis of the spray, which suggests the influence of extinktion. From these distributions it can be concluded that reliable results can be obtained up to approximately half of the spray radius.

The normalized distributions shown in figure 8 represent the results of the variation of the injection pressure. Approximately 1 ms after the start of injection the main droplet volume has passed the measurement position and after about 2 ms a significant reduction in the number of droplets and the droplet volume, respectively, is observed. With an increase in the injection pressure less relatively large droplets (> 30 mm) are detected in all time intervals.

A comparison of the droplet distributions for all three nozzles at an injection pressure of 600 bar (figure 9) shows, that during the whole injection duration the droplet diameters are clearly smaller in the case of SHN015. Significantly less droplets > 20 µm are recorded. However, the difference between SHN03 and BHN is not significant.

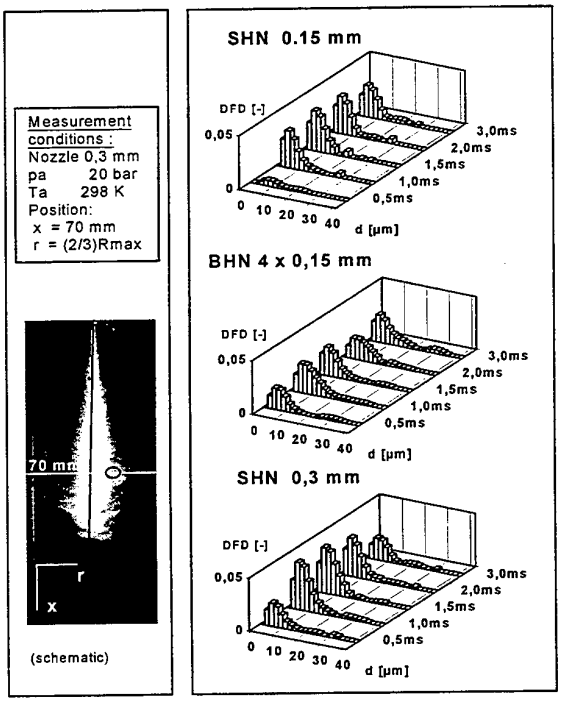

Figure 9 Droplet distributions for the variation of nozzle hole diameter

It becomes obvious from figure 10 that in all cases the largest droplets are present in the tip of the spray. During the main part of the injection a decrease in droplet sizes occurs and towards the end of injection increasing diameters could be observed again. An increase in the injection pressure from 250 bar to 1000 bar results in a decrease of the mean volumetric diameter (d_{30}) of about 20 %.

The analysis of the measured data for the whole injection provides the summarized effects of the variation of the nozzle hole diameter and the injection pressure. Figure 11 presents the integrated droplet volume distributions divided into three main droplet size classes. For each nozzle a trend towards smaller droplet sizes can be observed with an increase in the injection pressure. The proportion of droplets > 20 µm becomes smaller in all cases while the other droplet size classes show different tendencies. Furthermore, it can be seen from figure 10 that the mean droplet diameters for the SHN015 are significantly smaller than those for the other two nozzles. The SHN03 generates slightly larger droplets compared to BHN, however, this difference is far smaller than that between both nozzles and the SHN015. The spray images taken by the CCD-camera confirm these tendencies.

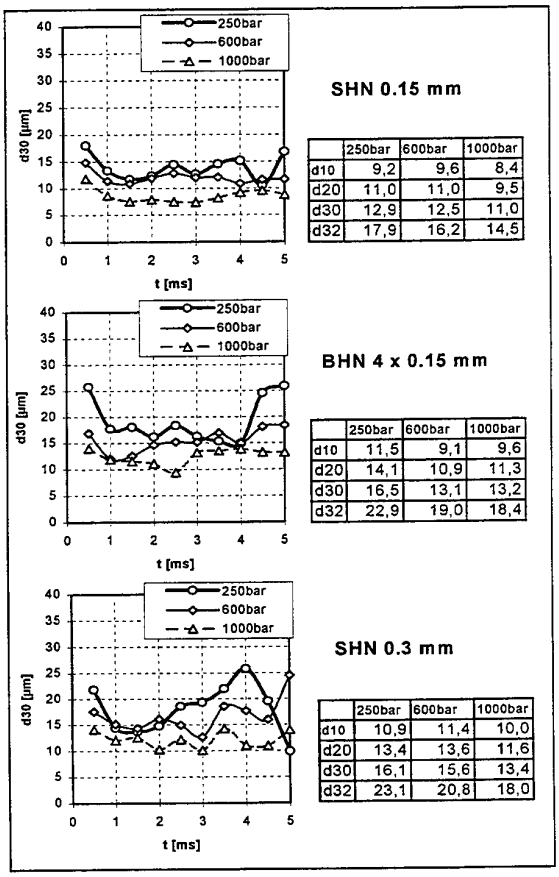

	250bar	600bar	1000bar
d10	9,2	9,6	8,4
d20	11,0	11,0	9,5
d30	12,9	12,5	11,0
d32	17,9	16,2	14,5

	250bar	600bar	1000bar
d10	11,5	9,1	9,6
d20	14,1	10,9	11,3
d30	16,5	13,1	13,2
d32	22,9	19,0	18,4

	250bar	600bar	1000bar
d10	10,9	11,4	10,0
d20	13,4	13,6	11,6
d30	16,1	15,6	13,4
d32	23,1	20,8	18,0

Figure 10 Mean diameters for the variation of injection pressure and nozzle hole diameter

The results underline that the altered fuel volume flow out of the nozzle does not influence the droplet formation through the flow conditions in the nozzle orifice but because of the changed conditions in the spray during its

development in the air. The larger fuel volume flow causes better 'flying' conditions for the single droplets in the shadow of the spray tip and therefore the droplets show a reduced tendency towards break-up.

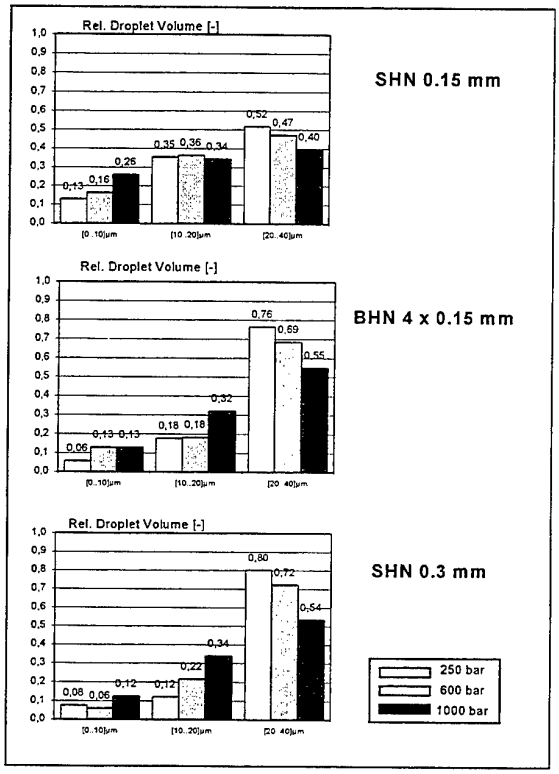

Figure 11 Integrated droplet distributions for the variation of injection pressure and nozzle hole diameter

5.3 Variation of fuel viscosity

The fuel properties were varied by mixing diesel fuel (DF) with a heavy fuel (HF) typically used in diesel engines on board of ships. Through a certain selection of the mixing ratio fuel mixtures were produced having kinematic viscosities in the range from 4 mm²/s to 30 mm²/s (27°C). The investigations were carried out under the conditions shown in figure 5.

It can be seen from figure 12 that with an increase in the viscosity the mean values of the droplet size distributions shift towards larger diameters. Moreover, the distributions show a broader range of droplet sizes. An overall view of the temporal change in the volume flow density at three radial distances from the spray axis for several fuel viscosities gives figure 13. A tendency towards a concentration of droplets in the spray tip can be observed with increasing viscosity. Furthermore, the number of droplets as a function of time increases faster from the periphery of the spray towards the axis. Thus, for diesel sprays more droplets were detected in the periphery while from approx. 0.5 Rmax the number of droplets recorded in heavy fuel sprays became larger.

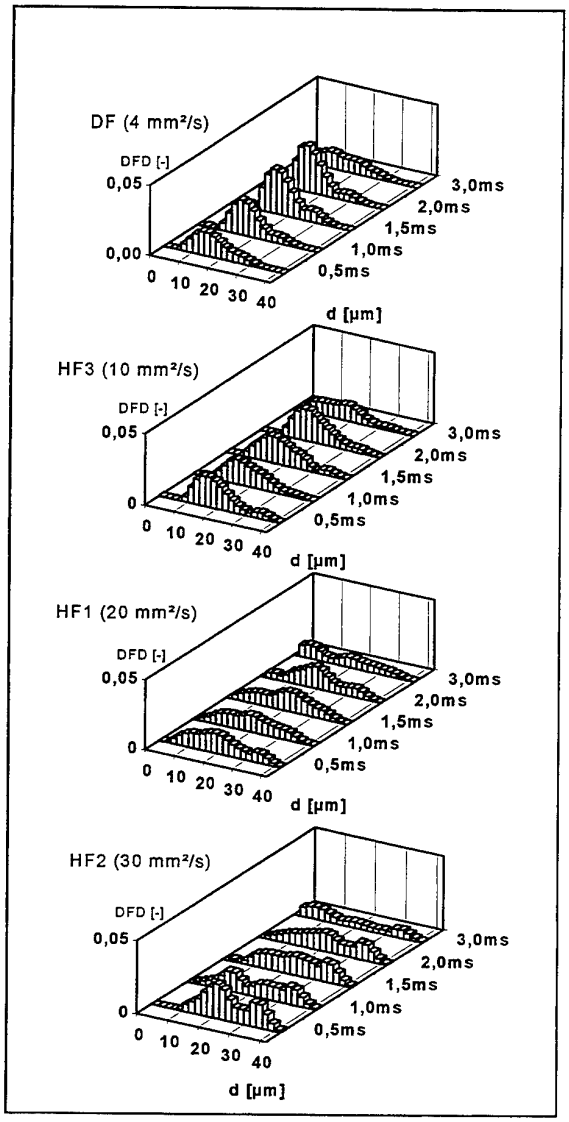

Figure 12 Droplet distribution for the variation of viscosity

The time averaged mean diameters show an increase both with an increase in the viscosity and for each fuel with radial approach to the spray axis. The increasing viscosity leads to a significant increase in the number of droplets in the size range from 10 ...20 µm and to an increase in the mean diameters (figures 14 and 15).

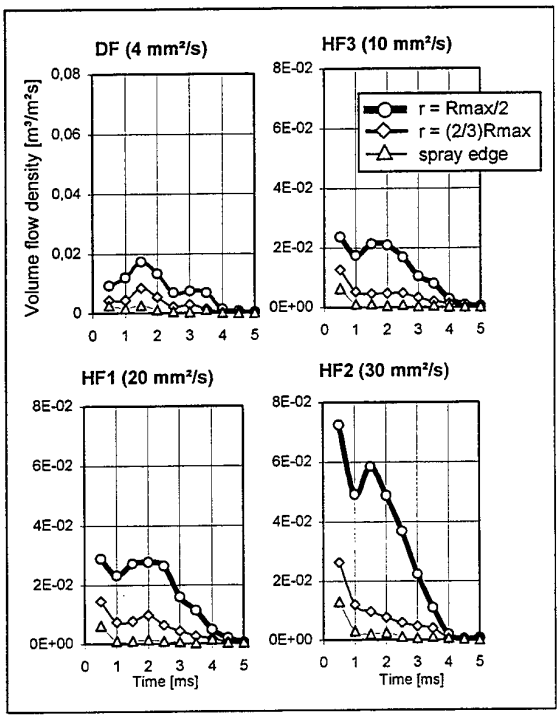

Figure 13 Volume flow density depending on spray radius and time

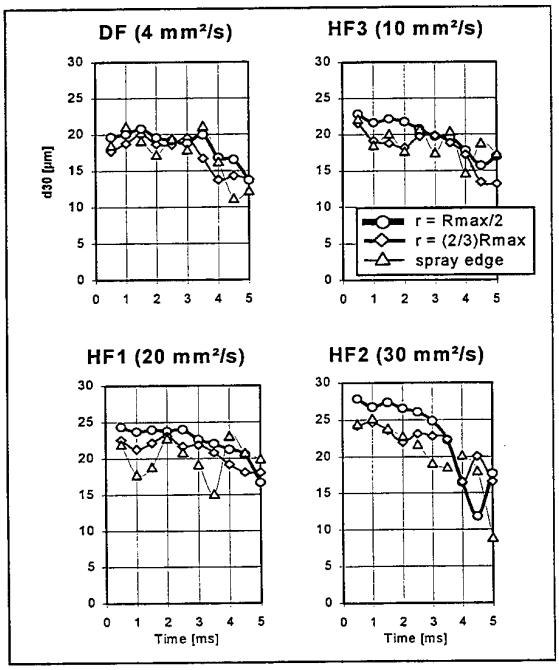

Figure 14 Mean volumetric diameter (d_{30}) depending on spray radius and time

By means of interpolation and linear approximation of the sauter mean diameters (d_{32}) for the whole field of variation of injection pressure and kinematic viscosity (single results were not shown because of limited space) the diagram in figure 16 was built. It can be concluded that an increase in the injection pressure can to a certain extent compensate the increasing droplet diameters caused by an increase in the viscosity. In order to obtain the same droplet sizes with a heavy fuel having a viscosity of 20 mm²/s compared to diesel fuel the pressure had to be increased from 500 bar to 900 bar. It has to be taken into consideration, however, that a change in the viscosity also means temporal changes of the spray geometry and, therefore, causes different conditions for the following processes.

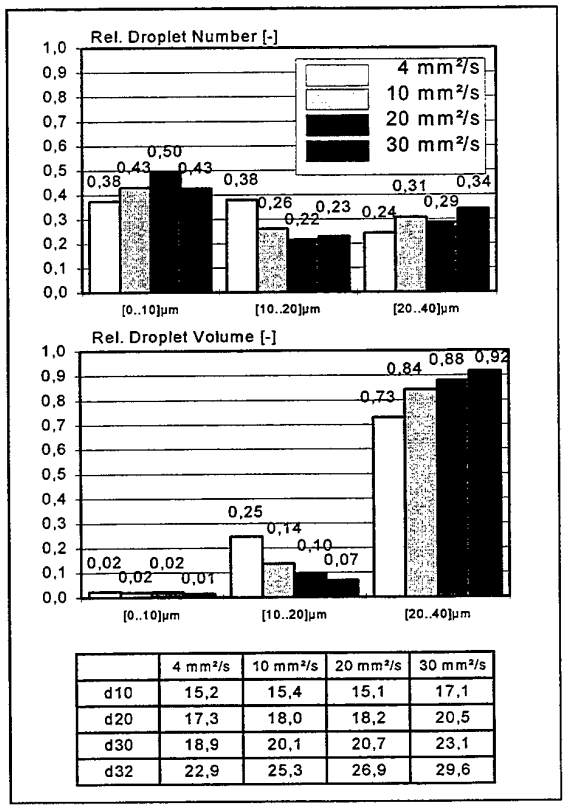

	4 mm²/s	10 mm²/s	20 mm²/s	30 mm²/s
d10	15,2	15,4	15,1	17,1
d20	17,3	18,0	18,2	20,5
d30	18,9	20,1	20,7	23,1
d32	22,9	25,3	26,9	29,6

Figure 15 Integrated droplet distributions and mean diameters

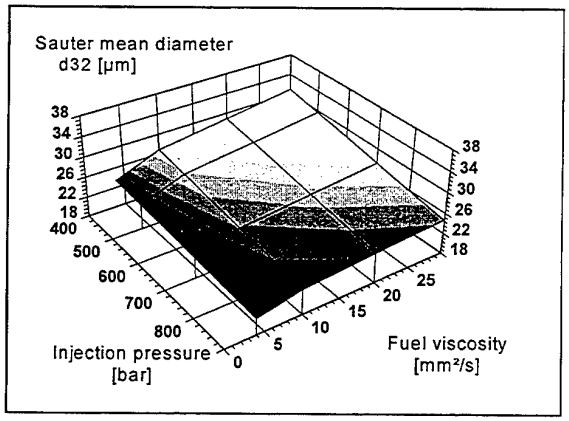

Figure 16 Summarized results for the variation of viscosity

6. CONCLUSIONS

The variation of the nozzle hole diameter and the number of holes could prove that the reason for the influence of the fuel volume flow on the droplet distributions does not lie in the flow conditions in the nozzle hole but in the changed conditions for the interaction of the droplets with the air during the spray development, i.e. the increase in the droplet concentration. An increase in the volume flow at the nozzle hole causes an increase in the fuel concentration in the spray and, consequently, droplet size distributions with an increasing proportion of larger droplets. A reduction of the nozzle hole diameter without changing the fuel volume flow of the spray leads to only slightly finer atomization. The increasing injection pressure supports the generation of smaller droplets and a temporal correlation between pressure and droplet diameter could be detected.

Using heavy fuels with higher viscosities causes a rise in the droplet diameters and increasing spray tip velocities. With an increase in the fuel viscosity an increasing dependence of the droplet diameters on the injection pressure was recorded. With a nearly constant spray angle the increase in the kinematic viscosity leads to an increasingly change of the droplet concentration in the radial direction of the spray. Furthermore the temporal change of the droplet concentration becomes stronger.

7. ACKNOWLEDGEMENT

This research work has been carried out with the financial support of the german Joint venture of Industrial Research Associations AIF (B 94 37) and the Research Association Internal combustion engines (FVV).

8. REFERENCES

/1/ Koo, J.-Y.; Martin, J. K.: Comparisons of Measured Drop Sizes and Velocities in a Transient Fuel Spray with Stability Critera and Computed PDF's; SAE 910179

/2/ Pitcher G.; Wigley G.: The Droplet Dynamics of Diesel Fuel Sprays under Ambient and Engine Conditions; ASME Laser Anemometry Advances and Applications Vol. 2, 1991

/3/ Dibelius G.; Funcke J.: Experimentelle Untersuchungen zur Zerstäubung und Verdampfung von Kraftstoff unter dieselmotorischen Bedingungen; Kolloquium des SFB 224 der RWTH Aachen, 1988 und 1990

/4/ Münch K.-U.: Anwendung der zweidimensionalen Mie-Streulichttechnik zur Diagnose des Ein-spritzprozesses im Brennraum eines direkteinspritzenden PKW-Dieselmotors; BEV Heft 93.1; Erlangen, 1993

/5/ Heinze, T.; Schmidt, T.: Fuel Air Ratios in a Spray, Determined between Injection and Autoignition by Pulsed Spontaneous Raman Spectroscopy; SAE 892102

/6/ Watson, D. J.; Tech, B.: Laser Diffraction Measurements in Transient Spray Conditions; ICLASS 1985

/7/ Eifler, W.: Untersuchungen zur Struktur des instationären Dieseleinspritzstrahles im Düsennahbereich mit der Methode der Hochfrequenz-Kinematografie; Dissertation ; Universität Kaiserslautern ; 1990

/8/ Schaffitz, W.; Bauer, W.; Prescher, K.: Ausbreitung von Kraftstoffstrahlen in Dieselmotoren; MTZ Nr. 47 (10); 1986

/9/ Xu, M.; Hiroyasu, H.: Development of New Opical Technique for Measuring Diesel Spray Penetration; SAE 902077

/10/ Zhigang, L.; Jiahua, W. : Atomizing Mechanism and Characteristics of Atomizing Channel Injector ; SAE 900226

/11/ Wendig, D.: Untersuchungen zur Kraftstoffverteilung im Brennraum von Dieselmotoren mit Hilfe der Holografie; Dissertation ; Universität Rostock ; 1985

/12/ Reuter, U. : Kammerversuche zur Strahlausbreitung und Zündung bei dieselmotorischer Einspritzung ; Dissertation ; RWTH Aachen ; 1989

/13/ Megahed, M.; Roosen, P. : Einfluß der Düsengeometrie auf die Dieselstrahlausbreitung ; MTZ 54 (12) ; 1993

/14/ Lakshminarayan, P. A.; Dent, J. C. : Interferometric Studies of Vapourising and Combusting Sprays ; SAE 830244

/15/ Arcoumanis, C.; Hadjiapostolou, A.; Whitelaw, J. H.: Flow and Combustion in a Hydra Direct-Injection Diesel Engine ; Int. Congress Detroit, 1991 ; SAE 910177

/16/ Fuchs, H.; Pitcher, G.; Wiesler, B.; Wigley, G.; Winklhofer, E. : Einspritzstrahlstruktur ; FVV Heft 499 ; 1992

/17/ Arcoumanis, C.; Cossali, E.; Paal, G.; Whitelaw, J.H. : Transient Charakteristics of Single-Hole Diesel Sprays ; SAE 890314

/18/ Hosoya, H.; Obokata, T. : Effect of Nozzle Configuration on Characteristics of Steady-state Diesel Spray ; SAE 930593

/19/ Pitcher, G.; Wigley, G. : The Effect of Needle Opening Pressure on the Atomisation of Diesel Sprays ; 2. Seminar on Exper. Methods in Engine Research and Development ; London ; 1991

/20/ Hirojasu, H.; Arai, M. : Structures of Fuel Sprays in

Diesel Engines ; SAE 900475
/21/ Hirojasu, H.; Arai, M.; Tabata, M. : Diesel Fuel Spray of High Viscosity Fuel ; MESJ Vol. 14, No. 1, 1986
/22/ Astachow, A.; Fitzky, G.; Krüger, G.: Kraftstoffzerstäubung ; FVV Heft 539 ; 1993
/23/ Beljaew, S. P. : Opto-elektronische Methoden zur Aerosoldiagnostik, Energie-Verlag, Moskau, 1981
/24/ Fißman, H.; Jerkovic, A.; Trampe, A.: Optische Aerosolmeßverfahren für extrem hohe und niedrige Partikelkonzentrationen, Technisches Messen tm 56 (1989) 5 R., Oldenburg Verlag
/25/ Don Holve; Sidnes A.; Self,: Optical particle sizing for in situ measurements, Part 1, Applied optics, Vol. 18, No. 10, 1979

CHARACTERIZATION OF SPRAY FLOWS UNDER HIGH FUEL TEMPERATURE USING PHASE DOPPLER ANEMOMETER

Tomio Obokata, Tsuneaki Ishima and Kouichi Uehara
Department of Mechanical System Engineering, Gunma University,
1-5-1, Tenjin-cho, Kiryu, 376 Japan

Tetsuji Koyama
Tsukasa Sokken Co., LTD
1-19-4, Tamazutsumi, Setagaya, Tokyo, 158 Japan

Kazumitsu Kobayashi and Masayoshi Tukagoshi,
Unisia Jecs Co.,
1671-1 Kasukawa, Isesaki, 372 Japan

ABSTRACT

Effects of fuel temperature on the characteristics of the intermittent-cyclic spray have been experimentally clarified using the phase Doppler anemometer. The spray was initiated from the air assisted fuel injector. The injection frequency was 50Hz, and the pressures of the liquid fuel (n-heptane) and air were 250kPa and 147kPa, respectively. The fuel temperature was changed from 293K (20°C, room temperature) to 413K (140°C).

Experimental results showed that the mean velocity of the droplets increase with the fuel temperature. The Sauter mean diameter increased in the fuel temperature region from 293K to 343K for intermittent spray and from 293K to 323K for continuous steady spray. After the regions, it was decreased. The droplets with higher fuel temperature and larger diameter have smaller decaying ratio of the velocity. These features are well explained by the analyses using grouped data classified by the droplet diameter or temporally divided velocity history of the intermittent spray. Evaluation of the droplet size distribution has also been performed by a log-hyperbolic (LH3) type fitting function.

1. INTRODUCTION

Spray characteristics are one of the dominant phenomena to affect the performance of internal combustion engines. In this field, a phase-Doppler anemometer (PDA) allows one to perform local and instantaneous measurement of both particle size and velocity. Many investigators have studied the subject with the PDA [1-5]. They indicated successfully the experimental data of particle size and velocity not only for steady condition but also for intermittent spray. Differences between continuous and intermittent sprays were also show in them [5]. Since the fuel spray is injected intermittently in the actual engine, establishment of evaluating methods of it is needed for spray characterization.

The authors' group has investigated an intermittent gasoline type spray initiated from an air assisted spray injector [6, 7]. The injector was proposed for obtaining better quality of air/fuel mixture. In these experiments, a time dividing analysis proposed by Obokata and Long [5], a size distribution using 3-parameters log-hyperbolic function (LH3) reconsidered by Xu et al [8]. and a size classification method were used for evaluating the spray. They indicated that the spray cloud of air assisted injector had smaller droplet diameter than that of existing system (pintle injector). An effect of the fuel temperature was also reported in the study [7]. The high fuel temperature resulted in increase in the droplet diameter and velocity. In those studies, however, it was difficult to have detail discussion on the effect of the fuel temperature because alternative fuel of Laws which was used for spray instead of gasoline was a composite fuel.

The present work was undertaken to clarify the effect of the fuel temperature on the characteristics of the intermittent spray initiated from the air assisted injector by using PDA system. An pure fuel of n-heptane was chosen for the present study. Its evaporation temperature is 371.4K and that value is lower than that of the Laws (423K). The characteristics of the intermittent spray are discussed by using the time dividing analysis and by using velocity information on droplets group classified by diameter. Whole and time divided size distributions of the spray droplets have also been discussed with 3-parameters log-hyperbolic function.

2. EXPERIMENTAL APPARATUS

2.1 Fuel Injection System

Figure 1 shows the inner mixing type air assisted fuel injection nozzle. The injector had a mixing chamber which was mounted on a pintle type fuel injector. The fuel was intermitted by the needle valve and the assisted air

continuously flowed in the nozzle. The nozzle outlet was 2mm in diameter. The frequency of injection was 50Hz, the pressure of fuel was 250kPa and that of air was 147kPa. The n-heptane was used for injection instead of gasoline. Typical fluid properties of n-heptane, Laws and gasoline are listed in Table 1. The fuel was injected into atmosphere which had normal room temperature and pressure. Flow rate of fuel was changed by valve opening duration, Δt=2.5ms, 4.5ms, 6.5ms (intermittent condition) and ∞ (steady condition). Figure 2 shows a schematic diagram of the injection tester used in this experiment. Spray flow and radial directions set Z-axis and r-axis, respectively, and the origin of the coordinates was set at the center of the nozzle outlet. Fuel temperature was varied from 293K (20℃) up to 413K (140℃). The fuel flowed through a copper pipe which was in a thermostatic oil bath and the temperature of fuel was set the certain value. The temperature of the assisted air was not controlled and was around 293K.

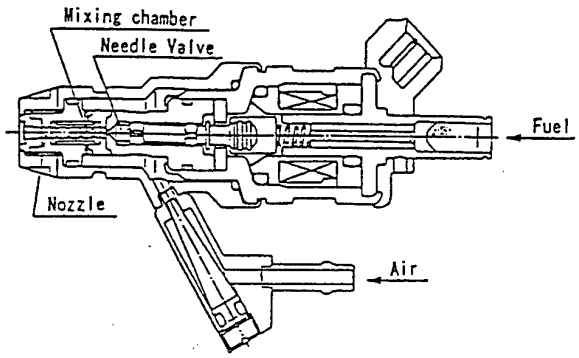

Figure 1 Cross section of air assisted fuel injector.

2.2 Phase Doppler Anemometer

A phase Doppler particle analyzer of Aerometrics (PDPA) was used to measure the droplet velocity and diameter. The diameter of the measuring volume was adjusted to more than five times of the expected maximum particle diameter, to remove measurement errors which would be affected by the Gaussian distribution of light intensity of the measuring volume [9]. The diameter of the measuring volume used in this experiment was about 0.3mm and the total intersection angle of incident beams was 1.5° and forward scattering mode was used with the off-axis angle of 30° from the incident beams. The measuring diameter range was chosen the range from 3.4~510.5 μm at 1.385 of refractive index of the fuel. High voltage of the detectors was set as 350V.

3. RESULTS AND DISCUSSIONS

3.1 Distribution of Droplet Velocity and Diameter of the Spray

Table 1 Physical properties of the fuels.

		n-heptane	Laws	Gasoline
Density kg/m^2	(20℃)	684	797	746
Kinematic viscosity m^2/s	(20℃)	0.61×10^{-6}	1.12×10^{-6}	0.54×10^{-6}
Refractive index	(20℃)	1.385	1.433	1.410
Surface tension N/m	(20℃)	20.9×10^{-3}	26.4×10^{-3}	22.5×10^{-3}
Coefficient of volume expansion ℃$^{-1}$		1.22×10^{-3}	0.66×10^{-3}	0.83×10^{-3}

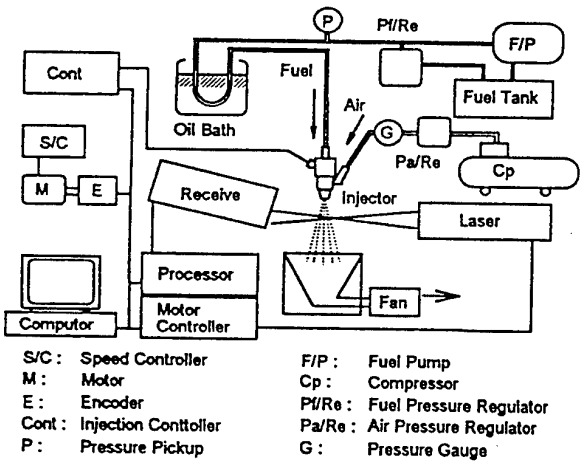

Figure 2 Experimental set up

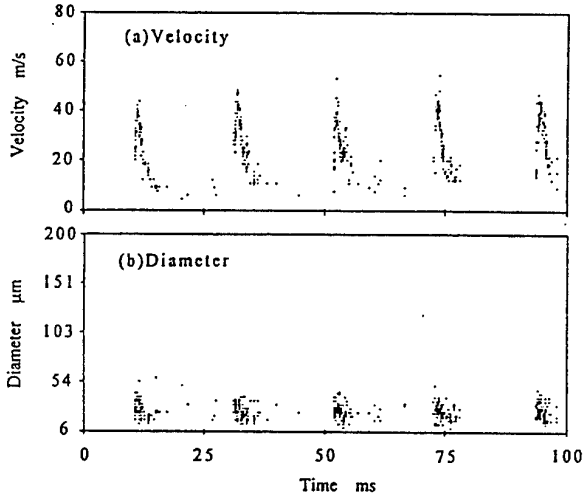

Figure 3 Time series of droplets size and velocity (Z=50mm, r=0mm, Δt=2.5ms and fuel temperature 413K)

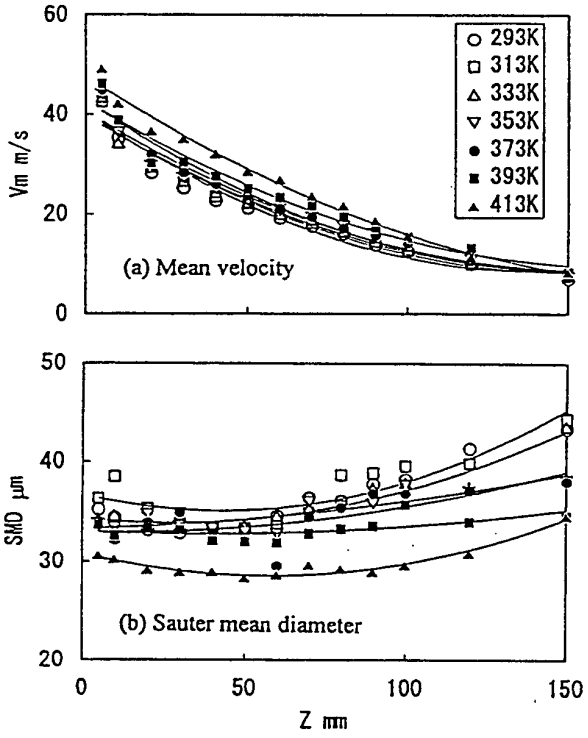

Figure 4 Axial distributions of droplets mean velocity and Sauter mean diameter with various fuel temperatures (r=0mm Δt=2.5ms).

Time series of droplets velocity and diameter measured at Z=50mm on the spray center line (r=0mm) are plotted in Figure 3 where the fuel temperature is 413K, the valve opening duration Δt=2.5ms and the flow rate of the air Q=0.255Nl/s. In this figure, the instantaneous maximum data rate is about 20kHz and the mean data rate is 10kHz.

Axial distributions of droplet mean velocity (V_m) and Sauter mean diameter (D_{32}) on the centerline (r=0mm) at the all period of intermittent spray with various temperatures are plotted in Figures 4(a) and (b). The mean velocity decreases along downstream distance (Figure 4(a)). The Sauter mean diameter decreases slightly just after the nozzle exit and after then increase with downstream distance (Figure 4(b)). The value at the initial point (Z=5mm) is much smaller than that of the Laws used in the previous work [7]. The decreasing rate of them at the upstream is also smaller than that of the Laws. In the downstream, the range of the values are almost same as that of the Laws. In the upstream, atomization and breakdown at n-heptane is much active than Laws and therefore the Sauter mean diameter is decreased. In the region, the Laws spray probably has a lot of non-spherical droplets due to their large kinematics viscosity. Then, the large value of the Sauter mean diameter is also explained by an incomplete atomization in n-heptane. In the downstream, the breakdown becomes inactive and small droplets disappear or their diameters become smaller than

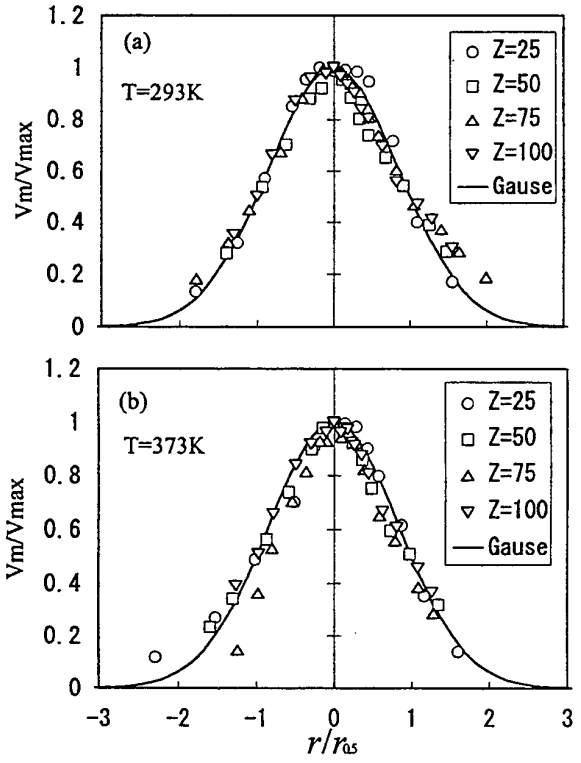

Figure 5 Radial distributions of mean velocity.

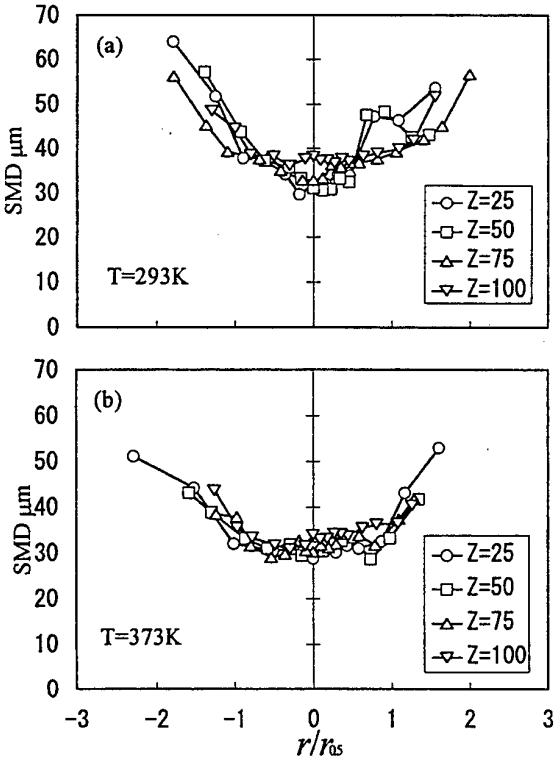

Figure 6 Radial distributions of Sauter mean diameter.

the measuring range of PDA due to evaporation. The tendency is also caused by that small droplets with slower velocity are overtaken and pushed away from the centerline by large droplets or merged into those [5]. These tendencies of the velocity and the diameter are little influenced by the fuel temperature. At the 413K of the fuel temperature, both of the mean velocity and the Sauter mean diameter have a different feature from those for another fuel temperature condition. Since the fuel temperature of 413K is higher than the evaporation temperature of the n-heptane, the evaporation seems to affect the results at the condition. The actual fuel temperatures would be lower than the given values because the fuel was cooled by the assisted air and the atmosphere. Then, the fuel droplets were able to exist in the measuring region and the PDA gives information on their velocity and diameter.

Figures 5(a) and (b) show the radial distributions of mean velocity. In these figures, fuel temperatures are 293K (room temperature) and 373K, and the measurement axial positions are Z=25mm, 50mm, 75mm and 100mm. The mean velocity and radius are normalized by the maximum mean velocity (V_{max}) on the axis and by the half-value width of the velocity distribution curve ($r_{0.5}$). The velocity distributions are close to the Gaussian distribution which is indicated by the solid curve (Gauss). The velocity at the outskirts of the spray is slightly greater than the Gaussian distribution. This feature is caused by the detection of droplets spreading out from the spray center and velocity bias at the LDA measurement near the edge of jet. Figures 6(a) and (b) show the Sauter mean diameter with non-dimensional radius. The distribution shape of the Sauter mean diameter has a minimum value around the center (r=0mm). The edge of the spray becomes asymmetric due to measurement uncertainty and decreasing data rate or absence of droplets. The Sauter mean diameter at the edge for the low fuel temperature spray is larger than that for the high fuel temperature. The distributions of the mean velocity have similar tendency for the both temperature conditions.

To clarify the effect of the fuel temperature on spray characteristics, the mean velocity and the Sauter mean diameter, which were measured at Z=50mm on the spray center line (r=0mm) with various fuel flow rates, are illustrated in Figures 7 (a) and (b), respectively. The fuel flow rate is changed by the valve opening duration Δt, and flow rates at fuel temperature of 293K are 5.1mg/stroke, 10.1mg/stroke, 15.2mg/stroke and 1.8g/s at Δt=2.5ms, 4.5ms, 6.5ms and ∞ (steady continuous spray),

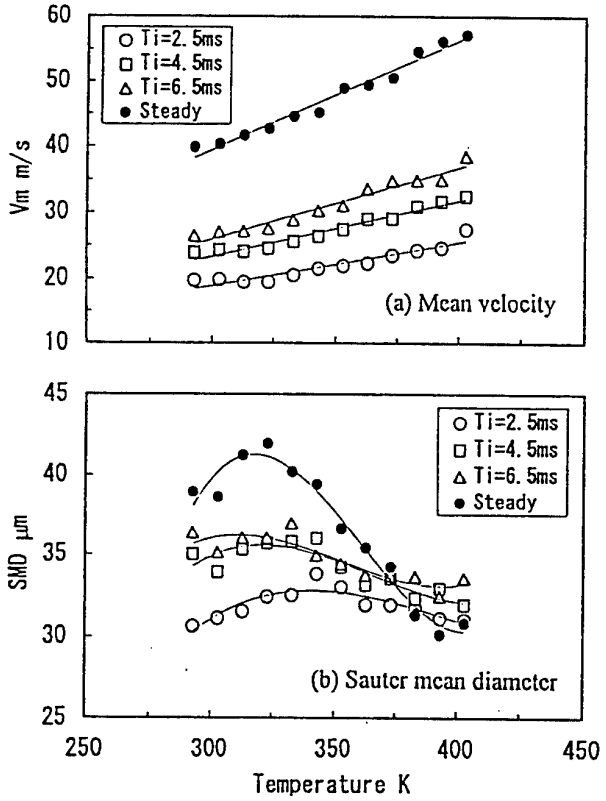

Figure 7 Mean velocity and Sauter mean diameter with various fuel temperature and various fuel flow rate (Z=50mm, r=0mm)

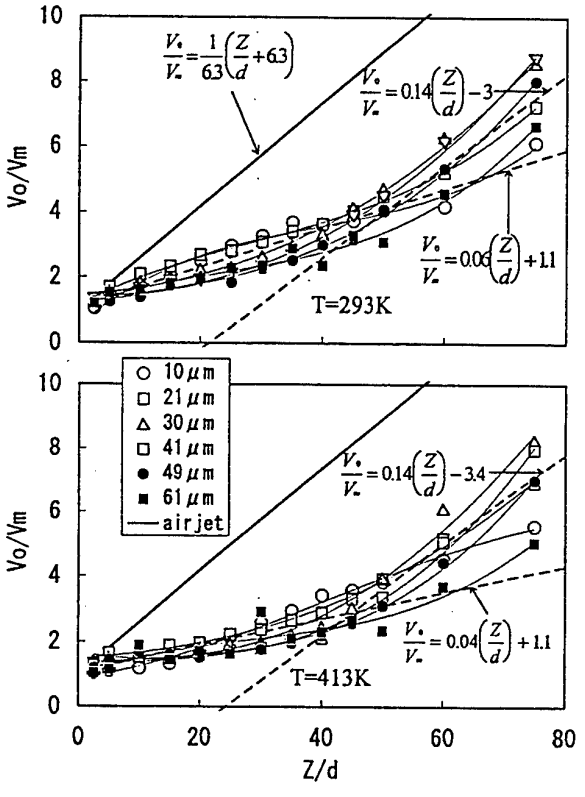

Figure 8 Decay of mean velocity at classified droplets on the centerline (r=0mm, Δt=2.5ms)

respectively. The mean velocity increases with increasing fuel temperature and fuel flow rate. The Sauter mean diameter increases in the region from 293K to 343K for intermittent spray and from 293K to 323K for continuous spray, after the region, they decrease. The high fuel temperature causes fuel evaporation, and it also causes promotion of the atomization due to decrease in the fuel kinematics viscosity and in the fuel surface tension. The increase in Sauter mean diameter can be explained that the small droplets tend to decrease or lose their diameter due to

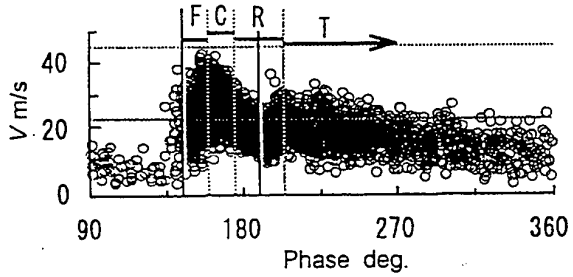

Figure 9 Example of phase matched plot of droplets velocity.

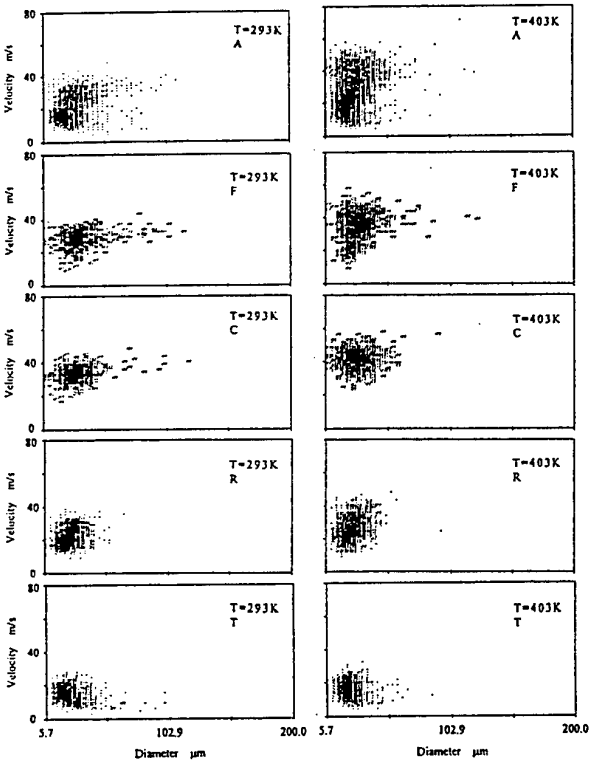

Figure 10 Correlation between droplet velocity and diameter at each divided part of spray (Z=50mm, r=0mm, Δt=2.5ms)

the evaporation because their total droplet surface area is greater than that of large droplets with same total fuel volume. In the region with increasing in the Sauter mean diameter, the evaporation affected the spray. After the region, the decrease in the fuel surface tension and the kinematics viscosity can mainly influence on the spray characteristics and therefore the Sauter mean diameter decreases. For increasing the fuel flow rate, duration of the injecting of the fuel becomes long where the large droplets with high velocity rush in the flow field (see also Figure 3). Then, the mean velocity and the Sauter mean diameter increase due to passing many fuel droplets with large diameter and high velocity in higher flow rate.

3.2 Velocity Decay at Droplets Group Classified by Diameter

The PDA measurement can provide a diameter and a velocity of each droplet. Figures 8(a) and (b) show decays of the mean velocity (Vm) at each classified size where V_0 is the exit velocity at the nozzle estimated from measured data and d is diameter of the nozzle outlet (d=2mm). An interval of the classified size diameter was set as about 4μm by the PDA system and six classified sizes were chosen for the figures. In these figures, a straight line indicates a theoretical decay line of air circular jet [10]. The experimental results indicate non-liner change in the decay of the droplet velocity although the decay of the velocity for the air is linear. Virtual origin seems to be shift to reverse axial direction with increasing the diameter of the droplet. Each droplet has a similar velocity at the origin. In the

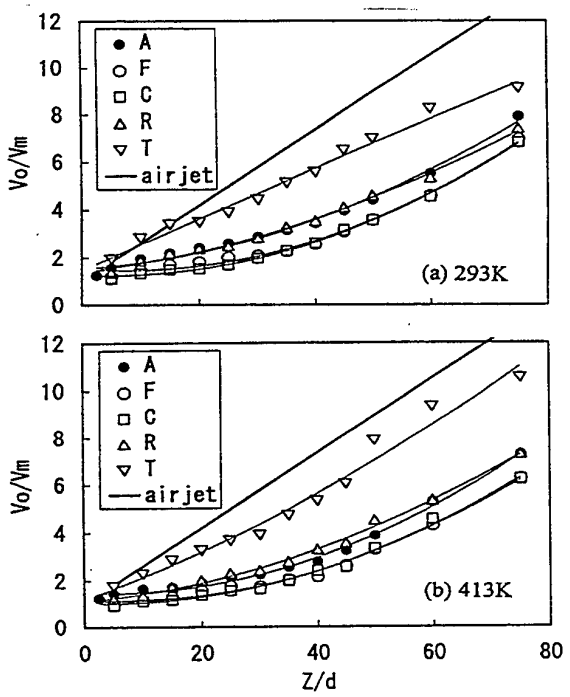

Figure 11 Axial distribution of the mean velocity of each temporal part (r=0mm, Δt=2.5ms).

upstream of Z/d ≦ 50, the small classified droplets has large velocity decay compared with the large droplets. In contrast, the small particle has small velocity decay in the downstream. In the downstream of Z/d ≧ 50 for 293K of fuel temperature, the velocity decay rate of the each droplet size can be observed to become almost same rate as air jet. The larger droplet keeps its velocity longer distance due to its large inertia depending on its diameter. Therefore, the large classified size droplets have smaller velocity decay. Comparison between the both conditions of the fuel temperature indicates small velocity decay for high fuel temperature in the whole experimental region. For high fuel temperature, the velocity decay rate maintains smaller than that for the low fuel temperature.

3.3 Time Dividing Analysis of Intermittent Spray

In order to estimate the intermittent spray, the temporal data of velocity and diameter were divided into some parts according to their phase angle [5-7]. This estimating method was named time dividing analysis. The method is explained as follows: Figure 9 shows an example of ensemble plots of velocity for intermittent spray, where the time axis of Figure 3 was converted into the injection phase angle. A duration ($t_{0.5}$) where the droplet velocity is larger than the half value of the maximum velocity is determined on the figure. The duration was divided by three parts. The first and the second $t_{0.5}/3$ duration is represented by fore part (F) and central part (C). Next duration of $2t_{0.5}/3$ is defined as rear part (R). The rest of the duration is represented by the tail part (T).

Figure 10 indicates correlation between droplets velocity and size for intermittent spray with time dividing analysis for fuel temperature of 293K and 413K at the Z=50mm and on the centerline (r=0mm). The data of entire spray (A) is also shown in the figure. A critical difference between the correlations of both fuel temperature conditions exists in F and C. The correlations at the parts of R and T are not sensitive to the fuel temperature. In the parts of F and C under the high fuel temperature condition, it can be observed an existence of a lot of droplets with large velocity. It is caused by that the droplets have a small velocity decay as indicated in Figure 8 and that they can reach a certain distance remaining a large velocity. In the parts of R and T, an instantaneous flow rate of the fuel is very low and the assisted air continuously flows in the nozzle. Since the assisted air cools the fuel, the fuel temperature would be lower than the given value. Therefore, the correlations at R and T are insensitive to the fuel temperature.

Figure 11 shows the axial distribution of the mean velocity of each temporal part. For the high fuel temperature, the droplet velocity remains large in the parts of F, C and R. This result is caused by the small velocity decay.

Figure 12 shows the axial distribution of the Sauter mean diameter. The Sauter mean diameter at the F and C is larger than that at the R and T. It will be supposed that the

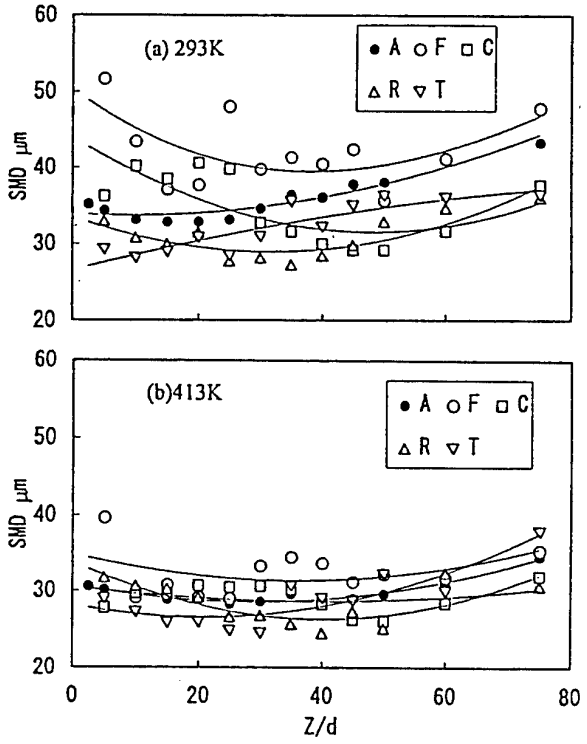

Figure 12 Axial distribution of Sauter mean diameter of each temporal part on the centerline (r=0mm, Δt=2.5ms).

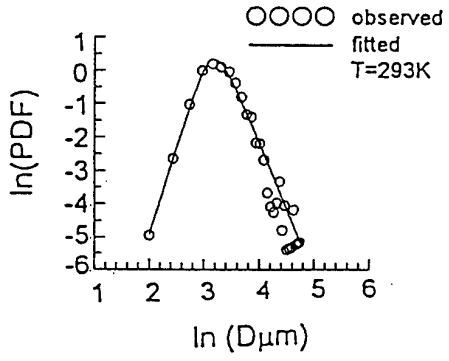

Figure 13 Example of measured droplet size distribution with result of log-hyperbolic fitting (Z=50mm, r=0mm, T=293K, Δt=2.5ms)

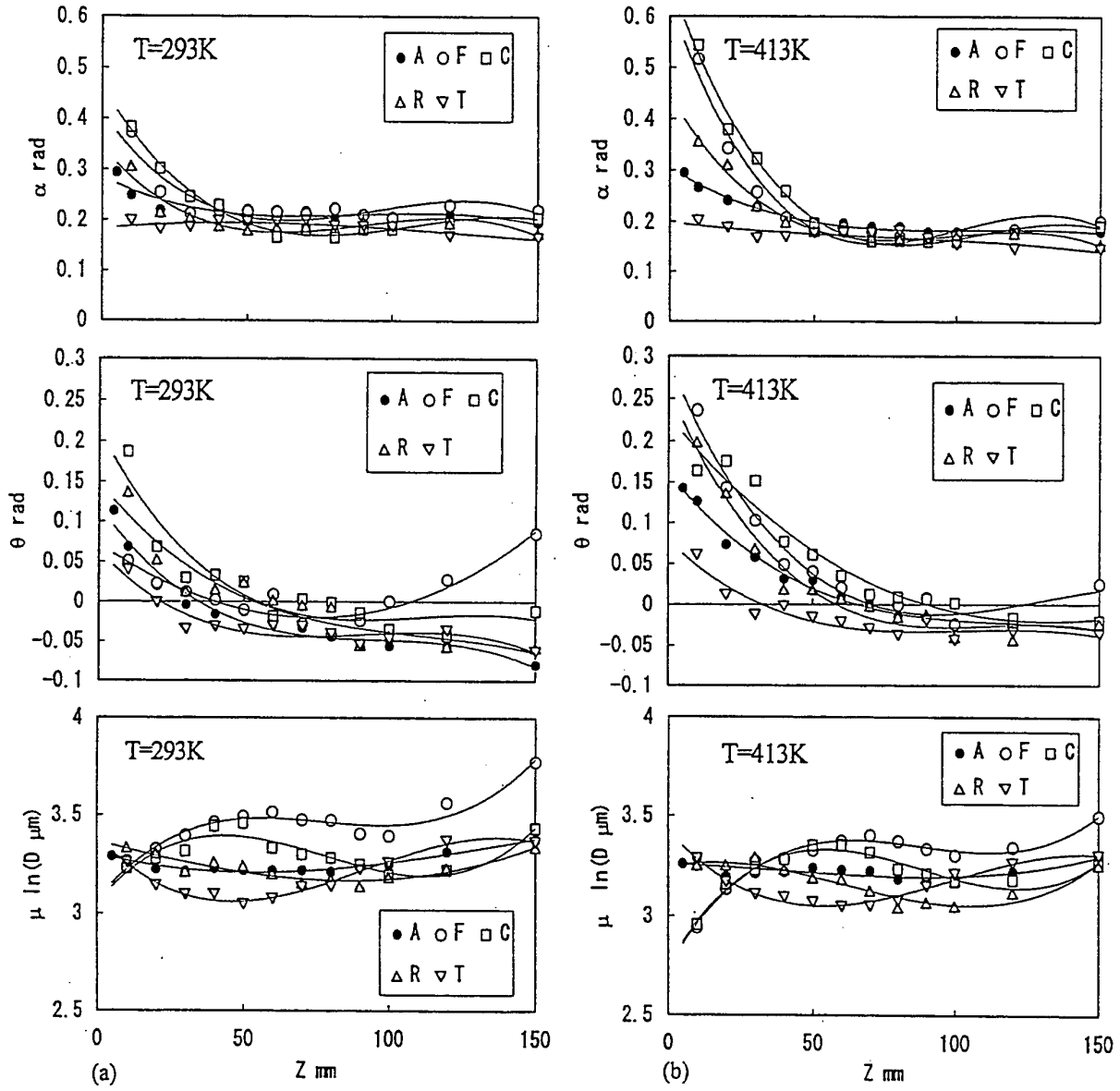

Figure 14 Distribution of three parameters of LH3 (r=0mm, Δt=2.5ms)

large droplets were accumulated in the F and C. At the high fuel temperature, the variance among the values of the parts becomes undistinguished. It is related with the decrease in the fuel kinematics viscosity and the fuel surface tension.

3.4 Evaluation of Droplet Size Distribution

Recently, the three parameter log-hyperbolic function (LH3) was reconsidered for evaluating the distribution of droplet diameters [8]. The function provided a good fitting curve for Diesel type spray [5] and gasoline type spray [6, 7]. This method plots the particle sizes and number density distribution on a diagram of logarithmic scales and fit a hyperbolic curve to the size distribution. The function represented by the hyperbolic curve has three parameters, α, θ and μ. The α defines the opening angle of the hyperbola, the θ is angle of the axis of the hyperbola relative to the coordinate system, and the μ is the location parameter defining the peak of the distribution. Since these parameters of α, θ and μ are related to the shape of the fitting curve, the droplet size distribution can be discussed by using them. Figure 13 shows an example of the measured size distribution of the droplets with the result of the LH3. In the figure, the abscissa is logarithmic scale of

droplet diameter of the histogram and the ordinate is logarithmic scale of the probability density. The result of the LH3 is obtained by using maximum likeness estimation proposed by Barndorff & Nielsen [11]. The fitting curve of the LH3 provides a good approximation to the size distribution of the air assisted spray. Figure 14 indicates the variation of the three parameters. For high fuel temperature, the α have more extent than that for the low fuel temperature at just after the nozzle exit. These parameters of θ and μ have a similar tendency with each temperature condition. The LH3 seems to be useful for describing the characteristics of the spray.

4. CONCLUDING REMARKS

In order to clarify the effect of the fuel temperature on the characteristics of the intermittent fuel spray initiated from the air assisted injector, the experimental study has been performed under the conditions of the fuel temperature changing from 293K to 413K. N-heptane which is one of the pure fuel was used for detail discussion. The concluding remarks are indicated as follows:

1. The mean velocity of the droplets in the fuel spray become large with increasing fuel temperature. These phenomena tend to become remarkable with increase in fuel flow rate. Axial flow velocity patterns are similar to each temperature condition.
2. The Sauter mean diameters increase in the region from 293K to 343K for intermittent spray and from 293K to 323K for steady continuous spray. After the region, they decrease.
3. For high fuel temperature, correlations between droplet velocity and diameter are different from that of room temperature of fuel. In the results of the correlation at high fuel temperature, the number of droplets with high velocity becomes larger than that for the low fuel temperature.
4. From the results of diameter classified velocity for various fuel temperatures, small decay of the droplet velocity is observed in high fuel temperature and in large diameter droplets.
5. The difference in the correlation at the different fuel temperature is observed at the fore and central parts of the spray cloud with time dividing method. In the result of the part of F and C under the high fuel temperature condition, it can be observed an existence of a lot of droplets with large velocity.
6. Log-hyperbolic function (LH3) well fits the droplets size distributions of the spray. The three parameters at the LH3 are useful for describing the characteristics of droplets size distribution of the spray.

REFERENCES

1. Hosoya, H. and Obokata, T. 1993, Effect of Nozzle Configuration on Characteristics of Steady-State Diesel Spray, SAE Paper No. 930593.
2. Coghe, A. and Cossali, G. E. 1994, Phase Doppler Characterization of a Diesel Spray Injected into a High Density Gas under Vaporization Regimes, Proc. of 7th Int. Symp. on Appli. of Laser Techniques to Fluid Mech., Lisbon, Paper No. 36. 3.
3. Kobashi, K. et al. 1990, Measurement of Fuel Injector Spray Flow of I.C.Engine by FFT Based Phase Doppler Anemometer, Proc. of 5th. Int. Symp. on Appli. of Laser Techniques to Fluid Mech., Lisbon, Paper No. 21. 2.
4. Vannobel, F. et al. D. 1992, Phase Doppler Anemometry Measurements on a Gasoline Spray Inside the Inlet Port and Downstream of the Induction Valve: Steady and Unsteady Flow Conditions, Proc. of 6th Int. Symp. on Appli. of Laser Techniques to Fluid Mech., Lisbon, Paper No. 25.1.
5. Obokata, T. and Long, W.Q. 1994, LDA/PDA Characterization of Conical Spray for Diesel Engine, Proc. of 6th. Int. Conference on Liquid Atomization and Spray Systems., Rouen, Paper No. IC94/90.
6. Obokata, T. et al. 1994, PDA Analysis of Transient Spray Flows Initiated from Air Assisted Injector, Proc. of 7th Int. Symp. on Appli. of Laser Techniques to Fluid Mech., Lisbon, Paper No. 36.5.
7. Obokata, T. et al 1995, Characterization of Spray Flow Initiated from Air Assisted Injector Using Phase Doppler Anemometer, FED-Vol. 229 Laser Anemometry, ASME
8. Xu, T.-H. et al. 1991, The Three-Parameter Log-Hyperbolic Distribution and its Applications to Particle Sizing, Proc. Int. Conf. on Liquid Atomization and Spray systems, ICLASS 91, Gaithersburg, Paper No.31, pp. 315-324.
9. Grèhan, G. et al. 1991, Evaluation of Phase Doppler System using Generalized Lorenz-Mie Theory, Proc. Int. Conf. Multiphase Flows. Tsukuba, pp. 291-294.
10. Rajaratnam, N. 1976 Turbulent Jets. Elsevier Scientific Publishing Company, Amsterdam.
11. Barndorff and Nielsen, O. 1977, Exponentially Decreasing Distributions for the Logarithm of Particle Size, Proc. R. Soc. of London, A. 353, pp. 401-419.

SPRAY FORMATION AND DISPERSION OF SIZE-CLASSIFIED FUEL DLOPLET OF AIR-ASSIST INJECTOR

Yuji Ikeda, Tsuyoshi Nakajima
Department of Mechanical Engineering
Kobe University
Rokkodai, Nada, Kobe 657 JAPAN
and
Noboru Kurihara
Ministry of International Trade and Industry
Umezono 1, Tsukuba 305 JAPAN

ABSTRACT

The droplet characteristics of the air-assisted gasoline injector was investigated. A Phase Doppler technique was used to measure droplet diameter and its velocity. The size-classes technique was employed and found to be the best way to understand what kind of droplet is existing in shear flow induced mushroom vortex at spray shell. The detail spray characteristics near nozzle was discussed and the double shell structure was found. The droplets of less than 20 μm can be entrained into mushroom vortex, while the larger of over 30 μm penetrates straight to downstream. The slip velocity and relative Reynolds number were used in data analysis in order to understand the momentum transfer occurence region due to strong drag force. The spray animation was demonstrated with the ensembled / size-classified droplet, which was found to be the powerful tool to understand spray formation and dispersion process.

1. INTRODUCTION

Fuel spray formations by gasoline injector [*Lenz (1990), Heywood (1988), Arcoumanis (1988), Beck, et al. (1986), Nuti (1990),* and so on.] have been used in internal combustion engines in order to improve engine performance and reduce exhaust emission. Understanding of mixture formation requires data as each fuel droplet velocity, diameter, evaporation rate, mass flux, entrained air, drag coefficient, spray shape, penetration and so on. Direct injections have been implemented even for small engines such as a two-stroke engine [*Sato & Nakayama (1987), Schechter, et al. (1991), Nuti (1986), Kenny, et al. (1993)*] in order to improve fuel consumption as lean combustion, dynamic range by stratified charge and derivability having stable combustion which can be achieved by reducing misfiring. When injected, the fuel spray penetrates into air by forming spray tip and spray shell surrounded by entrained air. The shape, spray angle and penetration of injected spray can be measured by visualization techniques as photo, lasersheet [*Kuwahara, et al. (1994), Shioji, et al. (1991)*], exciplex [*Felton (1993)*] and LIF [*Fujikawa, et al. (1995)*], but detailed information of each fuel droplet and its time history can not be obtained by planer measurements. The planar image methods can provide two-dimensional image of spray formation at a certain period which is indispensable for understanding of spatial spray structure, but can hardly provide sufficient temporal resolution.

On the other hand, one point measurement technique for spray study such as a phase Doppler technique (PDA or PDPA) can provide very high temporal resolution of droplet velocity and diameter, but this is only one point measurement, so that instantaneous spatial structure of spray can not be obtained. These two techniques are trade-off relationship in spatial and temporal resolution in order to understand the velocity variation, and so on.

When PDA (or PDPA) is applied for injector, a measuring system set up should not be the same as that used for steady spray such as spray burner. A system set-up optimization should be done in order to achieve high data rate, accepted rate, spherical ratio vary with time even a cycle. The bin number (time-window) should be carefully chosen in consideration of data number and required time-window.

In data analysis, the conventional droplet representation as Sauter mean diameter (SMD) is not enough to understand the evaporation process. A size-classified data analysis [*Presser, et al. (1995), Kawahara, et al. (1995)*] is one of the option to interpolate the physics of droplet dispersion and evaporation. This size-classified techniques have been applied in steady spray experiment and very simplified case [*Edwards & Rudoff (1990), Edwards, et al. (1990), Seay, et al. (1995), Hodges, et al. (1994)*]. The use of this size-classified technique for injector is one of a subject for future spray research. The mass flux measurement and agglomeration should be discussed to understand gasfication process and mixture formation. It is the best way for PDA to implement this size-classes method in injector study.

We have measured the spray formation process by PDA and showed an ensemble averaged Sauter mean diameter (SMD) velocity vector as a planar image [*Ikeda, et al. (1995)*].

The purpose of this investigation is to measure each droplet characteristics and classified into several groups in order to characterize droplet dynamic such as follow or penetration and dispersion process of droplet at high shear flow region and spray tip by means of slip velocity and relative Reynolds number of each size-classified droplet.

2. EXPERIMENTAL APPARATUS

An air-assisted injector used in this experiment was a practical injector for the two-stroke marine engine of over 22 kW (30 ps) as shown in Fig. 1 [*Ikeda, et al. (1995)*]. A fuel was injected in a cavity and then an air injector was operated by opening a poppet valve.

Figure 2 shows an experimental apparatus. All experiments were carried out under non-combustion and open air condition. The pressure difference of air and fuel was set up to 100 kPa and the air pressure was varied for different engine load conditions. A crankangle was set up and its timing signal was used to demonstrate an actual operating condition. The injector drive voltage was used as a starting trigger signal and the set-up timing was used as reference signal. The experiment was done under open air condition and surrounding air was sucked out by a blower to prevent from adhesion of fuel on to the optics. An argon-ion laser was used and the laser power at the measurement volume was set up over 300 mW [*Ikeda, et al. (1992)*]. For optimizing the measurement systems, four types of optics have been tried to optimize this measurement system having high data rate and less measurement uncertainly as shown in Table 1. Since a bandwidth of a processor was fixed, measurable velocity and diameter were determined by the size and the fringe spacing of measurement volume. Long focal length is desirable, but the resolution in velocity and diameter decrease, furthermore, the light scattered intensity from large measurement volume causes low SNR (Signal-to-Noise ratio) signal [*Ikeda, et al. (1990, 1991)*]. The small measurement volume is the best way to increase SNR. On the contrary, the maximum velocity and diameter were limited due to small fringe spacing and its measurement volume size. In this way, the optimization process is a very important factor in actual measurements to enhance reliability and data rate.

A drysolvent which has a refractive index of 1.427 was used as a fuel instead of gasoline. The specific density of the drysolvent of 0.77 g/cm3 is very similar to that of gasoline (0.7-0.8g/cm^3). The scattering angle of 68 degree was determined by first order refraction angle [Pitcher, et al. (1990)]. An ensemble averaged technique using a phase locking method of one degree resolution was implemented [*Ikeda, et al. (1995)*].

3. MEASUREMENT RESULTS

3.1 Two Dimensional Image of Spray

Direct pictures of the injected spray are shown in Fig. 3 [*Ikeda, et al. (1995)*]. It is clear that there is mushroom vortex induced by shear stress at spray shell. The spray tip velocity calculated from these picture is about 64 m/s. For farther discussion, a YAG laser sheet was used to take a two dimensional spray image as shown in Fig. 4. These shots are direct pictures at a certain cycle. It is well known that there is a cycle -to-cycle variation in this kind of air-assist injector. Then, two pictures at different cycle at the same timing are shown in the same figure. These picture results indicate the importance and need to analyze the spray by 2-D image having high temporal resolution, but the laser sheet visualization could not provide time variation information

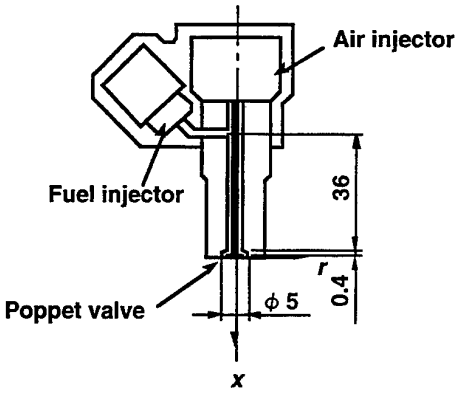

Fig. 1 Schematic of air-assist injector

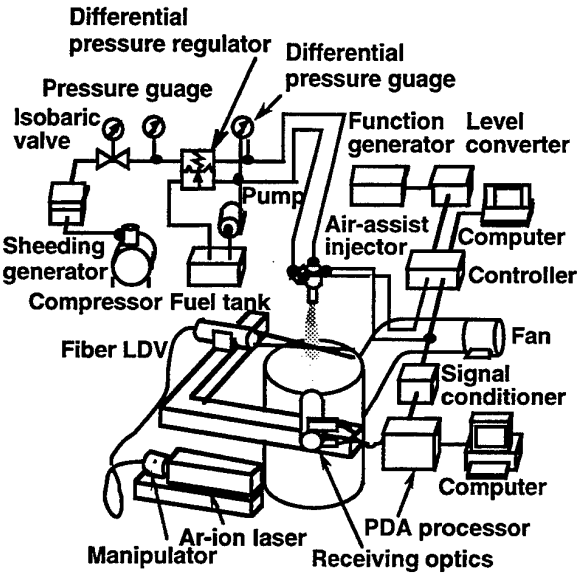

Fig. 2 Schematic of experimental apparatus

Table 1 Performance of FLDV probe for PDA measurement

	Type A	Type B	Type C	Type D
Forcal length (mm)	300.0	600.0	310.0	600.0
Spot diameter (μm)	63.0	126.0	228.0	440.0
Fringe spacing (μm)	2.6	5.2	4.3	8.3
Fringe number	24	24	54	53
Maximum diameter (μm)	50.7	101.4	81.7	157.5
Maximum velocity (m/s)	31.6	47.1	128.2	248.0
Minimum velocity (m/s)	-7.9	-15.7	-25.6	-49.6
Wavelength (nm)	632.8	632.8	514.5	514.5

where,
Focal length of receiving optics : 310 mm
Band widht of signal processor : 36 MHz
Frequency shift : 40 MHz

and diameter information. This is a trade-off relation. Once we use one point measurement we shall loose the cycle-to-cycle variation information and spatial structure variation. Even by one point measurement with ensemble averaged data, the two dimensional image of spray can be demonstrated its spatial structure as shown in Fig. 5. The Sauter mean diameter (SMD) having its velocity vector are shown in this figure.

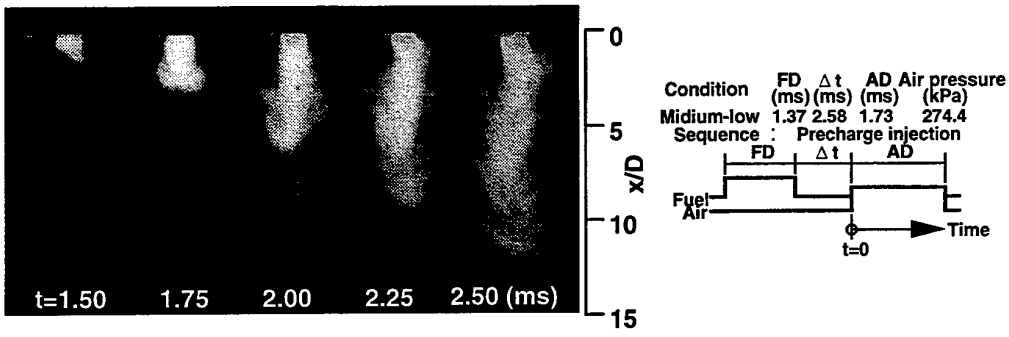

Fig. 3 Direct picture [*Ikeda, et al. (1995)*]

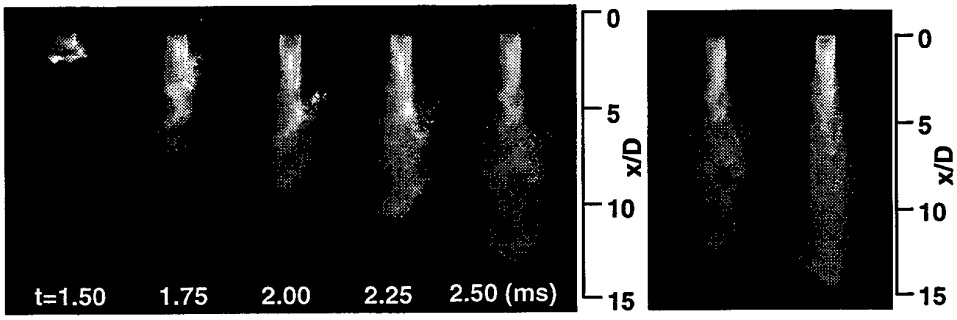

Fig. 4 Laser light sheet image (Cyclic Variation)

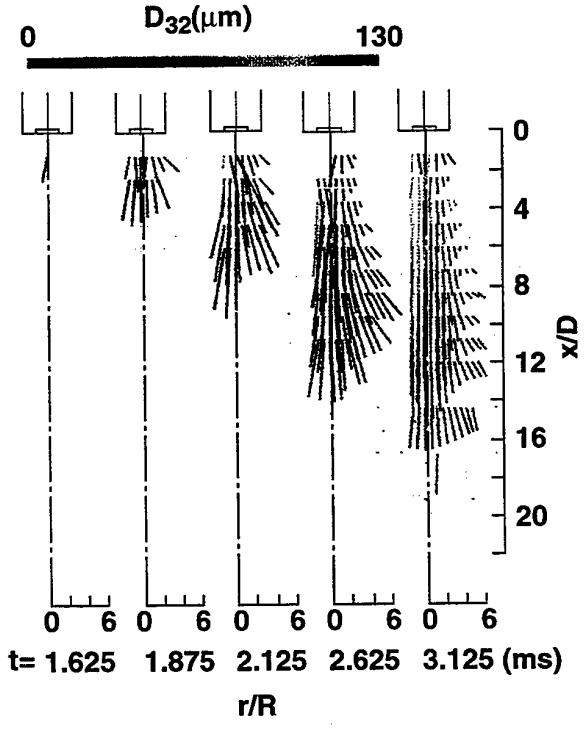

Fig. 5 SMD velocity vector [*Ikeda, et al. (1995)*]

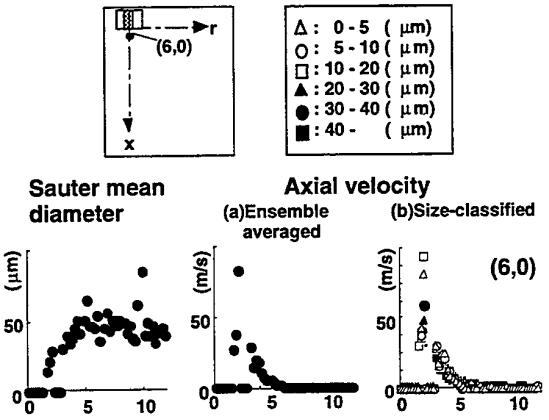

Fig. 6 Spray characteristics near nozzle

3.2 Spray Tip Characteristics near Nozzle

Figure 5 shows that small droplets injected at an early period and the larger one caught up with the spray tip. Near nozzle at 6 mm, further characteristics is examined in Figs. 6 and 7. Figure 6 shows the Sauter mean diameter, ensemble averaged axial velocity and size-classified axial velocities on the center axis near nozzle (6 mm). It is found that there are two peaks in all three figures, which mean the spray tip travels and passes at a point, and secondary spray tip exists and catch up with it, or spray shell at the tip may be double shell structure. The first velocity peak was over 80 m/s in the ensemble averaged, but this maximum velocity was due to small droplet less than 20 μm as shown in figure. The sec-

ond velocity peak has less velocity differences for each size-classes. The first peak is over 80 m/s but the second one is about 30 m/s.

In droplet diameter, the SMD is increasing with time and the SMD can be estimated around 40 - 50 μm in spray tail, which can hardly be understood with size-classified data. The SMD has been a very effective value to discuss spray characteristics but the value is not fit to these phenomena as accelerated and entrained.

For understanding these spray tip, droplet diameter distributions at 6 and 18 mm on the center axis are shown in Fig. 7. Near nozzle, the peak of droplet diameter distribution is the same diameter, while the second peak of diameter distribution is almost flat at 18 mm. It is assumed this is due to droplet agglomeration, which can hardly be explained in this measurement.

Anyway, these are two velocity peaks in the spray tip, and the first one was yielded by small droplet of less than below 20 μm.

3.3 Droplet Characteristics on the Center Axis

These two velocity peaks disappeared in downstream over 18 mm as shown in Fig. 8. This distance of 50 mm is almost the same as a cylinder stroke in two stroke engine. Near nozzle the SMD increases with time, in which two velocity peaks exist. At 30 mm, there is only one velocity peak. Here, the SMD shows its value over 90 μm which can not be understood by this nozzle characteristics. This SMD velocity peak decreases, but still shows the larger value of 60 μm. At 54 mm, the size-classified data shows very little discrepancies in each class velocity.

For further understanding of spray tip development, axial slip velocity, radial slip velocity and relative Reynolds number are shown in Fig. 9. An air velocity was defined as the droplet velocity of less than 5 μm.

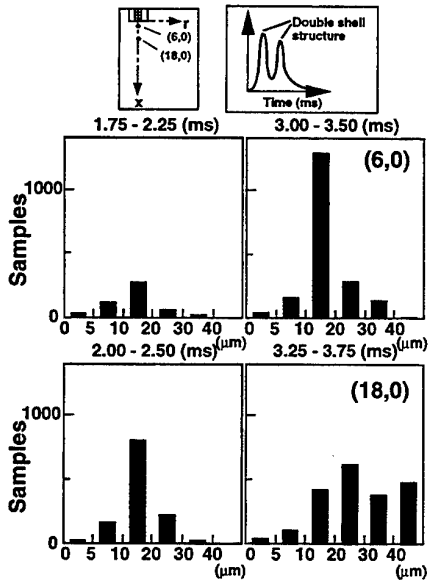

Fig. 7 Droplet diameter distribution at double shell stracture

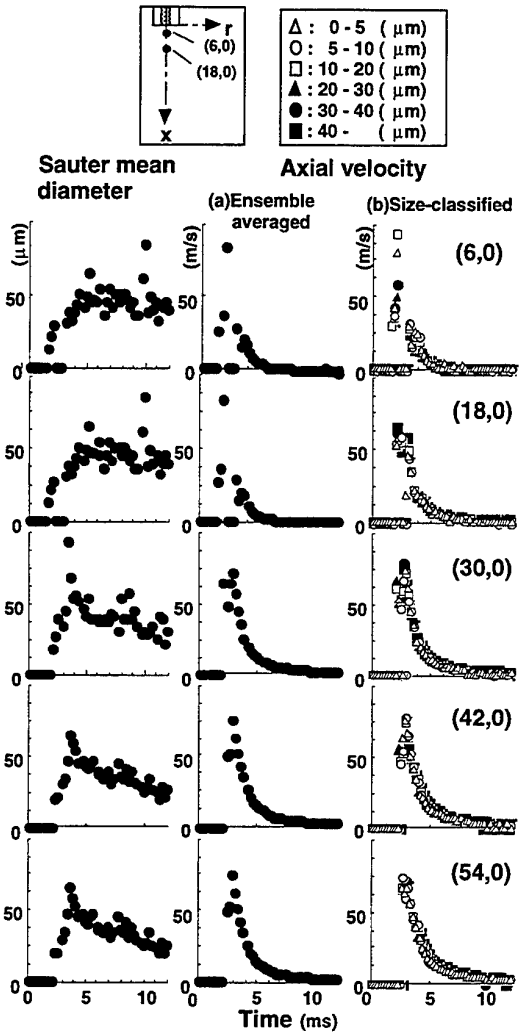

Fig. 8 Spray characteristics on the axis

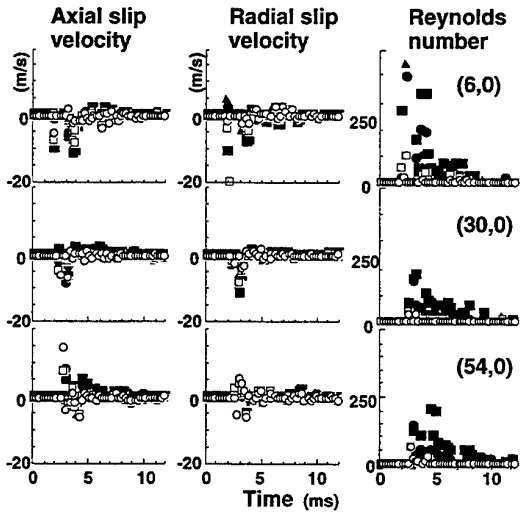

Fig. 9 Slip velocity and Reynolds number

At 6 mm, there are two negative peaks both in axial and radial slip velocities. Both velocities show that the larger droplet moves slowly and the smaller one travels very fast. The first and second peaks have the same characteristics.

At 54 mm, the smaller droplet moves faster than the air motion which indicates positive slip velocity. This is due to that the compressed air moves the droplets downstream near nozzle, then the droplet accelerated. At a certain distance the air motion was decreased by loosing its momentum, but the accelerated droplet increases its velocity and remains it. Then, the slip velocity changes its unit from negative to positive.

Relative Reynolds number was calculated with its averaged diameter of each size-classes and its averaged velocity in order to demonstrate a followable limit. Near the nozzle the limit size of the influenced droplet is about 10 - 20 μm, while its influenced droplet size increases with distance.

3.4 Spray Shell Characteristics

Here, the details droplet characteristics at spray shell will be discussed. As easily predicted, there is strong shear region at spray shell region due to strong drag force. A droplet momentum will be decreased and the droplet evaporates. There is the mushroom vortex as shown in Figs. 3 and 4.

It is found that the SMD is not a best representative value for spray characteristics in acceleration region on the center axis where droplets collapse and large droplets push the previous droplet downstream. Then let's see that at strong shear region. Figure 10 shows the SMD, ensemble averaged axial velocity, size-classified velocity of axial and radial directions.

There is no obvious two velocity peaks as observed on the center axis near nozzle, but it is possible to see that there is same hollow in velocity. In axial velocity, the velocity peak increases with distance, which is the contrary on the center axis. Near nozzle, small droplets exist for long period, while the small droplet looses its velocity and larger droplets have large axial velocity.

In the SMD, There are very ambiguous peaks, which was yielded after axial velocity peak. This is due to droplet aggravation at spray tail. It is also found the it is very difficult to discuss the spray characteristics just by the SMD.

In radial velocity, small droplets travels to outside near nozzle, but at distance droplet radial velocity decays rapidly and shows negative value which can be understood the negative pressure on the center line. At spray tail, larger droplets show larger radial velocity than the smaller.

The slip velocity and relative Reynolds number are shown in Fig. 11. Near nozzle, the positive slip velocities were caused both in axial and radial directions. The small droplet of 10 - 20 μm has larger slip velocity, which can be understood that the droplet under 10 - 20 μm can follow to turbulent air motion but the larger droplet over 10 - 20 μm will have drag and its trajectory will not the same as that of air.

3.5 Size-Classified Velocity Vector

The size-classified velocity vectors of less than 10 μm and over 30 μm are shown in Figs. 12 and 13.

At 1.875 ms, the smaller droplet has large velocity and its angle is large, while the large droplet shows less velocity.

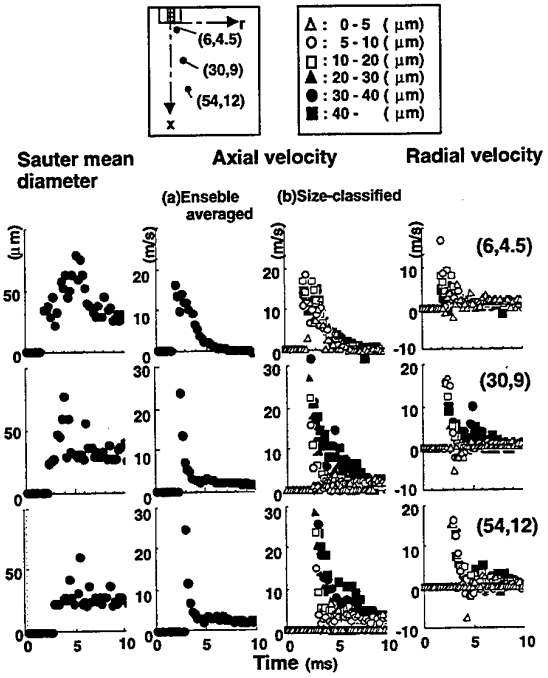

Fig. 10 Droplet dynamics at spray shell

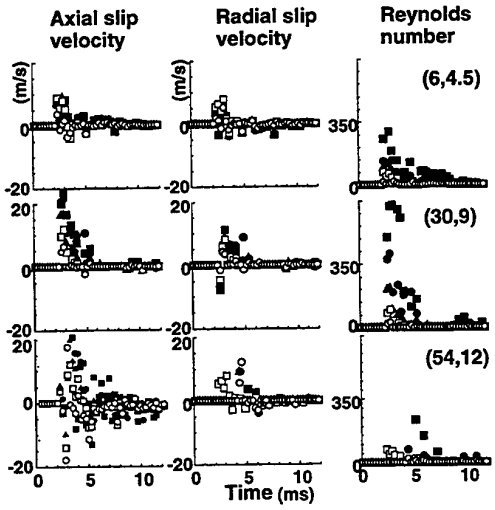

Fig. 11 Slip velocity and Reynolds number at spray shell

The velocity vector of the small droplet started to rotate in counter-clock wise direction at spray shell due to strong shear flow. In this mushroom vortex, the small droplet velocity decreases rapidly and diminishes.

On the other hand, the large droplet velocity vectors show a shear flow induced vortex at its spray shell and injected angle is almost straight.

For better understanding, four size-classified droplet velocity vectors are freezed at 2.875 ms as shown in Fig. 14. Obviously, there is shear flow induced mushroom vortex in the small droplet. At spray tip, the small droplet slows larger

velocity than the larger. The larger droplet vectors have straight and narrow injection angle. There are no larger droplets of over 30 μm at the spray shell region. (x/D<7).

The spray angle of each size classes and momentum decay should be quantified in order to understand evaporation process and mixture formation. Then, the air motion and turbulent energy intensity profiles are shown in Fig. 15. The large turbulent energy area shown in dark spot means strong shear flow region. At early injection period, the larger spot locates at the center axis. The dark area appears at the spray shell region in the next stage. The slip velocity vector shows the large vector angle at the strong shear region.

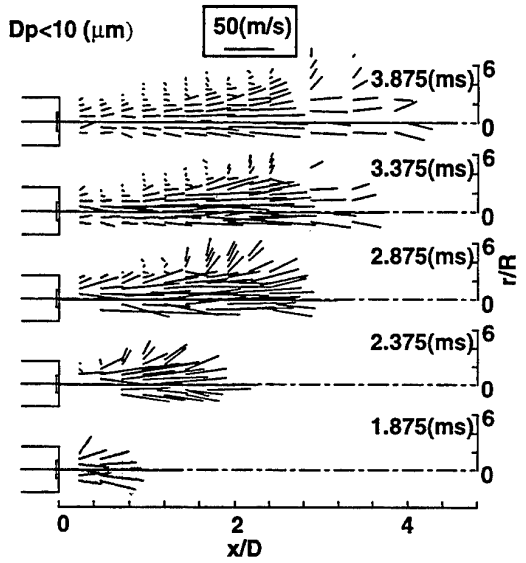

Fig. 12 Small droplet dynamics

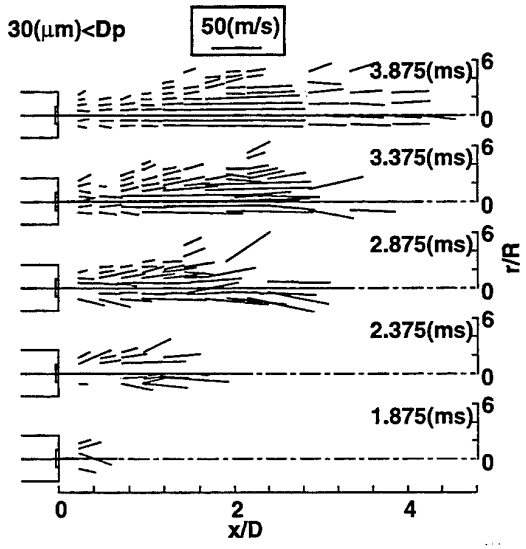

Fig. 13 Large droplet trajectory

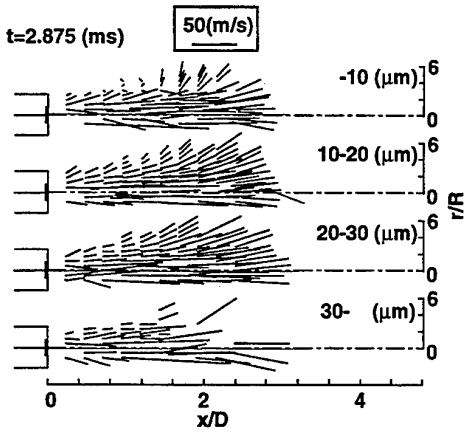

Fig. 14 Size-classified droplet dynamics at 2.875 msec

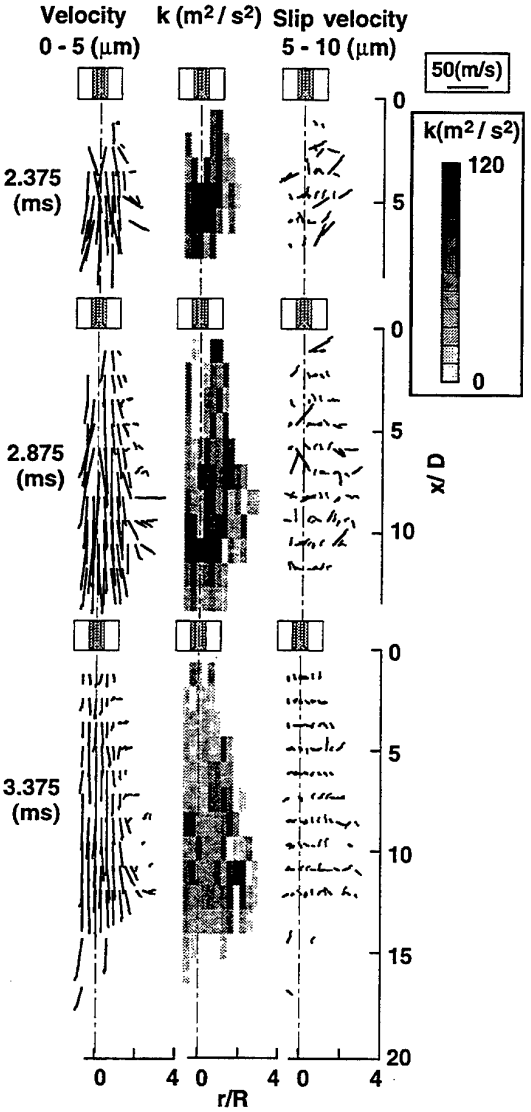

Fig. 15 Air flow motion, turbulent kinetic energy and slip velocity of small droplet

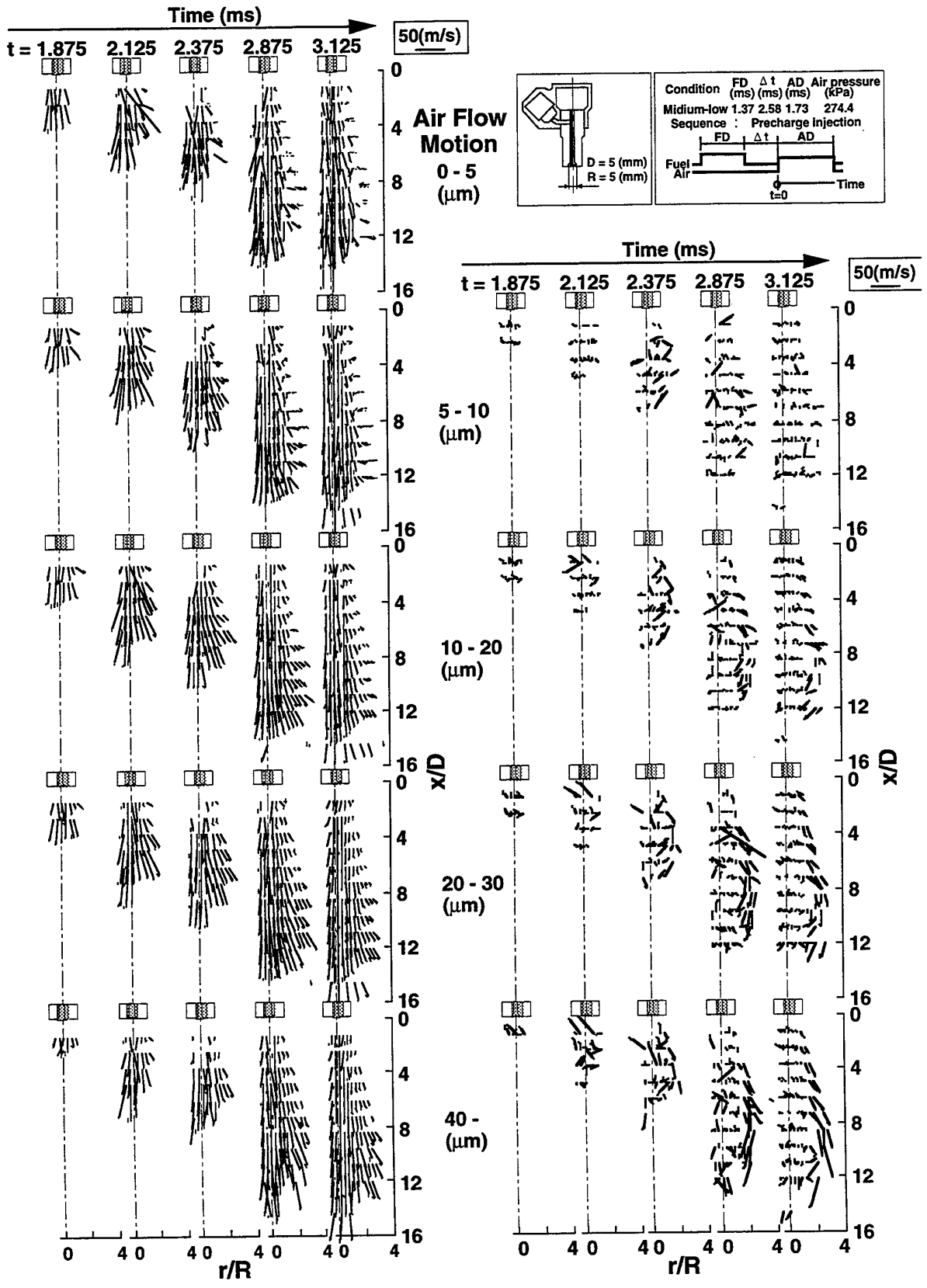

Fig. 16 Size-classified droplet velocity and slip velocity vector

3.6 Spray Animation

The spray animation of size-classified droplet, slip velocity vector with air flow motion are shown in Fig. 16. It is quite nice to see how injection processes are taken and the momentum decay and acceralation processes looks like. In an early period, the small droplet has large velocity and influenced by the shear flow. The mushroom vortex was caused at the spray shell and consisted of small droplet of less than 10 μm. The larger droplet penetrated straight to downstream. The large slip velocity vector area was the strong shear region in which droplet evaporates due to strong drag force.

The PDA is a one point measurement technique, however, this kind of spray animation is the one of breakthrough in spray research.

4. CONCLUSION

The spray characteristics of air-assisted gasoline injector has been investigated by phase Doppler measurements. The summarize is as follows:

A two-dimensional planer image of size-classified droplet was demonstrated to understand the spatial structure of spray formation. It is found that the Sauter mean diameter is not the best representation value at accelaration region, and the size-classes technique is very useful to understand detail spray characteristics. The slip velocity and relative Reynolds number was implemented to show the momentum transfer region which is due to strong drag force. The mushroom vortex was formed by the strong shear flow at spray shell and consists of the small droplet of 10 - 20 μm. A double spray tip structure was found near nozzle, which diminish rapidly with distance. The droplet larger than 30 μm penetrates almost straight to downstream. It is found that this spray animation can be the most powerful tool to understand momentum transfer process.

ACKNOWLEDGMENT

This research has been supported by the Grant-in Aid for Scientific Research, The Ministry of Education, Science, Sports and Culture, Government of Japan.

REFERENCES

Arcoumanis, C., 1988, Internal Combustion Engines, Academic Press.

Beck, N. J., et al., 1986, Electric Fuel Injection for Two-Stroke Cycle Gasoline Engines, SAE Paper No. 861242.

Edwards, C.F., et al., 1990, Measurement of Correlated Droplet Size and Velocity Statics, Size Distribution, and Volume Flux in a Steady Spray Flame, Fifth International Symposium of Laser Techniques to Fluid Mechanics, Lisbon.

Edwards, C.F. & Rudoff, R. C., 1990, Structure of a Swirl-Stabilized Spray Flame by Imaging, Laser Doppler Velocimetry, and Phase Doppler Anemometry, Twenty-Third Symposium on combustion, pp.1353-1359.

Felton, P. G., 1993, Fluorescence Imaging of Engine Sprays, Res. Paper ASI on Unsteady Combustion, L38.

Fujikawa, T., et al., 1995, Visualization Study of Misfire Phenomena under Light-Load Conditions in a 2-stroke Engine, Transactions of JSME, Vol.61-590.

Heywood, J. B., 1988, Internal Combustion Engine Fundamentals, McGraw Hill Book Co.

Hodges, J.T., et al., 1994, Analysis of Droplet Arrival Statistics in a Pressure-Atomized Spray Flame, Twenty-Fifth International Symposium on Combustion, pp. 353-361.

Ikeda, Y., et al., 1990, A Compact Fibre LDV with Perforated Beam Expander, Measurement Science and Technology. 1, pp. 260-264.

Ikeda, Y., et al.,1991, Scavenging Flow Measurements in a Fired Two-Stroke Engine by Fiber LDV, SAE Transaction, Section 3, Vol. 100, pp. 981-989, Paper No. 910670.

Ikeda, Y., et al., 1992, Flow Vector Measurements at the Scavenging Ports in a Fired Two-Stroke Engine, SAE Transaction, Section 3, Vol. 101, pp. 635-645, Paper No. 920420.

Ikeda, Y., et al., 1995, Spray Formation of Air-Assist Injection for Two-Stroke Engine, SAE Paper No. 950271.

Kawahara, N., et al., 1995, Droplet Followability and Slip Velocity Analysis of Evaporating Spray on Gun-Type Oil Burner, PARTEC95, pp. 593-602.

Kenny, R. G., et al., Application of Direct Air-Assisted Fuel Injection to a S.I. Cross-Scavenged Two-Stroke Engine, 1993, SAE Paper No. 932396.

Kuwahara, K., et al., 1994, Influence of Flow Field Structure after the Distortion of Tumble on Laser-Burn Flame Structure, Internal symposium, COMODIA94, pp. 84-94.

Lenz, H. P., 1990, Mixture Formation in Spark-Ignition Engines, Society of Automotive Engineering, Inc.

Nuti, M., 1986, Direct Fuel Injection : An Opportunity for Two-Stroke S.I. Engines in Road Vehicle Use, SAE Paper No. 860170.

Nuti, M., 1990, A Variable Timing Electronically Controlled High Pressure Injection System for 2T S.I. Engines, SAE Paper No. 900799.

Pitcher, G., et al., 1990, Sensitivity of Dropsize Measurements by Phase Doppler Anemometry to Refractive Index-Changes in Combusting Fuel Sprays, Fifth symposium on Applications of Laser Techniques to Fluid Mechanics, pp. 227-247.

Presser, C., et al., 1995, Interpretation of Size-classified Droplet Velocity Data in Swirling Spray Flames, AIAA Paper 95-0283.

Sato, T. & Nakayama, M., 1987, Gasoline Direct Injection for a Loop-Scavenged Two-Stroke Cycle Engine, SAE Paper No. 871690.

Schechter, M. M., et al., 1991, High Speed Fuel Injection System for 2-Stroke D.I. Gasoline Engine, SAE Transaction, Paper No. 910666.

Seay, J., et al., 1995, Atomization and Dispersion from a Radial Airblast Injector in a Subsonic Crossflow, AIAA Paper 95-3001.

Shioji, M., et al., Visualization of Turbulent Eddies in a Free Jet by a Laser Sheet Method, 1991, Transactions of JSME, Vol. 57-544.

SESSION 14

Aerodynamic Rotating Machines II

NEAR WAKE L.V. INVESTIGATION ON HOVERING ROTOR BLADES

J. Ramos, M. Nsi Mba, D. Favier and E. Berton

IRPHE/ASI Laboratory, UMR 138 of CNRS, University of Aix-Marseille I & II
163 Avenue de Luminy, Case 918, 13009 Marseille, France

ABSTRACT

This paper concerns an experimental investigation of the rotor aerodynamic field in hovering flight. The study emphasizes the characterization of the flowfield in the immediate vicinity of the blade and in its near wake.

The analysis of the near wake characteristics shed by a hovering rotor blade, is supported by measurements performed on the 3D velocity field around the blade and in the wake (determined by means of a long focal length laser velocimetry method). In the present study, a detailed survey of the rotor blade near wake region has been performed to directly measure the streamwise velocity deficit.

A specific L.V. data processing method based on the momentum equation applied around a blade section and in its near wake, has been developped to identify the contribution of the profile drag component to the total sectional drag coefficient.

1. INTRODUCTION

The design and the accurate prediction of the hovering rotor performance requires nowadays a realistic knowledge of several aerodynamic parameters induced by both the vortical wake and the rotor blades (see Caradonna (1990), Landgrebe (1986), Ramachandran et a. (1989), Steinhoff et a. (1987)). Among such parameters a better knowledge of drag mechanisms will constitute a valuable aid in the numerical modeling of local and overall airloads (see Favier et a. (1987), Maresca et a. (1988), Steinhoff et a. (1987)).

In order to investigate such drag mechanisms previous works from the present group (Berton et a. (1994), Favier et a. (1994), Ramos et a. (1994), Silva et a. (1993)) have been devoted to develop Laser Velocimetry methods capable to determine sectional loads contributions to overall hover performance. For instance a Laser Velocimetry methodology, so called KME-method (for Kutta and Momentum Equation) have been derived for determining the total lift and drag sectional coefficients along the blade span.

The present paper is focusing on development of a new flow scanning technique based on laser velocimetry to determine the near wake characteristics shed by a hovering rotor blade, and on a correlation with the blade profile drag. What follows is a brief description of the experimental methodology (section 2) based on a Laser Velocimetry measurement of the flow field around the blade sections. The methodologies associated to the theoretical analysis of the blade near wake characteristics and to the blade profile drag determination method (WMD-method for Wake Momentum Deficit) are described in section 3. Some examples of the results provided by such methods are also presented in section 3. An estimation of the efficiency of the WMD-method developped for determining the profile drag contribution to the total drag is also included.

2. EXPERIMENTAL SET-UP AND MEASUREMENTS METHODS

2.1 Experimental Facility Description

The model-scale of rotor (from the Aeroflight Dynamics Directorate-AFDD at Nasa Ames) is set up on the hovering test rig of the S1-Luminy wind tunnel. The test stand itself is mounted on an anti-vibration pad within the wind tunnel test hall.

The photograph in Figure 1 shows the rotor model mounted for testing in the hovering flight configuration. Shown in the foreground is the rotor hub with the L.V. optics traverse visible in the background. Note the orientation of the rotor disc plane. The rotor is mounted by means of an horizontal supporting mast, so that the center of the rotation is located 2.90 m above the ground. The rotor

drive shaft terminates in a right-angle gear box which can be rotated to allow any desired inclination of the rotor hub. An inverted orientation (thrust down, wake up) was chosen so that the distance between the rotor hub and the ceiling in this configuration is 13 m (6.5 rotor diameters).

2.2 Rotor Model Description

The rotor system tested was a 2 bladed, 2.13 m diameter, teetering rotor configuration with rectangular tip blades. The blades are of a stiff graphite composite construction designed to minimize aeroelastic deformations. Key geometric features of these blades are summarized in Table 1. The rectangular tip blades employ a constant VR-12 profile and twist rate from root to tip.

Table 1. Description of AFDD 1/7 scale rotor

Number of blades	2
Rotor radius	1066.8 mm (42.0 in)
Inboard chord	89.4 mm (3.521 in)
Blade aspect ratio	11.928
Cutout	.28R
Thrust-weighted solidity	.05027
Twist distribution	15.428 deg @ .28R 8.72 deg @ .86R 6.30 deg @ 1.0R
Airfoil distribution	VR-12, 3 deg tab

2.3 Measurements Procedures

Several measurements techniques suited for surveying the flow in the near and far wake regions and around the blades have been developed (see Berton et a. (1994), Favier et a. (1994), Ramos et a. (1994), Silva et a. (1993)) including X-wires anemometry and a long focal (2m to 2.5m) L.V. technique.

Overall forces measurements (averaged thrust and torque) are performed by means of a 6-components balance mounted on the rotor hub. Tip vortex path are measured by means of a hot-wires technique which allows the determination of the wake position as a function of the blade azimuth.

The three-dimensional velocity field is measured by a fiber optic laser velocimeter system. In the vicinity of the blade the velocity components U,V and the axial component W are determined by L.V. in a fixed coordinates system. Figure 1 provides a view of the L.V. system showing the traverse, optics, and the beam intersection forming the L.V. measuring volume. A glycerin-based smoke generator was used to seed the flow. Use of a 500 step encoder provides an azimuthal resolution of 0.72 deg (approximately .15 chords at .75R). The velocities used in our analyses are statistical averaged over an average minimum of 30 to 40 samples per time step. Detailed characterization of the flowfield is made possible by a combination of the .1 mm step resolution afforded by the laser optics traverse and the .3 mm diameter of the L.V. system measuring volume. The initiation and synchronisation of the instantaneous acquisition data are realized by means of a photo-cell delivering the azimuthal origin (Ψ = 0 deg). Figure 2 presents typical axial and tangential velocity time histories obtained using the present L.V. system. These figures also show that the L.V. system is capable of resolving periodic flow features such as those which define the blade passage (at 90 deg and 270 deg).

3. RESULTS AND DISCUSSION

3.1 Analysis of the Blade Near Wake Characteristics

Using L.V. application for performing the scanning of the flow field involves a detailed survey of the rotor blade near wake region to directly measure the streamwise velocity deficit. Figure 3 describes the notations and parameters used in the present study in order to carry out an accurate characterization of the flowfield in the near wake of the blade (see Favier et a. (1994)).

Wake velocity measurements were performed for a low-lift operating condition at θ=2 deg for collective at 1200 RPM and three radial stations, 0.55R, 0.75R, and 0.85R.

From the L.V. measurements a detailed description of the wake shed from the airfoil section into consideration can be obtained as exemplified in Figure 4 at r/R=0.75. The plots represent the evolution of the profile of tangential velocity deficit in the wake of the airfoil section at low pitch value (θ=2 deg). To characterize the velocity deficit profile within the wake sheet, the L.V. survey was tightened to ΔZ=1mm step size in the axial direction. Figure 4 presents the measured tangential velocity field as a function of the distance from the blade trailing edge. Note the loss of profile resolution between 2 to 3 chords aft of the blade trailing edge, as the wake sheet is convected downward out of the refined survey grid region.

Figure 5 presents in greater detail, a typical velocity deficit profile measured for a radial section r/R=0.75, within the wake sheet at a distance x/c=2 from the airfoil trailing edge. Convection of the wake downstream of the airfoil is shown in Figure 6, by the evolution of the maximum profile peak velocity as a function of distance from the blade trailing edge, which presents a linear behaviour.

An other wake characteristic parameter is L, defined as the width of the wake at the half value of the maximum velocity deficit. Figure 7 shows the

linear evolution of this wake limits parameter as a function of the distance from the blade trailing edge.

Assuming self-preservation, it can be shown from application of the equations of motion and mass conservation that the velocity distribution in the wake, is represented approximately by (see Favier et a. (1994)) :

$$\frac{\Delta U}{\Delta U_m} = e^{-4\ln(2)\frac{\eta^2}{2}} \qquad (1)$$

where ΔU is the mainstream velocity defect, ΔUm the maximal velocity defect at Z=0, and $\eta=Z/L$ where L is defined as indicated above.

Figure 8 presents an example of comparisons between this theoretical formulation, and the L.V. measurements at the distances x/c=1,5 and x/c=2,6 (c is the chord lengh), and shows the validity of equation (1) in the case of a rotor blade near wake for low values of θ.

Also, it has been shown by Favier et a. (1994) that the evolution of the wake centre-line velocity defect can be modelled according to the following formulation :

$$\Delta U_m = \frac{K}{\sqrt{\frac{x}{c}}} \qquad (2)$$

where K is a constant.

Dissipation of the wake downstream of the airfoil (as evidenced by a reduction in the profile's peak velocity) is shown in Figure 9. In this Figure, experimental results obtained at the radial station r/R=0.75, are compared with the theoretical formulation (2). It is shown that both the equations (1) and (2) provide very good approximations of the experimental data.

3.3 WMD-Method For Profile Drag Determination

Expressed in terms of the fixed frame perturbation velocity measured by the L.V. system, the profile drag determination method, sketched in Figure 10, has been already described in details by Ramos et a. (1994), Silva et a. (1993).

The WMD-method for the determination of profile drag, is based on the application of the momentum equation to the measured velocity profile in the wake. As shown in Figure 10, the profile drag coefficient at a given radial section of the blade is determined as a function of the wake velocity deficit in the near wake of the airfoil. Using the present L.V. system, the WMD method can easily be applied to the case of a hovering rotor. The assumptions on which the WMD formulation is based, namely that no pressure forces contribute to the streamwise momentum, and that no net streamwise momentum flux exists across the control surfaces normal to the freestream, are fair approximations for the case of a hovering rotor at low lift conditions. Ideally the integration is performed far enough downstream from the airfoil that the static pressure across the wake is equivalent to that of the undisturbed freestream.

The WMD-method has then been applied to the tangentiel velocity deficit profile measured in the wake to get the profile drag contribution Cdp as sketched in Figure 10. In the flow conditions of Figure 4, at the low pitch angle value θ=2 deg and r/R=0.75, the Cdp coefficient can be directly determined as a function of the downstream distance from the airfoil trailing edge.

A simple trapezoidal integration algorithm centered on the tangential velocity profile peak velocity and bounded by the profile zero crossings provided the evolution of the Cdp coefficient shown in Figure 11 as a function of the distance x/c behind the blade trailing edge. The results in Figure 11 indicate that for a distance x/c>2 from the trailing edge, the profile drag Cdp derived from the integrated wake deficit profile has a constant value. For distance x/c < 2 the sharp decrease in the Cdp values is to be attributed to the fact that the wake is not yet completely developped at such distances close to the trailing edge.

At a trailing distance of x/c>2 chords, the C_{dp} values calculated from the measured wake momentum deficits at 0.75R, is approximately 0.0092. The result compare favourably with the .0090 Cdp value commonly quoted for the VR-12 airfoil at similar Reynolds numbers. Figure 11 suggests that the integration of the results stabilizes within the second chord length aft of the trailing edge, remains fairly constant over the next 6 chord lengths, and slowly diminishes beyond 8 chord lengths. This behavior appears to be due to the wake dissipation with distance behind the trailing edge.

5. CONCLUSIONS

The present paper has concerned an experimental investigation of the drag mechanisms occuring on a helicopter rotor blades in hovering flight. The experimental approach conducted by means of local measurements has been focused on determining the 3D velocity field around the blade and in its wake. An effort in evaluating and improving the prediction efficiency of the profile drag contribution to the total sectional drag has been done by developping specific L.V. data processing method based on the momentum equation applied around a blade section.

In the present study, a detailed survey of the rotor blade near wake region has been performed to directly measure the streamwise velocity deficit. From such data sets, a theoretical analysis has been carried out in order to determine the characteristics of the flowfield in the immediate vicinity of the blade and in its near wake for low collective pitch conditions.

ACKNOWLEGMENTS

The authors wish to thank the support provided by the "Direction des Recherches Etudes et Techniques" under Grant 92/061. The authors would also like to acknowledge the U.S. and French Project officers of the US/France MOU for their contribution to this joint research work.

NOMENCLATURE

b	Number of blades
c	Constant blade chord, (c=0.05 m)
Cl,Clt	Total lift coefficient of airfoil sections
Cd,Cdt	Total drag coefficient of airfoil sections
Cdp	Profile drag coefficient of airfoil sections
Cdi	Induced drag coefficient of airfoil sections
C_T	Rotor thrust coefficient
C_Q	Rotor power coefficient
Γ	Blade circulation along the span, ($m^2.s^{-1}$)
n	Blade rotational frequency, (rps)
P	Static pressure, (Pa)
θ	Collective pitch angle at r/R=0.75, (deg)
θ_v	Blade twist law, (deg)
r	Radial distance from the rotation axis, (m)
R	Rotor blade radius, (R=0.75 m)
Ro	Root cut out, (Ro=0.22R)
σ	Rotor solidity (σ=bc/πR)
T,Q	Rotor thrust and torque, (N, N.m)
u, l	Upper and lower side of the blade sections
U,V,W	Radial, tangential and axial velocities
V_e	Rotational tip speed ($V_e = \Omega R$), $m.s^{-1}$
Ω	Angular rotational frequency, (Ω=143 $rad.s^{-1}$)
ψ, ψ_b	Angular blade rotation, (deg)

REFERENCES

Berton, E., Favier D., Maresca, C., Nsi Mba, M. 1994, Airloads determination on the hovering rotor using a laser velocimetry technique, AGARD, 75th Fluid Dynamics Panel Meeting and Symposium on Aerodynamics and Aeroacoustics of rotorcraft, Berlin, Germany.

Caradonna, F.X. 1990, The application of CFD to rotary wing flow problems, AGARD FDP, Special Course on Aerodynamics of Rotorcraft, VKI.

Favier, D., Nsi Mba, M., Barbi, C., Maresca, C. 1987, A free wake analysis for hovering rotors and advancing propellers, Vertica, Vol. 11, n°3, pp. 493-511.

Favier, D., Maresca, C., Nsi Mba, M., Berton, E., Ramos, J. 1994, Etude expérimentale et numérique de l'écoulement autour des pales d'un rotor d'hélicoptère en vol stationnaire ou en vol d'avancement, DRET Contract, n°92/061, Final Report.

Landgrebe, A.J. 1986, Overview of helicopter wake and airloads technology, Proc. of 12th European Rotorcraft Forum, Paper n°18, Garmish-Partenkirchen.

Maresca, C., Favier, D., Nsi Mba, M., Barbi, C. 1988, Validation à l'aide d'essais en soufflerie de codes de calcul du champ aérodynamique de rotors et d'hélices dans des conditions de vol variées, AGARD Conf. CP, n°437 on Validation of Computational Fluid Dynamics, Lisbon.

Ramachandran, K., Tung, C., and Caradona, F.X. 1989, Rotor hover performance prediction using a free-wake, computational fluid dynamics model, J. of Aircraft, Vol. 26, pp. 1105-1110.

Ramos, J., Nsi Mba, M., Berton, E., Favier, D., Silva, M. 1994, A laser velocimetric investigation of the airloads and performance of a model helicopter rotor in hover, American Helicopter Society Aeromechanics Specialists Conf., Paper n° 8.1, San Francisco.

Ramos, J., Berton, E., Nsi Mba, M., Favier, D. 1994, Etude de l'écoulement autour et dans le sillage proche des pales d'un rotor par une méthode de vélocimétrie laser, 4ème Congrès Francophone de Vélocimétrie Laser, Poitiers-Futuroscope.

Silva, M., Favier, D., Ramos, J., Nsi Mba, M., Berton, E. 1993, An experimental investigation of the drag mechanisms of a helicopter rotor in hovering flight, Proc. of 19th European Rotorcraft Forum, Paper n°18, Cernobbio.

Steinhoff, J., Ramachandran, K. 1987, A vortex embedding method of free wake analysis of helicopter rotor blades in hover, Proc. of 13th European Rotorcraft Forum, Paper n°2-11, Arles.

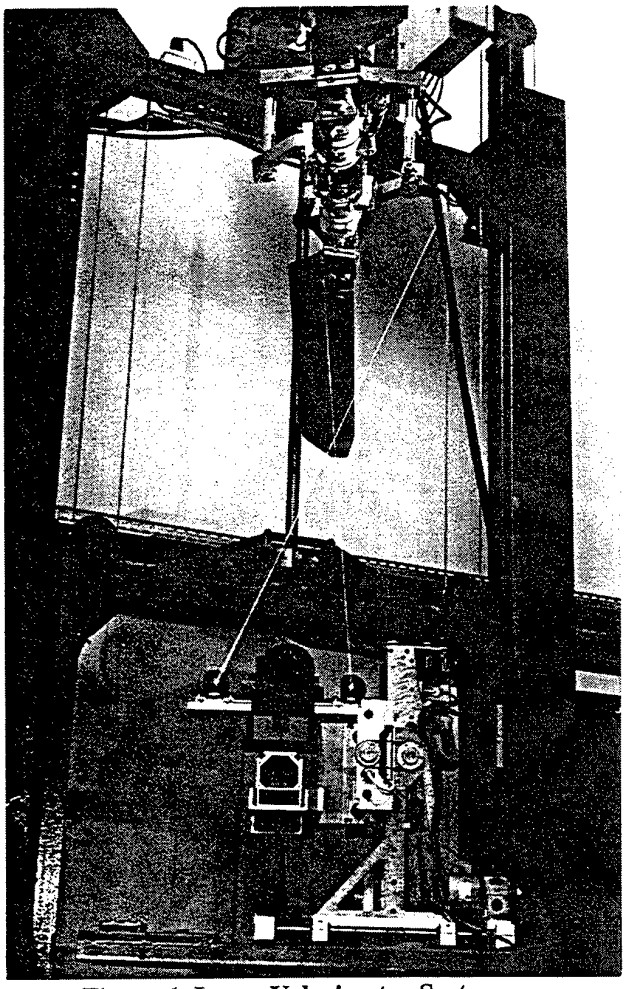

Figure 1. Laser Velocimetry System

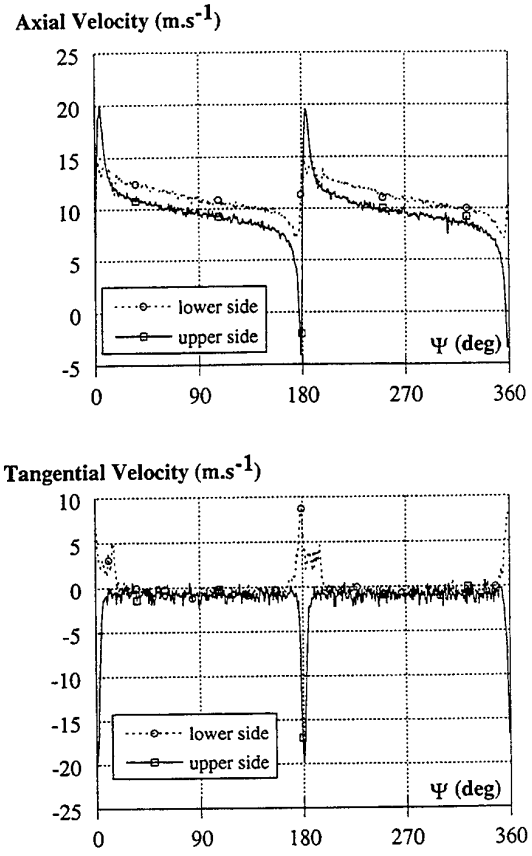

Figure 2. Typical LV axial and tangential velocity time histories r/R=0.75; θ=6 deg; Ω=125.7 rad.s^{-1}

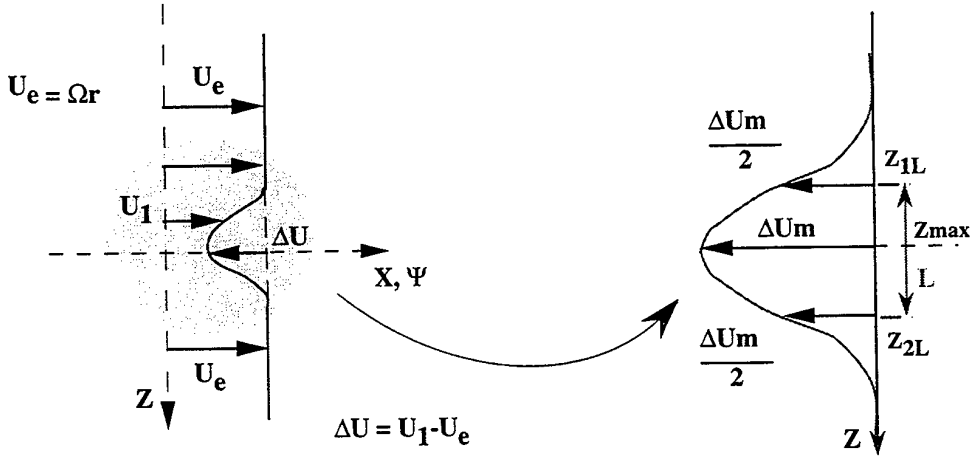

Figure 3. Parameters and notations used in an airfoil wake characterization

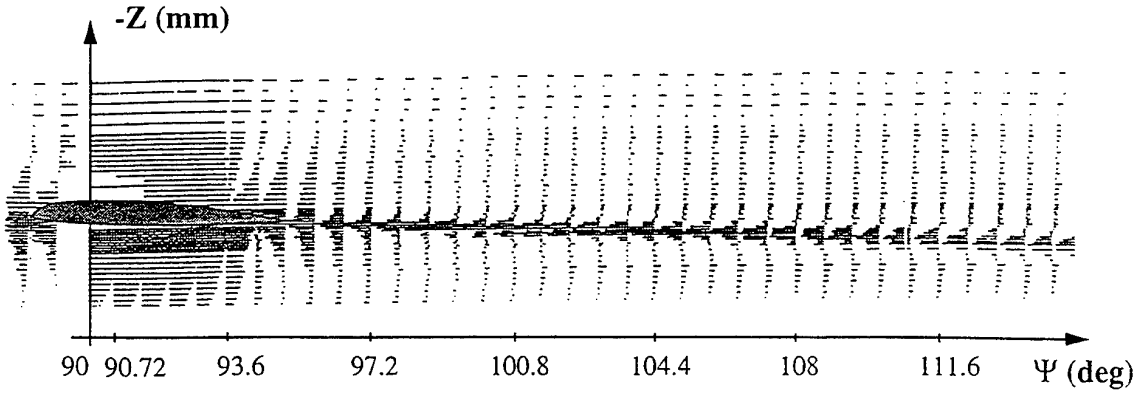

Figure 4. Measured tangential velocity field showing the evolution of the tangential velocity profile with distance from the blade trailing edge ; θ=2 deg; r/R=0.75; Ω=125.7 rad.s^{-1}

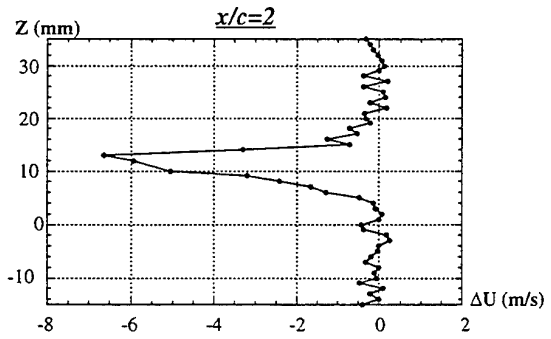

Figure 5. Tangential velocity profile in detail ; θ=2 deg; r/R=0.75

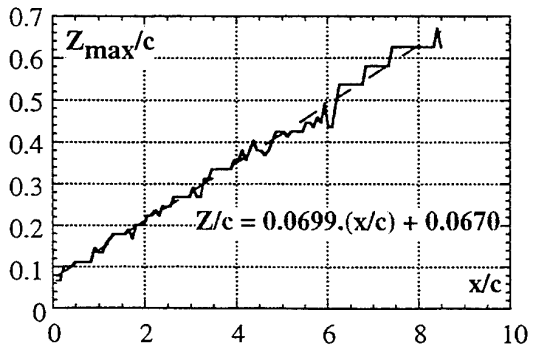

Figure 6. Trailing edge position θ=2 deg; r/R=0.55

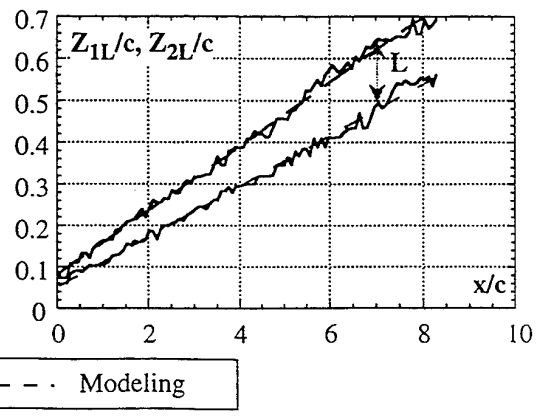

Figure 7. Evolution of the width L with distance behind blade trailing edge

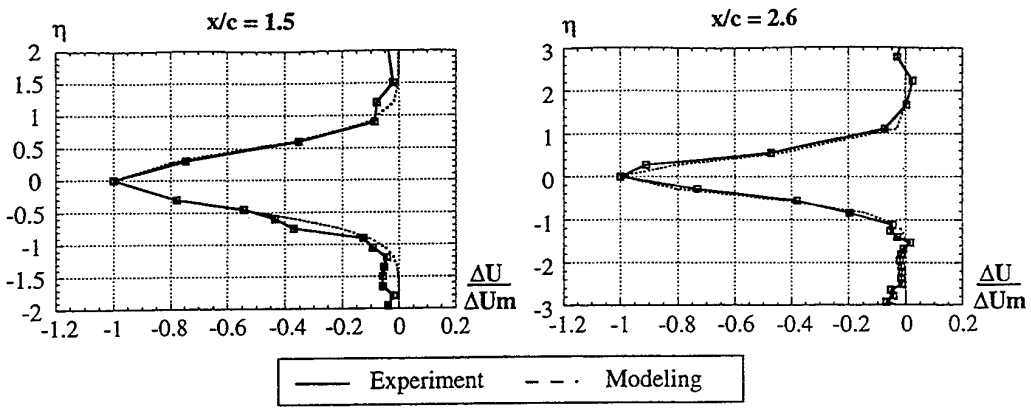

Figure 8. Comparisons on the velocity distribution in the wake ;θ = 2 deg ; r/R = 0.55

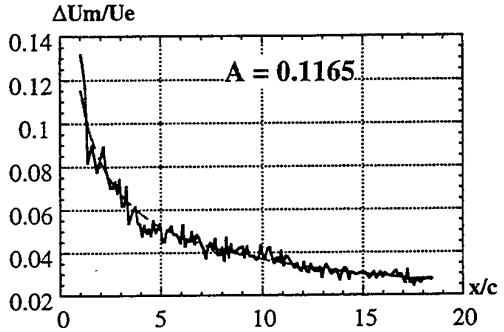

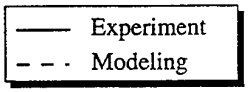

Figure 9. Comparison on the variation of the maximum velocity defect θ = 2 deg ; r/R = 0.75

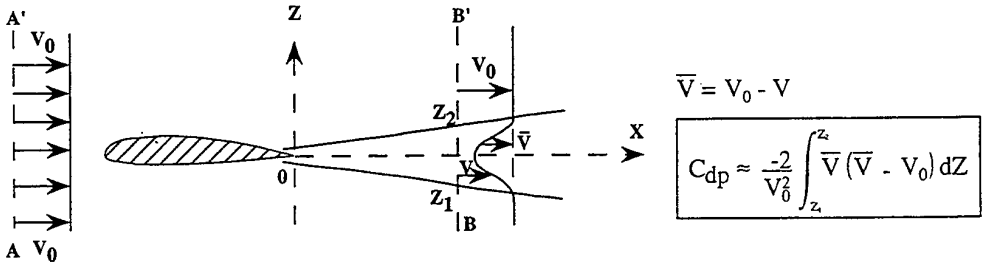

Figure 10. Determination of profile drag coefficient

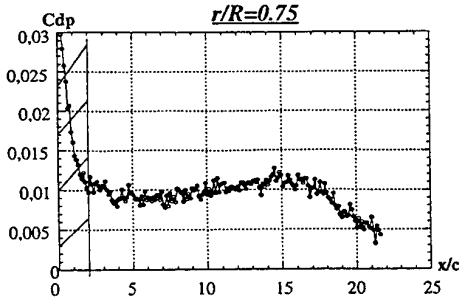

Figure 11. Profile drag coefficient derived from integrated velocity profiles ; θ=2 deg; Ω=125.7rd.s^{-1}

THE APPLICATION OF LASER ANEMOMETRY TO EDDY CAPTURE IN A PROPELLER INFLOW

J.M.Harden and M.V.Lowson

Department of Aerospace Engineering
University of Bristol, England.

ABSTRACT

The statistical properties of a turbulent flow at a point may be measured using either laser or hot-wire anemometry. However, data relating to the modification of individual flow structures precludes the use of such techniques in a conventional manner, especially in regions of high Reynolds stress. It is this type of measurement, made with a Dantec 3D laser Doppler anemometer (LDA) in a novel configuration, which is described for the flow through the axisymmetric contraction produced upstream of a 0.63 m diameter model propeller operating under high thrust conditions. The principal modifications to the conventional LDA configuration involved separating the measurement points of two optic heads, use of a 3 axis traverse mechanism to move the measurement points relative to one another, and an alignment set-up which enabled direct output of analogue velocity data. Eddy capture was assessed on-line using space-time correlations performed on a Brüel & Kjær (B&K) frequency analyser. The technique, which allowed data on individual eddies to be taken even in regions of highly turbulent, highly cyclical flow close to the propeller blades, is described in detail and a series of results presented.

1. INTRODUCTION

The performance of any given propeller is determined by the attitude of the blades with respect to the oncoming airstream. Consideration of mean flow quantities enables the determination of propeller performance in terms of thrust produced and power absorbed (Glauert, 1948). However, individual eddy structures not represented in a time-averaged realisation of the flow also affect performance in a number of ways. Interaction of turbulence with the blades leads to localised variations of lift, drag, induced velocity and contraction ratio across the span, with repercussions for overall thrust and power characteristics as well as noise radiation (Goldstein, 1976). These effects are of greatest importance for propellers operating under high thrust, low advance ratio conditions, where the axisymmetric contraction produced upstream of the blades is most severe. Such conditions occur in the take-off and climb phases of flight, during which large scale turbulent structures occurring naturally, as well as those caused by buildings, landscape features and other aircraft, are encountered at low altitude.

The behaviour of individual gusts and eddies under the influence of a propeller inflow is therefore of some importance, but investigation of the processes involved is hampered by difficulties in obtaining meaningful data. Single point measurements using hot-wire or LDA techniques can provide information on eddy size and structure through analysis of autocorrelations (ESDU, 1974), but are inappropriate for regions of high Reynolds stress and turbulence intensity, where the turbulence changes appreciably in a streamwise distance equal to the size of the largest eddies (Bradshaw, 1971). Such conditions are a feature of the flow under discussion. Cross-correlation of velocity signals measured at two points simultaneously can provide the data required, but hot-wire methods using multiple probes are again of limited value. In order to capture any given eddy at two points, the second probe must be inserted on or close by the streamline passing over the first. The result is a degraded correlation performance due to the interference caused by the upstream probe's wake.

The versatility and non-intrusive nature of the LDA meant that it was the only technique capable of providing the data needed, but only after significant modifications to the standard operating configurations used at Bristol University. The experimental requirements were principally for the simultaneous measurement of velocity from two separate points, incorporating the ability to move one point relative to the other in order to trace the progress of eddies throughout the area of interest. The facility for changing the velocity component under consideration was also necessary, as was measuring each component directly to enable instantaneous analogue output of signals. Cross-correlations could thus be assessed on-line, rather than via post-processing techniques.

2. EXPERIMENTAL PROCEDURE

2.1 Propeller Rig And Measurement Conditions

The test facility used was the upper working section of the Aerospace Engineering department's largest

wind tunnel at Bristol University, the cross section of which measures 2.13 m x 1.52 m (7 ft x 5 ft). Onset flow speeds of up to V_∞=60 m/s are possible, with the level of turbulence approximately 4.5 % across the speed range of interest.

The propeller rig comprised two distinct parts: the section located within the wind tunnel was restricted to those structural components necessary to hold the propeller in place and transfer drive to it. The bulkier components including the motor and much of the drive transfer mechanism were housed beneath the tunnel to minimise airflow interference.

The propeller itself was located at the tunnel mid-section, with the tip of the nose-cone designated as the origin for the purposes of the measurement axes. The co-ordinate system and measurement area of interest, as well as the propeller and rig components are shown in Figure 1. The measurement plane is XZ oriented, where the X axis is aligned with the onset flow direction, and the Z axis is vertical. In terms of the transverse Y direction, the plane is level with the tip of the propeller nose-cone. Due to the axisymmetric nature of the propeller inflow contraction, there is no mean flow into or out of the measurement plane in the Y direction. To reduce any flow impedance effects caused by the propeller supporting structure, only positive Z locations were used.

Low advance ratio (low J) running conditions were used to produce inflow conditions comparable to actual propellers operating at low altitudes. The mean streamlines illustrating the inflow distortion for a typical setting are shown in Figure 2.

2.2 LDA Set up

Two optic heads, each equipped with 1600 mm focal length lenses, were installed in gimbal mounts and positioned to allow access to the measurement plane. The optic head emitting a pair of blue beams was fixed in position with its gimbal mount attached to an immovable framework. The second optic head, emitting a pair of green beams, was set on a fully automated 3 axis Dantec traverse mechanism.

Both beam pairs were aligned separately, ensuring the Y position of the measurement point for the fixed optic head was within the measurement plane. The transverse position of the measurement point for the second optic head was less critical during alignment, as correct in-plane positioning could be finalised subsequently using the traverse mechanism. The alignments were performed via a quantitative technique based on the use of a pin-hole light meter with a 20 micron aperture, developed by Rickards et al (1993). Each optic head was set to operate in the back-scatter mode, with the gimbal mounts adjusted for no sweep or dip relative to the measurement plane. In this manner, U or W (X or Z sense) velocities could be measured directly, without the need for post-processing co-ordinate system transformations. To swap between components, the optic heads were rotated within the gimbal mounts by 90°.

For initial tests using this technique, the blue beam (fixed optic head) measurement point was set close to the upstream limit of the measurement plane (Figure 3). The downstream head was thus able to traverse throughout the rest of the plane in an attempt to capture eddies swept along mean flow streamlines from the upstream position. Subsequent experiments have involved repositioning of the fixed head at various points throughout the propeller inflow.

The optic heads were connected by fibre optic cables to a 5 Watt argon-ion Spectra Physics laser (Figure 4). Processing was performed by two Enhanced Burst Spectrum Analysers (BSAs) which featured the facility for velocity signal analogue output. On-line cross-correlation of these signals was performed by a dual channel B&K frequency analyser which also supported single-point autocorrelation and spectral analysis functions. An instantaneous assessment of eddy capture using cross-correlation of the analogue outputs was important due to the large area of interest and the severity of the flow distortion: post-processing methods would have entailed a large number of extra (and subsequently redundant) measurements.

3. RESULTS AND DISCUSSION

An example of how the technique of eddy capture was used in the highly oscillatory flow region close to the propeller blades is given in Figure 5. In this experiment, the separation of the two measurement points is over 600 mm in the streamwise direction. An 80 mm difference in Z positions reflects the contraction of the flow. The simultaneous turbulent velocity measurements from the two positions (5b and 5c) show significant differences: signal 1 is varying in a random manner, but signal 2 is oscillating at the blade passing frequency due to the proximity of the propeller.

Figures 5d) and 5e) show how single-point autocorrelations are ineffectual in this situation. Although the autocorrelation time span for signal 1 can provide, in this case, information on the extent of the W component of turbulent eddies in the flow direction, the signal 2 autocorrelation prevents any meaningful comparison due to the dominance of the blade pass effect. Furthermore, even if information on eddy size and structure could be obtained from Figure 5d), any conclusions regarding the development of the eddies from the upstream position depend on assuming that the mean flow streamlines do actually pass through both points. Due to the flow contraction and the bunching of streamlines as the propeller is approached (Figure 2), accurate positioning of the downstream beam focus at the most favourable point for catching the developing eddies becomes virtually impossible without direct feedback on the similarity of the two signals.

Despite the cyclical nature of the flow near the blades, the turbulent gusts and eddies which made up velocity signal 1 are not swamped by the propeller induced disturbance as they are ingested. Indeed, sufficient traces

of these eddies are represented in the downstream signal to produce a peak in the cross-correlation shown in Figure 5f). This plot contains useful information on the development of individual flow structures acted on by the propeller inflow regime, and directly relates the data from one point to another. The magnitude of the correlation peak is an indication of how intact an eddy has survived the journey between points - a 'frozen' eddy, a concept put forward by G.I.Taylor, would register a peak magnitude of 1. The time span of the peak provides size and structure information which, in this case, is in the direction of the mean flow. Furthermore, the transit time shows exactly how fast the eddies travelled between stations - this is not necessarily the mean flow speed.

The blade pass effect may be removed from the traces in Figures 5b) and 5d) by the use of filters on the Enhanced BSA analogue outputs. For some applications, the frequency of the disturbance to be removed may be close to that of the eddies being captured, in which case a filter would degrade the cross-correlation signal. Hence it is important that the basic method is robust enough to operate in the affected region as shown.

The technique described has been used for a wide range of experiments concerning the ingestion of coherent turbulent structures by the model propeller (Harden, 1996). Some of the initial results made with the LDA in the configuration described are presented below.

Figure 6 shows two-component eddy capture along a propeller inflow streamline. As the separation of the measurement points increases, so to does the position of peak correlation. In terms of the average eddy size in the mean flow direction, the U component correlation time spans can be seen to be greater than the W component spans. This is because the direction of the U component velocity fluctuations is closely aligned to the mean flow direction, thus increasing the effective readings. In terms of peak magnitude, the decay of the U component peaks is more marked, probably due to the variation in blade pass disturbance between components. However, both U and W component eddies can still be traced to a downstream position behind the tip of the nose-cone.

Figure 7 shows the same kind of results, but this time the positional variation of the downstream optic head is in the Z direction. W component results are presented, and again the eddy time spans are short because the individual measurements still reflect average size in the mean flow direction. This experiment was repeated at several operational settings and the peak magnitude variations with Z position are shown in Figure 8. Propeller advance ratio thus appears to have little effect on the shape of the distributions, but the overall plots are shifted down as advance ratio decreases. This corresponds to an increase in the severity of the inflow contraction with decreasing advance ratio - the eddies are simply following the mean flow. Similar plots for U component velocities yield the same results, but the distributions are narrower. Hence the average eddy size in the vertical direction is greater for the W component of turbulent velocity. This expected result is the reverse of the streamwise observations from Figure 6.

4. CONCLUSIONS

Simultaneous two-point velocity measurements using a laser Doppler anemometer may be used to reveal data on the development of eddies in a turbulent flow. By using on-line processing of analogue signals, large surveys taking data which proves mostly redundant can be avoided.

Cross-correlations of velocity from the measurement points can be used to detail the progress of eddies ingested by a model propeller operating under high thrust conditions. Two component eddy capture is possible throughout the propeller inflow, even within the highly oscillatory flow region close to the blades. Data on eddy size, strength and velocity can be used to show the impact of the inflow contraction on these turbulent structures at a range of operational settings.

5. ACKNOWLEDGEMENTS

This work was supported under EPSRC Grant GR/J 15407 in co-operation with Dowty Aerospace Propellers, Gloucester, England. Thanks goes to these establishments.

6. REFERENCES

Bradshaw, P. (1971) An Introduction to Turbulence and its Measurement. Pergamon Press.

ESDU 74030 (1974) Characteristics of Atmospheric Turbulence Near the Ground.

Glauert, H. (1948) The Elements of Aerofoil and Airscrew Theory. Cambridge University Press.

Goldstein, M.E. (1976) Aeroacoustics. McGraw-Hill, pp. 161-293.

Harden, J.M., Lowson, M.V., (July, 1996) Unsteady Propeller Flows Due To Turbulence Ingestion. R. Aero. Soc. Unsteady Aerodynamics Conference, London.

Rickards, J., Swales, C., Brake, C.J., Barratt, R.V. (1993) An Improved Alignment Technique Enabling Cross-coupled Operation of a Laser Doppler Anemometer for Small Scale Flow Surveys. 5th Int. LDA Conference, Veldhoven, The Netherlands.

Taylor, G.I. (1935) Statistical Theory of Turbulence. Proc. Roy. Soc. A., vol 156.

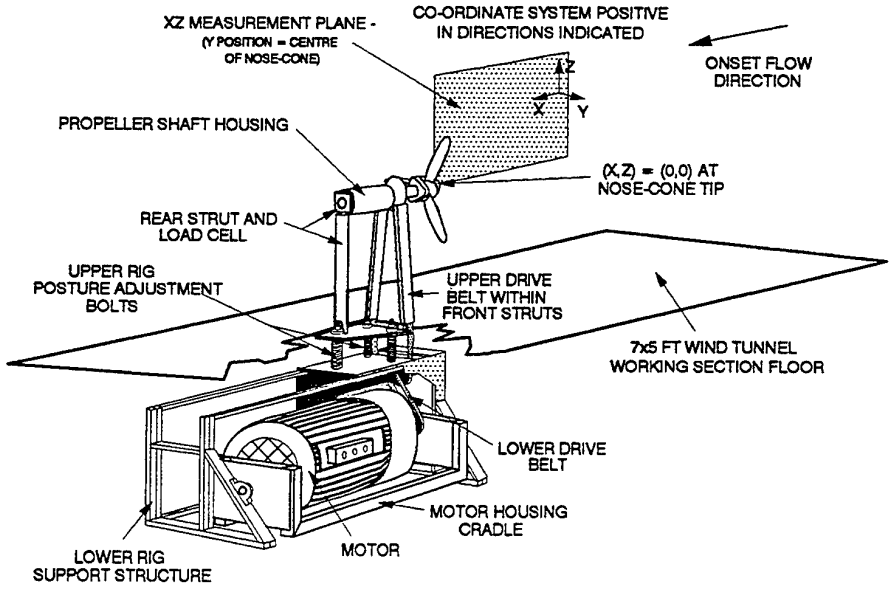

Figure 1 Propeller Rig And Measurement Plane

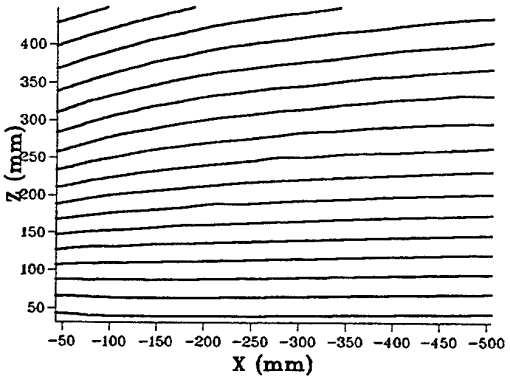

8 m/s ONSET FLOW

4000 RPM (J=0.19)

Figure 2 Propeller Mean Inflow Streamlines

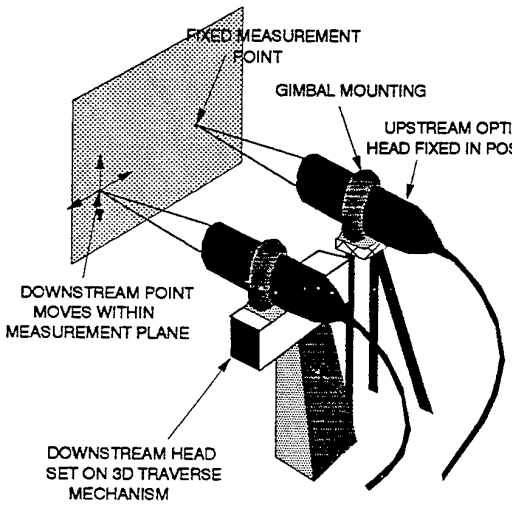

Figure 3 LDA Set Up

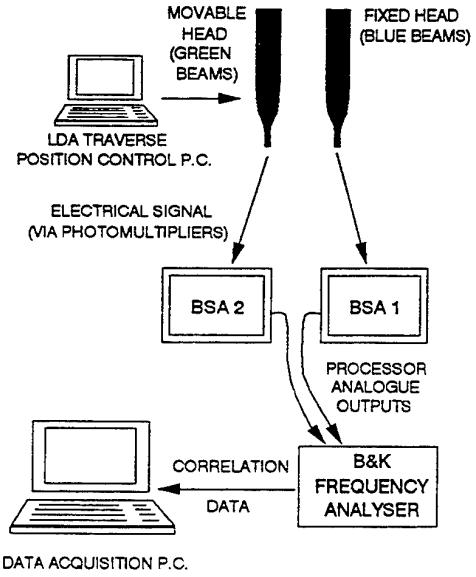

Figure 4 Data Acquisition

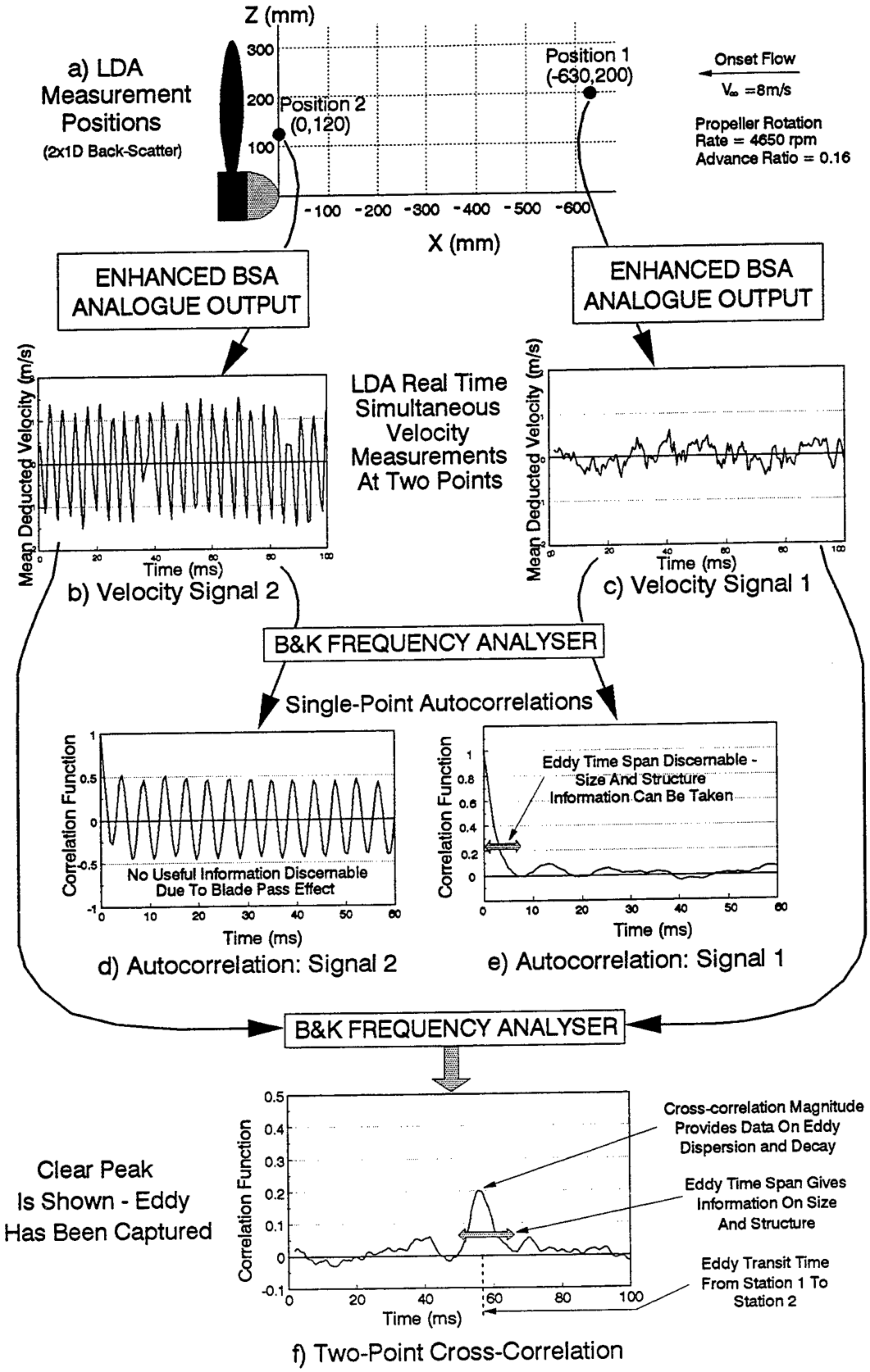

Figure 5 Method Of Eddy Capture (W Component) In The Propeller Inflow At Advance Ratio (J) = 0.16

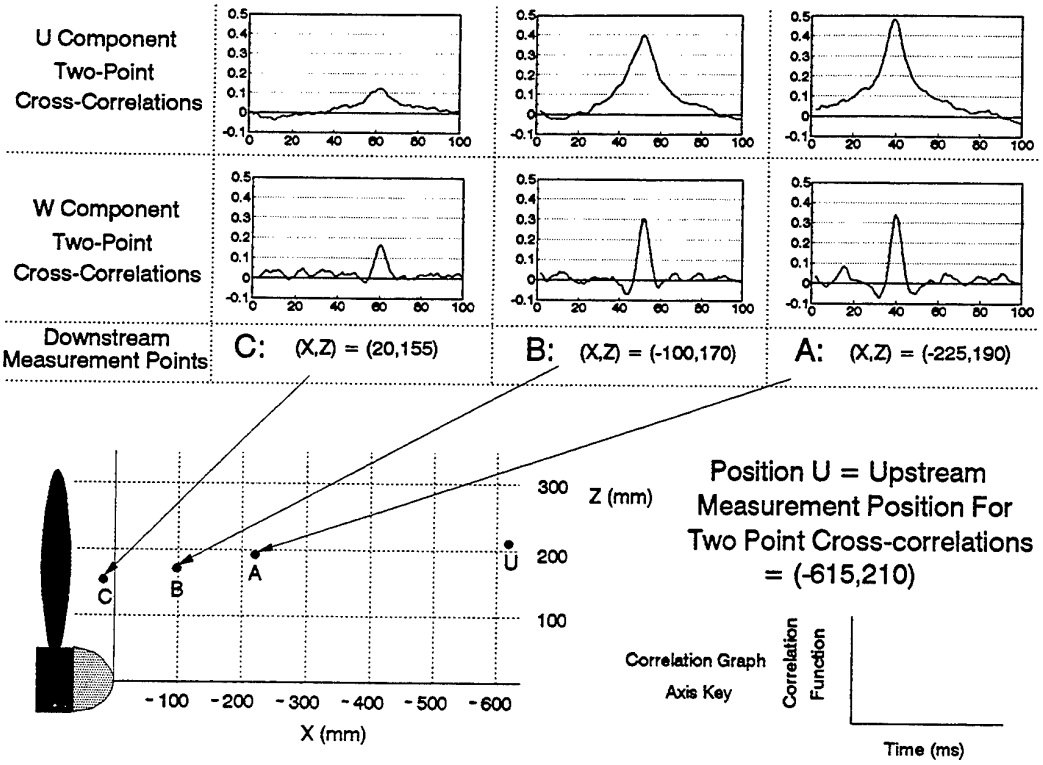

Figure 6 Two Component Eddy Capture In The Propeller Inflow. LDA Measurements at J=0.23 (V_∞=8m/s; 3330 rpm)

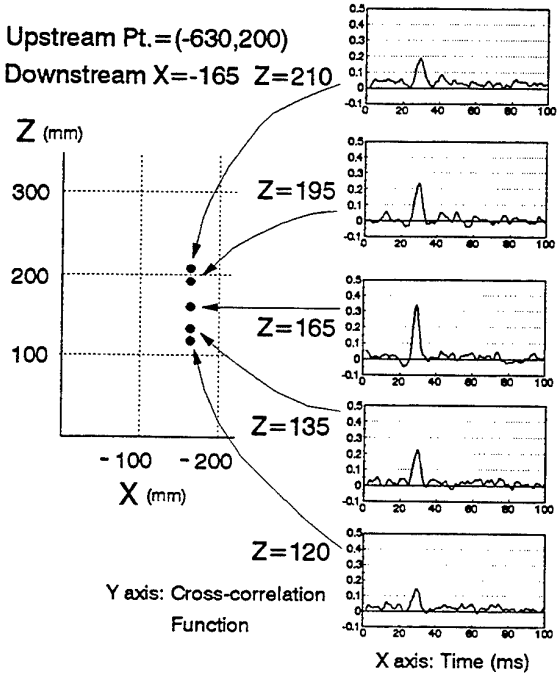

(V_∞=16m/s; 4000rpm)

Figure 7 W Component Cross-Flow Correlations

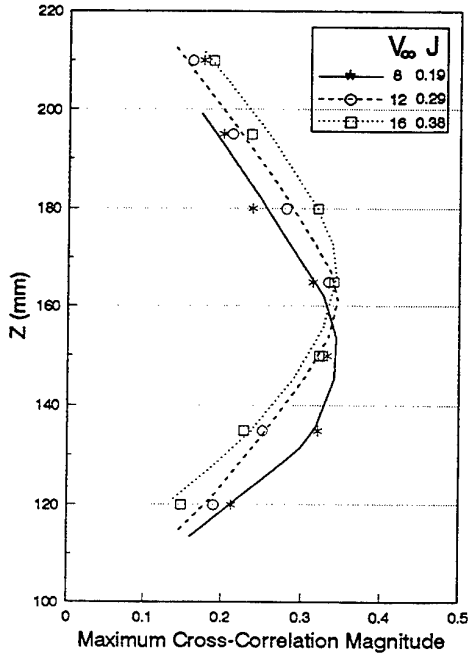

(W Component, 4000 rpm)

Figure 8 Peak Cross-Flow Correlation Values

MEASUREMENT OF VORTICAL STRUCTURES ON A HELICOPTER ROTOR MODEL IN A WIND TUNNEL BY LDV AND PIV

M. Raffel, U. Seelhorst, C. Willert, H. Vollmers, K.A. Bütefisch, J. Kompenhans

Institut für Strömungsmechanik
Deutsche Forschungsanstalt für Luft- und Raumfahrt (DLR)
Bunsenstraße 10, D-37073 Göttingen, Germany

ABSTRACT

Measurements of blade vortex interactions at a helicopter rotor model were performed by three component laser Doppler velocimetry (3D-LDV) and conventional (two component) particle image velocimetry (PIV). The results are in good correspondence in general, but also illustrate the different properties of both techniques.

1 INTRODUCTION

With increasing use of civil helicopters the problem of noise emission of helicopters has become increasingly important within the last decades. Helicopter noise has been subject of many research projects (Lowson 1991). Blade vortex interactions (BVI) have been identified as a major source of impulsive noise. As BVI-noise is governed by the induced velocities of tip vortices, it depends on vortex strength and miss-distance, which itself depends on vortex location, orientation, and convection speed relative to the path of the advancing blade. Blade vortex interaction can occur at different locations inside the rotor plane depending on flight velocity and orientation of the blade tip path plane. It has to be distinguished between parallel blade vortex interaction (angle between leading edge and vortex axis is $\approx 0°$) and orthogonal blade vortex interaction (angle between leading edge and vortex axis is $\approx 90°$). The noise emission of parallel blade vortex interaction is considerably larger (Cardonne et al. 1988, Splettstößer et al. 1990). Investigations of the accoustic near and farfield (Ehrenfried et al. 1991, Burley et al. 1991) were based on the interaction of the blade with vortices, which were described by mathematical models. Information about the structure and strength of the real rotor tip vortices and their interaction with the blade were not available for a long period. It is understood, that the study of these phenomena is of particular interest for progress towards quieter helicopters. In our investigations the vortical structures at a helicopter rotor model in a wind tunnel has been studied by optical measurement techniques, since only non-intrusive techniques are capable to obtain velocity data within the rotor plane. Measurements of local flow vectors at positions close to the rotor blade tips were performed by three component laser Doppler velocimetry (3D-LDV) and conventional (two component) particle image velocimetry (PIV). Since a comparison of LDV and PIV data acquired in a wind tunnel from the same rotor model have been performed for the first time, a blade position has been chosen where vortex positions and their orthogonal interactions with the blade are well known and are easily reproducible (see Fig. 1, case A). Additionally, the parallel interaction of a blade with vortices further downstream have been investigated by PIV (see Fig. 1, case B).

2 ROTOR AND TEST MATRIX

The LDV and PIV measurements have been performed at the same helicopter rotor model of the Department of Aerospace Engineering (ILR) of RWTH Aachen, developed and instestigated in detail by Beesten (1994). The rotor model, had a radius of 0.5 m and four NACA 0015 blades (chord length = 54 mm) with rectangular tips. It was driven by a toothed belt and an electric 65 kW engine. The rotor model was fully articulated and had flapping hinges. The rotor was installed in the open test section of the ILR Aachen low-speed wind tunnel.

For the investigation of orthogonal blade vortex interaction LDV and PIV measurements have been taken at an azimuth angle of $\psi \approx 90°$ (advancing blade side) in a plane directly behind the blade (see Fig. 1, case A). The free stream velocity was set to U = 15.7 m/s and the rotor speed to f = 25 rev/s resulting in an advance ratio of $\mu \approx 0.2$. The tip path plane was tilted by an angle of $\alpha_{TPP} = -3°$ against the mean flow (forward flight), the collective part of the angle of attack was $\upsilon_{coll} = 10°$, and the cyclic pitch was $\upsilon_{cycl} = \pm 3.5°$ resulting in trimmed condition. The Reynolds number, based on the main chord length and blade tip velocity, was $Re \approx 278.000$.

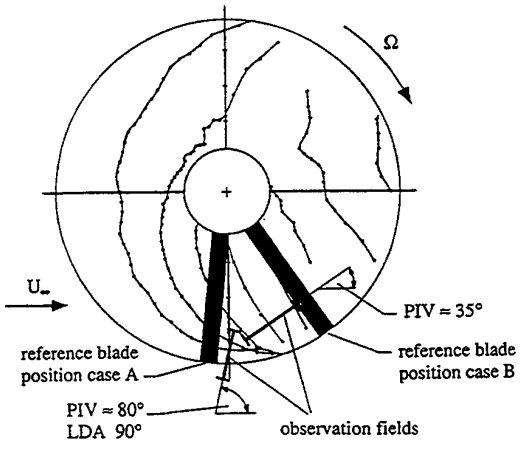

Figure 1: *Sketch of the pathes of the tip vortices at an advance ratio of $\mu = 0.2$, viewing direction parallel to the rotor axis, according to Beesten (1994) - not to scale.*

For the investigation of parallel blade vortex interaction PIV measurements were obtained at an azimuthal angle of $\psi \approx 60°$ (advancing blade side) in a plane orthogonal to the reference blade at ≈ 60% chord (see Fig. 1, case B). In this case, descent flight conditions was chosen, for which a high impulse noise has been observed during earlier accoustic measurements (Beesten 1994). The free stream velocity was set to U = 31.4 m/s and the rotor speed to f = 50 rev/s again resulting in an advance ratio of $\mu \approx 0.2$. The tip path plane was tilted by an angle of $\alpha_{TPP} = +4°$ against the mean flow (descent flight) and the collective part of the angle of attack was set to $\upsilon_{coll} = 11°$ in order to generate very strong tip vortices. The cyclic pitch was $\upsilon_{cycl} = \pm 3.5°$ again resulting in a trimmed condition. The Reynolds number was Re ≈ 340.000.

3 3D-LDV SET-UP

A new implementation of the 3D-LDV at the DLR Institute for Fluid Mechanics brought major improvements concerning sensitivity, data rate and third component resolution (Seelhorst et al. 1993). As can be seen in Figure 2, the system was operated in a back scatter, off-axis mode. A 6 Watt argon-ion laser was used as light source. The three most intensive laser lines (476.5 nm, 488 nm, 514.5 nm) were utilized to distinguish the different velocity components. Each of the laser beams was divided into two individual beams with similar intensity, one superimposed with a Bragg shift of 40 Mhz for ambiguity removal. The beams were coupled into single mode glass fibres and were launched into the probe volume with individual transmitting optics. For good resolution of the third velocity component the angle between the optical axis was about 30°. The effective size of the probe volume was approximately 0.25 mm in diameter and 1 mm in length. The tracer particles used were the same for LDV and PIV measurements: they consisted of dispersed oil, with an average diameter of less than 1 µm. The receiving optics of the system, operating in back-scatter mode, had an aperture of 500 mm in order to gather enough light for a sufficient data rate. The received light, containing information of all three velocity components, was coupled into a multi-mode glass fibre, which transmits the light to a prism system, where it was divided into single wavelengths and then converted into an electrical signal by photo-multipliers.

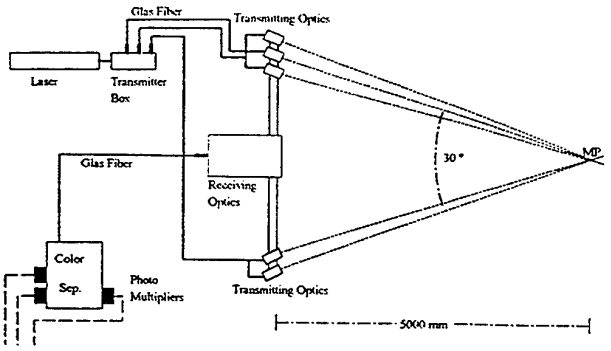

Figure 2: *Sketch of the 3D-LDV system.*

After digitization of the signals a fast Fourier analysis led to the Doppler frequency. When the signals of the three components coincided the velocity data was stored together with the actual time and measuring position.

Based on the assumption of a periodic flow field with respect to the rotor revolution, conditional sampling was used to get time dependent information of the flow field. A trigger signal from the rotor axis was shifted with a time delay to any chosen azimuthal position of the rotor blade with an accuracy of 0.3%. At this position the clock of the data acquisition system was set to zero. Data acquisition was then started for a time window, corresponding to a preselected azimuthal window or a time needed for the flow structure to pass through the probe volume. Usually data was acquired just within a small azimuthal window.

Converting time information into spatial information can be done in different ways. Here, the transformation of the time information into an azimuthal angle was done by the following equation:

$$\Psi = \Psi_0 + 2\pi \cdot f \cdot t, \quad \text{where } f \text{ is the rotor speed.}$$

The transformation of the time information into a spatial information of the flow structure as for example its length l was done by analysing the convection speed of the flow structure:

$$l = U_{conv} \cdot t \cdot$$

Using the conditional sampling mode to acquire time resolved velocity data, which is later converted into spatial velocity data, leads to an inaccuracy due to the fact that flow structures may change during the measuring time. This has to be balanced against the significant reduction of measuring time.

A 'position monitoring system' gave access to blade motion parameters (lead-lag motion, pitching motion and angle of incidence) at a preselected radial position of the blade.

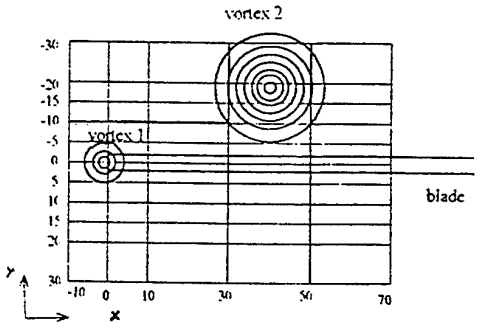

Figure 3: *Measurement grid and expected position of vortices.*

4 LDV RESULTS

As shown in Figure 1, LDV measurements were obtained behind the advancing blade at an azimuthal angle of $\psi \approx 90°$ (0.2 chord length behind the blade tip, rotor blade normal to mean flow). The measurement grid is shown in Figure 3 together with the locations of the tip vortices as expected after analysis of flow visualization data as obtained by Müller and Staufenbiel (1987). The origin of the coordinates was set to the point of intersection of the tip path of the reference blade (without aerodynamic load) and the observation area. The displacement of the tip path under load condition as measured by the position monitoring system was Y = 10 mm.

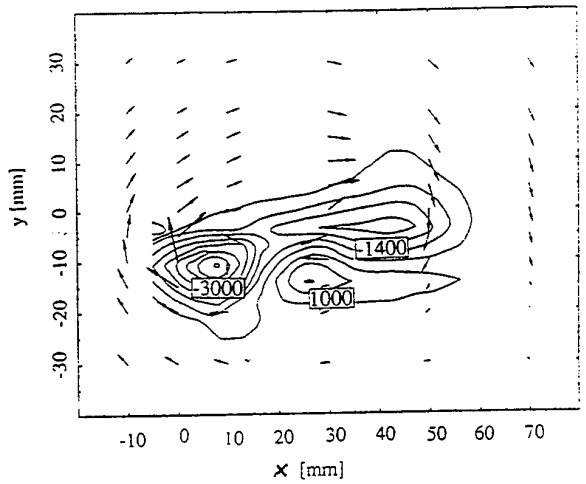

Figure 4: *Velocity vector plot (2D) as measured by LDV and the vorticity contours obtained from 3D-data.*

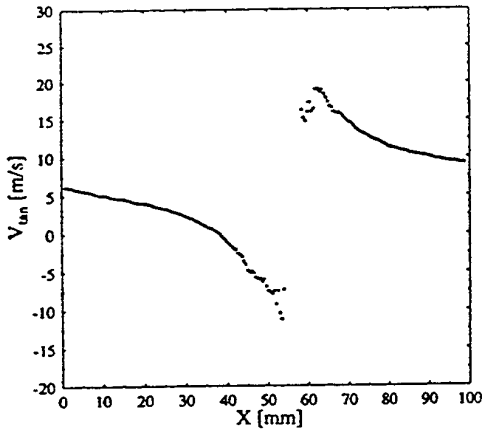

Figure 5: *Tangential velocities along a line through the vortex center obtained by 3D-LDV.*

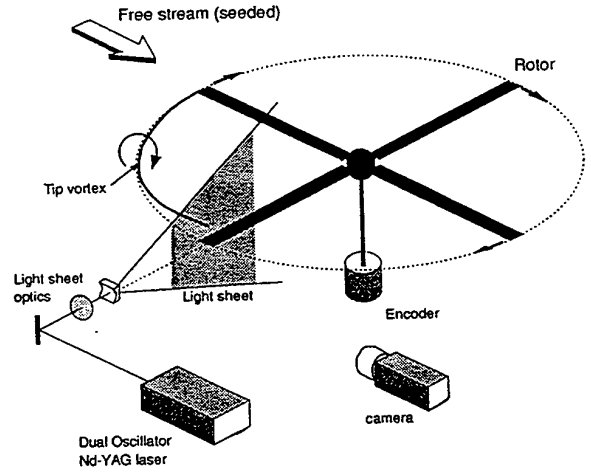

Figure 6: *Main components of the PIV set-up for investigating the rotor-vortex interaction.*

First, vector plots were computed from velocity data to give a general impression of the flow velocity field. Figure 4 clearly shows the vortex locations inside the measurement grid. At this azimuthal position a vortex could be observed, which has just been generated (age ≈ 0 ms, position corrected by the tip displacement X = 5 mm, Y = 2.5 mm). The vortex generated by the 90° advancing blade (age ≈ 10 ms, position corrected by the tip displacement X= 40 mm, Y = 5 mm) was located closer to the reference blade than expected (see also Fig. 3). The location of the vortex generated by the advancing blade results in an interaction with the reference blade, which generates a vortex of opposite sign. Since there was only little time between the generation of the tip vortices and their measurement (max. 10 ms) the cycle-to-cycle variations can be expected to be small compared to the measurement grid.

In Figure 5 the tangential velocity profile of a tip vortex is shown along a line through the vortex center. For the measurement of the profile, the resolution was increased considerably. From theis data the vortex core radius has been estimated to 8.9% of the blade chord with a maximum tangential velocity of 16 m/s.

5 PIV RECORDING SYSTEM

During the last decade PIV has increasingly been used to measure instantaneous flow velocity fields. This technique, in contrast to LDV, requires no conditional sampling. PIV allows to capture the flow velocity in a two-dimensional plane of the flow within a few microseconds. It therefore enables to obtain data of the entire velocity field even in case of large cycle-to-cycle variations. The fact, that the recording time, necessary for the application of PIV (≈ 12 µs), is small compared to the time required for one revolution cycle (≈ 40.000 µs) makes PIV an ideal tool for the investigation of flow fields in rotor aerodynamics.

During the last years a PIV system has been developed at DLR which can be operated under rough environmental conditions in wind tunnels (Kompenhans et al. 1994). This system utilizes a two-oscillator Nd:YAG pulse laser system with a pulse energy of 2 × 70 mJ for illumination of an area of up to 20 × 30 cm^2 of the flow field. The recordings are taken with a 35 mm photographic camera and are analyzed by a fully digital evaluation system (Willert 1995). The tracer particles used were the same as for LDV. The main components of the set-up are shown in Figure 6 in the configuration used to observe orthogonal blade vortex interaction.

Due to the synchronization scheme shown in Figure 7 the recording of the PIV images could be performed phase locked with the motion of the helicopter rotor model. Therefore cycle-to-cycle variations of the flow field could be investigated by analysing up to 100 recordings (more than 2000 independent velocity vectors each) taken at the same azimuthal angle of the reference blade. However, only the two in-plane components of the velocity vectors could be measured by means of the photographic PIV system. Examples of digital 2D-PIV measurements performed during the same measuring campaign are presented by Willert et al. (1996).

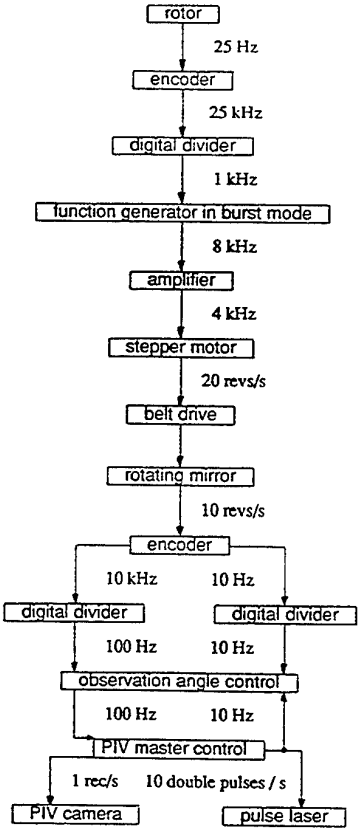

Figure 7: *Synchronization scheme of PIV data acquisition.*

6 PIV RESULTS

PIV measurements of orthogonal blade vortex interaction (case A) were taken at an azimuthal angle of $\psi \approx 90°$ on the advancing blade side. The observation area was nearly parallel to the trailing edge of the blade and orthogonal to the axis of the vortices. Figures 8a,b show two different instantaneous velocity vector fields from a set of 100 PIV recordings obtained at this angle. The origin was fixed to the tip of the trailing edge of the blade as it passed through the image plane with full aerodynamic load. Figure 8c is the velocity field obtained by averaging all 100 PIV data sets, and below (Fig. 8d) an estimate for the mean out-of-plane vorticity component is given. The tip vortex (A), which has just been generated (age $\approx$ 0 ms), was located at Y = 7.5 mm, Y = 2.5 mm. A tip vortex (B) previously generated by the 90° advancing blade (age $\approx$ 10 ms), is now located at X = 22 mm, Y = 25 mm. The cycle-to-cycle variations of these two vortices were small enough such that they are properly resolved in the average velocity field. Close inspection of Figures 8a and 8b does however show some variations in the shape of the vortices. Also, a third vortex structure (C), generated by the 180° advancing blade, can be observed. As this vortex intersects the rotor plane at the same time the blade intersects the image plane, it is sliced by the blade (i.e. orthogonal BVI) such that only its remnants can be observed in the velocity field of Figure 8. Due to small cycle-to-cycle variations this third vortex is sliced differently each time which results in the structure to be essentially lost in the averaged velocity field (Figure 8c). In Figure 9 the tangential velocity profile of a tip vortex (age $\approx$ 0 ms) from a single PIV velocity data set has been plotted along a line through the

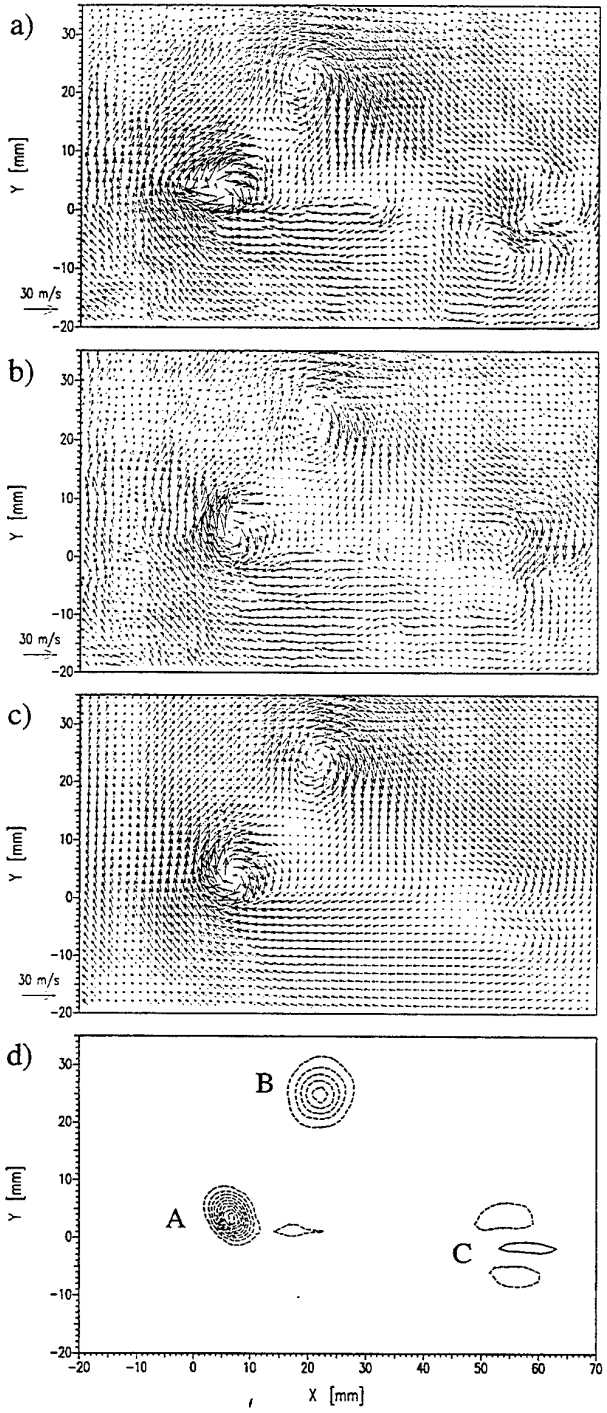

Figure 8: *Two examples (a,b) of 100 instantaneous velocity vector fields as obtained by PIV at $\psi \approx 90°$. Below (c) the averaged velocity field and (d) the corresponding vorticity estimate, $\omega_{z,,}$ is shown. (Contour levels spaced at 1000/s, dashed contours indicate negative values). Only subregions of the 210 mm by 150 mm fields are shown for clarity.*

vortex center. From these data the velocity core radius has been estimated to be 7.4% of the blade chord, compared to 8.9% by the LDV method. The maximum tangential velocities (±24 m/s) are 33% higher than those obtained by LDV. The discrepancy may be due to the averaging nature of the LDV method.

Measurements of parallel blade vortex interaction (case B) were taken at an azimuthal angle of $\psi \approx 60°$ (advancing blade side). The observation area was oriented orthogonal to the leading edge of the blade, orthogonal to the vortices axis and located at 60% of span (e.g. inside the rotor plane). Instantaneous velocity fields, the average of 35 velocity fields and the estimated mean out-of-plane vorticity component are plotted in Figures 10 and 11. The contour of the blade could be easily determined in the recordings and is labelled with (A). Vortex strength, convection speed, and the miss-distance between blade and vortex can easily be determined by analysing the PIV data. Significant cycle-to-cycle variations can be observed for the vortices, labelled (B), (C), and (D), which were generated 270°, 360°, 450° earlier, respectively. For instance vortex (D) is nearly invisible in the averaged velocity field of Figure 10c, as as it interacted most with the blade (A) as it passed through the observation field.

7 DISCUSSION

The LDV measurements yielded fundamental results concerning the structure of the blade tip vortex. In addition to geometric parameters like location of the vortex relative to the rotor plane and orientation of the vortex axis in space, the vortex core size, axial velocity, vortex strength, and vorticity distribution had been derived from 3D-LDV data. Although blade motion and local velocity had been measured simultaneously, phase averaging and the rearrangement of velocity data, which could only be measured pointwise, to a complete velocity field causes significant problems. Aperiodic flow phenomena, even of small amplitudes, can result in a spatial averaging and therefore reduce spatial resolution.

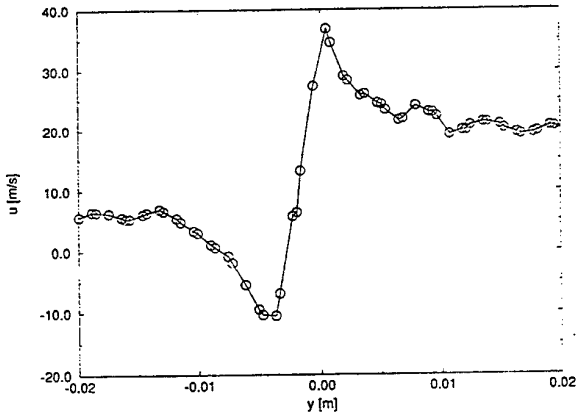

Figure 9: *Tangential velocitiy along a line through the vortex center as obtained by a single PIV recording.*

However, recent LDV measurements in large aerodynamic facilities show that 3D-LDV data of high quality can be obtained with good spatial resolution (Splettstößer et al. 1995).

In spite of the difficult experimental conditions high quality PIV data were obtained with sufficient spatial resolution. The time needed for data acquisition can be considerably decreased compared to LDV measurements. A specially developed synchronization scheme allowed the comparison of momentaneous flow field measurements at exactly the same phase angle of the rotor revolution and therefore the study of aperiodic features of the flow. Also with PIV the location of the vortex relative to the rotor plane, vortex core radius, convection speed, vortex strength and vorticity could be measured. However since conventional PIV measures only two velocity components, data, like the orientation of the vortex axis in space and axial velocity of a vortex, cannot be derived without changing viewing direction. Using a second camera in stereoscopic view would allow to measure all three velocity components without averaging data of different cycles.

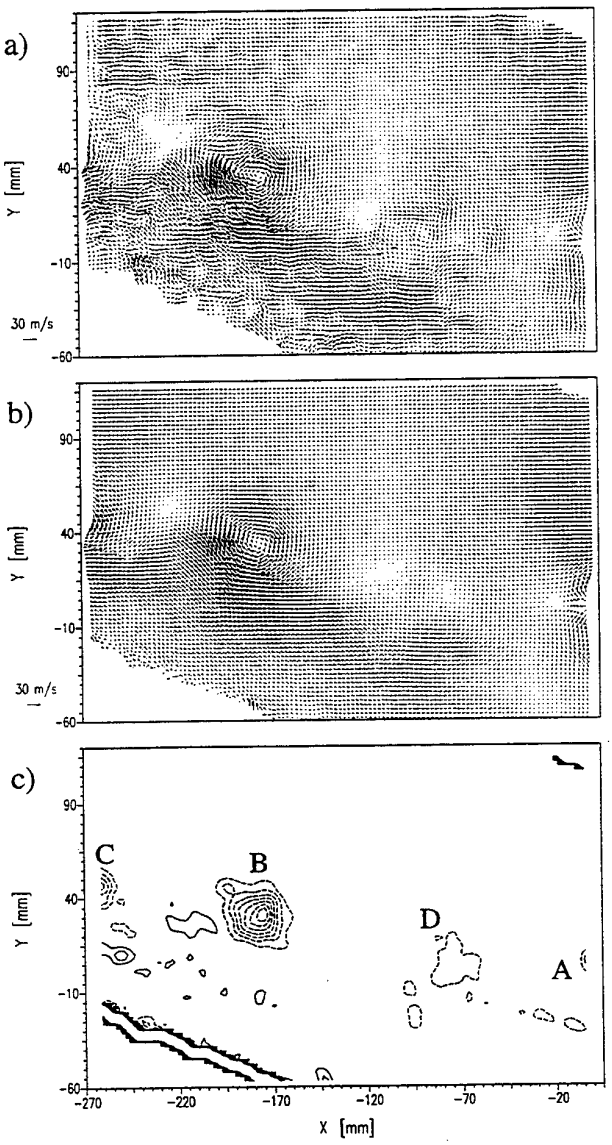

Figure 10: *Instantaneous velocity vector field (a) as obtained by PIV at $\psi \approx 60°$. Below (b) the averaged velocity field of such 35 fields and (c) the corresponding vorticity estimate, $\omega_{z,,}$ is shown. (Contour levels spaced at 500/s, dashed contours indicate negative values).*

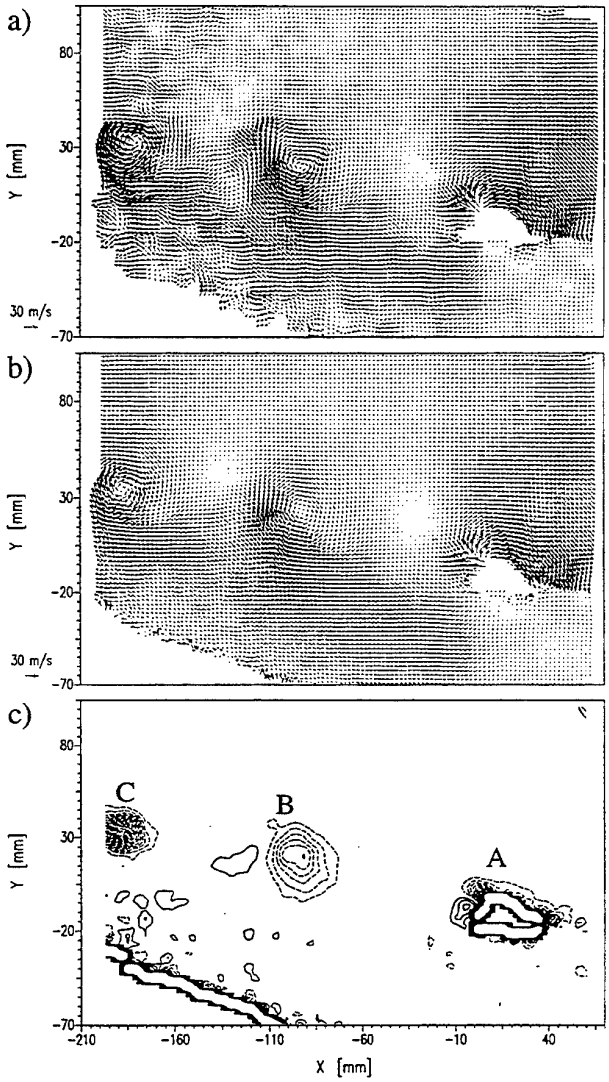

Figure 11: Same *as Fig. 10 but at an azimuth angle of* $\psi \approx 65°$.

LITERATURE

B.M.J. Beesten "Nichtplanare Rotorblattspitzen im Hubschraubervorwärtsflug" Dissertation vorgelegt an der RWTH-Aachen, 1994.

C.L. Burley, H.E. Jones, M.A. Marcolini, W.R. Splettstößer "Directivity and prediction of low frequency rotor noise" *AIAA 91-0592*, Aerospace Science Meeting, Reno, USA 1991.

F.X. Cardonne, J.L. Lautenschläger, M.J. Silva "An experimental study of rotor-vortex interaction" *AIAA 88-0045*, Aerospace Science Meeting, Reno, USA 1988.

K. Ehrenfried, G.E.A. Meier, F. Obermeier "Sound produced by vortex-airfoil interaction" Proc. of the 17th European Rotorcraft Forum, paper 63, Berlin, Germany 1991.

J. Kompenhans, M. Raffel, A. Vogt, M. Fischer, B. Bretthauer, H. Vollmers, B. Stasicki "Investigation of Unsteady Flow Fields in Wind Tunnels at High Flow Velocities by Means of Particle Image Velocimetry" Proc. of the 2nd International Conference on Experimental Fluid Mechanics *ICEFM*, Ed. M. Onorato, *Levrotto & Bella*, pp. 90-102, Turin, Italy 1994.

M.V. Lowson "Progress towards quieter civil helicopters" Proc. of the 17th European Rotorcraft Forum, paper 59, Berlin, Germany 1991.

U. Seelhorst, K.A. Bütefisch, K.H. Sauerland "Three component Laser Doppler Velocimeter development for large wind tunnel" *ICIASF* '93 Record, paper 33, Saint Louis, France, 1993.

W.R. Splettstößer, K.J. Schultz, R.M. Martin "Rotor blade-vortex interaction impulsive noise source localization" *AIAA Journal*, Vol. 28 No. 4, 593-600, 1990.

W.R. Splettstößer, R. Kube, W. Wagner, U. Seelhorst, A. Boutier, F. Micheli, E. Mercker "Key results from a higher harmonic control aeroacoustic rotor test (HART) in the german-dutch wind tunnel" Proc. of the 21th European Rotorcraft Forum, St. Petersburg, Russia, 1995.

C.E. Willert "The fully digital evaluation of photographic PIV recordings" to appear in *Applied Scietific Research*, 1995.

C.E. Willert "High-speed digital video camera systems and related software for application of PIV in wind tunnel flows". 8. Int. Symp. on Appl. of Laser Techniques to Fluid Mech., Lisbon, Portugal, 1996.

ACKNOWLEDGEMENT

The sientific and technical support given by Prof. Neuwerth, Dr. Beesten, Dr. Gitek, and the team of the RWTH-Aachen low-speed wind tunnel is greatly appreciated.

THREE COMPONENT LDA STUDY OF THE FLOW FIELD SURROUNDING THE HELICOPTER LANDING PAD OF A FRIGATE

Swales, C., Rickards, J., Crompton, N.
Terry, N., Breeze, G.

Department of Aerospace Engineering
University of Bristol
Bristol, England

ABSTRACT

At present most naval vessels above approximately 4000 tons have a helicopter landing deck to the rear of the ship. However, the box-like superstructure associated with these ships is known to generate flows of a highly turbulent and three dimensional nature which strongly interfere with the landing and take-off stages of the helicopter's sortie. The operating envelope of the helicopter therefore becomes limited and in extreme conditions the blades may impact on the helicopter fuselage. To date this operating envelope, and any understanding of the fluid mechanisms involved, has mainly been established at sea - a costly and hazardous solution. This paper describes how the unique combination of a 3 component LDA and an atmospheric wind tunnel should lead to a cheaper and safer method of establishing the flight envelope and to recommendations for improvements to the superstructure design.

1. INTRODUCTION

1.1 Ship/Helicopter Interface Aerodynamics

In recent times the majority of naval ships above a few thousand tons have included provision for a helicopter. They have become an integral part of shipboard operations, with reconnaissance and logistic support being two of the primary roles that the helicopter is required to fulfil. For these ships the landing area for the helicopter has traditionally been at the rear (aft) of the ship, with a hangar included slightly forward of the flight deck. However, this has proved to be a hostile area for the helicopter and pilot alike and there is therefore considerable new interest in the subject of ship aerodynamics. Described in this paper is one approach - use of a three component laser Doppler anemometer (LDA) to acquire velocity measurements above the flight deck of a 1:200 scale model ship within an atmospheric wind tunnel.

Classically, the aerodynamics of ships has received only scant attention as the hydrodynamic issues have been assumed to dominate. The result of this is detailed consideration of the hull design, but little attention to the superstructure. The latter, therefore, conventionally comprises an array of sharp-edged box-like structures, the design of which is influenced by practical rather than aerodynamic considerations. Unfortunately, strong, highly turbulent, and highly three-dimensional flows can be generated by these essentially sharp edged bluff bodies (Healey and Rhoades (1992)). This type of flow might have a limited influence on the performance of the ship, but its effect on a helicopter attempting to land or take-off can be substantial. Often retro-fitted, it is infact the helicopter hangar which can create the strongest flow disturbance.

The steady (low frequency) and unsteady (high frequency) flow effects are both important but in different ways. The steady flow effects, substantial but predictable, are caused by the structure of the ship. For example, for an ahead wind (zero yaw) the helicopter hangar creates a down-draught aft which, on landing, requires the pilot to increase power to maintain a constant rate of descent. In extreme cases the downwash may be such that there is insufficient power to safely control the descent.

The unsteady (high frequency) effects are generated by the freestream flow and shedding from the ship structure. These effects cause short term disturbances to the aircraft and tend to be sudden and unpredictable, increasing pilot workload. In some cases strong and sudden vortical gusts lead to blade strikes where the rotating blades impact on the helicopter fuselage. These occur during rotor engagement and disengagement, when the rotor becomes much more susceptible to onset velocities and the blade loads become more imbalanced. In the most extreme cases this has led to the complete loss of a helicopter.

The complex flow generated by the ship superstructure and by the high level of turbulence inevitably leads to a severely limited operating envelope for a particular helicopter/ship combination and poor operating conditions for the pilot even within this

envelope. If the helicopter is to operate from the flight deck the ship may have no option but to alter course and/or speed to produce suitable flight conditions. This, increasingly, is an unacceptable compromise.

There is therefore a requirement to improve the ship/helicopter operating envelope by reducing the influence of, and increasing resistance to, the onset flow. However, this has to be achieved without any significant increase in the cost of either the helicopter or the ship. Finally this has to be for any ship/helicopter combination, relative wind speed and direction, visibility and sea state.

A parallel issue is that of defining the operating envelope for a particular ship/helicopter configuration. Historically this has been achieved by testing at sea, a technique referred to as dynamic interface testing. It is however a laborious and expensive method and subject to the "co-operation" of the natural elements. For economic reasons a particular dynamic interface test may have to be curtailed - a more limited operating envelope than may actually be required may then ensue.

1.2 Wind Tunnel Testing

To circumvent the vagaries of nature Healey (1992) was one of the first to test a model ship within a wind tunnel configured to simulate the atmospheric boundary layer. Healey states that the complex shapes and separation of airflow around many corners made it very difficult to apply the principles of CFD and generate realistic computer models. In addition Healey reports that the recirculating zones give rise to "unsteady flows with extreme velocity gradients and turbulence intensity levels that are too high to be measured with hot-wire anemometers". The use of a laser Doppler anemometer to overcome the limitations of the hot-wire is clearly expressed.

The problem of the turbulence intensities being too high for hot-wire measurement is clearly addressed by the LDA. However, the high spatial resolution required for measurements within regions of steep velocity gradient cannot be assumed for long throw optics. However, if the light is collected off-axis then the length of the *effective* measurement volume is much reduced.

Unlike the hot-wire, when a 3D system is employed three components of velocity (mean and turbulence) are measured simultaneously both temporally and spatially. Again this is imperative where such complex, small scale, three-dimensional flows are believed to exist.

Finally, it is the non-intrusive nature of the LDA which, for this study, is its greatest asset. In regions of strongly recirculating flow whichever way the hot-wire probe is aligned data must be acquired from within the wake of the probe. Comparative tests with the LDA showed the hot-wire, due to its inability to discriminate direction as well as magnitude, to be ineffectual in regions of reversed flow. Flow tests where the hot-wire was mounted vertically within a downward flow the results were again erroneous.

This study was therefore configured to show how the unique combination of a 3 component LDA and an environmental wind tunnel could be employed for the study of ship aerodynamics with particular emphasis on the region above the helicopter landing deck.

2. EXPERIMENTAL CONFIGURATION

2.1 Atmospheric Boundary Layer Simulation

The department's Industrial Aerodynamics closed-circuit wind tunnel has over a number of years established itself as an important facility for studying building aerodynamics. The working section of the wind tunnel measures 1m by 2m, with a maximum speed of 15m/s. Upstream of the working section a mixing grid, a step, and a range of distributed surface roughness elements can be arranged which enable wind simulation over different terrains. For this investigation it was necessary to model strong winds blowing over rough seas, at a linear scale of 1:200.

In the field of building aerodynamics it has been established that when undertaking wind tunnel testing three features associated with high speed atmospheric winds need to be simulated properly. These features are the shear of the velocity profile (i.e. the variation of wind speed with height above the ground), the level of turbulence, and the sizes (or scales) of the turbulent fluctuations. If these are ignored, as for example by White and Chaddock (1967) who carried out tests in a wind tunnel with uniform velocity and very low turbulence intensities, the flow generated by the model is unrepresentative of the real environment.

The mean velocity profile and turbulence produced by the wind tunnel simulation are shown in Fig. 1. The results were obtained from measurements taken using a single hot wire anemometer. A comparison was made with the results from ESDU data sheets (see references). For these tests the full-scale wind speed was chosen to be approximately 50kts, the maximum windspeed under which helicopter-ship operations can occur. The surface roughness parameter, z_0, is set to 0.0084 which corresponds to a rough sea region. It can be seen that there is good agreement between the wind tunnel velocity measurements and the ESDU data. Without the boundary layer simulation the relative velocities would be higher than for the true conditions. In addition the turbulence intensities would be 2 or 3 times lower had no simulation been employed.

A spectrum of the turbulent fluctuations measured 200mm above the wind tunnel floor is shown in Fig. 2. For comparative purposes, the well known modified von Karman spectrum has been plotted with the measured spectrum. The von Karman spectrum shown has been derived using the linear scaling of the model, together with the velocity scaling ratio of the wind tunnel operating speed and the full scale wind speed. The combination of these scaling factors means that effectively

the results measured in the wind tunnel occur fifteen times faster than would occur in the full scale situation. The good agreement between the spectra shown in Fig. 2 shows that the sizes (or scales) of the simulated turbulent fluctuations have also been modelled correctly.

The observation that the shear, turbulence level and turbulence scales have all been simulated in the wind tunnel satisfies criteria specified by the British Standards Institute (see references). These criteria correspond to the best present-day practice of environmental wind tunnel testing techniques.

2.2 Wind Tunnel Model

A 1:200 scale model of a typical Royal Navy Type 23 'Duke' Class frigate was constructed, and painted matt black to reduce the effects of flare. The dimensions of this model are shown in Fig. 3. It can be seen from this figure that the rear deck of this ship design is dominated by a large hangar, aft of which is the helicopter landing deck platform. Around the model of the frigate, a number of nuts were randomly scattered. These nuts act as small roughness elements, and are necessary to ensure that the boundary layer passing over the ship model retains its turbulent nature. The model was mounted on a turntable, thereby enabling a range of yaw angles to be set.

Reynolds number effects (often also called model scale effects) mean that the flow pattern can be different for models compared to their full scale counterparts. For Reynolds numbers of practical interest, air cannot follow a surface having sudden changes of surface direction. Instead, air flow tends to separate away from the surface at such corner points. As can be seen in Fig. 3 most of the model of the frigate has sharp edges. Hence the air flow will always separate from these edges at both model and full scales. Therefore, measurements obtained from this small scale model testing will produce the same results as would be obtained at full scale.

2.3 LDA System and Configuration

The LDA employed was a full 3 component Dantec Fibre-Flow system (Fig. 4). The light source is a 5 Watt Spectra-Physics 2016 Stabilite Argon-ion laser. Ten metre-long fibre optic cables enable the three dominant wavelengths to be transmitted from the beam-splitter unit to two independently mounted 1600mm focal length optic heads - green (514.5nm) and blue (488nm) beams are emitted from one optic head (referred to as the 2D head), violet beams (476.5nm) from a second (1D) optic head. The gimbal mounts within which the optic heads are set can be dipped and swept to provide the required optical configuration. The optic heads can also be rotated within their respected gimbal mounts in order to produce a more balanced system where the velocity recorded by each of the three channels is of approximately the same magnitude. Finally both gimbal mounts are affixed to a high precision 3-axis Dantec traverse which enables a 600mm by 600mm by 600mm grid to be configured with a step size accurate to 0.005mm. Fig. 4 shows that the LDA is mounted external to the working section of the Industrial Aerodynamics wind tunnel. Optical access provided no difficulties.

Collection of the scattered light can be achieved by both optic heads, and hence two distinct modes of operation are possible. In the backscatter mode the light scattered by the seeding particles passing through the intersection of the beams from one optic head is collected by the same optic head; in the cross-coupled mode the light is collected "off-axis" by the other optic head. In both cases the collected light passes down the fibre-optic cable to three "filtered" photomultipliers. The resulting signal from each photomultiplier is then fed to an Enhanced Burst Spectrum Analyser - one for each wavelength. The method of accurately determining the frequency/velocity calibration factor and the elements of the measured/required velocity transformation matrix is described below. A 133MHz Pentium provided the computer hardware to control both the data acquisition and the traverse movement.

The experimental requirement was for three-component, non-intrusive, and directionally unambiguous velocity data. These criteria were successfully met by the above system. The further important requirement of ensuring good spatial resolution cannot however be assumed for such small beam included angles (focal length 1600mm, separation 115mm). It is well established that off-axis light collection reduces the effective measurement volume size. There is however a detrimental effect on the data rate, attributed to both the fact that the number of seeding particles passing through the measurement volume must inevitably be proportional to the size of the volume itself, and to the considerable difficulty in ensuring adequate alignment of the system.

Practical experience (Swales (1994)) suggests that for the system at Bristol operating in the backscatter mode the system rarely drifts out of alignment - the position of the measurement volume may drift slightly but the beams and the collection volume drift "together" and hence the system remains aligned. Most importantly the level of alignment is not always critical. However, if the light is collected off-axis the beams and the collection volume are associated with two independent optic heads. Aligning the collection volume to the intersection of the beams is therefore much harder to achieve and any slight drifting of either optic head, caused for example by slight vibration, will result in rapid misalignment and hence a significant drop in data rate. The former problem was solved by the development of a quantitative alignment technique, the latter by small but crucial modifications to the optic head clamping mechanism.

As described by Swales et al. (1993) the improved alignment technique, rather than relying on visually interpreting and improving the concentricity of images caused by the beams being passed through an objective lens, simply requires acting on the output of a multimeter. A low meter reading corresponds to an increased amount of light being detected by a light

dependent resistor mounted behind a 20 micron diameter pinhole (Fig. 5). This, due to the Gaussian light intensity distribution across a beam, corresponds in turn to the centre of the beam being aligned at the front face of the pin-hole. The technique of aligning first the two collection volumes and then the individual beams is shown schematically in Fig. 5. The result of employing this quantitative alignment technique has been the ability to consistently (approximately 98% of the time) achieve a level of alignment sufficiently high to operate in the cross-coupled mode without a detrimental effect on the data rate. The success of the technique is such that data rates in the cross-coupled mode are now higher than could be achieved previously in the backscatter mode by using the conventional alignment method.

2.4 Velocity Transformation Matrix

The direction of the measurement vectors are determined by the optical configuration. The three components of velocity have therefore to be transformed into values relative to the traverse and eventually relative to the wind tunnel working section.

The technique of determining the elements of the transformation matrix is based on determining the coordinates of the intersection of the six beams with two planes at a known separation, followed by the application of simple vector algebra. The accuracy of the technique is guaranteed through the use of the pin-hole alignment meter described above - by positioning the pin-hole meter at a suitable position the centre of a laser beam can be aligned to an accuracy of 0.01mm to the pin-hole, and the corresponding traverse "X" and "Z" coordinates noted. The process, with the pin-hole meter's position fixed, is repeated for all six beams, each time noting the traverse coordinates. This is then repeated for the traverse at a second "Y" position corresponding to the beams being intersected by a second plane. Finally the 12 sets of traverses are inserted into a spreadsheet which uses simple vector algebra to determine both the three calibration factors and the elements of the transformation matrix. Fig. 6 illustrates the key features of the technique. Analyses within the department have shown the error induced by inaccurate measurements of the beam vectors to be minimal (Mac Manus et al. (1996)). For this study a further rotational matrix had to be applied, and the accuracy of this transformation was dependent on the accurate measurement of the yaw angle of the ship.

3. RESULTS AND THEIR DISCUSSION

Detailed data was recorded with the 1:200 scale generic frigate at both zero yaw (ship axes directly in line with the wind tunnel axes and hence the onset flow) and at a yaw angle of 30 degrees. Nine traverses were configured for both yaw angles, with each traverse comprising a rectangular grid with over 300 points reaching from the flight deck to twice the height of the hangar, and over three times the width of the ship. Nine traverses were configured, each at a different "X" position, from 5mm to 245mm downstream of the hangar.

Fig. 7 shows the three resolved components of velocity (U, V, and W) for the zero yaw case 25mm downstream of the hangar. Of note is the symmetry of these contour plots. Away from the influence of the hangar the streamwise velocity (approximately -3m/s (the negative value is due to sign convention)) approaches the undisturbed wind tunnel velocity. There is very little structure except immediately behind the hangar (height 30mm) where a region of positive velocity exists, corresponding to a reversed flow region, typical of the near-wake caused by a bluff body. The velocity across the deck, V, reaches maximum values (positive and negative) immediately behind the sides of the hangar, with zero velocity immediately behind the centre of the hangar.

It is in many respects the vertical velocity which is of greatest importance to the pilot, as on landing the helicopter will have to cross a strong region of downwash (shown as positive velocities in Fig. 7). For the case 5mm downstream of the hangar, the velocity varies by 51% V_a, where V_a is the velocity at the ship's anemometer, in only 84cm full scale vertical distance. By 25mm downstream of the hangar the shear layer, which emanates from the sharp edges of the superstructure, is rather thicker but the effects are still considerable.

Fig. 8 shows a vector plot for a rectangular traverse at a constant 20mm from the flight deck (one third of hangar height) depicting the characteristic momentum deficit profile associated with the wake of a solid body. The flow is very symmetrical and predominantly in the streamwise direction. The near-wake, with its strong 'stagnated' region, extends over approximately one third of the deck length. Fig. 9 shows that the far-wake is bounded by a shear layer which reattaches to the flight deck at about 60mm, or about 50% flight deck length. This U-W vector plot clearly demonstrates the strong recirculating region immediately behind the hangar through which the helicopter has to fly.

Figs. 10 and 11 show contour plots of the streamwise velocity 5mm downstream of the hangar for the zero yaw and the 30 degree yaw case respectively. The zero yaw case is similar to that already described for Fig. 7. The 30 degree yaw case shows the contrast between the leeward and windward sides of the ship (left and right respectively in Fig. 11). On the windward side there is a very sharp boundary between the undisturbed flow and that immediately behind the hangar. On the leeward side there is a more gradual change, and in contrast to the zero yaw case the effects of the ship are still substantial right up to the maximum height of the traverse, ie. to twice the height of the hangar.

The vector plots shown in Figs. 12 and 13 confirm the strong contrast between the leeward and the windward side. For the 30 degree yaw case, almost three-quarters of the flight deck is engulfed in a very turbulent flow. The near-wake is still present but the recirculation on the leeward side (negative traverse positions) of the

hangar face is larger than that on the windward side. Both vector plots confirm the existence of crosswinds, which in reality can be so strong that there is insufficient roll cyclic or rudder control to maintain the proper heading relative to the ship.

There are several features of note in Fig. 13, including two strong regions of vortical flow, one 5mm below the top of the hangar and one to the leeward side of the ship. These are simply extensions of the basic concept of vortex corner flows, in this case caused respectively by the flow forming along the windward roof edge of the hangar and by the airflow passing over the main superstructure. In addition, immediately either side of the location of the hangar there are relatively strong updraughts, confirming observations previously made by Woodfield and Tomlinson (1995).

From the sample of results presented and by Crompton and Terry (1996) it is evident that the box-like superstructure poses significant problems to the pilot and helicopter alike, and that there is considerable scope for improvements to be made. The results confirm that the regions of highly three dimensional or recirculating flow are extensive, thereby unsuitable for hot-wires. However the problem is a complex one with many different and interlinked mechanisms. It is an area where the LDA is ideally suited. Furthermore without a dedicated traverse the large number of individual stations making up the grid would have taken too long with the hot-wire. With the LDA acquiring 3 component data it is possible to complete a 300 point traverse in 20 minutes, though for these tests longer sampling times were employed.

The quality of the LDA data is self-evident from the vector plots. There are no spurious data points and all the results appear consistent. The usual issues of LDA measurement accuracy exist, but these are beyond the scope of this paper.

4. CONCLUSIONS

The unique combination of an atmospheric wind tunnel and a 3 component laser Doppler anemometer has led to an economic and practical alternative to the dynamic interface method of establishing the operating envelope of a given helicopter/ship combination. This is an important development and should lead to a greater understanding of the importance of improved superstructure design for non-aviation ships. As expected the initial results have shown there to be very strong shear layers and significant regions of recirculating flow.

ACKNOWLEDGEMENTS

The assistance provided by Dantec Measurement Technology (UK) during these and other tests is very much appreciated.

REFERENCES

Crompton, M.J. and Terry, N.F. 1996 Effects of the Flow Over the Flight Deck of a Typical Type 23 Frigate in Helicopter Flight Characteristics, Department of Aerospace Engineering, University of Bristol, Report No. 758.

Healey, J.V., and Rhoades, M.M. 1992 Flight Deck Aerodynamics of a Non-aviation Ship, Journal of Aircraft, Vol. 29, No. 4.

Healey, J.V. 1992 Establishing a Database for Flight in the Wake of Structures, Journal of Aircraft, Vol. 9, No. 4.

Loezos, S. 1967 Effect of an Ambient Turbulence Component on Model Carrier Turbulence Data, DTNSRDC Aerodynamics Lab, Report 1131.

Mac Manus, D.G, Eaton, J.A., Barrett, R.V., Rickards, J., Swales, C. 1996 Mapping the Flow Field Induced by Suction through a Hybrid Laminar Flow Control Perforation using a High Resolution LDA, 34th AIAA Aerospace Sciences Conference, Reno, US.

Swales, C., Rickards, J., Brake, C.J., and Barrett, R.V. 1993 Development of a Pin-hole Meter for Aligning Three Dimensional Laser Doppler Anemometers, Dantec Information, Vol. 12.

Swales, C. 1994 Advanced LDA Techniques for Measurement of 3D Boundary Layer Velocity Profiles on a Helicopter Rotor, PhD Thesis, University of Bristol, Department of Aerospace Engineering.

White, H.E. and Chaddock, D.R. 1967 Comparison of Full Scale and Model Data of the Wind Velocity over the CVS-16 Flight Deck, DTNSRDC Report 2368, Aerodynamic Report 1128.

Woodfield, A. and Tomlinson, B. 1995 Ship Airwakes - A New Generic Model for Piloted Simulation, AGARD Flight Vehicle Integration Symposium on Flight Simulation.

ESDU Data sheet No. 85020 with Amends A to F. Characteristics of Atmospheric Turbulence Near the Ground. Part II: Single Point Data for Strong Winds (Neutral Atmosphere). April 1993.

BSI CP3: Chapter V: Part 2: September 1972. Code of Basic Data for the Design of Buildings. Chapter V, Loading. HMSO.

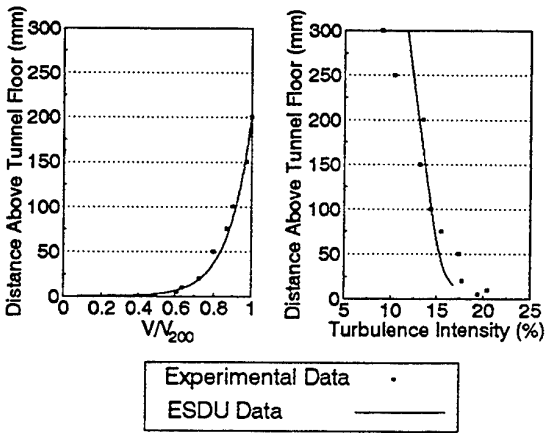

Fig. 1 Velocity Profiles From Boundary Layer Simulation

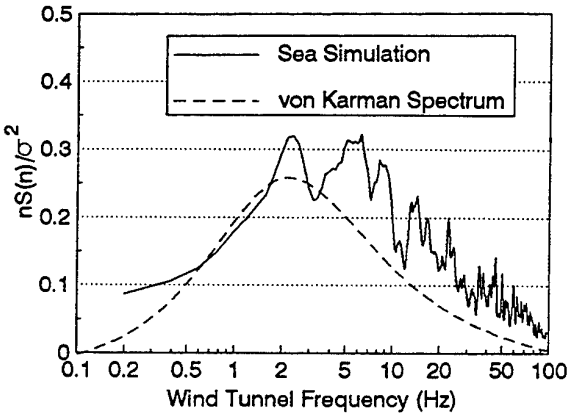

Fig. 2 Spectrum of the Turbulent Fluctuations 200mm above Wind Tunnel Floor

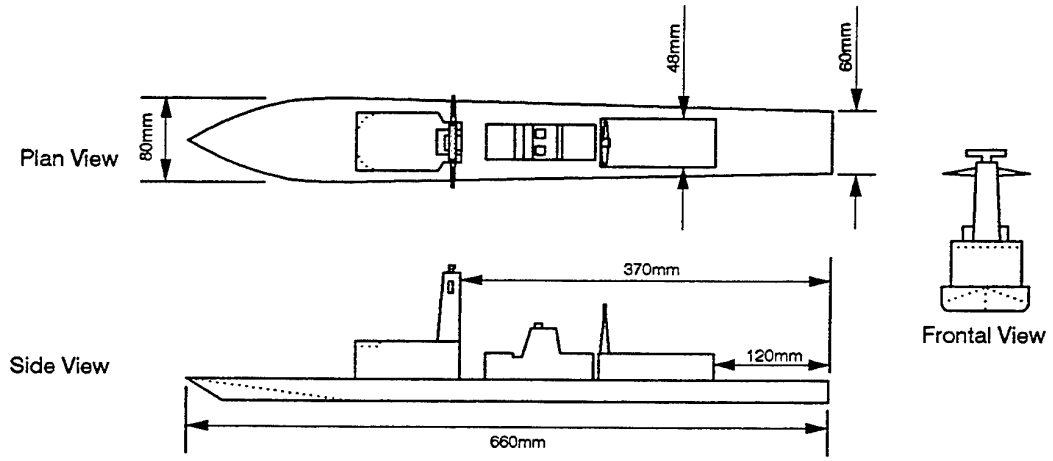

Fig. 3 1:200 Scale Model of a Type 23 "Duke" Class Frigate

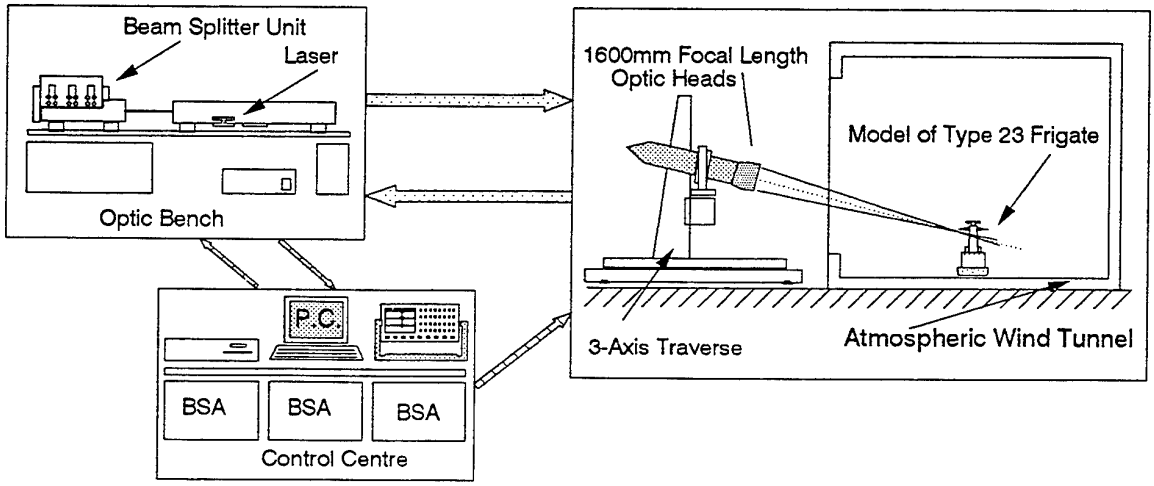

Fig. 4 Schematic Showing Principal LDA Components

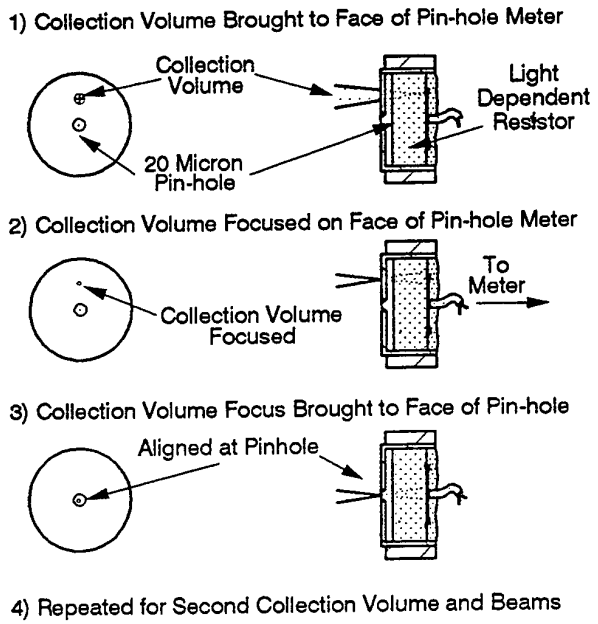

Fig. 5 Schematic of Quantitative Pin-hole Meter Alignment Technique

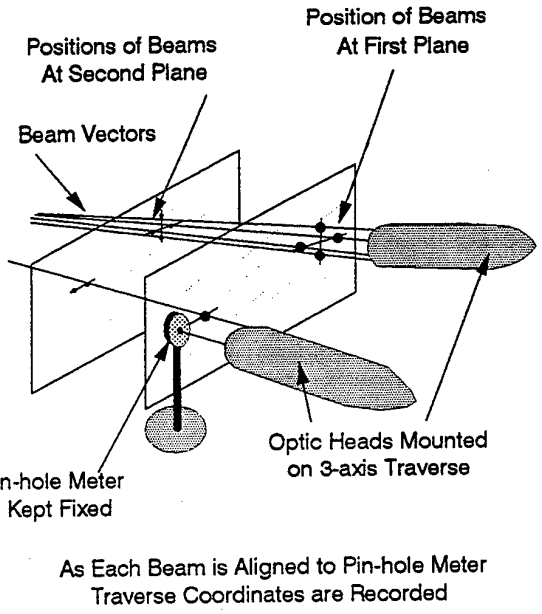

Fig. 6 Method of Determining the Elements of the Transformation Matrix

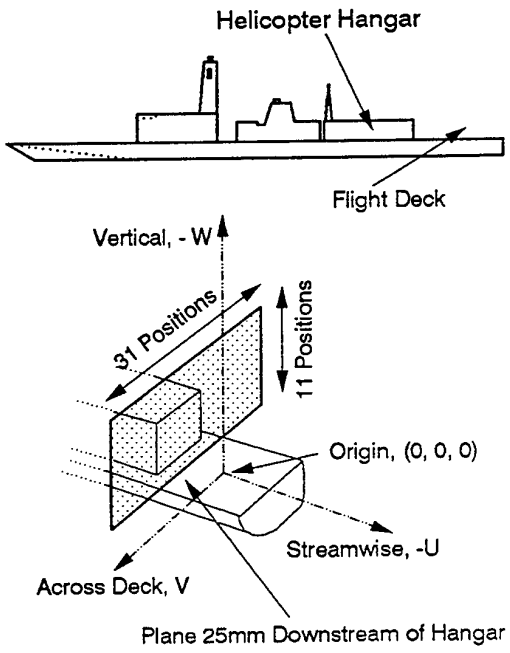

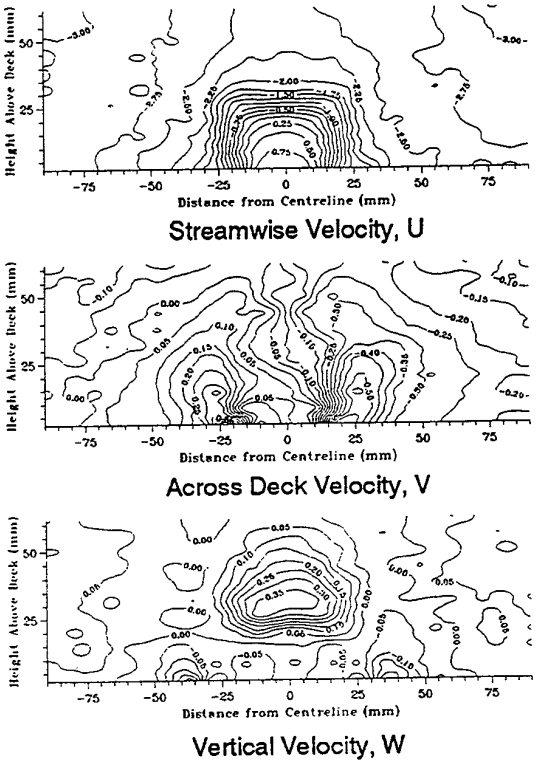

Fig. 7 Three Component Contour Plots, 25mm Behind Hangar, Zero Yaw

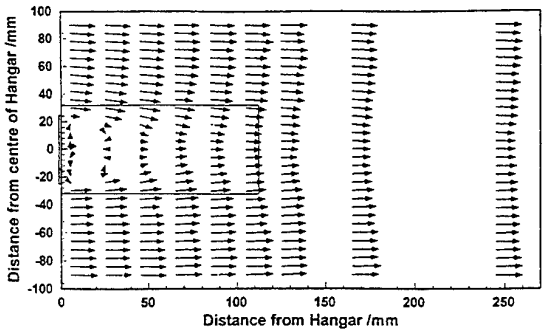

Fig. 8 Vector Plot at Zero Yaw, Z=20mm

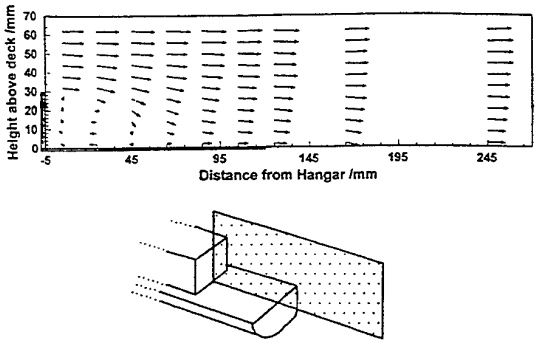

Fig. 9 Vector Plot at Zero Yaw, Y=0mm

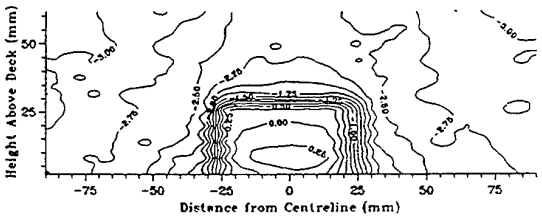

Fig. 10 Streamwise Velocity Contour Plot (Zero Yaw Angle)

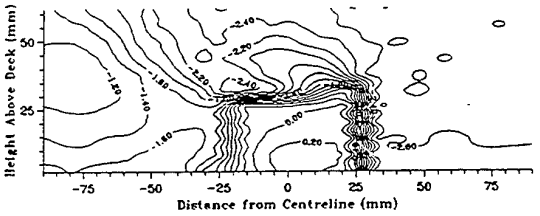

Fig. 11 Streamwise Velocity Contour Plot (30 Degree Yaw Angle)

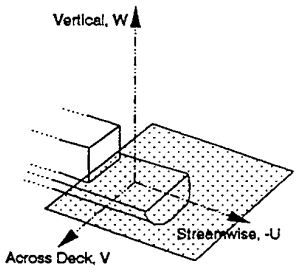

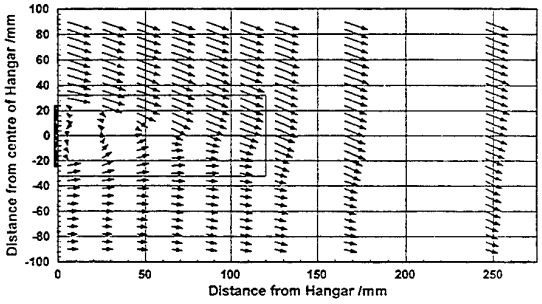

Fig. 12 Vector Plot at 30 Degrees Yaw and Z=20mm

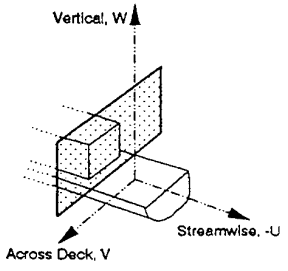

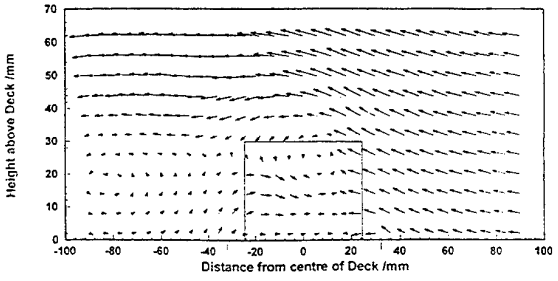

Fig. 13 Vector Plot at 30 Degrees Yaw and X=25mm

VORTEX INVESTIGATION ON A RETREATING HELICOPTER BLADE WITH 3D LASER VELOCIMETRY IN DNW

A. Boutier, J. Lefèvre, F. Micheli

Office National d'Etudes et de Recherches Aérospatiales
BP 72 - 92322 Châtillon CEDEX - France

ABSTRACT

As part of the HART program (Higher Harmonic Control Aeroacoustic Rotor Test, jointly conducted by US Army, NASA, DLR, DNW and ONERA), a series of tests have been made in the German Dutch Wind Tunnel (DNW) on a helicopter rotor with 2 m long blades, rotating at 1040 r.p.m.; several flight configurations, with an advance ratio of 0.15 and a shaft angle of 5.3°, have been studied with different higher harmonic blade pitch angles superposed on the conventional one (corresponding to the baseline case). Helicopter external noise is mainly generated by the Blade Vortex Interaction; therefore the vortex must be characterized before its interaction with the blade, which means that its viscous core radius, its strength and its distance to the blade have to be determined by non intrusive measurement techniques. The flow on the retreating side has been analyzed with an especially designed 3D laser velocimeter, and, simultaneously, the blade tip attitude has been determined in order to get the blade-vortex miss distance, which is a crucial parameter in the noise reduction.

A 3D laser velocimeter, in backscatter mode with a working distance of 5 m, was installed on a platform 9 m high and flow seeding with submicron incense smoke was achieved in the settling chamber using a remotely controlled displacement device. Acquisition of instantaneous velocity vectors by an IFA 750 yielded mean velocity and turbulence maps across the vortex as well as the vortex position, intensity and viscous radius. The blade tip attitude (altitude, jitter, angle of incidence) was recorded by the TART method (Target Attitude in Real Time) which makes use of a CCD camera on which is formed the image of two retroreflecting targets attached to the blade tip and lighted by a flash lamp. In addition to the mean values of the aforementioned quantities, spectra of their fluctuations have been established up to 8 Hz.

1. INTRODUCTION

In flight conditions of take-off and landing, helicopters generate high external noise when rotor blades interact with the tip vortices shed by the preceding blades. The reduction of this phenomenon, known as Blade Vortex Interaction (BVI) noise, has required a better insight into the mechanisms which create it. It was shown that the BVI noise intensity strongly depends on the vortex strength as well as on the blade-vortex miss distance, parameters which can be influenced by superposing a higher harmonic blade pitch angle on to the conventional one: this process is called Higher Harmonic Control (HHC) (Spiegel et al 1992).

The HART (HHC Aeroacoustic Rotor Test) programme (Gmelin et al 1995) has been jointly conducted by US Army, NASA, DLR, DNW and ONERA in order to improve physical understanding and modelling of the HHC effects on BVI noise and vibration generation by means of theoretical and experimental studies.

Various experimental studies were performed in DNW (German Dutch Wind Tunnel, Emmeloord, The Netherlands) (Kube et al 1994). In this paper we shall particularly focus on the way the flowfield has been characterized in details by ONERA on the retreating side, using laser velocimetry in connection with the TART method (Target Attitude in Real Time) which sampled at each turn the blade tip attitude. These non intrusive optical methods allow an accurate description of the vortex before it interacts with the blade (vortex core radius, vortex strength), as well as vortex location relative to the blade in flight (blade-vortex miss distance); all these parameters are fundamental in noise generation and reduction. Three flight configurations have been mainly studied, with an advance ratio of 0.15 and a shaft angle of 5.3°, in order to understand the involved phenomena: a baseline case, a second case with an HHC adjustment for which noise is

minimized, and a third case where vibrations are minimized.

The experimental environment at DNW, due to the size of the facility, presented a series of specific difficulties which were overcome by developing dedicated instruments and new measuring procedures which are reported in this paper. This technical challenge has contributed to the extension of the application domain of laser velocimetry to very large scale industrial facilities. Preliminary data processing was done very often in quasi real time in order to check the vortex location in the measured field; then a complete data reduction was achieved, taking into account both velocity fields and blade position measurements.

2. EXPERIMENTAL ENVIRONMENT

The experimental difficulties mainly come from the large sizes of the facility and of the rotor model; in fact the same spatial resolution as in smaller facilities is required. This is the first time that such optical techniques have been implemented in DNW. Moreover since the flow is periodic, stroboscopic measurements must be used, leading to long data acquisition times which must be minimized.

The model of the helicopter rotor (provided by DLR) is attached to the DNW sting mechanism in the open jet test section (10 x 8 m^2); the blade is 2 m long, its chord is 120 mm wide, the rotation speed is set at 1040 r.p.m.. The rotor plane is at a height of nearly 10 m relative to the ground. Since the vortex core must be evaluated to a fraction of a chord, a field of a few hundred mm^2 must be accurately analyzed at an altitude of 10 m relative to the ground, i.e. at blade level. Optical and mechanical setups must be installed outside the main flow, which requires a working distance of 5 meters.

To measure the highly three dimensional flow, a 3D laser velocimeter was installed on a platform 9 m high; its emitting optics must create a small probe volume (400 μm in diameter as usually in smaller wind tunnels, in order to have an appropriate spatial resolution) at a 5 m working distance, and the receiving optics must have an aperture of nearly f/10 to detect the submicron particles which are the only ones able to follow the important flow velocity gradients (existing, of course, in vortices); thus beam expanders (5x magnification) are used in the emitting part and a Cassegrain telescope, 450 mm in diameter, is placed in the receiving part. The scale of the facility has required the use of large and expensive optics in order to keep the same measurement quality for laser velocimetry as that usually obtained in smaller research facilities.

In order to minimize disturbances at the probe volume level, flow seeding is usually performed in a wind tunnel far upstream, in the settling chamber; but at DNW this settling chamber is 50 m upstream of the test section and is 30 m wide and 18 m high. Since the flow is deflected as it passes across the rotor disc, adequate seeding of the vortex (which is always very difficult) requires control of the seeding point in the settling chamber: the seeding apparatus was installed on the DNW motorized transverse mechanisms and was remotely controlled.

The flow is periodic; so statistics are done for each point of the analyzed field at the same blade azimuth. Starting from a synchronization pulse delivered by the rotor at each turn (i.e. every 57 ms), data must be acquired within a short temporal window (typically 80 μs) in order to freeze the phenomenon. Under these conditions the measurement probability is strongly reduced (by a factor one thousand compared to a continuous flow), and, even if the flow seeding provides a high data acquisition rate (continuous display of 50 kHz), a velocity map of a vortex may require several hours. A measurement strategy has been developed in order to reduce this measurement time to less than half an hour.

3. LASER VELOCIMETER DESCRIPTION

3.1 Optical and Mechanical Setups

The aerodynamic department of ONERA currently uses a 3D laser velocimetry bench for measurements in research wind tunnels at Chalais-Meudon. The maximum displacements along the three axes XYZ in this apparatus are 600 mm. This setup has been the basis of the device used in DNW, but specific components have been added in order to extend its working distance from 2 m to 5 m in the backscatter mode.

The Spectra-Physics 171 argon laser, emitting 10 W all lines, as well as the 2D beam dividing system creating 2 green beams (λ = 514,5 nm) and 2 blue beams (λ = 488 nm) which are coaxial, are fixed on the horizontal translation systems XY. The frequency shift which is induced on both green and blue components by a pair of acousto-optic modulators (Bragg cells) is fixed at 5 MHz (Boutier et al 1984). These 4 beams are directed vertically by mirrors towards the emitting optics, composed of a Cassegrain beam expander (x 5) and a doublet (corrected for chromatism), 200 mm in diameter and having a 5 m focal length (Boutier et al 1990). This optics axis makes an angle of 15° with the Y axis of the velocimeter.

For the third (violet) component (λ = 476,5 nm), a fiber optic device has been added in order to minimize the weight that the Z vertical translation slide must hold. This translation slide also holds the heavy green-blue emitting device and the large Cassegrain telescope which receives light scattered by particles crossing the probe volume. The Spectra-Physics 2040 argon laser emitting 2 W on the violet line, as well as the rigid mechanical box enclosing optics which allow the division of the violet beam into two beams (separating plate, mirrors and two Bragg cells introducing also a 5 MHz frequency shift), are installed on the ground of the wind tunnel on a structure of Microcontrole rails set on a stable wooden table. At the ouput of this box, two Dantec manipulators are used to couple the violet laser beams into two monomode, 20 m long, optical fibers. At its other end, each of these fibers

is fitted with a beam expander (x 5) and focusing optics with a focal length adjustable between 2.5 and 5 m. These two ends, each having a cylindrical shape, are separated by 120 mm and are fixed on a beam rigidly linked to the Z slide; their mean line of sight makes an angle of 15° with the Y axis, and is symmetrical to the green-blue axis with respect to the receiving telescope axis parallel to Y. Each of the violet emitting optics is equipped with fine adjustments (optics displacements with micrometer screws) in order to ensure the overlap of the violet beams inside the probe volume.

Light scattered by particles crossing the probe volume is gathered by a Cassegrain telescope, with a primary mirror 450 mm in diameter, which is placed 5 m from the sample volume and has a magnification of 2. The image of the probe volume, situated slightly behind the primary mirror (after reflexion on the secondary mirror which is a lens silvered on its rear face) is transferred by a collimating lens which sends the collected light towards several dichroic plates which successively isolate the green, blue and violet flux. Each monochromatic flux then impinges on a separate photomultiplier tube, with an appropriate interferential filter in front of it. This telescope has an axis parallel to the Y axis, and is situated at an equal distance from the green-blue emitting optics and from the third violet component optics; therefore the mean angle between the emitting and receiving axes is 15°. The general arrangement of the optics on the platform 9 m high is given in Figure 1.

An equilibrium on the the intensities of the beams arriving in the probe volume has thus been achieved: each laser beam of each color has a power of 300 or 400 mW. In the probe volume, 400 μm in diameter, the fringe spacings are deduced from measurements with a theodolite (Boutier et al 1986); the found values are 19.96 μm (green component), 18.23 μm (blue component) and 19 μm (violet component). Then a matrix (also determined by theodolite measurements) transforms the frame in which components are measured into the wind tunnel frame (U along the horizontal axis parallel to the main flow axis, V along the Y horizontal axis perpendicular to X, W along vertical Z axis directed upwards). The green and blue components are nearly symmetrical (at 45°) relative to the horizontal plane.

The acquisition and signal processing devices, as well as the piloting system of the XYZ bench, are installed in a shelter placed in the DNW hall.

Blade vortex interaction is predicted by codes to occur at 306° azimuth and 0.87 R (R is blade radius equal to 2 m). Since the vortex must be characterized before this interaction creating noise, the probe volume has been set at 298° and 0.8 R, assuming a vortex trajectory quasi parallel to the main flow axis X.

3.2 Flow Seeding

Two types of aerosols have been successively injected into the wind tunnel: glycol smoke which allows a visual observation (via a video camera) of the zone where particles are passing about the laser velocimeter probe volume, then incense smoke which provides the submicronic size distribution required for the measurement quality.

The ouputs of these injectors are linked to the smoke emitting point (in the settling chamber) by long flexible tubes (but temperature resistant). At the emitting point the two tube ends are placed side by side and fixed on a plate which can move vertically along Z and crosswise along Y. These displacements have amplitudes of several meters (settling chamber 30 m wide, 18 m high) and are motorized. The location of the injection point is monitored from the "command" shelter where the signal processors and computers are installed, with a display of the injection point positions.

The glycol smoke generator, which can run a very long time, is installed inside the settling chamber on a trolley which moves along Y. It is controlled (electric commands) through a 30 m long cable, the end of which is set outside the settling chamber. For each test, this glycol smoke is injected in order to roughly find the injection point location, then is stopped in order to use the incense smoke.

The incense smoke generator is located outside the aerodynamic circuit because it is necessary to change the granules which are consumed every 3/4 of an hour. A temperature resistant tube leads the smoke inside the settling chamber up to the mobile injection point (over a length of 40 m). The injection pressure of the smoke is regulated from the "command" shelter taking into account the data acquisition rate and the signals visualized on oscilloscopes.

3.3 Data Acquisition

Signals from the photomultipliers are processed by an IFA 750 of TSI, Inc., and are permanently visualized on 3 oscilloscopes. The PHASE software is used; for each particle, the "date" is recorded and the 3 signals are obtained in "simultaneous" mode, which provides the instantaneous velocity vector (allowing the computation of all turbulence parameters).

A PC computer manages the whole experiment. Its three main functions are the followings: acquisition of data from the IFA 750, driving of the stepping motors of the XYZ laser velocimeter bench, and acquisition of the blade turn numbers; these are delivered by an interface box, allowing an interactive mode with another PC, via the Data Link card, acquiring blade tip attitudes (TART method).

A counter continuously displays the number of validated data points during the observation window of the IFA 750, which allows one to visually optimize the position of the seeding point. Optimum seeding occurs when this counter increases as quickly as possible.

Starting from a pulse delivered by the rotor when the tested blade is at 180° azimuth (i.e. against the wind), the TSI RMR device creates a measurement window: blade azimuths corresponding to the beginning and the end of the vortex observation are entered; they precede the 298°

azimuth (retreating blade) where the laser velocimeter probe volume is set. Practically when the blade achieves a rotation of 45° (at 1040 r.p.m.), the vortex moves downstream (at the wind tunnel speed of 33 m/s) a distance of two blade tip chords (i.e. 240 mm, when its core is estimated to be a few tenths of a chord). At each turn of the same instrumented blade, instantaneous velocity vectors are recorded and dated relative to the beginning of the measurement acquisition window. For each altitude Z, 10000 instantaneous velocity values are recorded for "detailed" maps; only 2000 values are recorded when a "rough" map is established.

For data processing, at each Z altitude, the acquisition window is separated into equal intervals: for a "detailed" map, the angular resolution is 0.5° for a 45° observation window, which means 90 classes where nearly 100 particles per class are expected if acquisitions are evenly distributed, because in fact 10 000 particles are recorded over the whole observation window. For a "rough" map, which purpose is to see if the vortex is well detected, the resolution is lower (2.5°), with still 100 particles per class, but only 2 000 particles are recorded on the whole window, which is quicker.

The test strategy consists of recording for each vortex a rough map and processing it in real time (acquisition takes 15 minutes, then data processing and interpretation take 10 minutes), in order to choose the appropriate parameters for the detailed exploration. These parameters include probe volume altitudes and synchronization azimuths so the detailed data will be centered on the vortex.

All detailed measurements have been performed with a 50 μs coincidence window, when a 0.5° class is 80 μs wide. For each validated particle, are associated its temporal location (within 1 μs), the number of the turn at which it was acquired, as well as the blade tip attitude provided by the TART method.

The probe volume is located at 0.8 R along the radius R (equal to 2 m) at the fixed azimuth of 298°; its altitude Z varies to map the vortex. In other words, for each Z value, for X and Y fixed, we observe the vortex moving in front of a fixed probe volume. One of the purposes of the data processing is to evaluate the convection velocity of the vortex (modulus and angle). This velocity is nearly equal to wind tunnel speed (33 m/s), while blade tip moves at 220 m/s. This convection velocity is used to reconstruct in fixed coordinates (Z, X) the velocity field measured in (Z, ψ) coordinates.

In each class 0.5° wide (90 classes for each altitude Z) are computed mean and r.m.s. values, skewness and flatness factors, as well as the Reynolds shear stresses. All statistics made on less than 5 data points inside a class are eliminated.

For each map, the total number of points varies between 5 000 and 10 000 (50 to 100 lines, which are different values of Z, each one having 90 classes of 0.5°). At worst, 5% of the data are rejected. For instance data are rejected when a blade blocks a laser beam, preventing the collection of three components in coincidence. Vortex cores have relatively few particles, but are never empty.

In order to restore the observed phenomena at best, rough maps of the different parameters (mean velocities and turbulence) in frame (Z, ψ) must be transformed into maps in the frame (Z, X); therefore a constant convection velocity of the vortex must be defined.

In fact the laser velocimeter observes the vortex translation at a fixed point at altitude Z. We assume that during this observation time the vortex does not distort and that this structure moves at a constant convection velocity. The value of the convection velocity is obtained by computing the mean velocity over the whole measured field, for each test configuration. With this strategy, a detailed vortex map is acquired within half an hour (the initial idea was of course to open a window of 80 μs for a fixed value of ψ and to move the probe volume along Z and X). This approach reduces data acquisition time by a factor of 90, because the 90 classes along X are simultaneously acquired (with the assumption of a constant vortex convection velocity during the observation time of 8 ms). Practically, half an hour is a more convenient time for observation than fifty hours.

4. BLADE TIP ATTITUDE MEASUREMENT

In order to determine the attitude of the blade tip in real time, a method has been developed and successfully tested during these HART tests. It has been called the TART method: Target Attitude in Real Time.

Two targets of scotchlite (thin self-adhesive material composed of glass marbles, used as a retroreflecting device) are stuck at the tip of the instrumented blade: they are 4 mm in diameter and set 70 mm apart. They are illuminated by a flash emitting 1 μs pulses, synchronized with the rotor. The same synchronization pulse as the one used for laser velocimetry is used, but with a different delay, in order to record the blade attitude at 298° during laser velocimetry measurements.

A Lhesa CCD camera looks at these targets with a variable focal length objective (80 to 300 mm), allowing a magnification of 0.35 at a 5 m working distance. Interface and software specific to this configuration (developed under Labwindows) allow real time acquisition on a PC of the barycentres of the two target coordinates (x1, y1) and (x2, y2) illuminated by the flash.

The minimum time between two successive acquisitions is 40 ms, when the rotor rotation period is 57 ms. The half sum of barycentre ordinates (x1 + x2)/2 gives blade altitude; the half sum of barycentre abscissa (y1 + y2)/2 gives information on horizontal jitter of blade tip. The pitch angle of the blade tip is given by (x2 - x1)/(y2 - y1).

Four targets stuck along a rectangle, accurately measured under laboratory conditions, are installed on the blade: in order the rectangle to be horizontal, we push on blade tip with a telescopic mast 10 m high (and fitted with an adjustable rod 1 m long). Reference data are recorded

for a blade position at rest. This provides camera magnification and its angle relative to an horizontal. Simultaneously a triangulation by theodolites set on the ground provides the blade tip altitude in the rotor frame. Another theodolite looking at blade tip gives the corresponding incidence angle. All data gathered in flight are refered to the initial calibration data and allow the determination of blade tip altitude and incidence angle in rotor frame at any moment.

For each file which accumulates instantaneous values relative to hundreds or thousands of rotations, mean and r.m.s. values of the following parameters concerning blade tip are computed: altitude, jitter in mm along X and angular jitter, incidence angle.

In the TART method, one pixel of the camera used corresponds to 0.3 mm in the field analyzed. Therefore it is the resolution of the method for altitude and jitter measurements of the two spot barycentres. Angular resolution on pitch angle determination would be 0.3° if we considered one pixel uncertainty along a vertical axis relative to a 70 mm horizontal basis (distance separating the two targets); but practically, as each target covers several pixels, because of the horizontal fluctuations of one pixel for determination of each of the two barycentres, the angular resolution is improved and reaches: $(0.3/70 - 0.3/70.3) \times 180/\pi = 10^{-3}$ degree.

5. VORTEX CHARACTERISTICS

5.1 Laser Velocimeter Display

Acquired velocity maps in frame (Z, ψ) are transformed into (Z, X) frame by taking into account the vortex convection velocity. For (u, w) components, the values in m/s of the horizontal Vcx and vertical Vcz components of this convection velocity have been computed: (34, -8) for the baseline case, (34.9, -6.3) for the minimum noise case and (34.4, -6.9) for the minimum vibration case. This procedure allows a description of the state of the vortex when it arrives on the retreating blade at 298°, and seen by an observer situated on the laser velocimeter platform. Z and X coordinates are deduced from the measured coordinates Zm and ψ by the following formula:

$$Z = Zm + (298 - \psi)(\pi/180) \times Vcz \times \omega^{-1} \quad (1)$$

$$X = (298 - \psi)(\pi/180) \times Vcx \times \omega^{-1} \quad (2)$$

Notice that $\omega = 2\pi f$, with f = 17.5 Hz because the rotor rotates at 1 040 r.p.m..

For each configuration the following maps are drawn:
- mean velocity: the three components $(\bar{u}, \bar{v}, \bar{w})$, then the vectors $(\bar{u}, \bar{w})$ in a vertical plane (Z, X)
- turbulence levels: r.m.s. values $(\overline{u'^2})^{1/2}$, $(\overline{v'^2})^{1/2}$, $(\overline{w'^2})^{1/2}$, and the shear stresses $\overline{u'v'}$, $\overline{u'w'}$, $\overline{v'w'}$
- vorticity ζ in vertical plane (Z, X).

Vorticity ζ is defined by the following expression in each point of the measurement networking, and thus takes into account adjacent points: $\zeta = dw/dX - du/dZ$. This vorticity display has been a convenient visualization means, which has been used to point out vortex presence within a very short delay after the end of a map acquisition.

The four most important parameters which are deduced from velocity and turbulence maps are the followings:
a) location of the vortex core in the rotor frame
b) location of the vortex core relative to the blade; this position is computed by taking into account the results of blade tip altitude provided by the TART method
c) vortex core radius
d) vortex intensity, deduced from circulation calculation.

The most typical figures (extracted among the Minimum Vibration results) and which have been used for data reduction and interpretation are:
* Figure 2: vector field $(\bar{u}, \bar{w})$
* Figure 3: $\bar{u} = f(Z, \psi)$ non convected field; this representation allows to point out the blade wake in the foreground; interaction of this wake with the vortex structure explains the difficulties found further to compute vortex strength from a circulation evaluation on a closed contour surrounding the vortex.
* Figure 4: $\bar{u}$ field, horizontal component of mean velocity along X
* Figure 5: $\bar{u} = f(Z)$ profile; it is established at value ψt corresponding to vortex core location (see explanations 3) and 4) in section 5.2)

5.2 Vortex Core Location

The evaluation of the vortex core location has been achieved in seven different ways, for the three flight configurations:
1) from the representation of isovorticity contours, plotting of target center where lines which are quasi concentric become more confined;
2) in Figure 2 representing the projection $(\bar{u}, \bar{w})$ of mean velocity vectors in vertical plane (X, Z), plotting of the central point around which vectors seem to wind;
3) starting from the figures representing isovalue lines of axial $\bar{u}$ component (Figure 4) and of vertical $\bar{w}$ component (a similar figure has been drawn), these figures looking like "butterflies", plotting of vortex center altitude Zt in u map and of its position Xt (or ψt) in $\bar{w}$ map; this plotting corresponds to the axis of symmetry of the "butterfly";
4) for Xt defined in 3), i.e. for a fixed blade azimuth, evolution of axial u component is drawn as a function of Z (Figure 5); vortex center is thus defined as the mean of Z values corresponding to curve extrema (see arrows). The values of these extrema of axial u component are nearly symmetrical relative to convection velocity;
5) starting from Figure 5, the vortex center is defined as the curve inflexion point;
6) for Xt defined in 3), i.e. always for a fixed blade azimuth, profile $(\overline{u'^2})^{1/2} = f(Z)$ is drawn, i.e. axial velocity fluctuations which usually characterize turbulence (however they also integrate velocity gradients due to the vortex position fluctuations from one turn to another); these curves show a maximum at vortex center;

7) for Xt defined in 3), i.e. always for a fixed blade azimuth, profile u'w' = f(Z) is drawn, which is the evolution of the shear stress; the zero crossing of this profile is also characteristic of the vortex center.
Table 1 provides the coordinates Zt and ψt of the vortex center as determined by the 7 methods described before (non convected velocity fields, in rotor frame).

It clearly appears that method 4) is the least accurate one and provides results which are not consistent with those from other methods; results from this method 4) are thus rejected and the mean value of the other methods is kept for each configuration. Starting from table 1, the Zt altitude and ψt azimuth of vortex center values finally kept are: (-12 mm, 258°) for baseline case, (-45 mm, 269°) for the minimum noise case, (+18 mm, 262°) for the minimum vibration case.

Nevertheless, these altitudes Zt are not measured at a 298° blade azimuth. Since the blade position was measured by the TART method at 298°, in order to obtain consistent results at 298° azimuth, especially concerning the blade-vortex miss distance, we now compute the altitude Z't which the vortex core would have, taking into account its convection speed, when the blade moves from ψt to 298°. The formula allowing us to transform measured Zt altitudes at azimuths ψt to values of altitudes Z't at 298° azimuth are:

$Z't = Zt + Zc$ with $Zc = Vcz \times T(\psi t \rightarrow 298°)$

$T(\psi t \rightarrow 298°)$ is the time the blade takes for this azimuth modification, giving that rotation period is 57 ms:

$T(\psi t \rightarrow 298°) = 0.057 \times (298 - \psi t)/360$ s

The vortex center altitudes Z't finally kept at 298° azimuth, in the rotor frame, for the retreating blade are the followings: -62 mm for baseline case, -74 mm for minimum noise case and -21 mm for minimum vibration case; notice that the altitude corrections Zc are respectively -50 mm, - 29 mm and -39 mm.

5.3 Vortex Radius and Strength

The vortex, having a priori a trajectory in a quasi horizontal plane, but with its axis not parallel to Y axis, is seen by the laser velocimeter in perspective; this effect is minimized when analyzing data along a vertical axis at ψt fixed. The radii are then determined from curves of the Figure 6 type, distance between extrema giving 2 Rt. The vortex radii found are: 30 mm for the baseline and minimum vibration, but 50.5 mm for the minimum noise.

Circulation, representative of vortex strength, is usually computed by integrating velocity components over a closed contour surrounding the vortex core; when gradually going away from the vortex core, a constant value must be found. This type of calculation did not ever ended at a constant value because, in all recorded velocity fields, influence of blade wake is very close to the vortex (in Figure 3 the wake is the small "hill" in foreground); the vortex could also have vanished. Therefore circulation has been computed along the following formula (Batchelor 1972):

$$\Gamma = (\pi/1,2763) \times \Delta W_{pk\,pk} \times 2\,Rt$$

$\Delta W_{pk\,pk}$ is the velocity gap between extrema of curve of Figure 5. The circulation has a constant value of 2.4 m²/s.

5.4 Blade Tip Attitude

The mean altitude of the blade remains constant for each configuration, the r.m.s. value of the data being of the order of 1 mm; however a slow variation with a 1 mn period has been pointed out during all recordings, as shown in Figure 6 where the peak to peak fluctuation amplitude reaches 4 mm: this phenomenon has been recorded over more than 4 000 rotations, i.e. during nearly 4 mn. On a PC with the Easyplot software, a frequency analysis has been performed up to 8 Hz (rotor frequency is 17.5 Hz), with a magnification on the 0 - 0.2 Hz domain in order to clearly show the main 0.017 Hz frequency (which corresponds to a 1 mn periodicity). The blade tip jitter has a constant mean value, with a peak to peak amplitude also equal to 4 mm (r.m.s. value of 0.9 mm); the transformation of these data into angular jitter provides a r.m.s. value of 0.03° and a peak to peak value of 0.1°. Mean value of the incidence angle remains constant (thus over 4 mn), but with a r.m.s. value of 0.2° (peak to peak value of 0.5°). Spectrum analysis of jitter and incidence angle fluctuations do not point out any significant frequency.

Let us notice that blocking the sting supporting the rotor makes the periodic phenomenon disappear in the altitude fluctuations.

5.5 Blade-Vortex Miss Distance

Position of vortex core altitude has been determined at the end of section 5.2; the TART method provides mean values of blade tip altitude. Then we can calculate the blade-vortex miss distances at 298° azimuth, which are: - 35 mm for baseline, - 54 mm for minimum noise and 15 mm for minimum vibration (Z axis is directed upwards, thus negative distances mean that the vortex is under the blade).

This final result clearly points out that noise reduction seems to be directly correlated to the fact that the vortex goes far away from the blade before interaction (due to the chosen HHC), and that when it is closer, it induces a minimum of vibrations. This kind of result constitutes a first bank of data for further interpretations, in correlation with all the other measurements achieved.

6. CONCLUSION

The characterization of a vortex having a ten centimeter size in such a large scale facility as DNW (8x10 m² test section size, with rotor blades 2 m long and turning at 10 m from the ground) was really a challenge.

Two new apparatus, providing complementary data, have been designed and used, with the aim of providing the

same data quality as the one usually obtained in smaller research facilities.

Now an ONERA 3D laser velocimeter, already operational for 10 years, is able to perform reliable measurements with a working distance of 5 m and a spatial resolution of 400 μm, thanks to the use of the following key elements:

* large optics, partly already designed in the past for tests in the pressurized wind tunnel F1 of Le Fauga-Mauzac ONERA center
* a new technology based on monomode optical fibers for the third component
* the employment of a new signal processor (the IFA 750 TSI correlator).

The TART method (composed of a stroboscope, a Lhesa camera and a PC with a specific software) allows now accurate determination of the attitude of a target on which two retroreflecting circles are stuck: mean values and fluctuations of the target position (as well as its local incidence) in a plane perpendicular to the line of sight are acquired at a 20 Hz rate, with a spatial resolution of a few tenths of a mm and an angular resolution lower than a hundredth of a degree.

The results provided by the laser velocimeter, coupled to those of the TART method, constitute an important data base concerning the structure (radius, intensity, fluctuation levels) and the position relative to the blade of the vortex before it interacts with the blade. Helicopter noise reduction process thus begins to be better understood, the key parameter being the blade-vortex miss distance, which must be increased by appropriate settings of the rotor blades in flight. Finally all non intrusive technology is now available to study other modifications which can be brought to helicopter rotor characteristics with the aim of improving rotor performances.

ACKNOWLEDGEMENTS

This work has been achieved with the financial support and the encouragements of contracts from Ministry of Defense (DGA - DRET/6 and STPA/HE). The recognition of the authors goes also to their ONERA colleagues (G. Losfeld, D. Soulevant and R. Soares) who very actively participated in the tests at DNW.

REFERENCES

Batchelor (1972). Fluid dynamics. Cambridge University Press.

Boutier A; d'Humières Ch; Soulevant D (1984). Three dimensional laser velocimetry: a review. Proc. 2nd Int. Symp. on Applications of Laser Anemometry to Fluid Mechanics, Lisbon, Portugal, 2-5 July 1984.

Boutier A; Lefèvre J (1986) Accurate calibration of 3D fringe laser velocimetry with a theodolite. Proc. 3rd Int. Symp. on Applications of Laser Anemometry to Fluid Mechanics, Lisbon, Portugal, 7-9 July 1986.

Boutier A; Lefèvre J; d'Humières Ch; Coponet D; Soulevant D (1990). Laser velocimetry in large industrial facilities. Proc. 5th Int. Symp. on Applications of Laser Techniques to Fluid Mechanics, Lisbon, Portugal, 9-12 July 1990.

Gmelin B; Heller H; Mercker E; Philippe JJ; Preisser JS; Yu YH (1995), The HART programme, a quadrilateral cooperative research effort. Proc. 51st Annual Forum of American Helicopter Society, Fort Worth, TX, May 1995.

Kube R; Splettstoesser WR; Wagner W; Seelhorst U (DLR); Yu YH (AFDD); Boutier A; Micheli F (ONERA); Mercker E (DNW) (1994), Initial Results from the Higher Harmonic Control Aeroacoustic Rotor Test (HART) in the German-Dutch Wind Tunnel. Proc. 75th AGARD Fluid Dynamics Symposium CP552 (Panel on Aerodynamics and Aeroacoustics of Rotorcraft), Berlin, 10-13 October 1994.

Spiegel P; Rahier G; Michea B (1992), BVI Noise: Prediction and Comparison with Flight and Wind Tunnel Tests. Proc. 18th European Rotorcraft Forum, Avignon, September 1992.

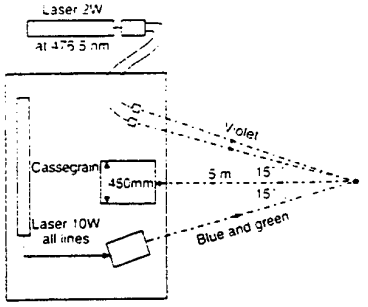

Figure 1: Optical configuration of the 3D laser velocimeter used

Configuration	Vorticity 1)	Vector map 2)	Butterflies 3)	$\overline{u}=f(Z)$ mean Z 4)	$\overline{u}=f(Z)$ Inflexion 5)	Max $(\overline{u'^2})^{1/2}=f(Z)$ 6)	Zero $\overline{u'w'}=f(Z)$ 7)
Baseline	- 8 258°	- 14 259°	- 12 258°	- 27 258°	- 12 258°	- 17 258°	- 12 258°
Minimum Noise		- 51 268°	- 38 269°	- 73 269°	- 45 269°	- 47 269°	- 57 269°
Minimum Vibration	19 264°	16 263°	20 262°	13 262°	16 262°	16 262°	23 262°

Table 1: Coordinates of the vortex center deduced from 7 different methods; the first number is the altitude in mm in rotor frame, and the second number is the azimuth in degree.

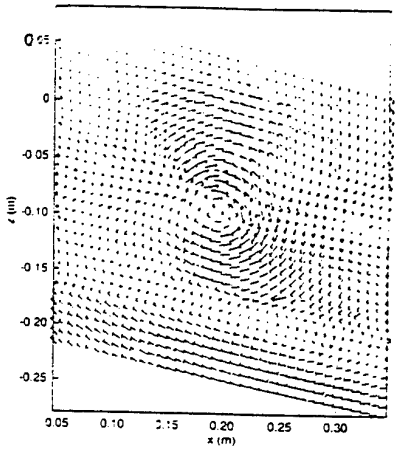

Figure 2: Field ($\overline{u}$, $\overline{w}$)

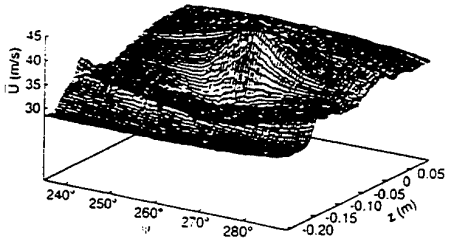

Figure 3: Profile $\overline{u}$ = f(Z, ψ)

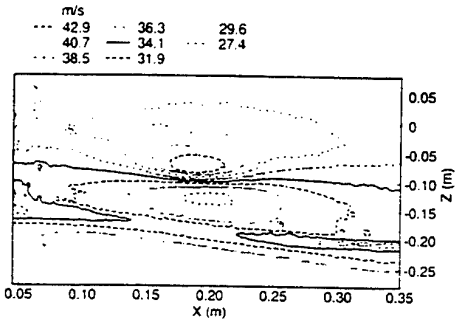

Figure 4: Field $\overline{u}$

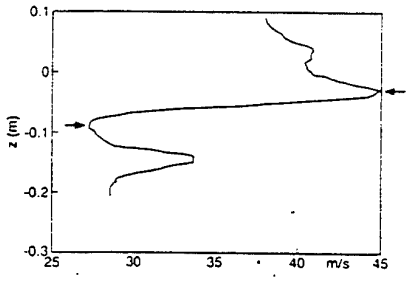

Figure 5: $\overline{u}$ = f(Z)

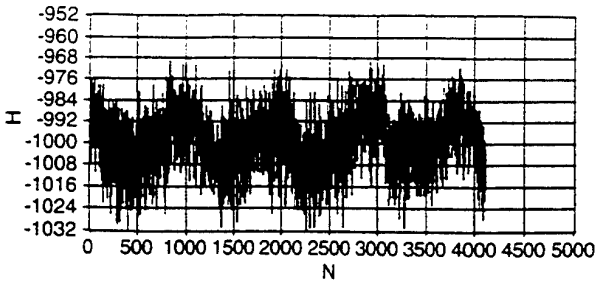

Figure 6: Evolution of altitude H (1/10 mm) as a function of the number of turns N in baseline case

SECONDARY FLOW IN AXIAL FLOW FANS OF NON-FREE VORTEX OPERATION

J. Vad and F. Bencze

Department of Fluid Mechanics
Technical University of Budapest, Hungary

ABSTRACT

The fine structure of the three-dimensional flow field downstream of an isolated axial flow fan rotor was measured using Laser Doppler Anemometry (LDA). The blading was designed for non-free vortex operation. Secondary flow characteristics were examined for design and off-design flow rates. Interacting flow phenomena, such as flow due to spanwise changing circulation, passage vortex and corner stall were observed. Radial transport processes were related to secondary flow. The tip leakage flow was found to be partially blocked by the secondary flow caused by non-free vortex operation. Close to the casing wall, vortical flow motion was detected for design flow rate. It was compared with a leakage vortex observed in a free vortex operating rotor of similar geometric and operating parameters. Though these vortices behave similarly, their origin must be different, as is concluded.

1. INTRODUCTION

The flow developing in rotors is closely related to the aerodynamical losses and noise of an axial flow fan. Losses represented by secondary flow, endwall and blade boundary layers can be identified and influenced through knowledge of flow field fine structure. Fluid mechanical processes taking place inside axial flow rotor passages have a great complexity. Thus, three-dimensional flow measurements must be carried out in the rotating system to learn more about these phenomena and to widen the experimental basis of theoretical models.

The most desirable manner of investigation involves three-dimensional flow study inside blade passages. Stauter(1993) took such measurements in the tip region of a compressor using a three-dimensional LDA system. A widespread way of study demanding relatively simpler measurement technique is to deduce the flow characteristics inside the blading on the basis of three-dimensional flow measurements downstream of axial flow blade rows.

Many of the rotors -mostly compressors- under such investigation were of free vortex design and operated at the design point. As a result, the endwall boundary layer flow was distinguishable relatively well from the mainstream of insignificant secondary motion. Only a few authors, e.g. Inoue and Kuroumaru(1984) extended their measurements to the whole downstream region of blade passages. Studies of Hunter and Cumpsty (1982), Inoue et a.(1986) and Inoue and Kuroumaru (1989) concentrated on the leakage flow in the blade tip region.

A number of publications are also available for off-design (non-free vortex) circumstances. Dring et a.(1982) and Goto(1992) obtained results in the whole downstream region. Experiments of Hunter and Cumpsty (1982), Inoue et a.(1991) and Lakshminarayana et a.(1995) were restricted again to the vicinity of the casing wall. In case of bladings of non-free vortex operation a secondary flow (abbrev. NFVO flow for "flow due to non-free vortex operation") develops inside the blade passage as a result of spanwise changing blade circulation. The NFVO flow takes probably part in formation of endwall boundary layers since it transports medium to lower and higher radii. It may also influence the development of the leakage jet and thus, change the effect of tip clearance size on tip clearance losses. Despite this, the above studies connect the underturning zone and the vortical motion (if any) near the casing wall solely to the leakage flow.

The main goal of the survey presented here was to point to the possible influence of NFVO flow on flow phenomena near the hub and casing wall. For this purpose, three-dimensional LDA measurements have been carried out downstream of a fan rotor designed for non-free vortex operation. Secondary flows have been examined from hub to tip, for design and off-design conditions.

2. EXPERIMENTAL EQUIPMENT

A ducted axial flow fan facility has been built for automatic characteristic and efficiency curve measurements at Technical University of Budapest, Department of Fluid Mechanics. Its schematic view is shown in Figure 1.

The rotor blading was designed for ideal total head rise changing along the radius as a power function with a power exponent of 1.2. The design and characteristic curve calculation method based on two-dimensional cascade data is described by Somlyódi (1970). The geometrical and design flow characteristics of the fan are given in Table 1. (A compressor studied by Inoue et a.(1986) which we compare to our rotor is also characterized in Table 1.) The blades have a spanwise uniform chord length of 136 mm and thickness of 2 mm. Further blading characteristics are shown in Table 2. Figure 2 shows the measured and calculated characteristic and efficiency curves. The studied cases of lower-than-design ($\overline{\Phi}$=0.4), design ($\overline{\Phi}$=0.5) and higher-than-design ($\overline{\Phi}$=0.58) volume flow rate are called cases L, D and H, respectively.

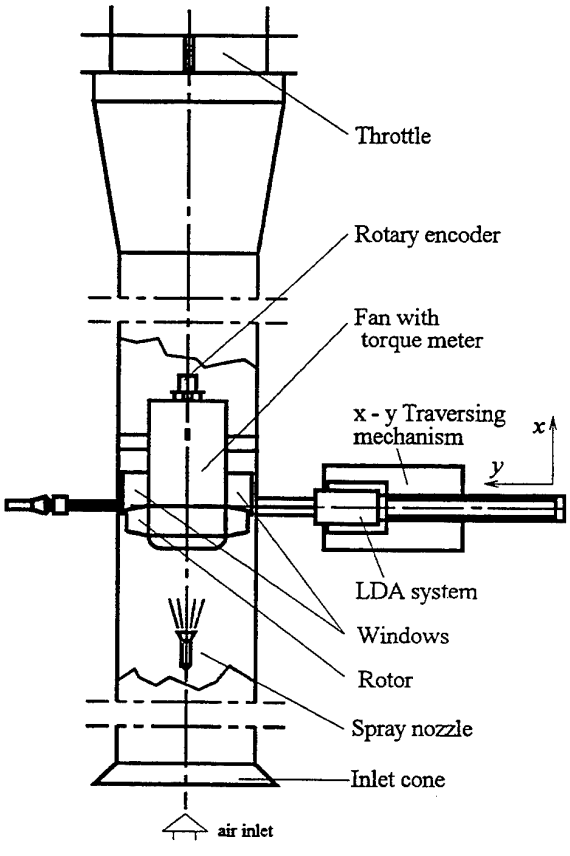

Figure 1. Experimental equipment

Table 1. Fan geometry and design flow conditions

	Authors' fan	Rotor of Inoue et a.(1986)
Configuration	isolated rotor	isolated rotor
Operation	non-free vort.	free vortex
Inlet condition	uniform axial	uniform axial
Blading	circular arc	NACA 65
Blade number	12	12
Rotor speed /(rev/min)	1200	1300
d_t /mm	624	449
d_h/d_t	0.683	0.600
$t/(r_t-r_h)$	0.030	0.034*
t/ℓ_t	0.022	0.026*
$Re_{bt}/10^5$	3.974	2.677*
$\overline{\Phi}$	0.5	0.5
$\overline{\Psi}$	0.41**	0.35**
η	0.78**	0.84**

* Calculated by the authors from Inoue et a.(1986)

**Read at design flow rates from Fig.2 and Inoue et a.(1986), Fig.3

Table 2. Blading geometrical and design characteristics

	root	midspan	tip
r /mm	213.0	262.5	312.0
radius of curvature/mm	318.0	394.2	475.3
solidity	1.22	0.99	0.83
stagger*/deg	43.2	49.3	53.8
inlet flow angle*/deg	53.8	59.3	63.4
exit flow angle*/deg	57.3	52.8	48.9
lift coefficient	0.77	0.82	0.86

* Stagger and design angles are taken in relative system from axial direction.

Division of $\overline{\Psi}$ values by the related η data derives the "measured" $\overline{\Psi}_{id}$curve (B). Calculation supplies diagram (A) and blade-to-blade averaged $\hat{\Psi}_{id}(R), \hat{\Phi}(R)$ distributions in any operating point. The latter will be taken as the basis of comparison between the measurements and the "ideal case". Curve A passes through the design point of $\overline{\Phi}$ = 0.5, $\overline{\Psi}_{id}$ = 0.58. Curves A and B do not coincide because the design and calculation method does not take the flow rate reducing effect of boundary layers into account. This effect must be eliminated during comparison. For this purpose, operating points L, D and H are marked on curve B. They are projected horizontally onto curve A. The $\hat{\Psi}_{id}(R), \hat{\Phi}(R)$distributions calculated for "reference points" derived this way will serve as reference to be compared with measurement results, as discussed below.

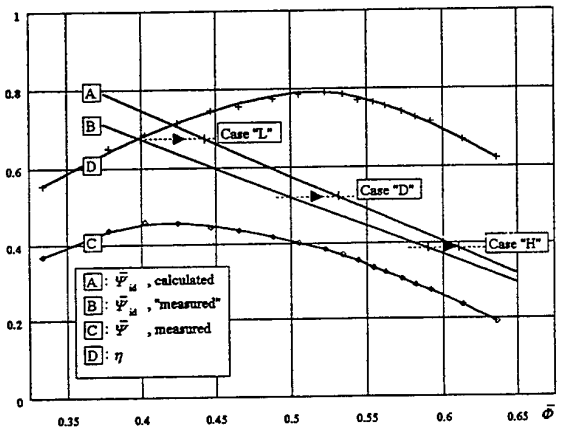

Figure 2. Fan characteristic and efficiency curves

3. LDA MEASURING TECHNIQUE

To measure the three-dimensional velocity field downstream of the rotor, LDA technique was chosen as a powerful, non-intrusive tool of high spatial and temporal resolution. The LDA available was a single component DISA 55L Mark II type with a Spectra-Physics Model 124B He-Ne laser.

A forward-scattering method had to be elaborated, due to the low laser power. Relatively low levels of reflecting noise are typical within the arrangement. Figure 3 shows the setup in which the laser beam plane is perpendicular to the duct axis. The velocity field is assumed stationary in the rotating system. Let us take a flow field element characterized by constant c_θ, c_r, c_x values. E.g. c_θ denotes c_θ multiplied by the tangential unit vector. If the measuring volume is positioned to a $-y$ coordinate from the duct symmetry plane, the magnitude of a certain projection of $c_\theta + c_r$ perpendicular to the beam bisector can be measured when the flow element passes the measuring volume. Targeting to $+y$ coordinate, we can measure the magnitude of another projection of $c_\theta + c_r$.

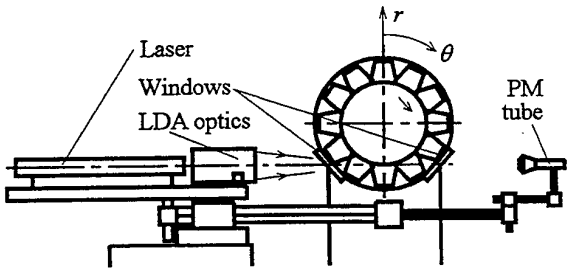

Figure 3. Downstream view of LDA arrangement

The measured mean velocities are functions of $|c_\theta + c_r|$ and the known geometry. Thus, c_θ and c_r can be calculated. Taking such symmetric measurements along the chord perpendicular to the duct axis, the downstream region of blade passages can be swept from hub to tip, to map c_θ and c_r. Aligning the beam plane parallel to the duct axis and rotating the optical bench so that the beam closer to the trailing edges is perpendicular to the duct axis, the magnitude of a projection of $c_\theta + c_r + c_x$ is measured. Using the appropriate geometrical relationship and the already known c_θ, c_r data c_x is derived.

The duct has been equipped with uncoated plane windows downstream of the blading (Brewster incidence condition is nearly fulfilled). To minimize flow disturbance, the inner window surfaces are tangential to the inner casing surface in the heigth of the measuring chord and their declination from the duct wall is less than the blade tip clearance.

A Bragg cell is operated in the path of one beam producing a 40 MHz frequency shift. The photomultiplier (PM) tube is aligned off the LDA axis. The LDA optical bench supporting the transmitting and receiving system is built up to a computer-controlled x-y traversing mechanism. An incremental rotary encoder has been connected to the fan driving motor, to measure rotor speed and angular position.

An Airbrush spray nozzle seeds the flow field with distilled water droplets. To reduce surface tension, detergent is added to the water at an optimized concentration. Droplet size distribution was measured in another LDA configuration by the visibility method. With appropriate trigger level adjustment, droplets with approx. 7 μm mean diameter are used for seeding. The diameter values scatter within an approx. 2 μm wide band.

A personal computer operates data acquisition and traversing. It performs all the calculations and evaluation. Velocity data are determined using fast Fourier transformation software. Further details of the measuring technique can be found in Vad et a.(1995).

The angular coordinate is read out with $\pm 0.3^\circ$ uncertainty at rotor speed of 1200 RPM.The effective measuring volume length is approx. 4 mm, which may be too large for measurements within boundary layers. Measurements have been resolved to cells of 5 mm in radial and 1° in tangential direction. More than 100 data have been collected for every cell and their ensemble averages are used in velocity calculation. The central angle of the measuring region was set to 35° (1 1/7 pitch) downstream of one certain blade passage to measure one blade wake region contiguously and to check periodicity in results. The measuring plane perpendicular to the duct axis was set at x/ℓ=0.147 from the tip trailing edge.

Table 3. General experimental uncertainty

	c_θ	c_r	c_x
Bias limit/(u_t /100)	1.8	0.3	0.1
Precision limit/(u_t /100)	1.0	0.1	0.6
Uncertainty/(u_t /100)	2.1	0.32	0.61

The relatively large droplet size causes bias error predominantly in measuring c_θ. Bias errors occur due to alignment errors and deformations. They increase slightly with relative angular deviations near the hub. "Precision errors" occur mainly due to the limited number of cell data as well as fluctuation in rotor speed and air density. During evaluation, spatial filtering of the velocity maps is executed to diminish the effect of random errors in identification of flow phenomena. Table 3 summarizes the velocity error limits valid for all the observed operating points. The error estimation procedure is described in Bencze and Vad(1996). The laser beams were lead through the gap between the rotor and the motor casing situated behind. This gap causes some disturbance in downstream radial velocity field, as measurements with removed blades suggest. Thus, bias limit for c_r is $0.02u_t$ in the two cell rows closest to the hub. Qualitative conclusions can be taken in this region, but the results seem to fail to satisfy e.g. continuity law ($c_{r\,h}=0$).

4. RESULTS AND DISCUSSION

The measurement annulus sector region is transformed to a rectangle during representation. The plots are extended to 40 deg range by duplicating the starting section to get a better view of flow structure. Methods used by Inoue et a.(1986) are followed in this flow field study.

Secondary flow maps are shown in Figure 4. Secondary flow was defined by a velocity component perpendicular to the relative flow direction given by the adequate reference distributions. Figure 4 also shows segments of $\partial c_x/\partial x = 0$ lines in the wake region, which were determined by numerical differentiation using the continuity equation. They cover the wake centers, by the authors' definition. Figure 5 shows the axial velocity plots.

In Figure 6, exit flow angle deviation, pitch angle and relative kinetic energy defect factor contour maps can be seen for case D. These values are calculated as follows, respectively (superscript * denotes reference values):

$$\beta-\beta^* = \cos^{-1}\left[\left(w_x^2+w_r^2\right)^{1/2}/w\right]-\cos^{-1}\left(w_x^*/w^*\right)$$

$$\gamma=\tan^{-1}\left(w_r/w_x\right)$$

$$\zeta=\left(w^{*2}-w^2\right)/w^{*2}$$

The defining expression of ζ had just the opposite sign in Inoue and Kuroumaru(1984). Axial velocity was higher and tangential velocity was lower than design in the mainstream in their measurements. This results in excess relative velocity (negative energy defect values), as published ζ plots of the above authors confirm as well. Since their definition would give positive values for the mainstream, its validity is doubtful.

Streamwise vorticity was calculated by numerical differentiation using the following equation:

$$\xi_s=(1/r)\left\{-\partial(r\cdot c_\theta)/\partial r+\partial c_r/\partial\theta\right\}\cos\beta-(\partial c_x/\partial r)\sin\beta$$

This equation is almost the same as in the work of Inoue et a.(1986) but here the part containing $\partial c_r/\partial x$ had to be neglected assuming that $\partial c_r/\partial x \ll \partial c_x/\partial r$, as in Lakshminarayana et a.(1995). Streamwise vorticities are presented in a form nondimensionalized by 2ω, in Figure 7.

Tip and and hub regions are of strong vorticity. To avoid contour line piling up in these zones, but to show detailed vorticity structure outside of them as well, Fig.7 is prepared for cases D and H as follows. Contour line values have a step of 0.2 between the line of value 1.0 near the casing wall and the line of value -2.0 near the hub (bold lines). Step value is 1.0 out of the middle region.

Dotted contour lines indicate zero values in Figs. 6-7.

Results are discussed separately for cases D,H and L.

4.1 Operating Point D

For case D, Fig.4 represents the wake flow, the NFVO flow, the passage vortex near the hub, the stall at the suction side blade root and the vortical motion near the casing wall. From this point on,the lattest will be compared to the leakage vortex observed by Inoue et a.(1986) behind a rotor characterized in Table 1. Data of Table 1 (and Table 2, adding that tip solidity and stagger were 1.00 and 56.2° for their rotor, respectively) support the comparability. Some discrepancy is shown in downstream measuring location (x/ℓ_t=0.068 for their published data). This would impair comparison only in higher solidity cases where the vortex reaches the adjacent blade and starts to interact with the wake, as Inoue and Kuroumaru(1989) experienced.

A deficiency in the present study is the lack of inlet flow data. Meixner(1994) measured the upstream axial velocity profiles for fans of non-free vortex design. In his experiment, axial uniform inlet condition seemed to be closely fulfilled at design and off-design points as well.

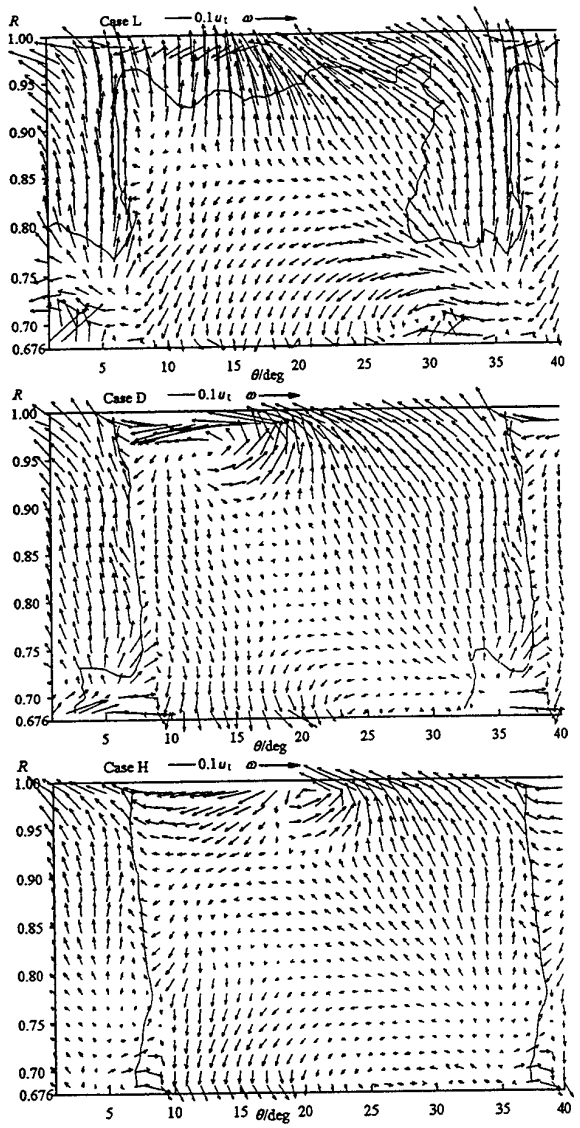

Figure 4. Secondary flow maps. $U(c_r)=0.003\,u_t$
$U(w_n)=0.018\,u_t$ (component normal to relative streamline)

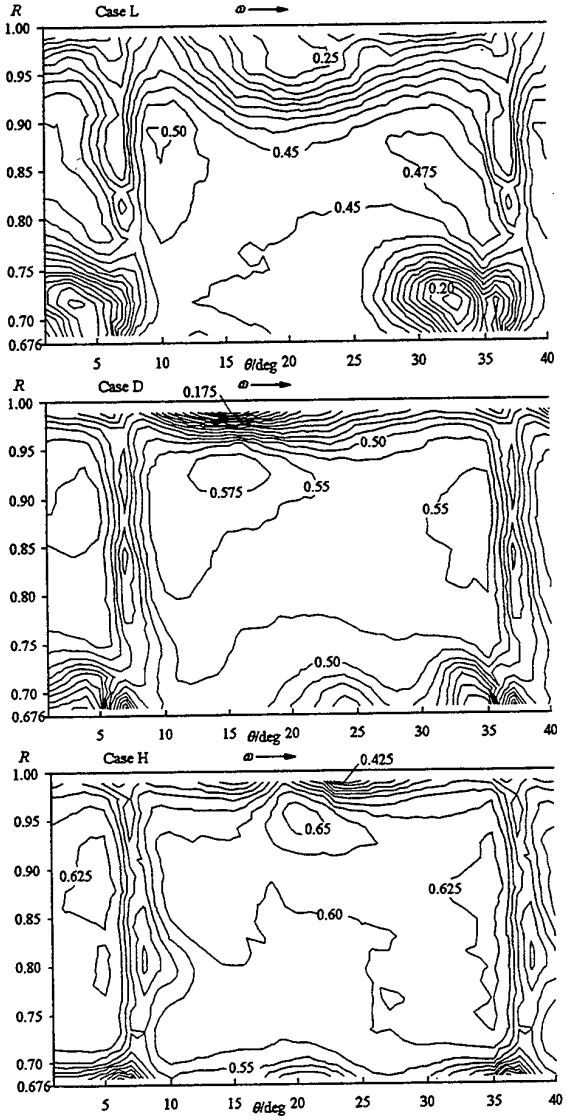

Figure 5. c_x / u_t contour plots. $U(c_x)=0.006\ u_t$

Some higher gradients were present only in the vicinity of the nose cone and casing wall. Inoue and Kuroumaru(1989) concluded that flow structure near the casing wall does not change considerably with the thickness of inlet casing wall boundary layer. Besides, inlet boundary layers are naturally developed (thin) for both rotors to be compared. Considering the above references, the lack of inlet flow measurements is not critical.

In Fig.4, the drastic suction side outward NFVO flow appears to block the leakage flow. Thus, the vortical motion near the casing wall is not definitely a leakage vortex.

Since it must derive rather from the NFVO flow, it will be called NFVO vortex. Minimum and maximum values in exit flow deviation and pitch angles within the NFVO vortex agree well with the results of Inoue et a.(1986). However, different tendencies are observed in the vortex regions. In Fig.6A, the range of high underturning does not include the tip region of the blade wake. This is evidence for leakage flow blockage. The pitch angle distribution (Fig.6B) is highly antisymmetric. The inward flow is concentrated in a small region of high pitch angle gradients. Axial velocities in Fig.5 show not a slight but a rapid increase in axial velocity as one moves from the

vortex towards the pressure side. These details suggest that medium stagnates at the tip and is scraped by the blade.

Analzying Figs. 4-6, flow phenomena near the casing wall can be described as follows. The outward NFVO flow transports medium to higher radii. This medium starts to interact with the casing wall boundary layer. It moves towards the pressure side and rolls up into the NFVO vortex. The medium originating from the casing wall boundary layer stagnates at the blade tip and is scraped by the blade since the outward NFVO flow in the adjacent passage blocks a possible leakage jet. The scraped fluid is connected to the inward NFVO flow and is pushed out of the blade passage. The strong NFVO vortex motion causes an absolute minimum and maximum in axial velocity field.

A consequence of non-free vortex operation is inhomogeneity in downstream axial velocity. Since zones of higher axial velocity and NFVO flow branches overlap (Figs. 4 and 5), one can conclude that transport phenomena within the NFVO flow and the related scraping process cause spanwise change in axial velocity.

Near the hub, the passage vortex extends to the zone of inward NFVO flow (Fig. 4). High and disordered velocity values show the existence of a corner stall at the suction side blade root. The overturning branch of the NFVO vortex, the underturning branch of the passage vortex and the inward and outward NFVO flow branches nestle close to a small symmetrical zone of neglectable secondary motion, as a result of their interaction.

The maximum in kinetic energy defect (Fig.6/C) and in dimensionless vorticity (Fig.7) within the NFVO vortex is in good agreement with results in Inoue et a.(1986) and the defect structures are very similar as well. The vortex centres (loci of maximum energy defect) almost coincide. At the suction side blade root, low energy fluid accumulates in a stall zone, connecting to the passage vortex. The overturning zone of the passage vortex also accumulates medium of energy defect, having a positive vorticity. Fig.7 shows a contra-rotating vortex below the NFVO vortex as a result of its interaction with the main stream.

The vorticity in the wake is generally negative, indicating uniformly increasing circulation (Fig.7), that decreases to zero just near the tip (positive vorticities). This suggests that spanwise decrease in total head rise to zero does not actually depend on blade action, it is mainly caused by the secondary flow phenomena near the casing wall. Though the stage performance is reduced, the blade acts almost as if the reducing effects would not occur. Thus, the shaft power does not decrease considerably.

4.2. Operating Point H

Tendencies established for case H differ only quantitatively from those for case D. The NFVO flow is weaker(Fig.4).

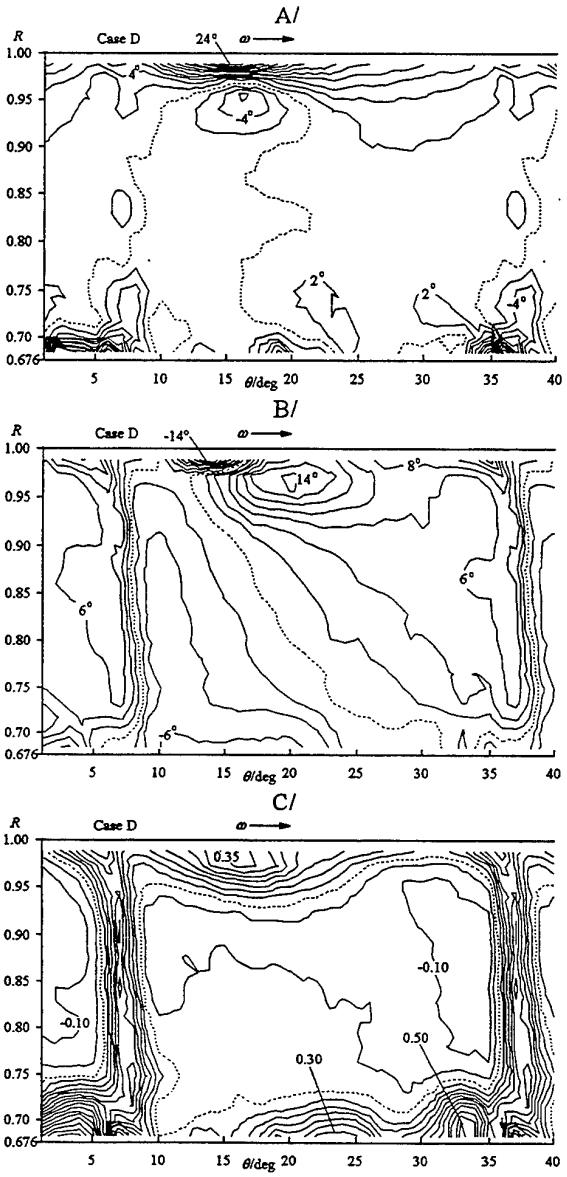

Figure 6. Exit flow angle deviation (A), pitch angle (B) and relative kinetic energy defect factor (C) plots for case D.
$U(\beta-\beta^*)=1.5°$, $U(\gamma)=1°$, $U(\zeta)=0.05$

Thus, the leakage flow blockage is not as strong as for case D. (Exit flow angle deviation and pitch angle plots not presented here show lower gradients). Thus, the leakage flow and the NFVO flow roll up together into a combined vortex. Since the NFVO flow and the scraping is weaker, the spanwise change in axial velocity is less (Fig.5), behaving as expected. The passage vortex starts to fade into the slightly linked branches of the NFVO flow.

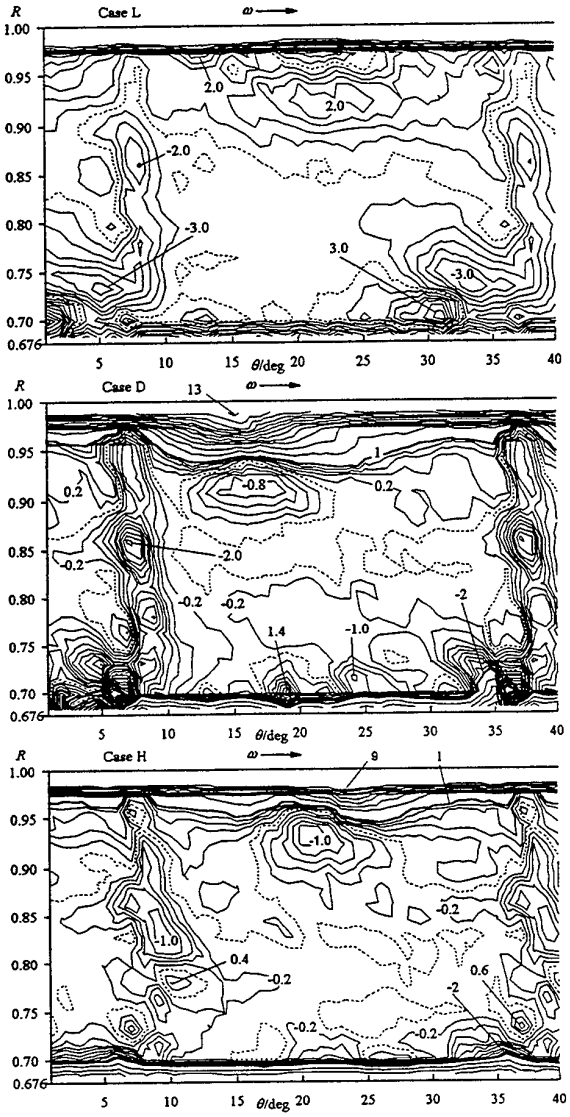

Figure 7. Plots of $\xi_s / 2\omega . U(\xi_s) = 0.5(2\omega)$

4.3. Operating Point L

At the suction side blade root, corner stall and passage vortex result in extended zones of reduced axial velocities (Figs.4,5) and low energy fluid accumulation. The NFVO flow is united with the passage vortex in closed loops. In the upper half-passage,a drastic outward flow exists as a result of a general loss in static pressure. The suction side loss flow blocks the leakage flow, causing fluid stagnation and some scraping process. A small portion of the suction side loss flow appears to start rolling up, but the pressure side loss flow dissipates this motion.

This dissipating region is indicated by an extended zone of positive vorticity near the casing wall. Fig. 7 does not give evidence of any structured vortical motion. The passage vortex core is represented by positive vorticity, smoothing to the corner stall zone of negative vorticity.

The vorticity in the wake shows that the blade could still perform nearly constant total head rise also within the upper half-passage. However, the aerodynamical losses reduce the static pressure immediately close to the blade and influence the whole region between the casing wall and the radius of most rapid change in circulation (minimum rotation within the wake), originating the loss flow.

5. CONCLUSIONS

1/ As our measurements show, the leakage jet forming near the blade leading edge tends to be partially blocked by the suction side outward NFVO flow developing inside bladings of non-free vortex operation. Due to the blockage, fluid stagnation and some scraping occurs on the tip pressure side. The blocking and scraping effect weakens with blade loading reduction. In case of downstream flow field investigations, secondary flow vector maps must be completed with exit flow angle deviation and pitch angle contour plots to demonstrate these tendencies.

The available studies dealing with non-free vortex operating rotors generally do not suggest such tendency. Dring et a.(1982), Hunter and Cumpsty(1982) and Goto(1992) do not publish exit flow angle deviation distribution. The relatively weak NFVO flow in Goto(1992) allows the leakage flow to dominate. Besides, the tip vortex observed by him downstream the blading seems already to interact with the adjacent blade, making the assessment difficult. The blading studied by Hunter and Cumpsty(1982) produced relatively weak NFVO flow. Downstream measurements of Lakshminarayana et a.(1995) at off-design point must be highly influenced by the inlet guide vane and do not show a structured NFVO flow. However, measurements of Meixner(1994) show some tendency indicating leakage flow blockage and stagnation.

The leakage flow blockage raises the question: are the fans producing relatively strong NFVO flow less sensitive to tip clearance size from the viewpoint of losses than non-free vortex operating fans? To answer this question, further studies must be made.

2/ Above a certain threshold in loading, considerable pressure losses come into existence. As a result, drastic outward flow forms near the casing wall, which restricts the NFVO flow to lower radii and blocks the tip clearance flow. Near-stall measurements of Inoue et a.(1991) provide similar secondary flow maps.

3/ For moderate loading, the NFVO flow and the leakage flow can roll up into a combined vortex, in which the proportion of the NFVO flow depends on the degree of the leakage flow blockage (blade loading). At the design point, the observed vortex behaved similarly to a leakage vortex formed in a free vortex operating rotor of similar geometric and operating parameters. The strong NFVO vortex motion results in absolute maximum and minimum in axial velocity. The NFVO vortex interacts with the main stream and a contra-rotating vortex comes into existence. For high loading, formation of any vortex is suppressed near the casing wall, due to the strong outward loss flow.

4/ The NFVO flow and a related scraping process are responsible for spanwise change in axial velocity.

5/ The outward and inward NFVO flow branches tend to link and the passage vortex tends to fade into the NFVO flow, for off-design circumstances.

ACKNOWLEDGEMENTS

The experimental work was supported by OTKA (Hungarian National Found for Science and Research) under contract T 16950.

NOMENCLATURE

c	=absolute velocity	U	=uncertainty
d	=diameter	w	=relative velocity
ℓ	=blade chord length	x,y	=Cartesian coordinates
M	=torque	β	=rel. exit flow angle
Δp	=stage total pressure rise	γ	=pitch angle
Q	=volume flow rate	ν	=kinematic viscosity
r	=radial coordinate	θ	=tangential coordinate
R	$=r/r_t$ dimensionless radius	ρ	=density
t	=tip clearance	ω	=rotor angular velocity
u	=peripheral speed	ξ_s	=streamwise vorticity

ζ =relative kinetic energy defect

$Re_{bt} = w_{it}\ell_t/\upsilon$ =blade tip Reynolds number

$\overline{\Phi} = Q\Big/\left[u_t\pi\left(d_c^2 - d_h^2\right)/4\right]$ =flow rate coefficient

$\overline{\psi} = \Delta p\Big/\left(\rho u_t^2/2\right)$ =total pressure rise coefficient

$\eta = \overline{\Phi}\,\overline{\Psi}/M\omega$ =efficiency

SUBSCRIPTS

c =casing wall
i =rotor inlet
id =ideal
h =hub
t =blade tip

REFERENCES

Bencze, F., and Vad, J., 1996, Investigation on Flow Field of Axial Flow Rotating Machinery, 1st T16950 Report to the National Found for Science and Research, Technical University of Budapest (in Hungarian)

Dring, R. P., Joslyn, H. D., and Hardin, L. W., 1982, An Investigation of Axial Compressor Rotor Aerodynamics, TRANS ASME J Eng Power, Vol. 104,pp. 84 - 96.

Goto, A., 1995, Three-Dimensional Flow and Mixing in an Axial Flow Compressor with Different Tip Clearances, TRANS ASME J Turbomachinery, Vol. 114, pp. 675 - 685.

Hunter, I. H., and Cumpsty, N. A., 1982, Casing Wall Boundary-Layer Development Through an Isolated Compressor Rotor, TRANS ASME J Eng Power, Vol. 104, pp. 805 - 818.

Inoue, M., and Kuroumaru, M., 1984, Three-Dimensional Structure and Decay of Vortices Behind an Axial Flow Rotating Blade Row, TRANS ASME J Eng Gas Turbines Power, Vol. 106, pp. 561 - 569.

Inoue, M., Kuroumaru, M., and Fukuhara, M., 1986, Behavior of Tip Leakage Flow Behind an Axial Compressor Rotor, TRANS ASME J Eng Gas Turbines Power, Vol. 108, pp. 7 - 14.

Inoue, M., and Kuroumaru, M., 1989, Structure of Tip Clearance Flow in an Isolated Axial Compressor Rotor, TRANS ASME J Turbomachinery, Vol. 111, pp. 250 - 256.

Inoue, M., Kuroumaru, M., Iwamoto, T., and Ando, Y., 1991, Detection of a Rotating Stall Precursor in Isolated Axial Flow Compressor Rotors, TRANS ASME J Turbomachinery, Vol. 113, pp. 281 - 289.

Lakshminarayana, B., Zaccaria, M., and Marathe, B., 1995, The Structure of Tip Clearance Flow in Axial Flow Compressors, TRANS ASME J Turbomachinery, Vol. 117, pp. 336 - 347.

Meixner, H. U., 1995, Vergleichende LDA-Messungen an ungesichelten und gesichelten Axialventilatoren, Dissertation, University of Karlsruhe

Somlyódi, L., 1970, Design and Characteristic Curve Calculation for Axial Flow Fans, Doctorate Thesis, Technical University of Budapest (in Hungarian)

Stauter, R. C., 1995, Measurement of the Three-Dimensional Tip Region Flow Field in an Axial Compressor, TRANS ASME J Turbomachinery, Vol. 115, pp. 468 - 476.

Vad, J., Bencze, F., Füredi, G., and Szombati, R., 1995, Fluid Mechanical Investigation on Axial Flow Fans, Proceedings of the 10th Conference on Fluid Machinery, Budapest, pp. 500 - 509.

SESSION 15

Particles & Markers

SEEDING FOR LASER VELOCIMETRY IN CONFINED SUPERSONIC FLOWS WITH SHOCKS

J. Lepicovsky
NYMA, Inc., NASA LeRC Group, Brook Park, OH 44142

R.J. Bruckner
NASA LeRC, Cleveland, OH 44135

INTRODUCTION

There is a lack of firm conclusions or recommendations in the open literature to guide laser velocimeter (LV) users in minimizing the uncertainty of LV data acquired in confined supersonic flows with steep velocity gradients. This fact led the NASA Lewis Research Center (LeRC) in Cleveland (Ohio, USA), and the Institute of Propulsion Technology of DLR in Cologne (Germany) to a joint research effort to improve reliability of LV measurements in supersonic flows. Over the years, NASA and DLR have developed different expertise in laser velocimetry, using different LV systems: Doppler and two-spot (L2F). The goal of the joint program is to improve the reliability of LV measurements by comparing results from experiments in confined supersonic flows performed under identical test conditions but using two different LV systems and several seed particle generators. Initial experiments conducted at the NASA LeRC are reported in this paper. The experiments were performed in a narrow channel with Mach number *2.5* flow containing an oblique shock wave generated by an immersed *25-dg* wedge.

BACKGROUND

Laser velocimetry (LV) is approaching the state of a mature experimental technique. Advances in laser Doppler anemometer (LDA) signal processors allow reliable measurement of signal frequencies up to *100 MHz*. The advent of LDA frequency-based processors allows measurements at poor signal-to-noise ratios (SNR). Integrated optics and fiber-optics links have solved many problems in optical access to measurement locations in complicated flow arrangements.

The only aspect of laser velocimetry that has not progressed at all in recent years is the technique of flow seeding, which seems to be a straightforward, uncomplicated task without the sophistication of LV signal processing. Consequently, very often, not enough attention is paid to flow-seeding problems, and lessons learned in low-speed subsonic flows are often directly applied to high-speed flow situations. Unfortunately, such an approach may result in serious measurement errors in high-speed flows with steep velocity gradients.

If a laser velocimeter system (optics and electronics) is viewed as a black box, then the signal generating seed particles are the actual velocity transducers. From this point of view, laser velocimetry (including all particle tracing optical techniques) is unique in that it is the only experimental technique in fluid dynamics where measurements at high flow velocities are often carried out using "uncalibrated transducers".

In theory, the requirements for seeding in high-speed flows with steep velocity gradients are simple: light, monodispersed, spherical particles with high surface reflectivity at the wavelength of detectable laser light. The low particle density is required to enable particles to follow the rapid flow changes. Monodispersity is crucial for post-measurement corrections of recorded velocities to true flow velocities and minimizing apparent velocity turbulence in regions of steep velocity gradients. High reflectivity should assure a good SNR for the LV signal. In practice, however, meeting these requirements at the point of measurement is very difficult.

SEEDING METHODS FOR SUBSONIC FLOWS

In subsonic applications, seed particles can be injected into the flow in solid, liquid, or gaseous forms. The available dry powders consist of polydispersed, non-spherical particles of relatively high density. The mechanics of dry particle delivery systems is complicated; particles tend to agglomerate in the delivery mechanism, which results in clusters of large particles injected into the flow. Consequently, the resulting seed particles follow flow changes poorly.

From a practical point of view, it is much easier to spray fluids into the airflow than to inject powders. Several well established methods can be categorized into five groups: (1) spraying a volatile carrier liquid that contains solid particles; (2) spraying non-volatile liquids dispersed into small droplets; (3) atomizing liquids and

injecting the mist into the flow; (4) vaporizing a liquid and injecting the resulting fog into the flow; and (5) burning (or reacting) solid or liquid components and injecting the resulting smoke. All these methods are used in subsonic flows with good results, however, the user must remember that there are some limitations.

The first method (Group 1) uses a carrier liquid with polystyrene latex (PSL) spheres. This approach relies on evaporation of the volatile carrier liquid (alcohol) and leaving the solid PSL spheres in the flow. The evaporation process has to be completed in the flow ahead of the point of measurement. The major advantage is that the resulting seeds are monodispersed with a known diameter.

The second method (Group 2, non-volatile liquid droplets) generates relatively large polydispersed droplets. Various separators or impactors are applied to narrow the droplet size range. In reality, the size spectrum at the point of measurement is not known with sufficient accuracy.

The third method (Group 3, liquid atomizing) generates polydispersed submicron-size fine droplets. A number of seeds may be below the detectable size for LDA systems. Scattered light from undetectable particles generates a high level of background noise that results in a significant decrease in SNR.

The fourth method (Group 4, vaporization e.g. "theatrical smoke") and the fifth method (Group 5, burning products - smoke bombs) are used only marginally.

SEEDING IN SUPERSONIC FLOWS

Several researchers have experimented with various seeding techniques in supersonic flows. Parobek et al. (1986) and O'Heren et al. (1983) discussed flow experiments that were carried out in boundary layers or free stream conditions without shocks in the flow. The experiment of Lepicovsky et al. (1985) dealt with free jets seeded with aluminum oxide powder. Samimy & Abu-Hijleh (1989) pointed out significant effects of laser Doppler velocimeter (LDV) system parameters on the results obtained in high-speed flows using polydispersed seed particles. In many instances parameters such as laser power, photomultiplier tube (PMT) gain, LV processor gain and threshold, and others are set subjectively and inconsistently, which results in large experimental errors.

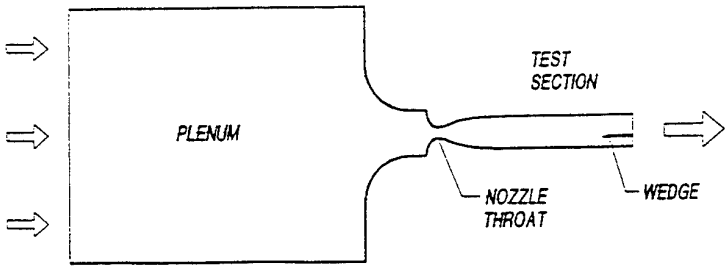

Figure 1. Supersonic wind tunnel.

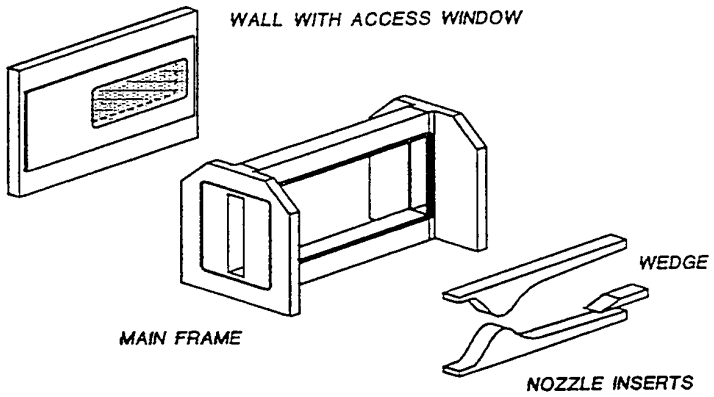

Figure 2. Supersonic test section.

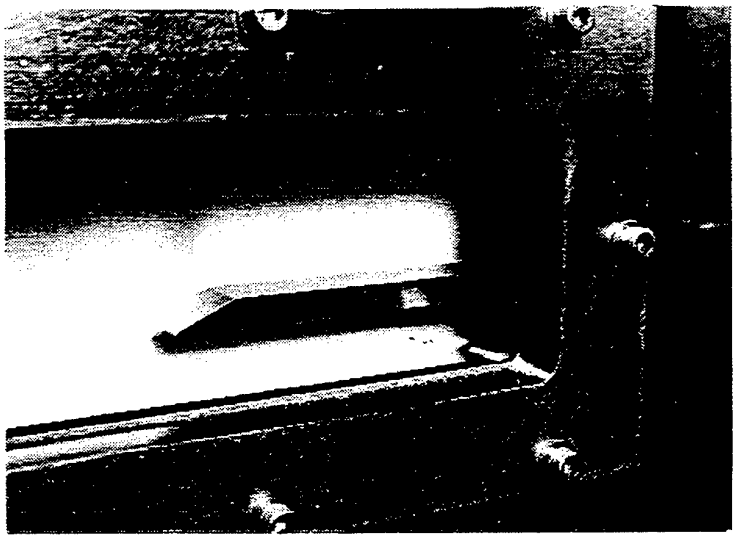

Figure 3. Supersonic test section.

Intuitively, monodispersed seeds (e.g. PSL particles, Group 1) are the most suitable ones for applications in confined supersonic flows. It is our experience, however, that the presence of carrier-liquid vapors in the flow constitutes a significant problem. In supersonic flows, due to the flow acceleration between the plenum and the test point conditions, the flow temperature drops below the dew point and the carrier liquid vapors condense back on the PSL spheres. The process results in liquid droplets of various diameters larger than the individual PSL spheres. The carrier liquid droplets around the PSL spheres are then the actual signal generators. As a result, we may know the PSL particle diameter exactly, but we do not know the diameter of the signal generating droplets.

The Group 4 and 5 methods lead to different difficulties. The fourth method (vaporization) often results in massive condensation at the beginning of the supersonic velocity region. Frequently the condensate accumulates on the test-channel walls and is driven over the access windows. Liquid on the windows causes detrimental laser beam refractions, which results in losing the beam intersection and measurement volume.

Finally, using the last method (smoke bombs) leads to heavy depositions of soot or tar-like substances on flow surfaces and access windows, resulting very often in short test runs and costly cleanups. In our experience these last two methods are not suitable for confined supersonic flows.

TEST APPARATUS

A supersonic wind tunnel with a test section free stream Mach number of *2.5* was designed and tested to provide a research tool for development work on LV flow-seeding techniques [Bruckner & Lepicovsky (1994)]. A schematic diagram of the tunnel is shown in Figure 1. The tunnel consists of a cylindrical plenum of internal volume of *1* m^3 and an exit bellmouth with an attached convergent-divergent nozzle, followed by a straight duct *813 mm* long that maintains a supersonic flow along the entire length. The nozzle was designed for Mach number 2.5. The nozzle throat area is *25* by *36 mm*, resulting in a plenum/throat contraction ratio of *650:1*. A drawing of the test section is shown in Figure 2; and a photograph in Figure 3. A *25-dg* wedge, located in the test section, generates an oblique shock at its tip followed by an expansion fan at the end of the wedge. The wedge is *21 mm* wide. There is a *7.5 mm* gap between the side walls and the wedge.

The LV system used in this study is a two-component, backscatter system assembled from DANTEC and TSI optical components. The system uses a Coherent Ar-Ion laser operated at total power of *2 W*; the receiving optics has an f-number of *2.5* and a focal length of *250 mm*; the fringe spacing for channel 1 (green) is *11.16* μm and *10.78* μm for channel 2 (blue); the diameter of the measurement volume is *120* μm. A TSI IF750 processor collected the LV data.

The flow was seeded in the plenum, ahead of the supersonic nozzle and the test section. Location of the seeding sprayers or tubes is depicted separately for each case described.

A schematic diagram of the flow structure generated in the test section by the inserted wedge is in Figure 4. The coordinate system used in the experiments is depicted in Figure 5.

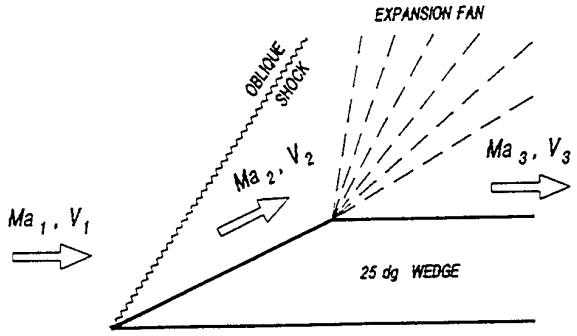

Figure 4. Shock wave structure.

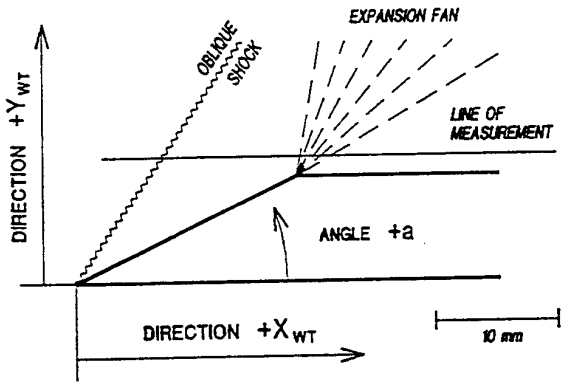

Figure 5. Test coordinate system.

RESULTS AND ANALYSIS

Three sets of results in this paper summarize the initial experiments conducted on Group 1 to 3 seeders at NASA LeRC. Each set consists of plots of velocity, velocity-angle distributions, and velocity histogram data. There is also a sketch for each particular seeding configuration.

Velocity and velocity-angle plots show variations over the oblique shock and expansion fan region. The velocity based on pressure measurements and 1-D theory of compressible flow is also shown in the plots. The tunnel velocity ahead of the shock wave was determined from the plenum total pressure and temperature and wall static pressure close to the wedge tip. In the velocity histogram plots, the data is shown for both velocity components at several axial positions in the investigated region.

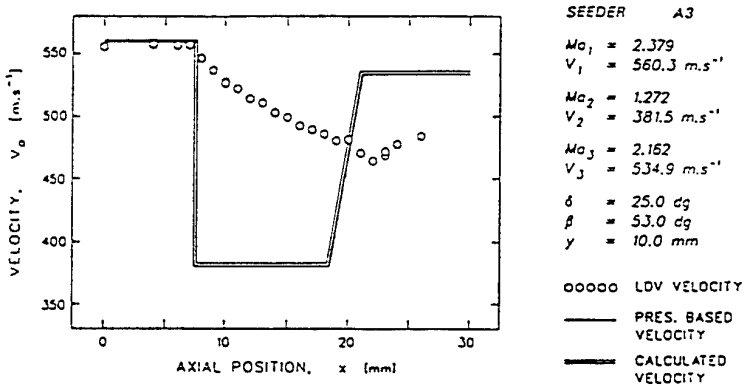

Figure 6. Velocity distribution (Seeder A3).

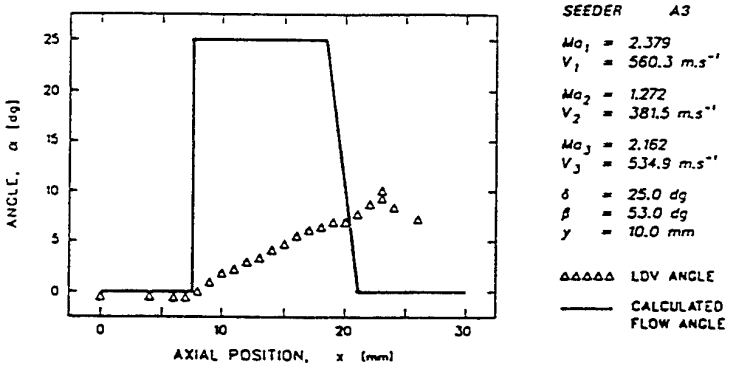

Figure 7. Flow angle distribution (Seeder A3).

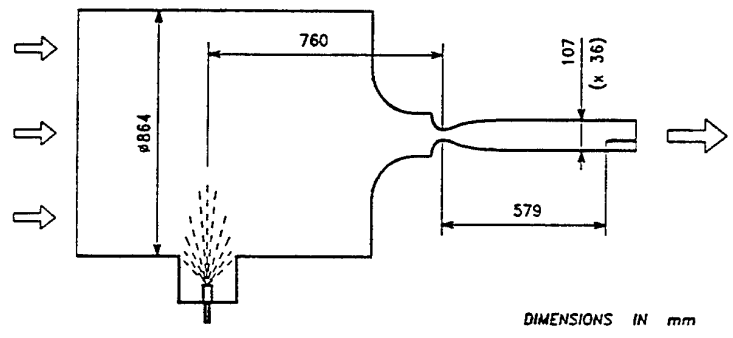

Figure 8. Test configuration (Seeder A3).

The first set of data (Figures 6 to 9) shows the results using the NASA seeder with polystyrene latex particles (PSL) suspended in alcohol. The PSL particle diameter was *1.1 μm*. This seeder fits the Group 1 description presented above. As seen from the velocity and velocity-angle distributions (Figures 6 and 7), the seeded particles follow the flow changes extremely poorly. The seeder sprayer injects the alcohol/particle mixture perpendicular to the flow (Figure 8, Seeder A3). It must be stressed here that no differences appeared whether the seeding was with an alcohol/PSL mixture or with pure alcohol only. Obviously, the LV signal was generated by alcohol droplets only and the droplets may or may not have contained the PSL particles inside. Consequently, the assumption that the carrier liquid evaporates and the PSL particles will generate the LV signal is not valid here. This is a textbook example of possible large errors in LV data if users extrapolate experiences from subsonic to supersonic laser velocimetry. The plots in Figures 6, 7, and 9 are for pure alcohol only. The histograms in Figure 9 show a single peak behind the oblique shock for both channels, which may indicate more or less uniform diameter for all the droplets. There was no visible contamination of the window in the shock region for pure alcohol. For the mixture alcohol/PSL, a noticeable window contamination with the PSL particles was observed in the wedge region.

There is an interesting detail in the expansion fan region. For the case of volatile fluid (pure alcohol), the velocity recovery behind the expansion fan is clearly noticeable. Further, the histograms for this region at x_{WT} = *20* and *22* exhibit two peaks. This may indicate changes in diameter for some droplets in the region between the shock and the fan.

The second set of data (Figures 10 to 13) was acquired using a seeder equipped with a Laskin nozzle generating oil droplets (glycol). This seeder belongs in Group 2 as outlined above. Detailed description of the seeder is given by Rabe & Sabroske (1994). The seeder performed very well in subsonic applications [Rabe & Sabroske (1994)], however, in our particular case the performance was not satisfactory. The velocity and velocity-angle distribution plots in Figures 10 and 11 indicate that here again the

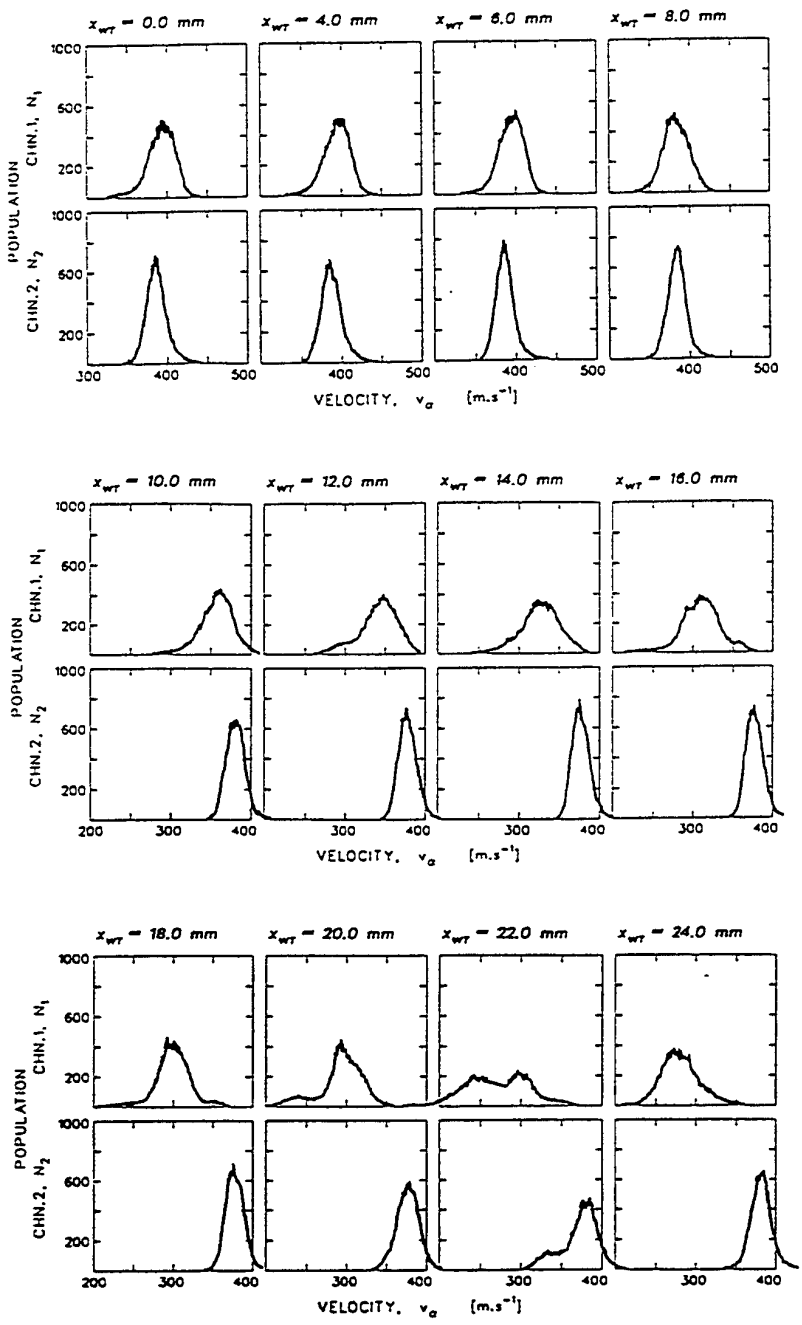

Figure 9. Velocity histograms (Seeder A3).

seeder produced oil droplets that follow the flow changes poorly. The position of the seeder delivery tube is shown in Figure 12. A glance at velocity and angle-distributions reveals that there is barely any improvement over the results from the first set. The velocity histogram plots (Figure 13) show deterioration of the LV signal in the shock wave region (there was noticeable contamination on the inside of the window at x_{WT} = *6* and *8*). After the shock, there are dual-peak histograms on channel 1 for x_{WT} = *10* and *12* and single peak histograms on channel 2. The two-peak histograms cannot be attributed to oblique shock wave oscillations. It seems that the left peak on channel 1 migrates to a lower velocity region faster than the right peak with increasing distance from the shock. A possible explanation is that the seeder generates 'two groups' of droplets of different mean diameters.

The third set (Figures 14 to 16) shows the results for a seeder based on the TSI six jet atomizer. The seeder belongs to Group 3. The seeds were injected in the flow in the same way as shown in Figure 12. The velocity and angle distributions indicate satisfactory agreement with expected flow velocity and angle variations. Generally, the results are good; however, some problems are not yet fully understood. First, when we used pure alcohol in the atomizer, no LV velocity data were recorded; the PMT signal contained only noise. This indicates that the size of the seeds was below the detection limit. Then, PSL particles of *1.1* μm in diameter were mixed with alcohol. The data in Figures 14 through 16 were acquired for the alcohol/PSL mixture. Even after adding the PSL particles, we still could not detect any data in front of the shock wave (very low SNR); however, behind the shock there was a strong LV signal. A very sharp and repeatable divide appeared to be at x_{WT} = *9*, just past the oblique shock. The sharp divide indicates a sudden change in the seed visibility (increased SNR).

At this point, we can only speculate on the physics behind these observations. A sudden increase in visibility can be caused by several factors such as increased particle size or drop in the background noise or increased particle surface reflectivity. There is also a possibility of coalescence of particles behind the shock. The effect of agglomerating submicron particles into larger droplets behind the shock would be twofold. First, it would lead to a larger diameter in the resulting droplets; second, it would lower the background noise radiation by reducing the population of fine submicron particles. In

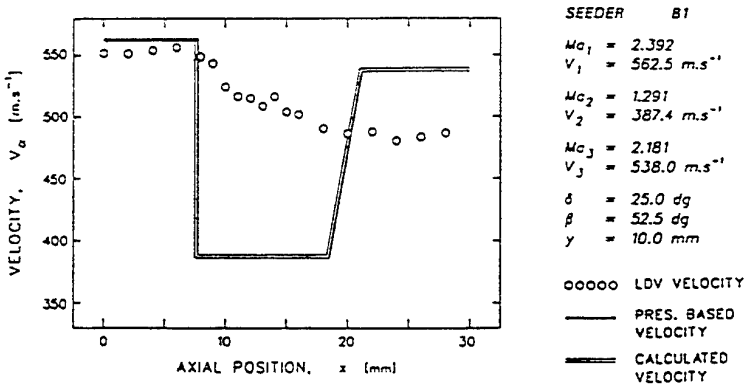

Figure 10. Velocity distribution (Seeder B1).

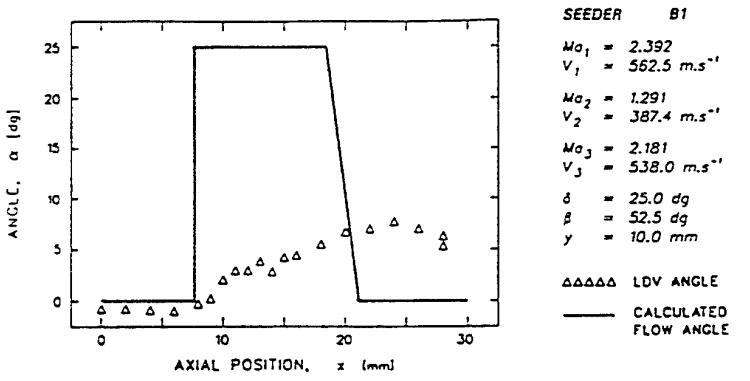

Figure 11. Flow angle distribution (Seeder B1).

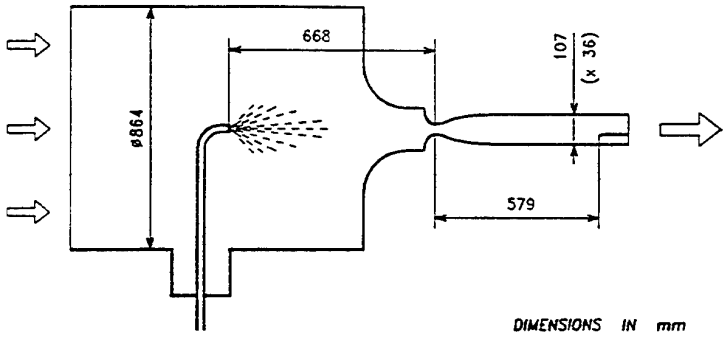

Figure 12. Test configuration (Seeders B1 and D1).

any case, the LV signal behind the shock is generated by relatively small diameter seeds as manifested in the velocity and angle distributions in Figures 14 and 15. Obviously, additional effort is needed to explain these observations fully.

CONCLUSIONS

The study demonstrated the possibility of large experimental errors in LV data acquired in confined supersonic flows with shock wave structures. The lessons learned about flow seeding at subsonic velocities cannot be blindly applied to supersonic flow conditions. Because our knowledge about seeding for confined supersonic flows is not adequate, we recommend always arranging for a pilot experiment using a wedge shock generator to test particle response at the point of measurement. Of course, the pilot tests should be run at the actual flow conditions of the desired experiment, using the actual seeding technique. The settings of the LV system should be maintained between the pilot study and actual testing. It is our experience that the experimenter should rely on a tested seed-particle response at particular flow conditions rather than rely on knowledge of seed particle sizes acquired by other means e.g. out of flow particle sizers.

Acknowledgement

The authors are grateful to Dr. L.J. Bober of the NASA LeRC Propulsion System Division and Mr. K.C. Civinskas of the Turbomachinery Technology Branch for their continuing support.

References

Parobek, D.M., Boyer, D.L., and Clinehens, G.A. 1986, Recent Developments in Liquid Flow Seeding Techniques for Use with LV Measurements, Paper AIAA-86-0769.

O'Heren, C.H., Parobek, D.M., and Weissman, C.B. 1983, Laser Velocimeter Developments for Surveying Thin Boundary Layers in a Mach 6 High Reynolds Number Flow, Air Force Wright Aeronautical Laboratories, Report AFWAL-TR-82-3111.

Lepicovsky, J., Ahuja, K.K., Brown, W.H., and Burrin, R.H. 1985, Coherent Large-Scale Structures in High Reynolds Number Supersonic Jets, NASA CR-3592.

Samimy, M. and Abu-Hijleh, B.A.K. 1989, Performance of Laser Doppler Velocimeter with Polydisperse Seed Particles in High-Speed Flows", Journal of Propulsion, Vol. 5., No.1, pp.21-25.

Bruckner, R.J. and Lepicovsky, J. 1994, A Supersonic Tunnel for Laser and Flow-Seeding Techniques, Paper AIAA-94-1825, also NASA TM 106588.

Rabe, D. & Sabroske, K. 1994, Laskin Nozzle Performance For Laser Flow Measurement Seeding, Paper AIAA-94-0044.

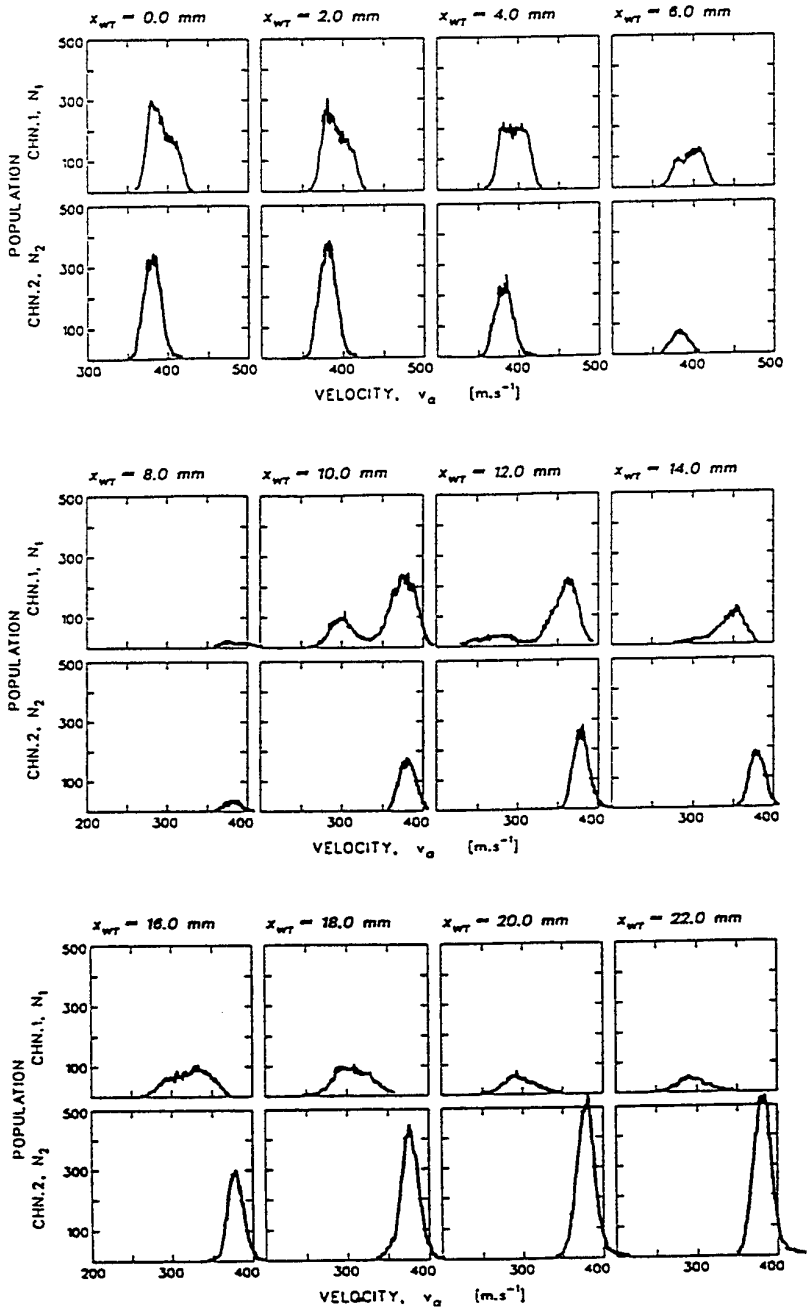

Figure 13. Velocity histograms (Seeder B1).

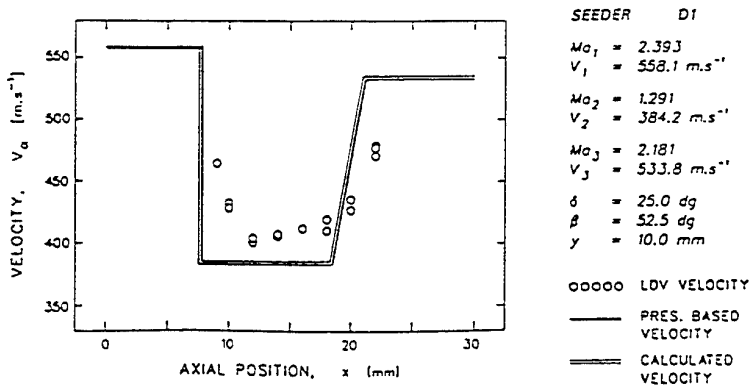

Figure 14. Velocity distribution (Seeder D1).

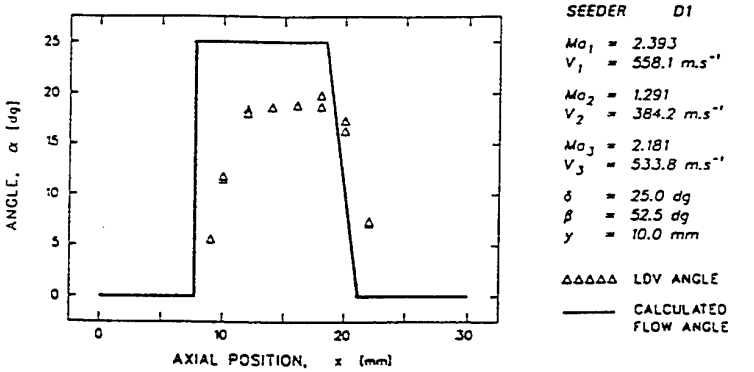

Figure 15. Flow angle distribution (Seeder D1).

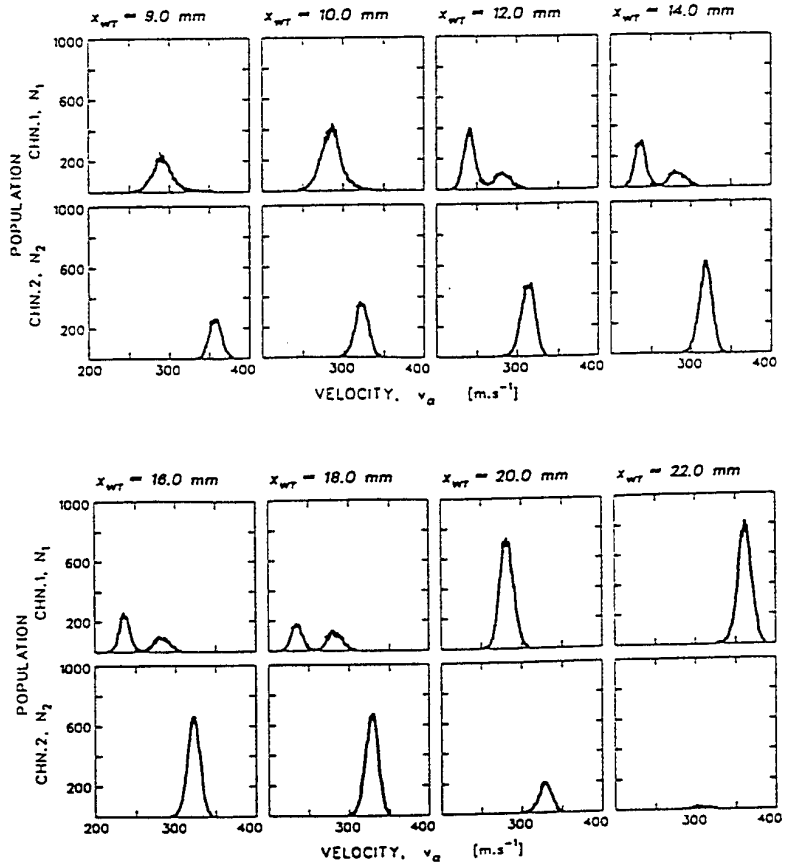

Figure 16. Velocity histograms (Seeder D1).

A REPEATABLE LASER-GENERATED LOCALIZED PERTURBATION FOR APPLICATION TO FLUID MECHANICS

J. D. Schmisseur
Wright Laboratory
Wright-Patterson AFB, OH 45433-7005

S.P. Schneider, T.R. Salyer and S.H. Collicott
School of Aeronautics and Astronautics
Purdue University
West Lafayette, IN 47907-1282

ABSTRACT

A method has been developed for generating repeatable, localized, controlled perturbations by photoionizing air using the focused beam from a frequency-doubled Nd:YAG laser. Characterization of the perturbation is ongoing in the Mach 4 low-noise environment of the Purdue University Quiet-Flow Ludwieg Tube. Constant temperature anemometer measurements reveal that the perturbation convects at the freestream velocity of the facility and has a diameter of approximately 5 mm while in the nozzle and test section. Application of the perturbation to the flowfield around a forward facing cavity has revealed the existence of a receptivity mechanism in the form of a resonance of the subsonic region near the stagnation point.

1. INTRODUCTION

Understanding how the boundary layer transitions from laminar to turbulent flow is critical for the accurate prediction of skin friction and heat transfer on supersonic vehicles. As reviewed in papers by Reshotko (1994) and Bushnell (1989), disturbances which facilitate the transition process are introduced into the boundary layer from both external and surface sources. The former include acoustic waves, particles, and freestream variations in vorticity and entropy. *Receptivity* describes the signature of externally-originating disturbances in the boundary layer, and the resulting response of the instability modes. The response of the boundary layer to a controlled perturbation originating in a low-disturbance freestream environment must be studied to obtain unambiguous information on the boundary-layer receptivity. Accurate interpretation of such information will represent a significant advancement in understanding the physics of transition.

Currently, the receptivity of the boundary layer on a 4:1 elliptic cross-section cone is being studied in the Purdue University Quiet-Flow Ludwieg Tube. Controlled disturbances are applied to the quiet-flow environment of the Ludwieg tube through introduction of a localized, laser-generated perturbation. The perturbation, which is a region of hot air, and its motion in the flowfield are shown schematically in Fig. 1.

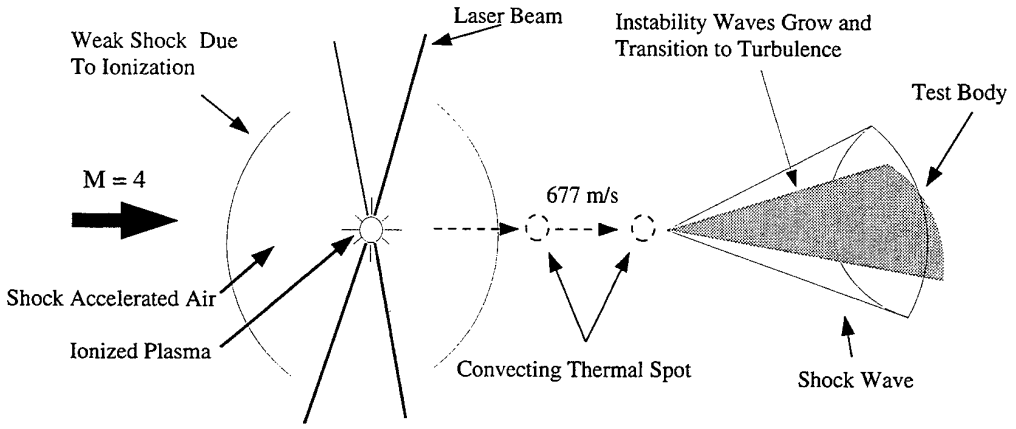

Fig. 1. Schematic of perturbation application

2. AN OPTICALLY-GENERATED PERTURBATION

Controlled perturbations are produced by photoionizing the air with a laser focused at the desired origin of the disturbance. As reported by Zel'dovich and Raizer (1966), although air is transparent at lower intensities, there exists a threshold intensity above which a multi-photon absorption process can produce ionization. As seen in Fig. 1, the initial disturbance consists of a plasma core surrounded by a region of non-ionized air and the shock wave produced during ionization. After the end of the laser pulse, the plasma core relaxes and remains as a region of hot recombined gas, referred to as the *thermal spot*. As shown in the earlier work of McGuire (1994), the thermal spot does not expand as rapidly as the shock does. Instead, the thermal spot convects with the local velocity of the flowfield and forms the portion of the disturbance useful as a local perturbation. The shock wave weakens and approaches a spherical shape with increasing distance from the plasma core as reported by McGuire (1994).

The formation of the disturbance relies on the intensity (average power per unit area in the focal region) of the laser pulse. Thus, both the energy in the laser pulse and the size of the focus affect the ionization process. A minimum intensity, known as the *threshold intensity*, is required to initiate ionization. (Zel'dovich and Raizer (1966), McGuire (1994), Armstrong, et a. (1983)) The intensity threshold varies with the gas pressure as $I_{th} = B P^{\alpha}$ where I_{th} is the threshold intensity, B is a constant which accounts for the efficiency of the energy coupling from the laser pulse to the air, and P is the pressure. Dewhurst (1978) reported a value for α of -0.55 for nitrogen and oxygen while McGuire (1994) reported a value of -0.60 for air. Once the intensity threshold for the onset of ionization has been surpassed, increasing intensity results in increasingly strong perturbations as measured by shock wave strength. (McGuire (1994))

A frequency-doubled Nd:YAG laser is operated at a pulse rate of 10 Hz with a wavelength of 532 nm. The laser is injection-seeded to narrow the line width, which also smoothes the pulse shape in time. This was found by McGuire (1994) to significantly increase the shot-to-shot repeatability of the perturbation over unseeded operation. The pulse duration is approximately 7 ns with a maximum pulse energy near 260 mJ. The beam diameter is approximately 8 mm at the laser head with a 90% fit to Gaussian in the nearfield and 95% fit to Gaussian in the farfield when injection-seeded, as quoted by the manufacturer. Variation in the injection-seeded pulse energy has been measured to be around 3% over a duration of several minutes as reported by Schneider, et a. (1995).

A schematic of the optical system is shown in Fig. 2. To prevent back reflections off the test section windows from damaging optics, the focusing beam is tilted 5 degrees from the window normal. The tilt increases aberrations, but not sufficiently to hinder system performance. Several focusing lenses were damaged by back reflections before the system tilt was incorporated. The system consists of a -38 mm focal length plano-concave singlet and two 150 mm focal length air-spaced doublets. The negative lens and the first doublet form a beam expander which expands the original beam diameter by a factor of four, from 8 mm to 32 mm. The second doublet focuses the collimated beam into the test section. The focusing lens has an F/# of 5. Using commercial optical design software, the diameter of the focused beam was determined to be 0.02 mm. For comparison, the diffraction limited spot diameter is 0.002 mm.

Initially, difficulty was encountered in maintaining the position of the perturbation within the test section. Since the Ludwieg Tube is subject to axial forces (*i.e.* recoil and vacuum forces) during the operation of the facility, the optical system, which is bolted to the test section, occasionally shifts by several millimeters with respect to the laser beam. Adjusting the mirrors to recenter

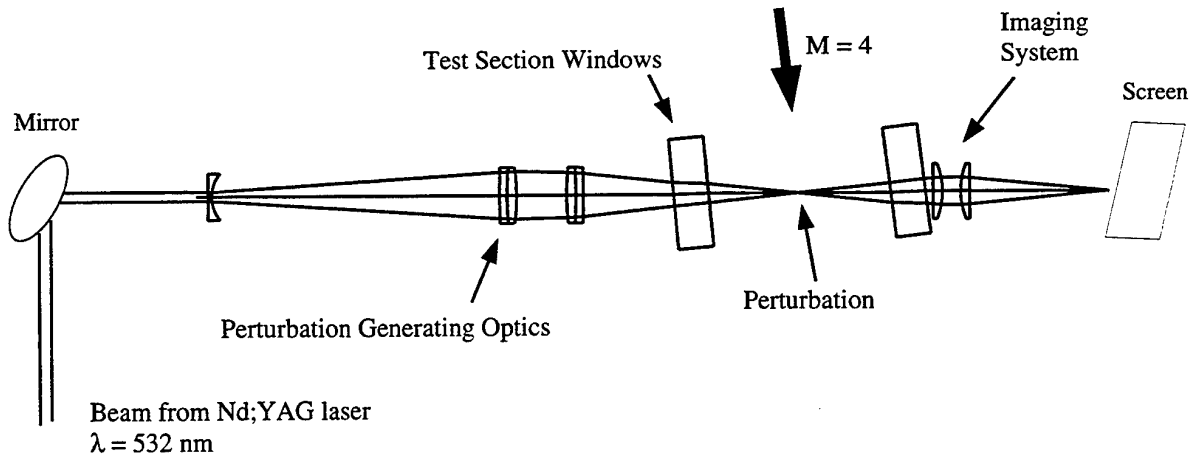

Fig. 2. Optical system for generating perturbations in the Ludwieg tube

the beam in the lenses changes the position of the perturbation. This problem is alleviated by imaging the perturbation as the beam passes out of the test section. A one-to-one imaging system, consisting of a pair of 75 mm focal length singlets, is installed on the same support bracket holding the perturbation optics but on the opposite side of the test section (Fig. 2). The perturbation location is repeated inside the test section by adjusting the spot-generating optics before the run so that the image of the perturbation is at a fixed position on a screen outside the test section.

3. THE PURDUE QUIET-FLOW LUDWIEG TUBE

Supersonic quiet-flow facilities with freestream noise levels an order of magnitude less than those in conventional facilities are a relatively recent development. (Beckwith, et a. (1990), Schneider and Haven (1995)) It is critical to maintain laminar boundary layers in quiet-flow nozzles since turbulent boundary layers radiate acoustic noise into the test core. Major features of most quiet-flow facilities, designed to prevent the introduction of instabilities into the nozzle, include the following (Fig. 3) :

1) Flow entering the nozzle is low-noise
2) Test gas is filtered to keep particles out of the nozzle
3) Nozzle surface finishes, especially in the throat, are kept exceptionally smooth.

The useful portion of the flowfield is known as the *quiet-flow test core*. The characteristics marking the onset of uniform supersonic flow form the upstream boundary of the quiet-flow test core while the characteristics originating at the location where turbulence begins in the wall boundary layer form the downstream limit. Greater test core lengths are obtained by delaying transition in the wall boundary layers.

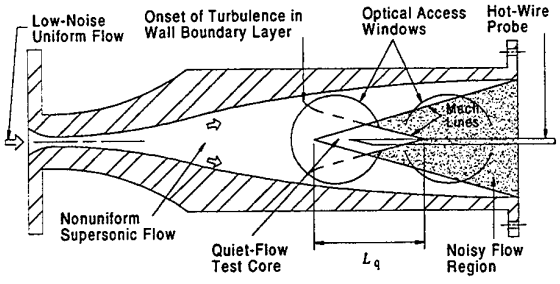

Fig. 3. Schematic of the Purdue Quiet-Flow Nozzle. (courtesy D. W. Ladoon)

The Purdue Quiet-Flow Ludwieg Tube is a long pipe called a *driver tube* with a converging-diverging nozzle on the end. The Purdue facility is based on a 0.305 m dia. driver tube that is 20.7 m long. A smooth contraction tapers from the driver tube to the nozzle throat, which is followed by the 96 x 109 mm Mach 4 rectangular nozzle. The nozzle, shown schematically in Fig. 3, is polished to a surface smoothness of 25-50 μm in the throat region. Optical access is provided by 76 mm dia. windows in the flat sidewalls. From the nozzle, flow exits into a test section, diffuser and vacuum tank. A diaphragm between the diffuser and the vacuum tank separates the high-pressure test air from the evacuated vacuum tank. Supersonic flow in the nozzle is initiated when the diaphragm is broken and the resulting expansion wave moves upstream into the driver tube. Total pressure fluctuations in the nozzle are approximately 0.06 percent for driver tube pressures less than 103 kPa. A detailed description of the facility is given by Schneider and Haven (1995).

Although the reflected expansion wave passing through the driver tube causes a change in stagnation conditions, supersonic flow persists until the pressure ratio is insufficient for sustaining shock-free flow through the nozzle. Thus, although the stagnation conditions (and, hence, Reynolds numbers) are constantly decreasing, numerous brief segments of high-quality constant-condition flow are obtained between passages of the reflected expansion waves. (Schneider, et a. (1994)) For this experiment, stagnation (driver tube) pressures were typically around 99 kPa while the stagnation temperatures were 21-27 degrees Celsius. Initial freestream unit Reynolds numbers were approximately 4.5 million per meter.

4. INSTRUMENTATION

Measurements of the convecting thermal spot are made with a constant temperature anemometer (CTA), the TSI IFA 100, using the standard bridge with no signal conditioning. The hot wire sensing element is a 0.0038 mm diameter tungsten wire mounted between two 0.076 mm dia. needles spaced 0.51 mm apart. The typical frequency response of the wire is around 120 kHz, operating at an overheat ratio of approximately 1.7. The sting-mounted hot-wire probes are positioned in the flowfield with a traverse which allows the sensor to be moved both vertically and in the streamwise direction along the transverse centerline of the test section.

The output bridge voltage is sampled at rates between 250 kHz and 10 MHz in both continuous and segmented data records using LeCroy 9304AM digital oscilloscopes. The continuous data records contain 250,000 points sampled between 50 and 250 kHz while the segmented records consist of 50 segments of 5,000 points sampled at rates between 1 and 10 MHz. Each segment in the segmented data sets is triggered from the synch pulse generated by the laser Q-switch circuit.

5. RESULTS

5.1 Freestream Measurements of the Thermal Spot

The first CTA bridge response to passage of the thermal spot after supersonic quiet-flow begins is shown in Fig. 4 for four different tube runs. Since the quiet portion of the run is approximately four seconds in duration and the laser operates at 10 Hz, about 40 thermal spot passages are recorded in a single run. The data in Fig. 4 were collected at the same vertical traverse location, near the thermal spot centerline, with varying streamwise distances from the thermal spot origin. The distance from the perturbation origin to the hot-wire is shown near the arrow which signifies the approximate beginning of the thermal spot passage over the hot-wire. To facilitate comparison, the undisturbed voltage has been subtracted from each signal. Driver tube pressures and temperatures were around 99 kPa and 22-24 C while the laser energy was approximately 227 mJ/pulse. The initial decrease in bridge voltage located at time = 0 (when the laser fires) is noise associated with the radio frequencies produced when the gas is ionized. A second larger voltage decrease, beginning about 21 μs after the laser fires for the case where the hot wire was 15 mm from the perturbation, corresponds to the passage of the thermal spot. Calculation of the thermal spot convection velocity using the time to peak bridge response at several streamwise locations indicates that the perturbation moves at the facility freestream velocity, around 680 m/s.

The entire set of segments collected during the quiet portion of a single run is plotted in Fig. 5. Each segment is triggered by the synch output of the laser Q-switch (10 Hz). Due to pre-triggering of the oscilloscope the first segment collected after flow was initiated is segment number 11. This is the same segment plotted in Fig. 4 for the response a distance of 15 mm from the perturbation origin. As seen in Fig. 5, the thermal spot is consistently formed with every laser pulse until the end of the data acquisition. Note that the amplitude of the CTA response decreases during the run. This amplitude attenuation is presumed to be due to a reduction in the energy transferred from the laser to the gas as the freestream density decreases during the run. For some runs the spot is not formed in the last few segments of the run as the freestream density drops below the threshold required for ionization at the laser energy of 224 mJ/pulse.

Although the CTA response to individual thermal spots varies by 5-10 %, presumably due to shot-to-shot variations in the laser, the average response over the first ten segments is consistent for similar driver tube conditions and laser pulse energies. The CTA response averaged over the first ten segments is shown in Fig. 6 for the data collected during three separate tube firings. Driver tube conditions and laser pulse energies were similar to those for Fig. 4. To facilitate comparison, the mean bridge voltage before the introduction of the perturbation has been subtracted. As seen in Fig. 6, the shape of the hot-wire response to the thermal perturbation is similar in all three traces. The rms of the three peaks is about 10 percent of the mean, as shown on the figure. Although three traces is not a statistically significant sample, it appears that the thermal spot is sufficiently repeatable for application as a localized perturbation.

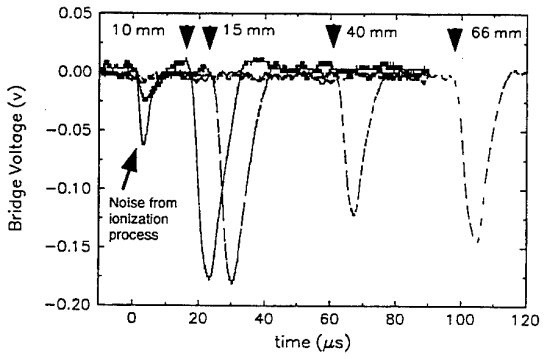

Fig. 4. CTA response to thermal spot at four streamwise positions. Responses shown are the first response after quiet-flow is initiated. The hot-wire distance from the perturbation origin is noted next to the arrow which indicates the beginning of the CTA response.

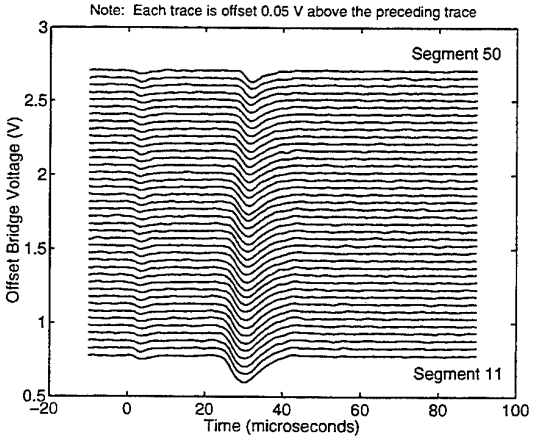

Fig. 5. All data segments after the onset of quiet-flow for a single run.

By vertically traversing the hot wire the profile of the convecting thermal spot has been determined. Three-dimensional plots of the averaged response of the hot-wire to the first ten thermal spot passages are shown in Fig. 7 for multiple vertical locations at distances of 15 and 66 mm downstream from the spot origin. The sign of the voltage has been changed to facilitate viewing the traces. All data in Fig. 7 were collected at ambient driver tube conditions (P ~ 98.6 kPa, T = 21-27 C) with the laser pulse energy between 220 and 225 mJ/pulse. Using the convection velocity of 677 m/s, the time signal has been transformed to a length scale. The vertical dimension is the distance from the approximate spot center. The nonuniform vertical increments between traces are due to the data collection process. Although the shape of the convecting perturbation may be roughly determined by inspection of the traces in Fig. 7, the contour plots of constant voltage shown in Fig. 8 are more useful in this regard.

From inspection of Figs. 7 and 8, the thermal spot exhibits little change in the brief time required for convection between the two streamwise survey positions. Similar observations of relatively slow thermal spot growth were made by McGuire (1994) on the benchtop. Visual inspection of Fig. 8 indicates that the full-width-at-half-maximum spot diameter is approximately 5 mm in the streamwise direction at both survey positions. The vertical diameter is roughly 4 - 5 mm at the survey location 15 mm from the origin and slightly smaller, approximately 3 mm, 66 mm from the origin. At the downstream (66 mm) location the hot-wire peak response to the spot passage is diminished, which may be due to the cooling of the thermal spot. With respect to the vertical width, the effective length of the spot in the freestream direction appears elongated due to the limited frequency response of the hot wire. This bandwidth limitation may contribute to the apparent constant streamwise length of the passing thermal spot.

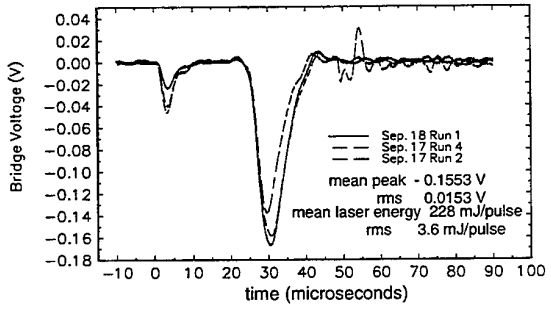

Fig. 6. Averaged CTA response to the first ten thermal spot passages after quiet-flow is initiated. The fluctuations after the peak in the trace for Sep. 17 # 4 are due to a single noisy data segment. Note that the mean voltage before introduction of the perturbation has been removed to facilitate comparison.

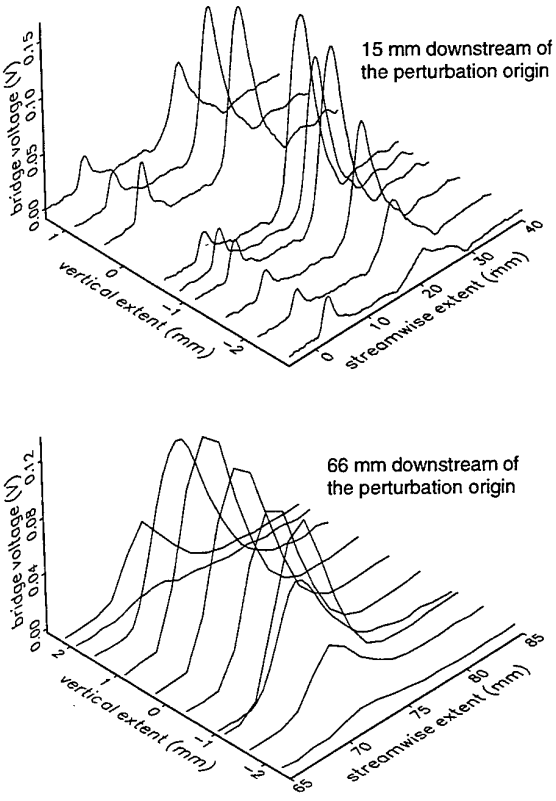

Fig. 7. Average CTA response to the first ten thermal spot passages at several vertical positions.

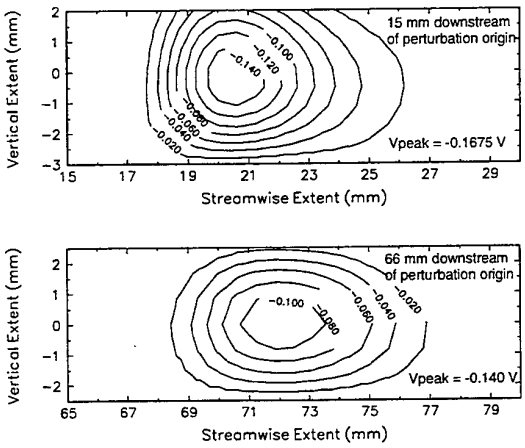

Fig. 8. Contours of constant CTA bridge voltage at two streamwise distances from the perturbation origin. The mean voltage before the introduction of the thermal spot has been removed to examine the effects of the thermal spot passage.

Finally, although only uncalibrated results have been shown in this paper, ongoing efforts are being made to calibrate the response of the CTA to the thermal spot passage. Calibration of the hot-wire response has been complicated by the substantial temperature rise associated with the thermal spot passage. The resulting change in effective overheat ratio during the thermal spot passage prevents calibration of the bridge response using a simple mass flux vs. CTA voltage output technique. Alternative data reduction techniques are currently being examined.

5.2 Application to Nose-cavity Flowfield

The combination of the thermal spot perturbation and the quiet flowfield of the Ludwieg Tube has produced unambiguous measurements of receptivity effects in the subsonic nose region of the flowfield around a forward-facing cavity. A schematic of the model is shown in Fig. 9. A Kulite dynamic pressure transducer is located in the nose of the model in a movable plug which forms the base of the cavity. The response to the introduction of the thermal spot, shown in Fig. 10, consists of a ringing of the subsonic region in the cavity after the delta-function-like passage of the perturbation. The variation of ringing frequency and oscillation decay as a function of the cavity length to depth ratio is the topic of current work by Ladoon, et a. (1997). The resonance of the subsonic nose region clearly demonstrates a receptivity mechanism present in the flowfield. The detection of such a mechanism without ambiguity is made possible by the application of the thermal spot perturbation to the quiet flowfield.

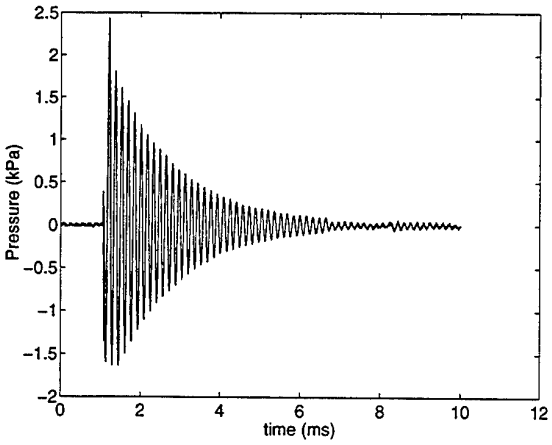

Fig. 10. Typical cavity base pressure trace showing cavity resonance induced by the thermal spot perturbation. L/D = 1.064 (Ladoon, et a. (1997))

6. SUMMARY

A repeatable method of generating controlled perturbations in supersonic flowfields using the focused beam from a Nd:YAG laser to locally ionize the air has been developed. Characterization of the perturbation is ongoing in the Purdue University Quiet Flow Ludwieg Tube. The thermal spot generated by the perturbation

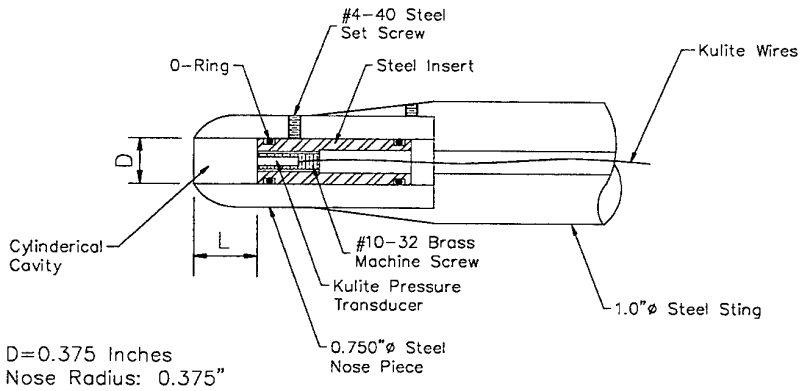

Fig. 9. Schematic of the forward facing cavity model. (Ladoon, et a. (1997))

convects at the freestream velocity of the facility and has a diameter of approximately 5 mm while in the nozzle and test section. Application of the perturbation to the flowfield around a forward-facing cavity has revealed the existence of a receptivity mechanism in the form of a resonance of the subsonic region near the stagnation point. The thermal perturbation is currently being applied to receptivity experiments. Potential applications include velocity measurement in hypersonic facilities and use as a plasma generator for the study of plasma dynamics in supersonic flowfields.

7. ACKNOWLEDGMENTS

The research is supported by the Air Force Office of Scientific Research under grants F49620-94-1-0067 and F49620-94-1-0326. Additional support and equipment has been provided by a gift from the Boeing Company and a gift in memory of K.H. Hobbie. The hot wires were designed and constructed by George Tennant and the hot-wire traverse design was improved by Joe Zachary.

8. REFERENCES

Armstrong, R.A., Lucht, R.A., and Rawlins, W.T. 1983, Spectroscopic investigation of laser-initiated low-pressure plasmas in atmospheric gases, Applied Optics, vol. 22, no. 10.

Beckwith, I., Chen, F., and Malik, M. 1990, Transition research in low-disturbance high-speed wind tunnels, in Laminar-Turbulent Transition, Springer-Verlag, New York.

Bushnell, Dennis, M. 1989, Notes on Initial Disturbance Fields for the Transition Problem, in Instability and Transition, ed. M.Y. Hussaini and R.G. Voigt , vol. 1, pp. 217, Springer-Verlag, New York.

Dewhurst, R.J. 1978, Comparative data on molecular gas breakdown thresholds in high laser-radiation fields, Journal of Physics D, 11(16):L191-L195, Letter to the Editor.

Ladoon, D.W., Schmisseur, J.D., and Schneider, S.P. 1997, Laser-Induced Resonance in a Forward Facing Cavity at Mach 4, Submitted to 35th AIAA Aerospace Sciences Meeting, Reno, NV.

McGuire, J.M. 1994, Fluid Dynamic Perturbations Using Laser Induced Breakdown, Master's Thesis, Purdue University, W. Lafayette, Indiana, USA.

Reshotko, Eli 1994, Boundary Layer Transition and Control, AIAA 32nd Aerospace Sciences Meeting, Reno, NV, AIAA paper 94-0001.

Schneider, S.P., McGuire, J.B., Collicott, S.H., Salyer, T.R., and Schmisseur, J.D. 1995,
Laser Generation of Controlled Localized Perturbations for Boundary-Layer Transition Research, Proc. IEEE ICIASF Conference, Dayton, pp. 11.1-11.11.

Schneider, S.P., and Haven, C.E. 1995, Quiet-Flow Ludwieg Tube for High-Speed Transition Research, AIAA Journal, vol. 33, no. 4, pp. 688-693.

Schneider, S.P., Haven, C.E., McGuire, J.B., Collicott, S.H., Ladoon, D., and Randall, L.A. 1994, High-Speed Laminar-Turbulent Transition Research in the Purdue Quiet-Flow Ludwieg Tube, 18th AIAA Aerospace Ground Testing Conference, Colorado Springs, CO, AIAA paper 94-2504.

Zel'dovich, Ya. B. and Raizer, Yu. P. 1966, Physics of Shock Waves and High-Temperature Hydrodynamic Phenomena, ed. Hayes, W.D., and Probstein, R.F.,pp. 338-348, Academic Press, New York.

Observations of Fluid Flow Produced in a Closed Cylinder by a Rotating Lid Using the PHANTOMM (PHoto-Activated Non-intrusive Tracking of Molecular Motion) Flow Tagging Technique

Scott R. Harris Richard B. Miles Walter R. Lempert

Department of Mechanical and Aerospace Engineering
Princeton University
Princeton NJ 08544

Abstract

Using the PHANTOMM flow tagging technique we obtain quantitative measurements of velocity as well as visualizations similar to those obtained with standard laser sheet fluorescence techniques of the flow in a cylinder driven by a rotating end wall. In addition, the axisymmetric Navier-Stokes equations are solved numerically using a vorticity-stream function formulation. The computed flow is compared to measurements in order to evaluate and validate the PHANTOMM technique so that one can be confident of measurements in flow regimes where accurate computations are not available.

1 Introduction

The phenomena of vortex breakdown has been the subject of much attention because of its practical importance in many different situations, as well as its attraction as a fundamental problem in fluid mechanics. Experiments by Vogel [13, 14] showed that the flow produced by a rotating end wall inside a closed cylindrical container can undergo vortex breakdown under certain conditions. Only two non dimensional parameters, the aspect ratio $\delta = \frac{H}{R}$ and the Reynolds number $Re = \frac{\Omega R^2}{\nu}$, completely determine the flow in this geometry. Escudier [3] extended the work of Vogel and examined this system using laser sheet fluorescence dye visualizations over the range $1000 \leq Re \leq 4000$ and $1.0 \leq \delta \leq 3.5$ and found that in this parameter range, the flow could undergo up to three breakdowns as well as become unsteady. Because of its simple geometry and completely specified boundary conditions, this flow is an excellent system, both computationally and experimentally, in which to study fundamental issues related to vortex breakdown.

The small number of experimental parameters combined with the simple geometry makes it possible to perform accurate experiments and numerical simulations. Together these features make this flow a nearly ideal setting in which to develop and characterize the PHANTOMM flow tagging technique, while still studying non-trivial fluid mechanics.

2 PHANTOMM Flow tagging

Flow tagging is a technique where a spatially continuous pattern is "written" into a flow field by means of an optical resonance. The displacement of this pattern is subsequently tracked or "interrogated" by means of Laser Induced Fluorescence (LIF) imaging. The displacement that occurs during the elapsed time interval between the tagging and interrogation processes results in a measurement of velocity. In the gas phase, examples of flow tagging methods include Raman Excitation plus Laser-Induced Electronic Fluorescence (RELIEF) [9] and multi-photon dissociation of water vapor, followed by (A,X) fluorescence from hydroxyl radical LIF [2].

In the liquid phase, we have previously reported a new flow tagging technique based upon the use of caged dye Photo-Activated Fluorophores (PAF's), which we

have termed PHoto-Activated Non-intrusive Tracking of Molecular Motion (PHANTOMM) [7]. PAF's are nominally fluorescent dyes that are rendered non fluorescent by the strategic attachment of a chemical caging group. The caging group is photolytically cleaved upon absorption of ultraviolet light, generally from a laser. After photolysis, the original fluorescent dye is recovered and can be tracked using laser sheet imaging techniques for times limited only by the inter-species diffusion of the un-caged tracer molecules into the surrounding caged tracer solution. The technique is akin to ordinary dye visualization except that the dye is produced in situ in a specific pattern determined by the tagging beam location. The PHANTOMM technique is very similar in many respects to Laser Induced Photochemical Anemometry (LIPA), which is based on the use of either photochromic or phosphorescent tracer materials [6, 15, 4].

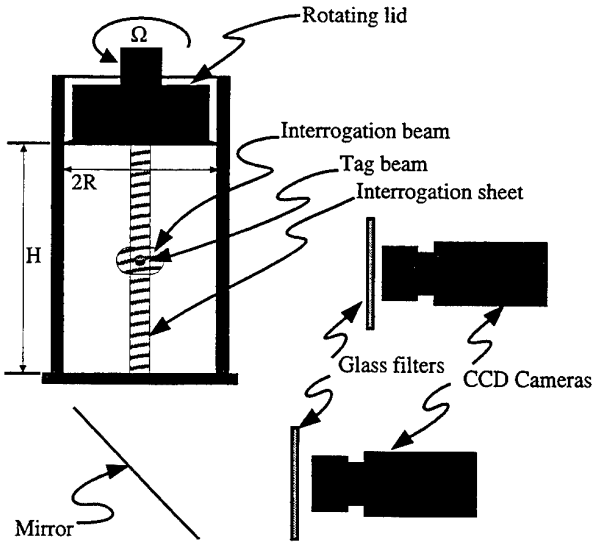

Figure 1: Side view of the experimental setup. Only one interrogation source is used at a time.

3 Experimental procedure

Dextran carboxy fluorescein with a molecular weight of 3000 g/mole was used as a tracer material in the work presented here. A typical concentration used in these experiments is 0.5 mg/l. The caging group is photolyzed upon the absorption of a single UV photon in the region of 350 nm. Lines are tagged in these experiments using the third harmonic of a Q-switched Nd:YAG laser. Typical tag beam energies were approximately 20 mJ per pulse.

The resulting un-caged dye behaves essentially like ordinary fluorescein dye, strongly absorbing in the region of 490 nm, with re-emission between 520–620 nm. Pulse outputs of approximately 100 mJ with a duration of approximately 2 μs from a flash lamp pumped dye laser using LD490 dye in methanol were used for interrogation. Since the fluorescence from the interrogated line is shifted significantly in frequency compared to the interrogation beam, a simple glass filter (OG530) can be used to block stray elastic scattering from the experiment. Fluorescence from the lines is imaged onto a standard CCD (Cohu model 4810) cameras and stored in a freeze frame unit between interrogations. The images in the freeze frame unit are digitized with a Scion LG-3 frame grabber and stored in real time on the hard disk of a Power Macintosh 7500 for later processing.

A schematic diagram of the apparatus used in these studies is shown in figure 1. The inner cylinder is a precision bore quartz cylinder with an inside diameter of 66.17 mm and a wall thickness of 2.06 mm. The bottom end of the cylinder is bonded to a quartz disk with silicone sealant. Because of the quartz construction, lines can be tagged from the side, as well as from the bottom. Provisions have been made in this apparatus for a square water bath to surround the inner cylinder to stabilize the temperature of the fluid in the inner cylinder, as well as to provide some degree of index matching. The outer water bath was not used in the experiments presented here.

The rotating disk at the upper end of the cylinder is driven by a variable speed DC motor. A 256 pulse-per-revolution shaft encoder and frequency counter are used to monitor the rotation rate of the shaft. A type K thermocouple located near the top of the rotating disk monitors the temperature of the fluid. Using water as the working fluid, the range of Reynolds numbers attainable is $0 \leq Re \leq 7800$. A simple motor change allows for even higher Reynolds numbers. In addition, the rotating disk can be translated vertically resulting in an available aspect ratio range $0 \leq \delta \leq 5$

Lines were tagged horizontally in the R-Z plane where Z-direction is along the axis of the cylinder. Figure 2 shows a top view of the optical setup as well as detail of the placement of the tagging and interrogation beams. The UV tagging beam from the laser was focused with a 500 cm focal length lens, resulting in a beam waist of approximately $25\mu m$.

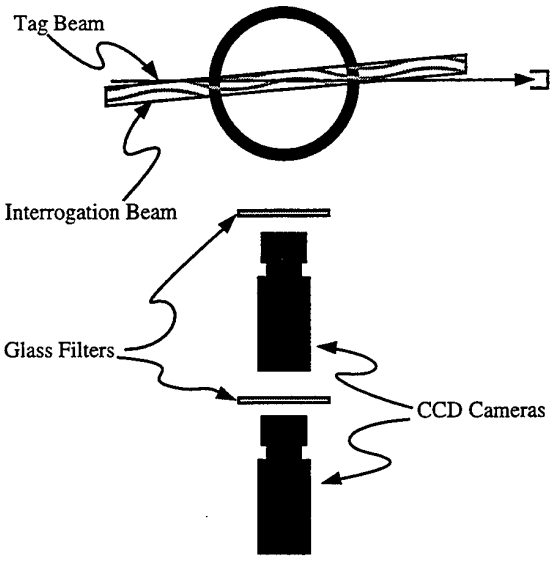

Figure 2: Top view of the experimental setup. Interrogation sheet is not shown

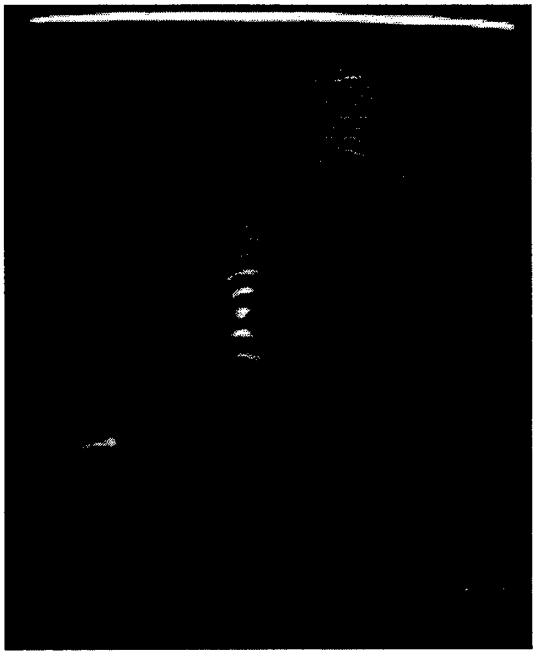

Figure 3: Image of several PHANTOMM lines tagged and interrogated at one second intervals $Re \approx 960$ and $\delta = 2.0$.

The light from the dye laser was focused into the experiment in one of two ways. In the first case, the beam from the dye laser was formed into a sheet approximately 1.0 cm thick that spanned the inner cylinder and was directed into the apparatus from below.

Because there is a finite (order milliseconds) time for the un-caging process to occur, the interrogations are made 5 milliseconds after the tag. In a slow flow, such as this one, the first interrogation is essentially at the tag position, and can be used as an excellent approximation to the tag position when calculating velocities.

Figure 3 shows a series of lines tagged into the flow at one second intervals where $Re \approx 960$ and $\delta = 2.0$. The motion of the PHANTOMM lines show that there is no stagnation point above the tag position. As the flow spirals upwards towards the rotating lid, the tagged fluid elements move out of the interrogation sheet and therefore, the lines appear shorter. After one quarter revolution the tagged fluid begins to move back into the sheet and the lines begin successively to appear longer.

Figure 4 shows two breakdown bubbles at $Re \approx 1890$ and $\delta = 2.0$. The bubble structure is visualized by tagging many lines into the flow. The slow re-circulation in the bubbles keeps the un-caged fluorescent dye originating from the middle of the PHANTOMM lines localized, while parts of the tagged lines outside the bubble are distributed over a much larger region and contribute to the faint background fluorescence. The structure of the bubbles appears somewhat blurred because the interrogation sheet is relatively thick to allow for azimuthal motion of the tagged lines.

In the second case, the interrogation beam was focused in to a cylindrical volume approximately 1 cm in diameter, roughly collinear with the tag beam inside the experimental volume. A second camera viewed the experiment from the bottom via a 45 degree front surface mirror. Figures 5 and 6 show the side and bottom views of the same tag and interrogations pairs spaced by one second. The reynolds number is 996 and $\delta = 2.0$.

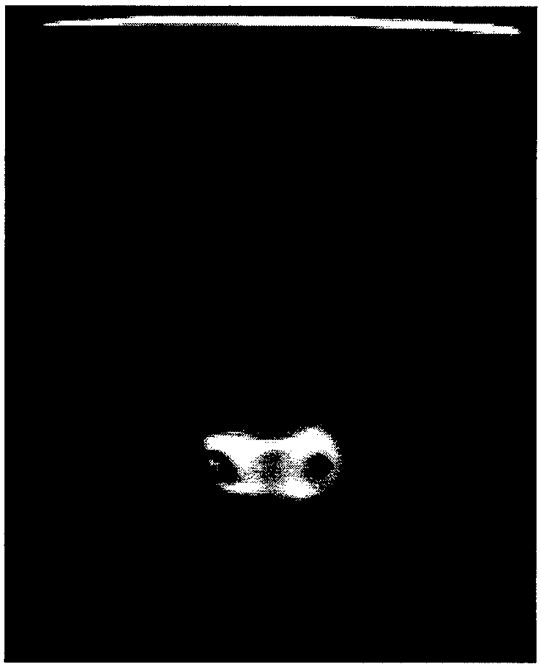

Figure 4: Two breakdown bubbles and PHANTOMM lines showing the axial velocity profile in the region of the lowest bubble. $Re \approx 1890$ and $\delta = 2.0$.

4 Numerical simulations

There are four parameters that define the flow: R, H, Ω, and ν. Time, length, and velocity are non-dimensionalized by Ω, R, and ΩR respectively. From these four dimensional parameters, one can define two non-dimensional parameters.

$$Re = \frac{\Omega R^2}{\nu} \tag{1}$$

and

$$\delta = \frac{H}{R} \tag{2}$$

If we define a stream function by (3) it automatically satisfies the axisymmetric form (i.e. $\frac{\partial}{\partial \theta} = 0$) of the continuity equation in cylindrical coordinates.

$$v_r = -\frac{1}{r}\frac{\partial \psi}{\partial z}, v_z = \frac{1}{r}\frac{\partial \psi}{\partial z} \tag{3}$$

Figure 5: Tag and interrogation pair of PHANTOMM lines from the side. See figure 6 for corresponding bottom view. $Re = 996$ and $\delta = 2.0$.

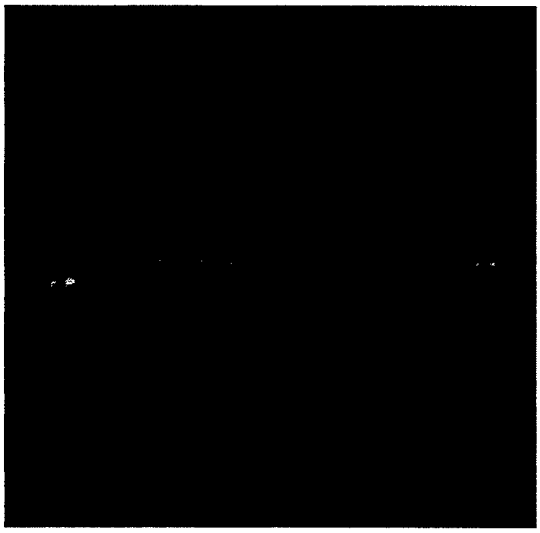

Figure 6: Tag and interrogation pair from figure 5 view from below. $Re = 996$ and $\delta = 2.0$.

Using (3) we find that the azimuthal component of vorticity is

$$\omega_\theta = \frac{1}{r^2}\frac{\partial \psi}{\partial r} - \frac{1}{r}\left(\frac{\partial^2 \psi}{\partial r^2} + \frac{\partial^2 \psi}{\partial z^2}\right) \tag{4}$$

Plugging equation (3) into the azimuthal momentum equation and non dimensionalizing results in (5).

$$\begin{aligned} \frac{\partial v_\theta}{\partial t} &= \frac{1}{r}J(v_\theta) + \frac{v_\theta}{r^2}\frac{\partial \psi}{\partial z} + \\ &\quad \frac{1}{Re}\left[\frac{\partial^2 v_\theta}{\partial z^2} + \frac{\partial^2 v_\theta}{\partial r^2} + \frac{1}{r}\frac{\partial v_\theta}{\partial r} - \frac{v_\theta}{r^2}\right] \end{aligned} \tag{5}$$

Taking $\frac{\partial}{\partial z}$ of the r-momentum equation and $\frac{\partial}{\partial r}$ of the z-momentum equation and using (3) we obtain (6).

$$\frac{\partial \omega_\theta}{\partial t} = J\left(\frac{\omega_\theta}{r}\right) + 2\frac{v_\theta}{r}\frac{\partial v_\theta}{\partial z} + \frac{1}{Re}\left[\frac{\partial^2 \omega_\theta}{\partial z^2} + \frac{\partial^2 \omega_\theta}{\partial r^2} + \frac{1}{r}\frac{\partial \omega_\theta}{\partial r} - \frac{\omega_\theta}{r^2}\right] \quad (6)$$

Where, in the above equations,

$$J = \frac{\partial \psi}{\partial z}\frac{\partial}{\partial r} - \frac{\partial \psi}{\partial r}\frac{\partial}{\partial z} \quad (7)$$

Associated with equations (4), (5), and (6) are these boundary conditions.

$$\left.\begin{array}{r} \psi(0,z) = v_\theta(0,z) = \omega_\theta(0,z) = 0 \\ \psi(1,z) = v_\theta(1,z) = 0,\ \omega_\theta(1,z) = -\frac{1}{r}\frac{\partial^2 \psi}{\partial r^2} \\ \psi(r,0) = 0,\ v_\theta(r,0) = r,\ \omega_\theta(r,0) = -\frac{1}{r}\frac{\partial^2 \psi}{\partial z^2} \\ \psi(r,\delta) = v_\theta(r,\delta) = 0,\ \omega_\theta(r,\delta) = -\frac{1}{r}\frac{\partial^2 \psi}{\partial z^2} \end{array}\right\} \quad (8)$$

Equations (4), (5), and (6) are approximated using second order accurate finite differences on a uniform mesh with equal spacing in the R and Z directions, except for the term J defined in (7) which is approximated by a method given by Arakawa [1]. The kinematic relationship between azimuthal vorticity and stream function is solved for ψ at each time step using a Gauss-Seidel method with multigrid acceleration. Once a new ψ is computed, the evolution equations for v_θ, (5) and ω_θ, (6) are advanced in time using a second order Runge-Kutta scheme.

Because the solution of (4) does not require the values of ω_θ on the boundaries of the flow, the boundary conditions on ω_θ are implemented at the end of each time step by using a Taylor expansion for ψ one grid point in from the boundary.

In the cases presented here, where the flow achieves a steady state, time is marched forward until the left hand sides of (5) and (6) go to zero. Further details on vorticity-stream function codes for this flow of this type can be found in the papers by Lopez, Neitzel, and Davis [8, 11, 10].

Figures 7 and 8 show the results obtained with this code for two cases that were also studied experimentally. In both computations, the grid used was relatively coarse with 65 points in the Z-direction and 33 along the radius. The time step was 0.04.

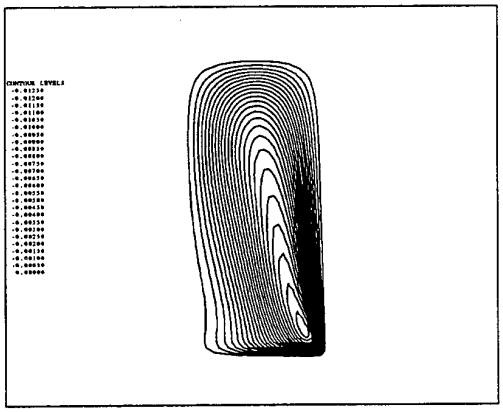

Figure 7: Contour lines of computed stream function in the R-Z plane. $Re = 996$ and $\delta = 2.0$. The rotating wall is at the bottom of the figure.

5 Determination of velocity from PHANTOMM images

In order to make quantitative measurements based on images such as those in figure 5 and 6 two issues must be considered. First, features in the digitized image must be related to physical dimensions in the experiment. Secondly, distortion of the image caused by passage through surfaces in to the experiment must also be considered.

In order to relate features in a digitized image to physical dimensions in the experiment a simple model for the imaging system based on a pinhole camera approximation is used. This model is extended to include radial distortion of the image caused by the lens as well as an offset between the center of the imaging system and the center of the digitized image. This model is very similar to one developed by Tsai for machine vision applications [12].

Figure 9 shows the coordinate frames used in the camera model. The point (X_0, Y_0, Z_0) corresponds to the origin of the laboratory frame. A point in this frame (X_l, Y_l, Z_l) is assumed to project through a pinhole to the point (X_c, Y_c) located in the image plane of the CCD camera. Radial distortion, in principle, causes a slight shift of this point to the point (X_d, Y_d) The basic equations for a pinhole camera are given by (9). Dimensions between the image plane and object plane are simply scaled by similar triangles. X and Y are the distance from the camera axis in the image and object planes. $\frac{Z_{object}}{f}$ simply is the

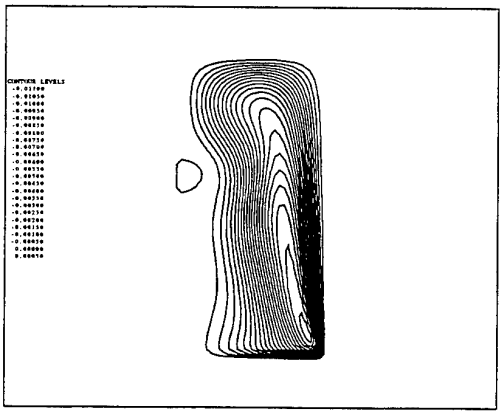

Figure 8: Contour lines of computed stream function in the R-Z plane. $Re = 1586$ and $\delta = 2.0$. The rotating wall is at the bottom of the figure.

magnification factor of the imaging system.

$$\frac{X_{object}}{Z_{object}} = -\frac{X_{image}}{f} \qquad (9)$$
$$\frac{Y_{object}}{Z_{object}} = -\frac{Y_{image}}{f}$$

Allowing for the axes in the laboratory frame to be translated in all three directions, we find that.

$$\frac{X_l - X_0}{Z_l + Z_0} = -\frac{Xc}{f} \qquad (10)$$
$$\frac{Y_l - X_0}{Z_l + Z_0} = -\frac{Yc}{f}$$

Approximating any radial distortion in the imaging system by the first non-zero term in its Taylor expansion we can write that

$$X_c = X_d(1 + \kappa r^2) \qquad (11)$$
$$Y_c = Y_d(1 + \kappa r^2)$$
$$r^2 = X_d^2 + Y_d^2$$

where X_c and Y_c are the coordinates of the point in the image plane due to a perfect pinhole projection. X_d and Y_d are the coordinates of the same point after radial distortion has occurred. Experimentally, for the lenses used in these experiments, κ is usually small.

Introducing a physical scale for the size of pixels on the CCD and allowing for the center of the digital image to be different from the center of the imaging system we can write

$$X_d = S_x(X_p + X_f) \qquad (12)$$
$$Y_d = S_y(Y_p + Y_f)$$

S_x and S_y relate the size of an individual pixel to physical dimensions on the CCD. X_f and Y_f account for the fact that experimentally the center of the digital image usually does not correspond to the center of the imaging system.

Combining equations (10), (11), and (12) we get that

$$\begin{aligned} X_l &= X_0 - (Z_l + Z_0)\frac{S_x(X_p + X_f)}{f} \times \\ &\quad [1 + \kappa(S_x^2(X_p + X_f)^2 + S_y^2(Y_p + Y_f)^2)] \\ &= F_x(X_p, Y_p; X_0, Y_0, Z_0, S_x, S_y, \kappa, f, X_f, Y_f) \\ Y_l &= Y_0 - (Z_l + Z_0)\frac{S_y(Y_p + Y_f)}{f} \times \\ &\quad [1 + \kappa(S_x^2(X_p + X_f)^2 + S_y^2(Y_p + Y_f)^2)] \\ &= F_y(X_p, Y_p; X_0, Y_0, Z_0, S_x, S_y, \kappa, f, X_f, Y_f) \end{aligned} \qquad (13)$$

The unknown model parameters X_0,Y_0,Z_0,S_x, S_y, κ, f, X_f, and Y_f are found by taking several images of a calibration grid at several different distances from the camera and minimizing the average squared error in feature position given by (14)

$$\chi^2 = \frac{1}{N}\sum_{i=1}^{N}[(X_i - X_{l_i})^2 + (Y_i - Y_{l_i})^2] \qquad (14)$$

Typical values of χ^2 are $2\text{x}10^{-4}$ implying an average computed error in location of approximately 0.015 inches.

The second issue of the distortion caused by viewing the image through the walls of the experiment is addressed by tracing a family of rays generated by the camera model from every point on the line back through a model of the experimental setup. Figure 10 show several representative rays traced back into a model consisting of two concentric cylinders. The outer cylinder has an index of refraction corresponding to quartz, while the inner cylinder's index is that of water.

The position of the tag and interrogation line are obtained by fitting a Gaussian line shape with a linearly varying background to the intensity distribution in each

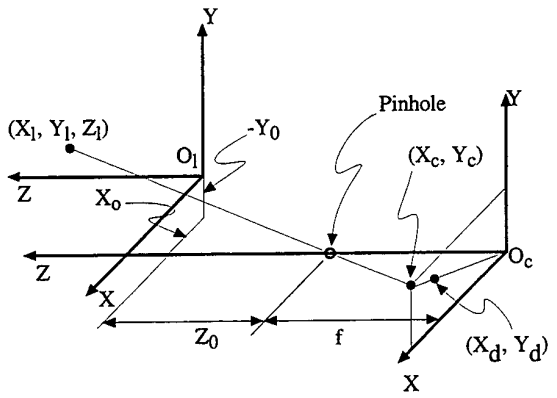

Figure 9: Coordinate frames used in the camera model.

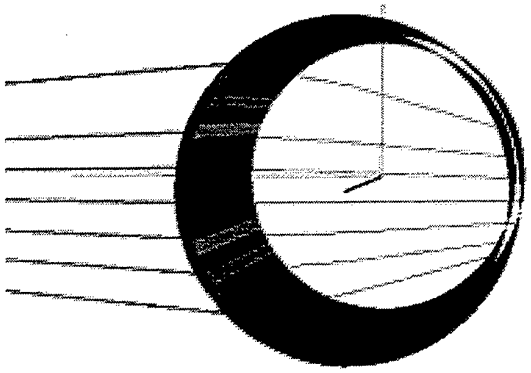

Figure 10: View of the 3D ray tracing procedure. Several rays corresponding to the line in figure 5 come from a pinhole source from the left and are traced back into the model.

vertical column of pixels in the recorded image. Generally, in this way, line centers can be located to an accuracy of 0.1 pixel.

In the current analysis, the tagged line motion is assumed to be planar, and the corrected line positions inside the experiment are calculated by intersecting the surface generated by tracing the rays back into the experiment with a plane in which the motion is assumed to occur (The R-Z plane in this case). Once both the tag and interrogation position is computed in this way, a measure of velocity can be computed using (15).

$$V \approx \frac{\Delta X}{\Delta T} \tag{15}$$

6 Results and Discussion

Figure 11 shows a measurement of velocity in the Z-direction obtained by tagging a line in the R-Z plane 0.856 R from the non rotating wall compared with vertical velocities at this location from the computations described above. Ray traced positions for both the tag and interrogation line were used to compute a series of line displacement measurements; these values were then divided by ΔT resulting in a velocity measurement.

As was pointed out in [5], so long as the spatial velocity gradients in the region the line traverses between tag and interrogation are small, (15) is a good measure of velocity.

Figure 12 shows the measured line displacement compared with the position of a line obtained by integrating a "numerical" line forward one second. In this way, one can obtain a direct comparison between the experiment and the data without the assumptions inherent in (15).

Figures 13 and 14 show the same comparisons between computed velocity and line displacement for motion in the R-θ plane.

It is important to note that in all measurements presented here, velocities and line displacements were computed assuming that the tagged lines motion remained planar. This assumption simplifies the ray tracing procedure as described previously. However, because the line motion is clearly non-planar this assumption introduces error in the calculated line position and resulting velocity measurements. We are currently implementing a three-dimensional ray tracing procedure in which rays from two cameras are traced back to their intersection in the experimental volume.

Several other possible sources for the discrepancy between computation and experiment exist and are currently being investigated. Reynolds number is experimentally determined by measuring the temperature of the water, rotation rate of the lid, and radius of the cylinder. Computations at Reynolds numbers 30 above and below 996 were run to evaluate the effects of inaccurate temperature measurements on computed velocity profiles in the region of interest. Only very small differences were found, and these alone can not account for the discrepancy shown. Although the measurement of Ω is believed to be quite accurate, since it affects the Reynolds num-

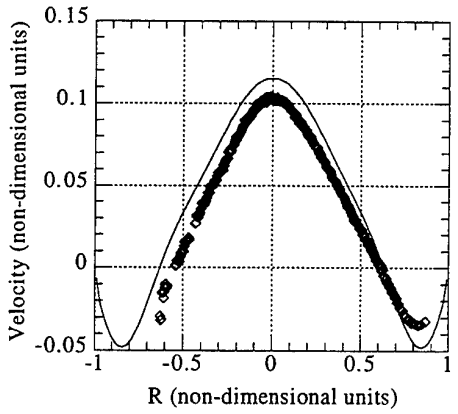

Figure 11: Non-dimensional velocity in the Z-direction computed (solid line) and measured (diamonds) along a line in the R-Z plane 0.856 R from the non-rotating wall. $Re = 996$ and $\delta = 2.0$.

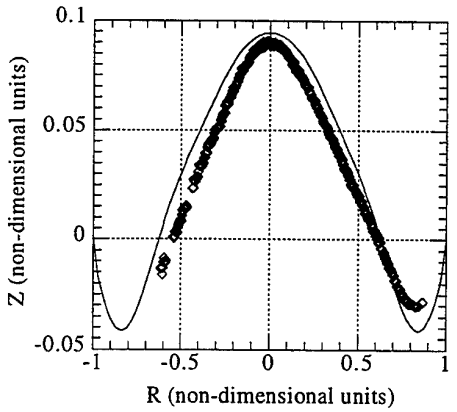

Figure 12: Computed (solid line) and measured (diamonds) non-dimensional line displacement after 1 s of an initially horizontal line tagged at 0.856 R in the R-Z plane. $Re = 996$ and $\delta = 2.0$.

ber as well as the non-dimensionalization of experimental velocity measurements, errors here could be quite significant.

The ray tracing procedure employed to remove optical distortion requires knowledge of the indices of refraction of the quartz cylinder and water. These were obtained from tabulated values, but may not accurately reflect the actual index of refraction of the cylinder or water at the wavelengths where the PHANTOMM dye fluoresces. The data should be re-analyzed with slightly different indices of refraction used in the ray tracer in order to quantify the sensitivity of measured velocity to errors in index of refraction.

7 Conclusions and future work

We have demonstrated the utility of the PHANTOMM technique simultaneously obtain quantitative velocity data in two planes in a highly three-dimensional flow field. A procedure has been outlined for removing the distortion due to imaging through curved surface with an imperfect optical system.

Measured velocity profiles have been compared to numerical simulations. Tagged lines have also been directly compared to "numerical" lines generated by forward integration of the computed flow. comparing measured velocity data to Future work will focus on resolving small remaining discrepancies between experimental data and the numerics, followed by experiments at higher Reynolds number where computations do not exist.

8 Acknowledgments

This work is supported by the National Science Foundation, Roger Arndt technical monitor. The authors wish to thank Mr. Philip J. Howard for constructing the apparatus and Professor Garry L. Brown for many illuminating discussions.

References

[1] Akio Arakawa. Computational design for long-term numerical integration of the equations of fluid motion: Two dimensional incompressible flow. Part 1. *Journal of Computational Physics*, 1:119–143, 1966.

[2] L.R. Bodeker. Velocity measurement with enhanced OH flow tagging. *Optics Letters*, 14:473–475, 1989.

[3] M.P. Escudier. Observations of the flow produced in a cylindrical container by a rotating endwall. *Experiments in Fluids*, 2:189–196, 1984.

[4] R.E. Falco and D. Nocera. Quantitative multipoint measurements and visualizations of dense

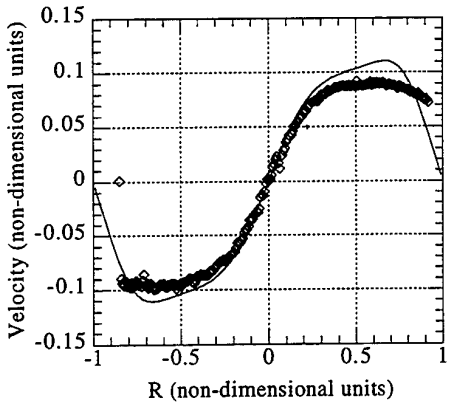

Figure 13: Non-dimensional velocity in the θ-direction computed (solid line) and measured (diamonds) across the diameter of the flow in the R-θ plane 0.856 R from the non-rotating wall. $Re = 996$ and $\delta = 2.0$.

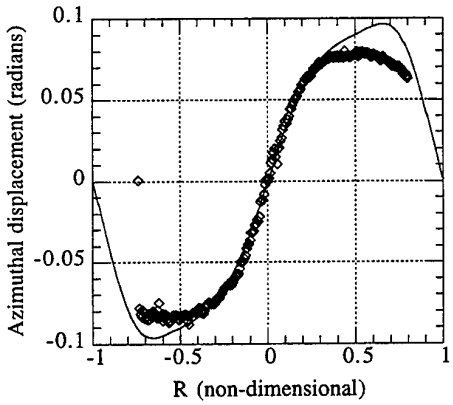

Figure 14: Computed (solid line) and measured (diamonds) non-dimensional line displacement after 1 s of a line tagged across the diameter of the flow 0.856 R from the non-rotating wall. $Re = 996$ and $\delta = 2.0$.

liquid-solid flows using Laser Induced Photochemical Anemometry (LIPA). In M.C. Roco, editor, *Particulate Two-Phase Flow*, pages 59–126. Butterworth-Heinemann, Boston, 1993.

[5] S.R. Harris, W.L. Lempert, et al. Quantitative measurements of internal circulation in droplets using flow tagging velocimetry. *AIAA Journal*, 34(3):449–454, March 1996.

[6] G.R. Johnson, E. Marschall, and J.H. Esdorn. Improved flow visualization technique for quantitative velocity measurement in small test volumes. *Review of Scientific Instruments*, 56:256, 1985.

[7] W.R. Lempert, K. Magee, K.R. Gee, and R.P. Haugland. Flow tagging velocimetry in incompressible flow using PHoto Activated Non intrusive Tracking Of Molecular Motion (PHANTOMM). *Experiments in Fluids*, 18:249–257, 1995.

[8] J.M. Lopez. Axisymmetric vortex breakdown part 1. Confined swirling flow. *Journal of Fluid Mechanics*, 221:553–552, 1990.

[9] R.B. Miles, J.J. Connors, E.C. Markovitz, P.J. Howard, and G.J. Roth. Instantaneous profiles and turbulence statistics of supersonic free shear shear layers by Raman Excitation plus Laser Induced Fluorescence (RELIEF) velocity tagging of oxygen. *Experiments in Fluids*, 8:17–24, 1989.

[10] G.P. Neitzel. Numerical computations of time-dependent taylor-vortex flows in finite-length geometries. *Journal of Fluid Mechanics*, 141:pp. 51–66, 1984.

[11] G.P. Neitzel and Stephen H. Davis. Centrifugal instabilities during spin-down to rest in finite cylinders. numerical experiments. *Journal of Fluid Mechanics*, 102:pp. 329–352, 1981.

[12] Roger Y. Tsai. a versatile camera calibration technique for high-accuracy machine vision and metrology using off-the-shelf TV cameras and lenses. *IEEE Journal of Robotics and Automation*, RA-3(4):323–344, August 1987.

[13] H. U. Vogel. Experimentelle Ergebnisse über die laminare Strömung in einem zylindrischen Gehäuse mit darin rotierender Scheibe. Technical report, Max-Planck-Institut. Bericht 6, 1968.

[14] H. U. Vogel. Rückströmungsblasen in Drallströmungen. Festschrift 50 Jahre Max-Planck-Institut für Strömungsforschung 1925–1975, 1975.

[15] V.N. Yurechko and Y.S. Ryazantsev. Fluid motion investigation by the photochromic flow visualization technique. *Experimental Thermal and Fluid Science*, pages 273–288, 1991.

QUANTITATIVE VELOCITY MEASUMENTS IN TURBULENT TAYLOR-COUETTE FLOW BY PHANTOMM FLOW TAGGING

M. Biage*, Scott R. Harris†, W. R. Lempert£ and A. J. Smits §

Department of Mechanical & Aerospace Engineering
PRINCETON UNIVERSITY, Princeton, New Jersey 08544, U.S.A

ABSTRACT

Quantitative velocity measurements have been performed in Taylor-Couette flow using the PHANTOMM flow taggign technique. The results illustrate the expected three-dimensional features of the flow and the presence of Taylor cells at low Taylor numbers. Moreover, these results showed the gradual transition to turbulence with increasing Taylor numbers. The spectral density function and the autocorrelation function were computed for the 211 x 10^3 to 110 x 10^9 range of Taylor numbers studied. The flow structure, for Taylor numbers less than 5.97 x 10^7, is dominated by larger torroidal eddies with a wavelength the same order as the gap size. When the Taylor number becomes larger, the flow structure displays more irregular motions. Nevertheless, even for the highest Taylor number studied in this work, the structure is far from random, and the flow exhibits an almost periodic behavior. We can take Ta = 6 x 107 as a number that characterizes the transition of the flow structure from one dominated by the Taylor cells to one where the irregular motions predominate. We can associate these irregular motions with the Görtler instability or instability of the second kind. The results also show the potential of the PHANTOMM technique to investigate the spatial instabilities in confined flow.

1. THE PHANTOMM TECHNIQUE

The ability to obtain accurate, high spatial resolution velocity data over a wide range of Reynolds numbers poses a significant challenge to existing optical diagnostic techniques. Flow tagging is an optical diagnostic in which a laser beam is used to "write" a spatially continuous pattern into a specific region of the flow field. The temporal evolution of the initial pattern is tracked ("interrogated") through Laser-Induced Fluorescence (LIF) imaging. The displacement within the elapsed time interval constitutes a measurement of velocity, with an absolute accuracy limited only by the ability to determine position and time.

Flow tagging based on caged dye Photo-Activated Fluorphores (PAF) (McCray 1989). PAF tracers has been termed as Photo-Activated Nonintrusive Tracking of Molecular Motion (PHANTOMM). Caged dye PAF's are organic dye molecules in which a chemical caging group has been attached in order to quench the normally bright laser fluorescence. The caging group is photolytically cleaved upon exposure of the molecule to ultraviolet (UV) light, typically, but not necessarily, from a laser. Upon photolysis, the original dye is recovered which can be tracked indefinitely using ordinary laser sheet fluorescence imaging approaches (Dahm et al. 1990). As was discussed by Lempert (1995), the uncaged dye exhibits an extremely intense fluorescence, with the result that low concentrations (less than 10^{-6} M) are required. As in ordinary dye visualization, the fluorescence is Stokes-shifted so that simple long-pass colored glass filters can be used to attenuate elastic scattering from the laser. This produces high contrast images which are conducive to measurements at high Reynolds number. In many respects, the technique is similar to Laser-Induced Photochemical Anemometry (LIPA), in which time lines are written into a flow using photochromic phosphorescent materials (Falco and Nocera 1993).

The capabilities of the technique to measure velocity in high-speed flow are directly linked to the optical and chemical properties of the PAF tracers. In particular, it should be pointed out that, while there is no limit to the maximum time between cage-breaking (tag) and interrogation (since the photochemical change is permanent), there is a minimum time dictated by the kinetic rate for the cage-breaking photolysis process. The finite

* Associate Professor, Department of Mechanical Engineering, Federal University of Uberlandia, Uberlandia-MG, Brazil, 38400-902; Visiting Fellow (1995), Department of Mechanical and Aerospace Engineering, Princeton University, Princeton, NJ, USA, 08544.
† Graduate Student, Department of Mechanical and Aerospace Engineering, Princeton University, Princeton, NJ, USA, 08544.
§ Professor, Department of Mechanical and Aerospace Engineering, Princeton University; Associate Fellow, AIAA, Princeton, NJ, USA, 08544.
£ Research Scientist, Department of Mechanical and Aerospace Engineering, Princeton University, Princeton, NJ, USA, 08544.

rate results in a time lag between the firing of the tagging laser and the evolution of sufficient dye in its fluorescent form to be interrogated with sufficient signal-to-noise. The magnitude of the signal-to-background ratio is a function of the caged dye purity, as well as the sheet thickness. This ratio needs to be adjusted by experiment (Lempert 1995).

2. THE TAYLOR-COUETTE FLOW AND OBJECTIVES

The flow between concentric cylinders has proved to be a remarkably rich problem in fluid dynamics. Interesting phenomena have been observed and examined since the early work of Taylor (1923) who found that for certain combinations of the rotation rates and geometry, the flow in the gap between the two cylinders became unstable. This instability is in the form of counter-rotating vortex pairs with their axes in the circumferential direction. Part of the fascination with the Taylor-Couette problem is how such a simple flow geometry can produce such complexities. One particularly interesting aspect of the study of the Taylor-Couette flow is the transition from laminar to turbulent flow. One of the inducements to understand the transition process in Taylor-Couette flow is the possibility of finding a general model of transition.

Some of the studies in Taylor-Couette flow have suggested that the structure of the flow is composed of large Taylor cells throughout the gap, typically due to the Taylor instability, and a thin boundary layer on the wall of the inner cylinder where the instability has been found to be characteristic of the Görtler instability. The disturbances in the boundary layer are of the form of counter-rotating vortex pairs with axes in the circumferential direction, with motion similar to that of the Taylor cells (Wei et al., 1992; Smith and Townsend, 1982). It should be noted that the Görtler instability is not limited to Couette flow geometries. The Taylor-Görtler instability may also be an important mechanism for the control of transition in a boundary layer along curved surface, for both compressible and incompressible turbulent flows.

The aspects of the Taylor-Couette flow described in the paragraph above have not been investigated in detail by quantitative velocity measurements. The hot wire anemometer is not adequate for this study because it affects adversely the flow structure within the small gaps. Also, it is not possible to get information about the global features of the large Taylor cells since it is inherently a single-point technique. This aspect may also restrict the use of LDV (Laser Doppler Anemometry). On the other hand, the PHANTOMM technique can extract interesting facts of the structure of the flow because the spatial measurements with this technique provide information that happens along a line. The statistical treatment of the spatial changes of velocities can help to show the main aspects of the flow.

For these reasons we studied the Taylor-Couette flow using the PHANTOMM technique. The study had a primary objective to characterize the performance this technique to measure velocities in incompressible turbulent flow in high Reynolds number. Also, we have carried out a treatment of the measurements with aim to understand the structure of the flow as a function of Taylor number, in the range where the flow goes from laminar to turbulent. The measurement procedure will be explained in the next section.

3. EXPERIMENTAL SYSTEM

3.1 Taylor-Couette Experimental Apparatus

The inner and outer cylinders of the Taylor-Couette are made of Plexiglas. The inner cylinder was machined to a radius of $R_i = 3.14$ *cm*. The nominal inside radius of the outer cylinder is $R_o = 8.18$ *cm* and the variation in the inner radius around the circumference at fixed height was determined by visual inspection to be less than *1%*. The height of the cylinders is $L = 102$ *cm;* giving an aspect ratio $\Theta = L/d = 20$ (d is the gap length), which is large enough to minimize end effects. The top and bottom endplates are stationary. The temperature of the system was not controlled but the ambient temperature of the room was constant between 22 and 25°C. The experimental system is mounted on a vibration-isolation table. The cylinders are driven by variable speed DC motors that allow uniform and stable rate of rotation for both cylinders. The rotation rates of the inner and outer cylinders can be chosen independently and co-rotating and counter-rotating cases are possible. A small He-Ne laser was directed on to a small black tape spot on the wall of the inner cylinder, and the signal was captured by photo diode, to allow the rotation frequency to be measured with the aid of a digitizing oscilloscope. The Taylor number was varied by changing the rotation frequency of the inner cylinder. In our experiments only the inner cylinder rotated, $\mu = 0$ (see Eq. 8). Since 0.355 μm light is attenuated by Plexiglas, the outer cylinder was fitted at its midpoint with a small quartz window, approximately 1 cm in diameter, to facilitate tagging. The working fluid was a water solution with Dextran Carboxy fluorescein that was used as a trace material. A typical concentration used in these experiments is 0.5 mg/l.

3.2 Optical Apparatus

In the optical configuration used in this study, the tagging is performed using the third harmonic of a Q-switched Nd:YAG laser at 0.355 μm. Single-pulse energies between 40 mJ and 60 mJ were used, depending upon the experiment. Lines were tagged along the radial axis (the r-direction), where the UV tagging beam from the laser was focused with a 30 cm focal length lens, resulting in a beam waist of approximately 10 μm. The interrogation was performed using a flash lamp pumped dye laser using LD490 dye in methanol with no interactive line-narrowing optics. The dye laser is capable of pulse outputs between 50-400 mJ with a pulse duration of approximately 2 μs. The interrogation beam is formed into a sheet that, for the lateral recording, emerged from the top of the experimental apparatus. The sheet, approximately 2 cm thick, was

formed by mirrors and cylindrical lenses with positive and negative focal length. This sheet was located in the (r,z) plane in the annular space between the cylinders, where the z- direction is along the axis of the cylinders. For recording from the top view, similar optics were used to place the sheet in the (r, ϕ) plane. It covered all the gap. Also, this sheet had a thickness of approximately 2 cm. A colored glass filter (OG530) was used to block stray elastic scattering from reaching the camera. Fluorescence from either the line or the image of the vortex pair and cells was imaged onto a standard CCD camera, stored in a freeze frame unit between interrogations, and recorded on a VHS VCR. The delay between the tagging and interrogation lasers was adjusted by a 4-channel digital delay/pulse generator. The maximum repetition rate was 10 Hz.

4. RESULTS

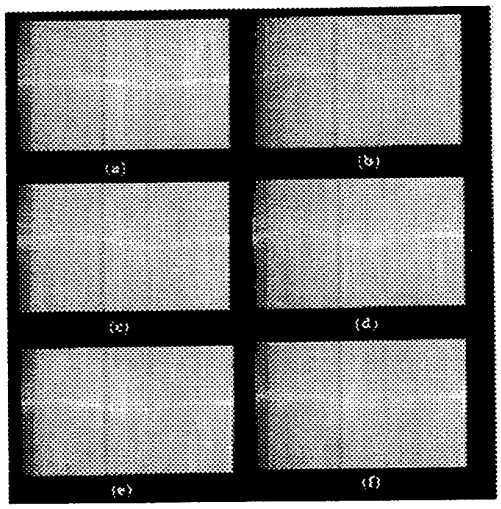

Fig. 1 Representative PHANTOMM line images for $Ta=0.21x10^5$ (Re=154), in the (r,z) plane. The images from (a) to (f) correspond to the interrogation lines with $\delta t=1$ second. Two seconds of delay occur between sucssive pictures.

For a cylindrical geometry (r,θ,z), where r, θ and z represent the radial, azimuthal and vertical axial directions, the basic-state velocity vector is $\vec{V}=(v_r,v_\theta,v_z)$, where v_r, v_θ and v_z represent the radial, tangential and axial velocity components. Rayleigh (1916) showed that the necessary and sufficient condition for the existence of an inviscid axisymmetric instability is:

$$\frac{d\left(\Gamma^2\right)}{dr}<0 \qquad (1)$$

anywhere in the flow. Γ is the circulation defined as $\Gamma=rV_\theta$.

The instability in Taylor-Couette flow is governed by the Taylor Number T_a defined by

$$Ta=Re^2\,\delta \quad , \quad Re=\frac{V_i d}{\nu} \qquad (2,3)$$

$$V_i=R_i\Omega_i \quad , \quad d=R_o-R_i \qquad (4,5)$$

$$\delta=\frac{d}{\bar{r}}\left(1-\mu^2\right) \qquad (6)$$

$$\bar{r}=\frac{R_i+R_o}{2} \quad , \quad \mu=\frac{\Omega_o}{\Omega_i} \qquad (7,8)$$

where ν is the cinematic viscosity, R_i and R_o are the radii of the inner and outer cylinders, respectively, Ω_i and Ω_o and are the angular velocities of the inner and outer cylinders. When the outer cylinder is fixed and the inner cylinder is rotating about its axis $\mu=0$. This case is that was studied in this work.

We have applied the PHANTOMM technique to measure the instantaneous velocities in the (r,z) and (r,θ) planes. Images from both views were recorded at 40 different Taylor numbers in the range $0.21x10^5<Ta<0.11x10^{12}$ and for several different delays between tagging and interrogation.

Figures 1 to 3 show the representative PHANTOMM line images. Fig. 1 shows the images in the (r,z) plane, for the lower value of the Taylor number, $Ta=0.21x10^5$. The lines indicate a flow structure typical the Taylor cells. The flow has a rotational laminar structure with a positive velocity close to the outer cylinder wall and a negative velocity from the center to the inner cylinder wall. This flow configuration is completely steady, and the Taylor cells cover the complete gap. As described in Biage et al. (1996), the cells have an inflectional point that characterizes the shift in the velocity sign. This point constitutes an equilibrium center that moves along the central line in the radial direction. When this point approaches of one of the cylinder walls the rotational sense of the cells changes. This is the flow typical of low Taylor numbers. Fig. 2 presents the line images of the flow in the (r,θ), for the same experimental condition of Fig. 1. In this figure we can observe three-dimensional characteristics of the flow. The lines close to the outer cylinder wall are affected by the axial flow in the vertical direction. The region of the gap core has an appearance of nozzle due the interaction of the flow in the (r,θ) plane with one in the (r,z) plane. The flow structure shows in the Fig. 2 indicates a larger velocity in the central region of the gap than that for the inner cylinder wall because of the nozzle effect. When the Taylor number increases the regular feature of the flow in the (r,z) plane changes and the coherence of the Taylor cells shrinks. At the same time, fluctuations with higher frequencies appear in the flow. For example, Fig. 3 shows the flow line structures for higher Taylor number.

Fig. 4 shows a typical view of the interrogation lines, overlaid with an estimate of the center of gray scale intensity as a function of r. The center of intensity was found using a peak searching algorithm. For the measurements in the (r,z) plane, this algorithm took the point that corresponds to the maximum gray scale intensity

over a vertical line (each picture had 646 vertical lines). This point coincides with the centerline of the interrogation line image with an error less than ±2%. For the measurements in the (r,θ) plane, the center of intensity was found by peak searching algorithm in the following way: as a first approach, using the same procedure described above for the (r,z) plane. Normally, the center of intensity found by this procedure did not coincide with the centerline of the interrogation line as a function of r. To correct this divergence, we have taken a set of points with 30-40 pixels distributed in the radial direction around the each maximum point, which was determined by the first approach, and then we evaluated the radial maximum intensity over the interrogation line. These points that correspond to the maximum radial intensity coincided with the centerline of the interrogation line, with the same precision mentioned above. Even the critical cases, where the flow had higher level of fluctuation, this analysis worked well.

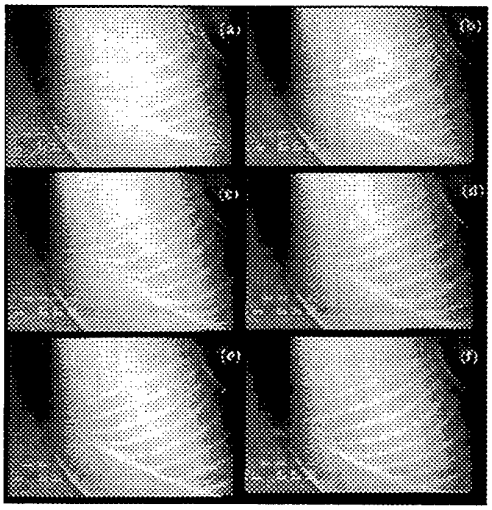

Fig. 2 Representative PHANTOMM images for $Ta=0.21x10^5$ (Re=154), in the (r,θ) plane. δt=20 ms for each first line image and δt=1 second between sucessive lines. Two seconds of delay between successive pictures.

The calibration of the image magnification was performed external to the experimental system because of the difficulty of performing this in-situ. We utilized an image of a grid placed in the same optical geometry used for the experiments. In this calibration, we did not apply corrections of the distortion caused by viewing the tagged lines through the cylindrical surface in the (r,z) plane. Also, we did not correct the distortion caused by the mismatch of the indices-of-refraction for air-water. However, by comparison of known gap length to that determined using the calibration measurements, we estimate the error to be less than 3%. The principal effect of the cylindrical surface is to compress the radial scale of the image very near the outer wall. The z-axis is not affected, except for a very small translation. This translation was minimized by positioning the camera at the same height as that of the tagging laser. A conservative estimate of the absolute velocity uncertainty introduced by these effects is less than ±5%.

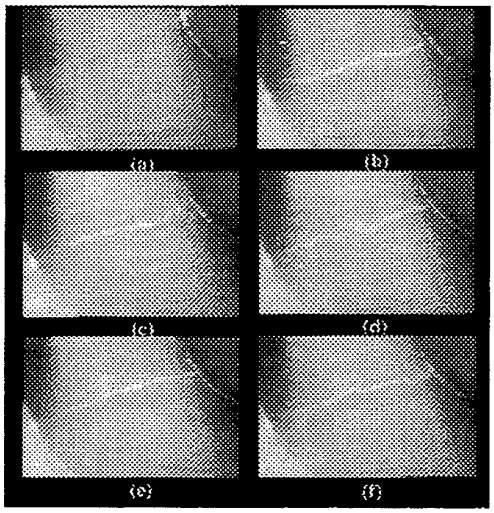

Fig. 3 Representative PHANTOMM images for $Ta=2.45x10^8$ ($Re=1.66x10^4$), in the (r,θ) plane. (a) baseline image with δt=1 ms and the images from (b) to (f) correspond to the interrogation lines with δt=1 ms. One second of delay between successive pictures.

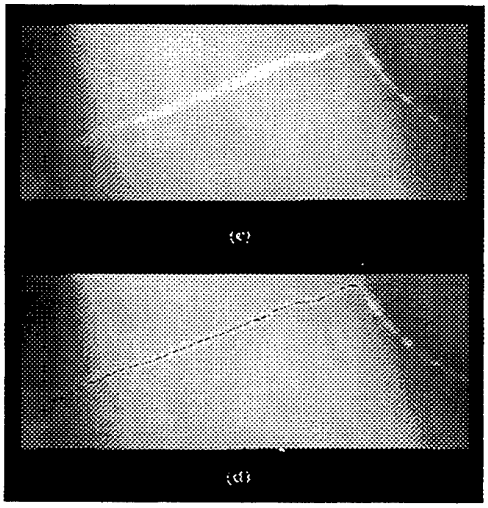

Fig. 4 (a) typical view of the interrogation line in the (r,θ) plane. 15 ms after tagging for $Ta=5.96x10^7$ (Re=8176) and (b) the corresponding fitted line position.

Figures 5 to 8 show the dimensionless instantaneous velocities across the gap for the planes (r,θ) and (r,z) for several Taylor numbers in the range of 0.21 x

$10^5 < Ta < 0.11 \times 10^{12}$. These figures were put on the same scale in order to illustrate the relative fluctuations in the two planes as a function of Taylor number. In all situations, the flow exhibits large spatial fluctuations.

Figures 5 and 6 show the velocity profiles for several Taylor numbers in the (r,θ) plane. In Fig. 5, which corresponds to $Ta = 0.21 \times 10^5$ (Re = 154), we observe that the velocity in the gap center achieves a velocity two times greater than the linear velocity of the inner cylinder wall. This occurs because of the three-dimensionality and the resulting streamwise convergence, as indicated earlier. The mean velocity in the (r,θ) plane becomes less affected by the three-dimensional characteristic of the flow as the Taylor number increases. Moreover, the outflow velocity profile evolves with the Taylor number, and it achieves an almost constant slope (about 0.42) when the Taylor number becomes larger than 5.96×10^7. One can see this tendency in the velocity profiles of Figs. 5 and 6. This behavior permits the enhancement that the outflow velocity profile is led for a universal profile in high Taylor number

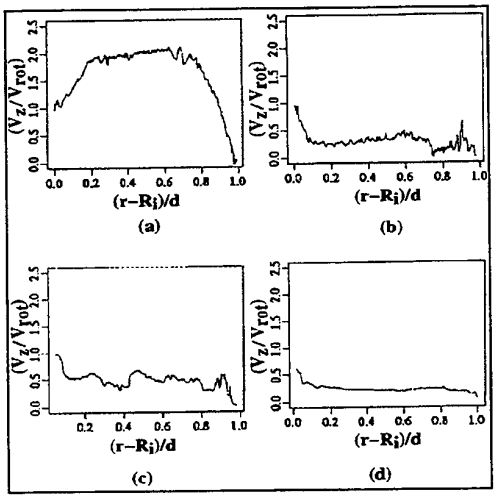

Fig. 5 Dimensionless instantaneous velocities along the gap, in the plane (r,θ). (a) $Ta=0.21 \times 10^5$, (b) $Ta=6.02 \times 10^6$, (c) $Ta=5.96 \times 10^7$ and (d) $Ta=2.45 \times 10^8$.

Almost all the variation of the angular momentum occurs within the two wall boundary layers since surface stresses are expected to be nearly proportional to the 7/5 power of the rotational velocity, according to Smith and Townsend (1982). One can observe that the boundary layer in the inner cylinder wall is concentrated in a region within 0.07 of the gap length. The thickness of the boundary layer shrinks when the Taylor number increases. For larger Taylor numbers, this thickness is less than 0.03 of the gap length. This boundary layer thickness on the outer cylinder wall is larger than that of the inner cylinder wall. However, the flow in this outer boundary layer appears to be more disturbed, fluctuating more intensity close to the wall. This fact suggests that flow in the boundary layer on the outer cylinder is more affected by curvature. It must be repeated, however, that optical distortions are maximum near the outer wall, and, it is, therefore, difficult to quantify the boundary layer thickness.

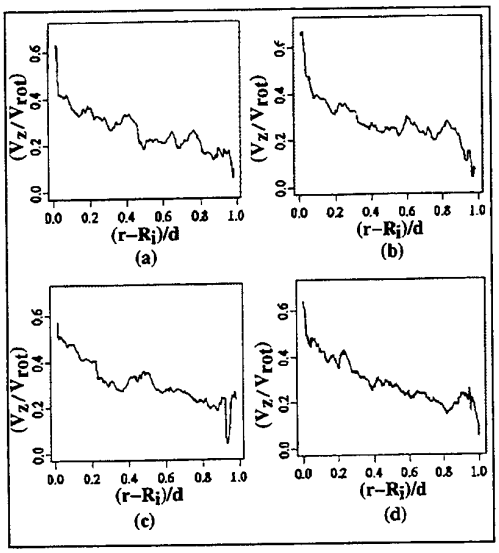

Fig. 6 Dimensionless instantaneous velocities along the gap, in the plane (r,θ). (a) $Ta=1.63 \times 10^9$, (b) $Ta=4.76 \times 10^9$, (c) $Ta=2.0 \times 10^{10}$ and (d) $Ta=0.11 \times 10^{12}$.

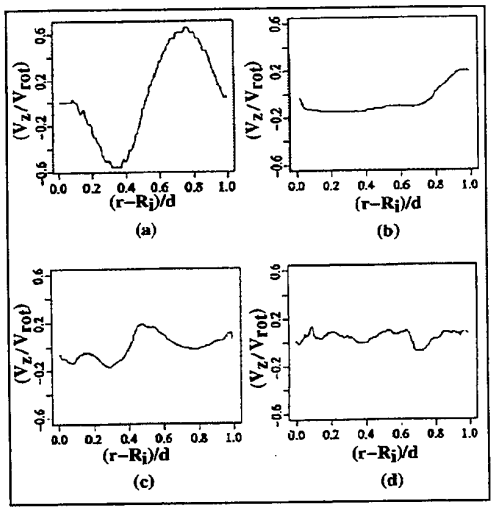

Fig. 7 Dimensionless instantaneous velocity along the gap in the (r,z) plane. (a) $Ta=0.21 \times 10^5$, (b) $Ta=6.02 \times 10^6$, (c) $Ta=5.96 \times 10^7$ and (d) $Ta=2.45 \times 10^8$.

The velocity profiles shown in the Figures 7 and 8 correspond to the (r,z) plane measurements. One can observe in the Figure 7.a that the velocity profile is characteristic of a laminar rotational flow, typical of

Taylor cells with a very slow circulation velocity. When the Taylor number increases (from $Ta=5.96x10^7$), the characteristic of laminar rotational flow disappears and is replaced by flow with larger fluctuation with irregular aspects. At all Taylor numbers, the mean velocity is zero in (r,z) plane.

We have evaluated the angular-momentum ratio defined by the following equation:

$$\left(\frac{\Gamma}{\Gamma_{rot}}\right)=\left(\frac{v_i r}{v_{rot}R_i}\right) \qquad \text{with} \quad i=\theta \text{ or } z \qquad (9)$$

where, v_i is the velocity in the θ and z direction, v_{rot} is the rotational velocity and R_i is the radius of the inner cylinder.

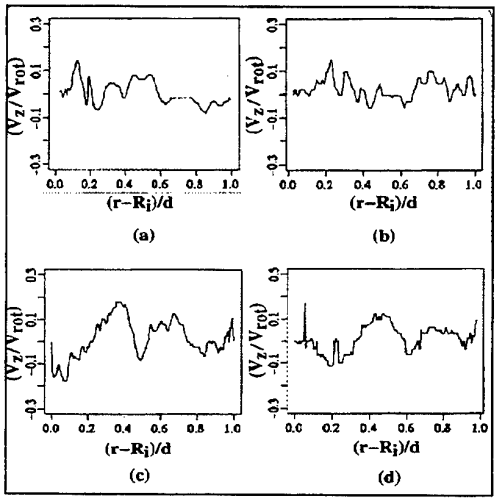

Fig. 8 Dimensionless instantaneous velocity along the gap in the (r,z) plane. (a) $Ta=4.76x10^9$, (b) $Ta=2.0x10^{10}$, (c) $Ta=0.48x10^{11}$ and (d) $Ta=0.11x10^{12}$.

The mean angular-momentum is almost constant across the gap for larger Taylor numbers. For the measurements in the (r,θ) plane, the mean angular-momentum ratio is close to 0.50, when the Taylor numbers are larger than $6.02x10^6$ (this value is the same found by Smith and Townsend, 1982). This fact suggests that for high Taylor number the outflow is not affected by the curvature effect associated with the cylinder surfaces, and in this it is similar to boundary layer flow in channels. Nevertheless, for the measurements in the (r,z) plane, the mean angular-momentum ratio is constant and it is zero, also, when Taylor numbers are larger than $6.02x10^6$. In the same way, the outflow in this plane is not affected by the curvature of the cylinder surfaces.

From the Equation 9, we can have one equation to determine the outflow velocity in the plane (r,θ), for Taylor numbers larger than $6.02x10^6$, which may approximate the outflow velocity in region of 90% of the gap. This equation is the following:

$$v_\theta = 0.5 v_{rot}\left(\frac{R_i}{r}\right) \qquad (10)$$

The spatial one-dimensional and one-sided spectral density function gives further information about the flow behavior. For example, the spectral density function of a periodic signal gives a maximum in the characteristic wave number of the signal. In case the dynamic system has a quasi-periodic behavior, then the spectral density function presents several maxima that correspond to the wave numbers of unrelated phenomena. On the other hand, the spectral density function for a random signal has a continuous spectral representation over a large bandwidth of wave numbers that characterizes a disordered behavior. The degree of disorder of a system is associated with the wave number bandwidth of the spectral representation. The spectral density function may be evaluated by the following equation (Bendat and Poersol, 1985 and Tennekes and Lumley, 1972):

$$G_{xx}(K_i)=\frac{2}{n_d N\Delta d}\sum_j^{n_d}\left|X_j(K_i)\right|^2 \qquad i=0,1,\ldots,\frac{N}{2} \qquad (11)$$

where x(r) is the recorded signal of the measurements along the gap with a zero average. It follows that each record of x(r) is $x_j(r)$ that corresponds to the instantaneous measurements for $j=1,2,\ldots,n_d$. X_j is the finite Fourier transform over N digital values distribute along the gap with width d. K_i is the discrete wave number for $i=1,2,\ldots$. Finally, n_d is the averaging operation that was of order ten in our calculation.

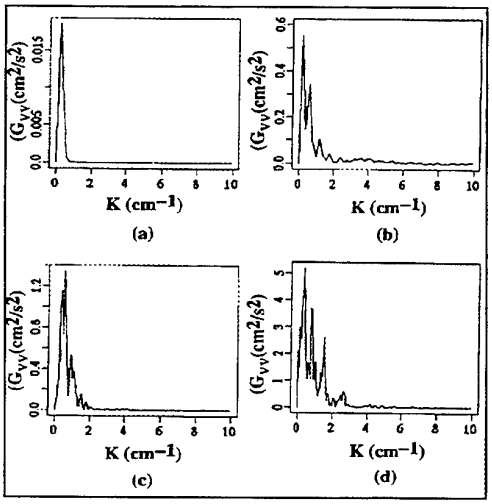

Fig. 9 One-dimensional and one-sided spectral density function in the (r,z) plane. (a) $Ta=0.21x10^5$, (b) $Ta=6.02x10^6$, (c) $Ta=5.96x10^7$ and (d) $Ta=2.45x10^8$.

The spectral density function was determined, for the (r,z) plane using the instantaneous velocity signal, in

this case $x(r)=v_z(r)$. The spectral density function was also evaluated, for (r,θ) plane using the angular momentum $(x_j(r)=rv_z(r))$. Note that the average velocity profile changes significantly along the gap. One Fundamental wave number with large amplitude that represents the average velocity oscillation along the gap appears in the spectral density function. The amplitude of the fundamental wave number is much larger than the amplitudes correspond to the wave numbers of the intrinsic oscillation of the instantaneous velocity. In this case, the qualitative feature of the spectral density function is better analyzed using the instantaneous angular momentum rather than the velocity.

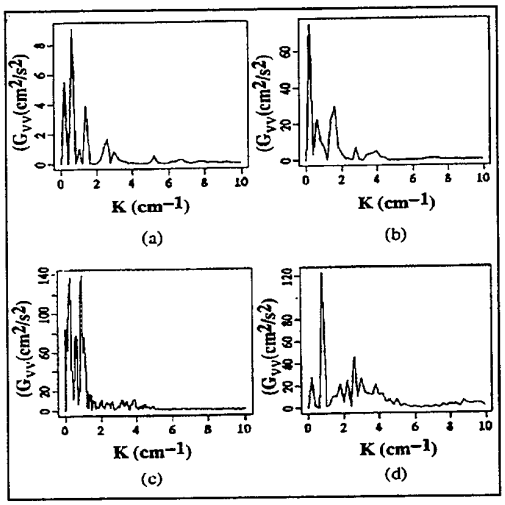

Fig. 10 One-dimensional and one-sided spectral density function in the (r,z) plane. (a) $Ta=1.63x10^9$, (b) $Ta=4.76x10^9$, (c) $Ta=2.0x10^{10}$ and (d) $Ta=0.11x10^{12}$.

Figures 9 and 10 show the spectral density function for several Taylor numbers in the range $0.21x10^5<Ta<0.11x10^{12}$. Physically, these figures represent the energy flow as a function of the wave number. The flow feature is typically toroidal eddies with a regular wave number ($K=0.198$ cm^{-1}), that is, the Taylor cells, which have a characteristic scale with the same dimension of the gap (see also the flow visualization presented in Biage et al. (1996)). The spectral density function represents other maxima with significant energy (amplitude) when the Taylor number increases. In reality, the flow becomes more irregular, with important contributions on characteristic scales less than the fundamental scale (approximately 0.198). The Figures 9.d and Figure 10 support this analysis. We can conclude that the flow is almost perfectly periodic, for Taylor number less than $5.96x10^7$. For Taylor number larger than this, the flow structure is quasi-periodic with contributions from several characteristic wavelengths. This flow structure persists for the higher Taylor numbers studied in this work (Fig. 10.d). While we have presented only the spectral density function for the (r,z) plane, the measurements in the (r,θ) plane gave the same results.

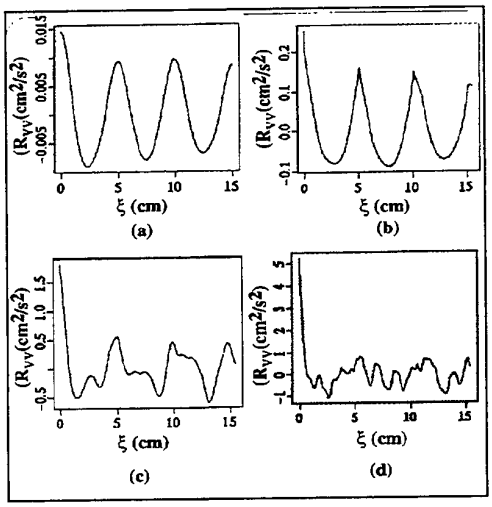

Fig. 11 One -dimensional auto_correlation in the (r,z) plane. (a) $Ta=0.21x10^5$, (b) $Ta=6.02x10^6$, (c) $Ta=5.96x10^7$ and (d) $Ta=2.45x10^8$

The degree of coherence of the oscillations may be assessed more precisely from measurements of the auto-correlations of the instantaneous velocity. The spatial one-dimensional auto-correlation function characterizes the similitude of one variable in a position r with their values in another position $(r+\xi)$, where ξ is the wavelength. The periodic or quasi-periodic signals keep theirs internal similitude along the space. We can say that a system behavior is predictable, because if one know the signal characteristic of a specific position, one can predict the signal behavior of another position $(r+\xi)$ (Bendat and Piersol, 1985). The similitude rate of a signal is obtained in the auto-correlation function by taking the ratio of the principal maximum ($\xi=0$) to the secondary maxima. When the flow is random, the auto-correlation function tends to zero quickly when ξ increases and the secondary maxima disappear. A random signal is non-predictable because it progressively loses its internal similitude.

To estimate the unbiased one-dimensional auto-correlation function, we use the following equation (Bendat and Poersol, 1985 and Tennekes and Lumley, 1972):

$$R_{xx}(\xi)=\frac{N}{N-m}\hat{R}_{xx}(\xi), \qquad \text{with} \quad m=1,\ldots,N-1 \qquad (12)$$

where ξ represent the oscillation wavelengths, R_{xx} are auto-correlation function, $\hat{R}_{xx}$ is the biased auto-correlation function computes from the Fourier transform of the two-sided spectral density function estimated from a sequence

of 2N values. The other variables are the same as for the spectral density function.

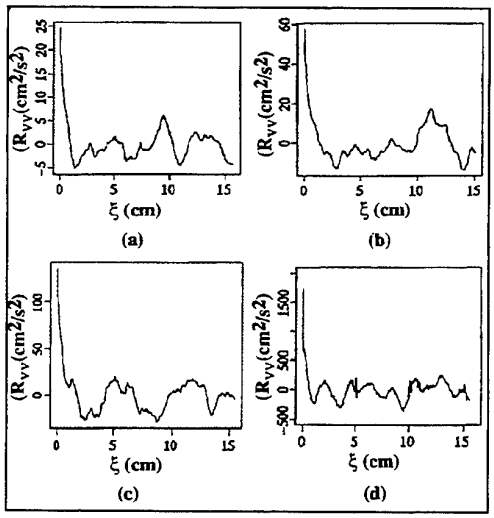

Fig. 12 One -dimensional auto_correlation in the (r,z) plane. (a) Ta=1.69x10^9, (b) Ta=4.76x10^9, (c) Ta=2.0x10^{10} and (d) Ta=0.11x10^{12}.

To compute more accurately the auto-correlation function and verify the coherence of the velocity fluctuation, we have evaluated the auto-correlation function from a sequence of ten samples of the instantaneous velocity. This procedure indicates the coherence of the signal much more clearly.

Figures 11 and 12 show the auto-correlation function for several Taylor numbers in the range of $0.21x10^5<Ta<0.11x10^{12}$. The flow structure for Taylor numbers less than $5.97x10^7$ is dominated by larger toroidal eddies that cover the gap, with a wavelength the same order as the gap characteristic length. When the Taylor number becomes larger, the flow structure shows irregular fluctuations similar to quasi-periodic signal. Nevertheless, even for the highest Taylor number studied in this work, the flow is far from a random and exhibits quasi-periodic behavior. We can take the Ta=$5.96x10^7$ as a number that characterizes the transition of the flow structure from one dominated by Taylor cells to another where the irregular motions of fluctuations are predominant in the flow. If we use the visualization study presented in Biage et al. (1996), we can associate this irregular motion as the Göltler instability or instability of second kind. The same observation could have been extracted from the auto-correlation function evaluated from the instantaneous velocity in the (r,θ) plane.

In conclusion, the full interpretation of these figures gave a new understanding of the structure of the Taylor-couette flow. The results also show the potential of the PHANTOMM technique for investigating spatial instabilities in confined flows.

5. ACKNOWLEDGMENTS

We thank the Air Force Office Scientific Research, contract number F49620/93/1/0427 and National Science Foundation that have been supported this research. Also, we thank the CNPq (National of Scientific and Technologic Development of the Brazil Government) that has supported the grant for Mr. Biage.

6. REFERENCES

- BARCILON, A. and BRINDLEY, J., 1984, Organized structrures in Taylor-Couette flow. J. Fluid Mech., 143,29.
- BENDAT, J. S. And PIERSOL, A. G., 1986, RANDOM DATA: Analysis and measurement procedures, John Wiley & sons.
- BIAGE, M.; HARRIS, S. R.; LEMPERT, W. R. and SMITS, A. J., 1996, Visualization study of Taylor-Couette flow: A description of the transition to turbulence, to be published in the 27th AIAA Fluid Dynamics Conference, New Orleans-LA, USA.
- DAHM, W.J.A. and DIMOTAKIS, P.E., 1990, Mixing at large Schmidt number in the self-similar far field of turbulent jets, J. Fluid Mech.,. 217, p. 299.
- FALCO, R.E. and NOCERA, D., 1993, Quantitative Multi-Point Measurements and Visualization of Dense Liquid-Solid Flows Using Laser-Induced Photochemical Anemometry (LIPA), in: Particulate Two-Phase Flow (ed. M.C. Roco) Boston: Butterworth-Heinemann.
- HARRIS, S. R., LEMPERT, W. L., HERSCH, L., BURCHAM, C. L., SAVILLE, D. A. And MILES, R. B., 1995, Flow tagging measurements of internal circulation in droplets. AIAA paper, 95-0168.
- LEMPERT, W. R., MAGEE, K., GEE, K. R. and HAUGHLAND, R. P.,1995, Flow tagging velocimetry in incompressible flow using Photo-Activated Nonintrusive Tracking of Molecular Motion (PHANTOM). Exp. in Fluids., 18, 249-257.
- McGRAY, J. A. and TRENTHAM, D. R. Properties and uses of photoreactive caged compounds. Annu. Rev. Biophys. Chem. 18, 239-270, 1989.
- SMITH, G. P. and TOWNSEND, A. A. 1982. Turbulent Couette flow between concentric cylinders at large Taylor number. J. Fluid Mech. 123, 187.
- RAYLEIGH, l. 1916, On the dynamics of revolving fluids. Scientific Papers. 6, 447-53.
- TAYLOR, G. I. 1923. Stability of a viscous liquid contained between two rotating cylinders. Phil. Trans. R. Soc. Lond. A 223, 289.
- TENNEKES, H and LUMLEY, J. L. A First Course in Turbulence. The MIT Press, 1972.
- WEI, T.; KLINE, E. M.; K-LEE, S. and WOODRUFF, S., 1992, Gortler vortex formation at the inner cylinder in Taylor-Couette flow. *J. Fluid Mech.*, 245, 47.

MEASUREMENTS OF VELOCITY AND TEMPERATURE IN TURBULENT FLOW USING LASER PHOTOTHERMAL EFFECT WITH THE NEW INTERFEROMETERS

Noboru Nakatani*, Takanori Oshio* and Toshiya Sakabe**

*Ashiya University
13-22, Rokurokuso-cho, Ashiya, Hyogo 659, Japan
**Nara National College of Technology
22, Yata-machi, Yamato-kooriyama, Nara 639-11, Japan

ABSTRACT

This paper describes measurements of velocity and temperature using photothermal effect in turbulent flow. We developed a new differetial interferometer for detecting small phase variation caused by photothermal effect without influence of turbulent phase fluctuation. The detected fringe point of the interferometer is scanned repeatedly by moving a photomultiplier. An electric system for operarting compulsorilly the interferometer at maximum inclination point of fringe intensity curve is constructed. Using jet of nitrogen gas mixed with ethylene gas, it is confirmed that this method is a useful tool to measure velocity and temperature in turbulent flow. Lastly, the advanced interferometers are proposed.

1. INTRODUCTION

The laser Doppler velocimeter (LDV), which has some advantages such as non-perturbing quality, capability of remote operation and high spatial resolution, has been well developed to measure flow velocity. However, the LDV [Durst, Melling and Whitelaw (1981)] needs to seed scattering particles in flow. Recently, to be freed from this problem, velocimeters using photothermal effect have been investigated [Nie, Hane and Gupta (1986)]. In this study we investigated on measurements of flow velocity and temperature using laser photothermal effect. The non-intrusive methods of temperature measurement in a flame that have been proposed and demonstrated (CARS [Attal, Mueller-Dethlefs, Debarrc and Taran(1982)] or LIF [Daily (1977)] rely on a measurement of Boltzman dsitribution among rotational sublevels of the molecules. Therefore, one must assume that the thermal equilibrium exists, which is not always found to be the case. These techniques have further following problems; Signal intensity obtained by CARS is very weak because of using non-linear effect. LIF is suffered from quenching effect. Photo-acoustic deflection spectroscopy free from these problems was proposed by Rose, Salamo and Gupta (1984) to measure gas temperature. Propagation velocity of a photoacoustic pulse (sound) produced by the heating and the thermal expansion of the pump laser-irradiated region is detected by deflection of probe beams. The fast refractive variation caused by the sound is about a fifth of that caused by a photothermal effect. We needed to increase detection sensitivity for obtaining reliable data. The fiber heterodyne interferometer which we developed [Nakatani et al. (1989), (1991)] can not be used for this purpose because of low response. In the previous study, in order to increase the detection sensitivity of the fast refractive variation, we developed a differential interferometer [Nakatani et al.(1994)]. The operation point of the interferometer is set on the maximum inclination of fringe intensity curve by the use of a piezomechanical translator. The time-of-flight method measuring the difference between phase at two focal points was used for measuring flow velocity and temperature. In turbulent flow, however, it is difficut to set the operation point of this interferometer because of the large phase vari-

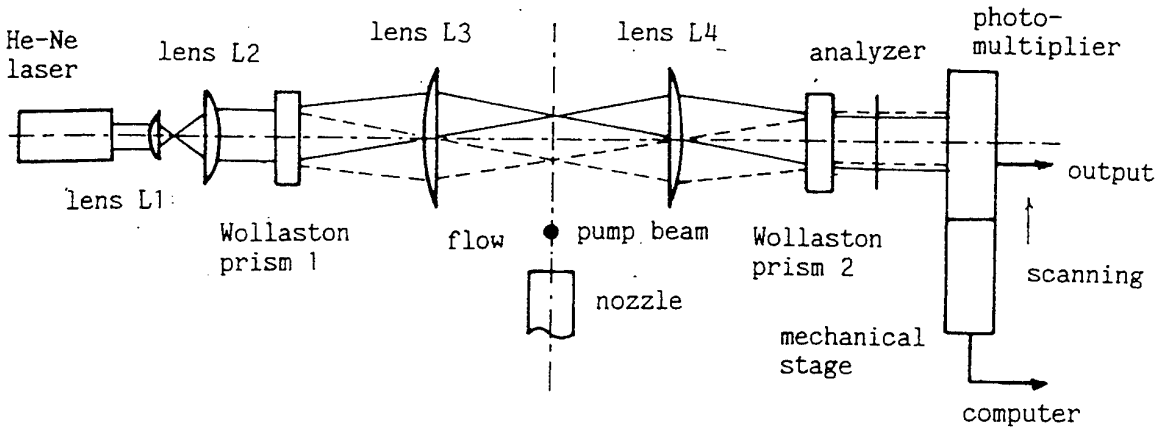

Figure 1 Schematic diagram of a new differential interferometer for measurements of velocity and temperature in turbulent flow using laser photothermal effect. The interferometer is compulsorily operated at maximum inclination point of fringe intensity curve by an electric system.

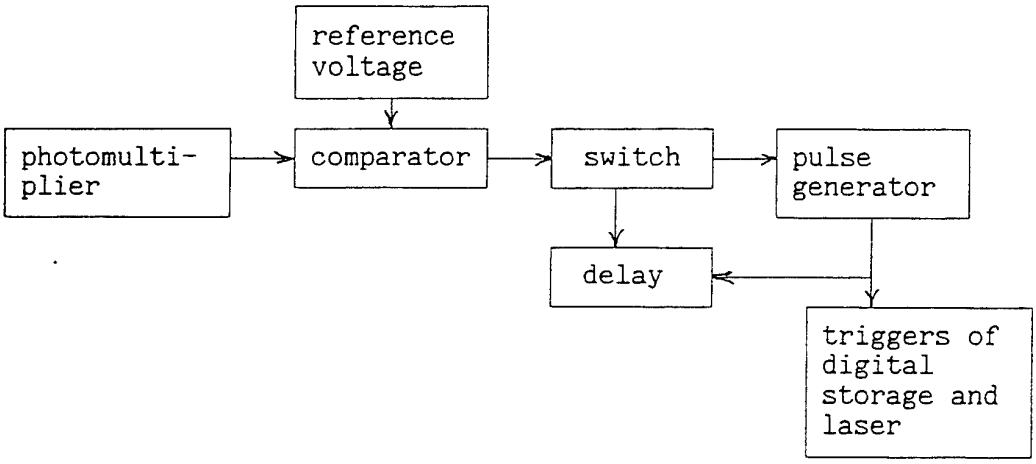

Figure 2 Block diagram of an electric system for operating compulsorily the interferometer at maximum inclination point of fringe intensity curve.

ation around a limited measuring part.

In this study for eliminating this difficulty we describes a new differential interferometer operated compulsorily at maximum inclination point of fringe intensity curve by an electeric system. Using turbulent jet of nitrogen gas mixed with ethylene gas, it is confirmed that this method is a useful technique to measure temperature and velocity in turbulent flow. Lastly, two new interferometers using fibers and phase conjugators are proposed.

2. NEW DIFFERENTIAL INTERFEROMETERS

A laser beam is passed through a Wollaston prism for dividing two beams and obtaining two focal points of time-of-flight method. The detection point of the two beam interferece fringes is scanned repeately by moving the photomultiplier and the electric triggering system is used for operating com-

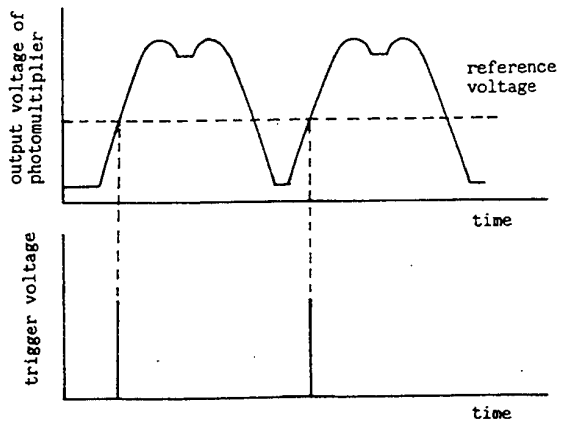

Figure 3 Triggering data storage in the electric system shown in Fig. 2.

pulsorily the interferometer at maximum inclination point of fringe intensity curve. The experimental set up of the constructed interferometer is shown in Figure 1. A He-Ne laser of wavelength 632 nm, power 5 mW and beam diameter 1 mm was used as the light source. The laser beam is expanded to 10 mm diameter by lenses L1 and L2 for making focal point small. The expanded two beams is passed through a Wollaston prism 1 of 10 mrad or 2.5 mrad in dividing angle α for dividing two beams. The divided beams are focused on two points with a spherical lens L3 of F_3= 100 mm or 200 mm in focal length. The distance between the two focal points is 0.5 mm, 1 mm and 2 mm for α = 2.5 mrad and F_3= 200 mm, α = 10 mrad and F_3= 100 mm, and α = 10 mrad and F_3 = 200 mm, respectively. When puff of phase variation by photothermal effect passes through the two focal point, the phases of the beams is varied. The beams are collimated with a spherical lens L4 of 100 mm or 200 mm in focal length, and are passed through a Wollaston prism 2 of 2.5 mrad or 10 mrad in combining angle α for combining two beams and increasing visibility of interference fringe. The Wollaston prism 2 is set at a little back distance from the back focal point of the lens L4 for making broad interference fringes. The two beams of orthogonally electric vectors are interferenced through an analyzer. The interference light is received with a photomultiplier through a rectangular slit of 1 mm x 150 μm for increasing visibility. The difference between the phases of the beam for upstream focal point and the beam for downstream focal point changed the intensity of interference fringe. As the two beams are close to each other, the phase variation at the two focal points is detected mainly. The fringe detecting point of the interferometer is scanned repeatedly by moving a photomultiplier for searching maximum inclination point of fringe intensity curve. The photomultiplier is mounted on a mechanical stage driven by a step motor. The output of the photomultiplier is put into an electric triggering system and a data storage. The electric triggering system is constructed for operating compulsorily the interferometer at maximum inclination point of fringe intensity curve. The trigger pulse is used for triggering a pumping pulse laser and the data storage. The block diagram of the electric triggering system is shown in Figure 2. The output voltage V_P of the photomultiplier is compared with the reference voltage V_R set the voltage at the maximum inclination point of fringe intensity curve. When V_P crosses either over V_R or under, a pulse geneartor generates a pulse for triggering a digital storage and a pumping laser as shown in Figure 3. After 1.5 s from a pulse generation, the pulse generator is switched on again by the pulse passed through the delay. A TEA CO_2 pulse laser is used as a pumping beam to produce photoacoustic sound and phtothermal puff. The time-of-flight method is used to measure photoacoustic sound-velocity for gas temperature measurement and velocity of photothermal puff for flow velcoty measurement. The analyzing method of the signals of the interferometer was described [Nakatani et al. (1994)] for obtaining sound velocity and flow velocity.

An advanced differential interferometer using fibers and a laser diode is shown in Figure 4. This system is compact in light source part and need not move the detector for scanning fringe compared with the Figure 1. The current modulation of a laser diode driver leads to the wavelength modulation of the laser diode. The output of the laser diode is divided into two beams by the use of

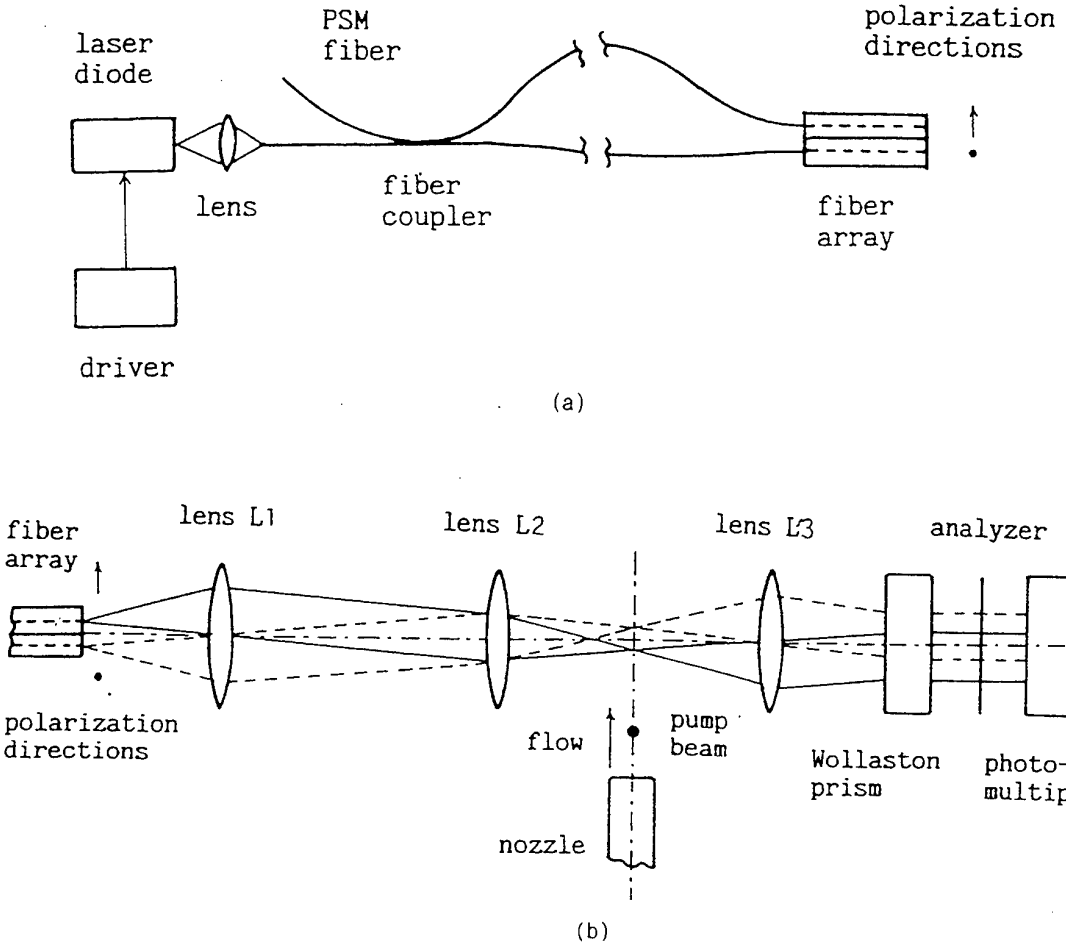

Figure 4 Schematic diagram of a differential interferometer using a laser diode and fibers. (a): Light source part, (b): measuring part.

a fiber couppler. One output fiber of the couppler is longer than that of another fiber for moduating interference fringe. The end part of the output fibers is paralell to each fiber and a fiber array. The two output beams are collimated by a lens L1 and are focused by a lens L2. The focal points are measuring part. The beams are collimated by a lens L3 and are passed through a Wollaston prism for combining two beams and increasing visibility. The Wollaston prism is set at a little back distance from the back focal point of the lens for making broad interference fringes. The two beams of orthogonally electric vectors are interferenced through an analyzer. The light of the interference fringe is received by a photodetector. The operation point of the interference fringe can be scanned by the modulation fringe without moving the detector. The electric system shown in Fig. 2 is used for operating compulsorily the interferometer at maximum inclination point of fringe intensity curve.

A new constructed fiber interferometer using two self-pumped phase conjugater (SPPC) is shown in Figure 5 for eliminating the influence of phase variations in the fiber used and around limited measuring part. A photo-refractive crystal of Ce-$BaTiO_3$ is used as the SPPC. The response time of the crystal

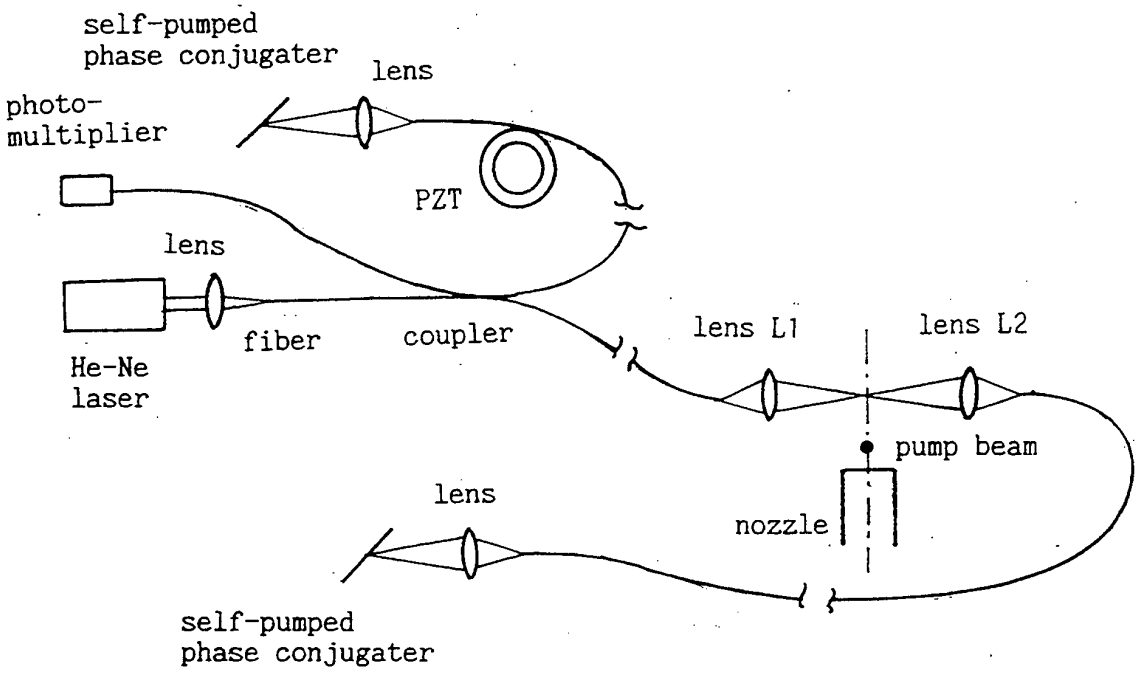

Figure 5 Schematic diagram of a fiber interferometer using two self-pumped phase conjugators for measurements of velocity and temperature in turbulent flow of a large flow field.

to phase variation is 1 s. This interferometer is useful to eliminate the influence of slow phase variation. The length of the measuring part can be changed by changing the focal lengths of the lenses L1 and L2. The operation point of the interference fringe can be scanned by the use of a piezo mechanical translator (PZT). The electric system shown in Fig. 2 is used for operating compulsorily the interferometer at maximum inclination point of fringe intensity curve. This interferometer is useful to measure large flow field.

3. PHASE FLUCTUATION OF THE DIFFERENTIAL INTERFEROMETER IN TURBULENT FLOW MEASUREMENT

We investigated on phase fluctuation of the differetial interferometer shown in Figure 1 in various optical parameters in turbulwnt flow meaurement. The nozzle of 4.7 mm in diameter is used. Nitrogen gas mixed with ethylene gas is used as a fluid. Reynolds number is 3400. The phase variation arises from large-scale air entrainment by the jet and turbulent mixing. The output variations of the photomultiplier were measured in various optical parameters. The power spectrum densities of the outputs are shown in Figure 6. Figures (a)$\sim$(c) are in turbulent state and (d) is in laminar state. Figure (a) (the focal length of the lens L3 F_3 = 100 mm, the dividing angle of the Wollaston prism 1 α = 10 mrad, the distance between two focal points d = 1.0 mm) shows largest phase variation because of largest focusing angle. The phase variation of Figure (b) (F_3 = 200 mm, α = 10 mrad, d = 2.0 mm) is larger than that of Figure (c) (F_3 = 200 mm, α = 2.5 mrad, d = 0.5 mm) because of large distance between two focal points. The power spectrum densities in the optical conditions (a)$\sim$(c) and in laminar state are same as shown in Figure (d).

To reduce the influence of phase fluctuation in turbulent flow, it is concluded that the focal length of the focusing lens should be made longer and that the distance between the two focal points should be made shorter.

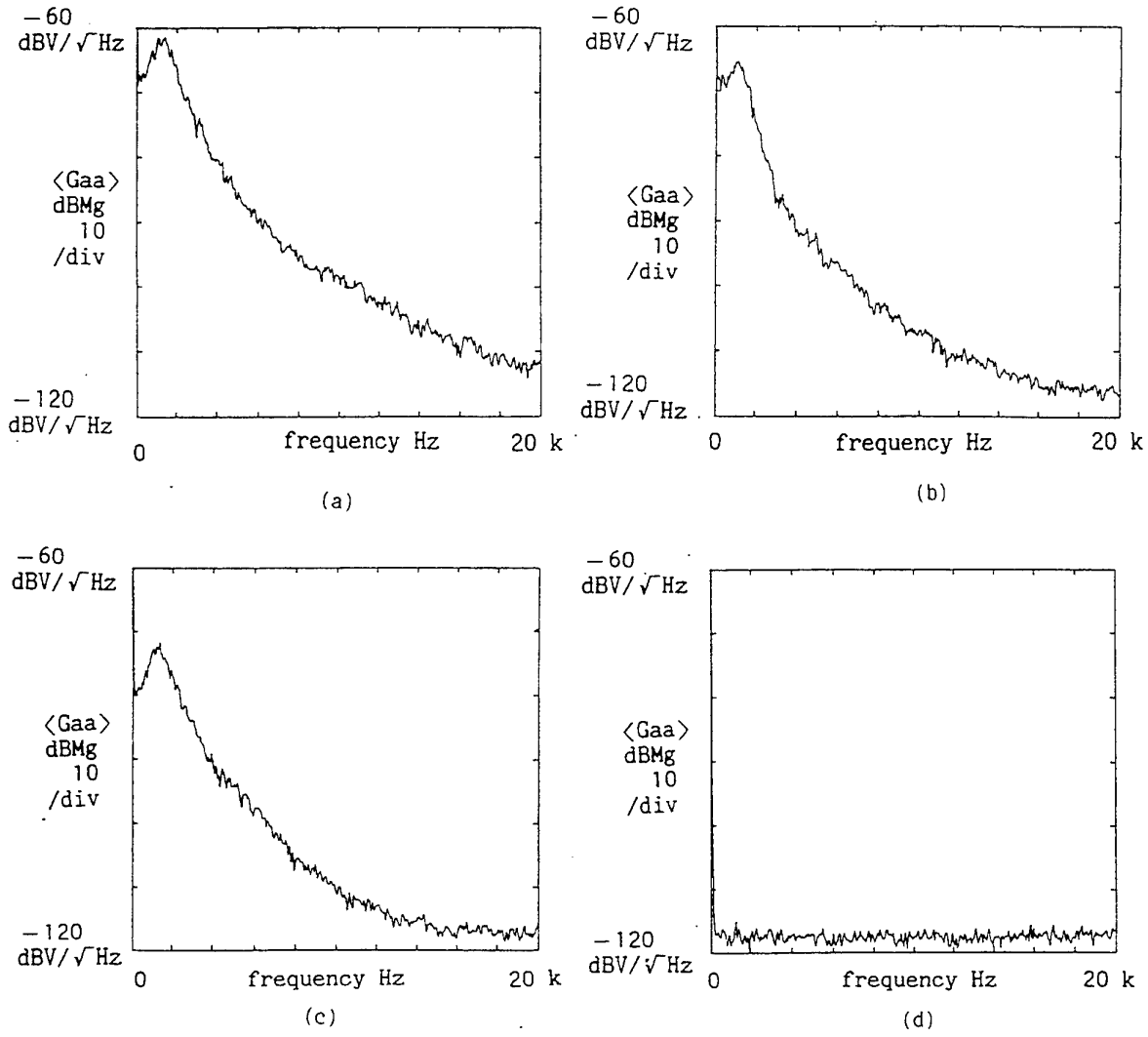

Figure 6 Power spectrum densities of fluctuation of phase difference. (a) ~ (c) are in turbulent state. 0 dBv = 8.35 λ (λ : wavelength 632.8nm). (a): The focal length of the lens L3 F_3 = 100 mm, the divding angle of the Wollaston prism 1 α = 10 mrad, the distance between two focal points d = 1.0 mm, (b): F_3 = 200 mm, α = 10 mrad, d = 2.0 mm, (c): F_3 = 200 mm, α = 2.5 mrad, d = 0.5 mm, (d): in laminar state for optical conditions (a)~(c).

4. MEASUREMENT OF FLOW TEMPERATURE AND VELOCITY

Using jet of nitrogen gas mixed with ethylene gas, it is confirmed that this method is a useful technique for measuring flow temperature and velocity. The interferometer shown in Figure 1 was used in this experiment. In turbulent flow of Reynolds number 3400 the variation of phase difference put out from the photomultiplier is shown in Figure 7. Figure 8 shows a typical oscilloscope trace of a photoacoustic signal in temperature measurement. The trace shows that the measurement is not influenced with turbulent phase fluctuation. The velocity obtained from the elapsed time 2.70 μs and the distance between the two focal points d

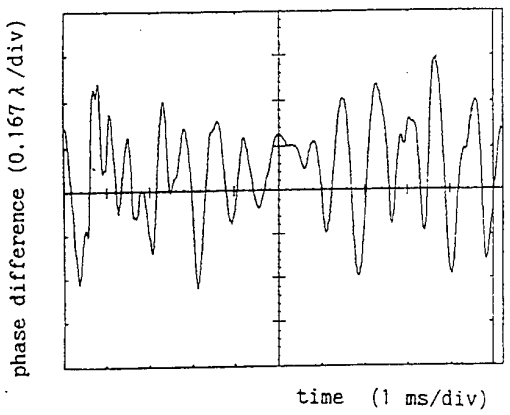

Figure 7 Typical oscilloscope trace of variation of phase difference in turbulent flow. Reynolds number is 3500. λ is wavelength.

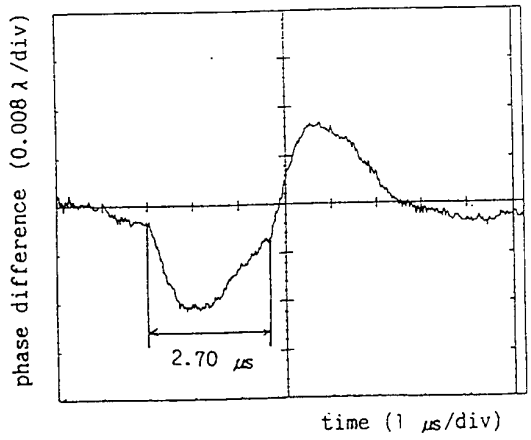

Figure 8 Typical oscilloscope trace of photoacoustic signal for temperature measurement in turbulent flow. The distance d between the two focal points is 0.98 mm.

= 0.98 mm is 363 m/s. Figure 9 shows a typical oscilloscope trace of a photothermal signal in flow velocity measurement. The trace shows that the measurement is not almost influenced with turbulent phase fluctuation. The flow velocity obtained from the elapsed time 75.3 μs and the distance between the two focal points d = 0.98 mm is 13.0 m/s.

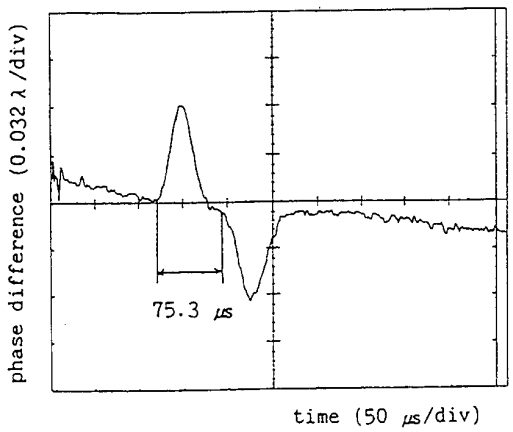

Figure 9 Typical oscilloscope trace of photothermal signal for measurement of velocity in turbulent flow. The distance d between the two focal points is 0.98 mm.

The sound velocity is 350 m/s. The temperature is given as

$$T = (M/\gamma(T)R) \cdot V_s^2, \qquad (1)$$

where M is average molecular weight of the gases in the flame, R is the universal gas constant, V_s is the sound velocity, and $\gamma(T)$ is the temperature-dependent average specific heat ratio at constant volume. The obtained temperature 297 k is almost same as room temperature. These experimental results show that the system is useful to measure velocity and temperature in turbulent flow.

ACKNOWLEDGEMENTS

The research work leading to this paper was performed under the supervision of President Satoru Ogasahara of Ashiya University.

REFERENCES

Attal, B., Mueller-Dethlefs, K., Debarrc, D. and Taran, J. P. E. 1982 Resonant CARS Spectroscopy of C_2. Appl. Phys. B 28, 121.
Daily, J. W. 1977 Saturation Effects in Laser Induced Fluorescence Spectroscopy. Appl. Opt. 16, 568.
Durst, F., Melling, A. and Whitelaw, J. H.

1981 Principles and Practice o f Laser-Doppler Anemometry. Academic Press.
Nakatani, N., Inagaki, J., Yamada, T. and Sakabe, T. 1989 A Photothermal Velocimeter Using an Optical Fiber Heterodyne Interferometer Free from External Disdturbance. Proc. of the 3rd Int. Conference on Laser Anemometry Advances and Applations, Swansea, 35.1.
Nakatani, N. and Oshio, T. 1991 A Photothermal Velocimeter Using an Optical Fiber Heterodyne Interferometer with Differentiation of Phases at Two Points. Applications of Laser Techniques to Fluid Mechanics, Springer-Verlag, Berlin, 331.
Nakatani, N., Oshio, T., Kataoka, T. and Kishida, K. 1991, Simultaneous Measurements of Flow Velocity and Concentration with a Photothermal Velocimeter Using an Optical Fiber Heterodyne Interferometer. Laser Anemometry Advances and Applications vol. 1, ASME, New York, 83.
Nakatani, N., Oshio, T., 1994 Measurements of Gas Flow Velocity and Temperature Using Laser Photothermal Effect with a Differential Interferometer. Proc. of the 7th Int. Symp. on Applications of Laser Techniques to Fluid Mechanics, Instituto Superior Tecnico, 32-5-1.
Nie, Y. X., Hane, K. and Gupta, R. 1986 Measurements of Very Low Gas Flow Velocities by Photothermal Deflection Spectroscopy. Appl. Opt. 25, 3247.
Rose, A, Salamo, G. J. and Gupta, R. 1984 Photoacoustic Deflection Spectroscopy: a New Specie-Specific Method for Combustion Diagnostics. Appl. Opt. 23, 781.

SESSION 16

Engines III

EVALUATION OF TIME AND SPATIAL TURBULENCE SCALES IN A D.I. DIESEL ENGINE

G. Valentino, M. Auriemma, F.E. Corcione, R. Macchioni, G. Seccia

Fluidynamics & Combustion Division
National Research Council, Istituto Motori, Naples, Italy

ABSTRACT

A general procedure to estimate time and spatial autocorrelation function of non-stationary in-cylinder LDV data is given. The method was applied to the tangential component of the instantaneous velocity within a motored single-cylinder d.i. Diesel engine (0.435 liter, 21:1 compression ratio) equipped with a re-entrant combustion chamber using a Laser Doppler Velocimetry (LDV) system. Moreover, a two-probe volume LDV system was used to measure directly the spatial autocorrelation coefficient along the radial direction of the tangential velocity component.

Measurements of the instantaneous velocity were carried out on a horizontal plane at 5 mm below the engine head for different radii from 70 degrees before TDC to 30 degrees after TDC of both the compression and expansion strokes. The engine was motored at 1,000, 1,500, and 2,000 rpm, respectively. An ensemble-averaging technique was performed to analyze data estimating the integral time scale from the single point autocorrelation function. The spatial integral length scale was also computed through the Taylor's hypothesis. Further, the direct estimate of the lateral integral length scale was also performed measuring the spatial autocorrelation coefficient of the velocity fluctuation for different separations.

1. INTRODUCTION

The complex nature of the flow field in an internal combustion engine in terms of its non-stationarity, and non-homogeneity has been a matter of investigation using both Hot Wire Anemometry (HWA), Tindal et al., 1982, Catania, 1985 and Laser Doppler Velocimetry (LDV), Witze et al., 1984, Bertoli et. al, 1985, Hall & Bracco, 1987, Fansler & French, 1988.

The turbulent field can be characterized by the following parameters: the mean motion, turbulence intensity, and spatial and time scale. However, the interpretation of the in-cylinder single-point measurements, to compute correctly those parameters, is still a matter of controversy. In fact, the development of algorithms suitable for processing the parameters of interest must challenge the presence of cycle-to-cycle variation in the mean flow that ranges on time scales of milliseconds that are the same orders of magnitude as typical temporal scales of turbulence, Catania & Mittica, 1990, Fraser & French, 1988. Moreover, to give reliable results on spatial scales, simultaneous multi-point measurements should be made to evaluate the integral length scale without invoking the Taylor's hypothesis. During the last decade measurements of the lateral integral length scale have been made in engines by simultaneous multi-point measurements in a variety of engine speed and combustion chamber shape, Ikegami et al., 1987, Glover et al., 1988, Fraser & Bracco, 1988, Corcione & Valentino, 1990. The characterization of the flow in terms of turbulent scales is assuming an important role for the calibration of turbulence models in 3-D numerical codes, Han et al., 1996.

The present paper aims at focusing the procedure to evaluate time and spatial scale from LDV measurements carried out within a single cylinder direct injection (d.i.) diesel engine. Both, single point and multi-point measurements have been carried out during compression and expansion to provide results of integral time and spatial scale. The paper is organized as follows: in the next section the experimental set-up is given, while the section following gives detail about the time and spatial autocorrelation procedure. Further, will be given the results and a summary of the main points obtained.

2. EXPERIMENTAL SET-UP

2.1 Engine

Tests were carried out on an optically accessed engine able to run at high speed without lubricating oil. The engine, representative of a modern light-duty Diesel engine for passenger cars, was manufactured by modifying a commercial single-cylinder diesel engine of 86 mm bore, 75 mm stroke, and a volumetric compression ratio of 21:1. To use combustion chambers with different geometry and to make LDV measurements along horizontal planes located at different distance below the engine head, the engine was equipped with a quartz window on the head. The size of the

quartz window (30 mm diameter) allowed to investigate the squish area and half part of the chamber even if the combustion bowl axis had an offset of 6 mm with respect to the cylinder axis. In order to avoid oil vapor within the measurement volume, the engine was run without lubricating oil using sealing bearings on the engine crank-shaft and connecting rod, and with auto-lubricating bronze-teflon piston rings. Moreover, to avoid the passage of oil vapor from the bottom of the engine towards the cylinder and combustion chamber, the engine crank-shaft was sealed. These devices greatly reduced the problem of window fouling and allowed the engine to run up to 15 min. at 1,000 rpm, 10 min. at 2,500 rpm. These temporal intervals were further increased using as seeding molybdenum disulfide (MoS_2), self-lubricating particles ($1\mu m$) instead of conventional titanium dioxide (TiO_2) particles that are very abrasive for pistons and cylinders.

2.2 LDV System

The LDV system comprises an argon-ion laser which utilizes the two lines at 488 and 514.5 nm, standard optics by Dantec working in backscatter mode, two photomultipliers, and two burst spectrum analyzers (BSA). The signal quality of the individual component was improved by introducing an optical fiber between the laser beam output and the standard optics. The system can extract Doppler frequencies from bursts with a very poor signal to noise ratio, and provides a high data rate at high engine speeds with more than 80% of validated data. An optical shaft encoder, with a basic resolution of 0.1 crank angle degree, was connected directly to the engine crank-shaft to drive a trigger device for the two BSA's. Data were sent to a PC computer via a IEEE488 parallel interface and analyzed off-line.

2.3 Two-Probe Volume LDV System

The system, used to make in-cylinder measurements of the spatial autocorrelation coefficient under motoring conditions, was a two-probe volume LDV system, Corcione et al., 1996, made by a four beam LDV system that produces two-probe volumes. One probe volume is fixed, another one can be moved from 0 to 15 mm, allowing the simultaneous measurement of the same velocity component in two adjacent spatial locations. First, the system was successfully tested in a cylindrical duct on a steady-state test rig in a flow with controlled grid-generated turbulence. The scattered light coming from the two-probe volumes is collected by the two photomultipliers and analyzed by the BSA's. The coincident data were checked by an off-line software based on the shaft-encoder resolution. The acceptance window width of coincident data was checked from 0.1 to 0.3 crank angle interval with no meaningful difference in the results. As a result, the coincidence interval was set at 0.2 degree at 1,000 rpm and 0.3 degree at 1,500 rpm ($33\mu s$ at both engine speeds)

The instantaneous tangential component of the velocity was measured at 1,000 , 1,500, and 2,000 rpm in the crank angle range of 100 degrees about TDC: from -70° before TDC to 30° after TDC. Figure 1 shows the gometry of the combustion chamber used in the present tests and the location of the measurement points (A, B). Measurements of the tangential velocity component were taken on the horizontal plane at z=5 mm below the engine head and at 20, and 16 mm from the cylinder axis, respectively. Further, the lateral integral length scale was directly computed, at r=20 mm (A) from the cylinder axis, as the integral of the spatial autocorrelation coefficient measured for adjacent separations at 1,000 and 1,500 rpm. MoS_2 particles of about $1\mu m$ were supplied, by means of a cyclone chamber, into the intake duct. Data treatment was performed using ensemble-averaging the instantaneous velocity data collected on about 1,000 consecutive engine cycles in which the data validation was in the range 80 to 90% depending on the engine speed.

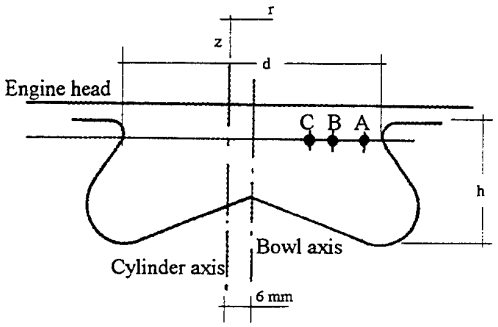

Figure 1. Combustion chamber shape and location of measurement points.

3. DATA PROCESSING

3.1 Time Autocorrelation Function

For a given stationary flow and a fixed point P of the flow field, denoted $\underline{U}(t)$ the fluid velocity vector at the instant t and (x_1, x_2, x_3) three cartesian axes, let put $U_k(t)$ the velocity component for the generic x_k axis. Referring from now on to a particular component $U_k(t)$, we will simply denote it $U(t)$. In the conventional statistical approach, averaging with respect to time, it's possible to evaluate a mean velocity $\overline{U}$, a fluctuation u about the mean velocity, and a turbulence intensity $u' = \sqrt{\overline{[u(t)]^2}}$ Hinze,1975. Considering all pairs of velocities $U(t)$ and $U(t+\Delta t)$ for a fixed delay time Δt, a *time autocorrelation coefficient* (TAC) can be defined as:

$$R_t(\Delta t) = \frac{\overline{u(t)u(t+\Delta t)}}{u'^2}$$

$$\overline{u(t)u(t+\Delta t)} = \lim_{T\to\infty} \frac{1}{T}\int_0^T u(t)u(t+\Delta t)dt$$

This coefficient should be regarded as an index which expresses how well fluctuations remember their earlier behavior after a time delay Δt.

If we take into account non-stationary flows, such as those within reciprocating engines, to compute the TAC the previous procedure must be reviewed, Fansler & French, 1988. In this case it's possible to generalize all the mentioned process considering N identical experiments i and referring to the velocities $U(P_0,t_0,i)$ collected for *homologous* points P_0 and instants t_0. It is possible to compute the TAC applying an *ensemble average procedure* to engine cycles that can be regarded as single experiments characterized by similar conditions. Particularly, homologous points P_0 will be defined by the same position P inside the cylinder while homologous instants t_0 will be characterized by the same crank-angle ϑ. Considering an ensemble of N engine-cycles, and denoted $U(\vartheta,i)$ the instantaneous velocity corresponding to the crank-angle ϑ and to the engine-cycle i, applying the ensemble-average technique, it will be possible to determine a mean velocity $\overline{U(\vartheta)}$, a fluctuation $u(\vartheta,i)$ of the instantaneous velocity about the mean velocity itself, and a turbulence intensity $u'(\vartheta)=\sqrt{\overline{[u(\vartheta,i)]^2}}$. For a fixed pair of crank angles ϑ and $\vartheta+\Delta\vartheta$, considering the contributions of all engine-cycles, the TAC will be then defined as:

$$R_t(\vartheta,\Delta\vartheta)=\frac{\overline{u(\vartheta)u(\vartheta+\Delta\vartheta)}}{u'(\vartheta)u'(\vartheta+\Delta\vartheta)}$$

where:

$$\overline{u(\vartheta)u(\vartheta+\Delta\vartheta)}=\frac{1}{N}\sum_{i=1}^{N}u(\vartheta,i)u(\vartheta+\Delta\vartheta,i)$$

The TAC, hence, defines the correlation between fluctuations related to different crank angles ϑ comparing their distribution about the mean velocity. For each ϑ it will be possible to determine a function $R_t(\vartheta=const,\Delta\vartheta)$ which shows the correlation between velocities versus time delay. It must be noted that this procedure does not consider the possibility that some of the velocities $U(\vartheta,i)$ could be missing. In fact, collecting data by in-cylinder LDV measurements, for each engine-cycle there could be some crank angles having missing data. Since we need to work only on collected data, the problem can't be solved interpolating missing data and the procedure will have to be further refined. If, at the crank angle ϑ, we denote $N_{(\vartheta)}\le N$ the number of cycles in which the velocity $U(\vartheta,i)$ is valid, in order to consider the chance of missing data, first of all we should define the mean velocity and the turbulence intensity as follows:

$$\overline{U(\vartheta)}=\frac{1}{N_{(\vartheta)}}\sum_{i=1}^{N}U(\vartheta,i)\qquad u'(\vartheta)=\sqrt{\frac{1}{N_{(\vartheta)}}\sum_{i=1}^{N}[u(\vartheta,i)]^2}$$

where contributions to the summation exist only for cycles in which the velocity $U(\vartheta,i)$ exists. Now if, related to a fixed pair of crank angles $(\vartheta,\Delta\vartheta)$, we denote $N_{(\vartheta,\Delta\vartheta)}\le\left\{N_{(\vartheta)},N_{(\vartheta+\Delta\vartheta)}\right\}\le N$ the number of cycles in which both velocities $U(\vartheta,i)$ and $U(\vartheta+\Delta\vartheta,i)$ are valid, the term $\overline{u(\vartheta)u(\vartheta+\Delta\vartheta)}$ can be computed as follows:

$$\overline{u(\vartheta)u(\vartheta+\Delta\vartheta)}=\frac{1}{N_{(\vartheta,\Delta\vartheta)}}\sum_{i=1}^{N}u(\vartheta,i)u(\vartheta+\Delta\vartheta,i)$$

where contributions to the summation exist only when both velocities $U(\vartheta,i)$ and $U(\vartheta+\Delta\vartheta,i)$ in the cycle i are valid. Carrying out this procedure, it is possible to get quite correct results if $N_{(\vartheta,\Delta\vartheta)}$ is not too small compared to $N_{(\vartheta)}$ and $N_{(\vartheta+\Delta\vartheta)}$. In fact, the instantaneous velocities related to the valid fluctuations, contributing to the summation, represent a quite big part of those used to evaluate the mean velocities $\overline{U(\vartheta)}$ and $\overline{U(\vartheta+\Delta\vartheta)}$ which determine the value of the turbulence intensity and the TAC itself. We want to point out that, for a fixed pair of instants $(\vartheta,\Delta\vartheta)$, the formula of the TAC was initially made to compare the distributions of the velocities about their mean velocity. In detail, the formula of the TAC was made to work on fluctuations about a mean velocity evaluated considering only those velocities related to the valid fluctuations contributing to the TAC. Therefore, the TAC can be computed taking into account, for each pair of instants $(\vartheta,\Delta\vartheta)$, the mean velocity, the fluctuation, and the turbulence intensity based just on the contribution of those cycles in which both velocities $U(\vartheta,i)$ and $U(\vartheta+\Delta\vartheta,i)$ are valid. Denoted $U_{(\vartheta,\Delta\vartheta)}$ the velocities belonging to those cycles in which both velocity estimates are valid and sorted them as a series from 1 to $N_{(\vartheta,\Delta\vartheta)}$ it can be written that:

$$\exists\begin{Bmatrix}U(\vartheta,i)\\U(\vartheta+\Delta\vartheta,i)\end{Bmatrix}\Leftrightarrow\begin{Bmatrix}U_{(\vartheta,\Delta\vartheta)}(\vartheta,j)=U(\vartheta,i)\\U_{(\vartheta,\Delta\vartheta)}(\vartheta+\Delta\vartheta,j)=U(\vartheta+\Delta\vartheta,i)\end{Bmatrix}$$

$$\text{with}\quad\begin{cases}i=1,\dots,N\\j=1,\dots,N_{(\vartheta,\Delta\vartheta)}\end{cases}$$

Considering only the contribution of these velocities, we may define, at the crank angle ϑ (the same for $\vartheta+\Delta\vartheta$), the mean velocity, the fluctuation, and the turbulence intensity as:

$$\overline{U_{(\vartheta,\Delta\vartheta)}(\vartheta)} = \frac{1}{N_{(\vartheta,\Delta\vartheta)}} \sum_{j=1}^{N_{(\vartheta,\Delta\vartheta)}} U_{(\vartheta,\Delta\vartheta)}(\vartheta, j)$$

$$u_{(\vartheta,\Delta\vartheta)}(\vartheta, j) = U_{(\vartheta,\Delta\vartheta)}(\vartheta, j) - \overline{U_{(\vartheta,\Delta\vartheta)}(\vartheta)}$$

$$u'_{(\vartheta,\Delta\vartheta)}(\vartheta) = \sqrt{\frac{1}{N_{(\vartheta,\Delta\vartheta)}} \sum_{j=1}^{N_{(\vartheta,\Delta\vartheta)}} \left[u_{(\vartheta,\Delta\vartheta)}(\vartheta, j)\right]^2}$$

Finally, the TAC will be defined as:

$$R_t(\vartheta, \Delta\vartheta) = \frac{\overline{u_{(\vartheta,\Delta\vartheta)}(\vartheta) u_{(\vartheta,\Delta\vartheta)}(\vartheta + \Delta\vartheta)}}{u'_{(\vartheta,\Delta\vartheta)}(\vartheta) u'_{(\vartheta,\Delta\vartheta)}(\vartheta + \Delta\vartheta)}$$

$$\overline{u_{(\vartheta,\Delta\vartheta)}(\vartheta) u_{(\vartheta,\Delta\vartheta)}(\vartheta + \Delta\vartheta)} =$$

$$= \frac{1}{N_{(\vartheta,\Delta\vartheta)}} \sum_{j=1}^{N_{(\vartheta,\Delta\vartheta)}} u_{(\vartheta,\Delta\vartheta)}(\vartheta, j) u_{(\vartheta,\Delta\vartheta)}(\vartheta + \Delta\vartheta, j)$$

The possibility to estimate the TAC for a fixed pair of crank angles $(\vartheta, \Delta\vartheta)$ is connected to the assumption that:

$$N_{(\vartheta,\Delta\vartheta)} \geq N_{min} > 0$$

where $N_{min} > 0$ is an arbitrary value chosen to achieve a confident statistics. To improve the statistics of TAC, each $R_t(\vartheta, \Delta\vartheta)$ has been replaced with a new one $R_{t_{ref}}(\vartheta, \Delta\vartheta)$ obtained by an average of all the $R_t(\vartheta', \Delta\vartheta)$ related to instants ϑ' internal to a *reference range* ξ_{ref} around ϑ sufficiently small to assume the velocity field *locally stationary* over the reference range. If $\gamma > 0$ is the encoder resolution while $\alpha = m\gamma$ and $\beta = m'\gamma$ (m, m' integer and positive) are the increments respectively of ϑ and $\Delta\vartheta$, we can denote $N_{ref} = 2n_{ref} + 1 = 2int(\xi_{ref} / 2\alpha) + 1$ the number of instants ϑ' internal to the reference range ξ_{ref} and $N'_{ref}(\vartheta, \Delta\vartheta) \leq N_{ref}$ the number of coefficients $R_t(\vartheta', \Delta\vartheta)$ really estimated in this range, so that:

$$R_{t_{ref}}(\vartheta, \Delta\vartheta) = \frac{1}{N'_{ref}(\vartheta, \Delta\vartheta)} \sum_{i=-n_{ref}}^{n_{ref}} R_t(\vartheta + i\alpha, \Delta\vartheta)$$

where, obviously, contributions to the summation exist only if it has been possible to estimate the coefficient $R_t(\vartheta + i\alpha, \Delta\vartheta)$. Using this procedure, a coefficient $R_{t_{ref}}(\vartheta, \Delta\vartheta)$ can be estimated even if $N_{(\vartheta,\Delta\vartheta)} < N_{min}$ provided that there is at least one instant $\vartheta' = \vartheta + i\alpha$ internal to ξ_{ref} for which: $N_{(\vartheta',\Delta\vartheta)} \geq N_{min}$. If some TACs are still missing they can be obtained by a linear interpolation. In this paper, using a 1,000-cycles ensemble, the TACs were estimated for the tangential component of the fluid velocity varying ϑ between -70 and +30° about the TDC with an increment $\alpha = 0.6$ ° and considering, for each ϑ, a series of instants $\vartheta + \Delta\vartheta$ obtained varying $\Delta\vartheta$ between 0 and 30° with an increment $\beta = \alpha$; the value of N_{min} was set to 20 but the values of the accepted $N_{(\vartheta,\Delta\vartheta)}$ ranged between 100 and 800 depending on the particular pair of crank angles. The reference range ξ_{ref} was set at 5°, having checked that this did not change the trend of the TACs.

Figure 2 shows an example of the autocorrelation function computed for the point B (r=16 mm from the cylinder axis) at $\vartheta = 0°\,(TDC)$, and three engine speeds. The plot shows a continuously decaying pattern, as could be expected for higher time delay, and a decrease of the integral below the curve, until $R_t \approx 0$, as the engine speed increases. Similar results were obtained at different crank angles and locations as will be reported in the following.

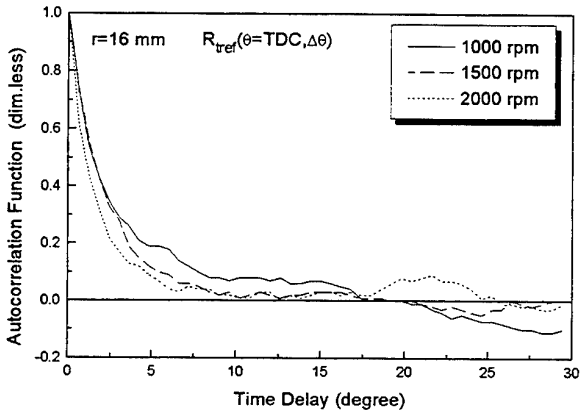

Fig. 2. Autocorrelation function estimated at $\vartheta = 0°\,(TDC)$

For each function $R_{t_{ref}}(\vartheta = const, \Delta\vartheta)$, it's possible to determine an *integral time scale* defined as:

$$L_t(\vartheta) = \int_0^{\Delta\vartheta^*} R_{t_{ref}}(\vartheta, \Delta\vartheta) d(\Delta\vartheta)$$

where $\Delta\vartheta^*$ is the delay time $\Delta\vartheta$ corresponding to the first minimum where $R_t \approx 0$ or $R_t < 0$. To improve the statistical quality of $L_t(\vartheta)$, at each ϑ, an average of all the scales $L_t(\vartheta')$ was carried out for a *reference range* ψ_{ref} around ϑ small enough to consider the flow *locally stationary*. Given $K_{ref} = 2k_{ref} + 1 = 2int(\psi_{ref} / 2\alpha) + 1$, $L_{t_{ref}}(\vartheta)$ can be computed as:

$$L_{t_{ref}}(\vartheta) = \frac{1}{K_{ref}} \sum_{i=-k_{ref}}^{k_{ref}} L_t(\vartheta + i\alpha)$$

Further, for a stationary and homogeneous (*ergodic*) flow, in which fluctuations are low enough compared to the mean velocity, can be considered valid *Taylor's hypothesis*:

$$\frac{\partial}{\partial t} = -\overline{U}\frac{\partial}{\partial x}$$

where $\overline{U}$ is the time-average that, because of homogeneity, must be equal to the space-average. Although, the in-cylinder flow field is neither stationary nor homogeneous, and fluctuations are often quite big compared to the mean velocity, we can generalize the Taylor's hypothesis assuming the flow field *locally stationary and homogeneous*. Therefore, passing through Taylor's hypothesis, it's possible to define the *integral longitudinal length scale* as:

$$L_{f_T}(\vartheta) = \overline{U(\vartheta)} L_{t\,ref}(\vartheta)$$

where the index T highlights the assumption of Taylor's hypothesis. Finally, for *isotropic turbulence*, the *lateral length scale* is given by the following equation:

$$L_{g_T}(\vartheta) = \frac{L_{f_T}(\vartheta)}{2}$$

3.2 Spatial Autocorrelation Function

Considering the non-stationary and non-homogeneous in-cylinder flow, denoted (x_1, x_2, x_3) the cartesian axes, let put $P \equiv (x_1,0,0)$ a particular location of the flow field on the x_1 axis. Denoted $U_k(x_1,\vartheta,i)$ the fluid velocity component for the generic x_k axis, the location P, the crank angle ϑ and the engine-cycle i, carrying out ensemble-averages, it's possible to define a mean velocity $\overline{U_k(x_1,\vartheta)}$, a fluctuation $u_k(x_1,\vartheta,i)$ about the mean velocity itself and a turbulence intensity $u'_k(x_1,\vartheta,i) = \sqrt{\overline{[u_k(x_1,\vartheta,i)]^2}}$. If we consider another point $P' \equiv (x_1 + \Delta x_1,0,0)$, in relation to the velocity component U_k, it's possible to define a *spatial autocorrelation coefficient* R_{sk} as:

$$R_{sk}(x_1,\Delta x_1,\vartheta) = \frac{\overline{u_k(x_1,\vartheta)u_k(x_1+\Delta x_1,\vartheta)}}{u'_k(x_1,\vartheta)u'_k(x_1+\Delta x_1,\vartheta)}$$

$$\overline{u_k(x_1,\vartheta)u_k(x_1+\Delta x_1,\vartheta)} = \frac{1}{N}\sum_{i=1}^{N} u_k(x_1,\vartheta,i)u_k(x_1+\Delta x_1,\vartheta,i)$$

In particular, we will obtain the *longitudinal autocorrelation coefficient* when $k = 1$ while we will have the *lateral autocorrelation coefficient* $k = 2,3$. In order to estimate these coefficients, it's necessary to collect data by simultaneous measurements in two different locations corresponding to the points $P \equiv (x_1,0,0)$ and $P' \equiv (x_1 + \Delta x_1,0,0)$, respectively. Facing the problem of missing data, denoted $U_{k(x_1,\Delta x_1)}(x_1,\vartheta,i)$ and $U_{k(x_1,\Delta x_1)}(x_1+\Delta x_1,\vartheta,i)$ the coincident velocities U_k really collected at the same crank angle ϑ of the same cycle i in both locations, and $N_{(x_1,\Delta x_1)}(\vartheta) \le N$ the total number of these coincident velocities it is possible to sort these velocities as a series from 1 to $N_{(x_1,\Delta x_1)}(\vartheta)$:

$$\exists\begin{Bmatrix} U_k(x_1,\vartheta,i) \\ U_k(x_1+\Delta x_1,\vartheta,i) \end{Bmatrix} \Leftrightarrow$$

$$\Leftrightarrow \begin{Bmatrix} U_{k(x_1,\Delta x_1)}(x_1,\vartheta,p) = U_k(x_1,\vartheta,i) \\ U_{k(x_1,\Delta x_1)}(x_1+\Delta x_1,\vartheta,p) = U_k(x_1+\Delta x_1,\vartheta,i) \end{Bmatrix}$$

$$\text{with } \begin{cases} i = 1,\ldots,N \\ p = 1,\ldots,N_{(x_1,\Delta x_1)}(\vartheta) \end{cases}$$

Based on the contribution of coincident data, it is possible to evaluate a mean velocity, a fluctuation, and a turbulence intensity as follows:

$$\overline{U_{k(x_1,\Delta x_1)}(x_1,\vartheta)} = \frac{1}{N_{(x_1,\Delta x_1)}(\vartheta)} \sum_{p=1}^{N_{(x_1,\Delta x_1)}(\vartheta)} U_{k(x_1,\Delta x_1)}(x_1,\vartheta,p)$$

$$u_{k(x_1,\Delta x_1)}(x_1,\vartheta,p) = U_{k(x_1,\Delta x_1)}(x_1,\vartheta,p) - \overline{U_{k(x_1,\Delta x_1)}(x_1,\vartheta)}$$

$$u'_{k(x_1,\Delta x_1)}(x_1,\vartheta) = \sqrt{\frac{1}{N_{(x_1,\Delta x_1)}(\vartheta)} \sum_{p=1}^{N_{(x_1,\Delta x_1)}(\vartheta)} \left[u_{k(x_1,\Delta x_1)}(x_1,\vartheta,p)\right]^2}$$

R_{sk} is then defined as:

$$R_{sk}(x_1,\Delta x_1,\vartheta) = \frac{\overline{u_{k(x_1,\Delta x_1)}(x_1,\vartheta)u_{k(x_1,\Delta x_1)}(x_1+\Delta x_1,\vartheta)}}{u'_{k(x_1,\Delta x_1)}(x_1,\vartheta)u'_{k(x_1,\Delta x_1)}(x_1+\Delta x_1,\vartheta)}$$

$$\overline{u_{k(x_1,\Delta x_1)}(x_1,\vartheta)u_{k(x_1,\Delta x_1)}(x_1+\Delta x_1,\vartheta)} =$$

$$= \frac{1}{N_{(x_1,\Delta x_1)}(\vartheta)} \sum_{p=1}^{N_{(x_1,\Delta x_1)}(\vartheta)} u_{k(x_1,\Delta x_1)}(x_1,\vartheta,p)u_{k(x_1,\Delta x_1)}(x_1+\Delta x_1,\vartheta,p)$$

Obviously, it is possible to estimate R_{sk} only if $N_{(x_1,\Delta x_1)}(\vartheta) \ge N'_{min} > 0$, applying a linear interpolation to each function $R_{sk}(x_1 = const, \Delta x_1 = const, \vartheta)$ to determine the missing coefficients. For each function $R_{sk}(x_1 = const, \Delta x_1, \vartheta = const)$, it's possible to determine a *longitudinal* and a *lateral integral length scale* as:

$$L_f(x_1,\vartheta) = \int_0^{\Delta x_1 *} R_{s1}(x_1,\Delta x_1,\vartheta)d(\Delta x_1)$$

$$L_{g_k}(x_1,\vartheta) = \int_0^{\Delta x_1 *} R_{sk}(x_1,\Delta x_1,\vartheta)d(\Delta x_1) \qquad k = 2,3$$

where $\Delta x_1 *$ is the separation Δx_1 corresponding to the first minimum where $R_{sk} \approx 0$. In the paper we assumed $x_1 \equiv r, x_3 \equiv z$, figure 1, while x_2 was assumed as the tangential direction and the lateral integral length scale was measured along the radial axis for the tangential component.

For isotropic turbulence $R_{s2} = R_{s3} \Rightarrow L_{g_2} = L_{g_3} = L_g$ and this is the assumption we made to compare these length scales with those obtained from the time scales passing trough Taylor's hypothesis.

4. RESULTS AND DISCUSSION

Figure 3 shows the integral time scale computed as the integral of the time autocorrelation function for the point located at r=16 mm from the cylinder axis at three engine speeds. To improve the statistics at each crank angle, L_t was averaged, as shown in the data processing section, setting the reference interval $\psi_{ref} = 7°$.

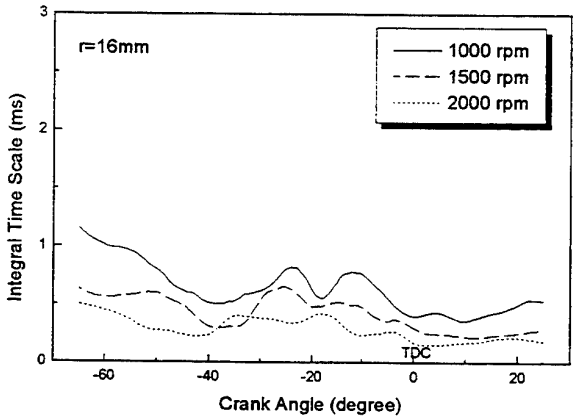

Fig. 3. L_t vs. crank angle at different speeds for r=16 mm.

Values of L_t ranged from a maximum of 1ms, in the middle of compression at 1,000 rpm, to a minimum of 0.2 ms, around TDC at 2,000 rpm, showing a decrease along the compression and an almost constant trend during the first 20° of the expansion. A similar result was obtained at r=20 mm from the cylinder axis, figure 4. The overall trend is an inverse scaling of the integral time scale with engine speed.

Figures 5 and 6 show the lateral integral length scale estimated through the Taylor's hypothesis for both locations. It can be noted a decrease of the lateral integral length scale along the compression stroke and a minimum of about 1 mm is reached around TDC for both locations. This trend is physically reasonable because spatial scales are sensitive to the global geometrical changes therefore, a reduction is expected as the piston approaches TDC. Moreover, $L_{g_T}(\vartheta)$ shows no sensitivity with engine speed. Focusing the attention on the figure 6, a decrease of integral length scale can be observed at 2,000 rpm. It can be explained considering the different behavior of the mean velocity and turbulence intensity for the location closer to the wall that gives higher values of fluctuation matched to a non-linear behavior for mean velocity at higher engine speeds, Corcione & Valentino, 1994.

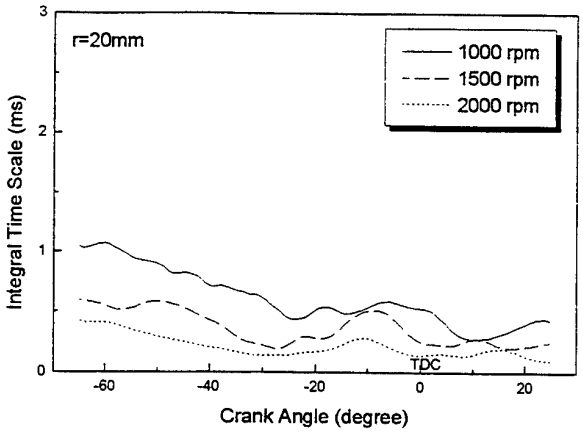

Fig. 4. L_t vs. crank angle at different speeds for r=20 mm.

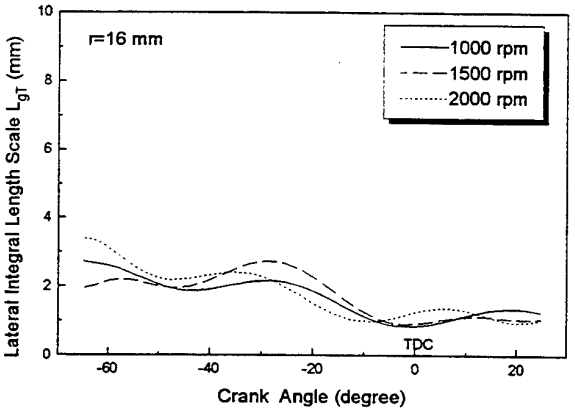

Fig. 5. L_{g_T} vs. crank angle at different speeds for r=16 mm

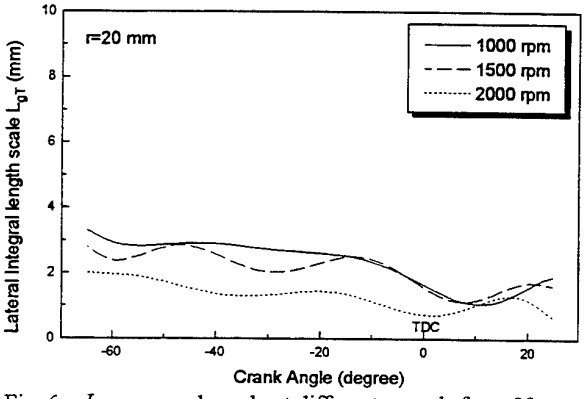

Fig. 6. L_{g_T} vs. crank angle at different speeds for r=20 mm

It is interesting to compare the lateral integral length scales estimated by using the Taylor's hypothesis and those computed by the direct measurement of the spatial autocorrelation coefficient. We want to remind that for the computation of the time autocorrelation function and spatial autocorrelation function only the ensemble averaged fluctuations have been involved therefore, the correlation

takes into account the behavior over all temporal and spatial scales.

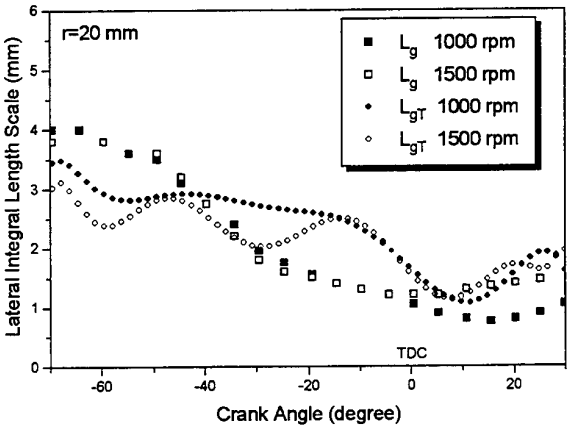

Fig. 7. L_{g_T} and L_g versus crank angle at two engine speeds.

Figure 7 shows the comparison between L_{g_T} and L_g at two engine speeds, 1,000 and 1,500 rpm, for the point located at r=20 mm from the cylinder axis. The results show that the overall range is between 1 and 4 mm but some differences between L_{g_T} and L_g exist. In fact, for both engine speeds, differences up to 40% are given during the compression stroke. The gap between L_{g_T} and L_g decreases approaching TDC in which almost overlapped values can be noted as consequence of a more isotropic turbulence around TDC. L_{g_T} and L_g show a decreasing trend along the compression and a light increase along the expansion. In addition, integral length scale, L_g, is not sensitive to engine speed along the compression stroke in which almost overlapped values have been obtained for both engine speeds tested. That can be explained considering that the integral length scale can be considered as a mean velocity times the integral time scale and reminding the different trend for the mean velocity and the integral time scale with engine speed. In fact, the mean velocity has a positive scaling (almost linearly) with engine speed, Corcione & Valentino (1994), whereas the integral time scale, as can be noted looking at figures 5 and 6, has a negative trend with engine speed.

5. CONCLUSIONS

A general method to compute time and spatial autocorrelation function for a non-stationary flow such as that within a reciprocating engine has been developed. The procedure, based on the analogy with stationary flows, computes time and spatial autocorrelation coefficients using an ensemble-averaging technique.

Experimental tests have been carried out to collect LDV data within the cylinder of a d.i. diesel engine, optically accessible. The instantaneous tangential velocity has been collected at three engine speeds, 1,000, 1,500, and 2,000 rpm, whereas two point simultaneous velocities have been collected, at 1,000 and 1,500 rpm, to compute the spatial autocorrelation coefficient.

Evaluation of integral time and spatial scale of turbulence performed by the non-stationary autocorrelation function has been a powerful method to investigate the turbulent structure of in-cylinder flow field. The analysis applied to the tangential velocity fluctuation has provided the following main results:

- the integral time scale decreases along the compression stroke, reaching a minimum around TDC. A more uniform distribution but with a light increase pattern during the first 20° of compression was found for both locations. Moreover, the integral time scale shows an approximate inverse scaling trend with engine speed.

- the integral spatial length scale computed by means the spatial autocorrelation function shows a decrease along the compression stroke, reaches a minimum of about 1 mm around TDC, and then increases along the expansion. Its comparison with values obtained from the integral length scale through the Taylor's hypothesis has shown that although, the trend is the same, a difference up to 40% remains.

6. NOMENCLATURE

K_{ref}, number of crank angles ϑ included in the reference range ψ_{ref}.

L_f, integral spatial longitudinal scale; L_{f_T}, integral spatial longitudinal scale obtained passing through Taylor's hypothesis.

L_g, spatial lateral integral scale; L_{g_T}, spatial lateral integral scale obtained passing through Taylor's hypothesis.

L_t, integral time scale; $L_{t_{ref}}$, integral time scale obtained by averaging all the $L_t(\vartheta)$ related to crank angles ϑ internal to the reference range ψ_{ref}.

N, number of cycles; $N_{(\vartheta)}$, number of valid velocities at the crank-angle ϑ; $N_{(\vartheta,\Delta\vartheta)}$, number of cycles in which velocities at the crank-angles ϑ and $\vartheta+\Delta\vartheta$ are valid; $N_{(x_j,\Delta x_j)}$, number of coincident velocities simultaneously collected in both locations x_j and $x_j+\Delta x_j$ in relation to a fixed ϑ.

N_{min}, minimum value accepted for $N_{(\vartheta,\Delta\vartheta)}$; N'_{min}, minimum value accepted for $N_{(x_j,\Delta x_j)}$

N_{ref}, number of crank angles ϑ in the reference range ξ_{ref}; N'_{ref}, number of $R_t(\vartheta, \Delta\vartheta)$ really estimated for a fixed $\Delta\vartheta$ and crank angles ϑ internal to the reference range ξ_{ref}.

R_t, time autocorrelation coefficient; $R_{t_{ref}}$, time autocorrelaion coefficient obtained by averaging all the $R_t(\vartheta, \Delta\vartheta)$ related to a fixed $\Delta\vartheta$ and to crank angles ϑ internal to the reference range ξ_{ref}.

R_s, spatial autocorrelation coefficient.

t, time.

U, instantaneous velocity; $\overline{U}$, ensemble-mean velocity; u, fluctuation about mean velocity; u', turbulence intensity.

$U_{(\vartheta,\Delta\vartheta)}$ instantaneous velocity belonging to one of those cycles in which both velocity estimates related to the crank angles ϑ and $\vartheta+\Delta\vartheta$ are valid; $\overline{U_{(\vartheta,\Delta\vartheta)}}$, ensemble-mean velocity; $u_{(\vartheta,\Delta\vartheta)}$, fluctuation about the mean velocity; $u'_{(\vartheta,\Delta\vartheta)}$, turbulence intensity.

$U_{(x_j,\Delta x_j)}$ instantaneous velocity simultaneously collected in both locations x_j and $x_j+\Delta x_j$; $\overline{U_{(x_j,\Delta x_j)}}$, ensemble-mean velocity; $u_{(x_j,\Delta x_j)}$, fluctuation about the mean velocity; $u'_{(x_j,\Delta x_j)}$, turbulence intensity.

x_j, cartesian axis.

α, increment of the crank-angle ϑ.

β, increment of the delay $\Delta\vartheta$.

γ, encoder resolution.

ϑ, crank-angle.

ξ_{ref}, reference range to average R_t,.

ψ_{ref}, reference range to average integral time scales.

Δ, difference; Δx_j*, separation along the x_j axis corresponding to the first minimum of $R_s(x_j = const, \Delta x_j, \vartheta = const)$; $\Delta\vartheta$*, time separation corresponding to the first minimum of $R_t(\vartheta = const, \Delta\vartheta)$.

$\exists$, symbol of existence

7. REFERENCES

Bertoli, C., Corcione, F.E., Police, G., Valentino, G., 1985, Effect of Inlet Port Geometry on Turbulent Air Flow in the Combustion Chamber of a Diesel Engine, Int. Symposium on Diagnostic and Modeling of Combustion in Reciprocating Engines, pp. 273-283, Tokyo.

Catania, F.E., 1985, Induction System Effects on the Fluid-Dynamics of a D.I. Automotive Diesel Engine, ASME Diesel & Gas Engines Symposium, ETCE, 85-DGP-11.

Catania, F.E. & Mittica, A., 1987, Induction System Effects on the Small Scale Turbulence in a High-Speed Diesel Engine, Energy-sources Technology Conference and Exhibition, New Orleans, 87-ICE-38.

Catania,F.E. & Mittica,A., 1990, Energy-sources Technology Conference and Exhibition, New Orleans, Paper 90-ICE-12.

Corcione, F.E. & Valentino, G., 1990, Turbulence Length Scale Measurements by Two-Probe-Volume LDA System, SAE paper 902080.

Corcione,F.E. & Valentino, G., 1994, Analysis of In-Cylinder Flow Processes by LDA, Combustion & Flame 99: 387-394.

Auriemma, M., Corcione F.E., Macchioni, R., Seccia, G., Valentino, G., 1996, LDV Measurements of Integral Length Scales in an IC Engine, SAE 961161.

Fansler, T.D & French, D.T., 1988, Cycle-Resolved Laser-Velocimetry Measurements in a Reentrant-Bowl-in-Piston Engine, SAE paper 880377.

Glover, A.R., Hundleby, G.E., Hadded, O., 1988, An Investigation into Turbulence in Engines using Scanning LDA, SAE paper 880379.

Hall, M.J. & Bracco, F.V., 1987, A Study of Velocities and Turbulence Intensities Measured in Firing and Motored Engines, SAE paper 870453.

Hadded, O., Denbratt, I., 1991, Turbulence Characteristics of Tumbling Air Motion in Four-Valve S:I: Engines and their Correlation with Combustion Parameters, SAE paper 910478

Han, Z., Reitz, R.D., Corcione, F.E., Valentino, G., 1996, Interpretation of $k-\varepsilon$ Computed Turbulence Length Scale Predictions for Engine Flows, To be presented at Twenty-sixth Int. Symposium on Combustion, Napoli.

Hinze, J.O.,1975, Turbulence, McGraw-Hill, New York.

Ikegami, M., Shioji, M., Nishimoto, K., 1987, Turbulence Intensity and Spatial Integral Scale During Compression and Expansion Strokes in a Four-Cycle Reciprocating Engine, SAE paper 870372.

Tindal, M.J., Williams, T.J., Aldoory, M., 1982, The Effect of Inlet Port Design on Cylinder Gas Motion in Direct Injection Diesel Engines, Flows in I.C. Engines, ASME, New York.

Witze, P.O., Martin, J.K., Borgnakke, C., 1984, Conditionally-Sampled Velocity and Turbulence Measurements in a Spark Ignition Engine, Combustion Science and Technology, Vol. 36, pp. 301-317.

CHARACTERISTICS OF FLOWS THROUGH THE INLET PORTS OF MULTI-VALVE ENGINES

Z. Mahmood, K. Ng and M. Yianneskis

Centre for Heat Transfer and Fluid Flow Measurement
Mechanical Engineering Department
King's College London
London. WC2R 2LS. U.K.

ABSTRACT

The in-cylinder flow motion in a Ford Zetec dual-intake valve engine has been examined experimentally by laser-sheet flow visualisation and laser-Doppler anemometry. For steady flow investigations, a replica of the engine inlet ports and cylinder was produced into a transparent Perspex block. A mixture of turpentine and tetraline liquids was employed as the working fluid. The influence of intake valve lift on flow structure was examined, initially with both inlet valves having equal lifts, and then with one inlet valve kept closed, to determine the effects of inlet valve disablement.

The results have been used to validate corresponding steady flow numerical investigations and good agreement is noted for mean velocity data. Simulations of flow in a Zetec engine under motored conditions are also presented, together with experimental data obtained using a 3D stereoscopic visualisation technique and an optical engine.

1. INTRODUCTION

The advantages of four-valve per cylinder technologies in spark-ignition (S.I.) engines over two-valve designs include greater volumetric efficiency, increased specific engine power output and higher fuel efficiency (Newton et al, 1989). The present trends towards the use of lean-burn strategies in multi-valve S.I. engine configurations have called for a comprehensive understanding of the manner in which pre-combustion in-cylinder flow fields may be manipulated, to create optimum levels of turbulence immediately prior to combustion.

A large number of studies have been made, in recent years, into the tumble and swirl motions produced in four-valve engines. Rönnbäck et al (1991) studied the effect of tumble intensity on pre-combustion turbulence. It was indicated that the kinetic energy imparted by a high-tumble design to the flow during induction is partly maintained during the compression stroke, and produces large turbulent length scales and turbulence intensities at the point of ignition. This was also noted by Omori et al (1991).

Kent et al (1989) tested six intake configurations, based on three cylinder head designs. They observed that tumble was the dominant motion when both intake valves were open, while strong swirl was created when one valve was kept closed. By adding valve masking to the open valve, the axis of the swirl was inclined, to introduce an intense tumble component to the flow.

In a combined steady flow and reciprocating engine study, Arcoumanis et al (1994) examined the tumble-generating characteristics of a four-valve engine cylinder head. The results showed that the tumble vortex ratio calculated with steady flow using a tumble adaptor was similar to that in a motored engine at inlet valve closure, and that the tumble produced by the four-valve design in a motored engine led to over 60% greater volume-averaged turbulence levels than two-valve designs. Furthermore, by adding sleeves to the intake ports, Arcoumanis et al were able to intensify the tumble during induction, resulting in even higher mean velocity and turbulence levels at the point of ignition.

The greater turbulence levels produced by high tumble systems lead directly to improvements in engine combustion, fuel economy and emissions characteristics, as shown by Endres et al (1992) and Hu et al (1992) for example. Hence, optimisation of engine cylinder head design is important in order to achieve superior performance characteristics.

In the present study, the mean velocity and turbulence characteristics of the flow in the Zetec engine have been investigated with a view to acquiring an understanding of the influence of inlet port design on in-cylinder flow structure. Detailed experimental studies and numerical modelling using computational fluid dynamics (CFD) are used to provide a description of the three-dimensional flow field inside the engine cylinder, under both steady flow and motored engine conditions.

2. FLOW CONFIGURATION

2.1 The Ford Zetec Engine

The two inlet ports of the Ford Zetec engine are designed to produce a strong tumbling flow motion into the cylinder during the induction stroke. Figure 1 shows the inlet port and cylinder head geometry. Some engine parameters for the 1.8 litre model have been provided on Table 1 overleaf.

2.2 The Steady Flow Experimental System

The steady flow investigations were performed using a Perspex replica of the intake ports and cylinder of the Zetec engine. A mixture of rectified oil of turpentine and teraline

Table 1 Specifications of the 1.8 litre Ford Zetec engine

Displacement:	1796 cm^3
Bore:	80.6 mm
Stroke:	88.0 mm
Mean compression ratio:	10:1
Intake valve diameter:	32.0 mm
Exhaust valve diameter:	28.8 mm
Intake valve opening:	6° BTDC
Intake valve closure:	222° ATDC

liquids in the proportions 68%:32% by volume was employed as the working fluid. The refractive index of the liquid mixture (1.489 at 25°C) was identical to that of the Perspex material used for the test section, enabling complete optical access to laser light for flow visualisation and LDA measurements. The density of the mixture was 893.5 kg/m^3 and the kinematic viscosity was 1.71 x 10^{-6} m^2/s. As the mixture had a low viscosity, turbulent flow was readily achieved in the cylinder. The similarity of liquid and air flow through engine inlet ports has been previously demonstrated (Cheung et al 1990).

Tests carried out using LDA to determine the effect of liquid mass flowrate on in-cylinder flow structure under steady flow conditions revealed that in-cylinder velocities scaled well with mass flowrate. The remaining experiments presented here were conducted with the liquid mass flowrate set at 1.54 kg/s (Re = 30000).

For flow visualisation studies, minute air bubbles created within the experimental rig were used as tracers. A 2W Argon-Ion laser operating at a wavelength of 514.5 nm was used as the light source. The laser beam was passed through a cylindrical lens to produce a sheet of light, which was directed onto the test section using mirrors. Recordings of the flow were made using a CCD video camera.

The laser-Doppler anemometer was operated in forward-scatter fringe mode. The anemometer consisted of a 10 mW Helium-Neon laser, a rotating diffraction grating, associated optics and a photomultiplier. Table 2 provides the principal LDA system characteristics.

Table 2 Principal LDA system characteristics

Laser light wavelength:	632.8 nm (red)
Frequency shift between first-order beams:	3.38 MHz
Measurement volume diameter:	78.0 μm
Measurement volume length:	1.00 mm
Number of interference fringes:	19
Frequency to velocity conversion factor:	4.096 m/s/MHz
Half-angle of laser beams:	4.50°

The signal processing system comprised a frequency counter and a computer interfaced to the counter and installed with data processing software. As the liquid mixture already contained a sufficient quantity of micron-sized contaminant particles, artificial seeding of the flow was not required for the LDA studies. Further details of the experimental techniques are provided in Mahmood and Yianneskis (1995).

2.3 Computational Fluid Dynamics

A three-dimensional grid of the inlet ports and cylinder of the Zetec engine was produced using CAD data provided by Ford Motor Company Limited. The STAR-CD software was used with the SIMPISO numerical scheme and the k-ε turbulence model to calculate the flow. Initially, CFD calculations were performed under steady flow conditions at a number of different inlet valve lift settings. These predictions were compared with experimental data obtained by LDA to determine the accuracy of the numerical model, before modifying the grid to calculate flows in a reciprocating engine. Details of the computational model have been provided in Chen et al (1996) and Mahmood et al (1996).

2.4 Stereoscopic Visualisation in a Motored Optical Engine

The flow processes in a motored optical engine fitted with a Zetec cylinder head were investigated using a 3D flow visualisation and velocity measurement technique. High speed engine flows were modelled at greatly reduced engine speeds by employing a heavy gas, sulphur hexafluoride (SF_6), at pressurised inlet conditions as the working fluid instead of air. Previous work on the experimental facility showed that dynamic similarity is achieved for flow in the engine cylinder (Ma et al 1986 a and b).

For global instantaneous flowfield studies, the entire cylinder volume was illuminated through a Perspex piston crown by light from a 5W Argon-Ion laser. For some experiments, selected planes inside the cylinder were illuminated with a laser light sheet. Hollow glass spheres of approximately 100 micron diameter were used as tracer particles. The flow was observed by two CCD video cameras, which were positioned to focus onto the cylinder axis. The images from the cameras were interlaced by a multiplexer and recorded onto S-VHS video tape.

During the data processing stage, the left and right fields of the video recordings were separated by a de-multiplexer, and a sequence of images were grabbed using a digital frame store connected to a personal computer. Matching pairs of streaks on the 2D images from each camera were identified and tracked, and this information was used to arrive at a 3D representation of the in-cylinder flow field.

3. RESULTS AND DISCUSSION

3.1 Flow Visualisation

Detailed flow visualisation recordings were made under a number of different conditions; firstly with both inlet valve lifts set equal, and then with the lift of one inlet valve varied relative to the other. Figure 2 shows a typical video recording of the flow structure in the vertical plane x = -17.6 mm (through the centre of one inlet valve) with the inlet valve lifts both set at 10 mm.

The figure shows a strong jet of fluid issuing into the cylinder from the right of the valve head. A vortex seen towards the right of Figure 2 dominates the flow structure inside the cylinder, and corresponds to the early development of tumble flow during the induction stroke of a reciprocating engine. An elliptic vortex is created adjacent to the tumble-like vortex by fluid passing at the left of the valve head.

3.2 LDA Measurements with 10 mm Inlet Valve Lifts

Mean velocity results for flow in the plane x = -17.6 mm are shown on Figure 3, for the 10 mm valve lift case (Chen et

al 1996). As was noted from the flow visualisation study (see Figure 2), the velocity vectors indicate that the flow in the inlet ports is uniform and ensemble-averaged velocities are around 1.75 m/s. A high velocity jet flow is apparent at the right of Figure 3, with lower velocity magnitudes towards the centre of the plane.

Measurements taken in the horizontal planes showed that the flow structure is symmetric about the plane of symmetry of the cylinder head. Two pairs of counter-rotating vortices are created when the valve lifts are equal, with the largest velocity magnitudes at locations close to the cylinder wall (Mahmood and Yianneskis 1995). The highest r.m.s. velocity magnitudes were measured in regions of steep mean velocity gradients at the edges of the inlet jet.

3.3 LDA Measurements with One Inlet Valve Closed

At part load operating conditions, by keeping one of the two inlet valves in a four-valve engine closed, or by applying port de-activation strategies, it is possible to generate swirl and tumble structures which are stronger than those produced with both valves open (Kent et al 1989, Stone et al 1993). At low engine speeds, this can lead to more stable combustion of lean mixtures and improvements in fuel economy. Such strategies have already been applied to modern lean-burn engines, as illustrated by the Honda VTEC-E deactivation system, and the swirl control mechanisms present in Toyota induction system designs.

In the present study, Valve 1 (as labelled on Figure 1) was kept closed and the lift of Valve 2 was set at 10 mm. Figure 4(a) presents mean velocity vectors in the plane x = -17.6 mm. As the liquid mass flowrate through the one open port was kept the same as when both inlet valves were open, velocities inside the port are higher. In this instance, velocity magnitudes of up to 3.9 m/s were measured inside the open port, around twice those in the previous case.

A complex flow structure was generated inside the cylinder. Flow visualisation experiments showed that a strong inclined swirling motion results in the cylinder volume. Figure 4(a) indicates that a high velocity jet results from flow over the left side of the inlet valve. This produces a strong vortex underneath the inlet valve which rotates in the opposite direction to the tumble-like vortex mentioned earlier. High velocity magnitudes are present at locations closest to the cylinder wall, as seen at the right of Figure 4(a) - typically around 2.2 m/s.

The flow field in the vertical plane x = 17.6 mm is shown on Figure 4(b). This is a plane through the centre of the closed inlet valve. The velocity vectors indicate the presence of one vortex, which covers almost the entire plane. This figure shows the motion that takes place over one half of the cylinder under steady flow conditions when one inlet valve is disabled. The vectors towards the top of the cylinder have a low angle of inclination, indicating that swirl is the dominant motion in this region. Further down the plane, the W-component of the mean velocity becomes larger, as the liquid spirals down the cylinder.

LDA measurements made in several horizontal planes inside the test section ilustrated the strong swirl characteristics of this configuration. Figure 4(c) shows profiles of the mean V-velocity component in the z = -30 mm plane. A well defined clock-wise swirl is apparent, with large velocity magnitudes at regions close to the cylinder walls.

The steep velocity gradients seen from the mean velocity results and the shearing action of the flow produced high turbulence levels inside the test section. Magnitudes of r.m.s. velocities were on average twice as high for this case, as when both inlet valve lifts were set at 10 mm.

3.4 Comparison of Steady Flow CFD and LDA Results

Detailed comparisons were made of the computed and measured velocity results in both vertical and horizontal planes, for each equal valve lift case studied. Figure 5 presents a typical plot from the 10 mm valve lift case, comparing the CFD calculations of the mean V-velocity component in the z = -20 mm plane with experimental results. It can be seen that there is good agreement between both sets of data, implying that the CFD model has predicted the main features of the flow well. Mean velocity characteristics in other valve lift cases were also calculated with good accuracy (Chen et al 1996, Mahmood et al 1996).

Turbulence levels were generally found to be under predicted by the CFD model. This may be partly due to the implicit assumption of isotropic turbulence in the k-ε turbulence model, and the presence of instabilities in real complex three-dimensional flows, which are not accounted for in the computational method.

3.5 Motored Engine Results

The motored engine CFD simulations were performed at a part load operating condition and an engine speed of 2000 rpm. The induction and compression strokes were modelled. The data for boundary conditions, including wall temperatures and the initial cylinder pressure were provided by Ford Motor Company Limited and were calculated using a one-dimensional gas dynamics code.

Figure 6(a) shows the mean flow in the x = -17.6 mm plane at 88° ATDC crankangle during the induction stroke. A strong tumbling motion develops inside the cylinder as the intake air passes over the combustion chamber roof, down the cylinder wall and across the piston surface. As the piston approaches BDC induction, the tumbling motion persists inside the cylinder volume.

The tumble vortex was seen to intensify during the compression stroke as its size was reduced, due to conservation of angular momentum (Gosman et al 1985). Figure 6(b) shows the computed flow structure at 330° ATDC crankangle during the compression stroke. A well-defined tumble motion exists inside the cylinder close to TDC compression. The development of the tumble during induction in the plane of symmetry of the cylinder head (x = 0 mm) is shown on Figures 7(a) and 7(b), at 104° ATDC and 178° ATDC crankangle.

For the experimental studies, the engine was motored at 42 rpm with 1.22 bar inlet manifold pressure, giving an equivalent engine speed of 2200 rpm at 1/4 load. Figures 8(a) and 8(b) show the development of the flow during the induction stroke at 100° ATDC and 173° ATDC crankangle in the x = 0 mm plane. The camera positions did not allow viewing of the entire cylinder. Comparisons of the particle tracks with Figures 7(a) and 7(b) indicate that qualitatively, the flows have been well-predicted by the CFD model. The experimental results show a less well-defined flow structure than the predictions, and this is because Figures 8(a) and 8(b)

present instantaneous pictures of the flow, compared to the averaged results of the numerical model.

4. CONCLUSIONS

A combined experimental and computational study was undertaken into the pre-combustion in-cylinder flow motion in the Ford Zetec engine, under both steady flow and motored engine operating conditions.

Experimental results obtained by laser-sheet visualisation and LDA showed that a strong tumble-like flow occurs in the cylinder with steady flow, when both inlet valve lifts are identical. With one inlet valve closed, a strongly inclined motion was noted inside the cylinder.

CFD simulations of flow in a motored Zetec engine showed the development of a well-defined tumble motion during the induction stroke. The tumble flow was maintained during the compression stroke up to crankangles close to TDC compression. Qualitative comparisons of the numerical results with experimental data obtained by a stereoscopic flow visualisation method showed that the main features of the flow were satisfactorily reproduced by the CFD model.

ACKNOWLEDGEMENTS

The authors gratefully acknowledge financial support provided for this work by the Engineering and Physical Sciences Research Council under grant GR/J65693 and Ford Motor Company Limited. Technical advice and assistance provided by Dr. Gopal Ganti and Mr. Bob Marshall of Ford Motor Company Limited is also acknowledged.

REFERENCES

Arcoumanis, C., Bae, C.S. and Hu, Z. 1994, Flow and Combustion in a Four-Valve Spark-Ignition Optical Engine, SAE Paper 940475.

Chen, A., Mahmood, Z., Yianneskis, M. and Ganti, G. 1996, Three-Dimensional Simulation of the Flow Through a Twin-Intake Port Engine, Paper C499/055/96, Proc. 3rd I.Mech.E. Int. Conf. 'Computers in Reciprocating Engines and Gas Turbines', pp. 239-248.

Cheung, R.S.W., Nadarajah, S., Tindal, M.J. and Yianneskis, M. 1990, An Experimental Study of Velocity and Reynolds Stress Distributions in a Production Engine Inlet Port Under Steady Flow Conditions, SAE Paper 900058.

Endres, H., Neusser, H.-J. and Wurms, R. 1992, Influence of Swirl and Tumble on Economy and Emissions of Multivalve Engines, SAE Paper 920576.

Gosman, A.D., Tsui, Y.Y. and Vafidis, C. 1985, Flow in a Model Engine with a Shrouded Valve - A combined Experimental and Computational Study, SAE Paper 850498.

Hu, Z., Vafidis, C., Whitelaw, J.H., Chapman, J. and Head R.A. 1992, Correlation Between In-Cylinder Flow, Performance, and Emissions Characteristics of a Rover Pentroof Four-Valve Engine, Paper C448/026, Proc. I.Mech.E. Conf. 'Combustion in Engines', pp. 157-164.

Kent, J.C., Mikulec, A., Adamczyk, A.A., Mueller, S.R., Stein, R.A., and Warren, C.C. 1989, Observations on the Effects of Intake-generated Swirl and Tumble on Combustion Duration, SAE Paper 892096.

Ma, T.H., Davies, M. and Collings, N. 1986 a, Low Speed Dynamic Similarity Modelling of I.C. Engines, SAE Paper 860239.

Ma, T.H., Marko, K., Li, P. and Davies, M. 1986 b, Dynamic Similarity Helps Laser Flow Visualisation for In-Cylinder Measurements, Paper 865036, Proc. XXI FISITA Congress, pp. 1.259 - 1.264.

Mahmood, Z. and Yianneskis, M. 1995, Velocity and Turbulence Characteristics of Steady Flow Processes in the Ports and Cylinder of a Ford Zetec Engine, Report EM/95/02, Mech. Eng. Dept., King's College London.

Mahmood, Z., Chen, A., Yianneskis, M. and Ganti, G. 1996, On the Structure of Steady Flow Through Dual Engine Intake Ports, International Journal for Numerical Methods in Fluids, (In Press).

Newton, K., Steeds, W. and Garret, T.K. 1989, Chapter 4 - Constructional Details of the Engine, The Motor Vehicle, 11th Edition, Butterworths International.

Omori, S., Iwachido, K., Motomochi, M. and Hirako, O. 1991, Effect of Intake Flow Pattern on the In-Cylinder Tumbling Airflow in Multivalve S.I. Engines, SAE Paper 910477.

Rönnbäck, M., Le, W.X. and Linna, J.-R. 1991, Study of Induction Tumble by Particle Tracking Velocimetry in a 4-Valve Engine, SAE Paper 912376.

Stone, C.R., Carden, T.R. and Podmore, I. 1993, Analysis of the Effect of Inlet Valve Disablement on Swirl, Combustion and Emissions in a Spark-Ignition Engine, Proc. I.Mech.E. 'Journal of Automobile Engineering', Vol. 207, No. D4, pp. 295-305.

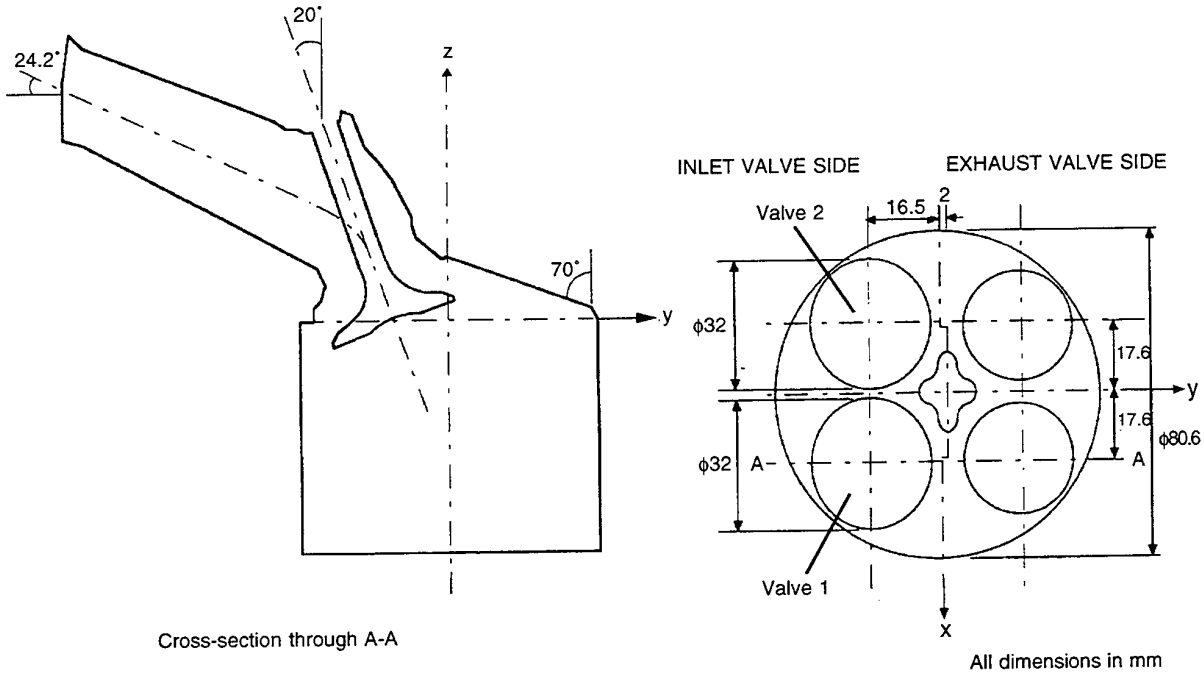

Figure 1 Outline of the inlet ports of the Ford Zetec engine in a vertical plane through one inlet valve and major cylinder head dimensions

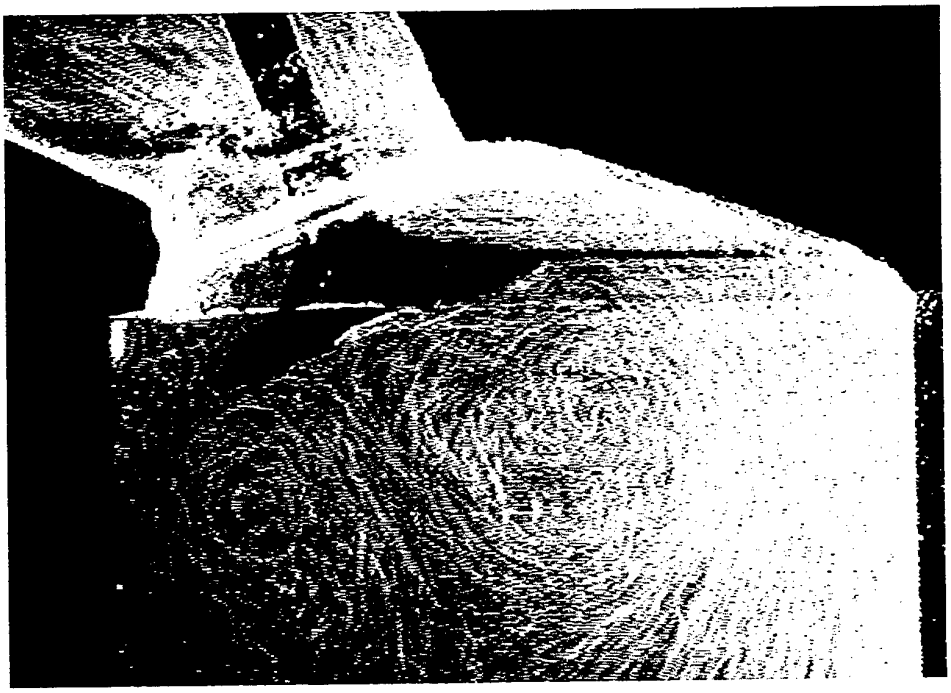

Figure 2 Still frame from flow visualisation study of steady flow through the intake ports and cylinder of the engine model, with 10 mm valve lifts

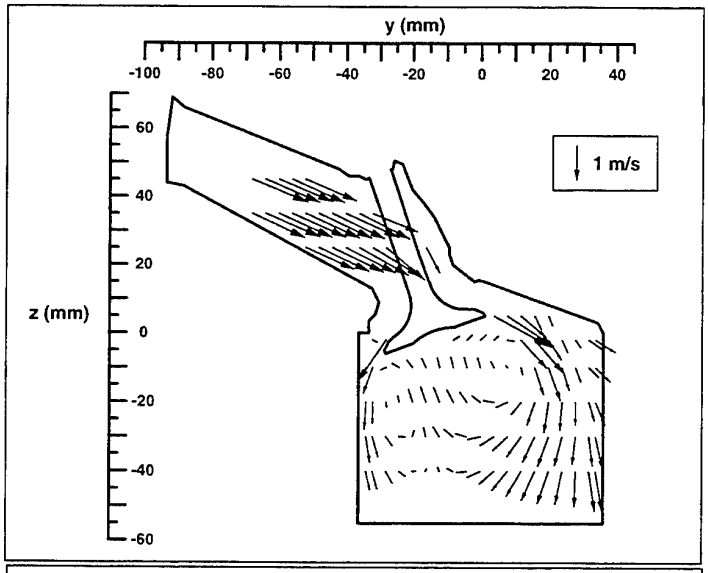

Figure 3 Velocity vectors for flow in the plane x = -17.6 mm with 10 mm valve lifts

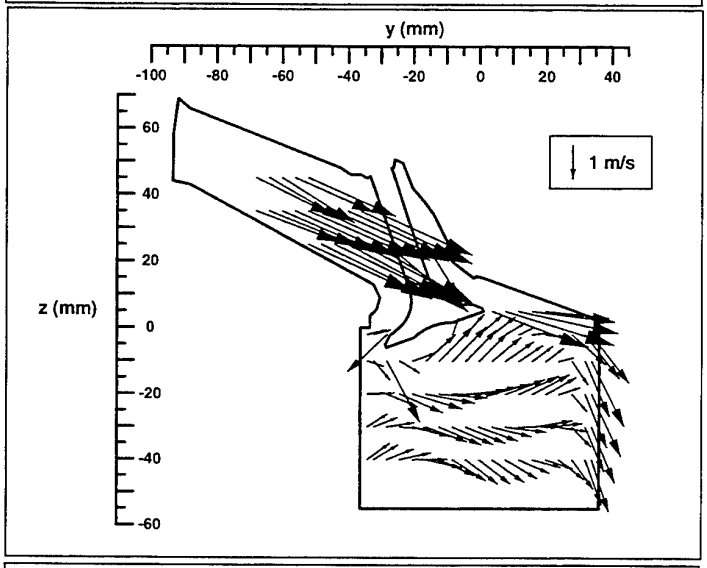

Figure 4(a) Velocity vectors for flow in the plane x = -17.6 mm with one inlet valve closed

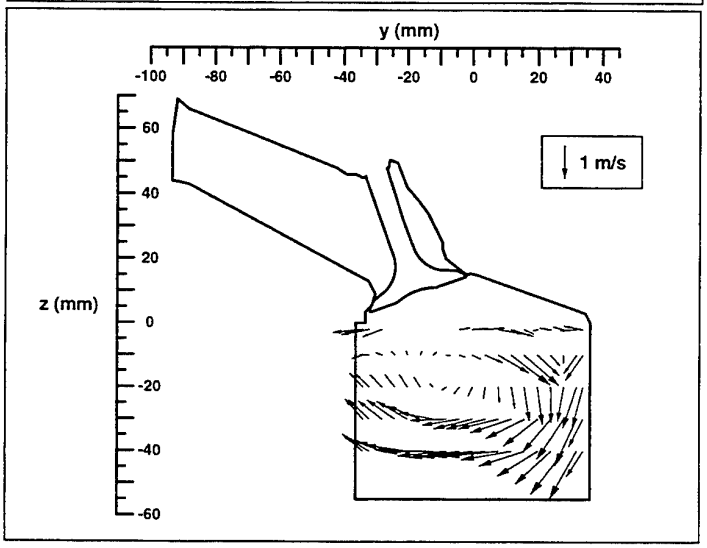

Figure 4(b) Velocity vectors for flow in the plane x = 17.6 mm with one inlet valve closed

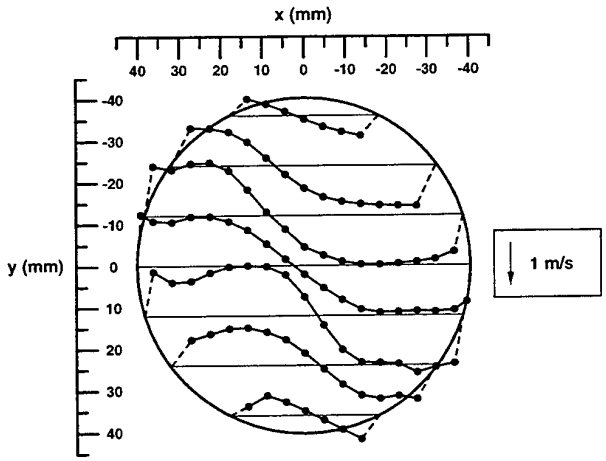

Figure 4(c) Profiles of the mean V-velocity component in the z = -30 mm horizontal plane with one inlet valve closed

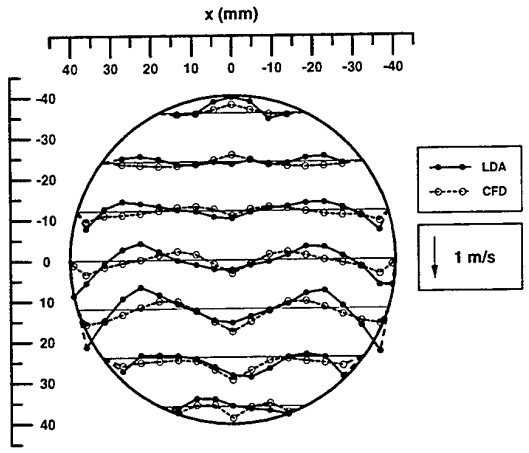

Figure 5 Comparison of computed and measured V-component velocities in the z = -20 mm plane, with 10 mm valve lifts

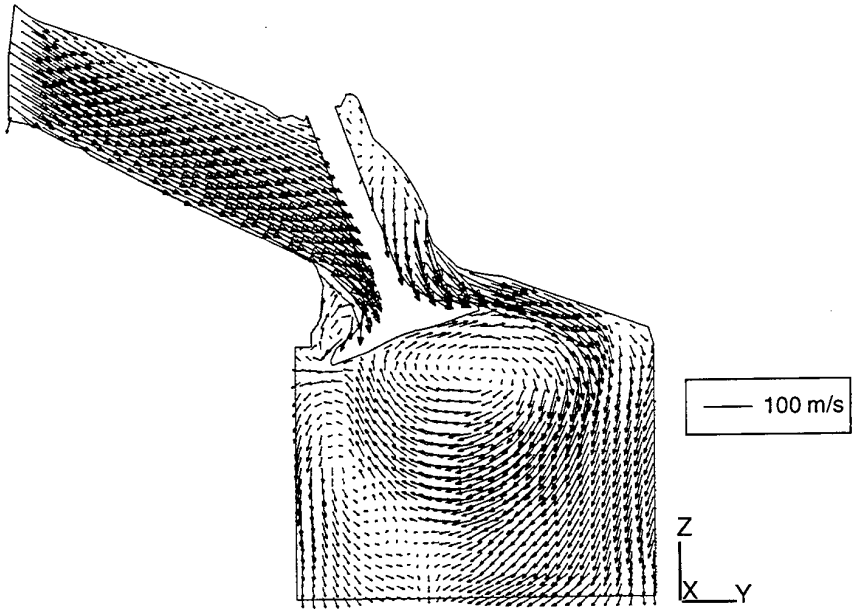

Figure 6(a) Mean velocity vectors of flow in the vertical plane x = -17.6 mm at 88° ATDC crankangle (induction stroke)

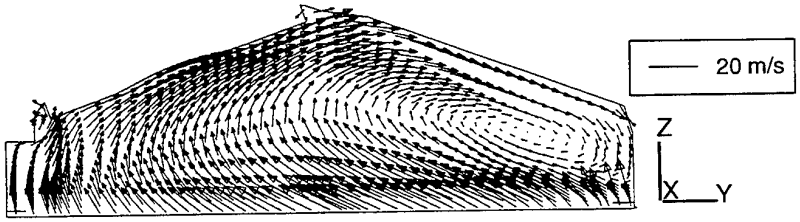

Figure 6(b) Mean velocity vectors of flow in the vertical plane x = -17.6 mm at 330° ATDC crankangle (compression stroke)

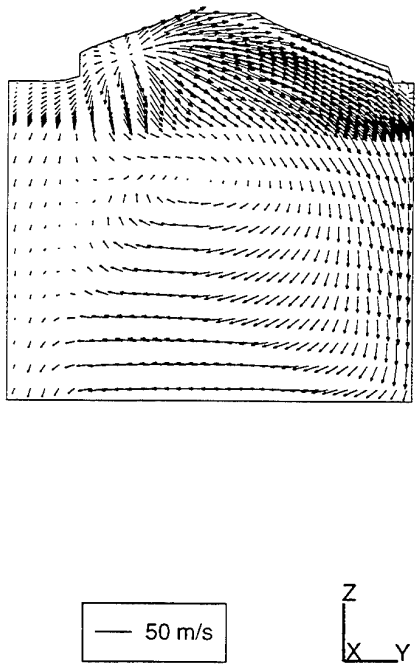

Figure 7(a) Calculated mean velocity vectors for flow in the x = 0 mm plane at 104° ATDC crankangle

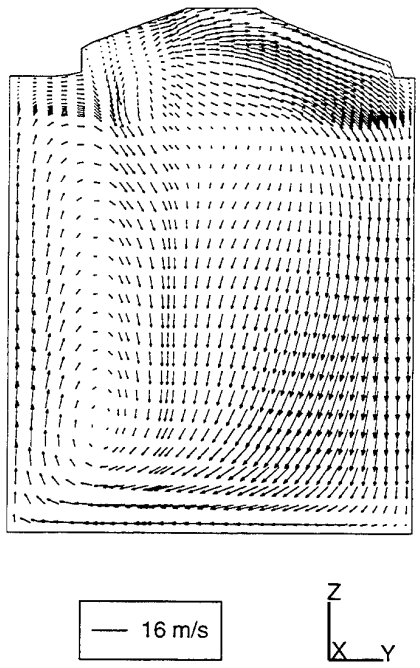

Figure 7(b) Calculated mean velocity vectors for flow in the x = 0 mm plane at 178° ATDC crankangle

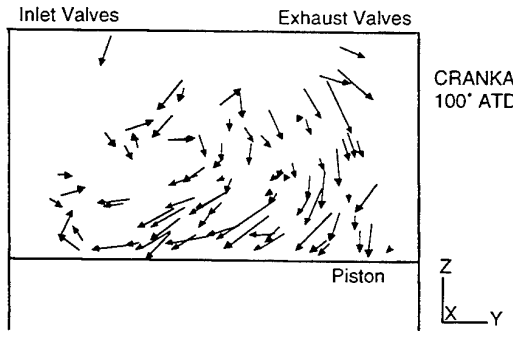

Figure 8(a) Particle trajectories obtained from processed images, showing the instantaneous flow pattern in the x = 0 mm plane at 100° ATDC crankangle

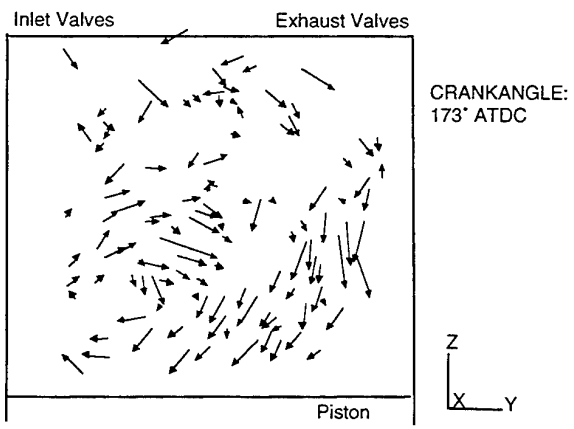

Figure 8(b) Particle trajectories obtained from processed images, showing the instantaneous flow pattern in the x = 0 mm plane at 173° ATDC crankangle

STEADY INTAKE FLOW CHARACTERISTICS THROUGH A DIESEL FOUR-VALVE CYLINDER HEAD

C Arcoumanis, B. French* and J M Nouri

Department of Mechanical Engineering
Imperial College of Science, Technology & Medicine, London, England

* Diesel Engineering, Ford Motor Co. Ltd

ABSTRACT

The annular flow around the two intake valves of a production four-valve diesel cylinder head has been investigated by laser Doppler velocimetry under steady flow conditions at a mass flowrate of 85 kg/h corresponding to an engine speed of 1000 rpm. The results showed that the primary valve generates much stronger swirl than the secondary valve, which in turn generates more than 20% of the mass flow. When both valves are open, the generated swirl and mass flow levels fall between those obtained with the primary and secondary valves but much closer to the former than to the latter. The exit flow around the intake valves was found to be non-uniform, with more pronounced the case of the primary valve, with the maximum exit flow present at the planes which are in-line with the inlet port axis and the minimum exit flow at the planes towards the end of the helical ramp of the port. Similar non-uniform flows were observed when both valves were open except for the two planes of the primary valve which are affected by the jet flow exiting from the secondary valve. Turbulence, in general, was anisotropic with maximum levels of about $5V_p$ (V_p = mean piston speed) near the cylinder head.

INTRODUCTION

The importance of the in-cylinder air and fuel motions on the performance and emissions of direct-injection Diesel engines has long been recognised. The desirable condition is to achieve rapid mixing between the swirling air and injected fuel in order to complete combustion within a short crank angle interval close to TDC. High fuel-air mixing rate, which in turn controls the fuel burning rate, is even more important in passenger car diesels where the mixing time scale is very short relative to engines at the large end of the size range. Improved understanding of the characteristics of the induction air motion over a wide range of speeds is a prerequisite for the development of high speed direct-injection (HSDI) diesels, as the legislation on NO_x and particulate emissions becomes worldwide more stringent.

The present experimental investigation aims to quantify the exit flow characteristics generated by the two intake helical ports of an advanced four-valve Diesel cylinder head in terms of the flow discharge and swirl coefficients and the mean/rms velocity profiles as a function of the valve lift. These results are expected to assist the development of multidimensional computer models, which require accurate experimental data as boundary conditions, and to allow the design of these ports to be improved by achieving higher volumetric efficiency especially at high engine speeds.

FLOW CONFIGURATION AND INSTRUMENTATION

The four-valve cylinder head of a production Ford diesel engine was mounted on a steady flow rig, as shown in figure 1. Ambient air was drawn through the two inlet ports by a five-stage centrifugal suction pump which was controlled by a bypass flow regulator. The mass flow rate was determined by a British Standard orifice plate, 1042, with an accuracy of ±1.3%. Digital and U-tube manometers were used to measure the upstream pressure of the orifice plate, the air pressure drop across the orifice plate and the pressure drop through the inlet manifold and the cylinder head assembly. The ambient air pressure and temperature were measured with a mercury barometer and a thermometer, respectively. The two inlet ports were of helical type and produced different levels of swirl; they are referred to here as primary (higher swirl) and secondary (lower swirl). An open-ended acrylic cylinder was fitted to the cylinder head with a bore diameter of 88mm, a wall thickness of 6mm and a length four times the bore diameter, which provided optical access for the laser Doppler velocimeter. At the end of the acrylic cylinder four interconnected pressure tappings were made to monitor the pressure drop across the cylinder head prior to its connection to a settling chamber.

To obtain the swirl coefficient generated by the intake ports, either individually or jointly, a commercial torque meter (Quadrant Scientific) was placed four bore diameters downstream of the cylinder head. The meter consists of a honeycomb which converts the angular momentum to torque and a measuring device which gives the induced torque with an accuracy of ±0.5%. The torque meter was calibrated over the measuring range with balance weights and the linearity of the response of the meter was found to be very satisfactory as shown in figure 2. The laser Doppler velocimeter comprised a water-cooled argon-ion laser (Spectra Physics) operating with a wavelength and power of 0.514 μm and 300 mW respectively, a diffraction-grating to divide the laser beam into two of equal intensity and provide frequency shifts up to 12 MHz, a collimating and a focusing lens to bring the two beams to an intersection volume, a photomultiplier (Dantec 55X34), and a frequency counter (TSI model 1990) interfaced to a microcomputer using a DMA board (Dostek 1400). The intersection volume was approximately 757 μm in length and 42 μm in diameter, with a fringe spacing of 4.6 μm. The signals from the

photomultiplier were processed by the counter to form ensemble averages from 4000 individual velocities.

The measurement position and the magnitude of the velocity components were corrected, when required, for refraction effects of the laser beams through the cylindrical wall. Uncertainties due to velocity gradients were minimised by aligning the smaller dimension of the intersection volume along the velocity gradient, except for the swirl component, and by collecting the light 30° off-axis. Statistical uncertainties were also minimised by considering a large number of samples and the maximum counting ambiguity of the TSI instrument, having a clock frequency of 1000 MHz, was 0.5% of the Doppler frequency shift. The overall maximum uncertainty in the measurements of mean and rms velocities is estimated to be 5% and 10%, respectively.

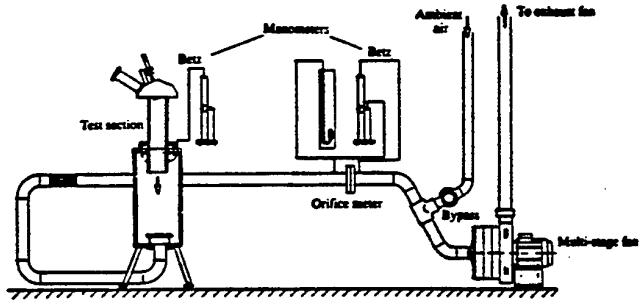

(a) Diagram of steady flow rig

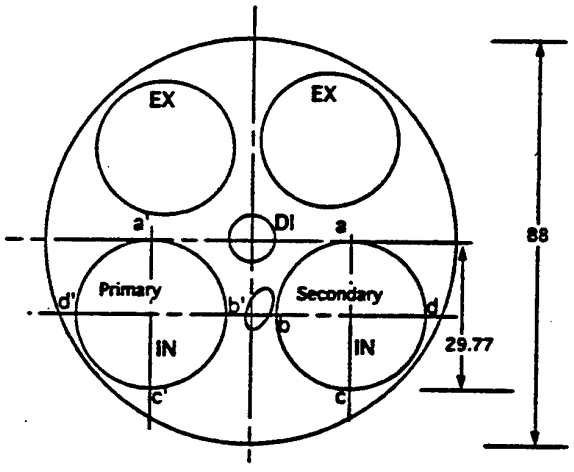

(b) Diagram of cylinder head

Fig. 1 Schematic diagrams of flow circuit and cylinder head together with measuring locations around the intake valves (dimensions in mm)

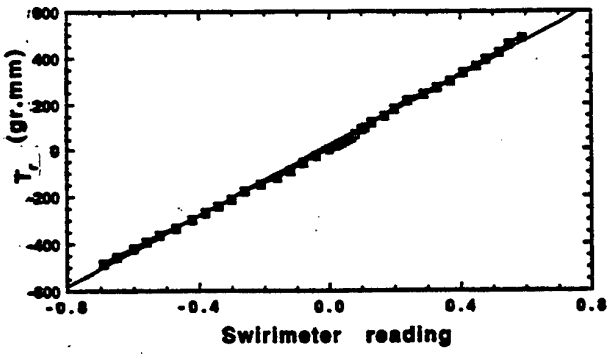

Fig. 2 Calibration curve of the swirl impulse meter.

The flow was seeded with silicone oil droplets which were generated by an air-blast atomiser and introduced into the flow in the plenum chamber upstream of the inlet ports. This atomiser had been shown to produce droplets with Sauter mean diameter, d_p, of less than 2 μm and this corresponds to an effective Stokes number of less than 0.1, implying that droplets do follow the mean flow even with the occasional larger droplet and, thus, the uncertainty due to the wide size range of the droplets can be considered to be negligible.

3. RESULTS AND DISCUSSION

Measurements of the discharge, flow and swirl coefficients and the three components of the mean and rms velocities around the intake valves were obtained at constant mass flow rates as a function of the valve lift. For comparison purposes, three test cases were examined, first when only the primary valve was open, second when the secondary valve was open and thirdly when both valves were open. The initial tests reported here were made at a mass flow rate of 85 kg/h through the inlet ports, which corresponds to an engine mean piston speed of V_p=3.155 m/s for a stroke of 94.6mm and an engine speed of 1000 rpm. Subsequent tests were performed at a mass flow rate corresponding to 3000 rpm in order to examine the flow behaviour at higher speeds where the volumetric efficiency of the engine was found to deteriorate (Arcoumanis et al, 1995).

3.1 DISCHARGE, FLOW AND SWIRL COEFFICIENTS

The discharge coefficient is defined as the ratio of the measured mass flow rate, m, through the port and valve assembly for a given valve lift, L, and a pressure ratio, to the isentropic mass flow rate, m_i, through an ideal nozzle, i.e.

$$C_d = \frac{m}{m_i} \qquad (1)$$

and

$$m_i = A_l \sqrt{[2P_o\rho_o \frac{\gamma}{\gamma-1}(\frac{P}{P_o})^{2/\gamma}\{1-(\frac{P}{P_o})^{(\gamma-1)/\gamma}\}]} \quad (2)$$

where P/P_o is the pressure across the port and valve assembly, P_o and ρ_o are ambient pressure and density, γ is equal to 1.4, and A_l is the curtain area defined as $A_l=\pi N D_h L$ where N is the number of intake valves and D_h is the valve head diameter (=29.77mm).

The flow coefficient is defined as the ratio of the measured mass flow rate to the theoretical mass flow rate through the valve inner sit area and is expressed as:

$$C_f = \frac{m}{\rho V_o A_i} \quad (3)$$

where A_i is the valve inner sit area, $A_i = \frac{\pi N D_i^2}{4}$ where D_i is the valve inner sit diameter (=26.2mm) and V_o is the head velocity derived from the pressure drop across the valve using the compressible flow equation:

$$V_o = \sqrt{[\frac{2\gamma}{\gamma-1}\frac{P_o}{\rho_o}\{1-(\frac{P}{P_o})^{(\gamma-1)/\gamma}\}]} \quad (4)$$

The swirl coefficient is essentially the ratio of the flow angular momentum to its axial momentum. With the impulse torque meter the simplest definition according to Heywood (1988) is

$$C_s = \frac{8T_r}{mV_oB} \quad (5)$$

where T_r is the induced torque and B is the bore diameter. The variation of the discharge, flow and swirl coefficients with valve lift is presented in figure 3 for a constant mass flow rate of 85 kg/h. The discharge coefficient, C_d, shows in all cases a sharp decrease up to a valve lift of L/D=0.083 (or 2.5mm) and a slightly smaller decrease thereafter; no measurements were obtained at valve lifts less than L/D=0.067 for the cases when only the primary or the secondary valve was open because the mass flow rate of 85 kg/h could not be achieved. The results also show that the secondary valve produces a much higher discharge coefficient than the primary valve at all lifts except at the very low lifts (less than 0.083) where the difference becomes very small; for example, at full lift (L/D=0.275 or 8.2mm) the C_d with the secondary valve is 20% higher than the primary valve. When both valves are open, C_d reduces from a value of 0.78 at the lowest lift to a value of 0.33 at full lift and the results follow those of the primary valve very closely in that C_d is higher with the primary valve up to L/D=0.1 and consistently lower afterwards; the C_d with the primary valve open is higher by 5.6% at L/D=0.067 while at full lift it is lower by 4%.

Unlike the C_d variation, the flow coefficient based on the inner valve sit cross-sectional area, C_f, shows an increase with increasing valve lift for all cases. Its values increase sharply and linearly up to a valve lift ratio of 0.125 after which the rates of increase reduce considerably until L/D=0.2 and then remain almost constant with a small and gradual increase until the full lift L/D of 0.275. The differences between the C_f values for different flow cases are similar to those of C_d, so that at full lift the value of C_f when the secondary valve is open is higher by 14% and 20% than the corresponding values when both valves are open and when the primary valve is open, respectively.

The results of the swirl coefficient, C_s, show marked differences between the three flow cases but in a reverse order to that of the discharge coefficient, that is the highest swirl coefficient is generated by the primary valve followed by that when both valves are open while the lowest swirl coefficient is generated by the secondary valve which produced the highest coefficient of discharge. With the secondary valve open the C_s increases mildly with valve lift to a maximum value of 0.16 at L/D=0.15 and then reduces very slowly so that at full lift it is 0.125. The results of the primary valve and for the case when both valves are open exhibit similar trends in which the C_s values increase sharply until L/D=0.14 and then the rate of increase reduces till L/d=0.2 after which it increases again. At full lift, the swirl coefficient generated by the primary valve is 0.675 compared to 0.125 when only the secondary valve is open. The value of C_s when both valves are open at full lift is 0.49 which is 27.5% lower and 390% higher than those of the primary and secondary valve, respectively. These results confirm that when a higher degree of swirl is required, as for example at low speeds to improve mixing, the use of the primary valve is necessitated and when a higher mass flow rate is required, as for example at high speeds, both valves should be used.

3.2 VELOCITY MEASUREMENTS

The three velocity components around the intake valves were measured for all three flow cases at a mass flow rate of 85 kg/h and full valve lift, 8.2mm. Measurements were taken at different axial locations from the tip of the valves to a distance 2mm from the cylinder head in circumferential positions a, b, c and d around the secondary valve (SV) and a', b', c' and d' around the primary valve (PV) as shown in figure 1(b), with a radial distance from the tip of the valve head of 0.5mm for the axial and radial velocity components and 1mm for the swirl component. The mean and rms velocities are normalised in all cases with the mean piston speed, V_p, equal to 3.155 m/s at 1000 rpm. The results are presented as velocity profiles and in vector forms and the three flow cases are examined below separately.

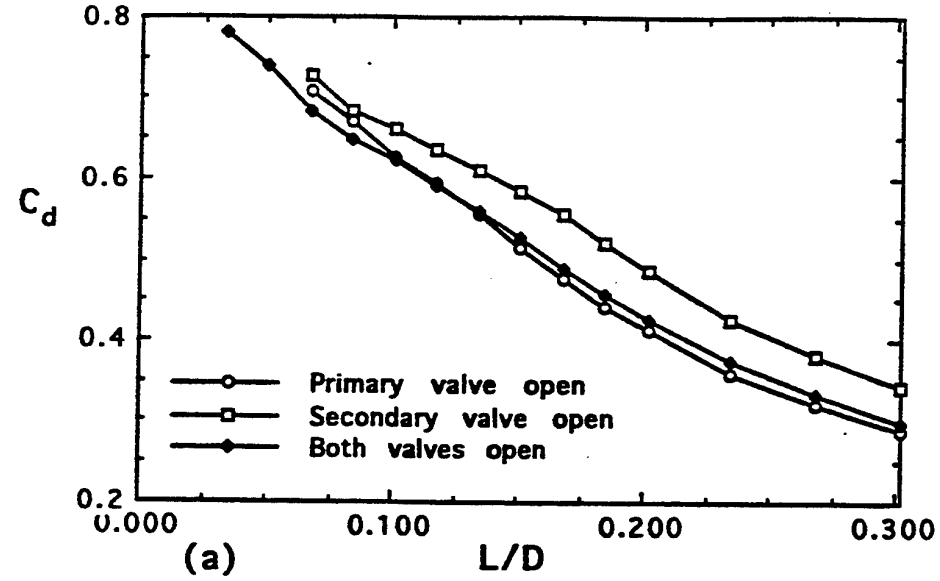

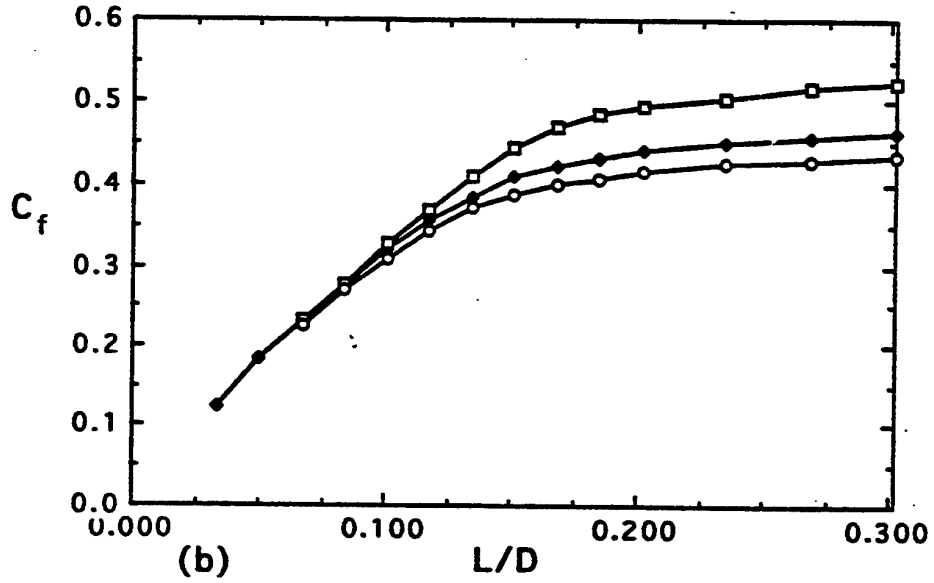

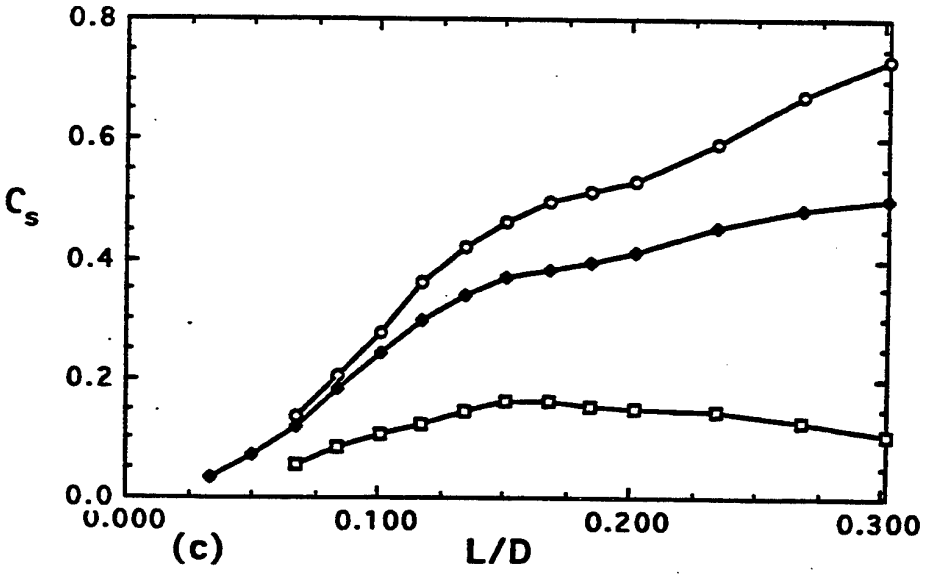

Fig. 3 Variation of discharge and swirl coefficients at a constant mass flow rate of 85 kg/h and as a function of valve lift; (a) discharge coefficient, (b) flow coefficient, (c) swirl coefficient.

3.2.1 PRIMARY VALVE OPEN

The measured velocity profiles and deduced vectors around the primary valve are shown in figure 4 together with the position of the valve and the cylinder wall. The axial flow at the exit planes, figure 4(a), shows a non-uniform distribution of the axial velocity around the valve so that the velocities are lowest with a maximum of $5V_p$ at plane b', upstream of the end of the helical ramp of the port, and then increase considerably in the clockwise direction to the largest values in plane a' with a maximum value of $18V_p$; the maximum velocities in planes c' and d' are around $12V_p$ and $16V_p$, respectively. Surprisingly, the velocity profile across the valve gap in plane c' exhibits a double peak which may be due to the proximity of the measuring plane to the edge of the helical ramp of the port.

A similar non-uniformity can be seen in the circumferential distribution of the radial mean velocity, figure 4(b), with maximum values in plane a' of $24V_p$ which are more than 50% higher than the maximum values in planes b' and c'. Like the axial flow at plane c', a similar double peak profile can be seen here with a minimum value in the middle of the valve gap. It is also interesting to note that despite the cylinder wall proximity at plane d', the axial and radial velocities in this plane are larger than those in plane b' where the cylinder wall is at a much larger distance. This is because plane d' is more aligned with the axis of the inlet port, which is directed along the wall of the cylinder, than plane b' and the results emphasise the dominant influence of the port position on the flow around the intake valves.

The swirl velocity distribution around the valve, figure 4(c), is more uniform and reduced in magnitude than the other two velocity components, with the lowest values in plane b', similarly to the axial and radial velocity, and largest values in plane d' with magnitudes of up to $13V_p$; the velocity in all planes increases from the tip of the valve towards the cylinder head. The relative magnitude of the axial/radial and radial/tangential velocities indicates a variation of the discharge and angular flow directions, respectively, which will be discussed again when the velocity vectors are presented later. The rms velocity variation of all three components follows the trends of the mean flow with the velocities not uniformly distributed around the valve periphery; the anisotropy of the flow is evident from the comparison of the three rms components. The level of turbulence is, however, relatively high in all three components varying from $1V_p$ to $5V_p$.

The non-uniformity of the discharging flow around the valve is more evident from the vector addition of the axial and radial velocity components shown in figure 4(d), with largest and lowest values at planes a' and b', respectively. The results also reveal that the flow angle with respect to the valve axis varies slightly along the gap, so that in general the flow angle tends towards the valve axis as the flow approaches the valve tip; the reverse axial velocity at the tip of the valve and just below it is an indication of the reverse flow being part of the recirculation zone formed beneath the valve head. The flow angle variation from one plane to another is also evident so that the average flow angle at planes a', b', c' and d' is 43°, 66°, 38° and 50°, respectively. The vector addition of the radial and tangential mean velocity components, shown in figure 4(e), reveals more clearly the flow pattern around the valve and indicates that the flow angle with respect to the valve radius varies only slightly within the valve gap expect in plane d' where the flow angle close to the cylinder head wall, at z=2.2mm, is much larger than that close to the tip of the valve, at z=6.2mm. The variation of the flow angle around the valve periphery changes, however, more drastically with the average values at a', b', c' and d' being 25°, 30°, 34.5° and 45°. Similar trends have been reported by Arcoumanis et al. (1987) and Haghgooie et al. (1984) for helical ports in two-valve heads.

3.2.2 SECONDARY VALVE OPEN

Similar measurements to those of the primary valve were made around the secondary valve and are shown in figure 5. Similar trends to those observed with the primary valve can be seen here but the distribution of the axial and radial velocities, figures 5(a) and (b), along the valve gap and around the periphery of the valve is more uniform in the case of the secondary valve; the maximum axial velocities in planes a, b, c and d are $12.5V_p$, $17V_p$, $13V_p$ and $7.5V_p$, and the corresponding maximum radial velocities are $15V_p$, $19V_p$, $16V_p$ and $7.5V_p$. It is also evident that the maximum axial and radial flow is in plane b which is expected since this plane is in-line with the inlet port axis; planes a and c seem also to benefit from this proximity. The swirl velocity presented in figure 5(c) shows a more uniform distribution around the valve than that of the primary valve but with slightly smaller magnitudes. All mean velocity components in plane d are smaller than in the other planes due to its proximity to the end of the ramp of the port and also due to the confinement by the cylinder wall. The values of normal shear stresses presented as rms velocities are high, like in the case of the primary valve, and follow the mean flow variation; their levels vary from values as low as $1V_p$ just below the valve tip to a maximum of $5V_p$ close to the cylinder head and in the region of the strong shear layer above the tip of the valve.

The mean flow variation described above can be seen more clearly in figures 5(d) and (e) where the vector addition of the velocities is presented. The axially and radially discharging flow around the valve, figure 5(d), shows a good degree of uniformity except in plane d where the flow is significantly reduced for the reasons explained previously. The flow angle with respect to the valve axis varies from plane to plane so that at planes a, b, c and d the angles are 45°, 59°, 59° and 45°, respectively, and tends to become more axially directed as the flow approaches the tip of the valve. The vector addition of the radial and tangential mean velocity components, figure 5(e), shows that there is a small variation in the flow angle within the valve gap and that the flow angle reduces as the flow approaches the valve head. The variation of the flow angle around the valve periphery is also small so that the average flow angles at planes a, b, c and d are 29°, 9°, 25° and 32°, respectively,

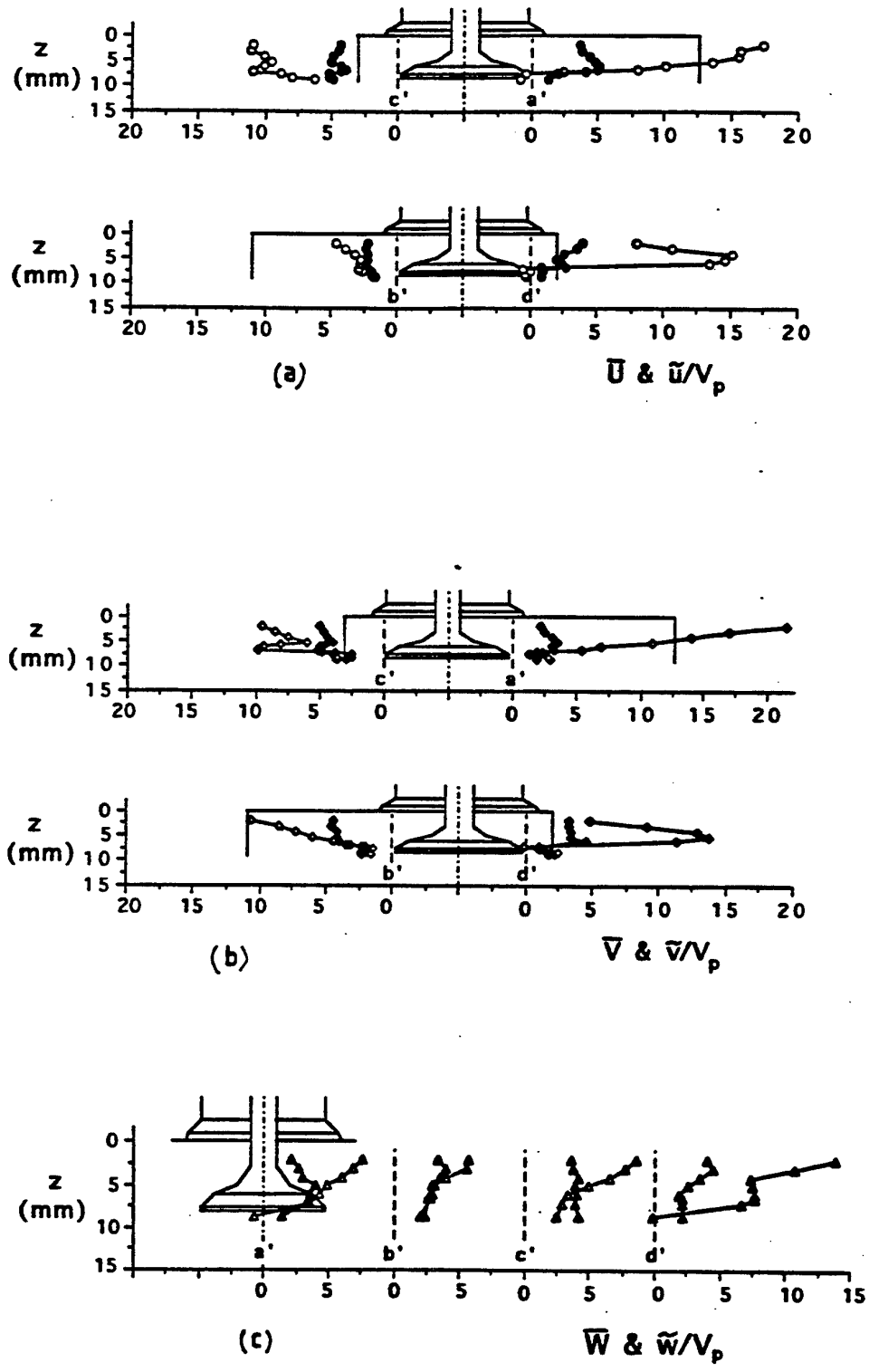

Fig. 4 Primary valve exit flow for full lift; (a) axial mean and rms velocity, (b) radial mean and rms velocity, (c) tangential mean and rms velocity, (d) Vector addition of the axial and radial mean velocity components, (e) Vector addition of the radial and tangential mean velocity components.

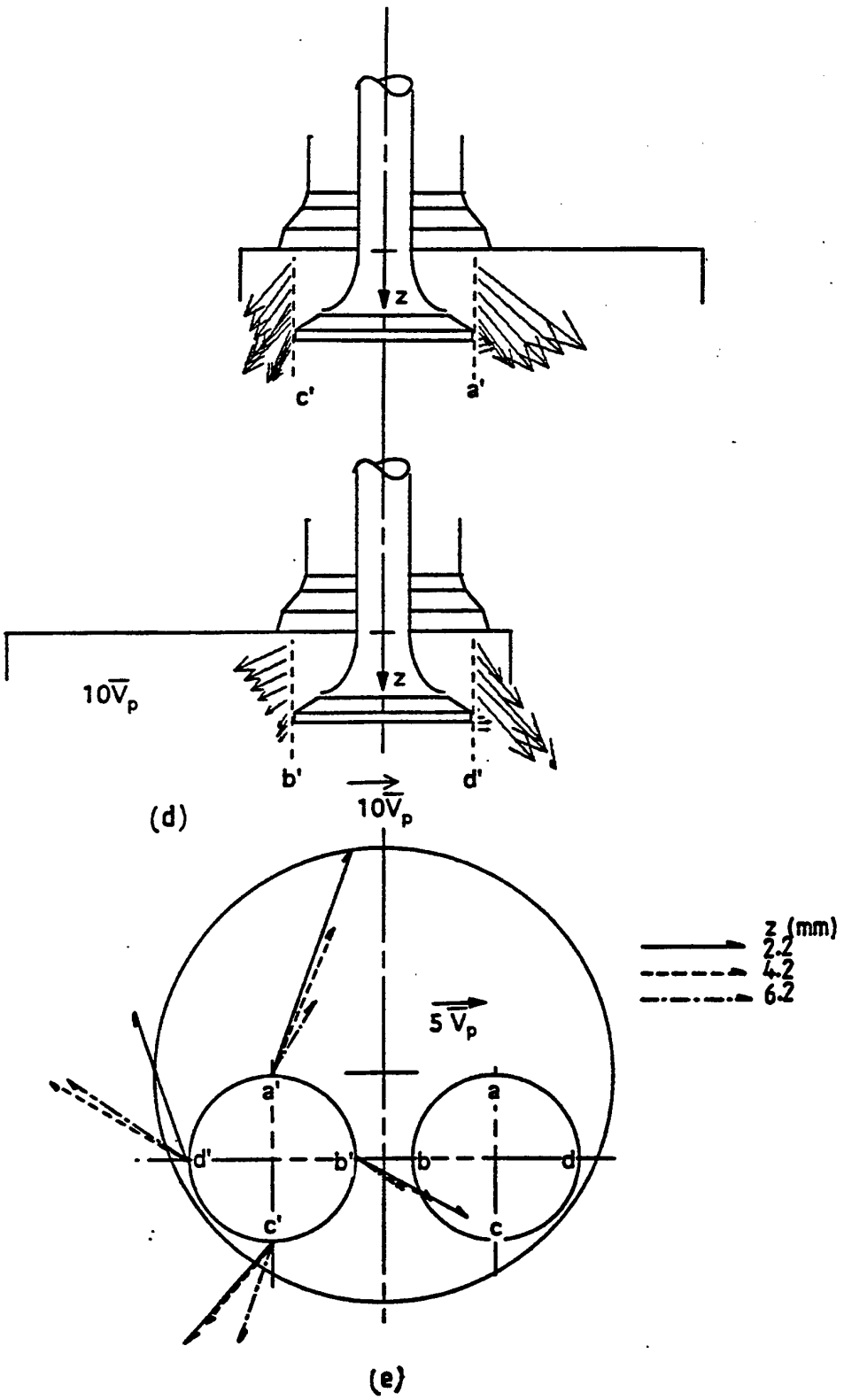

Fig. 4 Primary valve exit flow for full lift; (a) axial mean and rms velocity, (b) radial mean and rms velocity, (c) tangential mean and rms velocity, (d) Vector addition of the axial and radial mean velocity components, (e) Vector addition of the radial and tangential mean velocity components.

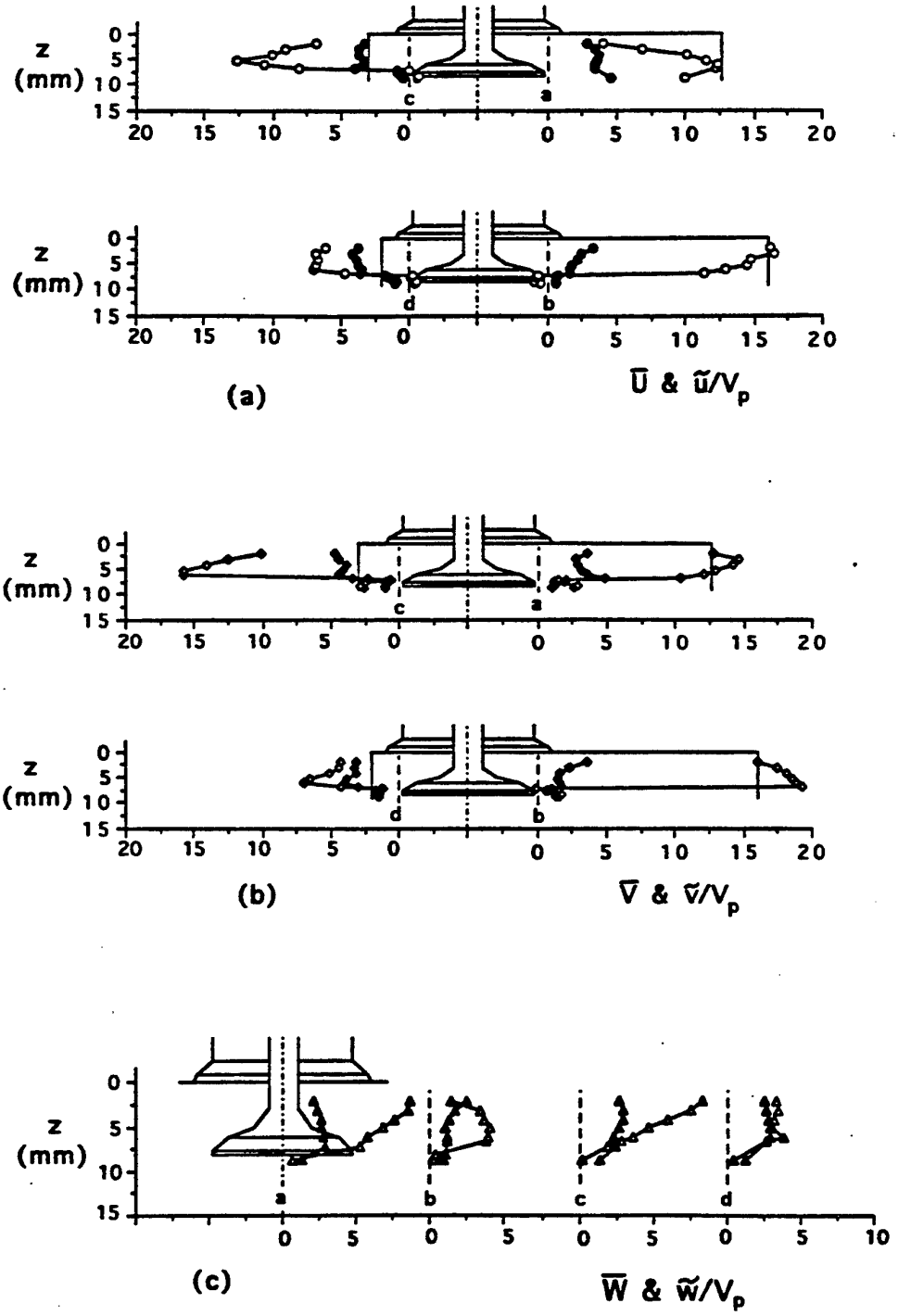

Fig. 5 Secondary valve exit flow for full lift; (a) axial mean and rms velocity, (b) radial mean and rms velocity, (c) tangential mean and rms velocity, (d) Vector addition of the axial and radial mean velocity components, (e) Vector addition of the radial and tangential mean velocity components.

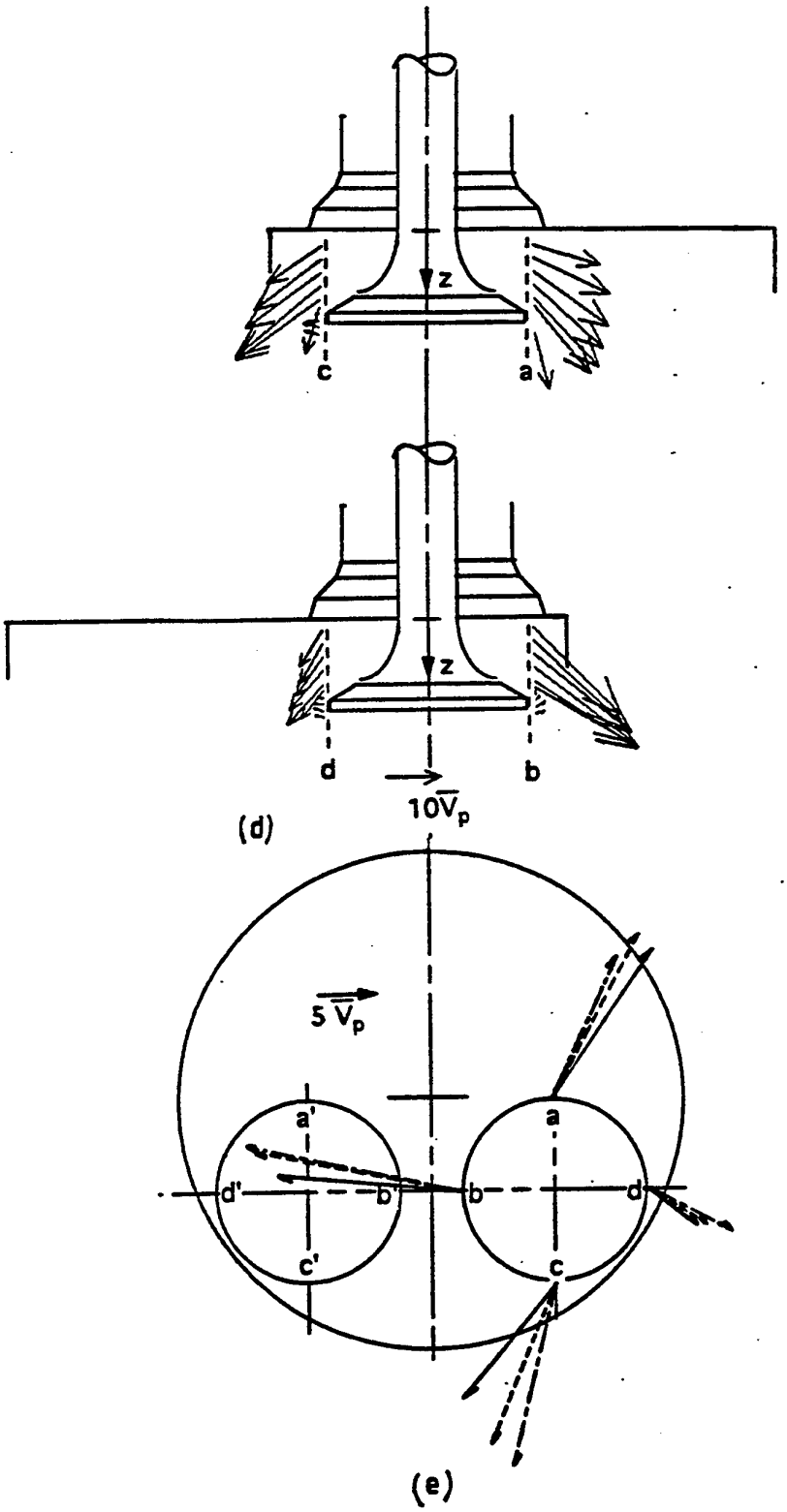

Fig. 5 Secondary valve exit flow for full lift; (a) axial mean and rms velocity, (b) radial mean and rms velocity, (c) tangential mean and rms velocity, (d) Vector addition of the axial and radial mean velocity components, (e) Vector addition of the radial and tangential mean velocity components.

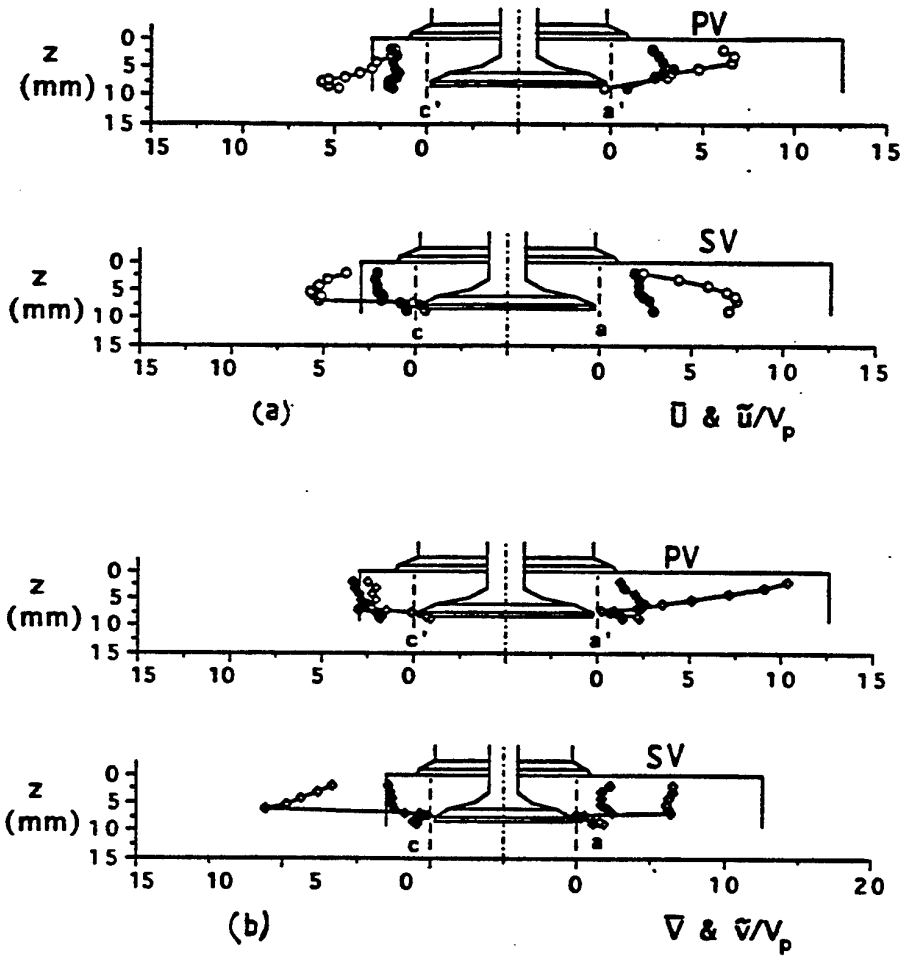

Fig. 6 Primary and Secondary valve exit flow for full lift; (a) axial mean and rms velocity at planes a-c and a'-c', (b) radial mean and rms velocity at planes a-c and a'-c', (c) tangential mean and rms velocity, (c) axial mean and rms velocity at planes b-d and b'-d', (b) radial mean and rms velocity at planes b-d and b'-d', (e) tangential mean and rms velocity.

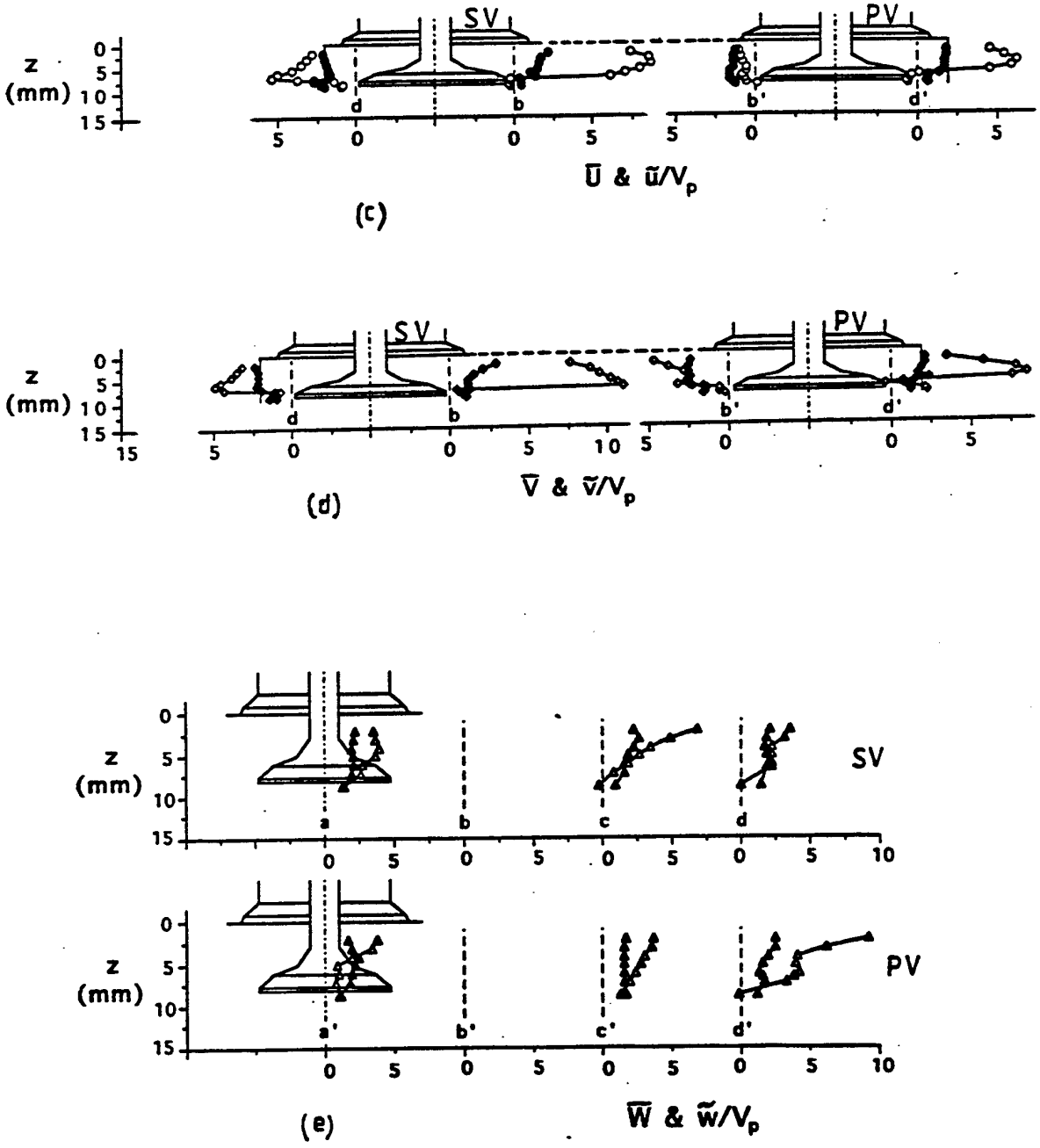

Fig. 6 Primary and Secondary valve exit flow for full lift; (a) axial mean and rms velocity at planes a-c and a'-c', (b) radial mean and rms velocity at planes a-c and a'-c', (c) tangential mean and rms velocity, (c) axial mean and rms velocity at planes b-d and b'-d', (b) radial mean and rms velocity at planes b-d and b'-d', (e) tangential mean and rms velocity.

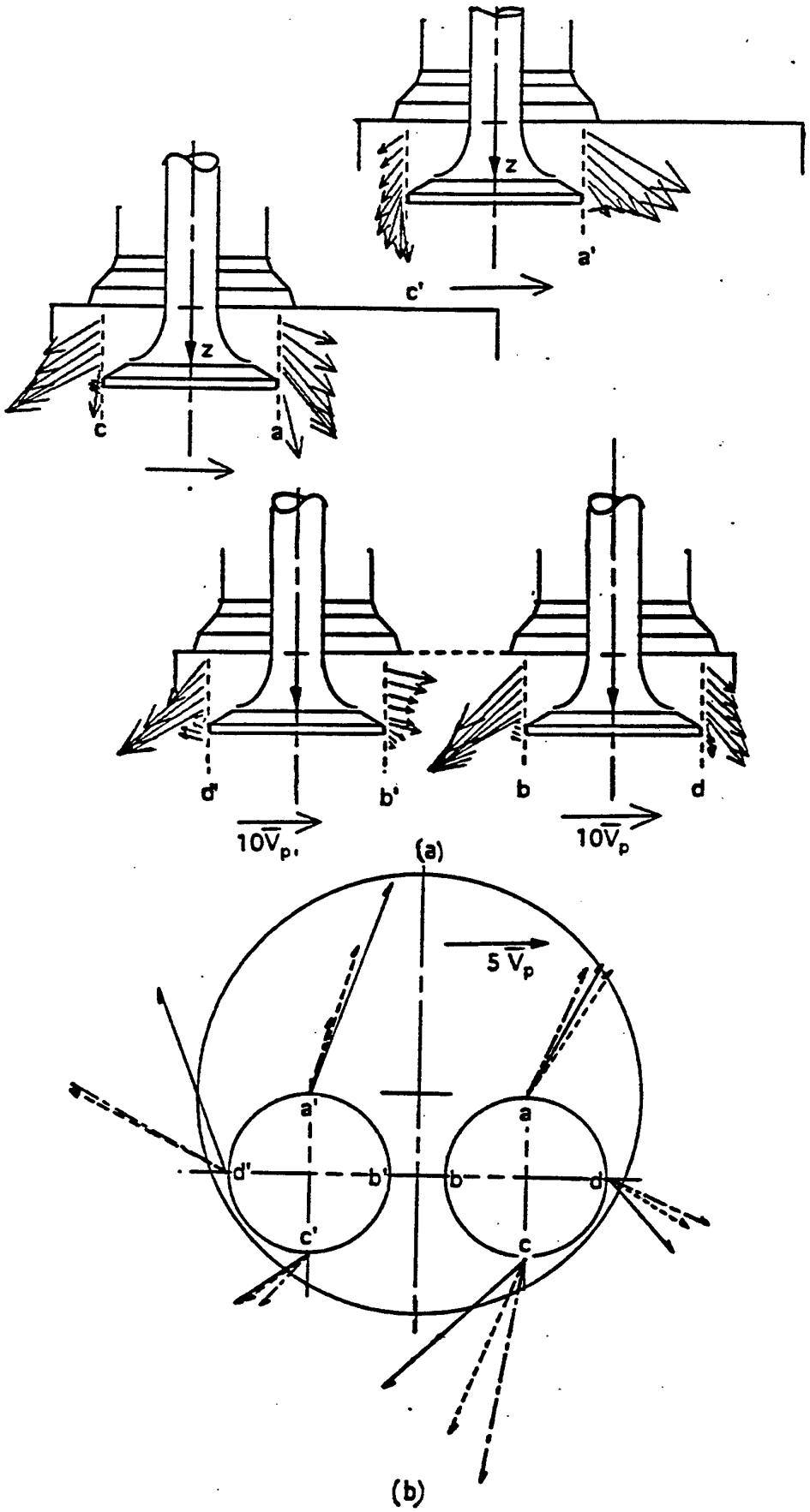

Fig. 7 Primary and Secondary valve exit flow for full lift; (a) Vector addition of the axial and radial mean velocity components, (b) Vector addition of the radial and tangential mean velocity components.

which are smaller than those of the primary valve suggesting lower overall swirl levels.

3.2.2 BOTH VALVES OPEN

Measurements were also obtained when both valves remained open and at the same lift and mass flow rate of 85 kg/s to the two previous cases when either the PV or the SV was open; the results are presented in figures 6 and 7. Due to the presence of the valve head and stem in front of the laser beams, the measurement of the tangential velocity at planes b and b' was not possible. The variation of the mean and rms velocity profiles of all three components around the valve is presented in figure 6 and shows similar trends to the corresponding profiles obtained when one of the valves was open, but with much smaller magnitudes, around half, which is expected since the annular flow area here is twice as large as with one valve open; because of the different scaling between the flow cases, direct comparison is not straightforward. The distribution of the rms velocities indicates the high level of turbulence intensities in all three components with values of around $0.4V_p$ in plane b and c to a maximum of $3.4V_p$ in plane c'.

The interaction between the two flows discharging from the intake valves can be better seen in vector form in figure 7(a). The flow angle of the discharging flow around the SV is slightly affected, with the largest changes in plane b where the flow angle becomes smaller by up to 5°. The discharging flow at plane b' of the PV is however affected by the strong jet coming from the opposite direction and evident in plane b of SV so that the flow profile exhibits a bimodal distribution; this in turn is affecting the flow at plane b of SV too, although to a smaller degree, by reducing the flow angle as shown above. The flow in plane a' seems to be unaffected, but at c' the flow changes considerably compared to the flow when only the PV valve was open, and in such a way that the flow angle reduces from 55° close to the cylinder head to nearly zero at the tip of the valve head. This implies that the radial flow is impaired by the incoming strong jet from plane c of the SV which is directed along the wall by the surrounding liner and by the impingement of the two discharging jets at planes b and b'. This effect at plane c' can also be seen in figure 7(b), where the addition of the radial and tangential mean velocities is presented, from the increase in the flow angle relative to the valve radius (50.5° compared to 34.5°) and the smaller magnitude compared to the case when the PV was only open. This in turn resulted in lower flow angles in planes d' and a' by 3° and 7°, respectively, compared to the case when only the PV valve was open. The average flow angles at the planes around the SV seem to be unaffected.

4. CONCLUSIONS

The steady flow characteristics around the two intake valves of a production four-valve diesel cylinder head were investigated by laser Doppler velocimetry for a mass flowrate of 85 kg/h corresponding to 1000rpm engine speed and the most important findings are summarised below.

The discharge and flow coefficients of the primary valve were lower than those of the secondary valve at all valve lifts, with a maximum difference of more than 20% around the maximum lift; when both valves were open the values of the coefficients were in between but much closer to those of the primary valve. The reverse trend was observed for the swirl coefficient in that the primary valve was generating much higher swirl than the secondary valve by more than sixfold; in the case when both valves were open, the value of the swirl coefficient was again found to fall between the values obtained with the two individual valves.

The discharging flow around the primary valve was found to be non-uniform with the maximum flow observed at planes which are in-line with the inlet port axis and the minimum flow at planes towards the end of the helical ramp of the port; this non-uniformity of the flow was found to be less pronounced around the secondary valve. When both valves were open the discharging flow from the secondary valve was little affected by the opening of the primary valve, while its effect on the exit flow of the primary valve was much more substantial, especially in two out of the four examined planes of the primary valve where the local flows were found to be greatly modified by the jet flow exiting from the secondary valve.

The distribution of the turbulence intensity was found not to be uniform around the valves, following the trend of the mean flow. The turbulence was, in general, anisotropic in all cases with maximum levels of up to $5V_p$ near the cylinder head and in the strong shear layer just above the valve tip for the case of the individual valves being open; with both valves open the maximum turbulence intensity was about $3.4V_p$.

Overall, it is clear that certain improvements in the design of production four-valve diesel cylinder heads are desirable and necessary in order to reduce the interaction between the flows discharging from the two intake valves. This effect is expected to be more pronounced at the higher air flowrates corresponding to the higher end of the speed range of passenger car diesel engines where volumetric efficiency deteriorates.

ACKNOWLEDGEMENTS

The authors would like to thank Mr Roy Horrocks of Ford for his contribution to the research programme, Dr H. M. Xu for many discussions and useful suggestions during the course of this work and Paul Bruni for the setting up of the experimental rig.

REFERENCES

Arcoumanis, C., Vafidis, C. and Whitelaw, J. H. (1987) Valve and in-Cylinder flow generated by a helical port in a production diesel engine. Trans. ASME J. Fluid Eng., **109**, 368-375.

Arcoumanis, C., French, B. and Nouri, J.M. (1995) "Steady intake flow characteristics through a diesel four-valve cylinder head (Part 2: high flowrates), Report TF/95/25b, Mechanical Engineering Department, Imperial College.

Haghgooie, M., Kent, J. C. and Tabaczynski, R. J. (1984) Intake valve cylinder boundary flow characteristics in an internal combustion engine. Comb. Sci. Tech., 38, 49.

Heywood B. J. (1988) Internal Combustion Engine Fundamentals. McGraw-Hill International Edition, Chapter 8.

LASER DOPPLER MEASUREMENTS OF THE INSTANTANEOUS VOLUME FLOW RATE IN PERIODICALLY OPERATING SYSTEMS

D. Trimis, M. Weclas, F. Durst

Lehrstuhl für Strömungsmechanik
Universität Erlangen-Nürnberg
Cauerstr. 4, D-91058 Erlangen / Germany

ABSTRACT

Research and development work carried out to provide a method to measure accurately instantaneous flow rates in periodically operating systems is summarized in this paper. The instantaneous flow rate is reconstructed from axial velocity time series measured by a laser Doppler anemometer on the center-line of a capillary pipe flow. The theoretical background on which the evaluation of the instantaneous flow rate is based is provided. It is shown that the axial mean velocity is sufficient to reconstruct the periodically varying flow rate and the pressure gradient. The application of the proposed method is described and an instrument suggested that can be employed in many fields where fast, periodically varying flow rates occur, and instantaneous information is needed.

1. INTRODUCTION

Fuel injection systems are devices that provide, over a finite time span, fuel injection through the nozzle and shape the fuel jet or fuel film in such a way that spray formation occurs. The nozzle geometry and the instantaneous flow rate of the fuel through the nozzle define the spray's initial properties; surrounding fluid properties are also important. Since there is no measuring system available that directly measures the instantaneous fuel flow rate through the nozzle, one usually uses secondary information that defines this flow rate (e.g. time-varying pressure, needle lift, nozzle geometry). All these parameters can easily be measured nowadays and it is also known that they somehow define the instantaneous flow rate through the nozzle. However, it remains unknown how the flow rate is related to them. Calibration is usually provided by static calibration of the flow rate versus pressure by neglecting the dynamic effects resulting from the needle opening, the fuel supply line, and the combustion chamber itself. The above-mentioned, commonly accepted procedure to provide information on the instantaneous fuel injection flow rate is far from being sufficient to provide the basis for advanced research and development work into spray injection systems. At LSTM-Erlangen, a method has been developed to perform instantaneous flow rate measurements as they occur during fuel injection.

2. MEASUREMENT TECHNIQUE AND INSTRUMENTATION

2.1 Theoretical Derivations

The principle for a measuring technique for instantaneous periodic volume flow rates has been described in detail in *Durst et al. (1996)*. The analytical solution of *Lambossy (1952)* for the velocity field of the harmonic oscillating fully developed laminar pipe flow, which is driven by a time-varying pressure gradient is used and extended for an arbitrarily time-varying pressure gradient, which may be expressed by means of a Fourier expansion. The linearity of the governing equation permits the resultant velocity field to be computed as a superposition of *Lambossy*' s solutions by taking

into the summation each of the n terms of the pressure gradient:

$$U(r,t) = -\frac{R^2 p_0}{4\nu}\left[1-\left(\frac{r}{R}\right)^2\right] + \sum_{n=1}^{\infty}\left[\frac{p_n}{n\omega} i e^{in\omega t}\left(\frac{J_0\left[i^{3/2}Ta_n\, r/R\right]}{J_0\left[i^{3/2}Ta_n\right]} - 1\right) + C.C.\right]$$

The instantaneous flow rate is therefore given by:

$$\dot{V}(t) = \frac{\pi R^2}{2}\left[\frac{R^2 p_0}{4\nu} + \sum_{n=1}^{\infty}\left[\frac{p_n}{n\omega} i e^{in\omega t}\left(\frac{4i^{1/2}J_1\left(i^{3/2}Ta_n\right)}{Ta_n J_0\left(i^{3/2}Ta_n\right)} - 2\right) + C.C.\right]\right]$$

where $U(r,t)$ is the axial velocity distribution across the pipe, $\dot{V}(t)$ is the instantaneous volume flow rate, *C.C.* is the complex conjugate, *Ta* the Taylor number, r the radial distance from the pipe center-line, R the pipe radius, J_0, J_1 the Bessel function of zero and first order, ω the frequency of oscillation and ν the fluid kinematic viscosity. Computing the pressure gradients p_0 and p_n permits the time-varying flow rate $\dot{V}(t)$ to be calculated. The above derivations applied to the center-line velocity of a fully developed laminar pipe flow can be processed to yield the coefficients of the appropriate Fourier terms, which can subsequently be employed to compute the instantaneous volume flow rate through the pipe, see *Durst et al. (1996)*.

Validation of the above formula is limited to fully developed laminar flow conditions.

2.2 Practical realisation

A measuring instrument very suitable for the accurate measurement of the instantaneous flow rate of periodically varying fully developed laminar pipe flow was built at LSTM-Erlangen. The instrument is based on the LDA technique for center-line velocity measurements, see *Bopp et al. (1989), Durst et al. (1993)*. The test-rig consisted of a pressure vessel which was filled with a liquid used in the experiments as a working fluid. The pressurized gas in the vessel pushed the working fluid through the pipe system including a test section with a glass pipe of typical internal diameter d = 2 or 3 mm. Inside this glass pipe the measurement volume of the LDA system was positioned on the center-line of the pipe (Fig. 1) and the time-dependent velocity distribution over a large number of cycles was measured.

Time variations of the flow in the pipe were driven by an injector mounted at the end of the glass pipe. Within each cycle, predetermined opening times could be selected, and each period was divided into 1000 slots (phases τ) within which the velocity data were collected over a large number of cycles. An ensemble-averaging procedure was used to calculate the mean velocity on the pipe center-line. At the exit of the valve the liquid was collected to perform the mass balance. The LDA-system (Fig. 1) includes an He-Ne laser (30 mW in the TEM_{00} mode, λ = 0.6328 µm). The laser beam was passed through a beamsplitter, resulting in two output beams of equal intensity. These were passed through Bragg cells to provide a relative frequency shift (from a few kHz to a few Mhz). The crossing point was positioned on the center-line of the glass pipe. The diameter of the measurement volume was 47 µm, its length was 190 µm, and the interference fringe spacing was 1.794 µm. Light scattered from the measurement volume was collected in the forward direction and was passed on to an avalanche photodiode (APD). Its output signal, containing frequency (velocity) information, was processed with a LDA signal processor (TSI 1980).

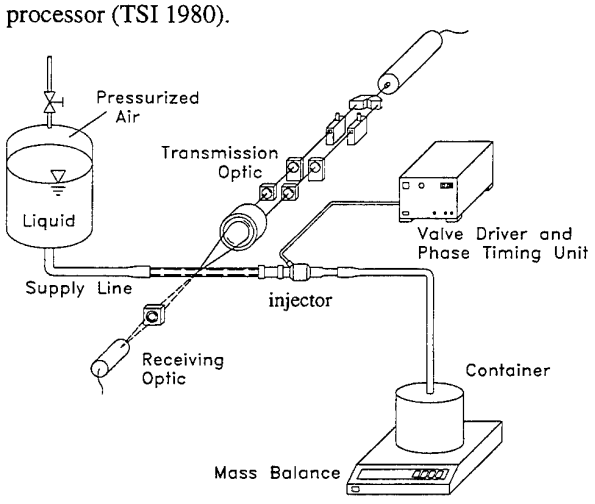

Fig. 1 Scheme of the test rig for instantaneous flow rate measurements

The counter was connected to an interface board, which transferred the data to an IBM-compatible PC. Additionally, the information of the phase was also transferred to the PC.

3. APPLICATION OF LDA FLOW RATE METER TO OPERATING GASOLINE INJECTORS

3.1 Overall characteristics of operating injetion systems

Some examples showing the main features and capabilities of the technique are presented below on the basis of experiments performed on gasoline injectors. The distributions of center-line velocity phase series and corresponding reconstructed flow rates for different valve operating frequencies at τ = 10 % opening time of the valve are shown in Fig. 2.

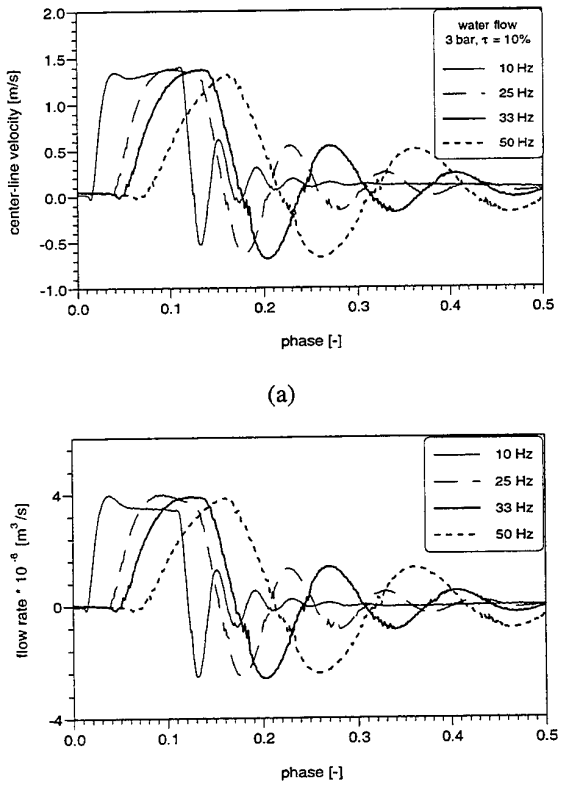

Fig. 2 Center-line velocity time series (a) and reconstructed flow rate (b) for p = 0.3 MPa τ = 10% and different frequencies (water flow)

Significant wavy effects after valve closing are clearly observed. As shown, temporal distributions of axial velocity and flow rate correspond to the valve opening period with some offset (phase shift), which depends significantly on the operating frequency, as shown in Figure 3.

The distributions of the center-line velocity and the corresponding reconstructed flow rates for different opening periods of the valve at f = 10 Hz are shown in Fig. 3.

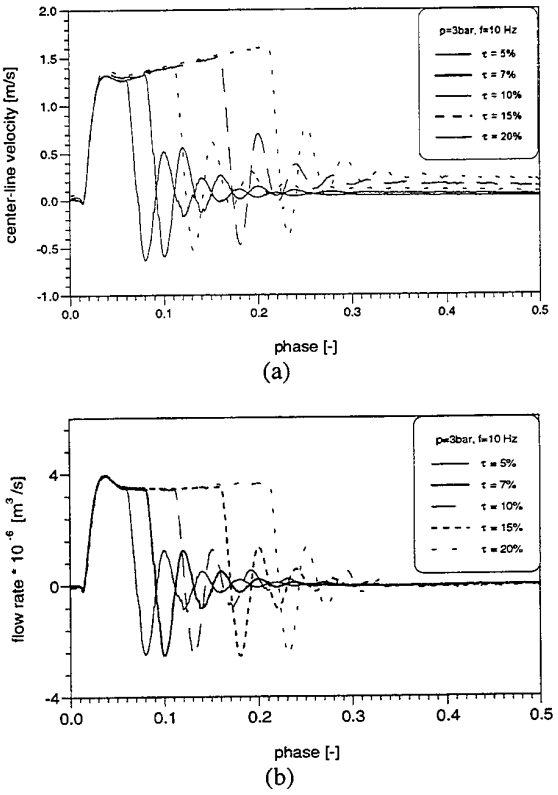

Fig. 3 Center-line velocity time series (a) and reconstructed flow rate (b) for p=0.3 MPa f=10Hz and different opening times (water flow)

In figs. 4 and 5 the opening characteristic of the valve is presented for different frequencies in absolute time scale. In order to verify the independence of the injection characteristics from the operating frequency, the opening procedure of the valve is presented in absolute-time series for two different frequencies and opening durations. The operating parameters were chosen in such a way that the resulting absolute opening time t of the valve was kept constant.

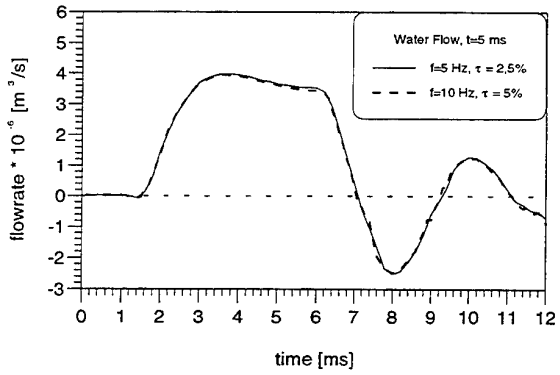

Fig. 4 Reconstructed flow rate at valve opening in absolute time scale for t=5 ms opening duration

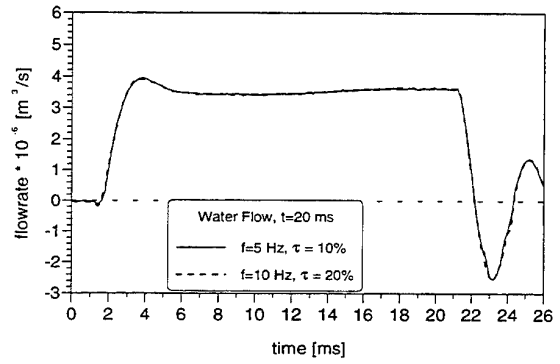

Fig. 5 Reconstructed flow rate at valve opening in absolute time scale for t=10 ms opening duration

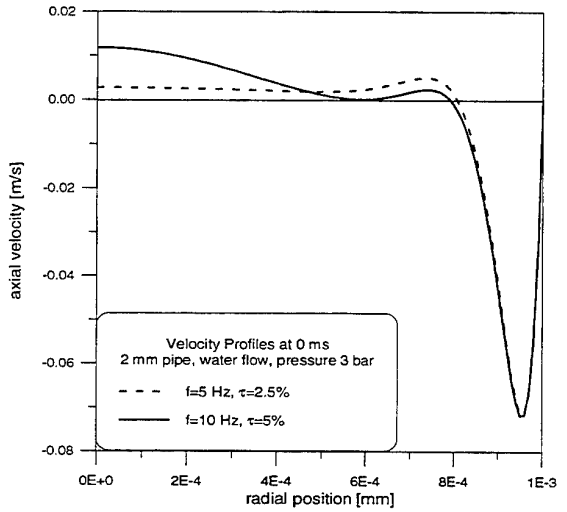

Fig. 6 Velocity profiles correspondent to fig. 4 at an absolute time of 0 ms

Although the operating frequency and relative opening duration are different (absolute opening time is constant) the reconstracted flowrate distributions are almost identical. However, the reconstructed velocity profiles in the test section are different because of the different operating conditions, resulting in different dynamic characteristics of the flow system, as shown in fig.6 at the start of the period.

The situation with lower frequency (dashed line) is more similar to a "plug flow" whereas the case at higher frequencies (solid line) is the velocity profile more developed. This is because at lower frequencies the flow had time to settle down after the valve closing (except at the boundaries).

According to the above findings, it is sufficient to present the full injector characteristics at different opening durations only at a single operating frequency. Examples of differential and integral injection characteristics of gasoline injector are given in fig. 7.

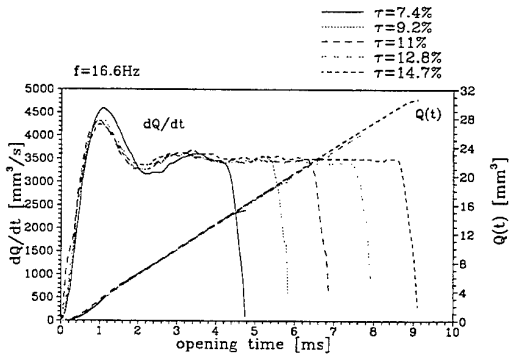

Fig. 7 Differential and integral injection characteristics (gasoline flow)

The flowrate distribution indicates that the amount of injected liquid is basically dependent on the absolute opening time of the valve. This result has significant implications for electronically controlled gasoline injection systems in IC-engines.

3.2 Tests with different pipe diameters

The validity of the technique was also investigated by comparing data for the same mean flow rates but for different internal diameters of the glass (test) pipe, as shown in Fig. 8. The data are

compared for two pipe diameters (d = 2 and 3 mm). For significantly different center-line velocity distributions the reconstructed flow rate is very similar (within the repeatability of the flow conditions). The reconstructed flow rates are very similar for both pipe diameters investigated. However, differences in the wavy effects are clearly observed due to significant differences in the pressure waves penetration through the test section, especially after the valve closing. For the larger pipe these fluctuations are significantly reduced.

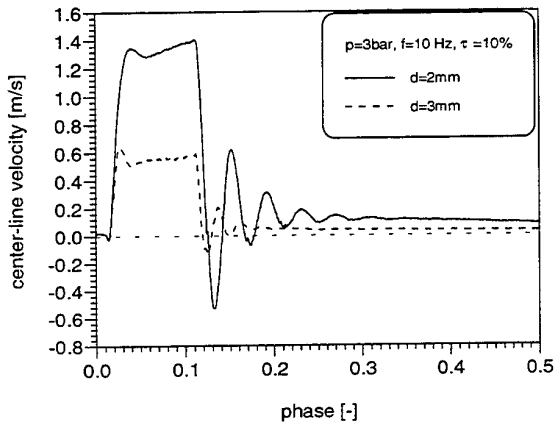

(a)

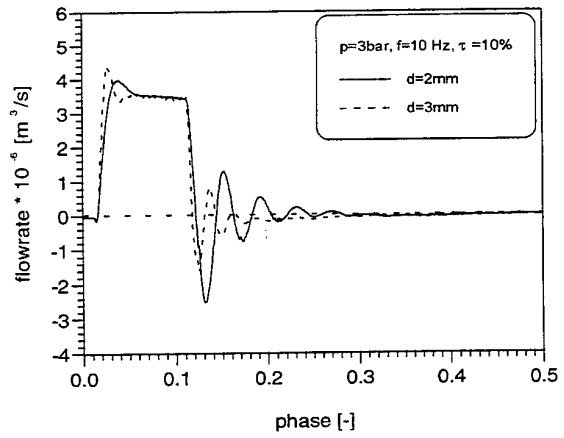

(b)

Fig. 8 Center-line velocity time series (a) and reconstructed flow rate (b) for p=0.3 MPa f=10 Hz t=10 % and different pipe diameters (water flow)

In fig. 9 the reconstructed velocity profiles for both pipe diameters at same operating conditions and at an absolute time of 2 ms are presented.

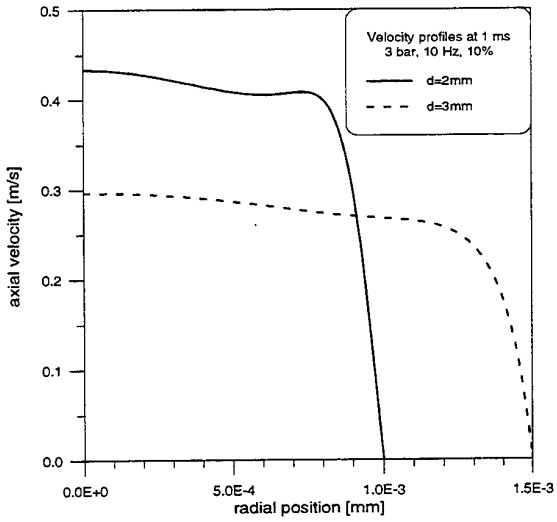

Fig. 9 Reconstructed velocity profiles at 1 ms absolute time corresponding to fig. 8

As shown in fig. 8 the transient characteristics at opening and closing are different for the two pipe diameters. The larger pipe diameter is characterized by steeper flowrate gradients at the beginning of the opening. The flowrate level during the open period is the same for both pipe diameters. After valve closing, the oscillations of the pipe flow are reduced in amplitude and frequency for the larger pipe (3mm) in comparison to the smaller pipe (2mm). By comparing the two curves of fig. 8a one can see that the acceleration of the fluid elements in the centre of the pipe is the same for both pipe diameters. However, in the case of the smaller pipe, larger velocities have to be reached in order to get the same flowrate, which is basically defined by the pressure losses of the injector. This results in longer times until the highest velocity is reached in the case of the smaller pipe. The same behaviour is observed during the oscillations that occur when closing the valve (same acceleration rate, higher velocities resulting in longer times for the smaller pipe diameter).

Because of the significant differences in the velocity level between the two pipe diameters (fig 8a) the velocity profiles in fig. 9 at 2 ms are correspondently different. However, the smaller pipe has a more "developed" velocity profile, because of the

larger velocities across the entire pipe section. However the integrated injection characteristics are practically the same for both investigated pipe diameters as shown in fig. 10.

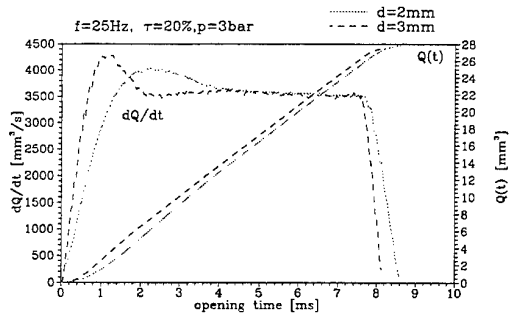

Fig. 10 Differential and integral injection characteristics for two pipe diameters

4. CONCLUSIONS

The presented technique shows that the center-line axial velocity of a fully developed oscillatory laminar pipe flow is suitable for computing the instantaneous volume flow rate. For these measurements the LDA technique provides velocity information with sufficient time and spatial resolution. A laser Doppler flow rate meter has been built and applied to operating gasoline injectors. The only requirements for the application of the instrument are the following:

- arbitrary periodic flow conditions;
- laminar flow;
- sufficient entrance and outlet lengths in order to have a fully developed laminar oscillatory flow;
- transparent fluid with tracer particles, in order to make LDA measurements possible;
- a phase-timing unit or an angle encoder in order to build phase averages of the recorded velocity-time series.

The demonstrations included frequencies that are of technical relevance, i.e. for injection systems employed in the automobile industry.

As shown, for a given injector, the instantaneous flow rate distribution over the valve opening period is independent of the operating frequency and depends only on the opening duration.

In general, the increase in flow rate is a function of the opening characteristic of the electromagnetic valve employed but also of all the elements incorporated in the pipe system. They all contribute to the time constant describing the increase in flow rate just after valve opening. Especially the upstream pipe diameter influences the time constant of the injection system. This results in different transient behaviour during the valve opening and closing but not during the open period of the injector.

REFERENCES

Bopp, S., Durst, F., Holweg, J., Weber, H. (1989), *A laser-Doppler sensor for flow rate measurements*, Flow Meas.Instrum., Vol. 1, No. 1, 31-38.

Durst F., Ismailov M., Trimis D (1996), *Measurement of instantaneous flow rates in periodically operating injection systems,* Exp. Fluids, Vol. 20, 178-188.

Durst, F., Teufel, M., Trimis, D., Weber, H. (1993), *Genaue Messungen kleinster Volumenstrome,* Wägen & Dosieren, Vol. 24, No. 2, 3-8.

Lambossy, P. (1952), *Oscillations forcées d'un liquide incompressible et visqueux dans un tube rigide et horizontal. Calcul de la force frottement,* Helv. Physica Acta 25, 371-386.

SESSION 17

Wall Flows I

A Study of Streaky Structures in a Turbulent Channel Flow with Particle Image Velocimetry

Z.-C. Liu [a),b)], R. J. Adrian [a)], T. J. Hanratty [b)]
[a)] *Department of Theoretical and Applied Mechanics*
[b)] *Department of Chemical Engineering*
University of Illinois
Urbana, Illinois 61801

Abstract

The streaky structures in a Reynolds number 6,800 turbulent channel flow are studied using PIV. Streamwise-spanwise planes at vertical locations y^+ = 16, 20, 50, 80, 110 and 385 are investigated. The fluctuating velocity fields clearly contain low- and high-speed streaks. Filtering techniques separate the streaks from small, roughly circular vortices that are evident in each of the fluctuating fields. The low-pass filtered field gives the low-speed and high-speed streaks, and the high-pass filtered field gives the same 'circular' vortices. The lowpass-filtered field contains larger, roughly circular vortices that occur in conjunction with the complementary streaks. This association is consistent with the low-speed streaks being formed by inclined vortices or hairpin vortices that are mere mature than the smaller vortices. The latter appear uncorrelated with the former.

Visual evaluation of the low-speed streak patterns in the PIV data indicates spanwise streak spacing that is consistent with previous investigations, i. e. $\lambda^+ \sim 100$ at the wall, and increases with increasing y^+. However, quantitative Fourier analysis shows that $\lambda^+ = 100$ is actually the weaker of several larger wavelength modes.

Introduction

Streaky structures containing low-momentum and high-momentum flows in the streamwise direction are important organized motions found in the near wall region of wall turbulence. Most experimental studies have been based on qualitative flow visualization with hydrogen bubble line or dye injection techniques (e. g. see Kline *et al*, 1967, Smith & Metzler, 1983). The present work studies the streaky structures in a turbulent channel flow at a moderate Reynolds number by using particle image velocimetry to examine the whole flow field quantitatively. Six streamwise-spanwise planes at different distances above the wall have been investigated. The PIV results show that in the buffer and logarithmic layers the fluctuating flow fields are full of low-speed and high-speed streaks. A new aspect of our work is that the quantitative nature of the PIV data makes it possible to observe compact vortices that occur at the sides of the streaky structures. A filtering technique applied to the velocity data clearly reveals different aspects of the total field. The streamwise scales of the streaks found in this study range from 500 to more than 1000 viscous units. The spanwise spacing appears to be about 100 viscous units at the wall, and it increases with the distance away from the wall, in accord with results of other researchers. However, the quantitative nature has a significant impact on the interpretation of the data. Fourier analysis in the spanwise direction reveals that estimation of the streak spacing from visual examination is misleading. There are, in fact, several larger wavelength modes that contain considerably more energy than the $\lambda^+ = 100$ mode. The latter is more visible, but less energetic than the others.

Experiment:

The experiments are performed in a 15.24 m long (x) water channel with a flat-wall and a rectangular cross section of $2h$ = 48.75 mm high (y), 609.6 mm wide (z). The fully developed turbulent water flow has a Reynolds number of $Re_h = U_b h/\nu$ =6,800 ($Re_\tau = u_\tau h/\nu = 395$), where U_b is the bulk velocity, u_τ is the friction velocity calculated using measurements of bulk velocity and Dean's correlation of the friction coefficient (Dean 1978), h is the half height of the channel, and ν is the kinematic viscosity of water. The temperature of the water is controlled during experiments to maintain the same viscosity and flowrate for all realizations. The channel is filled with tap water that is cleaned with 3 μm filters. Turbulent flow in this channel has been documented previously by LDV studies (Niederschulte, 1989 and Niederschulte et al, 1990), and comparisons of the time averaged moments of the u - and v - fluctuations through fourth order at Re_h = 2,777 and 18,000 agree well with the channel flow results of other investigators.

Particle image velocimetry is used as a quantitative flow visualization technique to record instantaneous velocity fields in horizontal planes of the channel flow (Adrian 1991). The test section of the channel has 5.5 cm x 15 cm optical windows on both sides and a 10.5 cm x 15 cm optical window on the top wall, which allow a double-pulsed laser light sheet to illuminate a horizontal plane of the flow from the side window and a camera to record the flow velocity field from the top window. A sketch of the channel and the optical arrangements for PIV measurements are shown in Fig. 1. Aluminum oxide particles with a nominal mean diameter, d_p = 9.5 μm, at a concentration of about 15 particles per cubic mm are seeded in the flow and illuminated by two 2J ruby laser pulses with pulse duration of 30 ns. The image size of a particle given by the present optical system is d_τ = 35 μm. The time separation between the two pulses can be adjusted for each of the planes at different distance away from the wall, to provide an average displacement of particle images of about a quarter of the interrogation spot size that satisfies the requirement for achieving a high detection rate during interrogation using autocorrelation (Keane & Adrian, 1990). When using the single-frame cross-correlation interrogation technique this

requirement is relaxed by adjusting the offset between two interrogation windows. Therefore, in the present work a fixed time separation, Δt = 1.2 ms, is used for all planes. A 16 mm laser beam is expanded in horizontal direction by a cylindrical lens with 150 mm focal length, and focused in the vertical direction by a spherical lens with 787.5 mm focal length to provide a light sheet that is 120 mm wide and 0.8 mm thick in the test section. A 100 mm by 125 mm large format camera with a *f#* 9 Schneider lens of 305 mm focal length is used to photograph the particle images at a magnification M = 0.928 on Kodak 4415 film. A 305 mm by 254 mm mirror is inserted in the optical path so that the camera can be positioned horizontally. No image shifting is needed in the second exposure because of the overwhelmingly positive streamwise velocities. The error due to the refractive index of water and the window is negligible since the optical path is less than 37 mm compared with the much longer path in air.

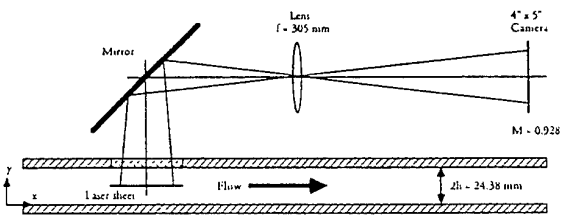

Fig. 1 Optical arrangement for PIV measurements in streamwise-spanwise (horizontal) planes of the channel flow (y^+=16, 20, 50, 80, 110 and 385) at Re_h=6,800.

Six horizontal planes parallel to the lower wall are studied. They are located at y^+=16, 20, 50, 80, 110 and 385, where y^+ is the distance away from the wall in terms of viscous unit. The planes are so chosen that the first two are in the buffer layer, the next three planes are in the logarithmic region, and the last one is close to the center of the channel. The streamwise ensemble mean velocity, $U(y^+)$, is shown in Fig. 2 together with data from DNS by Kim (1996). The dimensions of the measurement volume are determined by the laser light sheet thickness in the wall-normal direction, Δy_0 = 0.8 mm, and by the interrogation spot size, Δx_0 = 1.8 mm and Δz_0=1.35 mm. In terms of viscous wall unit they are Δx_0^+ = 21.7 ,Δy_0^+ = 12.96 and Δz_0^+ = 29.0. A velocity vector obtained from interrogation by correlation analysis corresponds to a volume average over $\Delta x_0 \Delta y_0 \Delta z_0$ (Adrian 1988). The smallest scales of motion are not resolved in the present studies, and there are some averaging effects in the near wall regions. However, the resolution is still enough to resolve the streaky structures in this study. More information about flow parameters in the present study are given in Table 1. Interrogation of PIV photographs is carried out with a high speed system (Meinhart et al 1993), consisting of a SUN 4/370 host workstation and eight 80 Mflop Mercury MC860 array processors, utilizing parallel array processing technology. A Videk Megaplus CCD camera with 1,024 x 1,024 pixel resolution acquires images from the photographs. The CCD array is divided into eight sub-arrays that are passed to each of the eight array processors. An Imaging Technology VSI-150 frame grabber equipped with double input buffers (1,024 x 1,024 x 16 bits), digitizes the images at a frequency of 20 MHz. This system can calculate over 100 velocity vectors per second from 128 x 128 pixel interrogation spots.

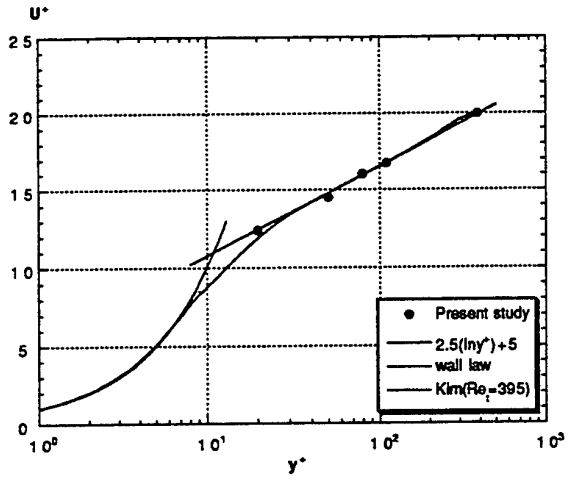

Fig. 2: The streamwise ensemble mean velocities. Solid circles are data points of PIV measurements for horizontal planes with six locations in wall-normal direction. The open circles are data from DNS.

Table 1: Flow parameters

Re_h ($U_b h/\nu$)	6,800
Re_τ ($u_\tau h/\nu$)	395
ν (cm^2/s)	9.269 x 10^{-3}
T (°C)	23.5
U_b (m/s)	0.258
u_t (mm/s)	15.036
ν/u_τ (mm)	0.06164
U_b^+	17.2
U_c^+	19.92
h^+	395.44
Δx_0^+	29.0
Δy_0^+	12.96
Δz_0^+	21.7

A single-frame, double-exposure cross-correlation technique is used to interrogate all 300 PIV photographs for six y-locations. The cross-correlation significantly improves the signal-to-noise ratio over autocorrelation by increasing the positive displacement peak (without significantly changing the fluctuating noise), reducing the self-correlation peak and negative displacement peak, and eliminating in-plane velocity gradient bias by removing in-plane image pair-loss (Keane and Adrian 1992). The sizes of the first and second windows of cross-correlation are chosen to be 128 pixels by 64 pixels in the streamwise and spanwise directions respectively. They are 1.8 mm by 1.35 mm in physical dimension, 29.0$^+$ by 21.7$^+$ in terms of viscous wall unit. The use of asymmetric cross-

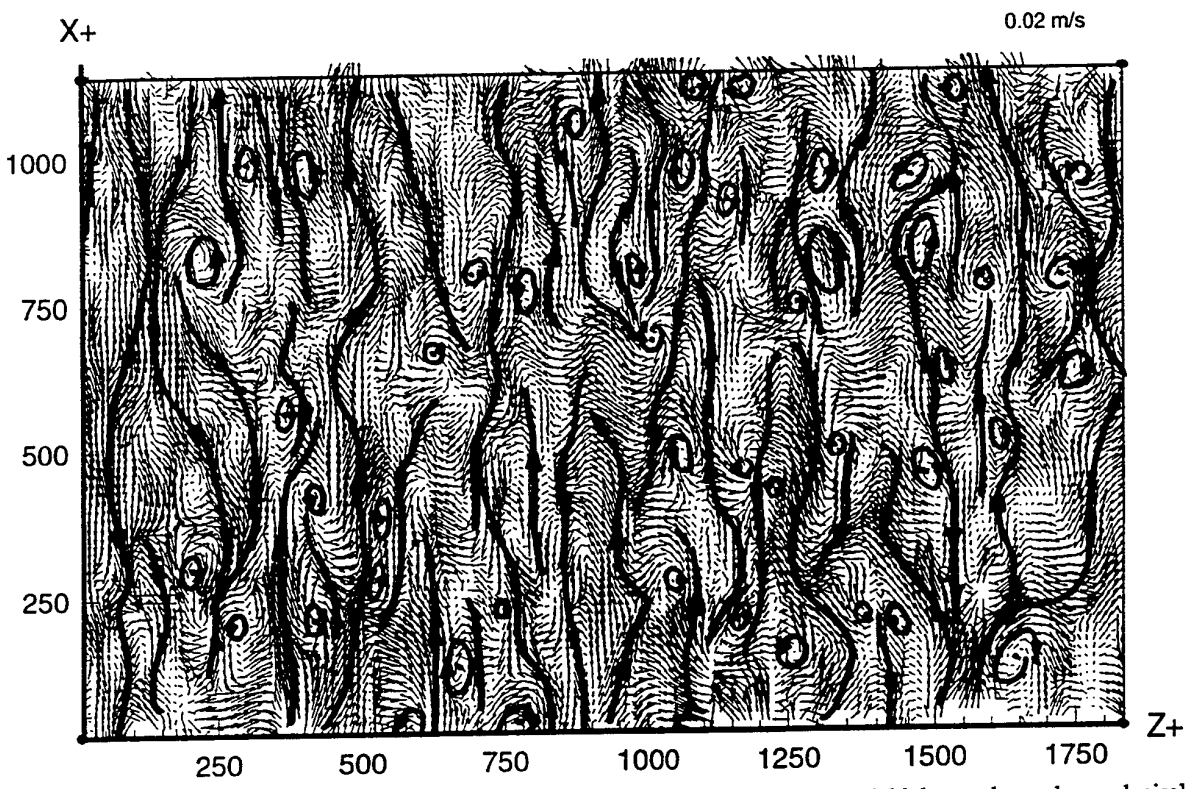

Fig. 3. Fluctuating velocity field at $y+ = 20$. Lines represent low-speed streaks and high-speed streaks, and circles represent vortices.

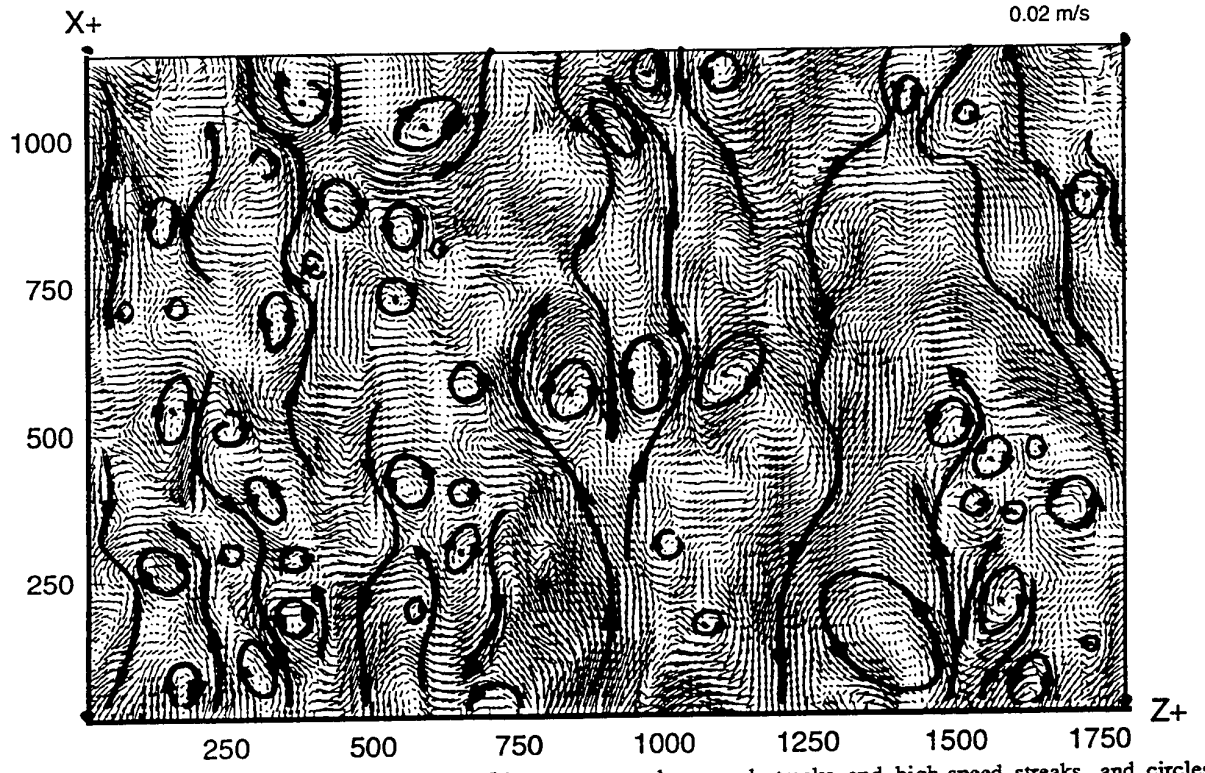

Fig. 4. Fluctuating velocity field at $y+ = 80$. Lines represent low-speed streaks and high-speed streaks, and circles represent vortices.

correlation windows is based on the consideration that the velocities and the scales in streamwise direction are larger than in the spanwise direction. The offset of the windows is set to be 16 pixels at the beginning of the interrogation to match the displacement of the image pairs and adaptively adjusted during the rest of interrogation to match the local displacements of image pairs. This adaptive windowing technique is important and necessary for high quality interrogation in cases where the dynamic range of velocity in the whole field is large. The interrogation with 50% overlap of interrogation windows meets the Nyquist sampling criterion, and gives about 12,000 to 20,000 vectors in a photograph for the six planes. The CCD camera's center-to-center distance between pixel is d_{pix} = 14 μm/pixel. This gives the ratio d_τ / d_{pix} = 2.5 pixel which is greater than two pixels per particle image criterion that is required for the finite resolution of the CCD chip to have negligible effect on the accuracy of measuring displacement of particle image (Adrian 1995).

Table 2: Parameters of interrogation using cross-correlation:

M	0.928
Δt (ms)	1.2
d_p (μm)	9.5
d_τ (μm)	40
d_{pix} (μm/px)	0.014
d_τ / d_{pix}	2.9
FFT window (px)	128 x 128
correlation window (px)	96 (z) x 128 (x)
window offset (px)	16
sampling overlap (%)	50
number of vectors	12000-20000

Raw vectors obtained from interrogation are validated, and invalid vector data are removed with an automatic post-interrogation procedure that replaces invalid vectors with alternatives from other correlation peak measurements (Meinhart 1994). The program runs in interactive mode on a Silicon Graphics workstations, and it can be executed in batch mode as well. Two main automatic techniques are applied to this vector validation process: bad vectors are removed when they fall outside a user assigned standard deviation from the mean, or their magnitude differences from the median of their surrounding neighbors are larger than a user specified value. The missing vectors due to removal can be replaced with alternative vectors that are supplied from other correlation peaks during interrogation, or from interpolation if there are no valid alternative vectors available. A Gaussian low-pass filter with a width of 0.75 grid size is used to remove noise that is still present in the vector field.

Fluctuating velocity fields

The ensemble mean streamwise velocity shown in Fig. 2, $U(y^+)$, is calculated by averaging the instantaneous streamwise velocity component, $\tilde{u}(x,y)$, at all points in the same plane, since the flow is homogeneous in streamwise and spanwise directions. Ensemble averaging is carried out over all realizations for each plane. Fluctuating velocity fields, $u(x,y)$, are obtained using Reynolds decomposition as usual:

$$u(x,y) = \tilde{u}(x,y) - U(y)$$

Fig. 3 and 4 depict the fluctuating velocity fields of realizations at y^+ = 20, 50 and 80. The streamwise direction of the flow is in x^+ direction.

The most striking features in these fluctuating fields are the low-momentum and high-momentum streaks aligned in the quasi-streamwise direction. The dashed lines on the figures identify low momentum streaks and the solid lines identify high momentum streaks. In the buffer layer at y^+ = 20 , Fig. 3, the streaks have an apparent spanwise spacing of about 100 viscous unit and a streamwise scale of 500 to more than 1000 wall units. Most low-speed streaks are narrower than the high-speed streaks. In the logarithmic layer as the distance from the wall increases, Fig. 4, the streak spanwise spacing becomes wider; also the streamwise scale becomes shorter.

At y^+ = 385 (not shown) close to the center line, streaks can barely be seen and may not exist. The streaks are not perfectly streamwise; they drift around in the spanwise direction, possibly with a coherent angle. The flow visualization indicates that some streaks seem to merge and some seem to divide. The individual spacings vary even within one realization at the same y -plane.

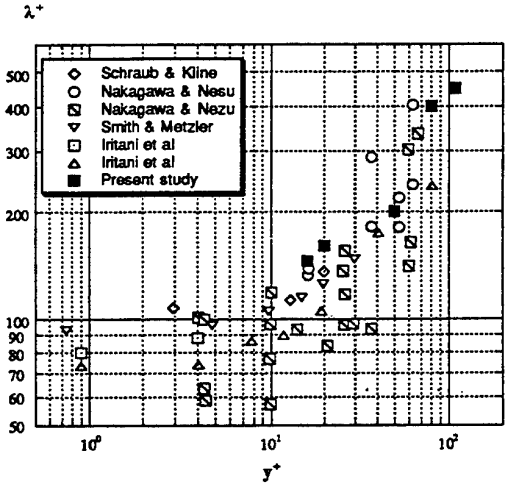

Fig. 5. Average spanwise streak spacings vs. distance away from the wall

Counting the numbers of low-speed streaks in the spanwise direction and averaging the count over all realizations for each y^+ -plane gives the average number per unit width. The reciprocal of this number is taken to be the mean spacing between low-speed streaks. The results are plotted in Fig. 5 together with results from other researchers collected by Kasagi (1988). When determined in this way (by flow visualization) the results of the present study agree well with those of previous researchers. Although one can find individual spanwise spacing of 100 at y^+ = 16 and 20 planes , the averaged spacing is somewhat larger than this typical value. The experimental

data in Fig. 6 from different researchers show that the averaged spanwise spacings deviate from 100 and increase, starting from around $y^+ = 10$, with increasing distance from the wall.

Another important feature that can be observed in the fluctuating fields is that vortices show up in the region between the low-speed streaks and the high-speed streaks, appearing singly or in pairs. The circles on the figures identify typical vortices of this type. Looking at the fluctuating fields Figs. 3 and 4 carefully, one can see that there is a weak partial coherent association of the streaks with the vortices. The vortices in the planes at $y^+ = 16$ and 20 show some elongation. As the distance from the wall increases the vortices become more circular and increase a little in size. This is consistent with a picture in which the planes cut through an inclined vortex whose inclination is small at low y and increases with y, as illustrated in Fig. 6.

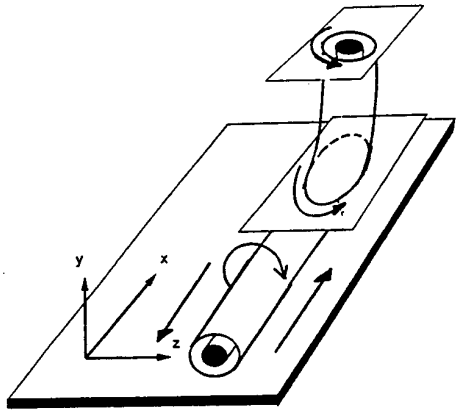

Fig. 6. cross-sections of a single inclined vortex observed in *x-z* planes located at various distances above the wall.

The connections between the streaks and the vortices suggest that they may be two aspects of a common vortex structure, either a single vortex that is tilted at an angle in the streamwise direction or a hairpin vortex whose legs are similar to those of the single ones. In the core of hairpin-like vortices the legs are quasi-streamwise vortices that generate low-speed fluid between them and high-speed fluid outside of them. The horizontal laser light sheet in the experiments cuts the tilted legs of the vortices and captures the cross-section of them between the low- and high-streaks, Fig. 6.

Recently, a direct numerical simulation by Zhou *et al* (1996) demonstrates that sufficiently strong hairpin vortices are capable of generating a hierarchy of secondary hairpin vortices that are aligned in the same streamwise direction, as shown in Fig. 7. They are associated with a strong low momentum flow by the interaction of the legs. A horizontally cut view of this structure at $y^+ = 80$ is given in Fig. 8 which demonstrates the association of low-speed streak with vortices. The vortices appear on both sides of the low-speed streak and between the low- and high-speed streaks. This is similar to what has been shown in Figs. 3 and 4 in the real flow.

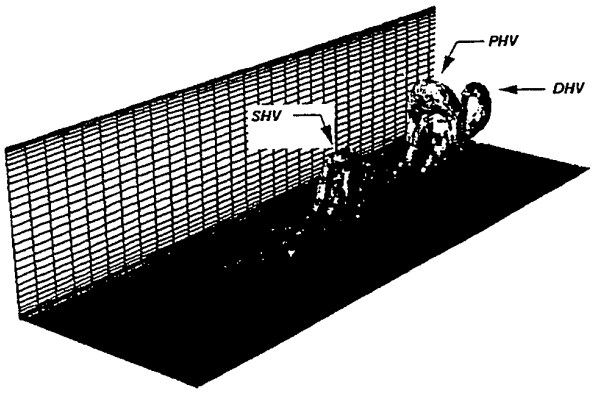

Fig. 7. A hierarchy of hairpin vortices from a DNS study. (PHV: primary hairpin vortex; SHV: generated secondary hairpin vortex; DHV: generated donwstream hairpin vortex)

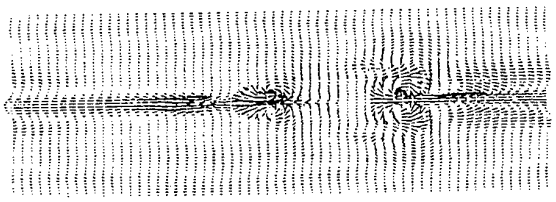

Fig. 8. A horizontal (streamwise-spanwise) cross-section of generations of the hairpin vortices shown in Fig. 7.

Filtered fields

In order to reveal the streaks and vortices more clearly, a filtering technique has been applied to the fluctuating velocity fields. Since the fluctuating fields exhibit apparently different scales in the streamwise direction, it is possible to use a properly chosen low-pass filter to decompose them into two scales.

$$u(x,y) = \bar{u}(x,y) + u_s(x,y)$$

The filtering operation is a convolution of the fluctuating field with a sinc filter function resulting in a low-pass filtered field that contains the large scales. The complimentary high-pass field contains the small scales (i.e. the subgrid scale in terms of large eddy simulation . A one-dimensional filter in the streamwise direction with sharp cut-off in spectral space, that has been used in LES study by many researchers, and it has also been chosen for the present work. Other types of filters such as a Gaussian filter or a top-hat filter could be used, but for separating the scales clearly the sharp-cut filter in the spectral space works best. The filtered field, $\bar{u}(x,y)$, is expressed by

$$\bar{u}(x,y) = \int g(x-x') \cdot u(x',y)dx'$$

while the subgrid field, $u_S(x,y)$, is expressed by

$$u_s(x,y) = \bar{u}(x,y) - \bar{u}(x,y)$$

where $g(x\text{-}x')$ is a filter of a sinc function form in physical space:

$$g(x-x') = \frac{2\sin[2\pi(x-x')/L_c]}{\pi(x-x')},$$

and L_C is the filter size in the *x*-direction. The Fourier transform of $g(x\text{-}x')$ is a sharp-cut filter in spectral space:

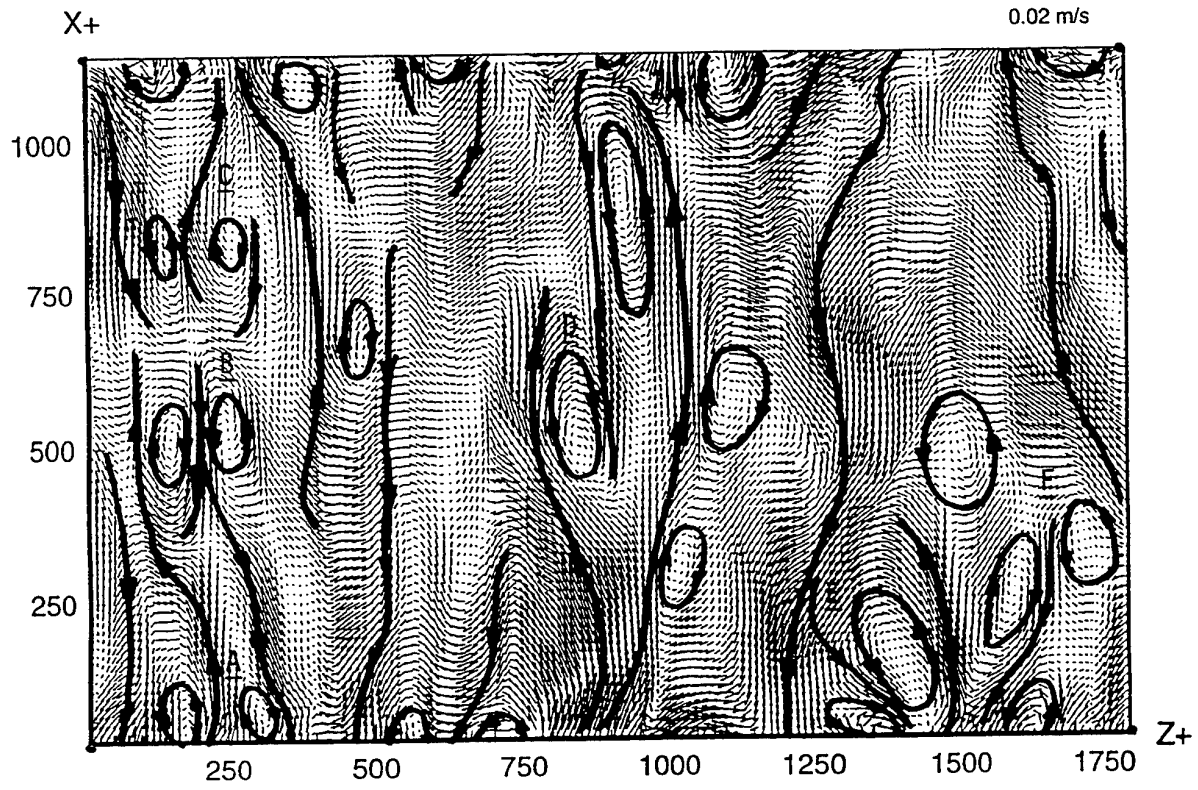

Fig. 9. The filtered field at y+ = 80 with length scales larger than L_c ($\lambda \geq 406^+$). Lines represent low-speed streaks and high-speed streaks, and ircles represent vortices.

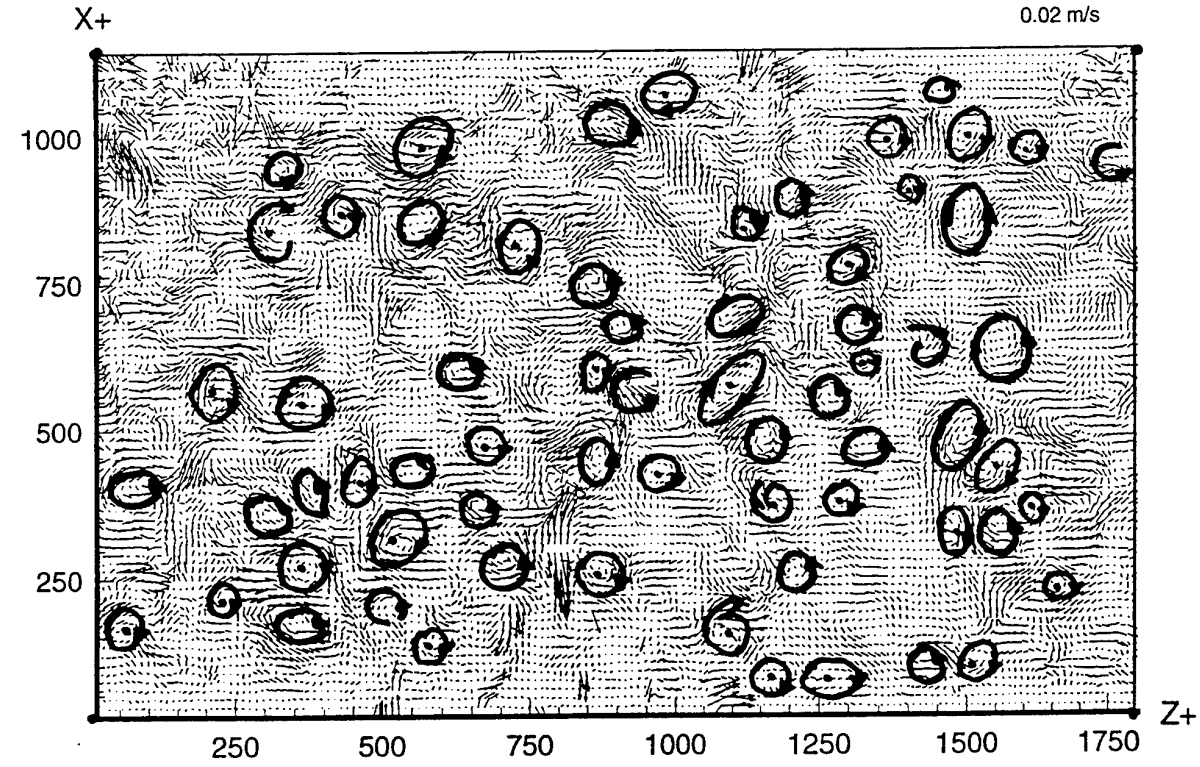

Fig. 10. The subgrid field at y+ = 80 with length scales less than L_c ($\lambda \leq 406^+$). Circles represent vortices.

$G(k)=1, \quad /k/ \leq k_c,$

$G(k)=0, \quad$ otherwise

where $k = 2\pi/\lambda$ and λ are the wavenumber and the wavelength of the scale in the flow, respectively. $k_C = 2\pi/L_C$ is the cut-off wavenumber of the filter.

Since the streaks are observed to have the scales at least 400 - 1000 wall units in the streamwise direction, the cut-off length scale, and therefore the filter size, L_C, is chosen to be about 406^+. (This value is also close to some of the published LES work.) Fig. 9 and Fig. 10 give a filtered field and a subgrid field at $y^+ = 80$ with the filter size $L_C = 406^+$. The filtered field resolves the scales in the streamwise direction larger than 406^+ and keeps all the scales in spanwise direction because of no filtering operated in this direction. The filtered field in Fig. 9 shows the low-speed streaks, high-speed streaks are roughly circular vortices whose diameters are of the order of 100 ~ 200 viscous units. The circular vortices are arranged along the sides of the streaks, and pairs of counter-rotating vortices often straddle a streak, suggesting that the streak is associated with a hairpin vortex. Examples of such pairs are labeled A - E in Fig. 9. Pairs B, D, E and F are associated with low-speed streaks and would correspond to hairpin vortices like those in Fig. 7 which creates second quadrant Reynolds stress events ($u < 0, v > 0$ in the region of the hairpin head). Pairs A and C are associated with positive u-momentum streaks, and would correspond to sweep or inrush events. Note that several vortices also occur without being part of the a pair.

The streaks in Fig. 9 have varying lengths, and sometimes they clearly terminate, as in the region between pairs B and C. However, the end of a streak may only signify displacement of the streak from the plane.

The small scale vortices in Fig. 10 all have diameters (based on visual estimation) between 30 and 100 viscous units. Their scales approximately one-half the scale of the 'circular' vortices in the low-pass filtered field. The locations of the small-scale vortices have little correlation with the larger-scale vortices. Overlaying Fig. 9 and 10 reveals almost no instances in which a small vortex and a large vortex coincide. There may be a tendency for the small vortices to cluster around streaks, but the trend is weak, and further analysis of this conjecture is needed.

Spanwise modes

It has been shown by visualization that he low-speed streak spacing at the wall is $\lambda^+ \sim 100$, and it increases with increasing y . However, PIV data permits quantitative evaluation of the spanwise modes of the streaky structures by Fourier analysis method.

Two-dimensional power spectra for each horizontal plane of the flow have been computed. The expression of the power spectrum is given by the Fourier transform of two

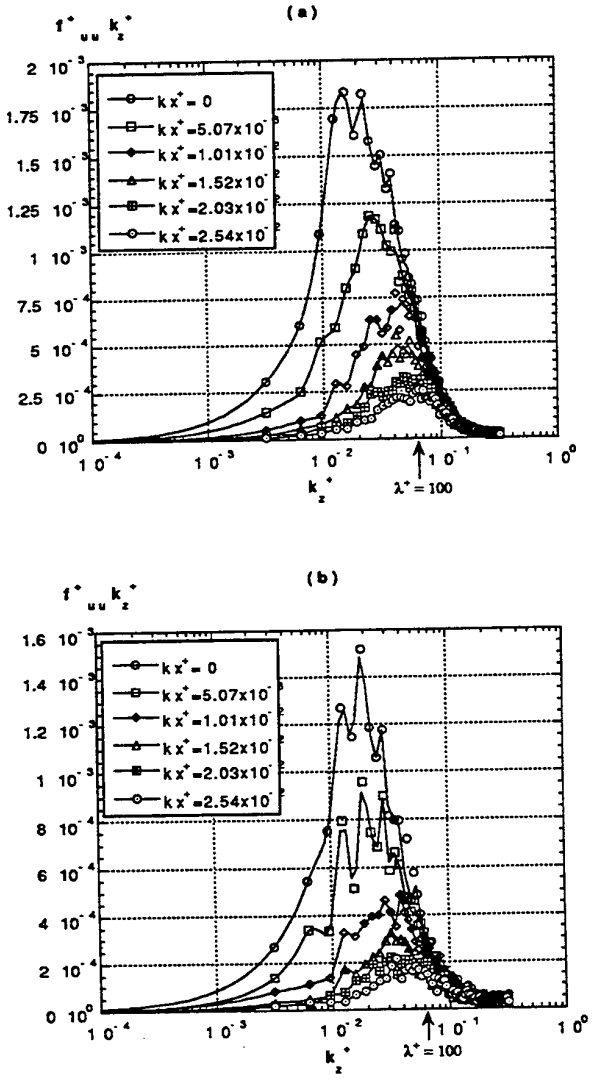

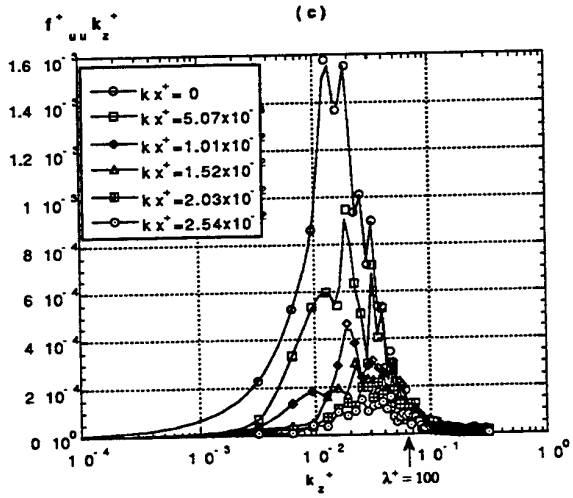

Fig. 11. Two dimensional power spectra of the streamwise velocity component, $\phi^+_{uu}(k^+_x, k^+_z)$, for the horizontal planes at (a) $y^+ = 20$, (b) $y^+ = 50$, (c) $y^+ = 80$.

point spatial correlation R_{ij}:

$$\phi_{ij}(k_x, y, k_z) = \iint R_{ij}(r_x, y, r_z) e^{-j(k_x \cdot r_x + k_z \cdot r_z)} dr_x dr_z$$

where k_x and k_z are the wave numbers in the streamwise and spanwise directions, related to the wavelengths, λ_x and λ_z., by $k_x = 2\pi/\lambda_x$ and $k_z = 2\pi/\lambda_z$. $R_{ij}(r_x,y,r_z)$ is the two-point correlation coefficient defined as:

$$R_{ij}(r_x, y, r_z) = \frac{\sum_x \sum_z u_i(x,y,z) u_j(x+r_x, y, z+r_z)}{\sqrt{\sum_x \sum_z u_i^2(x,y,z)} \sqrt{\sum_x \sum_z u_j^2(x+r_x, y, z+r_z)}}$$

where subscript indices i and j denote velocity components u and w, r_x and r_z are the separations of the two points in the streamwise and spanwise directions. The summations are carried out through all realizations. When made dimensionless, $k^+_x = 2\pi/\lambda^+_x$ and $k^+_z = 2\pi/\lambda^+_z$. The dimensionless power spectra become $\phi_{ij}(k^+_x, k^+_z)$.

Fig. 11 gives the two-dimensional power spectra versus spanwise wave numbers with streamwise wave numbers as parameters for three planes. The ordinate is the power spectrum multiplied by the spanwise wavenumber, and it represents the energy of modes in a wavenumber bandwidth k^+_z wide, centered on k^+_z.

The spectra in Fig. 11 reveal that the streamwise turbulent kinetic energy of mode with 100 wavelength ($k^+_z = 6.28 \times 10^{-2}$) is relatively weak in comparison to modes with larger scales of about 200^+, 400^+ and 600^+. the latter modes contribute much more to the total turbulent kinetic energy. The most energetic mode is the one with around 400^+ to 600^+ scale. This observation suggests that whereas the $\lambda^+ = 100$ mode is most readily observed mode by flow visualization, it is also one of the least important in respect to total turbulent energy. Much more attention should be given to the larger scale modes in the future work.

Conclusions

Streaky structures of a turbulent channel flow have been quantitatively studied with PIV. Low-speed streaks and high-speed streaks clearly show up in the fluctuating velocity fields in the buffer and logarithmic layers. The spanwise spacing of low-speed streaks at the wall, $\lambda^+ = 100$, can be visualized in the buffer layer. The spacing of individual low-speed streak varies even in one realization at the same y-plane, but generally agrees with earlier experiments which were also based on flow visualization. The average spacing found by visual inspection of the vector fields is somewhat larger then 100. The spacing also increases with increasing distance from the wall, as can be seen in the logarithmic layer. The streamwise scales of the streaks are about 500 to more than 1000 viscous units, and become shorter with increasing y.

Roughly circular vortices accompany the streaks seen in the low-pass and fluctuating velocity field, and more clearly in the subgrid fields. They appear at the sides of the streaks with sizes around 100 to 200 viscous units, and are elongated in the streamwise direction in the buffer layer and become more circular in the logarithmic layer. This feature of the vortices and their association with the streaks is consistent with inclined streamwise vortices or a hairpin vortices observed on a plane cutting through them horizontally. High-pass fluctuaing fields contain many roughly circular vortices whose diameters are of 50 ~ 100 viscous units. They appear to be uncorrelated with the larger vortices.

Fourier analysis gives more quantitative information about the streaky structures than the visual examinations of the streaks. Two-dimensional power spectra, measured at the six streamwise-spanwise planes, show that the streaky structures have many spanwise modes. The $\lambda^+ = 100$ mode is one of them, but it is not an energetic mode. The modes with larger spanwise scales dominate the turbulent kinetic energy. The most energetic mode occurs with scales around 400 to 600 viscous units.

Acknowledgments

This work was supported by ONR N00014-93-1-0552 and NSF CTS 92-00936.

References

Adrian, R.J., 1988, Statistical properties of particle image velocimetry measurements in turbulent flow, Laser Anemometry in Fluid Mechanics, p.115

Adrian, R.J., 1991, Particle-imaging techniques for experimental fluid mechanics, Ann. Rev. Fluid Mech., vol. 23, pp. 261-304

Adrian, R. J. 1995, Limiting resolution of particle image velocimetry for turbulent flow, Advances in Turbulent Research, pp. 1-19, Postech, Pohang, Korea

Dean, R. B. 1978, Reynolds number dependence of skin friction and other bulk flow variables in two-dimensional rectangular duct flow, J. of Fluids Engineering, vol. 100, pp. 215-223.

Kasagi, N., 1988, Structural Study of Near-Wall Turbulence and Its Heat Transfer Mechanism, Near-Wall Turbulence, Zoran Zaric Memorial Conference, pp. 596-619.

Kim, J., 1996, Private communication.

Keane, R.D., Adrian, R.J. 1990, Optimization of particle image velocimeters. Part 1: double pulsed systems, Meas. Sci. Technol., vol. 1, pp. 1202-1215.

Keane, R.D., Adrian, R.J. 1992, Theory of cross-correlation analysis of PIV images, Applied Scientific Research. vol. 49, pp.191-215.

Kline, S.J., Reynolds, W.C., Schraub, F.A., and Runstadler, P.W. 1967, The structure of turbulent boundary layers, J. Fluid Mech. vol. 30, part 4, pp. 741-773

Meinhart, C.D., Prasad, A.K., Adrian, R.J. 1992, Parallel digital processor system for particle image velocimetry, Meas. Sci. Tech. vol. 4, pp. 619-626.

Meinhart, C.D. 1994, Investigation of turbulent boundary-layer structure using particle-image velocimetry, PhD thesis, University of Illinois at Urbana-Champaign

Niederschulte, M.A. Turbulent flow through a rectangular channel. Ph.D. Thesis. (University of Illinois, Urbana, 1988).

Niederschulte, M. A., Adrian, R.J., Hanratty, T.J., 1990, Measurements of turbulent flow in a channel at low Reynolds numbers. Exp. Fluids 9, 222

Smith, C.R., Metzler, S.P., 1983, The characteristics of low-speed streaks in the near-wall region of a turbulent boundary layer, J. Fluid Mech., vol. 129, pp. 27-54

Zhou, J., Adrian, R. J., Balachandar, S. 1996, Autogeneration of near-wall vortical structures in channel flow, Phys. Fluids, 8 (1), pp 288-290

SPANWISE VORTICITY MEASUREMENTS IN A TURBULENT BOUNDARY LAYER USING LDV

C. L. Gan, L. Djenidi and R. A. Antonia
Department of Mechanical Engineering
University of Newcastle, N.S.W. 2308 Australia

ABSTRACT

An estimate of the spanwise vorticity in a smooth wall turbulent boundary layer is obtained using two-point LDV measurements. The results show that the estimate is in relatively good agreement with the spanwise vorticity obtained from DNS data. It is also found that there exists an optimal range of separations for two-point LDV measurements when determining $\partial u/\partial y$.

1. INTRODUCTION

Vorticity features prominently in the study of turbulence, and consequently numerous techniques have been developed for determining this quantity. It has been measured (at least the spanwise and wall-normal components) with relative success by hot-wire anemometry (see the review of Wallace and Foss, 1995) in various turbulent flows. However, there are situations where thermal anemometry methods is not adequate for such measurements. For example the measurement of the spanwise vorticity, defined as $\omega_z = (\partial v/\partial x) - (\partial u/\partial y)$ [lower case letters represent the fluctuating components; x, y and z refer to the streamwise, wall-normal and spanwise directions respectively], requires $\partial v/\partial x$ to be estimated. Unfortunately, this term cannot always be measured adequately by thermal anemometry. Indeed, the measurement of this quantity relies on finite-difference approximations of velocity gradients. In thermal anemometry methods and for small separations between the two hot-wires, the measurement at the downstream position may be contaminated by the wake of the upstream wire. Usually, to overcome this difficulty, Taylor's hypothesis is used for estimating the streamwise derivative; but in the near-wall region, where the flow is highly inhomogeneous, this hypothesis is not valid (Elavarasan et al., 1996). Clearly other methods are required in situations where hot-wires cannot be used.

Laser Doppler velocimetry (LDV) techniques are, in principle, quite reliable alternatives to hot-wire anemometry methods. Indeed, the non-intrusive nature of LDV and the relatively small measurement volume make these techniques a logical choice in situations where traditional hot-wire anemometry is not appropriate. For example, LDV provides a very effective means for measuring the wall shear stress (Ching et al., 1995). Yet, there have been only few attempts at measuring vorticity using LDV (Lang 1985 ; Agui and Andreopoulos, 1994). Perhaps, this is due to the fact that the same spatial and temporal resolution requirements which apply to hot-wire anemometry (Wallace and Foss, 1995) are also encountered in LDV. Also the need for seeding the flow and the uneven separation between samples may lead to further difficulties. Often, specially built optical components are required for carrying out reliable velocity measurements. However, new data acquisition systems have improved the performance of commercial LDV systems. The particular aim of the present paper is to demonstrate the effectiveness of using a commercial LDV system without any specially built optical components in estimating vorticity. It is a first rather modest step towards a more general goal of measuring all three vorticity components in turbulent boundary layers over different surface conditions. The paper reports LDA measurements of the spanwise component of vorticity.

2. EXPERIMENTAL FACILITIES AND TECHNIQUES

Measurements were performed in a constant

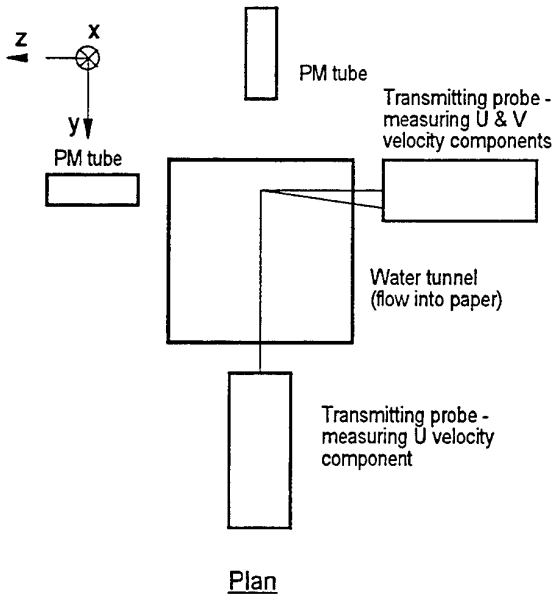

Figure 1: Schematic of LDV setup

head recirculating water tunnel. The test section of the vertical tunnel is 2 m long with a 250 mm square cross-section. Water flows from the head tank through a honeycomb and a 6:1, 3-D contraction at the tunnel inlet. Details of the water tunnel facility are in Ching et al. (1995). For this study, the freestram velocity was nominally 19 m/s, giving a momentum thickness Reynolds number of $Re_\theta = 700$.

A three component fibre optic LDV system (Dantec, 5W Ar-ion) is used in forward scattering mode. Dantec Burst Spectrum Analysers (BSA) are used to acquire the data. The two transmitting probes were set orthogonally to each other, as shown in Figure 1. The measurement volumes have a diameter of $d = 0.046$ mm ($d^+ = 0.4$, $d/\eta = 0.3$ at $y^+ = 15$; the superscript denotes normalisation with wall units and η is the Kolmogorov length scale) and a length of $l = 0.38$ mm ($l^+ = 3.5$, $l/\eta = 2.1$ at $y^+ = 15$). In the present experiment, ω_z', the rms spanwise vorticity, is approximated by

$$\omega_z' \approx \left[\overline{\left(\frac{\partial u}{\partial y}\right)^2} + \alpha\overline{\left(\frac{\partial u}{\partial x}\right)^2}\right]^{1/2} \quad . \qquad (1)$$

This empirical expression was suggested by Rajagopalan and Antonia (1993) who found that it gave reasonable estimates of ω_z', with $\alpha \approx 1.4$, by reference to the DNS data of Kim et al. (1987). They also noted that the value of α may depend on the Reynolds number and flow conditions.

To use Eq. (1), two-point measurements were carried out. Such measurements have already been performed successfully with LDV (e.g. Morton and Clark, 1971; Cenedese et al., 1991; Romano, 1993). The term $\partial u/\partial x$ is approximated by assuming Taylor's hypothesis.

3. RESULTS

$\partial u/\partial y$ Measurements

Antonia et al. (1993) reported that a separation in the range $2-4\eta$ is optimum when hot-wires are used to estimate $\partial u/\partial y$ with two-point mesaurements. When this separation is less than 2η, the uncertainty of measuring $\partial u/\partial y$ increases mainly due to contamination by electronic noise. This leads to an overestimation of $\partial u/\partial y$. It is not known whether LDV measurements would be superior to hot-wires for estimating $\partial u/\partial y$, where Δy is small. Obviously, it is important to ascertain if an optimal range of Δy exists for LDV measurements. The appropriate separation for measuring $\partial u/\partial y$ can be determined by measuring the spatial correlation in the y-direction, $R_{uu}(\Delta y)$, as detailed by Zhu and Antonia (1992). The variance $\overline{(\partial u/\partial y)^2}$ may be inferred from a Taylor series expansion of $R_{uu}(\Delta y)$, viz.

$$R_{uu}(\Delta y) \approx 1 - \frac{(\Delta y)^2}{2\overline{u^2}}\overline{\left(\frac{\partial u}{\partial y}\right)^2} \quad , \qquad (2)$$

at least for $y^+ > 10$. Figure 2 shows the variation of $(1 - R_{uu})$ as a function of Δy, on a semi-log scale. In this plot, a slope of 2 indicates separations which would yield good estimates of $\partial u/\partial y$. At both $y^+ = 20$ and 65, the measurements in the range $3 \leq \Delta y/\eta \leq 7$ agree relatively well with those of Zhu and Antonia (1992), and overlap the optimal separation range of $2 - 4\eta$ for hot-wires. However, for values of $\Delta y/\eta$ smaller than 1.5, the LDV data clearly show an anomalous trend: ideally, the data should decrease to 0 as $\Delta y/\eta$ decreases. It is possible that this anomaly is related to noise as reported by Antonia et al. (1993) in the context of hot wire measurements.

Using a separation of 0.7 mm for the two-point measurements ($\Delta y = 3.9\eta$ and 2.5η at $y^+ = 15$ and 100 respectively), $\partial u/\partial y$ in the wall region of a turbulent boundary layer was determined by a finite difference approximation. Figure 3 shows the distribution of $\partial u/\partial y$. It is in good agreement

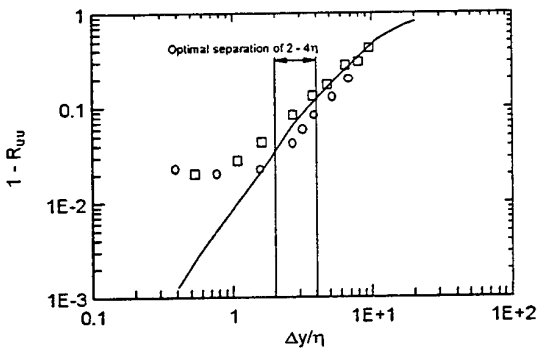

Figure 2: Variation of spatial correlation with separation. LDV data : □, $y^+ = 20$; ○, 65; —, hot wire data (Zhu and Antonia, 1992).

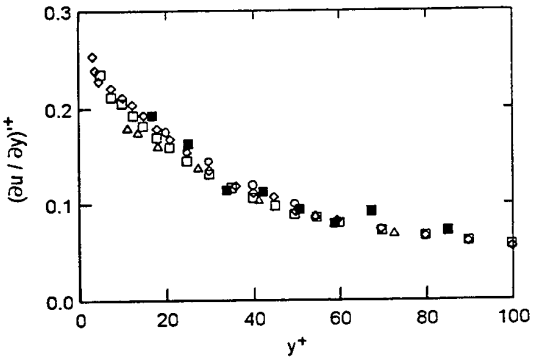

Figure 3: RMS $\partial u/\partial y$ in a smooth wall turbulent boundary layer. △, Balint et al. (1991); ○, Dubief (1996) $Re_\theta = 1150$; □, Dubief (1996) $Re_\theta = 940$; ◇, Dubief (1996) $Re_\theta = 540$; ■, present data.

with the hot-wire measurements of Balint et al. (1991) and Dubief et al. (1996). Estimates of ω_z', were made using Eq. (1), and $\alpha = 1.4$. Taylor's hypothesis was used to estimate $\partial u/\partial x$. The validity of this hypothesis was verified for $y^+ > 15$ by comparing the two-point longitudinal spatial correlation R_{uu} with the temporal autocorrelation of u. This verification is reported in Elavarasan et al. (1996).

ω_z' Measurements

Figure 4 shows the ω_z'-distribution in the wall region of a smooth wall turbulent boundary layer. The figure also includes DNS, hot-wire and other LDV data. Clearly, the present LDV data provide reasonable estimates of ω_z'. One cannot rule out the possibility that the agreement between DNS

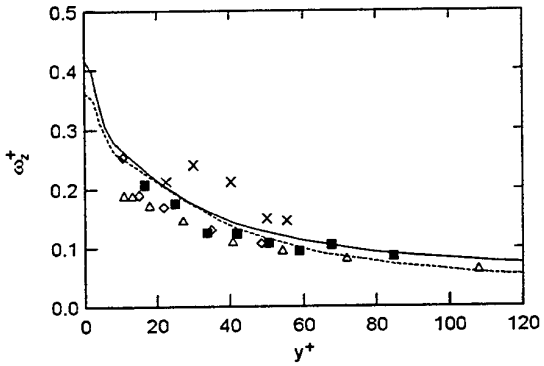

Figure 4: RMS spanwise vorticity in a smooth wall turbulent boundary layer. ×, Agui and Andreopoulos (1994); △, Balint et al. (1991); - - -, Kim et al. (1987); ◇, Rajagopalan and Antonia (1993); —, Spalart (1988); ■, present data.

and LDV data can be improved through a more appropriate choice of α. Interestingly, the present results support the use of Eq. (1) for measuring ω_z' when it is either difficult or impossible to measure the term $\partial v/\partial x$. Further LDV measurements will be carried out to determine $\partial v/\partial x$ directly.

4. CONCLUSIONS

The spanwise vorticity in a smooth wall turbulent boundary layer has been estimated using two-point LDV measurements, a configuration somewhat analogous to that involving two parallel hot-wires. The results indicate relatively good agreement with available experimental and DNS data. As with hot-wire measurements, there exists an optimal range of separations for two-point LDV measurements which minimises the uncertainty of measuring $\partial u/\partial y$.

ACKNOWLEDGEMENTS

We would like to thank Dr R. Elavarasan for his contribution to the experiments. The support of the Australian Research Council is acknowledged.

REFERENCES

AGUI, J. H. and ANDREOPOULOS, J. : 1994. Development of a new laser vorticity probe - LAVOR, *Ann. Symp. on Laser Anemometry, ASME Fluids Eng. Meeting*, Lake Tahoe, CA.

ANTONIA, R. A., ZHU, Y. and KIM, J. : 1993. On the measurement of lateral velocity derivatives in turbulent flows, *Expts. in Fluids*, **15**, 65.

BALINT, J-L., WALLACE, J. M. and VUKOSLAVCEVIC, P. 1991. The velocity and vorticity vector fields of a turbulent boundary layer. part 2. Statistical properties, *J. Fluid Mech.*, **228**, 53.

CENEDESED, A., ROMANO, G. P. and DI FELICE, F. : 1991. Experimental testing of Taylor's hypothesis by LDA in highly turbulent flow, *Expts. in Fluids*, **11**, 351.

CHING, C. Y., DJENIDI, L. and ANTONIA, R. A. : 1995. Low-Reynolds-number effects in a turbulent boundary layer, *Expts. in Fluids*, **19**, 61.

DJENIDI, L., DUBIEF, Y. and ANTONIA, R. A. : 1996. Advantages of using a power law in a low R_θ turbulent boundary layer, *Expts. in Fluids* (submitted)

ELAVARASAN, R., DJENIDI, L. and ANTONIA, R. A. : 1996. Check on Taylor's hypothesis using two-point LDV measurements in a turbulent boundary layer, *Eighth Int. Symp. on Applications of Techniques to Fluid Mechanics*, Lisbon (to appear)

KIM, J., MOIN, P. and MOSER, R. : 1987. Turbulence statistics in fully developed channel flow at low Reynolds numbers, *J. Fluid Mech.*, **177**, 133.

LANG, D. B. : 1985. Laser Doppler velocity and vorticity measurements in turbulent shear layer, Ph.D. Thesis, California Institute of Technology.

MORTON, J. B. and CLARK, W. H. : 1971. Measurements of two-point velocity correlations in a pipe flow using laser anemometer, *J. Phys. E : Sci. Instrum.*, **4**, 809.

RAJAGOPALAN, S. and ANTONIA, R. A. : 1993. RMS spanwise vorticity measurements in a turbulent boundary layer, *Expts. in Fluids*, **14**, 142.

ROMANO, G. P. : 1993. Two points velocity measurements using LDV : spatial and temporal analysis in a turbulent boundary layer, *SPIE Laser Anemometry Advances and Applications*, **2052**, 597.

SPALART, P. R. : 1988. Direct simulationof a turbulent boundary layer up to $R_\theta = 1410$, *J. Fluid Mech.*, **187**, 61.

WALLACE, J. M. and FOSS, J. F. : 1995. The measurement of vorticity in turbulent flows, *Ann. Rev. Fluid Mech.*, **27**, 469.

ZHU, Y. and ANTONIA, R. A. : 1992. The measurement of $\partial u/\partial y$ in the wall region of a turbulent channel flow, *Proc. Eleventh Australasian Fluid Mechanics Conference*, Hobart, 695.

AN LDA STUDY OF LONGITUDINAL VORTICES EMBEDDED IN A TURBULENT BOUNDARY LAYER

Hui-Liu Zhang*, Xin Zhang† and David W. Hurst‡

Department of Aeronautics and Astronautics
University of Southampton, Southampton SO17 1BJ, UK

and Michael W. Collins§

Department of Mechanical Engineering and Aeronautics
City University, London EC1V 0HB, UK

Abstract

A three-component Laser Doppler Anemometry(LDA) system was used to investigate the complex flow field generated by vortex generator jets in a turbulent boundary layer. The prominent feature of the flow is longitudinal vortices embedded in the boundary layer. The study was performed in a $3.5m \times 2.6m$ low speed wind tunnel. The non-intrusive measurement technique allows for reliable and accurate measurement of the velocity and turbulent stress field. Data obtained include time-averaged velocity and turbulent stress distributions on cross planes downstream of the jet exit. It was found that (i) the flow field of the longitudinal vortex generated by a rectangular jet is significantly different from that generated by a round jet in the magnitude of the cross velocity, but quite similar to that generated by a solid vortex generator; (ii) a strong injection flow from the surface between two contra–rotating longitudinal vortices generated by a row of contra–rotating jets can be observed, which is different from the single jet flow.

*Research Fellow
†Lecturer
‡Research Lecturer, now at Glasgow University
§Professor

1 Introduction

Longitudinal vortices have been widely used in flow and heat transfer control (Bushnel, 1992). A traditional method of vortex production — solid vortex generators, was first proposed by Taylor(1948) then developed by many researchers (Pauley & Eaton 1994, Wendt & Hingst 1994, and Zhu *et al.* 1995, among others). It is effective in generating a longitudinal vortex, but produces pressure loss, parasitic drag and hot spots at the same time. Furthermore, it does not provide possibilities for active control.

In the present study, we investigate a relatively new method of vortex production — inclined air jets (see Wallis 1952, Johnston & Nishi 1990, Compton & Johnston 1991, Pearcey *et al.* 1990, Zhang 1995, Zhang *et al.* 1996a,b). The inclined air jets generate longitudinal vortices which can be used for the same flow control purpose. The jets will not produce residual parasitic drag and hot spots. However, the applications of this method are rare due to (i) a lack of reliable data; (ii) a perception that the vortices are weak; and (iii) high costs due to high speed jet requirements.

In the past, the vortex flow produced by a single round jet was measured by Compton and Johnston (1991) using a five hole pressure probe. Strong interactions between the longitudinal vortex and boundary layer, and between the jet and oncoming flow were observed. The study was valuable

in that it provided a data base for theoretical and numerical model validation. However, the five-hole probe is intrusive and will not provide accurate measurement of the flow near the surface where strong cross flow interaction exists (Zhang 1995). This is one of the major motivations of the current study.

In this study, we attempt to address the problem of data quality associated with some of the earlier wind tunnel studies. In doing so, we hope that we can eventually provide reliable and accurate whole field data to assist in the current development of theoretical and numerical modelling methods. We use two examples to illustrate our points:

- a rectangular jet, and comparison with a traditional round jet (Compton & Johnston 1991), and
- an array of contra-rotating inclined jets.

2 Experimental Methods

2.1 Flow conditions and wind tunnel facility

Experiments were performed in a low speed closed circuit wind tunnel with a $3.5m \times 2.6m$ test section. A $2.43m$ long and $10mm$ thick aluminum flat plate was installed across the span of the test section, and supported at a height of $0.9m$ above the tunnel floor in order to create a well behaved boundary layer developed from the elliptic leading edge of the flat plate. The freestream velocity at the leading edge of the flat plate was $20m/s$, and the freestream turbulent intensity approximately 0.3%. The velocity increase due to the blockage was about 2.5% at the trailing edge of the plate. The boundary layer of interest developed on the upper surface of the plate with transition fixed by a $10mm$ wide sand strip (the size of the sand is $0.060mm$) located $100mm$ downstream of the leading edge.

For the single jet vortex generator, a rectangular jet with a $6.4 \times 27.3mm^2$ exit area (the aspect ratio is 4.3, and the exit area is equivalent to a round jet of $D = 15mm$ diameter) passed through the plate at pitch and skew angle of 45° into the incompressible turbulent boundary layer over it. For the multiple jets vortex generator, a row of round jets ($d = 75mm$ apart, totally 6 jets) with diameter $D = 15mm$, pitch angle $\alpha = 45°$ and skew angle β equal to either 45° or $-45°$ were issuing from the flat plate, producing a row of longitudinal vortices trailing over the surface. The ratio of the jet velocity V_j over the oncoming freestream velocity U_∞ was 2 for the single jet while $V_j/U_\infty = 1$ for the multiple jets. Figure 1 gives a schematic view of the flow field around two contra–rotating vortices produced by the multiple jets.

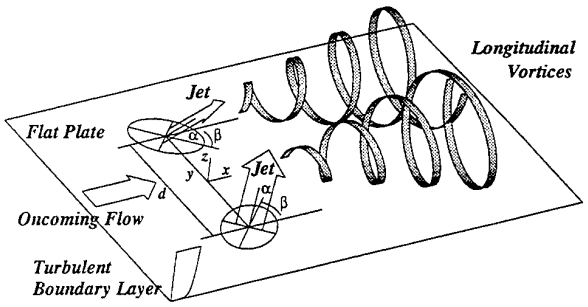

Figure 1: Schematic of the multiple jet flow field.

The position of the jet injection was located at $1.2m$ downstream of the leading edge of the plate, and the boundary layer thickness was about $35mm$ thick at this position. The Reynolds number based on the momentum thickness of the boundary layer was approximately 4,670 at this point.

2.2 Laser Doppler Anemometry Measurement

The mean velocity and turbulent intensity distributions were measured using a three–component DANTEC LDA system. It consists of an Ar–ion Laser, a 60×33 safety cover, a 60×40 transmitter, six 60×24 Fibre manipulators, two $60 \times 10/60 \times 11$ transducers, two 55×12 beam expanders and two 55×59 lenses, see Figure 2.

A seeding rake was positioned vertically in front of the plate upstream of the measurement point, releasing oil vapour produced by two DANTEC 55L18 seeding generators. The height of the seeding rake was about $150mm$, which covered the vertical area of interest which was about $60mm$ high above the plate surface. However, in the spanwise direction, the width of the seeding rake was only about $20mm$, so it was designed to allow horizontal movement over a range of $80mm$ in the spanwise direction in order to keep a high seeding density through the measurement volume.

The Doppler signals were analyzed by three DANTEC 57×11 Burst Spectrum Analyzers controlled by a Dell system 400 microcomputer. As the

three independent velocity components are acquired separately through the three laser beams, their cross products are meaningful only when the components are measured at the same time. In other words, only the velocity signals which arrived at the Burst Spectrum Analyzers at the same time can be used in data processing. Usually, thousands of velocity signals are necessary at each measurement point, this can be time consuming. In the present study, in order

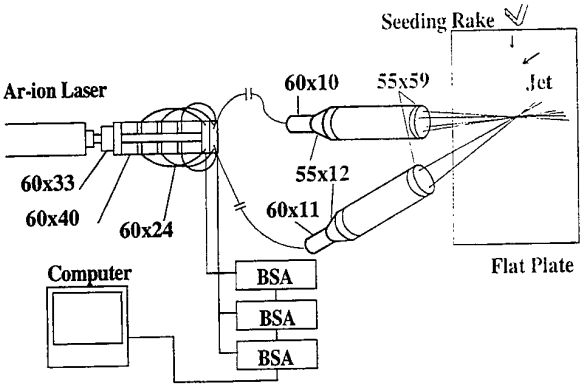

Figure 2: Schematic of the Laser Doppler Anemometer set–up.

to reduce the measurement time, one independent velocity component was arranged in alignment with the x–axis. The normal Reynolds stress in this direction can then be deduced directly from the measured data, irrespective of the arrival time of the other velocity component signals. Therefore, only the normal Reynolds stress $\overline{uu}$ will be presented in this paper.

2.3 Measurement accuracy

The uncertainty in the measurements of the LDA system was estimated at 1% for the mean velocity, and 3% for the streamwise turbulent normal stress. The minimum step of the traverse mechanism carrying the laser beams was 1±0.01mm.

The most difficult part of the acquisition process was the measurement of jet velocity due to the strong distortion of the velocity around the jet exit. In this study, the velocity at nine points across the jet exit (i.e. one point at the centre and eight points along the perimeter of the jet exit) were measured using a Pitot tube velocimeter, its uncertainty was estimated to be 3%. The average value was calculated as the jet velocity. The maximum deviation of the velocity at the jet exit from the nominated jet mean velocity was about 10%. The pitch and skew angles of the jet were fixed with an accuracy of about 0.5°.

For each cross plane of data, the measurement points ranged between 252 and 288 for the single jet flow, and between 294 and 391 for the multiple contra–rotating jets flow. The measurement points were uniformly distributed along the spanwise direction ($4mm$ between the two measurement points), while stretched along the vertical direction where the first measurement point was $2mm$ away from the plate surface and the maximum step was $4mm$. Typically, the measurement area in the cross section was $60 \times 130mm$ at $x = 10D$.

3 Results and Discussions

3.1 Single rectangular jet

The measured cross velocity field verifies the existence of a longitudinal vortex generated by the jet. Figure 3 shows the LDA measurement results of the

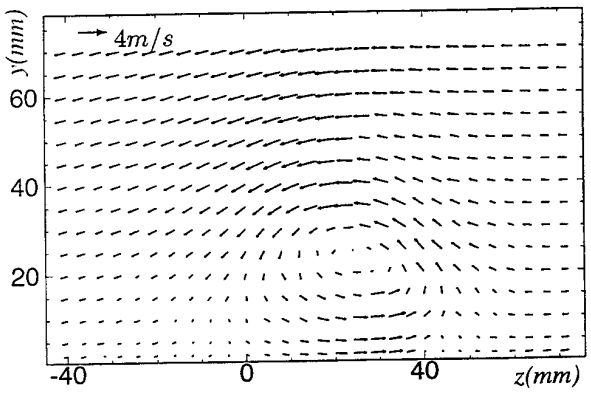

Figure 3: Cross velocity vector for the single rectangular jet at $x = 20D$. $\alpha = 45°, \beta = 45°$ and $V_j/V_\infty = 2$.

cross velocity at $x = 20D$ downstream of the jet exit for the single rectangular jet, where the swirling motion as well as the swirling centre can be easily identified. The highest cross velocity is approximately 3.5m/s, or about 17% of the oncoming flow velocity U_∞. It is more than two times larger than that found in Compton & Johnston(1991)'s measurements of a round jet vortex generator, where the maximum cross velocity was only 7% of U_∞. The present value is close to that measured by Eibeck & Eaton(1985)

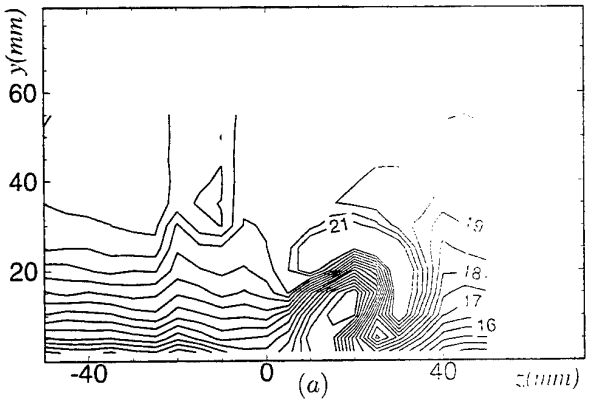

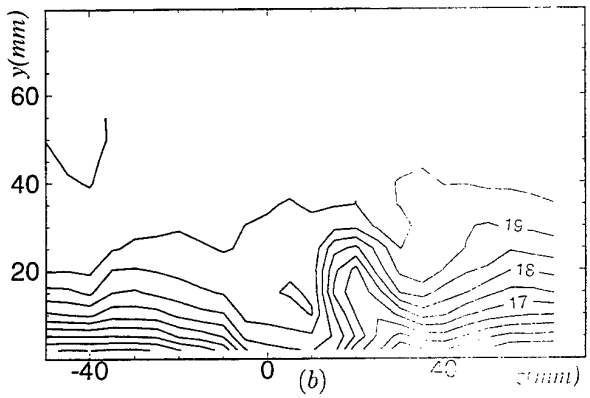

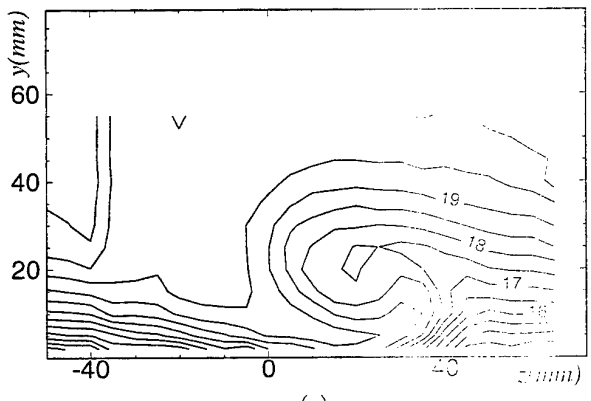

Figure 4: Streamwise velocity contours and s for the single rectangular jet at (a) $x = 5D$; (b) $x = 10D$ and (c) $x = 20D$.

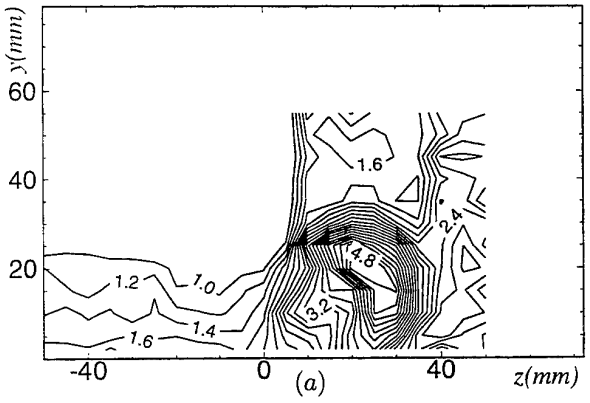

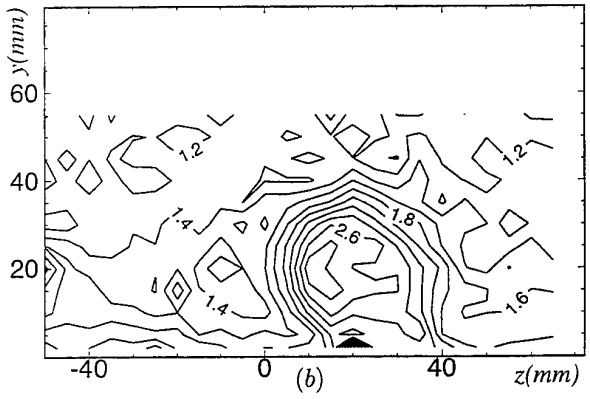

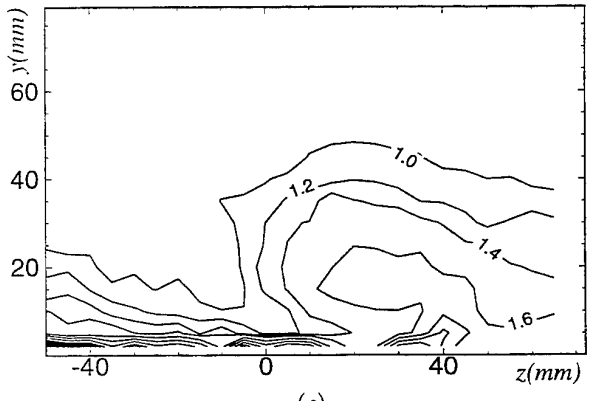

Figure 5: Contours of streamwise turbulence normal stress (m^2/s^2) for the single rectangular jet at (a) $x = 5D$; (b) $x = 10D$ and (c) $x = 20D$.

for a vane vortex generator flow. The longitudinal vortex thus generated by the rectangular jet cannot be designated as a "weak" vortex (Compton & Johnston, 1991).

The manipulation of the boundary layer by the longitudinal vortex can be better understood from the streamwise velocity contours, as shown in Figure 4 at three downstream locations for the single jet case. At $x = 5D$, although strong interaction between the oncoming flow and the air jet can be observed, the affected area is relatively small. The longitudinal vortex evolves continuously downstream. At $x = 10D$, the downwash flow to the left and upwash flow to the right become apparent. The thinning and thickening of the boundary layers in the downwash and upwash regions, respectively, can be clearly seen from Figure 4(b). At $x = 20D$, the longitudinal vortex has become well developed, with a low velocity core in the centre of the vortex. At this position, the thickness of the undisturbed boundary layer is about $39mm$. In contrast to the slightly thickened boundary layer in the upwash region ($45mm$), the boundary layer in the downwash region is thinned to about half of the depth of the undisturbed case. A high velocity region exists between the vortex centre and the wall due to the downwash flow which brings the high momentum fluid towards the wall from the outside of the boundary layer.

Substantial differences can be found again when the present results are compared with the round jet vortex generator study of Compton & Johnston(1991). Their measurements suggested that there was no low axial velocity core in the vortex. The present results of Figure 4(c) are much more similar to the results obtained by Eibeck & Eaton(1985) for a solid vortex generator, except that the position of the vortex is lower relative to the boundary layer. The reason for the similarity with the solid vortex generator results is probably that the rectangular jet behaves much like a vortex sheet which is rather similar to the vane in shape. Another possible cause is that the manipulation of the boundary layer by the vortex is determined not only by the position of the vortex in the boundary layer but also by the Reynolds number based on the characteristic length of the vortex generator. In the present case, the Reynolds number based on the nominated diameter of the air jet ($D = 15mm$) is about 20,600. In Eibeck & Eaton(1985)'s measurements the Reynolds number based on the height of the vane was approximately 22,000, which is much closer to the present result than Compton & Johnston(1991)'s results for the round jet vortex generator, where the Reynolds number based the diameter of the jet was only about 6,500.

The normal Reynolds stress ($\overline{uu}$) distributions in the x–direction at three cross sections ($x = 5D, 10D, 20D$) are given in Figure 5. At $x = 5D$, a very high level of $\overline{uu}$ distribution can be found in the vortex core area. The interaction between the air jet and the oncoming flow is the main reason for the high turbulence level in this area. As the vortex develops, the maximum $\overline{uu}$ value gradually decreases, while the area with high $\overline{uu}$ level enlarges. At $x = 20D$, fluid with low $\overline{uu}$ stress at the outer region of the boundary layer is drawn into the near wall region by the swirling motion of the vortex. The overall pattern of the $\overline{uu}$ contour is consistent with the streamwise velocity distribution (compare Figure 4c and Figure 5c).

3.2 Multiple contra-rotating round jets

Figure 6 shows the cross velocity vector of the multiple jets at $x = 20D$, where a strong injection flow from the plate surface between two contra–rotating longitudinal vortices can be observed, which is different from the single jet flow. This injection flow will strongly affect the distributions of the streamwise velocity and turbulence normal Reynolds stress $\overline{uu}$. The maximum cross velocity magnitude is about $2.2m/s$ at the centre line, or 11% of the oncoming flow velocity.

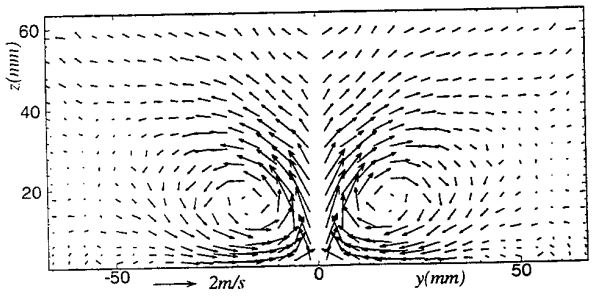

Figure 6: Cross velocity vector for the multiple jets at $x = 20D$. $\alpha = 45°, \beta = \pm 45°$ and $V_j/V_\infty = 1$.

The manipulation of the boundary layer due to the longitudinal vortices can be shown again by the streamwise velocity contours in Figure 7. At $x = 10D$, two low level streamwise velocity cores near the vortex centres can be found (Figure 7a),

and between the two cores the boundary layer is significantly thickened. With the development of the vortices the two vortex cores approach to merge with each other. Eventually only one low level streamwise velocity core can be observed after the strong interaction between the vortices (Figure 7*b* and *c*).

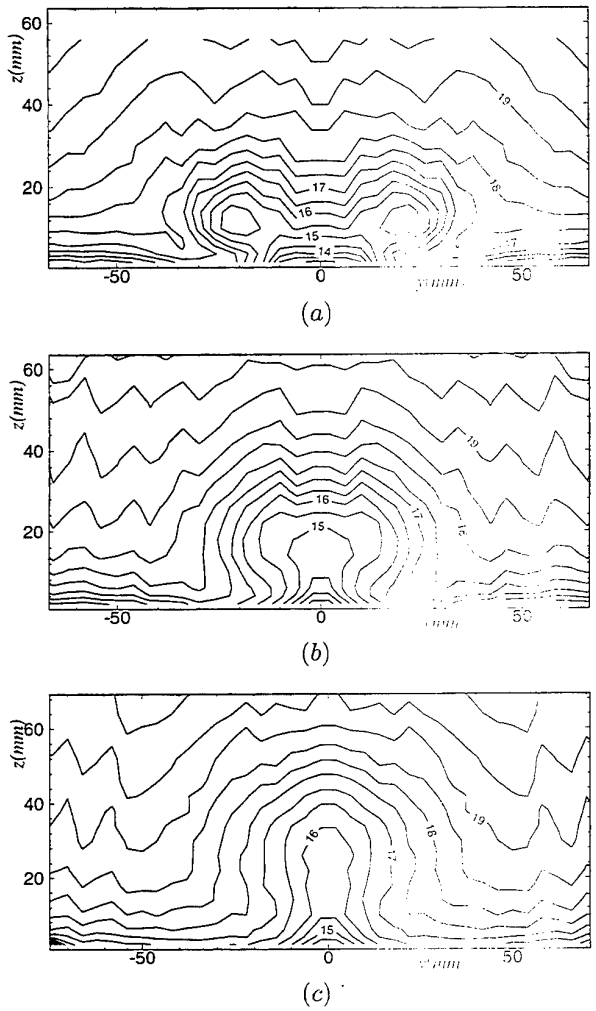

Figure 7: Streamwise velocity contours (m/s) for the multiple jets at (*a*) $x = 10D$; (*b*) $x = 20D$ and (*c*) $x = 30D$.

The normal Reynolds stress $\overline{uu}$ distributions in the x–direction for the multiple jets flow at three cross sections ($x = 10D, 20D$ and $30D$) are shown in Figure 8. At $x = 10D$ when the two vortices are still apart from each other, two separate high turbulence level zones can be found, corresponding to the vortex cores of low level streamwise velocity. When the two vortices merge with each other at $x = 20D$, the two high turbulence level zones amalgamate too, and form a single high turbulence level core which is slightly pushed away from the plate surface (Figure 8*b*). With the development of the vortices further downstream, the high turbulence level zone is isolated from the plate surface by a zone of low turbulence level. Therefore, for the multiple contra-rotating jets, one can expect a significant increase in the turbulence mixing between the contra–rotating longitudinal vortices as well as between the outer boundary layer and the near wall region.

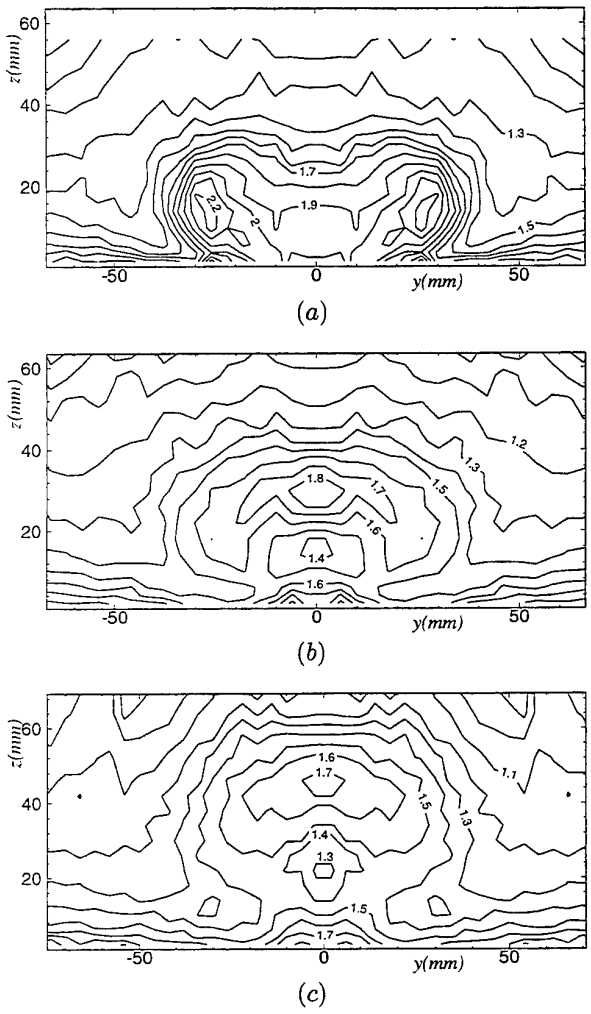

Figure 8: Contours of streamwise turbulence normal stress (m^2/s^2) for the multiple jets at (*a*) $x = 10D$; (*b*) $x = 20D$ and (*c*) $x = 30D$.

4 Concluding Remarks

An attempt has been made to study the complex flow field generated by inclined jets in a turbulent boundary layer using a three-dimensional LDA system in a low speed wind tunnel. The data obtained in the study contribute to the understanding of the flow physics and will be useful in the theoretical and numerical modelling efforts.

For the single rectangular jet, an important realization we have reached after studying all the test data so far is that the flow field of the longitudinal vortex generated by a rectangular jet is significantly different from that generated by a round jet in terms of the cross velocity, but quite similar to that generated by a solid vortex generator. The manipulation of the streamwise velocity and normal Reynolds stress distributions in the boundary layer can be found due to the strong upwash and downwash flow at both sides of the longitudinal vortex.

For the multiple contra-rotating round jets, it is found that the manipulation of the streamwise velocity distribution is not as strong as that for the single rectangular jet, but the turbulence mixing between the contra–rotating longitudinal vortices as well as between the outer boundary layer and the near wall region is greatly increased.

This study complements the existing numerical modelling exercise. Further experiments are being performed to study the effects of various jet parameters.

5 Acknowledgements

This research is supported by EPSRC under contract number GR/J17722. The authors wish to thank Professor H.H. Pearcey for his helpful comments during the research.

References

[1] Bushnell, D.M., 1992, Longitudinal Vortex Control — Techniques and Applications, *Aeronautical J.*, October 1992, pp.293–303.

[2] Compton, D.A. and Johnston, J.P., 1991, Streamwise Vortex Production by Pitched and Skewed Jets in a Turbulent Boundary Layer, *AIAA Paper 91–0038.*

[3] Eibeck, P.A. and Eaton, J.K., 1985, An Experimental Investigation of the Heat Transfer Effects of a Longitudinal Vortex Embedded in a Turbulent Boundary Layer, Report MD–48, Thermosciences Division, Dept. of Mech. Engrg., Stanford University.

[4] Johnston, J.P. and Mishi, M., 1990, Vortex generator jets — means for flow separation control, *AIAA Journal,* Vol.28, No.6, pp.989-94.

[5] Pauley, W. R. and Eaton, J. K., 1994, The effect of embedded longitudinal vortex arrays on turbulent boundary layer heat transfer, *Journal of Heat Transfer,* Vol.116, No.4, pp.871-9.

[6] Pearcey, H.H., Rao, K. and Sykes, D.M., 1993, Inclined Air–Jets Used as Vortex Generators to Suppress Shock–Induced Separation, *AGARD Fluid Dynamics Symposium Computational and Experimental Assessment of Jets in Cross Flow,* Winchester, U.K.

[7] Wendt, B. J. and Hingst, W. R., 1994, Flow structure in the wake of a wishbone vortex generator, *AIAA Journal,* Vol.32, No.11, pp.2235–40.

[8] Zhang X., 1995, Co- and Contra-Rotating Streamwise Vortices in a Turbulent Boundary Layer, *Journal of Aircraft,* Vol.32, No.6, pp.1095–1101.

[9] Zhang X., Zhang, H.–L. and Collins, M.W., 1996a, Some Aspects of Streamwise Vortex Production Using Air Jets, *AIAA Paper 96–0209.*

[10] Zhang, H.–L., Zhang X. and Collins, M.W., 1996b, Near Field Flow Calculation of Jet Generated Vortices in a Turbulent Boundary Layer, *The 3rd International Symposium on Engineering Turbulence Modelling and Measurements,* Crete, Greece.

[11] Zhu, J. X., Fiebig, M. and Mitra, N. K., 1995, Numerical investigation of turbulent flows and heat transfer in a rib-roughened channel with longitudinal vortex generators, *International Journal of Heat and Mass Transfer,* Vol.38, No.2, pp.495–501.

The differential speckle strophometry - a light scattering technique for the measurement of velocity gradients in turbulent fluid flow

R. Schulz and W. Staude
Universität Bremen, Fachbereich 1 - Physik
D - 2800 Bremen 33
Federal Republic of Germany

Abstract

A laser light scattering technique is described which allows the measurement of velocity gradients and their temporal correlation functions in fluid flow. This non-invasive and gauge-free technique was applied to a turbulent channel flow. Results of the measurements, including the turbulent energy dissipation and the enstrophy are presented.

1 Introduction

It is a well known fact that the light scattered by moving particles carries information on the velocity of these particles. The wide spread Laser Doppler Anemometry is a technique which in an ingenious way exploits this fact for the determination of flow velocities. But there is even more information contained in the scattered light. Thus we could show [1] in what way a velocity gradient of the flow influences the light scattered by immersed particles: The random intensity pattern (speckle pattern) produced by the randomly distributed particles within the fluid exhibits a *motion* if certain components of the velocity gradient tensor are different from zero. A theoretical treatment of this effect shows that each velocity component of the speckle motion is uniquely determined by a particular linear combination of the components of the velocity gradient tensor, the coefficients being dependent only on geometrical parameters describing the optical set-up. It is therefore possible to determine velocity gradient components of a flow by measuring components of the velocity of the random speckle pattern.

It is worth noting that the mentioned effect only occurs if *many* light scattering particles are in the region where the scattered light emerges, because the light pattern produced by only one scattering particle exhibits no motion. It is therefore not possible to understand the method described in this paper on the basis of the LDA measurement scheme.

A method to measure velocity gradients, which is based on essentially the same physical effect as the one just mentioned, was proposed by de Gennes [2], but it was not developed to a level, such that measurements comparable to the ones presented here can be performed.

It is obvious that a measurement scheme which is non-invasive and gauge-free has advantages over the hot wire technique, which was used by Balint et al. [3] to perform for the first time a systematic investigation of velocity gradient properties in a flow.

2 Theory

The velocity field $\vec{u}(\vec{r},t)$ within a flowing fluid is a smooth function in space and time. One can therefore perform a Taylor series expansion with respect to the spatial variables. If only a small volume within the fluid is considered, one can neglect all higher powers in the spatial variables than the first ones and gets

$$\vec{u}\,(\vec{r},t) = \vec{u}_o(t) + \hat{\Gamma}(t)\cdot\vec{r}. \qquad (1)$$

$\hat{\Gamma}(t)$ is the 3×3 velocity gradient tensor. $\vec{u}_o(t)$ is the mean value of the velocity within the considered volume if the origin of the coordinate system is taken to lie in the centre of mass of the considered volume. In turbulent flow both quantities are random functions of time.

Let us now consider a light scattering experiment as depicted schematically in figure 1. A laser beam is focussed into a small region within a flow seeded with small light scattering particles. Light emerging from the so called scattering volume passes a lens and can then be observed on a screen. We will assume that the scattering volume, i.e. the region from which scattered

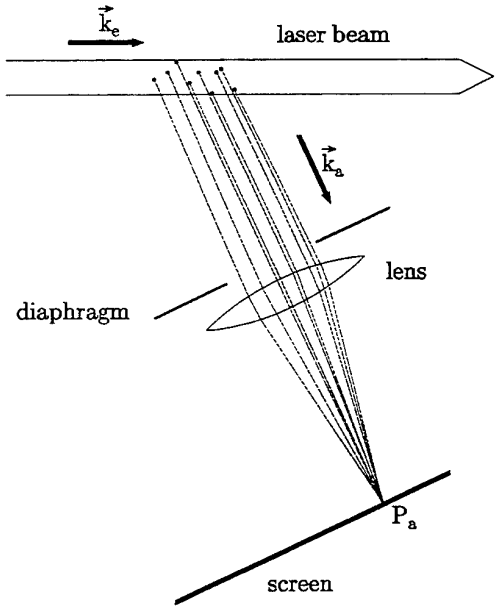

Figure 1: Schematic representation of a light scattering experiment. Light scattering particles which are hit by the laser light emit secondary waves. The dashed lines denote the light paths to a point on the focal plane. Their optical lengths determine the phases of the scattered light components at this point. The diameters of the laser beam and the diaphragm, respectively, determine the scattering volume.

light does reach the screen, is small enough such that the velocity field within this volume can be expressed by equation (1)

Within the scattering volume the illuminating light wave is assumed to be plane and can therefore be characterised by its wave vector $\vec{k}_e$. The direction of this vector is given by the propagation direction of the light wave, and its length depends on the wavelength of the light wave through the relation $|\vec{k}| = 2\pi/\lambda$.

The screen is placed in the focal plane of the lens. This assures that all light wave components emerging in the scattering volume, which travel in the same direction (i.e. have the same wave vector $\vec{k}_a$) are focussed on *one* particular point P_a on the screen. The relative phases of the just mentioned components determine the brightness at this point. If now the particles within the scattering volume move with *different* velocities, then the relative phases change and conesquently also the brightness at the point P_a.

In the case of a velocity field of the form given in equation (1) the phase changes are such that a motion of the pattern results. This is due to the fact that the relative phases of the secondary waves at an arbitrary point P_a at time t are identical to those of a point P'_a at a later time t'. An especially simple form of the velocity of the pattern is obtained [1] if it is expressed with the help of the temporal change $\dot{\vec{k}}_{a\perp}$ of the wave vector $\vec{k}_a$ which "points" towards the arbitrary point P_a:

$$\dot{\vec{k}}_{a\perp} = \left(\hat{\Gamma}\cdot(\vec{k}_e - \vec{k}_a)\right)_\perp \tag{2}$$

The index $\perp$ denotes that a pattern motion is described by a rotation of the wave vector, no change in the length of the wave vector of light can occur in a simple light scattering experiment.

With the help of geometrical optics one can relate the pattern velocity $\vec{u}$ on the screen to $\dot{\vec{k}}_{a\perp}$ and obtains

$$\vec{v}_\perp = \frac{\left(\hat{\Gamma}\cdot(\vec{k}_e - \vec{k}_a)\right)_\perp}{|\vec{k}_e - \vec{k}_a|}\cdot f \tag{3}$$

where f is the focal length of the lens.

Unforunately one observes not only a motion of the speckle pattern but superimposed random fluctuations known as speckle boiling. This is caused by the stochastic flux of scattering particles through the scattering volume, and by the parallel component of the vectors appearing on both sides of equation (2). This speckle boiling generally leads to very fast decorrelations of the pattern, which renders the measurement of the velocity a rather difficult task. Nevertheless we were able to develop several measurement schemes [4] for a reliabel determination of this velocity. One of this methods is based on differential properties of the pattern, this will be the topic of this paper. We could show [5] that the following relation holds between the pattern velocity component v_x say and derivatives of the pattern intensity $I(\vec{r},t)$ on the screen:

$$< v_x >= -\frac{< \dot{I}(\vec{r},t)\cdot\mathrm{sign}\,(I_x(\vec{r},t)) >}{< I_x(\vec{r},t)\cdot\mathrm{sign}\,(I_x(\vec{r},t)) >} \tag{4}$$

I_x denotes in this equation the spatial derivative of the intensity with respect to x, $\dot{I}$ is the temporal derivative, and sign is the sign-function with the properties:

$$\mathrm{sign}(x) = \begin{cases} 1 & \text{for } x > 0 \\ 0 & \text{for } x = 0 \\ -1 & \text{for } x < 0 \end{cases} \tag{5}$$

The brackets in equation (4) denote averaging, which for our measurement scheme will be temporal averaging.

Based on this equation it is possible to determine average values of the velocity gradient components as we have shown in [4].

An important extension of the briefly scetched method is obtained, if the light scattered in two different directions is used to measure correlations of velocity gradient components. Let us denote the light intensities on the two screens by $I^1(\vec{r}_1,t)$ and $I^2(\vec{r}_2,t)$, where the vectors $\vec{r}_i$ indicate points in these screen planes. One then has the following relation:

$$< v_i^1(t)v_j^2(t+\tau) >= \quad (6)$$
$$\frac{< \dot{I}^1(\vec{r}_1,t)\cdot\text{sign}\left(I_x^1(\vec{r}_1,t)\right)}{< I_x^1(\vec{r}_1,t)\cdot\text{sign}\left(I_x^1(\vec{r}_1,t)\right) >} \times$$
$$\frac{\dot{I}^2(\vec{r}_2,t)\cdot\text{sign}\left(I_x^2(\vec{r}_2,t)\right) >}{< I_x^2(\vec{r}_2,t)\cdot\text{sign}\left(I_x^2(\vec{r}_2,t)\right) >}$$

The "speckle-velocity crosscorrelation function" $< v_i^1(t)v_j^2(t+\tau) >$ is according to the theory scetched above directly proportional to a temporal correlation function of two different linear combinations of components of the velocity gradient tensor. If a sufficient number of these correlation functions for different scattering geometries is measured one can calculate any desired auto- or crosscorrelation function of gradient tensor elements.

In a general flow there are 9 auto- and 36 independent crosscorrelation functions. These numbers decrease if the flow under consideration has symmetry properties. For an incompressible fluid the numbers reduce to 8 and 28, respectively. This is due to the relation

$$\Gamma_{xx} + \Gamma_{yy} + \Gamma_{zz} = 0 \quad (7)$$

A channel flow which can approximately be viewed as two dimensional in the x-y-plane (the mean flow velocity is in the x-direction) has furthermore the following symmetries:

- invariance against reflexion at the x-y-plane
- invariance against translation in x-direction
- invariance against translation in z-direction

These symmetry properties reduce the number of independent correlation functions to 8 and 10, respectively.

3 The measurement scheme

The derivatives of the light intensity which appear in the equations (4) and (6) cannot be measured directly. Consequently one is forced to measure spatial and temporal differences, which requires two detectors at different locations which perform successive intensity measurements.

The time interval between successive intensity measurements (the so called sample time) must be chosen in a way that intensity changes during that time are only small. This requires the possibility to adjust the sample time according to the pattern velocity. In our experiments we used sample times from 5 - 50 μs depending on the flow properties. The mutual distance of the two detectors was about one tenth of the speckle size in the screen plane, this assures sufficiently small spatial intensity differences.

Gauge measurements with these parameters on the flow within a rotating cuvette show at most 5% deviations of the values obtained with our measurement scheme from the true gradient values.

The intensity measurements were done with photomultipliers in the photon count mode. A measure for the average intensity within a sample time is then the number of detected photons during this time. These numbers were counted electronically and after each sample time fed to the memory of a PC. After a certain time the data transfer to the PC was interrupted, and the calculation of the correlation functions according to expressions derived from equations (4) and (6) was started. This procedure was repeated until the scatter in the calculated correlation functions was considered sufficiently small.

The resulting measurement time varied between 10 and 40 minutes. This amounts to an averaging over a number of sample times of the order of magnitude of 10^8. This number can be reduced considerably if the light intensity is increased. The measurements cited in this paper were performed with an average of detected photons per sample time of not more than 5.

4 The flow

We did the measurements on a flow in an open water channel with the dimensions of $500\times18\times3$ cm^3. All results cited in this paper refer to a Reynolds number R_e of 4200, where R_e is defined by

$$R_e = \frac{u\cdot d}{\nu} \quad (8)$$

Here d is the channel width, u the centre line velocity, and ν the kinematic viscosity. The measurements were done at 3.5 m from the inlet and 16 cm above the channel bottom. The critical Reynolds number of this channel was determined to be 2400. The temperature of the water was controlled to better then 0.5 degrees. The seeding was done with latex particles with a particle size of $\approx$ 200 nm.

5 The optical set-up

An argon laser of maximum power of 3 W served as the light source. The laser was run in the TEM_{oo} mode at wave length of 488 nm and a power of 300 mW.

In order to obtain a sufficient large number of independent correlation functions we built a set-up where the illuminating light wave could be switched by use of a Pockels cell between two antiparallel directions. Both light beams were directed with mirrors and lenses into the flow in a way that the waists of the two beams had equal size and coincided.

The scattered light was observed in two perpendicular directions, which were also perpendicular to the directions of the illuminating light beams. The resulting scattering volume was almost spherical of a diameter of 150 μm.

With this set-up we could measure 8 auto- and 16 crosscorrelation functions of the speckle velocities in the two observation planes. This was sufficient to calculate all non-vanishing correlations functions of the components of the velocity gradient tensor.

For measurements at different distances from the channel wall we could translate the whole optical set-up with respect to the flow channel.

6 Results

Examples of measured correlation functions of the speckle velocity are shown in figures 2 and 3.

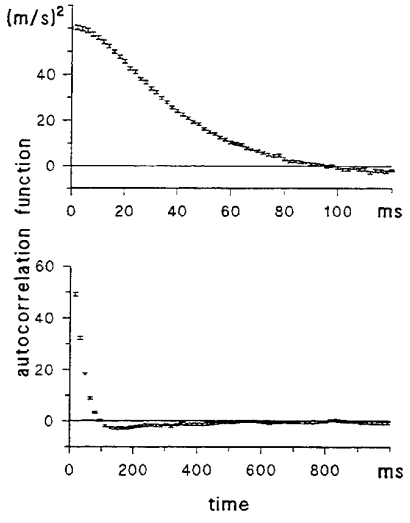

Figure 2: Example of a measured autocorrelation function of the speckle velocity. Note the different scales!

From a set of 24 correlation functions measured for one definite position of the scattering volume within the flow we calculated the correlation functions of the components of the velocity gradient tensor. It should be noted that this calculation is not straight forward since not all of the measured correlation functions are linear independent, and therefore, the data are not compatible with each other. We did the calculation by use of a least mean square fit procedure.

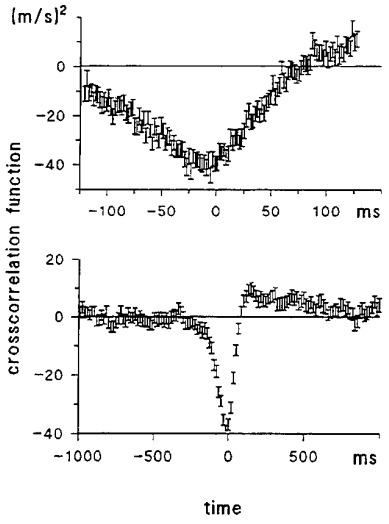

Figure 3: Example of a measured crosscorrelation function of the speckle velocity. Note the different scales!

Examples of these correlation functions are shown in the figure 4, where the autocorrelation functions of the z-component of the vorticity for different distances y^+ from the channel wall are plotted.

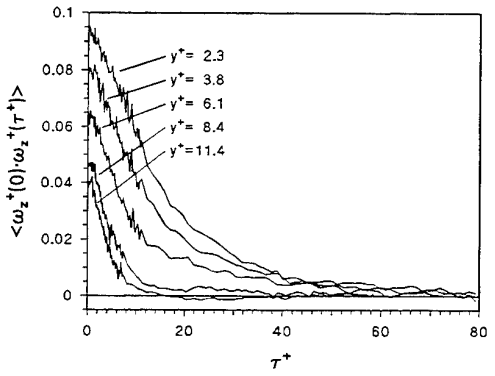

Figure 4: Autocorrelation functions of the z-component of the vorticity for different wall distances y^+.

In this figure as well as in the following ones we used scaled variables, which can be calculated from the kinematic viscosity ν of the fluid and the so called wall gradient γ_W. This is the derivative of the mean flow

velocity at the wall in the direction normal to the wall. One then has the following scaled variables:

$$\begin{aligned} \vec{u}^+ &= \frac{\vec{u}}{\sqrt{\nu \cdot \gamma_W}} \\ \tau^+ &= \tau \cdot \gamma_W \\ y^+ &= y \cdot \sqrt{\frac{\gamma_W}{\nu}} \end{aligned} \tag{9}$$

From the zeroth channels of the correlation functions we calculated the turbulent energy dissipation ϵ^+,

$$\epsilon^+ = \sum_{i,j=1}^{3} \left\langle \left(\frac{du_i^+}{dx_j^+} + \frac{du_j^+}{dx_i^+} \right)^2 \right\rangle \tag{10}$$

and the enstrohpy ω^+,

$$\omega^+ = \frac{1}{2} \cdot \sum_{i,j=1}^{3} \left\langle \left(\frac{du_i^+}{dx_j^+} - \frac{du_j^+}{dx_i^+} \right)^2 \right\rangle . \tag{11}$$

In these two equations the symbols u_i^+ denote the flutuating parts of the velocities according to the Reynolds decomposition.

The results are shown in the figures 5 and 6.

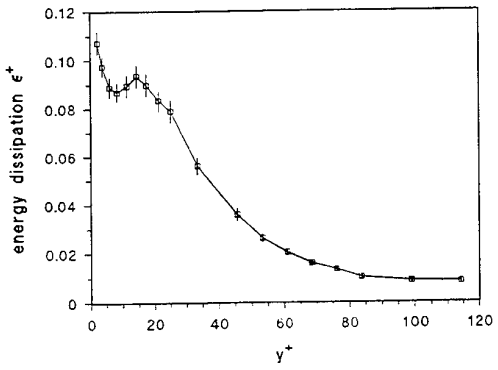

Figure 5: The turbulent energy dissipation in a channel flow as a function of the wall distance y^+. All quantities scaled according to equations (9)

The examples shown in this paper clearly demonstrate the power of the differential speckle strophometry for measurements of correlations and correlation functions of velocity gradient components. It is also possible to use the effect of speckle motion for measurements of momentaneous velocity gradient values, as was shown in [6]. It is furthermore worth noting that our method is especially suited for measurements at locations in flows where the velocity is low, as for instance near walls or stagnation points. This is due to the fact that in these cases the speckle boiling is very slow. The method

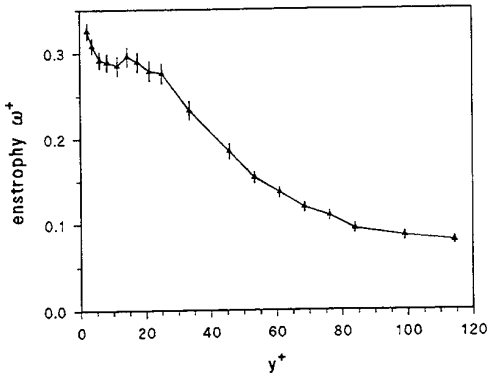

Figure 6: The enstrophy in a channel flow as a function of the wall distance y^+. All quantities scaled according to equations (9)

can also be extended to measure two-point correlation functions, measurements of this type are presently being performed.

References

[1] Keveloh, C. and Staude, W. 1988, The measurement of velocity gradients in laminar and turbulent flow, J. Phys. D: Appl. Phys. vol. 21, pp. 237-245

[2] de Gennes, P.G. 1977, Principe de nouvelle mesure sur les écoulements par échauffements optique localisés, J.Physique Lett. vol. 38, pp. L-1 - L-3

[3] Vukoslavčević, P., Wallace, J.M., and Balint, J.-L. 1991, The velocity and vorticity vector fields of a turbulent boundary layer. Part 1: Simultaneous measurement by hot wire anemometry, Part 2: Statistical properties, J.Fluid.Mech., vol. 282, pp.25-86

[4] Breyer, H., Kriegs, H., Schulz, R., and Staude, W. 1993, The measurement of velocity gradients in fluid flow by laser light scattering, Part2: Statistical properties of gradients, Exp. in Fluids, vol. 15, pp. 240-246

[5] Staude, W. 1996, The velocity of random time-dependent patterns and its experimental determination, J.Phys. D, vol. 29, pp. 307-314

[6] Kriegs, H. and Staude, W. 1995, A laser pulse technique for the measurement of time-resolved velocity gradients in fluid flow, Meas. Sci. Technol vol. 6, pp. 653-662

SESSION 18

2D PIV and PTV

HIGH-SPEED DIGITAL VIDEO CAMERA SYSTEMS AND RELATED SOFTWARE FOR APPLICATION OF PIV IN WIND TUNNEL FLOWS

Christian Willert,* Markus Raffel, Boleslaw Stasicki and Jürgen Kompenhans

Center for Quantitative Visualization (CQV)
c/o DLR, Institut für Strömungsmechanik,
Bunsenstraße 10, D-37073 Göttingen, Germany

ABSTRACT

Two particle image velocimetry (PIV) recording systems, based on electronic imaging, for use in industrial wind tunnel environments are presented. The first camera contains two independently triggerable, standard interline transfer CCD sensors which view the same area of interest through a beam splitter. Each sensor has a minimal exposure time of 0.8 μs and can be triggered within 1 μs. The asynchronous reset allows the camera to be directly triggered by a pulsed laser with repetition rates differing from standard video framing rates, and thus can provide two distinct images, separated by a short time interval, for dual-frame, single-exposure PIV application. Captured images are digitized and stored within the camera and are transferred to a PC through the parallel port interface. The residual misalignment of the two sensors is accounted for through software.

The second system utilizes a high resolution, full frame interline transfer CCD sensor which, contrary to the other, captures all lines of the pixel array. Adequate timing synchronization with the pulsed laser enables the camera to also provide closely spaced image pairs. The minimal time delay can be as low as 2 μs.

Images recorded by either system use the same multiple-pass, cross-correlation analysis software, whose algorithms are briefly described. Two examples of actual applications are given: the flow issuing from a jet nozzle was imaged by the high-speed video camera at close proximity. The high resolution system was applied in the study of helicopter rotor aerodynamics. The formation and evolution of a tip vortex behind the advancing blade was captured normal to the free stream of the wind tunnel. Here a large number of PIV recordings (200) could be obtained in a short time (4 minutes) which implies a possible reduction in wind tunnel operation cost.

1. INTRODUCTION

Particle image velocimetry (PIV) enables the instantaneous measurement of a large number of velocity vectors. Adrian (1991) and Hinsch (1993) give detailed descriptions of various implementations of the method which has been under continual development for the past 15 years. The most widespread implementation of the method images seeding particles suspended in the flow under investigation by illuminating them with a pulsed laser light sheet which is oriented normal to the imaging axis of the camera. The camera records the positions of the particle images using at least two closely spaced illumination pulses. By measuring the particle image displacement, either by particle tracking or locally applied statistical methods, the two-dimensional projection of the local velocity vector can be estimated using the magnification factor, M, and the laser pulse delay, τ.

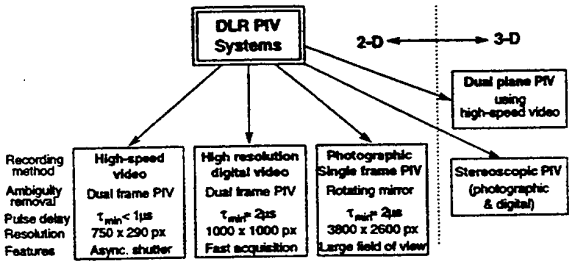

Figure 1. Particle image velocimetry systems currently available (left) and under development (right) at DLR for use in wind tunnels. The left-most two systems are described in this paper.

In the past years the PIV method has gained continual acceptance as a valuable fluid mechanics research tool in a wide variety of applications. In most cases however, the method was employed in laboratory settings in which the setup and data acquisition times were secondary with respect to obtaining high quality data. A different approach toward the application of PIV was taken at the German Aerospace Research Establishment (DLR) where the Measurement Sciences Division has been developing PIV systems since 1986. The principle aim in these efforts was to provide PIV systems for application in a wide variety of DLR wind tunnel facilities. This imposed a number of additional requirements not present in typical laboratory environments: The PIV system has to be easily portable and its components need to be mod-

* Affiliated with DNW-NWB, DLR-Braunschweig.

ular to adapt to each tunnel's unique features. Reliability is of principle concern due to the high cost of operating larger wind tunnels such as the Deutsch-Niederländischer Windkanal (DNW) with its 6 m x 8 m test section. Another set of requirements arises from the fact that nearly all applications of PIV at DLR take place in air at moderate to high speeds: small seeding particles are needed to accurately follow the flow, even at transonic speeds across shocks, which in turn requires the use of high-powered pulsed lasers in conjunction with high quality imaging equipment, especially when the observation areas and distances are increased. The seeding equipment itself has to be capable of producing large quantities of particles to seed large volumes of air. Finally, a third set of requirements is motivated by reducing the time between the actual PIV recording and the availability of the recovered PIV vector data sets.

The currently existing PIV systems at DLR are outlined in Figure 1. To the left, PIV is implemented in its classical form, namely recording the two-dimensional projection of the particle displacements from within a light sheet. Toward the right, systems capable of recovering the out-of-plane (third) velocity components are indicated and are still in a developmental phase. Of the three systems toward the left, the photographic, single-frame/double-exposure recording approach has been in use the longest (Kompenhans & Höcker, 1988). Image shifting by means of a rotating mirror (Raffel & Kompenhans, 1995) and recently through the use of a birefringent crystal plate, now enable PIV measurements over the entire spectrum of DLR's wind tunnel flows. Through the recent implementation of digital interrogation methods based on high resolution scans of the photographic recording (Willert, 1996) the achievable spatial resolution could be increased by a factor of two over the existing Young's fringe method of interrogation. The digital approach significantly reduces processing time because there no longer is a need to produce a high-contrast contact copy of the recording prior to interrogation. As films can be developed and dried within an hour, there now are multiple chances for feedback into the experiment during the course of a day.

An almost immediate availability of the PIV data is possible by using video based approaches to PIV recording, indicated to the left of Figure 1. This big advantage is opposed by a reduction in spatial resolution such that the photographic recording method continues to be a valuable tool for high resolution PIV measurements. As a matter of fact the video and photographic approaches are currently used in conjunction in the wind tunnel environment: the video approaches are often used

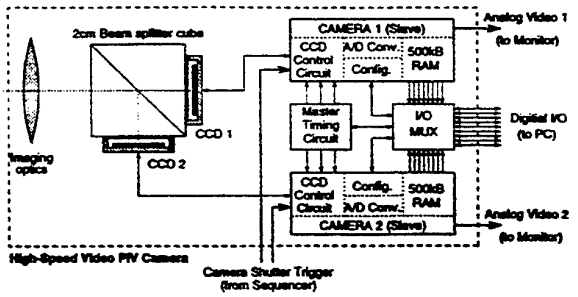

Figure 2. Schematic layout of the high-speed, dual sensor PIV camera.

to locate areas of interest in the flow field, which then can be mapped at greater spatial resolution using photography. This article describes two video based PIV systems currently in use at DLR. Each system has a number of advantages over the other which allows the coverage of a wide spectrum of applications, some of which will be given herein.

2. A HIGH-SPEED VIDEO CAMERA

Aside from reducing the time between image acquisition and PIV data availability, one of the primary reasons for using a video based approach to PIV recording is to completely remove the directional ambiguity issue by separating the two exposures of the particles in the flow field onto two separate recordings. But due to the relatively low frame rate of conventional video, typically 25 Hz (CCIR video standard) or 30 Hz (RS-170 video standard), this dual-frame/single-exposure approach was initially limited to low speed applications in water (Willert & Gharib, 1991). The later use of frame transfer CCD sensors permitted the pulse delay, τ, to be reduced from 33.3 ms (i.e. video frame rate) to 2 ms providing PIV recordings at a 15 Hz frame rate (Gharib et al., 1992; Hornung, Willert & Turner, 1995). Alternatively, video cameras based on interline transfer CCD sensors have been used to reduce the exposure delay to 160 μs (Huang & Fiedler, 1994) and 10 μs (Lecordier et al., 1994) by exposing the sensor once before and once after the interline transfer event in which case the recovered images only have half the vertical resolution. One major disadvantage of using standard video cameras for dual-frame/single-exposure PIV recording is that they generally cannot be triggered fast enough to capture rapidly occurring, asynchronous events in wind tunnel flows, such as from rotor blades or airfoil flapping.

In an effort to provide a video based PIV system suitable for capturing unsteady events in wind tunnel flows, a special camera has been designed at DLR. The camera system is based on previous experiences gained in the design and use of

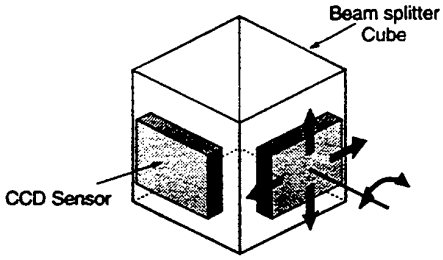

Figure 3. Coarse sensor alignment over three degrees of freedom.

a special, patented, high-speed video camera containing eight sensors with a burst frame rate of 1 million frames per second (Stasicki & Meier, 1995; Raffel et al., 1994). The optical design of this eight-sensor camera is such that its sensitivity is reduced by a factor of eight in comparison to a standard, single sensor CCD camera. This makes its application to imaging the light scattered off small (1 μm) oil droplets in air difficult unless the supplied laser illumination is increased accordingly.

The high-speed video camera featured in this article has a very similar electronic design as the eight sensor version but contains only two sensors which view the same area by means of a beam splitter. This arrangement makes the camera four times more sensitive to light than the original design. A schematic layout of the camera is shown in Figure 2. In essence the system contains two camera modules which are slaved to a third, sensorless, master camera that provides timing signals allowing the active cameras operate exactly synchronous. This was necessary since the electronic impulses present during the asynchronous reset event of one sensor interfered with its neighboring counterpart and resulted in a deterioration of the acquired images.

Each of the two camera modules has its own 8-bit A/D converter and memory to store a full image containing 741 by 574 pixels. The frame memories can be read out through a multiplexer and digital interface using the parallel port of a standard personal computer (PC). Additional frame-grabbers are therefore not needed. Analog video outputs permit the simultaneous viewing of the camera signals on standard video monitors. The cameras' configuration parameters, such as, integration (shutter) times, trigger and acquisition modes, are stored in EEPROM within the system and can be read or modified from the PC using the parallel port interface. Configuration and data retrieval is performed using dedicated MS-Windows or DOS programs; recorded images are stored as Bitmap or TIFF files.

Each of the camera modules within the system is freely triggered using TTL pulses. The internal

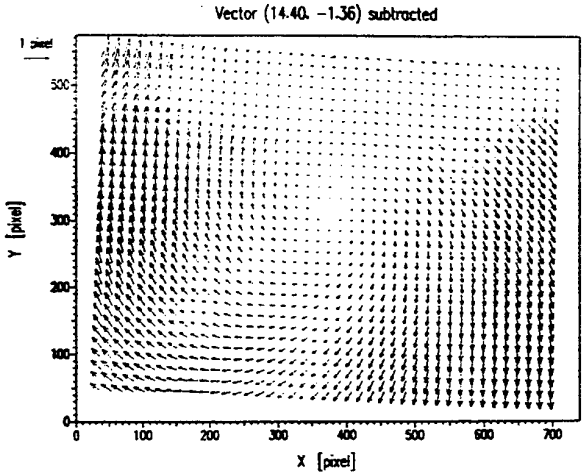

Figure 4. Raw PIV displacement data obtained through cross-correlation processing of stationary random dot pattern. The data shows the residual misalignment between the two sensors of the high-speed video camera.

Table I. Statistics for the residuals of the least squares fit to the data in figure 4.

Window Size (pixel^2)		RMS-Fluct. (pixel)	Max. Deviations (pixel)
64^2	X-Shift	0.023	(-0.080,0.084)
	Y-Shift	0.040	(-0.112,0.140)
32^2	X-Shift	0.047	(-0.198,0.175)
	Y-Shift	0.088	(-0.278,0.452)

delay for camera reset is on the order of 1 μs. The minimum exposure time for the sensor is 0.8 μs, which corresponds to the time required to shift the accumulated charge from an exposure into the interline storage wells. As both camera modules can be triggered individually, there is no minimum delay, τ, for its operation. The effective minimum delay without cross-talk from one to the other sensor is given by the minimum exposure time, $\tau_{min} = 0.8\,\mu$s.

2.1. SENSOR ALIGNMENT AND CALIBRATION

The two CCD sensors are mounted on two faces of the beam splitter as shown in Figure 3. The sensors are packaged in circular cases and are held by circular brass fittings which allows each sensor to be rotated fully and translated on the order of $\pm 100\,\mu$m. With the aid of an alignment fixture the sensors can be aligned within a few pixels by overlaying the two video signals onto one monitor.

The residual misalignment between the two sensors is accounted for through software as described next: the simultaneous recording of a random dot

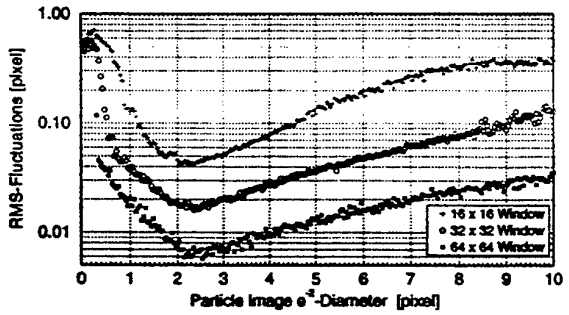

Figure 5. RMS measurement uncertainties in dual-frame, cross-correlation PIV as a function of particle image diameter based on simulated particle images with a density of 0.01 particles/pixel.

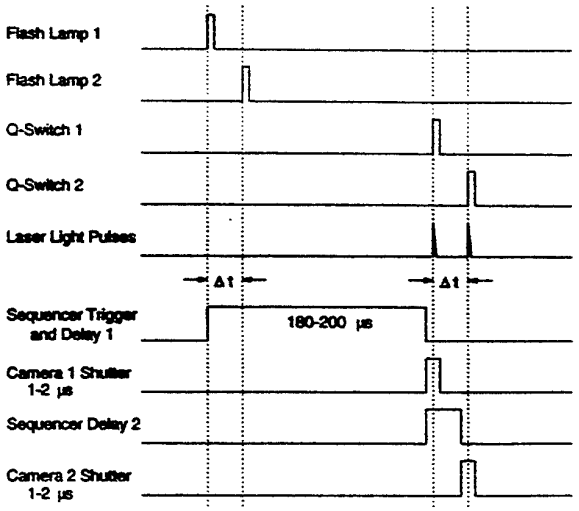

Figure 6. Timing diagram showing the synchronization between the pulsed laser and the camera.

pattern or of actual seeding particles is used to estimate the shift of the sensors on a pixel-by-pixel basis. The recorded image pair is interrogated using the same cross-correlation software as is used for evaluating actual PIV image pairs. The resulting displacement data (Figure 4) is then used to compute a second degree least squares fit which provides a very precise estimate of the misalignment which can be described with very few parameters. This alignment vector field only needs to be determined once and is removed from the displacement data of an actual PIV measurement prior to its conversion to velocity.

The residuals of the least squares fit, summarized in Table I, give an estimate for the obtainable measurement uncertainty. The data shows that both the RMS-fluctuations and maximum deviations approximately double when the interrogation window is reduced from 64^2 pixels to 32^2 pixels. Further, the vertical uncertainty is approximately twice as large as the horizontal which is due to the reduced vertical resolution associated with the field storage mode of the interline CCD sensors. In the alignment dot pattern (random black dots on white paper) given herein the diameter of the recorded artifical particle images ($\approx$ 5 pixels) was about twice that of typical particle images recorded in air. Experience and simulations, such as summarized in Figure 5, have shown that particle images of 2-3 pixel diameter produce the lowest measurement uncertainty.

2.2. PIV APPLICATION ON A FREE JET

In its first application, the dual-sensor camera was used to record PIV images of the flow issuing from a 2.5 cm jet nozzle with an exit velocity of 60 m/s. The seeding was provided by 1 μm oil droplets which were generated using pressurized air passing through Laskin nozzles immersed in olive oil. A constant stream of seeded air was introduced in the settling chamber of the jet facility, but no external seeding was used.

PIV recordings were obtained at the nozzle as well as further downstream at a high magnification using a 60 mm/f2.8 lens. The small field of view (45 mm by 30 mm) was chosen in order to test the camera's operation with short time delays, τ. Delays down to $\tau = 3\,\mu$s with exposure times of 1.5 μs were tested successfully in this manner. A further decrease in timing was hampered by a 1 μs jitter of the analog laser timing circuitry, a problem which since has been solved. Figure 6 illustrates the timing sequence to trigger the camera off the laser which operated at 10 Hz and 40 mJ per pulse. Using the first flash lamp trigger pulse, a sequencer provided the necessary TTL pulses to trigger the sensor exposure simultaneously with the actual laser light pulses. The delay between the pockels cell (Q-switch) and the first light pulse was too short ($< 1\,\mu$s) to allow the camera to be triggered in this alternative fashion. In the current application the camera captured image pairs at a 10 Hz rate of which selected pairs were transferred to and stored on the host computer for subsequent PIV data retrieval. The exposure delay was set to $\tau = 10\,\mu$s during which the particles moved on the order of 0.6 mm near the nozzle orifice (about 9 pixels in the image plane, $M = 15.21$ pixel/mm). In a later implementation both the laser and camera could be controlled using the same sequencer such that the exposure delay, τ, is set in only one place.

2.3. PIV ANALYSIS SOFTWARE

Before the recorded images could be analyzed by the cross-correlation software, several operations

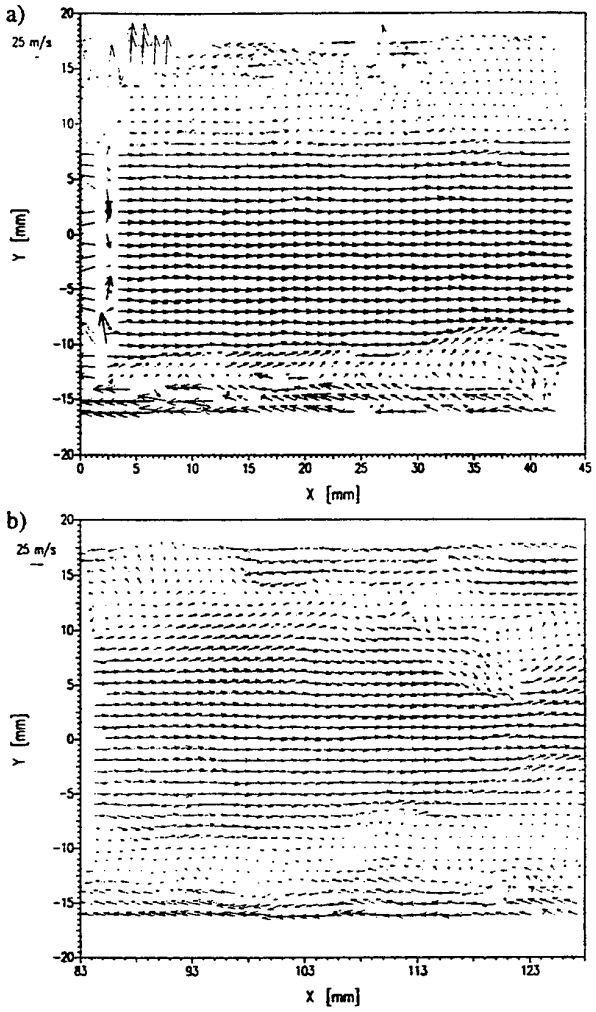

Figure 7. Velocity vector map for a jet flow with 25 mm nozzle diameter (located at $x = 0$, $y = 0$). The data on the top is recorded at the nozzle, while the bottom is recorded 80 mm further downstream. Half the exit velocity (i.e. 30 m/s) has been subtracted.

were performed: First, the images recorded from the off-axis face of the beam splitter were flipped horizontally to account for the reflection. Secondly, since only every other line of the pixel array in the interline CCD sensors was exposed, the missing lines were linearly interpolated. It should be noted however, that this operation of course can not generate the particle image data which was missed in the original recording. Rather, this operation was performed to allow easier handling and viewing of an undistorted image.

The core of the evaluation procedure is based on a cross-correlation analysis using small (32^2 pixel) interrogation windows similar to that described by Willert & Gharib (1991). The interrogation windows are overlapped 50% (16 pixels). The cross-correlation analysis program implements a multiple pass algorithm in which a number of passes (typically 3 passes) are used to offset the interrogation window with respect to each other in accordance to the local displacement vector. This procedure, described by Westerweel, Dabiri & Gharib (1995), has the advantage of significantly reducing the measurement uncertainty and improving the signal to noise ratio (i.e. higher data yield). Between each of the interrogation passes an outlier search algorithm eliminates vectors which deviate significantly from their neighbors to prevent the following interrogation to lock onto the suspect displacement data. In the final pass, the peak detection algorithm is limited to a smaller search region within the correlation plane to recover displacement data which may not otherwise be found. No outlier detection and replacement is performed after the last pass of the interrogation. Since the interrogation windows can only be shifted by integer amounts the multiple pass algorithm converges after typically three passes and generally requires approximately twice the interrogation time as the standard, single-pass interrogation.

Once the displacement data has been determined it is corrected with the sensor alignment data that was obtained using the least squares analysis described in the previous section. Finally the data is converted to velocity using the known magnification factor, M, and exposure delay, τ. Figure 7 shows two examples of PIV vector maps obtained for the jet flow using the multiple-pass interrogation procedure. No additional data validation or smoothing was applied here. The large number of outliers on top and bottom of figure 7a is due to the lack of particle images in these regions because no external seeding was applied. Further downstream (Figure 7b) the seeding covered the entire field of view and therefore resulted in a vector map with very few outliers.

As shown in Figure 5 the measurement uncertainty varies with particle image diameter. In the present recordings the particle image diameters are on the order of 2 to 4 pixel such that a conservative estimate for the 32^2 pixel interrogation window is ± 0.03 pixel (or ± 0.047 pixel from Table I) which translates to ± 0.2 m/s or approximately 0.5% of the exit velocity. Since the vertical resolution of the sensor is only half as good, the measurement uncertainty in this direction should be on the order of ± 0.4 m/s. These estimates may be on the optimistic side since they only are valid for gradient-free regions of the flows and because the simulations shown in Figure 5 do not include effects due to recording noise, missing particle image data (due to uncaptured video lines), particle loss by three-dimensional motion as well as other effects.

3. A HIGH RESOLUTION CROSS-CORRELATION VIDEO CAMERA

In spite of its numerous advantages the high-speed video camera described in the previous section has a significantly lower spatial resolution than photographic film and thus can only be used to map small areas within the flow field. Given the interrogation window of 32^2 pixel the dual-sensor camera provides approximately 23 by 18 discrete vectors. Standard 35 mm photographic film, digitized at 100 pixels per millimeter, yields about 56 by 37 discrete vectors at comparable measurement uncertainty (a 64^2 pixel interrogation window is required; see Willert, 1996).

To fill the large gap in spatial resolution, a third camera system has been designed. In this case the camera's sensor incorporates a full-frame interline CCD technology which has recently become available. Contrary to the more common interline transfer CCD sensors, as used in the high-speed video camera, these sensors are capable shuttering (exposing) and storing the entire array of pixels, not just every other line. Thus, these sensors immediately offer twice the vertical resolution when the CCD is used in the shuttered mode. A standard resolution camera of this type (768 x 484 pixels) was first used for high-speed PIV measurements in air at the California Institute of Technology as part of the collaboration in the Center of Qualitative Visualization (Vogt et al., 1996).

Following this general approach, the present PIV camera system additionally features a non-standard, high resolution, digital video format consisting of 1000 by 1000 square pixels with a 15 Hz frame rate. Using a 32^2 pixel interrogation window this translates to a spatial resolution of 31 by 31 discrete vectors. The digital video signal of the camera can not be viewed using a standard video monitor. Rather, the camera has its own digitizer and memory and provides the video signal in a digital form which is captured by an interface card in a PC. The interface card transfers the digital data directly into the computer's memory (RAM) at roughly 20 Mbyte/s and thereby allows a contiguous sequence of frames to be viewed and captured.

To permit the recording of two full frames in short succession the camera had to be exactly synchronized with the laser. Unlike the high-speed camera system described before, which was slaved to the laser's pulse generator, the high resolution camera provides the timing for the pulsed laser. A special frequency divider/multiplier was designed to synchronize the 15 Hz frame rate of the camera with the 10 Hz of the pulsed Nd-YAG laser. This

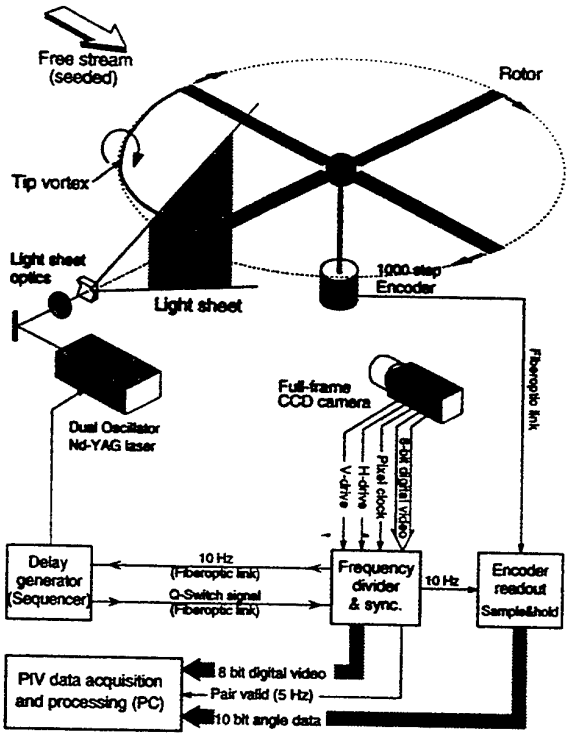

Figure 8. PIV system used in the study of tip vortex interaction with a model rotor.

allows the generation of PIV image pairs at a 5 Hz rate. The phase of the timing signals is set such that the first laser light pulse occurs shortly before the interline transfer event within the sensor, while the second laser light pulse occurs shortly thereafter. This procedure is similar to those described by (Lecordier et al., 1994) and (Huang & Fiedler, 1994). The minimal delay, τ, between the pulses has been confirmed down to $\tau_{min} = 1\,\mu s$ at low light levels. However, τ increases to $5 - 10\,\mu s$ for high saturation levels of the exposed pixels.

3.1. PIV MEASUREMENTS OF HELICOPTER TIP VORTICES

A challenging application for this high resolution, cross-correlation video camera was the study of tip vortices generated by and interacting with a model helicopter rotor in simulated free flight and descent. The experiments were undertaken in the open test section of the low speed wind tunnel of the Department of Aerospace Engineering of RWTH Aachen. The fully actuated rotor of 1 m diameter consisted of four NACA 0015 blades (chord length = 54 mm) with rectangular tips and was driven by a 65 kW electric motor. Two flight configurations were studied, simulated free flight at 1500 rpm and a free stream velocity of $U_\infty = 15.7$ m/s, and simulated descent at 3000 rpm and $U_\infty = 31.4$ m/s. PIV measurements results of the former are briefly described

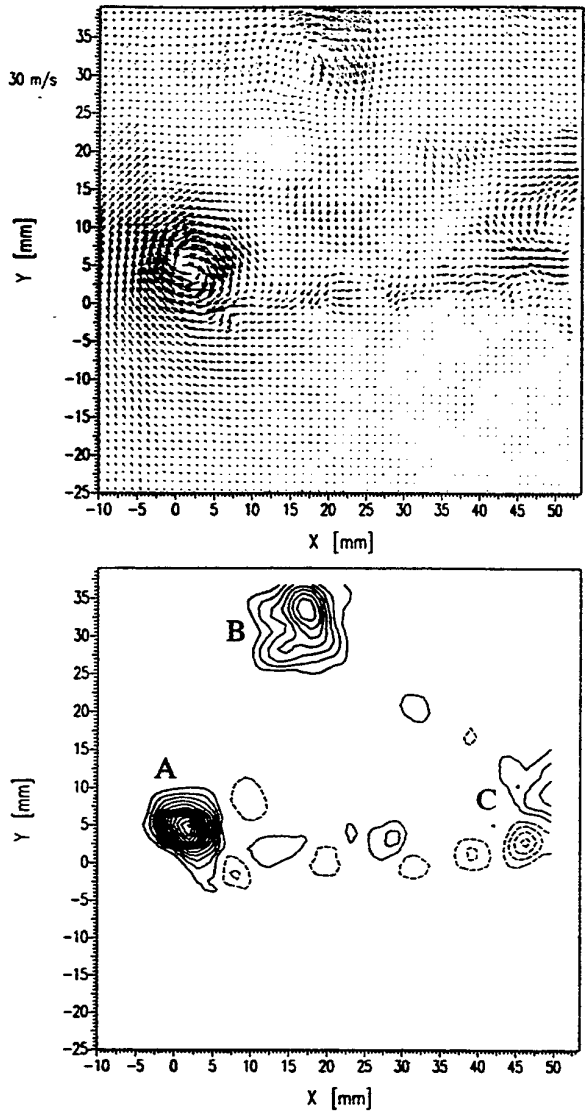

Figure 9. Velocity vector map (top) and corresponding vorticity estimate, ω_z, (bottom) for the flow behind an advancing rotor blade. One of the four blades, rotating at 1500 rpm in the $y = 0$-plane at a free stream of $U_\infty = 15.7$ m/s, has just left the imaging plane. The contour levels are spaced at 2000 $\sec^{-1}$; solid contours indicate negative values for ω_z.

here; more detailed results on both cases are given in (Raffel et al., 1996).

Figure 8 outlines the PIV system incorporating the high resolution, cross-correlation video camera. As the camera could not by operated asynchronously, but rather provided the timing for the pulsed laser, the PIV recording could not be performed at desired azimuthal angles of the rotor. Instead, it was decided to record a large number of PIV images (200) which were coded with the azimuthal angle (0.36° resolution) at the instant of the first laser light pulse (Q-switch trigger). To prevent spurious interference from the wind tunnel and rotor motors or from the laser, a number of signals were transmitted using fiber optic cables.

The plane of the light sheet was oriented nearly normal to the free stream on the advancing side of the rotor. The PIV camera, fitted with a 180 mm/f2.8 lens was located 1.5 m downstream and imaged an area 65 x 65 mm^2. Due to the short residency time of the particles flying normal to the 1 mm thin light sheet the pulse delay was set at $\tau = 7\,\mu s$. This translated to an out-of-plane particle loss of less than 15%. In this configuration 200 image pairs (i.e. 400 MBytes) were captured within four minutes covering the entire range of azimuthal angles.

The same multiple-pass, cross-correlation software as previously described was used to recover the displacement data. During the acquisition the laser power was limited to 60 – 70 mJ per pulse which was insufficient to saturate the sensor and produce adequately sized particle images; many particle images thus only covered 1-2 pixels. As a result the measurement uncertainty was on the order of ±0.1 pixel. The maximum displacements were limited to less than three pixels around the strongest vortex due to the short pulse delay of $\tau = 7\,\mu s$. As a consequence, the measurement uncertainty was large compared to the measured displacements. Nevertheless, the displacement data quality could be improved by first oversampling the images during interrogation (32^2 pixel interrogation window), then Gaussian-filtering the data and finally desampling back to a 50% overlap. In the future the problem should be resolved by using a high powered laser (300 mJ/pulse) which was recently acquired.

Figure 9 shows one example of the 200 PIV image set that was acquired with the high resolution, cross-correlation camera. The tip of the rotor blade is located at $x = 0$ cm, $y = 0$ cm with the vertical rotor axis located at $x = 50$ cm. Three different vortices can be seen: the strong vortex (A) to the left was generated by the rotor blade, which just passed through the light sheet. A second, weaker vortex (B) can be seen near the top of the observation area, and was generated by the blade 90° forward of the current blade. As the current blade moves away from the observation area, the newly formed vortex will move up to this position. Later, the vortex will move further inward and down into the rotor plane where it will be 'hit' by an advancing blade. The remnants of this third, 180° old, vortex (C) can be seen near the right edge of Figure 9.

4. POTENTIAL APPLICATIONS AND OUTLOOK

The application of the high-speed digital video camera to a high speed air jet at close proximity implies a wide range of other possible PIV applications in the area of internal aerodynamics. In the example given here, the camera operated at $\tau \approx 10\,\mu s$ and was able to record high velocities in a small field of view. By reducing the pulse delay to $\tau_{min} \approx 1\,\mu s$, the velocity may be increased tenfold, allowing the measurement of transonic or supersonic internal flows, such as in turbines or internal combustion engines.

The asynchronous shutter capability of the high-speed video camera allows its application in bright ambient conditions where standard sensors would be flooded by light. This means that the camera can be used to record PIV images in luminous flows such as flames. Further, the combination of the camera's asynchronous reset and asynchronous shutter enable its application to stochastically (non-periodic) occurring events. Also, a continuous illumination, such as by a CW-laser, can be used to generate light pulses by solely operating the electronic shutters in the camera and thereby makes the usual opto-mechanical or electro-optical shutter devices in the path of the laser beam unnecessary.

The high resolution cross-correlation camera fills the gap in spatial resolution between the high-speed video camera and photographic 35 mm PIV recording. Although it can not be operated asynchronously the combination of digital image capture and high-speed data transfer (20 MByte/s) allow a large number of PIV recordings to be recorded in a short time. The acquisition software was devised in such a manner that captured image pairs could be interrogated within 30 seconds allowing the camera's observation area to be shifted to the area of interest during the operation of the tunnel. This procedure was exercised during the helicopter rotor studies. This also allowed the photographic PIV acquisition to be quickly aimed at the area of interest to provide PIV recordings of similar spatial resolution but larger field of view. The complementary use of electronic imaging, for obtaining a large quantity of PIV recordings, and photographic imaging, for capture of fewer, but highly detailed, PIV recordings, make both approaches equally valuable for application of PIV in industrial wind tunnels. It is anticipated that these PIV recording systems, at their current state of development, can cover a large spectrum of applications in a large scale facility such as the Deutsch-Niederländischer Windkanal (DNW).

REFERENCES

Adrian, R. J. 1991, Particle-imaging techniques for experimental fluid mechanics, *Ann. Rev. Fluid Mech.*, **23**, pp. 261-304.

Gharib, M.; Weigand, A.; Willert, C. & Liepmann, D. 1992, Experimental studies of vortex reconnection to a free surface: A physical flow model, Proc. *19th Symposium on Naval Hydrodynamics (ONR), Seoul, Korea, 23-28 August 1992.*

Hinsch, K.D. 1993, Particle image velocimetry, in *Speckle Metrology*, ed. R.S. Sirohi, pp. 235-323, Marcel Dekker, New York.

Hornung, H.; Willert, C. & Turner, S. 1995, The flow field downstream of a hydraulic jump, *J. Fluid Mech.*, **287**, pp. 229-316.

Huang, H.T. & Fiedler, H.E. 1994, Reducing the time-interval between successive exposures in video-PIV, *Exps. Fluids*, 17, No. 5, pp. 356-357.

Kompenhans, J. & Höcker, R. 1988, Application of particle image velocimetry to high speed flows, in *von Karman Institute for Fluid Dynamics, Lecture Series 1988-06, Particle Image Displacement Velocimetry*, pp. 67-83, Brussels, March 21-25.

Lecordier, B.; Mouqualid, M.; Vottier, S.; Rouland, E.; Allano, D. & Trinite, M. 1994, CCD recording method for cross-correlation PIV development in unstationary high-speed flow, *Exps. Fluids*, 17, No. 3, pp. 205-208.

Raffel, M.; Kompenhans, J.; Stasicki, B.; Bretthauer, B. & Meier, G.E.A. 1994, Velocity measurement of compressible air flows utilizing a high-speed video camera, *Exps. Fluids*, 18, No. 3, pp. 204-206.

Raffel, M. & Kompenhans, J. 1995, Theoretical and experimental aspects of image shifting by means of a rotating mirror system for particle image velocimetry, *Meas. Sci. Tech.*, 6, pp. 795-808.

Raffel, M.; Seelhorst, U.; Willert, C.; Vollmers, H.; Bütefisch, K.A. & Kompenhans, J. 1996, Measurement of vortical structures on a helicopter rotor model in a wind tunnel by LDV and PIV, Proc.: *8th Intl. Symposium on Appl. of Laser Techniques to Fluid Mechanics, Lisbon*, paper 28.1.

Stasicki, B. & Meier, G.E.A. 1995, A computer controlled ultra high-speed video camera system, SPIE Proc. *21st Intl. Congress, High-Speed Photography and Photonics, Taejon, Korea, 29 Aug. - 2 Sep. 1994*, SPIE Vol. 2513, pp. 196-208.

Vogt, A.; Baumann, P.; Gharib, M. & Kompenhans, J. 1996, Investigations of a wing tip vortex in air by means of DPIV, Proc. *19th AIAA Advanced Measurement and Ground Testing Technology, New Orleans, LA., 17 - 20 June 1996.*

Westerweel, J.; Dabiri, D.; Gharib, M. 1995, Noise reduction by discrete image shifting in DPIV, in *Flow Visualization VII*, ed. J. Crowder, pp. 688-694, Begell House, New York.

Willert, C. & Gharib, M. 1991, Digital Particle Image Velocimetry, *Exps. Fluids*, **10**, pp. 181-183.

Willert, C. 1996, The fully digital evaluation of photographic PIV recordings, *Appl. Sci. Res.*, to appear.

HIGH-RESOLUTION DIGITAL TWO-COLOR PIV (D2CPIV) AND ITS APPLICATION TO HIGH FREESTREAM TURBULENT FLOWS

S. Gogineni and D. Trump
Systems Research Laboratories
2800 Indian Ripple Road
Dayton, OH 45440

L. Goss
Innovative Scientific Solutions, Inc.
3845 Woodhurst Ct.
Beavercreek, OH 45430

R. Rivir
Wright Laboratory
Aero Propulsion and Power Directorate
Wright-Patterson AFB, OH 45433

D. Pestian
University of Dayton Research Institute
300 College Park
Dayton, OH 45469

ABSTRACT

An extension of two-color Particle Image Velocimetry (PIV) is described in which the recording media (color film) is replaced with a high-resolution (3060 x 2036 pixel) color CCD sensor. Incorporation of the sensor eliminates the time associated with film development and digitization. Use of color allows the removal of directional ambiguities without resorting to polarization-based image-shifting techniques. For comparing the performance of the color CCD sensor with conventional color film, PIV images were obtained on a sand-blasted surface undergoing a known translation and rotation under comparable lighting and camera conditions. Good agreement was obtained between the two recording media, indicating that the behavior of the color CCD sensor is similar to that of 400-ASA color film. This digital two-color PIV (D2CPIV) technique was used for studying simulated turbine film-cooling flows to obtain more detailed characterization of the coolant-injection phenomena and their interaction with freestream disturbances. This technique allowed near-real-time optimization of the PIV parameters which resulted in higher valid vector density and shear-layer resolution.

NOMENCLATURE

d	film-cooling-hole diameter (1.905 cm)
R	coolant blowing (mass flux) ratio ($\rho_c U_c / \rho_\infty U_\infty$)
Re	Reynolds number based on film-cooling-hole diameter
Tu	turbulence intensity (u'/U)
U	mean local streamwise velocity (m/s)
x	streamwise distance measured from the downstream lip of the injection hole (cm)
y	vertical distance from the injection surface (cm)

1. INTRODUCTION

The PIV technique has been in use for a number of years to measure velocity distributions in planar cross sections of aerodynamic flowfields (Adrian 1991). One of the difficulties involved in implementing this velocimetry technique is the 180-deg. directional ambiguity which results from the inability to determine the temporal sequence of the particle pairs. Several techniques have been developed to resolve this ambiguity problem; most involve imposing a shift between consecutive image exposures by means of scanning or rotating mirrors (Adrian 1986), pulse tagging (Grant and Liu 1990), calcite crystals (Landreth and Adrian 1988), or polarizing beam splitters (Lourenco 1993). For overcoming the difficulties inherent in these techniques, a two-color PIV system was developed (Goss et al. 1991). The advantages of this system are: 1) the directional ambiguity is resolved using the color coding of the particle images, which is inherent in the system, 2) higher data yields and signal-to-noise levels are attainable, and 3) the technique is suitable for both reacting and non-reacting flowfields.

In early experimental approaches involving the PIV technique, the particle images were recorded on photographic film. However, this type of recording is time consuming because of the need to develop the film before digitization and subsequent computer processing. This disadvantage can be overcome by recording the particle images directly onto a two-dimensional CCD array. This approach has been recognized by several investigators. Cho (1989) proposed that the double-exposed digital images be obtained by digitizing single-exposed video images and adding the successive images. Okada et al. (1990) used liquid-crystal television (LCTV) having a resolution of 320 x 320 pixels. Willert and Gharib (1991) developed digital PIV and used cross correlation of the original-image frames acquired in succession to obtain an accurate measurement of the

displacements without directional ambiguity. Lourenco et al. (1994) introduced a fully digital and operator-interactive PIV system which utilized a CCD area sensor (1320 x 1035 pixel), resulting in significant improvements over earlier CCD-based PIV systems. This system has been successfully implemented in a wide variety of flow regimes.

The extension of the two-color PIV technique to include CCD cameras has been hampered in the past by the lack of commercially available high-resolution color CCD camera systems. Goss et al. (1994) attempted to utilize a single CCD camera and dichroic mirror to record the two-color PIV images of a stagnation-point flow. However, several problems were encountered, including a nonuniform shift across the image and degraded signal-to-noise ratios. Because of recent developments in high-resolution color cameras, the difficulty in utilizing color CCD cameras for two-color PIV has significantly decreased.

The present paper describes the extension of two-color PIV by recording the color images onto a single, high-resolution, digital (3060 x 2036 pixel) color CCD sensor, thus eliminating the processing time and subsequent digitization time of color film and the complexities associated with conventional image-shifting techniques. For demonstrating the direction-resolving capabilities of the D2CPIV technique and evaluating the spatial resolution capabilities, a test was performed using a sand-blasted rotating wheel. Results from this study indicate that the high-resolution color CCD sensor is comparable to 400-ASA color film in sensitivity, spatial resolution, and data quality.

This D2CPIV technique was also used to study simulated turbine film-cooling flows in order to provide a more detailed characterization of the coolant-injection phenomena and their interaction with the freestream disturbances. These types of flows are important because many state-of-the-art turbine stages employ film cooling to permit near-stoichiometric combustor operating temperatures. Film-cooling air is injected through rows of small (0.5 - 0.8 mm diameter typical) holes in the blade surface. The coolant air is supplied from the compressor exit flow and is maintained at essentially constant pressure.

2. EXPERIMENTAL SETUP AND PROCEDURES

2.1 Facility Description

The open-loop film-cooling wind tunnel, as shown in Figure 1, has been described in detail by Bons et al. (1994, 1995). The main flow passes through a conditioning plenum containing perforated plates, honeycomb, screens, and a circular-to-rectangular transition nozzle. Downstream of the transition nozzle, at the location of the film-cooling station, low freestream turbulence levels of 0.7% (± 0.05) can be achieved, with velocity and temperature profiles being uniform to within 1% at the film-cooling station. High freestream turbulence levels up to 17% can be achieved at the film-cooling station. A single row of 1.905-cm film-cooling holes at an injection angle of 35 deg to the primary flow is investigated. The length-to-diameter ratio of the film-cooling holes evaluated is 2.4. The ratio of integral turbulence scale to film-hole diameter is in the range 2.88 - 4.23, depending on the turbulence level and turbulence-generation mechanism (Bons et al. 1994). The ratio of momentum thickness to hole diameter typically is 0.05. The film-cooling-hole Reynolds numbers (Re) are 10,000, 20,000, and 40,000. The ratio of micro scale to film-hole diameter is in the range 0.1 - 0.39. The ratio of temperature or density of the film flow to the primary flow is typically in the range 1.07 - 1.09. The variation in blowing ratios (R = 0.7 - 1.5) is achieved effectively by varying the velocity ratio of the film-flow to the primary-flow velocity.

2.2 Two-Color PIV System

The two-color PIV system uses color for temporal marking of the seed particles in the flow field. The green (532-nm) laser output from a frequency-doubled Nd:YAG laser and the red (640-nm) laser output from a Nd:YAG-pumped dye laser (DCM dye) are combined by a dichroic beam splitter and directed through sheet-forming optics. The laser-sheet energy is typically 20 mJ/pulse, with a thickness of < 1 mm at the test section. The temporal delay between the two lasers is a function of gas velocity, optical magnification, and interrogation spot size. In the present

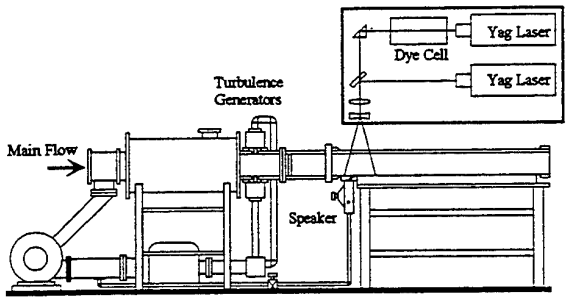

(a)

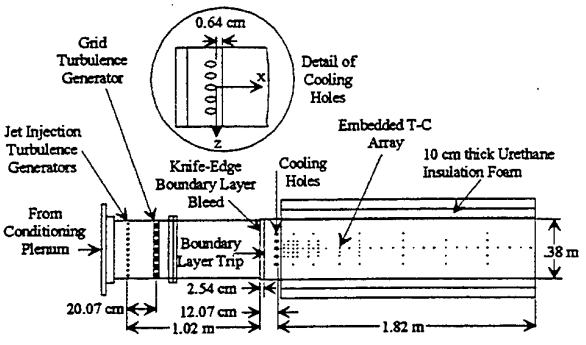

(b)

Fig. 1 Schematic diagram of experimental setup. (a) side view, (b) top view.

experiments, the time delay between the two color lasers is set at 10 μsec for flows at Re = 40,000.

The film-cooling flow is seeded with sub-micron size particles, and the Mie scattering from the seed particles is recorded on a Kodak DCS 460 CCD array. This CCD sensor has a resolution of 3060 x 2036 pixels, and each pixel is 9 μm square. The CCD camera has a built-in 12-bit analog-to-digital converter for increased dynamic range and a frame rate of 1 frame/sec. It also features a PC-MCIA storage drive which delivers about 26 exposures, with each PIV image occupying ~ 18 Mbytes. A 105-mm micro lens with an f-number 5.6 is used to record the images.

The color response of the DCS 460 CCD array is accomplished by overlaying the individual pixels of the camera with a series of red, green, and blue color filters. The green- and red-laser outputs are situated near the peak of the transmission of the green and red camera filters, respectively. Because the camera was built to respond, in part, as a human eye to color, most of the pixels are green-sensitive. The relative percentages of green, blue, and red pixels are 50%, 25%, and 25% respectively. The distribution of the red and blue pixels is random for minimizing straight-edge effects. The output from the camera controller to the computer is a 24-bit RGB tiff image; thus, the 12-bit ADC camera output must be mapped into three 8-bit colors, each having a spatial resolution equivalent to the chip size (3060 x 2036). This is accomplished through proprietary software developed by Kodak which involves interpolation to increase the spatial resolution of the camera. Because of the proprietary nature of this interpolation software, it was not known whether the resulting resolution of the color camera would be sufficient for accurate PIV measurements. This study was also directed toward evaluation and demonstration of the use of the Kodak color CCD camera for PIV studies.

2.3 Data Analysis

Once the PIV image has been captured and digitized, the velocity field is obtained using a cross-correlation technique. To improve the analysis of the seeded flow field, the output of the linear camera was convolved with a logarithm-like function prior to cross-correlation analysis. The present cross-correlation technique is based on intensity maps of the red and green images of the scattered light.

Consider the intensity distributions of the red and green images r(x,y) and g(x,y) and their corresponding Fourier transforms R(α,β) and G(α,β). The two-dimensional cross-correlation function

$$\begin{aligned} h(x,y) &= \int_R \int_R r(\alpha,\beta)\, g(x+\alpha.y+\beta)\, d\alpha\, d\beta \\ &= F^{-1}[F(r(x,y))\, F(g^*(x,y))] \\ &= F^{-1}[R(\alpha,\beta)\, G^*(\alpha,\beta)] \end{aligned} \quad (1)$$

is employed to determine the magnitude and direction of the average velocity over the interrogation area. (Note that unlike in processing methodologies that are based on autocorrelation, the direction of the velocity vectors is uniquely determined.)

The correlation function is calculated over small segments (interrogation domains) of the PIV image. The dimensions of each interrogation domain are dependent on particle density, estimated local velocity gradients, particle-image size, and desired spatial resolution. The maximum displacement of each particle must be less than one-half the interrogation spot. In the present experiments, the interrogation domain measured 64 x 64 pixels, corresponding to 2 x 2 mm in the measured flow. For enhancing the overall resolution, the interrogation domains are overlapped by one-half the domain size. The peak of the correlation map corresponds to the average velocity displacement within the interrogation spot. An intensity-weighted peak-searching routine is used to determine the exact location of the peak to sub-pixel accuracy. The number of particle pairs normally necessary to ensure a desirable signal-to-noise ratio is reduced to four or five pairs when the cross-correlation analysis is employed.

2.4 Uncertainty Analysis

The experimental uncertainties are calculated based on knowledge of the instrumentation used and a simple root-mean-square error analysis (Kline and McClintock 1953). This method assumes that contributions to uncertainties arise mainly from unbiased and random sources. Uncertainty in the velocity measurement arises from the time required to keep the large out-of-plane velocities and fluctuating components within the laser sheet during both pulses. The resulting number of pixels, typically 10, of displacement and the sub-pixel resolution of 0.1 pixels then dictate the uncertainty of ± 1%. The spatial resolution in the data presented is 4 mm. The data are acquired at a resolution of 2.0 mm using 32 pixels/mm for a spatial-resolution accuracy of ~ 0.3%.

3. RESULTS AND DISCUSSION

3.1 Calibration of the System

For testing the ability of the color CCD camera to capture images of sufficient quality for PIV analysis and for demonstrating the directional resolving ability of the two-color PIV system, "calibration" displacements were obtained by recording the speckle patterns from a sand-blasted surface undergoing uniform translation and rotation. The output from the green and red lasers was sent unexpanded onto a scattering plate which diffusely scattered the light onto the sand-blasted surface. In the case of uniform translation, the displacements for each translation were generated by recording the single-exposed digital image (green at the initial position and red after a small translation) and then numerically adding the two images. Extreme care was taken to prevent any movement of the camera or the stage between exposures. Cross-correlation analysis was employed to process these images using a 64 x 64 pixel interrogation size. The processed translation data which contain about 6000 vectors showed uniform displacements throughout the

interrogation region, and the rms value of the translational horizontal component was found to be 0.011 mm. The displacements for the uniform rotational case were generated by spinning the wheel and exposing the speckle pattern from both green and red lasers on the same frame. Figure 2(a) shows a typical speckle pattern of the rotational image, and Figure 2(b) shows the velocity data which clearly indicate the ability of the two-color approach to resolve the directional ambiguity. In order to compare results obtained with the color CCD sensor and film, a line passing through the center of rotation with zero horizontal displacement was examined. Because the tangential velocity of a rigid body undergoing rotation varies directly with the radial distance from its center and its rotational speed, a simple deterministic relationship exists between the actual and measured velocities. Velocity measurements were obtained using both the color CCD sensor and color film (400 ASA) under identical conditions such as magnification, recording lens, aperture, and rotational speed. The film image was digitized at a resolution of 2700 pixels/in., yielding an image size of ~ 3000 x 2000 pixels.

These images were interrogated using spot sizes ranging from 32 x 32 to 256 x 256 pixels. Figure 3 shows a comparison of the actual and measured velocities for both film and CCD sensor, with the images being processed using a 128 x 128 spot size. This shows that the data obtained using the high-resolution CCD sensor are very comparable to the film data. The proprietary interpolation software developed by Kodak appears to be effective in maintaining equal red, green, and blue pixel spatial resolution, even though the color pixels are not distributed equally through the color CCD sensor.

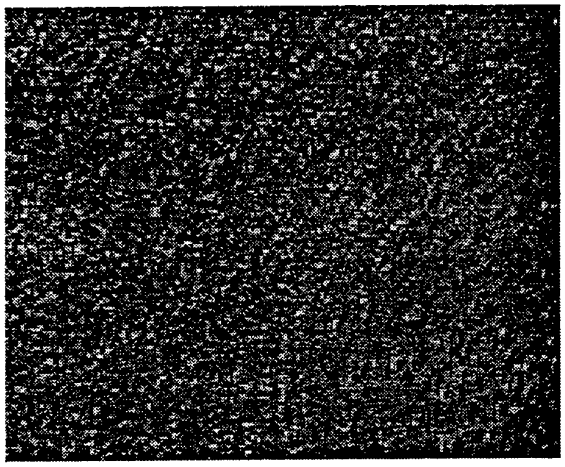

(a)

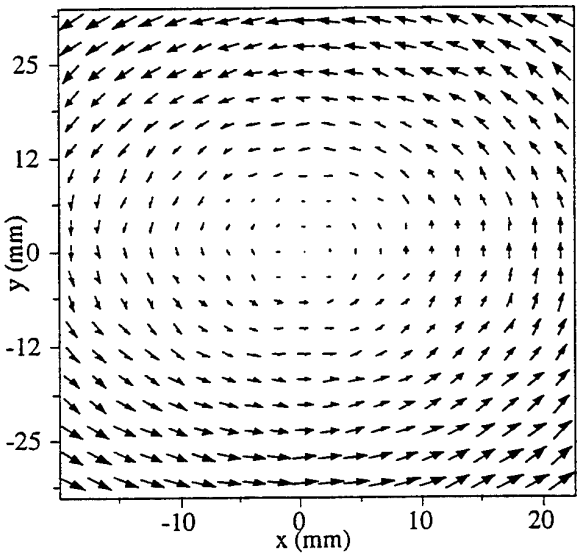

(b)

Fig. 2 Rotational data showing the direction-resolving capability of the D2CPIV technique. (a) speckle pattern, (b) velocity field

3.2 Application to Simulated Turbine Film-Cooling Flows

For further demonstrating the ability of the system to capture the complex flow features in quantitative form, simulated turbine film-cooling flows were considered. These flows occur in a very hostile, unsteady environment where velocity and temperature disturbances exceed 20%. The freestream and film-cooling wall conditions in these flows exceed those encountered in a classical, fully turbulent boundary layer. Accurate modeling of these flows has proved to be difficult due to the high-level unsteadiness. These flows have been investigated by Gogineni et al.

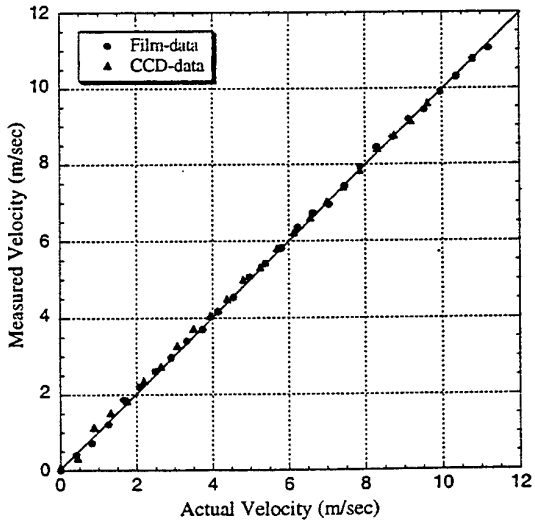

Fig. 3 Comparison of film and CCD data

(1995, 1996) using the conventional two-color PIV technique for Re = 20,000, with R varying from 0.5 to 1.5 and Tu from 1 to 17%. It was shown that turbulence clearly increases the film spread for R = 0.7. It was also observed that a linear relationship exists between the jet-exit slopes and both Tu and R for R < 1.0.

In the present study PIV measurements were made using a CCD sensor for Re = 10,000, 20,000, and 40,000 at freestream Tu levels of 1 and 17% by varying R from 0.7 to 1.5. These flow conditions were selected to understand the influence of high Reynolds number and high freestream turbulence on film-cooling effectiveness. Since the instantaneous realizations are not representative of mean flow behavior, 10 images were recorded for each condition. Figures 4(a) - 4(c) show typical double-exposed, two-color PIV images for R = 0.7 and Tu = 1% as Re is varied from 10,000 to 40,000. In these photographs, only the film-cooling flow is seeded with sub-micron size particles. When Re is increased, the shear-layer frequency over the film hole increases dramatically. The dominance of the film hole in setting the shear layer frequency over the film hole is reduced to 0.75 of the film hole diameter as Re is increased to 40,000. In all three photographs, a second, parallel shear layer is detected in the leading-edge exit region. This can be associated with separation from the inside entrance lip of the film-cooling hole. The shear-layer roll up is observed to be opposite that which would be expected for R = 0.7. The observed roll up results from the film tube boundary layer and a lack of seeding in the freestream. Figures 4(d) - 4(f) show the corresponding instantaneous velocity distributions. For clarity purposes, only a few of the measured vectors are shown in each frame.

Figures 5(a) - 5(c) show the PIV images when R is increased to 1.5 and Tu to 17%. At R = 1.5, the scale of the shear layer after the film-cooling hole increases or the frequency decreases as compared to R = 0.7 in Figure 4. Figures 5(d) - 5(f) show the corresponding instantaneous velocity dis-tributions. The CCD digitization allowed near-real-time optimization of the seeding and laser-sheet intensities which resulted in higher valid vector density and shear-layer resolution.

4. CONCLUSIONS

A new implementation of the two-color PIV technique is described where conventional color film is replaced with a high-resolution color CCD sensor. The proprietary interpolation software developed by Kodak is effective in maintaining equal red, green, and blue pixel spatial resolution, even though the pixels are not equally distributed. It was determined that optimum results in seeded flow fields are obtained by applying a logarithm-like function to the camera image prior to cross-correlation analysis. Tests on a rotating wheel showed the directional-resolving capabilities of the two-color approach, and the system was successfully applied under simulated turbine-flow conditions. The CCD sensor contributed significant improvement to the optimization of seeding and laser-sheet intensities for the simulated turbine high freestream flows.

ACKNOWLEDGMENTS

This work was performed under partial sponsorship of the Air Force Office of Scientific Research Project 2307S, with Dr. James McMichael as program manager. The work was also supported by Wright Laboratory, Aero Propulsion and Power Directorate, Wright-Patterson Air Force Base, Ohio, under USAF Contract Nos. F33615-90-C-2033 (with SRL) and F33615-95-C-2507 (with ISSI). The editorial assistance of Marian Whitaker (ISSI) is greatly appreciated.

REFERENCES

Adrian, R. J. 1991, Particle Imaging Techniques for Experimental Fluid Mechanics, Ann. Rev. Fluid Mech., vol. 23, pp. 261-304.

Adrian, R. J. 1986, Image Shifting Technique to Resolve Directional Ambiguity in Double Pulsed Velocimetry, Appl. Opt., vol. 25, no. 21, pp. 3855-3858.

Bons, J., MacArthur, C. and Rivir, R. 1994, The Effect of High Free Stream Turbulence on Film Cooling Effectiveness, ASME Paper No. 94-GT-51, 39th International Gas Turbine and Aeroengine Congress and Exposition, The Hague, Netherlands.

Bons, J., Rivir, R., Mac Arthur, C. and Pestian, D. 1995, The Effect of Unsteadiness on Film Cooling Effectiveness, AIAA Paper No. 95-0306, 33rd Aerospace Sciences Meeting and Exhibit, Reno NV.

Cho, Y. C. 1989, Digital Image Velocimetry, Appl. Opt. vol. 28, pp. 740-748.

Gogineni, S., Rivir, R., Pestian, D. and Goss, L. 1996, PIV Measurements of Flat Plate Film-Cooling Flows with High Freestream Turbulence, AIAA Paper No. 96-0617, 34th Aerospace Sciences Meeting and Exhibit, Reno, NV.

Gogineni, S., Rivir, R., Pestian, D. and Goss, L. 1995, High Freestream Turbulence Influence on Turbine Film-Cooling Flows, Winner of the 13th Annual Fluid Mechanics Gallery of Fluid Motion Photo Contest, 48th APS/DFD Annual Meeting, Irvine, CA (to appear in a special issue of Phys. Fluids, September 1996).

Goss, L. P., Post, M. E., Trump, D. D. and Sarka, B. 1991, Two-Color Particle-Image Velocimetry, J. Laser Appl., vol. 3, pp. 36-42.

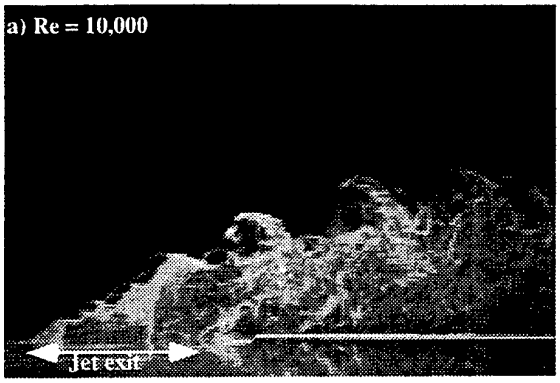

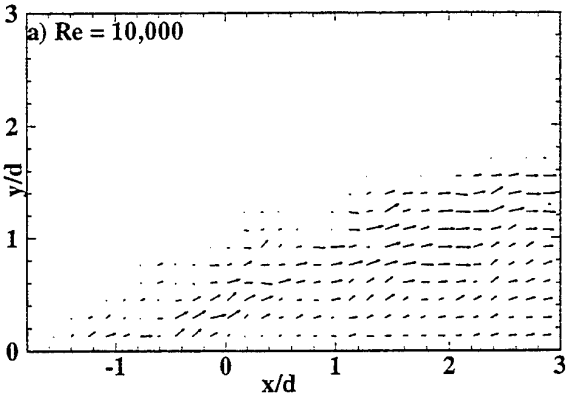

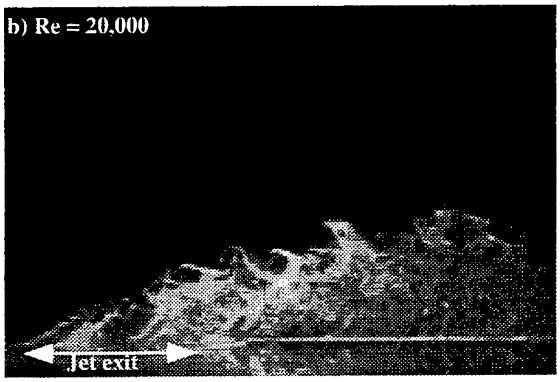

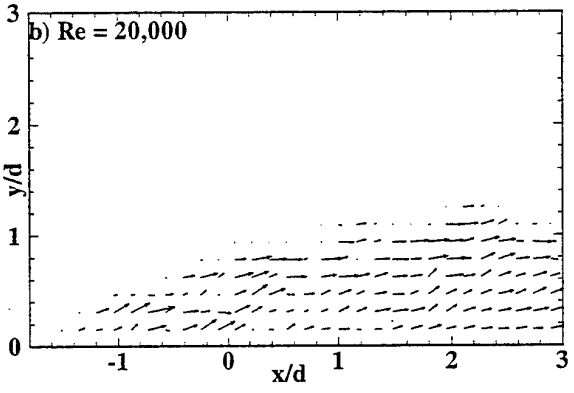

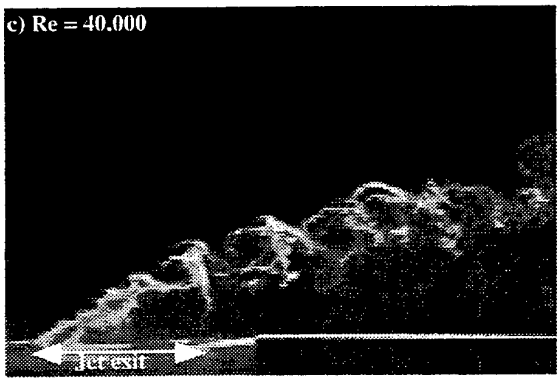

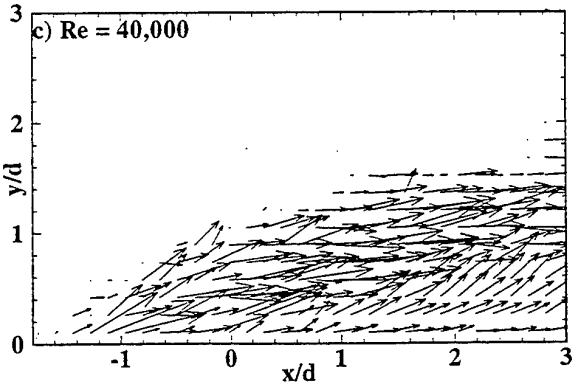

Double exposed PIV images

Instantaneous velocity distribution

Fig 4. Effect of Re on film-cooling flows (R = 0.7, Tu = 1%)

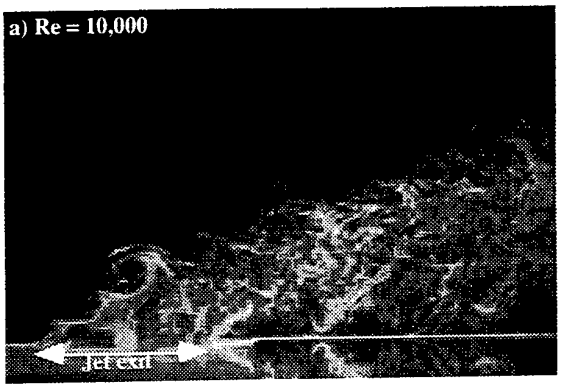

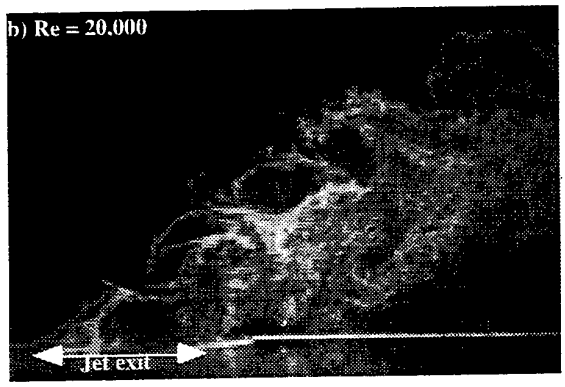

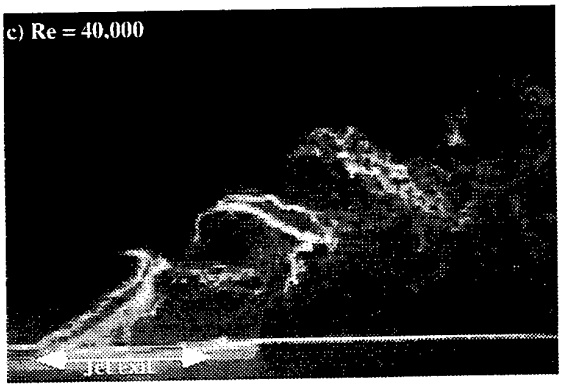

Double exposed PIV images

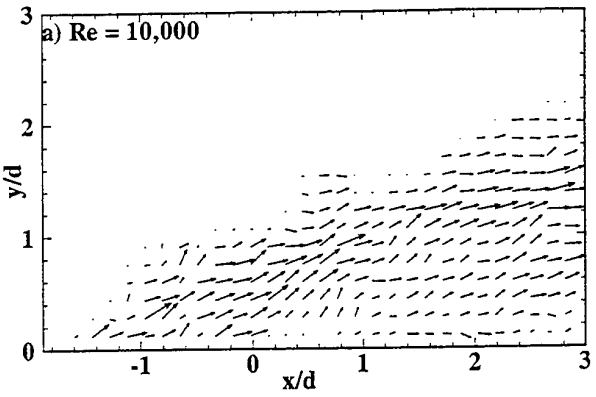

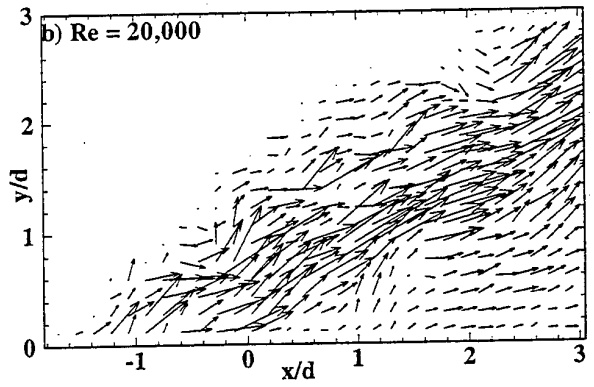

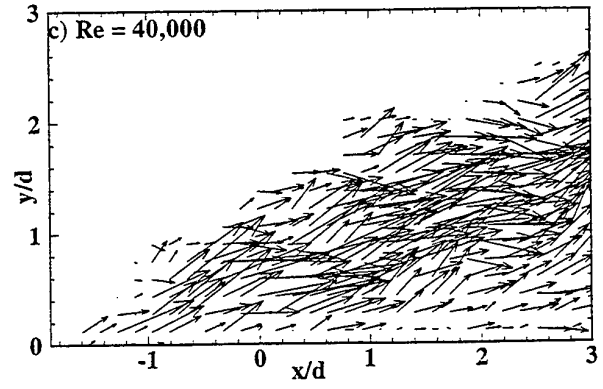

Instantaneous velocity distribution

Fig 5. Effect of Re on film-cooling flows (R = 1.5, Tu = 17%)

Goss, L. P., Trump, D. D. and Frank, J. 1994, Two-Color Particle-Imaging Velocimetry Employing a Single CCD Camera, Combustion Fundamentals and Applications (Proceedings 1994 Technical Meeting, Central States Section, The Combustion Institute), pp. 237-242, The Combustion Institute, Pittsburgh, PA.

Grant, I. and Liu, A. 1990, Directional Ambiguity Resolution in Particle Image Velocimetry by Pulse Tagging, Exp. Fluids, vol. 10, pp. 71-76.

Kline, S. J. and McClintock, F. S. 1953, Describing Uncertainties in Single-Sample Experiments, Mech. Eng., vol. 75, pp. 3-8.

Landreth, C. C. and Adrian, R. J. 1988, Electro-Optical Image Shifting for Particle Image Velocimetry, Appl. Opt. vol. 27, pp. 4216-4220.

Lourenco, L. M. 1993, A Velocity Bias Technique for PIV Measurements of High Speed Flows, Appl. Opt., vol. 32, no. 12, pp. 2159-2162.

Lourenco, L. M., Gogineni, S. P. and LaSalle, R. T. 1994, On-Line Particle Image Velocimeter: An Integrated Approach, Appl. Opt., vol. 33, no. 13, pp. 2465-2470.

Okada, E., Enomoto, H., Fukuoka, Y. and Minamitani, H. 1990, Instantaneous Particle Image Velocimetry with Electronic Specklegram, in Proceedings of Applications of Laser Techniques to Fluid Mechanics, ed. R. J. Adrian, D. F. G. Durao, F. Durst, M. Maeda and J. H. Whitelaw, pp. 464-475, Springer-Verlag, New York.

Willert, C. E. and Gharib, M. 1991, Digital Particle Image Velocimetry, Exp. Fluids, vol. 10, pp. 181-193.

VISUALIZATION OF STRUCTURE IN A TURBULENT BOUNDARY LAYER USING A STEREOSCOPIC PARTICLE IMAGE VELOCIMETER

Z. C. Liu, R. J. Adrian and C. D. Meinhart
Department of Theoretical and Applied Mechanics
University of Illinois, Urbana, Illinois 61801

W. Lai
TSI, Inc., St. Paul, Minnesota 55164

ABSTRACT

Development of a stereoscopic particle image velocimeter for the measurement of three-dimensional vectors on a planar domain is described. The camera is based on two high-resolution video cameras. Experiments in a turbulent boundary layer at $Re\theta = 2525$ demonstrate its applicability to the measurement of three-dimensional turbulent flow. In addition to the quantitative value of the out-of-plane component, it is found that having the complete three-dimensional vector also significantly improves the qualitative visualization of the flow.

1. INTRODUCTION

The extension of particle image velocimetry to measurement of three-dimensional velocity vector fields is both desirable and achievable. Hinsch (1995) reviews many of the techniques used for three-dimensional measurements. In general, there are two classes of measurement techniques: those which measure three-dimensional velocity vectors on full three-dimensional domains, i.e. volumes, and those that measure three-dimensional vectors on planar domains, i.e. light sheets. Three-dimensional volumetric measurements can be performed by using holographic techniques (Barnhart *et al.*, 1994, Meng and Hussain, 1995), by using photogrammetric particle tracking techniques (Maas *et al* 1993, Brodkey 1977, Nishino *et al* 1991), or by scanning laser light sheets rapidly (Brucker 1995). Photogrammetric methods use three or four cameras to view particles from several different directions. Volumetric measurements are in general difficult and require equipment that is rather different than the standard planar PIV equipment using a laser light sheet and a single camera. Holographic systems require a unique set of techniques and apparatus, and three-dimensional particle tracking systems involve multiple cameras and specialized software, plus they place demands on the optical access required to view the flow field. However, the most demanding aspect of volumetric measurements is the sheer number of velocity vectors that are obtained from the measurements. A modest 100x100x100 velocity grid measurement yields one million vectors, and if these measurements are to be repeated hundreds or even thousands of times for the purpose of statistical averaging, the amount of data is overwhelming. Thus, while volumetric measurements can be extraordinarily valuable for studying instantaneous flow field structures, they are often too rich in data to be used on a routine basis with present equipment.

An intermediate approach to three-dimensional measurements with PIV is to perform measurements of a three-dimensional velocity field on a planar domain. In this way, the number of vectors is the same as in ordinary two-dimensional planar PIV, but the third component contributes significantly to the experimenter's capability to visualize the flow, and the third component is valuable for the purposes of quantitative analysis of the flow. Further, full measurement of the three-dimensional vectors eliminates the perspective error that is inherent in monocular PIV systems (Adrian 1991, Prasad and Adrian 1993). This error can be quite significant if the flow has significant out-of-plane velocity component and the angular field-of-view is not small.

Systems operating with this capability can be designed using various aspects of image correlation (Robinson and Rockwell 1993), or the change in image magnification (Willert and Gharib 1992). However, the most common technique is the well-known stereoscopic method whereby one obtains a pair of images, each image viewing the particles in the illuminated light sheet plane from a different direction. Displacements of the particle images in the two different views differ because of the different viewing angles, and measurements of these displacements can be used to solve for the full three-dimensional displacement of particles. This technique can be applied to individual particles, as in particle tracking systems, or it can be applied to correlation technique for groups of particles. The correlation approach is desirable because three-dimensional velocity vectors can also be obtained on uniform grids, and the problem of matching individual pairs is solved automatically accounted. The limitation of this technique is that to assure good measurements of the out-of-plane component of velocity, the viewing angles between the stereo lenses must be substantial, of the order of thirty degrees, and the time between exposures of the images must be small enough that the particles remain within the thickness of the light sheet. These requirements have been explored amply and shown to be achievable and not inconvenient in practice (Troy 1994).

Stereographic systems of conventional form have been used by Arroyo and Greated (1991), Prasad and Adrian (1993), and Troy (1994). These experiments each used two photographic recordings, interrogated the

recordings to obtain displacements and then solved the stereo equations to obtain three-dimensional velocity vectors. The difficulty with using photographic film is the problem of registering the two pieces of film with respect to each other so that measurements of displacements locations in the first image can be identified precisely with locations in the second. This problem must be faced for each pair of photographic exposures that are taken in a stereo-photographic system. The registration process is more laborious and time consuming than developing the film itself, and it places a fundamental constraint on the utility of this method.

To make feasible extensive quantitative analysis of three-dimensional vector fields, it is necessary to make the image acquisition analysis process easy enough and fast enough to permit thousands of images to be taken for averaging purposes. To this end, the photographic recording must be eliminated, and replaced by videographic recording. Video cameras in a stereo system can be registered during the construction of the stereo camera and by this means they can be aligned once and for all, thereby eliminating all future efforts at registering the two images. The registration can be accomplished both by means of mechanical alignment during construction, and by electronic image processing alignment during the experimental stage. The electronic alignment is necessary in situations where an aberrating medium is placed between the object plane and the cameras, because the registration that was originally achieved in the construction of the camera is distorted by the medium. In this case, a calibration procedure can be used to correct for aberrations, provided they are not so severe as to completely destroy the images of the individual particles.

In this paper, the design and construction of a stereographic camera based on video recording is described, and some of the procedures used in the aberration calibration and correction process are explained. The system is applied to the visualization of three-dimensional vector field structure in a low Reynolds number turbulent boundary layer.

2. STEREOSCOPIC PIV SYSTEM

The stereoscopic camera is shown schematically in Fig. 1. The camera lenses L_1 and L_2 lie in a plane parallel to the object plane defined by the laser light sheet. They are offset laterally by d_{L1} and d_{L2}, respectively. Since the camera arrays also lie in a plane parallel to the object plane, the magnification of each lens is constant, equal to

$$M_0 = d_i / d_o, \qquad (1)$$

where d_i and d_o are the image and object distances, respectively. Within the angular field indicated by the solid lines each lens images point objects with resolution and distortion that are within the specification of the lens. In the object plane the size of the region that can be imaged with good resolution by both lenses, the 'joint field', is determined by the intersection of the respective angular fields. The lateral offsets d_{L1} and d_{L2} are chosen to be the largest values that still permit the angular fields to overlap over the desired region in the object plane, i.e. to make the joint field as large as possible while still keeping the angle between the lenses large enough to achieve small measurement error for the z-component of velocity. Nominally, d_{L1} and d_{L2} are equal, and the angle between the axes of the two lenses is 24.4 degrees. According to Prasad and Adrian (1993) the error in the z-component of velocity is about twice the error in the in-plane components of velocity when the angle between the axes of the lenses exceeds 30 degrees.

The field of view of each CCD array is simply the area of the array mapped onto the object plane. As in Prasad and Adrian (1993) and Troy (1994), offsetting the cameras laterally in the image plane overlaps their respective fields of view. Each camera sees nearly the same region in the flow, thereby maximizing the size of the joint field of view. This design is relatively simple to layout, but care must be taken to ensure that tolerances in the focal lengths of the lenses and in the orientations of the individual elements of the system are taken into account, either mechanically, or by careful calibration.

The joint field of view increases by more than a factor of two if the lenses are tilted towards each other so as to completely overlay their angular fields. This method, called 'angular displacement', has been discussed by Gauthier and Riethmuller (1988) and more recently by Prasad and Jensen (1996). Its principle advantage is the larger joint field of view, and its principal disadvantage is the more complicated alignment that is needed, which also involves using magnification that varies across the field of view. Only the simpler lateral offset method will be considered here, although angular offset can be easily accommodated by the present camera.

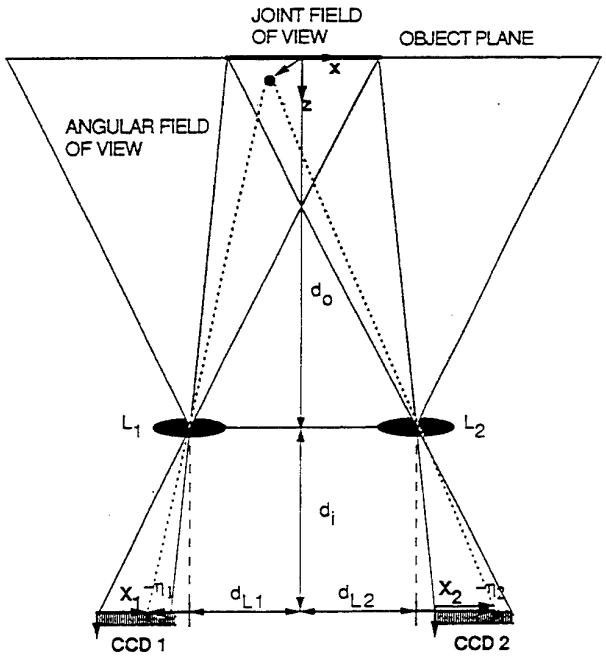

Figure 1. Schematic of the stereoscopic camera.

The camera uses two Kodak *Megaplus 4.2* CCD video cameras, each with 2029 x 2044 pixels resolution. Since the camera is intended to image a 100-300 mm field of view in the flow, and the CCD chip dimension is only 18 mm, the magnification of the system is substantially less than unity. M = 0.23 for the present system. Two Nikon *EL-Nikkor* 302.5 mm F/5.6 enlarging lenses that are optimized for normal operation at large magnification are ultilized to provide the appropriate small magnification with little aberration, minimal distortion and large aperture (53.6 mm). The angular field of view of this lens is 57 degrees. Images are normally acquired at F/9. The video cameras and two lenses are mounted on a 3-D translation stage. The stage provides the six degrees of freedom needed to position and focus the cameras and to accurately register them with respect to each other. For the wind tunnel experiments, $D_o = 1617$ mm and $d_i = 372$mm.

The rest of the stereoscopic system is shown in Fig. 2. Illumination of the flow field is provided by two Continuum Lasers Nd:YAG lasers with a wavelength of 532 nm at pulse frequency of 10 Hz. Each laser delivers up to 200 mJ/pulse of energy with a pulse duration of 8 nsec. The laser beam is formed into a sheet of about 1 mm thickness in the test section. To resolve directional ambiguity, image shifting is normally needed. However image shifting was not used for the present measurements because of the strong mean flow in comparison with the turbulence intensity in the boundary layer. If directional ambiguity were a problem the cameras could be replaced by 1k x 1k cross-correlating camera. Timing for the sequence of laser pulses and the image capture with the cameras is provided by a TSI, Inc. *Laser Pulse* synchronizer box.

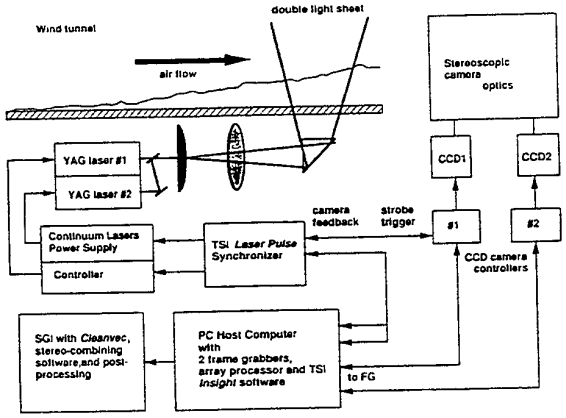

Figure 2. Stereoscopic system.

3. IMAGE ANALYSIS

The image analysis procedure is described in Fig. 3. The capture and analysis of images is controlled by *INSIGHT*, a Windows-based software package supplied by TSI, Inc. The software controls the simultaneous image capture by the video cameras. Image analysis to determine the velocity vectors on each image plane is performed by the autocorrelation technique. The outcome determine the velocity vectors on each image plane is performed by the autocorrelation technique. The outcome of the analysis is a pair of displacement vector fields, ΔX_1 and ΔX_2 that are functions of the camera coordinates, X_1 and X_2. The vectors in these fields are tested for validity using procedures described by Meinhart, *et al.* (1996), and invalid vectors are either

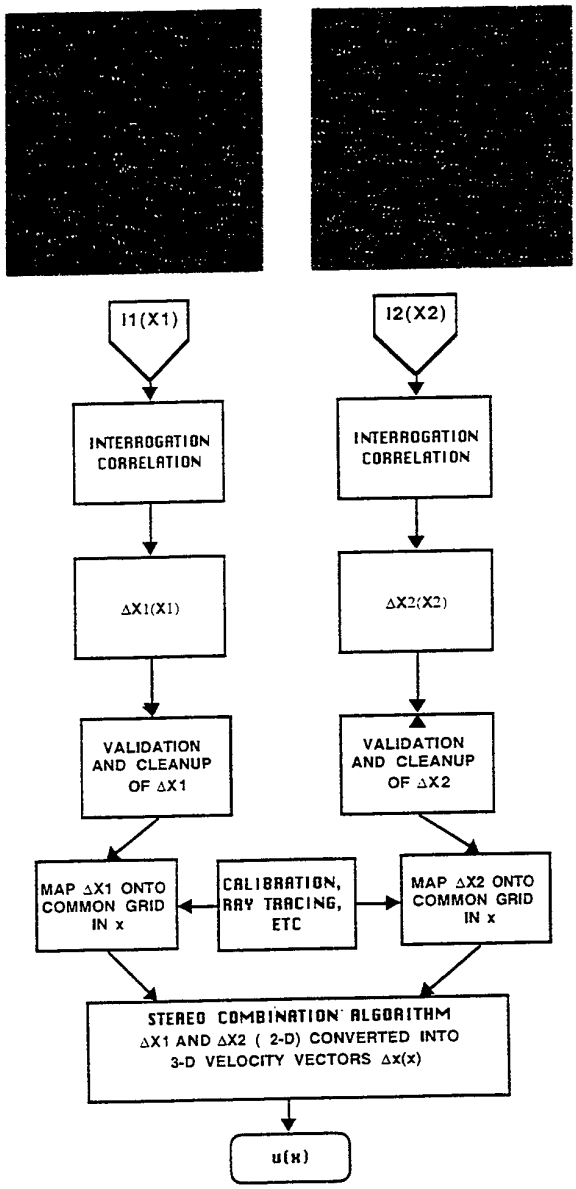

Figure 3. Image analysis procedure.

replaced by second or third choice vectors from the autocorrelation interrogation, replaced by interpolated values, or simply removed. Typically the fraction of invalid vectors is less than 2%. Corrections for the mis-registration of the images, and the variation of the magnification factors are all performed in a post-processing package. Effectively, this step maps the displacement vectors from a grid in each of the CCD

array image planes onto a common grid in the object plane. This step is necessary in general if there is any distorting medium between the object plane and the camera, such as a water-air interface (Prasad and Adrian 1993). In the present experiment the 6.35 mm thick glass windows of the wind tunnel cause the images to be displaced laterally by 0.55 mm. Since this shift is nearly constant, it is most easily accounted for by mechanical alignment in the initial layout of the cameras. In more general cases of nonlinear distortion it is better to calibrate the distortion and correct for it in software. The procedures for doing this will be discussed elsewhere.

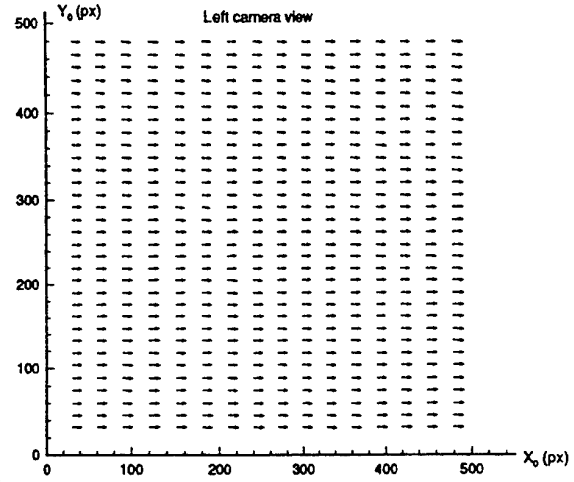

(a)

Lastly, the stereoscopic equations are applied to compute the third-component of the velocity vectors. For the ideal camera system shown in Fig. 1 the image of a point particle at x is mapped by lens ℓ onto a location η_ℓ in the $\mathbf{X}_\ell$-plane on camera ℓ given by

$$-\eta_1 = \frac{-d_i}{d_o - z}\left[(x + d_{L1})\hat{\mathbf{x}} + y\hat{\mathbf{y}}\right], \qquad (2a)$$

$$-\eta_2 = \frac{-d_i}{d_o - z}\left[(x - d_{L2})\hat{\mathbf{x}} + y\hat{\mathbf{y}}\right] \qquad (2b)$$

where carats denote unit vectors. Three-dimensional displacement of the particle by an amount $\Delta\mathbf{x}$ results in two-dimensional displacements $\Delta\eta_\ell$ that are found by taking the increment of (2). The result depends on the z-location of the particle at the time of the first exposure. However, PIV correlation analysis gives an estimate of the *volume average* of the displacements of the particles that lie in the measurement volume defined by the thickness of the light sheet and the area of the interrogation spot. By integrating the equation for the image displacement over such a volume and by making use of the normally large ratio of the object distance to the light sheet thickness, Prasad and Adrian (1993) have shown that the volume averaged displacements are given by

$$\Delta\overline{\eta}_1 = M_o\left[\Delta x + \frac{\left(x + d_{L1}\right)}{d_o}\Delta z\right]\hat{\mathbf{x}} + M_o\left[\Delta y + \frac{y}{d_o}\Delta z\right]\hat{\mathbf{y}} \qquad (3a)$$

$$\Delta\overline{\eta}_2 = M_o\left[\Delta x + \frac{\left(x - d_{L2}\right)}{d_o}\Delta z\right]\hat{\mathbf{x}} + M_o\left[\Delta y + \frac{y}{d_o}\Delta z\right]\hat{\mathbf{y}} \qquad (3b)$$

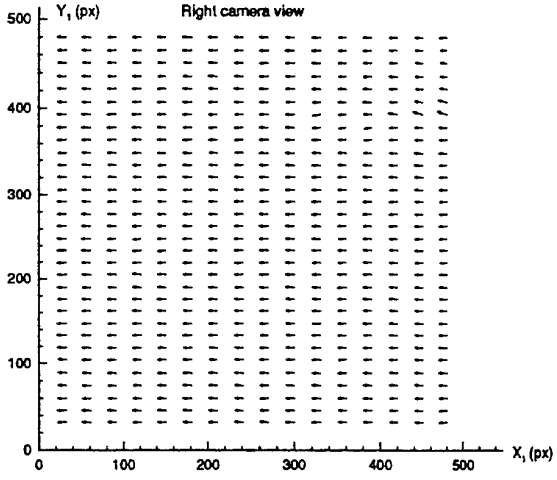

(b)

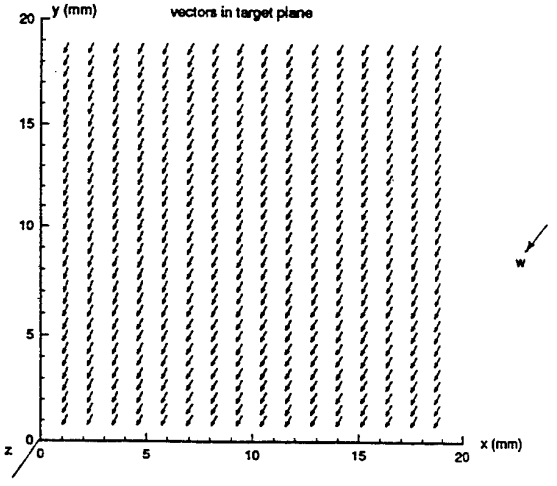

(c)

Figure 4. Image displacement fields due to a pure out-of-plane translation. (a) Camera 1, $-\eta_1(\mathbf{X}_1)$; (b) Camera2, $-\eta_2(\mathbf{X}_2)$; (c) Three-dimensional displacement field, $\Delta\mathbf{x}(\mathbf{X})$.

Given the two two-dimensional vector displacements $\Delta\eta_1, \Delta\eta_2$ three of the equations in (3) can be solved for $\Delta x, \Delta y, \Delta z$, and the fourth can be used to obtain a second estimate of Δy. Alternatively, the two Δy-equations can be added together to obtain a slightly more robust equation. The three-dimensional velocity vector is, of course, found by dividing three dimensional displacement by the time between exposures.

Figure 4a and 4b show the displacement fields that result on cameras 1 and 2, respectively when the object field undergoes a pure, uniform displacement in the z-direction. Solving equation (3) for the three-dimensional particle displacement yields the field shown in Fig. 4c.

4. TURBULENT BOUNDARY LAYER MEASUREMENTS

The turbulent boundary layer measurements were performed in an eiffel-type low-turbulence boundary layer wind tunnel with a working section 914 mm wide x 457 mm high x 6.096 m long. The free stream turbulence intensity at the test section inlet is less than 0.2% for free stream velocities less than 10 m/sec. The turbulent boundary layer was produced on a flat plate placed 100 mm above the floor of the test section. The boundary layer was tripped by the a 4.7 mm diameter wire which spanned the boundary layer plate just downstream of the leading edge. Optical access to the boundary layer was provided from the side by float glass windows, and from below by 610 mm wide x 2.748 m long float-glass windows.embedded in the boundary layer plate. The stereo PIV measurements presented here were performed at a free stream velocity of 3.4 m/sec, which produced a Reynolds number based on the momentum thickness θ of Re_θ=2575 at the location of the measurements. All measurements were made with the light sheet in the x-y plane of the flow, where x is streamwise and y is normal to the wall.

Figure 5 shows the (u,v) components of one realization of the flow field. A constant convection velocity of 3000 mm/s has been subtracted to make the fluctuations more visible. The edge of the turbulent boundary layer lies around 50 mm above the wall in this realization. As observed in earlier work, there is an internal layer close to the wall that grows in a manner similar to that of an ordinary boundary layer. This internal layer, seen as a region of uniformly low momentum that extends from the wall up to about 20 mm, is capped by a collection of several intense spanwise vortices.

The w-component of velocity is shown in Figure 6 by plotting its contours in gray-level form . It is immediately clear that the values of the w-component are frequently as large or larger than the other components. There is a tendency for the w-contours to align along the same 30 degree inclination that is observed in the u-v field. There is also a tendency for the sign of the w-component to be positive on one side of a 30 degree line and negative on the other, indicating a large-scale rotation about an inclined axis. The strength of the w-component and its coherent organization shows that one must be very cautious in interpreting the two-dimensional fields in a data set such as Figure 5.

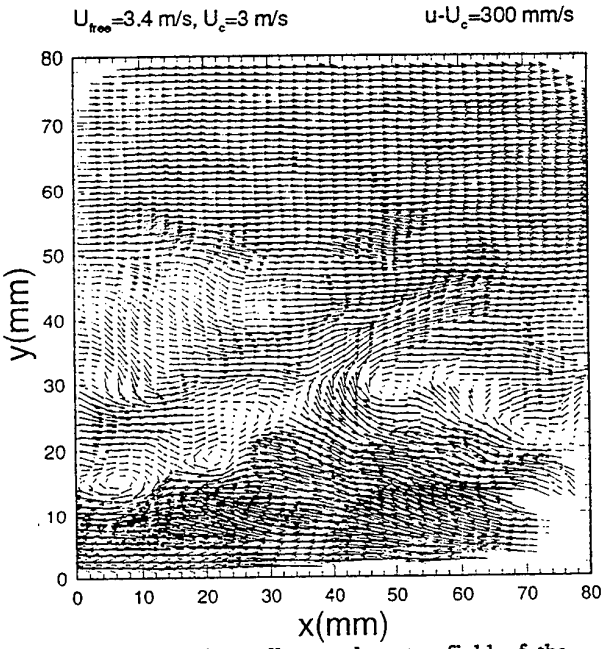

Figure 5. Streamwise-wall normal vector field of the turbulent boundary layer.

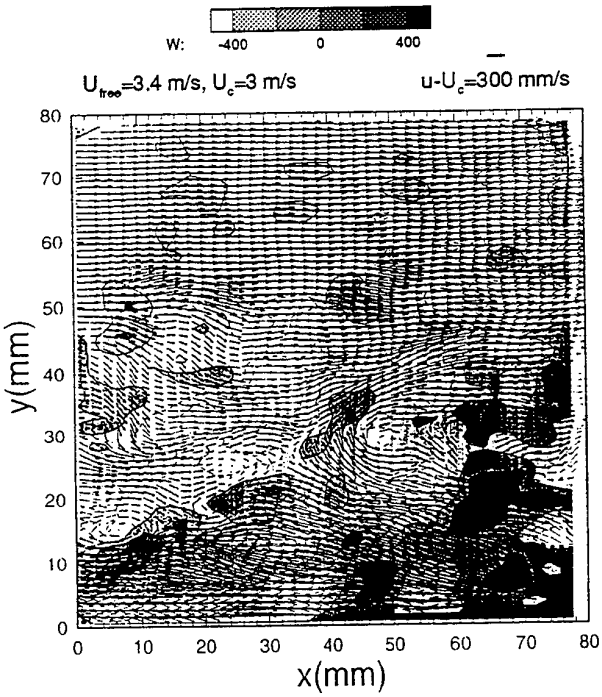

Figure 6. Field of the spanwise turbulent velocity superimposed on the streamwise-wall normal field from Fig. 5.

The three dimensional vectors are shown in end view, i.e. looking at the x-y plane along the x-axis, in

Figure 7a, and in oblique view in Figure 7b. The growth of the internal low-momentum layer is very evident in Figure 7b.

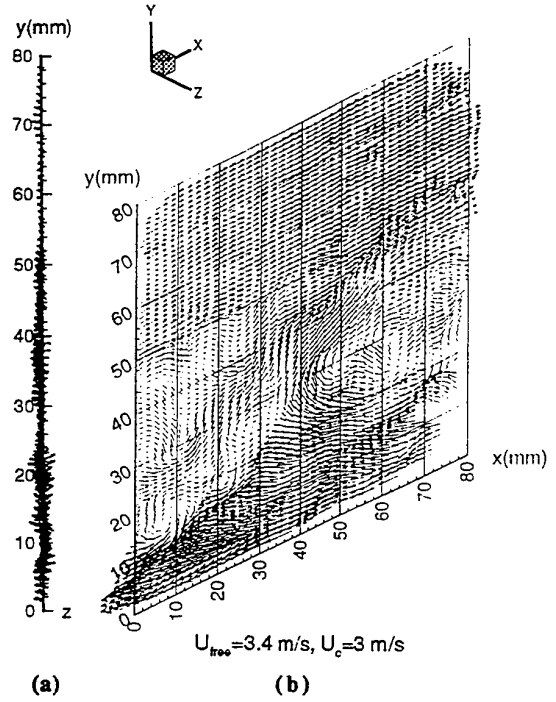

Figure 7. Three-dimensional vectors on the x-y plane. (a) end view; (b) oblique view.

5. SUMMARY

Stereoscopic PIV corrects for perspective error as well as providing the out-of-plane component. It requires a special camera, but otherwise it uses essentially the same hardware as a monocular PIV. Videographic recording increases the ease of use substantially by eliminating the necessity of registering photographic images. The present system has been used to measure thousands of frames in experiments that required only a few days to set up. Although the video-based PIV system has less resolution than a photographic system, it is encouraging that it is still able to resolve many of the important features of the turbulent boundary layer that have only recently been discovered by photographic PIV. The results are very similar to those obtained by photographic PIV. Thus, while the video system clearly has a role to play in the acquisition of data for analysis by statistical averaging, it also provides enough resolution to be of considerable value in visualizing the flow.

Acknowledgments

This work was supported by the United States Air Force Office of Scientific Research, the United States Office of Naval Research, and TSI, Inc.

References

Adrian, R. J. 1991, Particle-imaging techniques for experimental fluid mechanics, Ann. Rev. Fluid Mech., vol. 23, pp. 261-304.

Arroyo, M.P. and Greater, C.A., 1991, Stereoscopic particle image velocimetry, Meas. Sci. Tech. Vol. 2, pp. 1181-1186.

Barnhart, D.H., Adrain, R.J. and Papen, G.C., 1994, Phase-conjugate holographic system for high resolution particle image velocimetry, Appl. Opt., Vol. 33, pp. 7159-7170.

Brodkey, R.S., 1977, Stereoscopic visual studies of complex turbulence shear flows, *Flow Visualization*, (Ed. Asanuma, T.), New York: McGrow-Hill, pp. 117-122.

Brucker, C., 1995, 3D-PIV using steroscopy and a scanning light-sheet: application to the 3D unsteady sphere wake flow. *Flow Visualization VII*, (Ed. Crowder, J.P.), New York: Begell House, pp. 715-720.

Gauthier, V. and Riethmuller, M.R., 1988, Application of PIDV to complex flows: measurements of the third component. *Von Karman Institute Lecture Series on Particle Image Velocimetry*. Rhodes-Saint-Genese: von Karman Institute for Fluid Dymanics.

Hinsch, K.D., 1995, Three-dimensional particle velocimetry, Meas. Sci. Tech. Vol. 6, pp. 741-753.

Meinhart, C.D., Barnhart, D.H. and Adrain, R.J., 1996, Interrogation and Validation of 3-D vector fields, *Development in Laser Techniques and Applications to Fluid Mechanics.*, Springer: Berlin, pp. 379-391.

Meng, H. and Hussain, F., 1995, In-line recording and off-axis viewing (IROV) technique for holographic particle velocimetry, Appl. Opt. Vol. 34. pp. 1827-1840.

Nishino, Y., Kasagi, S. and Hirata, M., 1989, Three-dimensional particle tracking velocimetry based on automated digital image processing. ASME J. Vol. 111, pp. 384-391.

Prasad, A.K., and Adrian, R.J., 1993, Stereoscopic particle image velocimetry applied to liquid flows, Exp. Fluids, Vol. 15, pp. 49-60.

Prasad, A.K., Jensen, K., 1995, Saheimpflug stereocamera for particle image velocimetry in liquid flows, *Appl. Opt.*, Vol. 34, pp. 7092-7099.

Robinson, O., and Rockwell, D., 1993, Construction of three-dimensional images of flow structure via particle tracking techniques, Exp. Fluids, Vol. 14, pp. 257-270.

Troy, V., 1994, A study of Turbulent Penetrative Thermal Convection Using Stereoscopic Particle Image Velocimetry. *M.S. thesis*, University of Illinois, Urbana.

Willert, C.E.,. and Gharib, M., 1991, digital particle image velocimetry, Exp. Fluids, Vol. 10, pp. 181-193.

FIBRE OPTIC PIV STUDIES IN AN INDUSTRIAL COMBUSTOR

D J Anderson†, C A Greated‡, J D C Jones, G Nimmo§ and S Wiseall§

Department of Physics, Heriot-Watt University, Riccarton, Edinburgh EH14 4AS, UK

†Now at: Sharp Laboratories of Europe, Oxford, UK
‡Department of Physics and Astronomy, University of Edinburgh, UK
§Applied Science Laboratory, Rolls-Royce plc, Derby, UK

1. INTRODUCTION

The objective of the work described in this paper was to develop a robust optical fibre beam-delivery system for particle image velocimetry (PIV) capable of delivering Q-switched pulses from frequency-doubled Nd:YAG lasers with pulse energies in 20 mJ range. The stimulus for the work was the requirement to make PIV measurements in an industrial-scale combustion test-rig, where optical access was too limited to accommodate bulk-optic beam delivery. Our basic requirement was to measure flow velocities of up to 60 ms^{-1} in a region of dimensions approximately 0.1 × 0.1 m, in the presence of high levels of unwanted ambient light generated by the combustion process. The maximum tolerable cross-sectional diameter of the light-sheet-forming optics was about 12 mm, which were required to operate at temperatures >200 °C, with combustion temperatures of around 2 000 K.

We have shown previously that it is feasible to use optical fibres to deliver Q-switched laser pulses for PIV measurements [Anderson et al, 1995]. However, to accommodate the high instantaneous peak powers of the laser pulse it is necessary to use fibres of large core diameter in order to reduce the power density sufficiently to avoid damaging the fibres. An inevitable consequence of the large core diameter is a low beam quality, which in turn leads to relatively thick laser light sheets in the PIV system, with consequently reduced energy densities and poorer spatial resolution. A compromise exists: larger fibres allow the transmission of higher pulse energies, but with poorer beam quality.

One of the objectives of this paper is therefore to show that the compromise between pulse energy and light sheet quality can be improved by using a bundle of fibres, rather than a single fibre, in the delivery system. To a rough approximation, the light sheet quality is set by the core diameter of any one of the fibres used in the bundle, whereas the maximum pulse energy scales with the number of fibres in the bundle. Delivery bundles were an integral design concept in the PIV system that we developed and successfully demonstrated for measurements in an industrial combustion test rig.

We shall first discuss the fundamental limitations that apply when using optical fibres for the delivery of pulsed laser power, indicating the increases in core size necessary to accommodate pulse energies typical of PIV requirements. We shall accordingly demonstrate the difficulty of using single optical fibres in PIV systems, not only arising from limited pulse energy handling capacity, but exacerbated by objective laser speckle induced by interference between light propagating as different guided modes in the large core diameter multimode fibre. We shall then introduce the concept of fibre bundles for beam delivery, and indicate the advantages that they confer in terms of shifting the energy-quality compromise. We shall also explain techniques available for reducing the problem of speckle. We shall illustrate our discussions by describing the design and performance of a practical fibre delivery system, and outline its successful application in combustion measurements.

2. OPTICAL FIBRE BEAM DELIVERY

Optical fibres are now very well established as a useful technology in the design of optical systems for many types of laser instrumentation used in fluid mechanics, exemplified by the fibre delivery systems for laser anemometers used for single-point measurements, of both Doppler difference and transit

types. Such delivery systems are now commercially mature.

Fibre systems were developed for these purposes for their now accepted advantages of flexibility in design, allowing active parts of the measurement system to be separated from an optical probe deployed in the measurement region by fibre cables. The general requirement is the ability to guide CW laser beams to form small laser beam waists constituting the measurement volume. For this purpose, single-mode optical fibres are the preferred choice, where the small core diameter (typically 5 μm for visible wavelengths) gives extremely high quality delivered beams—the ability of the single-mode fibre to spatially filter the input beam means that the delivered beam quality is often higher than that of the laser itself. Such delivery systems are used to deliver average laser powers of up to about 10 W, at wavelengths as short as 488 nm (see for example Jackson et al 1984).

Requirements for beam delivery in PIV are typically very different. Here, the requirement is to produce a laser light sheet (see, e.g., Koga et al 1987), rather than a tightly focused laser 'spot', where the need for temporal resolution dominates. Two techniques have been used to give the necessary temporal resolution, based either on beam scanning or pulsed laser illumination. In the first technique, a laser beam is scanned to generate an illuminating sheet, where although the duration of the laser illumination is long, the scanning action ensures that any given point in the sheet is illuminated only briefly. Scanning systems have the advantage of allowing relatively inexpensive and easily controlled modulated CW lasers to be used, with low peak powers. Thus delivery systems similar to those available for single-point anemometers are appropriate. Scanning systems are valuable in the investigations of relatively low speed flows, typically used for hydrodynamic studies, but the temporal resolution is inadequate for higher-speed aerodynamic flows. Furthermore, the requirement for beam scanning, usually achieved mechanically, mitigates against the development of robust and compact light-sheet forming optics. For reasons both of flow speed and practicality of probe design, scanning techniques for light sheet formation were unsuitable for our intended application.

Different types of laser system have been used to produce pulsed illumination for PIV. Simple systems are able to use a CW laser, which is gated using an external modulator, often of the acousto-optic type. Such systems can give only limited peak power, no higher than the average power of the un-modulated laser. However, they are simple to design, with undemanding requirements for the beam delivery system, and are appropriate for producing light sheets of small dimensions, where the limited pulse energy can still give adequate energy density to produce acceptable PIV particle images provided that the flow velocity is low.

To satisfy the light sheet dimensions and flow velocities present in our application, as defined above, the most appropriate type of laser source was a Q-switched and frequency-doubled Nd:YAG laser, thus operating at a wavelength of 532 nm. Such requirements are typical in PIV experiments (see for example Kompenhans and Raffel, 1993). We required a delivered pulse energy of about 20 mJ. The pulse duration was about 6 ns, leading to an instantaneous peak power of about 3 MW, which may be compared with the power levels of a few watts typically present in a single-point laser anemometer.

2.1 Damage mechanisms in optical fibres

It is useful to first review briefly the mechanisms that limit the maximum power that can be transmitted by an optical fibre. An ultimate limit is set by the dielectric breakdown of the materials from which the fibre is fabricated. Almost all fibres are made from fused silica, doped to produce the refractive index profiles need to achieve waveguiding. The damage threshold for fused silica for 1 ns pulses is around 1 kJ cm^{-2}. However, practical fibres fail to approach the bulk damage threshold.

In very high average power fibre delivery systems, typical of those encountered in industrial material processing applications, power-induced fibre damage is caused by thermal processes: light escaping from the fibre core propagates in the cladding and is absorbed at the cladding-buffer interface where it is absorbed, leading to an excessive rise in temperature and consequent damage.

However, in pulse power delivery applications, such as the present requirement for delivery of 10 mJ pulses at a repetition rate of <100 Hz, the average power is much too low for thermal damage mechanisms to be relevant. Instead, the power is limited by the onset of various non-linear effects: semi-permanent photorefractive effects; non-linear scattering; and self-focusing.

Photorefractive effects are already familiar from experience with single-mode optical fibres used for CW beam delivery in single-point laser anemometers. In the early development of fibre delivery systems for

argon ion lasers with powers of a few watts, a gradual deterioration in the fibre transmission was noted. It is now well understood that the loss of performance resulted from semi-permanent photorefractive changes arising from the interaction of the laser power with the germania dopant typically used to raise the refractive index of the core of the fibre. Such effects are a strong function of wavelength, typically observable at power densities of 5 MW cm^{-2}. Once the origin of the problem had been recognised, it was possible to develop single-mode fibres specifically for high-average power transmission of short-wavelength visible light, in which the core germania dopant was avoided. Conversely, the ability to use a laser to modify the refractive index of a fibre core has been exploited to produce refractive index gratings, leading to a new range of optical fibre components with wavelength-selective properties, the so-called in-fibre Bragg gratings.

It is thus straightforward to specify pure silica core fibres for power delivery, avoiding problems of photorefractivity, but still subject to the effects of stimulated scattering and self-focusing. Two stimulated scattering phenomena are possible: stimulated Raman scattering and stimulated Brillouin scattering. Typically, the Brillouin threshold is lower, reducing with smaller laser linewidths or longer fibres, and observable in single-mode fibres with power levels as small as milliwatts, but serious only at power levels of watts.

However, in our experiments we determined that self-focusing was the phenomenon most seriously affecting our ability to deliver high pulse energies. Self-focusing is a non-linear optical phenomenon: a change in refractive index roughly proportional to the power density is induced by the laser beam. Hence, in a medium where a beam propagates in which the power density is greatest at the centre of the beam, a refractive index profile distribution is generated with a maximum on axis, analogous to a lens, thus causing the beam to focus. Self-focusing becomes significant in fibres with core diameters of 200 μm (suitable for PIV delivery) at power levels as low as 100 kW.

The power handling capacity limit set by self-focusing in optical fibres may be understood as follows. When power is coupled into an optical fibre, then with symmetrical alignment of the input beam to the optical axis of the fibre, the power density is a maximum on the axis of the fibre. As we shall describe below, we typically coupled power into fibres where the input beam was conditioned to have only a weak divergence. Power is thus coupled preferentially into *meridional modes* of the fibre (Su et al, 1992), sharpening the axial intensity maximum. At the input face of the fibre, care was taken to distribute the beam over the full core area. However, the effect of the central intensity maximum is to induce self-focusing, so causing the guided beam to concentrate on the fibre axis, generating higher power densities than were present at the input face.

Evidence for the self-focusing hypothesis was provided by inspection of the fibres which had failed after exposure to laser pulses of excessive energy. The centre of the damage was at a distance up to 40 mm into the fibre, with disruption of the core-cladding interface. The exact damage mechanism remains to be established, but one possibility is as follows: the short laser pulses focused within the fibre generate ultrasound pulses that travel outwards from the core of the fibre, encountering a discontinuity at the core-cladding interface, where energy is dissipated leading to mechanical damage. An effect of self-focusing would thus be for fibres to fail within their bulk rather than at the input surface, giving the impression of a lower bulk damage threshold than surface damage threshold, in distinction to normal experience with conventional optical components.

At greater distances into the fibre, the effect of inter-modal dispersion (Adams, 1981) is sufficient to induce differences of optical path between the guided modes of much greater than a wavelength, thus preventing the guided wavefront from being focused to a small region.

We suspect that self-focusing-induce damage may be exacerbated by the presence of micro-cracks in the input face of the fibre created by the preparation process—either polishing or cleaving. There is evidence that the damage threshold can be increased by annealing the fibre input face to remove micro-cracks, using a CO_2 laser as a local heating technique.

2.2 Damage threshold measurements

We conducted a set of experimental measurements to establish practical damage thresholds for fibres to be used in our PIV delivery system. The fibres chosen covered a range of core diameters, from 100 μm to 1 mm. They were fabricated with a pure fused silica core, to avoid photorefractive effects, and a doped cladding; thus they had a step refractive index distribution.

We chose step-index, rather than graded index fibres, for the following reasons. Graded index fibres show much less inter-modal dispersion than step-index fibres, so that speckle effects may be expected to be more severe (see section 2.3), and there is a

possibility of repeated self-focusing along the fibre. In any case, in a graded index fibre a greater proportion of the beam is guided close to the axis (Boechat et al, 1993), exacerbating self-focusing. Conversely, graded index fibres produce higher quality beams, and so may be useful for future lower pulse energy applications.

A disadvantage of the inter-modal dispersion is a temporal spreading in the output pulse. However, the effect is not serious in the present case. An upper limit for the pulse spreading may be estimated from

$$\Delta\tau < (n_1 - n_2)L/c$$

where n_1 and n_2 are the core and cladding refractive indices of the fibre of length L, and c is the speed of light. The numerical aperture of a fibre is given by $NA = (n_1^2 - n_2^2)^{1/2}$, where a typical practical value would be 0.3. Thus for a typical delivery fibre length of 10 m, the pulse-spreading is only 1 ns. In practice, the pulse spreading is much reduced, given that much of the optical power is guided in modes close to the optical axis, for which the intermodal dispersion is small.

In order to maximise the damage threshold of the fibres, the laser beam was conditioned to distribute power over the full core area of the fibre. It is common in the design of beam launching systems to condition the laser to produce a beam waist on the input face of the fibre, matching the core diameter and acceptance angle of the fibre. In the present experiments, the core diameters were so high that a lens of excessive focal length would have been required to produce a beam waist on the entrance face matching the fibre core size. Instead, a lens of focal length 400 mm was used. The fibre was then positioned downstream of the lens where the beam had diverged to fill the entrance face. This technique has the advantage of slightly reducing the effects of self-focusing. Placing the fibre upstream of the focus in the converging beam is disastrous, since it allows *linear* focusing to take place. Results of the damage threshold measurements, as pulse energy versus core diameter, are shown in table 1. The observed damage morphology was the same in each case, shown by disruption of the core-cladding interface at a distance of a few cm into the fibre (see section 2.2). The maximum delivered pulse energy increased with core diameter, but not proportionately with core area; hence the larger fibres failed at smaller energy densities.

Table 1: Fibre energy damage thresholds measured using a Spectra Physics GCR12 Nd:YAG laser, delivering 6 ns Q-switched pulses at a wavelength of 532 nm and repetition rate of 10 Hz.

Fibre core diameter, μm	Energy damage threshold, mJ
200	1.5
400	7
600	9
1 000	14

2.3 Speckle noise

The number of modes guided by the fibre is given approximately by

$$M = \frac{1}{2} NA \left(\frac{\pi d}{\lambda} \right)^2$$

for large numbers of modes (Adams, 1981). In the present experiments, the range of propagation angles in the input beam is much less than the acceptance angle of the fibre. Consider the case of a fibre with a 200 μm core diameter, filled with a beam whose numerical aperture is about 10 mrad. Hence, the equation indicates that approximately 2 500 modes propagate. At the output of the fibre, these modes couple into free space. Hence, viewed in the far-field of the fibre output, the various modes interfere to produce speckle.

The effect of speckle is to produce an inhomogeneous light sheet. Essentially, we require that even in the 'dark' areas of the sheet, the energy density is sufficient to produce an acceptably exposed PIV image (Adrian and Yao, 1985). The degree of intensity modulation in the fibre far field can be described by its visibility, defined as

$$V = \frac{I_{max} - I_{min}}{I_{max} + I_{min}}$$

where I_{max} and I_{min} are the maximum and minimum intensities in the sheet. We adopted the following measures to reduce the speckle visibility, and hence the homogeneity of the light sheet. The ability of two modes to interfere to produce speckle depends on their mutual temporal coherence. However, the two modes have a relative path difference caused by intermodal dispersion. For values of intermodal dispersion large in comparison with the coherence length of the source, the visibility

of interference is low. Furthermore, high-order modes (those propagating with large angles to the axis) exhibit more intermodal dispersion than low-order modes. Thus we reduced the speckle visibility by using a long fibre and deliberately enhancing coupling to the higher-order modes. Mode coupling can be either intrinsic (caused mainly by scattering at the core-cladding interface) or extrinsic (induced by bending) (Su et al, 1994). By using a fibre length of >5 m we were able to reduce the speckle visibility to the acceptable level of 15 %, measured using a beam profiler based on a charge injection device camera and a digital frame grabber. Further reductions would have been possible by exploiting extrinsic mode coupling, although this would have also increased the divergence of the output beam, leading to a reduction in beam quality.

3. LIGHT SHEET PROPERTIES AND DELIVERY BY FIBRE BUNDLES

For the relatively large fibre core diameters used in these studies, geometrical optics offers a reasonable approximation for the purposes of optical design. A convenient measure of the quality of the beam emerging from the output of the fibre is the product of the near-field diameter and the far-field divergence. The near-field diameter is roughly equal to the fibre core diameter. The maximum possible far-field divergence is set by the numerical aperture of the fibre. However, in the present experiments, the input beam has a divergence much less than the acceptance angle of the fibre; thus, the fibre is *underfilled*, and the output beam divergence is much less than the numerical aperture of the fibre.

Consider the design of delivery system using a single fibre for pulse energies of >10 mJ. The practical results of the previous section indicate that a minimum core diameter, d_1, of about 1 000 μm would be required, thus setting the near-field profile diameter. The far-field divergence, even assuming a perfectly collimated input beam, is set by intrinsic mode coupling in the fibre, and the requirement to reduce speckle noise to an acceptable limit, feasible in our experiments with a divergence, θ, of 100 mrad, leading to a beam quality of 100 mm-mrad.

Our initial estimates based on requirements for energy density in the delivered light sheet indicated a requirement for a sheet of thickness approximately 1.5 mm, maintained over the dimension of the measurement region l of approximately 100 mm. The light sheet is produced by conditioning the output of the fibre first with a spherical lens and then a cylindrical one, to produce a magnification, m_1, of 1.2 in the plane of the sheet. Thus the thickness of the sheet at its centre is $t_o = m_1 d_1$, 1.2 mm with a divergence of $\theta_1 = \theta / m_1$, 82 mrad, so that the thickness has increased to

$$t_e = t_o + m_1 \theta l / 2$$

or 7.2 mm at the edges of the measurement volume. The single fibre is thus unable to give an acceptable compromise between delivered energy and beam quality.

Now consider the use of a bundle of optical fibres to deliver the beam. The bundle is formed into a cylindrical cross-section at its input and as a linear array at its output, figures 1 and 2. The input laser beam is conditioned to form a spot covering the entire input face of the bundle, so that the pulse energy E is shared between the N fibres forming the bundle, with each fibre carrying an energy E/N. Hence, adopting the simple approximate relationship that the damage energy scales with the area, then the required core diameter for each of the fibres is

$$d_N = d_1 / \sqrt{N}$$

where d_1^2 is the core diameter of a single fibre capable of withstanding a pulse energy of E. Consider now that the output from the linear array of fibres is conditioned as before, using a spherical and cylindrical lens. The thickness of the sheet at its centre is thus

$$t_o = m_N d_N$$

Thus the required magnification is

$$m_N = m_1 / \sqrt{N}$$

and the corresponding divergence in the plane is accordingly reduced, such that its thickness at the edges is now

$$t_e = t_o + m_1 \theta l / 2\sqrt{N}$$

For the case of a bundle comprising 19 fibres of core diameter 200 μm, we see that we can now achieve pulse energies of >20 mJ in a sheet with centre thickness 1.2 mm and edge thickness 2.5 mm over a

measurement volume of depth 100 mm, thus satisfying the requirements of our application.

A disadvantage of using bundles for beam delivery is the corresponding reduction in launching efficiency. The input faces are not perfectly packed, and light is lost both into the interstices and into the cladding of the fibre (hence indicating the advantage of specifying fibres with as thin a cladding as possible). It is also desirable to couple as nearly equal powers as possible into the various fibres of the bundle. This was achieved in practice by conditioning the input laser beam to form a spot somewhat larger than the area of the input face of the bundle, thus excluding the lower intensity wings of the beam, and exploiting only the central part of the beam where the intensity was roughly uniform; the price paid for the improvement in uniformity is a further loss of launch efficiency.

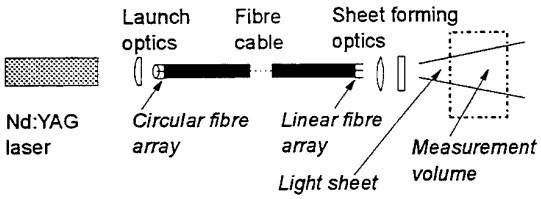

Figure 1: General arrangement for the fibre beam delivery system

We constructed a practical delivery system in the form of a bundle of 19 fibres. The number was chosen to be sufficient to satisfy our requirements for beam quality, whilst also giving efficient packing at the input face, in the form of a single central fibre, surrounded by an inner layer of six fibres and an outer layer of twelve fibres. Each fibre had a 200 μm diameter core and an outside cladding diameter of 220 μm. The core and cladding were pure and doped fused silica respectively. The fibres were each approximately 5 m long, sufficient both to suppress speckle by the combined effects of intrinsic mode coupling and intermodal dispersion, and to satisfy the requirement to keep the laser at an appropriate distance from the test rig. The fibres were formed into an array of circular cross-section at the input, and a linear array at the output.

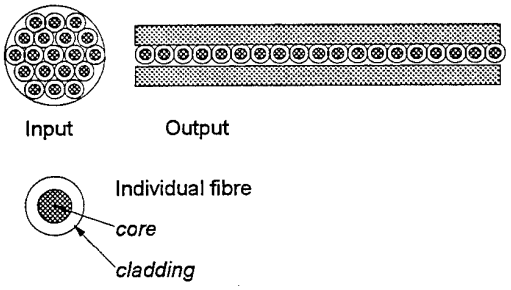

Figure 2: Arrangements of the input and output arrays for the fibre bundle

Light from the Q-switched and frequency doubled Nd:YAG laser was launched into the input end of the fibre bundle using a lens of focal length 400 mm. The lens was arranged to produce a laser spot on the entrance face of the fibre with a diameter of 1.4 mm, in comparison with a diameter of 1.1 mm for the bundle itself. The system gave launch efficiencies of up to 35 %, with pulse energies as high as 25 mJ, with reliable operation.

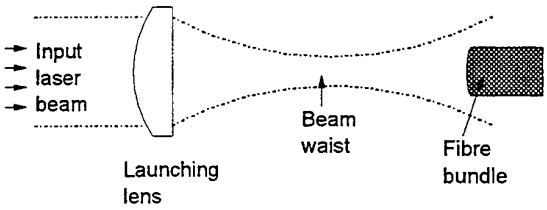

Figure 3: Arrangement for the launch optics

The light at the output end of the fibres had a numerical aperture (NA) of 104 mrad, much greater than the input NA of the laser beam (12.5 mrad) because of mode coupling in the fibre, but still less than the maximum NA of the fibre (440 mrad).

Optical arrangements for light-sheet formation are discussed, for example, by Prenel et al (1987). In our case, the light sheet was formed by conditioning the output from the linear array of fibres using a spherical lens with a focal length of 16 mm and a cylindrical lens of focal length 11 mm. The lenses were adjusted to form a light sheet with a thickness of 1.2 mm at its centre, and a maximum thickness of 2.5 mm over the entire 100 mm depth of the measurement region.

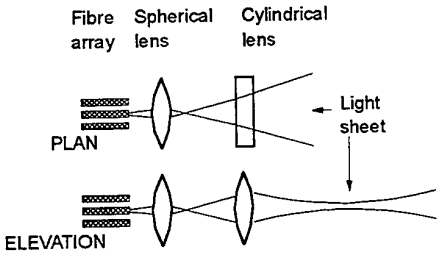

Figure 4: Optical arrangement for light sheet formation (three fibres only shown for clarity).

4. COMBUSTION TEST-RIG AND EXPERIMENTAL MEASUREMENTS

The tests were carried out on a Rolls-Royce Phase -V aircraft combustion rig, fuelled by a mixture of kerosene and pre-heated air, run in the ground-idle condition with an air-to-fuel ratio of just over 80. Temperatures in the combustor were of the order of 2 000 K, and the maximum velocities were of the order of 60 ms^{-1}.

The rig had quartz side windows which allowed access for the PIV photographs, but the fibre probe itself had to be inserted through an ignitor port which was only just over 12 mm in diameter. The combustion process generated soot and there were also unburned kerosene droplets in the chamber, so it was essential that the quartz windows and the output lens of the fibre probe were purged with air in order to keep them clean.

The fibre-optic arrangement was held in a chuck and inserted into a barrel which was threaded so that it could be screwed into the ignitor port. The light emerging from the fibre bundle passed through a spherical lens, and then a cylindrical lens, fixed into the barrel, the whole configuration sitting just proud of the inner skin of the combustor. Compressed air was forced through the system in order to cool it.

Seeding of the flow was achieved by introducing aluminium oxide powder into the pre-heated air stream before it entered the combustion chamber, using a device which produced a high intensity particle jet. The powder had a mean size of 3 μm.

The laser pulses were generated by a frequency doubled Q-switched Nd:YAG laser operating at 532 nm. For these tests, the energy per pulse was set at 9 mJ, corresponding to an illumination intensity of about 75 Jm^{-2} at the centre of the burner.

5. IMAGE CAPTURE AND RESULTS

The PIV images were captured on TMAX black-and-white film with an ASA rating of 400 using a Nikon 35 mm camera and 55 mm MicroNikkor lens. In order to discriminate between flame luminosity and laser light scattered from the seeding particles, the camera was synchronised with the laser pulses, using a shutter speed of 1/250 s. To further improve the discrimination, a bandpass interference filter with a centre wavelength of 532 nm and a bandwidth of 1 nm was attached to the front of the camera lens. The separation between laser pulses was typically 10 μs. It was found that an aperture of about *f*/8 gave the appropriate balance between depth-of-field, light enlargement and diffraction enlargement of particle images.

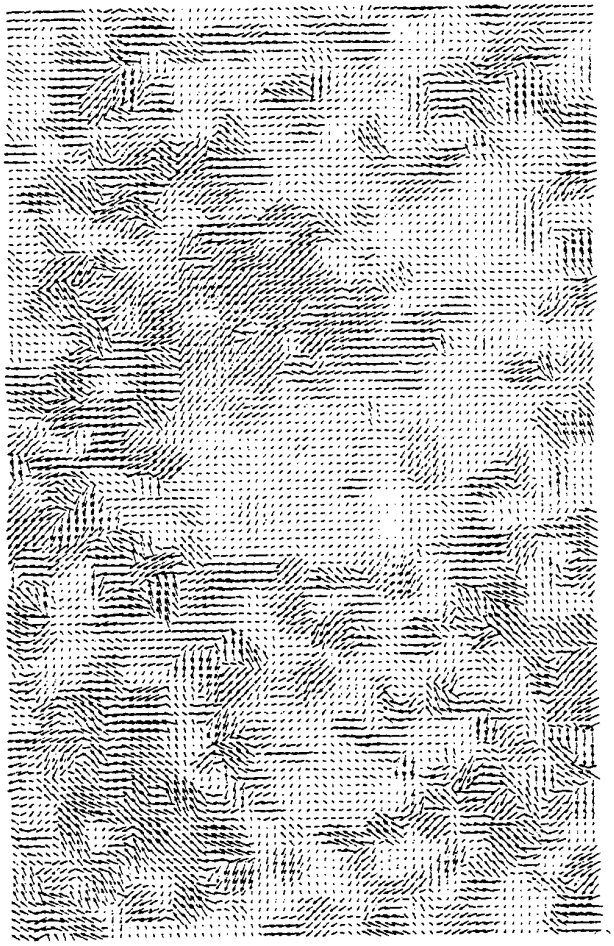

Figure 5: Typical velocity vector map, measured in the Rolls-Royce Phase-V aircraft combustion rig, using fibre optic illumination. The piv image was analysed by correlation using a 64x64 pixel resolution.

Once captured, the negatives were digitised and then analysed using direct digital FFT routines. A typical result is shown in figure 5. From these images it is possible to obtain useful information on the flow velocities within the combustor, and also on the fuel spray distribution adjacent to the injector nozzle.

6. DISCUSSION AND CONCLUSIONS

We have demonstrated successfully a fibre optic beam delivery system for > 25 mJ pulse energies from a Q-switched laser for use in practical PIV measurements. A key feature in making the system possible was the adoption of fibre bundles rather than individual fibres in order to deliver the beam.

Whilst successful, and useful in providing a flexible and robust means for beam delivery in situations with relatively poor optical access, the fibre system is inefficient in comparison with bulk-optic beam delivery, both in terms of loss of optical power and in deterioration of beam quality.

An obvious way of improving beam quality is to increase the number of fibres, so that each one could have a smaller core diameter. Diameters of 200 μm were adequate for our needs, but smaller ones are commercially available, with cladding outside diameters 10 % larger than the core diameter, down to at least 50 μm. Smaller diameters are feasible, but claddings thinner than a few μm lead to lossy fibres, as well as being difficult to handle. Thicker claddings increase the launching loss.

A significant power loss in our experiments arose from using only the inner part of the input beam in the interests of uniformity of intensity in the light sheet. If we had used a larger number of fibres, we could have used all of the beam. Although the outer fibres would then have been carrying lower energies, if they were distributed uniformly in the output linear array then a uniform-intensity light sheet would still have been produced.

Perhaps the greatest performance gains will arise from the frustration of self-focusing. One approach is to condition the input beam to reduce its spatial coherence (effectively, deliberately reduce the beam quality) so that self-focusing in the fibre could not lead to very high local intensities. Another solution which also reduces the effect of self-focusing is to use fibre tapers at the input end of the array.

In the long term, an interesting approach to high pulse energy transmission may be offered by hollow wave guides, where air is the core medium. At present, the losses of such fibres are too high and available core diameters are too large to be of interest for PIV, despite their successful use with CO_2 lasers (Su et al, 1995), but they are of sufficient potential value to monitor future developments.

ACKNOWLEDGEMENTS

This research was partially supported by the Engineering and Physical Sciences Research Council, UK.

REFERENCES

M J Adams 'An Introduction to Optical Fibre Waveguides' (Wiley, 1981)

R J Adrian and C-S Yao, Appl Opt 24 (1985) 44

D J Anderson, R D Morgan, D R McCluskey, J D C Jones, W J Easson and C A Greated, J Meas Sci Technol 6 (1995) 809

A.A.P. Boechat, D. Su and J.D.C. Jones, Appl Opt 32 (1993) 291 - 297

D A Jackson, J D C Jones and R K Y Chan, J Phys E Sci Instrum 17 (1984) 977

D J Koga, S D Abrahamson and J K Eaton, Experiments in Fluids 5 (1987) 215

J Kompenhans and M Raffel, Proc SPIE 2005 (1993) 425

J P Prenel, R Porcar and A El Rhassouli, Experiments in Fluids 5 (1987) 215

D. Su, A.A.P. Boechat and J.D.C. Jones, Appl Opt 31 (1992) 5816 - 5821

Daoning Su, Alvaro A P Boechat and Julian D C Jones, Opt and Laser Eng 20 (1994) 193

D Su, S Somkuarnpanit, D R Hall and J D C Jones, Opt Comm 114 (1995) 255 -261

MEASUREMENT OF VORTICAL FLOWS IN A LOW SPEED WIND TUNNEL USING PARTICLE IMAGE VELOCIMETRY

J.N.Stewart, Q.Wang, R.P.Moseley, P.W.Bearman and J.K.Harvey

Department of Aeronautics
Imperial College of Science, Technology and Medicine
London, UK

1 ABSTRACT

This paper describes the application of particle image velocimetry to the measurement of air flows in a 3m × 1.5m low speed wind tunnel. In particular the technique has been applied to the study of flows where the predominant velocity component is perpendicular to the plane of measurement. Results from studies of road vehicle wakes and swept wing aircraft flows are presented and discussed.

2 INTRODUCTION

The development of PIV (Adrian(1991)) over the last few years has enabled non-intrusive, virtually instantaneous measurements to be made over a large area of a complex flow field. These characteristics of the technique make PIV an ideal method for producing quantitative data on unsteady flow phenomena.

The PIV technique operates by measuring the displacement of small tracer particles as they translate with the flow field. A multiple pulse laser beam is formed into a light sheet and illuminates the particles at different instants in their motion. These images are recorded on photographic film and after development the film is automatically interrogated to yield velocity vectors. A conventional PIV arrangement utilises a single camera with its axis perpendicular to the plane of measurement. This type of system permits measurement of the components of velocity in the plane of the light sheet.

In cases where there is a significant velocity component perpendicular to the measurement plane, parallax distortions are present on the measured velocity components due to the out-of-plane velocity. This effect can be corrected for quite simply if the out-of-plane velocity is known. In some flows it may be adequate to assume that this is constant but for many complex flows where the out-of-plane velocity varies substantially, a double camera system is necessary for satisfactory correction.

The purpose of this experimental investigation is to advance the understanding of vortex behaviour in wakes and to compare instantaneous flow maps obtained using PIV with results achieved using time-averaged techniques. Two experimental cases will be discussed showing application of PIV to cross flow measurements in wakes.

The first of these cases is the wake of a typical passenger car model. A car is considered as a bluff body due to the large regions of separated flow generated. The drag experienced by a vehicle is directly related to the structure of the flow in its wake. Thus, it is essential to have detailed quantitative measurements in this part of the flow to enhance understanding of the drag creation mechanisms. Due to the lack of practical methods for instantaneous measurement of complex and unsteady flows most of the quantitative vehicle aerodynamics measurements made to date have used time-averaged techniques (Ahmed (1981), Bearman *et al* (1983), Cogotti(1987)).

The second case considered is the flow immediately downstream of a swept wing aircraft model. This experiment was carried out to test the ability of a stereo camera arrangement to remove parallax errors from the PIV vector field of a typical vortical flow.

3 PIV MEASUREMENT OF ROAD VEHICLE WAKES

3.1 PIV System Details

PIV measurements were made in cross flows in road vehicle wakes using the experimental arrangement shown in Figure 1.

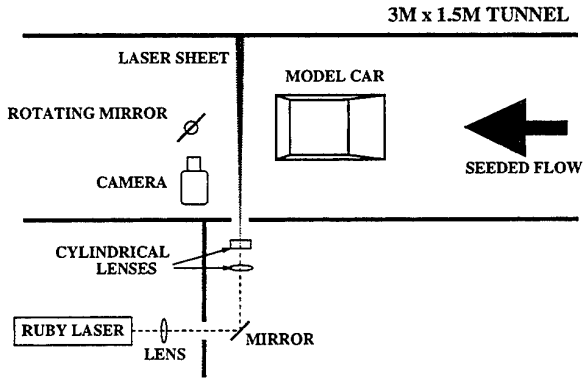

Fig. 1 Experimental Arrangement

The illumination required was provided by a Lumonics HLS4 ruby laser. This is capable of producing two red light pulses, each containing 5 Joules of energy. The pulse duration was 25ns and the pulse separation could be adjusted as required within a range of $1 - 400\mu$s.

The seeding material used was oil-based smoke produced by a Concept smoke generator. The smoke was introduced upstream of the model by a narrow pipe surrounded by an aerofoil housing. This arrangement was placed in the wind tunnel contraction, in order to minimise the disturbance to the flow. The average particle size, from an independent measurement, was 1μm.

Photographic film (Kodak Technical Pan) was used as the recording material because of its high resolution. A Bronica medium format camera fitted with a 110mm diffraction limited lens was used to photograph the flow field.

Image shifting was required to remove directional ambiguity on the two pulse PIV photographs. This was applied using a rotating mirror arrangement. The image shifting, laser firing and camera shutter operation were all controlled by a PC. Experiments were carried out in complete darkness with the camera shutter held open for 1 second while the laser firing was triggered by the rotating mirror.

Velocities in the plane of the light sheet were obtained by analysing PIV photographs using the autocorrelation technique. Small areas of the photographic negative were sequentially digitised and 128×128 pixel areas analysed using two-dimensional Fast Fourier Transform routines. These computational routines were carried out on a DSP32C digital signal processing card to enhance the speed of the operation. Sub-pixel resolution was obtained in determining particle separation by applying the Whitaker signal reconstruction technique (Lourenco and Krothapalli(1995)) to the autocorrelated data. During the post-processing stage a correction for the error caused by the rotation of the image shifting mirror was also applied to the data (Oschwald *et al* (1995)).

Parallax removal, in this case, was obtained by assuming that the out-of-plane velocity was constant and equal to the freestream velocity. A simple geometrical correction can be applied to correct the data under these assumptions (Grant *et al* (1994)). The assumption of constant axial velocity is incorrect for the central region of the vehicle wake but here the parallax error is small and hence the use of an inappropriate value leads to minimal error.

3.2 Experimental Results

The car model used for these experiments was a 1/8th scale Honda Accord. The testing was carried out at a Reynolds number of 1.4×10^5 based on the width of the model (freestream velocity of 10ms^{-1}). The measurements shown in this paper were taken from a cross-plane of the car wake with the laser sheet plane 0.23 car lengths downstream of the rear of the model.

The presence of an out-of-plane velocity component results in particles moving out of the measurement area between laser pulses which causes single, unpaired particle images to be recorded. These single images reduce the accuracy of the technique and their occurrence must therefore be minimised. For this case the laser sheet was approximately 4mm thick and the time separation between pulses was 60μs. This meant that a particle moving with the freestream velocity would travel 0.6mm between laser pulses. A large proportion (approximately 85%) of particles within the sheet should therefore be paired.

Figures 2 and 3 show examples of PIV results which demonstrate instantaneous velocity distributions captured under identical conditions at different times. The plots show the measurement plane, viewed from downstream with a projection of the rear of the model drawn to indicate the relative positions of the flow features. In these plots a number of features of the instantaneous flow can be seen. The flow is dominated by swirling features which tend to have a clockwise rotational sense on the left hand side and an anti-clockwise sense on the right. It is also noted that the instantaneous cross-plane structure differs significantly from that achieved by measuring mean velocities in the same flow using a split-film probe (a point measurement technique)

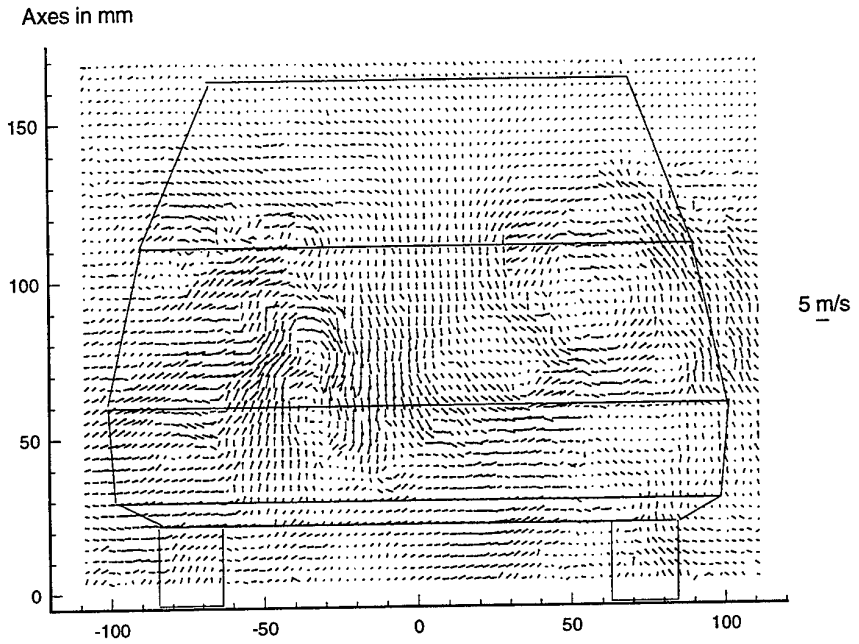

Fig. 2 Instantaneous flow behind car

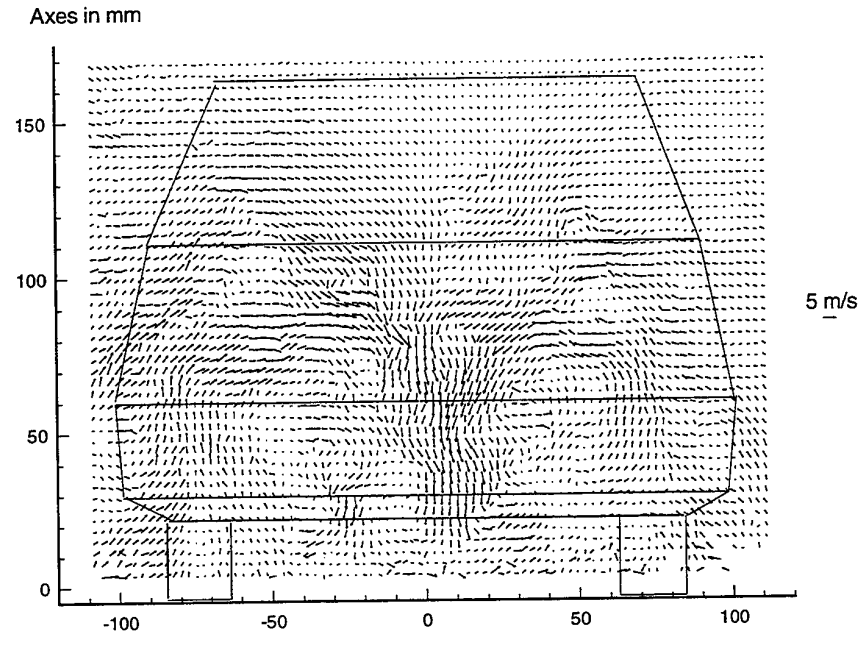

Fig. 3 Instantaneous flow behind car

and traversing the probe across the flow field to construct an array of vectors (Goh (1995)). This data is shown in Figure 4. Although this split-film probe plot shows only one half of the car wake, further results from the same reference show the wake to be symmetric. This time averaged data shows that the flow is dominated by a pair of strong symmetric vortices of opposite rotation. From instantaneous PIV data, it can be seen that the cross plane flow field consists of an asymmetric wake structure with a number of randomly placed vortices rather than a pair of vortices. In the central region of the car wake there is an area of strong downwards flow. The values of this downward component are approximately 55% of the freestream velocity.

The average of 10 instantaneous PIV pictures (including Figures 2 and 3) is shown in Figure 5. In the mean flow only two contra-rotating vortices appear with the expected rotational senses. In the instantaneous flow, although each side consists of a cluster of randomly positioned vortices, the overall direction of rotation of each side of the wake is the same as seen in the main flow surveys. After averaging, the small strong vortices disappear, and the flow is dominated by two larger but asymmetric vortices. In general the mean flow behind a bluff body should be symmetric. The asymmetry is expected to be due to the small number of PIV plots being used in the averaging process.

4 PIV APPLIED TO SWEPT WING AIRCRAFT FLOWS

4.1 Dual Camera PIV System

A dual camera system was constructed and implemented in the wind tunnel. A second identical Bronica camera was incorporated with a known vertical separation from the first. The camera film planes lay on the same plane. Mounting vertically had the advantage of allowing the same rotating mirror to be utilised by both cameras. The stereoscopic equations derived in Gauthier and Riethmuller (1988) were used to analyse the images.

Combining the upper and lower camera data enabled the component of velocity perpendicular to the plane of the laser light sheet to be resolved at each interrogation spot of the PIV photographs. Knowledge of this value allows the crossflow plane velocities to be accurately corrected for parallax errors. The out-of-plane velocity component is also calculated but with somewhat less accuracy than the in-plane components. The larger error in the out-of-plane component is caused by the use of the stereo combination to calculate an absolute velocity value rather than a correction as in the in-pane case.

Stereo photographs must have a common reference point to allow corresponding flow regions to be matched. In this case a thin wire crossed the measurement plane near the edge of the area photographed. This appeared as a dark spot on both negatives and was used as a reference point when initiating the interrogation process. As in Prasad and Adrian (1993), this work correlates the displacement of all particles within an interrogation spot rather than tracking particles individually.

4.2 Application to Swept Wing Aircraft Flows

The dual camera technique was applied to the measurement of velocities generated by the flow over the swept wing of a half aircraft model. The model was mounted with its baseplate 7cm above the tunnel floor and therefore out with the tunnel boundary layer. The experimental arrangement is shown in Figure 6. The results presented in this paper are for a sweep angle of 70° and an incidence of 8° and the laser sheet plane was 3cm (0.28 tip chord lengths) downstream of the wing tip trailing edge. The results presented were obtained with a free stream velocity of $15ms^{-1}$. The laser sheet used was 2mm thick and the time separation between laser pulses was $35\mu s$. Therefore 75% of particles moving with the freestream velocity should remain within the sheet. Although not shown in Figure 6, rotating mirror image shifting was used as in the car tests. The image shifting velocity applied to remove directional ambiguity was $20ms^{-1}$. When combining data from two separate cameras any errors present in the individual camera plots are magnified. Therefore it is crucial that any sources of error should be minimised. If the contribution of the actual in-plane velocity is very small in comparison to the superimposed image shifting velocity then the percentage error in the measured velocity may be high. The image shifting velocity must be kept as low as possible in order to maximise the contribution to the particle separation made by the in-plane particle motion, while ensuring that no directional ambiguity can possibly be present.

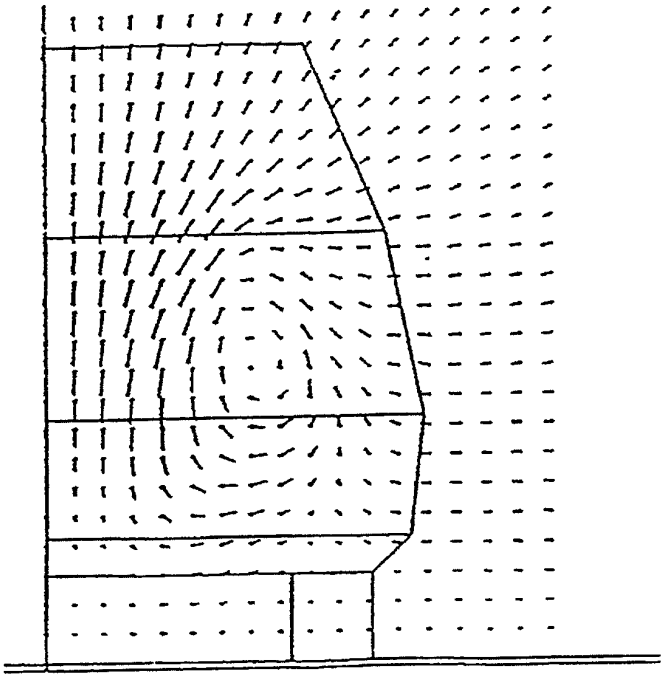

Fig. 4 Car time averaged flow
(taken from Goh(1995))

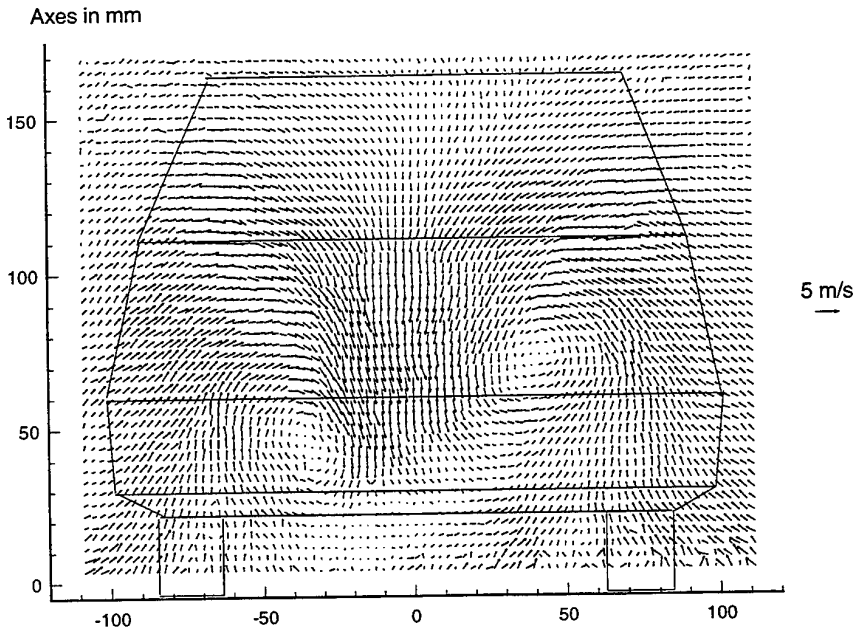

Fig. 5 PIV average flow behind car

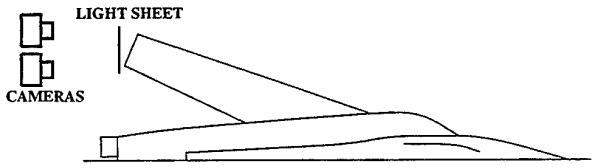

Fig. 6 Schematic of orientation for swept wing

Figure 7 shows a typical PIV vector plot from the upper camera. The vector plots represent the flow field in the plane to the rear of the wing, viewed from a downstream position with a projection of the wing tip drawn on the plot. The leading edge of the wing is situated at $(0, 0)$. The effects of parallax are shown on this plot. On the right of the plot parallax creates an apparent velocity to the right. This is more obvious to the upper right of the plot where parallax reinforces the actual in-plane velocity component. To the lower right actual and apparent velocities cancel to give very small measured velocities. Similar parallax effects occur on both the upper and lower extremes of the plot. In these cases the parallax causes an apparent vertical velocity component which enhances the actual vertical velocities near the top and reduces them near the bottom.

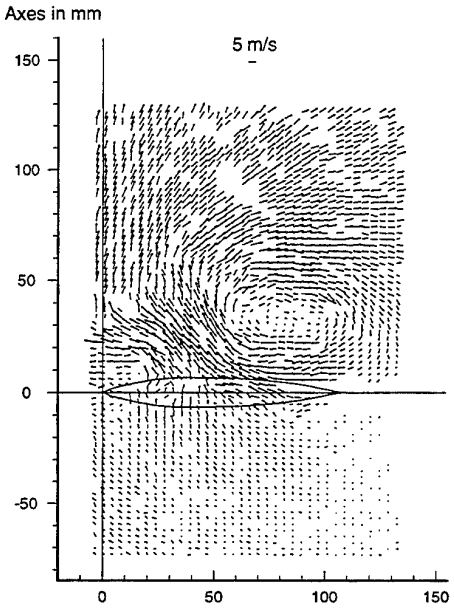

Fig. 7 Instantaneous flow with parallax present

The effect of combining the upper and lower camera data sets and the subsequent removal of the parallax error is shown in Figure 8. The effects of parallax towards the edges of the plot have been eliminated, allowing accurate measurements of the in-plane velocity components to be made. There are less velocity vectors present on the combined plot, in comparison to the upper camera plot. In order to produce parallax corrected data velocity vectors must be present at the corresponding co-ordinates in both upper and lower camera vector fields. A missing vector on either data set will result in a gap in the combined data.

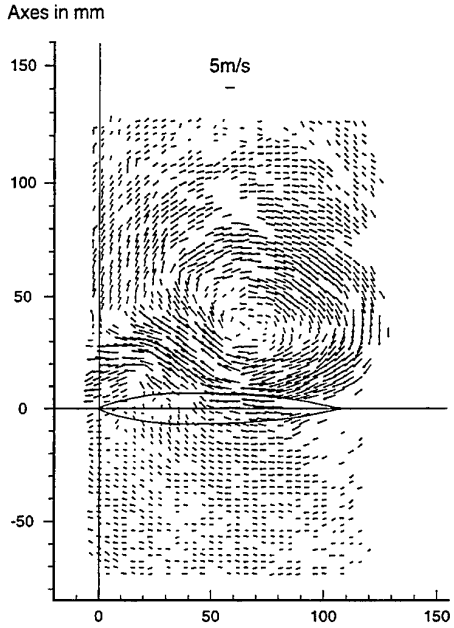

Fig. 8 Instantaneous flow with parallax removed

The results clearly show two vortex structures. The main vortex is situated (at about (65,35)) between the centre and trailing edge of the the wing and a secondary vortex towards the leading edge. The secondary vortex (at (15,15)) is caused by separation from the wing surface induced by the pressure field of the main vortex. These main vortical structures are separated by an area of strong flow containing cross flow velocities of up to 11ms^{-1}, 73% of the freestream velocity. Complicated small scale structures are also shown to be present in the flow. Comparison of the vector plots showed that in general the double vortex structure described was dominant but all demonstrated variation in vortex shape, structure and position. Figure 9 shows contours of constant vorticity generated from Figure 8. The velocity data was first interpolated to cover areas with gaps and then the vorticity equation was applied. On this figure contours of positive vorticity are white, with negative contours in grey. An intermediate range of

contours with values close to zero has been omitted to enable easy recognition of the highest vorticity values. The main areas of vorticity are obvious but the plot demonstrates that other vortical structures are present. All of the interesting flow structure occurs above the wing and so this area in particular was examined.

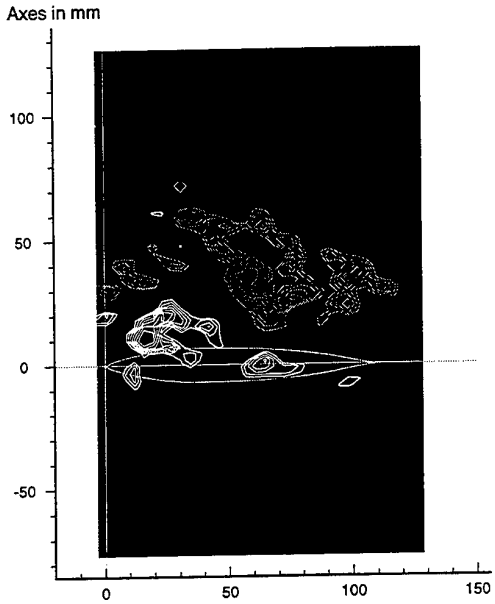

Fig. 9 Instantaneous vorticity

In order to obtain an estimate of the mean flow, 10 instantaneous flow maps were averaged. Although the number of sample instantaneous measurements is small the result of the averaging procedure (Figure 10) is to produce a vector diagram closely resembling those obtained using time mean measurement techniques, such as a pressure sensing probe. Vorticity data (Figure 11) shows that many of the smaller structures seen on individual maps disappear leaving only two dominant vortex structures and a weaker area of vorticity present near the trailing edge of the wing. These results suggest that the smaller structures are not due to systematic errors, but are actually present in the instantaneous flow. Therefore the vortical flows observed behind the swept wing are more complicated than time-averaged techniques would suggest.

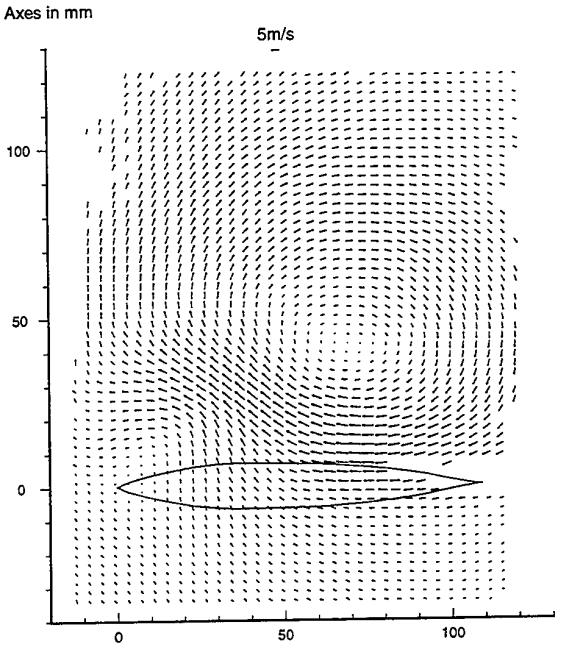

Fig. 10 Average of 10 data sets

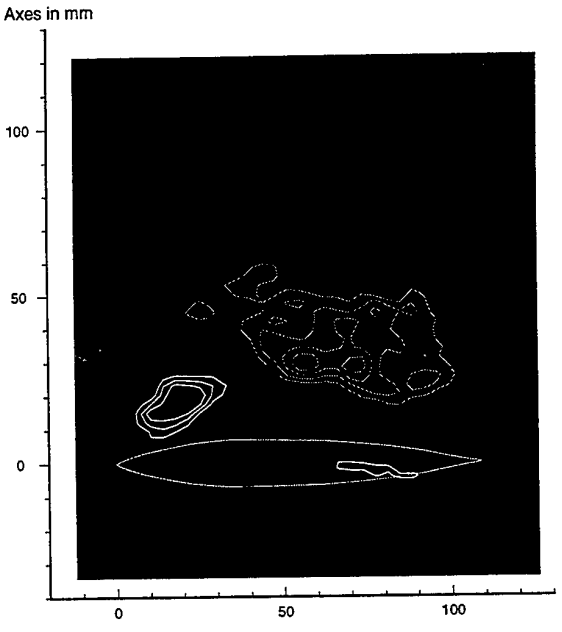

Fig. 11 Vorticity from averaged data set

5 CONCLUSIONS

From the passenger car model test several conclusions can be drawn. In this case parallax removal was carried out by assuming that the cross-plane velocity was equal to the freestream at all points in the field. The instantaneous flow in the cross-plane wake consists of mainly swirl type features which have a positive clockwise rotational sense on the left and the opposite sense on the right when viewed from behind the car. However, the instantaneous structure is significantly different from time-mean results. It consists of an asymmetric wake with several smaller and stronger vortices rather than only a pair of trailing vortices. In the middle of the car wake there is a strong downward flow where the instantaneous cross flow velocities are up to 55% of freestream velocity. The mean structure of the flow behind the car obtained by PIV is similar to that measured by split film probes. This gives confidence in the PIV results.

Tests on a swept wing aircraft model indicate that the stereoscopic translation method detailed in this paper has proved successful in achieving parallax removal from cross flow data sets. Parallax removal has been achieved for complex flow structures. Measurements of in-plane components using PIV revealed new details of the flow. PIV vector plots, which yield instantaneous data for a whole plane, show the presence of complex flow structures in addition to the vortex pattern expected. The two dominant vortices are separated by a region of relatively high cross flow velocity as in the road vehicle wake. In this case they can be as high as 73% of the freestream. The data also shows that the main vortices are composed of random patches of more intense vorticity which gyrate around the vortex centres.

Single and dual camera arrangements have been successfully applied to the measurement of complex unsteady air flows in a wind tunnel environment. Both test cases have revealed flow structures which were far more complex than expected. This type of flow information could not have been obtained using time-averaged techniques or single point probes. The development of instantaneous measurement techniques is therefore essential to further understanding of unsteady flow structures.

6 ACKNOWLEDGEMENTS

The passenger car measurements were funded by the Honda Research and Development Company and the swept wing measurements by British Aerospace Military Aircraft Division. The support of both is gratefully acknowledged.

7 REFERENCES

Adrian, R.J. 1991, Particle-Imaging Techniques for Experimental Fluid Mechanics, Rev. Fluid. Mech., vol. 23, pp. 261-304

Ahmed, S.J. 1981, Wake Structure of Typical Automobile Shapes, ASME J. Fluid Eng., vol. 103, pp. 162-169

Bearman, P.W., Davis, J.P. & Harvey, J.K. 1983, Measurement of the Structure of Road Vehicle Wakes, Int. J. Vehicle Design; Tech. Adv. in Vehicle Design Series, SP3; Impact of Aerodynamics on Vehicle Design, pp. 493-499

Cogotti, A. 1987, Flow Field Survey Behind Three Squareback Car Models Using a New Fourteen Hole Probe, SAE Paper 870243

Gauthier, V. & Riethmuller, M.L. 1988, Application of PIDV to Complex Flows: Measurement of the Third Component, VKI Lecture Series 1988-06

Goh, E.K. 1995, An Experimental Study into Time-dependent Characteristics of a Road Vehicle Wake Flow, Ph.D. thesis, Imperial College, University of London, U.K.

Grant, I., Pan, X., Wang, X. & Stewart, J.N. 1994, Correction for Viewing Angle Applied to PIV Data Obtained in Aerodynamic Blade Vortex Interaction Studies, Exp. Fluids, vol. 18, pp. 95-99

Lourenco, L. & Krothapalli, A. 1995, On the Accuracy of Velocity and Vorticity Measurements with PIV, Exp. Fluids, vol. 18, pp. 421-428

Oschwald, M., Bechle, S. & Welke, S. 1995, Systematic Errors in PIV by Realizing Velocity Offsets with the Rotating Mirror Method, Exp. Fluids, vol. 18, pp. 329-334

Prasad, A.K. & Adrian, R.J. 1993, Stereoscopic Particle Image Velocimetry Applied to Liquid Flows, Exp. Fluids, vol. 15, pp. 49-60

SESSION 19

Flows with Rotation

Combined Application of Particle Image Velocimetry (PIV) and Laser Doppler Anemometry (LDA) to Swirling Flows under Compression

J. Volkert, C. Tropea , R. Domann, W. Hübner

Lehrstuhl für Strömungsmechanik, University of Erlangen-Nürnberg, Cauerstr. 4
91058 Erlangen, Germany

Abstract

The velocity field of a strongly swirling flow has been examined using an LDA and PIV in combination. The PIV revealed an asymmetric component of the flow-field, in particular a movement of the swirl center away from the geometric center of the rotating cylinder. A statistical description of this asymmetric component has been developed, from which the *apparent* turbulence measured with an LDA has been estimated. These results are compared to the actual LDA measurements. The conclusion is that a large portion of the measured turbulence using a one-point technique (LDA) can be attributed to this effect and can also explain the previously observed discrepancy between experiment and numerical simulation.

1. Introduction

This paper investigates the use of PIV and LDA in a strongly swirling flow, however the methodology introduced to combine the results of the two measurement techniques for a better interpretation of the measured data has a much wider range of applications. It is the methodology which is considered to be the main contribution of this paper.

The problem will first be stated, using some of the experimental data for illustration. In the present case we are dealing with a swirling flow generated by a rotating cylinder, which after a period of constant rotational speed, is abruptly stopped and the resulting swirling flow is left to decay (spin-down). Optionally, the flow can also be subjected to compression during the spin-down phase, through movement of a piston. Figure 1 illustrates the velocity field in a radial plane at three time steps during the spin-down phase. Despite the exact axisymmetry of the cylinder, the center of flow rotation does not remain in the geometric center of the cylinder. A similar behaviour is noticed for the case of constant rotation of the cylinder.

A point velocity measurement (eg. LDA) will register not only turbulent fluctuations with time but also changes of the mean velocity (through movement of the swirl center) in the measured standard deviation. A two-dimensional numerical simulation (axisymmetric) will necessarily compute turbulence without this added component attributable to the precession of the rotation center. This problem is well known for measurements in internal combustion engines, usually referred to as the problem of cycle-to-cycle variations. Without defining too precisely what is meant by turbulence, efforts have been made to separate components of velocity fluctuations of low and high wavenumber, on the premise that the higher wave number fluctuations were turbulence, whereas the lower wave number fluctuations may not all be irreversibly lost energy. Previous approaches to this problem involved the use of filters in frequency domain [1,2], more elaborate decomposition schemes [3-5], scanning LDA measurements [6] and two-point velocity measurements [7].

Generally the problem arises because with LDA the velocity is only known at one point and any global flow movement cannot be deduced from such limited data. In this respect the PIV, being a whole-field technique, can be helpful. On the other hand, the PIV does not yet offer the required time and spatial resolution necessary for a statistical description of the turbulence field. Therefore a complementary combination of the two techniques is sought.

The approach used in the present experiment can be summarized briefly as follows. From PIV data similar to that illustrated in Fig. 1, statistics of the movement of the rotation center are derived by examining an ensemble of 50-100 repetitions of the one-shot experiment. These statistics are accumulated either for the constantly rotating cylinder or

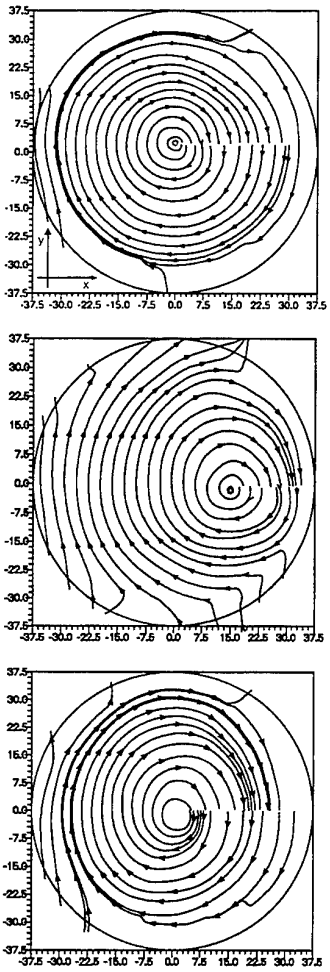

Figure 1: Streamline plots measured by PIV at different times during spin down showing the precession of the vortex core

for each time delay during the spin-down, and take the form of a joint probability density distribution in an x and y plane with its origin at the geometric center of the cylinder. Mean and RMS velocity profiles of the tangential velocity component on the same axial plane as the PIV measurements are then obtained with the LDA. The movement of the center of rotation, derived from the PIV data, is now used to postulate movement of the measured mean velocity profile (LDA), at least in a statistical sense. Knowing the spatial gradient of the mean velocity, the artifact (or apparent) turbulence appearing in the one-point LDA measurements, in addition to actual turbulent fluctuations, can be estimated. Of course the global movement of the flow will be a maximum in the center of the cylinder and reduce to zero at the cylinder wall. This must be taken into account by some spatial decay relation with respect to r of the joint probability function describing the center of rotation.

The remainder of the paper is organized as follows. The experimental apparatus is described in section 2 and the measuring equipment in section 3. The data processing of the PIV measurements is described in detail in section 4 and applied to the LDA measurements in section 5. Concluding remarks are given in section 6.

2. Experimental Apparatus

A Rapid-Compression-Machine (RCM) allows observation of the time-dependant behavior of an in-cylinder flow with a specified swirl strength under the influence of a one dimensional compression. Fig. 2 and Table 1 show the design and the dimensions of the RCM. With the current apparatus, the available range of operational parameters corresponds to those typically found in combustion engines, but also encompasses conditions in adherence with Rapid Distortion Theory.

The experimental operation consists primarily of two phases. The first phase is that related to the generation of swirl inside the cylinder. The cylinder consists of a rotating part (section $x_h + x_c$) and a non-rotating part (section x_s), see Fig. 2, where the rotating section is driven by an external motor. Both sections are separated by a small gap ($\Delta x = 1mm$).

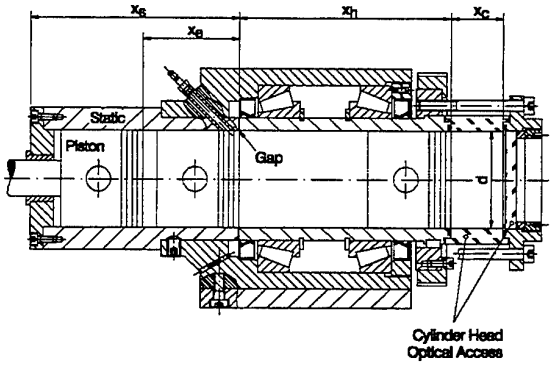

Figure 2 : Design of the Rapid Compression Machine

After stopping the cylinder rotation, a compression stroke is performed by a hydraulically driven piston. For optical access, the cylinder head (module section x_c) is made out of glass. Its length may easily be changed to enable experiments at different compression ratios $\epsilon_c = \frac{x_h + x_c}{x_c}$. Note that section x_e serves as acceleration length of the piston to its desired initial compression velocity when passing the gap.

	SIZE (MM)	DESCRIPTION
d	75.0	Cylinder diameter
x_e	74.0	Piston acceleration length
x_h	160.0	Stroke
x_c	40.0	Head clearance

Table 1 : Apparatus dimensions

Although the major goal of the overall project is to study the influence of compression upon the in-cylinder flow, experiments are also carried out without compression as a reference. The behaviour of the decaying swirl during the spin-down is discussed here, since its features, namely the precessing vortex core phenomenon, complicate the experimental evaluation of measurement data as mentioned in section 1 and described in the following.
The range of operating parameters for the swirl mode is characterized by the rotation rate of the cylinder. The motor used to drive the cylinder is capable of rotation rates up to 3000 rpm, with experiments being performed at 300 and 1200 rpm.

3. MEASUREMENT EQUIPMENT

3.1 Laser Doppler Anemometer

The two-component backscatter LDA system employed in the present study is shown schematically in Fig. 3.

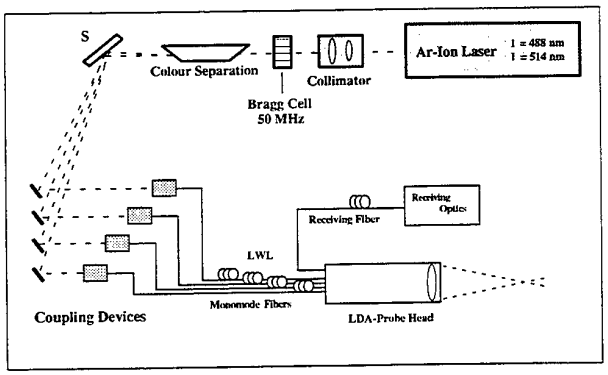

Figure 3: LDA Sending Optics

Transmitting Optics: The laser beam emitted by an Ar-Ion Laser is passed through the Bragg Cell, which operates at a nominal frequency of 50 MHz . The Bragg Cell acts as a beam splitter and frequency shifter. A colour separation prism follows. The power supply of the Bragg Cell driving unit is adjusted to yield nearly equal intensities for all beams. The four beams (one shifted and one unshifted beam of each color) are spatially separated by the use of mirrors before they are coupled into the monomode, polarization preserving fibers. The collimation before the Bragg Cell is used to condition the beam for the fiber launch.

2-COMPONENT-LDA PROBE		
LASER POWER/BEAM:	$P_{beam} \approx 40mW$ (GREEN)	
	$P_{beam} \approx 30mW$(BLUE)	
BEAM SEPARATION:	D = 22 mm	
NUMBER OF FRINGES :	N_f= 9.96	
FOCAL LENGTH f	120 mm	
	$\lambda = 488nm$	$\lambda = 514nm$
INTERS. HALF ANGLE ϕ	5.237 deg	5.237 deg
MCV DIAMETER d_m	25.82 μm	27.22 μm
LENGTH OF MCV l_m	281.65 μm	296.9 μm
FRINGE SPACING Δx	2.67 μm	2.82 μm
MCV : MEASUREMENT CONTROL VOLUME		

Table 2 : Specifications of the LDA probe

The fiber based system allows a relatively fast change of the probe head for application of different techniques (two-component / two-point measurements). In the present state a 36mm two-component probe is used, its specifications are given in Tab. 2.

Receiving Optics/Signal Processing: The light scattered from tracer particles is collected through the receiving aperture in backscatter mode and focused onto a graded index fiber of $50\mu m$ core diameter. Oil-water droplets (mixture 1:1) with diameters of $2\mu m \leq d_P \leq 5\mu m$ produced in a pressured air atomizer are used for seeding. The scattered light, which contains light coming from both measurement volumes, is directed to a colour separation optic based on a combination of three prisms. Two photomultipliers are mounted on the optics to detect the signals. Counter processors (TSI 1980) are used after passing the signals through a two-channel downmixer and bandpass filters. The data is transferred to a PC computer for further processing (Dostek 1400A LDA Interface).

3.2 Particle Image Velocimeter

Measurement System: For the PIV measurements presented in this work the *FlowMap* PIV System of Dantec MT was used, combined with a double pulsed frequency-doubled Nd:Yag laser (*Quanta Ray*, Spectra Physics). The data analysis procedure was based on vector processing by computing the autocorrelation function of double exposured interrogation areas. The details of the PIV measurements are as follows.
The in-cylinder flowfield was seeded by tracers as mentioned in section 3.1. A plane perpendicular to the cylinder axis was illuminated through the transparent cylinder head by a double pulsed light sheet ($\lambda = 532nm$). The light sheet was produced by a cylindrical lens, which was mounted at the end of a light transmitting system designed by tubes and

"joint-mirrors" (*light-guiding arm*). Due to the high laser power (peak energy $E_{Puls} = 300mJ$) a fiber based system was not feasible.
The CCD array of the *FlowSense* Camera comprises 1024 x 1024 pixels with a pixel size of $19\mu m$. The object/image magnification when mapping the whole flow field was $m = \frac{O}{I} = \frac{75mm}{19x1024\mu m} = 3.85$. The size of the interrogation areas was varied between 32x32 pixels and 128x128 pixels, giving a maximum spatial resolution of 1.172 mm. A velocity bias is incorporated by electronic pixel shift (displacing the first image a selected number of pixel lines) which allows the determination of the flow direction.

Synchronization with RCM Experiment: An important feature of the system is its capacity for controlling the timing of all hardware components. The experiments were synchronized as shown in Fig. 4.

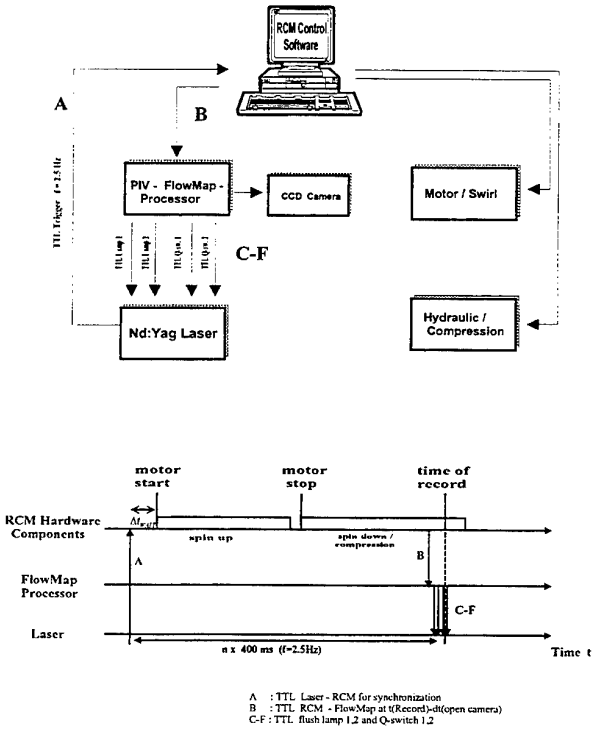

Figure 4: PIV Timing

Corresponding to the repetition rate of the laser and the readout time of the camera, measurements could be taken every 400 ms. Therefore, the program had to be synchronized with the periodically flashing pre-lamp of the laser. A TTL signal from the pre-lamp (**A**) was used to start the system: rotation - stopping the cylinder - start of compression. The PIV Processor was then triggered (**B**) to control the timing of the camera, the laser flash lamps and the Q-switches (**C-F**). By adjusting the time interval Δt_{WAIT}, measurements could be taken at every point in time after stopping the cylinder rotation.

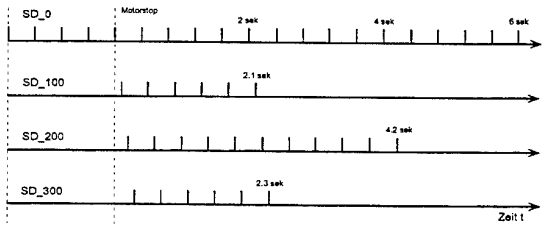

Figure 5: PIV timing pulses, showing 4 overlapping runs

As shown in Fig. 5, a series of time interleaved measurements have been carried out, beginning simultaneously with the motor stop and being delayed for 100ms, 200ms, and 300ms, respectively. In this way, a sampling of $\Delta t = 100ms$ until $2.4s$ after motor stop, $\Delta t = 200ms$ until $4.4s$ after motor stop and $\Delta t = 400ms$ for $t > 4.4s$ after motor stop has been achieved.

4. Data Processing

The processiong of the PIV data and their subsequent use to interpret the turbulence profiles measured with LDA can be divided into the following steps,

- determination of the swirl center location for a single PIV frame
- formulation of a joint probability function describing the local movement of the mean velocity gradient in the radial plane of the cylinder
- application of this function using measured mean velocity gradients to estimate artifact turbulence of LDA measurements

which are described in sequence below.

4.1 Swirl Center Location

Any attempt to localize the momentary position of the swirl center will necessary be an approximation, firstly because the flow by definition is no longer exactly axisymmetric and thus "center" must be newly defined and secondly because of the finite spatial resolution of the PIV velocity data.

Nevertheless a good approximation can be achieved by restricting the search to a more local area. Working on a $x - y$ coordinate system, the lines of zero $U, V, U+V$ and $U-V$ velocity are interpolated (Fig. 6a) leading to a first estimation of the swirl center

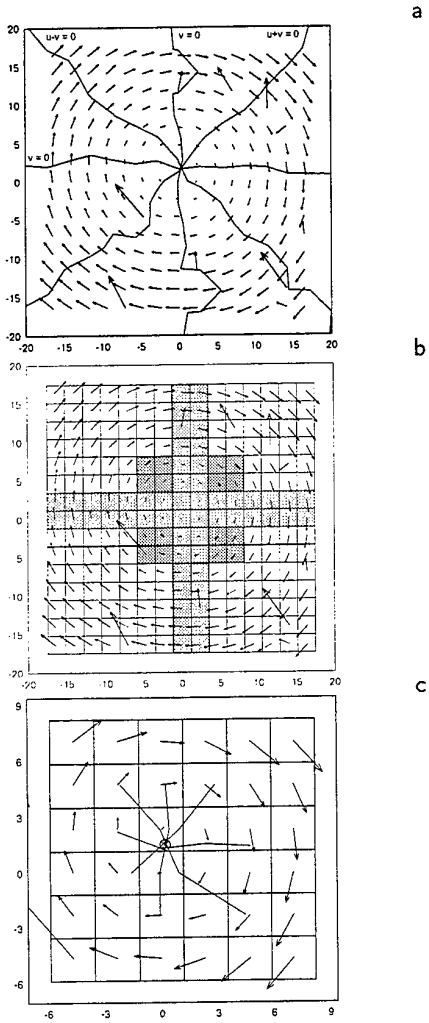

Figure 6: a) measured velocity field, b) first swirl center estimation and choice of reduced pixel set c) final interpolation of swirl center location

location and to a reduced set of interrogation spots for further analysis (Fig. 6b,c).
Again the lines of zero velocity are interpolated and this reduced set results in a zone where all lines cross. The center of a circle encompassing all crossings is specified as the swirl center. The movement of the swirl center, either in time for the constant rotation case or over an ensemble at equal time delays for the spin-down case, can now be expressed as a joint probability function in x, y.

The choice of this function and the estimation of its parameters is a rather sensitive step, since only a relatively small sample set is generally available. For the present work a Gaussian distribution is postulated

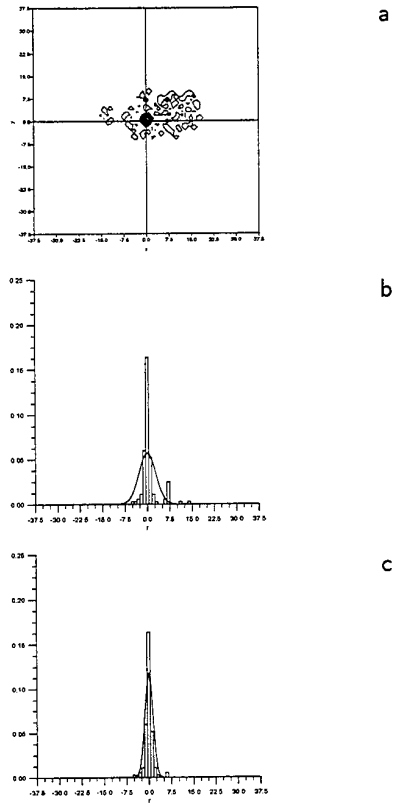

Figure 7: a) measured probability of swirl center movement, b) fitted Gaussian distribution for movement along the x axis, c) Gaussian fit using clipped data ($x < \pm 6.5$)

$$P_{sc}(x,y) = \frac{1}{2\pi\sigma_x\sigma_y} e^{-\frac{1}{2}\left[\frac{x^2}{\sigma_x^2}+\frac{y^2}{\sigma_y^2}\right]} \qquad (1)$$

where σ_x, σ_y are to be determined from the PIV measurements.

An example measured distribution is illustrated in Fig. 7a. Assuming that for $x = y = 0$ the variances σ_x and σ_y are equal for a sufficiently large sample size, the value of σ_x is taken as the variance of the measured distribution along the $y = 0$ diameter.

The subsequent fit is illustrated in Fig. 7b for the case of a constant rotation at 300 rpm. This particular case shows outlying values in the measured data. Some experimentation with data clipping (e.g. $x < \pm 6.5$) before the estimation of σ_x was performed, as discussed below and illustrated in Fig. 7c.

4.2 Movement of Mean Velocity Gradient

At the swirl center, the probability given in Equation (1) can be applied directly to describe move-

ment of the velocity gradient off center, for instance at the position x_0, y_0. However, the values of σ_x and σ_y are expected to decrease, ultimately becoming zero at the wall.

Two approaches were used to quantify this radial damping of σ_x, σ_y, a linear decay and a third order polynomial

$$\sigma_x = \sigma_x(0) f(x) \tag{2}$$

$$f(x) = 1 - \frac{x}{R} \quad \text{linear}$$

$$f(x) = a_0 + a_1 x + a_2 x^2 + a_3 x^3 \quad \text{3rd order polynomial}$$

where R is the cylinder radius. An expression for the movement of the local mean velocity gradient can therefore be given as

$$P_U(x', y', x_0, y_0) = \frac{1}{2\pi\sigma_x(x_0)\sigma_y(x_0)} e^{-\frac{1}{2}\left[\frac{x'^2}{\sigma_x(x_0)^2} + \frac{y'^2}{\sigma_y(x_0)^2}\right]} \tag{3}$$

where σ_x and σ_y are given as functions of x_0. The coordinates x', y' are now local to x_0, y_0 ($x' = x - x_0, y' = y - y_0$).

4.3 Application to Measured Mean Velocity Gradient

The strategy to estimate the apparent turbulent velocity measured by LDA is now to first describe the mean velocity field around the measurement point and then to use the above probability distribution to "sample" this field. The mean velocity field is known from LDA measurements and is assumed not to be influenced by the swirl center movement, at least to first order. Such a mean velocity profile is shown in Fig. 8, together with a numerical prediction using a full Reynolds Stress Model and low Reynolds number wall treatment, as described in detail in [8].

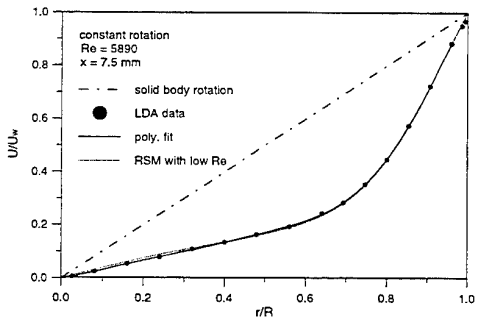

Figure 8: Radial profile of tangential velocity at 300 rpm

The mean tangential velocity is therefore available as an interpolation curve along the $y = 0$ diameter. A linear approximation can be used locally at the position (x_0, y_0) in the form

$$U_\Phi(x, y) = n(x_0) + m(x_0) \cdot r \tag{4}$$

where $n(x_0)$ and $m(x_0)$ is a local intercept and slope and r ist the radius from the geometric center. Out of the $y = 0$ diameter the y component of the velocity can be approximated by

$$U_y(x, y) = \frac{n(x_0)x}{\sqrt{x^2 + y^2}} + m(x_0)x \tag{5}$$

The measured variance of the fluctuating tangential velocity component can now be evaluated as

$$\bar{u^2}(x_0, y_0) = \int\int u_y^2(x, y) P_U(x', y', x_0, y_0) dx dy \tag{6}$$

Assuming a linear mean velocity gradient (Eq.4) this integral can be analytically solved :

$$n(x_0) = 0$$

$$\sigma_x = \sigma_y = \sigma(x_0)$$

$$\begin{aligned} \bar{u^2}(x_0, y_0) &= m^2\sigma_x^2(0)\left(1 - \frac{x_0}{R}\right)^2 + m^2 x_0^2 - \\ &\quad 2mx_0\bar{U}(x_0, y_0) + \bar{U}^2(x_0, y_0) \\ &= m^2\sigma_x^2(x_0) \end{aligned} \tag{7}$$

Alternative to Eq.(4), the actual measured mean velocity gradient can be used in the integral of Eq.(6), in which case a numerical integration using a 9 point quadrature method is suitable [9]. For this purpose the measured mean velocity profile is first approximated by a 7th order polynomial, as shown in Fig. 8.

5. Results and Discussion

The first results to be presented are taken from the case of constant cylinder rotation at 300 rpm and serve to illustrate the sensitivity of various processing parameters, as introduced above.

In Fig. 9 the choice of σ_x, σ_y, the integration limits and the mean velocity gradient is investigated. To begin, σ_x and σ_y were computed using Gaussian fit, as illustrated in Fig. 7b and applied with either a linear or polynomial decay function to a locally velocity gradient of the form Eq. (4). Fig. 9a compares the computed apparent turbulence with the actual turbulence (RMS) measured with the LDA. Two discrepancies are immediately obvious. In the

center ($r/R = 0$) the apparent turbulence is larger than the measured, which is physically impossible. Furthermore, the trend of the apparent turbulence towards the wall is to decrease, whereas the measured turbulence remains approximately constant.

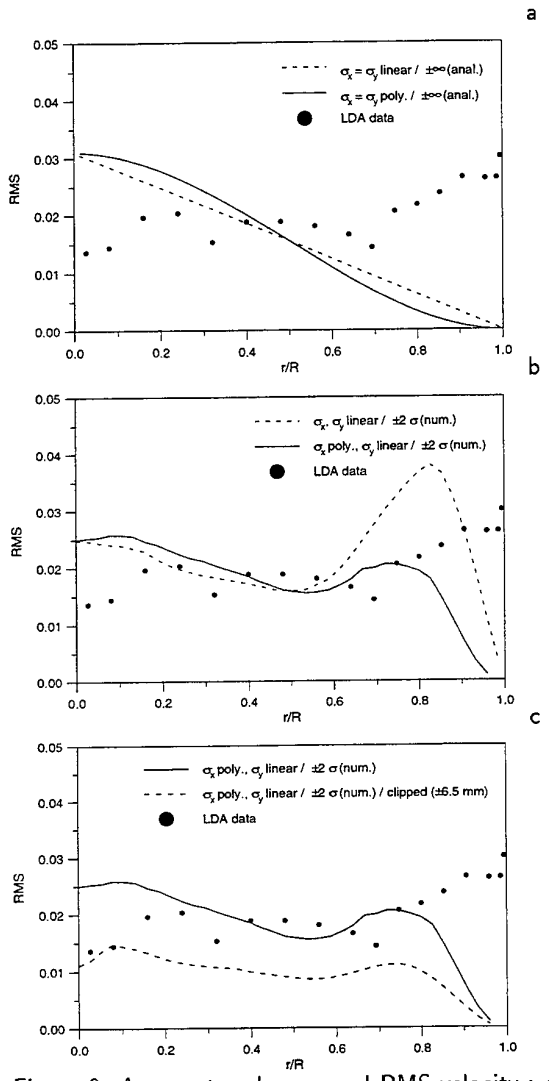

Figure 9: Apparent and measured RMS velocity : a) Gaussian fit for σ and linear mean velocity profile; b) restricted ($\pm 2\sigma$) numerical integration of actual mean velocity profile; c) as in b) with data clipping ($\pm 6.5mm$) for Gaussian fit

Physically the integration of a Gaussian distribution to $\pm\infty$ is unrealistic. Therefore the integration was repeated using limits of $\pm 5\sigma, \pm 4\sigma, \pm 3\sigma$ and $\pm 2\sigma$. In fact little difference was observed so that subsequent results were computed using $\pm 2\sigma$, which represents about 96% of the probability mass. The next step was to use the actual measured mean velocity gradient, as shown in Fig. 8, instead of the linear approximation, Eq. (4). The results are shown in Fig. 9b, which reflect also the increased gradient towards the wall. Still however, the apparent turbulence is larger than the measured turbulence in the center of the cylinder. Finally data clipping was applied before the Gaussian fitting of the measured probability of the swirl center movement, as illustrated in Fig. 7c. This lead to the results shown in Fig. 9c, which shows also the unclipped result for comparison. Clearly the initial estimates of σ_x, σ_y are very important and should be based on a larger number of single PIV frames to obtain the necessary certainty. Further results have therefore been computed using a polynomial decay of σ_x, a linear decay of σ_y, an integration limit of $\pm 2\sigma$ on the measured mean gradient and data clipping for the initial estimate of σ_x, σ_y. A final result for the constant rotation at 300 rpm is given in Fig. 10, where the LDA turbulence data have now been corrected by the estimated apparent turbulence.

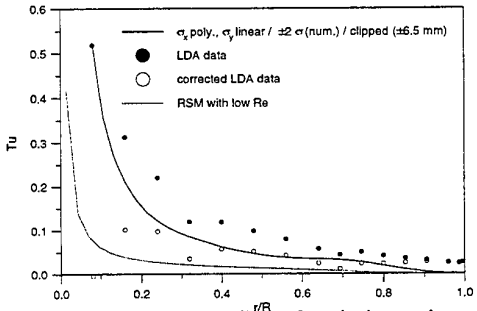

Figure 10: Radial profiles of turbulence intensity - comparison of numerical simulated data, estimated apparent turbulence, actual measured LDA data and "corrected" LDA data

The agreement with the results from numerical simulation is much improved, except near the wall. Numerically laminar flow conditions are predicted. Therefore the remaining variance in the LDA data is presumbly attributed to noise.
In Fig. 11 the measured mean velocity profile for one spin-down case is shown, including the polynomial fit for subsequent integrations.

The result of the analysis is given in Fig. 12, again showing the measured turbulence, the computed apparent turbulence and the corrected measurements. In this case, despite the clipping, the apparent turbulence is larger than the measured turbulence over large regions of the profile. This indicates clearly that the actual turbulence level is very low, in fact lower than the uncertainty in the corrected esti-

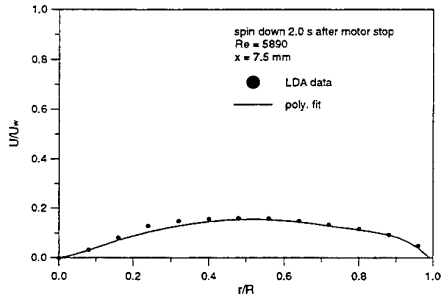

Figure 11 : Mean velocity profile - spin-down case

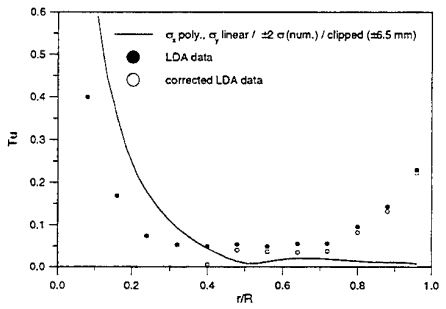

Figure 12: Radial profiles of turbulence intensity - comparison of estimated apparent turbulence, actual measured LDA data and "corrected" LDA data

mates.

6. Summary and Conclusions

In the present paper, a combined application of the LDA and the PIV techniques to investigate the contribution of large scale fluctuations to the turbulence intensities measured by LDA has been proposed and tested. A statistical description of the vortex motion based on PIV measurements allows the determination of *apparent* turbulence, which obviously is related to the precession of the vortex core. A better interpretation and even "correction" of the measured turbulence data is then possible. The presented methodology offers a better comparison of experimental and numerical results, even in the presence of three dimensional flow motion, which cannot be reproduced by numerical simulations. The results can be summarized as follows :

I: A significant part of the actual measured turbulence (LDA) can be attributed to the effect of vortex motion. "Correction" of the LDA data by estimated apparent turbulence leads to an improved agreement with results from numerical simulations.

II: For most of the presented results the apparent turbulence is larger than the measured turbulence. Since the number of single frames measured by PIV was limited to a maximum of 100, the certainty of the estimated probability distribution of the vortex core location, and therefore the first estimation of the σ_x, σ_y represents a very critical point.

III: Parametric studies showed the sensitivity of various processing parameters, such as the integration limits, the damping of σ_x and σ_y towards the wall and data clipping limits. Further work will be focused on a more reliable data analysis, based on an increased number of PIV frames, to increase the certainty of σ_x, σ_y- estimation. The data reduction procedure will be refined to show its potential for a wide range of applications as already mentioned before.

Acknowledgements

The authors gratefully acknowledge the support of DANTEC Measurement Technology, Skovlunde and Dantec/invent MT, Erlangen, who made the PIV equipment available. Also Spectra-Physics is acknowledged for the loan of the Nd-YAG laser. The work has been supported by the Deutsche Forschungsgemeinschaft (DFG Tr194/ 7-1). Thanks are also due to S. Jakirlic for providing the numerical predictions shown.

References

[1] Fansler,T.D. and French, D.T. (1988) *Cycle-Resolved Laser-Velocimetry Measurements in a Reentrant-Bowl-in-Piston Engine*, SAE 880377

[2] Brereton, G.J. and Kodal,A. (1991) *A Frequency-Domain Filtering Technique for Triple Decomposition of Unsteady Turbulent Flow*

[3] Rask, R.B. (1981) *Comparison of Window, Smoothed-Ensemble and Cycle-to-Cycle Data Reduction Techniques for Laser Doppler Anemometer Measurements of in-Cylinder Velocity*, **Fluid Mechanics of Combustion Systems**, ed. Morel, T., Lohmann, R.P. and Rackley, J.M., 11-20, ASME

[4] Hilton, A.D.M., Roberts, J.B. and Hadded, O. (1991) *Autocorrelation Based Analysis of Ensemble Averaged LDA Engine Data for bias-free Turbulence Estimates: A Unified Approach*, SAE 910479

[5] Daw, C.S. and Kahl, W.K. (1990) *Interpretation of Engine Cycle-to-Cycle Variation by Chaotic Tine Series Analysis*, SAE 902103

[6] Glover, A.R., Hundleby, G.E. and Hadded, O. (1988) *An Investigation into Turbulence in Engines using Scanning LDA*, SAE 880378

[7] Corcione, F.E. and Valentino, G. (1990) *Turbulence Length Scale Measurements by Two-Probe-Volume LDA Technique in a Diesel Engine*, SAE 902080

[8] Jakirlić, S. and Hanjalić, K. (1995) *A Second-Moment Closure for Non-Equilibrium and Separating High- and Low-Re-Number Flows*, Proc. 10th Symposium on Turbulent Shear Flows, The Pennsylvania State University, USA, August 14-16

[9] Abramowitz, M. and Stegun, I.A. (1970) **Handbook of Mathematical Functions**, New York, S. 892f.

[10] Heywood, J.B. (1987) *Fluid Motion within the Cylinder of Internal Combustion Engines - The 1986 Freeman Scholar Lecture*, Journal of Fluids Engineering, Vol. 109, 3-35

A LASER-DOPPLER ANALYSIS OF COOLING AND MIXING IN A RESEARCH COMBUSTOR

P. Anacleto, M.V. Heitor and A. L. N. Moreira

Instituto Superior Técnico
Mechanical Engineering Department
Av. Rovisco Pais, 1096 Lisboa Codex
Portugal

ABSTRACT

A laser-Doppler velocimeter is used to study the aerodynamics of the quenching process typical of a "Rich-burn, Quick-quench, Lean burn", RQL, gas-turbine combustor making use of a water model of a can-type combustor. The work extends previous analysis of the mean and turbulent flow in this type of combustors and includes consideration of four different combustor configurations, which were designed to allow to optimise the mixing and cooling efficiency of the quench modules in practical combustors with low-NO_x emissions.

1. INTRODUCTION

In a previous paper we have presented detailed velocity measurements of the mean and turbulent flow in a model combustor associated with the "Rich-burn, Quick-quench, Lean-burn" concept (hereinafter referred to as RQL, Anacleto et al., 1996), which consider the influence of different parameters on the performance of the combustor, such as the swirl level in the rich zone, the geometry of the quench holes, and the momentum of the inflowing jets on the internal flow field. The flows studied encompassed Reynolds numbers based on the bulk axial velocity at the outlet of the model about 10^5, which are representative of real combustor flows (Bahr, 1995; Joos and Pellisheck, 1995) and are extended in this paper to the study of a set of new combustor configurations.

Typically, an RQL combustor consists of three main zones, as follows: i) a fuel-rich primary zone where NO_x formation is reduced due to low temperature and non-stoichiometric conditions; ii) a quench zone, where the transition from fuel-rich to fuel-lean combustion should be obtained through rapid mixing of the rich mixture with dilution air jets, namely by accelerating the flow in order to limit the residence time in potential stoichiometric regions; and iii) a lean zone where the unburned products will burn for fuel-lean conditions. The work has been derived from the need to extend knowledge of preliminar full-scale combusting experiments, which have been shown to be limited in extent, time and the skills required. The prime objectives are to improve understanding of major flow features and of the effect of the details of the combustor geometry on the flow pattern, as well as to provide the basis for the numerical calculation of the flow in this type of combustors. In this context, the previous results have shown that the development of this type of combustors is particularly limited by the mixing pattern downstream of the quench zone, which is strongly influenced by the effectiveness of the penetration of the dilution jets at the quench stage. Other major questions include the effectiveness of the wall cooling and the carbon production in the primary zone. The solution of these technical problems demands a detailed understanding of the internal flow structure in these new type of combustors and this paper is aimed at studying the cooling and mixing patterns in the quench zone of a configuration with practical relevance.

It is known that measurements of the complete velocity field in real combustors under burning conditions are extremely difficult, if not impossible, and recourse has been made to the study of isothermal, constant density systems (e.g. Bicen et al., 1989; McGuirk and Palma, 1995). For these constant density experiments, the use of a water flow in a Plexiglas model is often preferred due to the possibility of optical access and the easy of laser-Doppler velocity measurements in water flows (Heitor, 1989). To achieve these objectives, a primary measure to consider in model combustors is to use similar flow splits along the combustor, namely through adequate control of primary and secondary flows (Anacleto et al., 1996). The work reported in this paper considers these aspects in terms of the analysis of the flow in a Plexiglass model of a practical RQL combustor, which was scaled at 1:1, keeping similar flow splits.

The model combustor is described in the following section. Section 3 describes briefly the experimental techniques and procedures used and Section 4 presents and discusses sample results obtained. The main conclusions of the work are summarised in section 5.

2. THE MODEL COMBUSTOR GEOMETRY

Figure 1 shows the layout of the test model, which consists of three different modules (namely, rich, quench and lean) assembled concentrically inside a larger peripheric can with a diameter of D0=125 mm and with 400 mm in length, so that a surrounding annular water flow is formed to feed the liner inlet ports accordingly to the related pressure drops. The model was immersed in a rectangular water tank to avoid the effects of refraction of the laser beams at the curved surface of the model.

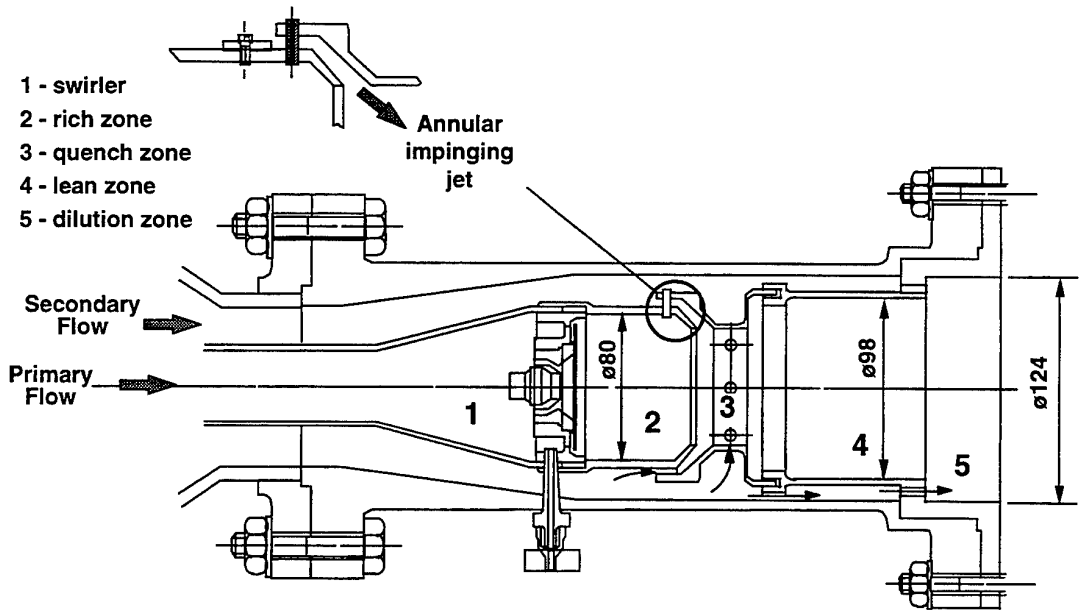

Figure 1. Schematic drawing of the model combustor

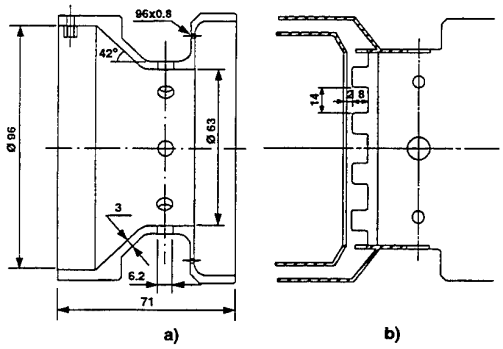

Figure 2. Schematic drawing of the quench module a) Basic configuration (Runs A and B); b) modified geometry (Runs C and D)

The primary flow enters the model via an inner stainless steel pipe with 40 mm inside diameter, which provides an orifice meter and a valve to measure and regulate the primary/secondary flow ratio. The primary flow is then directed to the head of the combustor through a diverging pipe. A coaxial swirler, similar to that used in the real combustor, is fitted around the fuel atomizer at the head of the model. For the results reported here the fuel atomizer was blocked.

The rich module consists of a cylindrical barrel of 80 mm internal diameter and 62 mm length. Figure 2a) shows the quench module, which is located just downstream of the rich module and consists of a 20 mm length truncated cone, providing a 5:8 area contraction and followed by a 20 mm length constant section of 63 mm inside diameter with eight holes disposed symmetrically along the wall. Part of the secondary stream is diverted through these holes, providing jets emerging normally to the direction of the primary stream to simulate the quench jets in practical combustors. At the junction of the rich with the quench module, there is an annular passage with 8 mm in width, which could be partially, or totally, blocked to allow the study of different mixing patterns in the combustor. Part of the secondary stream is diverted into the primary flow through this passage to simulate the wall-cooling jet in the practical combustors, which flows along the contraction wall at 42 degrees with the direction of the primary stream.

An additional ring, as presented in Figure 2b, can be assembled at the internal surface of the quench module, upstream of the single-row arrangement. It looks like a "crow" of eight teeth equispaced, dividing the original annular flow in eight distinguished jets. Between the rich module and those teeth, there is an annular gap of 2 mm to simulate the film cooling in practical combustors.

The third module, which simulates the lean zone in practical combustors, includes a 98 mm diameter cylinder with 76 mm in length. At the expansion between the quench and the lean zone, 96 small holes with 0.8 mm in diameter discharge part of the secondary fluid into the primary flow, which simulates the air used to cool the wall in this region.

Table 1. Flow Conditions

RUN	Main geometric features	mf (k/s)	$Re/10^5$	U_0 (m/s)
A	Basic configuration (Run 1 of Anacleto et al., 1996)	7.5	73	0.621
B	Absence of annular cooling jet	7.5	73	0.621
C	Cooling jet partially blocked, resulting in 8 jets located between each pair of quench jets	7.5	66	0.621
D	Similar to RUN C, but with 4 quench holes with an incresed diameter of Ø12 mm.	7.5	75	0.621

3. THE EXPERIMENTAL TECHNIQUES AND PROCEDURES

3.1 The Laser-Doppler Velocimeter

The mean and fluctuating velocities of the flow in the model combustor were measured by a laser-Doppler velocimeter based on a 2W Argon-Ion laser and operated in the dual-beam, forward-scatter mode with sensitivity to the flow direction provided by light-frequency shifting from acousto-optic modulation (Bragg cells), normally set at 2 MHz, figure 3. The light scattered by naturally occurring centres in the water was collected by a lens (focal length of 200 mm) and focused onto the pinhole aperture (0.3 mm) of a photomultiplier (OEI, type LD-0-810) with a magnification of 1.0. The output of the photomultiplier was band-pass filtered and the resulting signal processed by a commercial frequency counter (TSI 1980-B), which was operated in the single-measurement-per-burst mode with fixed cycles (N=8) validated in the time domain within 1%. The validated data were transferred to a laboratory 16-bit minicomputer, where the time averaged moments of velocity were evaluated.

The complete LDV system was mounted on a three-dimensional traversing unit, allowing the positioning of the laser-velocimeter control volume within + 0.25 mm. Measurements were obtained with the laser beams in the horizontal and vertical planes and by traversing the control volume along the horizontal and vertical directions to allow the determination of the axial, U, radial, V and tangential, W, mean and turbulent velocities.

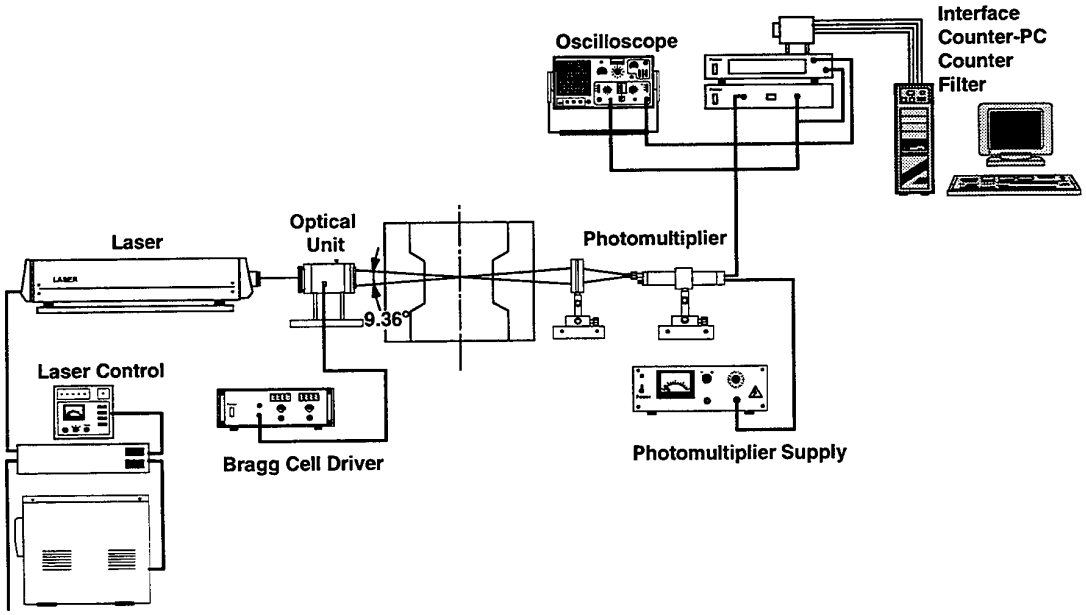

Figure 3. Schematic drawing of the laser velocimeter

Table 2. Flow Split along the Combustor
(as % of the total flow rate)

RUN	λ_p (%) (flowmeter)	λ_i (%)	λ_q (%)	λ_m (%)	λ_d (%)
1	24	29	10	—	27
2	24	38	11	—	27
3	15	31	13	8	33
4	25	0.0	18	—	57

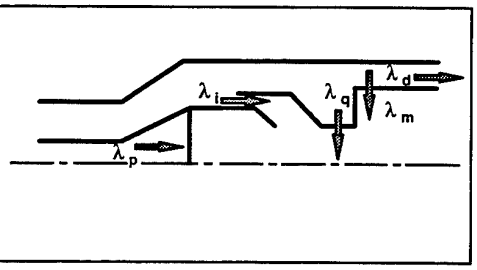

The accuracy of the laser-Doppler measurements presented here has been discussed by Anacleto et al. (1996) and is not repeated here. Spectral analysis of LDA signals was carried out by sampling and holding the velocity at each Doppler burst until another valid signal arrives. A mean sampling frequency of 2 KHz was used, suggesting that structures of the order of 1.0mm and above can be resolved. This is at least one order of magnitudes smaller than the expected length scales in the flow, which implies that the energy containing motions are resolved by the counter (Adrian and Yao, 1985).

3.2 The Flows Considered

A primary measure to guide the use of water models in the study of gas-turbine combustors is to establish adequate flow splits (e.g. Bicen et al., 1989). This has been achieved in the present work through a detailed analysis of the secondary flow, as described in Anacleto et al. (1996).

Table 2 summarises the flow split along the combustor for the four conditions specified in table 1, which allow to study the influence of the momentum of the inflowing jets on the internal flow field. The flows studied encompassed Reynolds numbers based on the bulk axial velocity at the outlet of the model, about 10^5, which are representative of real combustor flows.

4. RESULTS AND DISCUSSION

Figure 4 shows sample results characteristic of the mean flow along the model combustor for the four runs of table 1, which show that the main features of the flow are as follows: i) a swirl driven recirculation zone in the rich zone, which is surrounded by a shear layer characterised by large velocity fluctuations and limited in extent by the flow in the quench zone; ii) an outer recirculation zone of low intensity close to the wall in the rich zone, which is limited by the contraction at the entrance of the quench module; iii) a reduced penetration of the quench jets, in particular for Runs A, C and D, which is in part limited by the impingement of the annular cooling jet; and, except for Run B and partially for Run D, iv) a central core of fluid, rotating as a solid body, which extends along the centreline from the primary zone up to the exit of the combustor and exhibits a significant swirl component at the outlet of the lean zone.

The performance of this type of combustor is strongly influenced by the mixing rates at the quench stage and by the momentum transfer throughout the combustor (eg. Bahr, 1995). For example, the central core of rotating fluid up to the outlet of the model is a feature that should clearly be avoided in any combustor design. For the present flow conditions, it can be easily identified through the double "S" shape of the mean axial velocity profiles in the lean zone, figure 5, which is a direct result of the lack of penetration of the quench jets through the primary flow in Runs A and C. The analysis shows that improved mixing patterns at the quench zone can be achieved by increasing the penetration of the quench jets, namely by blocking the annular cooling jet (Run B) or by increasing the flow through the jets (Run D).

The results obtained for Run B, which considers with the inlet port of the cooling jet closed, shows that increasing the flow rate of the quench jets and the radial velocity at the entrance of the quench jets by about 60%, increases their penetration, but allows the central recirculation zone to extend up to the plane of the quench jets. In fact, the pressure distribution imparted by the annular jet in Run A is essential to keep the swirl induced recirculation zone within the rich zone of the combustor and, thus, to avoid combustion reactions to propagate down to the quench stage in practical combustors.

In addition, the annular cooling jet increases the axial velocity of the mainstream close to the wall, decreasing the momentum flux ratio between the quench jets and the crossflow and, consequently, the penetration the quench jets through the mainflow. However, it should be noted that this is not a suitable solution for practical RQL combustors, due to the lack of cooling in the front wall of the rich zone.

For the flow conditions of Run B, the primary flow interacts with a smaller mass rate of non-swirling fluid and the quench jets are only able to deflect the swirling flow towards the centreline. As a result, the core fluid in the quench module now rotates with an angular velocity about twice larger

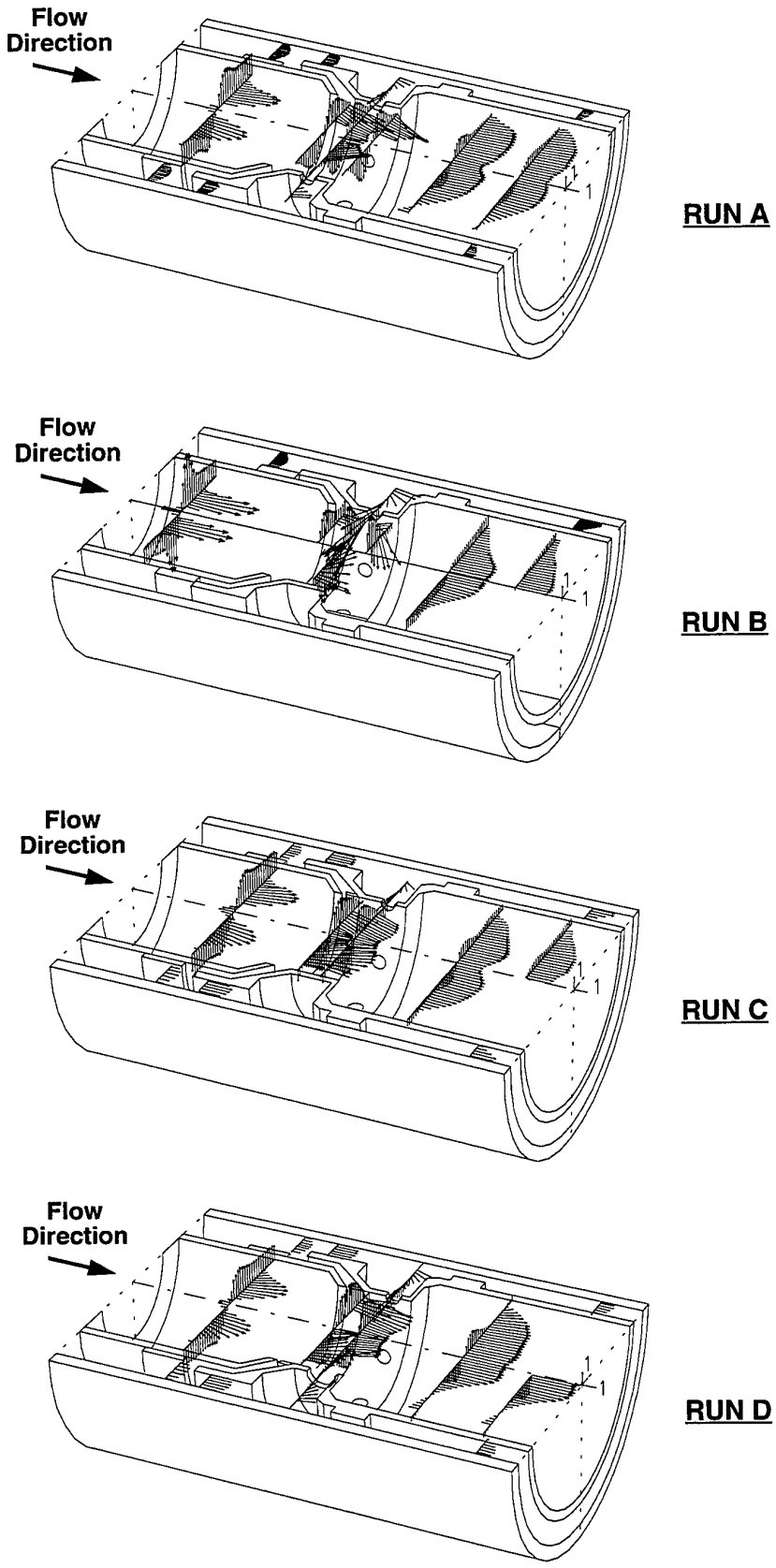

Figure 4 - Mean flow of patterns measured in the combustor

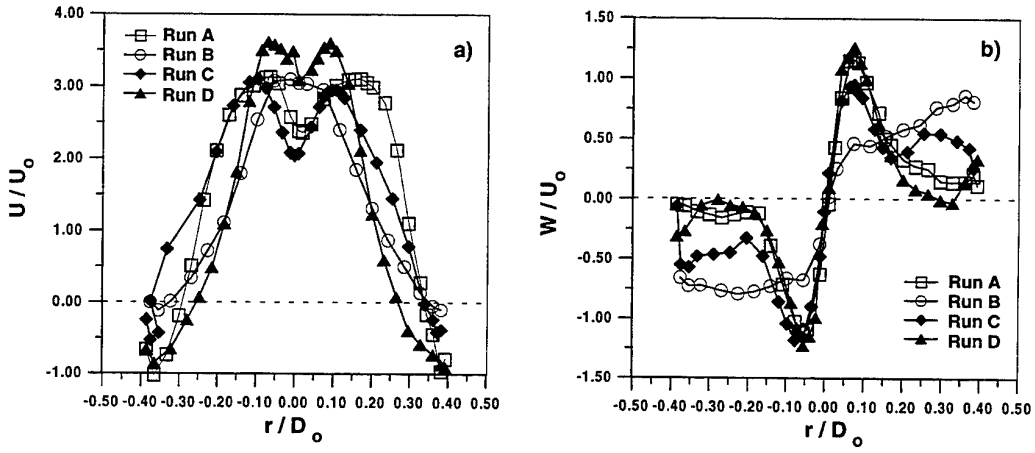

Figure 5 - Mean velocity profiles in the dilution zone (x/Do=1.17)
a) steramwise velocity component ; b) tangential velocity component

than in the standard case, Run A. At the lean zone, the axial mean velocity exhibits a single peak at the centreline, due to the absence of the annular cooling jet and the angular motion diffuses radially outwards, giving rise to a rotating pattern over all the cross-section of the combustor.

The results obtained for Run C quantify the effects of partially blocking the annular cooling jet in the flow pattern, figure 4c), and are associated with a decrease in the total mass flow rate of the cooling jets by about 20%, while that of the quench jets increased by about 30%. The quench holes arrangement is similar to that of the standard case, Run A, and, consequently, the quench jets emerges necessarily with a radial velocity 30% larger than that of the standard case. Despite the increase of the momentum flux ratio between the quench jets and the mainstream flow, the mean velocity field in the lean zone show quantitative features similar to those observed in the standard case, with the central vortex core extending up to the outlet of the model combustor. In general, the analysis shows that the increased penetration achieved by the quench jets is not enough to promote an efficient mixing downstream the quench zone.

On the other hand, when the flow rate of the quench jets is increased by to 80% of the standard case, the results for Run D shows that the axial mean velocity profile at the outlet of the lean zone, figure 4d), exhibits a single central peak, although the mean tangential velocity profile still suggests the existance of a rotating core. This results in a flow pattern closer to that theoretical desired for the combustor and confirms the need for an accurate adjusting of the geometry of the quench module, if the correct mixing pattern is to be established in the combustor.

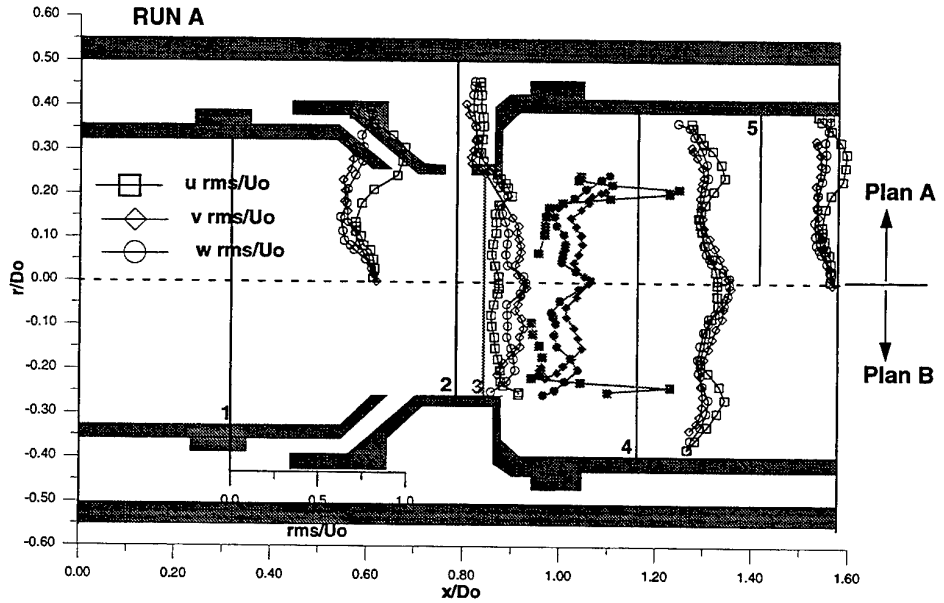

Figure 6. Turbulent velocity profiles along the combustor for RUN A.

We now turn to the analysis of the turbulent flow in the combustor and figure 6 shows sample profiles of axial, radial and tangential velocity fluctuations for Run A. The central flow in the primary zone is surrounded by a shear layer with large positive gradients of the mean axial and tangential velocities, where maximum turbulent fluctuations occur with local values up to $\sqrt{u'^2} = 1{,}9\ U_O$. These values are comparable with other published in the literature (eg. Koutmos and McGuirk, 1989; Palma and McGuirk, 1995), and suggest the likely representativity of the present flow pattern. The results are typical of high strained recirculating flows with swirl, suggesting the likely contribution of streamline curvature to turbulent production and transport. Although the detailed analysis of the turbulent flow requires plotting the results in streamline coordinates, figure 6 shows also that the magnitude of the axial velocity fluctuations in the primary zone is larger than those in the radial and tangential directions, with maxima differences up to 40%.

In spite of the lack of optical access, which precluded measurements to be obtained in the stagnation region, it is likely that the radial velocity fluctuations increase further downstream, as observed in other recirculating flows with a free stagnation point, because the relative magnitude of the three fluctuating velocity components is altered downstream of the quench module. These features suggest the likely importance of the generation of turbulent kinetic energy through the interaction between normal strains and normal stresses and are important to be noted because they imply that calculations using a scalar effective-viscosity turbulence model (eg. Coupland and Priddin, 1987, McGuirk and Palma, 1992) will be inaccurate, at least for the turbulence upstream of the exit of the combustor.

The velocity fluctuations in the quench zone peak in the highly strained shear layer surrounding the quench flow and show larger values in the axial direction in accordance with the generally accepted mechanism of production of turbulent kinetic energy by the interaction between turbulent motion and the mean rate of shear strain. As noted before, the tangential and radial velocity fluctuations in the central part of the flow have local maximum with values about twice larger than those of $\sqrt{u'^2}$. Similar trends have been reported by Green and Whitelaw (1983), and Koutmos and McGuirk (1989) and have been attributed by Bicen et al. (1989) to the impingement of opposed jets at the centreline.

The anisotropy of the turbulent flow observed so far in some zones of the flow may raise the question of whether velocity fluctuations are associated with unsteady mechanisms, such as precessing of the vortex core or vortex shedding in highly strained regions. The existence of such mechanisms would not only affect the performance of the combustor, but also would invalidate any attempt to simulate the flow with numerical models based on steady equations (McGuirk and Palma, 1995-b). In order to address this question, the probability density functions of velocity fluctuations and the related spectra were analysed and sample results are presented in figure 7. Bimodal probability distributions were not observed throughout the measurable flow, suggesting that instabilities, if present, do not contain enough energy to dominate over the turbulence generated fluctuations.

Figure 8 provides results of the turbulent velocities for the various runs considered in this paper and, in general, show characteristics similar to those discussed above for Run A. An exception to be noted is that derived from the fact that the quench jets in Run B induce large azimuthal gradients of mean and fluctuating velocities, which promotes turbulent mixing. In fact, the impingement of opposed jets in the centre of the combustor enhances turbulent production, giving rise to velocity fluctuations about five times larger than in the standard case. This is clearly observed either in the shear layer, where turbulent fluctuations are mainly due to shear induced mechanisms, or in the vicinity of the centreline where the contribution of normal strains to turbulence production is expected to be important (e.g. Heitor and Whitelaw, 1986).

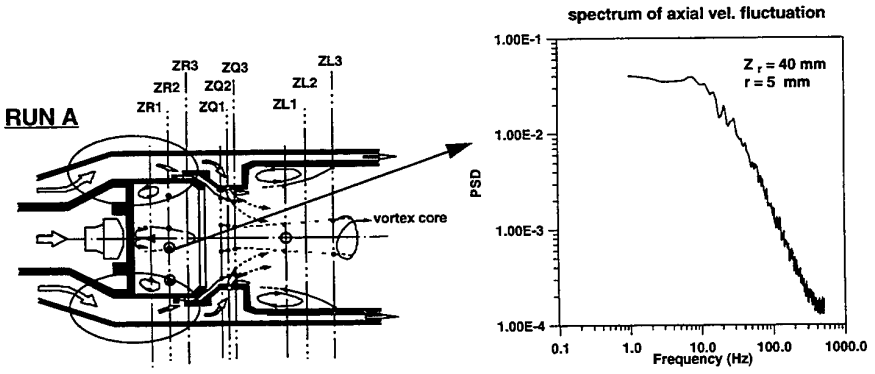

Figure 7 - Power Spectral density of velocity fluctuations obtained in the shear layer surrounding the central recirculation zone for Run A

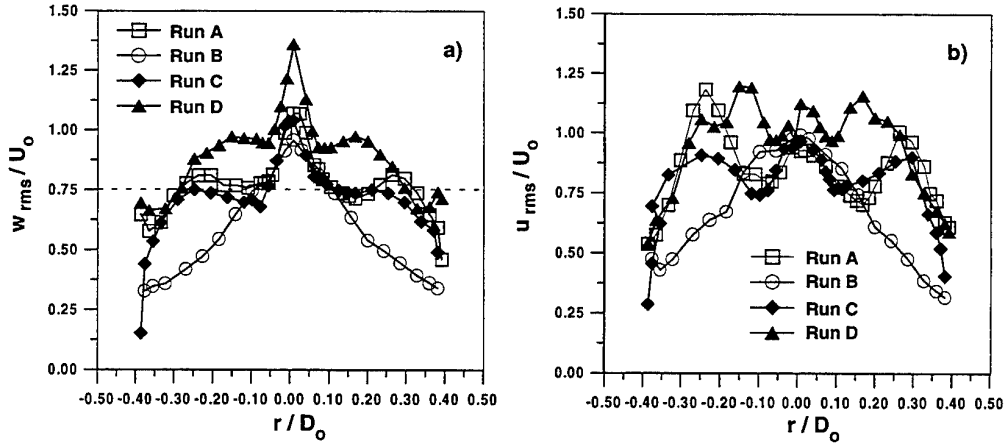

Figure 8 - Turbulent velocity profiles in the dilution zone (x/Do = 1.17)
a) rms of tangential velocity fluctuation
b) rms of axial velocity fluctuations

5. CONCLUSIONS

A laser-Doppler velocimeter was used to study the details of the mixing pattern typical of RQL combustors for four different geometric conditions. The results quantify the flow pattern induced by the annular jet used to cool the front wall of the rich module and by the quench jets. The analysis suggest that the optimum penetration of the quench jets is achieved without blocking the annular cooling flow, but by increasing the angle of the inlet section of the cooling jet at the entrance of the quench module.

Enhanced turbulent fluctuations can be achieved by increasing the momentum of the quench jets relatively to the axial momentum of the annular cooling jet. However, a serious limitation is expected since the pressure distribution imparted by the annular jet is essential to keep the swirl induced recirculation zone within the rich zone of the combustor, namely to avoid combustion reactions to propagate down to the quench stage in practical combustors.

ACKNOWLEDGEMENTS

The authors are pleased to acknowledge many useful discussions with Yves Bouchier, SNECMA, Hans Kaaling, VOLVO and Fabio Turrini, FIAT Avio. The rig was built in the Turin facilities of FIAT Avio and was adapted at the IST's workshop, under the BRITE/EURAM project "Low-Emission Combustion Technology", contract no. AER2-CT92-0036.

The contribution of Merss. Carlos Carvalho and Jorge Coelho in preparing the manuscript is appreciated.

REFERENCES

Adrian, R.J. and Yao, C.S. (1985). "Power Spectra of Fluid Velocities Measured by Laser-Doppler Velocimetry. ASME, Winter Annual Meeting, Miami Beach, Florida, November 17-22, 1995.

Anacleto, P. M., Heitor, M. V. and Moreira, A. L. N. (1996). "The Mean and Turbulent Flowfield in a Model RQL Gas-Turbine Combustor", Accepted for publication in "Experiments in Fluids".

Barh, D. (1995). "Aircraft turbine engine NO_x emission abatement". In: "Unsteady Combustion", eds. Culick, Heitor and Whitelaw, Kluwer Academic Publ., NATO ASI series, Vol. E306, pp 243-264.

Bicen, A. F., McGuirk, J. J. and Palma, J. M. L. M. (1989). "Modelling gas turbine combustor flow fields in isothermal flow experiments," Journal of Power Engineering, 203, pp 113-122.

Coupland, J. And Priddin, C. H. (1987). "Modelling the Flow and Combustion in a Production Gas Turbine Combustor", In: "Turbulent Shear Flows 5", eds. Durst et al., Springer-Verlag, pp 310-323

Green, A. S. and Whitelaw, J. H., 1983. "Isothermal models of gas-turbine combustors," Journal of Fluid Mechanics, 126, pp. 399-412.

Heitor, M. V. (1989). "Velocity and scalar measurements in model and real gas turbine combustors". In: "Instrumentation for Combustion and Flow in Engines", D. F. G. Durão et al. (eds.), Kluwer Academic Publ, Nato Asi Series, Vol E154pp 1-44.

Heitor, M. V. and Whitelaw, J. H. (1986). "Velocity, Temperature and Species Characteristics of the Flow in a Gas-Turbine Combustor," Combustion and Flame, 64, pp 1-32.

Joos, F. and Pellischeck; G. (1995). "Low Emission Combustor Technology". In: "Advances in Engine Technology", Ed. R. Dunker, John Willy & Sons.

Koutmos, P. and McGuirk, J.J., 1989. "Investigation of swirler/dilution jet flow split on primary zone flow patterns in a water model can-type combustor," Transactions of the ASME, Journal of Engineering for Gas Turbines and Power, 111, pp. 310-317.

McGuirk, J.J. and Palma, J.M.L.M. (1992). "Calculations of the Dilution System in an Annular Gas Turbine Combustor," AIAA Journal, Vol. 30, pp. 963-972.

McGuirk, J. J. and Palma, J. M. L. M. (1995a). "Experimental Investigation of the Flow Inside a Water Model of a Gas Turbine Combustor. Part 1: Mean and Turbulent Flowfield," Journal of Fluids Engineering, 117.

McGuirk, J. J. and Palma, J. M. L. M. (1995b). "Experimental Investigation of the Flow Inside a Water Model of a Gas Turbine Combustor. Part 2: Higher Order Moments and Flow Visualization". To appear in the Journal of Fluids Engineering, 117.

THE TURBULENT 3D FLOW FIELD IN A ROTATING ANNULAR FLUME

V. Spork, A. Cüppers and J. Köngeter

Institute of Hydraulic Engineering and Water Resources Management (IWW)
Aachen University of Technology, Germany

ABSTRACT

In this paper measurements of the flow field in a rotating annular flume are described. This flume contains of a rotating top lid and a rotating flume (Fig. 1) and is used for investigations on transport processes of cohesive sediments. Due to the curvature of the flume a complex 3D flow field is generated, resulting in unknown influences on the experimental results.

By simultaneous rotation of the top lid and of the flume itself optimised conditions for experiments can be established. To get values for the turning velocities of the top lid and the flume extensive studies of the flow field were made for the annular flume at the Institute of Hydraulic Engineering and Water Resources Management (IWW), Aachen University of Technology, Germany. The measurements were carried out with a 1D laser Doppler velocimeter system. All instruments are mounted on the rotating flume construction. Different ratios of top lid and flume speed as well as different water depths were investigated.

Optimised ratios could be determined for two different criteria in the annular flume. For an erosion experiment a uniform distribution of the bottom shear stress (criteria 1) is necessary and for deposition experiments minimised secondary flow circulations (criteria 2) have to be established in the flume.

Comparing the results of the annular flume experiments at the IWW with other investigations showed a good agreement, even if the annular flumes are not exactly comparable in dimensions.

1. INTRODUCTION

Rotating annular flumes (Fig. 1) are used for investigations on erosion and deposition processes of cohesive sediments. The annular flume (Fig. 1) consist of a circular flume (mean diameter: 3.25 m, channel width: 0.25 m) and a circular top lid (variable water depth). The top lid at the water surface drives the water and the rotational motion induces a secondary current in radial direction within the flume resulting in a complex 3D flow field. To minimise the secondary current near the bottom of the flume, the channel and the top lid can be rotated separately in both directions. The rotational speeds for the flume ω_f and the top lid ω_t as well as the ratio ω_t/ω_f have to calibrated carefully to get useful experimental conditions for investigations on cohesive sediment transport. In previous investigations the calibration of the rotational speeds of the top lid and the flume were done visually by observing the movement of plastic beads on the bottom of the flume and/or by the use of Prandtl tubes for velocity measurements (Spork et al. 1994). To improve this calibration and to get detailed information about the 3D flow field in the annular flume at the IWW extensive measurements were carried out by using the laser Doppler velocimetry (LDV) technique.

2. EXPERIMENTAL SETUP

2.1 Instrumentation

The measurements were done by using a 1D back scatter fibre optic 10 mw laser Doppler system (DANTEC FlowLite). This system was chosen, because the instruments have to be mounted on the flume and have been rotating with the channel, so that a water cooled and heavy laser system was not convenient for use. The focal distance of the front lens was 250 mm resulting in a measuring volume with a

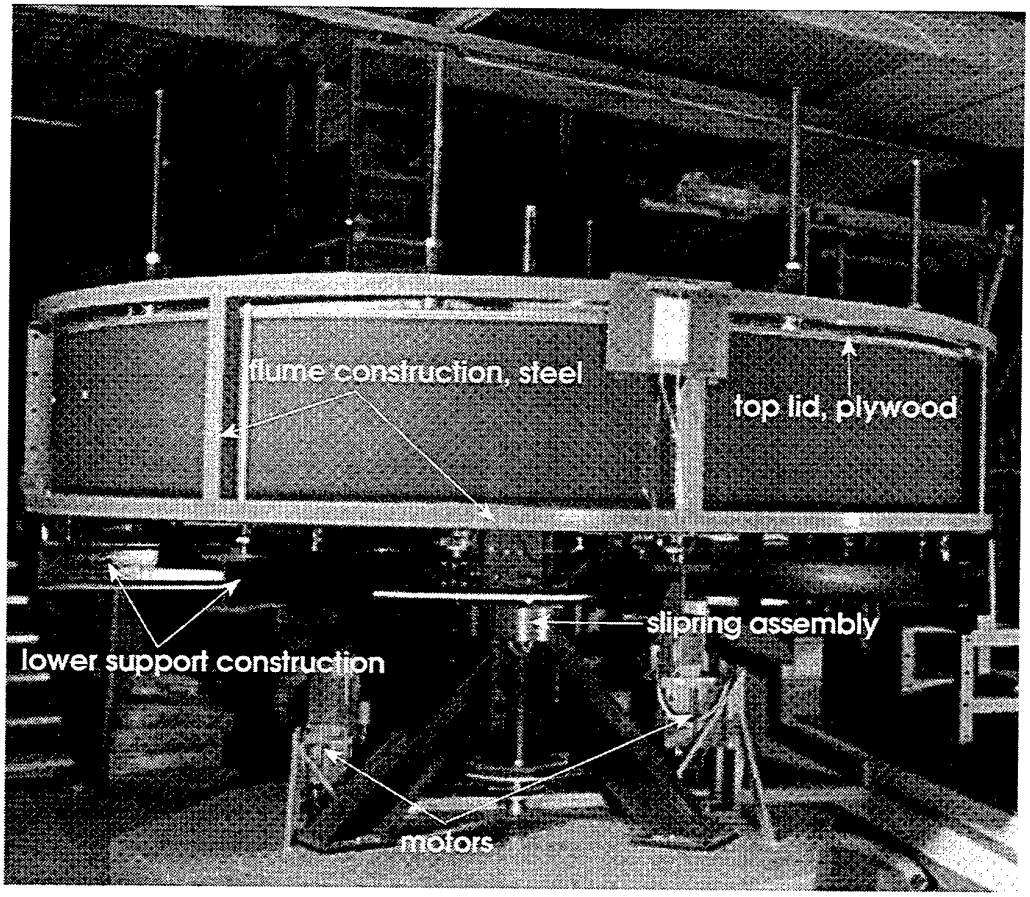

Fig. 1 Annular flume at the IWW, Aachen University of Technology

length of 1.92 mm and a width of 0.15 mm. A Fast-Fourier-Transformation (FFT) Doppler burst signal processing unit (DANTEC BSA) was used for data analysis. The probe was mounted on a traversing system which allowed radial and vertical displacement of the probe. For the measurements of the velocity components u and w the probe was mounted at the inner wall of the flume and for the velocity components u and v at the bottom of the flume (Fig. 2).

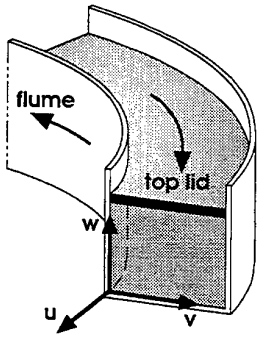

Fig. 2 Sketch of velocity components

All laser equipment and instruments were mounted on the lower support construction of the flume and were rotating with the flume. Power was transmitted by a slipring assembly (Fig. 1) and an IEEE interface was established in the same way. In this configuration the measurements could be easily remote controlled by a PC from outside the flume.

All measurements were carried out at one cross section with a width of 0.25 m and a depth of 0.175 m respectively 0.25 m during the first experiments. To prove the results of this first calibration another series of experiments with a water depth of 0.325 m is actually carried out at the IWW. The near bottom region was measured at a level of 2, 5 and 10 mm. In horizontal direction the measuring mesh has a width of 10 mm, except for the side walls, where an additional measurement at a distance of 5 mm was performed (Fig. 3). The whole cross section was divided in 728 measuring points for a water depth of 0.25 m and in 520 measuring points (Fig. 3) for a water depth of 0.175 m. With the used traversing system it was possible to execute all measurements automatically. The

data collection, the traverse system and adjustment of the laser was controlled by a PC.

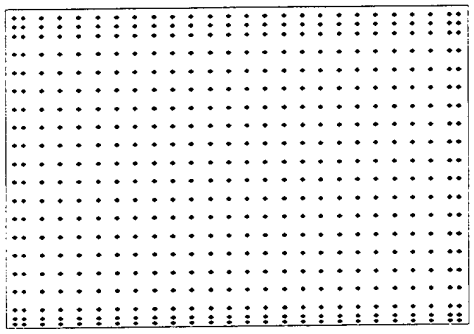

Fig. 3 Mesh of measuring points for a water depth of 0.175 m

The measuring period for each point was either limited by a time period of 100 sec or by a collection of 10000 bursts. In this way it was possible to get detailed and reliable information about the turbulent flow field at the cross section.

2.2 Correlation of different measurements

The different measurements from the side and the bottom had to be checked for correlation. This was possible by measuring the tangential flow velocity for both configurations and using the data for a correlation. About 24 to 36 points equally distributed within the cross section were chosen to be compared for the two configurations. In figure 5 the points which were used for this comparison are shown. The deviation at these points was found to be less than 8% for the tangential velocities. Figure 4 gives an example of the correlation for a water depth of 0.175 m, a flume velocity $\omega_f = 2.0$ rpm and a ratio $\omega_t/\omega_f = -1.8$.

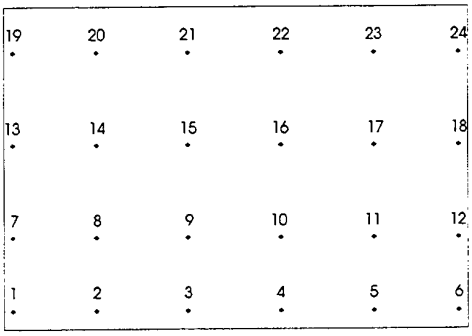

Fig. 5 Mesh of measuring points used for correlation for a water depth of 0.175 m

The good correlation between the side and bottom measurements proved the idea of using a 1D laser system. The restrictions by the rotating annular flume forced the IWW to use such a light weighted and air cooled system.

2.3 Turbulent fluctuations

The turbulent fluctuations $\overline{(u')^2}$, $\overline{(v')^2}$ and $\overline{(w')^2}$ can be determined directly with the velocity measurements. To get information about the turbulent fluctuations $\overline{(u'v')}$, $\overline{(u'w')}$ and $\overline{(v'w')}$ with an 1D laser system an additional measurement in the annular flume

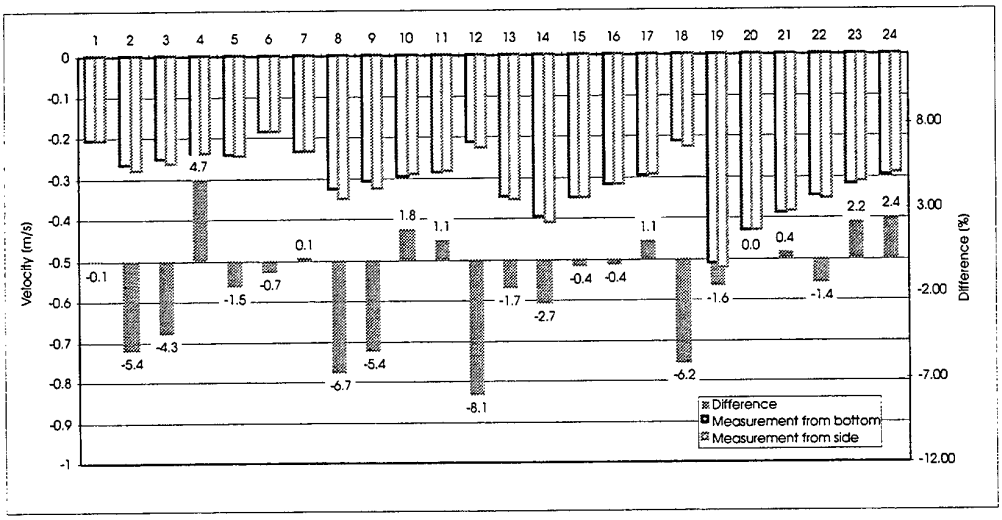

Fig. 4 Correlation of measurements from different positions for a water depth of 0.175 m, a flume velocity $\omega_f = 2.0$ rpm and a ratio $\omega_t/\omega_f = -1.8$, numbers on abscissa represent point numbers in Fig. 5

has to be carried out from the side and the bottom. In figure 6 a sketch of the adjustment and the velocity components is shown. The probe is positioned with an angel α (preferably 50 rad) to the main velocity directions and the velocity and statistics in plane P are measured.

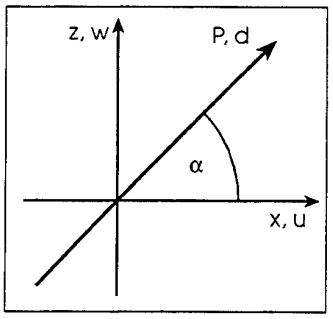

Fig. 6 Adjustment and velocity components for turbulent fluctuation measurements

With the help of the measurements in x- and z-direction it is possible to calculate the turbulent fluctuations $\overline{(u'\,w')}$ (Wiedemann 1984):

$$\overline{-u'\,w'} = -\frac{\overline{(d')^2} - \overline{(u')^2}\cos^2\alpha - \overline{(w')^2}\cos^2\alpha}{2\sin\alpha\cos\alpha} = \frac{\tau}{\rho} \quad (1)$$

Using the measurements in x- and y-direction with an additional measurement from the bottom the turbulent fluctuations $\overline{(u'\,v')}$ can be calculated respectively. The turbulent fluctuation $\overline{(v'\,w')}$ can not be derived, because measurements from inside the flume would have been necessary which was not possible due to disturbances of the flow field.

3. MEASUREMENTS

The experimental program was set up to determine the optimal ratios of rotational speeds ω_t/ω_f for deposition and erosion experiments as well as a relation between the water depth and the applied shear stress by changing the rotational speeds of the top lid and the flume. One has to distinguish between the two needs which can not be fulfilled simultaneously in an annular flume:

1 minimised secondary flow circulations for deposition experiments
2 uniform distribution of the shear stress near the bottom of the flume for erosion experiments

By previous calibrations with Prandtl tubes the approximate ratio ω_t/ω_f was already known for the annular flume at the IWW (Spork et al. 1994). The following experiments were carried out for a water depth of 0.25 m:

criteria 1: $\omega_f = 2.0$ ω_t/ω_f = -2.100, -2.150, -2.175, -2.200, -2.300
criteria 2: $\omega_f = 2.0$ ω_t/ω_f = -1.900, -1.925, -1.950, -1.975, -2.000
verification: $\omega_f = 0.5$ ω_t/ω_f = -1.975, -2.175
$\omega_f = 4.0$ ω_t/ω_f = -1.975, -2.175

and for a water depth of 0.175 m:

criteria 1: $\omega_f = 2.0$ ω_t/ω_f = -1.70, -1.80, -1.90
criteria 2: $\omega_f = 2.0$ ω_t/ω_f = -1.50, -1.60, -1.70
verification: $\omega_f = 0.5$ ω_t/ω_f = -1.80
$\omega_f = 4.0$ ω_t/ω_f = -1.80

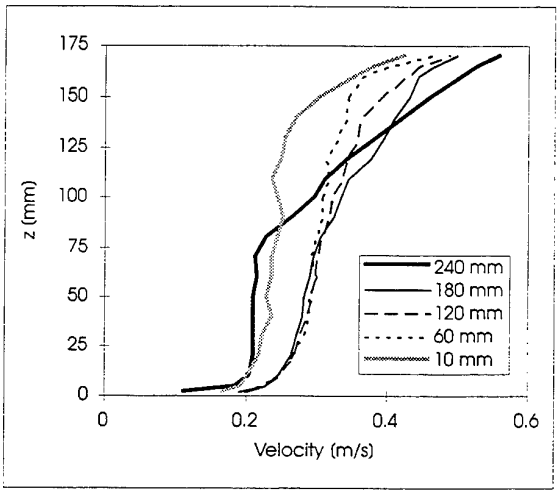

Fig. 7 Tangential velocity profiles over the cross section for ω_f= 2.0 rpm and ω_t/ω_f = 1.8

In figure 7 different tangential velocity profiles over the cross section are presented. It can be seen clearly that velocity increases from inside (10 mm) to outside (240 mm) of the flume, due to the fact, that a constant angle velocity results in higher velocity in tangential direction with increasing radius. This increase implies a non-uniform shear stress distribution.

All vector plots presented in the following have been smoothed once to give a homogeneous flow field.

3.1 Minimised Secondary Flow Circulations

In figures 8 to 10 the development of a large clockwise secondary flow circulation is visible, which is generated by the centrifugal forces at the top lid and dominates the flow field. Besides this the two much smaller counter clockwise secondary flow circulations at the bottom of the flume are generated by the flume itself. With increasing ratios the velocity of the top lid

increases simultaneously, while the generated secondary flow circulation grows and influences the flow at the bottom. Figure 9 represents the status of minimised secondary currents for the flow near to the bottom. The outward flow from the lower secondary flow circulations is interrupted by the flow from the large secondary flow circulation from the top lid.

Even if it is possible to establish experimental conditions with minimised secondary currents, the upward velocity is still in the magnitude of the fall velocity of fine material (outer side of the flume Fig. 8 to 10), implying a limitation in the use of annular flumes for deposition experiments (Booij 1994).

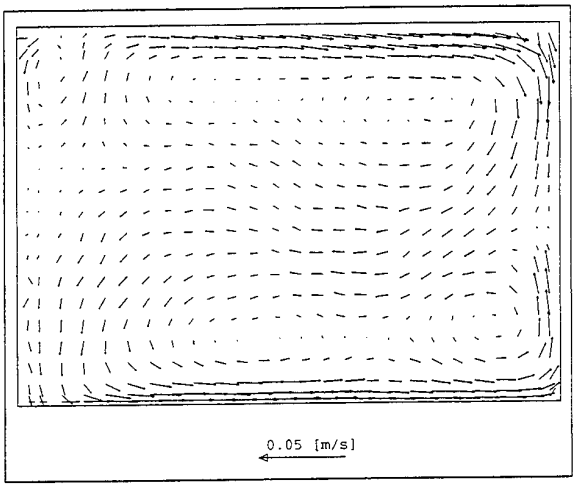

Fig. 8 Secondary flow field for ω_f= 2.0 rpm and ω_t/ω_f = 1.7, water depth: 0.175 m, left side represents inner wall

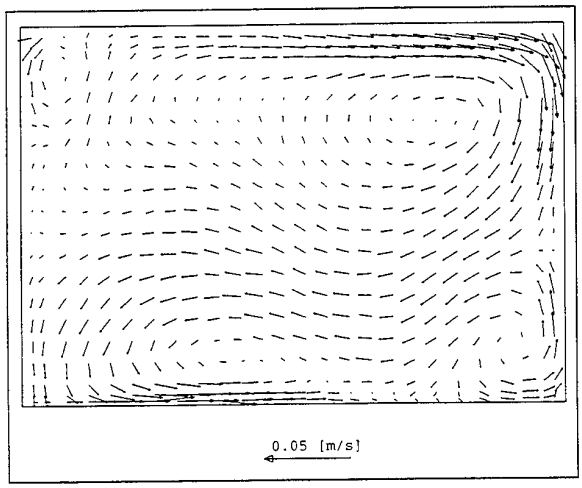

Fig. 9 Secondary flow field for ω_f= 2.0 rpm and ω_t/ω_f = 1.8, water depth: 0.175 m, left side represents inner wall

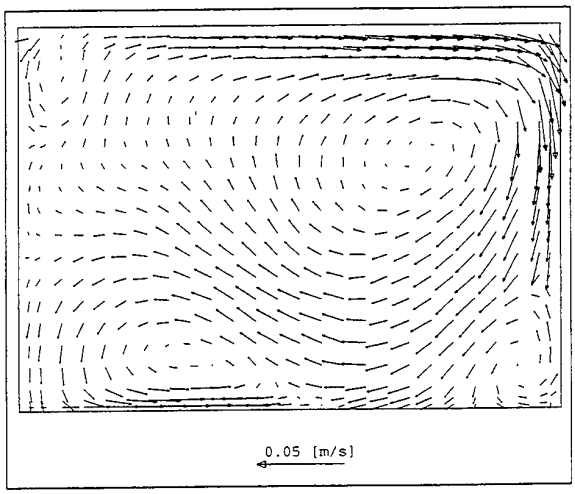

Fig. 10 Secondary flow field for ω_f= 2.0 rpm and ω_t/ω_f = 1.9, water depth: 0.175 m, left side represents inner wall

For a minimised secondary flow circulations (criteria 1) a ratio ω_t/ω_f = -2.175 was chosen for a water depth of 0.25 m and a ratio of ω_t/ω_f = -1.8 was chosen for a water depth of 0.175 m.

3.2 Uniform Shear Stress Distribution

As the measurements for deriving the turbulent fluctuations have not been finished yet, the IWW used the profile method to decide about the optimised ratio for criteria 2. The profile method uses the logarithmic law of the wall to determine the bottom shear stress. Thus the velocity distribution is necessary in the decision making process. Figure 11 gives an isoline plot of the tangential velocities for a ratio of ω_t/ω_f = -1.6. It is visible that the velocity distribution over the cross section is almost uniform near the bottom.

In figure 12 the velocity distribution for a ratio of ω_t/ω_f = -1.8 is presented. In this figure the distribution is not uniform. At the inner wall the gradient is lower than at the outer wall and the isolines do not represent a symmetric profile, resulting in differences in the shear stress distribution.

Out of figure 11 and 12 it can be seen that there is only a slight influence of the ratio on the shear stress distribution. The non sensitivity of the shear stress distribution was also proven by previous investigations (Spork et al. 1994, Booij 1994).

For a uniform distribution of the bottom shear stress (criteria 2) a ratio ω_t/ω_f = -1.975 for a water depth of 0.25 m and a ratio of ω_t/ω_f = -1.6 was chosen for a water depth of 0.175 m.

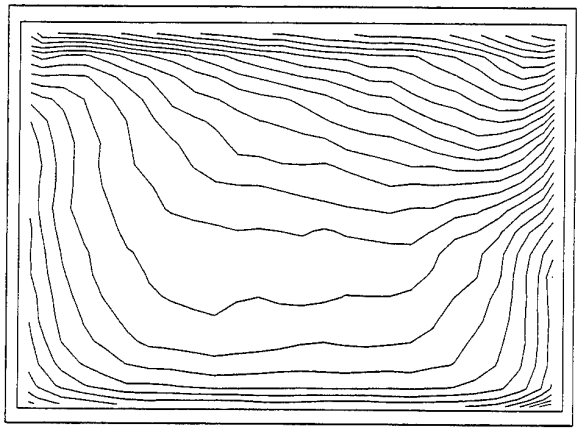

Fig. 11 Isolines of tangential flow velocity for ω_f= 2.0 rpm and ω_t/ω_f = 1.6, water depth: 0.175 m, left side represents inner wall

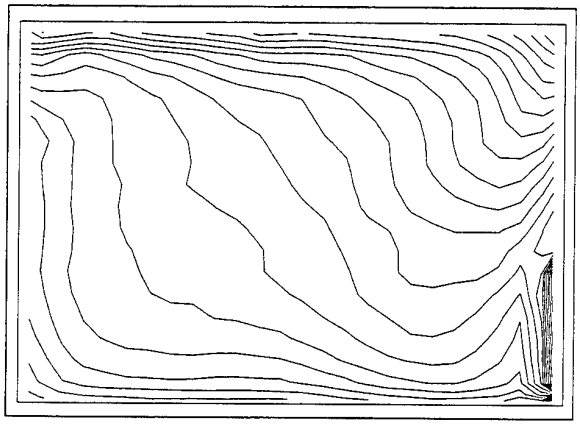

Fig. 12 Isolines of tangential flow velocity for ω_f= 2.0 rpm and ω_t/ω_f = 1.8, water depth: 0.175 m, left side represents inner wall

3.3 Verification of optimal ratios

In figure 13 a measurement with a flume velocity of 0.5 rpm and a ratio of ω_t/ω_f = 1.8 is given and in figure 14 the flume velocity is 4.0 rpm while the ratio is kept constant. Comparing these secondary flow patterns with figure 9 presenting the secondary flow at the same ratio but with a flume velocity of 2.0 rpm it can be seen that there is no or only slight change in the dimensions of the secondary flow circulations. Only the magnitude of the velocities increases with increasing turning velocities of the flume.

The series of experiments with flume velocities of 0.5 rpm and 4.0 rpm and the optimised ratios ω_t/ω_f showed that the ratio is independent from the rotational speed of the flume for the same water depth.

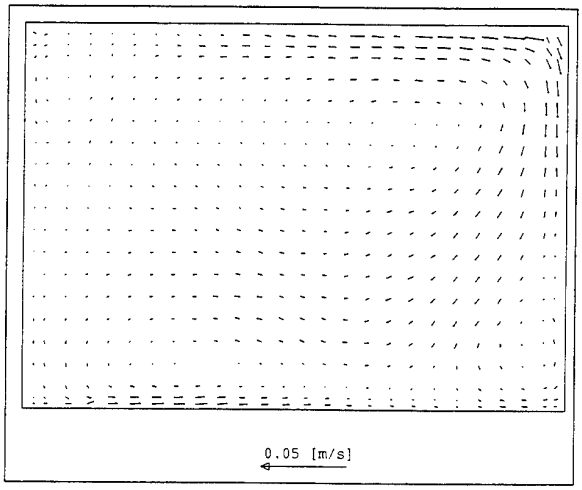

Fig. 13 Secondary flow field for ω_f= 0.5 rpm and ω_t/ω_f = 1.8, water depth: 0.175 m, left side represents inner wall

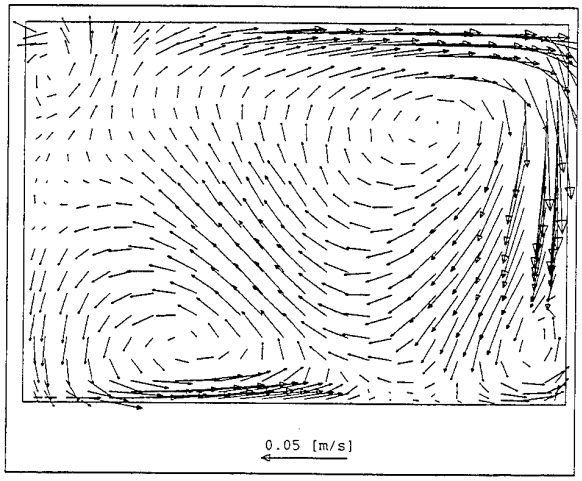

Fig. 14 Secondary flow field for ω_f= 4.0 rpm and ω_t/ω_f = 1.8, water depth: 0.175 m, left side represents inner wall

3.4 Comparison

As there are other annular flumes existing, which have calibrated as well, a comparison to those calibration measurements should be made. Annular flumes are constructed in different dimensions, resulting in different calibration values. To make the results comparable the ratio of water depth and channel width can be used. Also the diameter plays a role in the calibration measurements, as the curvature influences the secondary currents. Up to now only two other laser Doppler measurements are known in annular flumes, namely by

Krishnappan (1993) and Booij (1994) and one investigation with an electromagnetic current meter by Karelse (1990).

Krishnappan (1993) did not determine optimised ratios of ω_t/ω_f, so unfortunately a comparison is not possible. Especially because he did not carry out any detailed flow field investigations.

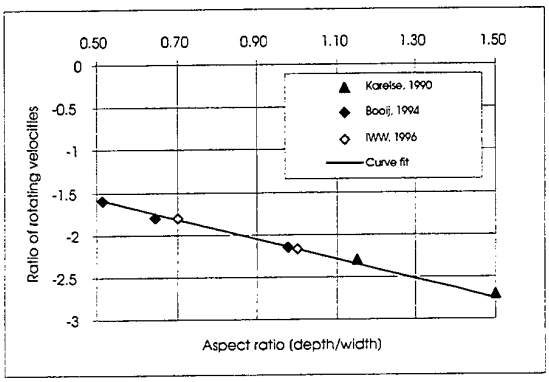

Fig. 15 Comparison with other annular flume investigations

Booij (1994) has done an accurate and extensive measuring program for the calibration of the annular flume at Delft University. The relative curvature (channel width/mean radius of the channel) for both flumes is comparable. For the annular flume at Delft University the relative curvature is 0.16 and for the annular flume at the IWW it is 0.154. The values of optimal ratios found in the investigations from Booij (1994) agree very much with those found in this investigation (Fig. 15).

Also the investigations by Karelse (1990) for the annular flume at Delft Hydraulics fit into a curve fit (Fig. 15), even if the relative curvature with a value of 0.19 is slightly different.

4. CONCLUSIONS

By using a 1D laser Doppler velocimetry system reliable information was obtained about the complex 3D flow field in the annular flume at Aachen University of Technology. The measurements for deriving the turbulent fluctuations are actually going on.

Optimal ratios ω_t/ω_f of rotational speeds of the top lid and the flume were determined. The criteria of minimised secondary flow circulations for deposition experiments as well as the criteria of a uniform bottom shear stress distribution over the cross section for erosion experiments can be fulfilled by using different ratios ω_t/ω_f. The ratios ω_t/ω_f are dependent on the ratio of water depth and channel width of the annular flume, but do not show a dependency on the absolute speed of the top lid and the flume.

Even minimising the secondary currents, the upward velocity components still stays high. Depending on the rotational speed of the top lid the upward velocity is in the order or may even be higher than the settling velocity of fine materials which shall be investigated in the flume.

A good agreement to other investigations was shown, proving either results as they were carried out with different measuring devices and annular flumes with slightly different dimensions.

It can be concluded that the laser Doppler velocimetry measurements gave a good calibration of the annular flume at the IWW and lead to a better knowledge and understanding of the complex flow field in annular flumes in general.

REFERENCES

Booij, R. 1994, Measurements of the Flow Field in a Rotating Annular Flume, Communications on Hydraulic and Geotechnical Engineering, Report no. 94-2, Delft University of Technology, Faculty of Civil Engineering, Hydraulic and Geotechnical Engineering Division, Delft

Karelse, M. 1990, Velocity and Bed Shear Stress Measurements in the Annular Flume, Rep. Z0159-52, Delft Hydraulics, Delft (in dutch)

Krishnappan, B. G. 1993, Rotating Circular Flume, Journal of Hydraulic Engineering, vol. 119, no.6, pp. 758 - 767

Spork, V., Ruland, P., Schneider, B. & Rouvé, G. 1994, A new Rotating Annular Flume for Investigations on Sediment Transport, International Journal of Sediment Research, vol. 9, no. 3, pp. 141 - 147

Wiedemann, J. 1984, Laser-Doppler-Anemometrie, Springer-Verlag, Berlin, Heidelberg, New York, Tokyo

A STUDY OF THE FLOWS IN A TORE® SLURRY TRANSPORTATION UNIT

M. G. Faram, N. Syred, T. O'Doherty

Division of Mechanical Engineering & Energy Studies
University of Wales, Cardiff, UK

ABSTRACT

The TORE® is a fully fluidic, non-moving part device, that utilises vortex flows for the fluidization and transportation of slurries. Laser Doppler anemometry has been applied to characterise the flows in the absence of the second phase. However, as a compromise, the TORE® was mounted in a confined region. These results are presented for a series of design variations.

Throughout, highest turbulence levels have been found to occur in a region close to the vortex centre, in the region of particle entrainment. Spectral analysis of data obtained in this region suggests the occurrence of a precessing vortex core (PVC), a phenomena which, it is believed, may be of importance in TORE® operation.

Subsequently, correlations have been made with corresponding performance data, and suggestions have been made as to which flow features, and hence, which design settings, are most suitable to give a particular set of output characteristics.

1. INTRODUCTION

The transportation of solid materials in suspension in a fluid medium is encountered in many engineering situations. Slurries are transferred between process stages, for example, in the mineral processing and chemical engineering industries, and also in the food production industry. Other situations include mineral recovery and dredging applications, the larger end of the scale being the long distance transportation of materials via cross country pipeline.

Slurry pumping equipment can be classified into two broad categories; direct and indirect pumping systems. Direct pumping systems are those in which the pre-mixed slurry material is pressurised directly by the primary displacement device. These include roto-dynamic and positive displacement pumps, respective examples being centrifugal and piston pumps. Indirect pumping systems are those in which the carrier fluid is pressurised prior to combination with the solid phase. Perhaps the most well known example of this is the jet pump.

Perhaps the most widely used type of slurry pump used presently is the centrifugal type. However, there are many problems associated with the use of such devices, and, indeed, other direct pumping devices. These problems have typically been associated with wear. In order to escape these problems, attempts have been made to develop various forms of non-moving part, fluidic pumps. Often, this has been at the expense of other pumping characteristics, and as a result such devices have currently obtained limited commercial success, often finding applications in those situations in which more conventional equipment would be inherently unsuitable.

The TORE® is a fully fluidic, non-moving part device, utilising vortex flows for the fluidization and transportation of slurries (US Patent: Drobadenko & Lukonina (1990)). It can be driven by a standard type water pump, and, given this, falls into the category of an indirect transport system. It was originally developed by the Moscow Geological Prospecting Institute of the former USSR, where trials were carried out during the 1980's in Russian mines. Subsequently, a company has been set up in the UK, Merpro Process Technologies Ltd, to seek commercial applications of the device. A number of installations now exist, mostly involving the TORE® as part of a larger overall process.

The objectives of the research in hand were to help to characterise the operation of the TORE® for a range of parameter variations, such that the mechanisms behind its operation could be more fully understood. Clearly, this would aid in future developments of the design.

The measurement of flow characteristics within the body of concentrated solid/liquid mixtures has many associated problems. Various non-intrusive techniques such as nuclear magnetic (NMR) imaging and pulsed neutron activation (PNA) have emerged, and have been successfully applied to relatively simple flow situations (Ding et al. (1993), Porges et al. (1988)). However, besides being inherently costly, such technologies are still somewhat specialised. Refractive index matching techniques used in conjunction with laser Doppler anemometry have also provided useful results (Wildman et al. (1992)), but have generally been applied to

fairly confined flow volumes. Given the potential limitations of these techniques with regards to the current studies, preliminary work has focused on the case in which the second phase was absent, but with the TORE® mounted in a confined vessel. This was to help to represent the confinement that might be imposed by a surrounding bed of solid material. LDA has been applied throughout.

The results of the flow characterisation studies are presented in the paper. The effect of the design variations considered are discussed with reference to results obtained during corresponding trial work carried out in which the second phase was present.

2. THE TORE® UNIT

Figure 1 shows a sectional view through a TORE® unit representative of that considered in the current research. A schematic representation of a typical installation in which the TORE® is mounted in a pressure vessel is shown in Figure 2.

The unit comprises of a swirl chamber, feeding to an annulus between a pair of concentric tubes. The swirl chamber is fed, tangentially, by a standard type water pump. The two tubes terminate at a point in the region of particle entrainment. The central tube, the slurry discharge, leads vertically up through the centre of the swirl chamber before connecting to the slurry pipeline. As a result of the turbulent swirling flow exiting from the annulus, mixing occurs between the solid and liquid phases. The mixed slurry material is then passed via the discharge tube to a slurry pipeline.

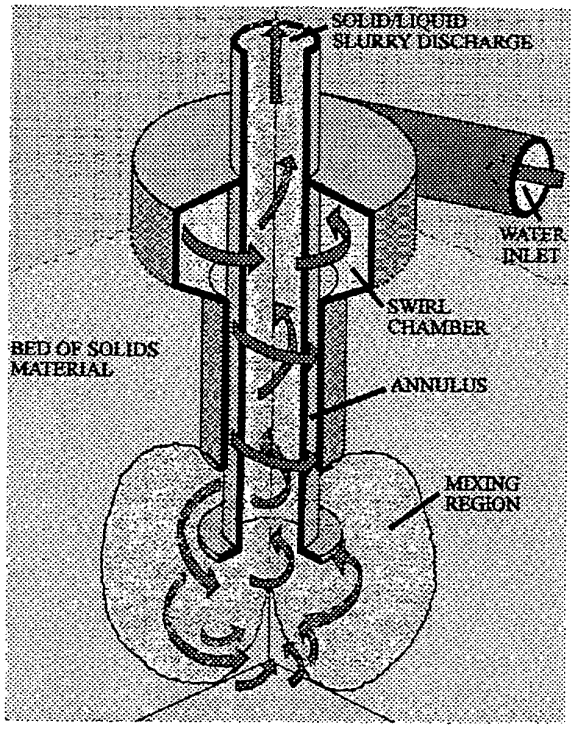

Figure 1 90° Section Through the TORE® (Schematic)

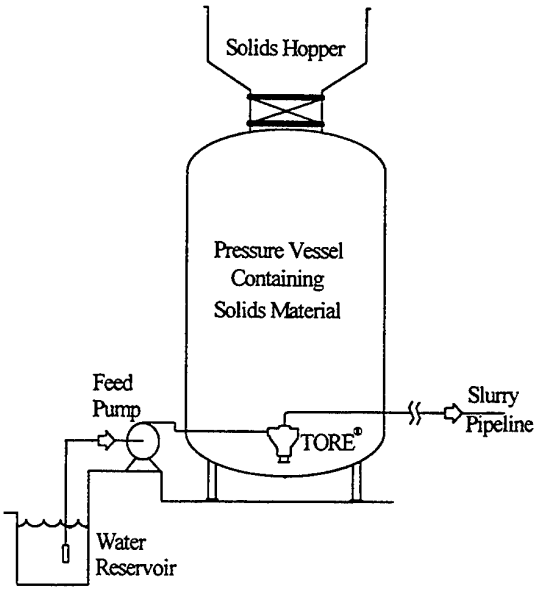

Figure 2 Typical Installation in a Pressure Vessel

Results obtained to date have revealed that, by adjustment of the design parameters, the slurry consistency can be varied over a broad range. With this versatility, it is envisaged that the device could be adapted for use in a wide variety of situations.

The TORE® investigated in the current work was one with a discharge diameter of 50 mm. The annulus inner/outer diameters were 60 and 80 mm respectively, giving an annulus to discharge area ratio of close to unity. The swirl chamber, fed by a single tangential inlet of 50 mm diameter, had an outer diameter of 175 mm, giving a geometrical swirl number of around 2.5 at the annulus exit.

The swirl chamber and inlet section of the unit were constructed of steel, while the inner/outer tubes were constructed of perspex. The tubes were interchangeable, allowing variation of their relative lengths, although for current trials, the central tube was set at 185 mm length from the point at which the annulus joins the swirl chamber. The discharge tube foot was also removable, allowing the effect of this design feature to be investigated.

3. EXPERIMENTAL TEST FACILITY

The overall objectives of the research at Cardiff were to study both the performance of the TORE® and the principles behind its operation. Since this was to involve both single phase and two phase studies, modifications to the test facility were necessary for each of the areas of investigation.

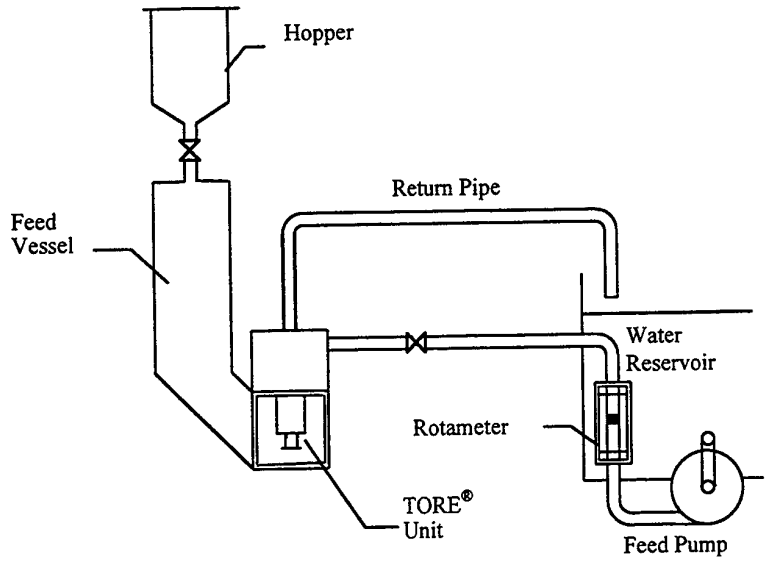

Figure 3 Schematic of the TORE® Test Facility

A schematic of the test facility, as it was arranged for the single phase studies, is shown in Figure 3.

The TORE® was mounted such that the inner/outer tubes projected downwards into a six sided chamber (270 x 200 x 200 mm), with a distance of 70 mm between the base of the inner tube and the floor of the chamber. The underside, and two of the vertical sides were fitted with polycarbonate windows to facilitate good visual/laser access. From a third side, a feeder vessel (horizontal area 0.06 m^2) was attached. This extended to a height of 1.1 m, connecting to a 50 mm diameter pipe. The pipe fed, via a valve, to a small perspex hopper. Throughout the LDA investigations, the valve was kept closed, ensuring that the inlet and outlet flowrates to the TORE® were equal.

Feed to the TORE® was provided by a general purpose centrifugal water pump. This fed via a bank of rotameters and a valve, allowing control and measurement of flowrate. The discharge from the TORE® was fed directly back to the main water reservoir.

For the purpose of trial work in which the solid phase was added, it was necessary to make a series of modifications to the test facility. This was to allow material to be transported continuously around a loop, allowing steady state samples to be taken, but avoiding the risk of contamination of the main water reservoir with solids. Firstly, the small perspex hopper was replaced with a much larger one of volume 0.6 m^3. The 50 mm diameter pipe and valve feeding from this was replaced with a 200 mm diameter open pipe. In order to ensure that the inlet flowrate to the TORE® was equal to the discharge flowrate, a jet pump was employed, fitted at a point 0.95 m above the base of the discharge pipe. This was fed, via a turbine flowmeter, from a multi-stage high pressure centrifugal pump. By careful adjustment of flowrates, the rate of fluid induction could be controlled. The original set of rotameters used on the TORE® inlet line were replaced with a magnetic flowmeter. Following induction via the jet pump, slurry material was fed back to the solids hopper. Overflow water was returned, via a system of weirs and a filter, back to the main feed reservoir. The discharge point was moveable, allowing slurries to be diverted to a 70 litre sampling vessel.

4. LASER ANEMOMETRY FACILITIES

For the laser velocity measurements, a Dantec fibre optic system was used, utilising a 5W argon-ion laser as the power source. Running at around 2W, this was used together with a 60X40 transmitter box which incorporated Bragg cell frequency shifting at 40 MHz to remove any directional ambiguity. The probe used throughout was a 60 mm diameter Dantec 60X10 one-dimensional probe, which provided a beam spacing of 38 mm. This, coupled with a lens transmission focal length of 160 mm, gave a control volume with a length of 0.66 mm in air.

Back scatter light was collected for processing via a Dantec Burst Spectrum Analyser and the associated Burstware software package.

The flow was seeded with small amounts of titanium dioxide coated mica. A sample of, typically around 1000 Doppler bursts was taken for each measurement point. Based on this sample, estimated errors are < 5 % with a confidence level of around 95 %.

Post processing of the data was carried out using the Tecplot software package, which allows mean and rms velocity contours to be plotted.

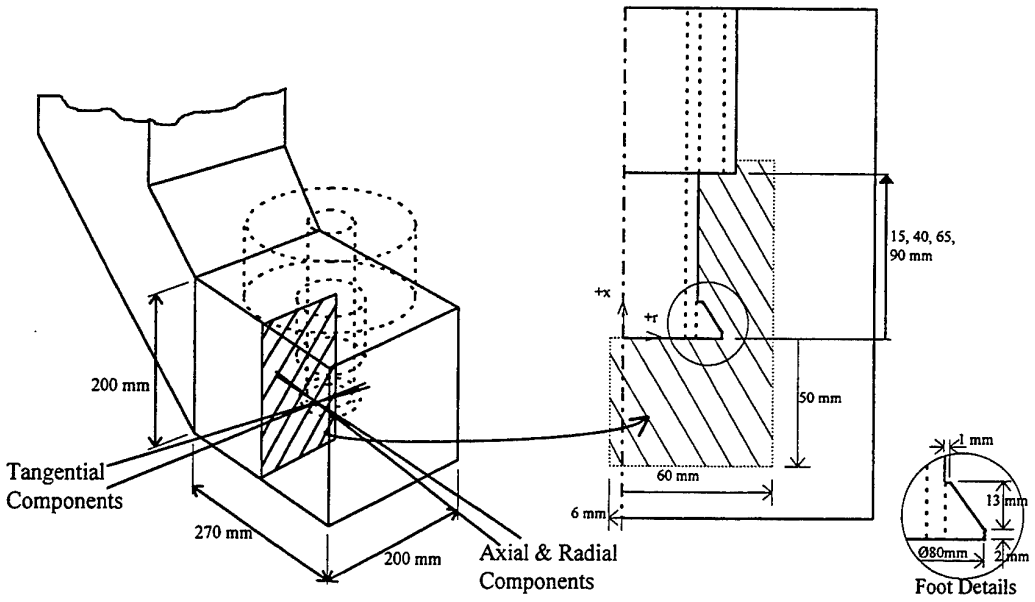

Figure 4 Measurement Regions and Foot Details

5. EXPERIMENTAL PROCEDURE

5.1 Laser Measurements

Tangential, axial and radial velocity measurements were taken via the side windows of the box in which the TORE® was mounted. These were taken in increments of 3 mm x 3 mm. The work concentrated on an area extending from the pipe centreline to a point 60 mm radially outwards, downwards 50 mm from the base of the foot, and up to a point a little above the end of the outer tube. The centreline was also crossed by 6 mm to ensure that the flow centre was included in the measurements. Measurements were taken for a number of inlet flowrates and a range of different outer tube sizes. The length of the central/discharge tube was not changed. For inner/outer tube spacings of 40, 65 and 90 mm, measurements were taken for an inlet flowrate of 230 l/min (corresponding to Re ≈ 108 000). For a 15 mm spacing, measurements were taken at 120, 200 and 290 l/min. All measurements were taken with a tapered central tube foot fitted. Details of the measurement region, and dimensions of the foot are shown in Figure 4.

5.2 Performance Trials

Throughout, the transportation of 14-25 Mesh sand (0.6 - 1.18 mm, SG 2.65) was considered. At the start, 700 kg of sand was added. Intermittent duplication of some of the tests confirmed repeatability and hence reliability of results.

For each run, settings were carefully adjusted such that the rate at which slurry was drawn away by the jet pump was matched closely with the rate of delivery to the TORE®, thus simulating a pressurised arrangement. For each setting, once a balanced state had been achieved, at least five samples were taken. For each sample, the time, weight and volume were recorded.

Design parameters varied included inlet flowrate, relative lengths of the inner/outer concentric tubes, and the design of the discharge tube foot, although the present paper reports only those results corresponding to the configurations for which LDA was applied. Using the obtained data, the slurry concentration has been calculated for each configuration. Since, in this situation, the jet pump was used largely as a tool, the slurry concentration calculated has taken into account the quantity of water added by the jet pump, and thus represents the pre-jet pump consistency.

6. FLOW CHARACTERISTICS

6.1 Overview

Throughout, the results of the laser measurements have revealed two fairly distinct sets of flow characteristics, the flows for the 15 and 40 mm tube spacing forming one set, and those for the 65 and 90 mm spacing forming the other. The most significant changes in flow features were found to occur between a 40 to a 65 mm tube spacing. For the 15 mm tube spacing, the following discussions refer, unless otherwise stated, to the cases in which the inlet flowrate was set at 200 l/min. The validity of comparisons with results obtained at 230 l/min is supported by the fact that in many cases, this configuration actually gave rise to higher velocity and rms levels in the regions of interest. Given this, the presented results mainly include those for the 15 and 65 mm configurations, these representing most clearly the principle features of the two sets. Salient features of both mean and rms characteristics observed in each of the individual sets of

Tube Spacing (mm)	Mean Velocities (m/s)	RMS Velocities (m/s)
15 (at 200 l/min)	Peak tang. ≈2.4 beneath foot, around r/R≈0.8 & ≈2.6 m/s at annulus exit. Axial max. close to CL of ≈2.4, & at annulus of ≈ -2.7. Radial max. ≈-2.0 close to CL, ≈0.9 at annulus.	Tang. rms peaks correspond to max. means & flow reversal region; ≈1.9 at centre, ≈1.1 at annulus exit. Axial & radial rms peaks; axial: ≈1.6 at centre, ≈1.1 below foot, radial: ≈2.4 at centre, ≈0.9 at annulus.
40 (at 230 l/min)	Peak tang. ≈2.9 beneath foot, around r/R≈0.3 & ≈3.7 m/s at annulus exit. Axial max. close to CL of ≈2.2, & at annulus of ≈ -2.1. Radial max. ≈-3.1 close to CL & ≈0.6 at annulus.	Tang. rms peaks correspond to max. means & flow reversal region; ≈2.2 at centre, ≈1.6 at annulus exit. Axial & radial rms peaks; axial: ≈1.5 at centre, ≈0.8 at annulus & below foot, radial: ≈1.4 at centre, ≈1.0 at annulus.
65 (at 230 l/min)	Peak tang. ≈1.6 beneath foot at around r/R≈0.8 & ≈3.0 at annulus exit. Axial max. close to CL of ≈2.4, & at annulus of ≈-2.5. Radial max. ≈-0.4 below foot at around r/R≈0.8 & ≈0.7 m/s at annulus.	Tang. rms peaks correspond to max. means & flow reversal region; ≈1.7 at centre, ≈1.3 at annulus exit. Axial & radial rms peaks; axial: ≈0.9 at r/R≈0.4, ≈0.9 m/s at annulus, radial: ≈1.6 below foot at r/R≈0.5, ≈1.3 m/s at annulus.
90 (at 230 l/min)	Peak tang. ≈1.5 beneath foot at around r/R≈0.5 & ≈3.6 m/s at annulus exit. Axial max. close to CL of ≈2.1, & at annulus of ≈ -2.2. Radial max. ≈-1.0 below foot edge at r/R≈0.8 & ≈0.7 m/s at annulus.	Tang. rms peaks correspond to max. means & flow reversal region; ≈1.8 at centre, ≈1.3 at annulus exit. Axial & radial rms peaks; axial: ≈1.1 at centre, ≈0.9 at annulus, radial: ≈1.9 at centre, ≈1.3 at annulus.

Table 1 Salient Flow Features at 200 and 230 l/min

results are outlined in Table 1. Figures 5 and 6, (a) - (c) show the mean velocities for the 15 and 65 mm cases. Figures 7 and 8 (a) - (c) show the corresponding rms values.

6.2 Tangential Direction

For each configuration, the peak tangential velocities, Figures 5 & 6 (a), are seen to occur at the point at which the flows exit from the annulus. It is evident that the flows 'flare' outwards, at an angle of around 30° for the 65 and 90 mm tube spacings. Notably, as the tube spacing is reduced, the rate of spread becomes less pronounced, the flows beginning to 'stick' to the foot more, following around to the discharge. The tangential flows beneath the foot represent a typical Rankine vortex structure, peaks occurring a short distance from the vortex centre in each case. For the 15 and 40 mm tube spacings, the peaks occur very close to the mouth of the discharge, also being of a higher value than for the 65 and 90 mm cases (Table 1). Of interest is the off-centred nature of the vortex relative to the geometrical centreline which is most evident for the larger spacings. This is most pronounced for the 65 mm tube spacing, originating at a point around r/R=0.3 adjacent to the discharge mouth, and slanting outwards from the centreline at around 30°, suggesting an unstable vortex. Subsequent spectral analysis of some of the LDA data has revealed the existence of time dependent flow features in the region below the foot. Dominant frequencies of the order 8 Hz have been identified at a position around r/R=0.6. Lower amplitude frequencies have also been identified, of around 0.2 Hz, at the centre of the flow, principally in the axial direction. It has been considered that this could represent the presence of a precessing vortex core (PVC), a three dimensional, time dependent coherent structure, also found to occur in swirl burners, cyclone dust separators, and other swirl devices (Syred et al. (1994)).

Throughout, the peak levels of turbulence, Figures 7 & 8 (a), correspond with the regions of maximum mean velocity, and also with the region of flow reversal at the vortex centre. The highest values have been found for the 15 and 40 mm tube spacing cases, Table 1, corresponding to the higher mean values also encountered for these configurations.

6.3 Axial Direction

The plots of mean axial velocity, Figures 5 & 6 (b), go further to illustrate the flaring of the flows which was observed for the 65 and 90 mm spacing cases, and also the tendency for the flows to 'stick' to the foot for the smaller spacings. As might be expected, peak velocities have occurred at the point of exit from the annulus, and also at the discharge mouth, close to the vortex centre, with a similar order of magnitude for each case. Notably, the line of flow reversal flares outwards, at around 40°, from the base of the foot for the 65 and 90 mm spacing cases. However, the reversal line pulls in towards the discharge mouth, slanting in the opposite direction, for both the 15 and 40 mm tube spacing cases.

The peak values of rms velocity, Figures 7 & 8 (b), correspond closely to the positions at which the peak tangential rms velocities occurred i.e. corresponding with the vortex centre and the annulus exit. Between the annulus and the discharge, there is also a brief increase in turbulence levels at a point adjacent to the foot, corresponding with the region of axial flow reversal. For the 15 and 40 mm tube spacings, this is very close to the foot. For the 65 and 90 mm spacings, however, this occurs at a point approaching the edge of the measurement region. Again, the peak values are significantly higher for the 15 and 40 mm tube spacing cases, the lowest being for the 65 mm spacing (Table 1).

6.4 Radial Direction

Figures 5, 6, 7 & 8 (c) show contour plots of radial mean and rms velocities for the 15 and 65 mm tube spacing cases. The overall peak mean radial velocities measured, Table 1, were those for the 15 mm tube spacing. Throughout, peak values have occurred at a point very close to the vortex centre, and also at the annulus exit. Notably for the 15 and 40 mm tube spacing cases, the flows are seen to divert towards the direction of the discharge very shortly after leaving the annulus. Consistently with other measurements, the peak turbulence levels have also been encountered in the

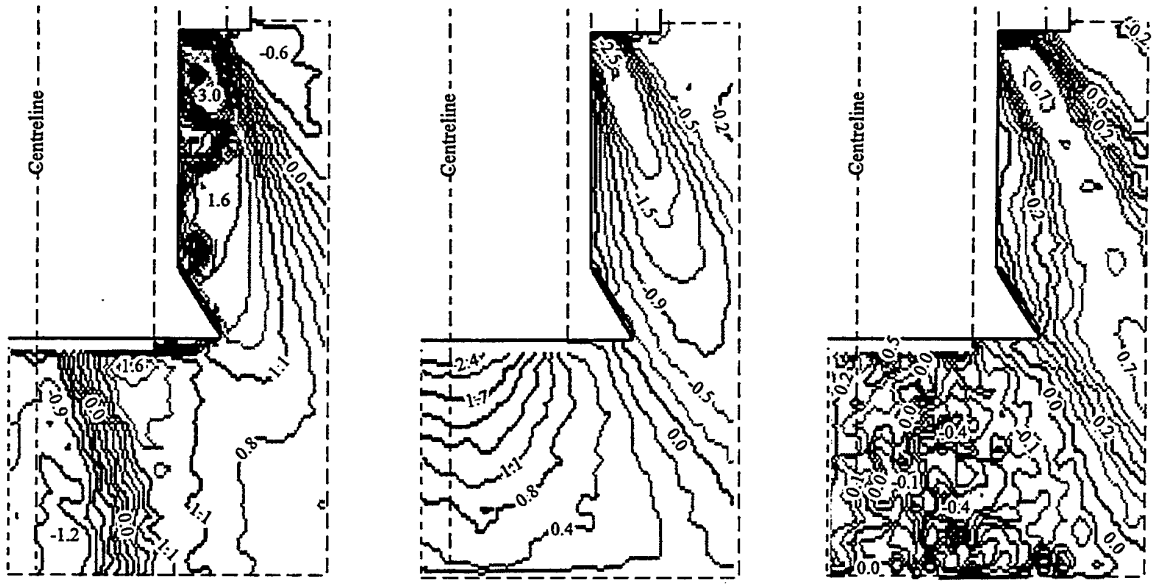

(a) Tangential (b) Axial (c) Radial

Figure 5 Mean Velocities for a 65 mm Tube Spacing (Inlet Flowrate 230 l/min)

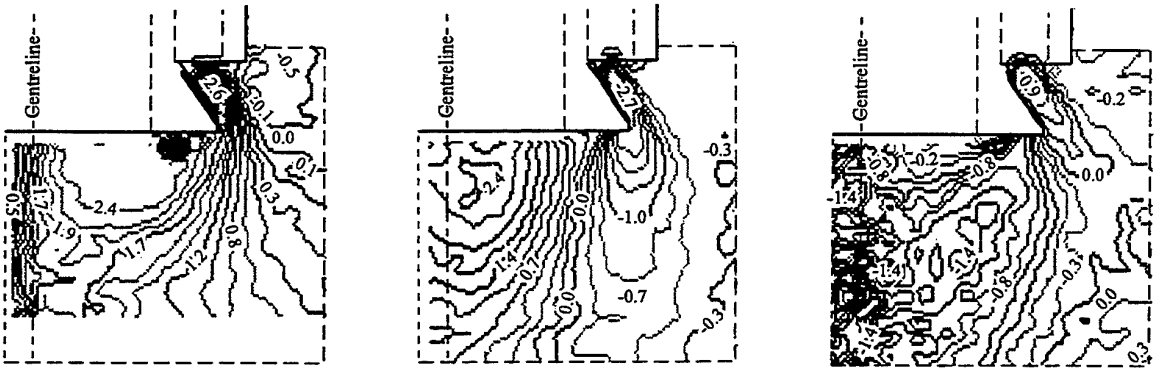

(a) Tangential (b) Axial (c) Radial

Figure 6 Mean Velocities for a 15 mm Tube Spacing (Inlet Flowrate 200 l/min)

regions corresponding with the vortex centre and the annulus exit. Interestingly, the 15 mm tube spacing, even with the smaller flowrate of 200 l/min, has given the highest turbulence levels overall, peaking at 2.4 m/s close to the vortex centre. Highest levels at the annulus exit have been for the 65 and 90 mm tube spacings, this corresponding also with the high degree of flow flaring encountered for these configurations.

6.5 Effect of Inlet Flowrate Variation

Table 2 illustrates the peak velocity and rms values measured for flowrate settings of 120, and 290 l/min. These were obtained for an inner/outer tube spacing of 15 mm. Throughout, the basic flow structure for both the mean and rms velocities was remarkably similar to that for the 200 l/min case. Comparing individual values (Tables 1 and 2), it is clear that incremental increase in inlet flowrate has given approximately proportional increase in both velocity and rms values. With care, it is considered that, within a limited range of flowrates, the results obtained for each set of design settings could be scaled up or down as required. This would eliminate the benefits to be gained from further detailed flow characterisation for more settings of flowrate.

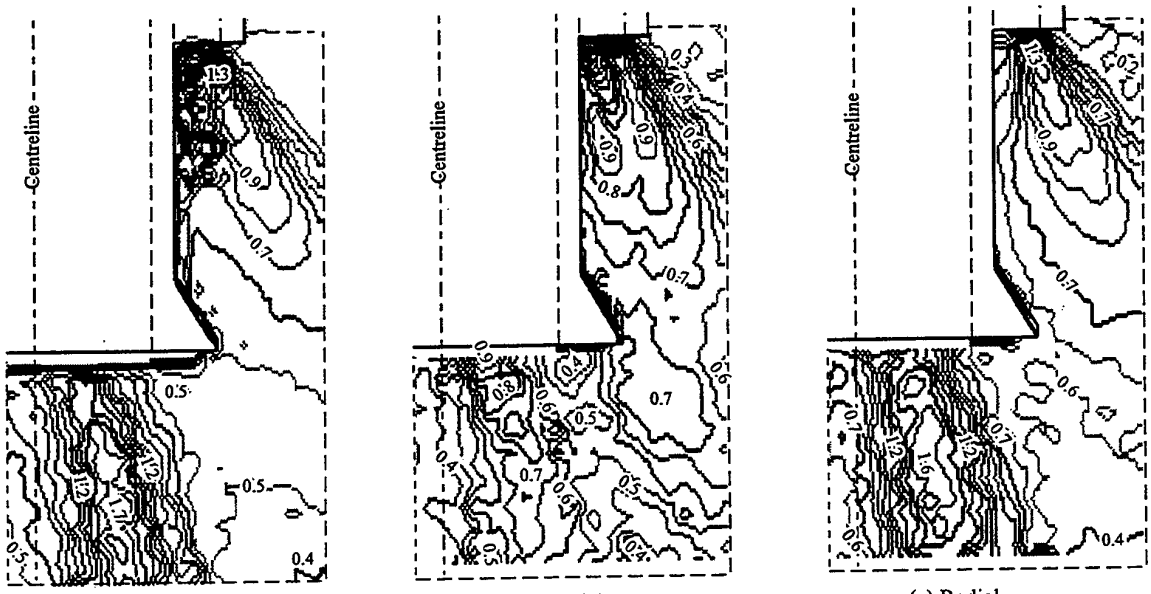

(a) Tangential (b) Axial (c) Radial

Figure 7 RMS Velocities for a 65 mm Tube Spacing (Inlet Flowrate 230 l/min)

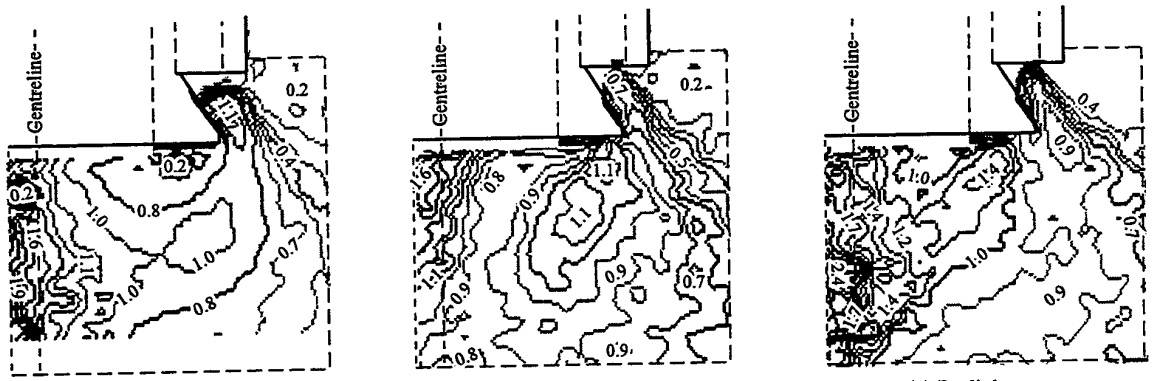

(a) Tangential (b) Axial (c) Radial

Figure 8 RMS Velocities for a 15 mm Tube Spacing (Inlet Flowrate 200 l/min)

7. TWO PHASE TRIALS

Mean discharge slurry concentration values for a range of flowrates for each of the relative tube spacings tested are shown in Figure 9. An observation based on these results, and indeed other trial work (not presented), has been that as the inlet flowrate to the TORE® is increased, the general trend is that the discharge concentration falls (with the isolated exception of the 90 mm case). It has been considered that this may be related to the fact that solids can only be removed as quickly as they can be replaced. Although the slurry concentration may be low at higher flowrates, the actual rate of removal is likely to be higher.

For TORE® inlet flowrates between 130 and 180 l/min, the slurry concentration in the discharge for the 90, 65 and 40 mm tube spacings has been close, varying a little above and below 30 % by weight. However, the 15 mm tube spacing has consistently given lower concentrations, falling from around 24 % wt. to 19 % wt. within the same range. Above a flowrate of 180 l/min, more variation is seen for each configuration. The 90 mm tube spacing has given a concentration of around 33 % at 230 l/min, showing an overall increase compared to the lower flowrates. On the whole, a 65 mm tube spacing has given the most steady values over the flowrate range, the lowest concentration being around 27 % wt. at 230 l/min. The 40 mm tube spacing has shown a far steeper concentration fall than for

Flowrate (l/min)	Mean Velocities (m/s)	RMS Velocities (m/s)
120 (15 mm tube spacing)	Tang.: ≈1.6 below foot (r/R≈0.8), ≈1.4 at annulus. Axial: ≈1.6 at CL, ≈-1.8 at annulus. Radial: ≈-1.2 at CL, ≈0.5 at annulus.	Tang. rms: ≈1.1 at centre, ≈0.6 at annulus. Axial rms: ≈1.0 at centre, ≈0.7 below foot. Radial rms: ≈1.5 at centre, ≈0.5 at annulus.
290 (15 mm tube spacing	Tangential: Not available. Axial: ≈3.4 at CL, ≈-4.0 at annulus. Radial: ≈-3.5 at CL, ≈1.1 at annulus.	Tang. rms: Not available Axial rms: ≈2.1 at centre, ≈1.7 below foot. Radial rms: ≈3.0 at centre, ≈1.3 at annulus.

Table 2 Salient Flow Features at 120 and 290 l/min

the other configurations, falling to around 22 % wt. at 230 l/min. Similar general trends have been observed in repeat runs in which the design of the discharge tube foot has been altered. For a 15 mm tube spacing, the slurry concentration falls down to around 17 % wt. at 210 l/min, the lowest concentration obtained overall, before showing an apparent increase of around 1 % as the flowrate is increased to 230 l/min. Alteration of the central tube foot design in other trial work has had most impact on performance for this setting.

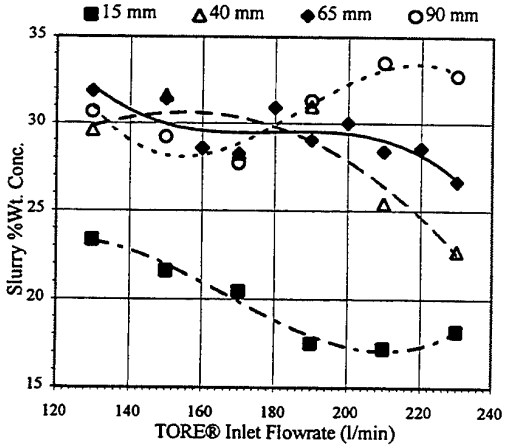

Figure 9 TORE® Performance Data

8. CONCLUSIONS

Overall, the results of the laser measurements have revealed some important features of the flows that exist in the TORE®. Interestingly, the results have fallen into two similar sets of characteristics, these being those for a 15 and 40 mm tube spacing, and those for a 65 and 90 mm spacing, the biggest changes taking place between the 40 and 65 mm setting. Variation of flowrate relative to a fixed tube spacing has shown only quantitative changes, general flow characteristics being of the same form.

The larger spacings have given a significant degree of flare of the flows as they leave the annulus. On the whole, this has been accompanied with reduced peak turbulence and tangential velocity levels in the region below the foot. Conversely, the smaller tube spacings have given a much more confined turbulent region, but with generally higher rms and tangential velocity levels in this area. The presence of a precessing vortex core (PVC), although not currently confirmed to occur in the two phase case, may be important in TORE® operation. Clearly, further research would be required to assess this.

Correlation of the results of flow characterisation with the corresponding trial results gives rise to some broad conclusions. For an inlet flowrate of 230 l/min, a consistent finding has been that as the inner/outer tube spacing is increased, the discharge slurry concentration also increases. This suggests that the increase in turbulence and peak tangential velocity levels has a controlling effect on the discharge concentration levels, giving a higher degree of slurry dilution for the smaller tube spacings. This is in contrast to the idea that a stronger vortex might lead to a higher rate of entrainment.

Overall, this research has helped to characterise TORE® operation, both in terms of operating mechanisms, and output performance.

ACKNOWLEDGEMENTS

The author, M. G. Faram would like to acknowledge the personal financial assistance provided by Merpro Process Technologies Ltd and EPSRC, both of the UK. [The TORE® is a patented product of Merpro Tortek Ltd.]

REFERENCES

Ding, J., Lyczkowski, R. W., Sha, W. T., Altobellini, S. A., Fukushima, E., 1993, Numerical Analysis of Liquid-Solids Suspension Velocities and Concentrations Obtained by NMR Imaging, Powder Technology, Vol. 77., No. 3.

Drobadenko, V. P., Lukonina, O. A., 1990, Method and Apparatus for Conveying Materials in Bulk by Liquid Pressure, United States Patent, Number 4978251.

Porges, K. G. A., Cox, S. A., Herszenberg, C., Kampschoer, C., 1988, Flow Speed Measurement and Rheometry by Pulsed Neutron Activation, ASME Fluids Engineering Division (Publication) FED, Vol. 75.

Syred, N., O'Doherty, T., Froud, D., 1994, The Interaction of the Precessing Vortex Core and Reverse Flow Zone in the Exhaust of a Swirl Burner, Proc. Instn. Mech. Engrs., Vol. 208.

Wildman, D. J., Ekmann, J. M., Kadambi, J. R., Chen, R. C., 1992, Study of the Flow Properties of Slurries Using the Refractive Index Matching Technique and LDV, Powder Technology, Vol. 73, No. 3.

LDA MEASUREMENTS OF AXIAL AND TANGENTIAL VELOCITY COMPONENTS IN A DMS CYLINDRICAL CYCLONE

B. Chiné [1, 2], F. Concha [2] and G. Ferrara [1]

[1] Dipartimento di Ingegneria Chimica, dell'Ambiente e delle Materie Prime
Universitá degli Studi di Trieste, Ple. Europa,1 34127 Trieste, Italia

[2] Departamento de Ingenieria Metalúrgica,
Universidad de Concepción, Casilla 53-C, Correo 3, Concepción, Chile

ABSTRACT

Measurements of axial and tangential velocity components have been made by laser-Doppler anemometry of a swirling flow of water in a two-stages cylindrical cyclone (Tri-Flo) used in dense medium separation (DMS) processes. A perspex model of 100 mm diameter was installed in an experimental rig and a back-pressure was applied at the tangential discharges of this cyclone. Two series of measurements were performed: a) a single stage was operated and the inlet Reynolds number varied and b) two stage were operated in two cases of equal and different values of back-pressure at the tangential exits. The results show the existence of two principal and opposite axial flows in the cyclone and a swirling flow changing from a forced vortex regime near the inlet regions to a Rankine vortex flow near the tangential exits. Asymmetry of the air-core was observed when the LDA signals were collected near the air-liquid interface. Finally the experimental data indicate that the flow depends strongly on the pressure conditions at the tangential exits.

1. INTRODUCTION

Dense medium separation (DMS) processes (also *sink and float* separation) have been known and applied industrially for the treatment of coal and metallic and non-metallic minerals for many years. Recently, there was a renewed interest in using DMS process for a number of new applications, such as industrial minerals processing, materials recycling, environmental technologies, etc.

DMS is a process applied to the separation of particles in a liquid or a fairly stable suspension of a predetermined density, chosen such that it is higher than the lighter constituents (*float*) and lower than the heavier constituents (*sink*). While in a static separator the essential separating force is gravitational in a dynamic DMS process, like that developed in a cyclone, a centrifugal movements is imposed to the flow so that the forces tending to separate heavies and lights are greater. Burt(1984) and Ferrara (1995) describe the different aspects of the separation in DMS processes.

One of the dynamic separators which is attracting greater interest is the DMS cylindrical cyclone Tri-Flo (Figure 1), because it seems to ensure high separation sharpness due to its multi-stage separation. The device, subject of the present work, consists of two equal cylindrical compartments connected through an axial orifice. Each compartment has an involute feed inlet, an involute outlet (*sink* discharge) and an axial *float* passage (vortex finder). The dense medium is fed through the *feed* inlets establishing a strong swirling flow with a central low pressure region, which causes the formation of an air-core along the axis of the vessel. The solid material enters axially into the first compartment, where the heaviest particles are separated in the vortex flow and are removed through the first involute outlet, while the lightest ones are carried forward into the second cyclone and are treated again to produce a new heavy class and a final *float* product. For one density separations the two stages are fed

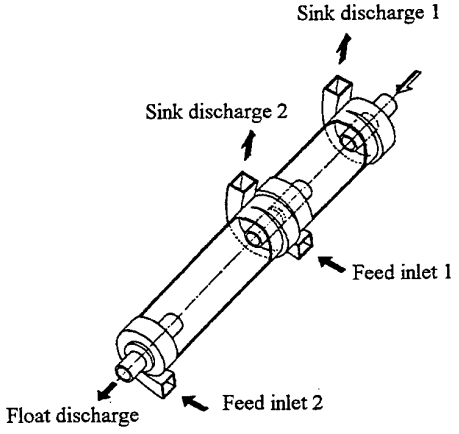

Fig. 1 The two stage Tri-Flo separator.

with the same medium, with the two *sink* flows being combined into a single product.

A comparison between the cylindrical separators and other vessels has often been the object of discussion, but compared to the large body of works dealing for example with the conical cyclone, a few investigations (Kirchberg and Schulze, 1968; Baranov *et al.*, 1984; Hacioglu and Turner, 1985) have been performed on the DMS cylindrical cyclones.

In order to obtain a more detailed knowledge of the characteristics of the flow and a better understanding of the separation process in the DMS cylindrical cyclone, it was decided to carry out measurements of velocities in the Tri-Flo centrifugal separator. Since intrusive measurements in cyclones could be of questionable values, being that vortex flows are sensitive to disturbances originated by the probes, it was decided to perform the measurements with a laser-Doppler anemometer, which permits a complete no-intrusive mapping of the flow field. The experimental work was performed in the laboratories of the Department of Metallurgical Engineering at the University of Concepción (Chile).

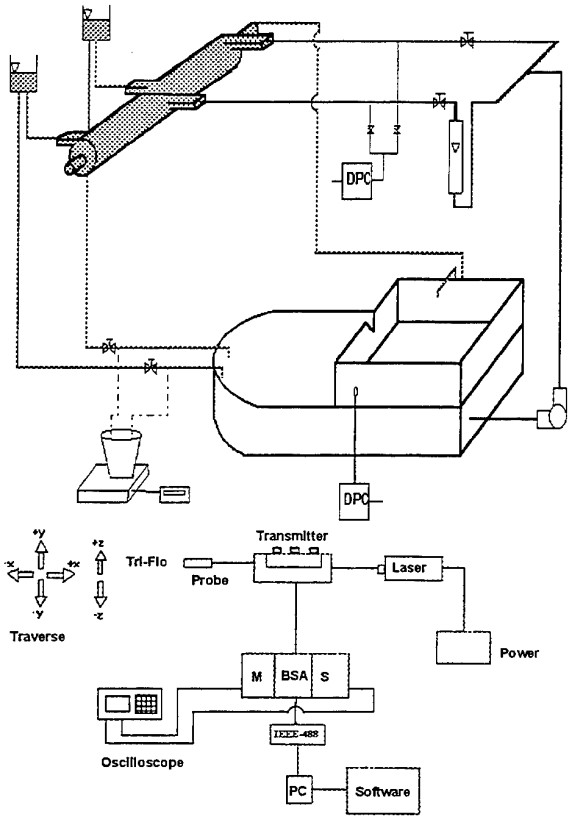

Fig. 2 The experimental rig.

2. EXPERIMENTAL SET-UP

This section describes briefly the experimental arrangement used during the investigation and which is shown in Figure 2. More details are given by Chiné (1995) in his research work.

2.1 Flow Configuration

A well machined perspex model of the Tri-Flo separator was installed in the closed rig (Figure 1) and was positioned with an inclination angle of 15° about the horizontal direction. This inclination was chosen in such a way that the cyclone was operated in the counter-current mode, i.e. in each compartment the *sink* flow moved upwards against the gravity. The geometric dimensions of the two equal cyclonic compartments are given in Table 1.

Water was utilised in the experimental test and it was admitted to the two stages of the cyclonic separator under controlled flow conditions. The fluid was pumped from a 0.665 m^3 sump and was split in two currents by a set of valves. *Feed* pressure and flow rates were monitored with a differential pressure cell and a rotameter. Back-pressure was applied at the two involute outlets (*sink* discharge) using a water column and the two flows, which discharged against the back-pressure, were measured by sampling volumes of water. The axial flow through the *float* exit was monitored with a differential pressure cell. The temperature of the fluid was controlled within 23÷24°C with a cooling coil in the installed sump.

2.2 Measurements Techniques

The velocity profiles inside the vessel were measured using the laser-Doppler velocimeter shown schematically in Figure 2. The velocimeter is a Dantec two component fibre optic system with Burst Spectrum Analysers (BSA) and an automatic computer controlled three component traverse system.

Coherent light with wavelength in the range 457÷514.5 nm from a 300 mW Argon-Ion laser was directed to a transmitter box where frequency shifting, to remove the direction ambiguity of the velocities (Durst *et al.*, 1981; Adrian, 1983), and colour separation were performed. A Bragg cell splits the light beam in two beams with a 40 MHz frequency shifting. These beams then pass through a dispersion prism which provides two

Table 1 Dimensions of the Tri-Flo model (mm)

Inner diameter	100
Length of each compartment	345
Wall width	10
Inlet section	20x20
Outlet section	25x25
Float discharge diameter	30
Orifice between stage 1 and 2 (diam.)	40

green (514.5 nm) and two blue (488 nm) light beams. The shifted and direct beams are led to output aperture, where fibre manipulators are used to focus the beams into fibre optic cables. Then a probe with a 160 mm focal length lens and a beam intersection angle of 0.236 rad causes the four beams to intersect. The same lens collect the scattered light coming back from the measurement volume, since the air-core doesn't permit the use of the forward-scattering mode. Finally the back-scattered light is separated into green and blue components and is directed onto two photomultipliers.

The Doppler signals were processed in two Burst Spectrum Analysers with fast Fourier transform in order to extract the Doppler frequencies. The BSA master for measuring the axial component of the velocity and the BSA slave for the tangential component were set to run in a continuos data collection mode. Data was transferred to a computer for processing via a IEEE-488 interface.

In order to map the velocity distribution throughout the cyclonic separator the probe was moved in front of the vessel using a highly accurate three component (x-y-z) traverse system, which was controlled by a computer via a RS-232 interface.

The BurstWare 2.0 software package was used to collect all the data, move the traverse, process the data and to present the results.

To minimise the optical refraction of the laser beams at the curved walls, the vessel was immersed in a water-filled jacket (Fingerson *et al.*, 1991), thus the change in refractive index, n, and hence the also the grade of refraction, on passing from the surrounding water (n=1.33) to the perspex (n=1.49) was smaller than it would have been in the absence of the jacket.

Measurements of the V axial and W tangential velocity components profiles were thus performed on the axial half plane placed on the sink discharges side. The laser beam intersection was moved on this half plane, from the wall towards the central air-core interface, using a radial step of 1.35 mm. For one predetermined operation condition eleven equally spaced radial velocity profiles were obtained for each cyclonic compartment. No velocity measurements were carried out close the wall. The position of the laser beam intersection within the fluid was calculated by employing the equations given by Gardavský *et al* (1989). Then, it was practically implemented using a relationship obtained by traversing the laser beam intersection between the opposite extreme locations at the inner side of the wall.

Finally, the fluid in the closed experimental rig was seeded with latex painting particles and a sample of 1000 velocity data was collected in each measuring point. Due to the small error, no refraction corrections were applied to the interference fringe spacing of the velocity data samples.

3. RESULTS AND DISCUSSION

Since the first observations made by A M. Binnie (Binnie and Hookings, 1948) evidence existed that swirling flows are very complex. In fact, air-core displacement, vortex core precession, recirculation etc. are important phenomena exhibited in cyclonic flows. In an interesting work Escudier *et al.* (1980) showed with the aid of LDA that, under a strong swirling flow regime, reverse flow in proximity of the axis of a vortex tube can occur.

During our LDA measurements it was possible to observe that the air-core was asymmetric and that the oscillations of air-liquid interface produced some problems when the data were collected near the air-core region. Figure 3 presents two LDA time series for the tangential velocity component W obtained in two successive measurement points (1.35 mm distant) near the air-core region, when the inlet Reynolds number was $6x10^4$. As soon as the measurement volume enters the displacement zone of the oscillating air-liquid interface some velocity data appear around the zero value (Figure 3a). Then, when the traverse moves to the successive point, placing the beam intersection closer to the interface, the number of zero values grows and the RMS value of the measurement is greater (Figure 3b). Raw estimations of the interface displacement and of the air-core diameter were made, thus establishing the measuring grid in the radial direction.

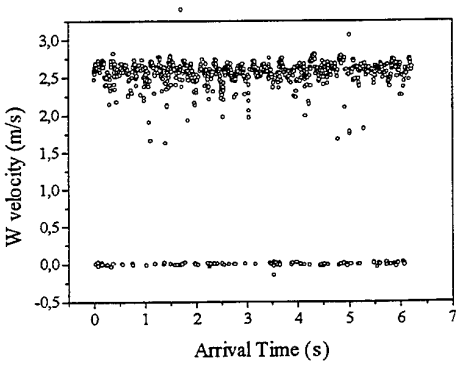

(a)

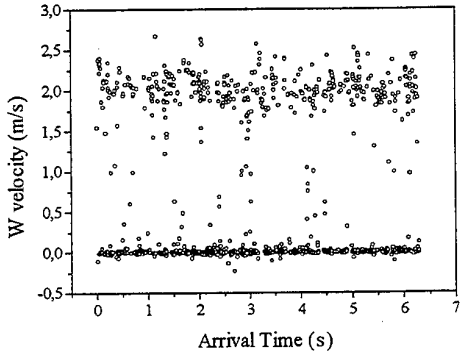

(b)

Fig. 3 Time Series for LDA data near the air-core.

3.1 Measurements With Only One Operating Stage

In this section we present results of axial and tangential velocity components obtained when the Tri-Flo was operated with only one stage. This case represents the swirling flow inside a counter-current cylindrical cyclone with axial and tangential discharges.

The radial profiles of the axial and tangential velocity components are shown in Figure 4 in eleven different sections inside the cyclone. The LDA data were obtained for a *Re* of $6.3x10^4$ by measuring in the second cylinder, where radial steps of 1.35 mm and axial steps of 25.2 mm were used (the section 1 was 7 mm distant from the closest vortex finder). The measurements of the V component show the existence of a complex flow

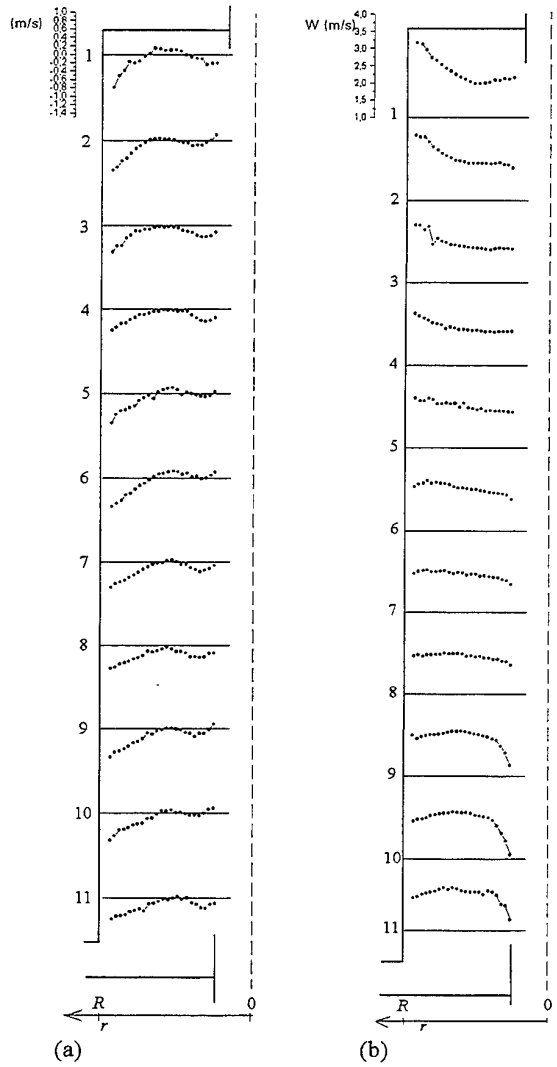

Fig. 4 LDA measurements of velocities (*Re*= $6.3x10^4$; backpressure=40 cm of water column); (a) axial velocity; (b) tangential velocity.

pattern inside the cyclone. There are two principal and opposite flows: a) the first negative flow moves near the wall against gravity to the involute discharge; b) the second positive flow near the air-core (*reverse* flow) moves to the axial exit. Between these principal opposite currents there are two adverse secondary flows, which confirm a more complex flow pattern than that of the swirling flows in conical cyclones. Nuttal in 1926 and Binnie in 1957, as reported by Nissan and Bresan (1961), observed a reversed flow located between two ascending currents in a cylindrical tube. On the other hand, the tangential velocity profiles of Figure 4 show a swirling flow changing from the inlet region to the involute outlet. In fact, on the side of the *feed* inlet W increases up to a maximum value as the radius increases and then it decreases near the wall. In the central sections the measurements suggest that changes of W with the radius are less pronounced. Finally, near the *sink* discharge, we can distinguish a rigid body rotation close to the air-core followed by decreasing tangential velocities as r increases, thus originating a flow pattern similar to a Rankine vortex. These results agrees with the investigations of Kirchberg and Schulze (1968), Baranov *et al.* (1984) and Hacioglu and Turner (1985) conducted for studying a counter-flow cylindrical cyclone.

3.2 Measurements With Two Operating Stages

A complete set of velocity data was taken to map the flow in the cyclone while it was operated in the standard mode (two stages). Table 2 gives the experimental conditions (a) and (b), to which the next figures will refer. The first measuring section was placed near the inlet region: at a distance of 20 mm from the vortex finder in the first vessel and at distance of 7 mm in the second one. The axial step used was of 23.1 mm in the first cylinder and of 25.2 mm in the second.

Some interesting results obtained for the tangential component in the first stage are shown in Figures 5 and 6. Figure 5 represents two plots of the W velocities measured in the section 1 and Figure 6 the data of the same velocity component in section 11. The shape of the profiles is similar to those presented in Figure 4, but the application of a second stage doubles the values of the W velocity in the first cyclone. In Figures 5 and 6 we can also see that only a small change of W is produced when the

Table 2 Experimental conditions

	1st STAGE		2nd STAGE	
	(a)	(b)	(a)	(b)
Re	$6.1x10^4$	$5.8x10^4$	$6.1x10^4$	$6.1x10^4$
Backpressure (cm of water column)	40	40	40	30
Feed pressure (kPa)	18.1	17.0	18.1	17.0

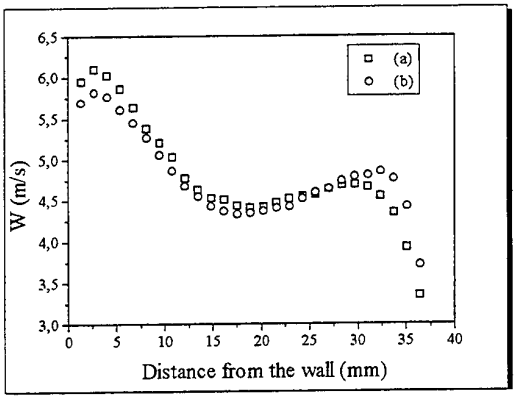

Fig. 5 Tangential velocity profiles in the section 1 of the 1st stage.

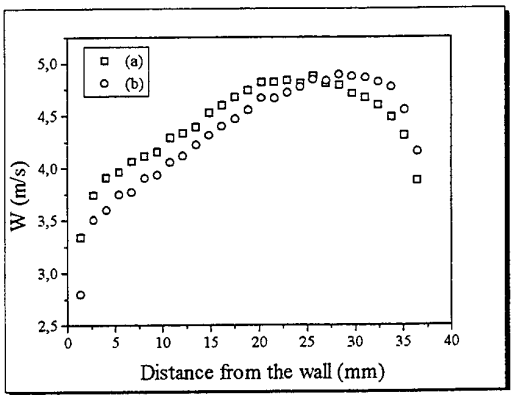

Fig. 6 Tangential velocity profiles in the section 11 of the 1st stage.

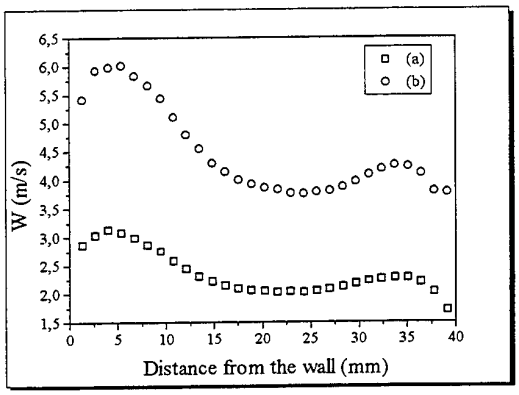

Fig. 7 Tangential velocity profiles in the section 1 of the 2nd stage.

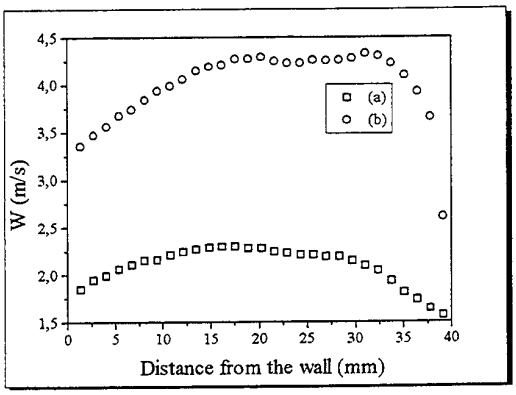

Fig. 8 Tangential velocity profiles in the section 11 of the 2nd stage.

back-pressure is lowered in the second stage. A different situation is encountered in the second cyclone (Figures 7 and 8). On the one hand, as it can be appreciated by comparing Figure 7 with the profiles of Figure 4, the W velocity is practically the same of the one operating cyclone case in the second stage. In this case the application of a lower back-pressure at the sink discharge of the second stage produces (see Figure 8) an important rise of the tangential component velocity in the second vessel. On the other hand, the axial velocity measurements give origin to the same patterns as shown in Figure 4.

These results would seem to confirm that the flow regimes inside the two stages of the separator are interrelated and depend strongly on the pressure condition at the exits. The centrifugal acceleration in the separator can be risen by the application of a second stage and by choosing appropriate values of the back-pressures. The radial homogeneity of the tangential velocity component in the middle of the vessel and the less severe radial change of the axial velocity component could explain the good performance of the cylindrical cyclones.

4. CONCLUDING REMARKS

Two components of velocities were measured in a multi-stage DMS cylindrical cyclone (Tri-Flo) by laser Doppler anemometry. This experimental technique proved to be a useful tool in characterising quantitatively the swirling flow in the centrifugal separator. The results show that the fluid flow pattern in the cylindrical cyclone is very complex. The axial and tangential velocity components, measured in a one-stage operating cyclone, confirm some former studies conducted with intrusive techniques. For a multi-stage operating cyclone, the results provide valuable insight into the dependence of the internal fluid flow on pressure conditions at the *sink* discharges.

ACKNOWLEDGEMENTS

We acknowledge the Research Doctoral Programme of the University of Trieste and the SALA Italiana. We also thank financial support from FONDEF, Codelco Chile and the University of Concepción through project MI-08 and Fondecyt through project 1941035.

REFERENCES

Adrian R.J., *Laser Velocimetry*, in Fluid Measurements, Goldstein R.J. editor, 1983, Springer-Verlag, Berlin, 161-163.

Baranov D., Kutepov A.M. and Ternovskii I.G., Flow Rate Characteristics and Hydrodynamics of a Counterflow Cylindrical Hydrocyclone, *Journal of Applied Chemistry* - USSR (English trad.), 57(5), 1984, 1181-1184.

Binnie A.M. and Hookings G.A., Laboratory Experiments on Whirlpools, *Proceedings of Royal Society,* Series A 194, 1948, 398-415.

Burt O.R., Gravity Concentration Technology, *Developments in Mineral Processing* vol. 5, Fuerstenau D.W. advisory editor, 1984, Elsevier, Amsterdam, 139-183.

Chiné B., Studio Idrodinamico del Separatore Centrifugo Multistadio Tri-Flo, *Tesi di Dottorato di Ricerca*, Universitá di Trieste (Italia), 1995.

DANTEC Measurements Technology A/S, *BSA Enhanced: Installation and User's Guide*, 1994, Skovlunde, Denmark.

Durst F., Melling A. and Whitelaw J.H., *Principles and Practice of Laser Doppler Anemometry*, 1981, Academic Press, London, 342-346.

Escudier M.P., Bornstein J. and Zehnder N., Observations and LDA Measurements of Confined Turbulent Vortex Flow, *Journal of Fluid Mechanics,* 98, 1980, 49-63.

Ferrara G., State-of-the Art and New Developments in Dense Medium Separation Processes, Int. Conf. "*Mineral Processing: Recent Advances and Future Trends*", December 11-15, 1995, Kanpur, India.

Fingerson L.M., Adrian R.J., Menon R.K. and Kaufman S.L., *Data Analysis, Laser Doppler Velocimetry and Particle Image Velocimetry*, TSI Short Course Text, 1991.

Gardavský J, Hrbek J., Chára Z. and Severa M., Refraction Correction for LDA Measurements in Circular Tubes within Rectangular Optical Boxes, Dantec Information No 08, November 1989.

Hacioglu E. and Turner J.F., A Study of the Dynawhirlpool, *Proceedings of XV International Mineral Processing Congress*, June (1985), Cannes (France), 244-257.

Kirchberg H. and Schulze G., Study of the Flow and Separation Conditions in a Dyna Whirlpool Cylindrical Cyclone, 1968, Report N° 156 from Forschungsinstitut für Aufbereitung, Freiberg (Germany).

Nissan A.H. and Bresan V.P., Swirling Flow in Cylinders, *AIChE Journal* 7(4), 1961, 543-547.

SESSION 20

Sprays

COMPARATIVE MASS FLUX MEASUREMENTS IN SPRAYS USING PATTERNATOR AND PHASE-DOPPLER TECHNIQUE

K. Dullenkopf, M. Willmann, S. Wittig

Lehrstuhl und Institut für
Thermische Strömungsmaschinen
Universität Karlsruhe

F. Schöne, M. Stieglmeier

DANTEC/invent
Measurement Technology GmbH

C. Tropea, Chr. Mundo

Lehrstuhl für Strömungsmechanik
Universität Erlangen-Nürnberg

ABSTRACT

The Phase-Doppler technique has become one of the most important instruments in two phase flow research in recent years because of its capability to simultaneously measure diameter and velocity of spherical particles. However, the shortcomings of this technique with respect to volume flux measurement has become increasingly apparent. In order to study the performance of the different PDA instruments, comparative flux measurements in two characteristic sprays using a patternator and three phase-Doppler systems have been performed at the 'Institut für Thermische Strömungsmaschinen' of the University of Karlsruhe (ITS) in cooperation with the 'Lehrstuhl für Strömungsmechanik' of the University of Erlangen-Nürnberg (LSTM) and DANTEC/invent Measurement Technology GmbH in Erlangen.

The results of this study clearly indicate that especially in dense sprays, mass flux determination by the phase-Doppler technique is still critical. Further efforts to improve the reliability of the system and to identify the possible sources of errors are necessary. However, the DualPDA technique shows a significant improvement compared to the other instruments under investigation.

1. INTRODUCTION

For investigations of atomizer characteristics, measurement techniques are required which facilitate local measurements within a spray cone. In order to guarantee an optimal atomization process, one of the most important spray parameters to be analyzed is the local volume flux or mass flux in the two-phase flow produced. The mass flux is also an important quantity when evaluating transport processes of sprays, for instance evaporation or wall impact splashing. In fact, quantitative comparison between numerical simulation of dispersed two-phase flows and experiment rely almost entirely on an accurate measurement of local mass flux.

Essentially only two measurement instruments are suitable for this kind of investigation. On one hand, there is the patternator, characterized by a systematic arrangement of tubes collecting droplets and accumulating their liquid volume for a sufficient duration. On the other hand, phase Doppler techniques (PDA) provide local volume flux and mass flux information. In addition to the capabilities of a patternator, the non-intrusive phase Doppler technique provides local measurement of particle velocity and size distributions. Furthermore, the PDA is more widely applicable in flow configurations in which the main flow/spray direction is not well defined, e.g. in the case of recirculation. In such two-phase flows the patternator represents a disturbance which is unacceptable.

Although in the past years the phase Doppler instrument has become a powerful tool for spray characterization with respect to the droplet size and velocity, errors of magnitude 100% and above regarding the mass flux have been reported. Such errors have been attributed to several different sources, including improperly sized droplets [Gréhan et al. (1991)], non-uniform reference area for the measurement [Saffman (1987), Durst et al. (1994)] or incorrect particle counts due to poor signal validation. More recently, considerable effects have been extended to minimize or compensate for such errors and thus increase the reliability of mass flux measurements made using PDA. Three such improved systems were available for the present study, in which the PDA instrument could be directly compared with patternator results in a spray for which the latter can be used with confidence. The aim of the present study is therefore to evaluate the achievable accuracy of the PDA instruments in measuring mass flux. The evaluation has been carried out for two spray nozzles, a pressure swirl nozzle and an airblast atomizer. In both cases the spray had a well defined mean flow direction.

The generality of the results presented here is limited. This becomes apparent, when the influencing factors of measuring accuracy are discussed in more detail below. Nevertheless some basic recommendations and guidelines can be derived from the results presented below.

The paper is organized in the following manner. The specific features of the various instruments used in this study are described in section 2. The operating details of each instrument and a general description of the experimental procedure are given in section 3. Measurement results are presented in section 4 and a discussion with conclusions is found in section 5. A general introduction to the

task of measuring mass flux and concentration is given below.

Basically there are two approaches to measuring mass flux using PDA. With the first approach, the number and size of droplets passing normal through a reference area per unit time are counted and the resulting volume flux is then multiplied by the density, as given in the equation below for the flux normal to the x direction.

$$f_x = \frac{\rho\pi}{6\Delta t}\sum_{i=1}^{N}\frac{D_i^3}{A_x(D_i)}\times\frac{|U_i|}{U_i} \qquad (1)$$

whereby the velocity is used only to determine the direction of the individual droplets. Note that the area is expressed as a function of the droplet diameter, a necessity with PDA instruments, since the detection probability of a droplet is fundamentally a function of droplet size and trajectory through the measurement volume. Several schemes have been proposed to account for this [Saffman (1987)] or to minimize the effect by devising an amplitude independent signal detection, for instance using the signal-to-noise ratio (SNR) [Qiu et al. (1994)]. Experience shows, that some influence of the signal amplitude always remains, particularly as the bandwidth of the size range is increased.

Eqn. 1 can often be found in a slightly modified form, for instance if the summation is not performed over each individual droplet but rather over groups of droplets of similar size

$$f_x = \frac{\rho\pi}{6\Delta t}\sum_{k=1}^{N_s}\frac{D_k^3 N_k}{A_k(D_k)}\times\frac{|U(D_k)|}{U(D_k)} \qquad (2)$$

where N_k is now the number of droplets in each size group, i.e. the number/size distribution and N_s is the number of segments the size distribution is computed in. Further modifications to this expression, to account for more turbulent flow-fields, i.e. flows in which the main flow direction is not primarily normal to A_x, have been discussed in Tropea et al. (1996) and will be described briefly in section 2.3.

A second approach to measuring the mass flux is to measure first the droplet size dependent concentration and then apply the droplet size dependent velocity to obtain the mass flux. This approach is implemented using size groups of droplets:

$$f_x = \frac{\rho\pi}{6\Delta t}\sum_{i=1}^{n} d_i^3 \frac{\sum_{j=1}^{m}\mathrm{Int}_{i,j}(d_{i,j})|\vec{u}|}{\iiint_{\mathrm{Vol}(d_i)}\overline{V}(d_j,x,y,z,t)\,dv} \qquad (3)$$

where i and j are the denotations for the individual size class and the individual sample in each size class, respectively. $\mathrm{Int}_{ij}(d_j)$ denotes the time-dependent integration of the envelope of the filtered Doppler signal of each measured individual sample, multiplied with its velocity component in the direction of interest. $\iiint_{\mathrm{Vol}(d_i)}\overline{V}(d_j,x,y,z,t)\,dv$ describes the spatial integration of the signal's envelope. The principle is further explained in section 2.4, however it is clear that the droplet velocity now plays a much more important role in the mass flux measurement than in eqn 1.

Considering briefly sources of error these can be identified readily from Eq. 2 as being:

- size measurement - particularly significant due to the third power dependence
- number count - depends on detection electronics and possible validation scheme
- reference area - depends on droplet size, optical configuration but possibly also on validation scheme

Note that in a polydisperse spray the smaller droplets will not influence the mass flux significantly, so that poor detection of small droplets should not be a major source of error, however small droplets sized as large droplets (e.g. slit effect [Durst et al. (1994)]) or large droplets sized as small droplets (trajectory effect) remain problems to be addressed. A further difficulty arises, when the validation rate is low, either due to high droplet densities with more than one particle in the probe volume, non-sphericity of the droplets or to other causes, such as trajectory effect validation. In such cases the mass of the rejected droplets is missed or discarded and there is no reliable way to compensate for this. Some instruments simply scale the measured number fraction by the inverse of the validation rate, which will only be correct if there is no correlation between validation and droplet size, which is definitely not the case for trajectory effect rejections.

A final, more subtle source of error is the alignment and adjustment of the instrument. For reasons which are not always completely understood, but which are clearly authentic, the measured mass flux may be very dependent on the optical alignment (transmitting and receiving side), the photo-detector high voltage, amplifier settings, etc. A robust system is one in which small changes in parameter settings have little influence on the reading or one in which an alignment and operating procedure is well enough prescribed to insure a high degree of repeatability. Although these aspects are to some extent subjective criteria, some attempt has been made to comment on system robustness below.

2. DESCRIPTION OF MEASURING EQUIPMENT

2.1.PATTERNATOR

The term adopted for the process to determine the spatial distribution in the spray cone is 'spray patternation' and therefore the instrument is called a 'patternator'. In contrast to the other instruments used in this study it can be classified as an extractive probing technique. Generally two different methods can be differentiated: Systems in which the total fluid in the spray is collected and systems using isolated probes or an array of probes in which only a fraction of the fluid in the spray is captured. The instrument used in this study belongs to the latter. It was especially designed at the 'Institut fuer Thermische Stroemungsmaschinen (ITS)' for the use in high speed sprays like airblast atomizers and as a reference tool for non-intrusive optical instrumentation like the Phase-Doppler-Analyzer.

Therefore, special care was taken in the design of the instrument to avoid disturbances in the flow field or the spray by the patternator. In contrast to most patternator systems described in the literature [McVey (1989)] the ITS device uses isokinetic sampling and a vacuum technique to minimize interference with the spray. The general layout is presented in Fig. 1. It consists of a sampling array made of 5mm stainless steel tubes. The tubes have an inner diameter of 4.8mm and an area of 18mm^2 to achieve a high spatial resolution. Up to 50 tubes can be arranged to examine the spatial flux distribution inside the spray. The sampling tubes are connected with flexible hoses to the collectors. By means of a vacuum control valve, sampling and transport conditions at the entrance to the tubes can be adjusted according to the spray under investigation. To restart the patternator after a measurement the collector bottles can automatically be emptied by means of a second vacuum connection.

After a certain period, typically 0.5 to 1 hour, the collection of the liquid is stopped and the height of the fluid is measured. By means of the collected volume, the time and the sampling area the spatially resolved volume flux can be calculated.

Comprehensive numerical and experimental tests have been performed in the development procedure of the ITS patternator to minimize systematic errors. The average error was found to be around 5%

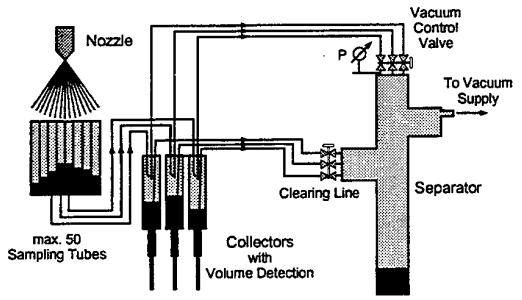

Fig. 1: Layout of the ITS patternator system

2.2 PDPA

The Phase-Doppler Particle Analyzer (PDPA) used in this study was one of the first generation AEROMETRICS counter-based instruments. A detailed description of the instrument was given by Bachalo (1984). In the following, only the relevant aspects concerning volume flux measurements are presented in detail. Table 1 contains the parameters chosen for the PDPA measurements.

At the ITS the AEROMETRICS software version 2.24 is used, which is, because of technical problems with updates, not the latest version. Unfortunately this program release gives obvious erroneous values for the measured volume flux. Therefore a post-processing program was developed at the ITS, which reads in raw data and calculates volume flux in the way described below. A comparison with the latest software version 2.27E gives identical values.

Transmitter:		
	axial	trans.
Laser wavelength [nm]	514.5	488
Laser power [mW]	100	
focal length [mm]	500	
beam separation [mm]	20	10
frequenzy shift [MHz]	1.2	0.8
Probe volume diameter [µm]	250	
Receiver:		
Off axis angle [°]	30	
focal length [mm]	500	
Aperture slit-width [µm]	100	

Table 1: Configuration of the PDPA

In principle, Eq. 2 is used, where the most critical parameter is the probe area of individual droplet size classes. Neglecting effects of the slit aperture, the probe volume has the shape similar to a cigar. The diameter of this 'cigar' is measured on-line in the direction of the main-flow. For this, an analysis of the probability density function of measured fringe counts for all events of each individual droplet size class is performed. The sharp edge in this probability density functions towards large fringe counts is taken to calculate the probe volume diameter by means of the fringe spacing. With the simplified assumptions of a Gaussian intensity distribution in the probe volume and a quadratic dependence of scattered intensity on droplet diameter, a fit for all measured droplet size dependent path lengths gives the required information about the individual probe-volume diameter values.

The slit aperture in the receiver optics cuts a disc out of the above mentioned 'cigar'. This disc represents the actual probe volume of the instrument. Assuming uniform flow in the main flow direction, the probe area is calculated from the measured diameter of the probe volume and the projected slit width:

Even if the influence of all parameters is not investigated in detail, it is clear, that this method suffers from several limitations:

- a large number of droplet size classes with a sufficiently high number of droplet counts is required in order to give sensible results for the probe volume diameter
- the limited number of fringes in the probe volume gives finite resolution to the measurements of the probe volume diameter. Increasing the fringe number indefinitely is however not possible due to constraints imposed by the sizing and velocity measurements.
- The method is extremely sensitive to trajectory deviations from the main flow direction, which can only be fully corrected using a 3 component velocity measurement.
- Gaussian beam effects usually result from particle trajectories through one side of the probe volume. If these droplets are rejected, the probe volume is no longer symmetric.

Determining the probe volume diameter along the main flow axis gives therefore, values which are too large for the probe-area perpendicular to the main flow direction.

Considering all the errors discussed in the introduction, it is clear that this method may be suitable for simple, well directed flows, but will lead to erroneous results under complex, technically relevant conditions.

2.3. DUAL-PDA

The DualPDA from DANTEC/invent is a specially designed PDA receiving optics recently developed and released. Due to the already mentioned shortcomings of conventional PDA systems leading to erroneous mass flux results when applied to relatively large, transparent particles, the new DualPDA was developed to enhance measurement accuracy. In particular, the accuracy of mass flux and concentration measurements are significantly improved. Furthermore, the trajectory effect [Gréhan et al. (1991)] and the slit effect [Durst et al. (1994)] leading to ambiguous particle sizes measurements, are eliminated by means of the new arrangement of the receiving apertures. The DualPDA actually combines two different types of Particle Dynamics Analyzers, a conventional PDA and a planar PDA as shown in Fig. 2.

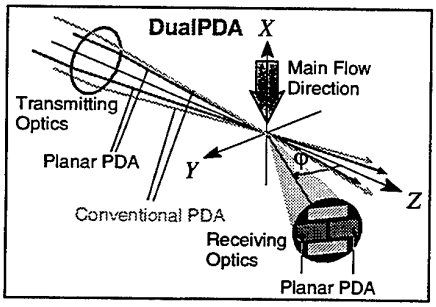

Fig. 2: Principle layout of the DualPDA

For the comparison measurements between patternator and DualPDA, the DualPDA was set up with an off–axis angle of 30° (Fig. 3).

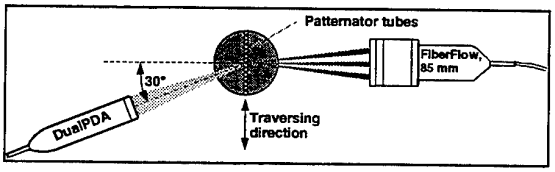

Fig. 3: Set up of DualPDA and patternator (top view).

Similar to conventional PDA systems, the DualPDA shows good performance under these conditions, therefore this angle is used for all the instruments. The transmission optics consisted of an air-cooled Ar-Ion Laser, a fiberoptic transmitter facilitating beam splitting and optical frequency shifting and a FiberFlow probe. A 2-D 85 mm probe was chosen because this type provides good flexibility regarding beam separation and thus enabling variation of measurement ranges. The parameters of the transmission optics chosen for all measurements are listed in Table 2.

Transmission Optics (FiberFlow, 85 mm)		
	conv.	planar
Laser wavelength [nm]	514.5	488.0
Laser power [mW]	approx. 60	
focal length [mm]	310	
beam separation [mm]	40	
frequency shift [MHz]	40	
probe volume diameter [μm]	150.5	
Receiving Optics (DualPDA)		
off-axis angle [°]	30	
focal length [mm]	310	
aperture-slit [μm]	100	
aperture mask	small particles	

Table 2: Configuration of the DualPDA

For processing of the Doppler bursts, a covariance signal processor (DANTEC/invent MultiPDA) was used. This device determines signal frequency and phase difference for both the conventional PDA and the planar PDA. Besides analog signal processing, this type of processor also conducts burst detection and the initial signal validation by an online determination of the signal-to-noise ratio.

The second feature of the quasi online signal validation is contained in the data acquisition software (SIZEware). It is a well known fact that the detection of nonspherical particles is crucial for reliable mass flux measurement. This check is performed by comparing the particle sizes measured with the conventional PDA to those measured with the planar PDA. Although this procedure is similar to the one incorporated in conventional 3–detector PDA systems, the reliability in the DualPDA setup is significantly improved as shown by Tropea et al. (1996).

Furthermore, an improved validation routine implemented in the software accounts for oscillations in the particle size / phase difference response curve occurring for small particles [Schöne et al. (1995)].

The calculation of the particle size dependent cross–sectional area, required for determining the mass flux, is based on the burst length method described by Saffman (1987). His method is modified to yield more accurate results in size classes with few particles, typically occurring at the upper end of the measured particle size distribution. Also both components ot the velocity are considered in computing the burst length [Tropea et al. (1996)]. A further improvement could be achieved taking rejected events into account for the calculation of the mass flux using the inverse of the validation rate as a scaling parameter.

2.4 QIU & SOMMERFELD - PDA

The basic principle of this signal processing technique is to account for the amplitude and integral intensity of the reflected and refracted light to determine the spatial volume concentration of the dispersed phase. From the volume concentration, the local mass flux can be calculated. A detailed description of the processing technique is given in Qiu & Sommerfeld (1995) and it will be only briefly described in this section.

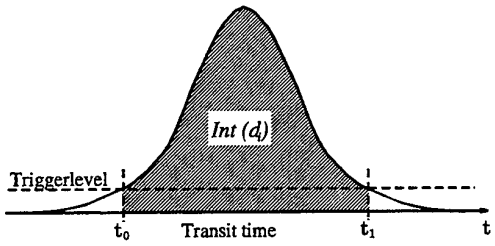

Fig. 4: Envelope of the filtered Doppler signal

The envelope of the band-filtered Doppler signal $V(_{di},x(t),y(t),z(t))=V(d_i,t)$ (see Fig. 4) of each aquired sample is integrated over the transit time as well as over the space, using the identity $ds = |\vec{u}|dt$. The indices i and j refers to the actual sample and to the size class in which the sample belongs to.

$$Int_{i,j}(d_{i,j}) = \int_0^{t_j} V(d_j,\tau)d\tau = \frac{1}{|\vec{u}|}\int_0^{s_j} V(d_j,t)ds \qquad (4)$$

Integrating over the measurement area and over all samples belonging to the considered size class gives

$$Int_j(d_j) = \frac{N_j}{\overline{A}(d_j)|\vec{u}|}\iiint_{Vol_j}\overline{V}(d_j)dv \qquad (5)$$

with the average size of the measurement area $\overline{A}(d_j)$ of the considered size class. $\overline{V}(d_j)$ is the envelope function averaged over all trajectories which the particles might have in the measurement volume. With the definition of the local volume concentration per size class

$$c_V(d_j) = \frac{\pi d_j^3 N_j}{6|\vec{u}_j|\overline{A}(d_j)\Delta t} \qquad (6)$$

one finally obtains

$$c_V(d_j) = \frac{\pi d_j^3}{6\Delta t}\frac{Int_j(d_j)}{\iiint_{Vol_j}\overline{V}(d_j)dv} \quad . \qquad (7)$$

The corresponding mass flux is obtained by multiplying the volume concentration with the velocity component in the considered direction.

$$f_x(d_j) = \frac{\pi\rho d_j^3}{6\Delta t}\frac{Int_j(d_j)\,u_{x,i,j}}{\iiint_{Vol_j}\overline{V}(d_j)dv} \quad . \qquad (8)$$

Summing Eq. 5 over all size groups gives the integral local mass flux.

$$f_x = \sum_{j=1}^{n} f_x(d_j) = \frac{\pi\rho}{6\Delta t}\sum_{j=1}^{n} d_j^3 \frac{Int_j(d_j)\,u_{x,i,j}}{\iiint_{Vol_j}\overline{V}(d_j)dv} . \qquad (9)$$

Therefore, with this signal processing algorithm the local mass flux can be determined with a standard, one dimensional PDA setup.

In the present measurements, the following optical arrangement was used: The transmitting optics consists of a He-Ne Laser with an output power of 15mW and a double Bragg cell unit for frequency shifting. The focal length of the transmitting and the receiving optics was 160 mm and 310 mm, respectively. An off-axis angle of 30° was chosen. In the receiving optics, two avalanche photodiodes (APD's) with slits of 150µm in width for spatial filtering were used.

The validation criterion for the signal acquisition are the following: frequency and phase validation as well as signal amplitude validation. The alignment of the optical setup, the high voltage and amplification of the APD's were adjusted in order to minimize the signal amplitude errors, the frequency and phase errors. In Table 3 the optical setup of the transmitting and receiving optics are summarized.

Transmitting optics	
Laser-wavelength [nm]	632.8
Laser Power [mW]	15
Focal length [mm]	150
Beam separation [mm]	10
Frequency shift [MHz]	1
Probe volume diameter [µm]	129
Receiving optics	
Off-axis angle [°]	30
Focal length [mm]	310
Aperture slits [µm]	150

Table 3: Configuration of the QS-PDA

3. DESCRIPTION OF THE EXPERIMENT

The experimental investigations were performed on a spray-test-rig at the ITS. This test rig consisted of a support for the atomizers with the control instrumentation for the nozzle and a tube 200mm in diameter containing the patternator rack and a flow straightener positioned 100mm below the nozzle exit. A blower shown in Fig. 5, established the background airflow. De-mineralized water at 20°C was used as test fluid. The spray rig is mounted on a stepper-motor driven traversing system. By means of the traverse the probe volume of the different phase-Doppler systems was positioned 2 mm above the center of the sampling tubes.

With each PDA instrument, preliminary measurements were performed to choose a suitable number of samples to achieve stable mean values. Typically 10,000 samples were used, except in some outer regions of the spray. During these preliminary tests each instrument was adjusted such that the measurement result was insensitive to small changes in settings of the processor or processing

scheme. In each case the alignment and adjustment, as well as the subsequent measurements, were performed by a person completely familiar with the particular equipment.

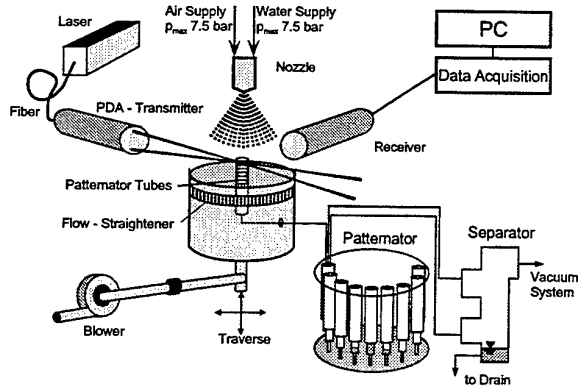

Fig. 5: Spray-test-rig with instrumentation

Two commercial atomizers have been used:

- *pressure swirl atomizer:*
  simplex pressure swirl atomizer type Monarch MTD-92, 1.35, 30°, R, pressure of the water: p_{water} = 5bar
- *airblast atomizer:*
  coaxial jet airblast atomizer type Schlick Model 970, form 0, Pressure of water: p_{water} = 0.5 bar, pressure of air: p_{air} = 3 bar.

In order to avoid problems with remounting of the atomizers, the alignment of the instruments and performance degradation of the atomizers, phase-Doppler and patternator experiments were performed simultaneously for each instrument. Results are plotted relative to the patternator values for each individual instrument according to Eq. 10.

$$f_{x,norm}(i) = \frac{f_x(i)}{\sum_{k=1}^{N} f_{x,pat}(k)} \qquad (10)$$

4. EXPERIMENTAL RESULTS AND DISCUSSION

The Sauter mean diameter values plotted in Fig. 6 and Fig. 7 for the pressure swirl atomizer and the airblast atomizer respectively, indicate that reproducibility between the different instruments and operators is within aprox. ±10%. A main reason for this discrepancy may be difficulties with the different adjustment of the atomizers relative to the instrument, as well as differences in atomizer performance. However, differences in that order of magnitude were also observed in other inter-laboratory tests. [Hassa et al. (1992)].

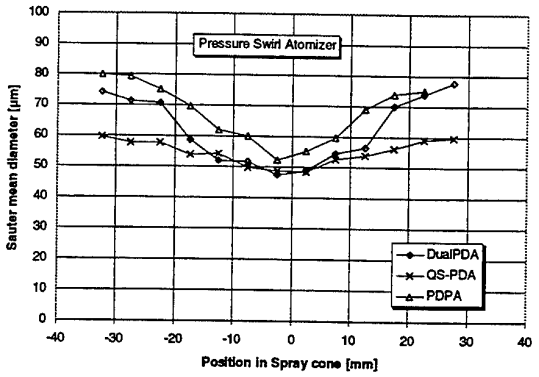

Fig. 6: Sauter mean diameter, pressure swirl atomizer

The measured distributions clearly indicate that the atomizers differed significantly in their spray characteristic. In general the pressure swirl atomizer produced a coarser spray. In addition, larger droplets occuring in the outer range of the spray typically result from ejection during the atomization process. For the coaxial airblast atomizer a more uniform distribution with the larger droplets in the center of the spray was found. These droplets resulted from the atomization process of the liquid core.

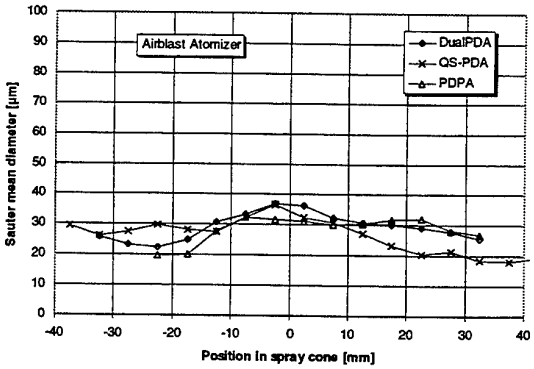

Fig. 7: Sauter mean diameter, airblast atomizer

Fig. 8 contains the comparisons of normalized mass flux in the spray of the pressure swirl atomizer between the three phase Doppler instruments and the patternator. The PDPA (top) shows the largest deviations, yielding only half or less of the patternator results over the entire spray cone. The QS-PDA generally achieves better results but it switched from overprediction at the center to underprediction at the edge of the spray cone. The best reproduction of the patternation in the center of the core is given by the DualPDA (bottom figure), whereas significant errors with this instrument only occur in the boundary areas of the spray, possibly due to a higher statistical variance.

The distributions in the spray of the airblast atomizer, see Fig. 9, indicate that for this spray type, significant errors occur in the mass flux determination based on phase-Doppler measurements for all three instruments.

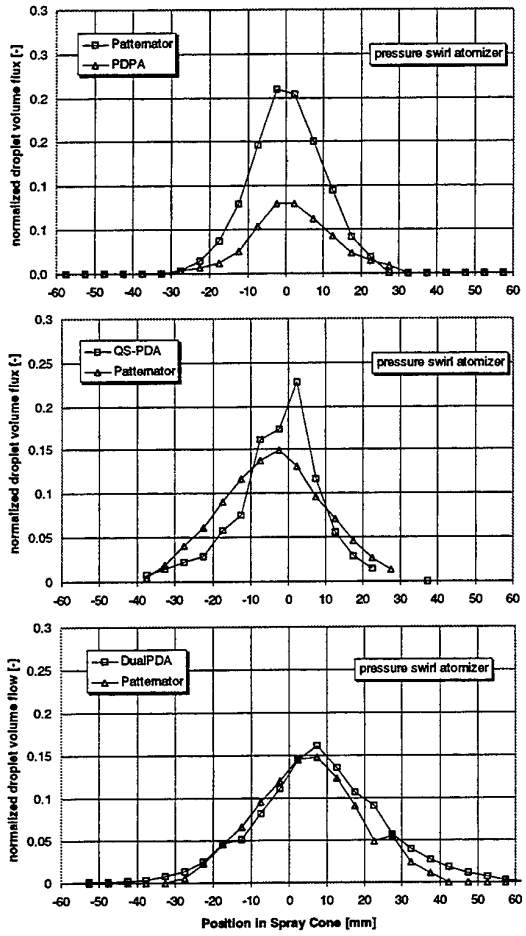

Fig. 8: Normalized volume flux, pressure atomizer

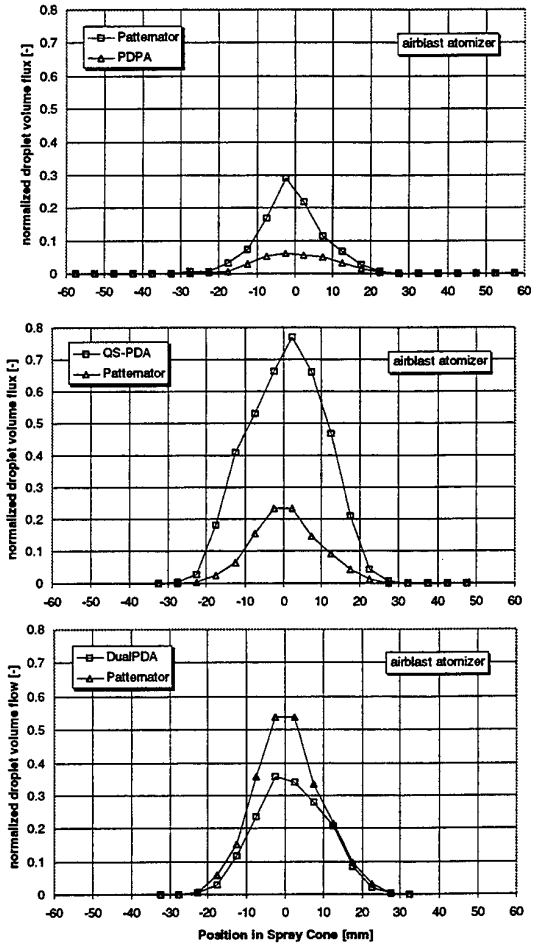

Fig. 9: Normalized volume flux, airblast atomizer

Their performance differs to the one shown previously. In this case the QS-PDA drastically overpredicts the patternator values, whereas the PDPA and the DualPDA underpredict.

To investigate these differences between the pressure swirl and the air blast atomizer, data rates and validation rates are listed in Table 4 and a further diagram has been prepared, showing profiles of the axial velocity (Fig. 10) for the pressure swirl atomizer and for the airblast atomizer (Fig. 11). The main difference between the two atomizers is seen to be the higher velocity and the higher data rate.

Comparing the measured velocity profiles for each of the atomizers, shows that all instruments are in close agreement with one another for the pressure swirl atomizer. This indicates that there were no fundamental errors in the

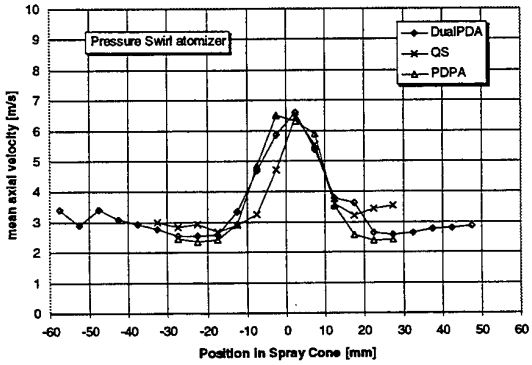

Fig. 10: Mean axial velocities, pressure atomizer

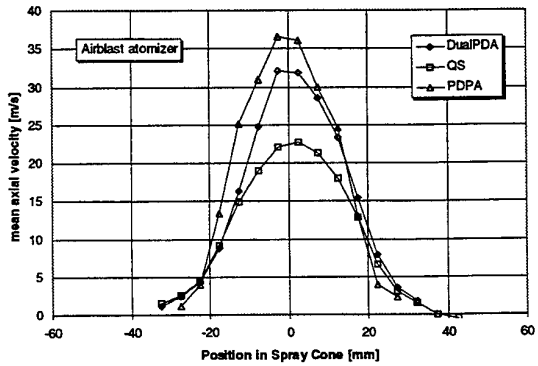

Fig. 11: Mean axial velocities, airblast atomizer

choice of optical and/or processor parameters, which would exclude validation on these grounds. Nevertheless, the QS-PDA shows slightly lowered velocities for the airblast atomizer spray, indicating possible difficulties with data processing.

	pressure swirl		airblast atomizer	
	data rate	val. rate	data rate	val. rate
DualPDA	6kHz	95%	35kHz	85%
QS-PDA	9kHz	99%	20kHz	85%
PDPA	3kHz	85%	13kHz	70%

Table 4: Peak data rate and validation

The validation rate in all cases was high, since this was a primary indicator of correct instrument adjustment during the preliminary measurements. Only the DualPDA used this information to adjust the measured mass flux. Specifically, the rejection due to non-sphericity was compensated using the inverse of this validation rate.

It appears, that the high data rate was an obstacle for obtaining correct mass flux measurements. The analysis of the PDPA raw data showed time gaps resulting from internal data transfer which were in the order of 5% of the total measurement time for the airblast atomizer. For the QS-PDA the nominal data rate was definitely exceeded with the airblast atomizer. The behavior of the detection electronics and the envelope integration circuit becomes unpredictable in these circumstances, which leads to unreliable estimates of the mass flux. Therefore, no further attempt to explain this result is undertaken. The DualPDA is specified at 100 kHz or 170 kHz for equidistant samples. The measured data rate of approximately 35 kHz therefore certainly lies below the nominal limits given by the manufacturers of the DualPDA. Nevertheless, depending on the arrival statistics of droplets even at 35 kHz some events will come in short sequence, such that they will fall in deadtimes of the processor. This acquisition time (or cycle time) for the DualPDA apparently lies at about 6 µs. Considerably, this could explain a portion of the missing mass flux of the airblast atomizer in the DualPDA measurements.

The reduced validation rate of the PDPA, which is obviously a reason for the unsatisfactory reproducibility of mass flux, results from several data rejection algorithms like phase check, nonsphericity check and intensity validation. In this case, especially the parameters for the intensity validation algorithms were found to have a strong influence on the measured mass flux. No reliable procedure for a correct adjustment of these parameters was found, yet. Nevertheless, based on the results it can be assumed, that a global correction with the inversed validation rate would give significantly better results.

5. CONCLUSION

These results indicate that modern phase-Doppler systems have reached a high level of reliability in characterizing sprays. The accuracy of measurements in typical pressure swirl atomizers sprays characterized by moderate mean diameters is quite good, especially with advanced instruments. However, the determination of the volume or mass flux especially in dense sprays remains a problem. As shown by this study significant errors occur in the widely used standard systems but even in advanced instruments. Further efforts to identify the sources of errors are still necessary to improve the reliability of the systems. However, the DualPDA technique does show a significant improvement compared to the other instruments under investigation.

REFERENCES

M. Aizu, F. Durst, G. Gréhan, F. Onofri, T.-H. Xu (1993): PDA System without Gaussian Beam Defects, Proc. 3rd Int. Conf. Optical Particle Sizing, Aug. 23-26, Yokohama, Japan, pp. 461-470

W.D. Bachalo, M.J. Houser (1984): Development of the Phase/Doppler Spray Analyser for Liquid Drop Size and Velocity Characterizations. AIAA 20th Joint Propulsion Conference, June 11-13, Cincinnati, Ohio

F. Durst, C. Tropea, T.-H. Xu (1994): The Slit Effect in Phase Doppler Anemometry, 2nd Int. Conf. on Fluid Dyn. Meas. and its Appl., Oct. 19-22, Beijing

G. Gréhan, G. Gousbet, A. Naqwi, F. Durst (1991): Evaluation of a Phase Doppler System using Generalized Lorenz-Mie Theory, Int. Conf. on Multiphase Flows '91, Tsukuba, Japan, pp. 291-296.

C. Hassa, M. Brandt, G. Cormack, H.L. Hawkins, A.K. Jasuja, I. Tam, R. Kneer, M. Laedoux, D. Liesiecki (1992): Cross correlation of three drop sizing techniques on an airspray fuel injector. 6th Int. Symp. on Appl. of Laser Techniques to Fluid Mechanics, Lisbon, 20th-23rd July.

A. Høst-Madsen, T. Nonn (1995): Quantization of Phase-Doppler Signals: How many bits are needed, Proc. 2nd Int. Conf. on Multiphase Flow, Apr. 3-7, Kyoto, Japan

J.B. McVey, J.B. Kennedy, S. Russel (1989): Application of Advanced Diagnostics to Airblast Injector Flows, Journal of Engineering for Gas Turbine and Power, Vol. 111, pp. 53-62.

H.H. Qiu, M. Sommerfeld, F. Durst (1994): Two novel Doppler signal detection methods for laser Doppler and phase Doppler Anemometry, Meas. Sci. Techn., 5, pp. 769-778

M. Saffman (1987): Automatic Calibration of Measuring Volume Size, Applied Optics, 26, pp. 2592-2597

F. Schöne, C. Tropea, T.-H. Xu, P. Haugen (1995): Mass Flux Measurements with Phase Doppler Anemometry, Proc. 1st Int. Symposium on Two-Phase Flow Modelling and Experimentation, Oct. 9-11, Rome, Italy

M. Sommerfeld, H.-H. Qiu (1995): Particle concentration measurements by phase Doppler anemometry in complex dispersed two-phase flows, *Exp. in Fluids*, Vol. 18, pp. 187-198

C. Tropea, T.-H. Xu, F. Onofri, G. Grehan, P. Haugen, M. Stieglmeier (1996): Dual Mode Phase Doppler Anemometer, Part. Part. Sys. Char., Vol. 13, No. 2, pp. 165-170

SPRAY VISUALIZATION AND PHASE DOPPLER ANEMOMETRY MEASUREMENTS OF CHARGED HYDROCARBON SPRAYS

J. S. Shrimpton, A. J. Yule, A. P. Watkins

Thermofluids Division,
Department of Mechanical Engineering, UMIST, Manchester, M60 1QD, UK.

ABSTRACT

The presented work is part of a project to assess the suitability of an electrostatic atomization technique for the combustion of liquid hydrocarbon fuel sprays. Due to the unique jet and drop breakup mechanisms that occur for electrostatically charged insulating liquids, such as hydrocarbon oils, these sprays contain large numbers of small drops. Also, since the relationship between drop charge and drop diameter is not linear smaller drops possess higher charge to mass ratios than their larger companions within the spray. Therefore the smaller drops are strongly repelled, away from the main body of the spray along the axial centreline and a stratification of the average (arithmetic mean) diameter occurs. Large drops, typically the same size as the orifice diameter remain near the spray centreline and the average drop diameter decreases at progressively larger radial displacements.

1. INTRODUCTION

Attempts have been made to atomize hydrocarbon fuels electrostatically during the past 25 years using existing electrostatic methods, (Law, 1978) but due to the difficulty in charging these insulating liquids and the low flow rates achieved, electrostatic atomization has not been a viable method for spraying oils. This has been due to the fundamental difficulty of encouraging charge, which is present on a conducting electrode, to migrate into an insulating liquid, without causing the electrical breakdown of the liquid. Electrostatic atomization of insulating liquids is possible by artificially enhancing the conductivity of the liquid, by the addition of an anti-static additive. This has been achieved by Gomez and Tang (1991), using heptane and phase Doppler anemometry (PDA) data for the charged spray was obtained. In the present work (Shrimpton, 1995) the objective was to produce burnable sprays from common industrial liquid fuels *ab initio*, that is without using additives or using additional atomization methods, such as centrifugal force or air-assist atomizer designs. The design of this atomizer uses the *charge injection* principle (Kelly, 1984) and electrostatically atomized combustible hydrocarbon sprays have been achieved (Shrimpton et al, 1996a). The maximum specific charge (ρ_V ,C/m^3) the spray may contain has been found to be a function of both flow rate (Q_L, cc/s) and most importantly the orifice diameter (d, μm) as shown in Fig. 1. Smaller orifice diameter liquid jets, since they possess greater surface area to volume ratios are able to contain more charge before inducing corona and losing charge to the gas phase. The increase in performance at higher flow rates is thought to be due to the decrease in the residence time of the charged species near the corona site at the jet surface as it emerges from the orifice. This allows a more uniform charge density profile across the orifice and increases the overall spray volumetric specific charge.

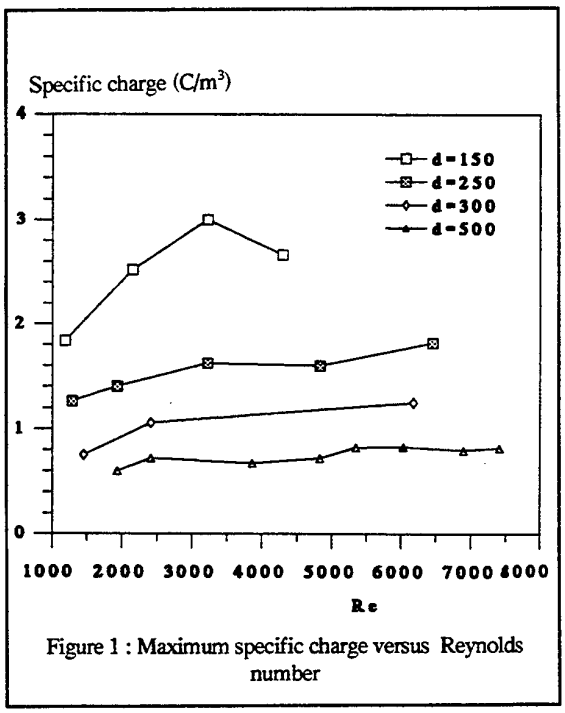

Figure 1 : Maximum specific charge versus Reynolds number

Phase Doppler anemometry results for the case of relatively lowly charged (ρ_V<-1C/m^3) hydrocarbon (kerosine) sprays have been previously described (Shrimpton et al, 1995) where a 500μm orifice diameter was used. It was shown that large numbers of small drops, typically 1/10 of the orifice diameter are produced at sufficient levels of charge injection. Larger drops, of

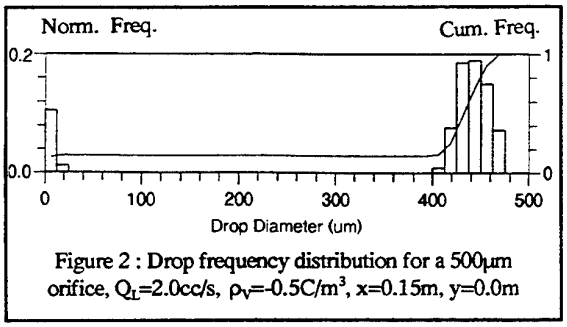

Figure 2 : Drop frequency distribution for a 500μm orifice, Q_L=2.0cc/s, ρ_V=-0.5C/m^3, x=0.15m, y=0.0m

diameters comparable to the diameter of the orifice contain most of the spray volume. In between these two drop populations, as shown by Fig. 2, no additional drops were recorded and this is quite unlike what one would expect from conventional, non-electrostatic atomizers, where one smoothly varying drop diameter versus frequency distribution is the norm. A discussion of the jet breakup dynamics and a detailed description of the electrical parameters particular to this design of atomizer are to be found in Yule et al.(1995). However these results relate only to the simple case of relatively lowly charged sprays, and the objective of the project, of which this paper gives some results, was directed towards high specific charge sprays, with sufficient numbers of small drops to sustain stable combustion. As noted above these 'highly' (defined by ρ_V>-1C/m^3) charged sprays may only be obtained by using small orifice diameters and the quantitative results in this paper describe charged hydrocarbon sprays produced from a 250μm diameter orifice.

3. EXPERIMENTAL

The nozzle design needed to be refined from the previous work (Shrimpton et al, 1995) to allow smaller orifice diameters, hence higher charge densities and better atomized sprays to be examined. This was possible by adopting the internal design as shown in Fig. 3, which optimised the nozzle on the basis of electrical, rather than liquid flow performance. The design allows the electrode tip to be placed in a region of high liquid velocity which strips the charge from the electrode much more efficiently than the previous design (Yule et al, 1995) without requiring the bulk flow to be especially high, which would require high injection pressures and restrict the turndown ratio available. The liquid fuel tested is as used previously for the lowly charged sprays (Shrimpton et al, 1995), that is a kerosine, sold commercially in the UK by Shell as '*homeglow 28*', which has a typical dynamic viscosity and density of 0.001N s/m^2 and 780 kg/m^3 respectively. Two sets of quantitative results are presented, for an orifice diameter of 250μm and flow rates of 0.5 and 1.67cc/s, which give mean injection velocities of 10 and 28 m/s respectively. The spray specific charges were -1.20 and -1.80C/m^3. These and additional information for a spray produced from an orifice diameter of 150μm are summarised in table 1, below.

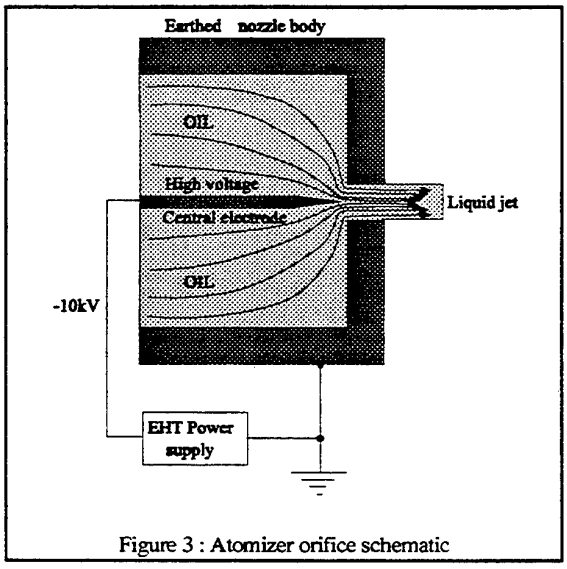

Figure 3 : Atomizer orifice schematic

Table 1: Atomizer operating conditions

Description			
Orifice diameter (d, μm)	250	250	150
Flow rate (Q_L, cc/s)	0.5	1.67	0.5
Mean injection velocity (m/s)	10	34	28
Specific charge (ρ_V, C/m^3)	-1.20	-1.80	-3.00

Results are presented for both qualitative and quantitative flow visualization to give a clearer understanding of the flow. For the qualitative study a 3W Ar^+ laser was used in conjunction with a cylindrical glass rod of 5mm diameter to illuminate a 0.15x0.15m section of the spray and the images were time averaged over 1 second, using ISO3200 black and white35mm film. The quantitative study used a 2D PDA system, kindly loaned to UMIST by DANTEC (UK) for the duration of the measurements. Due to the large radial velocities indicated above a two velocity component PDA system was particularly useful for the results presented in this section. The characteristic dimensions of the measurement system are given in table 2, below.

The off axis angle was the Brewster condition, and this angle was found to give the best linearity of phase shift versus drop diameter. A description of the Mie scattering analysis undertaken and the results for various off axis angles are given in Shrimpton et al. (1995).

Table 2: PDA system dimensions

Description	Value	Units
Laser power	100	mW
Light wavelength (u)	514.5	nm
Light wavelength (v)	415	nm
Beam separation	40	mm
Focal length (transmitting)	600	mm
Focal length (receiving)	600	mm
Measurement volume diameter	0.3	mm
Off axis angle	70.6	°
Refractive index (C_{10})	1.46	-

4. SPRAY VISUALIZATION RESULTS

Qualitative spray visualization results are presented for the three cases described in table 1. It is noted, for reference, that an uncharged 'spray' from this atomizer, at the conditions described in table 1, consists of stream of large drops moving along the spray centreline. Fig. 4 shows the case for a flow rate of 0.5cc/s and a specific charge of ρ_V=-1.20C/m^3. It is shown that the plume has expanded significantly and the outermost drops of the densely populated core exhibit moderate radial deflections. This figure clearly highlights the bimodal nature of most charged sprays. Recirculation is also observed at small axial displacements, near the injector, and this is due to small charged drops, produced from jet breakup, being attracted back towards the earthed atomizer body. For higher flow rates and specific

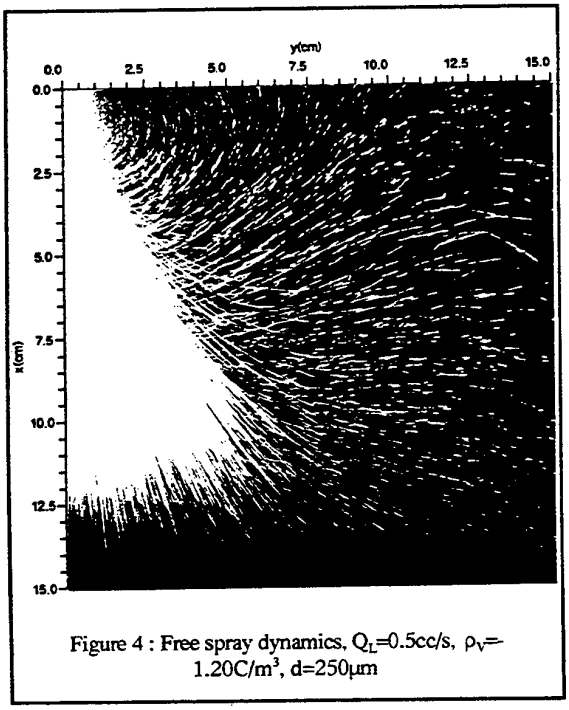

Figure 4 : Free spray dynamics, Q_L=0.5cc/s, ρ_V=-1.20C/m^3, d=250μm

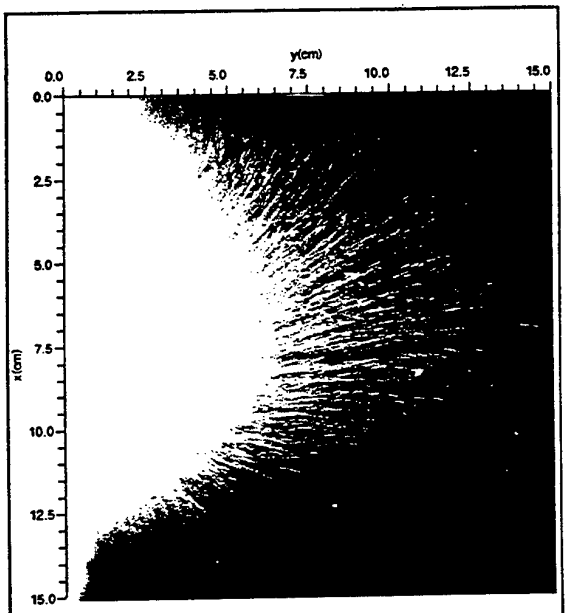

Figure 5 : Free spray dynamics, Q_L=1.67cc/s, ρ_V=-1.80C/m^3, d=250μm

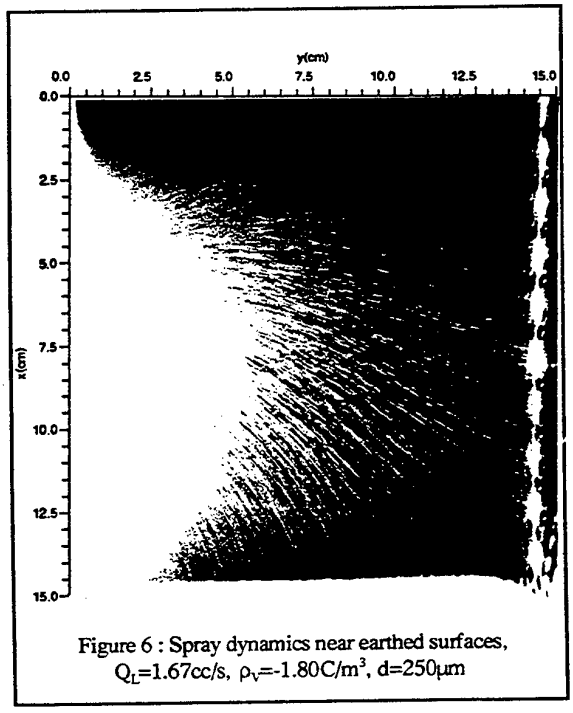

Figure 6 : Spray dynamics near earthed surfaces, Q_L=1.67cc/s, ρ_V=-1.80C/m^3, d=250μm

charge, shown in Fig. 5, with the earthed plate removed, the amount of scattered light increases significantly and the spray, under the influence of space charge forces expands to fill the volume illuminated. The sprays presented show strong radial forces acting on the drop trajectories and CFD modelling (Shrimpton et al, 1996b) has revealed that the radial electric field, due the approximate cylindrical symmetry, is at least an order of magnitude greater than the axial electric field generated by the charged drops near the centreline. The drop trajectories are very well ordered, typically emerging normally from the spray core and diverging at larger radial displacements. As shown in Fig. 6, for the same flow conditions as in Fig. 5, the effect of placing an earthed surface at x=0.15m and y=0.15m is pronounced. The smaller drops near the spray periphery appear to follow the electric field lines expected between the nozzle injector and the earthed plates. This shows that drop trajectories may be easily influenced away from the dense core of the spray, even by earthed plates and shows that the bulk spray charge has little influence away from the axial centreline. Results for a spray

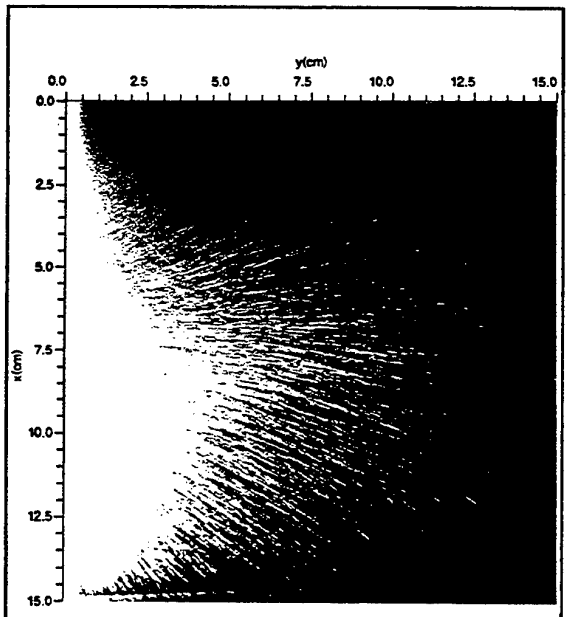

Figure 7 : Free spray dynamics, Q_L=0.5cc/s, ρ_V=-3.00C/m^3, d=150μm

produced by a 150μm orifice were also obtained and an example is shown in Fig. 7. The increase in specific charge (highlighted in Fig.1) produces still higher drop number concentrations and trajectory deflections. This is evident since a great deal of light is still scattered in Fig. 7, despite a flow rate only approximately 1/3 of the flow rate in Figs. 5 and 6.

5. DROP DIAMETER RESULTS

Quantitative results for the two flow rates using an orifice diameter of 250μm are now presented. Figure 8 shows the axial variation in drop diameter number distribution within the core for a flow rate of Q_L=0.5cc/s. The results are very different from

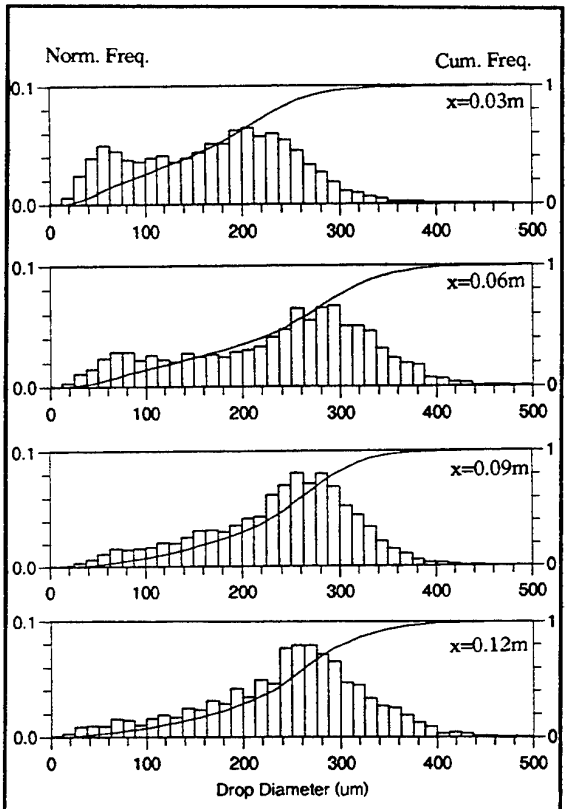

Figure 8 : Drop frequency distribution, Q_L=0.5cc/s, ρ_V=-1.20C/m^3, d=250μm at y=0.0m

the sprays presented in Fig. 2 for an atomizer with an orifice diameter of 500μm since the distribution is now continuous. The multi-modal character of the charged spray distribution is preserved but there are no intervals where drop diameters are not detected. At small axial displacements a range of drop sizes in the range 300>D>0μm predominate but as the axial displacement of the measurement volume from the injector was increased the frequency of the small drops decreased and ultimately a drop size distribution with a median approximately equal to the orifice diameter was produced. This is in common with results for the 500μm atomizer in that the most frequent large diameter drops are approximately equal to the orifice diameter. However the continuous nature of the size distribution is strikingly different for the sprays of higher specific charge reported here than for the previous, less highly charged sprays of Shrimpton et al (1995). A similar result was obtained for the Q_L=1.67cc/s flow rate shown in Fig. 9. In this case however the size distribution is skewed towards the smaller drops and the

most frequent large drop diameter is D=140μm. The mechanism for producing drop diameter distributions of this type for the case of charged sprays is not clear but significant aerodynamic forces,

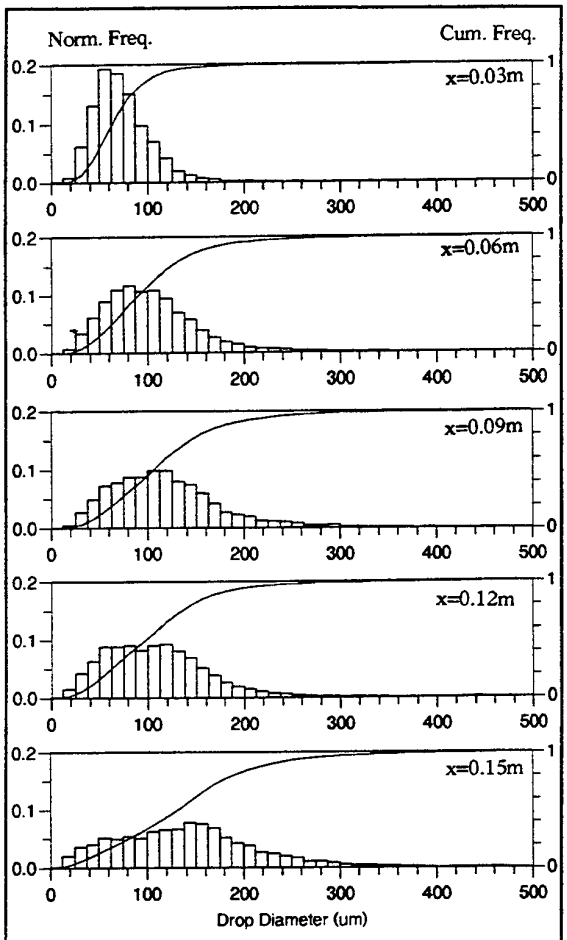

Figure 9 : Drop frequency distribution, Q_L=1.67cc/s, ρ_v=-1.80C/m^3, d=250μm at y=0.0m

and higher drop and charge concentrations would contribute to make any modelling attempt difficult. It is noted that the specific charge of the spray increases with flow rate as shown in Fig.1. Therefore the combination of larger electrical forces, combined with higher aerodynamic shear actually improves atomization performance at higher flow rates. This is achieved at minimal electrical energy input, since the power drawn from the high voltage supply is only of the order of tens of mW.

An understanding of the spray character may be obtained by examining the variation of the arithmetic mean diameter (D_{10}) throughout the 2D section of the sprays analyzed. Figures 10 and 11 show these drop diameter distributions for flow rates of 0.5 and 1.67cc/s respectively. The decrease in average diameter with increasing radial position is clearly shown in both cases, and as also is the expansion of the spray core, where the majority of the large drops are found, as the axial displacement from the atomizer increases. This stratification of drop diameter with radial displacement allows stable combustion to occur easily, since the small drops quickly evaporate and provide a stable flame seat (Shrimpton et al, 1996a). There is also evidence to suggest (Gomez, 1993) that evaporating charged drops rapidly and repeatedly break up and this acts to increase the overall evaporation rate.

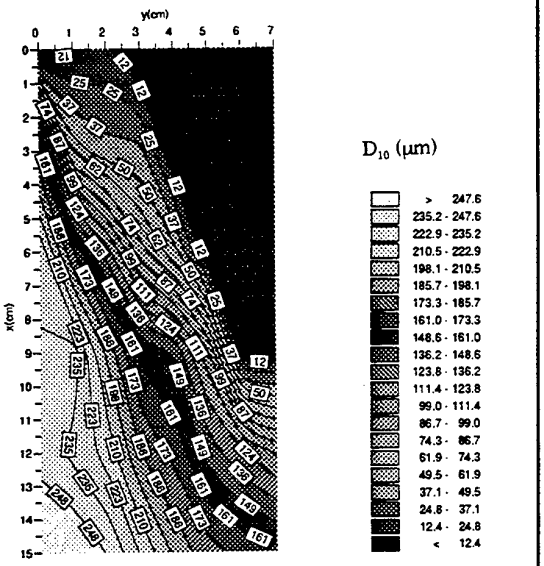

Figure 10 : D_{10} distribution, Q_L=0.5cc/s, ρ_v=-1.20C/m^3, d=250μm

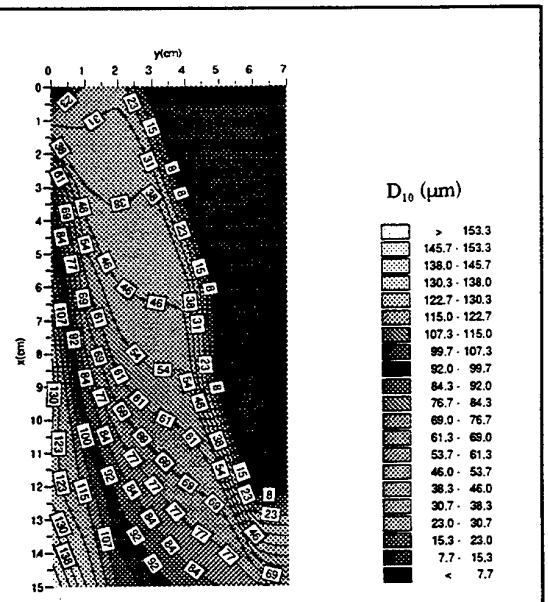

Figure 11 : D_{10} distribution, Q_L=1.667cc/s, ρ_v=-1.80C/m^3 d=250μm

6. DROP VELOCITY RESULTS

From the spray visualization and drop diameter results it has been shown that although a range of drop sizes are present the trajectories vary only gradually with respect to the spatial position in the spray. Figures 12 and 13 show the mean axial and radial velocity profiles at the measurement points plotted for the cases of Q_L=0.5cc/s, ρ_V=-1.20C/m^3, and Q_L=1.67cc/s, ρ_V=-1.80C/m^3 respectively. The general pattern of spray behaviour, first observed for the 500μm orifice diameter atomizer, of high

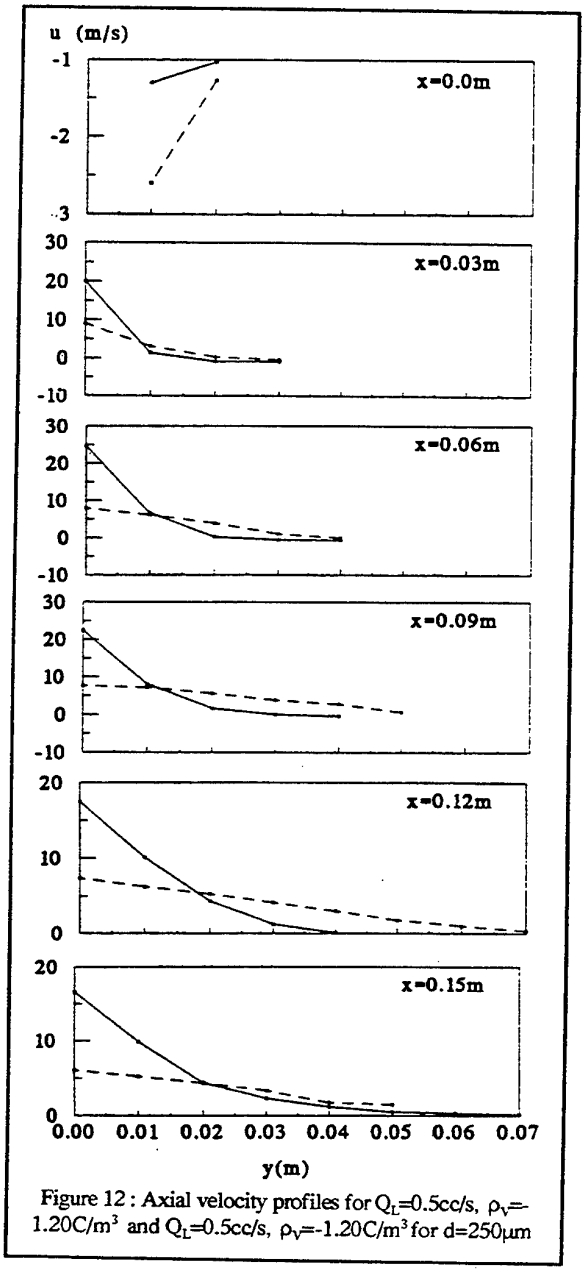

Figure 12 : Axial velocity profiles for Q_L=0.5cc/s, ρ_V=-1.20C/m^3 and Q_L=0.5cc/s, ρ_V=-1.20C/m^3 for d=250μm

axial velocity components and large radial accelerations in the spray core is repeated, even though the drop distribution is continuously varying, and radically different from the lower charged sprays described in Shrimpton et al. (1995).

An overview of the mean axial velocity profiles (Fig.12) shows that the axial velocity, in general, decreases with increasing axial displacement from the atomizer. This suggests that the initial momentum, from the liquid injection at the atomizer is transferred to the gas by drag forces. Indeed axial velocity versus drop diameter correlations at particular points along the spray centreline (Shrimpton, 1995) have shown that the drop axial velocity is proportional to the square of drop diameter, suggesting drag forces dominate. Of interest to charged spray dynamics is that the mean axial velocity for Q_L=1.67cc/s at x=0.03m (u=20.0m/s) is lower that the mean axial velocity at the next axial ordinate (x=0.6m) where u=24.6m/s, where, from the drag relation noted above, one would expect it to be lower. This behaviour is not repeated for the lower flow rate case presented here, nor was it observed from sprays produced by the atomizer with an orifice diameter of 500μm (Shrimpton et al, 1995). Predictions from a transient, turbulent two phase charged spray CFD code (Shrimpton et al, 1996b) showed that the axial electric field caused by the distribution of charge, on individual drops, throughout the spray changes direction between the atomizer and at an axial position where the spray core has spread out. Examination of the directions of the axial electric field and sign of the drop charge showed that the drops should be decelerated near the atomizer. This experimental evidence confirms that this phenomena does have an effect, providing sufficiently high spray specific charges are used and supports further development of the model.

Examination of the mean radial velocity profiles (Fig. 13) shows similar behaviour for both flow rates. In general the acceleration of the drops away from the spray centreline is highest for the spray with the larger spray specific charge. Due to the cylindrical symmetry the radial electric field along the spray centreline will be zero and this is the cause of the very small radial velocity components at these positions. Near the centreline the radial electric field is strong and decreases rapidly as radial displacement increases. Thus the radial velocity profiles are closely correlated with the strength of the radial electric field. Correlations between the radial velocity component and drop diameter at various measurement positions (Shrimpton, 1995) showed an approximately linear relationship.

Using several assumptions, this may be used to give an insight into the charge to mass ratios of charged drops as a function of drop diameter. Assuming the spray system has reached steady state and the drop drag force is balanced by the electrical force due to the interaction of the drop charge and the electric field caused by the charged spray then.

$$\overline{F_D} = \overline{F_E} \qquad (1)$$

For simplicity the drop drag is defined as the Stokes drag and for the radial component,

$$6\pi\mu_g D v = \phi E_y \qquad (2)$$

To test the charge to mass ratio versus drop diameter relationship, the assumption of constant surface charge density is used.

$$\frac{\phi_1}{D_1^2} = \frac{\phi_2}{D_2^2} \qquad (3)$$

This presumes that the charge relaxation time is much longer than the drop creation time and is thought to be a valid approximation for insulating liquids. It has already been pointed out that changes in the radial velocity component correlated closely with the strength of the radial electric field. However at the PDA measurements locations, fixed in space, for the steady state conditions for which results are presented, E_y will be constant. Therefore the only two variables in eqn (2) are the drop charge, ϕ and the drop diameter, D. By substituting eqn. (3) into eqn. (2) the relation between drop diameter and drop charge gives the following relationship between radial velocity and diameter.

$$\frac{v_1}{v_2} = \frac{D_1}{D_2} \qquad (4)$$

This relation is linear and provides indirect evidence that the assumption of eqn. (3) used in the charged spray modelling work (Shrimpton et al, 1996b) is valid. Admittedly there are several assumptions made in obtaining this result but it is felt that this may be the only way to obtain ensemble charge to mass ratio versus drop diameter measurements for charged sprays.

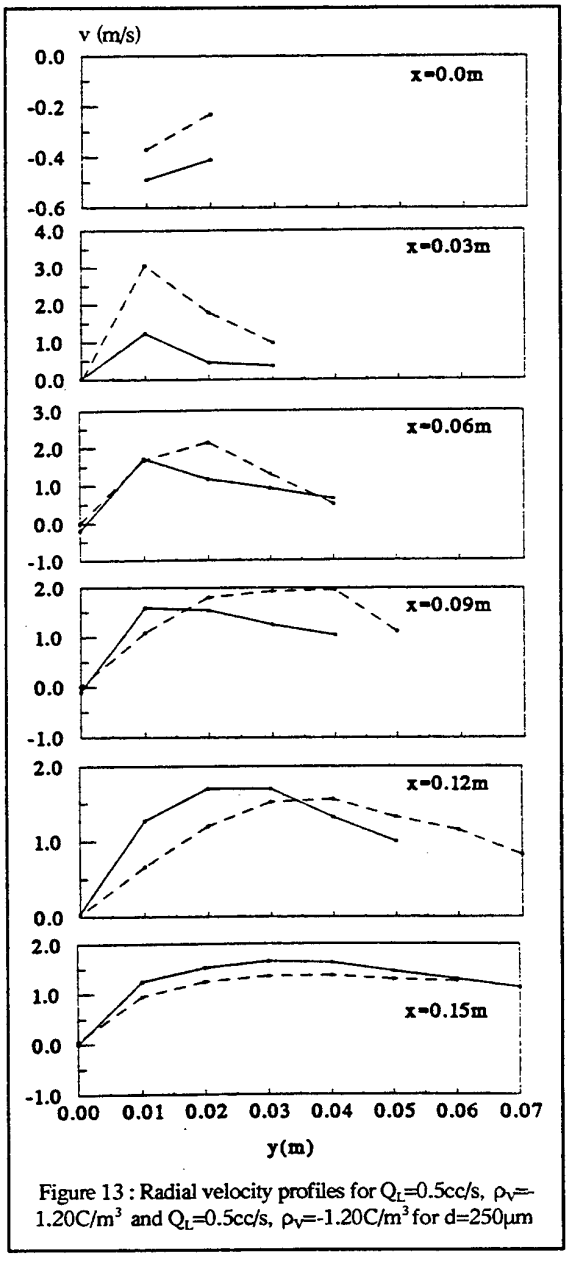

Figure 13 : Radial velocity profiles for Q_L=0.5cc/s, ρ_V=-1.20C/m^3 and Q_L=0.5cc/s, ρ_V=-1.20C/m^3 for d=250μm

CONCLUSIONS

The characteristics of highly charged hydrocarbon sprays have been presented and the drop diameter distributions have been found to be strikingly different from lower charged sprays from a similar atomizer. Average drop diameter decreases with increasing radial displacement from the spray centreline since the charge to mass ratios of the small drops is larger than that of more massive drops, which tend to populate the spray core. Radial velocities are closely linked to the magnitude of the radial electric field and a simple analysis of the relation between drop charge and drop diameter indicates a constant surface charge density assumption is valid.

ACKNOWLEDGEMENTS

The funding of the EPSRC and the loan of the 2D PDA equipment from Dantec (UK) are gratefully acknowledged.

NOMENCLATURE

Flow rate	Q_L	cc/s
Drop diameter	D	μm
Radial electric field	E_y	V/m
Force	F	N
Orifice diameter	d	μm
Axial velocity component	u	m/s
Radial velocity component	v	m/s
Drop charge	ϕ	C
Spray specific charge	ρ_V	C/m^3
Gas dynamic viscosity	μ_g	Ns/m^2

REFERENCES

Law S.E., 1978, "Embedded electrode electrostatic spraying charging nozzle", Trans. ASAE, pp. 1096-1104.
Gomez A. and Tang K., 1991, "Atomization and dispersion of

quasi-monodisperse electrostatic sprays of heptane. ", ICLASS-91, Gaithersburg MD, USA, pp. 805-812.
Shrimpton J.S., 1995, Electrostatic atomization and combustion of hydrocarbons oils", PhD thesis, UMIST, Manchester, UK.
Kelly A.J., 1984, "The electrostatic atomization of hydrocarbons", J. Inst. Energy, June, pp. 312-320.
Shrimpton J.S., Yule A.J., Watkins A.P. and W. Balachandran, 1995, "Size and velocity measurements in an electrostatically produced hydrocarbon spray", 1995, ASME/JSME LDA conference, August 1995, Hilton Head island, USA. August 13-18. vol 229 pp. 57-64.
Shrimpton J.S., Yule A.J., Watkins A.P. and W. Balachandran, 1996a, "Combustion of Electrostatically atomized hydrocarbon Sprays and the effect of applied electric fields", The Combustion Institute, Lisbon, Portugal, 1-4/4/96.
Yule A.J., Shrimpton, J.S., Watkins, A.P., Balachandran, W. and Hu, D, 1995, "Electrostatically atomized hydrocarbon sprays", Fuel, vol 74, No. 7, pp.1094-1103.
Shrimpton J.S., Yule A.J., and Watkins, A.P., 1996b, "Modelling of charged sprays including drop breakup", Paper to be presented at ECCOMAS-96, Paris, France.
Gomez A, 1993, "The electrospray : Fundamentals and applications", Invited Paper. 3rd World Conf. on Experimental Heat Transfer and Thermodynamics. Honolulu. Hawaii.

CHARACTERIZATION OF A PULSED FUEL INJECTOR

E. Haile, F. Lacas, D. Veynante and D. Durox

Laboratoire E.M2.C. du CNRS et de l'Ecole Centrale Paris
92295 Châtenay-Malabry Cedex, France

ABSTRACT

Two laser anemometric techniques are used to characterize a pulsed liquid fuel injector. Particle imaging velocimetry (PIV) is used to measure the an average spray velocity field, and to obtain information on the form of the spray. Phase Doppler anemometry (PDA) yields the average distributions of droplet size and axial velocity. Results are compared to mutually confirm and interpret the modification in the liquid spray characteristics induced by a time-varying upstream pressure. It is found that the information gained from each measurement technique is complementary, and that both are necessary to understand fully the other.

1 INTRODUCTION

Combustion processes find a wide range of applications, from transportation to commercial energy production, but are subject to pollutant formation and may lead to combustion instabilities. These problems can be overcome by actively introducing fluctuations in the oxidizer or fuel flow rates, see Candel (1992). Since the heat release rate is more sensitive to a modulation of the fuel flow rate, less effort is theoretically required to modify the combustion process when acting on this parameter than when acting on the air flow rate. However, while fluctuations at acoustic frequencies are relatively simple to produce in gaseous media, for industrial, liquid-fueled applications, there is a need for innovative technological solutions.

The response of the combustion process to unsteady fuel flow rates will depend on the influence of the liquid actuator on droplet dispersion and size and velocity distributions. Pressure fluctuations in the fuel supply line can interact with the atomization of the liquid fuel by the mechanical pulverizers typically encountered in industrial applications. Takahashi et al. (1995) have shown that large-amplitude high-frequency pressure fluctuations can change the dispersion angle of a liquid spray delivered by a mechanical atomizer. To quantify the effects of our new actuator on the droplet size and velocity distributions and the spray angle, optical diagnostic techniques were employed, as well as more classical measurement tools. This article presents the results of the characterization of a pulsed liquid fuel atomizer using phase Doppler anemometry (PDA) to measure the time-averaged droplet size and velocity distributions, particle imaging velocimetry (PIV) to measure the instantaneous droplet velocity field, and to compare with the PDA results, and hot film anemometer and piezo-electric pressure transducer signals to quantify the modulated fuel flow rate and pressure, respectively.

2 EXPERIMENTAL SET-UP

A domestic hot-water heater injector (Danfoss 0.50 gph 60° semi-hollow cone) is used, delivering 0.55 g/s, in conjunction with a rapid electrovalve (Fluid Automation Systems) to produce a pulsed spray of liquid heating fuel oil. The sintered bronze filter is removed from the injector and the valve is mounted in its place. The injector and valve are connected to a 2 liter reservoir of fuel oil pressurized under 9 bars of N_2. Four meters of flexible tubing (4 mm i.d.) lead from the reservoir to a 5 μm in-line filter, a piezo-electric pressure transducer and a hot film anemometer before the injector. The injector and fuel line are shown schematically in figure 1. The liquid used for the measurements is domestic fuel oil, average composition $C_{16}H_{30}$, density $\rho = 875$ kg/m^3. A refractive index $n \approx 1.45$ was chosen from values given in the literature for fossil fuels, see for example,

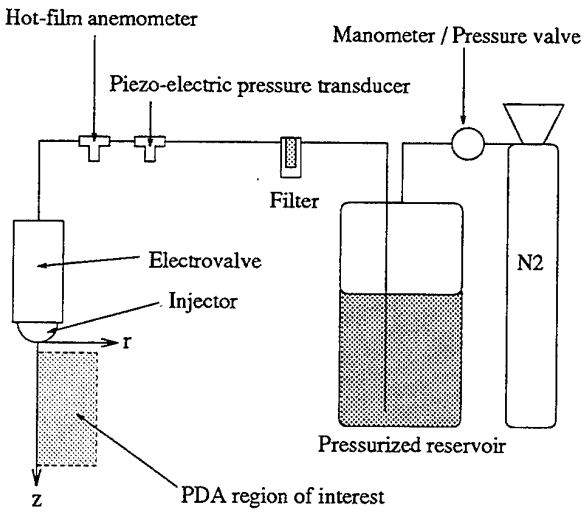

Figure 1: Schematic view of the injector, rapid electrovalve, piezo-electric pressure transducer, hot film anemometer, filter and fuel line.

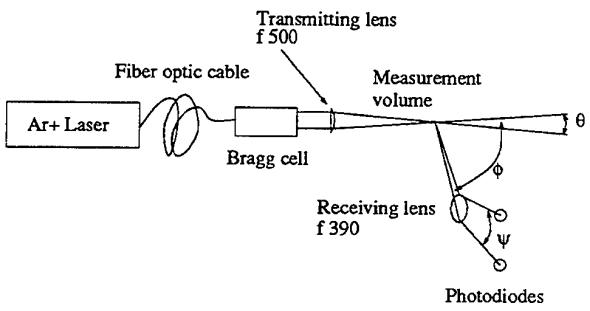

Figure 2: Phase Doppler anemometry set-up. The injector is placed upside-down in the measurement volume, and injects downwards.

Lide (1992).

The electrovalve is triggered with a square wave signal amplified by a 200 W amplifier when it is used in pulsed mode. The electro-mechanical response time is short enough to respond to frequencies up to 1000 Hz. In steady operation mode, a DC power supply is used to keep the valve open. The square wave signal, as well as the piezo-electric pressure transducer and hot film signals, are acquired by a PC equipped with an A/D converter for later signal processing.

The particle image velocimetry technique is discussed in detail by Adrian (1991). The set-up uses a 15 W 10 kHz Cu_{vap} laser. The beam is expanded into a laser sheet and collimated onto the injector axis by a concave cylindrical $f-100$ lens and a convex spherical $f450$ lens. At its focal point, the sheet is about 1 mm wide. An ultrarapid cine camera (NAC E-10) is used to image the laser light scattered at 90° by the droplets. The field of view extends from the injector 60 mm in the axial direction and ±40 mm in the radial direction. The camera functions at 8000 frames per second, and generates a synchronous pulse signal that triggers the laser. The 16 mm film is developped at 800 ASA, and has a grain size of approximately 1μm. The developped film is scanned at 2025 dpi ($\approx$ 800 pixels/mm). The scan resolution is inferior to that of the film, but the elevated developping temperature used to increase the image contrast probably degraded the film grain. The final image resolution is approximately 4 pixels/mm. A threshold is applied to the scanned images to eliminate the grain noise. This also inevitably filters-out some of the signal from the smaller droplets. Once processed, two successive images are divided into interrogation cells 40 pixels square, or about 4 mm square, and the intercorrelation of two corresponding cells in the two successive images is computed, to avoid ambiguity in the vectors' orientations, see Lecordier et al. (1994). The direct analysis technique presented by Cenedese & Paglialunga (1990) is used to evaluate the image intercorrelation. The maximum of the intercorrelation function gives the mean droplet displacement in the region of interest. A third-order polynomial fit was used to interpolate this maximum to increase the precision of the method to within $1/16^{th}$ of a pixel, which corresponds to 5 cm/s. In this manner, an instantaneous velocity field, locally averaged in space and over the distribution of droplet velocities, is obtained.

The phase Doppler anemometry set-up (INVENT GmbH) is shown in figure 2. A 10 W cw Ar^+ laser is connected by optical fiber to the emitting optics that separate and split the green and blue beams. The Bragg cell operates with zero frequency shift. The 514.5 nm beams are focused onto the measurement volume by a spherical f 500 lens, giving a convergence angle of $\theta = 5.7°$. The light scatered by the droplets crossing the measurement volume at $\phi = 45°$ from forward is collected by a spherical f 390 lens and a pair of photodiodes separated by 40 mm, or $\psi = 5.9°$. The diode signals are filtered and acquired with a digital oscilloscope. The oscilloscope communicates via an IEEE liaison with a PC, which processes the signals, and accumulates the droplet size and vertical velocity distribution statistics. In general, 1000 validated measurements are accumulated at each measurement point. The transmitting and receiving optics are mounted on a pneumatic microdisplacement table with two degrees of liberty, enabling a scan of the region of interest: 60 mm along the

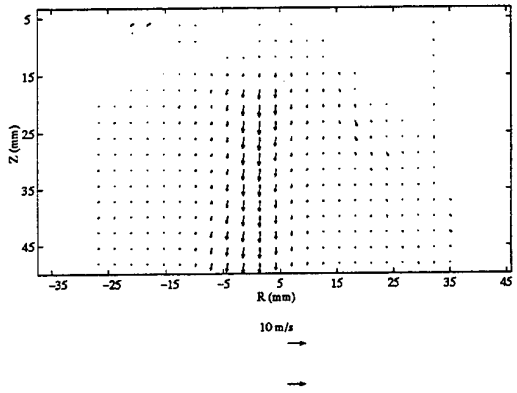

Figure 3: PIV results obtained for the continuous-mode injector.

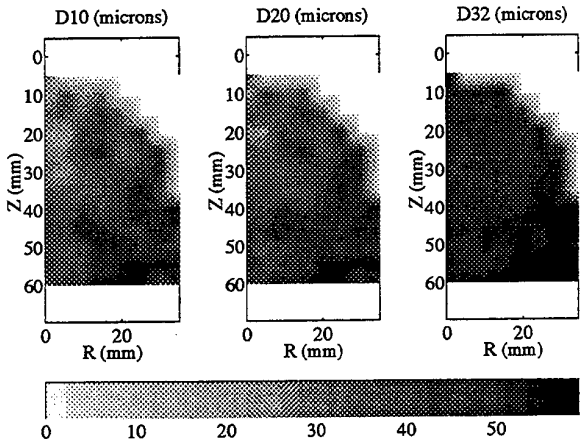

Figure 4: Average droplet diameters obtained by PDA for the continuous-mode injector.

spray axis and 35 mm in the radial direction, with an accuracy of ± 0.1 mm, see figure 1. For a detailed description of the technique, see Durst & Zaré (1975), Bauckhage & Flögel (1984) and Saffman et al. (1984)

3 RESULTS AND DISCUSSION

Figure 3 shows the modulus of the average droplet velocity field obtained by the intercorrelation PIV technique exposed in the previous section for the injector in continuous operating mode. The form of the spray is clearly visible. From the raw images and instantaneous velocity fields, one can see that the central region of the semi-hollow cone is dominated by closely-packed bursts of indistinguishable droplets, while the outer regions are a mixture of stagnated droplets falling under gravity or re-entrained by the spray, and individual high-speed droplets. The coordinates shown are relative to the injector, $r = 0$ corresponding to the injector axis, and $z = 0$ corresponding to the injector exit plane. The greatest average velocities (≈ 7 m/s) are attained in the central region of the spray, since the ensemble averaging of the results reduces vector amplitudes in sparsely populated zones. The deviation of the spray from the vertical near the bottom edge of the image is due to an angle between the image frame and the film's reference frame and appears during the scan of the latter.

Figure 4 shows the distribution of three average droplet diameters, the arithmetic average (D_{10}) the average squared diameter (D_{20}) and the Sauter mean diameter (D_{32}) for the injector in steady operation measured using the PDA technique. Note that the grayscale is different in each image in order to maximize contrast. The average diameters change little from the center to the periphery of the spray, and are within the manufacturers specifications. The observed increase in droplet size with distance from the injector is due to coallescence of smaller droplets in stagnated flow areas. The closely-packed droplets in the central column may be an effect of the width of the light sheet used in the PIV experiments. Since the PDA measurement volume is much smaller than the laser sheet, this technique is capable of resolving the individual droplets in these packets.

The average axial velocity of the droplets decreases with increasing distance from the injector, and one can note the relative importance of the velocity dispersion, figure 5, also for steady operation. Again, maximum average velocities are obtained near the injector axis, and are of the same order of magnitude as those found with the PIV technique. The agreement is not as good far from the injector, since the PDA set-up only measured the axial velocity component. The PIV results give the modulus of the measured two-dimensional velocity vectors. The agreement is not as good in the region between the central column of small droplets and the outer edges of the spray since the PIV technique is less biased towards slow droplets, which will reduce the measured locally averaged velocity. PDA will measure more of the faster droplets passing through the measurement volume during the data acquisition. What is more, since the Bragg cell operated with zero frequency shift, we probably rejected a good number of these slower droplets.

Also shown in figure 5 is the estimated numerical density of the droplets, which drops rapidly with distance from the injector. The edge of the spray pre-

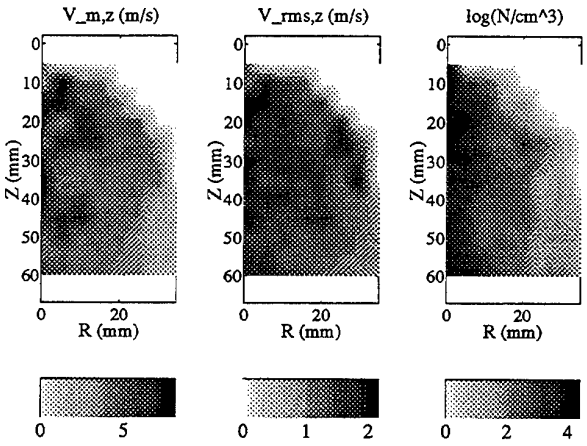

Figure 5: Average droplet vertical velocities and numerical density obtained by PDA for the continuous-mode injector.

sented in these results corresponds to the point beyond which the data acquisition rate dropped below a threshold value. As such, the PDA-measured spray angle differs from that seen with the PIV technique.

In order to account for the complexity of the spray characteristics, we represent the results by averaging over three classes of droplets: small droplets, whose diameter is $d \leq 30\mu$m, medium droplets, whose diameter is such that $30 < d \leq 60\mu$m, and large droplets whose diameter $d > 60\mu$m.

Figure 6 shows the size distribution averaged over the three droplet classes. This representation brings out the dominance of the small droplet class in the hollow cone of the spray. It also clearly shows that the edge of the spray is dominated by medium-sized droplets. The large droplets that do appear at the edges of the spray and of the region of interest probably result from collisions between smaller droplets, coalescing into the large droplets observed. This information is not apparent in the distribution of average droplet diameters, figure 4.

The local average mass fractions, figure 7, show that, although the small droplets near the axis account for more than 90% of all the droplets measured, they only transport about 16% of the mass of liquid fuel injected. Therefore, for combustion applications, other than flame stabilization, the Sauter mean diameter, which privileges larger droplets, is adequate to describe the distribution of liquid mass. In fact, most of the mass of liquid fuel is transported by the medium droplets, except for regions far from the injector, where the droplets would have evaporated in a combustor. The Sauter mean diameter for the spray falls into this class of droplets.

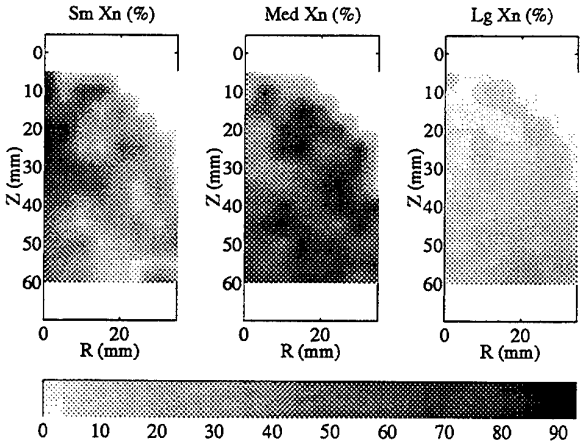

Figure 6: Size-averaged droplet size distribution for the continuous-mode injector.

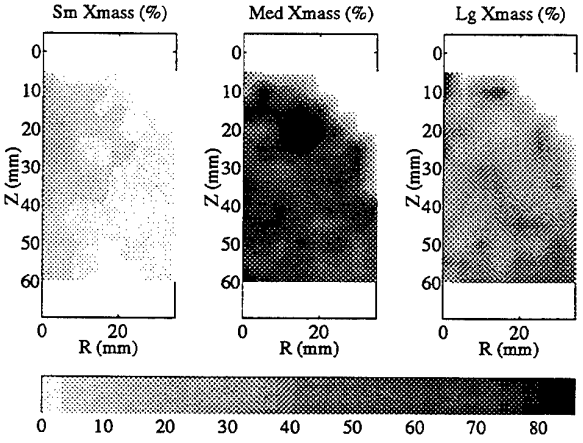

Figure 7: Size-averaged droplet mass distribution for the continuous-mode injector.

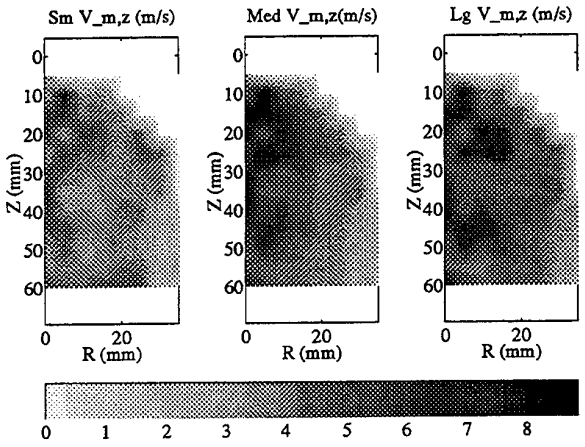

Figure 8: Size-averaged droplet mean vertical velocity for the continuous-mode injector.

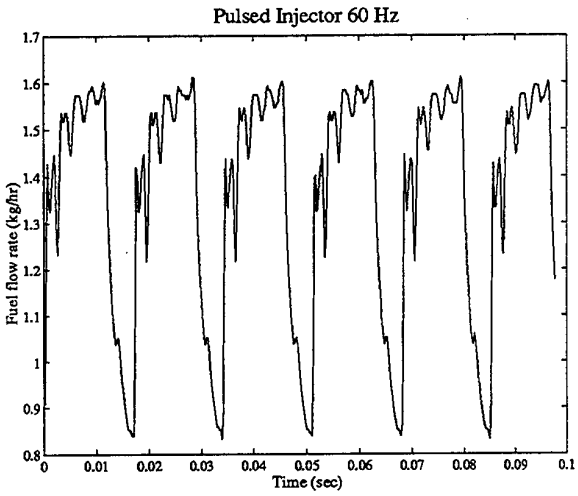

Figure 9: Instantaneous fuel flow rate measured by hot film with injector pulsed at 60 Hz.

The average vertical velocities of the three classes are given in figure 8. In general, the small droplets are slower than the medium and large droplets. All classes tend to slow down as they move away from the injector, which is normal. The fact that the large droplets are slightly slower than the medium droplets (the maximum large droplet velocity is about 8 m/s, while the maximum medium droplet velocity is around 8.5 m/s) belies their origins in droplet collisions.

When the valve is set in oscillation, the average liquid flow rate is reduced, as measured by hot film anemometry. Figure 9 shows the instantaneous fuel flow rate measured upstream of the injector. As might be suspected, the limiting factor in the valve's capacity to modulate the liquid flow rate is the mechanical closing time. The valve is opened by an electromagnet, therefore the opening time can be controlled, however, the valve is closed by a mechanical spring whose response time is limited. Therefore, the valve's operation is not entirely on/off, and at this frequency, the amplitude of the fluctuation is only about 40% of the average flow rate. As the frequency is increased, the quantity of fuel actually pulsed decreases. The high-frequency oscillations are due to the acoustics of the liquid fuel lign, and are the traces of reflected waves. The amplitude of these oscillations dies down with time and the fuel flow rate approaches its nominal value at this feed pressure.

Figure 10 shows that the maximum average droplet velocity measured by PIV is reduced by about 30% to around 5 m/s with the upstream fuel flow rate given above. This reduction is of the same order of magnitude as the reduction in the time-averaged fuel flow rate. Compared with the continuous-mode velocity field, here the edge of the spray seems to be less well-defined. The spray angle will open and close as the pressure upstream of the injector rises and falls. 100 individual velocity fields were again averaged to obtain this image, corresponding to 1.25 ms, which is a little less than one valve cycle, 1.67 ms.

The PDA-measured average droplet diameters and velocities are given in figures 11 and 12, respectively. The radial distance scale has been increased; the maximum radial coordinate in the images is 25 mm, instead of 35 mm for the continuous injector. The measured spray angle seems reduced by the valve's action; beyond 25 mm in the radial direction, the data rate drops below the threshold value chosen to define the spray's edge. Therefore, the droplets observed in this region with the PIV technique must only be present during a part of the valve's cycle. The time-averaged PIV image conserves the trace of these droplets as small velocities, while the probability of finding these droplets in the PDA measurement volume drops considerably.

Surprisingly, the average droplet sizes do not seem effected by the fluctuating fuel flow rate. As the pressure upstream of the nozzle drops, one would expect larger droplets or ligaments to be formed in the spray. Apparently, during the valve's closing, the pressure does not drop sufficiently to compromise the atomisation of the liquid before the valve opens again. What is more, the rapid rise time in the fuel flow rate indicates that the pressure behind the injector rises very rapidly to its optimal value. However, the droplets, having less momentum, seem to stagnate earlier, and the average diameters increase closer to

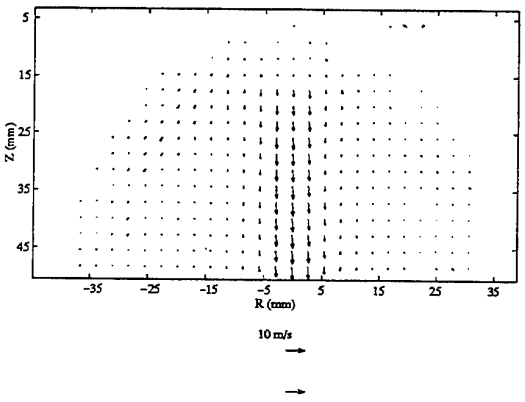

Figure 10: Average PIV-measured droplet velocity field for the injector pulsed at 60 Hz.

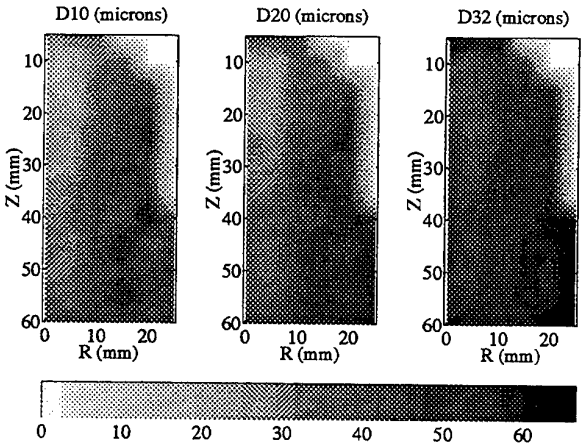

Figure 11: Average droplet diameters obtained by PDA for the injector pulsed at 60 Hz.

the injector than in the continuous operating mode.

The same reduction in average velocities observed with PIV when the valve pulses the liquid flow rate is measured by PDA, and the same order of magnitude of the maximum average velocity is found. The droplets have less initial momentum, and will therefore stagnate and coalesce closer to the injector. The spray structure seems to have changed, as well; the high-density region near the injector is widened in the radial direction and shortened in the axial direction.

As before, the PDA results are averaged over three droplet classes, depending on their diameters. Figure 13 shows the numerical distribution of the three classes. The high-density region observed in the numerical concentration plot (figure 12) is dominated by the small droplets, while the majority of the spray is dominated by the medium-sized droplets, which includes the Sauter mean diameter. It would seem that one of the effects of the valve's action is to increase the concentration of small droplets in the spray, and to modify the latter's internal structure. As can be seen in figure 14, up to 25% of the mass of liquid fuel in this region is now carried by the small droplets.

Figure 15 shows that the reduction in the average vertical velocity of the droplets effects all droplet categories equally. Therefore, there are no large droplets formed by the pulsed injector. The increase in droplet size when the valve modulates the fuel flow is due simply to the reduced droplet velocity, and increased coalescence.

The same measurements were carried-out for the valve pulsed at 600 Hz, but the results are not shown here for brevity. As the forcing frequency increases, the valve closes less and less, due to the slow me-

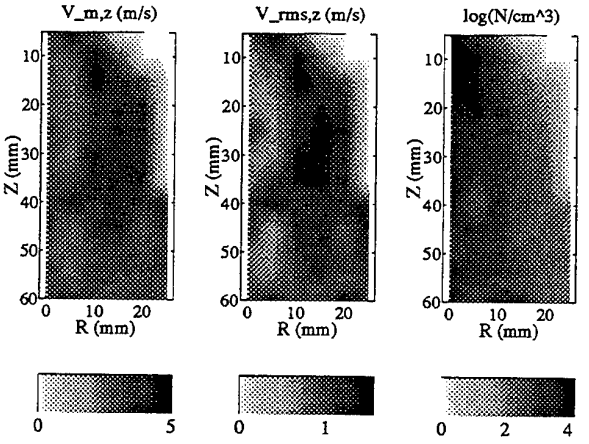

Figure 12: Average droplet vertical velocity component and numerical density obtained by PDA for the injector pulsed at 60 Hz.

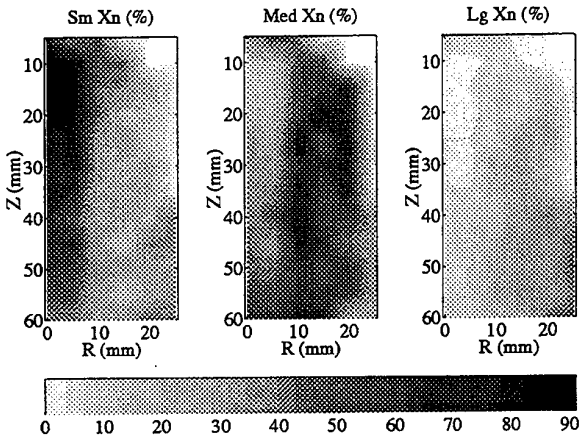

Figure 13: Size-averaged droplet size distribution for the injector pulsed at 60 Hz.

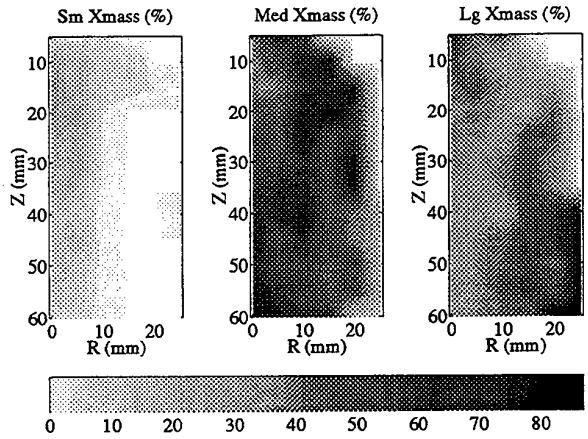

Figure 14: Size-averaged droplet mass distribution for the injector pulsed at 60 Hz.

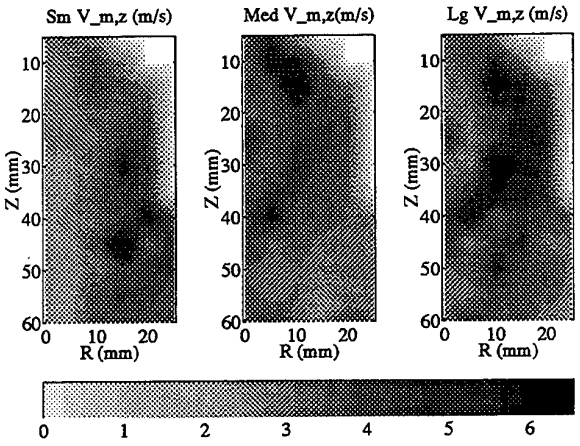

Figure 15: Size-averaged droplet mean vertical velocity component for the injector pulsed at 60 Hz.

chanical response time of the spring. As such, the amplitude of the flow rate modulation decreases. At 600 Hz, this amplitude is less than 10% of the maximum, steady flow rate. The PIV results are no different from the continuous-mode injector. The PDA results, however, show a reduced spray angle. The angle is wider than that observed when the valve operates at 60 Hz, and the average velocities increase with respect to the low-frequency case presented here.

4 CONCLUSIONS

Two different, complementary laser diagnostic techniques have been used to characterize a liquid heating fuel oil injector in a continuous operating mode, as well as with a pulsed fuel flow rate. Phase Doppler anemometry has been used to measure the dispersion of droplet sizes and velocities in the spray generated by the mechanical atomizer. Particle image velocimetry has been used to measure the instantaneous spray velocity field. Comparison of the two velocity fields shows that both techniques yield quantitatively the same results, if care is taken to compare comparable measurements. The PIV technique, while affording temporally resolved measurements, is biased towards the large droplets, since the scattered light intensity in Mie scattering increases nonlinearly with droplet diameter. What is more, PIV will locally average the measured velocities, thereby favoring the most dense droplet populations. PDA, on the other hand, will temporally average the results, thereby eliminating information about organized droplet clouds, that can be seen with PIV. PDA is also sensitive to droplet density and is bi-

ased towards fast droplets, and will ignore stagnated droplets, which can be seen with PIV, unless a Bragg cell is used. By comparing the results of these two experimental techniques, a more complete picture of the spray characteristics is obtained.

When the upstream pressure is actively modulated at acoustic frequencies, the average and instantaneous spray velocity distributions change. The spray angle and velocity are sensitive to average upstream injection pressure. However, on average, the size distribution does not change. The spatial distribution of the spray also changes when the valve modulates the liquid flow rate. Not only does the spray angle close, but inside the spray, the droplets formed are smaller in the central region. This central region is also larger under the effects of the valve. The same phenomena are observed at 600 Hz as for 60 Hz, with the exception that, as the excitation period approaches the mechanical cut-off frequency of the valve, the percentage of the fuel mass flow modulated by the valve's action is reduced. Thus, the droplet velocities, mean flow rate and spray angle increase.

These results are promising for a future application of this technology to active combustion control.

References

Adrian, R. J. (1991). Paticle-imaging techniques for experimental fluid mechanics. *Annu. Rev. Fluid Mech., 23*, 261–304.

Bauckhage, F. & Flögel, H. H. (1984). Simultaneous measurements of droplets size and particle velocity in nozzle sprays. In *2nd LDA Symposium, Lisbon.*

Candel, S. (1992). Combustion instabilities coupled by pressure waves and their active control. In *Twenty-Fourth Symposium (International) on Combustion*, (pp. 1277–1296). The Combustion Institute, Pittsburgh.

Cenedese, A. & Paglialunga, A. (1990). Digital direct analysis of a multiexposed photograph in PIV. *Exp. in Fluids, 8*, 273–280.

Durst, F. & Zaré, M. (1975). Laser Doppler measurements in two phase flows. In *LDA Symposium, Copenhagen.*

Lecordier, B., Mouqallid, M., & Trinité, M. (1994). Simultaneous 2D measurements of flame front propagation by high speed tomography and velocity field by cross correlation. In *Seventh Int. Symp. on Appli. of Laser Tech. to Fluid Mech.*, volume 1. Lisbon, Portugal.

Lide, D. R. (Ed.). (1991–1992). *Handbook of Chemistry and Physics* (72^{nd} Edition ed.). CRC Press.

Saffman, M., Buchhave, M., & Tanger, H. (1984). Simultaneous measurements of size, concentration and velocity of spherical particles by a laser Doppler method. In *2nd LDA Symposium, Lisbon.*

Takahashi, F., Schmoll, W. J., & Dressler, J. L. (1995). Characteristics of a velocity-modulated pressure-swirl atomizing spray. *J. Prop. and Power, 11*(5), 955–963.

APPLICATION OF EXTENDED PHASE-DOPPLER ANEMOMETRY IN LIQUID-GAS ATOMIZATION

J. Domnick[#], J. Raimann[#], G. Wolf[‡]

[#]Lehrstuhl für Strömungsmechanik
Universität Erlangen-Nürnberg, Cauerstr. 4, D-91058 Erlangen, FRG

[‡]Applikations- und Technikzentrum für Energieverfahrens-, Umwelt und Strömungstechnik (ATZ-EVUS), Rinostr. 1, D-92249 Vilseck, FRG

0 ABSTRACT

During the last years the investigation of atomization of molten metals was enforced by several groups of scientists (Bauckhage et al.(1991), Bergmann et al.(1991), Lavernia et al.(1992)). For the purpose of an improved quality of the powder produced on-line particle size measurements of the resulting powder were tested using different optical measurement techniques. Fraunhofer scattering systems and other intensity based light scattering instruments were used e.g. by Ridder et al. (1992) and Henein et al. (1992) for an on-line control of the process during supersonic gas atomization. Phase-Doppler anemometry was first applied and is still used by Bauckhage et al. (1988) in the molten metal spray of the spray compacting material process.

The present investigations, performed within the EU Brite/Euram project entitled "On-Line Process Control of Liquid Gas and Water Atomization by Extended Phase-Doppler Anemometry", aim to apply phase-Doppler and extended phase-Doppler anemometry in liquid gas atomization (LGA). In this contribution, the layout of the Phase-Doppler system used in a laboratory scale LGA unit are described and first measurement results in conventional gas atomization (CGA) as well as LGA, including also simultaneous measurements of molten metal and liquid gas droplets, are presented.

1 INTRODUCTION

The material properties of metal and alloy powders can be considerably influenced by cooling their melts very rapidly. By using appropriate methods cooling rates between 10^2 K/s up to more than 10^8 K/s can be achieved. The time for ordering effects in an atomic scale is short and the nucleation and growth of crystals are strongly reduced resulting in a fine-grained microstructure. Segregation effects in alloys can be avoided and new crystalline, supersaturated phases may be generated. Depending on the material crystal nucleation may even be completely suppressed so that the melt solidifies with an amorphous structure. Since the mechanical and/or the physical properties of these materials are dramatically changed and enhanced, respectively, rapid quenching and powder metallurgical technologies have gained an enormous significance during the past two decades for multiple applications.

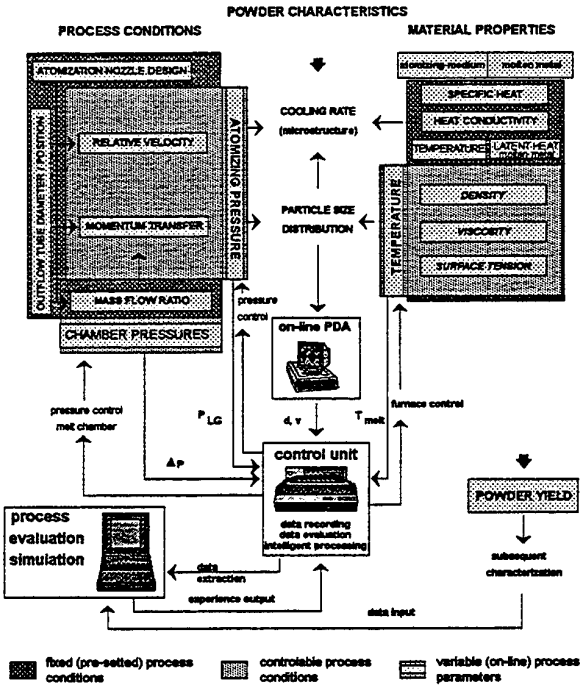

Fig. 1: Schematic representation of a suggested closed loop process control using phase-Doppler anemometry and appropriate data acquisition.

Powder production by atomizing the molten material ensures rapid cooling conditions and gas and water atomization (WA) processes are well established, industrially used techniques for this purpose. Gas (inert or air) or water jets are applied to disintegrate a molten metal stream resulting in rapidly solidified powder particles. The main parameters affecting the quenching rate during the atomization process may be summarized as the thermo-physical properties of both, melt and atomizing fluid, the relative velocities between the atomized melt droplets and the surrounding me-

dium and the droplet volume, as indicated by the schematic drawing in fig. 1.

High pressures have to be used in order to achieve high velocities and a finely dispersed droplet jet. With this respect, liquid atomization media provides some advantages compared to a gaseous atomizing medium. The higher specific mass results in an improved momentum transfer and more favorable thermo-physical properties (e.g. thermal conductivity) enhance heat exchange. However, the applicability of WA is restricted to metals or alloys with a low oxidation tendency. The LGA technique introduced a few years ago by Bergmann et al. (1988) appears to be a promising alternative for industrial powder production combining the advantages of both WA and CGA. Providing benefits similar to WA, the use of liquefied gas (e.g. N_2, Ar) allows atomization of melts without oxidation. Moreover, the cryogenic temperatures of the atomizing liquid further enhance cooling rates and the sudden evaporation of the atomizing medium with a volume expansion of factor 800 causes high turbulence inside the atomization region resulting in an enhanced atomization efficiency. Consequently, the achievable quenching rates are above 10^5 K/s. LGA already has been successfully employed for the production of powders exhibiting a high affinity to oxygen, i.e. rare earth alloys for hard magnetics (Wolf et al. 1994), where high quenching rates are essential in order to achieve a fine grained or even amorphous structure.

Beside the aim to achieve high quenching rates the yield of powder particles in a certain size range is essential for economic reasons. Fine powders are of growing interest for various applications, e.g. metal injection molding (MIM). The two most important parameters during the process that allow to adjust the process performance for a given nozzle geometry are the atomizing pressure and the mass flow ratio between atomizing fluid and melt (fig. 1). They can be varied within a certain range and have to be used to adjust the resulting particle size distribution. Hence, a tool is required which allows an on-line control of the atomization process. The aim of the present investigations was, therefore, to develop and to install a PDA set up enabling the on-line detection of particle size distributions during CGA and LGA of molten metals. This technique has to take into account the simultaneous presence of molten or already solidified metal particles and droplets of the cryogenic atomizing medium inside the atomized jet. First successful measurements have been carried out and the control scheme depicted in fig. 1 has partially been completed.

2 EXPERIMENTAL SET-UP

ATZ-EVUS has two atomization units of laboratory and pilot size, respectively, both being able to operate with (high pressure) gas or liquefied cryogenic gas. As shown in fig. 2, the units have separated melt and atomization chambers. By varying the pressure difference between the melt chamber and the atomization chamber the melt flow rate can be adjusted. The process steps during CGA and LGA are nearly identical. In order to achieve an efficient disintegration of the molten metal stream a "confined" atomization nozzle design is used where the drillings of the (liquid) gas nozzle are situated concentrically and very close to the melt feeding tube (fig. 3a). Therefore, the (liquid) gas jets impinge on the melt directly at the feeding tube orifice with a high velocity ensuring high quenching rates. The atomization jets exhibit a narrow and only slightly divergent shape with a diameter of approx. 10 (gas) to 30 mm (liquid gas) at a distance of 100 mm from the nozzle exit, which broadens with decreasing pressure. The laboratory unit used for the present experiments and the characteristics of the LGA process have already been described earlier in more detail (Wolf et al. 1994). This unit has been adapted for the application of the PDA (fig. 2), e.g. by the installation of windows to achieve the necessary optical access (see Domnick et al. 1995).

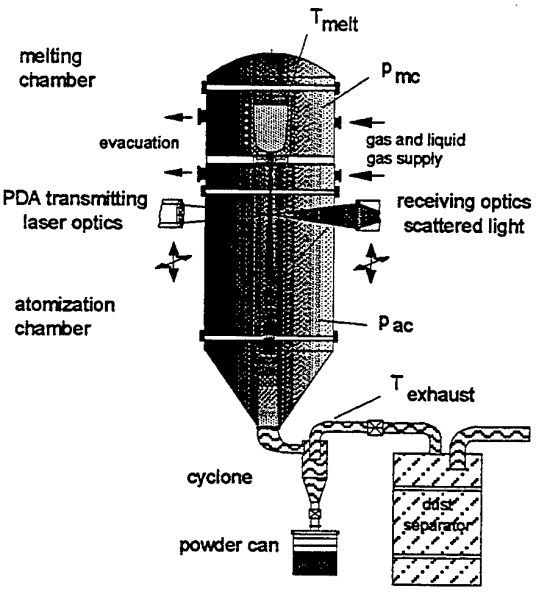

Fig. 2: Schematic illustration of the instrumented atomization unit including the PDA system installed.

The presented atomization experiments have been carried out with copper melts. Parameters has been varied as listed in table 1 in order to investigate their influence on the atomization characteristics and the PDA measurements performed:

Table 1: Atomization parameters settings

Parameter	Range
Melt superheat temperature	120 - 290 K
Melt feeding tube inner diameter	2,4 - 4,0 mm
Atomizing pressure	20 -70 bar (CGA) 10 -100 bar (LGA)
Mass flow ratio $m_{(L)Gas}/m_{Melt}$	0,5 -5 (CGA) 0,6 -10 (LGA)

Both gas and liquid gas atomized molten metals solidify with a spherical particle shape provided that no

chemical reaction with the melt occurs. Hence, the particles meet the requirements for being measured by phase-Doppler anemometry. The resulting particle size distribution is strongly influenced by the mass flow ratio, i.e. primarily by the applied atomizing pressure and the chosen inner diameter of the melt outlet.

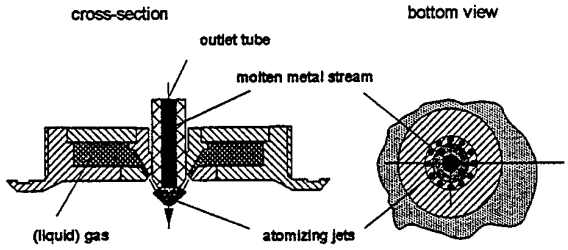

Fig. 3: a) Cross section and bottom view of the atomization nozzle used for the experiments

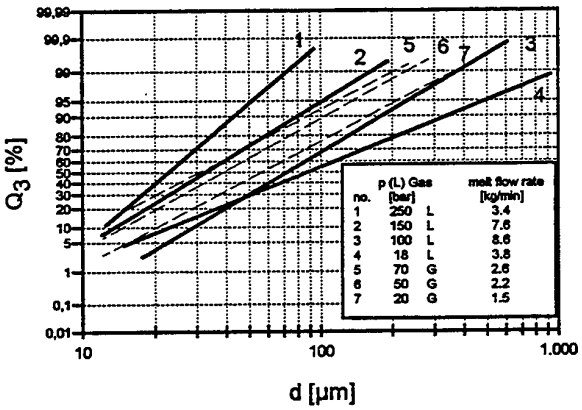

b) Log-normal distributions of typical Cu powders, gas and liquid gas atomized at various pressures and melt flow rates

In addition, the distribution widths varies with the parameters changed. Typical size distributions of Cu powders, gas and liquid gas atomized at different conditions, are shown in fig. 3b. In general, the variation of the median particle size with the applied mass flow ratio can be approximated by a function of the form $d_{m,30} = B + (m_{(L)Gas}/m_{Melt})^{-n}$ where B and n are constants depending on the melt properties. For the gas atomized copper of the present investigations values of B≈15 and n≈-0.4 have been derived.

3 OPTICAL CONSIDERATIONS

The phase-Doppler anemometry technique has already been applied to CGA (e.g. Bauckhage et al. 1991). During LGA, however, a technique is required that is able to distinguish between the melt and the atomizing liquid, delivering size and velocity information of both particulate phases independently. For this purpose, an extended phase-Doppler anemometer was installed.

The layout of such an extended PDA system depends on the optical properties of the observed materials. The classical extended PDA using two detector units at different scattering angles, as described e.g. by Brenn et al. (1994), measures the refractive indices of the particles, that can be used for the particle discrimination. The particulate phases have to differ by at least 0.1 in the refractive index.

Table 2: Properties of fluids considered

Material	Nitrogen (liquefied)	Copper (liq.)
Temperature		
T_b	77,33 K	
T_m		1357 K
Density	0,81 kg/l at T_b	8,0 kg/l at T_m
Surface Tension		1,303 N/m
Refractive Index	1,2-i 10^{-7}	1,5-i x (x=1-3)

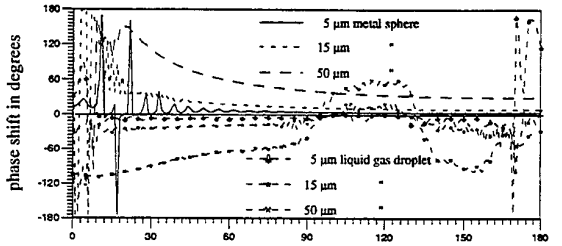

Fig. 4: Phase shift of melt and liquid gas droplets

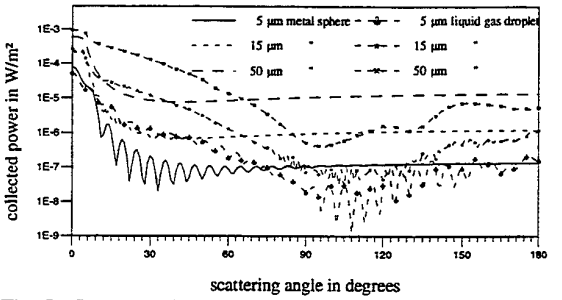

Fig. 5: Scattering intensity of melt and liquid gas droplets

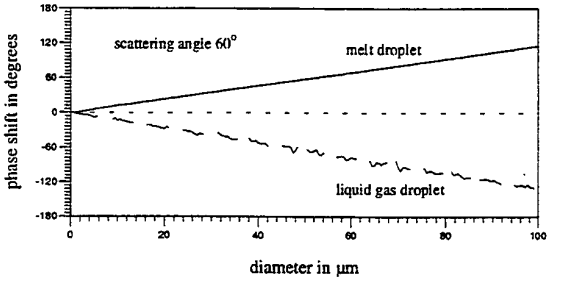

Fig. 6: Phase shift as function of diameter at a scattering angle of 60°

In the present case, the two fluids have completely different scattering properties (tab. 2). On the one hand, there is the atomization fluid (liquefied gas), which can be described as a transparent liquid, producing scattered light mainly due to refraction (at appropriate scattering angles).

On the other hand there is molten metal, which, as a perfect conductor, produces scattered light only due to reflection.

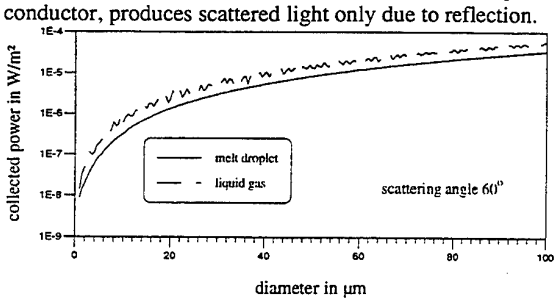

Fig. 7: Collected light power as function of diameter at a scattering angle of 60°

As well known from the derivation of the phase-Doppler principle, the phase shifts produced by reflection and refraction have opposite signs. This sign of phase can be utilized to discriminate between the different particulate phases, provided that only phase shifts between -180° and +180° are produced.

This, of course, has the disadvantage of reducing the size ranges to 50 % for a given PDA geometry, however, only one single detector unit is required. Mie-calculations have been performed to locate an appropriate scattering angle for the particles under consideration. In fig. 4 and 5., the phase shifts and the scattered light intensities for three different particle sizes of both phases are compared.

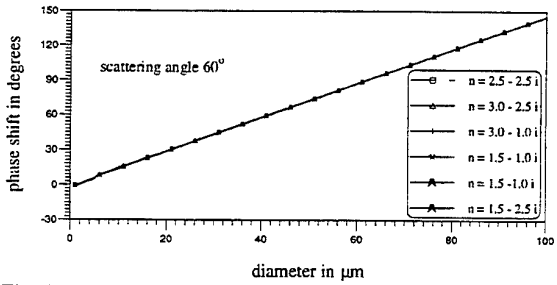

Fig. 8: Influence of variations in the complex refractive index of copper on the phase response

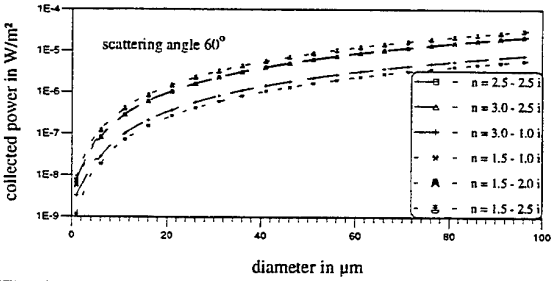

Fig. 9: Influence of variations in the complex refractive index of copper on the collected light power

Assuming that melt and liquefied gas droplets will have similar size distributions, an off-axis angle of 60° was chosen, yielding similar scattered light intensities for both phases. For this configuration calculations of the phase shift (fig. 6) and the scattered light intensity (fig. 7) as a function of the diameter in the range up to 100 µm were performed.

These calculations show very linear response curves with positive (melt) and negative (liquid gas) slopes of almost the same magnitude. Since different values for the complex refractive index of liquid copper can be found in literature (e.g. van der Hulst 1981), its influence on the phase-Doppler response function was verified.

As indicated by figs. 8 and 9, the final effect of the existing uncertainties can be neglected. Only the scattered light intensity shows some sensitivity to the imaginary part of the refractive index.

4 PRACTICAL IMPLEMENTATION OF THE SIGN OF PHASE METHOD

The present investigations have to be performed using a commercial PDA system (AEROMETRICS fiber based two-component system with DSA processor). Although custom made extended phase-Doppler systems have been realized at LSTM before, the necessary fast data acquisition and processing for an on-line process control

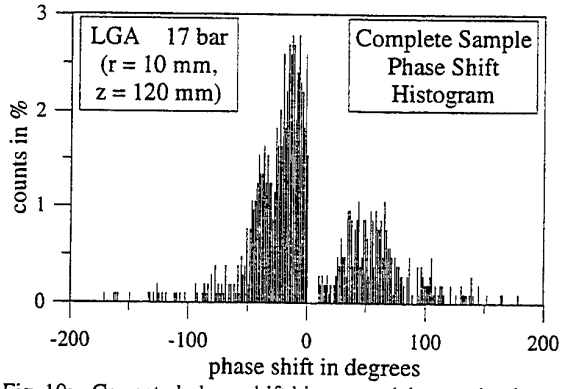

Fig. 10: Corrected phase shift histogram (phase redundancy turned off)

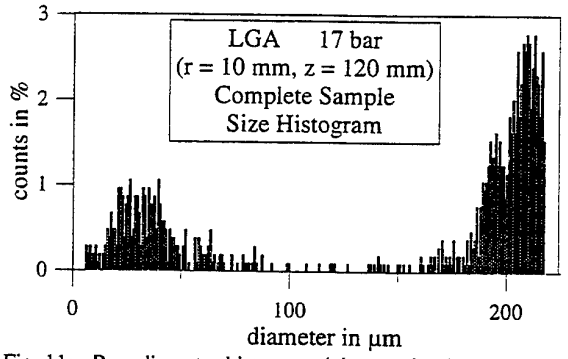

Fig. 11: Raw diameter histogram (phase redundancy turned off)

requires a high-speed system. Another advantage of the commercial system used is its high velocity bandwidth (up to 250 m/s) that is also required in the present application. However, the simultaneous measurement of refracting and reflecting particles during liquid gas atomization needs specific operating modes of the data processing software. As

a first step, the redundant phase measurements by three detectors in the receiving unit has to be switched off to enable measurements of phases with different signs. In this case, signal pairs having a 'wrong' sign of the phase shift (equivalent to a fringe movement in opposite direction) will appear with 360° phase shift offset. In fig. 10 the phase distributions for liquid nitrogen (negative phase) and melt droplets (positive phase) are shown.

The initial 0-360° phase axis has been transformed into a -180 to 180° phase axis. Finally, the size distributions of liquid gas and melt droplets are calculated from the individual phase factors for 1st order refraction and reflection at the scattering angle considered. In fig. 11 the corresponding

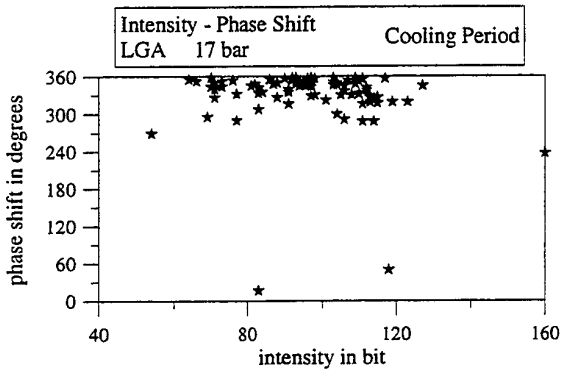

Fig. 12: Intensity - phase shift relation for the precooling period

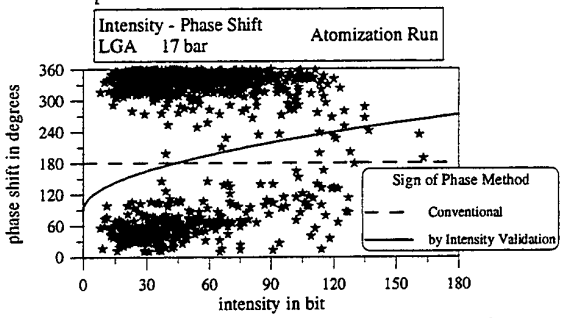

Fig. 13: Intensity - phase shift relation obtained during liquid gas atomization

raw size measurement of the DSA software is shown based on phases smaller and larger than 180°. As the orientation of the PDA receiving unit was adapted to dominant reflection, phases below this limit originate from melt droplets, while phases larger than 180° stem from liquid gas droplets. This approach yields only reasonable results if the size distributions are well separated and the absolute magnitude of the phases are always smaller than 180°. A slightly more flexible solution for the distinction between the different particulate phases is the usage of the signal intensities. The method of intensity validation that has been proposed to reduce the number of erroneous phase measurements (Bachalo et al. (1995)) is already realized in the DSA software. Fig. 12 shows measured phases versus intensity obtained in a measurement during the precooling period, where only liquid gas droplets are present. Using the DSA software, most of these samples would have been rejected due to too small intensities.

Fig. 13 shows a complete phase/intensity plot obtained in a typical LGA test, indicating two clearly distinguishable particle distributions. Instead of having a fixed phase limit, position and steepness of the parabolic shaped intensity discrimination curve may be adapted to the varying measurement conditions. The final setting of the curve has to be fitted according to the experiences obtained in CGA and LGA tests.

5 MEASUREMENTS IN CONVENTIONAL GAS ATOMIZATION

Preliminary tests for the realization and the verification of the on-line control have been performed during CGA. One major task of these experiments was to find a representative measurement location for the PDA that allows to make subsequent comparisons with off-line measuring techniques used to classify the final powder. Here, it should be pointed out that no traverse of the PDA system is feasible during the atomization tests due to the short response time necessary for a control loop. Thus, the PDA measurements will always deliver information only from a locally limited area inside the jet.

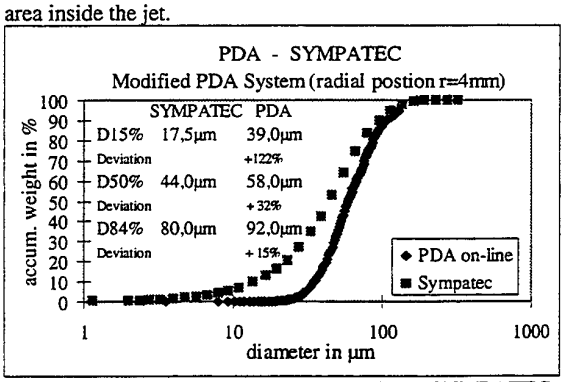

Fig. 14: PDA results compared with off-line SYMPATEC HELOS measurements

In the atomization unit of ATZ-EVUS, a representative point was determined to lie at a radial distance of a few mm from the centerline of the spray at 120 mm axial distance to the nozzle. Near this point the PDA results fit closely to the off-line sieving and SYMPATEC HELOS results. For comparison the PDA results were transformed into a cumulative volume distribution (fig. 14).

Although the PDA measurements show a certain underestimation of particles smaller than 50 µm, it could be demonstrated to be sensitive enough to detect variations in the relevant operation parameters, i.e. atomization pressure, molten metal temperature and nozzle diameter (see Domnick et al. 1995). The underestimation of small particles results from both a high number density in the melt droplet stream and a considerable amount of particles recirculating in the outer region of the atomization chamber. A typical PDA measurement obtained at the representative location mentioned above is shown in figs. 15 & 16. The distributions are

recorded with 1500 validated samples. Velocities up to almost 250 m/s could be measured at this location.

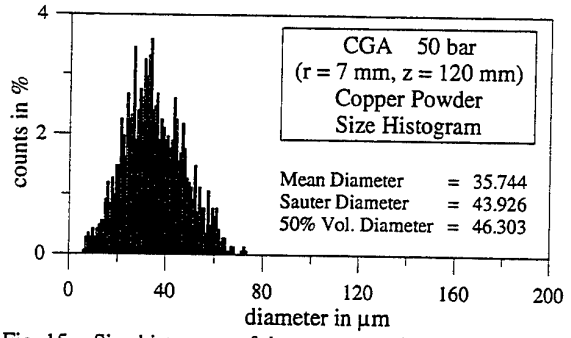

Fig. 15 Size histogram of the copper particles during CGA

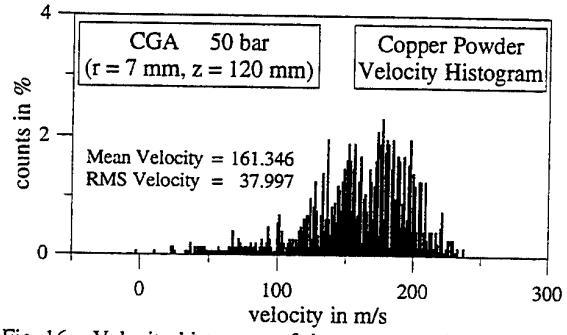

Fig. 16: Velocity histogram of the copper particles during CGA

Radial size and velocity profiles obtained in gas atomization are shown in figs. 17 & 18. In general, the mean diameters decrease with increasing radial distance as expected from a coaxial jet type of atomizing system. This is also true for the velocity profiles, exhibiting a reduction of the mean velocity and an increase in the RMS velocity towards the spray edge.

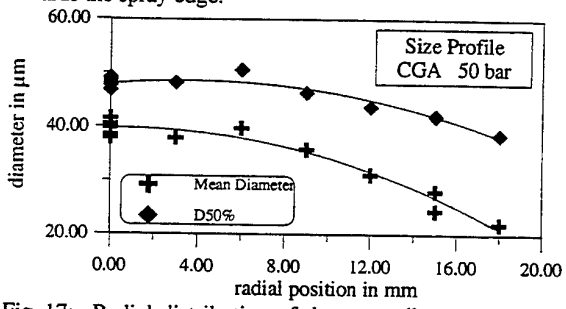

Fig. 17: Radial distribution of the mean diameters of the copper particles during CGA

Although the real mass flow rate varied during the experiment, the integrated mass flow rate based on the local PDA mass flux measurements (0.54 kg/min) corresponds reasonably with the true mean mass flux of 0.92 kg/min calculated from the melt consumption over the total experiment time. This result confirms again the applicability of phase-Doppler anemometry for the CGA process.

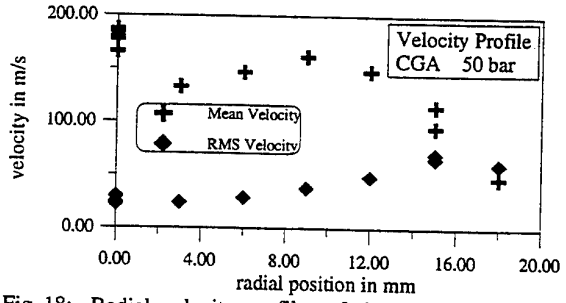

Fig. 18: Radial velocity profiles of the copper particles during CGA

6 MEASUREMENTS IN LIQUID GAS ATOMIZATION

Measurements during LGA were performed by using the modified sign of phase method described before. In figs. 19 to 22 the results of a representative atomization test is displayed in terms of powder and liquid gas sizes and velocities. Again, a total number of 1500 validated samples were taken, yielding stable mean diameters within a measuring time of 11 s. This measurement duration seems to be appropriate for the future realization of an on-line process control.

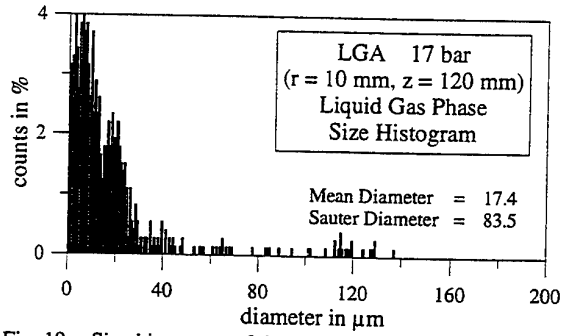

Fig. 19: Size histogram of the liquid gas phase

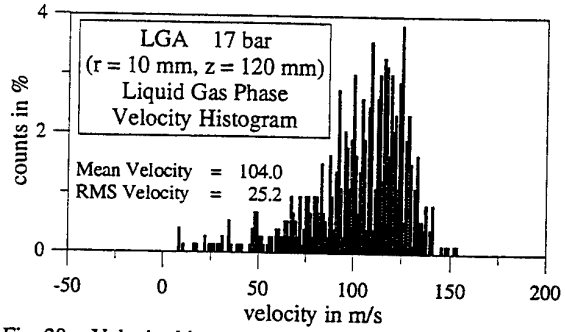

Fig. 20: Velocity histogram of the liquid gas phase

Applying the intensity validation for the discrimination as suggested, a small cross talk between the powder and the liquid gas fraction appears, leading to a few erroneous measurements in the upper part of the liquid gas droplet size distribution (fig. 19). Since the measurements have to con-

centrate on a stable estimation of the copper powder mean diameter, this cross talk seems to be acceptable.

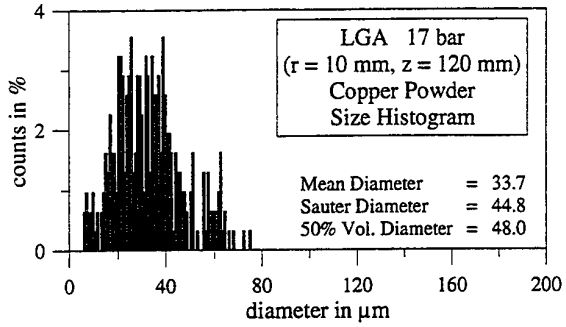

Fig. 21: Size histogram of the copper droplets / particles

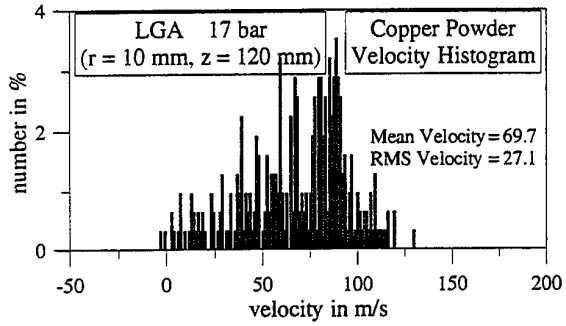

Fig. 22: Velocity histogram of the copper droplets / particles

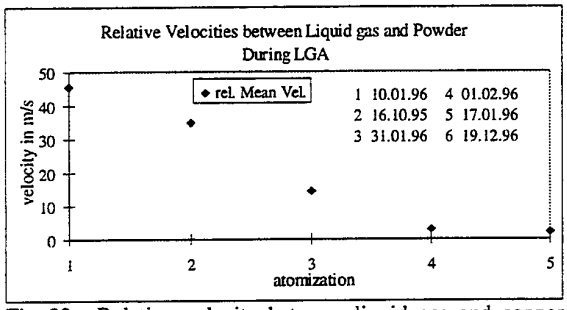

Fig. 23: Relative velocity between liquid gas and copper powder during LGA

Comparing the velocity histograms of liquid gas (fig. 20) and metal powder (fig. 22) a considerable difference in the mean velocities of liquid gas and melt can be detected. To clarify the significance of this effect, several atomization tests at similar conditions were performed. However, fluctuations of the process conditions cannot be fully avoided, e.g. a melt flow rate variation of 3 ± 1 kg/min for given outlet diameters of 2.3 - 3 mm. In addition, the void fraction at the nozzle of the usually boiling liquefied gas is dependent on the storage conditions. A stable temperature during the process can be achieved only by applying a pre cooling of the whole system. The influence of the void fraction on the exit velocity and the momentum transfer between liquefied gas and melt is not yet fully determined.

The atomization experiments in figs. 23 and 24 are arranged to have increasing diameters in terms of SYMPATEC results. Fig. 23 indicates, that increasing diameter correspondents to decreasing relative velocities.

Fig. 24 also depicts a systematic difference between the $D_{50\%}$ mean diameter measured on-line by PDA and off-line by the SYMPATEC Fraunhofer diffraction instrument as in CGA. The mean diameter of the gained powder (SYMPATEC results) differ only in a range between 92 µm and 108 µm due to the described condition variations.

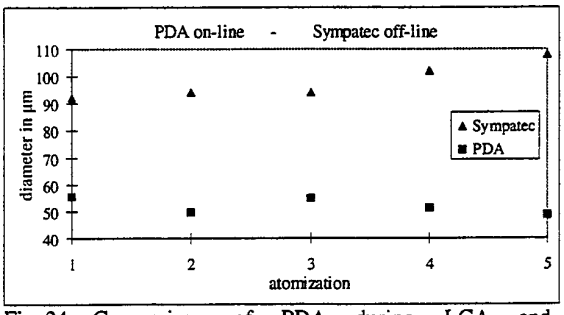

Fig. 24: Comparison of PDA during LGA and SYMPATEC off-line

7 FUTURE ON-LINE PROCESS CONTROL

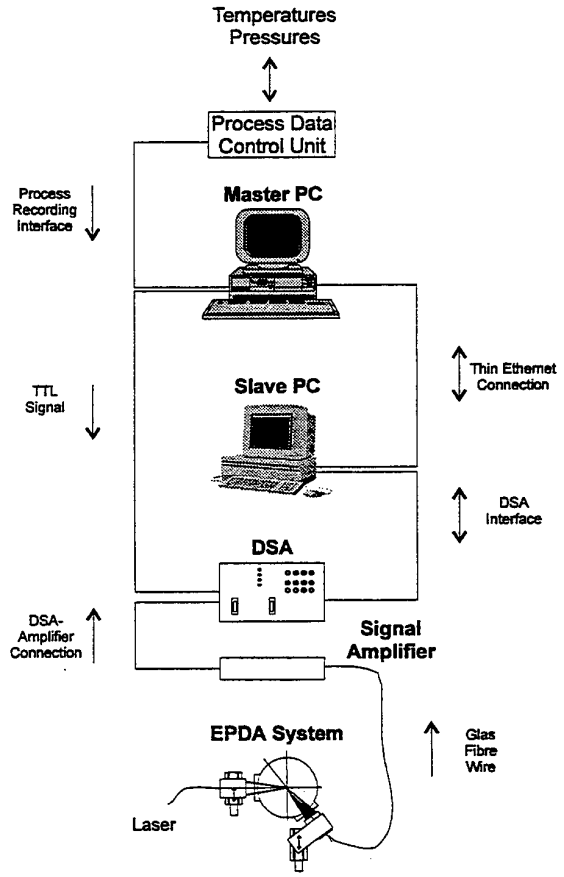

Fig. 25 Arrangement of hardware for the control loop in powder production

For the realization of an on-line process control several requirements for the PDA measurements must be fulfilled:

- The spatially and temporarily resolved results of the PDA measurements must correspond to the gained powder quality characterized off-line.
- The PDA measurements must be fast enough to enable a reasonable response time of the on-line control loop. So far, 1500 validated samples could be collected in approx. 10 s.
- The PDA measurements have to be transformed into a characteristic number, i.e. a mean diameter, that can be transferred to a control software executed by the master PC (see fig. 25).

As shown in fig. 25, the control loop will be realized by using two independent PCs connected via Thin Ethernet. Both computers are running under IBM OS/2, using the features of the IBM Peer utility. This operating system allows to establish a background connection between both computers and to realize a true multitasking of different programs running at the same time.

8 SUMMARY AND OUTLOOK

It could be shown, that the PDA technique is able to deliver reasonable results in both CGA and LGA. While a standard PDA system can be applied to CGA, LGA requires the distinction between liquid gas and melt droplets. Here, a modified extended phase-Doppler system based on a commercial instrument was successfully adapted. Discrimination between the two particulate phases is realized by using the sign of the phase in a -180° to 180° phase domain, slightly modified by additionally checking the intensity of the individual measurements. While during CGA a certain underestimate of small particles is obtained, measurements in LGA yield the opposite effect.. Nevertheless variations in the operating conditions can be detected on-line. Thus, phase-Doppler as well as extended phase-Doppler anemometry seem to be appropriate methods to be incorporated in a closed loop control.

In the near future, it is planned to extend the data base of measurements during CGA and LGA considerably. Therefor the reproducibility of PDA and EPDA measurements will be enhanced. A high pressure liquid gas pump will be applied for complementary investigations in atomizing pressures up to 250 bar. The on-line control loop as described above will be completed and tested during CGA first, before being adapted to LGA. Also, the PDA measurements will be used as inlet conditions for numerical simulations of the melt atomization process.

REFERENCES

H.W. Bergmann, J. Vetter, Q. Cai 1988, Die Erzeugung von Metallpulvern durch Verdüsung ihrer Schmelzen mit flüssigen Gasen, Steels & Met. Mag., Vol. 26, 10 (1988), 985-1003.

G. Wolf, M. Nöth, E. Schubert, V. E. Martin, H.W. Bergmann 1994, Production and Characterization of Liquid Gas Atomized Hard Magnetic NdFeB-Alloy Powders for Bonded Isotropic Magnets, Proc. of the Powd. Met. World Congr. , Paris, Vol. 3, 1745-1753.

U. Fritsching, H. Liu, K. Bauckhage 1991, The Influence of Spray Parameters on Local Mass Fluxes and Deposit Growth Rates during Spray Compaction Process, Proc. ICLASS-91, Gaithersburg, USA.

A. Emmel, H.W. Bergmann 1991, Comparison of Experimental Observations with Mathematical Calculations for Rapid Solidification Obtained by Melt Spun Ribbons and Atomized Particles, Modeling of Casting, Welding and Advanced Solidification Processes V, The Minerals, Metals & Materials Society.

E. J. Lavernia, T. S. Srivatsan, R. H. Rangel 1992, Atomization of Alloy Powders, Atomization and Sprays, vol. 2, pp. 253-274.

S. D. Ridder, S. A. Osella, P. I. Espina, F. S. Biancaniello 1992, Intelligent Control of Particle Size Distribution During Gas Atomization, The Int. Jour. of Powder Metallurgy, vol. 28, No. 2.

H. Henein, P. L. Meyer, D. J. Holve, M. A. Kuhni 1992, On-Line Measurement of Powder Size Distribution in Zinc Atomization, The Int. Jour. of Powder Metallurgy, vol. 28, No. 2.

K. Bauckhage, P. Schreckenberg, H. Vetters 1988, Atomization of Liquid Metals by Pressure Gas-Ring Nozzles, a New Application of Spray Systems for Spray Compacting Materials with Enhanced Properties, Proc. ICLASS-88, Sendai, Japan.

G. Brenn, J. Domnick, F. Durst, C. Tropea, T.-H.. Xu 1994, Investigation of Polydisperse Spray Interaction Using an Extended Phase-Doppler Anemometer, Proc. Seventh Int. Symp. on Appl. of Laser Tech. to Fluid Mech., vol. II, Lisbon, Portugal.

H. C. van de Hulst, T. K. 1981, Light Scattering by Small Particles, pp. 273, Dover Publications, New York.

W. D. Bachalo, S. V. Sankar, D. A. Robart, An Adaptive Intensity Validation Technique for Minimizing Trajectory Dependent Scattering Errors in Phase Doppler Interferometry, Proc. 4th International Congress on Optical Particle Sizing, pp. 1-14, Nürnberg, 1995.

J. Domnick, J. Raimann, G. Wolf, E. Schubert, H.W. Bergmann 1995, On-Line Characterization of Particle Jets During the Atomization of Molten Metal by High Velocity Cryogenic Liquid Gas Jets, Proc. ILASS-95, Nürnberg, Germany.

ACKNOWLEDGMENTS

Parts of this work were conducted within the frame of the EC project BRITE/EURAM No. 8209 entitled "On-line process control of liquid gas and water atomization by extended phase-Doppler anemometry". The authors gratefully acknowledge this financial support.

CONTROL OF DROPLET ATOMIZATION IN AN 'AIR-ASSIST' ATOMIZER

R. Aftel and A.K. Gupta
Department of Mechanical Engineering, University of Maryland, College Park, MD, USA

C. Cook and C. Presser
National Institute of Standards and Technology, Gaithersburg, MD, USA

ABSTRACT

Control of droplet atomization was studied by using air, nitrogen, argon and carbon dioxide as the atomizing gas in an 'air-assist' spray nozzle. The effect of these gases on droplet size, number density, and velocity was investigated in nonburning kerosene fuel sprays using a two-dimensional phase Doppler interferometer. The reference air-assisted case represents the most commonly used configuration. Results were obtained under conditions of constant atomizing gas mass and momentum flux. In sprays where the atomization gas was momentum controlled, droplets had similar size, velocity, and number density. In the sprays where the atomization gas was mass controlled, less dense gases, such as nitrogen, more effectively atomized the fuel in comparison to the denser gases. Thus, argon and carbon dioxide produced larger, slower moving droplets than air and nitrogen assisted cases in these fuel sprays. The results indicate that spray characteristics are independent of atomizing gas density when the gas momentum is held constant.

1.0 INTRODUCTION

The purpose of atomizing liquids is to break the liquid into a multitude of droplets. It is often desired to control the atomization process in order to produce a desired size distribution of droplets that are well dispersed spatially. Control of size and spatial distributions can provide several significant advantages in a variety of applications. For example, control of the droplet formation process is critical in combustion applications in which smaller, well-dispersed droplet sizes lead to reduced emissions, and in material synthesis processes (spray drying, powder atomization, and thermal spraying) in which control of droplet size and velocity can lead to advanced material properties and coatings.

One liquid atomization technique commonly used in the above-mentioned application is air-assisted atomization. The advantage of this technique over pressure-jet atomization (in which the liquid is supplied at elevated pressures) is that the atomizing air is used to control the liquid atomization without altering the properties of the liquid stream. Thus, liquid atomization is controlled by the interaction of the air with the expelled liquid. Several issues arise with regard to optimizing this interaction which are 1) what are the advantages and disadvantages of using different gases other than air, 2) what are the effects of atomizing gas properties (e.g., density) on the atomization process, and 3), when comparing different gases, on what basis should they be compared?

The motivation for this work was to provide a basis of comparison for spray flame characteristics using steam-assisted atomization. Since steam will affect the atomization process by means of its temperature and density, the current study was undertaken to isolate the density effects with different nonreacting gases. This study thus provides benchmark data and system operation criteria for the more complex steam-assisted experiments. The effect of N_2, Ar and CO_2 on the atomization characteristics of kerosene was investigated in this study using a commercially available 'air-assist' atomizer. Table 1 lists the densities of the gases used in the present investigation. It was of interest to determine if these gases influence atomization as a result of their different densities. Several studies have been carried out using air-assisted atomizers (Presser, et. al. 1988, Edwards, et. al. 1990), but little information exists on the advantages of using different gases other than air to influence spray and spray flame characteristics. Studies performed by Ingebo (1989) explored the effects of atomizing gas density on droplet atomization in sonic nozzles, and developed correlations describing the effect of density on droplet characteristics. However, these results are not applicable to air-assist atomizers because of the subsonic gas velocities within the atomizer. The effect of different atomizing gases in reacting flows where the atomizing gas participates chemically in the combustion process was recently studied by Aftel, et. al. (1996).

Table 1. Density of Selected Atomizing Gases

Gas (@138 kPa, 300 K)	Density (Kg/m^3)
Air	1.58
N_2	1.53
Ar	2.18
CO_2	2.41

2.0 EMPIRICAL RELATIONSHIP FOR INTERNAL MIXING ATOMIZERS

In order to compare one gas with another, it was important to ensure that the various gases were metered in such a way that the droplets formed would be unaffected by gas density. The atomization of liquid fuels within an air-assist atomizer occurs due to the interaction of the fuel and atomizing gas, and thus it was required to determine the controlling factors of this interaction. Earlier studies with air-assist atomizers were essentially limited to air as the atomizing fluid (Edwards, et. al. 1990, Presser, et. al., 1988) Typically, the mass flow rate of the atomizing gas was considered the controlling factor affecting the atomization process (Lefebvre, 1989). For any atomizing gas, a given mass flow rate would impart a unique momentum and energy to the fluid flow rate. Thus, the benefits derived from controlled momentum or energy remained unknown. A more comprehensive understanding of the correlation between atomizing gas flow and subsequent quality of atomization would therefore assist in the appropriate selection of the atomizing gas.

Wigg (1964) provided an empirical correlation for internal mixing air-assist nozzles that allowed for the fact that mass flux was not the only determining factor affecting droplet size. His correlation was dependent on mass flux, atomization gas density, and relative velocity between the fuel and air. The equation for mass median diameter was given according to:

$$MMD = 20\upsilon_L^{0.5}\dot{m}_L^{0.1}\left(1+\frac{\dot{m}_L}{\dot{m}_A}\right)^{0.5} h^{0.1}\sigma^{0.2}\rho_A^{-0.3}U_R^{-1.0} \qquad (1)$$

Under conditions where the fuel properties and flow rates are held constant, as was the case with the atomizing nozzle used in this investigation, Eq. 1 simplifies to:

$$MMD \propto \left(1+\frac{\dot{m}_L}{\dot{m}_A}\right)^{0.5} \rho_A^{-0.3}U_R^{-1.0} \qquad (2)$$

This expression indicates that the droplet median size produced from an air-assist atomizer using a given fuel is dependent on both the fuel and atomizing gas mass flow rates, atomizing gas density, and relative velocity between the atomizing gas and fuel. The mass flux of atomizing gas may be expressed as $\rho_A U_A$, and the momentum flux by $\rho_A(U_A)^2$. For example, if the density of the atomizing gas is doubled while maintaining the mass flux constant, the flow velocity of the atomization gas will be halved. Furthermore, we assume further that $U_A \approx U_R$ (since air-assisted atomizers are characterized by high velocity, low capacity atomizing gas supplied to a low pressure, low velocity fuel stream (Lefebvre (1989))). Given these assumptions, the ratio of droplet mass median diameters obtained for different atomizing gases can be expressed as:

$$\frac{MMD_1}{MMD_2} \propto \frac{\left(1+\frac{\dot{m}_L}{\dot{m}_1}\right)^{0.5} \rho_1^{-0.3}U_1^{-1.0}}{\left(1+\frac{\dot{m}_L}{\dot{m}_2}\right)^{0.5} \rho_2^{-0.3}U_2^{-1.0}} \qquad (3)$$

Assume a comparison where two atomizing gases are used where gas 1 is twice as dense as gas 2. For the mass controlled case, $\dot{m}_1 = \dot{m}_2$, and thus Eq. 3 can be simplified to:

$$\frac{MMD_1}{MMD_2} \propto \left(\frac{\rho_2}{\rho_1}\right)^{0.3} \frac{U_2}{U_1} = \left(\frac{\rho_1}{\rho_2}\right)^{0.7} \qquad (4)$$

Mass median droplet size will increase by 62% when the mass flow rate of the atomization gas is held constant. In the case where the momentum flux of the atomization gas is held constant, droplet median sizes are predicted in Eq. 2 to be nearly equal regardless of changes in atomizing gas density.

Mass median droplet size was estimated for the gases studied using Eq. 2 for atomization gas flows metered according to mass, momentum and energy flux rate ($0.5\rho_A(U_A)^3$). The results given in Table 2 show the importance of maintaining constant momentum flux between atomizing gases if the effects of gas density are to be reduced.

Although the Wigg correlation yields a relation for the mass median diameter, and not the Sauter mean diameter (SMD), the two quantities can be related if one assumes some probability density function. For example, if a Rosin-Rammler size distribution is assumed, one can derive the following relationship:

$$\frac{MMD}{SMD} = (0.693)^{1/q}\Gamma\left(1-\frac{1}{q}\right) \qquad (5)$$

It can be seen that the mass median diameter and the Sauter mean diameter have a fixed relationship given an assumed distribution, where q is a parameter describing the width of the droplet size distribution.

Table 2. Estimated Mass Median Droplet Diameter Relative to Air

Gas	Mass	Momentum	Energy
Air	1.000	1.000	1.000
N_2	0.977	0.999	1.007
Ar	1.252	1.008	0.939
CO_2	1.345	1.011	0.921

The ratios relative to air for the momentum and energy controlled flows were determined using the flowrates used in the experiments, which are given in the experimental apparatus section. The ratios shown in Table 2 demonstrate the effectiveness of using momentum flux control to maintain similar droplet sizes despite significant differences in atomizing gas density. Under conditions of mass flux

control, predicted droplet size varies by 27%. Under energy flux control conditions, the variation is reduced to 9%. Under momentum flux conditions, these differences are almost independent of density, with a 1% difference in median droplet size.

Analysis of Wigg's empirical correlation indicates that droplet diameter formed by an internal mixing air-assist atomizer will be nearly independent of atomizing gas density if operated under constant momentum conditions. The Wigg correlation is applicable to sprays operating in a quiescent environment, i.e., without the effects of external turbulent gas streams. However, realistically this is an unlikely situation in a combustor. It is therefore desirable to determine if the aforementioned findings are valid under actual burner operating conditions. Of particular interest is the determination of the impact of the atomizing gas in the near region of a burner since atomization quality will influence flame stability and emissions. In this study, a swirl-stabilized combustor was operated under nonreacting conditions. Swirling combustor air, normally used to ensure flame stability, shrouds the liquid fuel and atomizing gas in the region immediately downstream of the air-assist nozzle. The focus therefore is to determine to what extent the empirically derived results remain valid within an actual combustor flow field.

3.0 EXPERIMENTAL APPARATUS

A detailed description of the experimental spray burner facility has been well documented in other studies, and will not be described in detail here (see, for example, Presser, et. al. 1988, Presser, et. al. 1989). The experiments discussed here had a swirl number of S = 0.29 (swirl vane angle of 32°). In these experiments, kerosene was supplied at a rate of 4.1 kg/h. A commercially available full-cone air-assist nozzle was used and provided a full-cone 45° spray. The atomizing gas was introduced through a surrounding annulus and swirled within the nozzle. In the mass flow controlled cases, the mass flow rate of the atomizing gas (air, N_2, Ar or CO_2) was set to 1.64 kg/h. In the momentum controlled case, the momentum flux was set to 7.86×10^{-2} kg/m·h^2 at the flow meter. Combustion air flow in all cases was set to 210 kg/h, which is over two orders of magnitude greater than the atomizing gas flow. This provided an inlet equivalence ratio of approximately 0.28. In these experiments, a propane fueled afterburner placed about 60 cm downstream of the spray nozzle, was used to burn the fuel droplets before they entered the exhaust duct.

A two-component phase Doppler interferometer (PDI) (Bachalo, et. al., 1984) was used to determine fuel droplet size, number density and velocity, in the nonburning sprays. The data rates were determined as discussed in Presser, et. al. (1994). At every measurement point, 10,000 validated samples were recorded. Results were repeatable within a ±5% margin for mean particle size and axial velocity. Information on droplet size, velocity and number density were measured with the PDI from the spray centerline to the edge of the spray, in increments of 1.27 mm at an axial position (z) of 10 mm downstream from the nozzle, and increments of 2.54 mm at z = 15, 20, 25, 30, 35, 40, 50 and 60 mm.

4.0 RESULTS

Experimental results are presented for nonburning sprays while maintaining either the mass or momentum flux of the atomizing gas constant. Air was considered as the base line case. Since N_2 has a density similar to air, only one case was carried out for N_2, representing both the mass and momentum controlled cases. Ar and CO_2 had different densities to that of air and thus the data were obtained under conditions of both constant mass and momentum flux.

Results at z = 10 and 50 mm are presented and describe the salient features of droplet properties in different regions of the spray where the atomizing gas influences the spray features. The spray features described are the size and velocity distributions, as well as mean values for droplet size, axial velocity and number density.

4.1 Mass Flow Controlled Sprays

The variation of droplet Sauter mean diameter with radial position is presented in Fig. 1. Frames 'A' and 'B' of each figure present results for mass flux controlled atomization, while 'C' and 'D' denote momentum flux controlled atomization. The results presented in Fig. 1 indicate that droplet mean size is influenced differently for mass controlled and momentum controlled cases. For the case where the mass flux is held constant, atomization is affected by atomizing gas density. The influence of the gas density on droplet mean size is most significant in the region where the atomizing gas is the dominant gaseous stream relative to the surrounding combustion air. In this region, atomizing gas interacts with the liquid fuel, i.e., toward the spray centerline and at axial positions near the nozzle exit. Two regimes are denoted in Fig. 1A, namely 1) $0 < r < 12$ mm and 2) $r > 12$ mm. At $r \sim 12$ mm the fuel volumetric flux (results not shown) reaches a maximum and thus is indicative of the radial position where most of the fuel mass exists. This position is referred to as the 'spray boundary'. It is interesting to note that the peak in volumetric flux at z = 10 mm is off-axis although the nozzle is designed to form a full-cone spray. The reason is attributed to the fact that full-cone sprays behave as hollow-cone sprays immediately downstream of the nozzle due to the finite diameter of the orifice and filming of the fuel over the orifice surface. The differences between full- and hollow-cone sprays occurs further downstream where droplets in the full-cone spray disperse rapidly and fill in the central region of the spray more quickly than for a hollow-cone spray.

At the spray centerline and at z = 10 mm (see Fig. 1A), atomizing air produced droplets with a Sauter mean diameter of 25.5 μm, while N_2 formed an SMD of 20.6 μm. Droplet mean size in the Ar and CO_2 atomized sprays were considerably larger (29.2 and 30.0 μm, respectively). The

difference in size between the smallest and largest droplets at this location was 9.4 μm. It was observed that the Ar and CO_2 atomized sprays had a considerably wider size distribution, with a variance (RMS) on the order of 9 μm, as opposed to air and N_2, which had a variance of 7 μm. Although the droplet mean size produced by the air atomized spray on centerline at z = 10 mm was somewhat larger than expected, the results elsewhere for r < 12 mm are in closer agreement with the N_2 spray. The similarity in SMD between air and N_2 was expected due to the similarity in density. Near the spray boundary, at z = 10 mm and r > 12 mm, all the gases produced similar droplet mean sizes (within 3 μm), demonstrating the overriding influence of main combustion air in the outer regions of the spray.

surrounding combustion air begins to provide an influence on the central region of the spray.

Similar differences were noted for the axial velocity results for mass controlled atomization (see Fig. 2). Air and N_2 droplets had the highest velocities on the spray centerline at z = 10 mm (19.1 and 18.9 m/s, respectively), followed by Ar (15.9 m/s) and CO_2 (13.1 m/s). These differences were still found further downstream at z = 50 mm and the spray centerline, with air and N_2 atomized droplets having the largest velocities (11.4 and 10.2 m/s, respectively), followed by Ar (4.3 m/s) and CO_2 (3.3 m/s). At larger radial or axial distances from the nozzle, the effect of the surrounding combustion air on droplet velocity becomes more pronounced.

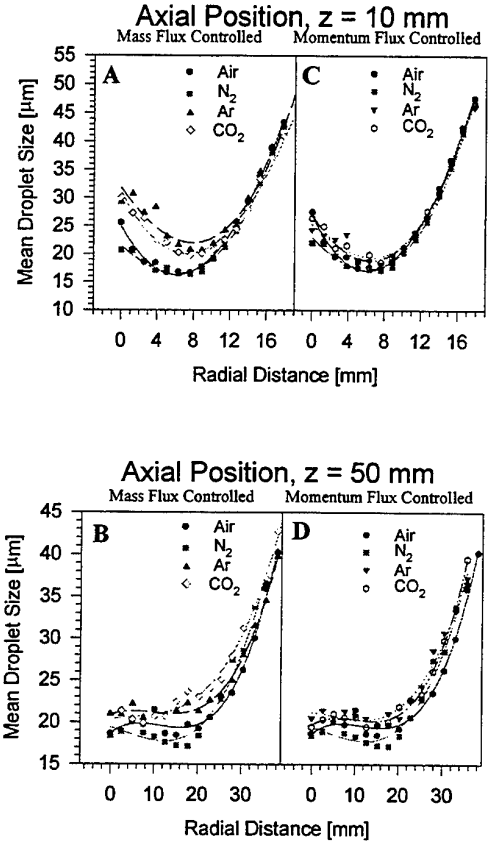

Figure 1. Sauter mean droplet size [μm] in nonburning sprays. (A) mass flow constant, z = 10 mm, (B) mass flux constant, z = 50 mm, (C) momentum flux constant, z = 10 mm, (D) momentum flux constant, z = 50 mm.

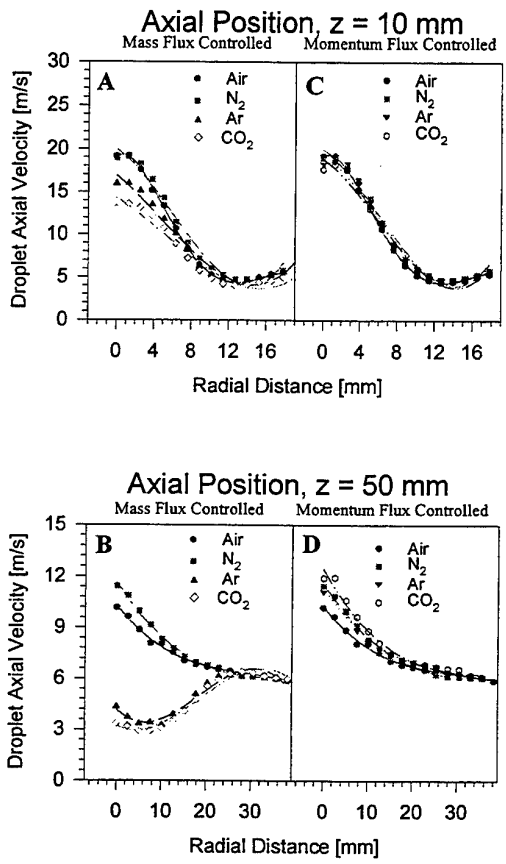

Figure 2. Axial droplet velocity [m/s] in nonburning sprays. (A) mass flow constant, z = 10 mm, (B) mass flux constant, z = 50 mm, (C) momentum flux constant, z = 10 mm, (D) momentum flux constant, z = 50 mm.

Near the spray centerline at z = 50 mm (see Fig. 1B), the mean droplet diameter with atomizing air was 18.7 μm, N_2 was 18.4 μm, Ar was 20.9 μm, and CO_2 was 20.2 μm, i.e. a difference of 2.5 μm. Differences between the sprays are also reduced at this downstream position, as the effects of the

The droplet number density for the mass controlled sprays is shown in Fig. 3. Since droplets may not be validated for a variety of reasons (Presser, et. al. 1994, Bachalo, 1986) and thus not included in the statistics, droplet number densities can be lower than the absolute number of detected droplets. The bias in the values of size and velocity distributions is

unknown since the repeatability of the measurement is generally within ±5%. For the measurements recorded in this study, typical validation rates were on the order of 70-80%. This indicates that around 20-30% of the droplets entering the probe volume are ignored. Therefore, these data can only be taken to describe qualitative trends, and explains why results do not vary according to atomizing gas density. As shown in Fig. 3A, Air and N_2 produce the highest peak number densities on the spray boundary (8000/cm^3), followed by CO_2 (7000/cm^3) and Ar (6400/cm^3). The results indicate that the peak values are found at an off-axis radial position as descried earlier.

At z = 50 mm, the number density is reduced as a result of droplet dispersion (see Fig. 3B). At this axial position, fewer data points (5000/position) were recorded due to reduced droplet number densities. Since the validation rates were reduced at this position, the resulting data had more scatter. CO_2 and Ar atomized sprays have higher number densities, followed by N_2 and air. Normally, number density is correlated with mean diameter (i.e., as SMD increases, number density decreases), however this feature is not present in this case (see Figs. 1B and 3B). This result indicates that the droplets produced in the N_2 and air atomized sprays were more dispersed at this axial location. Ar and CO_2 atomized sprays are less dispersed since the velocity of the atomization gas was strongly reduced in these atomization gas mass flow controlled experiments. The shift in the peak values to the centerline for the Ar and CO_2 cases also indicates that the reduced velocities leads to the full-cone spray features earlier than with the higher velocity air and N_2 sprays.

4.2 Momentum Flux Controlled Sprays

Momentum flux controlled sprays produced smaller size droplets (see Figs. 1C and 1D) traveling at higher axial velocities (Figs. 2C and 2D) droplets as compared with the mass flux controlled sprays. Recall that Wigg's correlation provided the same trends for droplet size. As in the mass flow controlled cases, air produced the largest droplets on the spray centerline at z = 10 mm (25.5 μm). N_2 produced droplets with a mean diameter of 20.6 μm. The air and N_2 data presented are identical to that shown in the mass controlled section, since as stated previously the densities of the two gases were close enough for one flow condition to satisfy both mass and momentum control. Air and N_2 were followed by Ar (22.7 μm), and CO_2 (24.6 μm), resulting in a difference of 4.0 μm between the smallest and largest droplets at this position of z = 10 mm. Denser atomizing gases continued to produce larger droplets for identical momentum fluxes, although the differences were strongly reduced in comparison to the mass controlled case. The droplet distributions were more similar in the momentum controlled cases than in the mass controlled cases, with typical distribution widths (RMS) on the order of 7 μm. These results suggest the implications of the Wigg correlation, namely, droplet mean size is independent of atomizing gas density for constant momentum control.

Near the spray boundary (r = 12 mm) at z = 10 mm there is little difference in droplet diameter between the momentum controlled cases, with a maximum difference of only 2 μm between the smallest and largest droplets at this location. At the spray edge, the differences are similarly reduced. Near the spray edge, the influence of the turbulent, swirling combustion air is expected to be significant, and this widens the size distribution of the droplets.

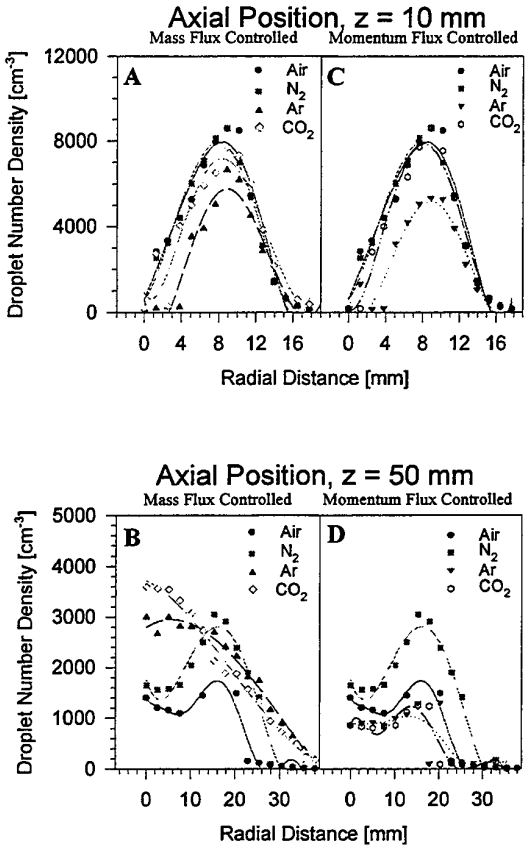

Figure 3. Droplet number density [droplets/cm^3] in nonburning sprays. (A) mass flow constant, z = 10 mm, (B) mass flux constant, z = 50 mm, (C) momentum flux constant, z = 10 mm, (D) momentum flux constant, z = 50 mm.

Differences in droplet mean size are again smaller at z = 50 mm, with the momentum controlled gases producing droplets with mean sizes within 2.1 μm of each other at the centerline. Towards the spray edge these differences are further reduced. However, the width of the size distribution increase, as previously stated.

In the momentum flux controlled cases, droplet velocities at z = 10 and z = 50 mm were similar, and are shown in Fig. 2. From these results, it is apparent that nearly identical droplet velocities can be produced with atomization gases of

differing densities by ensuring that the momentum flux of the atomization gases are held to a constant value.

Droplet number density for the nonburning momentum controlled sprays at z = 10 mm is presented in Fig. 3C. Compared with the data for the mass controlled case shown in Fig. 3A, it is apparent that the differences in number density between the various atomization gases are reduced in the momentum controlled case with the exception of the Ar case, which is anomalous. At z = 50 mm, Ar and CO_2 atomized sprays appear to have better dispersion, with lower number densities than the N_2 atomized spray. This is in contrast to that found in the mass controlled cases (compare Fig. 3B and 3D).

To summarize, droplet mean properties are nearly unaffected by changes in the atomization gas density as long as the atomizing gases are metered according to the momenta. This result can be of great significance when studying the effects of various atomizing gases, since it makes it possible to isolate the effect of gas density on the atomization process.

4.3 Droplet Size Distributions

Histograms of the droplet size distributions in the sprays are shown in Figs. 4A and 4B. In Fig. 4A, droplet size distributions at the spray centerline and z = 10 mm are shown for mass flux controlled air, nitrogen, argon and carbon dioxide respectively. The results show that the droplet size distribution is affected by the gas density for the mass controlled case which in turn influences the mean values. For both argon and carbon dioxide, the size distributions shift toward larger droplets and fewer smaller droplets.

The droplet total velocity distributions in the mass flux controlled cases at z = 10 mm and r = 0 mm are shown in Fig. 4B. When denser atomizing gases are used, the flow velocity of the gas is reduced in order to maintain a constant mass flux. This results in a shift of the distribution to lower velocities for Ar and CO_2. At other spatial positions where there is little difference in the mean properties, the size and velocity distributions also show little variation. Likewise, in the momentum controlled case, the size and velocity distributions are the same regardless of the atomizing gas.

5.0 CONCLUSIONS

Although the volumetric flux of atomizing gas is less than 1% of the total oxidizer flow, these results suggest that the atomizing gas plays a significant role in droplet formation and transport in the near region of the spray. Due to its availability in regions where droplets are forming, it may enhance mixing with the fuel. Also, comparing the mass and momentum controlled cases, it is clear that in the momentum controlled cases droplet atomization is significantly improved, i.e., droplet sizes are significantly smaller, axial velocities are higher, and number densities are greater.

The spray characteristics were found to be dependent on the atomizing gas density for the mass controlled atomization case. This result was supported by the Wigg correlation for mass median diameter as well as experimentally. Spray characteristics were found to be essentially independent of atomizing gas density in the momentum controlled case.

NOMENCLATURE

h	height of the air annulus within the atomizer
m_A	mass flow rate, atomization gas
m_L	mass flow rate, fuel
q	parameter of Rosin-Rammler size distribution
SMD	Sauter mean diameter (D_{32})
MMD	mass median diameter ($D_{0.5}$)
RMS	root mean square
U_A	atomizing gas velocity
U_R	relative velocity of the liquid fuel and atomization gas.
ν	fuel viscosity
Γ	Gamma function
σ	surface tension of the fuel
ρ	density

ACKNOWLEDGEMENTS

One of the authors (AKG) gratefully acknowledges the partial support of this research by the Office of Naval Research (project manager Dr. Gabriel Roy). Assistance provided by Joerg Schreck is also gratefully acknowledged.

REFERENCES

Aftel, R., Gupta, A.K., Cook, C., and Presser, C. 1996, Gas Property Effects on Droplet Atomization and Combustion in an 'Air-Assist' Atomizer, 26th Symposium (International) on Combustion, The Combustion Institute, Pittsburgh, PA (in press).

Bachalo, W.D., Houser, M.J., and Smith, J.N. 1986, Evolution and Behavior of Sprays Produced by Pressure Atomizers, AIAA Paper 86-0296.

Edwards, C.F. and Rudoff, R.C. 1990, Structure of a Swirl-Stabilized Spray Flame by Imaging, Laser Doppler Velocimetry, and Phase Doppler Anemometry, Twenty-Third Symposium (International) on Combustion, The Combustion Institute, Pittsburgh, pp. 1353-1359.

Gupta, A.K., Presser, C., Hodges, J.T., and Avedisian, C.T. 1996, Role of Combustion on Droplet Transport in Pressure Atomized Spray Flames, Journal of Propulsion and Power, vol. 12, no. 3.

Ingebo, R.D. 1989, Gas Density Effect on Dropsize of Simulated Fuel Sprays, AIAA/ASME/SAE/ASEE 25th Joint Propulsion Conference, Monterey, CA.

Lefebvre, A.H. 1989, Atomization and Sprays, Hemisphere Publishing Co., New York.

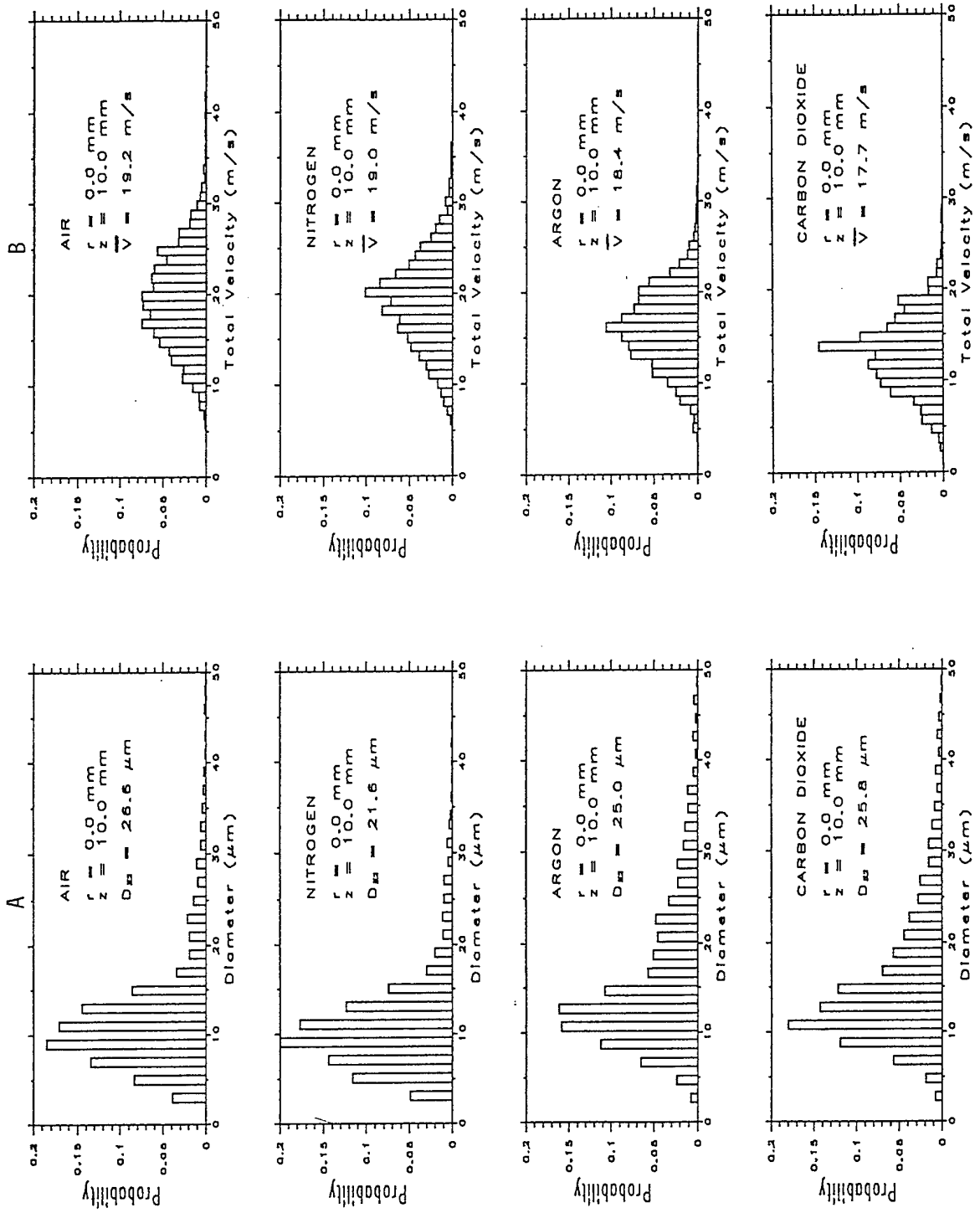

Figure 4. Histograms of droplet size distribution in nonburning mass flow controlled air, nitrogen, argon and carbon dioxide atomized sprays at spray centerline (r = 0 mm). (A) droplet size distribution (B) droplet total velocity distribution.

Presser, C., Gupta, A.K., and Semerjian, H.G. 1988, Aerodynamic Effects on Fuel Spray Characteristics: Air-Assist Atomizers, Heat Transfer in Combustion Systems, ASME Winter Annual Meeting, Chicago, pp. 111-119.

Presser, C., Gupta, A.K., and Semerjian, H.G. 1989, Droplet Velocity Measurements in a Swirling Kerosene Spray Flame, Heat Transfer in Combustion Systems, ASME Winter Annual Meeting, San Francisco, pp. 21-34.

Presser, C., Gupta, A.K., and Semerjian, H.G. 1993, Aerodynamic Characteristics of Swirling Spray Flames: Pressure-Jet Atomizer, Combust. Flame, vol. 92 pp.25-44.

Presser, C., Gupta, A.K., Semerjian, H.G., and Avedisian, C.T. 1994, Droplet Transport in a Swirl Stabilized Spray Flame, Journal of Propulsion and Power, vol. 10, no. 5, pp. 631-638.

Presser, C., Gupta, A.K., Avedisian, C.T., and Semerjian, H.G. 1994, Effect of Dodecanol on the Combustion of Methanol Spray Flames, Atomization and Sprays, vol. 4, pp. 207-222.

Wigg, L.D. 1964, Drop-Size Predictions for Twin Fluid Atomizers, J. Inst. Fuel, vol. 27, pp. 500-505.

AUTHORS' INDEX

Abe, N., 33.2.1
Achimastos, T.J., 38.5.1
Adrian, R., 23.1.1, 17.1.1
Aftel, R., 20.5.1
Akamatsu, F., 2.4.1
Akoh, E., 37.2.1
Anacleto, P., 19.2.1
Anders, K., 9.2.1
Anderson, D.J., 18.4.1
Antonia, R.A., 17.2.1, 29.1.1
Arcoumanis, C., 16.3.1, 25.1.1
Aroussi , A., 37.3.1
Astachow, G., 13.4.1
Auger, P.L., 34.4.1
Auriemma, M., 16.1.1
Azizi, L., 6.2.1
Azzopardi, B.J., 38.4.1

Bachalo, W.D., 2.3.1, 9.3.1
Balabani, S., 33.3.1
Baldwin, T., 33.5.1
Barcouda, M., 37.1.1
Barigozzi, G., 28.3.1
Barrientos, A., 26.3.1
Bearman, P.W., 18.5.1
Bénard, J., 37.1.1
Bencze F., 14.6.1
Benech, P., 34.4.1
Benedict, L.H., 36.1.1, 36.6.1
Bergmann, V., 3.1.1
Bernard, A., 26.5.1
Berton, E., 14.1.1
Beyer, W., 23.4.1
Biage, M., 15.4.1
Blümcke, E., 22.1.1
Boesiger, P., 33.5.1
Booij, R., 35.3.1
Borrett, N.A., 8.5.1
Botnar, R., 33.5.1
Boulouchos, K ., 13.2.1
Bourguignon, E., 7.1.1
Bousgarbiès, J.L., 26.5.1
Boutier, A., 14.5.1
Bräumer, G., 37.5.1
Breeze, G., 14.4.1
Brenn, G., 9.4.1
Brücker, Ch., 4.2.1, 26.1.1
Bruckner, R.J., 15.1.1
Brun, M., 22.5.1
Buresti, G., 30.3.1
Bütefisch, K.A., 14.3.1

Cahen, C., 37.1.1
Caldas, F., 7.3.1
Campi, A., 12.4.1
Campos, V.A., 37.5.1
Carosone, F., 21.2.1
Cartellier, A., 34.4.1
Castellini, P., 26.2.1
Cenedese, A., 21.2.1, 27.3.1
Chiné, B., 19.6.1
Christofori, K., 12.1.1
Coelho, P.M., 35.5.1
Coghe, A., 25.6.1
Cohn, R.K., 1.2.1
Collicott, S.H., 15.2.1
Collins, M.W., 17.3.1
Concha, F., 19.6.1
Cook, C., 20.5.1
Corcione, F.E., 16.1.1
Cossali, G.E., 25.6.1
Cremers, C., 11.5.1
Crompton, N., 14.4.1
Cüppers, A., 19.4.1

Dabiri, D., 30.1.1
Darabiha, N., 3.5.1
Delgado, A., 8.1.1
Denk, V., 8.1.1
Derville, A., 4.1.1
Dimopoulos, D.A., 38.5.1
Dimopoulos, P., 13.2.1
Djenidi, L., 17.2.1, 29.1.1
Domann, R., 19.1.1
Domnick, J., 20.4.1
Dopheide, D., 6.6.1, 34.1.1, 40.3.1
Draad, A.A., 29.3.1
Dracos, T., 4.6.1

Duarte, D., 7.3.1
Dufour, C., 11.4.1
Dufour, C., 31.2.1
Dullenkopf, K., 20.1.1, 25.2.1, 25.3.1
Dum, T., 32.2.1
Durox, D., 20.3.1
Durst, F., 6.3.1, 8.4.1, 16.4.1

Ebner, J., 25.2.1
Egan, D., 28.2.1
Egbers, C., 23.4.1
Eisele, K., 33.5.1
Ekmann, J.M., 10.3.1
Elavarasan, R., 29.1.1
Elder, R.L., 28.2.1
Elsäßer, A., 25.2.1, 25.3.1
Escudier, M.P., 1.1.1
Evenstad, J., 2.1.1

Faram, M.G., 19.5.1
Faure, M., 22.3.1
Favier, D., 14.1.1
Fentiman, N.J., 8.5.1
Fernandes, E.C., 39.1.1
Ferrão, P., 7.3.1
Ferrara, G., 19.6.1
Fick, W., 10.4.1
Fiedler, O., 12.1.1
Fitzpatrick, J.A., 36.5.1
Ford, H.D., 11.3.1
Founti, M.A., 38.5.1
Frederiksen, J.P. 37.2.1
French, B., 16.3.1
Frohn, A., 9.2.1
Furuichi, N., 31.5.1

Gallagher, M.W., 38.2.1
Gan, C.L., 17.2.1
Gasparetti, M., 12.4.1, 26.2.1
Gendrich, C.P., 1.2.1
Gharib, M., 30.1.1
Ghiglione, A., 28.3.1
Gjelstrup, P., 31.3.1
Glahn, A., 9.5.1
Gogineni, S., 18.2.1
Gökalp, I., 7.1.1
Goss, L., 18.2.1
Gottero, M., 35.1.1
Gouesbet, G., 6.5.1
Gougat, P., 38.3.1
Gould, R.D., 36.1.1, 36.6.1
Gouldson, I.W., 1.1.1
Gray, C., 7.4.1
Greated, C.A., 18.4.1
Gréhan, G., 6.5.1

Griffiths, A.J., 10.4.1
Grrem, R., 13.3.1
Gupta, A.K., 20.5.1

Hachiga, T., 31.5.1
Haile, E., 20.3.1
Hanratty, T.J., 17.1.1
Hanson, S.G., 40.2.1
Harden, J.M., 14.2.1
Harris, S.R., 15.3.1, 15.4.1
Hart, D.P. 21.1.1
Harvey, J.K., 18.5.1
Hassa, B., 26.6.1
Hassan, Y., 27.1.1
Heikal, M.R., 22.3.1
Heitor, M.V., 7.3.1, 19.2.1, 32.1.1, 39.1.1
Helbig, J., 26.6.1
Hensse, J., 13.4.1
Hermann, J., 39.2.1
Herve, P., 6.2.1
Herzog, P., 39.4.1
Hess, C.F., 6.1.1
Hicks, R.A., 10.1.1
Higashi, S., 33.2.1
Hirohata, T., 2.6.1, 10.5.1
Hirt, F., 33.5.1
Hishida, K., 29.4.1, 31.5.1, 35.2.1
Hishida, M., 2.5.1
Höfer, H., 28.1.1
Hoffman, R., 32.1.1
Höfken, M., 8.4.1
Hofmann, D., 1.3.1
Hofmann, F., 37.1.1
Hönig, R., 7.6.1
Host-Madsen, A., 31.3.1
Houssaye, G., 31.2.1
Hsu, C.T., 12.6.1
Huber, L., 38.3.1
Hübner, W., 19.1.1
Hurst, D.W., 17.3.1

Ibrahim K.M., 2.3.1
Iizuka, K., 35.2.1
Ikeda, K., 24.2.1
Ikeda, Y., 2.6.1, 10.5.1, 13.6.1, 40.5.1
Ikedo, S., 37.6.1
Imam, H., 40.2.1
Imbach, J., 10.2.1
Ishima, T., 13.5.1, 22.2.1
Ito, A., 11.5.1
Iuso, G., 35.1.1

Jackson, D.A., 25.5.1
Jackson, N., 22.3.1

Jaffre, D., 7.4.1, 7.5.1
James, S.W., 28.2.1
Johari, H., 30.1.1
Jones, J.D.C., 18.4.1
Jud, E., 33.5.1

Kappler, G., 7.6.1
Karlsson, R.I., 35.6.1
Kato, F., 21.4.1, 24.2.1
Katsuki, M., 2.4.1
Katz, J., 4.3.1
Kawaguchi, Y., 29.4.1
Kawahara, N., 10.5.1
Kendrick, D.W., 7.5.1
Kepner, J., 33.5.1
Kettl, H., 7.6.1
Kijima, M., 33.2.1
Kimura, I., 24.6.1
Klasine, R., 32.2.1
Kleitz, A., 6.2.1
Kobayashi, K., 13.5.1
Koizumi, M., 27.1.1
Kompenhans, J., 4.1.1, 14.3.1, 18.1.1, 28.1.1
Köngeter, J., 19.4.1
Koochesfahani, M.M., 1.2.1
Kost, F., 28.1.1
Koyama, T., 13.5.1
Krüger, G., 13.4.1
Kruse, M., 29.2.1
Kumada, M., 31.5.1
Kumpart, J., 12.1.1
Kurihara, H., 34.5.1
Kurihara, N., 13.6.1

Labahn, N., 12.1.1
Lacas, F., 20.3.1
Lachner, R., 7.6.1
Lading, L., 40.2.1
Larsen, P.S., 37.2.1
Lauren, T.S., 35.4.1
Lawes, M., 10.1.1
Le Roy, J.F., 11.4.1, 31.2.1
Lee, K.C., 8.5.1
Lefèvre, J., 14.5.1
Lehmann, B., 26.6.1
Leipertz, A., 1.3.1
Lempert, W.R., 15.3.1, 15.4.1
Lepicovsky, J., 15.1.1
Leporcq, B., 11.4.1, 31.2.1
Levy, Y., 39.3.1
Liard, V., 3.5.1
Lindvold, L.R., 40.2.1
Liu, Z.-C., 17.1.1
Lockey, R.A., 28.2.1
Logar, R.H., 32.2.1
Lowson, M.V., 14.2.1, 28.4.1
Lubarsky, E., 39.3.1
Lutz, M., 8.1.1

Macchioni, R., 16.1.1
Madarame, H., 27.1.1
Maeda, M., 2.5.1, 29.4.1, 35.2.1
Maeda, T., 2.5.1
Maekawa, M., 35.2.1
Mahmood, Z., 16.2.1
Marr, R., 38.1.1
Martel, C., 3.5.1
Martinez, R.E., 3.3.1
Mathur, M.P., 10.3.1
McCluskey, D.R., 35.4.1
McEwan, I.K., 38.2.1
Meier, U.E., 3.1.1
Meier, W., 3.1.1
Melling A., 6.3.1
Menon, R., 2.1.1, 12.2.1
Merkel, G.J., 4.6.1
Meyers, J.F., 11.1.1
Micheli, F., 14.5.1
Michou, Y., 7.1.1
Miles, P.C., 40.1.1
Miles, R.B., 15.3.1
Mimatsu, J., 31.5.1
Miozzi, M., 27.3.1
Miyate T., 32.3.1
Mokaddem, K., 7.5.1
Mordacci, A., 30.3.1
Moreira, A.L.N., 19.2.1, 32.1.1
Morikita, H., 2.5.1
Moseley, R.P., 18.5.1
Most, J.M., 10.2.1
Müller, E., 36.2.1
Müller, H., 6.6.1, 34.1.1
Münch, K.-U., 1.3.1
Mundo, Chr., 20.1.1
Mungal, M.G., 3.3.1
Muñiz, L., 3.3.1

Nakajima, T., 2.6.1, 10.5.1, 13.6.1, 40.5.1
Nakatani, N., 15.5.1
Naqwi, A., 2.1.1, 2.2.1
Narumi, A., 11.5.1
Nash, E.C., 28.4.1
Nattrass, S.R., 25.5.1
Ng, K., 16.2.1
Nielsen, N.F., 37.2.1
Nijenboer, F.J., 31.4.1
Nimmo, G., 18.4.1
Nino, E., 3.4.1
Nobach, H., 36.2.1
Nocera D.G., 1.2.1
Nouri, J.M., 16.3.1

Nsi Mba, M., 14.1.1

O'Doherty, T., 10.4.1, 19.5.1
Obokata, T., 13.5.1
Ogino, F., 32.3.1
Ohba, K., 37.6.1
Ohta, Y., 22.2.1
Ohtake K., 32.3.1
Okamoto, K., 24.2.1, 27.1.1
Okamoto, S., 33.2.1
Oldenburg, M., 8.2.1
Onorato, M., 35.1.1
Onori, R., 12.4.1
Orglmeister, R., 8.6.1
Orthmann, A., 39.2.1
Oshio, T., 15.5.1
Ovalle, E., 26.3.1
Ozawa, M., 24.6.1

Panidis, Th., 12.5.1
Paone, N., 3.4.1, 26.2.1
Pap, E., 8.2.1
Perrin, M., 7.4.1, 7.5.1
Persson, N.J., 35.6.1
Pestian, D., 18.2.1
Peters, W.D., 23.5.1
Piana, J., 3.5.1
Pickering, S.J., 37.3.1
Pinchemel, B., 11.4.1, 31.2.1
Pinho, F.T., 8.3.1, 35.5.1
Piqueiro, F.M., 8.3.1
Podoleanu, A.Gh., 25.5.1
Poireault, B., 10.2.1
Poppe, C., 7.3.1
Porporato, A., 36.3.1
Potz, D., 13.4.1
Prescher, K., 13.4.1
Presser, C., 20.5.1
Proença, M.F., 8.3.1
Qiu, H.H., 12.6.1
Raffel, M., 4.1.1, 14.3.1, 18.1.1, 28.1.1
Raimann, J., 20.4.1
Rambert, A., 38.3.1
Ramos, J., 14.1.1
Rasmussen, J.J., 35.4.1
Rath, H.J., 23.4.1
Ren, K.F., 6.5.1
Reuber, J., 22.1.1
Revel, G.M., 3.4.1
Richon, J.B., 7.4.1
Rickards, J., 14.4.1
Ridolfi, L., 36.3.1
Riethmuller, M.L., 9.1.1
Rist, D., 7.6.1
Rivir, R., 18.2.1
Robart, D.M., 9.3.1
Rodrigues, A.H., 35.5.1
Rolon, J.C., 7.5.1
Romano, G.P., 27.3.1
Ronneberger, O., 4.1.1
Rose, B., 40.2.1
Rossi, G.L., 12.4.1
Roth, N., 9.2.1
Rothlübbers, C., 8.6.1
Rys, F.S., 4.6.1

Saito, K., 11.5.1
Sakabe, T., 15.5.1
Sakurai, A., 37.6.1
Salyer, T.R., 15.2.1
Samenfink, W., 25.2.1, 25.3.1
Sankar, S.V., 9.3.1
Santos, A.M., 8.3.1
Sawa, K., 37.6.1
Schäfer, M., 8.4.1
Schanen Duport, I., 34.4.1
Scheffler, T., 8.6.1
Schmid, A., 7.6.1
Schmid, H.-J., 37.4.1
Schmisseur, J.D., 15.2.1
Schneider, S.P., 15.2.1
Scholten, J., 36.5.1
Scholten, J.W. 33.1.1
Schöne, F., 20.1.1
Schraml, S., 1.3.1
Schulz, R., 17.4.1
Seasholtz, R.G., 24.1.1
Seccia, G., 16.1.1
Seelhorst, C., 14.3.1
Shen, X., 31.1.1
Sheppard, C.G.W., 10.1.1
Shibata, Y., 21.4.1
Shimizu, I., 21.4.1, 24.2.1
Shrimpton, J.S., 20.2.1
Siekmann, H., 8.6.1
Simmons, K., 37.3.1
Simon, L., 36.5.1
Smits, A.J., 15.4.1
Socoliuc, M., 22.5.1
Sommerfeld, M., 12.5.1
Spork, V., 19.4.1
Stasicki, B., 18.1.1
Staude, W., 17.4.1
Stenum, B., 35.4.1
Stewart, J.N., 18.5.1
Stieglmeier, M., 20.1.1
Stricker, W., 3.1.1
Strunck, V., 6.6.1, 40.3.1
Susset, A., 7.4.1
Swales, C., 14.4.1, 28.4.1
Syred, N., 19.5.1

Takamoto, M., 34.5.1
Takeda, C., 22.2.1
Talamelli, A., 30.3.1
Tanzini, G., 30.3.1
Tao, B., 4.3.1
Taplin, S.R., 25.5.1
Tashtoush, G., 11.5.1
Tatam, R.P., 11.3.1
Tatam, R.T., 28.2.1
Tawaraya, Y., 29.4.1
Tedeschi, G., 12.2.1
Teixeira, J.C.F., 37.5.1
Terry, N., 14.4.1
Theisen, D., 7.6.1
Többen, H., 34.1.1
Tokuhiro, A., 35.2.1
Tournois, G., 39.4.1
Tran, P.X., 10.3.1
Trimis, D., 16.4.1
Tropea, C., 9.4.1, 19.1.1, 20.1.1, 36.2.1
Troy, V., 23.1.1
Trump, D., 18.2.1
Tsunoda, K., 33.2.1
Tsushima, S., 2.4.1
Tukagoshi, M., 13.5.1
Tukker, J., 35.3.1
Tummers, M.J., 36.4.1

Ubaldi, M., 28.3.1
Uehara, K., 13.5.1
Ullum, U., 37.2.1
Umhauer, H., 37.4.1
Urabe, T., 37.6.1

Vad, J., 14.6.1
Valeau, V., 39.4.1
Valentino, G., 13.2.1, 16.1.1
Valière, J.C., 39.4.1
Van Beeck, J.P.A.J., 9.1.1
Van Maanen, H.R.E., 31.4.1, 36.4.1
Venart, J.E.S., 23.5.1
Veynante, D., 3.5.1, 20.3.1
Volkert, J., 19.1.1
Volkholz, P., 6.3.1
Vollmers, H., 14.3.1
Vortmeyer, D., 39.2.1
Vyrodov, A.O., 3.1.1

Wagner, S., 29.2.1
Wang, Q., 18.5.1
Watkins, A.P., 20.2.1
Webb, D.J., 25.5.1
Weclas, M., 16.4.1
Weigand, A., 30.1.1
Weiß, C., 38.1.1
Westerweel, J., 29.3.1
Whitelaw, D.S., 25.1.1
Whitelaw, J.H., 25.1.1
Wigley, G., 32.2.1, 38.1.1
Will, S., 1.3.1
Willert, C., 4.1.1, 14.3.1, 18.1.1, 28.1.1
Willmann, M., 9.5.1, 20.1.1
Wiseall, S., 18.4.1
Wittig, S., 9.5.1, 20.1.1, 25.2.1, 25.3.1
Witze, P.O., 13.3.1, 40.1.1
Wolf, G., 20.4.1
Wolley, R., 10.1.1

Xu, T.-H., 9.4.1

Yabe, A., 29.4.1
Yianneskis, M., 8.5.1, 16.2.1, 33.3.1
Yule, A.J., 20.2.1

Zaidi, S.H., 38.4.1
Zangl, P., 39.2.1
Zhang, H.L., 17.3.1
Zhang, J., 4.3.1
Zhang, X., 17.3.1
Zhang, Z., 33.5.1
Zhongming, M., 31.1.1
Zunino, P., 28.3.1